Open-Shell Formulation of the Fragment Molecular Orbital Method

Spencer R. Pruitt,[†] Dmitri G. Fedorov,[‡] Kazuo Kitaura,[‡,§] and Mark S. Gordon*,[†]

Department of Chemistry, Iowa State University, Ames, Iowa 50011, RICS, National Institute of Advanced Industrial Science and Technology (AIST), 1-1-1 Umezono, Tsukuba, Ibaraki 305-8568, Japan, and Graduate School of Pharmaceutical Sciences, Kyoto University, Sakyo-ku, Kyoto 606-8501, Japan

Received August 18, 2009

Abstract: Performing accurate calculations on large molecular systems is desirable for closed- and open-shell systems. In this work, the fragment molecular orbital method is extended to open-shell systems and implemented in the GAMESS (General Atomic and Molecular Electronic Structure System) program package. The accuracy of the method is tested, and the ability to reproduce reaction enthalpies is demonstrated. These tests also demonstrate its utility in providing an efficient means to model large open-shell systems.

1. Introduction

Recently, a large number of fragment-based methods[1−6] have been developed, including the fragment molecular orbital (FMO) method.[7−10] The aim of these methods is to treat complex molecular species efficiently, while retaining ab initio accuracy, by dividing the system into many much smaller fragments. However, few of these methods are capable of treating open shells.[11] Several wave function types have already been interfaced with FMO;[12−17] however, most of them are for closed-shell methods. The only exception is the multiconfiguration self-consistent field (MCSCF method),[14] which can treat both closed- and open-shell species. Although the MCSCF method is very useful in some systems, it is also desirable to have a single-reference open-shell method, which could be efficiently combined with restricted open-shell (RO) second-order Møller−Plesset perturbation theory (MP2)[18] or coupled cluster theory (CC).[19]

[†] Iowa State University.
[‡] AIST.
[§] Kyoto University.
* To whom correspondence should be addressed. E-mail: mark@si.msg.chem.iastate.edu.

Open-shell systems play a very important role in many processes, for instance, in radical chemistry,[21] electron transfer,[22] and many transition metal compounds.[23] In addition, transition states in chemical reactions involve breaking chemical bonds and thus possess considerable open-shell character. Although more difficult cases such as transition metal complexes may require a more sophisticated treatment (e.g., MCSCF), in many organic, inorganic, and biochemical systems, the open-shell character can be well described by an open-shell single-reference wave function. Therefore, it is useful to be able to perform large-scale calculations of open-shell systems with single-reference methods. The FMO method is particularly appealing in this regard, since it has been shown to accurately reproduce fully ab initio calculations with high accuracy.[9,10] Due to the inherently parallel nature of the method, it also scales almost linearly with system size.

2. Methodology

The *n*-body FMO energy (FMO*n*) of *N* fragments is given by[8]

$$E^{\text{FMO2}} = \sum_I^N E_I + \sum_{I>J}^N (E_{IJ} - E_I - E_J) \tag{1}$$

$$E^{\text{FMO3}} = E^{\text{FMO2}} + \sum_{I>J>K}^N (E_{IJK} - E_I - E_J - E_K - \Delta E_{IJ} - \Delta E_{JK} - \Delta E_{IK}) \tag{2}$$

where

$$\Delta E_{IJ} = E_{IJ} - E_I - E_J \tag{3}$$

and E_I, E_{IJ}, and E_{IJK} are the monomer (single fragment), dimer (fragment pair), and trimer (fragment triple) energies, respectively, computed in the electrostatic field of other fragments.[8]

This expression is also used for the restricted open-shell FMO method, which is an extension of the closed-shell method, described in detail elsewhere.[10] The computational scheme is methodologically similar to that of the FMO-based MCSCF or time-dependent[23] density functional theory (TDDFT), with one fragment chosen to be the open-shell fragment. There are two types of dimers and trimers in an open-shell system: (a) open-shell, if they include the open shell fragment; (b) closed-shell otherwise. The electrostatic field added to all monomer, dimer, and trimer calculations is computed from the total density of either open- or closed-shell fragments. The covalent boundaries are treated exactly as in the closed-shell FMO,[7,9,10] that is, by assigning two electrons from the detached bond to one fragment and none to the other, for the pair of fragments between which a bond is detached.
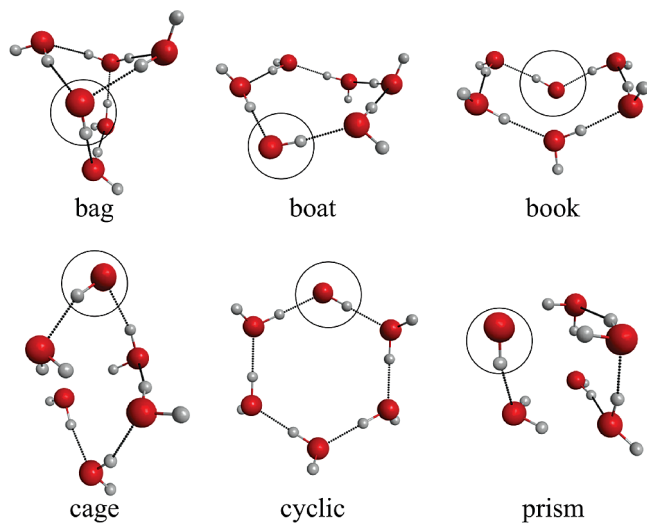
Figure 1. The six isomers of OH(H2O)5 clusters used for testing. Open-shell OH molecules are circled, and the naming convention is from ref 26.

Table 1. Absolute Errors between ab Initio ROMP2 and FMO-ROHF for Six OH(H2O)5 Clusters

	absolute errors (kcal/mol)			
	aug-cc-pVTZ			
isomer	FMO2-ROHF	FMO3-ROHF	FMO2-ROMP2	FMO3-ROMP2
prism	0.2	0.0	0.0	−0.1
cage	1.4	0.1	1.3	0.1
bag	2.8	0.0	2.7	0.1
cyclic	1.7	0.1	1.6	0.3
boat	1.7	0.1	1.6	0.3
book	1.4	0.1	1.3	0.2

The FMO energy has been implemented for the RO-based Hartree−Fock method (ROHF), MP2 (ROMP2), and CC (ROCC). In FMO-ROHF, the densities of all fragments are optimized self-consistently on the basis of the ROHF density of the open-shell fragment, whereas in FMO-TDDFT all densities are optimized for the ground state, from which excitations are evaluated following the TDDFT theory.

In addition, a multilayer scheme[25] was also implemented in which several layers with varying levels of electronic structure theory (HF, MP2, and CC) can be defined. The multilayer FMO method uses the notation of listing the wave functions in increasing order of layers, for example, FMO2-ROMP2:ROCC means that the fragment densities are obtained self-consistently at the uncorrelated level (ROHF) and used in the correlated

Table 2. Comparison of the ROMP2 Relative Energies[a] of Six OH(H2O)5 Clusters

	relative energies (kcal/mol)		
	aug-cc-pVTZ		
isomer	ROMP2	FMO2-ROMP2	FMO3-ROMP2
prism	0.0	0.0	0.0
cage	1.4	2.7	1.6
bag	2.5	5.2	2.7
cyclic	3.9	5.5	4.3
boat	4.7	6.3	5.0
book	8.8	10.2	9.1

[a] Zero energy for all methods is set to be the prism isomer.

calculations at the ROMP2[26] (Z-averaged perturbation theory) level for the less important fragments (substituents) and ROCC[19,20] (completely renormalized CR-CC(2,3) method) for (for example) a reaction center. Dimer calculations are performed at the lower level of the two layers to which the two fragments belong. In the case of the reaction described below, there was only one fragment in the higher level, so that all dimer calculations were done with ROMP2. The same basis set is used in both layers.

Especially for CC, which is a very steeply scaling method (N^7) with the system size N, the use of FMO is beneficial even for very small systems, such as that with only three fragments discussed below. In addition to the computational cost scaling, CC requires very large memory; the huge memory demand prevented the full ab initio CC calculations while the FMO-CC computations are feasible.

The open-shell FMO code was parallelized with the generalized distributed data interface (GDDI),[27,28] using a two-level hierarchical scheme. Since the open-shell MP2 method in GAMESS (General Atomic and Molecular Electronic Structure System)[29] is fully parallelized, it can take advantage of both levels of GDDI. This is not the case for the open-shell CC code, which can only take advantage of the inherent coarse-grained level parallelism of the FMO method using GDDI. The load balancing is dynamic (optionally static) and follows a general algorithm[28] with all fragments (closed- and open-shell) distributed over groups in GDDI. All methods discussed here have been implemented in GAMESS.

All calculations discussed here used the default values of thresholds. The exception is that, for water clusters, the Mulliken point charge representation[8] of the electrostatic potentials in the FMO method was used (i.e., fragment calculations are done in the field of point charges derived self-consistently from the fragment densities, and fragment calculations are repeated until their densities converge with respect to the field;[7,8,10] dimers are computed in the converged field only once). Spherical basis functions were used throughout, and the core electrons (e.g., 1s on C and O) were not correlated in MP2 and CC.

3. Tests

3.1. Open-Shell FMO2 and FMO3 Calculations on OH(H2O)5 Clusters. A preliminary test of the open-shell FMO method employed clusters of six water molecules. The ability to accurately model the solvated OH radical has implications in biological applications and atmospheric processes.[30] The large charge transfer present in solvated OH clusters adds an additional degree of difficulty, providing an excellent test case for the open-shell FMO method.

The structures of the six clusters shown in Figure 1 were determined by optimizing previously determined minima[31] with MP2 and the aug-cc-pVTZ basis set.[32] To create the open-shell test systems, one hydrogen atom was arbitrarily removed from one of the water molecules in each cluster (doublet spin multiplicity). Fragments were chosen by placing the open-shell OH in a fragment with both nearest neighbor H2O molecules, while placing the other H2O molecules in fragments by themselves, with the exception of the prism and bag isomers. For these two isomers, there were two other H2O molecules with a significant interaction between them. This required them
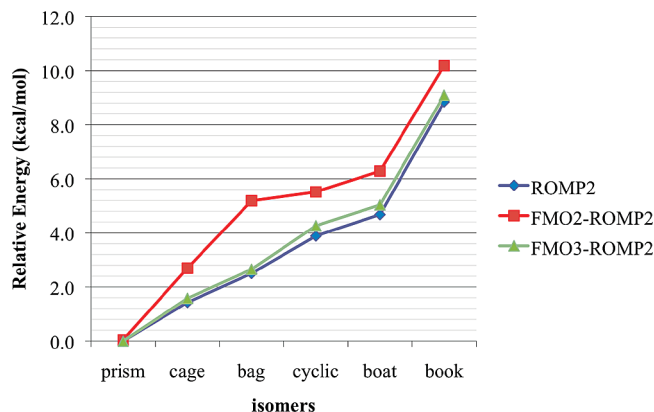
Letter

J. Chem. Theory Comput., Vol. 6, No. 1, **2010** **3**

Figure 2. Graph of the relative energies of the six $OH(H_2O)_5$ clusters computed using ab initio ROMP2, FMO2-ROMP2, and FMO3-ROMP2.

Table 3. Absolute Errors between ab Initio ROMP2 Calculations and FMO2-ROMP2 for the RAFT Reaction

	absolute errors (a.u.)		
	6-311G(d,p)		
	ROMP2	FMO2-ROMP2	error (kcal/mol)
reactant 1	−518.94377299	−518.94481925	−0.7
reactant 2	−1235.33260039	−1235.33407266	−0.9
product	−1754.31552043	−1754.31616825	−0.4

to be placed into one fragment together, while the open-shell OH was placed in a fragment with only one nearest neighbor. The final fragmentation scheme created four FMO monomers for all isomers.

Errors for FMO2-ROHF calculations (Table 1) relative to ab initio calculations are between 0.2 and 2.8 kcal/mol, while the errors are between 0.0 and 2.7 kcal/mol for FMO2-ROMP2. The addition of ab initio three-body interactions with FMO3-ROHF significantly reduces the error to 0.0−0.1 kcal/mol, while the error for FMO3-ROMP2 falls to 0.1−0.3 kcal/mol. The improvement in accuracy for FMO3 is not a surprising result, as the importance of three-body effects in water has been shown previously.[12,33]

Relative energetics (Table 2) are of similar accuracy, with the ordering of isomers being captured correctly with both FMO2 and FMO3, illustrated in Figure 2. The choice of fragments is important for the accurate reproduction of the relative energies, especially for FMO2 and in systems in which

fragments may have very strong interactions such as charge transfer. These strongly interacting fragments should be grouped together to improve accuracy.

For the small water clusters computed, we note that FMO2-ROMP2 takes about the same time as ab initio ROMP2, whereas FMO3-ROMP2 takes about three times more, and the crossover size (when FMO owing to its nearly linear scaling becomes faster) may be just a few more molecules. Considering the distributed memory requirements of the ab initio ROMP2 calculations (~2 GB of RAM) versus that of the FMO2-ROMP2 calculation (~512 MB of RAM) or the FMO3-ROMP2 calculation (~1 GB of RAM), the open-shell FMO method is capable of providing accurate energies at a much lower cost. One can imagine that, as the size of the cluster *N* increases, the memory requirement of the *ab initio* calculation will also increase substantially (~N^4); however, for FMO it will remain the same, no matter how large the cluster is.

3.2. Multilayer FMO2 Calculation of the Reversible Addition−Fragmentation Chain Transfer (RAFT) Reaction Enthalpy (Figure 3). As a further test of the open-shell FMO method, the initiation step in the RAFT reaction[34,35] was chosen as a small test case. The initiation step consists of two reactants, one an open-shell radical (doublet spin multiplicity), that combine to form an open-shell radical product. Initial structures were optimized using DFT with the B3LYP functional and the
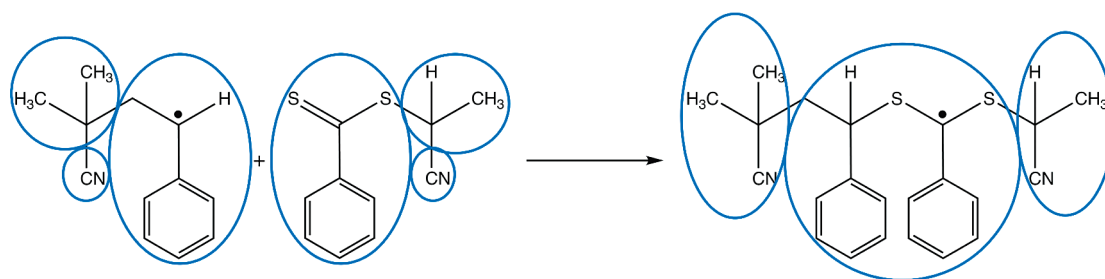

Figure 3. Reaction scheme for the RAFT reaction with the choice of FMO fragments shown in blue.
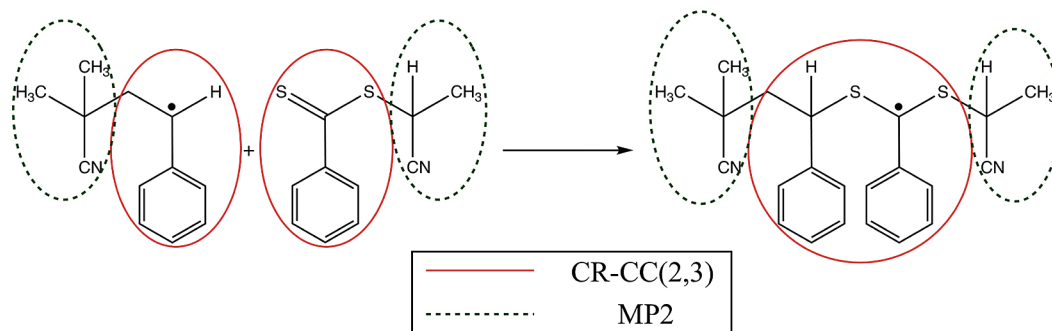

Figure 4. Reaction scheme for the RAFT reaction with the multilayer FMO details: higher layer fragments (CC) are circled in red, and lower levels fragments (MP2) are in green dashed circles.

Table 4. Calculated Enthalpy of the RAFT Reaction Using ab Initio ROMP2, FMO2-ROMP2, and FMO2-MP2:CR-CC(2,3)

basis set	method	energy (a.u.)			enthalpy (kcal/mol)
		reactant 1	reactant 2	product	
3-21G	FMO2-ROMP2	−515.27782025	−1228.15256231	−1743.46127536	−19.4
3-21G	FMO2-MP2:CR-CC(2,3)	−515.37480438	−1228.23664205	−1743.63878524	−17.2
6-311G(d,p)	FMO2-ROMP2	−518.94481925	−1235.33407266	−1754.31616825	−23.4
3-21G	ROMP2	−515.27782024	−1228.15256232	−1743.46133847	−19.4
6-311G(d,p)	ROMP2	−518.94377300	−1235.33260039	−1754.31552043	−24.6

6-31G(d) basis set.[36] FMO2-ROMP2 single point energy calculations using the 6-311G(d,p) basis set were performed with the fragmentation scheme shown in Figure 3 (the unpaired electron is shown schematically; in practice, it is delocalized). Higher-level calculations were also performed, using the completely renormalized coupled cluster single and double excitations using left eigenstates for perturbative triple excitation corrections (CR-CC(2,3))[19,20] method with the 3-21G basis set to model the open-shell fragment, and MP2 with the 3-21G basis set to model the closed-shell fragments (FMO2-MP2:CR-CC(2,3)), shown in Figure 4. The reason for using a smaller basis set is the huge memory requirements for the CC code, which even for 3-21G was 8 GB, while for the 6-31G(d) basis set, the requirements are more than 32 GB.

Table 3 gives the absolute energy differences between ab initio ROMP2 and FMO2-ROMP2 for both reactants and the product of the RAFT reaction. The FMO2-ROMP2 method gives accurate energies, with errors between 0.4 and 0.9 kcal/mol. This accuracy in absolute energies translates to equivalent accuracy when calculating the reaction enthalpy (Table 4). Comparing the enthalpy from FMO2-ROMP2 using the 6-311G(d,p) basis set with the ab initio ROMP2 enthalpy, the error is only 0.9 kcal/mol. Calculations performed with the 3-21G basis set also show very good agreement between ab initio ROMP2 and FMO2-ROMP2 calculations. With the addition of the CC correction in the FMO2-MP2:CR-CC(2,3) calculation, the enthalpy changes by +2.2 kcal/mol. This suggests that the use of ROMP2 to calculate enthalpies is adequate in this case; however, a higher level of theory may be required in other instances to properly describe open-shell systems.

3.3. Excitation Energy Calculation of a Small Protein (1L2Y). As a model application to a larger system, consider the FMO2-ROMP2 triplet excitation energy using the 6-31+G(d) basis set of the Trp-cage miniprotein construct (1L2Y), with diffuse functions added to the carboxyls. The geometry has been taken from previous studies.[9] The protein consists of 20 amino acid residues and a total of 304 atoms. When a triplet excitation of one of the Trp-6 residue in the protein is specified and also the ground-state closed-shell calculation is performed, the calculations took 160 min each on four nodes containing two 2.66 GHz quad core Intel Xeon processors (32 CPUs total). In contrast, the full ab initio ROMP2 calculation containing 2610 basis functions, if the calculation was feasible, would require 1024 CPUs with 16 GB of RAM per CPU. The FMO-ROMP2 excitation energy was found to be 93.35 kcal/mol (4.05 eV).

4. Conclusions

The open-shell FMO method has been implemented in the GAMESS program package and parallelized using GDDI for the HF, MP2, and CC levels of electronic structure theory. The accuracy of the method was tested by calculating the absolute and relative energetics of open-shell molecular clusters. The ability of the method to reproduce reaction enthalpies was also tested using the RAFT reaction. It was demonstrated that in both cases the open-shell FMO method provides energies and properties within 0.0−2.0 kcal/mol of ab initio calculations.

The need for a single reference open-shell FMO method was fulfilled through this work, providing a scalable method for use on large chemical systems such as the RAFT reaction. The combination of accuracy and reduction in computational expense provides a means for accurate calculations on much larger open-shell radical chemical systems than was previously available.

References

(1) Söderhjelm, P.; Aquilante, F.; Ryde, U. *J. Phys. Chem. B* **2009**, *113*, 11085.

(2) Pomogaev, V.; Pomogaeva, A.; Aoki, Y. *J. Phys. Chem. A* **2009**, *113*, 1429.

(3) Xie, W.; Orozco, M.; Truhlar, D. G.; Gao, J. *J. Chem. Theory Comput.* **2009**, *5*, 459.

(4) Leverentz, H. R.; Truhlar, D. G. *J. Chem. Theory Comput.* **2009**, *5*, 1573.

(5) Suárez, E.; Díaz, N.; Suárez, D. *J. Chem. Theory Comput.* **2009**, *5*, 1667.

(6) Deshmukh, M. M.; Gadre, S. R. *J. Phys. Chem. A* **2009**, *113*, 7927.

(7) Kitaura, K.; Ikeo, E.; Asada, T.; Nakano, T.; Uebayasi, M. *Chem. Phys. Lett.* **1999**, *313*, 701.

(8) Nakano, T.; Kaminuma, T.; Sato, T.; Fukusawa, K.; Akiyama, Y.; Uebayasi, M.; Kitaura, K. *Chem. Phys. Lett.* **2002**, *351*, 475.

(9) Fedorov, D. G.; Kitaura, K. *J. Phys. Chem. A* **2007**, *111*, 6904.

(10) Fedorov, D. G.; Kitaura, K. *The Fragment Molecular Orbital Method: Practical Applications to Large Molecular Systems*; CRC Press: Boca Raton, FL, 2009.

(11) Korchowiec, J.; Gu, F. L.; Aoki, Y. *Int. J. Quantum Chem.* **2005**, *105*, 875.

(12) Fedorov, D. G.; Kitaura, K. *J. Chem. Phys.* **2004**, *120*, 6832.

(13) Fedorov, D. G.; Kitaura, K. *J. Chem. Phys.* **2004**, *121*, 2483.

(14) Fedorov, D. G.; Kitaura, K. *J. Chem. Phys.* **2005**, *122*, 054108.

(15) Mochizuki, Y.; Koikegami, S.; Amari, S.; Segawa, K.; Kitaura, K.; Nakano, T. *Chem. Phys. Lett.* **2005**, *406*, 283.

(16) Fedorov, D. G.; Kitaura, K. *J. Chem. Phys.* **2005**, *123*, 134103.

Letter

J. Chem. Theory Comput., Vol. 6, No. 1, 2010 **5**

(17) Chiba, M.; Fedorov, D. G.; Nagata, T.; Kitaura, K. *Chem. Phys. Lett.* **2009**, *474*, 227.

(18) Lee, T. J.; Rendell, A. P.; Dyall, K. G.; Jayatilaka, D. *J. Chem. Phys.* **1994**, *100*, 7400.

(19) Włoch, M.; Gour, J. R.; Piecuch, P. *J. Phys. Chem. A,* **2007**, *111*, 11359.

(20) Piecuch, P.; Włoch, M. *J. Chem. Phys.* **2005**, *123*, 224105.

(21) Pryor, W. A. *Free Radicals*; McGraw-Hill: New York, 1966.

(22) Griese, B.; Wang, M.; Gao, J.; Stoltz, M.; Müller, P.; Graber, M. *J. Org. Chem.* **2009**, *74*, 3621.

(23) Astruc, D. *Electron Transfer and Radical Processes in Transition-Metal Chemistry*; Wiley-VCH: New York, 1995.

(24) Chiba, M.; Fedorov, D. G.; Kitaura, K. *J. Chem. Phys.* **2007**, *127*, 104108.

(25) Fedorov, D. G.; Ishida, T.; Kitaura, K. *J. Phys. Chem. A.* **2005**, *109*, 2638.

(26) Aikens, C. M.; Fletcher, G. D.; Schmidt, M. W.; Gordon, M. S. *J. Chem. Phys.* **2006**, *124*, 014107.

(27) Fletcher, G. D.; Schmidt, M. W.; Bode, B. M.; Gordon, M. S. *Comput. Phys. Commun.* **2000**, *128*, 190.

(28) Fedorov, D. G.; Olson, R. M.; Kitaura, K.; Gordon, M. S.; Koseki, S. *J. Comput. Chem.* **2004**, *25*, 872.

(29) Schmidt, M. W.; Baldridge, K. K.; Boatz, J. A.; Elbert, S. T.; Gordon, M. S.; Jensen, J. H.; Koseki, S.; Matsunaga, N.; Nguyen, K. A.; Su, S.; Windus, T. L.; Dupuis, M.; Montgomery, J. A., Jr. *J. Comput. Chem.* **1993**, *14*, 1347.

(30) Seinfeld, J. H.; Pandis, S. N. *Atmospheric Chemistry and Physics: From Air Pollution to Climate Change*; Wiley: New York, 2006.

(31) Day, P. N.; Pachter, R.; Gordon, M. S.; Merrill, G. N. *J. Chem. Phys.* **2000**, *112*, 2063.

(32) (a) Dunning, T. H., Jr. *J. Chem. Phys.* **1989**, *90*, 1007. (b) Woon, D. E.; Dunning, T. H., Jr. *J. Chem. Phys.* **1995**, *103*, 4572.

(33) Xantheas, S. *Struct. Bonding (Berlin)* **2005**, *116*, 119.

(34) Coote, M. L.; Izgorodina, E. I.; Krenske, E. H.; Busch, M.; Barner-Kowollik, C. *Macromol. Rapid Commun.* **2006**, *27*, 1015.

(35) Chiefari, J.; Chong, Y. K.; Ercole, F.; Krstina, J.; Jeffery, J.; Le, T. P. T.; Mayadunne, R. T. A.; Meijs, G. F.; Moad, C. L.; Moad, G.; Rizzardo, E.; Thang, S. H. *Macromolecules* **1998**, *31*, 5559.

(36) Structures used for the RAFT reaction calculations were obtained from Professor Michelle Coote at the Austrailian National University.

JCTC Journal of Chemical Theory and Computation

Least-Action Tunneling Transmission Coefficient for Polyatomic Reactions

Rubén Meana-Pañeda,[†] Donald G. Truhlar,[‡] and Antonio Fernández-Ramos*,[†]

Department of Physical Chemistry, Faculty of Chemistry, University of Santiago de Compostela, 15782 Santiago de Compostela, Spain, and Department of Chemistry and Supercomputing Institute, University of Minnesota, 207 Pleasant Street S. E., Minneapolis, Minnesota 55455-0431

Abstract: We present a new least-action variational approximation for tunneling in polyatomic reactions based on the procedure developed by Garrett and Truhlar for atom−diatom reactions.[63] The method calculates the semiclassical ground-state tunneling probability at every tunneling energy by minimizing the value of imaginary action integral along a family of paths ranging from the minimum energy path to the straight path. The method is illustrated by applications to two hydrogen-atom abstraction reactions from methane using analytical potential energy surfaces.

1. Introduction

Tunneling is a quantum mechanical effect by which a particle can penetrate into classically forbidden regions of coordinate space.[1−3] Less than 10 years after the formulation of modern quantum mechanics, Wigner[4] and Bell[5] pointed out the importance of this effect in chemical kinetics. Tunneling is very sensitive to the mass of the particles involved in the tunneling motion and to the shape and height of the effective barrier being crossed. Tunneling often competes well with overbarrier processes at low temperatures for processes that involve the transfer of a proton or deuteron. It is well established that quantum tunneling effects require a multi-dimensional treatment and that they are important processes even at room temperature.[6−9] Because the likelihood of tunneling depends on the mass that is being transferred, the analysis of kinetic isotope effects is one of the chief means of getting insight into the reaction mechanisms of many processes of biological and technological importance.[10,11] Therefore, the treatment of quantum tunneling within a multidimensional framework is very important.

Variational transition-state theory with multidimensional tunneling contributions[12,13] (VTST/MT) has been shown to be capable of accounting for quantum effects on large systems[14,15] but the methodology for treating those effects still allows for some improvements. Here, we present a new approximation that leads to a more complete treatment of quantum tunneling effects in polyatomic chemical reactions.

In section 2, we present background necessary to understand the new work in the context of VTST/MT. Section 3 presents the new LAG4 approximation. Section 4 presents the application of the LAG4 method to the $H + CH_4 \rightarrow H_2 + CH_3$ and $^{15}H + CH_4 \rightarrow {}^{15}H - H + CH_3$ reactions using the Jordan and Gilbert (JG) potential energy surface.[16] Section 5 has concluding remarks.

2. Background

Variational transition-state theory (VTST)[12,13,17−26] is based on transition-state theory (TST), also called conventional transition-state theory, which was originally formulated by Eyring[27] and Evans and Polanyi.[28] TST calculates the one-way equilibrium flux through the transition state (a surface dividing reactants from products in phase space) and assumes that the transition state is a reaction bottleneck that separates reactants from products such that all trajectories that start in the reactants' region and cross the transition state do not recross it before becoming equilibrated as products; this is known as the no recrossing assumption. Furthermore, TST assumes that the Born−Oppenheimer approximation is valid and that the reactants are equilibrated canonically (in a fixed-temperature ensemble) or microcanonically (in a fixed-total-energy ensemble).

* Corresponding author. E-mail: qf.ramos@usc.es.
† University of Santiago de Compostela.
‡ University of Minnesota.

TST and VTST can be formulated unambiguously in a classical world,[29] and quantum effects on all degrees of freedom except the reaction coordinate can reasonably be included by quantizing their partition functions,[27] as justified to order $\hbar^2$ by Wigner.[4] Quantum effects on the reaction coordinate can be incorporated by the addition of a multiplicative multidimensional factor, called the tunneling transmission coefficient,[30-32] but this can only be accomplished consistently in VTST.[33] In fact, VTST/MT incorporates both recrossing (with respect to conventional TST) and quantum tunneling effects, although it needs more information than TST about the potential energy surface of the reaction. TST (without tunneling) needs information only about reactants and the transition state, whereas VTST/MT needs information at least about the reaction path that joins the transition state with reactants and products and sometimes also about a wider region called the reaction swath, which includes additional geometries on the concave side of the reaction path. In the present work, the reaction path is chosen as the minimum energy path (MEP) in isoinertial coordinates,[31,34] scaled to a reduced mass of μ, and the signed distance along this path is labeled as s. By convention, $s = 0$ indicates the location of the transition state, whereas $s < 0$ and $s > 0$ correspond to the reactant and product sides, respectively. The variational method that minimizes the one-way flux from reactants to products through trial dividing surfaces that cross the reaction path at various values of s in a fixed-temperature ensemble is called canonical variational transition-state theory or canonical variational theory (CVT).[20,35] The CVT rate constant for a bimolecular reaction at temperature T is given by

$$k^{\text{CVT}} = \sigma \frac{k_{\text{B}}T}{h} \frac{Q^{\text{GT}}(T, s_*^{\text{CVT}}(T))}{\Phi_{\text{R}}(T)} \exp\left[-V_{\text{MEP}}(s_*^{\text{CVT}}(T))/k_{\text{B}}T\right] \tag{1}$$

where σ is the symmetry number,[36,37] k_{B} and h are the Boltzmann and Planck constants respectively and $V_{\text{MEP}}(s_*^{\text{CVT}}(T))$ is the value of the potential on the reaction path at s_*^{CVT}, which is the location along the reaction coordinate of the dividing surface that minimizes the one-way flux rate constant. The quantized reactant partition function per unit volume is $\Phi_{\text{R}}(T)$, and $Q^{\text{GT}}(T, s_*^{\text{CVT}}(T))$ is the quantized generalized transition-state partition function at $s_*^{\text{CVT}}(T)$.

In this article, we are concerned with quantum effects on the reaction coordinate, which are incorporated by multiplying the CVT rate constant by a transmission coefficient, κ. The resulting rate constant is given by

$$k^{\text{CVT/SAG}}(T) = \kappa^{\text{CVT/SAG}}(T)k^{\text{CVT}}(T) \tag{2}$$

where SAG denotes semiclassical (vibrationally) adiabatic ground state. Neglecting κ is called the quasiclassical approximation.[15] The transmission coefficient, which rigorously is the ratio of the averaged quantum mechanical reaction probabilities to the model underlying TST or VTST without the transmission coefficient, is approximated by the ratio of the averaged SAG and quasiclassical probabilities. The SAG transmission coefficient is evaluated by using an effective potential that (in the first approximation under discussion here) is vibrationally adiabatic with the further approximation[21] that the vibrationally adiabatic potential curves of all of the vibrational excited states have the same shape as the ground-state vibrationally adiabatic potential curve, $V_a^{\text{G}}(s)$, so that all of the tunneling probabilities are evaluated with this potential, which is given in the harmonic approximation by

$$V_a^{\text{G}}(s) = V_{\text{MEP}}(s) + \frac{\hbar}{2}\sum_m \omega_m(s) \tag{3}$$

where $\omega_m(s)$ is a frequency of one of the $3N$-7 ($3N$-6 for linear molecules) generalized normal modes at s. In general, the harmonic approximation used in the evaluation of the vibrationally adiabatic potential is reasonable for polyatomic systems, a major exception being those systems presenting low-frequency internal rotations, for which it is important to include anharmonicity on those torsional modes.[38,39] (Low-frequency modes that are not torsions are also usually anharmonic.) Because the barrier height, V_a^{AG}, of the ground-state vibrationally adiabatic potential curve may be different from $V_a^{\text{G}}(s_*^{\text{CVT}}(\text{T}))$, the CVT/SAG transmission coefficient on the right-hand side of eq 2 is equal to an intrinsic transmission coefficient κ^{SAG} times the factor $\exp\{\beta[V_a^{\text{G}}(s_*^{\text{CVT}}(\text{T})) - V_a^{\text{AG}}]\}$ to make the transmission coefficient consistent in spite of the difference in the effective thresholds of the transmission coefficient and of the CVT rate constant. The intrinsic transmission coefficient is given by

$$\kappa^{\text{SAG}}(T) = \frac{\int_0^\infty dE P^{\text{SAG}}(E) \exp\left(-\beta E\right)}{\int_{V_a^{\text{AG}}}^\infty dE P^{\text{C}}(E) \exp\left(-\beta E\right)} \tag{4}$$

where $P^{\text{C}}(E)$ is the classical probability, which equals zero below V_a^{AG} and unity otherwise, so the transmission factor can be written as:

$$\kappa^{\text{SAG}}(T) = \beta \exp\left(\beta V_a^{\text{AG}}\right) \int_0^\infty dE P^{\text{SAG}}(E) \exp\left(-\beta E\right) \tag{5}$$

The semiclassical adiabatic reaction probability of the ground state $P^{\text{SAG}}(E)$ for the whole range of energies is given by

$$P^{\text{SAG}}(E) = \begin{cases} 0, & E < E_0 \\ \{1 + \exp\left[2\theta(\text{E})\right]\}^{-1}, & E_0 \leq E \leq V_a^{\text{AG}} \\ 1 - P^{\text{SAG}}(2V_a^{\text{AG}} - E), & V_a^{\text{AG}} \leq E \leq 2V_a^{\text{AG}} - E_0 \\ 1, & 2V_a^{\text{AG}} - E_0 < E \end{cases} \tag{6}$$

where E_0 is the lowest energy at which it is possible to have tunneling (this is the energy of the reactant zero-point level when the reaction is written in the exoergic direction) and $\theta(E)$ is the so-called action integral, actually the magnitude of the imaginary part of the action integral:

$$\theta(E) = \hbar^{-1} \int_{\tilde{s}_0}^{\tilde{s}_1} ds\{2\mu_{\text{eff}}(s)(V_a^{\text{G}}(s) - E)\}^{1/2} \tag{7}$$

where $\mu_{\text{eff}}(s)$ is the effective mass of the tunneling motion, and $\tilde{s}_0$ and $\tilde{s}_1$ are the classical turning points at a given

tunneling energy, E, in the reactant and product valleys, respectively. Both turning points have to obey the resonance condition:

$$V_a^G(\tilde{s}_0) = V_a^G(\tilde{s}_1) = E \qquad (8)$$

The simplest case for the evaluation of the action integral of eq 7 is when the coupling between the reaction coordinate and the transverse modes is neglected. In that case, the effective mass equals that of the isoinertial coordinate system, that is, $\mu_{eff}(s) = \mu$. This method is known as the zero-curvature tunneling (ZCT) approximation.[31] The ZCT method is not recommended for general use because it often seriously underestimates the tunneling contribution.[40,41] Wyatt[42] and Marcus and Coltrin[43,44] showed that the coupling enters the reaction-path Hamiltonian through the kinetic energy term producing a negative centrifugal effect that shortens the tunneling path by moving it toward the concave side of the reaction path. This is now called corner-cutting tunneling. Marcus and Coltrin derived a corner-cutting approximation to the transmission coefficient for the collinear H + H$_2$ reaction (for which the curvature of the MEP in isoinertial coordinates is small) by finding for that case a least-action path, that is, the tunneling path that minimizes eq 7, by incorporating the reaction path curvature (the centrifugal effect) into the effective mass. This method was extended to polyatomic systems by making the vibrationally adiabatic approximation for all bound modes of the transition state,[45] by modifying the effective mass to avoid the singularity in the reaction path Hamiltonian due to the breakdown of the natural collision coordinates when the reaction path curvature is large[46,47] and by properly including the simultaneous corner cutting in more than one mode of vibration.[48,49] The resulting method is called the centrifugal-dominant small-curvature semiclassical adiabatic ground-state (CD-SCSAG) approximation or simply the small-curvature tunneling (SCT) approximation.

For systems with large curvature of the isoinertial MEP, such as bimolecular reactions in which the hydrogen atom is transferred between two heavy atoms,[50] tunneling may be dominated by paths that lie very far from the MEP and, therefore, the adiabatic approximation may breakdown. The large-curvature ground-state tunneling (LCT) method[12,13,48,51−56] was designed for such cases. Other straight-path methods[57−59] have been put forward as well. The latest version of the LCT approximation is called LCG4.[13,56] At each tunneling energy, LCT includes a set of tunneling paths that are the straight trajectory between the two classical turning points at that energy plus the set of all lower-energy tunneling paths. To evaluate action integrals along these paths requires not only information in the potential valley around the MEP (the regions close to the MEP, which can be treated within the adiabatic approximation) but also information about the broader reaction swath on the concave-side of the MEP; this region is the locus of deep-tunneling paths that are vibrationally nonadiabatic. In the LCT approximation, tunneling into excited vibrational states of the products in the exoergic direction is also included;[55] tunneling into excited states is also included for thermoneutral reactions.[60] The LCG4

approximation is more accurate than the previous LCG3 approximation because it includes a nonquadratic correction in the nonadiabatic region. In general, the evaluation of the LCG4 transmission coefficients is quite demanding from the computational point of view, so two interpolated large curvature tunneling (ILCT) methods, called ILCT1D[61] and ILCT2D,[62] were proposed. The latter evaluates the LCG4 transmission coefficient with an error (with respect to the uninterpolated calculation) smaller than 1% but it reduces the computer time by more than one order of magnitude.

The SCT and LCT transmission coefficients cover the whole range of reaction-path curvatures, so it seems natural to built a transmission coefficient which, at every tunneling energy, chooses the largest between the SCT and LCT tunneling probabilities, or similarly (essentially equivalently), the smallest between the SCT and LCT imaginary action integrals. This approximation is called microcanonical optimized multidimensional tunneling (μOMT) method.[55] The μOMT tunneling probabilities are, therefore,

$$P^{\mu OMT}(E) = \max_E \begin{cases} P^{SCT}(E) \\ P^{LCT}(E) \end{cases} \qquad (9)$$

where $P^{SCT}(E)$ and $P^{LCT}(E)$ are the SCT and LCT probabilities evaluated within the CD-SCSAG and LCG4 approximations, respectively. However, these two approximations are just two particular cases of a more general method in which the tunneling path is variationally optimized by employing a criterion of least imaginary action. This method, which is called least-action ground-state tunneling (LAT) approximation, was developed some years ago for atom−diatom reactions, and it was shown to be superior to the SCT and LCT methods.[63,64] Other LAT methods using a family of paths similar to that described by Garrett and Truhlar[63] have also been developed for polyatomic reactions, although those methods were only used to compute tunneling splittings. For instance, Taketsugu and Kimihiko[65] used a multidimensional LAT method to obtain the least-action integral at a given tunneling energy. Similarly, Tautermann et al.[66] obtained the optimal tunneling path to predict ground-state tunneling splittings in symmetric polyatomic systems. So far though the LAT method has not been applied to evaluate thermal rate constants for polyatomic systems. However, it has been extensively applied to atom−diatom reactions[41] and compared with SCT and LCT approximations. Although all of the LCT calculations were performed using the LCG3 approximation, it was concluded that, for some cases the μOMT method was as accurate as the LAT method, but on average the latter was superior to the former.

The current μOMT method evaluates the large-curvature probabilities with the LCG4 approximation and it performs well for polyatomic reactions. However, it is interesting to know the effect of full optimization of the tunneling paths in a multidimensional framework in polyatomic reactions even when full optimization may be more expensive computationally than the current methods. In this work, we present a new version, which adds the following features to the previous LAT method: (i) it is now developed for polyatomic reactions, and (ii) it uses the same criteria for

Least-Action Tunneling Transmission Coefficient

J. Chem. Theory Comput., Vol. 6, No. 1, 2010 **9**

the specification of the adiabatic and nonadiabatic regions as the LCG4 method. Therefore, we label this version of the least-action tunneling method as LAG4.

3. Methods

LAG4, like LCG3 and LCG4, is always applied to a reaction in the exoergic or thermoneutral direction with the reactant in its ground vibrational state. The tunneling process may end in the product ground state or in an excited diabatic vibrational state of the product. In general one sums over the probabilities of producing each final state but, in many cases, one needs to consider only ground-state-to-ground-state tunneling, and this section will start with the ground-state-to-ground-state process.

The LAG4 approximation involves the minimization of the imaginary action integrals along a given set of paths, which are between the MEP and the straight path (which is the reference path for all the LCT methods, including the LCG4 approximation). At a given tunneling energy the end points of any particular tunneling path are given by $\tilde{s}_0$ and $\tilde{s}_1$ with the resonance condition given by eq 8. The mass-scaled Cartesian geometries of these two classical turning points that are located on the MEP are $\mathbf{x}(\tilde{s}_0)$ and $\mathbf{x}(\tilde{s}_1)$, respectively. The paths to initiate the search for the least-action are built as a function of a single parameter α, such that $\alpha = 0$ yields the MEP and $\alpha = 1$ yields the straight path. Therefore, $\alpha = 0$ and $\alpha = 1$ correspond to the ZCT and LCT transmission coefficients, respectively. We introduce a progress variable along the path, called $\xi(\alpha)$, which is in the interval $0 \leq \xi(\alpha) \leq \xi_P(\alpha)$, where $\xi_P(\alpha)$ is the total length of path at a given tunneling energy.

The lengths of the MEP and of the straight path are $\xi_P(0)$ and $\xi_P(1)$ respectively, so all the intermediate paths obey the condition $\xi_P(1) \leq \xi_P(\alpha) \leq \xi_P(0)$. The variable γ is defined by

$$\gamma = \frac{\xi(\alpha)}{\xi_P(\alpha)} \qquad (10)$$

The γ parameter is in the interval $[0, 1]$, being 0 at the reactants classical turning point and 1 at the products classical turning point. This parameter is useful to unify all of the paths with different α values to see how much relative progress there is along each of them. We prefer to use $\xi(\alpha)$ instead because in this case the length of the paths is explicitly used.

The mass-scaled Cartesian geometries for a given value of α, at a point $\xi(\alpha)$ along the path and at a given tunneling energy, are $\mathbf{x}[\alpha, \xi(\alpha), \tilde{s}_0]$. Thus, the mass-scaled Cartesian geometries along the MEP are given by $\mathbf{x}[0, \xi(0), \tilde{s}_0]$, whereas the ones along the straight path are

$$\mathbf{x}[1, \xi(1), \tilde{s}_0] = \mathbf{x}(\tilde{s}_0) + \xi(1)\hat{\boldsymbol{\eta}}[1, \xi(1), \tilde{s}_0] \qquad (11)$$

where $\mathbf{x}(\tilde{s}_0) = \mathbf{x}[0, 0, \tilde{s}_0]$. The parameter $\xi(1)$ indicates the progress along the straight path; $\hat{\boldsymbol{\eta}}[1, \xi(1), \tilde{s}_0]$ is the unit vector along the straight path, that is,

$$\hat{\boldsymbol{\eta}}[1, \xi(1), \tilde{s}_0] = \frac{\mathbf{x}(\tilde{s}_1) - \mathbf{x}(\tilde{s}_0)}{\xi_P(1)} \qquad (12)$$

where the length of the straight path is $\xi_P(1) = |\mathbf{x}(\tilde{s}_1) - \mathbf{x}(\tilde{s}_0)|$.

The MEP and the straight path are the extreme cases of a family of α−dependent paths, which are chosen as

$$\mathbf{x}[\alpha, \xi(\alpha), \tilde{s}_0] = (1 - \alpha)\mathbf{x}[0, \xi(0), \tilde{s}_0] + \alpha\mathbf{x}[1, \xi(1), \tilde{s}_0]$$

$$(13)$$

where $\mathbf{x}[0, \xi(0), \tilde{s}_0]$ and $\mathbf{x}[1, \xi(1), \tilde{s}_0]$ are the geometries along the MEP and along the straight path respectively with the same progress, that is, $\xi(0)/\xi_P(0) = \xi(1)/\xi_P(1) = \gamma$.

The imaginary action integral for each of these paths is a generalization of the imaginary action integral along the LCT straight path. At every tunneling energy, the paths of eq 13 are built as a function of the α parameter as shown in Figure 1. For small values of α the geometries along the path will be very close to those along the MEP and therefore motion along the entire path is treated as vibrationally adiabatic. For intermediate to large values of α, the path is divided into three regions. Regions I and III, located on the reactants and products sides respectively are treated as vibrationally adiabatic, and region II is vibrationally nonadiabatic.

The vibrationally adiabatic potential is obtained in such a way that the geometry $\mathbf{x}[\alpha, \xi(\alpha), \tilde{s}_0]$ is perpendicular to the gradient at that s value, that is,

$$\{\mathbf{x}[\alpha, \xi(\alpha), \tilde{s}_0] - \mathbf{x}[0, \xi(0), \tilde{s}_0]\} \frac{d\mathbf{x}[0, \xi(0), \tilde{s}_0]}{ds} = 0$$

$$(14)$$

The above equation may have multiple solutions but we are interested in the solution that makes s a continuous function of $\xi(\alpha)$. There is no guarantee that eq 14 will be met for any geometry along the tunneling path. To find the solution to eq 14 for a geometry $\mathbf{x}[\alpha, \xi(\alpha), \tilde{s}_0]$ starting from region I, a root search procedure is set up starting from the reactants side turning point $\tilde{s}_0$, that is, at $\xi(\alpha) = 0$. The value of s that satisfies eq 14 is $s_I[\alpha, \xi(\alpha), \tilde{s}_0]$. In the same way can be found a value $s_{III}[\alpha, \xi(\alpha), \tilde{s}_0]$ starting from products at the classical turning point $\tilde{s}_1$. If it is not possible to find a geometry along the MEP that satisfies eq 14, it means that there is no projection for that geometry of the tunneling path onto the modes perpendicular to the reaction path in the interval $[\tilde{s}_0, \tilde{s}_1]$. When this happens going from reactants to products, the nonadiabatic region in the reactants side starts at $\xi(\alpha) = \xi_I(\alpha)$, being $\xi_I(\alpha)$ the last value for which $s_I[\alpha, \xi(\alpha), \tilde{s}_0]$ exists. In the same way, the nonadiabatic region in products side starts at $\xi(\alpha) = \xi_{III}(\alpha)$, being $\xi_{III}(\alpha)$ the last value for which $s_{III}[\alpha, \xi(\alpha), \tilde{s}_0]$ exists.

It may occur that $\xi_{III}(\alpha) < \xi_I(\alpha)$, so there is an overlap between the adiabatic regions and the nonadiabatic region does not exist. In this case, the vibrationally adiabatic potential in the interval $[\xi_{III}(\alpha), \xi_I(\alpha)]$ is evaluated as:

$$\min(V_a^G[s_I(0, \xi(0)); \tilde{s}_0], V_a^G[s_{III}(0, \xi(0)); \tilde{s}_0]) \qquad (15)$$

Each of the two $s_i(0, \xi(0))$, $i = I, III$ values needed for the evaluation of the vibrationally adiabatic potentials $V_a^G[s_i(0, \xi(0)); \tilde{s}_0)]$ is obtained from eq 14.

In the case that $\xi_{III}(\alpha) > \xi_I(\alpha)$, the potential is nonadiabatic in the region II, which has boundaries $\xi_I(\alpha)$ and $\xi_{III}(\alpha)$ with regions I and III, respectively. Therefore, region I corresponds to $0 \leq \xi(\alpha) < \xi_I(\alpha)$, region II to
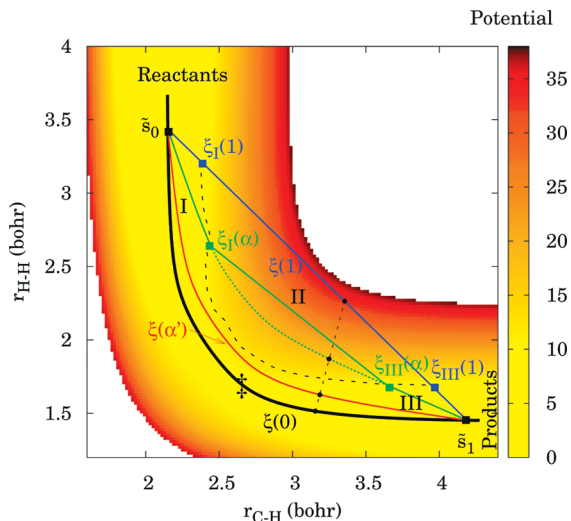
Figure 1. Plot of the JG PES (energy in kcal/mol) as a function of two distances; r_{C-H} is the distance between the carbon atom and the abstracted CH_4 hydrogen atom and r_{H-H} is the distance between the hydrogen atom and the abstracted CH_4 hydrogen atom. The graph also shows some possible reaction paths at a given tunneling energy with classical turning points given by $\tilde{s}_0$ and $\tilde{s}_1$ in the reactant and product sides, respectively. The reaction swath is partitioned into the adiabatic region of reactants (labeled as I), adiabatic region of products (labeled as III), and the nonadiabatic region (labeled as II and with boundaries given by a black dashed line). The symbol ‡ indicates the position of the saddle point, which is the conventional transition state. Four different paths are plotted as solid curves over the PES using eq 13. The four different values of α are 0 (black solid line), 0.10 (red line), 0.50 (green line), and 1 (blue line). The path with $\alpha = 0$ corresponds to the MEP and is labeled as $\xi(0)$. The path with $\alpha = 0.10$ (labeled as $\xi(\alpha')$) corresponds to a curved path passing through a region, which is completely vibrationally adiabatic. The path with $\alpha = 0.50$ (labeled as $\xi(\alpha)$) corresponds to a curved path, which crosses the nonadiabatic region with boundaries given by $\xi_I(\alpha)$ in the reactants side and by $\xi_{III}(\alpha)$ in the products side. In the nonadiabatic region, this path does not follow the curved path (green dotted line) but the straight path (green solid line). Finally, the path with $\alpha = 1$ (labeled as $\xi(1)$) corresponds to the straight path connecting the geometries of the MEP at the classical turning points. The nonadibatic region starts at $\xi_I(1)$ in the reactants side and ends at $\xi_{III}(1)$ in the products side. The black dashed line joining the straight path and the MEP indicates the progress along each of the four tunneling paths for a given value of γ (eq 10).

$\xi_I(\alpha) \leq \xi(\alpha) \leq \xi_{III}(\alpha)$, and region III to $\xi_{III}(\alpha) < \xi(\alpha) \leq \xi_P(\alpha)$. As shown in Figure 1, the path along regions I and III is given by eq 13, whereas the path along region II is a straight path between the boundaries, where the geometries are given by

$$\mathbf{x}[\alpha, \xi(\alpha), \tilde{s}_0] = \mathbf{x}[\alpha, \xi_I(\alpha), \tilde{s}_0] + \frac{\xi(\alpha) - \xi_I(\alpha)}{\xi_{III}(\alpha) - \xi_I(\alpha)} (\mathbf{x}[\alpha, \xi_{III}(\alpha), \tilde{s}_0] - \mathbf{x}[\alpha, \xi_I(\alpha), \tilde{s}_0]) \quad (16)$$

The nonadiabatic region is defined in the same way as for the LCG4 method, that is, the path is in the adiabatic region

when (i) the condition given by eq 14 is obeyed, (ii) all the generalized normal mode coordinates are within their vibrational turning points, (iii) the geometry $\mathbf{x}[\alpha, \xi(\alpha), \tilde{s}_0]$ lies within the single-valued region of the reaction path coordinates, and (iv) the adiabatic potential should be greater than or equal to the effective potential at the boundary of the nonadiabatic region; in the other case the nonadiabatic region is extended until this condition is met. On the other hand, if the adiabatic potential is smaller than the effective potential the difference is due to anharmonicity, so the effective potential is modified with a nonquadratic correction.

The imaginary action integral at every tunneling energy and for each α value along the paths of eq 13 is:

$$\theta(\alpha, \tilde{s}_0) = \frac{(2\mu)^{1/2}}{\hbar} \Big[\int_0^{\xi_I(\alpha)} d\xi(\alpha) \{ V_a^G[s_I(0, \xi(0); \tilde{s}_0)] - V_a^G(\tilde{s}_0) \}^{1/2} \cos \chi_0 \{ \tilde{s}_0, \hat{\boldsymbol{\eta}}[\alpha, \xi(\alpha), \tilde{s}_0] \} + \int_{\xi_I(\alpha)}^{\xi_{III}(\alpha)} d\xi(\alpha) \{ V_{eff}^{II}(\alpha, \xi(\alpha), \tilde{s}_0) - V_a^G(\tilde{s}_0) \}^{1/2} + \int_{\xi_{III}(\alpha)}^{\xi_P(\alpha)} d\xi(\alpha) \{ V_a^G[s_{III}(0, \xi(0); \tilde{s}_0)] - V_a^G(\tilde{s}_0) \}^{1/2} \cos \chi_1 \{ \tilde{s}_1, \hat{\boldsymbol{\eta}}[\alpha, \xi(\alpha), \tilde{s}_1] \} \Big]$$

$$(17)$$

The two cosines of eq 17, $\cos \chi_i \{ \tilde{s}_i, \hat{\boldsymbol{\eta}}[\alpha, \xi(\alpha), \tilde{s}_i] \}$ for $i = 0, 1$ are obtained as the dot products between the unit vectors $\hat{\boldsymbol{\eta}}[\alpha, \xi(\alpha), \tilde{s}_i]$ and the unit vectors tangent to the MEP at s_i, that is,

$$\cos \chi_i \{ \tilde{s}_i, \hat{\boldsymbol{\eta}}[\alpha, \xi(\alpha), \tilde{s}_i] \} = \hat{\boldsymbol{\eta}}[\alpha, \xi(\alpha), \tilde{s}_i] \frac{d\mathbf{x}(\tilde{s}_i)}{ds}, i = 0, 1 \quad (18)$$

The effective potential of eq 17 of the LAG4 method is the same as that of the LCG4 method, with the difference that now the geometries at which the potential is evaluated are functions of α and of the progress variable ξ, which also depends on α. Therefore, the effective potential is given by

$$V_{eff}^{II}(\alpha, \xi(\alpha), \tilde{s}_0) = V\{ \mathbf{x}[\alpha, \xi(\alpha), \tilde{s}_0] \} + V_{corr}^I(\alpha, \xi_I(\alpha), \tilde{s}_0) + V_{anh}^I(\alpha, \tilde{s}_0) + \frac{\xi(\alpha) - \xi_I(\alpha)}{\xi_{III}(\alpha) - \xi_I(\alpha)} [V_{corr}^{III}(\alpha, \xi_{III}(\alpha), \tilde{s}_0) - V_{corr}^I(\alpha, \xi_I(\alpha), \tilde{s}_0) + V_{anh}^{III}(\alpha, \tilde{s}_0) - V_{anh}^I(\alpha, \tilde{s}_0)] \quad (19)$$

The potentials $V_{corr}^i(\alpha, \xi_i(\alpha), \tilde{s}_0)$, $i = $ I, III correct for the zero-point energy in the modes that are still within their turning points. The potentials $V_{anh}^i(\alpha, \tilde{s}_0)$ incorporate anharmonic nonquadratic corrections to the effective potential in the same way as in the LCG4 method.

The optimum tunneling path (i.e., the LAG4 path) of the family of paths given by eq 13 is the one that minimizes the imaginary action integral of eq 17. The searching procedure is similar to the one described in ref 12, that is, the smallest value of $\theta(\alpha, \tilde{s}_0)$ is found by a quadratic search in α starting with a initial set of 11 equally spaced points. The optimum value of α at every tunneling energy is labeled as $\tilde{\alpha}$.

The tunneling amplitude of the LAG4 path initiated at $\tilde{s}_0$ is approximated using a primitive semiclassical expression

$$T_{\text{tun}}^{\text{LAG4}}(\tilde{\alpha}, \tilde{s}_0) = T_{\text{tun}}^{\text{LAG4}}(\tilde{\alpha}, \tilde{s}_1) = \exp\left[-\theta(\tilde{\alpha}, \tilde{s}_0)\right]$$

(20)

The LAG4 primitive probability, $P_{\text{prim}}^{\text{LAG4}}(E)$, is obtained from the tunneling amplitude of the previous eq 20 plus the contribution due to the vibrational motion perpendicular to the reaction coordinate along the incoming $T_0(E)$ and outgoing $T_1(E)$ trajectories at tunneling energy E

$$P_{\text{prim}}^{\text{LAG4}}(E) = |T_0(E) + T_1(E)|^2 + \left(\frac{\cos\chi_0\{\tilde{s}_0, \hat{\boldsymbol{\eta}}[\tilde{\alpha}, \xi(\tilde{\alpha})\tilde{s}_0] + \} \cos\chi_1\{\tilde{s}_1, \hat{\boldsymbol{\eta}}[\tilde{\alpha}, \xi(\tilde{\alpha}), \tilde{s}_1]\}}{2}\right)^2 \times \exp\left[-2\theta(\tilde{\alpha}, \tilde{s}_0)\right]$$

(21)

The tunneling amplitude of the incoming trajectory along the reaction coordinate is $\exp[-\theta(\tilde{\alpha}, \tilde{s}_0)] \times \cos\chi_0\{\tilde{s}_0, \hat{\boldsymbol{\eta}}[\tilde{\alpha}, \xi(\tilde{\alpha}), \tilde{s}_0]\}$ and that of the outgoing trajectory is $\exp[-\theta(\tilde{\alpha}, \tilde{s}_0)] \cos\chi_1\{\tilde{s}_1, \hat{\boldsymbol{\eta}}[\tilde{\alpha}, \xi(\tilde{\alpha}), \tilde{s}_1]\}$. The expression used in eq 21 is the average of the two tunneling amplitudes. Similarly the tunneling amplitude due to the all the vibrational degrees of freedom perpendicular to the reaction coordinate is averaged using $T_0(E)$ and $T_1(E)$, instead of using $2T_0(E)$, to inforce macroscopic reversibility. The expression for $T_0(E)$ is similar to the one given in ref 13 but evaluated along the LAG4 tunneling path ($\alpha = \tilde{\alpha}$) instead of along the LCG4 tunneling path ($\alpha = 1$).

The primitive probability of eq 21 can be greater than one because of the integration of the amplitudes over the incoming and outgoing trajectories, so it is enforced to go to $^1/_2$ at the maximum of the vibrational adiabatic potential V_a^{AG} by the expression

$$P^{\text{LAG4}}(E) = \left\{1 + \frac{1}{2}\frac{[P_{\text{prim}}^{\text{LAG4}}(V_a^{\text{AG}})^{-1}] - 1}{P_{\text{prim}}^{\text{LAG4}}(V_a^{\text{AG}})}P_{\text{prim}}^{\text{LAG4}}(E)\right\} \times \frac{1}{1 + [P_{\text{prim}}^{\text{LAG4}}(E)]^{-1}}$$

(22)

It is possible to include tunneling into excited vibrational states of products in the exoergic direction. It can be done easily by using the LAG4 approximation for the ground state and the LCG4 approximation for excited vibrational states. The procedure is described in detail in ref 13 and will not be discussed here. The LAT method in its LAG4 version has been implemented in *POLYRATE 2008*.[67]

4. Results and Discussion

In this section, we apply VTST/MT, including the LAG4 approximation for the evaluation of the transmission coefficients for two hydrogen abstraction reactions:

$$\text{H} + \text{CH}_4 \rightarrow \text{H}_2 + \text{CH}_3 \qquad \text{(R1)}$$

$$^{15}\text{H} + \text{CH}_4 \rightarrow {}^{15}\text{H} - \text{H} + \text{CH}_3 \qquad \text{(R2)}$$

Both reactions R1 and R2 were studied using the Jordan and Gilbert (JG) potential energy surface (their surface no. 2).[16] In the case of reaction R2, we just have changed the mass of the hydrogen, which is abstracting the proton, to that of a methyl group to observe the effect of the reaction-path curvature on the transmission coefficients. Both reactions are of the type A + BC → AB + C, where A, B, and C are atoms or groups of atoms. The reaction path curvature is a function of the skew angle, which in isoinertial coordinates is given by

$$\beta = \cos^{-1}\left(\frac{m_A m_C}{(m_A + m_B)(m_B + m_C)}\right)^{1/2}$$

(23)

The skew angle is close to 90° when B has a much larger mass than A and C and it is close to zero when the mass of A and C is much larger than the mass of B. For the latter, tunneling effects are more important because a light particle is being transferred between two heavy atoms (heavy-light-heavy system). For reaction R1, the skew angle is $\beta = 47°$, whereas for reaction R2 the skew angle is only $\beta = 20°$. From these values of the skew angle, we expect small values of $\tilde{\alpha}$ at all tunneling energies for reaction R1, because the reaction path curvature is small, whereas large values of $\tilde{\alpha}$ are expected for reaction R2. Indeed, this is the case at low tunneling energies, as shown in Figure 2, which plots the variation of θ with α for every tunneling energy for reactions R1 and R2. For any reaction-path curvature, the least-action path is always the path with the best compromise between length and energy, that is, between short paths with high barriers and long paths with low barriers. The two extreme cases are, on one hand, the straight path, which is the shortest path between two classical turning points but the most unfavorable from the energetic point of view and, on the other hand, the MEP, which is the longest path but the most favorable energetically. The transmission coefficients obtained using these two prescriptions are the LCT, for the straight path, and the ZCT, for the MEP.

For both reactions, at low tunneling energies and for the paths characterized by the optimum $\tilde{\alpha}$, there is an important area of the reaction swath that is vibrationally nonadiabatic and that involves a significant increase of the potential energy. That increase has to be compensated by shortening the length of the path. That compensation occurs for reaction R2, for which the curvature of the reaction path makes the straight path very short, but not for reaction R1, for which decreasing the length of the path does not compensate the increase in potential energy. This is why the incursion of the least-action path into the vibrationally nonadiabatic region is weaker for reaction R1 than for reaction R2. The sudden increase of the action integral observed in Figure 2 for reaction R2 at α values about 0.9 is due to the extension of the nonadiabatic region because for those paths there are geometries for which eq 14 is not satisfied. At high tunneling energies, the whole reaction swath is vibrationally adiabatic and, therefore, there is no rise in energy even for very short paths, so the least-action path coincides with the straight path.

The transmission coefficients and rate constants for reaction R1 are listed in Table 1 and Table 2 respectively, whereas the transmission coefficients for reaction R2 are listed in Table 3. The LAT results for reactions R1 and R2 show that SCT and LAT approximations underestimate the
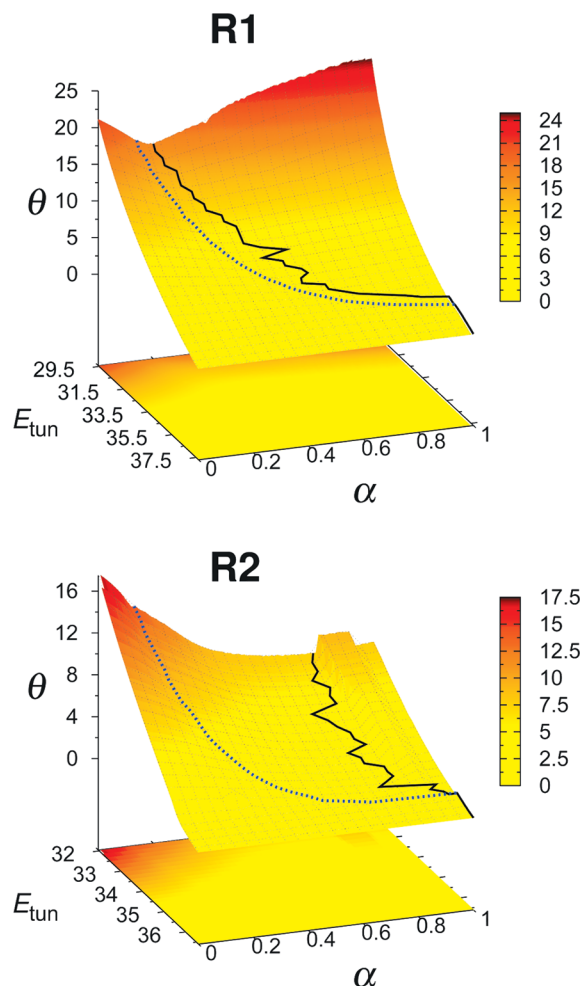
R1

R2

Figure 2. Graphs showing the variation of the imaginary-action integral with the α parameter at each of the tunneling energies (in kcal/mol) for reactions R1 and R2. The solid line indicates the locations of $\tilde{\alpha}$ at every tunneling energy. The dashed line indicates the lowest α value for which there is a nonadiabatic region when the paths given by eq 13 are followed in the direction from reactants to products.

Table 1. Transmission Coefficients for Reaction R1 on the JG Surface

T (K)	ZCT	SCT	LCT	μOMT	LAT
200	4.36	18.7	13.7	18.8	27.3
250	2.49	6.27	5.11	6.28	7.30
300	1.87	3.54	3.04	3.54	3.73
400	1.41	2.02	1.84	2.03	2.01
500	1.25	1.57	1.47	1.57	1.54

transmission coefficients for tunneling. As expected, SCT is better for small to intermediate curvature and LCT is better for large curvature. The μOMT transmission coefficient also underestimates tunneling but is the best choice when the LAT transmission coefficient is considered to be too expensive.

For reaction R1, we compare the thermal rate constants with accurate multidimensional quantum dynamical calculations[68] in the interval 200−500 K. There are also previous CVT/μOMT calculations[69] for the same interval of temperatures, which showed very good agreement with the previous quantum calculations. The CVT/LAT rate constants obtained in this work show even better agreement with the quantum

Table 2. VTST/MT Thermal Rate Constants (in cm³ Molecule⁻¹ s⁻¹) Compared to Accurate Quantal Ones for Reaction R1 on the JG Surface

T (K)	CVT/SCT[a]	CVT/LCT[a]	CVT/μOMT[a]	CVT/LAT[b]	accurate[c]
200	7.1(−21)[d]	5.2(−21)	7.1(−21)	1.0(−20)	9.0(−21)
250	4.3(−19)	3.5(−19)	4.3(−19)	5.0(−19)	5.5(−19)
300	7.8(−18)	6.7(−18)	7.8(−18)	8.2(−18)	9.8(−18)
400	3.6(−16)	3.3(−16)	3.6(−16)	3.6(−16)	4.0(−16)
500	4.1(−15)	3.8(−15)	4.1(−15)	4.0(−15)	3.8(−15)

[a] From ref 69. *[b]* This work. *[c]* From ref 68. *[d]* Powers of 10 in parentheses.

Table 3. Transmission Coefficients for Reaction R2 on the JG Surface

T (K)	ZCT	SCT	LCT	μOMT	LAT
200	2.98	4.62	31.3	31.3	36.5
250	2.08	2.83	11.3	11.3	12.5
300	1.69	2.12	6.14	6.14	6.59
400	1.35	1.56	3.10	3.10	3.23
500	1.22	1.34	2.16	2.16	2.22

results. The μOMT transmission coefficients are identical to the SCT ones, indicating that the least-action path is quite far from the straight path. Therefore, in this case the LCT transmission coefficients underestimate quantum effects. Sansón et al.[70] reached a similar conclusion for the H_2 + Cl reaction, which has similar skew angle to reaction R1. Because the skew angle for R1 is not large (small-to-intermediate curvature case), it is expected that the SCT transmission coefficient accounts well for tunneling. However, the comparison between SCT and LAT at $T = 200$ K shows that SCT underestimates tunneling at this temperature, although the difference is already small at room temperature. From the comparison of CVT/SCT and CVT/LAT with the accurate rate constants, it is difficult to know which of the two transmission coefficients is more accurate because both approximations lead to very good results; LAT could be more accurate than SCT because it finds the optimum tunneling paths in a set of paths at every tunneling energy and it includes nonadiabaticity; but SCT could also be more accurate because it incorporates a more accurate treatment of systems in the small-curvature limit.

When the curvature of the reaction path is large, as for reaction R2, SCT seriously underestimates tunneling at all temperatures in the range 200−500 K (Table 3) and, therefore, this approximation accounts poorly for quantum effects in this case. The LAT transmission coefficients are also larger than the LCT ones. The straight path used in the LCT method is a particular path in the family of paths generated by eq 13, and the LCT calculation corresponds, at every energy for which $\tilde{\alpha}$ does not equal 1 to an incompletely optimized LAG calculation (whereas SCT does not). Thus, whenever LCT differs from LAT, it gives less transmission probability. However, the LAT transmission factor is underestimated by LCT by only 14% at $T = 200$ K, and this percentage is reduced by half at room temperature.

To further analyze the tunneling, we examined, at every temperature, the integrand of eq 5, $P_W(E)$, which is the Boltzmann-weighted transmission probability. The value of P_W, with the zero of energy taken here as the maximum of
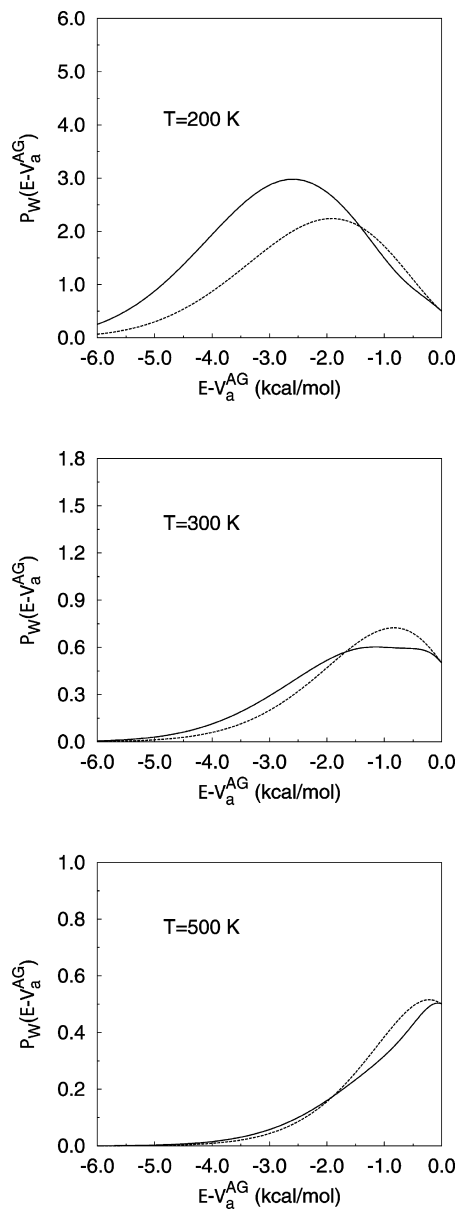
Least-Action Tunneling Transmission Coefficient

J. Chem. Theory Comput., Vol. 6, No. 1, 2010 **13**

Figure 3. Representation of the LAT (solid line) and μOMT (dashed line) Boltzmann-weighted probabilities versus tunneling energy at different temperatures for reaction R1. The tunneling energies labeling the abscissa are calculated using the maximum of the vibrationally adiabatic ground-state potential curve, V_a^{AG}, as the temporary zero of energy.

Figure 4. Same as Figure 3 but for reaction R2.

the vibrationally adiabatic ground-state potential curve, is shown at several temperatures for reactions R1 and R2 in Figures 3 and 4, respectively. The area under the curves gives the tunneling contribution to the transmission coefficients, which is clearly more important for reaction R2. Figures 3 and 4 also show how P_W varies with the tunneling energy for different transmission coefficients. Taking the LAT approximation as a reference approximation, we observe that for reaction R2 the μOMT curve follows closely the LAT curve, and as a consequence the μOMT transmission coefficients are quite similar to the LAT ones. For reaction R1, the μOMT transmission probabilities coincide with the SCT ones but that curve is quite far from the LAT curve at $T = 200$ K due to the difference in magnitude of the transmission coefficients. At $T = 300$ K and above the
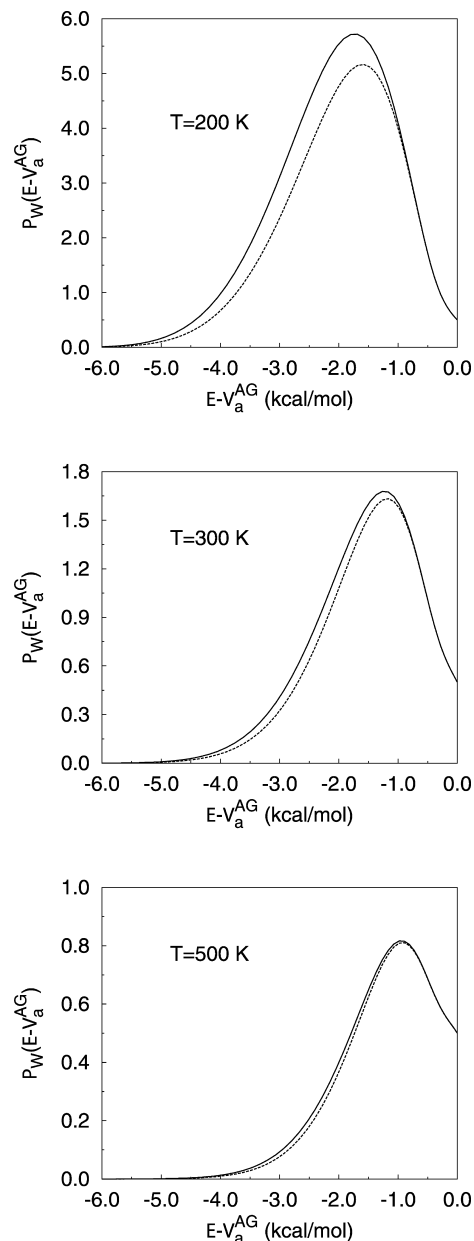
magnitude of SCT and LAT transmission coefficients is similar, and the curves are similar, but they differ in detail, with the μOMT (or SCT) probabilities being smaller at low tunneling energies, and bigger at high tunneling energies, when compared with the LAT probabilities. This behavior is observed even at $T = 200$ K and indicates that the SCT probabilities are too high at tunneling energies close to the top of the barrier. Another argument supporting this conclusion is offered during the discussion of the graphs depicted in Figure 5 and Figure 6.

The Boltzmann-weighted probability also allows one to identify the tunneling energy that contributes the most to each transmission coefficient. This characteristic energy is called representative tunneling energy (RTE), and it can be easily identified as the energy for which P_W has a maximum. The RTEs for reactions R1 and R2 obtained by each of the approximations for tunneling are listed in Tables 4 and 5, respectively. If the temperature is high, the maximum
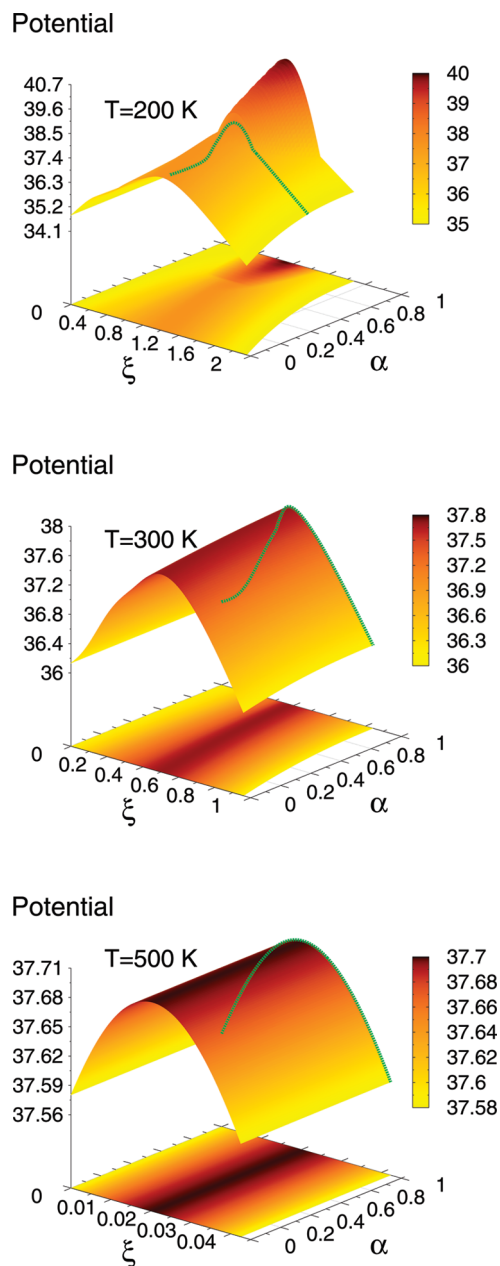
Potential

Potential

Potential

Potential

Potential

Potential

Figure 5. Effective potentials (in kcal/mol) at the representative tunneling energy for reaction R1 at different temperatures. The X axis is the length of the path, ξ (in a_0), and the Y axis is the α parameter (eq 13), which controls the curvature of the tunneling path. The green lines in each of the graphs are the least-action paths for that particular RTE. See text for details.

coincides with the top of the barrier, indicating that tunneling is unimportant. Whereas the LAT imaginary action integral and therefore the tunneling probability is the best compromise between length and energetics for the family of paths of eq 13, the RTE is the best compromise between the tunneling probability and the Boltzmann factor. It is obvious that at low temperatures the RTE is located at relatively low energies. In the limiting case, at $T = 0$ K the only contribution to the transmission coefficient comes from the tunneling probability at the lowest tunneling energy (i.e., the zero-point energy). As temperature increases, more energy levels are populated, and tunneling is possible at several
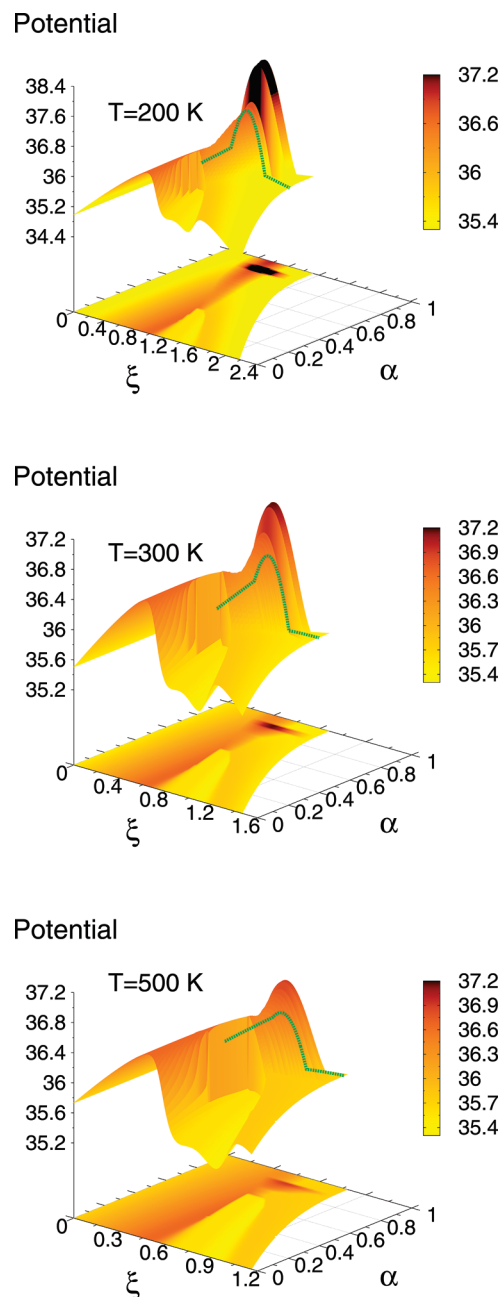
Figure 6. Same as Figure 5 but for reaction R2.

Table 4. Representative Tunneling Energies for Reaction R1 (in kcal mol^{-1})[a]

T (K)	ZCT	SCT	LCT	μOMT	LAT
200	37.03	35.68	36.07	35.68	34.75
250	37.29	36.42	36.14	36.42	36.11
300	37.42	36.81	36.18	36.81	36.16
400	37.61	37.21	37.46	37.21	37.45
500	37.70	37.39	37.59	37.39	37.58

[a] The maximum of the vibrationally adiabatic ground-state potential curve has an energy of 37.70 kcal mol^{-1}.

energies, and in this case we have to look for the least-action path at every tunneling energy. A quite different approach, known as the *instanton* theory[71,72] seeks, at every temperature (not at every energy) for a unique least-action periodic trajectory, called *instanton*, that represents all trajectories.

Least-Action Tunneling Transmission Coefficient

J. Chem. Theory Comput., Vol. 6, No. 1, 2010 **15**

Table 5. Representative Tunneling Energies for Reaction R1 (in kcal mol^{-1})^a

T (K)	ZCT	SCT	LCT	μOMT	LAT
200	35.90	35.81	35.01	35.01	34.95
250	36.14	35.86	35.34	35.34	35.11
300	36.28	36.00	35.53	35.53	35.52
400	36.57	36.23	35.71	35.71	35.71
500	36.65	36.37	35.74	35.74	35.74

^{a} The maximum of the vibrationally adiabatic ground-state potential curve has an energy of 36.66 kcal mol^{-1}.

Unfortunately, above a given critical temperature (usually for temperatures above 250 K) there is no *instanton* trajectory, although it is still possible to solve the problem approximately using analytical expressions.[73] There is a certain resemblance between RTE and *instanton* in the sense that, at every temperature, both indicate the most relevant region of the PES for tunneling.

Figures 5 and 6 depict effective potentials, which are given by eq 19 in the nonadiabatic region and by the vibrationally adiabatic ground-state potential in the adiabatic region, versus the length of the path for several values of α, taking as turning points the representative tunneling energies at $T = 200$, 300, and 500 K for reactions R1 and R2, respectively. Each of the graphs was generated by mapping the PES using eq 13. The green lines depicted in each of the graphs represent the least-action path. At $T = 200$ K the least action paths for both reactions, R1 and R2, have nonadiabatic regions, and the value of $\tilde{\alpha}$ is 0.62 and 0.83, respectively. For reaction R1 the ratio $\xi_P(\tilde{\alpha})/\xi_P(0)$ is 0.78 and the difference $V_{max}(\tilde{\alpha}) - V_a^{AG}$ is 0.64 kcal mol^{-1}, whereas for reaction R2 the ratio between lengths is 0.53 and the difference in energy is only 0.05 kcal mol^{-1}. Those numbers show that at $T = 200$ K the shortcut through the nonadiabatic region compensates the rise in energy for both reactions. This behavior is more noticeable for reaction R2, which exhibits a larger reaction-path curvature.

From the previous discussion it seems odd that, at $T = 300$ K, $\tilde{\alpha}$ is 1.00 and 0.93 for reactions R1 and R2 respectively but it is easily understood by taking into account that for the former reaction all members of the family of curves at that temperature from $\alpha = 0$ to $\alpha = 1$ lie completely in the adiabatic region, so the maximum of the effective potential is always the maximum of the vibrationally adiabatic ground-state potential, as shown in Figure 5. The consequence is that there is no energy penalty for shorter paths and, therefore, the least-action path coincides with the straight path. This circumstance does not occur for reaction R2, which has a nonadiabatic region for some values of α. Therefore, when the relevant part of the reaction swath is completely adiabatic the least-action path should be always the straight path and the probabilities obtained with the SCT approximation should not be larger than the LCT ones in that region of the PES. However this occurs for reaction R1, as shown previously in Figure 3. On the light of the values of the transmission coefficients obtained by the SCT and LAT approximations for R1 this issue seems unimportant, but in future work it would be interesting to analyze this behavior in more depth for a large number of reactive systems presenting varying amounts of reaction-path curvature.

In this work, we have used an analytical PES to show how the LAT approximation works for polyatomic systems. However, the method is very expensive in computer time, which is an obstacle for on-the-fly generation of the PES. The easiest solution to the problem is a brute-force approach consisting in the evaluation of several tunneling energies at the same time by parallelization of the method. A more reasonable approach would be to make use of different interpolation procedures to save computer time. The two graphs of Figure 2 give us a hint about a possible solution to the problem. In principle, it would be feasible to use a spline under tension similar to the one used in the ILCT2D[62] approximation, with the difference that, instead of interpolating tunneling paths and tunneling energies, we interpolate imaginary-action integrals and tunneling energies. It is possible to make the procedure even less expensive in computer time by interpolating the potential needed for the evaluation of the imaginary-action integral at every α value. A more detailed discussion about how to extend the LAT method to make it practical for its use within the direct dynamics approach will be presented elsewhere.

5. Concluding Remarks

We have extended the least-action tunneling (LAT) approximation to polyatomic reactions. The implementation is called least-action ground-state version 4 because it is based on the reactant ground state when the reaction is written in the exoergic or thermoneutral direction and because in the limit of large reaction-path curvature it reduces to the large-curvature tunneling (LCT) approximation carried out by the large-curvature ground-state version 4 (LCG4) method. The new method is more complete than the simpler microcanonically optimized multidimensional tunneling (μOMT) approximation, and in the tests presented here it is slightly more accurate. The method has been incorporated in the *POLYRATE* computer program.

References

(1) Gamow, G. *Z. Phys.* **1928**, *51*, 204.

(2) Eckart, C. *Phys. Rev.* **1930**, *35*, 1303.

(3) Johnston, H. S. *Gas Phase Reaction Rate Theory*; Ronald Press: New York, 1966.

(4) Wigner, E. *Z. Phys. Chem.* **1932**, *B19*, 203.

(5) Bell, R. *Proc. R. Soc. London, Ser. A* **1933**, *139*, 466.

(6) Garrett, B. C.; Truhlar, D. G. *J. Chem. Phys.* **1980**, *72*, 3460.

(7) Garrett, B. C.; Truhlar, D. G.; Bowman, J. M.; Wagner, A. F.; Robie, D.; Arepalli, S.; Presser, N.; Gordon, R. J. *J. Am. Chem. Soc.* **1986**, *108*, 3515.

(8) Alhambra, C.; Sanchez, M. L.; Corchado, J. C.; Gao, J.; Truhlar, D. G. *Chem. Phys. Lett.* **2002**, *355*, 388.

(9) Nagel, Z.; Klinman, J. P. *Chem. Rev.* **2006**, *106*, 3095.

(10) *Isotope Effects in Chemistry and Biology*; Kohen, A., Limbach, H. H., Eds.; CRC Press: Boca Raton, FL, 2006.

(11) *Hydrogen-Transfer Reactions*; Hynes, J. T., Klinman, J. P., Limbach, H. H., Schowen, R. L., Eds.; Wiley-VCH: Weinheim, Germany, 2007.

(12) Truhlar, D. G.; Isaacson, A. D.; Garrett, B. C. Generalized Transition State Theory. In *Theory of Chemical Reaction Dynamics*; Baer, M., Ed.; CRC Press: Boca Raton, FL, 1985; Vol. 4 pp 65−137.

(13) Fernández-Ramos, A.; Ellingson, B. A.; Garrett, B. C.; Truhlar, D. G. Variational Transition State Theory with Multidimensional Tunneling. In *Reviews in Computational Chemistry*; Lipkowitz, K. B., Cundari, T. R., Eds.; Wiley-VCH: Washington, D. C., 2007; Vol. 23 pp 125−232.

(14) Truhlar, D. G.; Gao, J.; Garcia-Viloca, M.; Alhambra, C.; Corchado, J.; Sanchez, M. L.; Poulsen, T. D. *Int. J. Quantum Chem.* **2004**, *100*, 1135.

(15) Pu, J.; Gao, J.; Truhlar, D. *Chem. Rev.* **2006**, *106*, 3140.

(16) Jordan, M.; Gilbert, R. *J. Chem. Phys.* **1995**, *102*, 5669.

(17) Wigner, E. *J. Chem. Phys.* **1937**, *5*, 720.

(18) Horiuti, J. *Bull. Chem. Soc. Jpn.* **1938**, *13*, 210.

(19) Keck, J. C. *Adv. Chem. Phys.* **1967**, *13*, 85.

(20) Garrett, B. C.; Truhlar, D. G. *J. Chem. Phys.* **1979**, *70*, 1593.

(21) Garrett, B. C.; Truhlar, D. G. *Acc. Chem. Res.* **1980**, *13*, 440.

(22) Pechukas, P. *Annu. Rev. Phys. Chem.* **1981**, *32*, 159.

(23) Truhlar, D. G.; Hase, W. L.; Hynes, J. T. *J. Phys. Chem.* **1983**, *87*, 2664.

(24) Truhlar, D. G.; Garrett, B. C. *Annu. Rev. Phys. Chem.* **1984**, *35*, 159.

(25) Truhlar, D. G.; Garrett, B. C. *Annu. Rev. Phys. Chem.* **1984**, *35*, 159.

(26) Truhlar, D. G.; Garrett, B. C.; Klippenstein, S. J. *J. Phys. Chem.* **1996**, *100*, 12771.

(27) Eyring, H. *J. Chem. Phys.* **1935**, *3*, 107.

(28) Evans, M. G.; Polanyi, M. *Trans. Faraday Soc.* **1935**, *31*, 875.

(29) Tucker, S. C.; Truhlar, D. G. *NATO ASI Ser. C* **1989**, *13*, 291.

(30) Hirschfelder, J. O.; Wigner, E. *J. Chem. Phys.* **1939**, *7*, 616.

(31) Truhlar, D. G.; Kupperman, A. *J. Am. Chem. Soc.* **1971**, *93*, 1840.

(32) Kuppermann, A. *J. Phys. Chem.* **1979**, *83*, 171.

(33) Garrett, B. C.; Truhlar, D. G.; Grev, R. S.; Magnuson, A. W. *J. Phys. Chem.* **1980**, *84*, 1730.

(34) Fukui, K.; Kato, S.; Fujimoto, H. *J. Am. Chem. Soc.* **1975**, *97*, 1.

(35) Garrett, B. C.; Truhlar, D. G. *J. Phys. Chem.* **1979**, *83*, 1052.

(36) Pollak, E.; Pechukas, P. *J. Am. Chem. Soc.* **1978**, *100*, 2984.

(37) Fernández-Ramos, A.; Ellingson, B. A.; Meana-Pañeda, R.; Marques, J.; Truhlar, D. G. *Theor. Chem. Acc.* **2007**, *118*, 813.

(38) Ellingson, B. A.; Lynch, B. A.; Mielke, S. L.; Truhlar, D. G. *J. Chem. Phys.* **2006**, *125*, 84305.

(39) Sturdy, Y. K.; Clary, D. C. *Phys. Chem. Chem. Phys.* **2007**, *9*, 2397.

(40) Truhlar, D. G.; Kuppermann, A. *J. Chem. Phys.* **1972**, *56*, 2232.

(41) Allison, T. C.; Truhlar, D. G. Testing the Accuracy of Practical Semiclassical Methods: Variational Transition State Theory with Optimized Multidimensional Tunneling. In *Modern Methods for Multidimensional Dynamics Computations in Chemistry*; World Scientific: Singapore, 1998; pp 618–712.

(42) Wyatt, R. E. *J. Chem. Phys.* **1969**, *51*, 3489.

(43) Marcus, R. A. *J. Chem. Phys.* **1966**, *45*, 4493.

(44) Marcus, R. A.; Coltrin, M. E. *J. Chem. Phys.* **1977**, *67*, 2609.

(45) Garrett, B. C.; Truhlar, D. G. *Proc. Natl. Acad. Sci. U.S.A.* **1979**, *76*, 4755.

(46) Skodje, R. T.; Truhlar, D. G.; Garrett, B. C. *J. Phys. Chem.* **1981**, *85*, 3019.

(47) Skodje, R. T.; Truhlar, D. G.; Garrett, B. C. *J. Chem. Phys.* **1982**, *77*, 5955.

(48) Lu, D.-h.; Truong, T. N.; Melissas, V. S.; Lynch, G. C.; Liu, Y.-P.; Garrett, B. C.; Steckler, R.; Isaacson, A. D.; Rai, S. N.; Hancock, G. C.; Lauderdale, J. G.; Joseph, T.; Truhlar, D. G. *Comput. Phys. Commun.* **1992**, *71*, 235.

(49) Liu, Y.-P.; Lynch, G. C.; Truong, T. N.; Lu, D.-h.; Truhlar, D. G. *J. Am. Chem. Soc.* **1993**, *115*, 2408.

(50) Babamov, V. K.; Marcus, R. A. *J. Chem. Phys.* **1978**, *74*, 1790.

(51) Garrett, B. C.; Truhlar, D. G.; Wagner, A. F.; Dunning Jr, T. H. *J. Chem. Phys.* **1983**, *78*, 4400.

(52) Garrett, B. C.; Abusalbi, N.; Kouri, D. J.; Truhlar, D. G. *J. Chem. Phys.* **1985**, *83*, 2252.

(53) Garrett, B. C.; Joseph, T.; Truong, T. N.; Truhlar, D. G. *Chem. Phys.* **1989**, *136*, 271.

(54) Truong, T. N.; Lu, D.-h.; Lynch, G. C.; Liu, Y.-P.; Melissas, V. S.; Stewart, J. J. P.; Steckler, R.; Garrett, B. C.; Isaacson, A. D.; González-Lafont, A.; Rai, S. N.; Hancock, G. C.; Joseph, T.; Truhlar, D. G. *Comput. Phys. Commun.* **1993**, *75*, 143.

(55) Liu, Y.-P.; Lu, D.-h.; González-Lafont, A.; Truhlar, D. G.; Garrett, B. C. *J. Am. Chem. Soc.* **1993**, *115*, 7806.

(56) Fernández-Ramos, A.; Truhlar, D. G. *J. Chem. Phys.* **2001**, *114*, 1491.

(57) Miller, W. H.; Ruf, B. A.; Chang, Y. T. *J. Chem. Phys.* **1988**, *89*, 6298.

(58) Ruf, B. A.; Miller, W. H. *J. Chem. Soc., Faraday Trans. 2* **1988**, *84*, 1523.

(59) Makri, N.; Miller, W. H. *J. Chem. Phys.* **1989**, *91*, 4026.

(60) Kreevoy, M. M.; Ostovic, D.; Truhlar, D. G.; Garrett, B. C. *J. Phys. Chem.* **1986**, *90*, 3766.

(61) Fernández-Ramos, A.; Truhlar, D. G.; Corchado, J.; Espinosa-Garcia, J. *J. Phys. Chem. A* **2002**, *106*, 4957.

(62) Fernández-Ramos, A.; Truhlar, D. G. *J. Chem. Theory Comput.* **2005**, *1*, 1063.

(63) Garrett, B. C.; Truhlar, D. G. *J. Chem. Phys.* **1983**, *79*, 4931.

(64) Lynch, G. C.; Truhlar, D. G.; Garrett, B. C. *J. Chem. Phys.* **1989**, *90*, 3102.

(65) Taketsugu, T.; Kimihiko, H. *J. Chem. Phys.* **1997**, *107*, 10506.

(66) (a) Tautermann, C. S.; Voegele, A. F.; Loerting, T.; Liedl, K. R. *J. Chem. Phys.* **2002**, *117*, 1962. (b) Tautermann, C. S.; Voegele, A. F.; Loerting, T.; Liedl, K. R. *J. Chem. Phys.* **2002**, *117*, 1967. (c) Tautermann, C. S.; Voegele, A. F.; Liedl, K. R. *J. Chem. Phys.* **2004**, *120*, 631.

Least-Action Tunneling Transmission Coefficient

J. Chem. Theory Comput., Vol. 6, No. 1, 2010 **17**

(67) Zheng, J.; Zhang, S.; Lynch, B. J.; Corchado, J. C.; Chuang, Y.-Y.; Fast, P. L.; Hu, W.-P.; Liu, Y.-P.; Lynch, G. C.; Nguyen, K. A.; Jackels, C. F.; Fernández Ramos, A.; Ellingson, B. A.; Melissas, V. S.; Villa, J.; Rossi, I.; Coitiño, E. L.; Pu, J.; Albu, T. V.; Steckler, R.; Garrett, B. C.; Isaacson, A. D.; Truhlar, D. G. *POLYRATE 2008*; University of Minnesota: Minneapolis, 2008.

(68) (a) Bowman, J. M.; Wang, D.; Huang, X.; Huarte-Larrañaga, F.; Manthe, U. *J. Chem. Phys.* **2001**, *114*, 9683. (b) Huarte-Larrañaga, F.; Manthe, U. *J. Chem. Phys.* **2002**, *116*, 2863.

(69) (a) Pu, J. C.; Corchado, J.; Truhlar, D. G. *J. Chem. Phys.* **2001**, *115*, 6266. (b) Pu, J.; Truhlar, D. G. *J. Chem. Phys.* **2002**, *117*, 1479.

(70) Sansón, J. A.; Sánchez, M. L.; Corchado, J. *J. Phys. Chem. A* **2005**, *110*, 589.

(71) (a) Miller, W. H. *J. Chem. Phys.* **1975**, *62*, 1899. (b) Coleman, S. *Phys. Rev. D* **1977**, *15*, 2929. (c) Benderskii, V.; Makarov, D. E.; Wight, C. H. *Adv. Chem. Phys.* **1994**, *88*, 1.

(72) Zhao, Y.; Yamamoto, T.; Miller, W. H. *J. Chem. Phys.* **2004**, *120*, 3100.

(73) Fernández-Ramos, A.; Smedarchina, Z.; Siebrand, W.; Zgierski, M. Z.; Rios, M. A. *J. Am. Chem. Soc.* **1999**, *121*, 6280.

JCTC Journal of Chemical Theory and Computation

Properties of a Method for Performing Adaptive, Multilevel QM Simulations of Complex Chemical Reactions in the Gas-Phase

M. Graham Guthrie,[†] April D. Daigle,[‡] and Michael R. Salazar*,[†]

Department of Chemistry, Union University, 1050 Union University Drive, Jackson, Tennessee 38305 and Department of Chemistry, Dartmouth College, 6128 Burke Laboratory, Hanover, New Hampshire 03755

Abstract: The properties of a new method of performing molecular dynamic simulations of complex chemical processes are presented. The method is formulated to give a time-dependent, multilevel representation of the total potential that is derived from spatially resolved quantum mechanical regions. An illustrative simulation is performed on a 110 atom system to demonstrate the continuity and energy conserving properties of the method. The effect of a discontinuous total potential upon the kinetic energy of the system is examined. The discontinuities in the magnitude of atomic force vectors due to changing the electronic structure during the simulation are examined as well as the effect that these discontinuities have upon the atomic kinetic energies. The method, while not conserving total energy, does yield canonical (NVT) simulations. The time reversibility property of the simulation with an extremely discontinuous total potential is discussed. The computational scaling associated with the formation of the spatially resolved, time-dependent groups is also investigated.

1. Introduction

Multiscale modeling of chemical processes has gained much popularity as theoreticians begin to move from what can be calculated on the atomic scale and attempt to join these results to give insight into the meso- and macroscopic scale. Often these simulations involve a mixture of a single high-level quantum mechanical (QM) region surrounded by a lower level molecular mechanical (MM) region. These so-called QM/MM simulations have proven enormously successful in studying many different chemical phenomena, and several review articles have recently appeared.[1−15] In particular, biochemical phenomena have proven to be a fruitful venue of application for chemical modeling via QM/MM methods.[1,4−6,8−10,12,16−20] In these QM/MM simulations, the chemical system is broken into differing regions because the QM calculations needed to understand the phenomena in the QM region, if applied to the whole system,

would be computationally prohibitive and would be an inefficient use of computer resources, since what happens inside the MM region only affects the QM region in a derivative manner.

Most often QM/MM methodology is formulated in a static manner, where the defined QM region (that may involve as little as a few atoms to multiples of tens of atoms or molecules) is connected to a defined MM region (typically involving orders of magnitude more atoms/molecules as that found in the QM region), and these regions remain fixed during the course of the simulation. Recently, however, time-dependent (or adaptive) partitioning between the QM and MM regions has provided a means of atomic exchange between regions, where the QM and MM regions are free to change as a function of the simulation time.[21−32] This feature is particularly important when studying chemical systems where the phenomena change significantly in time, such as complex reactive systems, solution dynamics, diffusion, and reactions on surfaces. Perhaps the primary difficulty in these dynamically defined QM/MM methods is the significant discontinuities in the total potential (and,

---

* Corresponding author. E-mail: msalazar@uu.edu.
† Union University.
‡ Dartmouth College.

QM Simulations of Complex Reactions

J. Chem. Theory Comput., Vol. 6, No. 1, 2010 **19**

perhaps, the atomic force field) and the result that the total energy is not a conserved quantity.[21,24−33] The recent adaptive partitioning method of Heyden and Truhlar[22,23] has been uniquely formulated in a manner that is able to make the connection between dynamically resolved QM and MM regions in a way that does not induce discontinuities in the potential energy and forces, which ensures microcanonical (NVE) ensemble simulations that conserve energy, angular, and linear momentum. The method connects the QM and MM zones through a buffer zone that ensures a smooth transition in the potential and atomic forces for atomic passage by means of $2N$ or N additional multilevel calculations of the buffer zone, where N is the number of groups in the buffer zone.

However, the significant discontinuities resulting in the total potential from time-dependent QM/MM methods has been shown not to induce deviations in the simulations themselves.[21,24,29] The reason for this is that the motions of the atoms in the simulation depend on the gradient of the potential (which yields the force field) and not on the potential itself. Thus, in order to have accurate and smooth simulations, the gradients must be continuous between time steps, not the potential. However, a discontinuous potential will not yield the conservation of the total energy (thus, not a microcanonical ensemble). In spite of this, simulations within the canonical ensemble (NVT) may be obtained from time-dependent QM/MM simulations, if the gradients are approximately continuous. Continuous gradients of the potential yield continuity in the kinetic energy and the smooth atomic motions between time steps where there may be a very large discontinuity in the potential.

When considering chemical systems that lend themselves to necessarily being studied by a time-dependent QM/MM methodology, perhaps the most compelling case is that of the simulation of gas-phase complex reactive processes. These complex processes may be spread over 1 000s of individual reactions with 100s of unique chemical species formed during the entire process.[34−39] In addition, the reactive channels have rates that are both temperature and pressure sensitive. Presently, the chemistry associated with these complex reactive processes is obtained through sophisticated methods of mechanistic postulation.[40−42] Mechanisms are postulated and reduced to the smallest number of reactions possible. Rate coefficients for the individual steps are obtained by fitting to experimental data through the design of experiments for the isolation of the individual reactions to obtain the rate coefficients and through the use of transition-state theory and/or molecular dynamics.[43] In this methodology of postulation and solving for the rate coefficients, the simulated dynamics of the chemical system are determined from the kinetics, rather than the reverse.

And that the kinetics determines the dynamics is for sufficient reason, since direct molecular dynamic simulations of these processes are extremely difficult and have only recently been performed through the use of empirical reactive force fields.[44−47] Consider, these systems are composed of individual reactions that may scale between picoseconds to as long as nanoseconds and between whole processes that are on the order of nano to microseconds. Furthermore,

because the chemistry involves so many reactive channels, 100s to 1 000s of atoms are needed in order to perform a meaningful simulation. Thus, simulation of these complex reactive gas-phase systems involves multiscale modeling in both time and system size, necessitating a time-dependent QM/MM methodology, if high-level QM calculations are to be used in order to understand these complex reactive processes.

In addition to requiring a time-dependent QM/MM methodology for the simulation of these complex gas-phase reactive processes, these systems further require a multilevel QM description of the potential. This is the case because a single level of QM theory will not be able to cover all the reactive and nonreactive collisional processes sufficiently well. Consider the treatment of a radical reaction at the same level of theory as a bath gas collisional process. A level of theory sufficient for the radical reaction is too high a level for bath gas collisions, and a level appropriate for the bath gas collisional process is insufficient for the radical reaction. Thus, these complex reactive gas-phase processes require a multilevel QM description due to the difficulties in obtaining accurate potentials for the diverse and numerous collisional processes.

One way of mitigating some of the computational difficulties associated with performing direct molecular dynamic simulations of these complex reactive processes has been suggested through the formulation of the total potential into time-dependent, spatially-resolved groups over which multiple levels of electronic structure may be applied.[29] This method allows one to avoid the use of a single level of electronic structure for all interactions within the simulation. Spatially resolved groups are formed during the course of the simulation, and an appropriate level of QM theory is applied to the groups depending on their chemical nature. This time-dependent, multilevel QM methodology allows the use of high levels of electronic structure for demanding reactive collisions, while also allowing use of lower levels of electronic structure for nonreactive collisional processes.

The subject of this work is an examination into the properties of such a time-dependent, multilevel QM molecular dynamics method. The method may be represented as nQM (QM1/QM2/QM3/..., where each QM level is for individual groups). The intergroup (group−group) MM interactions were set to zero for this study. A 110 atom nonreactive simulation is performed in order to examine the continuity properties of this adaptive nQM method. The simulation and levels of theory chosen for the various groups are described in Section II. Section III examines energy continuity and conservation properties that result from a time-dependent, multilevel QM description of the potential. The continuity of the atomic forces is examined in Section IV over two changes in groups where the QM levels describing the groups differ widely. The atomic kinetic energies of the atoms involved in the two groups are also examined. Section V examines the time reversibility of the simulations. The computational scaling associated with the formation of the groups is investigated in Section VI. The conclusions are given in Section VII along with a brief description of the future development of the computational tools in order to

perform direct molecular dynamic simulation of complex reactive processes in the gas-phase.

II. Illustrative Simulation

In order to examine the properties of a time-dependent, multilevel QM molecular dynamics methodology, a 110 atom simulation with 10 ethylene (C_2H_4), 10 carbon dioxide (CO_2), and 10 carbon monoxide (CO) molecules were placed into a cubic simulation cell of size 65 bohr per side and a total volume of 40.70 nm^3. The molecules were randomly placed in the simulation cell and equilibrated at a temperature of 300 K using ReaxFF,[48] giving an ideal pressure of 30.1 atm. After equilibration with ReaxFF, the atomic coordinates and velocities of the system were used as initial conditions for a nonthermostated simulation. For this 110 atom system, individual C_2H_4, CO_2, and CO molecules were treated at MP2/McLean and Chandler (MC), SVWN/6-31G, and RHF/STO-3G levels of theory, respectively. For groups mixed with combinations of molecular systems, the following rules were employed: combinations of molecules containing all three CO, CO_2, and C_2H_4 species, the RHF/STO-3G level of theory was employed; for CO and C_2H_4 only, the SVWN/6-31G level of theory was employed; for any combination of CO_2 and C_2H_4 with fewer than 20 atoms, the MP2/MC level of theory was used; for any combination of CO_2 and C_2H_4 with more than 20 atoms, the RHF/STO-3G level of theory was employed. Although not exhaustive, these rules were sufficient for the simulations reported herein. The 20 atom break was used to ensure that the simulation would not require more memory than available. The GAMESS electronic structure suite of programs was used to calculate the energy and gradients during the course of the simulation.[49] A 3.86 Å (7.30 bohr) diatom spatial cutoff was used to define the groups. Thus, any atom pair within this cutoff will be part of the same group (Section VI has more information on group formation). A larger spatial cutoff will have even better continuity properties than illustrated below.

In addition, the levels of electronic structure and basis sets were specifically chosen to ensure very significant changes in the level of theory used for describing the groups. In fact, it is recognized (and was such designed) that these selections represent poorer choices than would likely be used, resulting in much larger changes in the description of electronic structure when the groups change. Thus, the continuity properties outlined in this work were designed to be closer to the worst-case scenario, rather than the best that can be achieved.

III. Continuity and Conservation Properties

a. Potential and Total Energy. The 110 atom simulation began with a connectivity list given in Table 1 and a total potential energy of $-3.7522050175 \times 10^3$ Hartrees. A time step of 10 au of time (~0.242 fs) was employed for the simulation and Hamilton's 6N first-order equations of motion were solved using a velocity Verlet numerical integrator. Shown in Figure 1 are plots of the total potential energy (y-axis) and the energy conservation ($E(t) - E(0)$, secondary y-axis) as a function of simulation time, where the total
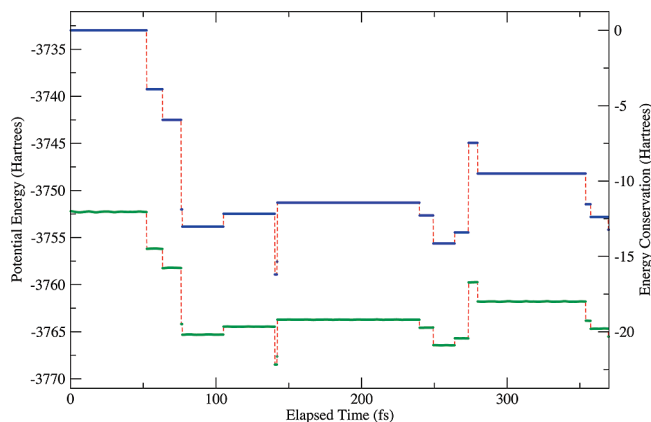

Figure 1. Continuity in the total potential energy (y-axis, green circles and red-dashed lines) and the conservation of total energy (secondary y-axis, blue circles and red-dashed lines) for an 110 atom simulation.

Table 1. The Groups at the Beginning of the 110 Atom Simulation

group size	number of members	molecules in group	level of theory
2	5	CO	RHF/STO-3G
3	3	CO_2	SVWN/6-31G
5	1	CO, CO_2	RHF/STO-3G
6	4	C_2H_4	MP2/MC
9	2	CO_2, C_2H_4	MP2/MC
11	1	CO, CO_2, C_2H_4	RHF/STO-3G
14	1	CO, 2 CO_2, C_2H_4	RHF/STO-3G
19	1	2 CO, CO_2, 2 C_2H_4	RHF/STO-3G

potential energy is shown as small green circles connected by red-dashed lines and the energy conservation is shown as small blue circles connected by red-dashed lines. This figure shows that the total potential energy begins smoothly with small oscillations in the total potential due to the intragroup interactions (vibrations and internal attractions and repulsions within the initial groups given in Table 1). At a simulation time of 52.5 fs, there is a discontinuous drop in the potential of 3.903 Hartrees, where a CO/CO_2/C_2H_4 11-mer group treated at the RHF/STO-3G level of theory dissociated to a CO/C_2H_4 8-mer plus a CO_2 3-mer, with each product group treated at the SVWN/6-31G level of theory. Continued changes in groups are seen at subsequent times of 63.4, 76.2, 76.9, 105.2, 140.5, 142.0, 142.2, 240.0, 249.4, 264.1, 273.6, 279.9, 354.1, 357.5, 369.4 fs with potential energy changes of −2.037, −5.947, −1.135, +0.848, −4.021, +0.850, +3.917, −0.851, −1.862, +0.733, +5.948, −2.042, −2.036, −0.844, −0.849 hartree, respectively.

In examining the conservation of energy, Figure 1 shows that energy is completely conserved (maximum value of -1.052×10^{-4} Hartrees) until the first change of groups at 52.5 fs where the total potential is discontinuous, resulting in the same discontinuity in the total energy. Also shown in Figure 1 is the result that, because groups are formed on the basis of internuclear spatial cutoffs, sometimes the groups (and, thus, levels of QM theory) change rapidly. This is best illustrated at time steps of 76.2, 140.5, and 142.0 where the groups remained unchanged for only 3, 6, and 1 time step, respectively, resulting in a rapidly changing total potential.
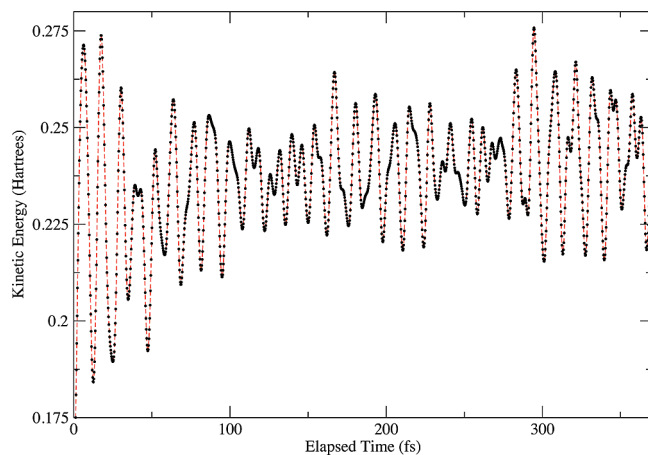
QM Simulations of Complex Reactions

J. Chem. Theory Comput., Vol. 6, No. 1, 2010 **21**

Figure 2. Continuity of the total kinetic energy for 110 atom simulation.
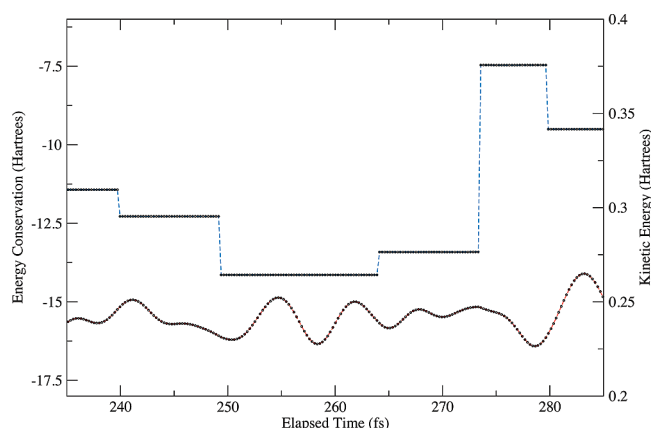

Figure 3. Total energy conservation (black circles connected with blue-dashed line) and continuity of the total kinetic energy (black circles connected by red line) in time window between 235 and 285 fs, where there are five changes in groups.

a. Kinetic Energy. Shown in Figure 2 is a plot of the kinetic energy for the 110 atom simulation of Figure 1 over the same time period. The kinetic energy at each time is shown as small black-filled circles connected by red-dashed lines. This figure shows that, while the total potential undergoes the radical discontinuities seen in Figure 1, the total kinetic energy remains continuous throughout. This is better illustrated in Figure 3, which shows the energy conservation (black circles connected by blue-dashed lines) and the kinetic energy (black circles connected by red-dashed lines) at times between 235 and 285 fs, where there were five changes in the groups and the resulting discontinuity in the total potential. As seen in this figure, the total energy undergoes large discontinuities (of over $+5.9$ Hartees at $t = 273.6$ fs), while the kinetic energy is continuous through all these changes, which yields very smooth atomic motions between these extremely large discontinuities in the potential.

To further examine the smoothness of the kinetic energy, the time derivative of the kinetic energy was calculated at each time step within the 235−285 fs simulation window displayed in Figure 3, and these results are shown in Figure 4. The time steps where there was a change in groups and the QM levels of theory used to describe those groups are shown as blue boxes. Figure 4 shows that the gradient of
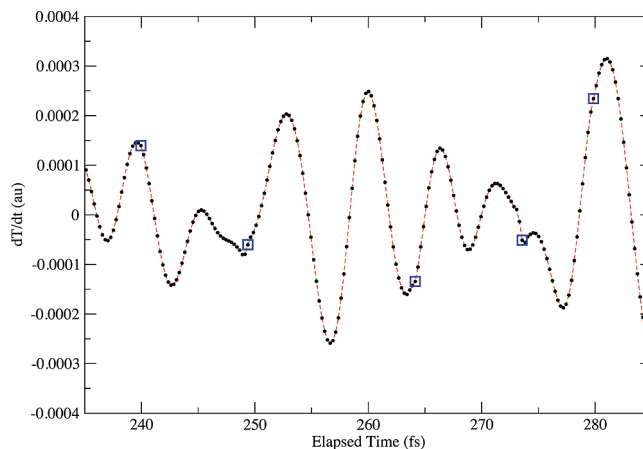

Figure 4. Time derivative of kinetic energy (T) in atomic units in 235−285 fs window. The blue boxes are where there is a change in groups.

the kinetic energy is continuous (C0 continuity), which alone is sufficient for a smooth and continuous kinetic energy. Furthermore, at all times where there was a change in groups and a resulting discontinuity in the total potential, the derivative of the kinetic energy immediately after the change is very smooth, with the possible exception of the point at 273.6 fs where there is a small kink. A similar kink is seen at $t = 248.9$ fs, where there was not a change in groups. Examining the second time derivative of the kinetic energy (time derivative of Figure 4, not shown) demonstrates that it is discontinuous in this short time window at a few of the times where there is a change in groups ($t = 249.4$, 264.1, and 273.6 fs). However, the second derivative of the kinetic energy is also discontinuous at times where there are no changes in the groups. The result of this analysis is that continuity of the time derivative of the kinetic energy is sufficient to guarantee a smooth and continuous kinetic energy. Figure 4 shows that this 110 atom simulation has a continuous derivative of the kinetic energy (and, thus, a smooth kinetic energy) when the potential undergoes frequent and significant discontinuities. In addition, the results of Figures 3 and 4 are for a spatial cutoff of 3.86 Å (7.30 bohr). Enlarging the spatial cutoff will improve the smoothness and continuity of the kinetic energy and the gradient of the kinetic energy, respectively.

IV. Atomic Force Continuity

The energy continuity and conservation properties of the 110 atom simulation shown in Figures 1−4 demonstrates that formulating the total potential as time-dependent, multilevel QM groups will result in a radically discontinuous potential with the resulting total energy not being a conserved quantity. However, examining the energy conservation plot of Figures 1 and 3 shows that as long as the groups remain unchanged, the total energy is a conserved quantity. Thus, what is changing with a change in groups is simply the reference total energy, $E(0)$. This is the case because the groups change at spatial cutoffs that are at, or near, the asymptotic region where the gradients of the potential will have approximately the same value, namely zero. Furthermore, the kinetic energy remained continuous despite very significant changes in the
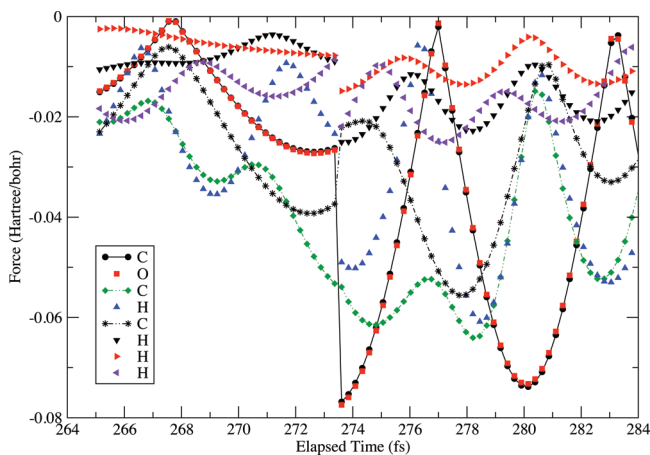
Figure 5. Continuity in the magnitude of the atomic force vectors for 8 of the 14 atoms involved in the change of groups at 273.6 and 279.9 fs.
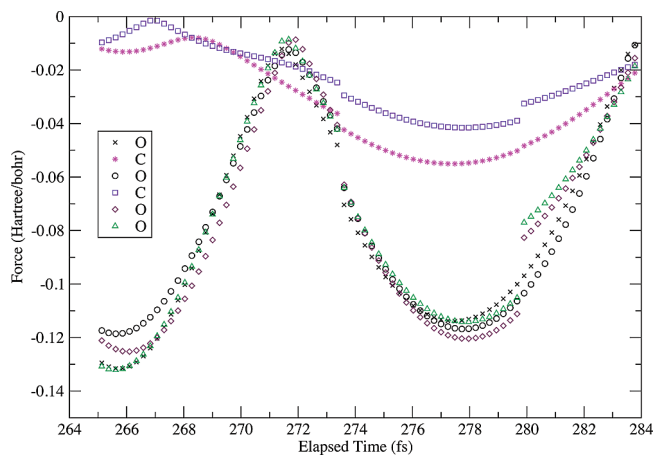

Figure 6. Continuity in the magnitude of the atomic force vectors for the remaining 6 of the 14 atoms involved in the change of groups at 273.6 and 279.9 fs.
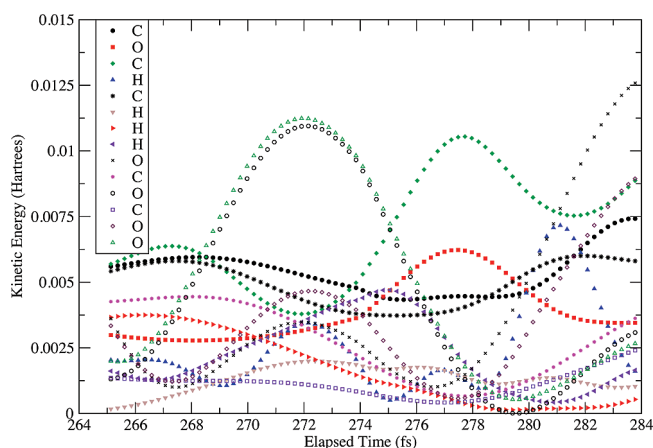

Figure 7. Continuity in the atomic kinetic energies of the 14 atoms involved in the change of groups at 273.6 and 279.9 fs.

level of theory and of basis sets used to describe the intragroup interactions (potentials and forces). During some changes, CO, CO_2, and C_2H_4 molecules went from a low-level RHF/STO-3G to higher levels of theory and larger basis sets of SVWN/6-31G and MP2/MC and vice versa. The levels of theory and basis sets were both chosen to illustrate that even with these large changes in the description of the electronic structure, where local bond distance minima and potential energy profiles will change with the change in levels of electronic structure theory, the kinetic energy remains continuous throughout.

In order to examine the changes in the intragroup atomic forces resulting from changes in QM levels of theory, the magnitude of the atomic force vectors were calculated over the range from 265 to 284 fs, where there were two different changes in groups that involved the same atoms. At 273.6 fs, a $(CO_2)_2$ 6-mer joined a C_2H_4/CO 8-mer to form a 14-mer supermolecule. The 6-, 8-, and 14-mer groups were treated at the MP2/MC, SVWN/6-31G, and RHF/STO-3G levels of theory, respectively. In addition, at 279.9 fs this same $(CO_2)_2$/C_2H_4/CO 14-mer group (RHF/STO-3G) dissociated into a CO_2 3-mer (MP2/MC) and a CO_2/C_2H_4/CO 11-mer (RHF/STO-3G). Shown in Figures 5 and 6 are the magnitude of the atomic force vectors between 265 and 284 fs for all 14 atoms involved in these 2 changes of groups. Lines connect the data for the C atoms in Figure 5 since they are more difficult to follow during this short time window. Figure 5 gives the atomic force vector for the C_2H_4/CO molecules, while Figure 6 gives the atomic force vector for the two CO_2 molecules. The large difference in electronic structure (and in potential energy) at 273.6 fs yielded discontinuities in the magnitude of the atomic force vectors for all atoms except the C atoms (filled green diamonds in Figure 5 and blue squares and purple asterisks in Figure 6). In all these cases, the atoms are going from being treated at a higher level of theory and a larger basis set to a lower level of theory and a very small STO-3G basis set. The subsequent change in groups at 279.9 fs, shown in both Figures 5 and 6, demonstrates that there are no discontinuities in the atomic force vector, except for the CO_2 molecule that leaves the 14-mer group. The atomic force vectors for this

CO_2 molecule are the blue squares, green up-facing triangles, and red diamonds in Figure 6. The largest discontinuity in Figures 5 and 6 was at 273.6 fs for the C and O atoms (of the CO molecule), in Figure 5 represented as the black-filled circles and red-filled boxes with a value of −0.0506 hartree/bohr. Thus, Figures 5 and 6 show that significant discontinuities may exist in the gradients of the intragroup potential due to the changes in electronic structure when there is a change in QM levels of theory at the spatial cutoff.

The atomic kinetic energies of the 14 atoms involved in the 2 group changes between 264 and 284 fs are shown in Figure 7. The atoms are given in the same order as shown in Figure 5 and then Figure 6. Although somewhat obscured due to the number of atoms represented in Figure 7, close inspection of the figure shows that, even though there are discontinuities in the magnitude of the atomic force vector at 273.6 and 279.9 fs, all the atomic kinetic energies evolve smoothly through these discontinuities. The kinetic energies of the C and O atoms (black filled circles and red filled boxes, respectively), where there was the largest −0.0506 hartree/bohr discontinuity in the atomic force vectors, also move smoothly through these discontinuities.
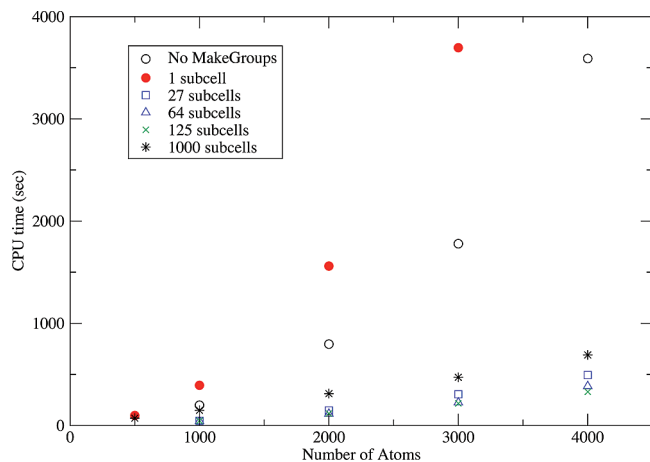
QM Simulations of Complex Reactions

J. Chem. Theory Comput., Vol. 6, No. 1, 2010 **23**

Figure 8. Computational scaling of simulations of N_2 at 300K and ~90 atm pressure with 500 time steps.

In order to examine the effect of a variable spatial cutoff on the discontinuity in the atomic gradients and atomic kinetic energies, single collisions between CO and C_2H_4 molecules were examined. Individual CO and C_2H_4 molecules were treated at the RHF/STO-3G and the MP2/MC levels of theory, while the CO/C_2H_4 supermolecule was treated at the SVWN/6-31G level of theory. Before performing the simulations, the geometries of the individual CO and C_2H_4 molecules were optimized using their respective levels of theory. Seven separate simulations were performed with spatial cutoffs of 4.3−7.3 bohr in increments of 0.5 bohr. The initial geometry of the collisions between the CO and C_2H_4 molecules was at their optimized geometries and at just outside the variable spatial cutoff from one another. The molecules were given center-of-mass velocities to push the molecules together but no internal kinetic energy. The molecules were given no internal kinetic energy in order to examine the effect of the discontinuity in the gradients upon the atomic kinetic energies, and it was not desired to have internal kinetic energy obscure the result. The discontinuity of the magnitude in the atomic force vectors due to the change in the levels of electronic structure was as large as 1.153×10^{-3} Hartrees/bohr, yet resulted in no discontinuities in the atomic kinetic energies across the spatial cutoff. These are precisely the results given above and displayed in Figures 7 and 8, with a spatial cutoff of 7.3 bohr. The difference between spatial cutoffs of 4.3−7.3 bohr is that there is only a very slight acceleration in the atomic velocities after the supermolecule is formed at 7.3 bohr because this spatial cutoff is near the asymptote, where the intermolecular gradients are very close to zero, regardless of the level of theory employed. With a spatial cutoff of 4.3 bohr, these intermolecular interactions are larger, resulting in larger accelerations and decelerations of the center-of-mass velocity vector after the change in levels of theory. Thus, the result of examining a variable spatial cutoff is that kinetic energy is still a continuous quantity, but a spatial cutoff that is too small will lead to sudden accelerations between the molecules, whereas a larger spatial cutoff will give rise to these accelerations in a slower, more physical manner.

V. Time Reversibility

One of the properties of classical molecular dynamic simulations is that they are time reversible. Given a set of initial conditions (atomic coordinates and velocities), one may propagate forward in time, and when the simulation is reversed arrive at the starting point in the exact same number of steps. Time reversibility was examined over the time window of Figure 3, where there are five discontinuities in the potential. The cumulative root-mean-square error (rms) in all the atomic Cartesian coordinates (in Å) at each time between 295 and 235 fs was calculated. The simulation was initialized with the atomic coordinates and the opposite velocities of the 295th fs time step when going forward in time and run for 60 fs using the same time step as before (10 au). This will cause the simulation to go back over the five discontinuities in the opposite direction. The rms error in the atomic coordinates rises slowly and in a very linear manner to reach a maximum value of 3.635×10^{-4} Å after 60 fs, and there is not additional error where there are changes in groups and discontinuities in the total potential. The rms error in the atomic coordinates has a cumulative effect because any deviation in a previous step will be carried through to the next time step. Fitting a slope to the rise in rms error over the 60 fs gives a value of 5.8694×10^{-6} Å/fs for a cumulative rms error of all 110 atomic Cartesian coordinates.

VI. Methodology

The method of performing molecular dynamic simulations by a time-dependent, multilevel QM description of the total potential has been programmed into a suite of programs called **A**ccelerated **Mol**ecular **D**ynamics with **C**hemistry (AMolDC). This multicomponent program divides the total potential into spatially resolved, time-dependent groups where differing levels of electronic structure may be employed over the individual groups in order to place appropriate levels of electronic structure for the various groups formed. Currently, the group−group (intergroup) interactions (MM) have not been implemented but may be computed by low-level QM calculations.

a. MakeGroups. As noted in the 110 atom simulation above, the QM regions are free to change definitions anytime during the simulation, as governed by spatial cutoffs, and it was observed that there may, indeed, be changes in the groups at every time step. Thus, the making of the groups of the simulation will necessarily take place on every time step and will, thus, need to be extremely efficient. In order to accomplish this task efficiently, the simulation cell is broken into link-listed subcells, i.e., each subcell has an explicit link to neighboring subcells. The making of all the groups within the simulation cell proceeds by looping over all the link-listed subcells. Once in a subcell, the groups are formed by looping over all the atoms within the given subcell and by connecting all atoms that are within the spatial cutoff of the atom being looped over. This connectivity list is then looped over to calculate the distance between these and other atoms in the given subcell and in any neighboring subcell, if the atom is within the spatial cutoff of the edge of the

subcell. This process continues until the connectivity list remains unchanged, at which time the process is repeated, being initialized for the next atom in the subcell. After all atoms within the subcell are searched, the next subcell is begun.

The MakeGroups module within AMolDC has been programmed in order to accomplish the task of making the spatially resolved groups at each time step in a simulation. In order to investigate the computational scaling of the MakeGroups module, simulations of N_2 at 300K were performed in which the nitrogens were randomly placed within a simulation cell and propagated for 500 time steps using a simple Morse potential for all internuclear distances. As the number of N_2 molecules was increased, the simulation cell size was adjusted to yield an ideal gas pressure of $\sim$90 atm at 300K. Shown in Figure 8 are the total simulation times without using the MakeGroups module (open circles) and with using the MakeGroups module with 1 subcell (red-filled circles), 27 subcells (open boxes), 64 subcells (open triangles), 125 subcells ($\times$), and 1000 subcells (*). One can see from this figure, the $O(N^2)$ scaling when not using MakeGroups (calculating all interatomic distances) and when using MakeGroups with only 1 subcell (the whole simulation cell). The computational overhead for the MakeGroups module is 1.45 times that of calculating all internuclear distances, as measured by the coefficient of the leading $O(N^2)$ term over the same simulation. However, when the simulation cell is divided into a distribution of $3 \times 3 \times 3$ link-listed subcells, the computational time is greatly reduced, and the computational expense goes from $O(N^2)$ scaling to $O(N)$ scaling. There is little computational difference (relative to the same simulation without MakeGroups) between a $3 \times 3 \times 3$, a $4 \times 4 \times 4$, and a $5 \times 5 \times 5$ division of link-listed subcells. Figure 6 shows that as one continues to increase the number of simulation cells, the computational time becomes more linear. Deviations from linearity come about from the $O(N^2)$ operations of calculating the internuclear distances of the molecules within the individual subcells. Saturation of the simulation cell with subcells, as given most closely by the $10 \times 10 \times 10$ division of link-listed subcells (asterisks), shows almost exactly linear scaling in the number of atoms. Even though the computational cost of MakeGroups is insignificant relative to high-level QM calculations, what is demonstrated in Figure 8 is that, because the total potential is assembled from time-dependent groups, one has the ability to reduce the total number of QM calculations in order to yield overall linear scaling with system size.

VII. Conclusions

The continuity and energy conservation properties of a time-dependent, multilevel QM methodology for the simulation of gas-phase reactive processes have been demonstrated by thoroughly examining a short 110 atom simulation. Although the 110 atom simulation was for nonreactive collisions, a simulation involving reactions will not change the properties illustrated, since all such reactions will be within the asymptotic spatial cutoff. The simulation of reactive processes will call for much higher levels of electronic structure methods to be employed. Simulations of a reactive system are currently being performed.

The principle illustrated in Figures 1−4 is that smooth simulations, within the canonical (NVT) ensemble, result from the framework of a time-dependent, multilevel QM description of the potential that undergoes radical discontinuities over the course of the simulation. However, whenever there is a change in the QM levels of theory, the kinetic energy smoothly traverses these times because the gradients of the potential are all approximately zero at the spatial cutoffs. In addition, Figures 5−7 show that the discontinuities that may result from changes in electronic structure for the intragroup interactions are also shown to not induce discontinuities in the kinetic energy. Thus, smooth atomic motions and continuity in the atomic and cumulative kinetic energy across the boundaries, where there may be significant changes in electronic structure, are also demonstrated.

With a multilevel QM description of the potential that is based on spatially resolved groups, one may place higher levels of theory for those intragroup interactions that demand such treatments (reactive processes) and lower levels of theory for simpler interactions (collisional processes). The AMolDC suite of programs (an nQM method) has been written in order to accomplish these goals. Computational studies show that reducing the total number of potential energy function calls allows the performance of nQM simulations that scale linearly with system size. Future applications will show the utility of a potential energy database (PESDatabase) module in which to store the high-level QM data of the various groups formed during a simulation. These high-level QM data will be used at subsequent simulation times to formulate fast numerical interpolations over the various groups. Thus, an extension in the system size and the simulation time for the direct simulation of complex reactive processes in the gas-phase is performed by the dividing of the total potential into spatially resolved, time-dependent groups over which multiple levels of electronic structures may be employed and the storing of these QM data for subsequent numerical interpolation, once the database is sufficiently populated.

References

(1) Hao, H.; Weitao, Y. *THEOCHEM* **2009**, *898*, 17.

(2) Zimmer, M. *Coord. Chem. Rev.* **2009**, *253*, 817.

(3) Bernstein, N.; Kermode, J. R.; Csanyi, G. *Rep. Prog. Phys.* **2009**, *72*, 026501.

(4) Kamerlin, S. C. L.; Haranczyk, M.; Warshel, A. *J. Phys. Chem. B* **2009**, *113*, 1253.

(5) Senn, H. M.; Thiel, W. *Angew. Chem., Int. Ed.* **2009**, *48*, 1198.

(6) Siegbahn, P. E. M.; Himo, F. *J. Biol. Inorg. Chem.* **2009**, *14*, 643.

(7) Sproviero, E. M.; McEvoy, J. P.; Gascon, J. A.; Brudvig, G. W.; Batista, V. S. *Photosynth. Res.* **2008**, *97*, 91.

(8) Blumberger, J. *Phys. Chem. Chem. Phys.* **2008**, *10*, 5651.

(9) Hu, H.; Yang, W. *Annu. Rev. Phys. Chem.* **2008**, *59*, 573.

(10) Woods, C. J.; Mulholland, A. J. *Chem. Modell.* **2008**, *5*, 13.

(11) Bo, C.; Maeras, F. *Dalton Trans.* **2008**, *22*, 2911.

(12) Sherwood, P.; Brooks, B. R.; Sansom, M. S. P. *Curr. Opin. Struct. Biol.* **2008**, *18*, 630.

(13) Takahashi, H.; Matubayasi, N.; Nakano, M. *Trends Phys. Chem.* **2007**, *12*, 59.

(14) Senn, H.; Thiel, W. *Top. Curr. Chem.* **2007**, *268*, 173.

(15) Lin, H.; Truhlar, D. G. *Theor. Chem. Acc.* **2007**, *117*, 185.

(16) Takahashi, H. *Front. Biosci.* **2009**, *14*, 1745.

(17) Miani, A.; Helfand, M. S.; Raugei, S. *J. Chem. Theory and Comput.* **2009**, *5*, 2158.

(18) de Visser, S. *Biochem. Soc. Trans.* **2009**, *37*, 373.

(19) Lodola, A.; Mor, M.; Siriak, J.; Mulholland, A. *Biochem. Soc. Trans.* **2009**, *37*, 363.

(20) Dybala-Defratyka, A.; Rostkowski, M.; Paneth, P. *Arch. Biochem. Biophys.* **2008**, *474*, 274.

(21) Bulo, R. E.; Ensing, B.; Sikkema, J.; Visscher, L. *J. Chem. Theory Comput.* **2009**, *5*, 2212.

(22) Heyden, A.; Truhlar, D. G. *J. Chem. Theory Comput.* **2008**, *4*, 217.

(23) Heyden, A.; Lin, H.; Truhlar, D. G. *J. Phys. Chem. B* **2007**, *111*, 2231.

(24) Dongwook, K.; Schatz, G. C. *J. Phys. Chem. A* **2007**, *111*, 5019.

(25) Praprotnik, M.; Kremer, K.; Delle Site, L. *J. Phys. A: Math. Theor.* **2007**, *40*, F281.

(26) Praprotnik, M.; Kremer, K.; Delle Site, L. *Phys. Rev. E: Stat. Phys., Plasmas, Fluids, Relat. Interdiscip. Top.* **2007**, *75*, 17701.

(27) Praprotnik, M.; Delle Site, L. Kremer, K. *Phys. Rev. E: Stat. Phys., Plasmas, Fluids, Relat. Interdiscip. Top.* **2006**, *73*, 66701.

(28) Praprotnik, M.; Delle Site, L.; Kremer, K. *J. Chem. Phys.* **2005**, *123*, 224106.

(29) Salazar, M. R. *J. Phys. Chem. A* **2005**, *109*, 11515.

(30) Hofer, T. S.; Pribil, A. B.; Randolf, B. R.; Rode, B. M. *J. Am. Chem. Soc.* **2005**, *127*, 14231.

(31) Kerdcharoen, T.; Morokuma, K. *Chem. Phys. Lett.* **2002**, *355*, 257.

(32) Kerdcharoen, T.; Liedl, K. R.; Rode, B. M. *Chem. Phys.* **1996**, *211*, 313.

(33) Delle Site, L. *Phys. Rev. E: Stat. Phys., Plasmas, Fluids, Relat. Interdiscip. Top.* **2007**, *76*, 47701.

(34) Pilling, M. J. *Proc. Combust. Inst.* **2009**, *31*, 27.

(35) Slavinskaya, N. A.; Frank, P. *Combust. Flame* **2009**, *156*, 1705.

(36) Blanquart, G.; Pepiot-Desjardins, P.; Pitsch, H. *Combust. Flame* **2009**, *156*, 588.

(37) Taatjes, C. A. *J. Phys. Chem. A* **2006**, *110*, 4299.

(38) Miller, J. A.; Pilling, M. J.; Troe, J. *Proc. Combust. Inst.* **2005**, *30*, 43.

(39) Matheu, D. M.; Dean, A. M.; Grenda, J. M.; Green, W. H. *J. Phys. Chem. A* **2003**, *107*, 8552.

(40) Frenklach, M. *Proc. Combust. Inst.* **2007**, *31*, 125.

(41) Susnow, R. G.; Dean, A. M.; Green, W. H.; Peczak, P. K.; Broadbelt, L. J. *J. Phys. Chem. A* **1997**, *101*, 3731.

(42) Feeley, R.; Frenklach, M.; Onsum, M.; Russi, T.; Arkin, A.; Packard, A. *J. Phys. Chem. A* **2006**, *110*, 6803.

(43) Oran, E. S.; Boris, J. P. In *Numerical Approaches to Combustion Modeling; Progress in Astronautics and Aeronautics Series*, Vol. 135; American Institute of Aeronautics and Astronautics: Washington, DC, 1991.

(44) Chenoweth, K.; van Duin, A. C. T.; Dasgupta, S.; Goddard, W. A. *J. Phys. Chem. A* **2009**, *113*, 1740.

(45) Zhang, L.; van Duin, A. C. T.; Zybin, S. V.; Goddard, W. A. *J. Phys. Chem. B* **2009**, *113*, 10770.

(46) Chenoweth, K.; van Duin, A. C. T.; Goddard, W. A. *J. Phys. Chem. A* **2008**, *112*, 1040.

(47) Strachan, A.; Kober, E. M.; van Duin, A. C. T.; Oxgaard, J.; Goddard, W. A. *J. Chem. Phys.* **2005**, *122*, 54502.

(48) van Duin, A. C. T.; Dasgupta, S.; Lorant, F.; Goddard, W. A. *J. Phys. Chem. A* **2001**, *105*, 9396.

(49) Schmidt, M. W.; Baldridge, K. K.; Boatz, J. A.; Elbert, S. T.; Gordon, M. S.; Jensen, J. H.; Koseki, S.; Matsunaga, N.; Nguyen, K. A.; Su, S.; Windus, T. L.; Dupuis, M.; Montgomery, J. A. *J. Comput. Chem.* **1993**, *14*, 1347.

JCTC Journal of Chemical Theory and Computation

Permutationally Invariant Polynomial Basis for Molecular Energy Surface Fitting via Monomial Symmetrization

Zhen Xie*,[†] and Joel M. Bowman*,[‡]

Mathematics and Computer Science Division, Argonne National Laboratory, 9700 S. Cass Avenue, Argonne, Illinois 60439 and Department of Chemistry and Cherry L. Emerson Center for Scientific Computation, 1515 Dickey Drive, Emory University, Atlanta, Georgia 30322

Abstract: We describe a procedure to develop a fitting basis for molecular potential energy surfaces (PESs) that is invariant with respect to permutation of like atoms. The method is based on a straightforward symmetrization of a primitive monomial basis and illustrated for several classes of molecules. A numerically efficient method to evaluate the resulting expression for the PES is also described. The fitting basis is used to obtain a new PES for H_3O^+ based on roughly 62 000 ab initio energies.

1. Introduction

The representation of potential energy surfaces (PESs) that are fits to electronic energies is a long-standing goal of computational chemistry.[1−3] Progress to extend this goal beyond three and four-atom systems has been made recently by using a fitting basis that is invariant with respect to all permutations of like atoms.[4] (Also consult this paper for a review of other recent approaches to fitting PESs.) The approach makes use of powerful algorithms from computational invariant polynomial theory. The key feature of this method is to compute the *primary* and *secondary* invariants for a particular molecule permutation group. Once the primary and secondary invariants are computed, every invariant polynomial basis function can be uniquely factorized as the product of secondary invariants with a polynomial of the primary invariants (typically this polynomial is just a product of some primary invariants when constructing the invariant basis functions). The computational efficiency of this representation comes from this factorization. Since every invariant polynomial can be written as the product of two invariant polynomials, hence in the real evaluation of the potential energy function, only N multiplications are needed to evaluate all the N basis functions, once the necessary

multiplication and additions are done to evaluate the primary and secondary invariants.

This method has been applied to a variety of molecules and molecular systems such as CH_5^+,[5−7] H_5^+,[8,9] C_2H_3,[10] $H + CH_4$,[11−13] $F + CH_4$,[14,15] malonaldehyde (CHOCH$_2$CHO),[16] $OH + NO_2$,[17] H_3O^+,[18] $HO_2 + NO$,[19] and $H_5O_2^+$ [20] and water dimer $(H_2O)_2$[21,22] and trimer.[23] The large set of primary and secondary polynomial for as many as 10 atom molecules was obtained with the commercial code magma.[24] This large library of fitting bases is available at the iOpenShell Web site.[25]

A much more straightforward approach to develop a permutationally invariant basis termed monomial symmetrization was briefly and only schematically described by Huang et al.[20] The method was described in more detail by Xie in his Ph.D. thesis[26] and was recently reviewed and illustrated for several molecules.[4]

The monomial symmetrization approach (MSA) appears prima facie to be much less efficient than the invariant polynomial approach, and so its presentation was mainly done as a pedagogical tool. In this paper, we describe a method to make this straightforward fitting procedure quite efficient and, thus, potentially competitive with the computational invariant polynomial approach. Another key point of the paper is to show that the implementation of the approach is straightforward and does not require access to the magma code.

* Corresponding author. E-mail: zhenxie@mcs.anl.gov.
† Argonne National Laboratory.
‡ Emory University.

Permutationally Invariant Polynomial Basis

J. Chem. Theory Comput., Vol. 6, No. 1, 2010 **27**

The paper is organized as follows: A brief review of the monomial symmetrization approach is presented in Section 2, followed by the algorithm to speed up the function evaluation process. The method is exemplified by an application for the PES of H_3O^+ in Section 3. A brief discussion including some possible new directions using this approach is given in Section 4. A summary and conclusions are given in Section 5.

2. Theoretical Background and Computational Details

2.1. Coordinate Representation of the Potential Energy Surface. The molecular PES, which we denote as V, should respect the key invariant properties of the physics. The well-known properties are overall translational and rotational invariances. A third property, one that is obvious but less well-known, is invariance with respect to all permutations of like atoms. This invariance has been noted in the classic book by Murrell and co-workers[1] and is at the heart of the approach recently reviewed by Braams and Bowman.[4] As noted in that review and the primary sources cited there, the ideal choice of coordinates for V should enable these invariance properties to be "built in". The full set of internuclear distances (of which there are $n(n-1)/2$ for a system of n atoms) almost satisfies this property. That is, these distances are invariant with respect to overall translation and rotation of the molecular system. They are not invariant with respect to permutation of like atoms; however, they are closed under these permutations, and this property has been exploited to make basis functions for the representation of V obey that invariance.

Before we show how this can be done using the MSA,[4,20,26] we make two important remarks. First, the full set of internuclear distances for molecules with more than four atoms is known as a redundant set of coordinates, since it is well-known that only $3n-6$ internal degrees of freedom are needed to specify an n atom molecular configuration. Thus, for n greater than four, there are more internuclear distances than internal degrees of freedom, and in that sense, the choice of all internuclear distances enlarges the space of variables for $n > 4$. Second, and independent of the value of n, internuclear distances are not a good choice of variables for a monomial or polynomial basis to represent V. This is because these distances become arbitrarily large when fragments form, and thus, V would diverge erroneously in these regions. Therefore, we and others use simple transformed variables that go to a constant in these regions. We have used several choices for these variables, some of which will be given below. A specific choice is made when we consider an application to the H_3O^+ PES. However, to investigate how these variables permute under permutations of like atoms, we need only consider the set of internuclear distances, and so we do so here.

We begin by labeling the n atoms in a molecule as 1, ..., n, and the $n(n-1)/2$ internuclear distances are given in lexical order as

$$(r_{1,2}, ..., r_{1,n}, r_{2,3}, ..., r_{2,n}, ..., r_{n-1,n})$$

At this point, it is worth noting that one choice of associated Morse variables that we have used extensively is $y_{i,j} = \exp(-r_{i,j}/\lambda)$. Also, we introduce a shorthand notation for these distances (or Morse variables), x_l, $l = 1, n(n-1)/2$, where the x_l are ordered according to the lexical ordering of $r_{i,j}(y_{i,j})$.

To proceed it is useful to consider a specific example of a tetraatomic molecule, A_4, and the six internuclear distances are

$$(r_{1,2}, r_{1,3}, r_{1,4}, r_{2,3}, r_{2,4}, r_{3,4})$$

and associated variables

$$(x_1, x_2, x_3, x_4, x_5, x_6)$$

The usual expression for V in terms of these variables is

$$V(x_1, x_2, x_3, x_4, x_5, x_6) = \sum_{a+b+c+d+e+f=0}^{k} C_{a,b,c,d,e,f} x_1^a x_2^b x_3^c x_4^d x_5^e x_6^f$$

(2.1)

where a, b, c, d, e, and f are all non-negative integers, and k is a positive integer that sets the maximum as the sum of all the exponents. (The coefficients $C_{a,b,c,d,e,f}$ would typically be determined by a standard linear least-squares fit to a data set of ab initio electronic energies.) Clearly this expression is not invariant with respect to permutations of like atoms. However, one can easily modify the expression so that it is. This procedure involves symmetrizing the monomials, as discussed in detail elsewhere,[4,26] which yields a sum of monomials with a single coefficient, which we denote as $D_{a,b,c,d,e,f}$.[4]

Continuing with the tetraatomic example, consider an example permutation of the four atoms where the original atom order (1, 2, 3, 4) is permuted to (4, 2, 1, 3). The internuclear distances change from

$$(r_{1,2}, r_{1,3}, r_{1,4}, r_{2,3}, r_{2,4}, r_{3,4})$$

to

$$(r_{4,2}, r_{4,1}, r_{4,3}, r_{2,1}, r_{2,3}, r_{1,3}) \equiv (r_{2,4}, r_{1,4}, r_{3,4}, r_{1,2}, r_{2,3}, r_{1,3})$$

or in the "x" notation:

$$(x_1, x_2, x_3, x_4, x_5, x_6)$$

maps to

$$(x_5, x_3, x_6, x_1, x_4, x_2)$$

Thus the monomial $x_1^a x_2^b x_3^c x_4^d x_5^e x_6^f$ maps to $x_5^a x_3^b x_6^c x_1^d x_4^e x_2^f$ ($\equiv x_1^d x_2^f x_3^b x_4^e x_5^a x_6^c$).

In order to complete the symmetrization, all permutations must be considered. We indicate the final result by

$$V = \sum_{a+b+c+d+e+f=0}^{k} D_{a,b,c,d,e,f} \mathcal{S}[x_1^a x_2^b x_3^c x_4^d x_5^e x_6^f] \quad (2.2)$$

where $\mathcal{S}$ is the operator that symmetrizes monomials. Examples of sums of symmetrized monomials were given for A_2B_2 and A_3B molecules elsewhere.[4] This was done by explicitly enumerating all the permutations and by showing how the internuclear distances permute. For a general molecule, the total number of permutations is just the direct

Scheme 1. Algorithm 1

Algorithm 1: Monomial symmetrization approach

   Data: k ;   // maximum total degree of monomials
   Data: $\mathscr{P}$;   // permutation group
   Result: B ;   // invariant basis functions set
   $B \leftarrow \emptyset$;
   $m \leftarrow [0 \cdots 0]$;
   while $deg(m) \leq k$ **do**
      | $\mathrm{orb}(m) \leftarrow \{p_i \cdot m | p_i \in \mathscr{P}\}$;   // p_i: a permutation
      | $B \leftarrow B \cup \mathrm{orb}(m)$;
      | $m \leftarrow m + 1$;   // get the next monomial
   end

---

product of permutations of sets of like atoms. For example, for molecule A_nB_m, the order of the direct product symmetric group is $n!m!$, and the full set of permutations of the sets of like atoms and how those map onto permutations of internuclear distances must be determined. We note that if the resulting monomials are reordered in lexical form 1, 2, 3, etc., then the effect of the mappings is equivalent to permuting the powers of the original "seed" monomial. We use this convention henceforth.

The generation of the permutation of internuclear distances (or equivalently the powers) has been automated with software we have written for any molecule,[27] and Algorithm 1 summarizes the process.

2.2. Algorithm for Efficient Basis Evaluation. Although the potential energy function as shown in eq 2.2 has the permutationally invariant property and we have Algorithm 1 to generate the basis function set, the terms (the symmetrized sum of monomials) are costly to evaluate, and so this representation is not nearly as efficient as the one based on primary and secondary invariants.[4] Clearly there exist strategies that can be used to speed up the evaluation of the symmetrized sum of monomials, which, henceforth, we denote as invariant polynomials. If the invariant polynomials could be factored into lower order invariant polynomials, considerable speedup would result. To our knowledge, however, this factorization cannot be done easily (primary and secondary invariants essentially do this, but the computation of primary and secondary invariants is difficult and complicated, as is the factorization).

Here we describe and demonstrate a less ambitious factorization scheme, which is a binary factorization plus remainder method, where the remainder is one or more invariant polynomials that may have already been computed. To describe this approach, we introduce some new notation and nomenclature. As noted already, an invariant polynomial (of some total degree) is the sum of all the monomials generated by acting all the possible permutations on a seed monomial. We denote this set of monomials as the orbit of the seed monomial m, and denote it as $\mathrm{orb}(m)$, which could be represented as $\mathrm{orb}(m) = \{m^{p_i} | p_i \in \mathscr{P}\}$. Hence eq 2.2 can be simplified as

$$V(x_1, x_2, x_3, x_4, x_5, x_6) = \sum_{a+b+c+d+e+f=0}^{k} D[abcdef] \left(\sum_{\mathscr{P}} \mathrm{orb}([abcdef]) \right) \quad (2.3)$$

where $[abcdef]$ is a shorthand notation for a general monomial $x_1^a x_2^b x_3^c x_4^d x_5^e x_6^f$.

Clearly, if $\sum_{\mathscr{P}} \mathrm{orb}([abcdef])$ could be evaluated effectively, then the whole potential energy function could be computed

effectively. One way to speed this process is to evaluate or build these orbits recursively, that is, to express the "later" orbits as some simple expression from the "earlier" ones, where the terms "later" and "earlier" are yet to be defined as the ordering of monomials.

For monomials with different total degrees, it is easy to order them according their total degree. For monomials with the same total degree, we order them according to the number of nonzero powers. For convenience, we order a monomial with more nonzero powers before another one with fewer nonzero elements but with same total degree, for instance, [010101] < [030000]. If two monomials have the same total degree and the same number of nonzero elements, then we order these monomials according to their lexicographical order, for example, [010101] < [101010]. This ordering scheme is made for later computational convenience. Similar to this ordering of monomials, we can also order the polynomials or orbits, and here the polynomials are ordered according to the "largest" monomials (ordered in the last position according to the monomial ordering) in it. Note that for molecules with greater than four atoms, the maximum total degree is typically much less than the number of internuclear distances there are no polynomials with, where every x_i has a nonzero power.

To illustrate the approach consider the polynomial $x_1^2 + x_2^2$, which is invariant with respect to the permutation of x_1 and x_2, and note that it cannot be simply decomposed as a product of two lower order polynomials. (It is, in fact, a primary invariant polynomial.) However, it can be given as a low-order product of invariant polynomials with a remainder:

$$x_1^2 + x_2^2 = (x_1 + x_2) \times (x_1 + x_2) - x_1 x_2 - x_1 x_2$$

As a result, if the polynomial $x_1 + x_2$ and $x_1 x_2$ are both in the invariant basis function sequence and both appear "earlier" than $x_1^2 + x_2^2$, then $x_1^2 + x_2^2$ could be easily evaluated with one multiplication and two subtractions. To evaluate $x_1^2 + x_2^2$ directly, we need two multiplications and one addition. Since multiplication is more expensive than addition or "subtraction", the decomposition should speed the evaluation. If such a decomposition can be found for a general invariant polynomial, the evaluation of the invariant basis function will be greatly sped up. Now the question comes to the existence and the uniqueness of this kind of decomposition. Unfortunately, neither of these is guaranteed. For a successful decomposition, which we will denote as a "usable decomposition", not only must the two polynomials that form the product be of a lower degree (which, of course, they are) but also the remainder polynomial must come "before" the polynomial becomes decomposed. This is not always the case. Another issue for the decomposition is the uniqueness. There exists various ways to factorize a high-degree monomial as a low-degree one; for example, a monomial [012101] can be factorized as

$$[012101] = [010001] \times [002100]$$

or

$$[012101] = [011101] \times [001000]$$

Scheme 2. Algorithm 2

Algorithm 2: Trial-and-error decomposition algorithm for all the permutationally invariant basis functions

Data: B ;   // invariant basis functions set
Result: D ;   // decomposition of $b_i \in B$
Result: M ;   // monomial set
$B_P \leftarrow \emptyset$;   // single term polynomial set
// populate the single term polynomial set
foreach $b_i \in B$ **do**
  if $|b_i| = 1$ **then**
    | $B_P \leftarrow B_P \cup b_i$;
  end
end
// trying to decompose every basis function
$M \leftarrow \emptyset$;
$i_M \leftarrow 0$;   // size index of M
foreach $b_i \in B$ **do**
  if $b_i \in B_P$ **then**
    | // deal with single term basis function
    | $M \leftarrow M \cup b_i$;
    | $i_M \leftarrow i_M + 1$;
    | $D \leftarrow D \cup [i, 0, i_M]$;   // 0 indicates failed decomposition
  else
    | // deal with multiple terms basis function
    | **if** $(\exists b_m, b_n, b_{l_1}, \cdots \le b_i) \vee (b_i = b_m \cdot b_n - b_{l_1} - \cdots)$ **then**
    | | // the basis function has a usable decomposition
    | | $D \leftarrow D \cup [i, 1, m, n, l_1, \cdots]$;   // 1 indicates successful
    | | decomposition
    | **else**
    | | // the basis function has no usable decomposition
    | | $M \leftarrow M \cup \mathrm{mono}(b_i)$;   // save the monomial set
    | | $D \leftarrow D \cup [i, 0, i_M + 1, \cdots, i_M + |b_i|]$; // record the sum of monomials
    | | $i_M \leftarrow i_M + |b_i|$;
    | **end**
  end
end
---

or any other two monomials whose sum of exponents are equal to the original exponents. Different factorizations of the monomials result in different remainder polynomials, and different factorizations may or may not lead to usable decomposition of a high-degree polynomial.

One practical approach to this factorization of polynomials is to list all the possible factorizations of the seed (it can be any monomial of the polynomial) of a high-degree polynomial. Denoting the high-degree polynomial as p_1, and one monomial in p_1 as m_1, we have $p_1 = \mathrm{orb}(m_1)$. Note that we do not distinguish the set of monomials as $\mathrm{orb}(m_1)$ and the polynomial, which is the sum of all the monomials in this set. Suppose p_2 is a polynomial arranged before p_1 in the invariant polynomial basis sequence. Then we can scan over all the monomials in p_2, to determine if there is one monomial (m_2) in p_2 that is a factor of m_1, then we can factorize m_1 as $m_1 = m_2 m_3$ and find the orbit of m_3 ($\mathrm{orb}(m_3)$) in the polynomial basis. Further suppose $p_3 = \mathrm{orb}(m_3)$. Then we can form the product $p_2 p_3$. The difference between $p_2 p_3$ and p_1 should be a sum of orbits of some other monomials (sum of some other invariant polynomials), and we try to minimize the number of remainder polynomials already computed. If it is not possible to find a usable decomposition, then we have to evaluate the polynomial by evaluating all monomials. All monomials within a polynomial that has no usable decomposition are pushed into a queue. The speed up for this process is determined partially by the size of the monomial queue. If most of the polynomials can be decomposed successfully, the size of the monomial queue

is small, and the efficiency of the approach is high. For monomials in the queue, the evaluation process could and is sped up by factorizing the later ones as the product of earlier ones.

In summary, all the possible monomials with total degrees less than some threshold are enumerated and grouped into orbits by the action of permutations. The sum of such monomials in an orbit is an invariant polynomial. They are arranged according to the polynomial ordering scheme, as defined above. Then the polynomials are decomposed into the product of two polynomials, and possibly subtracting a small number of same-order polynomials, if this is possible. Otherwise, the polynomial is kept as the sum of monomials. A factorization step is performed for every monomial from the previous step and evaluated as the product of two previous ones. In the following section, an example will be given to show the process.

The algorithms just described above are summarized as Algorithm 2, 3, and 4.

2.3. Example: Basis Functions for H_3O^+. H_3O^+ is an important molecule in chemistry, and it has three identical hydrogen atoms which make it a good example to illustrate the MSA process. Of course the results shown apply to any A_3B molecule.

The three H atoms are labeled as 1, 2, and 3, and the O atom is labeled as 4. Table 1 shows all the permutation actions on the internuclear distances and also on a general monomial [*abcdef*]. For demonstration purposes, *a*, ..., *f* are all different integers, in reality, some of them may be equal.

Scheme 3. Algorithm 3

Algorithm 3: Decomposition of a basis function (polynomial) b_i

Data: $B, b_i \in B$;   // invariant basis functions set, and one basis
Result: $b_i = b_m \cdot b_n - b_l \cdots, (m,n,l,\cdots \leq i)$ or fail
$D \leftarrow \emptyset$;   // usable decomposition set
$m_1 \leftarrow \text{seed}(b_i)$;   // $m_1 \in \text{mono}(b_i)$
foreach $b_j \in B \vee b_j < b_i$ **do**
  if $\exists m_2 \in \text{mono}(b_j) \vee m_1 = m_2 \cdot m_3$ **then**
    $b_m \leftarrow b_j$;
    $b_n \leftarrow \text{orb}(m_3)$;
    $p \leftarrow b_m \times b_n - b_i$;
    if $(\exists b_{l_1}, \cdots \in B) \vee (b_{l_1}, \cdots < b_i) \vee (p = \sum_i b_{l_i})$ **then**
      $D \leftarrow D \cup [i, m, n, l_1, \cdots]$;
    end
  end
end
if $D = \emptyset$ **then**
  return *fail*;
else
  return $d \in D : |d| \leq |d_i|, \forall d_i \in D$; // return the simplest decomposition
end

Scheme 4. Algorithm 4

Algorithm 4: Decomposition of monomials

Data: M;   // a monomial set
Result: H;   // the decomposition of monomials
$H \leftarrow \emptyset$;
foreach $m \in M$ **do**
  if $(\exists m_i, m_j \in M) \vee (m_i, m_j < m) \vee (m = m_i \cdot m_j)$ **then**
    $H \leftarrow H \cup [i, j]$;
  else
    $H \leftarrow H \cup m$;
  end
end

Table 1. Permutation of the H_3O^+ Molecule and Its Action on a General Monomial [*abcdef*]

permutation	atom labels	internuclear distance vector	permuted monomial
p_1	1 2 3 4	$(x_1, x_2, x_3, x_4, x_5, x_6)$	[*abcdef*]
p_2	1 3 2 4	$(x_2, x_1, x_3, x_4, x_6, x_5)$	[*bacdfe*]
p_3	2 1 3 4	$(x_1, x_4, x_5, x_2, x_3, x_6)$	[*adebcf*]
p_4	2 3 1 4	$(x_4, x_1, x_5, x_2, x_6, x_3)$	[*bdface*]
p_5	3 1 2 4	$(x_2, x_4, x_6, x_1, x_3, x_5)$	[*daebfc*]
p_6	3 2 1 4	$(x_4, x_2, x_6, x_1, x_5, x_3)$	[*dbfaec*]

Consequently, the orbit of a monomial [*abcdef*] may have less than six monomials, as shown in Table 2.

Table 2 lists all the invariant polynomial basis for molecule H_3O^+ up to degree 3. All those polynomials that have usable decomposition under the polynomial ordering scheme are indicated as a product of two other basis functions less some other basis functions. As for those that do not have a usable decomposition, the decomposition is written as the sum of monomials.

The factorization of all the monomials is shown in Table 3.

As we can see from Table 2, many basis functions have usable decompositions, i.e., can be expressed as the product of two lower degree basis functions, less some other basis functions that are at the same degree but come before the current invariant basis. As a result, the evaluation of those basis functions costs one multiplication with some addition. For those monomials, almost all could be factorized as a product of two previous ones, thus, significantly reducing the evaluation time—especially when the total degree of monomial increases. The monomials that cannot be factorized are those single variable terms, and they are trivial to evaluate.

2.4. Applications to Other Molecules. Relevant information about the monomial and the symmetrized monomial basis for a variety of molecules and total degree is given in Table 4. Columns three and four give the size of the monomial and symmetrized monomial (polynomial) basis for each example. The reduction in size for the polynomial basis is large. However, it is not as large as the order of the corresponding symmetric group; this reduction factor is approached only as the total degree approaches infinity. For example, for A_4, the maximum possible reduction is 24, and as seen for degree 8, the actual reduction is 15.4. Next, consider the number of polynomials and the percentage of the of all polynomials that have a usable decomposition shown in column five and six. The percent ranges from almost 100% to a low of 51.95%. The number of remainder monomials to be evaluated and the number that can be factored are given next. Finally, an "efficiency" column is included, which contains two values. The ratio of total monomials to total polynomials is given in parentheses, and the first number is the ratio of monomials to the sum of usable decomposition plus the monomials left.

Perusal of this table leads to the conclusion that the current factorization method works better for molecules with two or three identical atoms than for molecules with more identical atoms. On the other hand, the size of polynomial basis decreases by a larger factor for such molecules (since the order of the symmetric group increases).

The lack of usable decomposition of an arbitrary (invariant) polynomial in the present algorithm comes from the polynomial ordering scheme. It is not difficult to show that any high-degree invariant polynomial constructed by using monomial symmetrization approach can be represented as the product of two low-degree polynomials and as a remainder invariant polynomial of the same degree. If the polynomial ordering scheme can ensure that polynomials need to be subtracted are always come before the target polynomial, then the inefficiency factor could be removed, and we can claim that the monomial symmetrization approach is almost as fast as the computation invariant theory based approach. However, this ordering scheme is difficult to construct. A simple example may show the difficulty. Suppose that $x_1 + x_2$, $x_1^2 + x_2^2$ and $x_1 x_2$ are invariant polynomials, with respect to the permutation of x_1 and x_2. Both $x_1^2 + x_2^2$ and $x_1 x_2$ are of degree 2, and $x_1 + x_2$ is of degree 1, which always comes before the other two polynomials. $x_1^2 + x_2^2$ could be decomposed as

$$x_1^2 + x_2^2 = (x_1 + x_2) \times (x_1 + x_2) - x_1 x_2 - x_1 x_2 \tag{2.4}$$

and $x_1 x_2$ could be decomposed at

$$x_1 x_2 = (x_1 + x_2) \times (x_1 + x_2) - (x_1^2 + x_2^2) - x_1 x_2 \tag{2.5}$$

It is easy to rearrange eq 2.5 as

$$2x_1 x_2 = (x_1 + x_2) \times (x_1 + x_2) - (x_1^2 + x_2^2) \tag{2.6}$$

As can be seen, no matter what the polynomial ordering scheme is (whether $x_1 x_2$ comes before $x_1^2 + x_2^2$ or after it),

Permutationally Invariant Polynomial Basis

J. Chem. Theory Comput., Vol. 6, No. 1, 2010 **31**

Table 2. Invariant Polynomial Basis for Molecule H_3O^+ up to Degree 3

ID	degree	invariant polynomial basis	decomposition
B_0	0	[000000]	M_0
B_1	1	[000001] + [000010] + [001000]	$M_1 + M_2 + M_3$
B_2	1	[000100] + [010000] + [100000]	$M_4 + M_5 + M_6$
B_3	2	[000011] + [001001] + [001010]	$M_7 + M_8 + M_9$
B_4	2	[001100] + [010010] + [100001]	$M_{10} + M_{11} + M_{12}$
B_5	2	[000101] + [000110] + [010001] + [011000] + [100010] + [101000]	$B_1 \times B_2 - B_4$
B_6	2	[010100] + [100100] + [110000]	$M_{13} + M_{14} + M_{15}$
B_7	2	[000002] + [000020] + [002000]	$B_1 \times B_1 - B_3 - B_3$
B_8	2	[000200] + [020000] + [200000]	$B_2 \times B_2 - B_6 - B_6$
B_9	3	[001011]	M_{16}
B_{10}	3	[001101] + [001110] + [010011] + [011010] + [100011] + [101001]	$M_{17} + M_{18} + M_{19} + M_{20} + M_{21} + M_{22}$
B_{11}	3	[000111] + [011001] + [101010]	$B_2 \times B_3 - B_{10}$
B_{12}	3	[010110] + [011100] + [100101] + [101100] + [110001] + [110010]	$M_{23} + M_{24} + M_{25} + M_{26} + M_{27} + M_{28}$
B_{13}	3	[110100]	M_{29}
B_{14}	3	[010101] + [100110] + [111000]	$B_1 \times B_6 - B_{12}$
B_{15}	3	[000012] + [000021] + [001002] + [001020] + [002001] + [002010]	$B_1 \times B_3 - B_9 - B_9 - B_9$
B_{16}	3	[002100] + [010020] + [100002]	$B_1 \times B_4 - B_{10}$
B_{17}	3	[000102] + [000120] + [010002] + [012000] + [100020] + [102000]	$B_2 \times B_7 - B_{16}$
B_{18}	3	[001200] + [020010] + [200001]	$B_2 \times B_4 - B_{12}$
B_{19}	3	[000201] + [000210] + [020001] + [021000] + [200010] + [201000]	$B_1 \times B_8 - B_{18}$
B_{20}	3	[010200] + [020100] + [100200] + [120000] + [200100] + [210000]	$B_2 \times B_6 - B_{13} - B_{13} - B_{13}$
B_{21}	3	[000003] + [000030] + [003000]	$B_1 \times B_7 - B_{15}$
B_{22}	3	[000300] + [030000] + [300000]	$B_2 \times B_8 - B_{20}$

Table 3. Factorization of the Monomials from Those Basis Functions that do not have Usable Decomposition for H_3O^+ Molecule

ID	Monomial	factorization	ID	Monomial	factorization
M_0	[000000]	1	M_{15}	[110000]	$M_5 \times M_6$
M_1	[000001]	x_6	M_{16}	[001011]	$M_1 \times M_9$
M_2	[000010]	x_5	M_{17}	[001101]	$M_1 \times M_{10}$
M_3	[001000]	x_3	M_{18}	[001110]	$M_2 \times M_{10}$
M_4	[000100]	x_4	M_{19}	[010011]	$M_1 \times M_{11}$
M_5	[010000]	x_2	M_{20}	[011010]	$M_3 \times M_{11}$
M_6	[100000]	x_1	M_{21}	[100011]	$M_2 \times M_{12}$
M_7	[000011]	$M_1 \times M_2$	M_{22}	[101001]	$M_3 \times M_{12}$
M_8	[001001]	$M_1 \times M_3$	M_{23}	[010110]	$M_2 \times M_{13}$
M_9	[001010]	$M_2 \times M_3$	M_{24}	[011100]	$M_3 \times M_{13}$
M_{10}	[001100]	$M_3 \times M_4$	M_{25}	[100101]	$M_1 \times M_{14}$
M_{11}	[010010]	$M_2 \times M_5$	M_{26}	[101100]	$M_3 \times M_{14}$
M_{12}	[100001]	$M_1 \times M_6$	M_{27}	[110001]	$M_1 \times M_{15}$
M_{13}	[010100]	$M_4 \times M_5$	M_{28}	[110010]	$M_2 \times M_{15}$
M_{14}	[100100]	$M_4 \times M_6$	M_{29}	[110100]	$M_4 \times M_{15}$

there is always one nonusable decomposition. Unfortunately, either $x_1 x_2$ or $x_1^2 + x_2^2$ must be evaluated explicitly. (One or the other is in fact a primary invariant.)

In another case, suppose that we have invariants:

$$
\begin{aligned}
A &= x_1^4 + x_2^4 \\
B &= x_1^2 x_2^2 \\
C &= x_1 x_2^3 + x_1^3 x_2
\end{aligned}
\quad (2.7)
$$

and they could be decomposed as

$$
\begin{aligned}
A &= (x_1^2 + x_2^2) \times (x_1^2 + x_2^2) - (x_1^2 x_2^2 + x_1^2 x_2^2) \\
B &= (x_1 x_2^2 + x_1^2 x_2) \times (x_1 + x_2) - (x_1 x_2^3 + x_1^3 x_2) - x_1^2 x_2^2 \\
C &= (x_1 + x_2) \times (x_1^3 + x_2^3) - (x_1^4 + x_2^4)
\end{aligned}
$$

$$(2.8)$$

$x_1 + x_2$, $x_1^2 + x_2^2$, $x_1^3 + x_2^3$ and $x_1 x_2^2 + x_1^2 x_2$ are at a lower degree compared to A, B, and C, and so their values can be assumed to be known. However, the remainders do contain

A, B, and C and we wish to "disentable" these expressions. To do so first rewrite these equations as

$$
\begin{aligned}
A &= \alpha - 2B \\
B &= \beta - C - B \\
C &= \gamma - A
\end{aligned}
\quad (2.9)
$$

where

$$
\begin{aligned}
\alpha &= (x_1^2 + x_2^2) \times (x_1^2 + x_2^2) \\
\beta &= (x_1 x_2^2 + x_1^2 x_2) \times (x_1 + x_2) \\
\gamma &= (x_1 + x_2) \times (x_1^3 + x_2^3)
\end{aligned}
\quad (2.10)
$$

and then rewrite them in matrix form as

$$
\begin{bmatrix} 1 & 2 & 0 \\ 0 & 2 & 1 \\ 1 & 0 & 1 \end{bmatrix} \times \begin{bmatrix} A \\ B \\ C \end{bmatrix} = \begin{bmatrix} \alpha \\ \beta \\ \gamma \end{bmatrix}
\quad (2.11)
$$

This can be solved easily as

$$
\begin{aligned}
A &= \frac{1}{2}\alpha - \frac{1}{2}\beta + \frac{1}{2}\gamma \\
B &= \frac{1}{4}\alpha + \frac{1}{4}\beta - \frac{1}{4}\gamma \\
C &= -\frac{1}{2}\alpha + \frac{1}{2}\beta + \frac{1}{2}\gamma
\end{aligned}
\quad (2.12)
$$

This indicates that it is possible to further decouple intertwined polynomials and to obtain their usable decomposition simultaneously by solving a linear system. Solving the linear system is an extra cost for the decomposition, but it is an one-time cost and it will not be inherited in the future polynomial evaluation process. As a result, we can further speed up the polynomial evaluation process. We plan to investigate an implementation of this algorithm in the future.

3. Application to a Potential Surface for H_3O^+

The methods described in the previous section to automate the symmetrization of the monomial basis and to evalu-

Table 4. Information on Invariant Polynomial Basis Function Decomposition

molecule	max deg	tot mono.	tot poly.	usable decomp.	usable decomp. %	mono left	mono fact	efficiency
A_3	6	84	23	19	82.61%	8	4	3.11 (3.65)
A_3	8	165	41	37	90.24%	8	4	3.67 (4.02)
A_2B	6	84	50	46	92.00%	5	1	1.65 (1.68)
A_2B	8	165	95	91	95.79%	5	1	1.72 (1.74)
A_4	6	924	72	60	83.33%	88	81	6.24 (12.83)
A_4	8	3003	195	182	93.33%	112	105	10.21 (15.40)
A_3B	6	924	196	185	94.39%	33	26	4.24 (4.71)
A_3B	8	3003	590	579	98.14%	33	26	4.91 (5.09)
A_2B_2	6	924	291	282	96.91%	18	11	3.08 (3.18)
A_2B_2	8	3003	882	873	98.98%	18	11	3.37 (3.40)
A_2BC	6	924	502	494	98.41%	11	4	1.83 (1.84)
A_2BC	8	3003	1589	1581	99.50%	11	4	1.89 (1.89)
A_5	6	8008	140	94	67.14%	2368	2357	3.25 (57.20)
A_5	8	43758	580	443	76.38%	10158	10147	4.13 (75.44)
A_4B	6	8008	495	437	88.28%	807	796	6.44 (16.18)
A_4B	8	43758	2327	2216	95.23%	1953	1942	10.50 (18.80)
A_3B_2	6	8008	889	838	94.26%	390	367	6.52 (9.01)
A_3B_2	8	43758	4343	4249	97.84%	876	853	8.54 (10.08)
A_3BC	6	8008	1603	1565	97.63%	161	150	4.64 (5.00)
A_3BC	8	43758	8163	8121	99.49%	185	174	5.27 (5.36)
A_2B_2C	6	8008	2304	2278	98.87%	72	61	3.41 (3.48)
A_2B_2C	8	43758	11910	11884	99.78%	72	61	3.66 (3.67)
A_2BCD	6	8008	4264	4249	99.65%	22	11	1.87 (1.88)
A_2BCD	8	43758	22734	22719	99.93%	22	11	1.92 (1.92)
A_5B_2	4	12650	218	148	67.89%	4997	4975	2.46 (58.03)
A_5B_2	6	296010	2651	2080	78.46%	78066	77924	3.69 (111.66)
A_6B_3	3	9139	77	40	51.95%	5485	5448	1.65 (118.69)
A_6B_3	4	91390	327	208	63.61%	47533	47496	1.91 (279.48)

ate the subsequent terms by means of the decomposition procedure are applied to the PES of H_3O^+. There exists PESs for H_3O^+,[18,28,29] and an unpublished PES for this cation was obtained using the invariant polynomial approach previously[26] and was used as the "benchmark" PES both in terms of precision and speed of evaluations. The precision and speed of evaluation of the monomial symmetrization approach will be tested against this benchmark. In these fits, the internuclear distances (x) are replaced by the variables $(1.0 - \exp(-0.2x))^2$. This is a slightly different version of Morse variables[4] with the same goal to achieve a physically correct description, i.e., let the potential energy function approach to a constant in the limit of asymptotically large values of x.

Low-level direct dynamics calculations were run at several total energies to generate 61 604 H_3O^+ configurations. At these configurations, electronic energies were then obtained using the CCSD(T) method with aug-cc-pVTZ basis, as implemented in the code MOLPRO.[30] The energy range for these configurations is 29 674 cm^{-1} (84.84 kcal/mol). The maximum total degree for the polynomial basis is set to be 6. This is the same total degree used for the invariant polynomial fit. Since both approaches have the same number of basis functions, the number of coefficients is also the same. Note that the coefficient values are different because the basis functions from the two approaches differ. The coefficients for both fits were obtained with standard least-squares codes. The final root-mean-square error for both fitting approaches is 29 cm^{-1}, with the maximum absolute residual value deviation at 0.16 cm^{-1}. As expected, almost no difference is observed regarding the accuracy of these two approaches.

After obtaining the coefficients, we evaluated the energies for the molecule configurations in the original data set used for fitting three times. We obtained 184 812 potential function calls in total. The computational invariant theory approach took 8.77 s, and the modified monomial symmetrization approach took 9.50 s. It is about 8% less efficient for the monomial symmetrization approach, which is almost negligible. Comparing the details of these two approaches, one can see that slightly more time is consumed in evaluating and summing the monomials from those polynomial basis functions that cannot be effectively decomposed. For the H_3O^+ molecule, the number of monomials does not change when the maximum total degree of polynomial basis functions get higher and higher. As a result, the timing difference would be virtually the same.

4. Discussion

Perhaps the most striking practical effect of symmetrizing the monomial expression for the potential, eq 2.1, is the very large reduction in the number of terms and, hence, unknown linear coefficients to be determined. This was illustrated in Table 4 where the number of monomials in the unsymmetrized expression for V is compared to the number of symmetrized polynomials. The ratio of these two numbers approaches the order of the symmetric group in the limit of infinitely many terms in both expressions; however, as seen even for modest total orders, the reduction can be very big. Practically, this has allowed us to consider molecules with up to nine atoms and to deal with a relatively small linear algebra least-squares minimization. This very practical advantage is realized by using the full permutation group of a molecule.

This practical advantage in exploiting the full permutational symmetry also holds for molecular complexes. For example, consider the water dimer and trimer, where the order of the symmetric group is $4!2! = 48$ and $6!3! = 4\,320$, respectively. PESs for both the water dimer and trimer, using the full permutational symmetry, have been reported.[21,22,31] However, physically one knows that, for temperatures or total energies of interest, most of these permutations are infeasible, i.e., they must surmount high potential barriers to be realized. Thus, it would seem that using the full symmetric group, while greatly reducing the number of terms in V, is also physically irrelevant. Ideally one would like a representation that both greatly reduces the number of terms in V and only describes the feasible permutations. (In the case of water clusters, this would be the permutations of the H atoms associated with each monomer unit.)

If one is going to continue to use all the internuclear distances (probably with a standard many-body representation of the potential), then it seems clear that one will have to restrict the range of powers of some of the internuclear distances. These presumably would be the monomer internuclear distances, which undergo small amplitude motion. In fact, a rather primitive version of this type of restriction was used in a monomial representation of the global potential of H_2CO for the CO internuclear distance.[32] Further work along these lines is planned.

Also, as the observant reader has noted, the use of the Morse-type variables introduces a nonlinear range parameter. Generally we have used a single-range parameter, typically $2-3$ Bohr, for all variables. In principle, this parameter could be optimized and also made specific for a given set of internuclear distances, for example, all OH, HH, and OO distances. Doing so would turn the straightforward linear-least-squares optimization into a combination of linear and nonlinear optimizations. This may be worth considering; however, it involves a substantial increase in numerical complexity.

Finally we note that the library of primary and secondary invariant polynomials referred to in the paper does not include analytical expressions for partial derivatives. This may be added in the future; however, it will involve considerable symbolic computation. Clearly, using the monomial symmetrization described here makes this task much easier for the user. We plan to do this in the near future.

5. Conclusions

We have presented a straightforward monomial symmetrization scheme for the representing a multidimensional potential energy surface. We have proposed one scheme for efficient evaluation of the results terms in the representation and illustrated the approach by fitting roughly 62 000 electronic energies for H_3O^+. We also discussed several areas for future research. The codes described herein can be obtained by contacting either author.

Note Added after ASAP Publication. This article was released ASAP on November 23, 2009. The URL in reference 27 was updated, and the correct version was posted on November 30, 2009.

References

(1) Murrell, J. N. *Molecular Potential Energy Functions*; J. Wiley: Chichester, U.K., 1984.

(2) Schatz, G. C. *Rev. Mod. Phys.* **1989**, *61*, 669–688.

(3) Hollebeek, T.; Ho, T. S.; Rabitz, H. *Annu. Rev. Phys. Chem.* **1999**, *50*, 537–570.

(4) Braams, B. J.; Bowman, J. M. *Int. Rev. Phys. Chem.* **2009**, *28*, 577−606.

(5) Jin, Z.; Braams, B.; Bowman, J. *J. Phys. Chem. A* **2006**, *110*, 1569–1574.

(6) Christoffel, K.; Jin, Z.; Braams, B.; Bowman, J. *J. Phys. Chem. A* **2007**, *111*, 6658–6664.

(7) Mann, J.; Xie, Z.; Savee, J.; Braams, B.; Bowman, J.; Continetti, R. *J. Am. Chem. Soc.* **2008**, *130*, 3730.

(8) Xie, Z.; Braams, B.; Bowman, J. *J. Chem. Phys.* **2005**, *122*, 224307.

(9) Acioli, P.; Xie, Z.; Braams, B.; Bowman, J. *J. Chem. Phys.* **2008**, *128*, 104318.

(10) Park, W.; Park, J.; Park, S.; Braams, B.; Chen, C.; Bowman, J. *J. Chem. Phys.* **2006**, *125*, 081101.

(11) Zhang, X.; Braams, B.; Bowman, J. *J. Chem. Phys.* **2006**, *124*, 021104.

(12) Xie, Z.; Bowman, J.; Zhang, X. *J. Chem. Phys.* **2006**, *125*, 133120.

(13) Xie, Z.; Bowman, J. *Chem. Phys. Lett.* **2006**, *429*, 355–359.

(14) Czako, G.; Braams, B.; Bowman, J. *J. Phys. Chem. A* **2008**, *112*, 7466–7472.

(15) Czako, G.; Shepler, B.; Braams, B.; Bowman, J. *J. Chem. Phys.* **2009**, *130*, 084301.

(16) Wang, Y.; Braams, B.; Bowman, J.; Carter, S.; Tew, D. *J. Chem. Phys.* **2008**, *128*, 224314.

(17) Chen, C.; Shepler, B.; Braams, B.; Bowman, J. *J. Chem. Phys.* **2007**, *127*, 104310.

(18) Mann, J.; Xie, Z.; Savee, J.; Bowman, J.; Continetti, R. *J. Chem. Phys.* **2009**, *130*, 041102.

(19) Chen, C.; Shepler, B.; Braams, B.; Bowman, J. *Phys. Chem. Chem. Phys.* **2009**, *11*, 4722–4727.

(20) Huang, X.; Braams, B.; Bowman, J. *J. Chem. Phys.* **2005**, *122*, 044308.

(21) Huang, X.; Braams, B.; Bowman, J. *J. Phys. Chem. A* **2006**, *110*, 445–451.

(22) Shank, A.; Wang, Y.; Kaledin, A.; Braams, B.; Bowman, J. *J. Chem. Phys.* **2009**, *130*, 144314.

(23) Wang, Y.; Shepler, B. C.; Braams, B. J.; Bowman, J. M. *J. Chem. Phys.* **2009**, *131*, 054511.

(24) Bosma, W.; Cannon, J.; Playoust, C. *J. Symbolic Comput.* **1997**, *24*, 235–265.

(25) *iOpenShell*; iOpenShell: University of Southern California, Los Angeles, CA; http://iopenshell.usc.edu/.

(26) Xie, Z. Ph.D. thesis, Emory University, Atlanta, GA, 2008.

(27) MSA Code; Argonne National Laboratory, Mathematics and Computer Science Division: Argonne, IL; http://www.mcs.anl.gov/msa.

(28) Huang, X.; Carter, S.; Bowman, J. *J. Chem. Phys.* **2003**, *118*, 5431–5441.

(29) Rajamaki, T.; Miani, A.; Halonen, L. *J. Chem. Phys.* **2003**, *118*, 10929–10938.

(30) Werner, H.-J.; Knowles, P. J. Lindh, R. Schütz, M. MOLPRO, version 2002.6; University College Cardiff Consultants Limited: Wales, U.K.; 2003.

(31) Wang, Y.; Carter, S.; Braams, B. J.; Bowman, J. M. *J. Chem. Phys.* **2008**, *128*, 071101.

(32) Zhang, X. B.; Zou, S. L.; Harding, L. B.; Bowman, J. M. *J. Phys. Chem. A* **2004**, *108*, 8980–8986.

J. Chem. Theory Comput. **2010,** *6,* 35–47

35

JCTC Journal of Chemical Theory and Computation

Exploring Multidimensional Free Energy Landscapes Using Time-Dependent Biases on Collective Variables

Jérome Hénin,*[†,||] Giacomo Fiorin,[‡] Christophe Chipot,[§,⊥] and Michael L. Klein[‡]

*Center for Molecular Modeling, Department of Chemistry, University of Pennsylvania,
Philadelphia, Pennsylvania 19104, Institute for Computational Molecular Science and
Department of Chemistry, Temple University, Philadelphia, Pennsylvania 19122, and
Department of Physics and Beckman Institute for Advanced Science and Engineering,
University of Illinois at Urbana−Champaign, Urbana, Illinois 61820*

Abstract: A new implementation of the adaptive biasing force (ABF) method is described. This implementation supports a wide range of collective variables and can be applied to the computation of multidimensional energy profiles. It is provided to the community as part of a code that implements several analogous methods, including metadynamics. ABF and metadynamics have not previously been tested side by side on identical systems. Here, numerical tests are carried out on processes including conformational changes in model peptides and translocation of a halide ion across a lipid membrane through a peptide nanotube. On the basis of these examples, we discuss similarities and differences between the ABF and metadynamics schemes. Both approaches provide enhanced sampling and free energy profiles in quantitative agreement with each other in different applications. The method of choice depends on the dimension of the reaction coordinate space, the height of the barriers, and the relaxation times of degrees of freedom in the orthogonal space, which are not explicitly described by the chosen collective variables.

Introduction

A variety of approaches for accelerated sampling and mapping of free energy landscapes from molecular simulations have been proposed over the years (see refs 1–3 for reviews). Typically, these approaches have only been used by a limited number of groups that specialize in theory and method development. Only rarely have such methods been made readily available to the broad computational chemistry and biophysics community, as this requires well-documented implementations compatible with the standard tools of this community: parallel simulation programs capable of high-throughput, large-scale calculations. An implementation of the metadynamics approach of Laio and Parrinello[4] for mainstream simulation packages has been made available only very recently.[5]

The previous publicly available implementation[6] of the adaptive biasing force method[7,8] (ABF), in version 2.6 of NAMD,[9] has been applied successfully to a number of challenging cases. The domains of application of ABF include the recognition and association of peptides or proteins,[10–12] peptide− or protein−lipid interactions,[13–15] small molecules interacting in a confined environment,[16] cyclodextrin association with cholesterol,[17] steroid drugs,[18] and molecular ions,[19] as well as cyclodextrin self-assembly.[20] Translocation of molecules or ions through natural, transmembrane channel proteins[21–24] and transporters,[25] through synthetic pores,[26] and across simple liquid interfaces[27] have also been studied. Another class of applications involves conformational changes in peptides,[28,29] proteins,[30–32] and

---

* Corresponding author e-mail: jhenin@ifr88.cnrs-mrs.fr.

† University of Pennsylvania.

‡ Temple University.

§ University of Illinois at Urbana−Champaign.

|| Current address: Laboratoire d'Ingénierie des Systèmes Macromoléculaires, CNRS UPR9027, Marseille, France.

⊥ On leave from Equipe de Dynamique des Assemblages Membranaires, UMR CNRS/UHP 7565, Nancy Université BP 239, Nancy, France.

nucleic acids.[33] Despite the number and variety of such applications, that implementation carried significant technical limitations, particularly its restriction to one-dimensional free energy profiles.

When a low-dimension reduced representation comprised of a few degrees of freedom is used to describe a complex process, hidden barriers orthogonal to the chosen parameters are likely to exist. The orthogonal space random walk strategy[34,35] has been proposed by Zheng et al. as a means of overcoming such hidden barriers. While a promising idea, likely to be further explored and built upon in the future, it treats the orthogonal space using a single degree of freedom, which may or may not suffice to overcome hidden barriers effectively in complex examples; in many instances, a well-chosen degree of freedom may well yield better results. Still, the orthogonal space random walk approach has the advantage of generality, as it extends a predefined reaction coordinate space without requiring any additional physical insight into the particular process being examined.

Using collective variables well-adapted to the chemical or biophysical process under scrutiny is critical, and specific problems frequently require tailored variables. We recently developed a new code, the Collective Variables Module, for version 2.7 of the high-performance simulation program NAMD. This code supports a large set of commonly employed variables, offers the possibility to use polynomial combinations of such variables, and can be readily adapted to deal with atypical problems; the full list of features and technical details will be discussed elsewhere. In this contribution, we illustrate its most important application, that is, sampling multidimensional collective variable space and reconstructing free energy landscapes. Example simulations are presented, which make use of the first publicly released ABF implementation capable of multidimensional calculations, and are discussed alongside the results of identical simulations performed with the metadynamics method.[4]

In the following section, the theoretical framework underlying this ABF implementation is described, and its range of applicability as well as its technical limitations are discussed. Next, physical processes in four molecular systems are explored using ABF, conformational equilibria of *N*-acetyl-*N*′-methylalaninamide (NANMA), Met-enkephalin, and deca-alanine, as well as ion diffusion through a membrane-spanning peptide nanotube. The metadynamics approach is also applied to the NANMA and nanotube examples. The deca-alanine case is used to document the application of ABF to a three-dimensional reaction coordinate. The choice of reaction coordinate space, numerical behavior, and convergence of the simulations, as well as compared properties of the two methods, are discussed.

Methods

Defining Reaction Coordinates. The strategy described here consists of using ABF or metadynamics to map a complex, slow molecular process, based on simulated trajectories that are orders of magnitude shorter than its natural time scale. This can be achieved by navigating a carefully chosen reduced representation, the "reaction co-ordinate space", in an accelerated fashion. The minimum requirement for this approach to be useful is that the reduced representation resolves the end points of the transformation and, more generally, all states that one wishes to describe based on empirical knowledge of the system. For numerical efficiency of the sampling scheme, however, the chosen degrees of freedom should capture all kinetically significant regions of configuration space: the metastable intermediates and most probable transition pathways.

In chemical terminology, a reaction coordinate is a one-dimensional geometric parameter that can be used to measure the progression of a reaction.[36] Moving from the realm of chemical reactions to that of physical transformations in soft matter and biological systems, however, fluctuations along many degrees of freedom may become as important to the reaction kinetics as the progression along any particular pathway. One-dimensional descriptors then become less useful, while constructing single variables that may play this role becomes more cumbersome and less intuitive.

For the purpose of numerical simulations, the optimal situation is to achieve time scale separation, whereby all key slow degrees of freedom are described explicitly, so that other degrees of freedom coupled to the transformation relax on a short time scale, as compared to the length of the simulated trajectories. This time scale influences both the diffusion rate of the system in reaction coordinate space and the rate of convergence of quantities that are measured as a function of the reaction coordinates, such as the free energy gradient in ABF calculations.

Thermodynamic Integration in Configuration Space. This section gives a brief historical overview of the theoretical results that led to the ABF method.[7] The general principles of thermodynamic integration (TI) can be found in early work by Kirkwood[37] and Zwanzig.[38] In TI, the free energy derivative is computed as the ensemble average of an instantaneous force, F, acting on the reaction parameter ξ:

$$\frac{dA}{d\xi} = -\langle F \rangle_\xi \tag{1}$$

In most applications of TI to configurational variables, sampling along the reaction pathway is obtained by constraining the reaction coordinate, the so-called "blue moon ensemble". In one of the earliest cases, F was simply obtained as the force exerted by the solvent on two atomic ions, projected onto the interionic distance.[39] Shortly afterward, a general expression for the average force was proposed by Carter et al.[40] The expression features a Jacobian correction term, purely geometric in origin, and is based on an explicit set of generalized coordinates $(\xi, \mathbf{q})$ including the reaction coordinate ξ:

$$F(\xi, \mathbf{q}) = -\frac{\partial U(\xi, \mathbf{q})}{\partial \xi} + k_B T \frac{\partial \ln|J(\xi, \mathbf{q})|}{\partial \xi} \tag{2}$$

The explicit coordinate transform from (x_i) to $(\xi, \mathbf{q})$ is needed to define and compute both the Jacobian determinant $|J(\xi, \mathbf{q})|$ and the partial derivative $\partial U(\xi, \mathbf{q})/\partial \xi$ of the potential energy U. The latter quantity depends implicitly on the vector field $(\partial x_i/\partial \xi)$, hereafter referred to as "inverse gradient". This vector field can be thought of as the direction along which

an infinitesimal change in ξ is propagated in Cartesian coordinates, the complementary coordinates **q** being kept constant. By definition, at any point of configuration space, the dot product of the inverse gradient with the Cartesian gradient of ξ is unity.

A significant step toward lifting the requirement of a full coordinate transform was accomplished by Ruiz-Montero et al.,[41] who proposed to use an implicit set of complementary coordinates $\mathbf{q} \equiv (q_i)$ that would obey:

$$\nabla q_i \cdot \nabla q_j = \delta_{ij} \qquad (3)$$

$$\nabla \xi \cdot \nabla q_i = 0 \qquad (4)$$

Under these assumptions, a simpler expression holds:

$$F(\xi, \mathbf{q}) = -\frac{\nabla U \cdot \nabla \xi}{|\nabla \xi|^2} + k_B T \frac{(\nabla |\nabla \xi|) \cdot \nabla \xi}{|\nabla \xi|^3} \qquad (5)$$

In this formulation, the inverse gradient is replaced with a vector proportional to the gradient $\nabla \xi$, and no generalized coordinate other than ξ itself is involved. Den Otter and Briels noted,[42] however, that a set of complementary coordinates obeying eqs 3 and 4 is not guaranteed to exist and showed that, in fact, it does not exist in a case as simple as polar coordinates in two dimensions.

In a later publication,[43] den Otter put forward the visionary idea that the change in ξ can be propagated along an arbitrary vector field, provided that it satisfies orthonormality conditions similar to eqs 3 and 4. This obviates the need for a full coordinate transform, and the propagating field generalizes the role played by the inverse gradient (which is always a possible choice if a coordinate transform is available). Ciccotti, Kapral, and Vanden-Eijnden[44] extended den Otter's formalism to a multidimensional reaction coordinate $\boldsymbol{\xi} = (\xi_i)$, in the presence of a set of constraints of the form $\sigma_k(\mathbf{x}) = 0$. For each coordinate ξ_i, let $\mathbf{v}_i$ be a vector field ($\mathbb{R}^{3N} \to \mathbb{R}^{3N}$, where N is the number of atoms) satisfying, for all j and k:

$$\mathbf{v}_i \cdot \nabla \xi_j = \delta_{ij} \qquad (6)$$

$$\mathbf{v}_i \cdot \nabla \sigma_k = 0 \qquad (7)$$

The ith partial derivative of the free energy surface can then be calculated as the ensemble average of the following thermodynamic force:

$$F_i(\boldsymbol{\xi}, \mathbf{q}) = -\nabla U \cdot \mathbf{v}_i + k_B T \nabla \cdot \mathbf{v}_i \qquad (8)$$

Ciccotti et al. note that a set of vector fields $\mathbf{v}_i$ can always be constructed by orthonormalization. There is, however, no simple algorithm to evaluate the divergence of $\mathbf{v}_i$ numerically. This term involves the second spatial derivatives of (ξ_i), making numerical schemes potentially costly and subject to high variance. In practice, analytical derivation is often possible, although cumbersome; the present implementation relies on such analytical derivatives.

Adaptive Biasing Force Method for Multidimensional Coordinates. The ABF method was put forth in 2001 by Darve and Pohorille.[7] Its principle is to perform thermodynamic integration in configuration space based on an unconstrained simulation, in which a history-dependent bias is applied; this bias is designed to cancel the running estimate of the local free energy gradient. In the same contribution,

an estimator making use of a constraint algorithm was proposed. More recently, the same authors have described a new estimator for the free energy gradient, based on time derivatives of the reaction coordinates, and its use for multidimensional ABF calculations.[8]

The NAMD 2.6 implementation of the ABF method using eqs 2 and 8 (in the original one-dimensional version of den Otter) has been described previously.[6] In comparison, the present implementation offers a greatly extended range of applications by allowing multidimensional free energy surfaces to be computed, and by handling linear combinations of predefined variables. Multidimensional ABF may be implemented on the basis of various formulations of thermodynamic integration: this implementation relies on computation of free energy gradients based on eq 8, in arbitrary dimension, as published by Ciccotti et al.[44] The algorithm is otherwise identical to that described previously.[6–8] Much of the new code base is shared with the rest of the Collective Variables Module, which will be described in detail elsewhere. Increased flexibility does imply some restrictions on the way variables can be combined: as in the previous implementation, eq 7 has to be satisfied, should any degree of freedom be constrained. In addition, collective variables must obey eq 6. For modularity, program objects handling different collective variables function independently. As a result, the option of run-time orthogonalization suggested by Ciccotti et al.[44] is not available, and the orthogonality relationship 6 has to be enforced by construction of the variables. A trivial way of achieving this is to combine variables that depend on nonoverlapping sets of Cartesian coordinates, as illustrated by most of the ABF calculations discussed in the following sections. In the case of chloride permeation through the nanotube, the longitudinal and radial coordinates are orthogonal by construction.

The direct benefit of an ABF simulation, besides enhanced sampling in the molecular dynamics (MD) trajectory, is an estimate of the free energy gradient, discretized on a regular lattice. In dimensions higher than one, several numerical routes can be followed to integrate this gradient and obtain the free energy surface itself. Other groups have proposed[8,45] to expand the free energy on a basis of spline or Gaussian functions and minimize the square deviation of the gradient at a predefined set of control points. Here, a different approach is adopted: the free energy landscape is reconstructed on the basis of discrete Monte Carlo sampling of the lattice. Convergence is accelerated by introducing a history-dependent biasing potential, which is incremented locally at each step, much in the spirit of conformational flooding[46] or metadynamics.[4] This method has fewer tunable parameters than the aforementioned techniques, and it is natural to use the same lattice that was used to discretize the ABF calculation. Unlike the method based on smooth radial functions,[45] its convergence speed worsens rapidly as the dimension increases. ABF calculations, however, are unlikely to be performed in high dimension due to the computational obstacles that the current form of the algorithm entails. Indeed, only one ABF result in dimension higher than one has been reported so far,[8] that is, the two-dimensional Ramachandran map of NANMA. It is, nevertheless, conceivable that ABF

could be recast into a more scalable form, paving the way for higher-dimension applications.

Computational Details

Molecular Dynamics Simulations. All simulations reported here were carried out using version 2.7b1 of the molecular dynamics program NAMD.[9,47] Condensed-phase simulations were performed in the isobaric−isothermal ensemble. The pressure and the temperature were fixed at 1 bar and 300 K, respectively, employing the Langevin piston algorithm[48] and softly damped Langevin dynamics. Periodic boundary conditions were applied in the three directions of Cartesian space. Short-range Lennard-Jones and Coulomb interactions were truncated smoothly by means of a 12 Å spherical cutoff with a switching function applied beyond 10 Å. The particle-mesh Ewald method[49] was employed to compute long-range electrostatic interactions. The Verlet I *r*-RESPA multiple time-step integrator[50] was used with a time step of 2 and 4 fs for for updating short- and long-range forces, respectively. Covalent bonds involving a hydrogen atom were constrained to their equilibrium length. Gas-phase simulations were performed using a 0.5 fs time step, which is appropriate to ensure energy conservation, and bond lengths were not constrained. Other parameters were similar to those of condensed-phase simulations. The different chemical systems described in the present contribution were described by the all-atom CHARMM force field,[51] supplemented by the TIP3P water model.[52]

Free Energy Calculations. The present results were obtained using a software framework known as Collective Variables Module and implemented in NAMD, versions 2.7b1 and following. Detailed user-oriented documentation is available;[47] technical details will be published elsewhere.

Conformational Equilibrium of N-acetyl-N′-methylalaninamide. The first application consists of a proof-of-concept simulation of the prototypical, terminally blocked amino acid *N*-acetyl-*N*′-methylalaninamide (NANMA), often referred to as "alanine dipeptide".[53] Conformational sampling was performed in vacuum. The ϕ and ψ torsional angles of the backbone were handled as coupled variables covering each the full, $[-180°; +180°]$ range of the Ramachandran free energy map.[54] To increase the efficiency of the calculation, the latter map was split into four individual quadrants, corresponding to fully independent simulations. Each quadrant was discretized into bins $2.5° \times 2.5°$ wide, in which the force acting along the collective variables was accrued. In each quadrant, 25 ns of sampling was collected. A threshold of 100 force samples was set prior to application of the adaptive biasing force. Reconstruction of the complete free energy landscape was achieved by numerical integration of the two-dimensional gradients. The Ramachandran map was also sampled by means of the metadynamics algorithm. Sampling was collected from a 30 ns trajectory, and Gaussian biasing potentials of width 10° and height 0.1 kcal/mol were accumulated every 500 fs. The free energy difference between the C_{7eq} and C_{7ax} states was computed by integration over the corresponding regions V and V' of (ϕ, ψ)-space according to:

$$e^{-\beta \Delta A} = \frac{\int_V e^{-\beta \Delta A(\phi, \psi)} \, \mathrm{d}\phi \, \mathrm{d}\psi}{\int_{V'} e^{-\beta \Delta A(\phi, \psi)} \, \mathrm{d}\phi \, \mathrm{d}\psi} \tag{9}$$

Transition between the two lowest free energy states of the Ramachandran map, that is, C_{7eq} and C_{7ax}, which are stabilized by an intramolecular hydrogen bond formed between the carbonyl moiety of one terminus and the amino moiety of the other, was investigated with one-dimensional ABF, using as a collective variable the difference between two distance root mean-square deviations, $\xi = \mathrm{rmsd}(C_{7eq}) - \mathrm{rmsd}(C_{7ax})$. To ensure orthogonality of the variables according to eq 6, the two RMSDs were defined as two distinct subsets formed of six atoms of the peptide chain. Three independent, 20, 20, and 40 ns long, simulations were run, using a threshold of 5000 force samples prior to applying the adaptive biasing force along the chosen degrees of freedom.

Chloride Ion Permeation across a Peptide Nanotube. In this second application, translocation of an halide ion through a chemically engineered tubular structure is examined. Peptide nanotubes, which can be viewed as tailored synthetic ion channels, result from the self-assembly of cyclic peptides formed by alternated D-L-α-amino acids,[55,56] by means of a network of intermolecular hydrogen bonds.[57]

The peptide nanotube considered here consisted of eight stacked *cyclo*[LW]4 units, where underlined letters denote D-amino acids, immersed in a thermalized palmitoyl-oleoyl-phosphatidylcholine (POPC) bilayer formed by 48 lipid units, in equilibrium with 1572 water molecules. The complete molecular assembly was placed in a simulation cell of initial dimensions equal to $36 \times 41 \times 79$ Å^3. The two-dimensional free energy landscape delineating the translocation of a chloride ion across the tubular structure was determined along the longitudinal, ζ, and the radial, ρ, directions of the latter. Specifically, the model reaction coordinate was chosen as a subset of cylindrical polar coordinates: the distance separating the ion from the center of mass of the peptide nanotube, projected onto its long axis, in conjunction with the distance separating the ion from the axis. The reaction path spanned 40 and 3 Å in the ζ- and in the ρ-directions, respectively. In the ABF calculation, force samples were accrued in bins 0.1 Å wide. To increase the efficiency of the calculation, it was stratified into four nonoverlapping windows extending over 10 Å each in the ζ-direction and in which individual 30 ns trajectories were generated, corresponding to a total simulation time of 120 ns. A metadynamics simulation was performed using the same pair of variables, similarly split into four windows along *z*. Gaussian hills of width 0.3 Å and height 0.1 kcal/mol were added every 200 fs; the calculation was run for 44 ns.

Structure of Met-enkephalin in an Aqueous Solution. In this third application, a set of collective variables is utilized to explore the possible conformations of the short peptide Met-enkephalin in an explicit solvent. Met-enkephalin is an endogenous opioid, five-residue neurotransmitter peptide, YGGFM, found in mammals and known to inhibit the release of neurotransmitters upon activation of the relevant opioid receptors. On account of its small size and biological relevance, it has served as a paradigmatic system for

Multidimensional Free Energy Landscapes

J. Chem. Theory Comput., Vol. 6, No. 1, 2010 **39**

conformational search based on a variety of computational approaches.[58–72]

The molecular system consisted of Met-enkephalin immersed in a bath of 778 water molecules, which corresponds to a simulation cell of initial dimensions equal to $29 \times 29 \times 29$ Å^3. Conformational search was conducted in a two-dimensional space, combining the radius of gyration (R_g) of the short peptide to its distance rmsd with respect to a reference, helical structure. The reaction path spanned, respectively, 3.5 and 4.0 Å, in the R_g and rmsd directions. To ensure that the force measured along one variable does not act on the other (eq 6), two distinct subsets of atoms were defined to compute the distance rmsd and the radius of gyration, the five α-carbon atoms and all other heavy atoms of the peptide chain, respectively. The instantaneous force was accrued in bins 0.05 Å wide. No adaptive biasing force was applied below a threshold of 200 samples. The limited range covered by the two variables obviated the need for a stratification strategy. The two-dimensional free energy landscape reported in the present contribution was obtained from a total simulation time of 80 ns.

Conformational Landscape of Deca-alanine. To explore metastable conformations of deca-alanine in vacuum, starting points were chosen manually from preliminary ABF trajectories, and used as the seed for unbiased, 30 ns simulations, where relaxation and possible transitions to other local minima were monitored. Conformations typical of the long-lived, metastable conformers were extracted from these unbiased trajectories. The conformational free energy landscape of the peptide was then explored by means of ABF-biased simulations in one, two, and three dimensions. The one-dimensional calculation was based on the end-to-end distance d, that is, the distance between the carbonyl carbon atoms of residues 1 and 10. The duration of the simulated trajectory was 500 ns. The two-dimensional, 200 ns ABF calculation was based on both d and the minimal rmsd between the current structure and a typical β-hairpin conformation (structure E in Figure 6). The rmsd was calculated using α-carbon atoms only. Finally, a 400 ns three-dimensional ABF simulation was carried out: the set of collective variables was composed of three RMSDs, with respect to the typical α-helical, turn/3_{10}-helix, and ω-shaped turn, respectively. The structures of these conformers are described in the Results section. The three RMSDs were defined on the basis of α-carbon, carbonyl carbon, and peptide nitrogen atoms, respectively; these nonoverlapping sets of atoms ensured that eq 6 was obeyed.

Results and Discussion

Conformational Equilibrium of *N*-Acetyl-*N′*-methylalaninamide. In the past 30 years, the conformational equilibrium of NANMA has been investigated in ample detail, employing a variety of numerical approaches and potential energy functions.[4,8,53,73–93] Accurate reproduction of the gas-phase, two-dimensional Ramachandran free energy map, therefore, hardly constitutes a methodological prowess. Popular, well-established approaches like umbrella sampling[94] used in conjunction with the weighted histogram
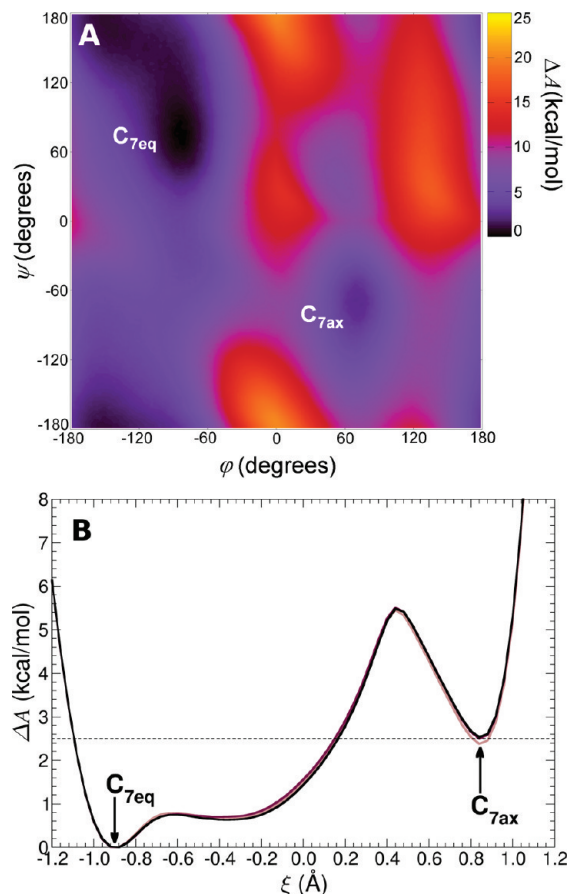

Figure 1. (A) Two-dimensional (ϕ, ψ) free energy landscape of *N*-acetyl-*N′*-methylalanylamide in the gas phase derived from a reference ABF calculation. (B) Free energy change along collective variable $\xi = \text{rmsd}(C_{7eq}) - \text{rmsd}(C_{7ax})$, the difference between the distance rmsd with respect to the C_{7eq} and C_{7ax} conformational states. The free energy profiles are obtained from independent 20 (light curve), 20 (dark curve), and 40 ns (black curve) ABF simulations.

analysis method[95] have proven to be perfectly adapted to rank with the desired accuracy the conformational states accessible to this paradigmatic peptide.[82] Furthermore, in several instances, NANMA has served as a discriminating test case for assessing the performance of novel numerical schemes.[8,83,96]

In the present work, determination of the two-dimensional free energy landscape of NANMA only represents the necessary preamble to an independent series of computations based on variables of higher collectivity than the mere ϕ and ψ torsional angles of the backbone. However predictable, the results of these preliminary free energy calculations depicted in Figure 1 agree quantitatively with previous investigations; see, for instance, ref 96. In particular, (ϕ, ψ)-integration over the basins corresponding to the C_{7eq} and C_{7ax} conformations, characterized by a long-lived intramolecular hydrogen bond, yields a free energy difference of 2.5 kcal/mol, in favor of the equatorial motif.[78,96]

The metadynamics calculation yields a free energy landscape identical to that determined by means of ABF (data not shown). Fast-relaxing, low-friction systems such as NANMA do not place high demands on the algorithms used to sample them, as demonstrated by early successes obtained

with limited sampling and unsophisticated algorithms. Meta-dynamics can be run with settings that result in high energy input (frequent accumulation of high hill potentials), without adverse consequences on the accuracy on the PMF. As a result, complete sampling can be obtained from a relatively short, 30 ns trajectory. As the ABF approach imposes that the system remains close to equilibrium, it requires a longer sampling time (100 ns). It is important to note, however, that this situation may not always occur in more delicate cases.

Transition between the lowest free energy states, C_{7eq} and C_{7ax}, of NANMA has been the object of a number of computational investigations published in the past decade.[83–85,89] In a nutshell, three possible, low free energy pathways can be considered to describe the (ϕ, ψ)-isomer-ization of the peptide. The first path connects the two conformations through the lowest point of the quasi-continuous free energy barrier arising around $\phi = 0°$. The second path uses the C_5, extended state as an intermediate between the C_{7eq} and C_{7ax} conformers, overcoming the free energy barrier located ca. $\phi = 120°$. Last, the third path partially overlaps with the previous one, yet, in lieu of diffusing in the wide basin that encompasses the C_5, C_{7eq}, and β conformations, visits the higher free energy states of the right-handed α-helix region.

As can be observed in Figure 1, the three independent free energy calculations that rely upon the use of variable $\xi = \text{rmsd}(C_{7eq}) - \text{rmsd}(C_{7ax})$ yield a consistent picture for the transition between C_{7eq} and C_{7ax}. Although a longer, 40 ns simulation has been performed for reference purposes, 20 ns appears to be ample to achieve convergence of the free energy. Each free energy profile possesses two distinct minima positioned almost equidistantly with respect to $\xi = 0$ Å and approximately 2.5 kcal/mol apart, in line with the measure based on the two-dimensional (ϕ, ψ) map. Interestingly enough, the three different curves exhibit a shallow free energy minimum emerging around -0.4 Å, which corresponds to an ensemble of C_5-like, extended states. This pseudominimum prefaces an abrupt, 5.6 kcal/mol barrier toward the C_{7ax} conformation, thereby suggesting that isomerization of NANMA proceeds through the second low free energy path outlined previously.

Chloride Ion Permeation across a Peptide Nanotube. Synthetic nanotubes resulting from the self-assembly of cyclic peptides are capable of conducting ions.[97] Synthesized with the proper amino-acid sequence, these nanotubes exhibit a pronounced tendency to insert as independent entities into the lipid bilayer, where they act as transmembrane channels.[98,99] Atomic-level mechanism and energetics of ion transport have been explored by means of complementary theoretical approaches.[100–102] In the light of calculations relying upon Poisson–Nernst–Planck theory, it has been suggested that conduction through open-ended tubular structures can be strongly modulated by the nature of the surroundings.[101,103,104] Such environmental effects on ion transport were subsequently quantified, employing free energy calculations, wherein a sodium ion was shuttled across the cavity of a peptide nanotube spanning the width of a fully hydrated POPC lipid bilayer.[26]
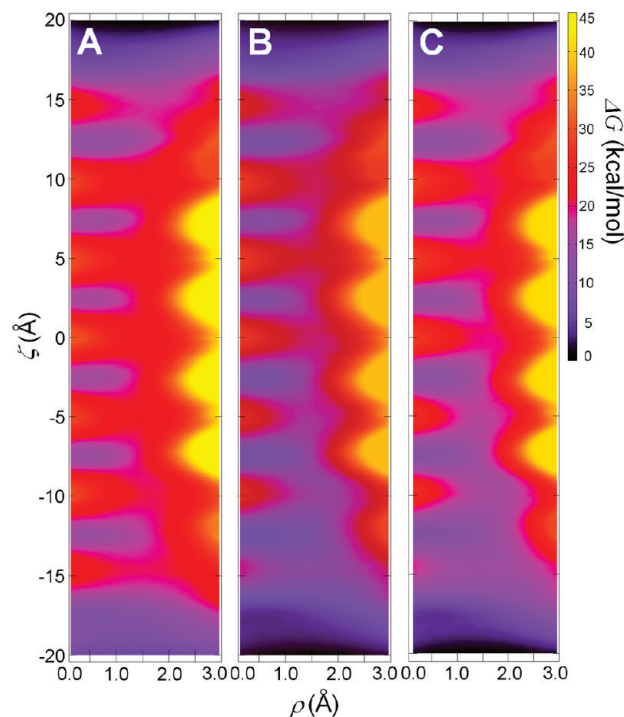

Figure 2. Comparison of the two-dimensional free energy landscapes characterizing the transport of a chloride ion in a peptide nanotube spanning a fully hydrated POPC lipid bilayer, using ABF, without (A) and with (B) periodicity-enforced integration of the gradients, and metadynamics (C). The free energy is measured concomitantly along the radial, ρ, and the longitudinal, ζ, directions of the membrane-spanning tubular structure.

In Figure 2, the two-dimensional (ρ, ζ) free energy maps delineating the translocation of a chloride ion in the same tubular structure are displayed, based on separate ABF and metadynamics calculations. From a methodological stand-point, the striking resemblance between the measured free energy landscapes ought to be underlined. Periodicity-enforced integration of the gradients obtained from the ABF calculation yields a free energy map that is by and large fully superimposable on that generated with metadynamics. A glance at the ABF maps reconstructed with and without periodicity suggests that introduction of the latter when integrating the gradients somewhat reshapes the free energy landscape, altering its expected symmetry with respect to $\zeta = 0$ Å.

In sharp contrast with sodium,[26] transport of chloride in the present peptide nanotube is markedly unfavorable. Translocation of the halide ion is burdened by a steep free energy barrier, on the order of 17 kcal/mol, at the mouth of the synthetic channel. This result is not completely surprising, given the radius of the pore formed by the stacked *cyclo*[LW]$_4$ peptide units, and the optimal aqueous coordination of chloride, found to be equal to ca. 6–8 at the experimental level,[105] and to about 7.5 on the basis of MD simulations in bulk water.[100] The significant free energy penalty arising at $\zeta = \pm15$ Å is, therefore, linked to a severe dehydration of the halide ion, entering the synthetic channel partially "naked".

Diffusion of the ion is further hampered by subsequent free energy barriers, ca. 7–8 kcal/mol high, emerging at the
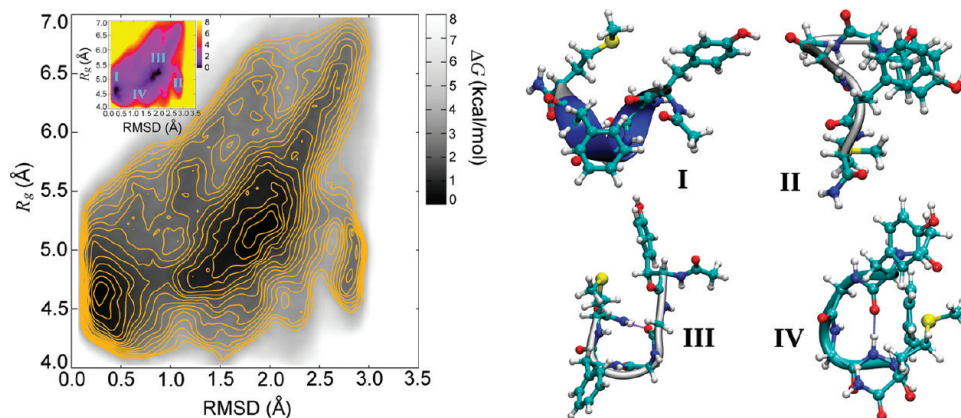
Figure 3. Two-dimensional (rmsd, R_g) free energy landscape of Met-enkephalin in aqueous solution. The position rmsd with respect to a helical conformation is measured over α-carbon atoms only. The radius of gyration, R_g, is evaluated over all heavy, but α-carbon atoms. Contours of the main two-dimensional map are separated by 0.5 kcal/mol. The **I**–**IV** key conformations of Met-enkephalin are charted on the inset free energy landscape and depicted to the right as cartoon and ball-and-stick representations. In the cartoon representation, color indicates secondary structure. Molecular graphics were rendered with VMD.[109]

midpoint between two adjacent cyclic peptides, the separation of which amounts to about 4.7 Å. Congruent with the simulations of the sodium ion,[26] in-plane coordination appears to be also the energetically preferred state for chloride. It is remarkable that the halide ion does not hop between cyclic peptides following a rectilinear path, collinear to the long axis of the synthetic channel at $\zeta = 0$ Å, but instead grazes the wall of the latter to form intermittent interactions with peptide amino moieties. This diffusion mode is reflected in a curvilinear low-free energy path apparent in Figure 2.

Structure of Met-enkephalin in an Aqueous Solution. On account of its unusual flexibility, Met-enkephalin can bind interchangeably either the δ, the κ, or the μ-opioid receptor, where it is anticipated to adopt distinct conformations. This, in large measure, rationalizes why experimental approaches have hitherto failed to propose a converging view of the native structure of this short peptide.[26,106,107] Although it is reasonable to believe that the marked flexibility of the backbone would be reflected in a generally flat free energy landscape, equilibrium MD simulations at a single temperature have proven to prevent exhaustive exploration of conformational space, the peptide chain being recurrently trapped kinetically in a random, unrepresentative conformation.[60] Despite its reduced length, Met-enkephalin, therefore, constitutes a pathological case for standard MD, but a well-suited candidate for more recent, multicanonical approaches, like replica-exchange MD,[108] aimed at enhancing ergodic sampling.

The two-dimensional free energy map of Figure 3 sheds light on the conformational space accessible to the short peptide along the directions of the position rmsd with respect to an arbitrary chosen helical motif and of the radius of gyration of the backbone. As has been commented on previously,[67] the free energy landscape of Met-enkephalin in aqueous solution consists of a rather wide, shallow basin, featuring a number of pronounced minima. At low distance rmsd and R_g, a compact, 3_{10}-helix motif (**I**) is observed, resulting primarily from the formation of an intramolecular hydrogen bond between the carbonyl group of residue i and

the amino group of residue $i + 3$, albeit transitory interconversion to an α-helical i to $i + 4$ hydrogen bond can be detected. Still at low R_g, but at a larger distance rmsd, around 2.8 Å, a free energy minimum (**II**) corresponding to an embryonic helix turn emerges about 2.1 kcal/mol higher than that of conformation **I**. A third minimum (**III**) can be found at a distance rmsd of 2.0 Å and an R_g of 5.2 Å, with a free energy equal to that of the helical motif **I** within statistical accuracy. Its U-shaped structure is essentially nonhelical, featuring an intermittent hydrogen bond formed between the terminal, blocking amino moiety and the carbonyl group of the first glycine residue. Last, a fourth conformational minimum (**IV**) can be found at a distance rmsd of 1.4 Å and an R_g of 4.8 Å, and corresponds to a free energy only 0.6 kcal/mol above that of structures **I** and **III**. In this free energy minimum, the peptide chain adopts a γ-turn conformation, often encountered in β-hairpin motifs.

It is apparent from the present results that, using a reduced set of collective variables and a single temperature, ABF is able to recover the complete free energy landscape of Met-enkephalin, virtually identical to that reported by Sanbonmatsu and Garcia on the basis of parallel-tempering MD simulations.[67] The (rmsd, R_g) two-dimensional map confirms, indeed, that this free energy landscape is relatively shallow and consists of essentially four distinct ensembles of conformations characterized by overall comparable free energies, barring structure **II**, and separated by appreciably low barriers.

The local minima are primarily distinguished by their rmsd value. Therefore, in this case, the second collective variable, R_g, is not essential to resolve the low free energy states, but it accelerates the sampling of transition pathways between them, and therefore the overall convergence of the calculation. The rmsd could be considered a one-dimensional reaction coordinate, while R_g is a degree of freedom in the orthogonal space that is included in the ABF calculation for numerical efficiency.

Conformational Free Energy Landscape of Deca-alanine. Deca-alanine in vacuum has been used several times as a computationally inexpensive and seemingly simple toy
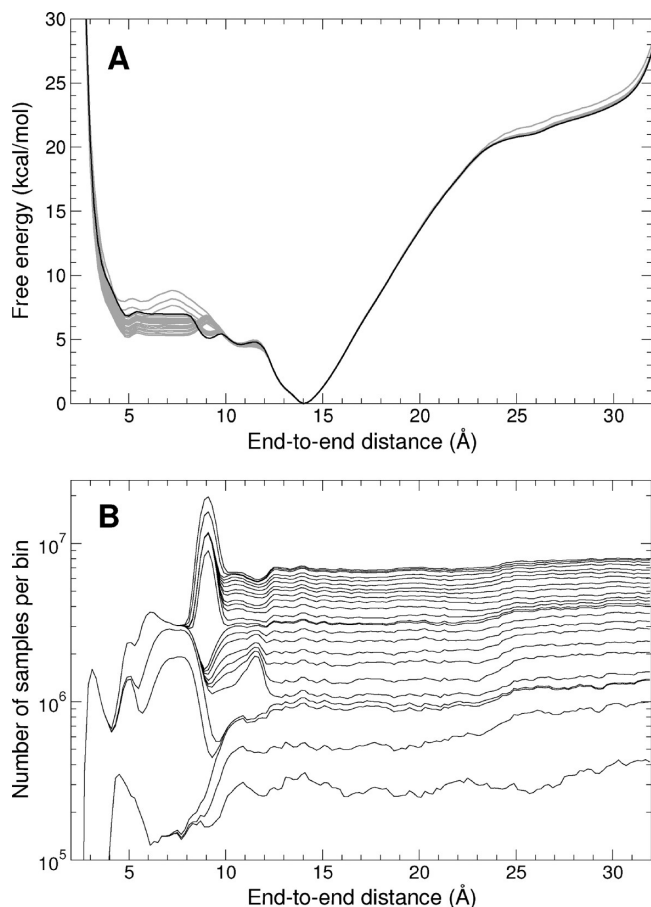
Figure 4. (A) One-dimensional free energy profile of deca-alanine in vacuum, as a function of the end-to-end distance. Intermediate results are plotted for every 20 ns period as gray lines; the final result of the 500 ns ABF simulation is shown as a dark line. (B) Sampling histograms (on a logarithmic scale) corresponding to the one-dimensional ABF simulation of deca-alanine. Each line is the full histogram at the end of a 20 ns period of the simulation.

model for conformational free energy calculations on peptides.[6,28,110–113] Stretching the peptide from its native, α-helical state to extended conformations, and back, is indeed a fairly straightforward transformation, for which relatively few pathways are possible. All simulations cited above, using the end-to-end distance of the peptide chain as a coordinate and various biasing schemes, achieve convergence and find potentials of mean force in good agreement with one another. Such simulations, however, only explore a small fraction of the conformational space available to deca-alanine. Indeed, when an attempt was made to sample the more compact conformations corresponding to end-to-end distances shorter than the α-helix length (i.e., less than 12 Å), it was found that several local minima, and the complex pathways linking them, were not resolved by that simple distance parameter. As a result, the complete free energy landscape of the peptide could not be mapped.[28]

As can be seen from Figure 4B, using ABF to sample the end-to-end coordinate d provides very uniform histograms for elongated structures, and uneven, sporadic sampling of the compact region. Thus, the potential of mean force shown in Figure 4A, while very accurate for d greater than 12 Å, is

not converged for smaller values. Furthermore, it does not exhibit clear features that could be related to the metastable conformations that can be identified in that region. The reason behind such nonuniform sampling of the low-d range is that d is a highly degenerate descriptor of most of the conformational space of deca-alanine. Even with an ideally converged adaptive bias canceling the free energy profile, some of the transitions would remain rare events, essentially because the enthalpic or entropic barriers are orthogonal to the direction of the bias.

Unbiased simulations starting from structures chosen from the ABF simulations indicate several metastable conformers whose lifetime is at least 30 ns. In order of increasing relative potential energy, these structures are the α-helix (0 kcal/mol), a loop containing a short 3_{10}-helical segment (3.5 kcal/mol), an ω-shaped loop composed of β and other turns (6.2 kcal/mol), a β-bridged loop (9.3 kcal/mol), a β-hairpin (9.8 kcal/mol), and a slightly expanded π-helix featuring transient i to $i + 5$ hydrogen bonds (11 kcal/mol). These conformations are represented in Figure 6.

To resolve the compact states that are merged in the one-dimensional landscape, the distance parameter was supplemented with a second degree of freedom, the position rmsd from a typical β-hairpin conformation. The results are represented in Figure 5. Although a large fraction of the reduced space is visited, sampling tends to accumulate in a few localized regions (Figure 5B), suggesting a failure of the collective variables to describe all of the free energy barriers in these regions. The global free energy minimum corresponding to the α-helix is clearly visible in the measured free energy landscape (Figure 5A). In contrast, the basins corresponding to metastable structures are almost coalesced and separated by low barriers, inconsistent with the long lifetimes of these conformers. Despite its limits, the two-dimensional profile is consistent with the one-dimensional free energy of 4 in the region containing the α-helix and the extended states.

Finally, a set of three RMSDs was chosen to try and resolve the numerous conformers of similar compactness of deca-alanine. The three-dimensional PMF is shown in Figure 6. In general, the differences in free energy between the metastable conformers and the α-helix are smaller than the potential energy differences, indicating significant entropy–enthalpy compensation. Indeed, the α-helix is more rigid than the other conformers. Because of the width of basins corresponding to individual conformers, and the short distance separating them in the reduced space, some conformers are still not perfectly resolved, in particular in the low free energy region containing the β-hairpin and β-bridge structures. Indeed, the local free energy minimum in that region contains conformations similar to both structures, whose similarity renders difficult to distinguish in a low-dimension representation. The free energy landscape is, however, sufficiently resolved for the complete conformational space to be explored at a much increased rate due to the adaptive bias. Here, because the full conformation space of flexible peptide is explored, the rmsd coordinate is not robust over its entire range. Specifically, at very high rmsd values, the structure becomes too dissimilar from the
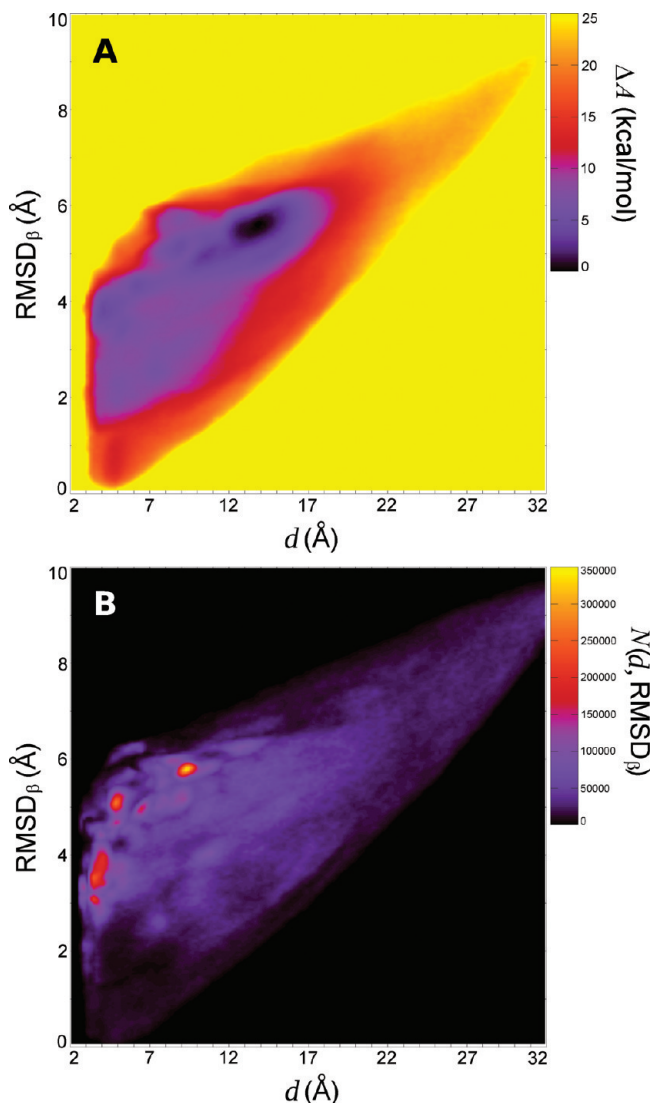
Figure 5. Two-dimensional ABF description of the conformations of deca-alanine in vacuum. The variables used for ABF are the end-to-end distance and the position rmsd with respect to a β-hairpin conformation. (A) Free energy landscape. (B) Sampling histogram at the end of the 200 ns simulation.

reference coordinates for the optimal rotation to be uniquely defined. In such regions of conformation space, the gradient of the rmsd is irregular and exhibits jumps, and hence forces measured or applied along that direction have little physical significance. It should nevertheless be noted that in more realistic applications, the relevant range of the rmsd will typically be limited to the region where the optimal rotation is unique, hence avoiding the issue altogether.

Deca-alanine exhibits a very structured, corrugated free energy landscape, featuring a rich set of metastable conformers. Although the peptide is of little intrinsic biochemical relevance, particularly in vacuum, it proves to be a challenging test case for conformational sampling algorithms.

Comparison of ABF and Metadynamics. The ABF and metadynamics schemes rely on several comparable parameters. The choice of collective variables is crucial in both cases. Metadynamics offers more flexibility in the choice and implementation of collective variables, because only the value and gradient of the variables are needed, not their

second derivatives. In the present implementation, any set of variables can be used together: there is no orthogonality requirement. Both methods require a width parameter, the Gaussian hill width in metadynamics and the bin width in ABF. This parameter defines the spatial resolution of both the time-dependent bias and the final PMF. Finally, a metadynamics simulation can be characterized by a filling rate, equal to the height of the Gaussian potential increments divided by the period of addition of such increments. This parameter controls how much work is performed on the system by the bias, and this quantity is typically constant for the complete duration of the simulation. The corresponding parameter of ABF, the threshold amount of sampling before the adaptive bias is enabled, is not equivalent to the filling rate. It has the dimension of a time rather than that of a power, and it only affects the initial behavior of the simulation. Once the amount of sampling is above that threshold, and neglecting the finite resolution of the lattice, the behavior of ABF is entirely specified by the algorithm, regardless of the values of tunable parameters.

In biased simulations that rely on reduced representations comprising few degrees of freedom, the most common shortcoming is the slow relaxation of other, "hidden" degrees of freedom, not included in the chosen set of collective variables. Under these premises, the underlying energy landscape of a given point in reduced space may change during the simulation, with the result that data collected previously become "stale", at least on the time scale of assisted diffusion in reduced space.[24] In principle, in the limit of ergodic sampling, even the slowest degrees of freedom are fully thermalized and convergence occurs. In practice, however, achieving this situation is highly dependent on the relevance of the reduced space as a reaction coordinate.

In any such nonideal situation, the exact form of history dependence of the biasing algorithm comes into play. Metadynamics is almost always performed with a constant height of the Gaussian hills, chosen to meet the desired accuracy through a theoretical estimate of the error.[114,115] This gives the method a finite memory time, which can be identified as the time required to explore the whole landscape. In this case, if relaxation of hidden degrees of freedom modifies the potential seen by the collective variables, metadynamics will fill up the minima of the "new" free energy landscape, until all memory of the previous landscape has been erased. It seems possible that such a situation might give rise to a cyclic behavior, where the locally measured free energy (on the time scale of metadynamics) oscillates between values corresponding to different basins, as dictated by transitions of hidden, slow degrees of freedom. This behavior might, however, be viewed as useful, in that it allows the method to recover from situations where inaccurate data have been collected, either as a result of deficiencies in the reduced representation or due to irreversible work performed by the metadynamics bias.

ABF, in contrast, has an effectively infinite memory time. Once a data point has been accumulated in the average, its weight decreases as the inverse of the total number of samples, that is, as $1/t$. For this reason, the oscillating behavior described above is unlikely. Instead, a commonly
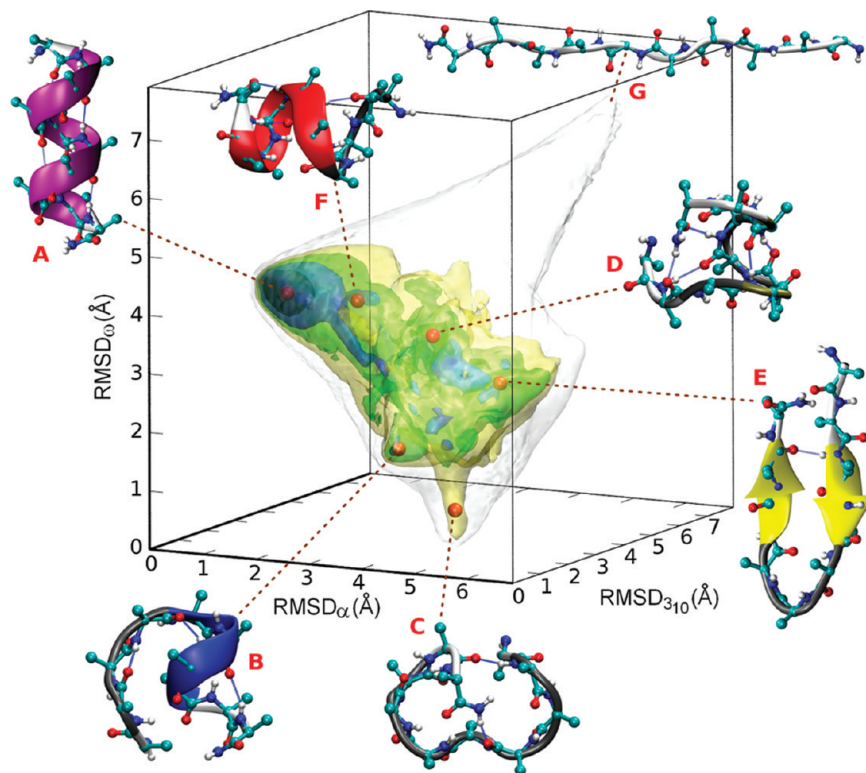
Figure 6. Three-dimensional conformational free energy landscape of deca-alanine, as a function of the rmsd with respect to ideal α-helical, ω-shaped γ-turn, and turn/3_{10}-helix conformations, respectively. The free energy was computed by numerically integrating the gradient obtained from a 400 ns ABF simulation. Free energy isosurfaces are shown for respective values of 3 (black), 6 (blue), 9 (green), 12 (yellow), and 24 kcal/mol (white). Average positions corresponding to metastable conformations are indicated by red spheres. Conformers are shown as ball-and-stick and cartoon representations, with color indicating secondary structure (purple, α-helix; blue, 3_{10}-helix; red, π-helix; gray, turn; yellow, β-strand; tan, β-bridge; white, unstructured). Hydrogen bonds are indicated as blue lines. The conformers are labeled using red capital letters: (A) α-helix, (B) turn/3_{10}-helix, (C) ω-shaped turn, (D) β-bridge, (E) β-hairpin, (F) π-helix, and (G) extended form (unstable).

observed effect of slowly relaxing hidden degrees of freedom is a change of the sampling behavior as the simulation progresses. Over time, the relative weight of newly accrued data in the average decreases, as does the responsiveness of the time-dependent bias to changes in the locally measured thermodynamic force. This is the desired behavior in the ideal context of a perfect reaction coordinate space, where all orthogonal degrees of freedom are either fast, or kinetically trapped and not relevant to the transformation under study. In real cases, the symptom is an initially efficient exploration of reduced space, followed by an increasing tendency to get trapped in local minima as they are "discovered" through relaxation in the orthogonal space and crossing of hidden barriers. This is observed, to a minor extent, in the 2D and 3D deca-alanine simulations described in the previous sections. Arguably, such behavior is indicative of failure of the reduced space to capture the reactive intermediates and pathways to a degree that allows for sampling over the intended (or technically feasible) time scale.

Metadynamics is designed as a nonequilibrium method, whereas ABF relies on equilibrium sampling from the canonical ensemble. In practice, ABF simulations go through an initial stage during which the estimate of the local free energy gradient evolves rapidly; then the running average is updated on a much slower scale, and eventually stabilizes altogether. Applying a biasing force based on the early, fast-fluctuating estimate of the free energy gradient may push

the dynamics into a nonequilibrium regime. This initial departure from equilibrium conditions can be greatly reduced in practice by delaying the introduction of the biasing force until after the large fluctuations of the running average have ended: this is accomplished by waiting for a preset number of samples to be accrued in a local bin.[6,8,28] Should any nonequilibrium effects occur, however, force samples measured in that phase are still taken into account in the average, and, as mentioned above, this contribution never vanishes. Any bias (typically, an overestimated free energy gradient) due to irreversible work performed in the beginning of the simulation will taint the final data, with a weight that only decays as $1/t$. In contrast, exponential convergence of ABF has only been proved under somewhat restrictive assumptions, including the use of a large number of replicas.[116] When a metadynamics run is carried out with constant hill height, irreversible work is performed throughout the simulation. This contribution may only be deemed to have been eliminated from the measured PMF once multiple sweeps have been observed (or, in higher dimension, multiple transitions between neighboring basins).

Both issues (slow hidden variables and irreversible work) can be alleviated by restricting the data set used to reconstruct the free energy, eliminating selected, problematic data. In metadynamics, this is achieved by stopping the simulation once the system leaves the relevant region of configuration space. In ABF, data collected in the initial, out-of-equilibrium

Multidimensional Free Energy Landscapes

J. Chem. Theory Comput., Vol. 6, No. 1, 2010 **45**

stage can be removed from the final average. Metadynamics performs well in low-friction systems such as the peptide nanotube example, because the filling rate (hill height divided by the hill accumulation period) can be increased while maintaining a level of irreversible work that does not hinder convergence.

Conclusion

An implementation of the ABF approach supporting multi-dimensional reaction coordinates based on sophisticated variables is proposed. This implementation is available in the scalable molecular-dynamics program NAMD, but can be readily incorporated into any MD platform. The method and its implementation have been tested on a variety of biomolecular systems. Multidimensional reaction descriptors improve the level of detail in which molecular processes can be mapped, as in the case of chloride permeation through a self-assembled peptide nanotube. In systems featuring particularly complex free energy landscapes, such as the multiple metastable conformations of deca-alanine, efficient sampling is only possible when applying the adaptive bias in a two- or three-dimensional reduced space. The work of constructing an appropriate reduced representation is made easier by the availability of variables such as the position rmsd, and the flexibility afforded by linear combinations of predefined variables.

Two of the test cases were used to compare directly ABF and the metadynamics method, applied on the same variables, under otherwise identical simulation conditions. Both approaches yield the expected results in terms of phase space exploration and sampling, and reconstruction of the free energy landscape. Neither can be said to be more efficient or accurate than the other on general grounds. Still, metadynamics does offer an inexpensive way to rapidly explore simple, fast-relaxing systems that are robust enough to withstand a high energy input, as is apparent from the toy model of NANMA, while ABF may constitute a safer option for more fragile systems. Differences are likely to become most apparent in difficult scenarios, where the two approaches react differently to incomplete sampling and nonequilibrium effects. Whereas metadynamics is much more likely to perform significant irreversible work in late stages of such simulations, ABF may become inefficient and sample reduced regions for disproportionate times.

The most crucial issue remains the choice of a reaction coordinate space. As illustrated in the deca-alanine example, describing a small system with seemingly limited phase space may require multiple parameters, fine-tuned to resolve nearby points of conformation space that, nevertheless, belong to different low free energy basins or pathways. More sophisticated collective variables will be developed to describe complex, frustrated free energy landscapes. The existing algorithms will evolve toward better scalability, or be replaced altogether by new sampling methods. In any event, it is essential for the progress of large-scale applications that new developments in sampling and free energy algorithms be kept in phase with state-of-the-art, parallel simulation software.

References

(1) Rodinger, T.; Pomès, R. *Curr. Opin. Struct. Biol.* **2005**, *15*, 164–170.

(2) *Free Energy Calculations. Theory and Applications in Chemistry and Biology*; Chipot, C., Pohorille, A., Eds.; Springer Verlag: New York, 2006.

(3) Lei, H.; Duan, Y. *Curr. Opin. Struct. Biol.* **2007**, *17*, 187–191.

(4) Laio, A.; Parrinello, M. *Proc. Natl. Acad. Sci. U.S.A.* **2002**, *99*, 12562–12565.

(5) Bonomi, M.; Branduardi, D.; Bussi, G.; Camilloni, C.; Provasi, D.; Raiteri, P.; Donadio, D.; Marinelli, F.; Pietrucci, F.; Broglia, R. A.; Parrinello, M. PLUMED: a portable plugin for free-energy calculations with molecular dynamics; 2009; arXiv:0902.0874v3 [physics.comp-ph]; arXiv.org ePrint archive, http://www.arXiv.org/abs/0902.0874 (accessed Nov. 9, 2009).

(6) Hénin, J.; Chipot, C. *J. Chem. Phys.* **2004**, *121*, 2904–2914.

(7) Darve, E.; Pohorille, A. *J. Chem. Phys.* **2001**, *115*, 9169–9183.

(8) Darve, E.; Rodríguez-Gómez, D.; Pohorille, A. *J. Chem. Phys.* **2008**, *128*, 144120.

(9) Phillips, J. C.; Braun, R.; Wang, W.; Gumbart, J.; Tajkhorshid, E.; Villa, E.; Chipot, C.; Skeel, R. D.; Kalé, L.; Schulten, K. *J. Comput. Chem.* **2005**, *26*, 1781–1802.

(10) Hénin, J.; Pohorille, A.; Chipot, C. *J. Am. Chem. Soc.* **2005**, *127*, 8478–8484.

(11) Xu, J.; Crowley, M. F.; Smith, J. C. *Protein Sci.* **2009**, *18*, 949–959.

(12) Halling-Brown, M. D.; Moss, D. S.; Sansom, C. E.; Shepherd, A. J. *Philos. Trans. R. Soc. London, Ser. A* **2009**, *367*, 2705–2716.

(13) Weronski, P.; Jiang, Y.; Rasmussen, S. *Biophys. J.* **2007**, *92*, 3081–3091.

(14) Gorfe, A. A.; Babakhani, A.; McCammon, J. A. *Angew. Chem., Int. Ed.* **2007**, *46*, 8234–8237.

(15) Gorfe, A. A.; McCammon, J. A. *J. Am. Chem. Soc.* **2008**, *130*, 12624–12625.

(16) Vaitheeswaran, S.; Thirumalai, D. *Proc. Natl. Acad. Sci. U.S.A.* **2008**, *105*, 17636–17641.

(17) Yu, Y.; Chipot, C.; Cai, W.; Shao, X. *J. Phys. Chem. B* **2006**, *110*, 6372–6378.

(18) Cai, W.; Sun, T.; Liu, P.; Chipot, C.; Shao, X. *J. Phys. Chem. B* **2009**, *113*, 7836–7843.

(19) Rodriguez, J.; Elola, M. D. *J. Phys. Chem. B* **2009**, *113*, 1423–1428.

(20) Rodriguez, J.; Semino, R.; Laria, D. *J. Phys. Chem. B* **2009**, *113*, 1241–1244.

(21) Treptow, W.; Tarek, M. *Biophys. J.* **2006**, *90*, L64–L66.

(22) Lamoureux, G.; Klein, M. L.; Berneche, S. *Biophys. J.* **2007**, *92*, L82–L84.

(23) Ivanov, I.; Cheng, X.; Sine, S. M.; McCammon, J. A. *J. Am. Chem. Soc.* **2007**, *129*, 8217–8224.

(24) Hénin, J.; Tajkhorshid, E.; Schulten, K.; Chipot, C. *Biophys. J.* **2008**, *94*, 832–839.

(25) Dehez, F.; Pebay-Peyroula, E.; Chipot, C. *J. Am. Chem. Soc.* **2008**, *130*, 12725–12733.

(26) Dehez, F.; Tarek, M.; Chipot, C. *J. Phys. Chem. B* **2007**, *111*, 10633–10635.

(27) Hénin, J.; Shinoda, W.; Klein, M. *J. Phys. Chem. B* **2008**, *112*, 7008–7015.

(28) Chipot, C.; Hénin, J. *J. Chem. Phys.* **2005**, *123*, 244906.

(29) Hénin, J.; Schulten, K.; Chipot, C. *J. Phys. Chem. B* **2006**, *110*, 16718–16723.

(30) Lee, E. H.; Hsin, J.; Mayans, O.; Schulten, K. *Biophys. J.* **2007**, *93*, 1719–1735.

(31) Blumberger, J.; Lamoureux, G.; Klein, M. L. *J. Chem. Theory Comput.* **2007**, *3*, 1837–1850.

(32) Kuang, Z.; Mahankali, U.; Beck, T. L. *Proteins* **2007**, *68*, 26–33.

(33) Spiegel, K.; Magistrato, A.; Carloni, P.; Reedijk, J.; Klein, M. L. *J. Phys. Chem. B* **2007**, *111*, 11873–11876.

(34) Zheng, L.; Chen, M.; Yang, W. *Proc. Natl. Acad. Sci. U.S.A.* **2008**, *105*, 20227–20232.

(35) Zheng, L.; Chen, M.; Yang, W. *J. Chem. Phys.* **2009**, *130*, 234105.

(36) *IUPAC Compendium of Chemical Terminology*, 2nd ed. (the "Gold Book"); McNaught, A. D., Wilkinson, A., Eds.; Blackwell Scientific Publications: Oxford, 1997.

(37) Kirkwood, J. G. *J. Chem. Phys.* **1935**, *3*, 300–313.

(38) Zwanzig, R. W. *J. Chem. Phys.* **1954**, *22*, 1420–1426.

(39) Ciccotti, G.; Ferrario, M.; Hynes, J. T.; Kapral, R. *Chem. Phys.* **1989**, *129*, 241–251.

(40) Carter, E, A.; Ciccotti, G.; Hynes, J. T.; Kapral, R. *Chem. Phys. Lett.* **1989**, *156*, 472–477.

(41) Ruiz-Montero, M. J.; Frenkel, D.; Brey, J. J. *Mol. Phys.* **1997**, *90*, 925–941.

(42) den Otter, W. K.; Briels, W. J. *J. Chem. Phys.* **1998**, *109*, 4139–4146.

(43) den Otter, W. K. *J. Chem. Phys.* **2000**, *112*, 7283–7292.

(44) Ciccotti, G.; Kapral, R.; Vanden-Eijnden, E. *ChemPhysChem* **2005**, *6*, 1809–1814.

(45) Maragliano, L.; Vanden-Eijnden, E. *J. Chem. Phys.* **2008**, *128*, 184110.

(46) Grubmüller, H. *Phys. Rev. E* **1995**, *52*, 2893–2906.

(47) Bhandarkar, M.; Brunner, R.; Buelens, F.; Chipot, C.; Dalke, A.; Dixit, S.; Fiorin, G.; Freddolino, P.; Grayson, P.; Gullingsrud, J.; Gursoy, A.; Hardy, D.; Harrison, C.; Hénin, J.; Humphrey, W.; Hurwitz, D.; Krawetz, N.; Kumar, S.; Nelson, M.; Phillips, J.; Shinozaki, A.; Zheng, G.; Zhu, F. *NAMD user's guide, version 2.7*; Theoretical biophysics group, University of Illinois and Beckman Institute: Urbana, IL, 2009.

(48) Feller, S. E.; Zhang, Y. H.; Pastor, R. W.; Brooks, B. R. *J. Chem. Phys.* **1995**, *103*, 4613–4621.

(49) Darden, T. A.; York, D. M.; Pedersen, L. G. *J. Chem. Phys.* **1993**, *98*, 10089–10092.

(50) Tuckerman, M. E.; Berne, B. J.; Martyna, G. J. *J. Phys. Chem. B* **1992**, *97*, 1990–2001.

(51) MacKerell, A. D., Jr. *J. Phys. Chem. B* **1998**, *102*, 3586–3616.

(52) Jorgensen, W. L.; Chandrasekhar, J.; Madura, J. D.; Impey, R. W.; Klein, M. L. *J. Chem. Phys.* **1983**, *79*, 926–935.

(53) Rossky, P. J.; Karplus, M. *J. Am. Chem. Soc.* **1979**, *101*, 1913.

(54) Ramachandran, G.; Ramakrishnan, C.; Sasisekharan, V. *J. Mol. Biol.* **1963**, *7*, 95–99.

(55) Ghadiri, M. R.; Granja, J. R.; Buehler, L. K. *Nature* **1994**, *369*, 301–304.

(56) Hartgerink, J. D.; Granja, J. R.; Milligan, R. A.; Ghadiri, M. R. *J. Am. Chem. Soc.* **1996**, *118*, 43–50.

(57) Bong, D. T.; Clark, T. D.; Granja, J. R.; Ghadiri, M. R. *Angew. Chem., Int. Ed.* **2001**, *40*, 988–1011.

(58) Roques, B. P.; Garbay-Jaureguiberry, C.; Bajusz, S.; Maigret, B. *Eur. J. Biochem.* **1980**, *113*, 105–119.

(59) Li, Z.; Scheraga, H. A. *Proc. Natl. Acad. Sci. U.S.A.* **1987**, *84*, 6611–6615.

(60) Perez, J. J.; Villar, H. O.; Loew, G. H. *J. Comput.-Aided Mol. Des.* **1992**, *6*, 175–190.

(61) Koča, J.; Carlsen, P. H. J. *J. Mol. Struct. (THEOCHEM)* **1995**, *337*, 17–24.

(62) Bartels, C.; Karplus, M. *J. Phys. Chem. B* **1998**, *102*, 865–880.

(63) Carlacci, L. *J. Comput.-Aided Mol. Des.* **1998**, *12*, 195–213.

(64) Mitsutake, A.; Hansmann, U. H.; Okamoto, Y. *J. Mol. Graphics Modell.* **1998**, *16*, 226–38, 262−3.

(65) Hansmann, U. H.; Okamoto, Y.; Onuchic, J. N. *Proteins* **1999**, *34*, 472–483.

(66) Shen, M.-y.; Freed, K. F. *Biophys. J.* **2002**, *82*, 1791–1808.

(67) Sanbonmatsu, K. Y.; García, A. E. *Proteins: Struct., Funct., Genet.* **2002**, *46*, 225–234.

(68) Evans, D. A.; Wales, D. J. *J. Chem. Phys.* **2003**, *119*, 9947–9955.

(69) Zaman, M. H.; Shen, M. Y.; Berry, R. S.; Freed, K. F. *J. Phys. Chem. B* **2003**, *107*, 1685–1691.

(70) Berg, B. A.; Hsu, H.-P. *Phys. Rev. E* **2004**, *69*, 026703.

(71) Zhan, L. X.; Chen, J. Z. Y.; Liu, W. K. *Biophys. J.* **2006**, *91*, 2399–2404.

(72) Ramya, L.; Gautham, N. *J. Chem. Theory Comput.* **2009**, *5*, 2180–2190.

(73) Hagler, A. T.; Honig, B. *Proc. Natl. Acad. Sci. U.S.A.* **1978**, *75*, 554.

(74) Brady, J.; Karplus, M. *J. Am. Chem. Soc.* **1985**, *107*, 6103.

(75) Mezei, M.; Mehrotra, P. K.; Beveridge, D. L. *J. Am. Chem. Soc.* **1985**, *107*, 2239.

(76) Ravishanker, G.; Mezei, M.; Beveridge, D. L. *J. Comput. Chem.* **1986**, *7*, 345.

(77) Anderson, A.; Hermans, J. *Proteins: Struct., Funct., Genet.* **1988**, *3*, 262.

(78) Tobias, D. J.; Brooks, C. L. *J. Phys. Chem.* **1992**, *96*, 3864–3870.

(79) Pellegrini, M.; Grønbech-Jensen, N.; Doniach, S. *J. Chem. Phys.* **1996**, *104*, 8639.

(80) Neria, E.; Fischer, S.; Karplus, M. *J. Chem. Phys.* **1996**, *105*, 1902.

(81) Bartels, C.; Karplus, M. *J. Comput. Chem.* **1997**, *18*, 1450–1462.

(82) Chipot, C.; Pohorille, A. *J. Phys. Chem. B* **1998**, *102*, 281–290.

(83) Smith, P. E. *J. Chem. Phys.* **1999**, *111*, 5568–5579.

(84) Apostolakis, J.; Ferrara, P.; Caflisch, A. *J. Chem. Phys.* **1999**, *110*, 2099–2108.

(85) Bolhuis, P. G.; Dellago, C.; Chandler, D. *Proc. Natl. Acad. Sci. U.S.A.* **2000**, *97*, 5877–5882.

(86) Andricioaei, I.; Dinner, A. R.; Karplus, M. *J. Chem. Phys.* **2003**, *118*, 1074–1084.

(87) Chekmarev, D.; Ishida, T.; Levy, R. M. *J. Phys. Chem. B* **2004**, *108*, 19487–19495.

(88) Jang, H.; Woolf, T. B. *J. Comput. Chem.* **2006**, *27*, 1136–1141.

(89) Branduardi, D.; Gervasio, F. L.; Parrinello, M. *J. Chem. Phys.* **2007**, *126*, 054103.

(90) Neale, C.; Rodinger, T.; Pomes, R. *Chem. Phys. Lett.* **2008**, *460*, 375–381.

(91) Kwac, K.; Lee, K. K.; Han, J. B.; Oh, K. I.; Cho, M. *J. Chem. Phys.* **2008**, *128*, 105106.

(92) Feig, M. *J. Chem. Theory Comput.* **2008**, *4*, 1555–1564.

(93) Velez-Vega, C.; Borrero, E. E.; Escobedo, F. A. *J. Chem. Phys.* **2009**, *130*, 225101.

(94) Torrie, G. M.; Valleau, J. P. *J. Comput. Phys.* **1977**, *23*, 187–199.

(95) Kumar, S.; Bouzida, D.; Swendsen, R. H.; Kollman, P. A.; Rosenberg, J. M. *J. Comput. Chem.* **1992**, *13*, 1011–1021.

(96) Rosso, L.; Abrams, J. B.; Tuckerman, M. E. *J. Phys. Chem. B* **2005**, *109*, 4162–4167.

(97) Sánchez-Quesada, J.; Isler, M. P.; Ghadiri, M. R. *J. Am. Chem. Soc.* **2002**, *124*, 10004–10005.

(98) Kim, H. S.; Hartgerink, J. D.; Ghadiri, M. R. *J. Am. Chem. Soc.* **1998**, *120*, 4417–4424.

(99) Tarek, M.; Maigret, B.; Chipot, C. *Biophys. J.* **2003**, *85*, 2287–2298.

(100) Asthagiri, D.; Bashford, D. *Biophys. J.* **2002**, *82*, 1176–1189.

(101) Hwang, H.; Schatz, G. C.; Ratner, M. A. *J. Phys. Chem. B* **2006**, *110*, 6999–7008.

(102) Hwang, H.; Schatz, G. C.; Ratner, M. A. *J. Phys. Chem. B* **2006**, *110*, 26448–26460.

(103) Mamonov, A. B.; Coalson, R. D.; Nitzan, A.; Kurnikova, M. G. *Biophys. J.* **2003**, *84*, 3646–3661.

(104) Aguilella-Arzo, M.; Aguilella, V. M.; Eisenberg, R. S. *Eur. Biophys. J.* **2005**, *34*, 314–322.

(105) Marcus, Y. *Ion Solvation*; Wiley and Sons: London, 1985.

(106) Khaled, M. A.; Long, M. M.; Thompson, W. D.; Bradley, R. J.; Brown, G. B.; Urry, D. W. *Biochem. Biophys. Res. Commun.* **1976**, *76*, 224–231.

(107) Smith, G. D.; Griffin, J. F. *Science* **1978**, *199*, 1214–1216.

(108) Sugita, Y.; Okamoto, Y. *Chem. Phys. Lett.* **1999**, *314*, 141–151.

(109) Humphrey, W.; Dalke, A.; Schulten, K. *J. Mol. Graphics* **1996**, *14*, 33–8, 27−8.

(110) Kumar, S.; Payne, P. W.; Vásquez, M. *J. Comput. Chem.* **1995**, *17*, 1269–1275.

(111) Park, S.; Khalili-Araghi, F.; Tajkhorshid, E.; Schulten, K. *J. Chem. Phys.* **2003**, *119*, 3559–3566.

(112) Minh, D. D. L.; McCammon, J. A. *J. Phys. Chem. B* **2008**, *112*, 5892–5897.

(113) Forney, M. W.; Janosi, L.; Kosztin, I. *Phys. Rev. E* **2008**, *78*, 051913.

(114) Laio, A.; Rodriguez-Fortea, A.; Gervasio, F. L.; Ceccarelli, M.; Parrinello, M. *J. Phys. Chem. B* **2005**, *109*, 6714–6721.

(115) Bussi, G.; Laio, A.; Parrinello, M. *Phys. Rev. Lett.* **2006**, *96*, 090601.

(116) Lelièvre, T.; Rousset, M.; Stoltz, G. *J. Chem. Phys.* **2007**, *126*, 134111.

JCTC Journal of Chemical Theory and Computation

Symmetry Conservation in Fukui Functions

Roberto Flores-Moreno*,†

*Departamento de Química, Centro de Investigación y de Estudios Avanzados del
Instituto Politécnico Nacional, Avenida Instituto Politécnico Nacional 2508,
A.P. 14-740, México, D.F., C.P. 07000, México*

Abstract: The problem of symmetry breaking in the evaluation of Fukui functions is addressed. It is also demonstrated that a reliable solution of the problem can be achieved using analytic methods. An automatic method that avoids occurrence of symmetry breaks has been implemented in a computer code and is described here. Negative regions of the Fukui function are shown to play a key role for the interpretation of reactivity. Example plots are presented for diatomic molecules, inorganic molecules, conjugated systems, and molecular cages. The potentiality of the Fukui functions as molecular scalar fields for prediction and analysis of regioselectivity is enhanced. Its advantages with respect to the use of condensed Fukui functions are discussed.

1. Introduction

Inspired by the pioneering works on molecular reactivity of Fukui,[1−3] Parr and Yang[4−6] have proposed an intrinsic local reactivity descriptor which they named the Fukui function[4] and defined it as the derivative of the molecular density with respect to the total number of electrons for a given external potential. This descriptor can be used to predict regioselectivity. Both nucleophilic and electrophilic molecular regions can be predicted.[7−10] It can also be used to do comparative studies of acidity or basicity.[11] Furthermore, the Fukui function plays a central role in the development and application of chemical reactivity theory.[6,8,12−16]

There are two principal ways in which the Fukui function has been used to predict regioselectivity. One may use the Fukui function itself or find molecular regions with nucleophilic and electrophilic character with the condensed Fukui functions.[17] The latter approach has the advantage of predicting reactive atomic centers. However, this coarse-grained approach also presents a number of disadvantages starting from the arbitrariness of the condensation procedures.[18] In addition, it hides information related to off-atom regions.

The purpose of this contribution is to address a problem in the evaluation and interpretation of Fukui functions of symmetric molecules: the breaking of symmetry. Once this problem is solved, plotting the Fukui functions emerges as the method of choice for analysis of regioselectivity instead of calculation of condensed Fukui function values. In fact, the extensive use of the condensed values[19−21] is one of the main reasons for the prevalence of the symmetry-breaking problem. Condensation hides this problem for many common systems.

This problem is very severe because it implies a violation of space symmetry. In the literature there are reports with erroneous Fukui function plots.[22,23] Probably because this problem is only relevant to systems with degenerate frontier orbitals (vide infra), many researchers have not paid attention to its occurrence. However, the problem occurs in the very important family of aromatic hydrocarbons which, by satisfying Hückel's $4n + 2$ rule, have degeneracies in the highest occupied molecular orbital (HOMO) and the lowest unoccupied molecular orbital (LUMO). Combination of efficient analytic methods with the results of the analysis presented here yield reliable molecular graphs of Fukui functions.

The paper is organized as follows. In section 2 the most widely used methods for the evaluation of Fukui functions are outlined and compared to the analytic formula. In section 3, the symmetry conservation problem is described

* E-mail: roberto.floresm@red.cucei.udg.mx.
† Current address: Departamento de Química, CUCEI, Universidad de Guadalajara, Blvd. Marcelino García Barragán 1451, Guadaljara Jal., C. P. 44430, México.

Symmetry Conservation in Fukui Functions

J. Chem. Theory Comput., Vol. 6, No. 1, 2010 **49**

and its solution is discussed. Application to a number of molecules is presented in section 4. Final remarks are given in section 5.

2. Methods for Evaluation of Fukui Functions

The following discussion is restricted to the Kohn−Sham approximation[24] of density functional theory (DFT),[6,25] but many of the observations and conclusions are applicable to other methods. A nondegenerate state is assumed. For degenerate ground states, extra corrections are required.[26]

The Fukui function, $f^{\pm}(\mathbf{r})$, is defined as the derivative of the density, $\rho(\mathbf{r})$, with respect to the total number of electrons, N, under a constant potential, $v(\mathbf{r})$:

$$f^{\pm}(\mathbf{r}) \equiv \left(\frac{\partial \rho(\mathbf{r})}{\partial N} \right)_v^{\pm} \tag{1}$$

The superscript signs are used to label left, −, and right, +, side derivatives. There are alternative (but equivalent for nondegenerate states[26]) definitions of the Fukui function.[27,28] Within the Kohn−Sham approximation of DFT, the density is given by a fictitious noninteracting system

$$\rho(\mathbf{r}) = \sum_i n_i |\psi_i(\mathbf{r})|^2 \tag{2}$$

Here, $\psi_i(\mathbf{r})$ denotes the ith molecular orbital and n_i is its occupation number. Assuming that the electronic density is well-defined and its one-sided derivatives with respect to N exist, the Fukui function can be evaluated by[5,29−31]

$$f^{\pm}(\mathbf{r}) = \sum_i \left(\frac{\partial n_i}{\partial N} \right)_v^{\pm} |\psi_i(\mathbf{r})|^2 + \sum_i n_i \left(\frac{\partial |\psi_i(\mathbf{r})|^2}{\partial N} \right)_v^{\pm} \tag{3}$$

Equation 3 is the exact formula for the evaluation of the Fukui function. The first term on the right-hand side accounts for the location from which the electrons are removed. The second sum collects contributions from the relaxation of orbitals. Equation 3 can be evaluated using perturbation theory.[32,33] In general it is assumed that electrons would leave from the HOMO and not from other orbitals. Justification for this assumption can be obtained by considering an ensemble of ionic states with different energies depending on whence electrons are removed or added in the neutral system. For the case where electrons are removed (left derivative), the highest population of these states in general corresponds to the state where electrons were removed from the HOMO because it is the orbital with the lowest energy. In an analogous way, occupation of the LUMO leads to an ensemble of anionic states. Population of other states is very low. For zero temperature, all other states with higher energy are empty. Therefore

$$\left(\frac{\partial n_i}{\partial N} \right)^- = \begin{cases} 1 & \text{if } i = \text{HOMO} \\ 0 & \text{otherwise} \end{cases} \tag{4}$$

$$\left(\frac{\partial n_i}{\partial N} \right)^+ = \begin{cases} 1 & \text{if } i = \text{LUMO} \\ 0 & \text{otherwise} \end{cases} \tag{5}$$

In the frontier approximation, the relaxation of orbitals is neglected. This is equivalent to assuming that second sum

in eq 3 vanishes. Thus, the left frontier Fukui function, $f_F^-(\mathbf{r})$, is given by[34]

$$f^-(\mathbf{r}) \approx f_F^-(\mathbf{r}) \equiv |\psi_{\text{HOMO}}(\mathbf{r})|^2 \tag{6}$$

Another, frequently used method for the evaluation of Fukui functions evaluates densities of the system with N electrons and the system with $N - 1$ electrons and approximates the Fukui function by their difference, $f_D^-(\mathbf{r})$:

$$f^-(\mathbf{r}) \approx f_D^-(\mathbf{r}) \equiv \rho_N(\mathbf{r}) - \rho_{N-1}(\mathbf{r}) \tag{7}$$

Equation 7 includes relaxation contributions in the evaluation of Fukui functions but also includes numerical errors and technical difficulties.[33] At 0 K, eq 7 is an exact formula[22] for the evaluation of $f^-(\mathbf{r})$ if the exact density is used. Our analytical results[33] and numerical calculations with fractional charge[21,33,35] yield different values because the exchange-correlation functional used in the calculations is not the exact one and, therefore, the density is not exact. Furthermore, incompletness of the basis sets used leads to a unbalanced treatment of ionic species, especially anions. One feature of analytic methods is that they yield results consistent with the approximate nature of the functional employed. For the exact functional, the analytic result is also the exact one. Whereas for approximate functionals analytic results are consistent, eq 7 presents errors that disappear only with the exact functional. This motivates us to pursue the use of analytic methods.

3. Symmetry Conservation

There have been publications related to the interpretation and application of Fukui functions where the reported graphs present an artificial symmetry breaking.[22,23] Those and our own previous results have motivated the following analysis. In this section, the particular cases of methane (CH_4), acetylene (HCCH), benzene (C_6H_6), and cubane (C_8H_8) are analyzed. This set includes linear, planar, and three-dimensional systems.

In many systems, HOMO and LUMO degeneracy appears as a consequence of symmetry. If only one of the frontier orbitals is considered for the removal or addition of electrons, then a symmetry break occurs in the corresponding Fukui function. Therefore, before discussing the Fukui function of the selected molecules, the HOMOs are presented in Figure 1. Note that lowercase letters are used to label different HOMOs in each molecule for further reference.

All the results presented in this contribution were obtained with a modified version of the deMon2k program.[36] The local density approximation with the VWN correlation functional was used.[37] The DZVP[38] basis and the GEN-A2[39−42] auxiliary sets were employed. The molecular plots were obtained with Sinapsis 0.3.[43]

3.1. Frontier Fukui Function. When only the HOMO a is used to evaluate $f_F^-(\mathbf{r})$, a symmetry break occurs. Figure 2 shows the results. For the evaluation of Fukui functions, all isosurfaces presented in this work were selected to satisfy $Nf(\mathbf{r}) = 0.1$, where N is the total number of electrons in the molecule. This choice is based on the fact that Fukui
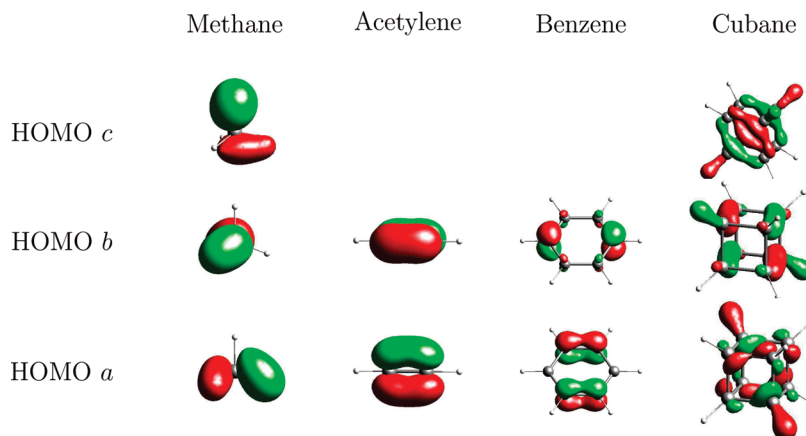
Figure 1. Isosurfaces taken at 0.1 au for HOMOs of the selected set of molecules.
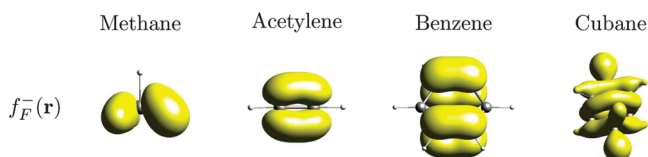

Figure 2. Symmetry break in frontier approximation to Fukui function evaluated as a^2.

functions integrate to an absolute value of 1.0 and, therefore, for larger molecules smaller absolute values of Fukui functions are found. This also reflects the fact that larger molecules are more able to accommodate extra charge.

The Fukui functions resulting from this method have a shape that resembles very closely that of the last occupied MO. They are also, by construction, positive semidefinite, i.e., $f_F^-(\mathbf{r}) \geq 0$. If one would attempt to predict regioselectivity with these plots, one would arrive at the wrong conclusion that some atoms are more reactive than others that are equivalent to them by symmetry. In order to recover the correct symmetry when the HOMO is degenerate, eq 6 should be modified to allow the possibility for the electrons to leave evenly from all of the HOMOs. Meneses et al.[44] have applied averaging of frontier orbitals. Cedillo has employed a similar procedure.[45] Unfortunately, no justification has been given for the legitimacy of this action. This is properly justified by the ensemble of ionic systems proposed above. Equations 4 and 5 should be substituted for the following more general forms:

$$\left(\frac{\partial n_i}{\partial N}\right)^- = \begin{cases} 1/D_{HOMO} & \text{if } \varepsilon_i = \varepsilon_{HOMO} \\ 0 & \text{otherwise} \end{cases} \quad (8)$$

$$\left(\frac{\partial n_i}{\partial N}\right)^+ = \begin{cases} 1/D_{LUMO} & \text{if } \varepsilon_i = \varepsilon_{LUMO} \\ 0 & \text{otherwise} \end{cases} \quad (9)$$

Here, ε_i is the energy for the ith MO and D_{HOMO} and D_{LUMO} are the order of degeneracy of the HOMO and LUMO, respectively. The frontier Fukui function should be corrected accordingly. For $f_F^-(\mathbf{r})$, the corrected formula is

$$f_F^-(\mathbf{r}) = \frac{1}{D_{HOMO}} \sum_i^{D_{HOMO}} |\psi_i(\mathbf{r})|^2 \quad (10)$$

with the sum running over all degenerate HOMOs. The correction of symmetry as a result of the generalization described by eq 10 is a consequence of group theory. If the frontier orbital did not belong to a degenerate set, then its value squared would yield a frontier density belonging to the totally symmetric irreducible representation.[46] For degenerate frontier orbitals, no single one of them can produce a totally symmetric density, but the direct product of all of their irreducible representations is the totally symmetric one. (This statement is better appreciated using complex character tables that allow separate handling of degenerate orbitals.[46]) This result is in accordance with the inclusion of all frontier orbitals in eq 10. The averaging preserves the normalization of the Fukui functions. In a recent paper[47] published while this work was in the reviewing process J. Martínez also points out the problem of symmetry breaking treated here. He reports some corrected plots with the frontier orbital approximation, including the one for HCCH presented here.[47]

Note that we are assuming a closed-shell system in the discussion, but the results just obtained are also valid for half-filled, open shells of degenerate frontier orbitals. Actually, this is the molecular counterpart of Unsöld's theorem.[48,49]

Figure 3 shows the results of this correction. Clearly, the resulting plots allow us to make reactivity predictions that do not violate molecular symmetry.

Unfortunately, the frontier approximation neglects relaxation contributions. Therefore, no attempt to interpret the resulting plots is made here. Nevertheless, this symmetric $f_F^-(\mathbf{r})$ serves as a starting point for evaluation of symmetrized analytic $f^-(\mathbf{r})$.

3.2. Finite Difference Method. In Figure 4, molecular densities for neutral and cationic systems are shown. Their difference is also evaluated to yield $f_D^-(\mathbf{r})$ as an approximation to the Fukui function. Positive values are in yellow and negative regions correspond to blue. Negative regions arise from relaxation contributions. Their existence has been pointed out.[20,22,50,51] We believe this can be properly understood only by using Fukui function plots and not by the condensed forms.

In ref 22, the plot $f_D^-(\mathbf{r})$ for acetylene was reported. Likewise, in ref 23, a contour plot for benzene was reported. In these reports, as in our plots of $f_D^-(\mathbf{r})$, artificial symmetry breaks occur. These artifacts originate in the method and

Methane   Acetylene   Benzene   Cubane
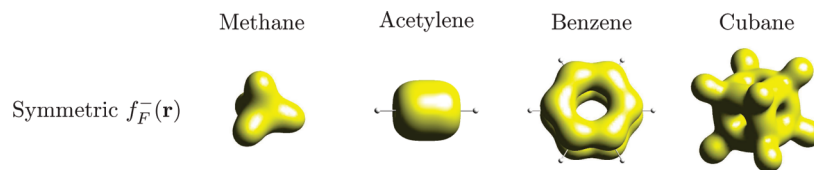
Symmetric $f_F^-(\mathbf{r})$

Figure 3. Symmetrized frontier approximation to Fukui function. Calculated using $(a^2 + b^2 + c^2)/3$ for methane and cubane and $(a^2 + b^2)/2$ for acetylene and benzene, according to eq 10.
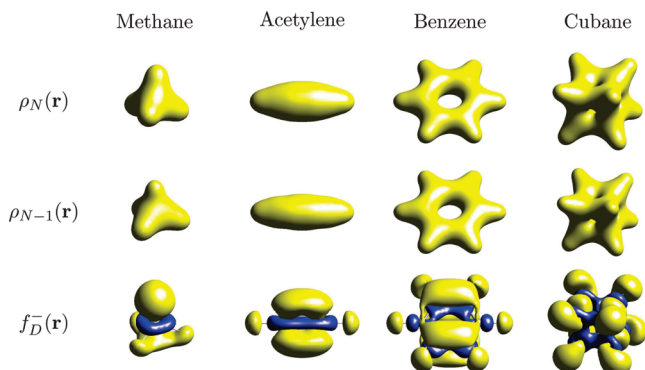
Methane   Acetylene   Benzene   Cubane

$\rho_N(\mathbf{r})$

$\rho_{N-1}(\mathbf{r})$

$f_D^-(\mathbf{r})$

Figure 4. Density of systems with N and $N − 1$ electrons and the resulting approximated Fukui function obtained from their difference. Isosurfaces taken at 0.1 au for densities.

support our position that it is preferable to not involve calculations on the $(N − 1)$-electron system in calculations on N-electron systems.[33]

The analysis of Figure 4 reveals why symmetry breaking has not been an issue in calculations of Fukui functions. The density of the N-electron system adapts to the molecular symmetry. In Figure 4 it can be observed that the density of the $(N − 1)$-electron system seems to follow the molecular symmetry. However, a careful analysis reveals that the density has a different symmetry. The deviations from symmetry are, for these molecules and others of similar size, about 1 order of magnitude smaller than the actual values of the density. Therefore, it is very hard to see the problem before actually evaluating the difference. On the other hand, people usually condense the difference instead of plotting it. Thus, hiding of the problem is very likely to occur.

Recovering adequate symmetry with the finite difference method is very difficult. More than one state of the $(N − 1)$-electron system should be calculated. For many currently used methods, it would be very demanding to identify the correct states and recover the corresponding density as required, resulting in more computer and human work that is error-prone. Thus, $f_D^-(\mathbf{r})$ is able to recover relaxation and

allows for the appearance of negative regions. Unfortunately, symmetry breaking is hard to prevent.

3.3. Analytic Method. The analytic method is also able to recover relaxation by means of linear response.[33] In addition, the symmetry break is readily corrected. The symmetrized frontier Fukui function is used as the starting point. The relaxation adapts automatically to the same symmetry. The response to a symmetric change in the density, arising in the frontier, is also symmetric. The forces responsible for relaxation represent a symmetrized change in the density and will cause a symmetrized relaxation. In Figure 5, plots of analytic $f^-(\mathbf{r})$ are shown without and with symmetry correction. Note how once symmetry has been corrected, the analytic method presents both positive and negative regions, with adequate symmetry.

Fukui function plots are very rich in information. Once the symmetry has been corrected, the plots calculated are reliable for the interpretation of reactivity. Their full potentiality for description of chemical reactivity is revealed. First, they show how changes in density are frequently outside of atomic regions. Negative regions are clearly an important feature.

4. Applications

In this section, the analytic Fukui functions, $f^-(\mathbf{r})$ and $f^+(\mathbf{r})$, are evaluated for different sets of molecules of current interest to chemistry and technology. Many of the Fukui functions shown below have never been displayed previously with adequate symmetry or their novel negative domains. Molecules with degenerate frontier orbitals are treated to show the range of applications that benefit from the present approach.

Henceforth, all plots correspond to symmetry-corrected Fukui functions.

4.1. Diatomic Molecules. Diatomic molecules are very simple reactive systems, but the symmetry problem in Fukui functions affects them in such a way that equivalent spatial directions for approaching the molecule would result in
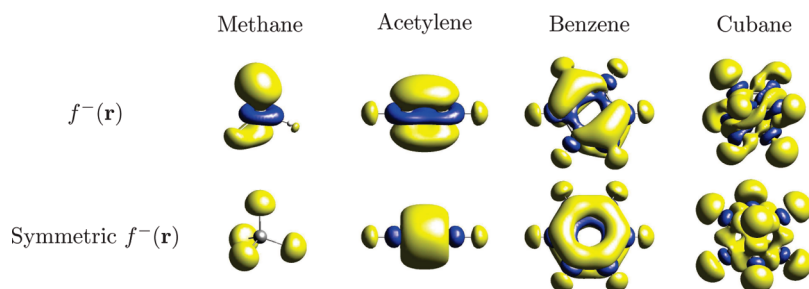
Methane   Acetylene   Benzene   Cubane

$f^-(\mathbf{r})$

Symmetric $f^-(\mathbf{r})$

Figure 5. Analytic Fukui functions before and after symmetrization.

Figure 6. Fukui functions for diatomic molecules.

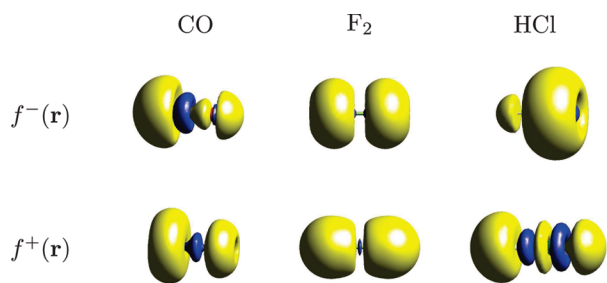**Figure 7.** Fukui functions for inorganic molecules.

Figure 8. Fukui functions for conjugated molecules.

different reactivities. This violates space isotropy and should be corrected. In Figure 6, the symmetry-corrected analytic Fukui functions for CO, F_2, and HCl are shown. For the case of CO only the LUMO is degenerate. For F_2 and HCl, only the HOMOs are degenerate.

For F_2, the symmetry of the Fukui functions is $D_{\infty h}$, whereas before the correction the symmetry was D_{2h}. For CO and HCl, the correction goes from C_{2v} to $C_{\infty h}$. In addition to the symmetry correction in Figure 6, one can see how negative regions in Fukui functions are always present. This is not the first time that such regions are detected or reported. Nevertheless, one of the results of this work is that it reveals how the appearance of negative regions is the rule rather than the exception. This result contrasts with the long-standing debate on the appearance, meaning, and legitimacy of negative values in condensed Fukui functions.

In linear molecules, such as the diatomic molecules of Figure 6, the condensation of unsymmetrical Fukui functions leads to the same values as the condensation of the symmetry-corrected form. These results provide good examples of how condensation hides the symmetry-breaking problem. Fortunately, this conclusion also implies that published condensed values such as those of refs 22 and 33 are correct. For nonlinear molecules, this fortuitous correction does not occur at all. Probably this is the reason that symmetric molecules are not frequently reported with Fukui functions.

A rationalization of negative regions of Fukui functions is possible with the analysis of the plots shown in this work. When a molecule loses electrons, there is a charge compensation that migrates toward the positive nuclear frame. Valence electrons will be attracted more strongly since the shielding has been lowered. This causes a net increase of core density. In the opposite case, if the molecule gains electrons, the charge compensation goes in favor of the electrons. The shielding increases in this case and core electrons can expand away from the nuclear framework, generating a depletion in core density. This is in agreement with the previous observations and analysis of Ayers et al.[22,50,51] This also explains why negative regions were not found close to hydrogens in the systems treated here.

4.2. Inorganic Systems. Generally, the Fukui function is used in the analysis of reactivity of organic molecules. There is no fundamental reason to restrict attention to those systems. On the other hand, calculation of charged systems happens to be more difficult in inorganic molecules, making application of the numeric d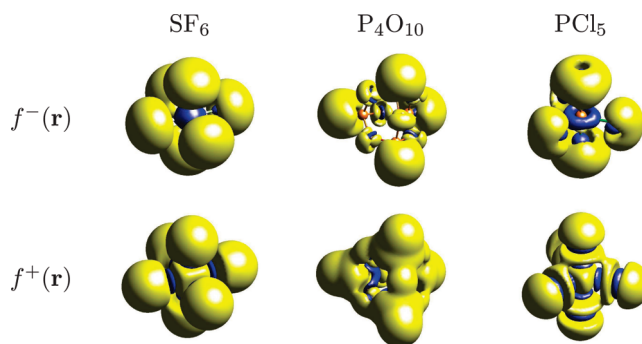ifference method more difficult. With the analytic method, charged systems are not calculated; only the neutral system is of interest. Therefore, we can proceed without worry to the treatment of inorganic molecules.
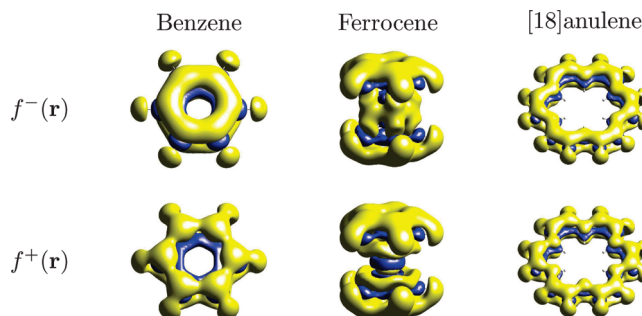
Examples of inorganic molecules are SF_6, P_4O_{10}, and PCl_5. P_4O_{10} and PCl_5 offer an opportunity for testing regioselectivity in a case where atoms of the same type appear in different conditions. Only the HOMO is degenerate for these systems. In Figure 7, one can observe how axial Cl atoms of PCl_5 are affected more upon removal of electrons. For the case of P_4O_{10}, oxygen atoms linked to a single P atom are the first source of electrons.

4.3. Conjugated Systems. Conjugated systems are very important in synthesis, in polymers and biological chemistry. Many of them have degenerate frontier orbitals. In particular the aromatic systems, by obeying Hückel's $4n + 2$ rule, present doubly degenerate frontier orbitals. In this section, benzene, ferrocene, and [18]anulene are treated as examples of conjugated molecules. While benzene is the prototype of all aromatic systems, ferrocene is the prototype of organometallic sandwich systems. [18]Anulene offers the possibility of testing atoms of the same type in different conditions. In Figure 8 the plots can be observed. For these three molecules both the HOMO and LUMO are doubly degenerate. It is interesting to note that $f^-(\mathbf{r})$ of ferrocene predicts that removal of electrons affects mostly the metal atom. This is in agreement with the experimental observation where it was found that Fe^{2+} oxidizes to Fe^{3+}.[52] In the cases of benzene and [18]anulene, the missing electrons come from the aromatic π-system. For addition of electron, $f^+(\mathbf{r})$ shows a clear tendency to localize. For [18]anulene, one can also conclude in electron transfer reactions that the external hydrogens are more likely to react than the internal hydrogens of the [18]anulene ring.
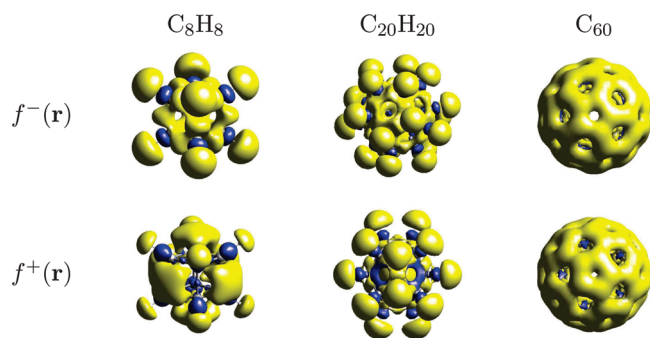
Symmetry Conservation in Fukui Functions

J. Chem. Theory Comput., Vol. 6, No. 1, 2010 **53**

Figure 9. Fukui functions for carbon molecular cages.

4.4. Molecular Cages. Molecular cages are very important in nanotechnology, in trapping of atoms and smaller molecules, and for the study of confinement effects.[53] They are also suitable for analyzing off-atom regions of Fukui functions.

Molecular cages C_8H_8, $C_{20}H_{20}$, and C_{60} are considered. Because of the number of degenerate frontier orbitals, the size of the systems, and the very small values of the calculated Fukui functions in these molecules, the calculation of symmetry-corrected functions by the finite difference method appears very hard to realize. This is a challenge for those who might be reluctant to employ analytic methods for the calculation of Fukui functions.

Figure 9 shows the analytic Fukui functions evaluated for these molecular cages. One can observe that removal of electrons from cubane affects mostly C−C bonds and the zones of hydrogen atoms. The addition of electrons to the same molecule would increase density in off-atom regions. In particular, there are zones out of the cubane box that increase density. In the opposite case, $C_{20}H_{20}$ shows that extra electrons would be better accepted inside the box.

In C_{60}, there is only one type of C atom, but there are two types of C−C bonds. If the symmetrized Fukui functions calculated here were condensed, then all atoms would show the same reactivity as expected. However, no information about the reactivity of bonds would be recovered. The direct analysis of these functions allows one to conclude that removal of electrons affects C−C bonds that are not part of the pentagons and addition of electrons would go to bonds on the C_5 motifs.

Note that the size of the systems that are being treated here is not small. For the case of C_{60}, about 900 basis functions and 2040 auxiliary functions are employed. Consider also that the calculations here shown do not exploit symmetry for efficiency. In an Intel Xeon 2.40 GHz CPU, the calculation of both Fukui functions took 7 h 41 min using a RAM under 512 MB. About 1 h of this time was consumed by the SCF calculation. This performance is to be expected from deMon2k,[36] which takes advantage of the variational fitting of the Coulomb potential[54,55] and other developments of auxiliary density functional theory.[56,57] It demonstrates that evaluation of analytic Fukui functions with linear response as described in ref 33 is very efficient and can be realized routinely for many chemically interesting systems. This method can help to extend the horizon of applications of Fukui functions in chemical reactivity theory.

5. Conclusions

Treating degenerate frontier orbitals on an equal footing, as dictated by 0 K statistical mechanics and molecular group theory,[46] corrects symmetry breaking in frontier Fukui functions and analytic Fukui functions for nondegenerate states. A number of symmetry-corrected Fukui function plots were evaluated to demonstrate the range of areas that can benefit from this development. The analysis of the plots presented here encourages the use of direct analysis of Fukui functions instead of the condensed forms.

The results of this work complement our recent effort to develop an efficient analytic method for reliable and reproducible calculation of Fukui functions.

Negative regions of Fukui functions appear in most graphs and can be rationalized on the basis of charge compensation. This is in agreement with previously published results.[22,50,51]

References

(1) Fukui, K.; Yonezawa, T.; Shingu, H. *J. Chem. Phys.* **1952**, *20*, 722–725.

(2) Fukui, K.; Yonezawa, T.; Nagata, C.; Shingu, H. *J. Chem. Phys.* **1954**, *22*, 1433–1442.

(3) Fukui, K. *Science* **1982**, *218*, 747–754.

(4) Parr, R. G.; Yang, W. *J. Am. Chem. Soc.* **1984**, *106*, 4049–4050.

(5) Yang, W.; Parr, R. G.; Pucci, R. *J. Chem. Phys.* **1984**, *81*, 2862–2863.

(6) Parr, R. G.; Yang, W. *Density Functional Theory of Atoms and Molecules*; Oxford University Press: New York, 1989; pp 87−104.

(7) Ayers, P. W.; Levy, M. *Theor. Chem. Acc.* **2000**, *103*, 353–360.

(8) Geerlings, P.; De Proft, F.; Langenaeker, W. *Chem. Rev.* **2003**, *103*, 1793–1873.

(9) Geerlings, P.; De Proft, F. *Phys. Chem. Chem. Phys.* **2008**, *10*, 3028–3042.

(10) Ayers, P. W.; Yang, W.; Bartolotti, L. J. In *Chemical reactivity theory: A density functional view*; Chattaraj, P. K., Ed.; CRC Press: Boca Raton, 2009; pp 255−268.

(11) Gupta, K,.; Giri, S.; Chattaraj, P. K. *New J. Chem.* **2008**, *32*, 1945–1952.

(12) Chermette, H. *J. Comput. Chem.* **1999**, *20*, 129–154.

(13) Ayers, P. W.; Anderson, J. S. M.; Bartolotti, L. J. *Int. J. Quantum Chem.* **2005**, *101*, 520–534.

(14) Chattaraj, P. K.; Sarkar, U.; Roy, D. R. *Chem. Rev.* **2006**, *106*, 2065–2091.

(15) Gázquez, J. L. *J. Mex. Chem. Soc.* **2008**, *52*, 3–10.

(16) Liu, S.-B. *Acta Phys.-Chim. Sin.* **2009**, *25*, 590–600.

(17) Yang, W.; Mortier, W. J. *J. Am. Chem. Soc.* **1986**, *108*, 5708–5711.

(18) Bultinck, P.; Fias, S.; van Alsenoy, C.; Ayers, P. W.; Carbó-Dorca, R. *J. Chem. Phys.* 207, *127*, 034102/1-11.

(19) Bultinck, P.; Carbó-Dorca, R. *J. Math. Chem.* **2003**, *34*, 67–74.

(20) Bultinck, P.; Carbó-Dorca, R.; Langenaeker, W. *J. Chem. Phys.* **2003**, *118*, 4349–4356.

(21) Roy, R. K.; Hirao, K.; Krishnamurty, S.; Pal, S. *J. Chem. Phys.* **2001**, *115*, 2901–2907.

(22) Melin, J.; Ayers, P. W.; Ortiz, J. V. *J. Phys. Chem. A* **2007**, *111*, 10017–10019.

(23) Martínez, J. I.; López, M. J.; Alonso, J. A. *J. Chem. Phys.* **2005**, *123*, 074303/1-9.

(24) Kohn, W.; Sham, L. J. *Phys. Rev.* **1965**, *137*, A1697–A1701.

(25) Hohenberg, P.; Kohn, W. *Phys. Rev.* **1964**, *136*, B864–B871.

(26) Cárdenas, C.; Ayers, P. W. *Private communication*, 2009.

(27) Fuentealba, P.; Contreras, R. In *Reviews in Modern Quantum Chemistry. A Celebration of the Contributions of Robert G. Parr*; Sen, K., Ed.; World Scientific Publishing Co.: River Edge, NJ, 2002; Vol. 1, pp 1013−1052.

(28) Ayers, P. W.; De Proft, F.; Borgoo, A.; Geerlings, P. *J. Chem. Phys.* **2007**, *126*, 224107/1-13.

(29) Cohen, M. H.; Ganduglia-Pirovano, M. V.; Kudrnovský, J. *J. Chem. Phys.* **1994**, *101*, 8988–8997.

(30) Ayers, P. W. *Theor. Chem. Acc.* **2001**, *106*, 271–279.

(31) Senet, P. *J. Chem. Phys.* **1997**, *107*, 2516–2524.

(32) Balawender, R.; Geerlings, P. *J. Chem. Phys.* **2005**, *123*, 124103/1-16.

(33) Flores-Moreno, R.; Melin, J.; Ortiz, J. V.; Merino, G. *J. Chem. Phys.* **2008**, *129*, 224105/1-6.

(34) Giambiagi, M.; Segre de Giambiagi, M. *Nuovo Cimento* **1990**, *12*, 139–141.

(35) Fitzgerald, G. *Mol. Simul.* **2008**, *34*, 931–936.

(36) Köster, A. M.; Calaminici, P.; Casida, M. E.; Dominguez, V. D.; Flores-Moreno, R.; Geudtner, G,; Goursot, A.; Heine, T.; Ipatov, A.; Janetzko, F.; del Campo, J. M.; Patchkovskii, S.; Reveles, J. U.; Vela, A. M.; Zuniga, B.; Salahub, D. R. *deMon2k*; The International deMon Developers Community, México, 2008.

(37) Vosko, S. H.; Wilk, L.; Nusair, M. *Can. J. Phys.* **1980**, *58*, 1200–1211.

(38) Godbout, N.; Salahub, D. R.; Andzelm, J.; Wimmer, E. *Can. J. Phys.* **1992**, *70*, 560–571.

(39) Andzelm, J.; Radzio, E.; Salahub, D. R. *J. Comput. Chem.* **1985**, *6*, 520–532.

(40) Andzelm, J.; Russo, N.; Salahub, D. R. *J. Chem. Phys.* **1987**, *87*, 6562–6572.

(41) Calaminici, P.; Flores-Moreno, R.; Köster, A. M. *Comput. Lett.* **2005**, *1*, 164–171.

(42) Calaminici, P.; Janetzko, F.; Köster, A. M.; Mejía-Olvera, R.; Zúniga-Gutiérrez, B. *J. Chem. Phys.* **2007**, *126*, 044108/1-10.

(43) Flores-Moreno, R. *Sinapsis 0.3*; México, 2009.

(44) Meneses, L.; Tiznado, W.; Contreras, R.; Fuentealba, P. *Chem. Phys. Lett.* **2004**, *383*, 181–187.

(45) Cedillo, A. *Unpublished results*.

(46) Hargittai, I.; Hargittai, M. *Symmetry through the eyes of a Chemist*, 2nd ed.; Plenum Press: New York, 1995; pp 247−249.

(47) Martínez, J. *Chem. Phys. Lett.* **2009**, *478*, 310–322.

(48) Unsöld, A. *Ann. Phys.* **1927**, *82*, 355–365.

(49) Blinder, S. M. *J. Math. Chem.* **1993**, *14*, 319–324.

(50) Ayers, P. W.; Morrison, R. C.; Roy, R. K. *J. Chem. Phys.* **2002**, *116*, 8731–8744.

(51) Ayers, P. W. *Phys. Chem. Chem. Phys.* **2006**, *8*, 3387–3390.

(52) Long, N. J. *Metallocenes. An introduction to sandwich complexes*; Blackwell Science: London, 1998; pp 134−137.

(53) Cerpa, E.; Krapp, A.; Flores-Moreno, R.; Donald, K. J.; Merino, G. *Chem.−Eur. J.* **2009**, *15*, 1985–1990.

(54) Dunlap, B. I.; Connolly, J. W. D.; Sabin, R. *J. Chem. Phys.* **1979**, *71*, 3396–3402.

(55) Mintmire, W.; Dunlap, B. I. *Phys. Rev. A* **1982**, *25*, 88–95.

(56) Köster, A. M.; Reveles, J. U.; del Campo, J. M. *J. Chem. Phys.* **2004**, *121*, 3417–3424.

(57) Flores-Moreno, R.; Köster, A. M. *J. Chem. Phys.* **2008**, *128*, 134105/1-10.

JCTC Journal of Chemical Theory and Computation

Rigorous Extraction of the Anisotropic Multispin Hamiltonian in Bimetallic Complexes from the Exact Electronic Hamiltonian

Rémi Maurice,*,[†,‡] Nathalie Guihéry,[†] Roland Bastardis,[§] and Coen de Graaf*,[‡,ll]

Laboratoire de Chimie et Physique Quantiques, IRSAMC/UMR5626, Université de Toulouse III, 118 route de Narbonne, F-31062 Toulouse Cédex 4, France, Departament de Química Física i Inorganica, Universitat Rovira i Virgili, Marcel·lí Domingo s/n, 43007 Tarragona, Spain, Laboratoire de Mathématiques, Physiques et Systemes, Université de Perpignan Via Domitia, 52 avenue Paul Alduy, 66860 Perpignan, France, and Institució Catalana de Recerca i Estudis Avançats (ICREA), Passeig Lluis Companys 23, 08010 Barcelona, Spain

Abstract: The magnetic anisotropy of the $[Ni_2(en)_4Cl_2]^{2+}$ (en = ethylenediamine) complex has been studied using wave function based computational schemes. The spin−orbit state interaction methodology provides accurate *ab initio* energies and wave functions that are used to interpret the anisotropy in bimetallic complexes. The extraction of the anisotropic spin Hamiltonian is performed using the effective Hamiltonian theory. This procedure which has successfully been applied to mononuclear complexes enables one to solve the weak exchange limit. It is shown that the standard coupled spin Hamiltonian only describes a part of the anisotropy of the molecule. Important higher order terms such as the biquadratic anisotropic exchange should be included in the model for an appropriate description of the anisotropy.

1. Introduction

The discovery of the unusual magnetic relaxation properties of the Mn_{12}-acetate cluster[1] triggered important research activity to find other molecule-based materials with similar magnetic properties. The interaction between different research areas in physics and chemistry proved to be a fruitful strategy in the design of new polynuclear species and the understanding of its peculiar magnetic properties.[2−7]

The basic requirements for systems to behave as single-molecule magnets (SMMs) are a high spin ground state of spin moment S and a sizable axial anisotropy characterized by an easy axis of magnetization and hence a negative zero-field splitting (ZFS) parameter D. These two factors lead to an energy barrier of $|D| \cdot S^2$ between the two states of opposite magnetization ($+M_s$ and $−M_s$). The presence of in-plane anisotropy leads to quantum tunneling effects which, on one hand, will speed the magnetization relaxation but, on the other hand, also introduce the possibility to study fundamental quantum phenomena such as coherence and interference effects. A detailed control over the anisotropy parameters would certainly be helpful in the development of new materials with higher energy barrier and higher blocking temperatures. Molecules with high nuclearities and/or high spin moments have been synthesized through an at least partially rational design.[8−11] Information about the anisotropy parameters D and E can be obtained from different experimental techniques, among which electron paramagnetic resonance (EPR) is particularly relevant.[12,13]

Theory also plays an important role in the description of the properties of SMMs. In the first place, theory provides important feedback to experiment by the interpretation of experimental data using model Hamiltonians.[14−18] Basically, there are two approaches to describe the magnetic phenomena in polynuclear systems: (1) the coupled spin Hamiltonian[19]

* Corresponding author phone: +33561556488; e-mail: rmaurice@irsamc.ups-tlse.fr (R.M.).

† Université de Toulouse III.

‡ Universitat Rovira i Virgili.

§ Université de Perpignan Via Domitia.

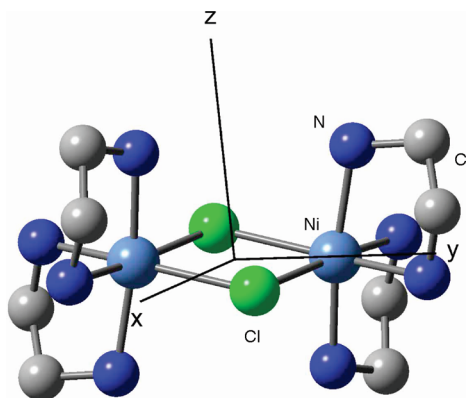ll Institució Catalana de Recerca i Estudis Avançats (ICREA).

Figure 1. Ball and stick representation of $[Ni_2(en)_4Cl_2]^{2+}$. Hydrogen atoms are omitted for clarity. The magnetic axes are shown. The angle between the magnetic *z* axis and the normal of the $Ni-(Cl_2)-Ni$ plane is 12°.

and (2) the giant spin Hamiltonian.[12] In the first model, the anisotropy of the molecule is obtained as resulting from the local anisotropies of the metal ions and the anisotropies of their interactions. In the giant spin approach, this information is lost and only the total spin of the ground state of the molecule is considered.

A second, more computational aspect of theory is the ability to derive magnetostructural correlations. This has a long-standing history in isotropically coupled magnetic centers, but recently the field has been extended to anisotropic spin moments.[20,21] Many of the computational studies of magnetic anisotropy are based on density functional theory.[20−26] The anisotropy is accounted for by a perturbational estimate of the effect of spin−orbit coupling on the lowest spin-free states.[23,24] Alternatively, a computational approach based on the *N*-electron wave function can be applied to study anisotropic effects in molecular magnetic systems, where the anisotropy can be addressed by perturbation theory[27] or variationally.[28−33]

Here, we present the *ab initio* description of the magnetic anisotropy in a bimetallic complex as a first step toward the theoretical study of anisotropy in larger, more interesting systems. The full *ab initio* description of the Mn_{12}-acetate complex is out of reach, but important information may be derived from bimetallic fragments that eventually can be extrapolated to polynuclear systems. The objective of our study is to validate and extract the multispin Hamiltonian to describe magnetic anisotropy, in particular in the weak exchange limit, i.e., for a weak isotropic exchange between the magnetic ions. For this purpose, a newly proposed procedure[34] based on the effective Hamiltonian theory is used to determine all the matrix elements of the effective Hamiltonian derived from the *ab initio* energies and wave functions and to consecutively extract all the spin operators that must be incorporated in the model Hamiltonian to reproduce at best the *ab initio* results. This methodology is applied to the $[Ni_2(en)_4Cl_2]^{2+}$ complex, shown in Figure 1.

Recently, high-field EPR data were published on this bimetallic Ni^{2+} complex.[35] These data were interpreted in terms of the coupled spin model, and values were given for the isotropic and axial anisotropic exchange interactions, in addition to the single-ion axial anisotropy parameter. The

relatively small number of atoms makes this complex the ideal candidate for a detailed *ab initio* exploration of the electronic structure including spin−orbit interactions.

The paper is divided in three major parts. The first part describes the computational strategy that we apply to obtain the *ab initio* energies and wave functions of the lowest electronic states including spin−orbit coupling (see the following section). In the second part of the paper, we extract the parameters of the standard coupled spin Hamiltonian including both axial and rhombic anisotropy (see section 3). Finally, the validity and physical content of the coupled spin Hamiltonian are analyzed (see section 4).

2. Ab Initio Treatment of $[Ni_2(en)_4Cl_2]^{2+}$

Spin−orbit effects are accounted for variationally by the spin−orbit state interaction (SO-SI) method introduced by Malmqvist and co-workers[28,29] and implemented in Molcas 7.[36] In this method, a spin−orbit interaction matrix is constructed using the CASSCF *N*-electron wave functions of the ground state and a collection of excited states as basis functions. Thus, the SO-SI scheme requires not only an accurate description of the ground state but also of the lowest lying excited states. Actually, in order to introduce dynamic correlation, the CASSCF energies on the diagonal elements of the spin−orbit state interacting matrix are replaced by energies obtained at a high level of correlation such as CASPT2 or Difference Dedicated Configuration Interaction (DDCI). This procedure presents several degrees of freedom which were previously studied in monometallic complexes[34] and provides accurate anisotropic parameters.

Difference Dedicated Configuration Interaction (DDCI) is one of the most accurate methods to determine relative energies of electronic states with important multiconfigurational character. DDCI involves a two-step procedure consisting of treating the nondynamical electron correlation effects in a small reference space, and subsequently includes dynamical correlation by CI calculations. The CI space is spanned by all single and double electron replacements with respect to the reference wave function except for the excitations that promote two electrons from the inactive orbitals into the virtual ones.[37] Although DDCI has been applied mainly to the calculation of energy differences between states with a common electronic configuration (i.e., the energy differences involved in magnetic coupling problems),[38−47] the method has also been successful in spectroscopic problems.[48−50] The bottleneck of the method is the size of the CI space, which is determined to a large extent by the size of the reference space. For the full computational characterization of the ground and first excited states of the Ni-dimer, it is necessary to construct a reference space that contains the 10 Ni-3d orbitals and the 16 electrons occupying these orbitals. This reference space leads to intractable CI spaces even when applying the DDCI selection rules.

Alternatively, dynamical electron correlation effects can be estimated perturbatively. The CASPT2 implementation of multiconfigurational second-order perturbation theory[51] may rival in precision with DDCI but is applicable to larger systems. The method has, however, a major drawback.
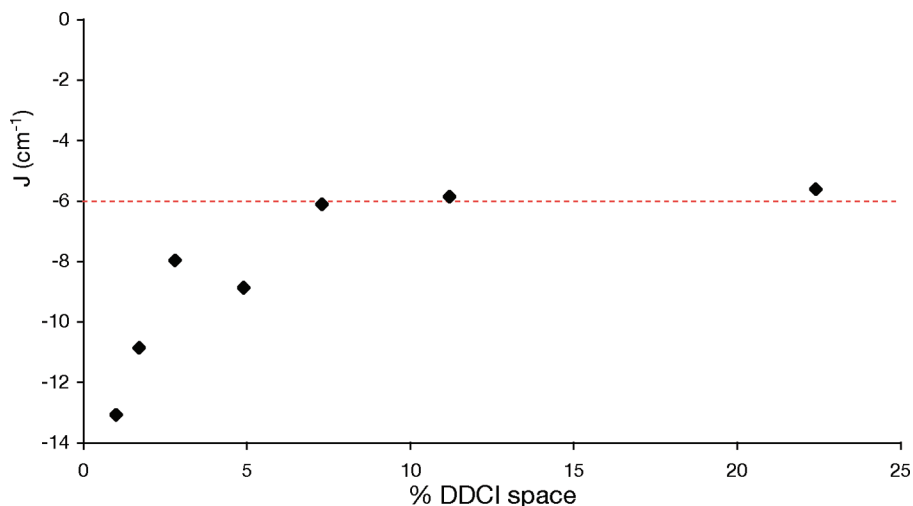
Figure 2. Magnetic coupling J (in cm^{-1}) as a function of the percentage of the space on which is performed the DDCI calculation.

Recently, it has been shown that CASPT2 cannot be applied to estimate magnetic coupling strengths for weakly coupled transition metals in bimetallic complexes.[52] Therefore, we adopted a two-step strategy to determine the spectrum of the Ni-dimer to take profit of the advantages of both methods. The relative energies of the lowest singlet, triplet, and quintet states, which arise from the magnetic coupling of the $S = 1$ spin moments on the Ni^{2+} ions, are calculated with DDCI, and the rest of the spectrum is calculated with CASPT2. Indeed, while a high precision is needed for these lowest states from which the spin Hamiltonian will be extracted, the CASPT2 precision is sufficient on the other excited states.[34] However, in order to ensure that the numerical errors have no consequences on the further qualitative conclusions, the results obtained using the CASSCF energies will be given for comparison.

2.1. Determination of the Isotropic J. The most common definition of the Heisenberg Hamiltonian in the field of magnetic anisotropy related to SMM is $\hat{H} = +J\hat{S}_i \cdot \hat{S}_j$, implying that $J > 0$ parametrizes antiferromagnetic coupling and $J < 0$ describes the ferromagnetic situation. The symmetry point group of $[Ni_2(en)_4Cl_2]^{2+}$ is C_i. This low symmetry makes the application of DDCI cumbersome. A straightforward procedure to reduce the computational cost of the DDCI calculation is to freeze the molecular orbitals (both occupied and virtual) that are less important for the energy difference between singlet, triplet, and quintet. A selection criterion based on orbital energies does not lead to a rapid convergence of the calculated J-values with the size of the MO space. A much better way to order the orbitals by increasing importance is obtained after the unitary transformation of the natural orbitals to so-called dedicated orbitals.[53] These orbitals are obtained by the diagonalization of the difference density matrix ρ_{diff}. For $[Ni_2(en)_4Cl_2]^{2+}$, the magnetic coupling involves three states, and the difference density matrix can be defined in several ways, which give practically the same results. Here we have chosen $\rho_{diff} = (\rho_Q - \rho_T) + (\rho_Q - \rho_S)$, where ρ is a density matrix and indexes Q, T, S refer to the low-lying quintet, triplet, and singlet spin−orbit free states, respectively. This reduction makes possible the DDCI calculation of the complex in the

Table 1. IDDCI Magnetic Coupling Parameter (in cm^{-1}) for $[Ni_2(NH_3)_8Cl_2]^{2+}$

method	iteration	$J(Q-T)$	$J(T-S)$
IDDCI	1	−2.00	−2.13
	2	−3.30	−3.37
	3	−4.44	−4.49
	4	−5.22	−5.29
	5	−5.70	−5.77
	6	−5.99	−6.06

unsymmetrized, experimental geometry. Figure 2 shows how J varies with the size of the CI space which depends on the number of occupied and virtual MOs considered in the generation of the CI space. For severe truncations, we observe large oscillations, but the magnetic coupling J converges rapidly to a value around -6 cm^{-1}. One may notice that the CASSCF value is -2.2 cm^{-1}. Since the angle $\widehat{NiLNi}$ (where L is a Cl^- ion) is close to 90°, the delocalization between the Ni ions is expected to be weak between the $d_{x^2-y^2}$ orbitals, and weak as well between the d_{z^2} orbitals due to their small overlap. As a consequence, either a weakly antiferromagnetic or a ferromagnetic value of J was expected. The enhancement of ferromagnetism with electron correlation shows that the spin polarization favors the highest spin states in this system.

A second strategy to reduce the length of the CI expansion is to symmetrize the molecule and replace the ethylenediamine external ligands by simpler model ligands. The symmetrization to C_{2h} symmetry does not imply large displacements; especially, the angles and distances in the central Ni_2Cl_2 unit remain practically unchanged. Furthermore, the effect of the external ligands on the magnetic coupling parameter has been proven to be weak as long as the nature of the atom coordinating the metal remains the same.[54] Results of the iterative DDCI procedure on this $[Ni_2Cl_2(NH_3)_8]^{2+}$ model complex are reflected in Table 1. This process optimizes at each iteration a new set of MOs by diagonalizing the average density matrix $\rho_{avg} = \rho_Q + \rho_T + \rho_S$. We adopted this strategy to make the results independent of the starting orbital set and to remove the largest part of the basis set dependency.[55] To check the importance of

Table 2. SO-SI Energies (cm^{-1}) and Weight of the Different |S, M_S⟩ Functions in the Low-Lying Spin Free Quintet, Triplet, and Singlet States Calculated in the CASSCF Space[a]

state	energy	|2, −2⟩	|2, −1⟩	|2, 0⟩	|2, 1⟩	|2, 2⟩	|1, −1⟩	|1, 0⟩	|1, 1⟩	|0, 0⟩
Ψ_1	0.000	0.41	0.00	0.09	0.00	0.41	0.00	0.00	0.00	0.06
Ψ_2	1.668	0.49	0.00	0.00	0.00	0.49	0.00	0.00	0.00	0.00
Ψ_3	8.752	0.00	0.49	0.00	0.49	0.00	0.00	0.00	0.00	0.00
Ψ_4	10.090	0.07	0.00	0.64	0.00	0.07	0.00	0.00	0.00	0.18
Ψ_5	12.014	0.00	0.00	0.00	0.00	0.00	0.00	0.97	0.00	0.00
Ψ_6	12.729	0.00	0.49	0.00	0.49	0.00	0.00	0.00	0.00	0.00
Ψ_7	19.719	0.00	0.00	0.00	0.00	0.00	0.49	0.00	0.49	0.00
Ψ_8	23.908	0.00	0.00	0.00	0.00	0.00	0.49	0.00	0.49	0.00
Ψ_9	29.498	0.00	0.00	0.24	0.00	0.00	0.00	0.00	0.00	0.74

[a] Ψ_1, Ψ_6, and Ψ_7 contain the |S, −M_S⟩ + |S, M_S⟩ combination. Ψ_2, Ψ_3, and Ψ_8 contain the |S, −M_S⟩ − |S, M_S⟩ combination.

the isotropic deviations from the expected Heisenberg splitting of the lowest energy levels, we calculated J from the energy difference of the singlet and triplet state ($J = E_T − E_S$) and from the triplet−quintet energy difference [($J = (1)/(2)(E_Q − E_T)$].

The results in Table 1 show that the DDCI energies follow almost perfectly the expected energy spacings (Heisenberg behavior), at difference with other Ni-dimers studied previously, which showed deviations up to 5% with respect to the Landé spacing.[56] The DDCI result converges in six iterations with respect to the shape of the natural orbitals to a J-value that is in perfect agreement with the result obtained with dedicated orbitals in the real complex.

2.2. Calculation of the Excited States. The singlet, triplet, and quintet states considered so far do not interact directly through spin−orbit coupling. The degeneracy of the M_S sublevels of these states is only lifted through the interaction with other excited states presenting a different spatial configuration. Previous studies on mononuclear Ni(II) complexes showed that the major effect on the spin−orbit splitting comes from the interaction between the ground state ($^3A_{2g}$ in the notation of the octahedral symmetry group) and the first excited triplet states ($^3T_{2g}$), which involves a single excitation of an electron from the t_{2g} to the e_g orbitals.[12,34] The next excited triplet state ($^3T_{1g}$) lies higher in energy and has a smaller interaction with the ground state because of the strong bielectronic excited character of this state. Extrapolating these findings to the Ni(II) dimer, we calculated the energies and wave functions of all 18 states that arise from the local $^3A_{2g} \rightarrow {}^3T_{2g}$ excitations.

State-averaged CASSCF calculations were performed for states with the same spin and spatial symmetry. The active space contains the 10 Ni-3d orbitals and 16 electrons, and dynamical correlation effects are estimated with CASPT2 for all electrons except those occupying the deep-core orbitals (1s, 2s, 2p, and 3s for Ni; 1s, 2s, and 2p for Cl; and 1s for C and N). The resulting spectrum shows three groups of six states at 0.92, 1.05, and ∼1.18 eV. Each group contains the singlet, triplet, or quintet spin coupled gerade and ungerade combination of the local $^3A_{2g} \rightarrow {}^3T_{2g}$ excitation on the left or right Ni(II) ion. The states arising from the next local triplet excitation start at 1.76 eV above the ground state and have not been considered in the determination of the spin−orbit resolved low-energy spectrum.

2.3. Effect of Spin−Orbit Coupling. Before analyzing the SO-SI results, it is preferable to make a proper choice

of the coordinate frame. Although the energies are of course independent of the axes, the expression of the wave function of the spin−orbit states is strongly influenced by this choice and the interpretation of the results may be severely hindered if the principal magnetic axis does not coincide with the z-axis of the coordinate frame. Following the procedure described in the study of the monometallic Ni(II) complexes,[34] we extracted the magnetic axes of the molecule. In both monometallic and polymetallic complexes the tensor which is diagonalized (in order to extract the magnetic axes frame) only describes the ground state. In the considered case, the tensor has therefore been extracted using a giant spin Hamiltonian (**S.D.S**) describing only the quintet ground state. The proper magnetic axes frame is shown in Figure 1.

Spin−orbit coupling splits the lowest singlet, triplet, and quintet states in nine states. The weights of the |S, M_S⟩ functions on which will be built the model anisotropic spin Hamiltonian in the wave functions of these states are given in Table 2. It can be noticed that the sum of these weights is close to 1 in each state, showing that this model space is appropriate; i.e., it contains the essential physics of the problem. The spectrum width (approximatively 30 cm^{-1}) is significantly increased by the spin−orbit coupling (spin−orbit free width = 3|J| = 18 cm^{-1}). At the CASSCF level |J| is much smaller. The width of the spin−orbit spectrum is 19 cm^{-1} which is still larger than the CASSCF spin−orbit free spectrum (3|J| = 7 cm^{-1}). This is a first indication of the importance of spin−orbit interactions and so of the magnetic anisotropy of this molecule. The axes frame almost coincides with the magnetic anisotropy axes frame, since the calculated wave functions show really small mixing of determinants that can interact due to the mismatch of the coordinate frame and the magnetic axes. Furthermore, we observe that the singlet and quintet strongly mix leading to a strong stabilization of the state dominated by the |2, 0⟩ determinant and that the energetic ordering of the states is not strictly the one that is expected in the strong exchange limit ($J \gg D, E$); the |1, 0⟩ has a lower energy than the |2, −1⟩ + |2, 1⟩ state. One should notice that the molecule shows not only axial anisotropy but also important rhombic anisotropy. The states that are dominated by the |S, M_S⟩ and |S, −M_S⟩ determinants are not degenerate as would be expected in the case of pure axial anisotropy.

Rigorous Extraction of Multispin Hamiltonian

J. Chem. Theory Comput., Vol. 6, No. 1, 2010 **59**

3. Parameter Extraction of the Standard Model Hamiltonian

The interpretation of the low-energy physics of bimetallic complexes with magnetic anisotropy is usually based on the following phenomenological model Hamiltonian:[57,58]

$$\hat{H} = J\hat{S}_a \cdot \hat{S}_b + \hat{S}_a \bar{\bar{D}}_a \hat{S}_a + \hat{S}_b \bar{\bar{D}}_b \hat{S}_b + \hat{S}_a \bar{\bar{D}}_{ab} \hat{S}_b + \bar{d}_{ab} \hat{S}_a \times \hat{S}_b \tag{1}$$

The first term describes the isotropic Heisenberg magnetic coupling of the local spin moments. The second and third terms account for the local single-ion anisotropies. The fourth term introduces a symmetric anisotropic exchange while the last term corresponds to the antisymmetric exchange. Since the studied complex is centrosymmetric, the antisymmetric exchange is strictly zero[59,60] (the local magnetic axes are colinear) and the $\mathbf{D}_a$ and $\mathbf{D}_b$ tensors are equal. Let us call D_a and E_a, respectively, the axial and rhombic anisotropy parameters of the local anisotropy tensors and D_{ab} and E_{ab} respectively, the axial and rhombic parameters of the symmetric anisotropic exchange tensors. As it will be shown later, the tensors $\mathbf{D}_a$, $\mathbf{D}_b$, and $\mathbf{D}_{ab}$ are diagonal in the same coordinate frame.

Several extractions can be performed from a given spectrum. The next paragraphs will compare different extractions and discuss their ability to reproduce the calculated spectrum.

First, we parametrize the model Hamiltonian in the strong exchange limit using the expressions shown in Figure 3,[58,61] as it is usually done. One should however note that the *ab initio* results show a significant spin mixing between the singlet and the quintet components which is not accounted for by the strong exchange extraction. To get reliable parameters, the extraction is performed using only those states which are not affected by the spin mixing. Indeed, an extraction performed by
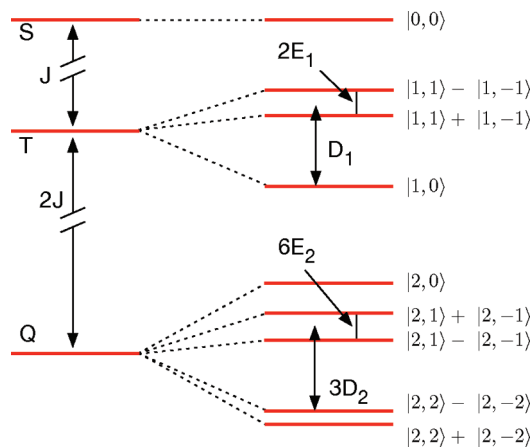

Figure 3. Energy levels of the quintet, triplet, and singlet states under the influence of spin−orbit coupling in the strong exchange limit: $D_1 = -D_a + D_{ab}$; $3D_2 = D_a + D_{ab}$; $E_1 = -E_a + E_{ab}$; $3E_2 = E_a + E_{ab}$.

optimizing the parameters in order to reproduce at best all the states of the spectrum would lead to nonphysically grounded parameters. Taking into account only axial anisotropies, $D_a = -9.43$ cm^{-1} and $D_{ab} = 0.36$ cm^{-1}. These parameters lead to the spectrum shown in the first column of Figure 4. To estimate the quality of the model spectrum, a mean percentage of error δ is defined as follows:

$$\delta = \frac{\sum_{i}^{N} |E_i^{abinitio} - E_i^{model}|}{N \times \Delta E^{abinitio}} \times 100 \tag{2}$$

where N is the number of calulated roots, $\Delta E^{abinitio} = 29.498$ cm^{-1} is the *ab initio* spectrum width, and $E_i^{abinitio}$ and E_i^{model} are, respectively, the *ab initio* and model energies.

For the strong exchange limit with axial terms only, δ is as large as 7.2%. Adding rhombic anisotropy improves the
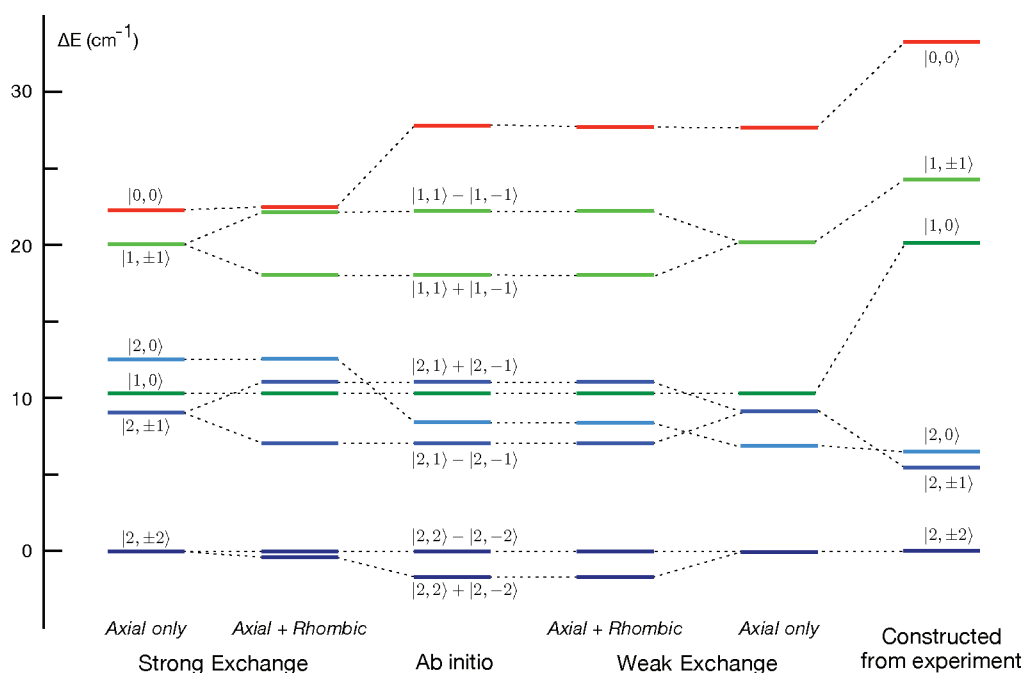

Figure 4. Comparison of the *ab initio* spectrum and model spectra obtained using different parametrizations.

model spectrum (second column, $\delta = 3.1\%$) and results in $E_a = -2.04$ cm^{-1} and $E_{ab} = 0.03$ cm^{-1}. The three states $|0, 0\rangle$, $|2, 0\rangle$, and $|2, 2\rangle + |2, -2\rangle$ which are strongly affected by the spin mixing between the singlet and the quintet are still poorly resolved by the model Hamiltonian in the strong exchange limit. At the CASSCF level, the anisotropic extracted parameters are of the same order of magnitude ($D_a = -7.07$ cm^{-1}, $D_{ab} = 0.30$ cm^{-1}, $E_a = 0.96$ cm^{-1}, and $E_{ab} = -0.39$ cm^{-1}) while $J = -2.60$ cm^{-1} is underestimated.

To further improve the representation of the *ab initio* spectrum by the model Hamiltanian, we follow the strategy outlined by Boča for the weak exchange limit, but never put to practice to the best of our knowledge. First, we determine analytically all model Hamiltonian matrix elements in the basis of the uncoupled $|M_{S_a}, M_{S_b}\rangle$ determinants (see Table 3). This 9×9 matrix is then transformed to the coupled $|S, M_S\rangle$ basis with the appropriate Clebsch−Gordan coefficients, and the five parameters of the model Hamiltonian can be determined by fitting the expressions of the eigenvalues of this Hamiltonian to the *ab initio* energies listed in Table 2. The Hamiltonian matrix in the coupled basis (given in Table 4) can be transformed into 2 smaller matrices: a 3 $\times$ 3 matrix spanned by the $|2, 2\rangle + |2, -2\rangle$, $|2, 0\rangle$, and $|0, 0\rangle$ functions and a 6×6 matrix within the $S = 1$ subspace, the $|2, \pm1\rangle$ determinants and the $|2, 2\rangle - |2, -2\rangle$ combination. Using the eigenenergies of $\Psi_{2, 3, 5-8}$, the parameters of the model Hamiltonian can be extracted from the 6×6 submatrix of the complete model Hamiltonian. Since the eigenstates of the 6×6 submatrix are not affected by the spin mixing, the parameters are practically identical to those extracted from the strong exchange limit. Nevertheless, in the weak exchange approach the three states affected by the spin mixing (see Figure 4, columns 4 and 5) are well reproduced and the overall error is 1.7% when rhombic anisotropy is neglected and only 0.07% when axial and rhombic terms are included. It is interesting to note that the lift of degeneracy between the $|2, 2\rangle$ and $|2, -2\rangle$ components is only correctly reproduced in the last extraction. This quantity (which determines the tunnel splitting) is crucial to understand the magnetization relaxation of SMMs at low temperature.

We also constructed the spectrum from the parameters that were extracted from the high-field EPR measurements reported by Herchel and co-workers.[35] Again, we only included axial terms as no estimates for E_a and E_{ab} were given in the paper. Using the parameters extracted from experiment ($J = -9.66$ cm^{-1}, $D_a = -4.78$ cm^{-1}, and $D_{ab} = -0.64$ cm^{-1}), we obtain a spectrum which exhibits a much smaller spin-mixing than the *ab initio* spectrum.

In summary, the largest differences between the *ab initio* spectrum and the spectrum extracted from experimental data is the degeneracy of the $|S, \pm M_S\rangle$ states in the latter one due to the absence of extracted rhombic anisotropy and the largest spin mixing in the *ab initio* spectrum.

4. Validity of the Model Hamiltonian

4.1. Transferability of the Single-Ion Anisotropy. Although the model Hamiltonian of eq 1 perfectly fits the *ab*

Table 3. Matrix Elements of the Model Hamiltonian for Bimetallic Ni(II) Complexes with Magnetic Anisotropy in the Uncoupled $|M_{S_a}, M_{S_b}\rangle$ Basis

$|M_{S_a}, M_{S_b}\rangle$	$|-1, -1\rangle$	$|-1, 0\rangle$	$|0, -1\rangle$	$|-1, 1\rangle$	$|0, 0\rangle$	$|1, -1\rangle$	$|1, 0\rangle$	$|0, 1\rangle$	$|1, 1\rangle$
$\langle-1, -1|$	$J + (2/3)(D_a + D_{ab})$	0	0	E_a	E_{ab}	E_a	0	0	0
$\langle-1, 0|$	0	$-(1/3)D_a$	$J - (1/3)D_{ab}$	0	0	0	E_a	E_{ab}	0
$\langle0, -1|$	0	$J - (1/3)D_{ab}$	$-(1/3)D_a$	0	0	0	E_{ab}	E_a	0
$\langle-1, 1|$	E_a	0	0	$-J + (2/3)(D_a - D_{ab})$	$J - (1/3)D_{ab}$	0	0	0	E_a
$\langle0, 0|$	E_{ab}	0	0	$J - (1/3)D_{ab}$	$-(4/3)D_a$	$J - (1/3)D_{ab}$	0	0	E_{ab}
$\langle1, -1|$	E_a	0	0	0	$J - (1/3)D_{ab}$	$-J + (2/3)(D_a - D_{ab})$	0	0	E_a
$\langle1, 0|$	0	E_a	E_{ab}	0	0	0	$-(1/3)D_a$	$J - (1/3)D_{ab}$	0
$\langle0, 1|$	0	E_{ab}	E_a	0	0	0	$J - (1/3)D_{ab}$	$-(1/3)D_a$	0
$\langle1, 1|$	0	0	0	E_a	E_{ab}	E_a	0	0	$J + (2/3)(D_a + D_{ab})$

Rigorous Extraction of Multispin Hamiltonian

J. Chem. Theory Comput., Vol. 6, No. 1, 2010 **61**

Table 4. Matrix Elements of the Model Hamiltonian for Bimetallic Ni(II) Complexes with Magnetic Anisotropy in the Coupled $|S, M_S\rangle$ Basis

$\langle S, M_S|$	$|2, -2\rangle$	$|2, -1\rangle$	$|2, 0\rangle$	$|2, 1\rangle$	$|2, 2\rangle$
$\langle 2, -2|$	$J + (2/3)(D_a + D_{ab})$	0	$[\sqrt{(2/3)}](E_a + E_{ab})$	0	0
$\langle 2, -1|$	0	$J - (1/3)(D_a + D_{ab})$	0	$E_a + E_{ab}$	0
$\langle 2, 0|$	$[\sqrt{(2/3)}](E_a + E_{ab})$	0	$J - (2/3)(D_a + D_{ab})$	0	$[\sqrt{(2/3)}](E_a + E_{ab})$
$\langle 2, 1|$	0	$E_a + E_{ab}$	0	$J - (1/3)(D_a + D_{ab})$	0
$\langle 2, 2|$	0	0	$[\sqrt{(2/3)}](E_a + E_{ab})$	0	$J + (2/3)(D_a + D_{ab})$
$\langle 1, -1|$	0	0	0	0	0
$|1, 0\rangle$	0	0	0	0	0
$|1, 1\rangle$	0	0	0	0	0
$|0, 0\rangle$	$[2/(\sqrt{3})](E_a - E_{ab})$	0	$[(\sqrt{2})/3](2D_a - D_{ab})$	0	$[2/(\sqrt{3})](E_a - E_{ab})$

	$|1, -1\rangle$	$|1, 0\rangle$	$|1, 1\rangle$	$|0, 0\rangle$
$|2, -2\rangle$	0	0	0	$[2/(\sqrt{3})](E_a - E_{ab})$
$|2, -1\rangle$	0	0	0	0
$|2, 0\rangle$	0	0	0	$[(\sqrt{2})/3](2D_a - D_{ab})$
$|2, 1\rangle$	0	0	0	0
$|2, 2\rangle$	0	0	0	$[2/(\sqrt{3})](E_a - E_{ab})$
$|1, -1\rangle$	$-J - (1/3)(D_a - D_{ab})$	0	$-E_a - E_{ab}$	0
$|1, 0\rangle$	0	$-J + (2/3)(D_a - D_{ab})$	0	0
$|1, 1\rangle$	$-E_a - E_{ab}$	0	$-J - (1/3)(D_a - D_{ab})$	0
$|0, 0\rangle$	0	0	0	$-2J$

Table 5. Single-Ion Anisotropy Parameters (cm^{-1}) Obtained for Different Representations of the Monomer Fragment[a]

	Ni(en)$_2$Cl$_2$	+AIMP	+Zn^{2+}	[Ni$_2$(en)$_4$Cl$_2$]$^{2+}$
D_a	−4.82	−6.11	−6.13	−9.43
E_a	1.32	1.33	1.34	2.04

[a] For convenience, the values of the complete bimetallic complex have been added in the last column.

initio spectrum, the single-ion anisotropy parameters D_a and E_a are not the same as those obtained in the monomer fragment (see below). The local $\mathbf{D}_a$ tensor is changed by the anisotropy of neighboring metallic centers in another way than that captured by the molecular anisotropy parameter D_{ab}.

To calculate the single ion anisotropy of the monomer, we constructed several models. The most crude representation is removing one side of the bimetallic complex to obtain the Ni(en)$_2$Cl$_2$ monomer. A refined model is obtained by replacing one of the Ni ions with an *ab initio* model potential[62] or a closed-shell (and hence isotropic) Zn^{2+}ion. The atoms of the two remaining ethylenediamine groups are replaced with LoProp atomic charges[63] to reproduce the electrostatic environment of the real complex. The anisotropy parameters listed in Table 5 are obtained from CAS(8,5)SCF calculations using CASPT2 energies and a SO-SI space that contains the lowest four triplet states of the monomer. These are the computational parameters used in the dimer translated to the monomer case.

The two more refined models show identical results, and we observe that the single-ion anisotropy calculated in the monomer is between 30% and 50% smaller than the D_a parameter of the dimer. Two hypotheses may be formulated: (1) Delocalization effects between the metal ions are not strictly identical in the embedded monomer (no delocalization), the dimer involving a Zn^{2+} ion (small delocalization between the Ni^{2+} and the closed shell Zn^{2+}), and the real dimer (more effective delocalization between the two Ni^{2+} ions). As a consequence, the resulting magnetic orbitals can be slightly different in the several calculations as well as the spin−orbit coupling involving these orbitals. (2) This could indicate a problem with the transferability of the single-ion anisotropy from monomers to polymeric systems, and the D_a parameter would not strictly parametrize the isolated single-ion anisotropy. In other words, the energy separations of the spin−orbit states would be partly caused by interactions that are present in the all electron Hamiltonian (i.e., in the *ab initio* results) but not included in the model Hamiltonian (eq 1).

4.2. Comparison with the Effective Hamiltonian. A rigorous check on the validity of the model Hamiltonian can be obtained by comparing it with an effective Hamiltonian spanned in the same basis. The effective Hamiltonian theory[64−68] is the bridge between the accurate *ab initio* results, which are difficult to interpret, and the easily understandable model Hamiltonians, which are in turn difficult to verify. By projection techniques, the *ab initio* information is reproduced in a small model space that hopefully contains all the essential physics. In a recent work on monometallic Ni(II) and 4-fold coordinated Co(II) complexes, we showed the validity of the standard Hamiltonian for zero-field splitting ($\hat{H} = \hat{S} \cdot \bar{\bar{D}} \cdot \hat{S}$) by comparing the model Hamiltonian to the corresponding effective Hamiltonian based on *ab initio* results.[34] Here, we follow the same procedure to check whether the model Hamiltonian of eq 1 contains all the important interactions for the magnetic anisotropy in bimetallic complexes.

In general, the effective Hamiltonian can be written as

$$\hat{H}^{\text{eff}} = \sum_i |\tilde{\Psi}_i\rangle E_i \langle \tilde{\Psi}_i| \tag{3}$$

where $\tilde{\Psi}_i$ are the orthogonalized projections on the model space of the exact (in practice, the *ab initio*) wave functions Ψ_i and E_i the energy eigenvalues. To ensure the Hermitic character of the effective Hamiltonian, we have applied an $S^{-1/2}$ orthonormalization of the projected vectors as proposed

by des Cloizeaux.[66] This procedure guarantees that the eigenvalues of the effective Hamiltonian are the same as for the all-electron Hamiltonian and that the corresponding eigenfunctions are the projections $\tilde{\Psi}_i$ of the eigenfunctions of the all-electron Hamiltonian onto the model space such that:

$$\hat{H}^{\text{eff}}|\tilde{\Psi}_i\rangle = E_i|\tilde{\Psi}_i\rangle \qquad (4)$$

In any arbitrary frame, the off-diagonal elements of the $\mathbf{D}_a$, $\mathbf{D}_b$, and $\mathbf{D}_{ab}$ tensors are nonzero. The corresponding analytical expression of the coupled-spin Hamiltonian matrix is given in the Supporting Information. The values of the matrix elements of the effective Hamiltonian (given in Table 6) show that the local anisotropy axes coincide with the magnetic axes of the molecule (determined from the giant spin Hamiltonian). All matrix elements arising from off-diagonal terms in the D_a and D_{ab} tensors are almost zero between the components of the quintet state (for which the axis frame has been extracted) and negligible between the other states components (see Supporting Information). Since the optimal orbital sets for the quintet, the triplet, and the singlet spin−orbit free states are different, it is not mathematically possible to define a proper magnetic axes frame shared by all these states. Nevertheless, the smallness of the off-diagonal terms of all these tensors shows that a proper magnetic axes frame can reasonably be determined for the study of the coupled-spin Hamiltonian and that these tensors can be considered as being diagonal in this axes frame.

A closer inspection reveals important differences between the model Hamiltonian matrix and the effective Hamiltonian matrix. The most spectacular difference between the two matrices concerns the $\langle 1, -1|\hat{H}|-1, 1\rangle$ matrix element. These determinants do not interact through the model Hamiltonian (see also Table 3), but the effective Hamiltonian shows a large matrix element equal to 8.6 cm^{-1}. Furthermore, $\langle -1, 0|\hat{H}^{\text{eff}}|0, -1\rangle \neq \langle -1, 1|\hat{H}^{\text{eff}}|0, 0\rangle$, while the model Hamiltonian predicts equal interactions for these determinants. The same occurs for the matrix elements $\langle -1, -1|\hat{H}|1, -1\rangle$ and $\langle -1, 0|\hat{H}|1, 0\rangle$, and the matrix elements $\langle -1, -1|\hat{H}|0, 0\rangle$ and $\langle -1, 0|\hat{H}|0, 1\rangle$.

In order to check that these unexpected results are not due to an artifact of CASPT2, the effective Hamiltonian has been extracted from the CASSCF spectrum and wave functions (see Supporting Information). The form of the effective Hamiltonian is similar, exhibiting nonzero elements and either small or large elements at the same place in the matrix. In this case the $\langle 1, -1|\hat{H}|-1, 1\rangle$ matrix element is equal to 6.4 cm^{-1} and the observed deviations between the model and the effective Hamiltonians are similar.

To account for the largest interaction that emerges from the effective Hamiltonian, it is necessary to include fourth-order interactions in the model Hamiltonian. The $|-1, 1\rangle$ determinant is coupled to $|1, -1\rangle$ by the $\hat{S}_a^+\hat{S}_a^+\hat{S}_b^-\hat{S}_b^-$ operator. A new model Hamiltonian including such fourth-order terms can be defined as:

$$\hat{H} = J\hat{S}_a \cdot \hat{S}_b + \hat{S}_a\bar{\bar{D}}_a\hat{S}_a + \hat{S}_b\bar{\bar{D}}_b\hat{S}_b + \hat{S}_a\bar{\bar{D}}_{ab}\hat{S}_b +$$
$$\vec{S}_a \otimes \vec{S}_a \cdot \mathbf{D}_{aabb} \cdot \vec{S}_b \otimes \vec{S}_b \qquad (5)$$

Table 6. Numerical Matrix Elements of the Effective Hamiltonian in the Uncoupled $|M_{S_a}, M_{S_b}\rangle$ Basis in the Magnetic Axes Frame

H^{eff}	$\lvert{-1,-1}\rangle$	$\lvert{-1,0}\rangle$	$\lvert{0,-1}\rangle$	$\lvert{-1,1}\rangle$	$\lvert{0,0}\rangle$	$\lvert{1,-1}\rangle$	$\lvert{1,0}\rangle$	$\lvert{0,1}\rangle$	$\lvert{1,1}\rangle$
$\langle{-1,-1}\rvert$	1.670	−0.001 + 0.002i	−0.001 + 0.002i	−0.706 − 0.011i	2.686 + 0.011i	−0.706 − 0.011i	0.000	0.000	0.002
$\langle{-1,0}\rvert$	−0.001 − 0.002i	16.278	−5.536	0.000	−0.010 + 0.035i	0.020 − 0.070i	2.042 + 0.013i	−0.053 − 0.012i	0.000
$\langle{0,-1}\rvert$	−0.001 − 0.002i	−5.536	16.278	0.020 − 0.070i	−0.010 + 0.035i	0.000	−0.053 − 0.012i	2.042 + 0.013i	0.000
$\langle{-1,1}\rvert$	−0.706 + 0.011i	0.000	0.020 + 0.070i	20.621	−1.309	8.599	−0.020 + 0.070i	0.000	−0.706 − 0.012i
$\langle{0,0}\rvert$	2.686 − 0.011i	−0.010 − 0.035i	−0.010 − 0.035i	−1.309	8.698	−1.309	0.010 − 0.035i	0.010 − 0.035i	2.686 + 0.011i
$\langle{1,-1}\rvert$	−0.706 + 0.011i	0.020 + 0.070i	0.000	8.599	−1.309	20.621	0.000	−0.020 + 0.070i	−0.707 − 0.012i
$\langle{1,0}\rvert$	0.000	2.042 − 0.013i	−0.053 + 0.012i	−0.020 − 0.070i	0.010 + 0.035i	0.000	16.278	−5.536	0.001 − 0.002i
$\langle{0,1}\rvert$	0.000	−0.053 + 0.012i	2.042 − 0.013i	0.000	0.010 + 0.035i	−0.020 − 0.070i	−5.536	16.278	0.001 − 0.002i
$\langle{1,1}\rvert$	0.002	0.000	0.000	−0.707 + 0.012i	2.686 − 0.011i	−0.707 + 0.012i	0.001 + 0.002i	0.001 + 0.002i	1.670

Rigorous Extraction of Multispin Hamiltonian

J. Chem. Theory Comput., Vol. 6, No. 1, 2010 **63**

where $\mathbf{D}_{aabb}$ is a fourth-order tensor, a 9×9 matrix, where a, $b = x$, y, z. The first two indices refer to site a, the other two to site b.

This new model Hamiltonian defined by the sum of the isotropic exchange, local and intersite anisotropy, and a term that describes the biquadratic anisotropic exchange significantly improves the comparison with the effective Hamiltonian. The $\langle -1, 1|H^{\text{eff}}|1, -1 \rangle$ matrix elements appear in the new model Hamiltonian as the $(1/4)(D_{xxxx} + D_{yyyy}) + D_{xyxy} - (1/2)D_{xxyy}$ fourth-order in-plane interaction. This is, however, not the only improvement. The fourth-order term also contains operators such as $\hat{S}_a^+ \hat{S}_a^+ \hat{S}_b^z \hat{S}_b^z$ and $\hat{S}_a^+ \hat{S}_a^z (\hat{S}_b^+ \hat{S}_b^z + \hat{S}_b^z \hat{S}_b^+)$, which cause differential contributions for the other matrix elements that were found to be different in the effective Hamiltonian and equal in the standard model Hamiltonian. The complete matrix representation of the new model Hamiltonian perfectly reproduces the symmetry of the numerical effective Hamiltonian, and its expression in the magnetic axes frame can be found in the Supporting Information. At the CASSCF level the model and effective Hamiltonians are also in perfect agreement.

This new definition of the model Hamiltonian for magnetic anisotropy involves the parametrization of at least 14 interactions, namely the isotropic exchange coupling (J), the local anisotropy parameters D_a and E_a, the anisotropic exchange parameters D_{ab} and E_{ab}, and nine parameters that define the fourth-order tensor. Actually, the 81 elements reduce to just 15 nonzero elements in an appropriate coordinate frame and finally to nine differents parameters due to the symmetry of the system. Nevertheless, there are only nine states in the model space, and there is no direct way to derive analytical expressions for the parameters, not even using all the information in the effective Hamiltonian. In any case, it is not very convenient to work with so many parameters.

The above presented analysis leads to the conclusion that fourth-order anisotropic interactions are non-negligible in Ni(II) polymetallic systems, and that the rigorous extraction of the magnetic anisotropy parameters is not possible without introducing any further approximation. Although the definition of the spin Hamiltonian as a sum of isotropic, second-order anisotropic, and fourth-order anisotropic terms leads to a better understanding of the physics, it does not provide the tools to describe the phenomenon in a practical manner due to the large number of parameters.

5. Conclusions

The extraction of the magnetic anisotropy parameters in bimetallic complexes has been performed within the coupled Hamiltonian formalism. The local anisotropic spin moments are coupled by isotropic and anisotropic exchange interactions to describe the total magnetic behavior of the molecule. The most important conclusions obtained from both CASSCF and CASPT2 calculations can be summarized in the following paragraphs.

The standard coupled Hamiltonian gives an excellent fit of the *ab initio* spectrum. However, the comparison of the matrix representation of this Hamiltonian and the effective Hamiltonian constructed from the calculated energies and wave functions shows important discrepancies. Therefore, it is concluded that while the effective parameters of the standard Hamiltonian enable one to reproduce the spectrum, this Hamiltonian does not contain all the operators required to describe the physics of the anisotropic exchange.

A rigorous description of the magnetic anisotropy in $[\text{Ni}_2(\text{en})_4\text{Cl}_2]^{2+}$ requires the use of fourth-order interactions. Test calculations on a bimetallic Co^{2+} complex show that sixth-order interactions appear in the effective Hamiltonian. Hence, the spin Hamiltonian should include spin operators up to order $2S_{\text{max}}$, in addition to the standard operators for local anisotropy, and isotropic and anisotropic exchange interactions. This Hamiltonian enables one to reproduce the matrix of the effective Hamiltonian extracted from the *ab initio* calculations.

In the giant spin approximation, the molecule is treated as an effective monometallic species with one (giant) spin for which the anisotropic properties can be determined. One important perspective will be the extraction of the giant spin Hamiltonian and the study of the effect of the coupled-spin fourth-order interactions in this formalism. Analytical relations between the multispin and giant spin Hamiltonian have to be found; this is the subject of ongoing research.

Supporting Information Available: Matrix elements of the standard coupled spin Hamiltonian in the $|M_{S_A}, M_{S_B}\rangle$ basis in an arbitrary coordinate frame, SO-SI spectrum of $[\text{Ni}_2(\text{en})_4\text{Cl}_2]^{2+}$ as function of the isotropic exchange J, orthonormalized projections of the *ab initio* wave functions on the $|S, M_S\rangle$ model space, effective Hamiltonian in the $|S, M_S\rangle$ space, effective Hamiltonian in $|M_{S_A}, M_{S_B}\rangle$ basis obtained with the CASSCF spin-free energies on the diagonal of the spin−orbit matrix, and the coupled spin Hamiltonian matrix extended with fourth-order interaction in the magnetic axes frame. This material is available free of charge via the Internet at http://pubs.acs.org.

References

(1) Sessoli, R.; Gatteschi, D.; Caneschi, A.; Novak, M. A. *Nature* **1993**, *365*, 141.

(2) Gatteschi, D.; Sessoli, R. *Angew. Chem., Int. Ed.* **2003**, *42*, 269.

(3) Gatteschi, D.; Sessoli, R.; Villain, F. *Molecular Nanomagnets*; Oxford University Press: Oxford, 2006.

(4) Aromí, G.; Aubin, S. M. J.; Bolcar, M. A.; Christou, G.; Eppley, H. J.; Folting, K.; Hendrickson, D. N.; Huffman, J. C.; Squire, R. C.; Tsai, H.-L.; Wang, S.; Wemple, M. W. *Polyhedron* **1998**, *17*, 3005.

(5) Delfs, C.; Gatteschi, D.; Pardi, L.; Sessoli, R.; Wieghardt, K.; Hanke, D. *Inorg. Chem.* **1993**, *32*, 3099.

(6) Yang, E.-C.; Wernsdorfer, W.; Zakharov, L.; Karaki, Y.; Yamaguchi, A.; Isidro, R. M.; Lu, G. D.; Wilson, S.; Rheingold, A. L.; Ishimoto, H.; Hendrickson, D. N. *Inorg. Chem.* **2006**, *45*, 529.

(7) Milios, C. J.; Inglis, R.; Vinslava, A.; Bagai, R.; Wernsdorfer, W.; Parsons, S.; Perlepes, S. P.; Christou, G.; Brechin, E. K. *J. Am. Chem. Soc.* **2007**, *129*, 12505.

(8) Müller, A.; Das, S. K.; Talismanova, M. O.; Bögge, H; Kögerler, P.; Schmidtman, M.; Talismanov, S. S.; Luban, M.; Krickemeyer, E. *Angew. Chem., Int. Ed.* **2002**, *41*, 579.

(9) Tasiopoulos, A. J.; Vinslava, A.; Wernsdorfer, W.; Abboud, K. A.; Christou, G. *Angew. Chem., Int. Ed.* **2004**, *43*, 2117.

(10) Larionova, J.; Gross, M.; Pilkington, M.; Andres, H.; Stoeckli-Evans, H.; Güdel, H. U.; Decurtins, S. *Angew. Chem., Int. Ed.* **2000**, *39*, 1605.

(11) Oshio, H.; Hoshino, N.; Ito, T.; Nakano, M.; Renz, F.; Gütlich, P. *Angew. Chem., Int. Ed.* **2003**, *42*, 223.

(12) Abragam, A.; Bleany, B. *Electron Paramagnetic Resonance of Transition Ions*; Dover Publications: Dover, NY, 1986.

(13) Bencini, A.; Gatteschi, D. *EPR of Exchange Coupled Systems*; Springer-Verlag: Berlin, 1990.

(14) Barra, A.-L.; Gatteschi, D.; Sessoli, R. *Phys. Rev. B* **1997**, *56*, 8192.

(15) Moragues-Cánovas, M.; Helliwell, M.; Ricard, L.; Riviere, E.; Wernsdorfer, W.; Brechin, E.; Mallah, T. *Eur. J. Inorg. Chem.* **2004**, 2219.

(16) Duboc, C.; Phoeung, T.; Zein, S.; Pécaut, J.; Collomb, M.-N.; Neese, F. *Inorg. Chem.* **2007**, *46*, 4905.

(17) Piligkos, S.; Bill, E.; Collison, D.; McInnes, E. J. L.; Timco, G. A.; Weihe, H.; Winpenny, R. E. P.; Neese, F. *J. Am. Chem. Soc.* **2007**, *129*, 760.

(18) Chibotaru, L.; Ungur, L.; Aronica, C.; Elmoll, H.; Pilet, G.; Luneau, D. *J. Am. Chem. Soc.* **2008**, *130*, 12445.

(19) Borrás-Almenar, J. J.; Clemente-Juan, J. M.; Coronado, E.; Tsukerblatt, B. S. *Inorg. Chem.* **1999**, *38*, 6081.

(20) Ruiz, E.; Cirera, J.; Cano, J.; Alvarez, S.; Loose, C.; Kortus, J. *Chem. Commun.* **2008**, 52.

(21) Cirera, J.; Ruiz, E.; Alvarez, S.; Neese, F.; Kortus, J. *Chem. Eur. J.* **2009**, *15*, 4078.

(22) Park, K.; Pederson, M. R.; Richardson, S. L.; Aliaga-Alcalde, N.; Christou, G. *Phys. Rev. B* **2003**, *68*, 020405.

(23) Pederson, M. R.; Khanna, S. N. *Phys. Rev. B* **1999**, *60*, 9566.

(24) Kortus, J.; Hellberg, C. S.; Pederson, M. R. *Phys. Rev. Lett.* **2001**, *86*, 3400.

(25) Neese, F. *J. Chem. Phys.* **2007**, *127*, 164112.

(26) Ribas-Arino, J.; Baruah, T.; Pederson, M. R. *J. Chem. Phys.* **2005**, *123*, 044303.

(27) Neese, F. *J. Am. Chem. Soc.* **2006**, *128*, 10213.

(28) Malmqvist, P.-Å.; Roos, B. O. *Chem. Phys. Lett.* **1989**, *155*, 189.

(29) Malmqvist, P.-Å.; Roos, B. O.; Schimmelpfennig, B. *Chem. Phys. Lett.* **2002**, *357*, 230.

(30) Llusar, R.; Casarrubios, M.; Barandiarán, Z.; Seijo, L. *J. Chem. Phys.* **1996**, *105*, 5321.

(31) Webb, S. P.; Gordon, M. S. *J. Chem. Phys.* **1998**, *109*, 919.

(32) de Graaf, C.; Sousa, C. *Int. J. Quantum Chem.* **2006**, *106*, 2470.

(33) Chibotaru, L.; Ungur, L.; Soncini, A. *Angew. Chem., Int. Ed.* **2008**, *47*, 4126.

(34) Maurice, R.; Bastardis, R.; de Graaf, C.; Suaud, N.; Mallah, T.; Guihéry, N. *J. Chem. Theory Comput.* **2009**, *5*, 2977.

(35) Herchel, R.; Boča, R.; Krzystek, J.; Ozarowski, A.; Durán, M.; van Slageren, J. *J. Am. Chem. Soc.* **2007**, *129*, 10306.

(36) Karlström, G.; Lindh, R.; Malmqvist, P.-Å.; Roos, B. O.; Ryde, U.; Veryazov, V.; Widmark, P.-O.; Cossi, M.; Schimmelpfennig, B.; Neogrady, P.; Seijo, L. *Comput. Mater. Sci.* **2003**, *28*, 222.

(37) Miralles, J.; Daudey, J.-P.; Caballol, R. *Chem. Phys. Lett.* **1992**, *198*, 555.

(38) Broer, R; Maaskant, W. J. A. *Chem. Phys.* **1986**, *102*, 103.

(39) de Graaf, C.; Illas, F. *Phys. Rev. B* **2001**, *63*, 014404.

(40) Cabrero, J.; de Graaf, C.; Bordas, E.; Caballol, R.; Malrieu, J.-P. *Chem. Eur. J.* **2003**, *9*, 2307.

(41) Herebian, D.; Wieghardt, K.; Neese, F. *J. Am. Chem. Soc.* **2003**, *125*, 10997.

(42) Gellé, A.; Munzarová, M. L.; Lepetit, M. B.; Illas, F *Phys. Rev. B* **2003**, *68*, 125103.

(43) Neese, F. *J. Chem. Phys.* **2003**, *119*, 9428.

(44) Calzado, C. J.; Malrieu, J.-P. *Phys. Rev. B* **2004**, *69*, 094435.

(45) Bastardis, R.; Guihéry, N.; Suaud, N. *Phys. Rev. B* **2007**, *75*, 132403.

(46) Le Guennic, B.; Petit, S.; Chastanet, G.; Pilet, G.; Luneau, D.; Ben Amor, N.; Robert, V. *Inorg. Chem.* **2008**, *47*, 572.

(47) Barone, V.; Cacelli, I.; Ferrati, A.; Prampolini, G. *Phys. Chem. Chem. Phys.* **2009**, *11*, 3854.

(48) García, V. M.; Caballol, R.; Malrieu, J.-P. *J. Chem. Phys.* **1998**, *109*, 504.

(49) Cabrero, J.; Caballol, R.; Malrieu, J.-P. *Mol. Phys.* **2001**, *100*, 919.

(50) Rodríguez, E.; Reguero, M. *J. Phys. Chem. A* **2002**, *106*, 504.

(51) Andersson, K.; Malmqvist, P.-Å.; Roos, B. O. *J. Chem. Phys.* **1992**, *96*, 1218.

(52) Queralt, N.; Taratiel, D.; de Graaf, C.; Caballol, R.; Cimiraglia, R.; Angeli, C. *J. Comput. Chem.* **2008**, *29*, 994.

(53) Calzado, C. J.; Malrieu, J.-P.; Cabrero, J.; Caballol, R. *J. Phys. Chem. A* **2000**, *104*, 11636.

(54) Bordas, E.; Caballol, R.; de Graaf, C. *THEOCHEM* **2005**, *727*, 173.

(55) García, V. M.; Castell, O.; Caballol, R.; Malrieu, J.-P. *Chem. Phys. Lett.* **1995**, *238*, 222.

(56) Bastardis, R.; Guihéry, N.; de Graaf, C. *J. Chem. Phys.* **2008**, *129*, 104102.

(57) Kahn, O. *Molecular Magnetism*; VCH Publishers: New York, 1993; pp 135−143.

(58) Boča, R. *Theoretical Foundations of Molecular Magnetism*; Elsevier: Amsterdam, 1999; pp 642−680.

(59) Dzyaloshinsky, I. *J. Phys. Chem. Solids* **1958**, *4*, 241.

(60) Moriya, T. *Phys. Rev.* **1960**, *120*, 91.

(61) Boča, R. *Coord. Chem. Rev.* **2004**, *248*, 757.

(62) Barandiarán, Z.; Seijo, L. *J. Chem. Phys.* **1988**, *89*, 5739.

(63) Gagliardi, L.; Lindh, R.; Karlström, G. *J. Chem. Phys.* **2004**, *121*, 4494.

(64) Bloch, C. *Nucl. Phys.* **1958**, *6*, 329.

(65) Bloch, C.; Horowitz, J. *Nucl. Phys.* **1958**, *8*, 91.

(66) des Cloizeaux, J. *Nucl. Phys.* **1960**, *20*, 321.

(67) Malrieu, J.-P.; Durand, P.; Daudey, J.-P. *J. Phys. A: Math Gen.* **1985**, *18*, 809.

(68) Heully, J.-L.; Malrieu, J.-P. *Chem. Phys.* **2009**, *356*, 76.

JCTC Journal of Chemical Theory and Computation

On the Structure and Geometry of Biomolecular Binding Motifs (Hydrogen-Bonding, Stacking, X−H···π): WFT and DFT Calculations

Kevin E. Riley,[*,†] Michal Pitoňák,[‡,§] Jiří Černý,[ǁ] and Pavel Hobza[*,‡,⊥]

Department of Chemistry, University of Puerto Rico, P.O. Box 23346, Rio Piedras, Puerto Rico 00931, Institute of Organic Chemistry and Biochemistry, Academy of Sciences of the Czech Republic and Center of Biomolecules and Complex Molecular Systems, Flemingovo nam. 2, 166 10 Prague 6, Czech Republic, Department of Physical and Theoretical Chemistry, Faculty of Natural Sciences, Comenius University, Mlynska Dolina CH-1, 842 15 Bratislava, Slovak Republic, Institute of Biotechnology, Academy of Sciences of the Czech Republic, 142 00 Prague 4, Czech Republic, and Department of Physical Chemistry, Palacký University, Olomouc, 771 46 Olomouc, Czech Republic

Abstract: The strengths of noncovalent interactions are generally very sensitive to a number of geometric parameters. Among the most important of these parameters is the separation between the interacting moieties (in the case of an intermolecular interaction, this would be the intermolecular separation). Most works seeking to characterize the properties of intermolecular interactions are mainly concerned with binding energies obtained at the potential energy minimum (as determined at some particular level of theory). In this work, in order to extend our understanding of these types of noncovalent interactions, we investigate the distance dependence of several types of intermolecular interactions, these are hydrogen bonds, stacking interactions, dispersion interactions, and X−H···π interactions. There are several methods that have traditionally been used to treat noncovalent interactions as well as many new methods that have emerged within the past three or four years. Here we obtain reference data using estimated CCSD(T) values at the complete basis set limit (using the CBS(T) method); potential energy curves are also produced using several other methods thought to be accurate for intermolecular interactions, these are MP2/cc-pVTZ, MP2/aug-cc-pVDZ, MP2/6-31G*(0.25), SCS(MI)-MP2/cc-pVTZ, estimated MP2.5/CBS, DFT-SAPT/aug-cc-pVTZ, DFT/M06-2X/6-311+G(2df,2p), and DFT-D/TPSS/6-311++G(3df,3pd). The basis set superposition error is systematically considered throughout the study. It is found that the MP2.5 and DFT-SAPT methods, which are both quite computationally intensive, produce potential energy curves that are in very good agreement to those of the reference method. Among the MP2 techniques, which can be said to be of medium computational expense, the best results are obtained with MP2/cc-pVTZ and SCS(MI)-MP2/cc-pVTZ. DFT-D/TPSS/6-311++G(3df,3pd) is the DFT-based method that can be said to give the most well-balanced description of intermolecular interactions.

Introduction

The structure, stability, and dynamic properties of biomolecular systems, such as proteins, DNA/RNA, and protein−ligand complexes, are influenced by several physical factors, the most important of which are solvation effects[1,2] and noncovalent interactions.[3–6] The mode of action of solvation effects in stabilizing biomacromolecules is generally seen

---

* Corresponding author. E-mail: kev.e.riley@gmail.com (K.E.R.); pavel.hobza@uochb.cas.cz (P.H.).

† Department of Chemistry, University of Puerto Rico.

‡ Institute of Organic Chemistry and Biochemistry, Academy of Sciences of the Czech Republic and Center of Biomolecules and Complex Molecular Systems.

§ Department of Physical and Theoretical Chemistry, Comenius University.

ǁ Institute of Biotechnology, Academy of Sciences of the Czech Republic.

⊥ Department of Physical Chemistry, Palacký University.

as being nonspecific in character, playing roles, for example, in the aggregation of hydrophobic amino acids in the core of globular proteins.[4,6] The roles that noncovalent interactions play in the structures and stabilities of biomacromolecules can be quite different than those played by solvation effects because of the presence of certain specific binding motifs that commonly occur in proteins and DNA (as well as other biomolecular structures), that lead to very stable interactions. The formation of these strong interactions can have a large impact on structure and, in the case of protein receptors that interact with particular ligands, can determine whether or not the receptor is activated.[7–9] Among the most common of these specific types of interactions are hydrogen-bonds (H-bonds) and stacking and X–H···π interactions (X is usually O, N, S, or C). It should be noted that dispersion, or van der Waals, interactions, which are generally fairly weak, represent a class of noncovalent interaction that is geometrically nonspecific, that is to say that they do not depend heavily on the relative orientation of the monomers, such as in the case of, for example, H-bonds. Although these types of interactions are weak, they are very important in biomolecular structure because of their pervasiveness throughout the structures of proteins, DNA and other biostructures. We will note here that, when we refer to dispersion interactions, we are describing the types of weak interactions, such as those between aliphatic molecules, whose attractive nature is largely attributable to London dispersion forces. In general, all types of noncovalent interactions contain some degree of a dispersion-type component. Likewise, even interactions between aliphatic molecules contain some contribution from electrostatic forces.

Noncovalent interactions are characterized by a very subtle energetic scale (with respect to geometric parameters), a property that is necessary for the fine-tuning and the diversity of biochemical processes.[10] As noted above, there are four classes of noncovalent interactions that play the largest roles in biomolecular structure, these are H-bonding and dispersion, stacking, and X–H···π interactions. We will note here that σ-hole bonding, which has been the subject of many recent investigations, also plays important roles in biology but, because it is fairly specialized and is not as ubiquitous as the other noncovalent bonding classes, this type of interaction will not be discussed here.[11–14] Among the interaction types, H-bonding is the best characterized and is known to be chiefly attributable to electrostatic forces (dipole–dipole interactions).[10,15,16] Dispersion interactions, as indicated by the name, are stabilized principally by London dispersion (part of van der Waals) forces.[10,15,16] Both dispersion and electrostatic forces contribute to the stabilization of stacked and X–H···π structures, with the largest energetic contribution for both these types of interactions coming from dispersion. It should be noted that, because of the enhanced electrostatic landscape of heterocyclic aromatic groups, interactions involving these moieties tend to be more attractive and to have larger electrostatic contributions than those involving phenyl rings. This is especially important when considering the extremely attractive stacking interactions between the nucleobases contained in DNA and RNA.[10,17]

The characterization of noncovalent interactions in biomolecules has been the subject of many experimental and theoretical investigations in (at least) the past two decades.[8–10,18–30] On the computational side, it has been possible for many years to properly characterize H-bonding interactions because these dipole–dipole dependent interactions can be described relatively well using one-particle methods, such as Hartree–Fock (HF) and density functional theory (DFT). Dispersion, stacking, and X–H···π interactions are largely dependent on dispersion forces, which can only be accurately described by (computationally expensive) high-level theoretical methods, such as the coupled cluster theory (CC) method using single, double, and perturbative triple excitations (i.e., CCSD(T)) along with large basis sets (at least aug-cc-pVTZ).[17,31] Because of the prohibitive cost of these types of calculations for all but the smallest complexes, there has been relatively little work done seeking to accurately characterize interactions that are heavily based on London dispersion forces. Over the past 15 years or so there have been many studies describing dispersion, stacking, and X–H···π interactions using the second-order Møller–Plesset perturbation theory method (MP2), a method that can be said to be of intermediate computational cost, with various basis sets.[10,16,32] It has been shown (for several different types of intermolecular interactions) that the results obtained with the MP2 method can be semiquantitative, with accuracies that are highly dependent on the basis sets that are employed.[32,33] Recently it has become possible to compute binding energies for molecular complexes with increasing accuracy by using techniques that take advantage of the fact that the CCSD(T) and MP2 binding energies exhibit very similar basis set behavior.[31,34] That is to say that the difference in binding energy computed using, for example, the aug-cc-pVDZ and aug-cc-pVTZ basis sets is roughly the same for both the MP2 and CCSD(T) methods. This basis set behavior allows one to compute the MP2 binding energy using the largest possible basis set (or extrapolate to the complete basis set limit (CBS)) and then add a CC correction term (ΔCCSD(T)), corresponding to the difference between the CCSD(T) and MP2 binding energies for a given (generally small or medium) basis set. At present, this scheme represents the most accurate technique for the determination of interaction energies for systems that cannot be treated using the CCSD(T) method, along with large basis sets. The use of this type of scheme along with MP2 binding energies that have been extrapolated to the complete basis set has been termed the CBS(T) method. The accuracy of the method was recently confirmed by performing the direct extrapolation of the CCSD(T) energies determined with the aug-cc-pVDZ and aug-cc-pVTZ basis sets.[17,35]

Most investigations concerned with the accurate characterization of noncovalent interactions in biomacromolecules have focused on obtaining accurate binding energies either by using the potential energy minimum (as determined at some lower level of theory) or the experimentally derived complex structures (such as those obtained from X-ray crystal structures). In this study, we investigate the types of noncovalent interactions that are relevant in biomolecular structure, focusing on the potential energy curves of these

interactions along the most important geometrical axis (i.e., directly along the dissociation pathway), meaning that the structure of a biomolecular cluster was optimized with respect to one geometry coordinate. There are several reasons that it is important to characterize not only minimum energy structures but also potential energy curves for these interactions. First, as noted above, noncovalent interactions are very sensitive to geometric parameters, and their strengths can often vary significantly with only a small geometric perturbation. This sensitivity can have a tremendous influence on the structures and the stabilities of proteins and nucleic acid compounds (DNA/RNA) and may be a large factor in determining whether or not a ligand (such as a hormone or pharmaceutical compound) successfully binds to a protein receptor. Formulating a deeper understanding of the behavior of noncovalent interactions as a function of geometric parameters can give us insights into the dynamics of biomolecular systems, giving us information that could be very valuable in the interpretation of vibrational (infrared) spectra of peptides, proteins, and nucleic acid compounds. Second, studying the potential energy curves for a variety of noncovalent interaction types can aid in determining the accuracy, in terms of converging to the geometric energy minimum, that can be expected of lower level (less computationally expensive) methods. This last point is very important because the structures obtained at these lower levels are often used for high-level binding energy analyses (as noted above) and because lower level theory is often used to obtain theoretical infrared spectra, which can potentially be useful in assigning peaks in experimentally obtained spectra. Finally, and this point is particularly significant for complex molecular systems, interactions at long ranges play a key role in complexes of extended systems, where the number of contacts at these distances grows extremely quickly.

It will be noted here that there are many degrees of freedom that must be considered in studying geometrical relationships in noncovalently bound systems. The goal of this work is to study potential energy curves along the dissociation pathways of several complexes, this is the coordinate that is generally considered to be the most important in terms of complex formation and dissociation. Further studies are underway in our laboratories to investigate the full geometrical dependence of noncovalent interactions on structures that have been fully gradient optimized at very high levels of theory (including estimated CCSD(T)/CBS).[36]

As noted above, the MP2 method has long been the method of choice for the computation of intermolecular interactions, producing binding energies that are generally semiquantitatively accurate at a reasonable computational cost. It has been shown that for the S26 test set of complexes, which contains H-bonded, dispersion-bound, and mixed (contributions from both electrostatics and dispersion) interactions, the MP2 method yields the best results when it is paired with the medium-sized cc-pVTZ and aug-cc-pVDZ basis sets (the S26 test set is related to the S22 test set described below).[32] The use of larger basis sets usually results in overestimation of binding energies, with electronic energies for complexes being too high relative to those of the

monomers. Generally the MP2 method treats H-bonding interactions fairly well but often greatly underestimates the binding energies of cyclic H-bonds, such as those found in nucleic acid base pairs. In terms of dispersion and stacking interactions, the MP2 method generally tends to (sometimes strongly) overestimate binding energies for these types of complexes, this is especially true when larger basis sets are used. It should be stressed that much of the success of the MP2 method can be attributed to error compensation effects stemming from the relative energies of a complex and from its constituent monomers. As a result of this, MP2 binding energies for intermolecular interactions do not generally converge to the correct value (as determined with CCSD(T)) with increasing basis set size. For example, the aug-cc-pVDZ basis set has been observed to obtain a more balanced description of binding energies for the S26 set than that of the aug-cc-pVTZ basis.

The use of smaller basis sets, such as those of the Pople-type 6-31G* family, along with the MP2 method allow for the treatment of larger systems and have been used with some frequency in past years when using larger bases was not possible. In some cases, these types of bases have been shown to yield very good binding energies. One example of a small basis set that has been extensively used for the treatment of noncovalent interactions is 6-31G*(0.25), which is a modified 6-31G* basis set for which the polarization functions have been modified to be more diffuse (change in exponential parameter from 0.80 to 0.25).[37] This basis has been shown to give reasonable results for binding energies of molecular complexes and has performed especially well for stacking interactions.[32] The surprisingly good agreement of MP2/6-31G*(0.25) and CCSD(T)/CBS binding energies for stacked systems has recently been shown.[38]

The past several years have seen the development of many new computational techniques that promise to provide well balanced and accurate descriptions of a wide variety of different types of noncovalent interactions at much lower computational costs than the CCSD(T), or even the CBS(T), method. A great number of these methods have been parametrized and/or tested using S22,[33] S26,[32] and JSCH2005[33] benchmark data sets; all complexes presented there are systematically given in their (estimated) global energy minima. A similar situation also exists for other noncovalent databases. It is, thus, highly desirable to test the performance of these methods not only for the stabilization energy but also for the geometry.

It is well know that one-particle methods, such as HF and DFT, generally fail to describe interactions that are strongly dependent on dispersion forces,[39] however, recently several DFT techniques seeking to take dispersion interaction contributions into account have been developed; here we will discuss two of these methods, DFT-D[40,41] and M06-2X.[22,42,43]

The DFT-D method deals with dispersion by using an empirical term describing the London dispersion energy. The DFT-D empirical dispersion term has been parametrized against the S22 binding energy test set, which includes H-bonded, dispersion-bound, and mixed (electrostatic and dispersion) complexes. The M06-2X functional is based on the reparameterization of the DFT

WFT and DFT Calculations

J. Chem. Theory Comput., Vol. 6, No. 1, 2010 **69**

functional in order to take dispersion effects into account; the parametrization was made on various data sets including a set of small noncovalent complexes. The M06-2X functional is a member of the M06 family of functionals, which, along with several other functionals (described at http://comp.chem.umn.edu/info/DFT.htm), represent an extensive effort by Truhlar and co-workers to develop density functionals with improved reliability for the computation of many molecular properties.[22,23,42–47] The performance of the M06-2X functional (as well as other functionals from the M06 family) was tested using the S22 data set.[43] In a recent assessment, Sherrill and co-workers note that the M05−2X and M06-2X descriptions of variously configured nucleic acids from the JSCH-2005 test set are not as well-balanced as that of the DFT-D/PBE/aug-cc-pVDZ method by Grimme.[48–50]

The DFT-symmetry adapted perturbation theory method (DFT-SAPT)[51–56] is the only method considered in this work treating molecular interaction differently than by the supermolecular approach. This technique has been shown to compute accurate binding energies for a variety of interaction types and has the great advantage of determining the total intermolecular interactions as a sum of physically meaningful components, such as electrostatic, exchange, induction, and dispersion terms. The method provides very good estimates of stabilization energies close to the CCSD(T) benchmark data. A very important advantage of the procedure is the fact that it is almost a genuine ab initio procedure, i.e., it does not contain any empirical parameter, except for those in underlying DFT functional, e.g., in the DFT-SAPT procedure.

The overestimation of the stabilization energy in dispersion-dominated complexes by MP2 was shown to be due to the fact that the supermolecular MP2 interaction energy includes the dispersion energy determined only at the uncoupled HF level. Dispersion energies are generally overestimated by 10−20% in comparison with accurate values.[57] In the past few years, several methods have been developed with the aim of improving the performance of MP2, in terms of their abilities, to accurately describe intermolecular interactions in a well balanced way (across all interaction types).[57,58]

The basis for the spin-component scaled MP2 method (SCS-MP2) is the parametrization of the parallel and antiparallel spin components of the MP2 correlation energy.[59] The parameters for the family of SCS-MP2 methods have been deduced from either theory or fitted against many test sets describing several atomic and molecular properties. In this work, we will only be concerned with the molecular interactions (SCS(MI)-MP2) variant of the method,[60] though there are several other variants that may produce good potential energy curves for intermolecular interactions (for example, SCSN-MP2).[61,62] This method, like DFT-D, has been parametrized against the S22 molecular interactions test set. The SCS(MI)-MP2 method has been shown to reduce the systematic overestimation of binding energies for dispersion-bound complexes seen with the MP2 technique and, thus, should be suitable for the description of a wide variety of molecular interaction motifs. The SCS(MI)-MP2 method

provides very good stabilization energies for stacked as well as H-bonded complexes, in contrast to the original SCS-MP2 method, which fails for the latter complexes.[17] All methods of the SCS-MP2 family contain empirical parameter(s). Sherrill and co-workers have recently carried out studies in which various SCS-MP2 methods (as well as DFT-based methods) are compared in terms of their ability to accurately produce potential energy curves for molecular complexes containing benzene as (at least) one of the monomers and the methane dimer.[61,63] One of the main conclusions of these studies is that SCS-MP2 methods, and particularly SCS(MI)-MP2, give reasonable potential energy curves for the systems considered, although binding energies for the methane dimer are strongly underestimated.

Recently an interesting property of the interaction energy calculated at the supermolecular MP3 level was recognized.[64] Tests carried out on the S22 as well as the JCSH2005 test sets revealed that MP3 underestimates stacking interactions roughly to the same extent as the MP2 overestimates them.[64] At the same time MP3 typically slightly increases the accuracy of the interaction energies of the H-bonded complexes. This was the basis for formulating the MP2.5 (or in general SMP3, Scaled MP3) method, i.e. the MP2 corrected by scaled $E^{(3)}$ (third-order correlation contribution). In the case of MP2.5, the scaling factor is 0.5, while in SMP3, the optimal scaling factor typically ranges from 0.45 to 0.65, depending on the type of molecular complex and the basis set applied. MP2.5 in general reproduces the CCSD(T) values very well (outperforms SCS(MI)-MP2 and all DFT methods mentioned above), but the scaling factor 0.5 is known not to be optimal for all kinds of molecular complexes and cannot be determined a priori, which could lead to errors of about $\pm 10\%$ of $E^{(3)}$. Fortunately (as shown further), SMP3, with a particular choice of the scaling factor, reproduces the CCSD(T) potential energy curves with almost a constant error along a wide range of geometry displacements. However, one main drawback of the method is in its N^6 scaling with system size, which means an order of magnitude slowdown compared to MP2 but a dramatic speedup compared to CCSD(T). The other advantage of the method is that it contains only one empirical parameter, the scaling factor.

There have been a number of studies carried out within the past several years in which high-quality potential energy curves for intermolecular interaction are produced.[17,31,65–81] In a recent work, Pitoňák et al. described both the (cyclic) H-bonding and stacking potential energy curves for the uracil dimer, the smallest nucleic acid complex, at various levels of theory, including the estimated CCSD(T)/aug-cc-pVTZ level.[17] One of the main findings made in this study is that the DFT-D, M06−2X, and SCS(MI)-MP2 methods produce potential energy curves for these interactions that are at least semiquantitatively accurate. The SCS(MI)-MP2 technique yielded particularly accurate results for both H-bonded and stacked systems, while the results obtained with the DFT-D and M06-2X methods were substantially better for the H-bonded complex than for the stacked one. It should be noted that Sherrill and co-workers have produced a number of high-quality potential energy curves for several interesting

intermolecular interactions,[31,63,65–70] among these are various configurations of the (substituted and unsubstituted) benzene dimer[31,67–69] and the H_2S−benzene[70] and methane−benzene complexes.[66] Extremely high-quality geometries and energies for the benzene dimer in various configurations have also been computed by Pulay and Janowski.[71] The geometries and interaction energies of stacked and H-bonded uracil dimers and stacked adenine−thymine pairs were studied by means of high-level quantum chemical calculations including CCSD(T) by Dabkowska et al.[72] It was found that geometry optimization with extended basis sets at the MP2 level underestimates the intermolecular distances compared to the reference CCSD(T) results, whereas the MP2/counterpoise-corrected gradient optimization agrees well with the reference geometries; therefore, this level (MP2/cc-pVTZ) was recommended for geometry optimizations. In a recent study Sponer and co-workers produced potential energy curves near the potential energy minima for several configurations of the uracil dimer using several electronic structure methods (including CBS(T)) and using an empirical potential-based method.[82] For these complexes, it was observed that the DFT-D, DFT-SAPT, and SCS(MI)-MP2 methods all generated curves that were in very good agreement with reference data. Tekin and Jansen produced high-quality, CCSD(T) and DFT-SAPT (both with aug-cc-pVTZ), potential energy curves for various configurations of the acetylene−benzene complex.[83] Tsuzuki and co-workers have produced high-quality CCSD(T) binding energies for a number of alkane dimers, including the propane dimer considered in this work, and have also generated MP2 potential energy curves for a number of conformations of the propane dimer.[76,84] Very recently Fusti Molnar et al. produced high-level estimated CCSD(T) potential energy curves for 20 of the 22 structures found within the S22 molecular interactions test set.[85]

One of the main goals of this article is to compute accurate potential energy curves for the most important classes of noncovalent interaction motifs relevant to biomolecular structure, in order to elucidate the properties of these types of interactions. To this end we have selected seven model systems representing the four major interaction categories to be studied here, these are: cytosine−benzene (stacked), adenine−benzene (stacked), and water−benzene (X−H···π) and propane (dispersion), methanol (H-bond), methylamine (H-bond), and formamide (H-bond, cyclic) dimers. Potential energy curves for each of these complexes have been computed at the estimated CCSD(T)/CBS level of theory, the highest level currently possible for the largest of these systems. Another principal aim of this work is to compare the performance of several lower-level methods in reproducing the potential energy curves of these complexes. The methods considered here include the MP2, which has long been used for the computation of binding energies of intermolecular interactions, and the relatively new SCS(MI)-MP2, DFT-SAPT, DFT-D, and DFT/M06-2X techniques. More specifically, the method/basis combinations that will be treated in this work are: MP2/cc-pVTZ, MP2/aug-cc-pVDZ, MP2/6-31G*(0.25), SCS(MI)-MP2/cc-pVTZ, DFT-SAPT/aug-cc-pVTZ, DFT-D/TPSS/6-311++G(3df,3pd), and DFT/M06-2X/6-311+G(2df,2p). It should be noted that some
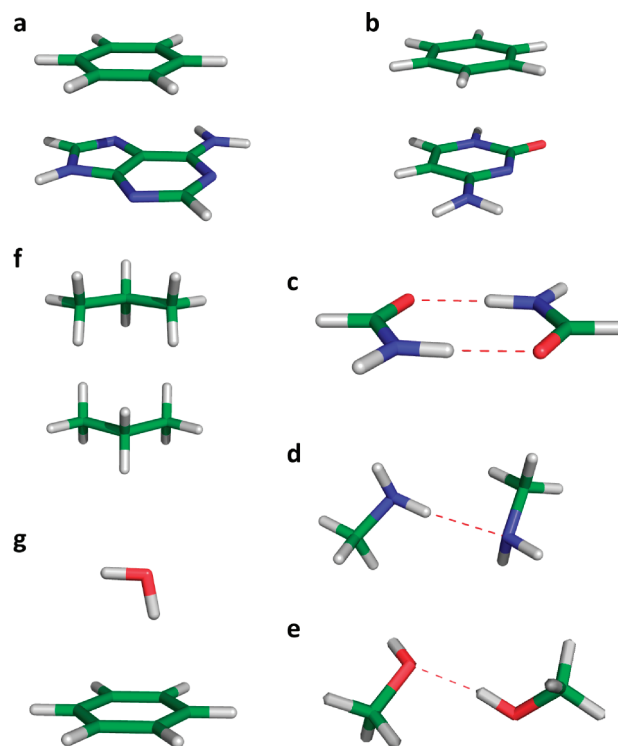

Figure 1. Molecular complexes considered in this work: (a) adenine−benzene, (b) cytosine−benzene, (c) formamide dimer, (d) methylamine dimer, (e) methanol dimer, (f) propane dimer, and (g) benzene−water.

of these methods, for example SCS(MI)-MP2, may yield better results when they are used along with larger basis sets. Our main purpose here is to evaluate the performance of several methods that could be used (and have been used) to treat relatively large systems relevant to biochemistry, as such we have chosen to use medium-sized basis sets for all of these methods.

Computational Methods

Structures of Studied Complexes. In order to investigate the noncovalent interactions of varying character, ranging from strongly electrostatic to strongly dispersive, we have included examples of four different interaction types into our study, these are:

- i. Stacking interaction: adenine−benzene and cytosine−benzene.
- ii. H-bonding interaction: methanol, methylamine, formamide dimers.
- iii. Dispersion interaction: propane dimer.
- iv. X−H···π interaction: benzene−water.

Structures of all complexes investigated are visualized in Figure 1. Initial geometries for the stacking systems were prepared by positioning the benzene ring in an ideal stacking position (i.e., perfectly flat) with its center directly above the center of either cytosine or adenine. The center positions of benzene and cytosine were determined as the average position of all atoms within the ring; in the case of adenine, the center of each ring was determined, and the overall molecular center was taken to be the position in the middle of these two points. The geometries of these monomers were

WFT and DFT Calculations

J. Chem. Theory Comput., Vol. 6, No. 1, 2010 **71**

determined at the B3LYP/6-31+G* level of theory. In order to generate the points for the potential energy curves of these systems, the monomers were simply separated in such a way that they remained parallel to one another.

The initial geometries of the methanol and methylamine complexes were determined at the estimated CCSD(T)/CBS level of theory, while the initial geometry of the formamide complex was taken directly from the S22 data set and computed at the MP2/cc-pVTZ level, using the counterpoise correction (CP) to account for the basis set superposition error (BSSE). Potential energy points for these systems were produced by modifying the H···O or H···N distances, such that the O−H···O or N−H···N angles remained constant. It should be noted that in the case of the formamide dimer, which contains a cyclic double H-bond, the H···N distances were modulated such that both H-bonds were consistently of the same length.

The initial structure for the propane dimer was obtained at the (CP-corrected) MP2/cc-pVTZ level of theory. Here, potential energy points were generated by modifying the distances between the monomers, such that the molecular planes defined by the three carbon atoms in each of the monomers were always parallel to one another and the molecules' centers of mass formed a line perpendicular to the two molecular planes.

In the case of the benzene−water complex, the initial geometry, as determined at the (CP-corrected) MP2/cc-pVTZ level of theory, was taken from the S22 data set. Here, points along the potential energy curve were produced by modulating the distance between the water and benzene monomers in a direction perpendicular to the plane defined by the benzene ring.

Electronic Structure Methods. High-level reference data for each of these curves were obtained using the CBS(T) method to estimate CCSD(T)/CBS results. These values are obtained by first computing the binding energies at the MP2/CBS level and then by adding a ΔCCSD(T) correction term:[10,34]

$$\Delta E^{\text{CCSD(T)}} = \Delta E^{\text{MP2}}_{\text{CBS}} + (\Delta E^{\text{CCSD(T)}} - \Delta E^{\text{MP2}})_{\text{small basis set}}$$

(1)

Here, $E^{\text{MP2}}_{\text{CBS}} = E^{\text{HF}}_{\text{CBS}} + E^{\text{corr, MP 2}}_{\text{CBS}}$ quantities were determined by extrapolating MP2 electronic energies to the complete basis set limit, using the extrapolation scheme of Helgaker and co-workers.[86] All MP2/CBS extrapolations were performed using electronic energies produced at the MP2/aug-cc-pVDZ and MP2/aug-cc-pVTZ levels of theory. As noted above, all ΔCCSD(T) correction terms were computed using the relatively large aug-cc-pVDZ basis set.

The success of this method in providing accurate binding energies is based on the fact that the CCSD(T) and MP2 methods exhibit basis set dependence that is very similar. Although the binding energies obtained using these two methods (with a particular basis set) can be quite different, the difference between these binding energies ($\Delta E^{\text{CCSD(T)}} - \Delta E^{\text{MP2}}$)$_{\text{small bassis set}}$ remains nearly constant regardless of the basis set used. It should be noted that binding energy results generally improve when larger basis sets are used to compute the ΔCCSD(T) term.

In a recent study, Pitoňák et al. produced very accurate interaction energies for the stacked and H-bonding uracil dimers by directly extrapolating CCSD(T) results to the complete basis set limit (using the aug-cc-pVDZ and aug-cc-pVTZ basis sets).[17] Here it was shown that the CBS(T) method, as implemented in this study (i.e., based on eq 1), produces accurate binding energies for these complexes, with errors no larger than 0.1 kcal/mol for the stacked structure and 0.2 kcal/mol for the H-bonding structure (both corresponding to errors of roughly 1.0%).

It should also be noted that the MP2 extrapolation to the complete basis set limit based on the aug-cc-pVDZ and aug-cc-pVTZ basis sets may cause some small binding energy errors, as these are the smallest basis sets for which this type of extrapolation can be carried out. Based on the H-bonding and stacking structures of the uracil dimer (as described above), it is seen that this extrapolation scheme underestimates the MP2/CBS binding energy of both structures compared to the aug-cc-pVTZ to aug-cc-pVQZ extrapolation by about 1%.[17] Jurečka et al. investigated the binding energies of four H-bonding and nine stacked nucleic acid pairs using MP2 extrapolation based both on aug-cc-pvDZ and aug-cc-pVTZ and on aug-cc-pVTZ and aug-cc-pVQZ.[33] For the H-bonding pairs, the smaller basis extrapolation scheme underestimated binding energies, with an average error of 1.8% (compared to the larger basis MP2 extrapolation), the largest error for these interactions was 2.0%. For the stacked structures, the average error of the smaller basis extrapolation was 1.4% (underbinding), with a maximum error of 2.6%. It should also be noted that, for one of the stacking pairs, the smaller basis extrapolation overestimated the binding energy by 1.2%. We expect that the errors present in our studies would not exceed those observed for the nucleic acid complexes described above. Fusti Molnar et al. have also noted the relatively small errors associated with MP2 extrapolation based on aug-cc-pVDZ and aug-cc-pVTZ.[85]

Here all CCSD(T)/aug-cc-pVDZ and MP2/aug-cc-pVDZ calculations were performed using the Molpro electronic structure package (Molpro 2006),[87] while MP2/aug-cc-pVTZ values were computed using the resolution-of-the-identity approach (RI-MP2)[88] with the Turbomole package.[89] The RI-MP2 approximation has been shown to introduce negligible errors.[90] MP2 and CCSD(T) computations were carried out using the frozen-core approximation in which the lowest lying molecular orbitals are constrained to remain doubly occupied in all configurations.

Here, we study the performance of MP2 along with the aug-cc-pVDZ, cc-pVTZ, and 6-31G*(0.25) basis sets for the description of the potential energy curves associated with the separation of molecular complexes. All MP2 curves were produced using the Molpro electronic structure package and incorporate the counterpoise correction in order to account for the BSSE.[91]

The DFT-D technique incorporates an empirical London dispersion energy term, which describes dispersion using the well-known C_6/R^6 formula.[41] The dispersion energy term also contains a damping function to account for overlap effects (most importantly at small values of R).

DFT-D parameters were fitted against the S22 data set of intermolecular interactions. In this work, we employ the DFT-D/TPSS/6-311++G(3df,3pd) technique using empirical coefficients optimized for noncounterpoise-corrected binding energy computations. DFT energies were computed using the Gaussian package (G03),[92] while the dispersion terms were obtained using an in-house Fortran program. For DFT calculations, fine grids and tight convergence were utilized for all calculations (i.e., INT(GRID=ULTRAFINE), SCF(CONVER=TIGHT)).

The M06-2X functional of Truhlar and co-workers (along with several other functional, M05, M05-2X, M06, M06-L, etc.) was developed to give improved results for several molecular properties.[22,42,43,45,47] One of the large goals achieved with many of these functionals was a much-improved description of dispersion forces. Here, we have employed the M06-2X functional along with the 6-311+G(2df,2p), using the Gaussian electronic structure package.[92] The counterpoise technique was employed to account for BSSE.

Both DFT-based methods considered here have been parametrized to be used along with specific basis sets and, in the case of DFT-D, functionals. Here we have used the basis sets (and functionals) recommended by the developers of these two methods in order to give the best results at reasonable computational costs.

The SCS(MI)-MP2 method obtains improved results for molecular interactions by scaling the MP2 parallel and antiparallel contributions to the correlation energy.[60] The main result of the spin parametrization in the SCS(MI)-MP2 method is the reduction of the overstabilization of dispersion interactions seen with MP2. The SCS(MI)-MP2 parameters were optimized against the S22 data set of molecular interactions. Here, SCS(MI)-MP2 calculations were performed along with the cc-pVTZ basis set, using Molpro. The counterpoise correction for BSSE was included.

DFT-SAPT uses monomer properties and electronic densities from DFT in order to compute interaction energies using the symmetry adapted perturbation theory (SAPT).[51–56] This is the only variant of the SAPT methods that can be practically used for systems containing more than a few atoms and is, thus, the most useful for computations on biomolecular systems. DFT-SAPT has been shown in several studies to obtain accurate binding energies for a wide variety of intermolecular interaction types. This method determines the total interaction energy as a sum of physically meaningful components, such as those arising from electrostatics, dispersion, induction, and exchange. The DFT-SAPT interaction energy is given as the sum of these components:

$$E_{int} = E_{pol}^1 + E_{ex}^1 + E_{ind}^2 + E_{ex-ind}^2 + E_{disp}^2 + E_{ex-disp}^2 + \delta HF \quad (2)$$

Some of these terms can be combined in order to define values that correspond to commonly understood physical quantities. The terms are commonly combined as such:

$$
\begin{aligned}
E(\text{elec}) &= E_{pol}^1 \\
E(\text{ind}) &= E_{ind}^2 + E_{ex-ind}^2 \\
E(\text{disp}) &= E_{disp}^2 + E_{ex-disp}^2 \\
\text{and} & \\
E(\text{exch}) &= E_{ex}^1
\end{aligned}
$$

These four quantities refer to the electrostatic (elec), induction (ind), dispersion (disp), and exchange–repulsion (exch) contributions, respectively, to the total interaction energy. The δHF term is an estimate of higher-order Hartree–Fock contributions and is determined as the difference between the HF interaction energy and the sum of all the first- and second-order contributions (obtained with the HF wave functions), with the exceptions of the dispersion and exchange–dispersion terms. Since the HF interaction energy is determined using a supermolecular description (including counterpoise corrections), the DFT-SAPT interaction energy constructed, as in eq 2, is not BSSE free. It is, however, true that the BSSE for the HF interaction energy is much smaller than that of the correlation interaction energy.

All DFT-SAPT computations have been carried out using the LPBE0AC potential along with the aug-cc-pVTZ basis set. This basis set can generally be viewed as the smallest basis that gives meaningful results with SAPT methods; the use of smaller basis sets will result in significant underestimation of the dispersion term and, thus, the binding energy. In a study of the binding in several configurations of the acetylene–benzene complex by Tekin and Jansen, it was found that DFT-SAPT/aug-cc-pVTZ produces binding energies that are up to ~5% lower than those of DFT-SAPT/CBS.[83]

The density fitting procedure was used to significantly reduce the computational cost of these calculations. It is necessary to compute a shift term involving the ionization potentials and the highest occupied molecular orbital (HOMO) energies for interacting monomers. These terms were obtained using the PBE0 functional along with the aug-cc-pVDZ basis set. DFT-SAPT calculations were performed using the Molpro package of programs. Here, it should be noted that DFT-SAPT/aug-cc-pVTZ computations on the adenine–benzene complex were not possible to obtain because of technical (convergence) difficulties.

MP3 (and thus MP2.5) calculations were performed using the L-CCD (linearized coupled clusters singles and doubles) module based on the Cholesky decomposed two-electron integrals implemented in the MOLCAS 7 program package,[93] where a 1.10^{-7} threshold for integral decomposition was used. Overall estimated MP2.5/CBS results were obtained analogously to eq 1:

$$\Delta E_{CBS}^{MP2.5} = \Delta E_{CBS}^{MP2} + \frac{1}{2}(\Delta E^{MP3} - \Delta E^{MP2})_{\text{small basis set}}$$

$$(3)$$

assuming that the $E^{(3)}$ term ($\Delta E^{MP3} - \Delta E^{MP2}$) converges, analogously to higher-order correction terms from CCSD(T), faster with the basis set than with the MP2. Just to illustrate the speedup of the MP3 calculation compared to the CCSD(T), a MP3 step of the single-point calculation of the cytosine–benzene complex using the aug-cc-pVDZ basis set
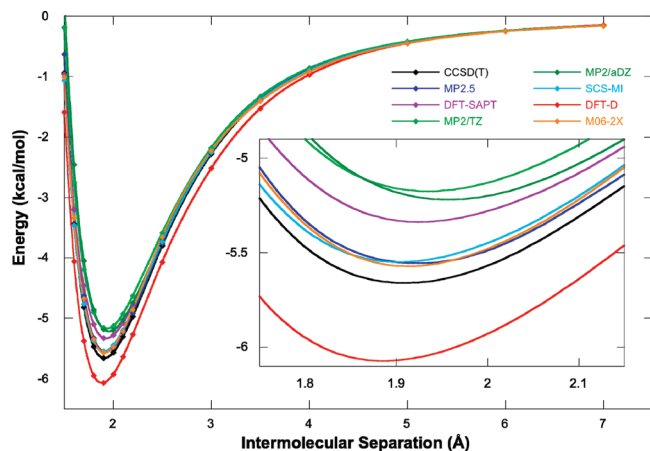
WFT and DFT Calculations

J. Chem. Theory Comput., Vol. 6, No. 1, 2010 **73**

Figure 2. Potential energy curves for the methanol dimer using several electronic structure methods (see text for exact description of methods used). CCSD(T) (black), MP2.5 (dark blue), DFT-SAPT (purple), MP2/TZ (light green), MP2/aDZ (dark green), SCS-MI (light blue), DFT-D (red), M06-2X (orange).
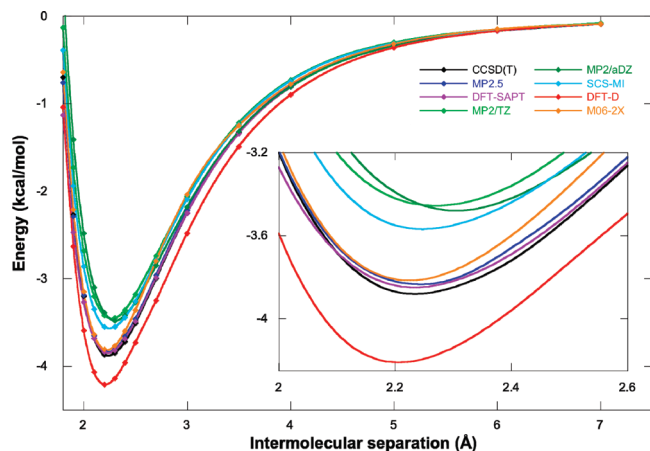

Figure 3. Potential energy curves for the methylamine dimer using several electronic structure methods (see text for exact description of methods used).

took 45 min on four cores of a 2.4Ghz Intel Core2 Quad processor machine, while the CCSD(T) step took 39 h on four 2.66 GHz four-core Intel Xeon E5430 processors. It should be noted, that the MP2 method is still roughly by an order of magnitude faster than MP3.

Results

Performance of MP2-, DFT-, and SAPT-Based Methods. *H-bonding Interactions.* Inspection of Figures 2−4 reveals that all of the computational methods studied here give similar interaction energy curves for the methanol (Figure 2), methylamine (Figure 3), and formamide (Figure 4) dimers, which are the three H-bonding complexes considered here. As would be expected for H-bonds whose properties are generally well described even by low-level methods, all of the computational techniques treated in this work give results that are, at least, semiquantitatively correct. It should also be noted that all of the methods considered here exhibit proper long-range behavior.
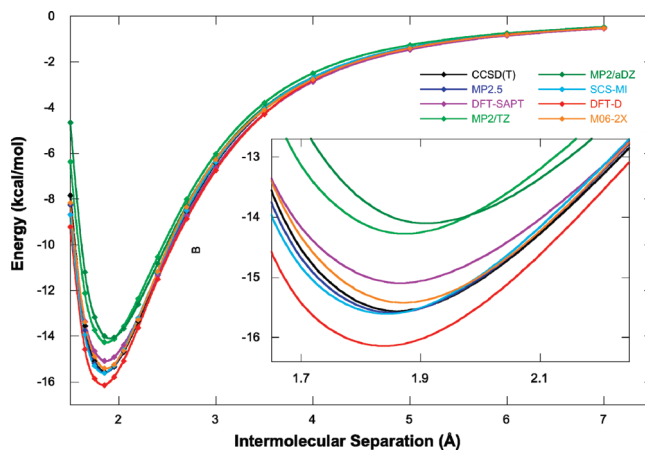

Figure 4. Potential energy curves for the formamide dimer using several electronic structure methods (see text for exact description of methods used).

The estimated MP2.5/CBS method produces extremely high-quality potential energy curves for these H-bonding systems, that are generally slightly underbound. The potential energy minima for all three complexes are at the same intermolecular separation as those of CCSD(T), with binding energies that are in error by no more than 2%. In general, MP2/aug-cc-pVDZ and MP2/cc-pVTZ tend to underbind these complexes by about 8−12%, with potential energy minima at slightly too large an intermolecular separation (by no more than about 0.01 Å, see Table 1). Still considering MP2, the minimum energy separation is slightly larger for the aug-cc-pVDZ basis set than for cc-pVTZ for all H-bonding systems. This finding agrees well with our previous conclusion mentioned above (Dabkowska et al.),[72] showing that counterpoise-corrected MP2/cc-pVTZ optimization yields reliable geometries well comparable with the CBS(T) ones. The SCS(MI)-MP2 method generally produces accurate results for the H-bonding complexes, matching the CBS(T) curves for the formamide and methanol dimers extremely closely. SCS(MI)-MP2 results for the methylamine dimer are not quite as accurate, with binding energies that are approximately 8% too high near the potential energy minimum. It should be noted that the curve produced with this method, although too shallow, is still in good agreement with CCSD(T) in terms of the location of the potential energy minimum. The fact that all calculations based on the MP2 procedure yield reliable distances of the minima is promising, since it allows one to optimize the structure of H-bonded complexes at this (rather cheap) level and then to perform a single-point calculation with some higher-level method providing accurate energies. DFT-SAPT produces very accurate potential energy curves for these H-bonding systems, with minima located at the same locations as those of CCSD(T) (to within 0.1 Å) and with binding energies that are slightly too high (underbound) for all complexes. The largest error in the binding energy at the potential energy minimum occurs for the methanol dimer, which is underbound by about 6%.

For each of the H-bonding complexes, DFT-D yields binding energies that are too large by about 4−9%. It should, however, be noted that this method predicts the proper

Table 1. Equilibrium Separation Distances and Binding Energies (in Parentheses) for Complexes/Methods Considered in This Work[a]
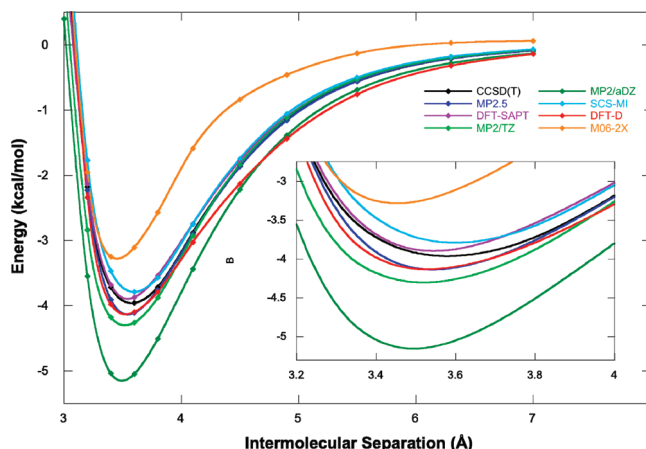
method	methanol	methylamine	formamide	adenine−benzene	cytosine−benzene	propane	benzene−water
CCSD(T)	1.91	2.23	1.86	3.40	3.56	3.81	2.41
	(5.66)	(3.88)	(15.56)	(5.28)	(3.97)	(2.04)	(3.26)
MP2.5	1.92	2.24	1.85	3.38	3.54	3.81	2.41
	(5.64)	(3.83)	(15.59)	(5.58)	(4.16)	(1.92)	(3.30)
DFT-SAPT	1.93	2.23	1.87	n/a	3.54	3.85	2.42
	(5.34)	(3.85)	(15.09)		(3.89)	(1.91)	(3.23)
MP2/TZ	1.94	2.27	1.87	3.30	3.51	3.87	2.47
	(5.17)	(3.46)	(14.27)	(6.84)	(4.33)	(1.64)	(2.93)
MP2/aDZ	1.96	2.30	1.91	3.30	3.49	3.89	2.50
	(5.22)	(3.48)	(15.00)	(7.69)	(5.19)	(1.72)	(2.98)
MP2/6-31	2.02	2.37	1.97	3.37	3.57	4.08	2.54
	(4.75)	(3.01)	(13.16)	(5.74)	(3.64)	(1.02)	(2.64)
SCS/TZ	1.90	2.25	1.84	3.36	3.58	3.90	2.47
	(5.66)	(3.57)	(15.62)	(5.87)	(3.79)	(1.49)	(3.06)
DFT-D	1.89	2.21	1.84	3.37	3.52	3.78	2.45
	(5.72)	(3.90)	(15.95)	(5.40)	(4.15)	(2.87)	(3.61)
M06-2X	1.91	2.23	1.87	3.31	3.46	3.65	2.36
	(5.57)	(3.81)	(15.43)	(5.10)	(3.31)	(2.09)	(3.58)

[a] CCSD(T) = estimated CCSD(T)/CBS, TZ = cc-pVTZ, aDZ = aug-cc-pVDZ, 6-31 = 6-31G*(0.25). MP2.5 refers to estimated MP2.5/CBS, DFT-SAPT refers to DFT-SAPT/aug-cc-pVTZ, DFT-D refers to DFT-D/TPSS/6-311++G(3df,3pd), and M06-2X refers to DFT/M06-2X/6-311+G(2df,2p). (See text for detailed descriptions of the complexes and the methods used; distances in Å and binding energies in kcal/mol.)
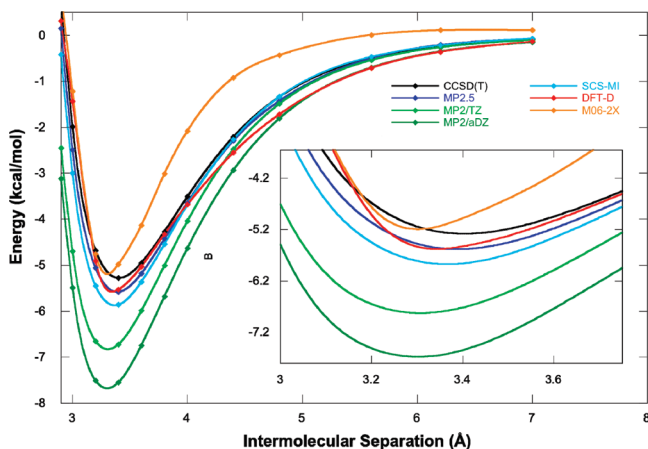
Figure 5. Potential energy curves for adenine−benzene using several electronic structure methods (see text for exact description of methods used).

Figure 6. Potential energy curves for cytosine−benzene using several electronic structure methods (see text for exact description of methods used).

locations of the potential energy minima for all three complexes (to within 0.02 Å, Table 1). The M06-2X functional gives excellent results for each of the H-bonding complexes, producing binding energies that are only very slightly too small. The potential energy curves given by this functional track the estimated CCSD(T) curves almost perfectly for both the formamide and methanol dimers and produce very good results for the methylamine dimer. In the case of the methylamine dimer, the M06-2X interaction energies, at points in the region of ascent from the potential energy minimum (moving radially outward), are too high (underbound) by about 0.15−0.20 kcal/mol. The fact that both DFT methods (and specifically the M06-2X) yield proper long-range behavior is not surprising, since the long-range contribution originates here in the dipole−dipole interaction, which is well described by the DFT functionals considered.

Stacking Interactions. Figures 5 and 6 give the potential energy curves for the interactions of adenine and cytosine

with benzene, respectively. In these figures it can be seen that the estimated MP2.5/CBS method yields very good potential energy curves for these complexes, with binding energies at the potential energy minimum that are overbound by approximately 4−6%. The fact that these binding energies are too low indicates that the magnitudes of the scaled $E^{(3)}$ corrections to the MP2/CBS results are smaller than those of the CCSD(T) corrections. One of the most prominent aspects of the data presented in these figures is the dramatic overbinding exhibited by the MP2 method when paired with both the cc-pVTZ and aug-cc-pVDZ basis sets. Overbinding is particularly strong for MP2/aug-cc-pVDZ, with minimum energy binding energies that are off approximately 42% for the adenine−benzene complex and by 27% for the cytosine−benzene complex. This result is not surprising, as it is well documented that the MP2 method, along with medium basis sets, generally tends to overbind for stacking interactions. It should also be noted that the MP2 method, with both basis sets, predicts the optimum intermolecular

WFT and DFT Calculations

J. Chem. Theory Comput., Vol. 6, No. 1, 2010 **75**

separations for these complexes to be slightly too small compared to those of estimated CCSD(T)/CBS results, but the difference is fairly small. As with H-bonded complexes, the counterpoise-corrected MP2/cc-pVTZ geometry is closer to the reference data than that of the MP2/aug-cc-pVDZ. In the case of cytosine−benzene, the MP2/cc-pVTZ method overbinds the minimum geometry by only about 5−10%. One of the goals in developing the SCS(MI)-MP2 method was to correct for the large overbinding effects seen with the MP2 method for stacked systems. In the figures, it can be seen that SCS(MI)-MP2 produces potential energy curves that are generally better than those given by MP2, with minimum energy binding energies that are within 10% of our reference values. Interestingly, this method overbinds by about 10% for the adenine−benzene complex, while underbinding by about 5% for the cytosine−benzene complex. For both complexes, the potential energy minima are located at approximately the same points for both SCS(MI)-MP2 and CCSD(T). DFT-SAPT results are available only for cytosine−benzene. For this complex, DFT-SAPT yields a very accurate potential energy curve, with a binding energy that is too high at the minimum by about 2%. One interesting aspect of the DFT-SAPT data depicted here is that the curve is slightly too shallow moving out (increasing the intermolecular separation) from the potential energy minimum. This shallowness is observed from the minimum (∼3.6 Å) out to about 4.2−4.4 Å.

The DFT-D technique obtains very good results for both of these stacking complexes, with minimum binding energies that are overbound by no more than about 5% for both the adenine−benzene and the cytosine−benzene systems. The locations of the potential energy minima are also in good agreement with estimated CCSD(T) results, although it should be noted that the optimum separation for the cytosine−benzene complex is slightly too short. Brief inspection of Figures 5 and 6 reveals that the features of the potential energy curves generated using the M06-2X functional are very different than those produced with estimated CCSD(T) interaction energies. For both complexes, this functional produces curves that are too steep near the minima, resulting in very narrow potential wells. In the case of the adenine−benzene complex, the optimum separation is predicted to be slightly too short, with a binding energy that is in good agreement with CCSD(T) results. However, for the cytosine−benzene complex, the minimum energy separation is too short by about 0.1 Å, with a binding energy that is approximately 20% too low. The incorrect long-range behavior of the M06-2X functional is due to the fact that the dispersion energy was covered by reparametrization of the exchange functional and not by the correlation one.

Dispersion Interactions. Potential energy curves of the propane dimer, whose chief mode of interaction is dispersion, for all methods considered here are given in Figure 7. It can directly be seen that MP2.5 and DFT-SAPT are the only methods producing good potential energy curves and that, among all of the MP2- and DFT-based methods, none can be said to be in excellent agreement with estimated CCSD(T) results. Both MP2.5 and DFT-SAPT give the correct location for the potential energy minimum, with binding energies that
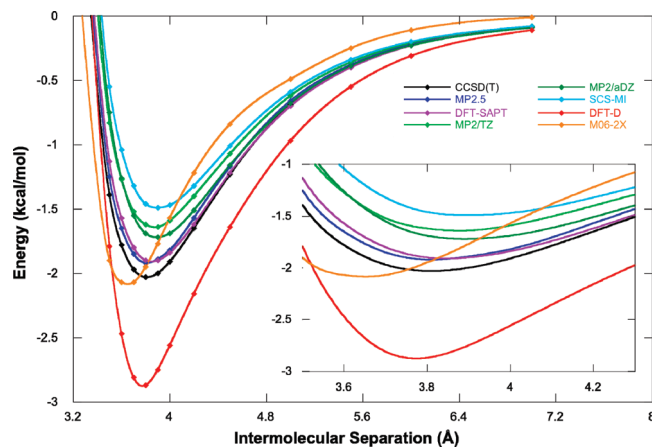

Figure 7. Potential energy curves for the propane dimer using several electronic structure methods (see text for exact description of methods used).

are underbound about approximately 6%. Among all other methods considered here, only DFT-D predicts the correct point for the potential energy minimum, at a separation of about 3.8 Å, but this method greatly overbinds the complex (by 0.84 kcal/mol or approximately 41%). This overbinding is most probably attributable to the fact that the S22 test set, from which DFT-D was parametrized, is heavily weighted toward sp²-hybridized carbons (aromatic systems). The MP2/aug-cc-pVDZ, MP2/cc-pVTZ, and SCS(MI)-MP2/cc-pVTZ methods all underestimate the binding energy of the propane dimer and all predict the potential energy minimum to be located at a separation close to 3.9 Å. The performance of SCS(MI)-MP2 is particularly disappointing, with a binding energy that is 0.54 kcal/mol too low. In terms of the binding energy at the potential energy minimum, the M06-2X DFT gives the best result, with a binding energy that is only 0.04 kcal/mol higher than that of the CCSD(T) result. This minimum is located at 3.65 Å, which is too small a separation. It should be noted that at longer ranges the potential energy curve produced by the M06-2X functional deviates significantly from that of CCSD(T) (and those of the other methods), with energies that rise too sharply in the range between the minimum and about 4.5 Å. The result is a potential energy well that is too narrow near the minimum. Notice that this method has very similar behavior for both stacked complexes described in the previous paragraph.

O−H···π Interactions. One of the most noteworthy aspects of the curves shown for the interaction between benzene and water in Figure 8 is the fact that, as in the case of the dispersion interactions, MP2.5 and DFT-SAPT are the only computational techniques whose potential energy curves closely match the CCSD(T) results. The MP2.5 method overbinds near the potential energy minimum, whereas DFT-SAPT tends to underbind, however, neither of these methods is in error by more than about 1% of the minimum. All MP2-based methods tend to underbind this complex, while the DFT-based methods both overbind. MP2/cc-pVTZ, MP2/aug-cc-pVDZ, and SCS(MI)-MP2 all produce curves whose minimum energy separations are too large (by about 0.05−0.1 Å) and whose binding energies are too
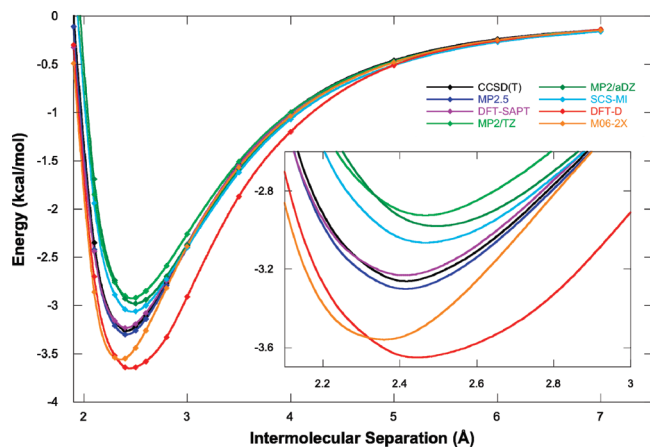
Figure 8. Potential energy curves for benzene–water using several electronic structure methods (see text for exact description of methods used).

low. The strongest underbinding tendencies are produced by the MP2/cc-pVTZ method, which is in error by approximately 10%. SCS(MI)-MP2 produces the best binding energy results for this mixed dispersion/electrostatic complex, with a binding energy that is within approximately 6% of the reference value. The binding energies produced at the potential energy minima for both DFT-D and M06-2X are overbound by approximately 10%. While DFT-D, like the MP2 methods, gives an optimum separation that is slightly too large, M06-2X gives a separation that is slightly too small (by 0.05 Å). It is also interesting to note that the curve produced with the DFT-D method appears to be somewhat too broad compared to the reference curve. Notice that, in this case, the long-range behavior is correct and well comparable with the reference CCSD(T) calculations. This might be explained by the fact that the electrostatic term represents the leading energy contribution.

Performance of the MP2/6-31G*(0.25) Method. In the Supporting Information, Figures S1–S7 give the MP2/6-31G*(0.25) potential energy curves, along with estimated CCSD(T)/CBS, MP2/cc-pVTZ, and MP2/aug-cc-pVDZ data, for all of the complexes considered in this work. One of the most striking aspects of these data is the fact that this method outperforms MP2/cc-pVTZ and MP2/aug-cc-pVDZ for both stacking interactions, being slightly overbound for the adenine–benzene complex and slightly underbound for the cytosine–benzene complex. This is in good agreement with previous results for stacked systems, where it was found that the 6-31G*(0.25) basis is among the best performers for MP2 binding energies of stacked systems.[32,72] It can also be seen in Table 1 that the potential energy minima obtained with MP2/6-31G*(0.25) are in very good agreement with the reference data. Unfortunately this method's exceptional performance for stacked systems does not translate to the other interaction motifs. It can be seen in the Supporting Information, Figures S3–S5, that MP2/6-31G*(0.25) is significantly underbound for all of the H-bonding complexes and also gives optimum intermolecular separations that are too wide (see also Table 1). Binding curves for the propane dimer and benzene–water complex are given in the Supporting Information, Figures S6–S7, respectively. MP2/6-31G*(0.25) is underbound and gives too large an optimum

intermolecular separation for both of these complexes. The most problematic case is clearly the propane dimer for which the method gives a binding energy that is far too weak (by a factor of 2) and an intermolecular separation that is about 0.3 Å too wide.

DFT-SAPT Decomposition of Interactions. As noted above, the DFT-SAPT technique determines the binding energy of a complex as a sum of physically meaningful terms, namely the electrostatic, exchange, dispersion, and induction contributions. Figure 9 gives the curves for DFT-SAPT decomposition terms for each of the interactions considered in this work (with the exception of adenine–benzene). In Figure 9, it can be seen that the two main components of all of these interactions are electrostatics and dispersion. However, in terms of their interaction energy components, the interaction types are quite different, being dominated either by electrostatics or dispersion or, as in the case of the benzene–water complex, by having large contributions from both electrostatic and dispersive forces.

Figure 9a, b, and c gives the DFT-SAPT decompositions for the H-bonded systems considered in this work. Here it can be seen that, as would be expected, electrostatics play the dominant role in stabilizing these complexes. At their potential energy minima, electrostatic effects account for about 59% of the total attractive forces in the methanol and formamide dimers. It is somewhat surprising that the electrostatic contribution found in the formamide dimer, which is bound by a cyclic network of two H-bonds, is not greater than that of the methanol dimer. It should be noted, however, that the induction and δHF contributions are both larger for the formamide dimer (13% induction) than for the methanol dimer (11% induction). It should be pointed out that induction is generally the biggest contributor to the higher-order terms within the δHF term. The methylamine dimer interaction is the weakest H-bonding interaction considered in this work and is also the least electrostatic in nature (54% electrostatic contribution to the total attractive energy). Dispersion interactions are ubiquitous throughout intermolecular interaction types and play a role in the stabilization of H-bonded complexes. Dispersion accounts for 22, 30, and 17% of the attractive interactions in the methanol, methylamine, and formamide dimers, respectively (at their potential energy minima).

The DFT-SAPT interaction energy analysis for the cytosine–benzene dimer is given in Figure 9d. Here it is apparent that dispersion is the dominant contributor to this stacking interaction, with electrostatics playing a lesser role. At its potential energy minimum (3.6 Å), the attractive interactions present in this complex are about 74% dispersion, 19% electrostatic, and 4% induction (2% δHF). Interestingly, the electrostatic interaction increases relative to the dispersion interaction as the separation distance grows shorter. For example, at a separation of 3.4 Å, dispersion is responsible for only 67% and electrostatics about 25% of the attractive interaction. It should be noted that, in cases where two heterocyclic aromatic groups are stacked, the contribution from electrostatics will generally be higher than in this heterocyclic aromatic and aromatic complex. As an example, in DFT-SAPT computations recently carried out on the
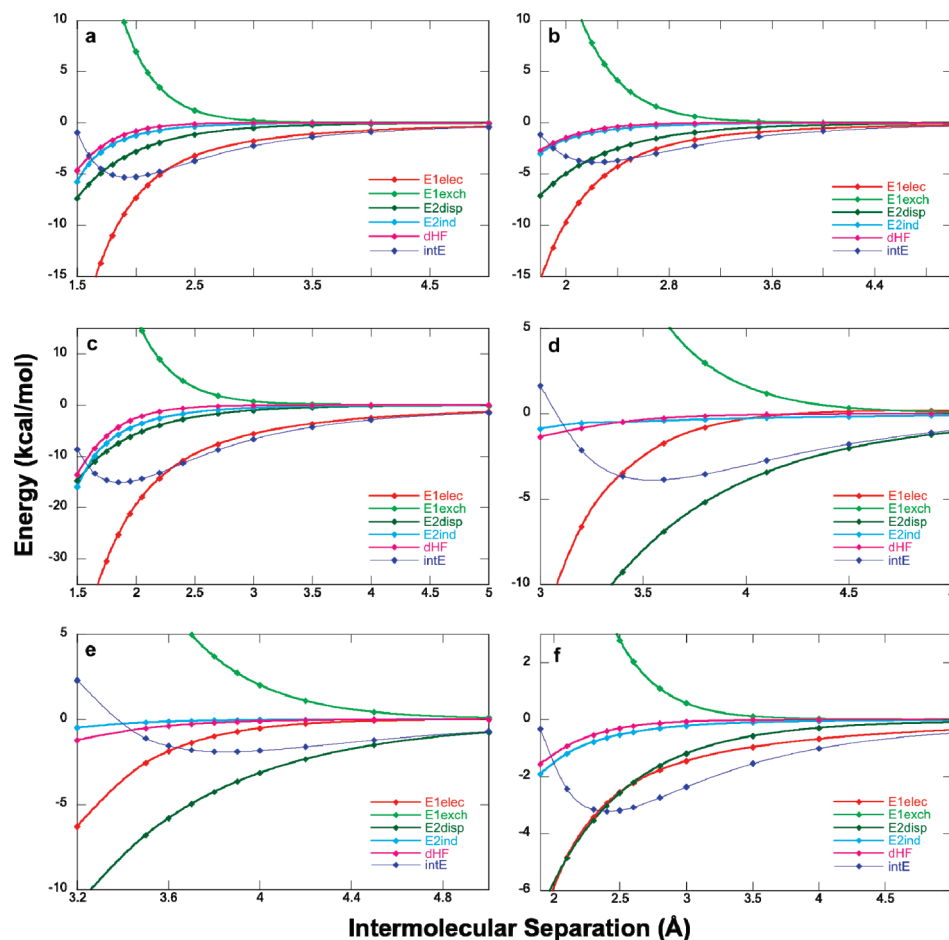
WFT and DFT Calculations

J. Chem. Theory Comput., Vol. 6, No. 1, 2010 **77**

Figure 9. DFT-SAPT interaction energy decompositions for: (a) methanol dimer, (b) methylamine dimer, (c) formamide dimer, (d) cytosine−benzene, (e) propane dimer, and (f) benzene−water. E1elec (red), E1exch (light green), E2disp (dark green), E2ind (light blue), dHF (pink), intE (dark blue).

stacked uracil dimer by Pitoňák et al., it was found that, at the potential energy minimum, dispersion describes approximately 52% and electrostatics 41% of the total attractive interaction.[17]

As in the case of the cytosine−benzene complex, the interaction in the propane dimer is dominated by dispersion forces (Figure 9e). This is, of course, an expected result as there are no strong dipole moments found in propane. At the potential energy minimum (3.9 Å), dispersion accounts for about 80% of the attraction in this complex, with electrostatics describing about 16%. The electrostatic contribution grows slightly more quickly than the dispersion contribution with decreasing intermolecular separation but not nearly as quickly as in the case of the cytosine−benzene complex. At a separation of 3.5 Å, dispersion describes approximately 67% and electrostatics 25% of the total attractive interaction.

The O−H···π interaction found in the benzene−water complex depends strongly on both dispersion and electrostatic contributions, with induction also playing an appreciable role in stabilizing the complex (Figure 9f). Between the distances of 1.9 and 2.6 Å, the contributions from dispersion and electrostatics to the overall attraction in this complex are almost identical (approximately 40−44%). Beyond 2.6 Å, the electrostatic term begins to have a larger relative attractive contribution relative to dispersion. The

increase in the relative electrostatic stabilization of the complex at larger distances can most likely be explained by the large spacial extent of benzene's π density and by the interaction between this π ring and water's positively charged hydrogen atom.

Conclusions

One of the major goals of this investigation is to determine the quality of several modern quantum chemical methods in describing potential energy curves for a variety of different types of intermolecular complexes. It has been found that, generally speaking, each of the methods applied in this work is capable of describing the H-bonding, stacking, dispersion, and O−H···π interactions considered here at least qualitatively. That is to say that each of the methods predicts bound states that correspond, upon gross inspection, to the particular interaction type being studied. In the cases of the two DFT-based methods, DFT-D and M06-2X, this is a major accomplishment considering the fact that just a few years ago it was widely acknowledged that existing DFT methods were incapable of describing noncovalent interactions, whose attractive forces are largely attributable to dispersion.

Here, we will summarize some of the general trends that have been observed in this study. As would be expected, the H-bonding interactions are generally well described by

each of the methods used here. MP2, combined with both the cc-pVTZ and aug-cc-pVDZ basis sets, has a strong tendency to underbind these types of interactions but provides reliable geometries. The former basis set yields better equilibrium geometries. The use of the spin-component scaled technique (SCS(MI)-MP2) with the cc-pVTZ basis improves the performance of MP2, but these binding energies are also generally slightly too low. The potential energy curves produced by MP2.5, M06-2X, and (to a lesser extent) DFT-SAPT match those obtained using the estimated CCSD(T)/CBS method (CBS(T)) very well. DFT-D tends to (sometimes strongly) overbind H-bonding interactions.

In terms of stacking interactions, the MP2 methods, as has been previously observed, have a strong tendency to overbind, this is especially true when MP2 is paired with the aug-cc-pVDZ basis set. The SCS(MI)-MP2 method greatly improves on the MP2 results, reducing the amount of overbinding significantly and, in the case of the cytosine−benzene complex, actually underbinding at the potential energy minimum. All calculations based on the MP2 procedure yield reliable distances of the minima, which allows for the structural optimization of various complexes at a rather cheap level (inclusion of the counterpoise correction is, however, necessary). The cc-pVTZ basis set yields better geometries than aug-cc-pVDZ ones. The MP2.5, DFT-SAPT, and DFT-D methods all produce potential energy curves that are in good agreement with those of CBS(T). The DFT/M06-2X potential energy curves for stacked systems are generally not in good agreement with the reference data, being strongly underbound for the cytosine−benzene complex, predicting incorrect minimum energy separations for both complexes, and are generally having curves with the wrong overall shape.

Only the relatively expensive MP2.5 and DFT-SAPT methods can be said to produce high-quality potential energy curves for the propane dimer. All MP2 methods, including SCS(MI)-MP2, tend to strongly underestimate the binding energy of this complex, while DFT-D very strongly overestimates it. DFT/M06-2X, on the other hand, obtains a reasonable value for the binding energy at the potential energy minimum but predicts the minimum to be at too small an intermolecular separation.

For the benzene−water complex MP2.5 and DFT-SAPT are, once again, the methods that produce the best results relative to those of CBS(T). As in the cases of H-bonding complexes and the propane dimer, all of the MP2 methods studied here underbind this O−H⋯π complex. Both DFT based methods, on the other hand, tend to overbind the complex, with DFT-D having a potential energy curve that appears to be much too broad.

Generally speaking, the only two methods that can be said to provide accurate potential energy curves for all of the complexes considered here, apart from the reference CBS(T) method, are MP2.5 and DFT-SAPT. Unfortunately, these methods are computationally very expensive and can only be used on complexes containing relatively few atoms (up to ∼60−80). Furthermore, DFT-SAPT has another two major disadvantages compared to other methods investigated in this work. First, the analytic gradients needed for optimization

of geometries have not been formulated or implemented yet, and second, in DFT-SAPT potential energy surface calculations, only rigid monomers can be considered (the deformation energy cannot be included). The MP2 method, long the "workhorse" used for computations on molecular complexes, only produces very good potential energy curves for H-bonding complexes, otherwise its performance can be said to be semiquantitatively accurate. MP2 results are generally better when the method is used in conjunction with the cc-pVTZ basis set, and this result agrees well with our previous finding.[72] The SCS(MI)-MP2/cc-pVTZ method, which seeks to improve the results of MP2/cc-pVTZ, is largely successful in this task, with improved potential energy curves for all of the noncovalently bound complexes with the exception of the propane dimer. In two of our previous studies, we thoroughly investigated the PES's of the uracil and adenine dimers, and in both studies, the SCS (MI)-MP2 method provided very good results, well comparable to those of the benchmark CCSD(T)/CBS method.[82,94] In the present study, SCS(MI)-MP2 gives very good results for all of the complexes with exception of the propane dimer. We believe that the reason for this is the same as disscussed above for the DFT-D method, which is the fact that SCS(MI)-MP2 as well as DFT-D were parameterized against the S22 set, which lacks systems containing carbon atoms having sp3 hybridization. On the other hand, the aromatic systems, such as DNA bases and benzene, are well represented in the set, and the method provides good results, even for complexes not included within the S22 set (e.g., adenine dimer or adenine−benzene complex). This finding is important and should be kept in mind when preparing data sets of the second generation. Among the much less computationally expensive DFT-based methods, DFT-D can be said to yield the best performance, giving accurate potential energy curves for H-bonding and stacking interactions. This method, however, tends to strongly overbind for both the propane dimer and the benzene−water complex. The M06-2X functional produces good results for H-bonding and O−H⋯π interactions but produces curves for stacked and dispersion-bound complexes that generally have the wrong overall shape.

WFT and DFT Calculations

J. Chem. Theory Comput., Vol. 6, No. 1, 2010 **79**

References

(1) Baldwin, R. L. *J. Mol. Biol.* **2007**, *371*, 283.

(2) Loladze, V. V.; Ermolenko, D. N.; Makhatadze, G. I. *J. Mol. Biol.* **2002**, *320*, 343.

(3) Berka, K.; Laskowski, R.; Riley, K. E.; Hobza, P.; Vondrasek, J. *J. Chem. Theory Comput.* **2009**, *5*, 982.

(4) Vondrasek, J.; Bendova, L.; Klusak, V.; Hobza, P. *J. Am. Chem. Soc.* **2005**, *127*, 2615.

(5) Vondrasek, J.; Kubar, T.; Jenney, F. E.; Adams, M. W. W.; Kozisek, M.; Cerny, J.; Sklenar, V.; Hobza, P. *Chem.−Eur. J.* **2007**, *13*, 9022.

(6) Riley, K. E.; Merz, K. M. *J. Phys. Chem. B* **2006**, *110*, 15650.

(7) Wilchek, M.; Bayer, E. A.; Livnah, O. *Immunol. Lett.* **2006**, *103*, 27.

(8) Meyer, E. A.; Castellano, R. K.; Diederich, F. *Angew. Chem., Int. Ed.* **2003**, *42*, 1210.

(9) Williams, D. H.; Stephens, E.; O'Brien, D. P.; Zhou, M. *Angew. Chem., Int. Ed.* **2004**, *43*, 6596.

(10) Sponer, J.; Riley, K. E.; Hobza, P. *Phys. Chem. Chem. Phys.* **2008**, *10*, 2595.

(11) Murray, J. S.; Lane, P.; Clark, T.; Politzer, P. *J. Mol. Model.* **2007**, *13*, 1033.

(12) Politzer, P.; Lane, P.; Concha, M. C.; Ma, Y. G.; Murray, J. S. *J. Mol. Model.* **2007**, *13*, 305.

(13) Riley, K. E.; Hobza, P. *J. Chem. Theory Comput.* **2008**, *4*, 232.

(14) Riley, K. E.; Murray, J. S.; Politzer, P.; Concha, M. C.; Hobza, P. *J. Chem. Theory Comput.* **2009**, *5*, 155.

(15) Sponer, J.; Leszczynski, J.; Hobza, P. *Biopolymers* **2001**, *61*, 3.

(16) Sponer, J.; Leszczynski, J.; Hobza, P. *Theochem* **2001**, *573*, 43.

(17) Pitonak, M.; Riley, K. E.; Neogrady, P.; Hobza, P. *ChemPhysChem* **2008**, *9*, 1636.

(18) Hobza, P.; Zahradnik, R. *Chem. Rev.* **1988**, *88*, 871.

(19) Hofstadler, S. A.; Griffey, R. H. *Chem. Rev.* **2001**, *101*, 377.

(20) Kollman, P. A. *Acc. Chem. Res.* **1977**, *10*, 365.

(21) Muller-Dethlefs, K.; Hobza, P. *Chem. Rev.* **2000**, *100*, 143.

(22) Zhao, Y.; Truhlar, D. G. *J. Chem. Theory Comput.* **2007**, *3*, 289.

(23) Zhao, Y.; Truhlar, D. G. *J. Chem. Theory Comput.* **2008**, *4*, 1849.

(24) Lee, E. C.; Kim, D.; Jurecka, P.; Tarakeshwar, P.; Hobza, P.; Kim, K. S. *J. Phys. Chem. A* **2007**, *111*, 3446.

(25) Dykstra, C. E.; Lisy, J. M. *Theochem* **2000**, *500*, 375.

(26) Hartmann, M.; Wetmore, S. D.; Radom, L. *J. Phys. Chem. A* **2001**, *105*, 4470.

(27) McConnell, T. L.; Wheaton, C. A.; Hunter, K. C.; Wetmore, S. D. *J. Phys. Chem. A* **2005**, *109*, 6351.

(28) Tsuzuki, S.; Uchimaru, T. *Curr. Org. Chem.* **2006**, *10*, 745.

(29) Rozas, I. *Phys. Chem. Chem. Phys.* **2007**, *9*, 2782.

(30) Rappe, A. K.; Bernstein, E. R. *J. Phys. Chem. A* **2000**, *104*, 6117.

(31) Sinnokrot, M. O.; Sherrill, C. D. *J. Phys. Chem. A* **2004**, *108*, 10200.

(32) Riley, K. E.; Hobza, P. *J. Phys. Chem. A* **2007**, *111*, 8257.

(33) Jurecka, P.; Sponer, J.; Cerny, J.; Hobza, P. *Phys. Chem. Chem. Phys.* **2006**, *8*, 1985.

(34) Jurecka, P.; Hobza, P. *Chem. Phys. Lett.* **2002**, *365*, 89.

(35) Pitonak, M.; Janowski, T.; Neogrady, P.; Pulay, P.; Hobza, P. Journal of Chemical Theory and Computation 2009, In Press: DOI 10.1021/ct900126q.

(36) Cerny, J.; Pitonak, M.; Riley, K. E.; Hobza, P. *J. Chem. Theory Comput.* **2009**, To be submitted.

(37) Sponer, J.; Leszczynski, J.; Hobza, P. *J. Phys. Chem.* **1996**, *100*, 5590.

(38) Rutledge, L. R.; Durst, H. F.; Wetmore, S. D. *J. Chem. Theory Comput.* **2009**, *5*, 1400.

(39) Johnson, E. R.; Wolkow, R. A.; DiLabio, G. A. *Chem. Phys. Lett.* **2004**, *394*, 334.

(40) Cerny, J.; Jurecka, P.; Hobza, P.; Valdes, H. *J. Phys. Chem. A* **2007**, *111*, 1146.

(41) Jurecka, P.; Cerny, J.; Hobza, P.; Salahub, D. R. *J. Comput. Chem.* **2007**, *28*, 555.

(42) Zhao, Y.; Truhlar, D. G. *J. Chem. Phys.* **2006**, *125*, 194101.

(43) Zhao, Y.; Truhlar, D. G. *Theor. Chem. Acc.* **2008**, *120*, 215.

(44) Zhao, Y.; Pu, J. Z.; Lynch, B. J.; Truhlar, D. G. *Phys. Chem. Chem. Phys.* **2004**, *6*, 673.

(45) Zhao, Y.; Schultz, N. E.; Truhlar, D. G. *J. Chem. Theory Comput.* **2006**, *2*, 364.

(46) Zhao, Y.; Truhlar, D. G. *J. Chem. Theory Comput.* **2005**, *1*, 415.

(47) Zhao, Y.; Truhlar, D. G. *Acc. Chem. Res.* **2008**, *41*, 157.

(48) Grimme, S. *J. Comput. Chem.* **2004**, *25*, 1463.

(49) Grimme, S. *J. Comput. Chem.* **2006**, *27*, 1787.

(50) Hohenstein, E. G.; Chill, S. T.; Sherrill, C. D. *J. Chem. Theory Comput.* **2008**, *4*, 1996.

(51) Hesselmann, A.; Jansen, G. *Phys. Chem. Chem. Phys.* **2003**, *5*, 5010.

(52) Hesselmann, A.; Jansen, G. *Chem. Phys. Lett.* **2003**, *367*, 778.

(53) Hesselmann, A.; Jansen, G. *Chem. Phys. Lett.* **2002**, *362*, 319.

(54) Hesselmann, A.; Jansen, G. *Chem. Phys. Lett.* **2002**, *357*, 464.

(55) Jansen, G.; Hesselmann, A. *J. Phys. Chem. A* **2001**, *105*, 11156.

(56) Hesselmann, A.; Jansen, G.; Schutz, M. *J. Chem. Phys.* **2005**, *122*.

(57) Cybulski, S. M.; Lytle, M. L. *J. Chem. Phys.* **2007**, *127*, 141102.

(58) Hesselmann, A. *J. Chem. Phys.* **2008**, *128*, 9.

(59) Grimme, S. *J. Chem. Phys.* **2003**, *118*, 9095.

(60) Distasio, R. A.; Head-Gordon, M. *Mol. Phys.* **2007**, *105*, 1073.

(61) Takatani, T.; Sherrill, C. D. *Phys. Chem. Chem. Phys.* **2007**, *9*, 6106.

(62) Hill, J. G.; Platts, J. A. *J. Chem. Theory Comput.* **2007**, *3*, 80.

(63) Sherrill, C. D.; Takatani, T.; Hohenstein, E. G. *J. Phys. Chem. A* **2009**, *113*, 10146.

(64) Pitonak, M.; Neogrady, P.; Cerny, J.; Grimme, S.; Hobza, P. *ChemPhysChem* **2009**, *10*, 282.

(65) Arnstein, S. A.; Sherrill, C. D. *Phys. Chem. Chem. Phys.* **2008**, *10*, 2646.

(66) Ringer, A. L.; Figgs, M. S.; Sinnokrot, M. O.; Sherrill, C. D. *J. Phys. Chem. A* **2006**, *110*, 10822.

(67) Ringer, A. L.; Sinnokrot, M. O.; Lively, R. P.; Sherrill, C. D. *Chem.−Eur. J.* **2006**, *12*, 3821.

(68) Sinnokrot, M. O.; Sherrill, C. D. *J. Phys. Chem. A* **2006**, *110*, 10656.

(69) Sinnokrot, M. O.; Valeev, E. F.; Sherrill, C. D. *J. Am. Chem. Soc.* **2002**, *124*, 10887.

(70) Tauer, T. P.; Derrick, M. E.; Sherrill, C. D. *J. Phys. Chem. A* **2005**, *109*, 191.

(71) Janowski, T.; Pulay, P. *Chem. Phys. Lett.* **2007**, *447*, 27.

(72) Dabkowska, I.; Gonzalez, H. V.; Jurecka, P.; Hobza, P. *J. Phys. Chem. A* **2005**, *109*, 1131.

(73) Peverati, R.; Baldridge, K. K. *J. Chem. Theory Comput.* **2008**, *4*, 2030.

(74) Tapavicza, E.; Lin, I. C.; von Lilienfeld, O. A.; Tavernelli, I.; Coutinho-Neto, M. D.; Rothlisberger, U. *J. Chem. Theory Comput.* **2007**, *3*, 1673.

(75) Williams, R. W.; Malhotra, D. *Chem. Phys.* **2006**, *327*, 54.

(76) Tsuzuki, S.; Uchimaru, T.; Mikami, M.; Tanabe, K. *J. Phys. Chem. A* **2002**, *106*, 3867.

(77) Jalkanen, J. P.; Mahlanen, R.; Pakkanen, T. A.; Rowley, R. L. *J. Chem. Phys.* **2002**, *116*, 1303.

(78) Jalkanen, J. P.; Pakkanen, T. A.; Rowley, R. L. *J. Chem. Phys.* **2004**, *120*, 1705.

(79) Jalkanen, J. P.; Pulkkinen, S.; Pakkanen, T. A.; Rowley, R. L. *J. Phys. Chem. A* **2005**, *109*, 2866.

(80) Rowley, R. L.; Tracy, C. M.; Pakkanen, T. A. *J. Chem. Phys.* **2006**, *125*, 154302.

(81) Rowley, R. L.; Tracy, C. M.; Pakkanen, T. A. *J. Chem. Phys.* **2007**, *127*, 025101.

(82) Morgado, C. A.; Jurecka, P.; Svozil, D.; Hobza, P.; Sponer, J. *J. Chem. Theory Comput.* **2009**, *5*, 1524.

(83) Tekin, A.; Jansen, G. *Phys. Chem. Chem. Phys.* **2007**, *9*, 1680.

(84) Tsuzuki, S.; Honda, K.; Uchimaru, T.; Mikami, M. *J. Chem. Phys.* **2006**, *124*, 7.

(85) Fusti Molnar, L.; He, X.; Wang, B.; Merz, K. M. *J. Chem. Phys.* **2009**, *131*, AN 065102.

(86) Halkier, A.; Helgaker, T.; Jorgensen, P.; Klopper, W.; Koch, H.; Olsen, J.; Wilson, A. K. *Chem. Phys. Lett.* **1998**, *286*, 243.

(87) Werner, H.-J.; Knowles, P. J.; Lindh, R.; Manby, F. R.; Schütz, M.; Celani, P.; Korona, T.; Rauhut, G.; Amos, R. D.; Bernhardsson, A.; Berning, A.; Cooper, M. J. O.; Deegan, A. J.; Dobbyn, A. J.; Eckert, F.; Hampel, C.; Hetzer, G.; LLoyd, A. W.; McNicholas, S. J.; Meyer, W.; Mura, M. R.; Nicklass, A.; Palmieri, P.; Pitzer, R.; Schumann, U.; Stoll, H.; Stone, A. J.; Taroni, T.; Thorsteinsson, T. *Molpro 7*, version 2006, University College Cardiff Consultants Limited: Cardiff, U.K.

(88) Feyereisen, M.; Fitzgerald, G.; Komornicki, A. *Chem. Phys. Lett.* **1993**, *208*, 359.

(89) Ahlrichs, R.; Bar, M.; Haser, M.; Horn, H.; Kolmel, C. *Chem. Phys. Lett.* **1989**, *162*, 165.

(90) Jurecka, P.; Nachtigall, P.; Hobza, P. *Phys. Chem. Chem. Phys.* **2001**, *3*, 4578.

(91) Boys, S. F.; Bernardi, F. *Mol. Phys.* **1970**, *19*.

(92) Frisch, M. J.; Trucks, G. W.; Schlegel, H. B.; Scuseria, G. E.; Robb, M. A.; Chesseman, J. R.; Zakrzewski, V. G.; Montgomery Jr., J. A.; Stratmann, R. E.; Burant, J. C.; Dapprich, S.; Millam, J. M.; Daniels, A. D.; Kudin, K. N.; Strain, M. C.; Farkas, O.; Tomasi, J.; Barone, V.; Cossi, M.; Cammi, R.; Mennucci, B.; Pomelli, C.; Adamo, C.; Clifford, S.; Ochterski, J.; Petersson, G. A.; Ayala, P. Y.; Cui, Q.; Morokuma, K.; Malick, D. K.; Rabuck, A. D.; Raghavachari, K.; Forseman, J. B.; Cioslowski, J.; Ortiz, J. V.; Baboul, A. G.; Stefanov, B. B.; Liu, G.; Liashenko, A.; Piskorz, P.; Komaromi, I.; Gomperts, R.; Martin, R. L.; Fox, D. J.; Keith, T.; AlLoham, M. A.; Peng, C. Y.; Nanayakkara, A.; Gonzalez, C.; Challacombe, M.; Gill, P. M. W.; Johnson, B. G.; Chen, W.; Wong, M. W.; Andres, J. L.; Head-Gordon, M.; Replogle, E. S.; Pople, J. A. *Gaussian 03*; Gaussian Inc.: Wallingford, CT, 2003.

(93) Aquilante, F.; De Vico, L.; Ferré, N.; Ghigo, G.; Malmqvist, P.; Neogrády, P.; Pedersen, T. B.; Pitonák, M.; Reiher, M.; Roos, B. O.; Serrano-Andrés, L.; Urban, M.; Veryazov, V.; Lindh, R. *J. Comput. Chem.* **2009**, In Press.

(94) Morgado, C. A.; Jurecka, P.; Svozil, D.; Hobza, P.; Sponer, J. *Phys. Chem. Chem. Phys.* **2009**, submitted.

JCTC Journal of Chemical Theory and Computation

Describing Both Dispersion Interactions and Electronic Structure Using Density Functional Theory: The Case of Metal−Phthalocyanine Dimers

Noa Marom,[†] Alexandre Tkatchenko,[‡] Matthias Scheffler,[‡] and Leeor Kronik*[,†]

Department of Materials and Interfaces, Weizmann Institute of Science, Rehovoth 76100, Israel, and Fritz-Haber-Institut der Max-Planck-Gesellschaft, Faradayweg 4−6, 14195 Berlin, Germany

Abstract: Noncovalent interactions, of which London dispersion is an important special case, are essential to many fields of chemistry. However, treatment of London dispersion is inherently outside the reach of (semi)local approximations to the exchange-correlation functional as well as of conventional hybrid density functionals based on semilocal correlation. Here, we offer an approach that provides a treatment of both dispersive interactions and the electronic structure within a computationally tractable scheme. The approach is based on adding the leading interatomic London dispersion term via pairwise ion−ion interactions to a suitably chosen nonempirical hybrid functional, with the dispersion coefficients and van der Waals radii determined from first-principles using the recently proposed "TS-vdW" scheme (Tkatchenko, A.; Scheffler, M. *Phys. Rev. Lett.* **2009**, *102*, 073005). This is demonstrated via the important special case of weakly bound metal−phthalocyanine dimers. The performance of our approach is additionally compared to that of the semiempirical M06 functional. We find that both the PBE-hybrid+vdW functional and the M06 functional predict the electronic structure and the equilibrium geometry well, but with significant differences in the binding energy and in their asymptotic behavior.

1. Introduction

Noncovalent interactions, of which London dispersion is an important special case, are essential to many fields of chemistry. Such interactions possess a significant component of electrostatic attraction between permanent or instantaneous dipoles and higher order multipoles and dominate in regions where there is little overlap of charge densities, i.e., at medium-range to long-range, as compared to the short-range chemical bond. In principle, exact density functional theory (DFT) should include accurate treatment of the long-range correlation, which is essential for describing noncovalent interactions.[1] However, van der Waals (vdW) interactions (a term that we use here interchangeably with London dispersion) are inherently outside the reach of (semi)local approximations to the exchange-correlation (xc) functional as well as of conventional hybrid functionals, based on semilocal correlation.[1,2]

Many strategies toward inclusion of van der Waals interactions in DFT calculations, at various levels of approximation, have been proposed. Many of those can be divided into three broad categories: (1) nonempirical methods, typically relying on the adiabatic connection theorem,[3] where the long-range correlation is either computed explicitly[4–11] or integrated with traditional xc functionals;[12,13] (2) semiempirically parametrized xc functionals, calibrated for data sets that include noncovalently interacting systems;[14–18] (3) pairwise addition of C_6/R^6 corrections to the internuclear energy expression, damped in the short-range while providing the desired long-range asymptotic behavior.[19–28] Such C_6/R^6 corrections are usually semiempirical but can be derived from first-principles considerations.[28]

Understandably, most of the literature on DFT computations of dispersively bound systems has focused on obtaining

* Corresponding author phone: +972-8-934-4993; e-mail: leeor.kronik@weizmann.ac.il.

† Weizmann Institute of Science.

‡ Fritz-Haber-Institut der Max-Planck-Gesellschaft.

correct geometries and binding energies. There are very important classes of systems, however, for which it is crucial to obtain a correct prediction of the electronic structure as well. An important example, on which we elaborate here, is that of small-molecule-based organic semiconductors. In such materials, intermolecular interaction in the molecular crystal is typically dispersive (or at least has a significant dispersion component), and geometry predicted using standard functionals can be highly inaccurate, as discussed, e.g., in ref 29. At the same time, an accurate description of the electronic structure is essential to understanding the relations between the chemical nature of the constituent molecules and their function in organic electronic devices.

A key question, then, is whether one can systematically obtain a sufficiently accurate theoretical treatment of both noncovalent interactions and the electronic structure, within a computationally tractable scheme that is preferably widely applicable and involves as little empiricism as possible. This is challenging because the electronic structure can be very sensitive to the type of functional used. A recurring reason for inadequate treatment of the electronic structure is the presence of self-interaction errors (SIE),[30,31] i.e., the spurious Coulomb interaction of an electron with itself in the Hartree term of the Kohn−Sham equation, which is not fully canceled out by approximate expressions for the exchange-correlation term. Local and semilocal functionals, e.g., the local-density approximation (LDA) and various flavors of the generalized gradient approximation (GGA), respectively, often exhibit significant SIE that results in a poor description of the electronic structure of organic molecules and crystals.[32,33] Hybrid xc functionals were found to mitigate the effect of the SIE significantly via the inclusion of a fraction of Fock exchange.[31–33] Therefore, a desirable scheme would combine a successful description of van der Waals interactions with a hybrid functional based description of the electronic structure.[34] This should be possible because the electronic structure is mostly sensitive to exchange and short-range correlation, whereas dispersive interactions mainly affect the total energies and geometries.

In principle, such a successful combination may be achieved within each of the three above-discussed strategies for treating van der Waals interactions. The most practical and successful representative of the first strategy (a nonempirical method relying on the adiabatic connection theorem) is the "vdW-DFT" functional of Dion et al.[13] (see ref 35 for some recent applications). It is based on a GGA (specifically revPBE[36]) exchange functional, combined with LDA for the local part of the correlation, on top of which the nonlocal correlation component is added. Although this nonlocal correlation can be combined with other functionals, results for, e.g., the binding energy may depend significantly on the underlying "parent" functional.[37] Therefore, we will not be discussing this approach here. Currently the most popular representative of the second strategy (semiempirical methods based on hybrid functionals) is the M06 family of functionals,[17] a family of meta-GGA functionals (i.e., functionals whose "semi-local" component includes kinetic energy spin-densities, in addition to the spin-densities and their gradients[31]) with varying fractions of exact exchange. This approach provides some flexibility in the choice of an appropriate functional, an issue elaborated below. However, the correct long-range R^{-6} behavior is still absent from such functionals even if medium-range noncovalent binding is well-achieved. The third strategy, addition of pairwise C_6/R^6 terms to the internuclear energy term, allows for the highest degree of flexibility in choosing independently the appropriate description of the electronic structure, on top of which a suitable dispersion correction is performed.

Obviously using C_6/R^6 corrections is not free from limitations either. First, the approach assumes that noncovalent interactions have little direct effect on the electron density and affect the system mainly by influencing the equilibrium geometry. Second, screening by the conduction electrons has to be addressed for metallic systems. Third, the short-range damping function may be problematic for the accurate description of short bond lengths. Fourth, Dobson et al.[38] have shown that summation over pairwise interactions may result in incorrect asymptotic behavior in certain special cases, e.g., low-dimensional (semi)metallic systems.

Here, we examine the degree to which a quantitative treatment of both the electronic structure and the dispersion interactions is achieved in practice. We show that this is indeed possible using the recently presented "TS-vdW" correction scheme,[28] in which the leading-order C_6 coefficients and vdW radii are determined in a first principles manner from the DFT ground-state electron density. These corrections are combined with the GGA of Perdew, Burke, and Ernzerhof (PBE)[39] with the one-parameter nonempirical PBE-hybrid (also known as PBEh or PBE0),[40] or with the three-parameter semi-empirical hybrid functional B3LYP.[41] We compare our results to those obtained from the M06 functional,[17] as well as to those obtained from the standard PBE and PBE-hybrid functionals and to pertinent experiments.

We have chosen two members of the metal−phthalocyanine (MPc) family as case studies for the above comparison, NiPc and MgPc. MPc's are highly stable organic semiconductors with a broad range of applications in, e.g., light emitting diodes, solar cells, gas sensors, thin film transistors, and even single molecule devices.[42] Specifically, their electronic structure has been shown to be highly sensitive to self-interaction errors.[32] Furthermore, it is known that $\pi-\pi$ and $\pi-$d interactions, which possess a dispersive component and are attributed to nonlocal electron correlations that occur in systems with spatially close-lying π orbitals,[43] play an important role in the stacking of molecules in MPc crystals. In transition metal Pc's, such as NiPc, $\pi-$d interactions affect the intermolecular distance in the stack.[44] In crystalline MgPc, $\pi-\pi$ interactions not only affect the intermolecular distance but also lead to a structural change in the molecular subunit as the Mg atom deviates from the molecular plane and shifts toward the azamethine N of the adjacent molecule (see also Figure 1), so that the basic unit of the MgPc crystal is, in fact, a dimer.[45,46] Thus, both NiPc and MgPc provide stringent test cases for a treatment of both geometrical and electronic structure.

Here, we calculate the binding energy curves, geometry, and electronic structure of NiPc and MgPc dimers. We find
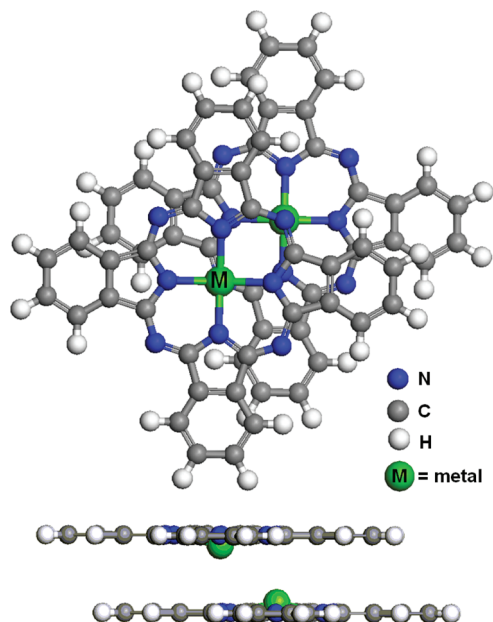
Figure 1. Schematic top-view and side-view of the MPc dimer. The metal atom of one molecule lies above the azamethine nitrogen of the other molecule. In the MgPc dimer, the Mg atom is shifted from the molecular plane, as shown in the side-view.

that PBE+vdW, PBE-hybrid+vdW, and M06 all yield similar geometries, but the electronic structure is well described only with the PBE-hybrid+vdW, the B3LYP+vdW,[47] and the M06 approaches. Moreover, we find significant differences in the binding energy between PBE-hybrid+vdW and M06. We attribute these differences to the long-range behavior of these two methods and show that they can be reduced by applying the TS-vdW C_6/R^6 correction to M06.

2. Methodology

a. TS-vdW Correction Scheme. In the TS-vdW[28] C_6/R^6 correction scheme used here, the pairwise vdW interaction, E_{disp}, added to the internuclear energy term, is given by

$$E_{\text{disp}} = -\sum_{j>i} f_{\text{damp}}(R_{ij}, R_{ij}^0) C_{6ij} R_{ij}^{-6} \qquad (1)$$

where C_{6ij} is the dispersion coefficient for the ij pair of atoms, R_{ij} is the interatomic distance, R_{ij}^0 is the sum of equilibrium vdW radii for the pair, and f_{damp} is a damping function discussed below. The novel feature of the TS-vdW scheme is that the parameters C_{6ij} and R_{ij}^0 are determined from first principles. The method yields significantly lower errors for the S22 database of molecular binding energies than empirical C_6/R^6 methods and has been recently shown to outperform the latter for water clusters.[48]

Briefly, the TS-vdW scheme is based on accurate *ab initio* computed reference values for free atom static dipole polarizabilities and C_6 coefficients,[49] a combination rule for deriving heteronuclear C_6 coefficients from homonuclear static dipole polarizabilities, and Hirshfeld partitioning[50–52] of the DFT electron density to calculate the relative polarizability of an atom inside a molecule. In this way, different

atomic hybridization states are inherently taken into account for different molecular geometries. Complete details are given in ref 28.

The damping function in eq 1 is needed to avoid the divergence of the R^{-6} term at short distances and reduce the effect of the correction on covalent bonds. A Fermi-type function was used here, in the form

$$f_{\text{damp}}(R_{ij}, R_{ij}^0) = \left[1 + \exp\left(-d\left(\frac{R_{ij}}{s_R R_{ij}^0} - 1\right)\right)\right]^{-1} \qquad (2)$$

where d determines the "steepness" of the damping function and s_R reflects the range of interaction covered by the chosen DFT exchange-correlation functional.[25] By fitting to the S22 database of Jurečka et al.,[53] which contains binding energies of 22 different weakly bound systems close to CCSD(T) basis set limit, the value of d was set to 20 and s_R was set to 0.94 for PBE and 0.96 for the PBE-hybrid.[28,54] A similar procedure for B3LYP yielded an s_R of 0.84, indicating that a smaller range of dispersion interaction is covered, likely due to a somewhat more repulsive exchange component than that of PBE or the PBE-hybrid. Finally, as discussed by Karton et al.,[55] the M06 functional yields attraction at intermediate range but still does not possess the correct long-range behavior. Therefore, the same fitting procedure was performed for M06 as well, yielding the s_R value of 1.16.

b. Computational Details. The routines for evaluation of energies and forces using the TS-vdW method have been implemented in the FHI-aims code[56] for consistent geometry optimizations. FHI-aims is an all-electron electronic structure code developed at the Fritz Haber Institute. It uses efficient numerical atomic-centered orbitals (NAO) as a basis set and allows one to achieve highly converged results with optimum efficiency in computer resources. In this work, the tier2 NAO basis set, which yields results that are similar in accuracy to those of the aug-cc-pVQZ Gaussian basis set for the S22 database, has been employed for geometry relaxation.

Additional calculations of single molecule geometry and dimer geometry of MgPc and NiPc were performed using the Gaussian[57] code with the PBE, PBE-hybrid, B3LYP, and M06 functionals. Calculations of the electronic structure of a single NiPc molecule were performed using the revPBE functional, the functionals M06L and M062X of the M06 family, and BLYP[58]-based functionals with similar fractions of exact exchange. The Def2-TZVP Weigend−Ahlrichs basis set[59] was used for all calculations, except for the MgPc M06 calculations, for which a larger all-electron cc-pVTZ basis[60] was used. Throughout this work, the single molecule geometry was optimized independently for each functional and basis set.

Binding energy curves were constructed using the PBE, PBE-hybrid, B3LYP, and M06 functionals, with and without C_6/R^6 corrections. The counterpoise (CP) method[61,62] was used to correct for basis set superposition errors (BSSE). In order to obtain dimer binding energy curves as a function of a single parameter, the intermolecular distance was varied under the assumption that the metal atom of one molecule lies directly above the azamethine nitrogen of the other molecule,[44–46] and that the metal atom is in the molecular plane. The latter assumption is consistent with experimental
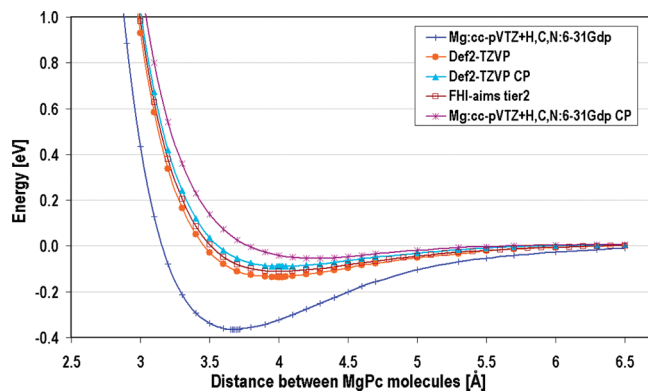
Figure 2. Binding energy curves for the MgPc dimer, obtained with the PBE functional using various basis sets. CP denotes use of the counter-poise correction method.

observations for the molecular stacks in crystalline NiPc.[44] Therefore, for NiPc the equilibrium geometry was deduced from the minimum of the binding energy curve. A full relaxation with the PBE+vdW functional has indeed confirmed that the monomers remain planar. As noted above, for the MgPc dimer the monomers do not remain planar.[45,46] Therefore, for this system a full geometry relaxation has additionally been carried out with all functionals used, so as to obtain realistic geometries.

The basis set convergence of our calculations was verified by direct comparison of the eigenvalues and binding energies obtained from PBE calculations of a MgPc dimer comprising two planar MgPc molecules at an interplanar distance of 4 Å, using both FHI-aims and Gaussian with the basis sets specified above. The two spectra were in good agreement with a maximal difference of 0.0065 eV and a mean error of 0.002 eV (the latter is equivalent to a relative mean error of 0.06%), for all eigenvalues larger than −15 eV. The binding energy obtained using the Gaussian code with the CP-corrected cc-pVTZ basis set was smaller by 20 meV than the value obtained using the FHI-aims code with the tier2 basis set, and smaller by 13 meV than that obtained with the tier3 basis set, which essentially recovers the complete basis set limit.

For additional insights into basis set convergence issues, Figure 2 shows binding energy curves of the MgPc dimer, calculated with PBE using a smaller, double-ζ (DZ) level basis set, consisting of an all electron cc-pVTZ basis set for the Mg atoms and the 6-31G(d,p) basis set for the H,C, and N atoms. Using a DZ basis set leads to an overbinding of 0.25 eV relative to the FHI-aims tier2 basis set and yields an intermolecular distance of 3.7 Å, as compared to 4.0 Å with the tier2 basis set. The CP procedure overcorrects this overbinding and results in an underbinding of 0.06 eV and an intermolecular distance of 4.3 Å. The larger, triple-ζ (TZ) basis set yields a distance of 4.0 Å, in agreement with the FHI-aims tier2 result. As expected, its CP correction is much smaller and reduces the binding energy by 0.05 eV, overcorrecting by only 0.02 eV compared to the tier2 basis. This close agreement between results obtained using different types of basis sets within different codes shows that our results are well-converged. Basis set convergence tests for the M06 functional are discussed in the Supporting Informa-

tion (SI). Importantly, we note that reliance on DZ basis sets may lead to spurious agreement between M06 and PBE+vdW binding energy curves, whereas the CP-corrected TZ basis set calculations reveal pronounced differences between the two curves, which are elaborated below. We note that while our TZ and tier 2 NAO calculations are sufficiently converged, BSSE errors can also be reduced substantially using diffuse functions. We have not utilized this route here because for the large systems studied in this work we have found that this introduces severe convergence difficulties.

3. Results and Discussion

Because we aim at a treatment of both the equilibrium electronic structure and the long-range dispersive interactions, we start our analysis by choosing which functionals are the most promising candidates for providing such a comprehensive treatment. For examining the TS-vdW C_6/R^6 correction scheme, we focus primarily on PBE and the PBE-hybrid as a prototypical semilocal and hybrid functional, respectively. We are well aware that B3LYP is likely the most popular choice for a hybrid functional but even so prefer the PBE-hybrid for several reasons. First, the PBE-hybrid and B3LYP yield essentially indistinguishable spectra for metal−phthalocyanines (ref 32 and cf. Figures 5 and 7 below), so we prefer to introduce as little empiricism as possible. This is especially so given that the PBE-hybrid has other advantages over B3LYP, e.g., yielding the correct result for the uniform electron gas limit and doing significantly better at predicting solid state atomization energies.[31,63] Furthermore, as noted above the range of dispersion interaction covered by the PBE-hybrid is somewhat higher than that of B3LYP. Nevertheless, because of its prominence in applications we do provide B3LYP results as well.

Next, we assess, using the NiPc electronic structure, which of the M06 family of functionals we should pursue. This family, constructed by Zhao and Truhlar,[17] consists of four different functionals, denoted as M06 (fractional Fock exchange), M06L (fully semilocal treatment of exchange, i.e., no fractional Fock exchange), M06−2X (with twice as much Fock exchange as in M06), and M06-HF (with 100% Fock exchange). Of those, M06 was recommended by Zhao and Truhlar for systems involving both transition metal chemistry and noncovalent interactions,[17] but it is instructive to consider the accuracy of the electronic structure obtained with other functionals of the M06 family. We additionally examine the electronic structure obtained from the revPBE GGA, primarily because the above-discussed "vdW-DFT" functional is based on it.

Figure 3 shows calculated eigenvalue spectra of the NiPc monomer, as well as the same spectra broadened by convolution with a 0.35 eV Gaussian to simulate the effective experimental resolution of ultraviolet photoemission spectroscopy (UPS) experiments performed by Ellis et al. on NiPc thin films,[64] also shown in the figure. We note that, strictly speaking, Kohn−Sham eigenvalues are not equivalent to quasiparticle excitation energies even if the exact xc functional is used.[31] Nevertheless, if a suitable approximate xc functional is used, they are often good approximations to electron removal energies.[31,33c,65] The figure compares the

Electronic Structure Using DFT

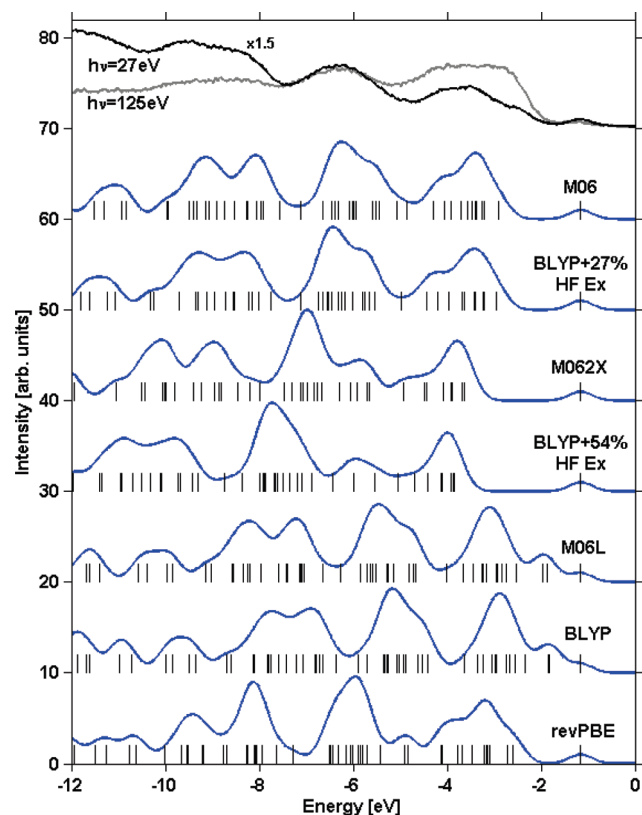*J. Chem. Theory Comput., Vol. 6, No. 1, 2010* **85**

Figure 3. Computed NiPc single molecule spectra, calculated with revPBE, different M06-variants, and BLYP-based single-parameter hybrid exchange-correlation functionals. Raw eigenvalue data, as well as the same data broadened by a 0.35 eV Gaussian, are shown. This facilitates comparison with the UPS data of Ellis et al.,[64] obtained for a 11.8 Å NiPc film at $\theta = 70°$, also shown in the figure.

Figure 4. Binding energy curves, obtained with different exchange-correlation density functionals, for (a) NiPc and (b) MgPc dimers, composed of planar molecules.

results of three M06 variants with corresponding one-parameter hybrids[66] based on BLYP,[58] a semiempirical GGA functional. To examine the role of exchange, in each case the M06-variant result is compared to a BLYP-based hybrid that has the same the fraction of Fock exchange. Two trends are immediately obvious: First, whereas the M06 spectrum agrees well with experiment, M06L and M06−2X yield spectra that do not. This agrees with the recommendation of Zhao and Truhlar. Second, the M06-variant spectra are remarkably similar (though, of course, not identical) to the corresponding BLYP-hybrid ones. This shows that, despite the many additional fitting parameters used in any M06 variant, the dominant factor in determining the electronic structure is the fraction of Fock exchange. In turn, the spectra obtained with BLYP and with BLYP+27% Fock exchange are remarkably similar to previously published spectra (ref 32 and cf. Figure 5 below), obtained with the nonempirical PBE and PBE-hybrid (i.e., 25% Fock exchange) functionals, respectively, further underscoring the dominant role of Fock exchange. Therefore, of the entire M06 family, only M06 is considered hereafter.

Interestingly, the leading (HOMO) and second peak of the revPBE spectrum are much closer to the spectra obtained from the hybrid functionals (BLYP+27% Fock exchange and M06) than to those obtained from the semilocal functionals (BLYP and M06L). We have observed a similar behavior

for other MPc's (not shown for brevity). Likely, this is at least partly because the exchange enhancement factor of revPBE was constructed by fitting to exact exchange-only calculations of total atomic energies.[67] This compensates to some extent for self-interaction errors and thus improves the fit to experiment in the higher-lying part of the spectrum. However, this comes at the price of distorting the shape of the third and fourth peaks. Because revPBE, while better than other GGAs in this respect, still fails to yield a satisfactory electronic spectrum, we do not discuss it further here.

We now turn to the binding energy curves of NiPc and MgPc dimers, shown in Figure 4, obtained using the PBE, PBE-hybrid, B3LYP, and M06 functionals, with and without the C_6/R^6 correction. Clearly, the uncorrected PBE and PBE-hybrid calculations underestimate considerably the strength of the noncovalent interaction and overestimate the inter-molecular distance in both dimers. The B3LYP calculations reveal no net attraction at all. This is a known tendency of semilocal and conventional hybrid functionals that has been demonstrated repeatedly for various systems (see, e.g., refs 1, 2, 13, 14, 19, 20, 22, 26). For both dimers, M06 significantly improves upon the semilocal and hybrid functionals, yielding binding energies that are higher by about 1.0 eV. However, the binding energies obtained with PBE+vdW, PBE-hybrid+vdW, and B3LYP+vdW are higher yet, by ∼0.7 eV as compared to M06. This difference between the TS-vdW corrected results and M06 is larger than the level of accuracy found in recent M06 studies of smaller dispersively bound systems,[55,68] likely due to the sheer size of the MPc molecules and the contribution of the π−d

Table 1. Intermolecular Distance in the NiPc and MgPc Dimers and Mg Atom Shift out of the Molecular Plane for the Latter[a]

	NiPc intermolecular distance [Å]	MgPc intermolecular distance [Å]	Mg atom shift [Å]
expt	3.24 [44]	3.172 (120 K), 3.185 (260 K) [45]	0.613 (120 K), 0.454 (260 K) [45]
PBE	4.2	3.79	0.88
PBE-hybrid	4.1	3.73	0.86
M06	3.30	3.30	0.61
PBE+vdW	3.22	3.29	0.56

[a] Calculated with the PBE, PBE-hybrid, M06, and vdW-corrected PBE functionals, compared to experimental values.

interaction. Furthermore, this difference can be traced back to the long-range behavior of the M06 functional, which is essentially the same as that of PBE or PBE-hybrid at intermolecular distances larger than 5.5 Å. For some applications, the latter difference may be practically unimportant if the near-equilibrium region is well-described. However, it is fundamentally important to realize that the hybrid meta-GGA approach does not possess the correct asymptotic behavior. This limitation may manifest itself practically as well, e.g., in systems where a cumulative effect of many long-range dispersive interactions is important.

For both dimers, the addition of the C_6/R^6 correction to the M06 functional recovers the correct long-range behavior and does not affect the equilibrium intermolecular distance. However the binding energy increases by ~1.0 eV, becoming ~0.3 eV larger than with PBE+vdW or PBE-hybrid+vdW. We note that the remaining difference may be attributed to the employed damping function. Since M06 already provides considerable attraction at the intermediate range, it may require a different model for the damping function. Without experimental or high-level quantum-chemical data for the binding energy, it is hard to say which functional yields a more accurate binding energy. However, the difference between PBE+vdW or PBE-hybrid+vdW and M06+vdW is significantly reduced (0.3 eV) as compared to the difference between uncorrected M06 and PBE(-hybrid)+vdW (0.7 eV).

To understand how well the approaches studied here do at geometry prediction, we have computed the equilibrium intermolecular distances obtained for the NiPc and MgPc dimers, as well as the shift of the Mg atom from the molecular plane for the latter. The computed values, compared to experimental data, are given in Table 1 (additional data on single molecule bond lengths and angles are given in the SI). As discussed above, PBE and PBE-hybrid significantly overestimate the equilibrium intermolecular distance of both dimers, whereas M06 and PBE+vdW yield values that are in good agreement with the experimental ones. The distance of the Mg atom from the molecular plane is underestimated by PBE and PBE-hybrid by ~0.3 Å, whereas it is within ~0.1 Å from experiment with PBE+vdW and within ~0.15 Å with M06. Full relaxation was not performed for M06+vdW, since the latter functional is not implemented in FHI-aims. However, on the basis of the binding energy curve of the planar dimer, we expect only minor changes from the uncorrected M06 dimer geometry.

Having accounted for dispersive interactions such that the correct equilibrium geometry was obtained, we now return to the electronic structure. Figure 5 shows calculated eigenvalue spectra of the NiPc dimer, as well as the same

Figure 5. NiPc single molecule (orange online) and dimer (blue online) spectra, calculated with different exchange-correlation functionals and broadened by a 0.35 eV Gaussian, compared to the UPS data of Ellis et al.,[64] obtained for a 11.8 Å NiPc film at $\theta = 70°$. The dimer eigenvalues shown are those obtained for the equilibrium geometry specified in Table 1, except for the PBE-hybrid+vdW and B3LYP+vdW eigenvalues that were calculated for the geometry obtained with PBE+vdW.

spectra broadened by convolution with a 0.35 eV Gaussian to simulate the effective experimental resolution of ultraviolet photoemission spectroscopy (UPS). The calculated spectra are compared to the single molecule spectrum calculated with PBE-hybrid, as well as to the thin film UPS data of Ellis et al.,[64] also shown in the figure.

As expected, the dimer PBE-hybrid spectrum is similar to that of the single molecule, with some level splitting due to the interaction between the two molecules. In previous work, it was shown that for the NiPc single molecule, as well as for other transition metal Pc's, the PBE functional fails qualitatively, primarily because of underbinding of localized orbitals due to self-interaction errors.[32] A similar picture is revealed for the NiPc dimer, where the spectra calculated with the hybrid functionals, PBE-hybrid and M06,

Electronic Structure Using DFT

J. Chem. Theory Comput., Vol. 6, No. 1, 2010 **87**
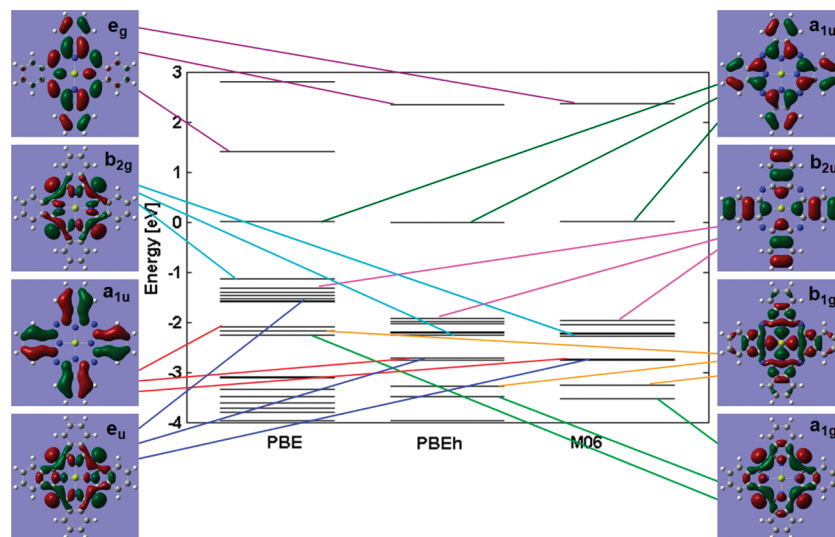
Figure 6. Energy and ordering of selected MgPc molecular orbitals, calculated with different exchange-correlation functionals. All spectra were shifted so as to align the highest occupied molecular orbital (HOMO). For clarity, only one example of each doubly degenerate e_g and e_u orbital is shown.

agree with experiment even at the overestimated intermolecular distance of 4.1 Å (obtained with the uncorrected PBE-hybrid). Contrary to the hybrid spectra, the PBE spectra are quite different from experiment. An obvious difference from experiment is that the PBE spectrum is "compressed"; i.e., there is a general narrowing of the gaps between peaks and more energy levels are "squeezed" into a given energy window. "Compression" of experimental spectra is a well-known tendency of semilocal functionals, which can be attributed to the comparison of Kohn−Sham eigenvalues with quasiparticle excitation energies.[31,69,70] (Note that in a hybrid calculation, unlike in a "true" Kohn−Sham one, one makes use of a nonlocal potential that can mimic the nonlocal self-energy. This may avoid the "compression" problem.[31,32]) Moreover, in the PBE spectrum there is a spurious peak between the experimentally observed first and second peaks and the subfeatures for the second peak are missing. This PBE distortion of the line shape remains with PBE+vdW geometry, but the PBE-hybrid+vdW and B3LYP+vdW retain the correct electronic structure.[47]

Figure 6 shows the eigenvalues of the MgPc molecule, obtained with different functionals, together with selected molecular orbitals and their energy positions. In agreement with trends observed for other transition metal Pc's,[32] the PBE spectrum of MgPc also appears to be affected by SIE. The b_{2g}, e_u, b_{1g}, and a_{1g} orbitals, localized over the central region of the molecule, are shifted to higher energies compared to the hybrid spectra, leading to a distortion of the PBE spectrum.

Figure 7 shows the calculated eigenvalue spectra of the MgPc dimer, as well as the same spectra, broadened by convolution with a 0.35 eV Gaussian to simulate the effective experimental resolution of UPS. Single molecule spectra obtained with PBE and PBE-hybrid are also shown. As expected, the dimer spectra are similar to those of the single molecule, obtained with the same functional, with some level splitting due to the interaction between the two molecules. Similarly to NiPc, the PBE spectra obtained for the PBE and PBE+vdW geometries appear compressed compared to
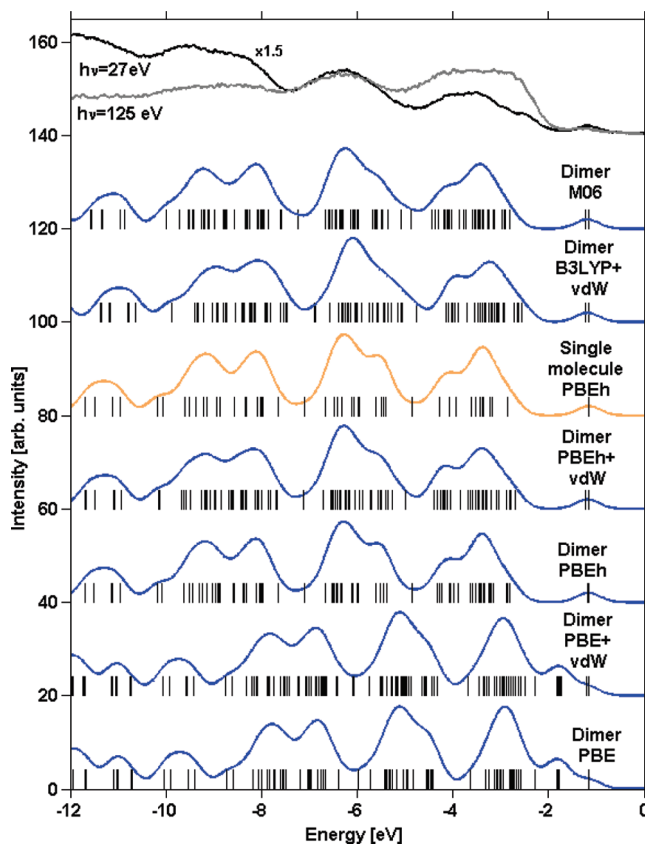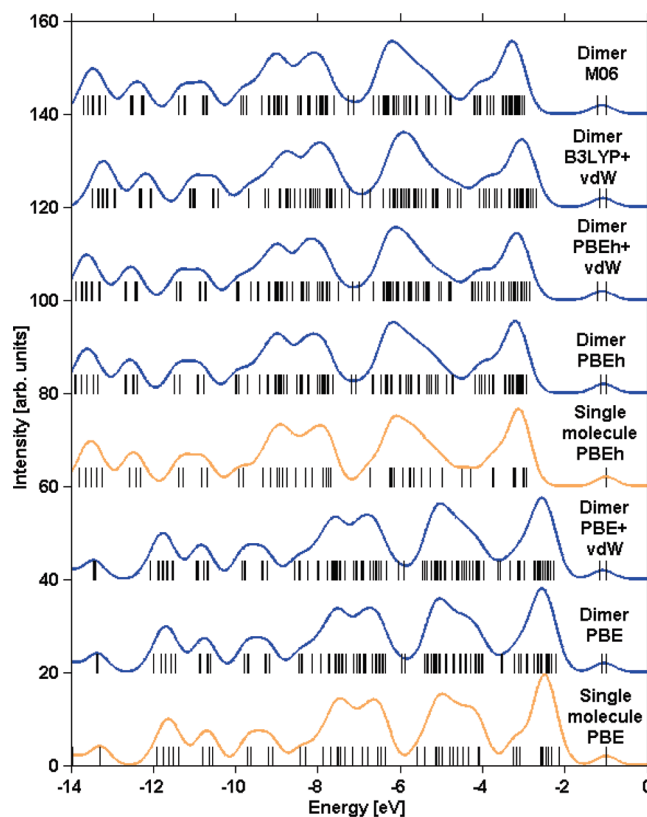

Figure 7. MgPc single molecule (orange online) and dimer (blue online) spectra, calculated with different exchange-correlation functionals and broadened by a 0.35 eV Gaussian. The dimer eigenvalues shown are those obtained for the equilibrium geometry specified in Table 1, except for the PBE-hybrid+vdW and B3LYP+vdW eigenvalues that were calculated for the geometry obtained with PBE+vdW.

the hybrid spectra. However, the differences in the line shape between the PBE and the hybrid calculations are not as visually obvious for MgPc as they are for NiPc, at least at the broadening level used.[71] Still, on the basis of the qualitative differences in molecular orbital ordering shown

in Figure 6, as well as on previous work on identifying self-interaction errors in similar[32] and other[33] organic molecules, we believe that the hybrid calculations are more reliable. A comparison against high-resolution experimental data could provide a definitive answer, should such data become available.

Even though PBE+vdW yields accurate geometries for the noncovalently bound systems studied here, it still fails to give a good description of the electronic structure, primarily due to self-interaction errors, whereas hybrid functionals yield spectra that are in good agreement with experiment (for NiPc) even with overestimated intermolecular distances. For both the NiPc and MgPc dimers, M06 provides good accuracy for the geometry and the electronic structure, but M06 does not capture the long-range asymptotics and yields a binding energy significantly lower than those obtained with the TS-vdW correction.

We therefore propose the following scheme for DFT calculations of systems involving noncovalent interactions: First, geometry relaxation can be performed with a PBE+vdW calculation, which is computationally less demanding than a corresponding PBE-hybrid+vdW calculation, yet yields binding energy curves that are practically identical to those obtained with the latter and in good agreement with pertinent experiments. This step is then to be followed by a calculation with the PBE-hybrid functional in order to obtain reliable electronic structure data.[72] Such a scheme is expected to provide a treatment of noncovalent interactions on the one hand and the electronic structure on the other hand. Since it is not based on a particular training set, it can be applied robustly to a wide range of materials.

4. Conclusion

The binding energy curves, geometry, and electronic structure of NiPc and MgPc dimers were calculated using the PBE, PBE-hybrid, B3LYP, and M06 functionals with and without a first principles C_6/R^6 correction. The PBE and PBE-hybrid functionals, inherently unsuitable for treating dispersive interactions, significantly underestimate the strength of the $\pi-d$ and $\pi-\pi$ interactions in the NiPc and MgPc dimers, respectively. Unlike PBE and PBE-hybrid, both M06 and PBE+vdW yield geometries in good agreement with experiment. However, PBE+vdW seriously distorts the electronic structure due to self-interaction errors.[47] Conversely, M06 does very well for the electronic structure but its binding energy is significantly different from that of PBE+vdW. This difference, which is accentuated by the sheer size of the system, reflects the fact that M06 does not possess the correct R^{-6} asymptote. Correcting the long-range dispersion brings M06 into much better agreement with PBE+vdW.

The binding energy curves obtained with PBE-hybrid+vdW are essentially indistinguishable from those obtained with PBE+vdW; i.e., both functionals possess the correct asymptotic behavior and do equally well on the geometry. But unlike PBE, PBE-hybrid (as well as B3LYP) mitigates the self-interaction errors and also describes the electronic structure well. Still, relaxation with PBE+vdW is less computationally intensive due to the absence of Fock exchange. Thus, although one can perform the entire calcula-

tion with the PBE-hybrid+vdW or the B3LYP+vdW scheme, it is often preferable in practice to perform the relaxation with PBE+vdW, followed by computation of the electronic structure with the PBE-hybrid.

We conclude that the thorny problem of obtaining a description of both geometry and electronic structure can be generally overcome by decoupling the two issues. We choose a functional that is appropriate to the electronic structure, but does not include a good description of dispersive interactions (e.g., PBE-hybrid), and augment it with first principles corrections for the leading terms of the dispersion interaction using the TS-vdW approach. This provides a robust and efficient scheme which we believe will find much use in future studies of organic electronic materials.

Supporting Information Available: Two figures and a table show additional information. This material is available free of charge via the Internet at http://pubs.acs.org.

References

(1) Kristyán, S.; Pulay, P. *Chem. Phys. Lett.* **1994**, *229*, 175.

(2) Pérez-Jordá, J. M.; Becke, A. D. *Chem. Phys. Lett.* **1995**, *233*, 134.

(3) (a) Langreth, D. C.; Perdew, J. P. *Solid State Commun.* **1975**, *17*, 1425. (b) Langreth, D. C.; Perdew, J. P. *Phys. Rev. B* **1977**, *15*, 2884.

(4) Aryasetiawan, F.; Miyake, T.; Terakura, K. *Phys. Rev. Lett.* **2002**, *88*, 166401.

(5) Fuchs, M.; Gonze, X. *Phys. Rev. B* **2002**, *65*, 235109.

(6) (a) Furche, F.; van Voorhis, T. *J. Chem. Phys.* **2005**, *122*, 164106. (b) Furche, F. *J. Chem. Phys.* **2008**, *129*, 114105.

(7) Marini, A.; García-González, P.; Rubio, A. *Phys. Rev. Lett.* **2006**, *96*, 136404.

(8) Harl, J.; Kresse, G. *Phys. Rev. B* **2008**, *77*, 045136.

(9) Rohlfing, M.; Bredow, T. *Phys. Rev. Lett.* **2008**, *101*, 266106.

(10) Janesko, B. G.; Henderson, T. M.; Scuseria, G. E. *J. Chem. Phys.* **2009**, *130*, 081105.

(11) Toulouse, J.; Gerber, I. C.; Jansen, G.; Savin, A.; Ángyán, J. G. *Phys. Rev. Lett.* **2009**, *102*, 096404.

(12) Kohn, W.; Meir, Y.; Makarov, D. E. *Phys. Rev. Lett.* **1998**, *80*, 4153.

(13) Dion, M.; Rydberg, H.; Schröder, E.; Langreth, D. C.; Lundqvist, B. I. *Phys. Rev. Lett.* **2004**, *92*, 246401.

(14) Adamo, C.; Barone, V. *J. Chem. Phys.* **1998**, *108*, 664.

Electronic Structure Using DFT

J. Chem. Theory Comput., Vol. 6, No. 1, 2010 **89**

(15) Kurita, N.; Inoue, H.; Sekino, H. *Chem. Phys. Lett.* **2003**, *370*, 161.

(16) Xu, X.; Goddard, W. A. *Proc. Natl. Acad. Sci.* **2004**, *101*, 2673.

(17) Zhao, Y.; Truhlar, D. G. *Acc. Chem. Res.* **2008**, *41*, 157. Zhao, Y.; Truhlar, D. G. *Theor. Chem. Acc.* **2008**, *120*, 215.

(18) (a) Tarnopolsky, A.; Karton, A.; Sertchook, R.; Gruzman, D.; Martin, J. M. L. *J. Phys. Chem. A* **2008**, *112*, 3. (b) Karton, A.; Tarnopolsky, A.; Lamère, J. F.; Schatz, G. C.; Martin, J. M. L. *J. Phys. Chem. A* **2008**, *112*, 12868.

(19) Wu, X.; Vargas, M. C.; Nayak, S.; Lotrich, V.; Scoles, G. *J. Chem. Phys.* **2001**, *115*, 8748.

(20) Wu, Q.; Yang, W. *J. Chem. Phys.* **2002**, *116*, 515.

(21) Johnson, E. R.; Becke, A. D. *J. Chem. Phys.* **2005**, *123*, 024101.

(22) (a) Neumann, M. A.; Perrin, M.-A. *J. Phys. Chem.* **2005**, *109*, 15531. (b) Neumann, M. A.; Leusen, F. J. J.; Kendrick, J. *Angew. Chem., Int. Ed.* **2008**, *47*, 2427.

(23) Nara, J.; Higai, S.; Morikawa, Y.; Ohno, T. *J. Chem. Phys.* **2004**, *120*, 6705.

(24) Grimme, S. *J. Comput. Chem.* **2006**, *27*, 1787.

(25) Jurečka, P.; Èerny, J.; Hobza, P.; Salahub, D. R. *J. Comput. Chem.* **2007**, *28*, 555.

(26) Tkatchenko, A.; von Lilienfeld, O. A. *Phys. Rev. B* **2008**, *78*, 045116.

(27) Silvestrelli, P. L. *Phys. Rev. Lett.* **2008**, *100*, 053002.

(28) Tkatchenko, A.; Scheffler, M. *Phys. Rev. Lett.* **2009**, *102*, 073005.

(29) Byrd, E. F. C.; Scuseria, G. E.; Chabalowski, C. F. *J. Phys. Chem. B* **2004**, *108*, 13100.

(30) Perdew, J. P.; Zunger, A. *Phys. Rev. B* **1981**, *23*, 5048.

(31) Kümmel, S.; Kronik, L. *Rev. Mod. Phys.* **2008**, *80*, 3.

(32) (a) Marom, N.; Hod, O.; Scuseria, G. E.; Kronik, L. *J. Chem. Phys.* **2008**, *128*, 164107. (b) Marom, N.; Kronik, L. *Appl. Phys. A: Mater. Sci. Process.* **2009**, *95*, 159.

(33) (a) Dori, N.; Menon, M.; Kilian, L.; Sokolowski, M.; Kronik, L.; Umbach, E. *Phys. Rev. B* **2006**, *73*, 195208. (b) Arantes, J. T.; Lima, M. P.; Fazzio, A.; Xiang, H.; Wei, S.-H.; Dalpian, G. M. *J. Phys. Chem. B* **2009**, *113*, 5376. (c) Körzdörfer, T.; Kümmel, S.; Marom, N.; Kronik, L. *Phys. Rev. B* **2009**, *79*, R201205. (d) Palummo, M.; Hogan, C.; Sottile, F.; Bagalá, P.; Rubio, A. *J. Chem. Phys.* **2009**, *131*, 084102.

(34) Naturally, one may go beyond DFT and use schemes like MP2+ΔvdW for obtaining the relaxed geometry. See Tkatchenko, A.; DiStasio, R. A., Jr; Head-Gordon, M.; Scheffler, M. *J. Chem. Phys.* **2009**, *131*, 094106. and many-body methods (quasiparticle excitations) for calculating the electronic structure.

(35) See, e.g., (a) Puzder, A.; Dion, M.; Langreth, D. C. *J. Chem. Phys.* **2006**, *124*, 164105. (b) Kleis, J.; Lundqvist, B. I.; Langreth, D. C.; Schröder, E. *Phys. Rev. B* **2007**, *76*, 100201. (c) Cooper, V. R.; Thonhauser, T.; Puzder, A.; Schröder, E.; Lundqvist, B. I.; Langreth, D. C. *J. Am. Chem. Soc.* **2008**, *130*, 1304. (d) Cooper, V. R.; Thonhauser, T.; Langreth, D. C. *J. Chem. Phys.* **2008**, *128*, 204102. (e) Hooper, J.; Cooper, V. R.; Thonhauser, T.; Romero, N. A.; Zerilli, F.; Langreth, D. C. *ChemPhysChem* **2008**, *9*, 891. (f) Lazić, P.; Crljen, Ž.; Brako, R.; Gumhalter, B. *Phys. Rev. B* **2005**, *72*, 245407. (g) Yanagisawa, S.; Lee, K.; Morikawa, Y. *J. Chem. Phys.*

2008, *128*, 244704. (h) Sony, P.; Puschnig, P.; Nabok, D.; Ambrosch-Draxl, C. *Phys. Rev. Lett.* **2007**, *99*, 176401.

(36) Zhang, Y.; Yang, W. *Phys. Rev. Lett.* **1998**, *80*, 890.

(37) (a) Vydrov, O. A.; Wu, Q.; Voorhis, T. V. *J. Chem. Phys.* **2008**, *129*, 014106. (b) Gulans, A.; Puska, M. J.; Nieminen, R. M. *Phys. Rev. B* **2009**, *79*, 201105.

(38) (a) Dobson, J. F.; McLennan, K.; Rubio, A.; Wang, J.; Gould, T.; Le, H. M.; Dinte, B. P. *Aust. J. Chem.* **2001**, *54*, 513. (b) Dobson, J. F.; White, A.; Rubio, A. *Phys. Rev. Lett.* **2006**, *96*, 073201.

(39) (a) Perdew, J. P.; Burke, K.; Ernzerhof, M. *Phys. Rev. Lett.* **1996**, *77*, 3865. (b) Perdew, J. P.; Burke, K.; Ernzerhof, M. *Phys. Rev. Lett.* **1997**, *78*, 1396 (E).

(40) (a) Perdew, J. P.; Ernzerhof, M.; Burke, K. *J. Chem. Phys.* **1996**, *105*, 9982. (b) Adamo, C.; Barone, V. *J. Chem. Phys.* **1999**, *110*, 6158. (c) Ernzerhof, M.; Scuseria, G. E. *J. Chem. Phys.* **1999**, *110*, 5029.

(41) (a) Stephens, P. J.; Devlin, F. J.; Chabalowski, C. F.; Frisch, M. J. *J. Phys. Chem.* **1994**, *98*, 11623. (b) Becke, A. D. *J. Chem. Phys.* **1993**, *98*, 5648.

(42) Applications of Phthalocyanines. In *The Porphyrin Handbook*, 1st ed.; Kadish, K. M., Smith, R., Guilard R., Eds.; Academic Press: San Diego, CA, 2003; *Vol 19*.

(43) Grimme, S. *Angew. Chem., Int. Ed.* **2008**, *47*, 3430.

(44) Schramm, C. J.; Scaringe, R. P.; Stojakovic, D. R.; Hoffman, B. M.; Ibers, J. A.; Marks, T. J. *J. Am. Chem. Soc.* **1980**, *102*, 6702.

(45) Janczak, J.; Kubiak, R. *Polyhedron* **2001**, *20*, 2901.

(46) (a) Mizuguchi, J. *J. Phys. Chem. A* **2001**, *105*, 1121. (b) Mizuguchi, J. *J. Phys. Chem. A* **2001**, *105*, 10719.

(47) At a given geometry, the "+vdW" part of the computation has no effect on the electronic structure by construction, as it is only added to the total energy. However, because the optimized geometry with the vdW corrections differs from the uncorrected one, some geometry-dependent changes in the electronic structure may ensue.

(48) Santra, B.; Michaelides, A.; Fuchs, M.; Tkatchenko, A.; Filippi, C.; Scheffler, M. *J. Chem. Phys.* **2008**, *129*, 194111.

(49) Chu, X.; Dalgarno, A. *J. Chem. Phys.* **2004**, *121*, 4083.

(50) Hirshfeld, F. L. *Theor. Chim. Acta* **1977**, *44*, 129.

(51) Nalewajski, R. F.; Parr, R. G. *Proc. Natl. Acad. Sci. U.S.A.* **2000**, *97*, 8879.

(52) (a) Johnson, E. R.; Becke, A. D. *Chem. Phys. Lett.* **2006**, *432*, 600. (b) Becke, A. D.; Johnson, E. R. *J. Chem. Phys.* **2007**, *127*, 124108.

(53) Jurečka, P.; Šponer, J.; Černy, J.; Hobza, P. *Phys. Chem. Chem. Phys.* **2006**, *8*, 1985.

(54) The s_R values found for PBE and PBE-hybrid are smaller than those found in conjunction with empirical determination of C_6 coefficients because we use *free-atom* vdW radii, which yield larger effective radii than the values reported by Bondi: Bondi, A. J. *J. Phys. Chem.* **1964**, *68*, 441.

(55) Karton, A.; Gruzman, D.; Martin, J. M. L. *J. Phys. Chem. A* **2009**, *113*, 8434.

(56) (a) Blum, V.; Gehrke, R.; Hanke, F.; Havu, P.; Havu, V.; Ren, X.; Reuter, K.; Scheffler, M. *Comput. Phys. Commun.* **2009**, *180*, 2175. (b) FHI-aims, Theory Department, Fritz-Haber Institute Berlin, http://www.fhi-berlin.mpg.de/aims/, accessed Jul 1, 2009.

(57) The calculations were performed using either revision C.01wis2 (2004) or revision E.01+MNG (2007) of the *Gaussian03* suite of programs . Frisch, M. J.; Trucks, G. W.; Schlegel, H. B.; Scuseria, G. E.; Robb, M. A.; Cheeseman, J. R.; Montgomery, J. A., Jr.; Vreven, T.; Kudin, K. N.; Burant, J. C.; Millam, J. M.; Iyengar, S. S.; Tomasi, J.; Barone, V.; Mennucci, B.; Cossi, M.; Scalmani, G.; Rega, N.; Petersson, G. A.; Nakatsuji, H.; Hada, M.; Ehara, M.; Toyota, K.; Fukuda, R.; Hasegawa, J.; Ishida, M.; Nakajima, T.; Honda, Y.; Kitao, O.; Nakai, H.; Klene, M.; Li, X.; Knox, J. E.; Hratchian, H. P.; Cross, J. B.; Bakken, V.; Adamo, C.; Jaramillo, J.; Gomperts, R.; Stratmann, R. E.; Yazyev, O.; Austin, A. J.; Cammi, R.; Pomelli, C.; Ochterski, J. W.; Ayala, P. Y.; Morokuma, K.; Voth, G. A.; Salvador, P.; Dannenberg, J. J.; Zakrzewski, V. G.; Dapprich, S.; Daniels, A. D.; Strain, M. C.; Farkas, O.; Malick, D. K.; Rabuck, A. D.; Raghavachari, K.; Foresman, J. B.; Ortiz, J. V.; Cui, Q.; Baboul, A. G.; Clifford, S.; Cioslowski, J.; Stefanov, B. B.; Liu, G.; Liashenko, A.; Piskorz, P.; Komaromi, I.; Martin, R. L.; Fox, D. J.; Keith, T.; Al-Laham, M. A.; Peng, C. Y.; Nanayakkara, A.; Challacombe, M.; Gill, P. M. W.; Johnson, B.; Chen, W.; Wong, M. W.; Gonzalez, C.; Pople, J. A. *Gaussian03*; Gaussian, Inc.: Wallingford, CT, 2003.

(58) (a) Becke, A. D. *Phys. Rev. A* **1988**, *38*, 3098. (b) Lee, C.; Yang, W.; Parr, R. G. *Phys. Rev. B* **1988**, *37*, 785.

(59) Weigend, F.; Ahlrichs, R. *Phys. Chem. Chem. Phys.* **2005**, *7*, 3297.

(60) (a) Dunning, T. H., Jr. *J. Chem. Phys.* **1989**, *90*, 1007. (b) Woon, D. E.; Dunning, T. H., Jr. *EMSL Basis Set Exchange*; https://bse.pnl.gov/bse/portal, accessed Apr 27, 2008.

(61) Boys, S. F.; Bernardi, F. *Mol. Phys.* **1970**, *19*, 553.

(62) Simon, S.; Duran, M.; Dannenberg, J. J. *J. Chem. Phys.* **1996**, *105*, 11024.

(63) Paier, J.; Marsman, M.; Kresse, G. *J. Chem. Phys.* **2007**, *127*, 024103.

(64) Ellis, T. S.; Park, K. T.; Ulrich, M. D.; Hulbert, S. L.; Rowe, J. E. *J. Appl. Phys.* **2006**, *100*, 093515.

(65) Chong, D. P.; Gritsenko, O. V.; Baerends, E. J. *J. Chem. Phys.* **2002**, *116*, 1760. (b) Gritsenko, O. V.; Baerends, E. J. *J. Chem. Phys.* **2002**, *117*, 9154.

(66) See eq 75 in ref 31.

(67) For dispersively bound systems, the similarity of revPBE exchange to exact exchange was discussed, e.g., in the context of the binding energy curve of the Kr dimer. See Langreth, D. C.; Dion, M.; Rydberg, H.; Schröder, E.; Hyldgaard, P.; Lundqvist, B. I. *Int. J. Quantum Chem.* **2005**, *101*, 599.

(68) (a) Hohenstein, E. G.; Chill, S. T.; Sherrill, C. D. *J. Chem. Theor. Comput.* **2008**, *4*, 1996. (b) Raju, R. K.; Ramraj, A.; Hillier, I. H.; Vincent, M. A.; Burton, N. A. *Phys. Chem. Chem. Phys.* **2009**, *11*, 3411.

(69) Hybertsen, M. S.; Louie, S. G. *Phys. Rev. B* **1986**, *34*, 5390.

(70) Jones, R. O.; Gunnarsson, O. *Rev. Mod. Phys.* **1989**, *61*, 689.

(71) A similar trend was observed previously for FePc and MnPc. See Marom, N.; Kronik, L. *Appl. Phys. A: Mater. Sci. Process.* **2009**, *95*, 165.

(72) Calculations of quasiparticle excitations at the optimized geometry may also be performed.

CT900410J

J. Chem. Theory Comput. **2010,** *6,* 91–99

91

JCTC Journal of Chemical Theory and Computation

Multilevel Fragment-Based Approach (MFBA): A Novel Hybrid Computational Method for the Study of Large Molecules

Jan Řezáč*,[†,‡] and Dennis R. Salahub[†]

Department of Chemistry, IBI—Institute for Biocomplexity and Informatics and ISEEE—Institute for Sustainable Energy, Environment and Economy, University of Calgary, 2500 University Drive NW, Calgary, Alberta, Canada T2N 1N4, Institute of Organic Chemistry and Biochemistry, Academy of Sciences of the Czech Republic and Center for Biomolecules and Complex Systems, 166 10 Prague 6, Czech Republic

Abstract: We present a novel method for the calculation of large molecules and systems, the multilevel fragment-based approach. It is based on dividing the system into small fragments followed by separate calculations of these fragments and the interactions between them. Unlike previous fragmentation-based methods, we use multiple computational methods for the individual calculations. Using an accurate method only to calculate local interactions and more approximate methods for interactions over larger distances, it is possible to achieve results very close to a more demanding fragmented calculation using the higher level method only. The number of calculations performed at the higher level scales linearly with the size of the system, which significantly improves the efficiency and allows this scheme to be used for very large systems. In this work, we have combined density functional theory with the more approximate density functional tight binding method and applied this method to the calculation of model peptides. Formulation of first derivatives of the total energy within this fragmentation scheme is also presented and tested.

Introduction

One of the important trends in modern computational chemistry is the application of quantum-mechanical (QM) methods to molecules and molecular systems of increasing size while achieving the greatest accuracy possible. This is not an easy task, because of unfavorable scaling of these methods with the system size. Even the most efficient ab initio methods, Hartree–Fock (HF) and density functional theory (DFT), in their most efficient implementations have $O(N^3)$ complexity. This algorithm complexity arises from a matrix diagonalization that is an indispensable part of all these calculations. Post-HF methods are even more demanding.

The ultimate goal is linear scaling. It is obvious that it can be achieved only by introducing some approximations, which in turn affect the accuracy of the results. Many approaches have been developed and published. All these methods can be divided into two very general groups: The first one is to set up the calculation of the whole system and then use approximations within the algorithms used to solve it (for a recent review of linear scaling methods, see refs 1, 2). The second group of methods relies on partitioning of the system into small fragments that are calculated separately and then composing the total energy and properties of the system from results obtained for the fragments. There is some overlap between these two groups, because some methods use the electronic structure of the fragments to build the electronic structure of the whole system, which is then used to obtain its properties. The adjustable density matrix assembler[3,4] (ADMA) and fragment molecular orbital[5–9] (FMO) methods are examples of this hybrid approach.

---

* Corresponding author. E-mail: rezac@uochb.cas.cz.

† University of Calgary.

‡ Academy of Sciences of the Czech Republic and Center for Biomolecules and Complex Systems.

In this work, we focus only on the pure fragment-based approach (FBA), exploiting the advantages of truly independent calculations of the fragments. Using only the final results of the calculations, such as the energy and its derivatives, this approach is independent of the method used and the calculations can be done using readily available software. This strategy also offers the possibility of lossless parallelization, because the calculations of the fragments can be distributed to multiple processors without any need of communication between them during the calculation.

There exist multiple methods based on the principle of fragmentation and independent calculation of the fragments: the molecular tailoring approach[10−13] (MTA) of Gadre et al., the molecular fractionation with conjugated caps[14−16] (MFCC), the kernel energy method[17,18] (KEM) devised by Huang, Massa and Karle, the generalized energy-based fragmentation (GEBF) by Li et al.[19] and others.[20−22] Most of these methods are designed to achieve linear scaling, and they do it by calculating interactions of a fragment with only a limited number of nearest surrounding fragments, selected either on the basis of their connectivity or by a distance cutoff. In large systems, the number of nearest neighbors of a fragment is practically constant and only kN interactions have to be calculated in a system consisting of N fragments. This incomplete description is an approximation that works well in systems where long-distance noncovalent interactions are negligible. This limits the use of these approaches to application to mostly neutral, nonpolar systems, because electrostatics is the strongest of these interactions. Noncovalent interactions play a crucial role in biomolecules, such as DNA and proteins, and their neglect can lead to serious errors. This issue will be explored systematically later in this paper.

This drawback has been addressed within the MFCC method by Li et al.,[14] who added all pairwise interactions between fragments into the scheme. The kernel energy method also uses all pairwise terms and was later extended to use higher-order terms up to four-body effects.[17]

In general, the linear scaling fragment-based methods rely on the calculation of a limited number of interactions between the fragments, neglecting the long-distance ones. Including all interactions is of course possible, but it brings quadratic scaling with the number of fragments. We present a novel approach that goes beyond the binary logic of selection of interaction and combines the advantage of calculating all pairwise terms with practically linear scaling. To do so, we combine multiple methods of calculation where they are appropriate. Only the local interactions are treated by the most accurate method, while all other interactions are also included but calculated at a more approximate and thus more efficient level. The scaling of the higher-level part of the calculation is linear, because we calculate only a limited (on average constant) number of interactions of each fragment with its neighbors. The lower-level part still scales quadratically, but its total cost is negligible compared to the higher-level part, because a more efficient method is used.

This multilevel fragment-based approach (MFBA) is in some respects related to previously reported MFCC calculations at the MP2 level,[14] where distinct distance cutoffs were used for the calculation of the correlation energy and the underlying HF calculations. On the other hand, the present MFBA scheme is, to the best of our knowledge, the first fragment-based method that combines completely independent methods, which opens up many new possibilities. The MFBA scheme is very general and its possible applications reach far beyond the single example described in this work. It can be applied to systems of moderate size, where we combine accurate ab initio calculations with more efficient ab initio calculations, semiempirical methods, or molecular mechanics. On the other end of the scale, we can combine more approximate atomistic methods, such as molecular mechanics, with a coarse-grained method used to calculate long-distance interactions (for example, as the interaction of multipoles representing the whole fragments). In this paper, we will focus on the first possibility, with the aim of achieving high accuracy by combining DFT with the more efficient self-consistent charge density functional based tight-binding (SCC-DFTB) method.[23]

The MFBA method is not limited to two levels of calculation. We can define more than one distance threshold and combine multiple methods in the calculation, utilizing different distance-dependent behavior of different types of interactions.

Our method of course shares some limitations with other fragment-based approaches. First, it can be applied only to molecules or systems that can be divided into fragments. The electronic structure of the fragments should represent the respective part of the molecule as closely as possible. It is not possible to cut a molecule with delocalized electrons, such as conjugated or aromatic systems. To limit the perturbation of the electronic structure, the fragments should be either independent molecules or connected by a chemical bond that can be cut and replaced by a suitable cap. We use hydrogen link atoms as the caps to treat C−C single bonds. Our scheme includes all pairwise interactions but neglects three-body and higher-order effects. Finally, apart from perturbation of the electronic structure of the molecule, adding link atoms to fragments introduces an additional error due to interaction of these atoms with the rest of the system. This problem has not been discussed before, and we will provide a detailed analysis and suggestions for how to minimize it.

The use of fragment-based methods is not limited to the calculation of the energy. Schemes for the calculation of first[13,14,24] and second[24,25] derivatives or electrostatic properties[26−28] have been proposed in the literature. We have formulated the calculation of first derivatives of the MFBA energy, which allows one to use the method for geometry optimizations. The simple scheme of composing the gradients reported for other fragment-based methods does not work in the MFBA scheme, and a more elaborate solution had to be developed.

Finally, we would like to discuss the relationship between MFBA and QM/MM or QM/QM′ methods.[29,30] Both approaches have in common the use of different computational methods combined to take advantage of the accuracy of the higher-level method and the efficiency of the other, and both have their specific uses. QM/MM methods are useful when
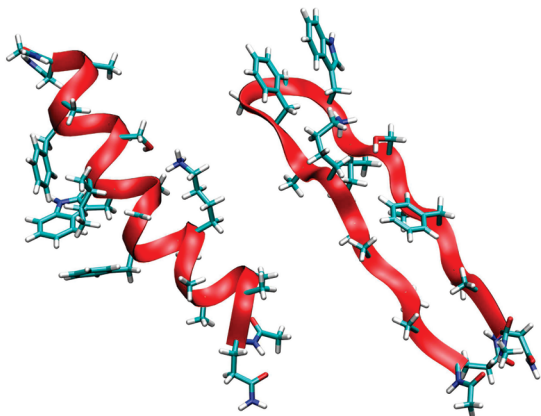
Multilevel Fragment-Based Approach

J. Chem. Theory Comput., Vol. 6, No. 1, 2010 **93**

Figure 1. Model 18-peptide in α-helix and β-sheet conformations. The sequence QAAAAKAFGGWISAFAAN features various noncovalent interactions between the side chains.

there is a localized region of interest, while the rest of the system acts only as an environment. MFBA, on the other hand, aims to achieve the accuracy of the high-level method for the whole system.

In the past, several hybrid schemes using fragment-based QM calculation have been proposed. It is worth mentioning that fragment-based calculations can be used as the QM part in a QM/MM calculation,[31] or it can be used to replace some terms in the MM forcefield.[32] Also, an equivalent of a QM/QM' scheme has been set up directly within one FMO calculation by separating the fragments into layers treated by different methods.[33]

The accuracy of the MFBA calculations and its comparison to a scheme neglecting long-distance interaction are demonstrated on a model system designed to be challenging. To make our conclusions relevant to applications in biochemistry, we have chosen a peptide in which electrostatic forces are important. We systematically study different states of the peptide, ranging from neutral to zwitterion forms, as well as an artificial hydrocarbon structure mimicking the same peptide. For each state, we calculate the energy difference between α-helix and β-sheet conformations (Figure 1). Although the MFBA approach can be applied to much larger molecules, the peptide was chosen to be relatively small (250 atoms), so that a full DFT calculation is still feasible and is used for comparison.

Methods

MFBA Formalism. Our fragmentation scheme is based on dividing the system into N fragments followed by calculations of these fragments and all of their pairs. In analogy with the kernel energy method, the total energy of the system is then expressed as a sum of energies of the fragments E_i and pairwise interaction energies ΔE_{ij} between them

$$E = \sum_{i=1}^{N} E_i + \sum_{i=1}^{N} \sum_{j=1}^{i-1} \Delta E_{ij} \qquad (1)$$

where interaction energy is defined as the difference between the energy of a pair of fragments E_{ij} and the energies of the isolated fragments

$$\Delta E_{ij} = E_{ij} - E_i - E_j \qquad (2)$$

This formulation is straightforward for noncovalent pairs, but the same can be applied to pairs of fragments connected by a covalent bond. To construct the fragments, the original chemical bond is replaced by a cap. For reasons described later, we are limited to the smallest caps possible, and we systematically use hydrogen atoms. This is the same approach as using hydrogen link atoms in QM/MM to terminate covalent bonds at the QM−MM boundary. In pairs (dimers) of fragments, the original bond between the fragments is conserved, and in the final summation, the added caps and the contribution of the new C−H bonds cancel out, leaving the contribution of the original C−C bonds that are conserved in the dimers.

In the MFBA method, the level of calculation for each fragment is decided using the following rules: All covalent dimers are calculated at the high level in order to describe the bond between the fragments accurately. For the rest of the pairs, the level is selected according to the distance of the fragments, evaluated as a minimal distance of their atoms. Pairs with distance below an arbitrary cutoff are calculated at the higher level, and other pairs are calculated at the lower level. Multiple cutoffs can be introduced if more than two methods are used for the calculations. The cutoff distance should be adjusted to the methods used, and it also represents the parameter balancing accuracy and efficiency. One important goal of this study is to show how the results change when the cutoff is varied in systems of different types.

Caps. The way that the system is divided into fragments may affect the accuracy of the results in multiple ways. To introduce as little perturbation as possible, we break only single C−C bonds, which are nonpolar, and replace them with C−H bonds, conserving well the original electronic structure of the fragment. The length of the newly formed C−H bond is calculated from the length of the C−C bond it replaces by multiplying it by a ratio of their average equilibrium distances. This value is not critical, since the contribution of these bonds cancels out in the summation.

Regarding only the electronic structure, the use of larger functional groups for the caps would be beneficial, but there is another reason why we use only hydrogen atoms. The added caps of course interact both with the rest of the fragment and with the other fragments. The major part of these interactions cancels out in the summation, but some interactions between the caps themselves do not and are an inherent source of error in this type of fragmentation schemes. Detailed analysis of an example is provided in the Appendix. To minimize this error, we have to use caps that interact as little as possible, hydrogen atoms being the best solution.

Gradient Calculation. The existing implementations[13,14] of gradient calculations in fragmentation-based methods compose the final gradients from gradients on the respective atoms in fragments using a scheme analogous to the energy calculation; the gradients on the caps are discarded. This may work in schemes where large caps are used and the original bonds at the boundary of each fragment are conserved, but it does not work when single atoms are used as the caps.

First, we compose the gradients on all but the cap atoms using a formula analogous to eq 1. Then, we go through all cap atoms in all fragments and apply the following correction to the atom in the original bond (with the appropriate sign from eqs 1 and 2). Since the position of the cap atom $\mathbf{r}_c$ is determined by the position of the atoms in the bond it replaces (atom in the fragment $\mathbf{r}_f$, the original atom it replaces $\mathbf{r}_o$) and the scaling factor g,

$$\mathbf{r}_c = \mathbf{r}_f + g(\mathbf{r}_o - \mathbf{r}_f) \qquad (3)$$

the gradient on the cap atom has to be projected on those two atoms:

$$\frac{\partial E}{\partial r_f} = \frac{\partial E}{\partial r_f} + (1 - g)\frac{\partial E}{\partial r_c} \qquad (4)$$

$$\frac{\partial E}{\partial r_o} = \frac{\partial E}{\partial r_o} + g\frac{\partial E}{\partial r_c} \qquad (5)$$

These equations are analogous to the ones used in subtractive QM/MM schemes.[34] This treatment works not only with MFBA, but it can be also applied to obtain gradients in the kernel energy methods, as it can be considered as a special case of MFBA calculation (with infinite cutoff distance for the high-level calculation of interactions).

In the current implementation, the selection of the methods is done once prior to the calculation. The use of this simplification in geometry optimization can be justified only when we do not expect substantial changes of the geometry. Updating the lists of fragment interactions during the calculation was not tested but is in principle possible. However, it might introduce problems caused by discontinuities of the potential energy surface.

Fragmentation. In this paper, we are working with peptides. Due to their polymeric nature, it is easy to break them into fragments. There is only one C—C bond in the peptidic backbone, the bond between C and C^α. To automate the fragmentation, we have developed a tool that identifies these bonds in a PDB file and prepares the input for fragmented calculation.

Implementation. For practical use, the MFBA calculation has to be automated. The implementation itself should be independent of the methods used for the particular calculation in order to take advantage of combining different methods. Our implementation is written in a high-level, object oriented programming language, Ruby.[35] It uses the Cuby (Chemistry in Ruby) framework, developed recently by one of the authors (J.R.). The framework provides unified access to external software packages used for the calculations and allows convenient manipulation of the results. Multiple simulation protocols, including geometry optimization and molecular dynamics algorithms, are available in Cuby and can be used with MFBA calculations. The resulting code is easy to use, as it needs only the geometry of the complete system and a simple definition of fragments (in the form of a list of bonds that are to be cut) as input. Currently, the following software packages and programs can be used for the calculations: AMBER,[36] deMon,[37] DFTB+,[38] Gaussian 03,[39] MNDO99,[40] MOPAC,[41] and Turbomole.[42]
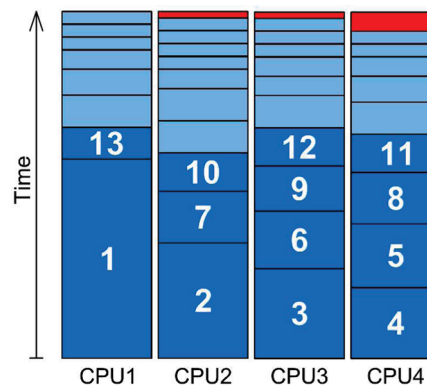
Figure 2. Calculations of fragments distributed to four processors using sorted queue. High-level calculations (darker blue, numbered) run first, faster low-level calculations fill the remaining time. This procedure minimizes the CPU time wasted while waiting for the last calculation (red).

Parallelization. The fragmented calculation can be made very efficient by simultaneous calculation of the fragments and their interactions. We have implemented a parallelization strategy that distributes these calculations to multiple nodes in a cluster and multiple processors on these nodes. The communication between the master node and other nodes, the initiation of the calculation, and retrieving the results use the widely available SSH protocol. When the calculation is run on a single multiprocessor computer, multiple threads are used to run the calculations in parallel, one at each processor.

To minimize the time of waiting for the last calculation to finish, we have implemented a simple queue system used to run the calculations on a given numbers of processors. This approach has been used previously in fragment-based methodology.[13] However, distributing the calculation to multiple nodes can lead to a situation where everything but the last calculation is finished and most allocated nodes have to wait for it. To minimize this waiting time, the calculation can be sorted by their expected length, as demonstrated previously for the FMO method.[43] In the MFBA scheme, multiple methods with different efficiency are used, but all the calculations can be put into one common pool because they are fully independent. The calculations in the pool are then sorted by the expected time of calculation, which is approximated from the method used and the number of atoms in the systems, and passed to a queue system balancing the load on multiple processors. The sorting ensures that the longest calculation will start first, and the shortest ones will then fill the remaining time with as little wasted time as possible (see Figure 2). This is particularly efficient in the case of the MFBA scheme, where there is only a limited number of demanding calculations.

Methods and Software Used. In this paper, we present MFBA calculations combining DFT and SCC-DFTB[23] calculations. All DFT calculations and the DFT part of MFBA calculations were carried out with the Turbomole package,[42] using the TPSS functional[44] and the TZVP basis set.[45] The resolution of identity approximation[46,47] was used to accelerate these calculations. In the case of the zwitterionic

Table 1. Energies of Model Structures Calculated Using DFT without and with Fragmentation and the Energy Difference between α-Helix and β-Sheet Conformations of the Peptide

model	conformation	E (au)		ΔE(α−β) (kcal/mol)	
		full	fragmented	full	fragmented
hydrocarbon	α	−4456.902	−4456.906		
	β	−4456.961	−4456.969	36.9	39.6
neutral	α	−6192.697	−6192.708		
	β	−6192.711	−6192.719	8.7	7.0
capped	α	−6193.111	−6193.145		
	β	−6193.098	−6193.027	−8.5	−11.2
zwitterion	α	−6020.733	−6020.782		
	β	−6020.903	−6020.950	106.9	105.2

peptide, a level shift of 0.5 au was used to improve convergence of the calculations.

The SCC-DFTB calculations were done in the DFTB+ code,[38] using the parameters set "mio". For the geometry optimization of model structures, empirical dispersion[48] available in the DFTB+ code was used (method abbreviated as SCC-DFTB-D).

Model Structures. The basis of all our test molecules is an 18-peptide of the sequence QAAAAKAFGGWISAFA-AN. It has net charge +1 due to the presence of a lysine (K) residue. Two conformers of this peptide were build using the program Ribosome,[49] an α-helix and an antiparallel β-sheet with the two glycine residues in the middle forming a β-turn. The orientation of the side chains, especially the aromatic groups, was adjusted manually to ensure favorable interactions. From this starting structure, four derivatives were prepared and their geometries optimized using the SCC-DFTB-D method.

The first structure is the peptide itself in zwitterionic form that would exist in solution. This serves as a model of a molecule with very strong intramolecular electrostatic interactions.

The second model is the same peptide with acetyl and N-methyl caps. The ends of the peptide chain are thus neutral, and the only charged group in the molecule is the lysine side chain. This model presents a structure where there are important electrostatic interactions between this charge and the other neutral, but polar, residues.

The third model is build from the second one by removing the proton from lysine, making it neutral, to further attenuate the effect of long-distance electrostatics.

Finally, we need a nonpolar model where there will be only a very small contribution of electrostatics. It was prepared from the previous model by replacement of all the peptide bonds (−CO−NH−) with the *trans*-alkene analog, −CH=CH−. The result is a hydrocarbon with functional groups originating from amino acid side chains. The optimized structures differ slightly from the geometry of the original peptide, but the overall conformation (helix and straight, parallel strands) is well conserved, the hydrogen bonds of the peptide replaced by weaker dispersion interactions. Interaction of the side chains stabilizes the structure further.

These four models are denoted zwitterion, capped, neutral, and hydrocarbon in the following text.

Performance of geometry optimizations was tested on a smaller model, a hexapeptide of the sequence FAGGAF with

acetyl and N-methyl caps in the α-helix conformation. The structure was prepared analogously to the large model.

Results

Comparison to Full Calculations. First, let us compare fragment-based calculations to full DFT ones. Here, the fragmented calculation uses only one level, the same DFT method as in the full calculation, and all pairwise interactions are included in the scheme. The results (Table 1) show the accuracy of the fragment-based approach itself. The error in relative energies caused by the fragmentation reaches 2.7 kcal/mol in the hydrocarbon and capped models. Errors in absolute energies are substantially larger, but the major part of them is systematic and is eliminated by working with the relative energies only. These errors have multiple sources: most important are the missing three-body terms; other sources of the error are differences in electronic structure of the fragments and the complete molecule, interactions between the caps, and the lack of higher-order terms. These problems arise from the approximate nature of the method, and their further investigation is beyond the scope of this paper.

For the following discussion of MFBA results, the fragmented DFT calculations will serve as the benchmark, because they represent the upper limit of its accuracy, because no interaction are calculated at the lower level.

Neglected Interactions and MFBA. The most important parameter of both MFBA and the linear scaling scheme neglecting long-distance interactions is the cutoff distance above which the interaction energy is calculated by the more approximate method or not calculated at all. To show the advantage of MFBA over neglect of the interactions and to determine the optimal value of the cutoff for further calculations, we have performed a set of calculations with varying cutoff on each model. The results are summarized in Table 2 and plotted in Figure 3. In addition to the final energy differences, the number of interactions calculated at the high level (average for both conformers) is listed, because it is an important measure of the efficiency of the method.

It is clear that the MFBA energies converge much faster to the benchmark fragmented DFT value. In all four cases, the results are a good approximation of the benchmark energy even when the cutoff is set to zero, which implies that only the covalent pairs are calculated at the high level.

When the interactions above the cutoff distance are neglected, reasonable results can be achieved only with very

Table 2. Energy Difference between Conformers as a Function of Cutoff Distance and Number of Pairs Calculated at the High Level, Calculated by MFBA and Fragmentation with Neglected Long-Distance Interactions[a]

method	cutoff (Å)	$\Delta E(\alpha-\beta)$ (kcal/mol)				number of pairs			
		hydrocarbon	neutral	capped	zwitterion	hydrocarbon	neutral	capped	zwitterion
frag. DFT	−	39.6	7.0	−11.2	105.2	171	171	171	153
neglected	0	26.9	89.0	73.6	27.4	18	18	18	17
	2	34.4	56.7	62.5	117.5	20	31	24	22
	3	41.1	43.7	19.7	129.7	49	47	47	42
	4	39.5	27.0	1.7	118.3	70	65	66	60
	5	39.6	27.5	2.3	112.9	79	70	70	65
	8	39.5	12.8	−7.9	138.0	110	99	101	92
	12	39.5	8.7	−10.5	114.2	138	125	127	116
	16	39.6	7.6	−11.2	116.7	159	146	149	135
	20	39.6	7.2	−11.0	117.0	167	161	162	147
MFBA	0	34.4	2.6	−9.6	114.5	18	18	18	17
	2	32.8	0.3	−9.8	105.3	20	31	24	22
	3	40.7	9.1	−10.0	106.2	49	47	47	42
	4	39.4	8.7	−8.9	106.9	70	65	66	60
	5	39.7	9.1	−9.3	106.1	79	70	70	65
	8	39.5	7.5	−10.9	105.2	110	99	101	92
	12	39.6	7.1	−11.2	105.4	138	125	127	116
	16	39.6	7.1	−11.2	104.4	159	146	149	135
	20	39.6	7.1	−11.2	102.7	167	161	162	147

[a] The results of fragmented DFT calculation including all the interactions are provided as a reference.
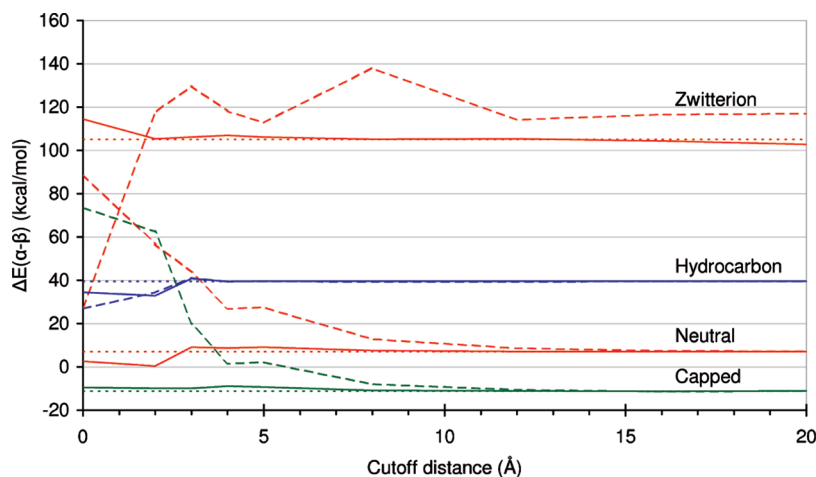
Figure 3. Energy difference between conformers as a function of cutoff distance. For each model (zwitterions, orange; hydrocarbon, blue; neutral, red; capped, green), the MFBA calculations (solid line) are compared to fragmentation scheme neglecting long-distance interactions (dashed line). The benchmark value, fragmented DFT calculation including all the pairwise interaction, is shown as dots.

large cutoff values. This behavior is more pronounced in the polar and charged systems, while in the nonpolar hydrocarbon model, the results are similar to the MFBA values, because the long-range interactions here are very weak. In the zwitterionic model, it is impossible to get good agreement with the benchmark energy when some of the interactions are neglected.

Generally, a cutoff of 5 Å is enough for consistent agreement with fragmented DFT calculation. This cutoff corresponds to about four calculations of pairs per fragment on average. Above 8 Å, the MFBA results are within 0.1 kcal/mol from the benchmark value.

Geometry Optimization. This work introduces the procedure for the calculation of derivatives of the total energy in the MFBA scheme and related methods, which allows one to apply this class of fragment-based methods to geometry optimizations.

We compare three variants of the method with full DFT geometry optimization: Fragmented DFT calculation (the KEM method), MFBA calculation combining DFT and SCC-DFTB, and the linear scaling scheme neglecting the long-distance interactions. The model system, an α-helical hexapeptide, is smaller than in the case of energy calculations. The peptide was divided into six fragments using the procedure described above. To put the method in a test, we use a small cutoff of 3 Å to select the interaction calculated at the higher level, which means that all pairs of fragments not connected by a covalent or hydrogen bond are calculated at the lower level or neglected. The discussion of the cutoff presented above suggests that using this cutoff distance should clearly reveal the differences between the methods.

The following convergence criteria were used: energy difference in the optimization step <0.006 kcal/mol, largest element of the gradient vector <1.2 kcal/mol/Å, and absolute

Multilevel Fragment-Based Approach

J. Chem. Theory Comput., Vol. 6, No. 1, 2010 **97**

Table 3. Comparison of Results of MFBA Geometry Optimization[a]

| | full DFT | MFBA | | |
		DFT	DFTB	neglect int
rmsd (Å)	−	0.04	0.06	0.10
ΔE (kcal/mol)	−	0.06	0.07	0.30
chain end−end distance (Å)	9.79	9.86	9.90	10.00
ALA2−ALA5 side chain distance (Å)	6.12	6.16	6.21	6.18
PHE1−PHE6 side chain distance (Å)	14.24	14.28	14.33	14.35
H-bonds in helix dist (Å)	7.17	7.25	7.29	7.38

[a] All noncovalent interactions in the model hexapeptide were calculated using the method listed in the table. Resulting geometries are compared to the geometry obtained by full DFT calculation by root mean square deviation (rmsd) of the Cartesian coordinates and by the energy difference calculated at the DFT level. Selected intramolecular distances are listed for illustration.

value of the gradient vector <1.2 kcal/mol/Å. The energy decreased smoothly during the optimizations. All four geometries obtained were very similar and the original structure of the peptide was conserved. The quality of the geometries was evaluated in two ways (the results are summarized in Table 3): First, we calculated the root-mean-square deviation (rmsd) between the DFT geometry and the one obtained by the fragment-based method (minimizing rmsd by translation and rotation of the geometries). Second, a full DFT calculation was performed on all the geometries and the energy is compared to that of the DFT geometry. Both the fragmented DFT calculation and MFBA combining DFT with SCC-DFTB yield results very close (0.04 and 0.06 Å, 0.06 and 0.07 kcal/mol) to the reference values. When the noncovalent interactions are neglected, the agreement is worse: rmsd 0.10 Å, energy difference 0.30 kcal/mol.

Conclusions

We have developed a novel fragmentation-based method combining multiple levels of calculations to maximize the accuracy and efficiency of calculations of large molecular systems: the multilevel fragment-based approach (MFBA).

This approach is not limited to the DFT/SCC-DFTB combination presented in this paper. While this combination allows very accurate calculations to be performed on molecules and systems containing hundreds of atoms, the same scheme can be used with both more accurate and more approximate methods.

The MFBA scheme is not limited to two levels of calculation. Multiple distance cutoffs can be used to select from multiple methods for each interaction.

The MFBA method was implemented in our modular framework, Cuby, which allows one to combine different methods. External software is employed to perform the calculations, multiple commercial or free computational packages and programs are supported now and other interfaces can be added easily.

Fragment-based calculations have an important advantage of efficient parallelization, because independent calculations of fragments can be distributed to multiple computers or processors. Our implementation allows this parallelization and uses an internal queue system and sorting of the calculations to use the allocated computational resources as efficiently as possible.

The performance of the MFBA method was demonstrated on model molecules derived from an 18-amino acid peptide. MFBA is superior to the fragmented calculation neglecting long-distance interactions while almost the same scaling and efficiency is conserved. MFBA works well even for charged systems where the scheme neglecting long-distance interactions fails. The accuracy of MFBA calculations is very close to the fragmented calculation using the higher level only that served as a benchmark for our calculations. However, further improvements are required to improve the absolute accuracy of the fragmentation-based method when compared to a full calculation.

We have derived the expressions for the calculation of gradients in the MFBA scheme, which opens applications of the method in geometry optimization and molecular dynamics. The same scheme can be applied to the kernel energy method.

Geometry optimization of a model hexapeptide has shown that even very approximate MFBA calculation can yield a geometry almost identical to that of a fragmented DFT calculation, and both these geometries are very close to the one from full DFT optimization. The agreement is better than in the case of energy calculations and makes MFBA an interesting choice for geometry optimizations of larger molecules.

Appendix

Error Introduced by Interaction of the Caps. The addition of the caps to the fragments is a source of error not only because they may not represent exactly the original electronic structure of the fragment, but also because they interact with each other and with the fragments themselves. A minor part of these interactions is not canceled in the final summation.

To demonstrate this issue, we will analyze the simplest system that can be treated with this fragmentation scheme, a linear system consisting of three fragments. The original system, the capped fragments, and their pairs are schematically depicted in Figure 4. Here, we identify all the interactions between the caps themselves and between the caps and the fragments and between the fragments in the pairs and express the energy of each of these subsystems as the sum of these interactions ΔE_{xy}, energies of the fragments without the caps $E_{f(x)}$ and energies of the caps alone $E_{c(x)}$.

The total summation (eq 1) for this system can be simplified using eq 2 to the following sum of the subsystems (the capped fragments and their pairs):

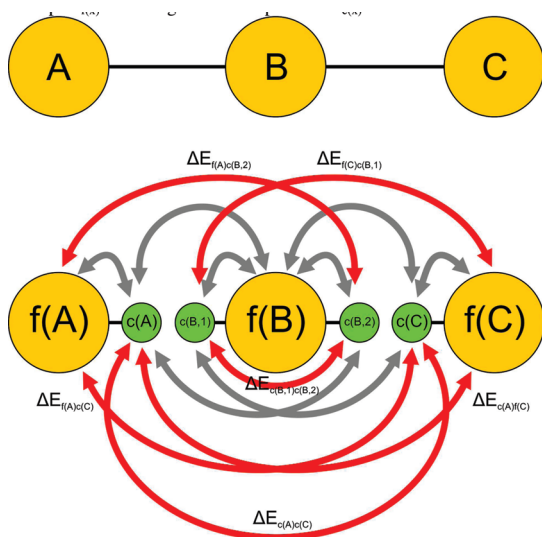$$E = E_{AB} + E_{BC} + E_{AC} − E_A − E_B − E_C \qquad (6)$$

Figure 4. Schematic representation of a system consisting of three fragments, before and after introduction of the caps. Interactions between the caps and other caps or fragments that are present in the calculation are shown, and those that are present in the final energy expression are highlighted red and labeled.

By substituting the subsystem energies by the sums of the contributions outlined above and simplifying the expression, we obtain the total energy as

$$
\begin{aligned}
E = {} & E_{f(A)} + E_{f(B)} + E_{f(C)} + \Delta E_{f(A)f(B)} + \Delta E_{f(B)f(C)} + \\
& \Delta E_{f(A)f(C)} - \Delta E_{c(B,1)c(B,2)} + \Delta E_{c(A)c(C)} + \Delta E_{f(A)c(C)} + \\
& \Delta E_{c(C)f(A)} + \Delta E_{f(A)c(B,2)} + \Delta E_{f(C)c(B,1)} \quad (7)
\end{aligned}
$$

while the desired total energy is only the sum of energies of the fragments and their interactions

$$
E = E_{f(A)} + E_{f(B)} + E_{f(C)} + \Delta E_{f(A)f(B)} + \Delta E_{f(B)f(C)} + \Delta E_{f(A)f(C)} \quad (8)
$$

and the remaining terms (eq 7 minus eq 8) are the artifacts introduced by interactions of the caps.

For this reason, the nature of the caps should be chosen in a way that these interactions are minimized. We use the smallest possible caps, hydrogen atoms. Another factor that affects this error is the size of the fragments, which determines also the distance between the caps. When larger fragments are used, this error will not be as pronounced as when the caps are close to each other and to the other fragment in a pair.

References

(1) Saebo, S.; Pulay, P. *Annu. Rev. Phys. Chem.* **1993**, *44*, 213–236.

(2) Wu, S. Y.; Jayanthi, C. S. *Phys. Rep.* **2002**, *358*, 1–74.

(3) Exner, T. E.; Mezey, P. G. *J. Phys. Chem. A* **2002**, *106*, 11791–11800.

(4) Exner, T. E.; Mezey, P. G. *J. Comput. Chem.* **2003**, *24*, 1980–1986.

(5) Fedorov, D. G.; Kitaura, K. *J. Chem. Phys.* **2004**, *121*, 2483–2490.

(6) Fedorov, D. G.; Kitaura, K. *Chem. Phys. Lett.* **2004**, *389*, 129–134.

(7) Fedorov, D. G.; Kitaura, K. *J. Chem. Phys.* **2004**, *120*, 6832–6840.

(8) Kitaura, K.; Ikeo, E.; Asada, T.; Nakano, T.; Uebayasi, M. *Chem. Phys. Lett.* **1999**, *313*, 701–706.

(9) Nakano, T.; Kaminuma, T.; Sato, T.; Fukuzawa, K.; Akiyama, Y.; Uebayasi, M.; Kitaura, K. *Chem. Phys. Lett.* **2002**, *351*, 475–480.

(10) Babu, K.; Gadre, S. R. *J. Comput. Chem.* **2003**, *24*, 484–495.

(11) Gadre, S. R.; Shirsat, R. N.; Limaye, A. C. *J. Phys. Chem.* **1994**, *98*, 9165–9169.

(12) Gadre, S. R.; Ganesh, V. *J. Theor. Comput. Chem.* **2006**, *5*, 835–855.

(13) Ganesh, V.; Dongare, R. K.; Balanarayan, P.; Gadre, S. R. *J. Chem. Phys.* **2006**, *125*, 104109.

(14) Li, S. H.; Li, W.; Fang, T. *J. Am. Chem. Soc.* **2005**, *127*, 7215–7226.

(15) Zhang, D. W.; Zhang, J. Z. H. *J. Chem. Phys.* **2003**, *119*, 3599–3605.

(16) Zhang, D. W.; Xiang, Y.; Zhang, J. Z. H. *J. Phys. Chem. B* **2003**, *107*, 12039–12041.

(17) Huang, L.; Massa, L.; Karle, J. *Proc. Natl. Acad. Sci. U.S.A.* **2008**, *105*, 1849–1854.

(18) Huang, L. L.; Massa, L.; Karle, J. *Int. J. Quantum Chem.* **2005**, *103*, 808–817.

(19) Li, W.; Li, S. H.; Jiang, Y. S. *J. Phys. Chem. A* **2007**, *111*, 2193–2199.

(20) Collins, M. A.; Deev, V. A *J. Chem. Phys.* **2006**, *125*, 104104.

(21) Deev, V.; Collins, M. A. *J. Chem. Phys.* **2005**, *122*, 154102.

(22) Bettens, R. P. A.; Lee, A. M. *J. Phys. Chem. A* **2006**, *110*, 8777–8785.

(23) Elstner, M.; Porezag, D.; Jungnickel, G.; Elsner, J.; Haugk, M.; Frauenheim, T.; Suhai, S.; Seifert, G. *Phys. Rev. B* **1998**, *58*, 7260–7268.

(24) Hua, W. J.; Fang, T.; Li, W.; Yu, J. G.; Li, S. H. *J. Phys. Chem. A* **2008**, *112*, 10864–10872.

(25) Rahalkar, A. P.; Ganesh, V.; Gadre, S. R. *J. Chem. Phys.* **2008**, *129*, 234101.

(26) Gao, A. M.; Zhang, D. W.; Zhang, J. Z. H.; Zhang, Y. K. *Chem. Phys. Lett.* **2004**, *394*, 293–297.

(27) Gadre, S. R.; Shirsat, R. N.; Limaye, A. C. *J. Phys. Chem.* **1994**, *98*, 9165–9169.

(28) Mueller, T. J.; Roy, S.; Zhao, W.; Maass, A.; Reith, D. *Fluid Phase Equilib.* **2008**, *274*, 27–35.

(29) Lin, H.; Truhlar, D. G. *Theor. Chem. Acc.* **2007**, *117*, 185–199.

(30) Senn, H. M.; Thiel, W. *Angew. Chem., Int. Ed.* **2009**, *48*, 1198–1229.

(31) Li, H.; Li, W.; Li, S. H.; Ma, J. *J. Phys. Chem. B* **2008**, *112*, 7061–7070.

(32) Soderhjelm, P.; Ryde, U. *J. Phys. Chem. A* **2009**, *113*, 617–627.

(33) Fedorov, D. G.; Ishida, T.; Kitaura, K. *J. Phys. Chem. A* **2005**, *109*, 2638–2646.

Multilevel Fragment-Based Approach

J. Chem. Theory Comput., Vol. 6, No. 1, 2010 **99**

(34) Dapprich, S.; Komaromi, I.; Byun, K. S.; Morokuma, K.; Frisch, M. J. *THEOCHEM* **1999**, *462*, 1–21.

(35) Ruby programming language. www.ruby-lang.org (accessed Aug 15, 2009).

(36) Case, D. A.; Cheatham, T. E.; Darden, T.; Gohlke, H.; Luo, R.; Merz, K. M.; Onufriev, A.; Simmerling, C.; Wang, B.; Woods, R. J. *J. Comput. Chem.* **2005**, *26*, 1668–1688.

(37) Köster, A. M.; Calaminici, P.; Casida, M. E.; Flores-Moreno, R.; Geudtner, G.; Goursot, A.; Heine, T.; Ipatov, A.; Janetzko, F.; del Campo, J. M.; Patchkovskij, S.; Reveles, J. U.; Salahub, D. R.; Vela, A. *deMon2k*; 2006 (http://www.demon-software-.com/public_html/program.html).

(38) Aradi, B.; Hourahine, B.; Frauenheim, T. *J. Phys. Chem. A* **2007**, *111*, 5678–5684.

(39) Frisch, M. J.; Trucks, G. W.; Schlegel, H. B.; Scuseria, G. E.; Robb, M. A.; Cheeseman, J. R.; Montgomery, J.; Vreven, T.; Kudin, K. N.; Burant, J. C.; Millam, J. M.; Iyengar, S. S.; Tomasi, J.; Barone, V.; Mennucci, B.; Cossi, M.; Scalmani, G.; Rega, N.; Petersson, G. A.; Nakatsuji, H.; Hada, M.; Ehara, M.; Toyota, K.; Fukuda, R.; Hasegawa, J.; Ishida, M.; Nakajima, T.; Honda, Y.; Kitao, O.; Nakai, H.; Klene, M.; Li, X.; Knox, J. E.; Hratchian, H. P.; Cross, J. B.; Bakken, V.; Adamo, C.; Jaramillo, J.; Gomperts, R.; Stratmann, R. E.; Yazyev, O.; Austin, A. J.; Cammi, R.; Pomelli, C.; Ochterski, J. W.; Ayala, P. Y.; Morokuma, K.; Voth, G. A.; Salvador, P.; Dannenberg, J. J.; Zakrzewski, V. G.; Dapprich, S.; Daniels, A. D.; Strain, M. C.; Farkas, O.; Malick, D. K.; Rabuck, A. D.; Raghavachari, K.; Foresman, J. B.; Ortiz, J. V.; Cui, Q.; Baboul, A. G.; Clifford, S.; Cioslowski, J.; Stefanov, B. B.; Liu, G.; Liashenko, A.; Piskorz, P.; Komaromi, I.; Martin, R. L.; Fox, D. J.; Keith, T.; Al-Laham, M. A.; Peng, C. Y.; Nanayakkara, A.; Challacombe, M.; Gill, P. M. W.; Johnson, B.; Chen, W.; Wong, M. W.; Gonzalez, C.; Pople, J. A. *Gaussian 03, Revision C.02*; 2004.

(40) Thiel, W. *MND099*; Max-Planck-Institut für Kohlenforschung: Mülheim, Germany, 1999.

(41) Stewart, J. P. *MOPAC2009*; Stewart Computational Chemistry: Colorado Springs, CO, 2008.

(42) Ahlrichs, R.; Bar, M.; Haser, M.; Horn, H.; Kolmel, C. *Chem. Phys. Lett.* **1989**, *162*, 165–169.

(43) Fedorov, D. G.; Olson, R. M.; Kitaura, K.; Gordon, M. S.; Koseki, S. *J. Comput. Chem.* **2004**, *25*, 872–880.

(44) Tao, J. M.; Perdew, J. P.; Staroverov, V. N.; Scuseria, G. E. *Phys. Rev. Lett.* **2003**, *91*, 146401.

(45) Schafer, A.; Huber, C.; Ahlrichs, R. *J. Chem. Phys.* **1994**, *100*, 5829–5835.

(46) Eichkorn, K.; Treutler, O.; Ohm, H.; Haser, M.; Ahlrichs, R. *Chem. Phys. Lett.* **1995**, *240*, 283–289.

(47) Eichkorn, K.; Weigend, F.; Treutler, O.; Ahlrichs, R. *Theor. Chem. Acc.* **1997**, *97*, 119–124.

(48) Elstner, M.; Hobza, P.; Frauenheim, T.; Suhai, S.; Kaxiras, E. *J. Chem. Phys.* **2001**, *114*, 5149–5155.

(49) Srinivasan, R. *Ribosome*; John Hopkins University: Baltimore, MD, 1997.

CT900413S

JCTC Journal of Chemical Theory and Computation

An Atomic Counterpoise Method for Estimating Inter- and Intramolecular Basis Set Superposition Errors

Frank Jensen

Department of Chemistry, University of Aarhus Langelandsgade 140,
DK-8000 Aarhus, Denmark

Received August 16, 2009

Abstract: An atomic counterpoise method is proposed to calculate estimates of inter- and intramolecular basis set superposition errors. The method estimates the basis set superposition error as a sum of atomic contributions and can be applied for both independent particle and electron correlation models. It is shown that the atomic counterpoise method provides results very similar to the molecular counterpoise method for intermolecular basis set superposition errors at both the HF and MP2 levels of theory with a sequence of increasingly larger basis sets. The advantage of the atomic counterpoise method is that it can be applied with equal ease to estimate intramolecular basis set superposition errors, for which few other methods exist. The atomic counterpoise method is computationally quite efficient, requiring typically double the amount of computer time as required for calculating the uncorrected energy.

Introduction

The calculation of weak intermolecular interactions by electronic structure methods has long been known to suffer from a systematic overestimation due to the incomplete basis sets used in practical calculations.[1−3] The reason for the overestimation is that each fragment in a complex can partly compensate for basis set incompleteness by utilizing basis functions on the other fragment(s), which commonly is denoted as basis set superposition error (BSSE). The counterpoise (CP) correction[4−8] is the most common method for estimating BSSE, while other approaches,[9,10] such as the chemical Hamiltonian approach,[11−14] has been less used.

For a complex consisting of two fragments, the CP correction is calculated by subtracting the fragment energy calculated in the regular basis set from the fragment energy calculated in the full basis set for the whole complex. While it is recognized that this is only an estimate of the BSSE, it has been demonstrated that the CP-corrected complexation energy converges more regular toward the basis set limiting value than the directly calculated value.[15−17]

While BSSE primarily has been associated with the systematic overestimation of the stability of intermolecular complexes, it has been recognized that intramolecular BSSE is a component of the change in, for example, relative conformational energies of a single molecule with respect

to changes in basis set.[18−20] The CP method has, in a few cases, been used to estimate intramolecular BSSE by dividing the molecule into nonbonded fragments and saturating dangling bonds, but the partitioning into fragments is nonunique, neglects the BSSE from the removed moiety, and requires involvement of the user.[21−24] Recently Asturiol et al. have attributed the artificial nonplanarity of aromatic systems at the MP2 level with certain Pople-type basis sets to intramolecular BSSE and have used a fragment approach to perform a CP correction.[25,26] Balabin has also used a fragment-based approach for estimating intramolecular BSSE in different conformations of small alkanes.[27]

The accurate calculation of conformational energies of systems with up to a few hundred atoms, like small peptides, is important for understanding, for example, biological recognition and for calibration of force field methods.[28] The relative energies of conformations with different degrees of compactness are very sensitive to intramolecular BSSE,[29−33] and there is clearly a need for methods capable of reducing this effect. The developments of explicitly correlated (F12) methods has the promise of calculating accurate correlation energies with basis sets of only triple-ζ quality,[34,35] and developments in linear scaling techniques will allow these methods to be applied to reasonably large system in the near future.[36] In such cases, the BSSE is likely to become a limiting factor for calculating accurate energies. In the present

An Atomic Counterpoise Method

J. Chem. Theory Comput., Vol. 6, No. 1, 2010 **101**

paper, we show that it is possible to define an atomic version of the CP correction that provides results similar to the well-known molecular CP for nonbonded fragments and that it can be used also for estimating intramolecular BSSE.

Computational Details

For a bimolecular complex A−B, the molecular counterpoise (MCP) correction is defined in eq 1.

$$\Delta E_{MCP} = E_A(Bas_A) - E_A(Bas_{AB}) + E_B(Bas_B) - E_B(Bas_{AB}) \quad (1)$$

Here $E_A(Bas_A)$ indicates the energy of fragment A in the regular basis set Bas_A, while $E_A(Bas_{AB})$ indicates the energy of fragment A in the combined basis set for both fragments and similar for fragment B.

The atomic counterpoise (ACP) correction is defined in eq 2:

$$\Delta E_{ACP} = \sum_A^{atoms} E_A(Bas_A) - E_A(Bas_{AS}) \quad (2)$$

Here $E_A(Bas_A)$ indicates the energy of atom A in the regular basis set Bas_A, while $E_A(Bas_{AS})$ indicates the energy of atom A in a subset of the full basis set, which always includes the regular basis function on A, and the subscript S indicates the additional subset of basis functions for atom A. In the intermolecular case, where the two fragments are not covalently bonded, the subset includes basis functions on all the atoms in the *other* fragment, but basis functions on atoms within the *same* fragment are excluded. In the intramolecular case, the subset includes basis functions on atoms separated from atom A in terms of bonding and distance, as discussed in the next sections. For the intermolecular case with fragments beyond a certain size, the ACP can be used to include both intra- and intermolecular BSSE. Galano and Alvarez-Idaboy have reported a very similar method denoted CP[aa] where Bas_{AS} includes all basis functions for the whole system,[37] and this is a special case of the current ACP. They used it for calculating intermolecular BSSE where the CP[aa] for the fragments were subtracted from the CP[aa] of the complex to provide an alternative to the conventional MCP that includes differences in intramolecular BSSE in each of the fragments. For calculating intramolecular BSSE, they partition the molecule into fragments and treat these as in the intermolecular case.

All calculations have been done using the Gaussian-03 program package[38] using unrestricted wave functions for open-shell species. The spin contamination for all atomic calculations is completely negligible. The geometries of all the systems are provided as Supporting Information.

Results and Discussion

Table 1 shows the molecular and ACP corrections for a T-shaped complex of two N_2 molecules (shortest intermolecular distance between atoms is 3.55 Å) as a function of increasingly larger basis sets of the correlation consistent type[39,40] at the HF and MP2 levels of theory. The MCP correction is a sum of two contributions for each of the two

Table 1. Molecular and ACP Corrections for a T-Shaped Complex between Two N_2 Molecules (kJ/mol)

basis set	HF		MP2	
	MCP	ACP	MCP	ACP
cc-pVDZ	1.32	1.18	1.71	1.55
cc-pVTZ	0.54	0.43	1.10	0.69
cc-pVQZ	0.25	0.15	0.56	0.28
cc-pV5Z	0.15	0.06	0.36	0.11
aug-cc-pVDZ	0.32	0.47	1.12	0.88
aug-cc-pVTZ	0.22	0.21	0.75	0.57
aug-cc-pVQZ	0.07	0.09	0.37	0.33
aug-cc-pV5Z	0.01	0.01	0.12	0.12

Table 2. Molecular and ACP Corrections for a Parallel Displaced Complex between Two Ethylene Molecules (kJ/mol)

Basis set	HF		MP2	
	MCP	ACP	MCP	ACP
cc-pVDZ	1.68	1.64	2.66	2.54
cc-pVTZ	0.60	0.48	1.20	0.97
cc-pVQZ	0.24	0.14	0.53	0.39
aug-cc-pVDZ	0.93	0.92	3.25	2.15
aug-cc-pVTZ	0.18	0.41	1.11	1.33
aug-cc-pVQZ	0.06	0.14	0.49	0.66

N_2 fragments, each employing all the basis functions. The ACP correction is a sum of four contributions for each of the four N atoms, each employing basis functions for three atoms, i.e., neglecting the basis functions on the directly bonded atom. It is seen that the two different methods of estimating the BSSE provide similar results and that they reduce to zero as the basis set approaches completeness. Table 2 shows similar results for two ethylene molecules in a face-to-face parallel displaced geometry with a shortest intermolecular distance between carbon atoms of 3.74 Å.

The benzene dimer has been a popular test case for evaluating the performance of different theoretical methods.[41,42] Table 3 shows the MCP and ACP corrections for a sandwich (S) and a T-shaped benzene−dimer complex, where the distance between the centers of the two ring systems is 3.6 and 5.0 Å, respectively. It is again seen that the ACP mirrors the MCP results quite closely at both the HF and MP2 levels of theory. The results in Tables 1−3, thus, show that the familiar MCP estimate of the BSSE can be reproduced quite accurately as a sum of atomic contributions, with the exact difference between the two estimates depending on the system and the basis set.

The results in Tables 1−3 have been obtained using atomic ground states for the ACP calculations, i.e., a triplet state for carbon and a quartet state for nitrogen. We have tested the sensitivity of the results to other choices, like a singlet state for carbon and a doublet state for nitrogen. For the N_2−dimer system (Table 1), the MP2 ACP result with the cc-pVDZ basis set changes from 1.55 to 1.74 kJ/mol when using the lowest energy doublet state as the atomic reference state instead of a quartet state, and both values can be compared to the MCP result of 1.71 kJ/mol. A significantly larger value of 4.95 kJ/mol is obtained if an excited doublet state corresponding to a $(2p_x)^2(2p_y)^1$ electron configuration is employed.

Table 3. Molecular and ACP corrections for a Sandwich (S) and a T-shaped Complex of Two Benzene Molecules (kJ/mol)

| | HF | | | | MP2 | | | |
| | S-complex | | T-complex | | S-complex | | T-complex | |
basis set	MCP	ACP	MCP	ACP	MCP	ACP	MCP	ACP
6-31G**	9.3	13.5	3.3	9.7	11.6	16.4	7.3	13.1
cc-pVDZ	5.0	7.0	2.7	4.3	8.7	10.4	6.8	7.4
cc-pVTZ	1.9	2.2	1.1	1.4	4.9	4.6	3.3	2.9
cc-pVQZ	0.8	0.7	0.5	0.4	2.2	2.1	1.6	1.3
6-31++G**	2.4	4.9	1.5	3.6	15.6	21.3	13.2	14.3
aug-cc-pVDZ	4.9	4.3	4.7	3.6	13.5	10.2	13.0	9.3
aug-cc-pVTZ	0.9	2.1	0.8	1.5	5.5	6.8	5.2	5.3
aug-cc-pVQZ	0.2	0.7	0.2	0.5	1.9	3.5	1.7	2.5

For the S-shaped benzene−dimer complex, the MP2 ACP results with the cc-pVDZ basis set change from 10.4 to 12.6 kJ/mol, if the lowest (open-shell) singlet state is used as the atomic reference state for carbon instead of a triplet state, while the corresponding results for the T-shaped complex are 7.4 and 8.5 kJ/mol. These values can be compared to the MCP results of 8.7 and 6.8 kJ/mol, respectively, for the two complexes. The ACP differences, due to using a singlet rather than a triplet atomic reference state, diminish for larger basis sets, and for the aug-cc-pVTZ basis set, for example, the values for the S- and T-shaped complexes change from 6.8 to 7.1 kJ/mol and from 5.3 to 5.5 kJ/mol, respectively.

These results show, as expected, that the ACP estimate of the BSSE increases as the electronic distribution of the atomic reference state becomes more and more diffuse. The premise of the ACP method is, thus, that the (local) electron distribution in the molecule resembles the distribution in the atomic reference state in terms of spatially diffuseness.

For estimating intermolecular BSSE, the ACP procedure offers little advantage over the corresponding molecular version, although the ACP method may be computationally less demanding for large fragments (see the Computational Considerations Section). For estimating intramolecular BSSE, however, the MCP procedure requires an ad hoc definition of an equivalent intermolecular reference system, which requires user involvement, is nonunique, and only recovers part of the BSSE.[21−24] The ACP method provides a common reference system for all molecules but requires the definition of atomic reference states and the subset of basis functions to be included in the CP calculations. The interpretation of BSSE in an intermolecular complex, as an artifact due to basis functions nearby in space but not directly bonded, suggests that the subspace in an intramolecular case should be limited to atoms sufficiently far removed in terms of bonding to effectively be considered as nonbonded atoms. This is in analogy to the situation in force field methods, where the nonbonded energy is only calculated for atoms that are at least three bonds apart, and contributions from atom pairs that are separated by exactly three bonds are sometimes reduced.[43] The number of bonds between atoms, which in an ACP sense is considered nonbonded, is therefore a free parameter which can be used to tune the performance.

While the magnitude of the intermolecular BSSE can be assessed by a MCP calculation, the magnitude of the corresponding intramolecular BSSE is more difficult to quantify. The commonly employed method consists of
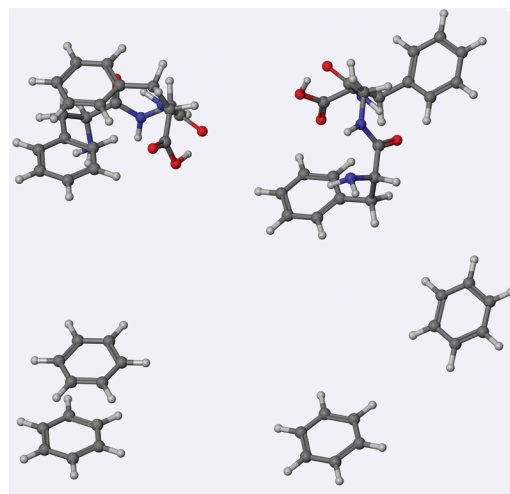
Figure 1. Folded and extended conformations of the FGF tripeptide and of the corresponding benzene dimer model systems used for calculating the results shown in Table 4.

evaluating the MCP for a suitable intermolecular model system.[21−24] Valdez et al. have estimated the intramolecular BSSE in folded and extended conformations of the phenylalanine−glycine−phenylalanine (FGF) tripeptide by partitioning the system into two benzene molecules with the same geometries, as shown in Figure 1.[23] The aug′-cc-pVDZ (aug′ indicates that diffuse functions are omitted for hydrogen) HF and MP2 MCP and ACP results using one to eight bonds for defining the subspace in eq 2 are shown in Table 4. As the model system neglects all atoms in the peptide backbone, the true intramolecular BSSE for each conformation will be significantly larger than that of the MCP estimate. However, the backbone structure of the two conformations is similar, and the difference in the MCP between the two conformations is, thus, expected to provide a reasonably accurate estimate of the difference in the intramolecular BSSE. The results in Table 4 show that the ACP estimate of the difference in intramolecular BSSE is relatively insensitive to the exact value of the number of bonds for defining the subspace in eq 2. The ACP(1) method is equivalent to the CP[aa] method of Galano and Alvarez-Idaboy[37] and appears to underestimate the BSSE difference, but all of the ACP(2)-ACP(8) results provide useful estimates of the difference in intramolecular BSSE between the two conformations. Given the uncertainty in the MCP estimate

An Atomic Counterpoise Method

J. Chem. Theory Comput., Vol. 6, No. 1, 2010 **103**

Table 4. Molecular and ACP Corrections for the Di-Benzene Complexes and the FGF Tripeptide Conformations in Figure 1 with the aug′-cc-pVDZ Basis Set (kJ/mol)[a]

	HF			MP2		
	folded	extended	Δ	folded	extended	Δ
MCP	4.3	0.2	4.1	13.7	0.8	12.9
ACP(1)	88.5	86.9	1.6	446.9	440.3	6.6
ACP(2)	58.0	54.8	3.2	176.1	164.4	11.7
ACP(3)	39.5	34.5	5.0	96.5	80.9	15.6
ACP(4)	26.6	20.1	6.5	59.6	42.3	17.3
ACP(5)	20.6	14.1	6.5	44.9	28.7	16.2
ACP(6)	16.3	10.3	6.0	35.2	20.3	14.9
ACP(7)	13.5	7.6	5.9	29.6	15.1	14.5
ACP(8)	12.2	6.4	5.8	26.7	12.8	13.9

[a] In the ACP(n) notation, n indicates the number of bonds between atoms for defining the basis set subspace in eq 2.

of the intramolecular BSSE, it is difficult to objectively select a unique lower bonded criterion based on the results in Table 4.

Another method for estimating the intramolecular BSSE is to compare the result with a given basis set to the basis set limiting result, but data for systems containing $50-100$ atoms, where intramolecular BSSE can be significant, is scarce. We have, in recent work, investigated the performance of conventional and local MP2 methods for predicting the energy difference between peptide conformations, including helical and extended structures of polyalanines with four, six, and eight amino acids (42, 62, and 82 atoms, respectively), as shown in Figure 2.[44] The local MP2 method calculates electron correlation using localized occupied orbitals, and a restricted set of virtual orbitals which significantly reduces the intramolecular BSSE compared to canonical MP2.[45-47] Table 5 shows the energy differences between the two conformations for the three peptides with the aug′-cc-pVDZ and aug′-cc-pVTZ basis sets. The basis set limiting value obtained by extrapolating aug′-cc-pVTZ and aug′-cc-pVQZ results[44] for the octaalanine peptide is $60-64$ kJ/mol, which the LMP2 method mirrors closely with both the aug′-cc-pVDZ and aug′-cc-pVTZ basis sets. The canonical MP2 method, on the other hand, overestimates the stability of the helical structure by ~30 and ~20 kJ/mol, respectively, which was attributed to differences in intramolecular BSSE. For the tetra- and hexa-alanine peptides, the MP2 and LMP2 results are much closer, which suggests that the BSSE almost cancels between the two conformations for these systems.

If the difference between the results from the local and canonical MP2 methods is taken as a measure of the difference in intramolecular BSSE, then this allows another probe of how many bonds atoms must be separated in order to be considered nonbonded in an ACP sense. Table 5 shows the difference in ACP calculated for the two conformations of the polyalanine peptides using different bond separations for defining the subspace in eq 2. The ΔACP values do not depend strongly on which bond criterion is used, but the best agreement is obtained using a four-bond criterion. The ACP(1) result, which is equivalent to the CP[aa] method, again appears to underestimate the difference in BSSE. It is worth noting that the ACP(4) results mirror closely the LMP2−MP2

differences for all three systems, including the small positive and negative values for the tetra- and hexa-alanines, and for both basis sets.

The two different independent methods for calibration, using either a suitable intermolecular model system or using the difference between local and canonical MP2 results, suggest that an ACP-type correction using a lower bonded criterion for defining the nonbonded subspace in eq 2 can provide a useful estimate of the intramolecular BSSE. From the limited results in the present paper, a value around four bonds appears to be a heuristic choice, at least for estimating differential BSSE between different conformations, but further studies may reveal a different optimum choice. The atomic reference state is another possible variable, but the results in Tables 1−5 suggest that ground atomic reference states can provide useful estimates of the BSSE for even quite polar systems, like poly peptides. The optimum choice of atomic reference states for charged systems, especially with strongly localized charges, will require careful calibration studies.

Computational Considerations

The MCP method requires calculations for each of the two fragments in a dimolecular complex, using all the basis functions for the whole complex, typically doubles the computational effort compared to calculating the energy of the complex and the two fragments. The ACP method requires N_{atom} calculations, each using a large fraction of all the basis functions for the whole system, which taken at face value would indicate a large computational overhead, especially if correlated methods are used. There are, however, a number of features that significantly reduce the computational cost:

1. Each calculation has only one atom and, thus, only a small number of occupied orbitals.
2. Hydrogen has only one electron and, therefore, no electron correlation energy.
3. If only the valence electrons are correlated, as is often the case, then the number of correlating electrons for non-hydrogen atoms is small.
4. Although each calculation has a large number of basis functions, many contribute only very little to the final results.

The latter point will automatically reduce the computational effort, if efficient integral-screening techniques are employed.[48] The computational time may also be reduced by a priori truncating the basis set based on a distance criterion. Figure 3 shows the magnitude of the HF and the MP2 ACP(4) corrections for the helical and the extended conformations of the octa-alanine peptide, as a function of a cutoff distance beyond which basis functions are excluded in the ACP calculations. With the aug′-cc-pVDZ basis set, the MP2 ACP(4) correction is calculated to within 0.5 kJ/mol of the limiting value with a cutoff distance of 10 Å (the dimensions of the two conformations are ~20 and ~30 Å, respectively). Given that the ACP only provides an estimate of the BSSE, there is little reason to refine the numerical value to an accuracy better than ~0.5 kJ/mol. The 10 Å cutoff limit corresponds qualitatively to a distance where the maximum overlap between basis functions on different atoms
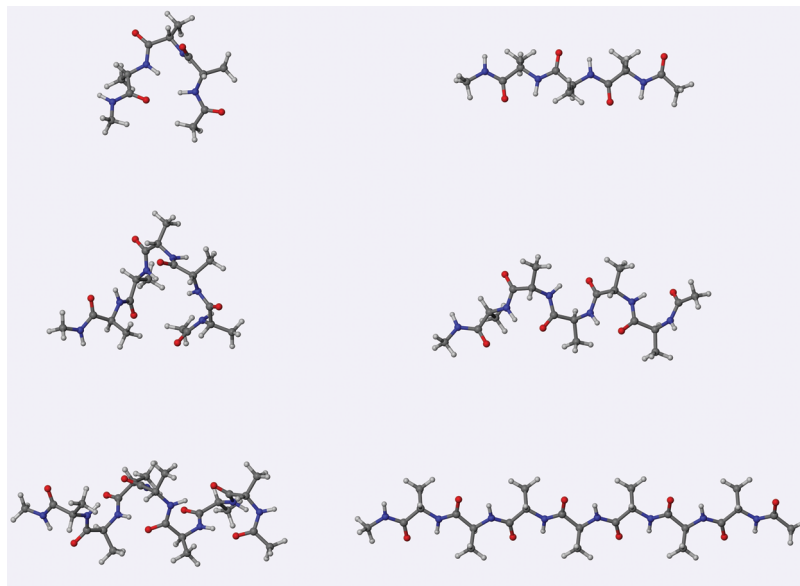
Figure 2. Helical and extended conformations of the tetra-, hexa-, and octa-alanine peptides used for calculating the results in Table 5.

Table 5. MP2 Energy Differences between the Extended and Helical Conformations of Tetra-, Hexa-, and Octa-Alanine Peptides Shown in Figure 2 as a Function of Basis Set (kJ/mol)[a]

		aug′-cc-pVDZ	aug′-cc-pVTZ	extrapolated
tetra-alanine	MP2	12.6	15.7	18.0
	LMP2	18.2	18.6	19.1
	LMP2−MP2	5.6	2.9	1.1
	ΔACP(1)	2.0	2.7	
	ΔACP(2)	3.1	1.4	
	ΔACP(3)	3.5	2.1	
	ΔACP(4)	4.3	3.0	
	ΔACP(5)	3.9	3.3	
	ΔACP(6)	4.4	3.1	
hexa-alanine	MP2	47.3	45.6	45.6
	LMP2	46.2	44.3	45.8
	LMP2−MP2	−1.1	−1.3	0.2
	ΔACP(1)	−0.4		
	ΔACP(2)	0.4		
	ΔACP(3)	1.3	−0.3	
	ΔACP(4)	−1.8	−1.4	
	ΔACP(5)	−0.6	−1.6	
	ΔACP(6)	2.0	1.1	
octa-alanine	MP2	−94.5	−84.0	−64.0
	LMP2	−60.1	−63.2	−60.2
	LMP2−MP2	34.4	20.8	3.8
	ΔACP(1)	17.5		
	ΔACP(2)	26.9		
	ΔACP(3)	32.0	15.4	
	ΔACP(4)	33.8	20.4	
	ΔACP(5)	27.1	20.3	
	ΔACP(6)	25.1	17.3	

[a] ΔACP(n) indicates the difference in ACP corrections between the helical and extended conformations, where n is the number of bonds between atoms for defining the basis set subspace in eq 2. Extrapolated indicates results extrapolated to the basis set limit from aug′-cc-pVTZ and aug′-cc-pVQZ results.[44]

drops below a certain critical value and will, thus, be smaller for basis sets without diffuse functions. For the cc-pVDZ basis set, the ACP(4) results (not shown) stabilize to the same level of accuracy at a cutoff distance of 7 Å, while basis sets employing multiple diffuse functions may require a cutoff distance larger than 10 Å.

The use of a lower bonded and an upper distance criterion reduces the number of basis functions for each ACP calculation, and the latter is especially effective for large systems. The distance criterion means that the overall computational effort for calculating the ACP scales linearly with the number of atoms in the system and is, of course, trivially parallelizable. For the benzene dimer, the computational time for an ACP calculation is slightly less than the time required for the MCP calculation. For the helical conformation of the octa-alanine peptide, the total computational time for the MP2 ACP(4) calculations is roughly twice that of the time for calculating the MP2 energy with
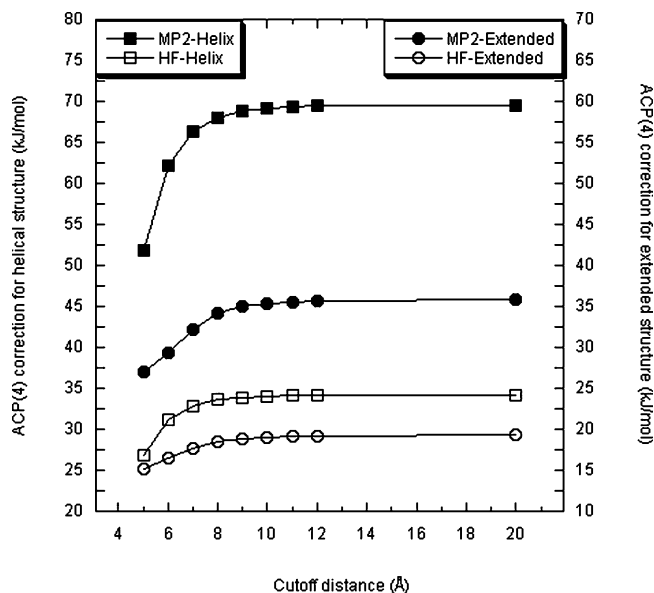
An Atomic Counterpoise Method

J. Chem. Theory Comput., Vol. 6, No. 1, 2010 **105**

Figure 3. HF and MP2 ACP(4) results (kJ/mol) for the helical and the extended conformations of the octa-alanine peptide as a functions of cutoff distance (Å).

the aug′-cc-pVDZ basis set, while the ACP(4) calculations only require one-third of the time for the MP2 energy for the extended conformation, due to the larger number of basis functions discarded by the distance criterion. For typical applications, the computational time for performing such a posterori ACP calculations is, thus, comparable to the time required for generating the BSSE uncorrected results.

We note that it is possible to improve the computational efficiency if the ACP corrections are generated as an integral part of the molecular energy calculation, rather than as an a posterori correction. In the current ACP procedure, a significant fraction of all the integrals over basis functions is regenerated for each atomic calculation, however, all of these integrals are also required for the molecular energy calculation. If the ACP calculations are performed at the same time as the molecular energy is calculated, then the overhead due to recalculating integrals N_{atom} times will be removed. This suggests that the ACP method provides a cost-efficient way of estimating BSSE, especially for intramolecular systems where few other methods are available.

Summary

We propose an atomic counterpoise (ACP) method, where the BSSE is estimated as a sum of atomic contributions, calculated as differences in energy in a regular basis set and in a subset consisting of basis functions on atoms separated by a minimum number of bonds. The computational efficiency can be improved by omitting functions on atoms separated by more than ∼7 or ∼10 Å for regular and augmented basis sets, respectively, without affecting the final results. Atomic ground states are used for all ACP calculations, but the results are not overly sensitive to using alternative atomic reference states. Differences in ACP values are also relatively insensitive to the exact value of the lower bonded criterion used, which indicates that the majority of

the difference in intramolecular BSSE between conformations is due to atoms remote in terms of bonding but close in physical space. From the (limited) results in the present paper, a value of four as the minimum bond criterion for including basis functions in the CP correction appears to be a heuristic choice, but further work may yield a different optimum value.

The ACP provides a method for estimating BSSE, which for intermolecular systems mirrors the results obtained with the molecular counterpoise method but can be applied with equal ease to estimate intramolecular BSSE as well. The ACP method is shown to work at both the HF and MP2 levels of theory, and it is likely that it will be equally useful for density functional and higher level electron correlation methods. The calibration has been done by comparing the intermolecular model systems and to the local MP2 results, which reduces the BSSE compared to canonical MP2. The use of local correlation methods for estimating BSSE requires a careful consideration of the parameters used for defining the local correlation space, while the ACP method can be used for both correlated and independent particle models. The ACP may, thus, be useful for estimating intramolecular BSSE for systems where elimination of the BSSE by enlarging the basis set is infeasible.

The ACP method, except ACP(1), will require ad hoc adjustments for systems where the bonding pattern is ambiguous, like transition structures and perhaps hydrogen-bonded systems, a feature it shares with the molecular counterpoise method. For charged systems, the ACP method may need to be modified by utilizing alternative atomic reference states for at least some of the atoms, and this will need to be investigated by careful calibration studies. Finally, we note that it is straightforward to define derivatives of the ACP corrected energy,[49] which should be useful for reducing artifacts in molecular structures due to intramolecular BSSE.

Supporting Information Available: Tables showing the molecular geometries used. This material is available free of charge via the Internet at http://pubs.acs.org.

References

(1) Chen, F.; Davidson, E. R. *Chem. Phys. Lett.* **2002**, *360*, 99.

(2) Tzeli, D.; Mavridis, A.; Xantheas, S. S. *J. Phys. Chem. A* **2002**, *106*, 11327.

(3) van Mourik, T. *J. Phys. Chem. A* **2008**, *112*, 11017.

(4) Jansen, H. B.; Ros, P. *Chem. Phys. Lett.* **1969**, *3*, 140.

(5) Boys, S. F.; Bernardi, F. *Mol. Phys.* **1970**, *19*, 553.

(6) Meunier, A.; Levy, B.; Berthier, G. *Theor. Chim. Acta* **1973**, *29*, 49.

(7) Van Duijneveldt, F. B.; van Duijneveldt-van der Rijdt, J. G. C. M.; van Lenthe, J. H *Chem. Rev.* **1994**, *94*, 1873.

(8) Valiron, P.; Mayer, I. *Chem. Phys. Lett.* **1997**, *275*, 46–55.

(9) Sadley, A. D. *J. Chem. Phys.* **1991**, *95*, 6706.

(10) Famulari, A.; Specchio, R.; Sironi, M.; Raimondi, M. *J. Chem. Phys.* **1998**, *108*, 3296.

(11) Mayer, I.; Vibok, A. *Mol. Phys.* **1997**, *92*, 503.

(12) Mayer, I. *Int. J. Quantum Chem.* **1998**, *70*, 41.

(13) Mayer, I.; Valiron, P. *J. Chem. Phys.* **1998**, *109*, 3360.

(14) Salvador, P.; Paizs, B.; Duran, M.; Suhai, S. *J. Comput. Chem.* **2000**, *22*, 765.

(15) Peterson, K. A.; Dunning, T. H. *J. Chem. Phys.* **1995**, *105*, 2032.

(16) Halkier, A.; Koch, H.; Jørgensen, P.; Christiansen, O.; Nielsen, I. M. B.; Helgaker, T. *Theor. Chem. Acc.* **1997**, *97*, 150.

(17) van Mourik, T.; Wilson, A. K.; Peterson, K. A.; Woon, D. E.; Dunning, T. H. *Adv. Quantum Chem.* **1999**, *31*, 105–135.

(18) Sellers, H.; Almlof, J. *J. Phys. Chem.* **1989**, *93*, 5136.

(19) Jensen, F. *Chem. Phys. Lett.* **1996**, *261*, 633.

(20) Senent, M. L.; Wilson, S. *Int. J. Quantum Chem.* **2001**, *82*, 282.

(21) Holroyd, L. F.; van Mourik, T. *Chem. Phys. Lett.* **2007**, *442*, 42.

(22) (a) Palermo, N. Y.; Csontos, J.; Owen, M. C.; Murphy, R. F.; Lovas, S. *J. Comput. Chem.* **2007**, *28*, 1208. (b) van Mourik, T. *J. Comput. Chem.* **2008**, *29*, 1. (c) Csontos, J.; Palermo, N. Y.; Owen, M. C.; Murphy, R. F.; Lovas, S. *J. Comput. Chem.* **2008**, *29*, 4.

(23) Valdes, H.; Klusak, V.; Pitonak, M.; Exner, O.; Stary, I.; Hobza, P.; Rulisek, L. *J. Comput. Chem.* **2008**, *29*, 861.

(24) Suarez, E.; Diaz, N.; Suarez, D. *J. Chem. Theory Comp.* **2009**, *5*, 1667.

(25) Asturiol, D.; Duran, M.; Salvador, P. *J. Chem. Phys.* **2008**, *128*, 144108.

(26) Asturiol, D.; Duran, M.; Salvador, P. *J. Chem. Theory Comp.* **2009**, *5*, 2574.

(27) Balabin, R. M. *J. Chem. Phys.* **2008**, *129*, 164101.

(28) Kaminsky, J.; Jensen, F. *J. Chem. Theo. Comp.* **2007**, *3*, 1774.

(29) van Mourik, T.; Karamertzanis, P. G.; Price, S. L. *J. Phys. Chem. A* **2006**, *110*, 8.

(30) Toroz, D.; van Mourik, T. *Mol. Phys.* **2007**, *105*, 209.

(31) Shields, A. E.; van Mourik, T. *J. Phys. Chem. A* **2007**, *111*, 13272.

(32) van Mourik, T. *J. Chem. Theory Comput.* **2008**, *4*, 1610.

(33) Valdes, H.; Pluhackova, K.; Hobza, P. *J. Chem. Theory Comp.* **2009**, *5*, 2248.

(34) Tew, D. P.; Klopper, W.; Neiss, C.; Hattig, C. *Phys. Chem. Chem. Phys.* **2007**, *9*, 1921.

(35) Knizia, G.; Adler, T. B.; Werner, H.-J. *J. Chem. Phys.* **2009**, *130*, 054104.

(36) Adler, T. B.; Werner, H.-J. *J. Chem. Phys.* **2009**, *130*, 241101.

(37) Galano, A.; Alvarez-Idaboy, J. R. *J. Comput. Chem.* **2006**, *27*, 1203.

(38) Frisch, M. J.; Trucks, G. W.; Schlegel, H. B.; Scuseria, G. E.; Robb, M. A.; Cheeseman, J. R.; Montgomery, Jr., J. A.; Vreven, T.; Kudin, K. N. ; Burant, J. C.; Millam, J. M.; Iyengar, S. S.; Tomasi, J.; Barone, V.; Mennucci, B.; Cossi, M.; Scalmani, G.; Rega, N.; Petersson, G. A.; Nakatsuji, H.; Hada, M.; Ehara, M.; Toyota, K.; Fukuda, R.; Hasegawa, J.; Ishida, M.; Nakajima, T.; Honda, Y.; Kitao, O.; Nakai, H.; Klene, M.; Li, X.; Knox, J. E.; Hratchian, H. P.; Cross, J. B.; Bakken, V.; Adamo, C.; Jaramillo, J.; Gomperts, R.; Stratmann, R. E.; Yazyev, O.; Austin, A. J.; Cammi, R.; Pomelli, C.; Ochterski, J. W.; Ayala, P. Y.; Morokuma, K.; Voth, G. A.; Salvador, P.; Dannenberg, J. J.; Zakrzewski, V. G.; Dapprich, S.; Daniels, A. D.; Strain, M. C.; Farkas, O.; Malick, D. K.; Rabuck, A. D.; Raghavachari, K.; Foresman, J. B.; Ortiz, J. V.; Cui, Q.; Baboul, A. G.; Clifford, S.; Cioslowski, J.; Stefanov, B. B.; Liu, G.; Liashenko, A.; Piskorz, P.; Komaromi, I.; Martin, R. L.; Fox, D. J.; Keith, T.; Al-Laham, M. A.; Peng, C. Y.; Nanayakkara, A.; Challacombe, M.; Gill, P. M. W.; Johnson, B.; Chen, W.; Wong, M. W.; Gonzalez, C.; Pople, J. A. *Gaussian*, Revision 03; Gaussian, Inc.: Wallingford, CT, 2004.

(39) Dunning, T. H., Jr. *J. Chem. Phys.* **1989**, *90*, 1007.

(40) Kendall, R. A.; Dunning, T. H., Jr.; Harrison, R. J *J. Chem. Phys.* **1992**, *96*, 6796.

(41) Sinnokrot, M. O.; Sherrill, C. D. *J. Phys. Chem. A* **2006**, *110*, 10656.

(42) Pitonak, M.; Neogrady, P.; Rezac, J.; Jurecka, P.; Urban, M.; Hobza, P. *J. Chem. Theory Comp.* **2008**, *4*, 1829.

(43) Jensen, F. *Introduction to Computational Chemistry*, 2nd ed.; Wiley: West Sussex, U.K.,2006, p 41−42.

(44) Kaminsky, J.; Mata, R. A.; Werner, H.-J.; Jensen, F. *Mol. Phys.* **2008**, *106*, 1899.

(45) Pulay, P. *Chem. Phys. Lett.* **1983**, *100*, 151.

(46) Schutz, M.; Hetzer, G.; Werner, H.-J. *J. Chem. Phys.* **1999**, *111*, 5691.

(47) Saebo, S.; Pulay, P. *J. Chem. Phys.* **2001**, *115*, 3975.

(48) Doser, B.; Lambrecht, D. S.; Kussmann, J.; Ochsenfeld, C. *J. Chem. Phys.* **2009**, *130*, 064107.

(49) Simon, S.; Duran, M.; Dannenberg, J. J. *J. Chem. Phys.* **1996**, *105*, 11024.

JCTC Journal of Chemical Theory and Computation

A General Database for Main Group Thermochemistry, Kinetics, and Noncovalent Interactions − Assessment of Common and Reparameterized (*meta*-)GGA Density Functionals

Lars Goerigk[†,‡] and Stefan Grimme*[,†]

Theoretische Organische Chemie, Organisch-Chemisches Institut, Universität Münster, Corrensstrasse 40 and NRW Graduate School of Chemistry, Universität Münster, Wilhelm-Klemm-Strasse 10, D-48149 Münster, Germany

Abstract: We present a quantum chemistry benchmark database for general main group thermochemistry, kinetics, and noncovalent interactions (GMTKN24). It is an unprecedented compilation of 24 different, chemically relevant subsets that either are taken from already existing databases or are presented here for the first time. The complete set involves a total of 1.049 atomic and molecular single point calculations and comprises 731 data points (relative chemical energies) based on accurate theoretical or experimental reference values. The usefulness of the GMTKN24 database is shown by applying common density functionals on the (*meta*-)generalized gradient approximation (GGA), hybrid-GGA, and double-hybrid-GGA levels to it, including an empirical London dispersion correction. Furthermore, we refitted the functional parameters of four (*meta*-)GGA functionals based on a fit set containing 143 systems, comprising seven chemically different problems. Validation against the GMTKN24 and the molecular structure (bond lengths) databases shows that the reparameterization does not change bond lengths much, whereas the description of energetic properties is more prone to the parameters' values. The empirical dispersion correction also often improves for conventional thermodynamic problems and makes a functional's performance more uniform over the entire database. The refitted functionals typically have a lower mean absolute deviation for the majority of subsets in the proposed GMTKN24 set. This, however, is also often accompanied at the expense of poor performance for a few other important subsets. Thus, creating a broadly applicable (and overall better) functional by just reparameterizing existing ones seems to be difficult. Nevertheless, this benchmark study reveals that a reoptimized (i.e., empirical) version of the TPSS-D functional (oTPSS-D) performs well for a variety of problems and may meet the standards of an improved functional. We propose validation against this new compilation of benchmark sets as a definitive way to evaluate a new quantum chemical method's true performance.

1. Introduction

The benefit of evaluating quantum chemical methods by benchmarking them against accurate experimental or theoretical energies was first realized by Pople and co-workers. Their work

culminated into the so-called G2/97 test set[1] and the enhanced versions G3/99[2] and G3/05.[3] However, these works mainly focused on atomization energies (or, equivalently, heats of formation). Electron and proton affinities and ionization potentials of small molecules played an additional minor role.

Truhlar and co-workers extended the idea of benchmarking by introducing databases covering a wide variety of different physicochemical properties, e.g., proton affinities, atomization energies, interaction energies of noncovalently bound

* Corresponding author. Telephone: (+49)-251-8336512. E-mail: grimmes@uni-muenster.de.

† Organisch-Chemisches Institut.

‡ Northrhine Westphalia Graduate School of Chemistry.

systems, barrier heights and reaction energies of diverse reactions, spectroscopic properties, transition-metal systems, and catalytic processes.[4−12] Truhlar and co-workers were also the first to carry out overall statistical analyses of combinations of different test sets to obtain one final number (e.g., an overall mean absolute deviation, MAD) for each tested method. Such an analysis makes an evaluation of any quantum chemical method and a comparison with other approaches more feasible. Important and popular benchmark sets introduced by other groups are, for example, the S22 set for noncovalent systems by Hobza and co-workers,[13] and the ISO34[14] set for isomerization energies of organic molecules, and the 'mindless-benchmark' set (MB08−165)[15] developed recently in our laboratory.

Having access to a plethora of different published benchmark sets, the question is which combination of these is the best to obtain a thorough insight into a given quantum chemical method's performance. First of all, the requirements for such a 'set-of-sets' are that a large cross-section of chemically relevant properties should be covered and that the specific subsets should be of an adequate size. Particularly for the evaluation of density functional theory (DFT) approximations, such a set is expected to be useful. Nowadays, it is well-known that a given density functional (DF), that performs well for a certain property, is not necessarily adequate for computing completely different types of systems. Actual research continues to develop DFs that are equally well applicable to a variety of different properties. Therefore, the aforementioned 'set-of-sets' would be a useful tool for determining whether this aim is reached or not. Furthermore, it can be sometimes seen that benchmark studies are only carried out for systems that are similar to those of the empirical fit sets with which the new functionals were generated. We think that it is crucial to distinguish between a fit and a validation set and that the latter one should also cover systems that were not included in the first one.

In this work, we present such a 'set-of-sets' (database), which covers a variety of 24 subsets for general main group thermochemistry, kinetics, and noncovalent interactions (GMTKN24). It covers atomization, relative, and reaction energies, electron and proton affinities, ionization potentials, barrier heights between conformers, and noncovalent interactions (inter- and intramolecular). The majority of sets is taken from the literature.[1,5,8−10,13−37] We also present new benchmark subsets that are combinations of already published data. These are the sets for barrier heights of pericyclic reactions (BHPERI), reaction energies involving small closed-shell molecules (G2RC), intramolecular London dispersion interactions (IDISP) and for cases that are difficult to treat with DFT methods (DC9). Furthermore, completely new sets were developed for this work. These are SIE11, the first set focusing on self-interaction error-related problems, and NBRC, describing oligomerization and hydrogen fragmentation reactions of ammonia/borane systems.

The GMTKN24 database's composition reflects many years of experience in benchmarking and applications of DFT methods to 'real-life' chemical problems. The range of properties covered by the GMTKN24 data set outperforms,

to the best of our knowledge, all other combinations of databases that have been previously proposed. Therefore, we think that GMTKN24 is highly representative for chemistry (excluding transition-metal chemistry). We propose that any quantum chemical method, that performs well for the entire database, can be really regarded as an accurate, robust, and useful method. GMTKN24 itself is also robust in a sense that adding or deleting one or two subsets does not qualitatively change the overall rating for the quantum chemical method under investigation.

This study focuses mainly on the evaluation of density functionals at the (*meta-*)generalized gradient approximation level (GGA). These functionals are still very important for the computation of the energetics and geometries of large systems. Particularly the physics community benefits from using GGAs for the calculation of solids and surfaces. Because they can be correct for slowly varying densities, these semilocal functionals are, in principle, better suited for solids than for molecules. Since Lee−Yang−Parr (LYP) correlation is not correct for a uniform gas, the 'LYP-based' functionals are less satisfactory than the Perdew−Burke−Ernzerhof based ('PBE-based') functionals for the equilibrium properties of metals.[38] With our new database, we are now able to investigate this difference also for molecules.

However, besides investigating (*meta-*)GGA functionals, the applicability of 'higher rung' functionals (i.e., B3LYP-D[39−41] and B2PLYP-D[30,31]) will also be tested in this study. We also want to note that functionals performing well for main group molecules need not perform well for solids. In particular, the best functional for main group chemistry, of those tested here, is B2PLYP, which diverges for solid metals.

Current DFs depend on a varying number of parameters, and there are two philosophies for determining these. The first one is the requirement of fulfilling physical boundary conditions (e.g., recovery of the uniform electron gas result for constant densities). Authors favoring this first approach argue that a DF should be as ab initio as possible and should be based on physical grounds. In 2005, Perdew et al. gave a 'recipe' for such an approach.[42] Examples are PBE[43] and its successor TPSS.[44] Contrary to that, the other main strategy of determining parameters is fitting them to accurate reference data. Such empirical DFs are, e.g., B3LYP,[39,40] HCTH,[45] the M05,[46,47] M06,[11,48,49] and M08[50] classes of functionals and the double-hybrid functionals B2PLYP[30] and mPW2PLYP.[51]

In the past, though, it was shown that, independent of the strategy with which the parameters are obtained, there is no clear right or wrong regarding the actual parameter values. Different values are more or less useful for the application to different chemical problems. Evidence for this are revised versions (with varying names) of the PBE,[52−57] TPSS,[58,59] BP86,[60] PW,[61] B3LYP,[62] B2PLYP,[16,63] and mPW2PLYP[16] functionals. In passing, it is noted that the improved performance of the revised functional versions could not always be confirmed by other researchers (for revPBE see, e.g., ref 64), which highlights the need for accurate and comprehensive benchmark sets, as outlined above.

Density Functional Thermochemistry

J. Chem. Theory Comput., Vol. 6, No. 1, 2010 **109**

Particularly for (*meta-*)GGA functionals, a variety of exchange and correlation functionals were proposed in the past, and with common quantum chemical codes, it is quite easy to arbitrarily combine these with each other. When doing this, though, the important question arises, whether the parameters of a certain exchange functional are optimal when combining them with a specific correlation functional. For example, one may ask, whether BLYP[65,66] would yield better results if the parameters were optimized according to this specific combination of Becke1988 exchange[65] with LYP correlation.[66] To the best of our knowledge, such an investigation has not been carried out yet.

Furthermore, our experience showed that, e.g., for thermodynamic properties, the TPSS *meta*-GGA functional yields similar results as the PBE functional. This happens, though, at a higher numerical complexity due to the inclusion of the kinetic energy density. Do physical boundary conditions lead to restrictions that inhibit improved performance of a certain DF, like TPSS? Would lifting these restrictions improve TPSS's performance compared to PBE? Finally, it is justified to ask how far one can go with an empirical fitting procedure for DFs, in general.

In this systematic study, we try to answer these questions. Based on a well balanced fit set, the parameters of the BLYP, mPWLYP, PBE and TPSS functionals are fully reoptimized. This reoptimization is carried out with an empirical dispersion correction (DFT-D)[41] to take into account long-range London dispersion effects and to partially withdraw a medium-range description of London dispersion by the semilocal functional parts. We think that this provides a better picture of a given functional's true performance.

The optimized functionals and their original versions will be benchmarked against the here presented GMTKN24 database. This allows a thorough evaluation of their performance for energetics. Furthermore, geometry optimizations of small first- and second-row and transition-metal compounds have been carried out, and the resulting bond lengths are compared to experimental data.

This manuscript is structured as follows: In the following section, Section 2, an overview of the GMTKN24 database is given. In Section 3, the computational details are explained. Section 4 describes the reparameterization procedure, including an overview of the fit set and a description of each functional. In Section 5, the results for the application to the GMTKN24 set and the optimized geometries are discussed.

2. The GMTKN24 Database

The herein presented database for general main group thermochemistry, kinetics, and noncovalent interactions covers a large variety of 24 different, chemically relevant subsets (GMTKN24). In Figure 1, an overview of these subsets is given. For each set, on average, the easiest and most difficult reactions (for GGA functionals) are shown. In Table 1, short descriptions for each part of the GMTKN24 database are given, including the number of entries, the specification of the reference values, and the relevant citations. Note that none of the reference data include zero point vibrational energies (ZPVEs) or thermal (enthalpic)

corrections. The type and source of reference data are given separately for each subset. By comparing different quantum chemistry programs with each other, we made sure that each entry is reliable and that the results are reproducible. Different codes with different technical setups, but for the same functional/basis set combination, typically produce differences for MADs of about 0.1 kcal mol^{-1} or less. Molecules that led to problems with orbital initial guesses or electronic-state symmetries were left out. We suggest to use an extended Hueckel initial orbital guess for open-shell species. All entries are shown in the Supporting Information, Tables S1−S24, and are available for download from our Web site.[67] The optimized coordinates of all systems can also be obtained from there. In total, the GMTKN24 database comprises 1.049 single point calculations and 731 data points (relative energy values).

2.1. The MB08−165 Subset. The 'mindless-benchmark' set (MB08−165) was recently introduced by Korth and Grimme.[15] It contains 165 randomly created so-called 'artificial molecules' (AMs) with varying constituencies. For these molecules, decomposition energies into their hydrides (for the main group elements 1−4) and homonuclear diatomics (main group elements 5−7) were calculated. For these reactions, estimated CCSD(T)/CBS reference values were computed. The reference data is listed in Table S1of the Supporting Information. See ref 15 for more details on the creation of the AMs and the reaction schemes. In contrast to other benchmark sets, MB08−165 is less biased toward certain chemical aspects, as it just contains artificial systems. Korth and Grimme assessed a variety of density functionals and could reproduce nicely the Jacob's Ladder scheme,[42] with higher-rung functionals yielding better results. We chose MB08−165 to be the first subset of our benchmark study, as it can be regarded as one of the most important of all 24 subsets. Compared to the other subsets, it contains a large number of reference values and involves rather high reaction energies: 180 single point calculations have to be carried out to compute all 165 decomposition energies; the average absolute energy of these reactions is 117.2 kcal mol^{-1}.

2.2. The W4−08 Subset. The W4−08 database by Karton et al. contains atomization energies of 99 small molecules.[16] The systems are dominated by dynamical correlation (e.g., H_2O and CH_4), and a few also include nondynamical correlation effects (e.g., O_3, C_2, and BN). Out of these 99 molecules, 16 are such multireference cases. Therefore, an additional analysis of this database without these cases is carried out (see Table 1). This subset is denoted as W4−08woMR. All reference data are based on W4 or higher levels of theory (see ref 16). For the complete W4−08 subset, 111 single point calculations have to be carried out. The average absolute atomization energy is 237.5 kcal mol^{-1} for the whole set and 261.5 kcal mol^{-1} for W4−08woMR. The W4−08 database is listed in the Supporting Information, Table S2.

2.3. The G21IP and G21EA Subsets. The G21IP subset contains 36 adiabatic ionization potentials of atoms and small molecules that were taken from the G2-1 set by Curtiss et al.[17] Note that G2-1 also includes the SH_2 molecule in its singlet and triplet, and N_2^+ in its $^2\Pi_u$ state, which are
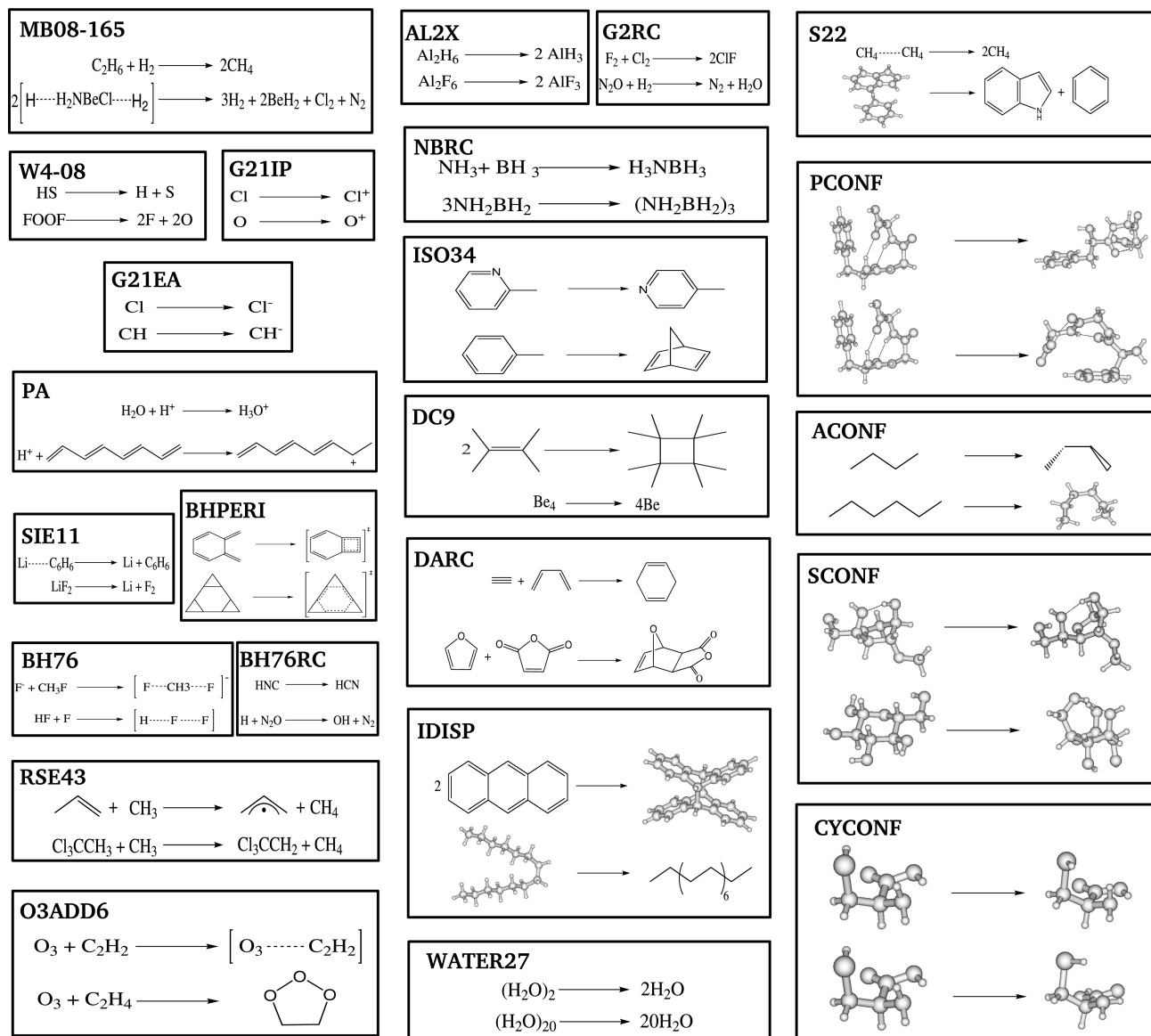
Figure 1. The subsets of the GMTKN24 database. For each set, on average, the easiest (top) and most difficult (bottom in each box) reactions (for GGAs) are shown.

problematic in unrestricted Kohn−Sham computations with some DFs. Thus, these cases were left out. The G21EA set contains 25 adiabatic electron affinities from the same work. Reference values are based on back-corrected experimental data. In total, 71 single point energies for G21IP and 50 for G21EA have to be calculated. The average absolute energies are 250.8 and 33.6 kcal mol^{-1}, respectively. The G21IP and G21EA databases are listed in Tables S3 and S4 of the Supporting Information.

2.4. The PA Subset. The PA database includes 12 adiabatic proton affinities. On the one hand, the PA set includes eight small molecules (H_2O, C_2H_2, SiH_4, PH_3, H_2S, HCl, and H_2) based on vibrationally back-corrected W1[18,68] reference values.[18] On the other hand, a homologous series of four conjugated polyenes (from ethene to all-*trans*-octatetraene) is included, that are taken from a study by Zhao and Truhlar.[5] Their reference values are based on estimated CCSD(T)/CBS results. Note that the polyenes from butadiene to octatetraene have a large impact on the complete subset's MAD because the results are influenced by the delocalization

error of density functionals. Therefore, they could also be made part of the self-interaction error subset (SIE11). However, from a chemical point of view, it is still justified to include them in the PA subset, as protonation of larger organic compounds is also a relevant issue that needs to be considered. In order to assess this subset, 24 single point energies have to be carried out. The average absolute reference energy is 174.9 kcal mol^{-1}. The PA database is shown in Table S5 of the Supporting Information.

2.5. The SIE11 Subset. The self-interaction error (SIE) is a severe flaw in common DFT methods, and finding appropriate correction schemes is still on the agenda of actual research.[69−73] Although several studies have been carried out on the SIE and, although it also plays a role in some of the subsets included in GMTKN24 (barrier heights, proton affinities), a set which exclusively deals with the SIE has, to the best of our knowledge, not been proposed yet.

The SIE11 subset comprises 11 systems, which are extremely prone to the SIE. Five of these are positively charged, and seven systems are neutral. Examples, are the

Density Functional Thermochemistry

J. Chem. Theory Comput., Vol. 6, No. 1, 2010 **111**

Table 1. Description of the Subsets within the GMTKN24 Database

set	description	no.	av |ΔE|[a]	ref method	reference
MB08-165	decomposition energies of artificial molecules	165	117.2	est. CCSD(T)/CBS	[b]
W4-08	atomization energies of small molecules	99	237.5	W4	[c]
W4-08woMR	W4-08 without multi reference cases	83	261.5	W4	[c]
G21IP	adiabatic ionization potentials	36	250.8	expt.	[d]
G21EA	adiabatic electron affinities	25	33.6	expt.	[d]
PA	adiabatic proton affinities	12	174.9	est. CCSD(T)/CBS and W1	[e,f]
SIE11	self-interaction error related problems	11	34.0	est. CCSD(T)/CBS	this work
BHPERI	barrier heights of pericyclic reactions	26	19.4	W1 and CBS-QB3	[c,g,h,i,j]
BH76	barrier heights of hydrogen and heavy-atom transfers, nucleophilic substitution, unimolecular and association reactions	76	18.5	W1 and theor. est.	[k,l]
BH76RC	reaction energies of the BH76 set	30	21.5	W1 and theor. est.	[k,l]
RSE43	radical stabilization energies	43	7.5	est. CCSD(T)/CBS	[m]
O3ADD6	reaction and association energies and barrier heights for addition of O_3 to C_2H_4 and C_2H_2	6	22.7	est. CCSD(T)/CBS	[n]
G2RC	reaction energies of selected G2/97 systems	25	50.6	expt.	[o]
AL2X	dimerization energies of AlX_3 compounds	7	33.9	expt.	[p]
NBRC	oligomerizations and H_2 fragmentations of NH_3/BH_3 systems	6	30.2	est. CCSD(T)/CBS	this work
ISO34	isomerization energies of organic molecules	34	14.3	expt.	[q]
DC9	nine difficult cases for DFT	9	35.7	theor. and expt.	[i,r,s,t,u,v,w], this work
DARC	reaction energies of Diels−Alder reactions	14	32.2	est. CCSDT/CBS	[p]
IDISP	intramolecular dispersion interactions	6	14.1	theor. and expt.	[q,x,y]
WATER27	binding energies of water, H^+ $(H_2O)_n$ and OH^- $(H_2O)_n$ clusters	27	82.0	est. CCSD(T)/CBS;MP2/CBS	[z]
S22	binding energies of noncovalently bound dimers	22	7.4	est. CCSD(T)/CBS	[aa]
PCONF	relative energies of phenylalanyl−glycyl−glycine tripeptide conformers	10	1.5	est. CCSD(T)/CBS	[bb]
ACONF	relative energies of alkane conformers	15	1.8	W1h-val	[cc]
SCONF	relative energies of sugar conformers	17	4.9	est. CCSD(T)/CBS	[dd,ee], this work
CYCONF	relative energies of cysteine conformers	10	2.1	est. CCSD(T)/CBS	[ff]

[a] Averaged absolute energies in kcal mol^{-1}, excluding ZPVEs. [b] Ref 15. [c] Ref 16. [d] Ref 17. [e] Ref 18. [f] Ref 5. [g] Ref 19. [h] Ref 20. [i] Ref 21. [j] Ref 22. [k] Ref 8. [l] Ref 9. [m] Ref 23. [n] Ref 10. [o] Ref 1. [p] Ref 24. [q] Ref 14. [r] Ref 25. [s] Ref 26. [t] Ref 27. [u] Ref 28. [v] Ref 29. [w] Ref 30. [x] Ref 31. [y] Ref 32. [z] Ref 33. [aa] Ref 13. [bb] Ref 34. [cc] Ref 35. [dd] Ref 36. [ee] G. Csonka, private communication. [ff] Ref 37.

dissociation of He_2^+ into He and He^+, the decomposition of LiF_2 into Li and F_2, or the binding energy of the lithium−benzene complex. The complete subset, including reference data, is shown in Table S6 of the Supporting Information.

Geometries were optimized with SCS-MP2[74]/TZVPP,[75] except for the LiF_2 decomposition (PBE[43]/TZVPP). The reference data were obtained as estimated CCSD(T)[76]/CBS values as by Jurečka and Hobza:[77]

$$E^{\text{CCSD(T)/CBS}} \approx E^{\text{MP2/CBS}} + (E_{\text{corr}}^{\text{MP2/small basis}} - E_{\text{corr}}^{\text{CCSD(T)/small basis}}) \quad (1)$$

According to the formalism by Halkier et al.,[78] an extrapolation to the complete basis set limit on the MP2 level (from cc-pVTZ to cc-pVQZ)[79] was carried out, and the difference between MP2 and CCSD(T) correlation energies on the cc-pVDZ[79] level was added (eq 1). For the LiF_2 decomposition, this difference was calculated with the cc-pVTZ basis.

The complete SIE11 subset involves 29 single point calculations and has an average absolute reaction energy of 34.0 kcal mol^{-1}.

2.6. The BHPERI Subset. The BHPERI subset contains 26 barrier heights of pericyclic reactions. The systems are taken from three publications and are shown in Table S7 of the Supporting Information. Ten reactions are taken from a work by Guner et al.[19] They include, among others, the ring-opening reaction of cyclobutene, the intramolecular Diels−

Alder reaction of *cis*-1,3,5-hexatriene, and the intermolecular Diels−Alder reaction of *cis*-butadiene with ethene. Reference values were based on CBS-QB3 calculations. Recently, Karton et al. published W1 reference values for 8 of these 10 reactions.[16] For the present study, we chose these eight W1 and the remaining two CBS-QB3 values as reference data. Furthermore, BHPERI includes nine 1,3-dipolar cycloadditions that were taken from a publication by Ess and Houk,[20] with improved reference values by Grimme et al. (CBS-QB3).[21] These reactions are based on diazonium, azomethine, and nitrilium betaines as 1,3-dipolar species. Finally, seven Diels−Alder reactions of different dienes with ethene are taken from the work of Dinadayalane et al. (CBS-QB3 reference values).[22] The final BHPERI set involves 61 single point calculations and has an average barrier height of 19.4 kcal mol^{-1}.

2.7. The BH76 and BH76RC Subsets. The BH76 subset is a combination of the HTBH38[8] and NHTBH38[9] databases by Truhlar and co-workers. HTBH38 contains forward and reverse barriers of 19 hydrogen atom transfer reactions. NHTBH38 comprises 38 barriers of 19 heavy-atom transfer, nucleophilic substitution, unimolecular, and association reactions. Reference values are based on W1 calculations and 'best theoretical estimates' (see refs 8 and 9 for more details). The combined BH76 test set involves 95 single point calculations and has an average barrier height of 18.5 kcal mol^{-1}. It is shown in Table S8 of the Supporting Information.

Having calculated the necessary reactants and products of the above-mentioned 36 reactions, it is straightforward to also compute the corresponding reaction energies. These are combined to another subset, denoted by BH76RC. In 6 of the 36 reactions, the reactants and products are identical (e.g., H + FH → HF + H), and therefore, the BH76RC set contains only 30 reactions. Reference values were calculated from reference data of the BH76 set. The final BH76RC set has an average reaction energy of 21.5 kcal mol^{-1} and is listed in Table S9 of the Supporting Information.

2.8. The RSE43 Subset. The RSE43 subset contains 43 radical stabilization energies (RSE), defined as H-abstraction energies for the reactions of hydrocarbons with a methyl radical (see ref 80 for a thorough discussion of RSEs). All relevant structures (B3LYP/TZVP) and reference values (est. CCSD(T)/CBS) are taken from a recent work by Neese et al.[23] Note that their study included the acetyl radical, which was herein excluded from the RSE43 set due to state ordering problems. The complete set comprises 88 single point calculations and has an average absolute RSE of 7.5 kcal mol^{-1} (Table S10, Supporting Information).

2.9. The O3ADD6 Subset. Recently, Zhao et al. carried out an assessment of a variety of different quantum chemical methods for the thermochemical properties of a multireference system.[10] They studied the addition reactions of ozone to ethane and ethyne. For each reaction the formation energy of the primary ozonide, the barrier height and the association energy of the van der Waals (vdW) complex were calculated. Geometries were based on M05/MG3S calculations, and reference values were obtained at the estimated CCSD(T)/CBS level. In this work, the same systems are investigated, and the resulting test set is denoted by O3ADD6. Geometries and reference data are the same as in the work by Zhao et al. The complete database includes nine single point calculations. The average absolute energy is 22.7 kcal mol^{-1}. The O3ADD6 subset is listed in Table S11 of the Supporting Information.

2.10. The G2RC Subset. The G2RC subset contains 25 reactions, whose reactants and products are part of the G2/97 set of heats of formation.[1] Based on vibrationally back-corrected experimental data from ref 1, reference energies were calculated. The 25 reactions and their reference values are shown in Table S12 of the Supporting Information. The G2RC set comprises 47 single point calculations and has an average absolute reaction energy of 50.6 kcal mol^{-1}. It contains similar (small) molecules as already included in BH76RC, which allows cross-checking, and is a test for internal consistency of the results for different methods.

2.11. The AL2X Subset. In 2008, Johnson et al. reported a systematic study of delocalization errors in density functionals and their implication for main group thermochemistry.[24] Their study contained, among others, a test set for the calculation of the binding energies of the dimers of seven aluminum compounds of the type AlX$_3$ (X = H, CH$_3$, F, Cl, and Br). As reference values, they used back-corrected experimental data. Here we denote this test set by AL2X. For this subset, 13 single point calculations have to be carried out. The average absolute dimerization energy is 33.9 kcal

mol^{-1}. The AL2X database is shown in Table S13 in the Supporting Information.

2.12. The NBRC Subset. The formation of nitrogen–boron bonds is sometimes difficult to describe with DFT methods, and indeed, the investigation of ammonia-borane adducts gave first evidence for problems of the popular B3LYP functional.[81] In this study, we present a new benchmark set, called NBRC, which describes oligomerization and hydrogen fragmentation reactions of ammonia/borane systems. It consists of six reactions, which are shown in Table S14 of the Supporting Information. These reactions are the dimerization of ammonia with borane to the NH$_3$BH$_3$ adduct, the H$_2$ abstraction yielding NH$_2$BH$_2$, and the subsequent dehydrogenation to NHBH. Furthermore, three cyclization reactions of NH$_2$BH$_2$ to the four-membered (NH$_2$BH$_2$)$_2$ and the six-membered borazine and (NH$_2$BH$_2$)$_3$ rings are considered. The reference values are based on estimated CCSD(T)/CBS computations (eq 1). The MP2/CBS limit was obtained from an aug-cc-pVTZ/QZ[82] extrapolation. The difference between the CCSD(T) and MP2 correlation energies was obtained with the cc-pVTZ basis. Effects due to the frozen core approximation were estimated at the MP2/cc-pwCVTZ[79] level. Geometries are based on PBE0[83]/TZVP[75] calculations. In order to calculate all reaction energies of the NBRC set, nine single point calculations have to be carried out. The average absolute reaction energy is 30.2 kcal mol^{-1}.

2.13. The ISO34 Subset. In 2007, Grimme et al. carried out an evaluation of quantum chemical methods for the calculation of 34 organic isomerization reactions (ISO34,[14] originally from refs 84 and 85). It turned out that some of these reactions are challenging tasks for common density functionals and that a benchmark study of new methods should include these types of reactions. These authors listed back-corrected experimental reference data that are also used in our work (see ref 14). The ISO34 set includes 63 single point calculations and has an average isomerization energy of 14.3 kcal mol^{-1}. It is shown in Table S15 of the Supporting Information.

2.14. The DC9 Subset. The DC9 subset comprises nine reactions that were shown to be difficult to treat with DFT methods. An overview of the DC9 set is given in Table S16 of the Supporting Information. The first system was discussed by Piacenza and Grimme, who carried out a systematic quantum chemical study on DNA base tautomers.[25] Among others, they investigated the tautomeric 2-pyridone/2-hydroxypyridine system. The reference value was obtained from QCISD(T)/TZV(2df,2pd)//B3LYP/TZV(2df,2pd) calculations. Note that the absolute reference value is rather small compared to that of the other reactions of this set. For many DFs, it is particularly difficult to predict the correct sign for this reaction, and deviations are often of the same magnitude as the actual reference value. Thus, although this reaction plays only a minor role in the overall statistics (note that, therefore, the second easiest reaction is shown in Figure 1), we still regard it as being important and, consequently, made it part of the DC9 subset.

The second entry describes the relative energy between the C$_{20}$ cage and its bowl isomer. The structures were taken from the work by Grimme and Mück-Lichtenfeld.[86] The

Density Functional Thermochemistry

J. Chem. Theory Comput., Vol. 6, No. 1, 2010 **113**

reference value was computed here at the estimated CCSD(T)/ CBS level (eq 1; MP2/CBS, difference between CCSD(T)/ cc-pVDZ and MP2/cc-pVDZ correlation energies).

The third case was taken from Woodcock et al.[26] They discussed the fact that DFT methods sometimes yield problematic results for the energetic differences between cumulenes and poly-ynes. Among others, they studied the energy separation of the hepta-1,2,3,5,6-hexaene and hepta-1,3,5-triyne (C_7H_4) isomers. The reference value is based on CCSD(T)/cc-pVTZ//MP2/cc-pVTZ calculations.

The fourth case is the dimerization of tetramethyl-ethene to octamethyl-cyclobutane. The reference value was calculated here on the SCS-MP2/TZVPP level of theory.

In 2006, Schreiner et al. published a study on the relative energies of several $(CH)_{12}$ isomers and showed that many DFs failed to correctly describe these energies.[27] For this work, two isomers were chosen that are labeled with the numbers 1 and 31 in the work of Schreiner et al. (see ref 27 for structures).

The sixth reaction is taken from a work by Lepetit et al., which dealt with an assessment of density functionals on carbo-[n]-oxocarbons and on their valence isomers.[28] For the DC9 set, carbo-[3]-oxacarbon and its valence isomer, as shown in ref 28, were taken from their work. Reference data, though, were recalculated here. They are based on an estimated QCISD(T)[76]/CBS level of theory (SCS-MP2/CBS with cc-pVTZ and cc-pVQZ; difference between the QCISD(T)/cc-pVDZ and SCS-MP2/cc-pVDZ correlation energies).

The seventh entry is the reaction energy for the 1,3-dipolar cycloaddition between ethene and diazomethane. This reaction was studied by Grimme et al.[21] and the reference value was determined at the CBS-QB3 level.

The eighth reaction describes the decomposition of a Be_4 cluster into beryllium atoms. The structure and reference value (CCSD(T)/CBS) were taken from a study by Lee.[29]

The last entry is the reaction of diatomic S_2 to the S_8. This reaction was also part of the first study of the double-hybrid functional B2PLYP.[30] The experimental reference value and the geometries were taken from that study (see ref 30 for more details).

The complete DC9 database includes 19 single point calculations. The average reaction energy is 35.7 kcal mol^{-1}.

2.15. The DARC Subset. In their work on the delocalization errors of DFT methods, Johnson et al. also investigated 14 typical Diels−Alder reactions.[24] These are the reactions of butadiene, cyclopentadiene, cyclohexadiene, and furane with ethene, ethyne, maleine, and maleinimide acting as dienophiles. Reference values are based on CCSD(T)/ CBS calculations. The complete DARC database comprises 22 single point calculations. The average reaction energy is 32.2 kcal mol^{-1}. It is listed in Table S17 in the Supporting Information.

2.16. The IDISP Subset. The IDISP set covers intramolecular London dispersion effects of large organic systems. The complete set and its reference values are shown in Table S18 of the Supporting Information. The first and the last two systems are taken from a study by Schwabe and Grimme.[31] These are the dimerization of anthracene, the hydrogenation

reaction of [2.2]paracyclophane yielding p-xylene, and the energetic differences between the linear and folded conformers of the $C_{14}H_{30}$ and $C_{22}H_{46}$ hydrocarbons. Structures and reference values were taken from the study by Schwabe and Grimme. They are based on theoretical or experimental data (see ref 31 for more details). The third reaction, in Table S18, is the isomerization of n-octane to iso-octane, which is also part of the ISO34 database.[14] The fourth reaction is the isomerization of n-undecane to 2,2,3,3,4,4-hexamethyl-pentane, which was shown in 2006 to be a problematic case for DFT methods by Grimme.[32] The reference value for this reaction is based on the SCS-MP2/cQZV3P//MP2/TZVP level of theory. The complete IDISP set involves 13 single point calculations. The average relative energy is 14.1 kcal mol^{-1}.

2.17. The WATER27 Subset. Recently, Vyacheslav et al. published a DFT study on the binding energies of water clusters.[33] Their assessment was based on 27 neutral $(H_2O)_n$, positively charged $H^+(H_2O)_n$, and negatively charged $OH^-(H_2O)_n$ clusters. As structures, their optimized B3LYP/ 6-311++G(2d,2p) geometries were taken. Reference data are based on either CCSD(T)/CBS or MP2/CBS calculations. We included this benchmark set as it can be regarded as a tough test for the description of strong hydrogen bonds and of long-range interactions. In the following, this set is denoted by WATER27. In total, 30 single point calculations have to be carried out for this set. The average binding energy of these clusters is 82.0 kcal mol^{-1}. The complete set is listed in Table S19 in the Supporting Information.

2.18. The S22 Subset. The S22 set was introduced in 2006 by Jurečka et al.[13] Since then it has become a very popular benchmark set for studying noncovalent interactions. It includes the binding energies of seven hydrogen bonded dimers, eight complexes with predominant London dispersion interactions, and seven mixed complexes, where both hydrogen bonds and dispersion effects are important. Geometries are based on CCSD(T) or MP2 calculations. Reference data are estimated CCSD(T)/CBS values (see ref 13 for more details). The complete set comprises 57 single point calculations. Its average binding energy is 7.4 kcal mol^{-1}. The S22 set is listed in Table S20 in the Supporting Information.

2.19. The PCONF Subset. In 2005, Řeha et al. carried out a thorough conformational study for the phenylalanyl−glycyl−glycine tripeptide.[34] Herein, we present a database denoted by PCONF, which is part of Řeha and co-workers' so-called 'Set 3' (see ref 34 for more details). In fact, we took the structures of the eleven most stable conformers of that particular set, which were obtained at the RI-MP2/cc-pVDZ level of theory. The relative energies, with respect to the most stable conformer, were calculated by Řeha et al. at the estimated CCSD(T)/CBS level of theory. These 10 relative energies, which are used as reference data for our study, have an average value of only 1.5 kcal mol^{-1}. The complete PCONF set is shown in Table S21 in the Supporting Information.

2.20. The ACONF Subset. The ACONF subset comprises 15 relative energies of n-butane, n-pentane and n-hexane conformers. The relative energies are based on the

completely staggered conformation for each molecule. Geometries and reference values are taken from a recent work by Gruzman et al.[35] The latter ones are based on W1h-val calculations. The complete set comprises 18 single point calculations and has an average absolute energy of only 1.8 kcal mol^{-1} (Table S22, Supporting Information).

2.21. The SCONF Subset. Recently, Csonka et al. carried out an evaluation study of DFs and of basis sets for a variety of different carbohydrate conformers.[36] They presented 3 test sets consisting of 15 D-allopyranose conformers (ALL15), 15 conformers of the five-membered ring system 3,6-anhydro-4-*O*-methyl-D-galactitol (AnGol15), and 4 β-D-glucopyranose conformers (GLC4). For each test set, Csonka et al. calculated the energetic differences relative to each most stable conformer.

The herein considered subset called SCONF combines the AnGol15 and GLC4 sets of Csonka et al. Geometries are based on their B3LYP/6-31+G* calculations. As reference data, the authors used MP2/aug-cc-pVTZ(-f) values. We regard this level of theory as insufficient and recalculated the reference data. For the AnGol15 subset the reference values are based on an estimated CCSD(T) extrapolation (eq 1). The MP2/CBS limit is based on aug-cc-pVDZ and aug-cc-pVTZ calculations. The difference between CCSD(T) and MP2 correlation energies was estimated with the cc-pVDZ basis set. The reference values for the GLC4 set were provided by Csonka in a private communication (MP2/CBS with aug-cc-pVTZ and aug-cc-pVQZ; difference between CCSD(T)/cc-pVTZ and MP2/cc-pVTZ). The reference values are shown in Table S23 of the Supporting Information. The notation of the different conformers is the same as in the original work (see ref 36 for more details). Compared to the original MP2 reference data, one can clearly see a difference between those and the herein presented CCSD(T)/CBS data.

The complete SCONF subset comprises 19 single point calculations and has an average conformational energy of 4.9 kcal mol^{-1}.

2.22. The CYCONF Subset. The CYCONF subset contains 10 relative energies of 11 cysteine conformers that were recently studied by Wilke et al.[37] Reference values are based on estimated CCSD(T)/CBS calculations (see ref 37 for more details). The average relative energy of this set is only 2.1 kcal mol^{-1} (Table S24, Supporting Information).

3. Computational Details

The CCSD(T)[76] calculations for obtaining reference data were done with MOLPRO Version 2006.1.[87] For QCISD(T)[76] calculations, the program RICC developed in our group was used.[88] All other calculations were carried out with a modified version of TURBOMOLE 5.9.[89-92] In general, the large Ahlrichs' type quadruple-ζ basis sets def2-QZVP were applied[93] that yield results quite close to the Kohn–Sham limit. For the calculations of electron affinities, diffuse s- and p-functions (for hydrogen only an s-function) were added from the Dunning aug-cc-pVQZ basis sets;[82] the resulting set is denoted by aug-def2-QZVP. Preliminary calculations for the WATER27 database showed that the results are very

basis set dependent. As negatively charged species are included in this set, we decided to add one diffuse s- and one diffuse p-function (taken from aug-cc-pVQZ) for oxygen. For example, this procedure reduced the MAD for this set from 8.2 to 3.8 kcal mol^{-1} in the case of BLYP-D.

For all (*meta-*)GGA calculations, the resolution of the identity (RI-J) approximation was applied.[94] For B3LYP[39,40] and the DFT part of B2PLYP,[30] the RI-JK approximation was applied.[95] For the perturbative part of the B2PLYP functional, the RI approximation was used as well.[92] Auxiliary basis functions were taken from the TURBOMOLE basis set library.[96] In all cases, SCF convergence criteria were set to 10^{-7} E_{h} and the TURBOMOLE grid m4 was used.[94] All open-shell calculations were done within the unrestricted Kohn–Sham formalism (UKS). Geometry optimizations with the (*meta-*)GGAs were carried out with a convergence criterion of 10^{-7} E_{h}, regarding the changes of the total energy between two subsequent optimization cycles.

The refitting procedure was applied to the BLYP,[65,66] mPWLYP,[61,66] PBE,[43] and TPSS[44] functionals. This procedure and subsequent benchmark calculations were carried out with the empirical dispersion correction, developed by Grimme (DFT-D).[41] This correction (E_{disp}) is added to the conventional Kohn–Sham DFT self-consistent field total energy $E_{\mathrm{KS-DFT}}$ (eq 2):

$$E_{\mathrm{DFT-D}} = E_{\mathrm{KS-DFT}} + E_{\mathrm{disp}} \tag{2}$$

with

$$E_{\mathrm{disp}} = -s_6 \sum_{i=1}^{N-1} \sum_{j=i+1}^{N} \frac{C_6^{ij}}{R_{ij}^6} f_{\mathrm{dmp}}(R_{ij}) \tag{3}$$

where E_{disp} is the dispersion energy, C_6^{ij} denotes the dispersion coefficient for atom pair ij, s_6 is a global scaling parameter, and R_{ij} is an interatomic distance. To avoid near singularities for small R and for electron correlation double-counting, a damping function f_{dmp} is applied, which is given by

$$f_{\mathrm{dmp}}(R_{ij}) = \frac{1}{1 + e^{-d(R_{ij}/R_r - 1)}} \tag{4}$$

Here, $d = 20$ is a damping parameter and R_r is the sum of atomic vdW radii. There is overwhelming empirical evidence that the actual value of d (e.g., in a reasonable range between $d = 15-25$) has only a minor impact on the results. For a more detailed description of the dispersion correction, see ref 41.

The DFT-D approach uses a scale factor to derive the atomic vdW radii ($r_{\mathrm{scal}}^{\mathrm{vdW}} = 1.1$ in the original work) from computed atomic electron densities. These original radii, however, lead to small double-counting effects with some functionals. Preliminary investigations carried out for this work showed that this choice of the scale factor, in particular, influences the description of hydrogen bonds. Therefore, we decided to rescale the radii in Table 1 of ref 41 by 1.04545 (i.e., $r_{\mathrm{scal}}^{\mathrm{vdW}} = 1.15$) for all reoptimized functionals. Furthermore, a fixed s_6 value of unity gives an asymptotically correct and consistent description of the London dispersion energy. Applying the DFT-D correction during the fitting procedure,

Density Functional Thermochemistry

J. Chem. Theory Comput., Vol. 6, No. 1, 2010 **115**

furthermore, reduces the very approximate description of dispersion effects by the semilocal DF.

The parameter optimization procedure is based on the fit set introduced in Section 4.1. The root-mean-square deviation (rmsd) for the complete fit set is calculated in each fitting cycle and is minimized. The, thus, obtained functionals are in the following denoted by the prefix 'o', which stands for optimized, while the suffix '-D' indicates the use of the dispersion correction (e.g., oPWLYP-D or oTPSS-D). To investigate the effect of the reoptimization procedure, calculations were also carried out with the original (*meta-*)GGA functionals. Again the empirical dispersion correction was applied, but this time in the originally proposed version, i.e., $r_{scal}^{vdW} = 1.1$ and the originally determined s_6 parameters: 1.20 (BLYP-D), 0.75 (PBE-D), and 1.00 (TPSS-D).[41] So far, no s_6 parameter for the mPWLYP functional has been published. Therefore, we determined it by calculations of the S22 test set (def2-QZVP basis). The optimal s_6 parameter was found to be 0.90, which yielded the lowest MAD of 0.60 kcal mol^{-1}. B3LYP-D and B2PLYP-D calculations were carried out with the original s_6 values of 1.05 and 0.55, respectively.[31,41]

4. Reoptimization of Common (*meta-*)GGA Functionals

4.1. The Fit Set. The database used for the fitting procedure consists of 143 entries, comprising seven different chemical properties. The complete set is shown in Table S25 of the Supporting Information. All reference data are ZPVE exclusive and without thermal corrections. The first 49 entries are atomization energies and 47 of them are taken from the G2/97 test set.[1] In addition to the 47 mentioned G2/97 systems, the total atomization energies of the adamantane and anthracene molecules, derived from experiment,[97] are included. These hydrocarbons have about the same size, but the uniformly accurate description of their unsaturated and saturated structures is difficult to achieve by DFs. The next 15 entries are total atomic energies.[98] As these energies are rather large, we scaled down the deviations between the investigated method and the reference data in order to be compatible with the other relative energies (see Table S25, Supporting Information). The fit set includes, furthermore, eight atomic ionization potentials and seven atomic electron affinities taken from the G2-1 test set.[17] As already mentioned above, density functional methods sometimes fail to correctly predict isomerization energies. Therefore, we included the difficult isomerization reaction from isooctane to *n*-octane, which is also part of the ISO34 database, with a weighting factor of 5. As the fitting procedure is carried out with the empirical dispersion correction, it was also important to include noncovalently bound systems. Therefore, we took the five smallest systems from the S22 database. These are the ammonia, water, formic acid, methane, and ethene dimers. Deviations from the reference values are scaled by 20 for the first 3 and by 30 for the last 2 systems. Finally, we included 58 decomposition energies from the MB08-165 subset, which involves rather small but still complicated artificial structures.

Table 2. Original and Reoptimized Parameters of the BLYP-D Functional

	β_{B88}	a_{LYP}	b_{LYP}	c_{LYP}	d_{LYP}	rmsd^a
BLYP-D^b	0.00420	0.04918	0.132	0.2533	0.349	10.01
oBLYP-D^b	0.00401	0.05047	0.140	0.2196	0.363	8.26

^{a} Root mean square deviation for the complete fit set in kcal mol^{-1}. All calculations were carried out with (aug)-def2-QZVP. ^{b} s_6 = 1.00 and r_{scal}^{vdW} = 1.15.

The fitting procedure itself was already outlined in the Computational Details Section. In the following, each reoptimized functional will be discussed.

4.2. The oBLYP-D Functional. The BLYP functional consists of Becke1988 (B88) exchange[65] combined with LYP correlation. The expression for B88 exchange is[65]

$$E_X^{B88} = E_X^{LDA} - \beta_{B88} \sum_\sigma \int \rho_\sigma^{4/3} \frac{x_\sigma^2}{1 + 6\beta_{B88}x_\sigma \sinh^{-1}x_\sigma} d^3r \tag{5}$$

where E_X^{LDA} is the LDA exchange energy, σ is the spin variable (for α and β spin, respectively), and x_σ is the reduced gradient variable, defined in eq 6:

$$x_\sigma = \frac{|\nabla\rho_\sigma|}{\rho_\sigma^{4/3}} \tag{6}$$

The parameter β_{B88} was originally obtained by a fit to the Hartree–Fock exchange energies of the six rare gas atoms from He to Rn. It was determined to be 0.00420 au (see Table 2).

Lee, Yang, and Parr derived the LYP correlation functional as a second-order gradient expansion of the Colle-Salvetti formula.[66,69] Miehlich et al. eliminated the second-order gradient from the LYP formula by partial integration and presented the following expression, which is usually implemented in DFT program packages (eq 7):[100]

$$E_C^{LYP} = -a_{LYP}\int \frac{4}{1 + d_{LYP}\rho^{-1/3}}\frac{\rho_\alpha\rho_\beta}{\rho} -$$
$$a_{LYP}b_{LYP}\int \omega\{\rho_\alpha\rho_\beta[2^{11/3}C_F(\rho_\alpha^{8/3} + \rho_\beta^{8/3}) +$$
$$\left(\frac{47}{18} - \frac{7}{18}\delta\right)|\nabla\rho|^2 - \left(\frac{5}{2} - \frac{1}{18}\delta\right)(|\nabla\rho_\alpha|^2 + |\nabla\rho_\beta|^2) -$$
$$\frac{\delta - 11}{9}\left(\frac{\rho_\alpha}{\rho}|\nabla\rho_\alpha|^2 + \frac{\rho_\beta}{\rho}|\nabla\rho_\beta|^2\right)] - \frac{2}{3}\rho^2|\nabla\rho|^2 +$$
$$\left(\frac{2}{3}\rho^2 - \rho_\alpha^2\right)|\nabla\rho_\beta|^2 + \left(\frac{2}{3}\rho^2 - \rho_\beta^2\right)|\nabla\rho_\alpha|^2\} \tag{7}$$

with

$$\omega = \frac{\exp(-c_{LYP}\rho^{-1/3})}{1 + d_{LYP}\rho^{-1/3}}\rho^{-11/3},$$

$$\delta = c_{LYP}\rho^{-1/3} + \frac{d_{LYP}\rho^{-1/3}}{1 + d_{LYP}\rho^{-1/3}}, \quad C_F = \frac{3}{10}(3\pi^2)^{2/3} \tag{8}$$

Table 3. Original and Reoptimized Parameters of the mPWLYP-D Functional

	b_{PW}	c_{PW}	d_{PW}	a_{LYP}	b_{LYP}	c_{LYP}	d_{LYP}	rmsd[a]
mPWLYP-D[b]	0.00426	1.6455	3.72	0.04918	0.132	0.2533	0.349	8.99
oPWLYP-D[b]	0.00402	0.8894	0.79	0.04960	0.144	0.2262	0.346	8.26

[a] Rmsd for the complete fit set in kcal mol^{-1}. All calculations were carried out with (aug)-def2-QZVP. [b] s_6 = 1.00 and r_{scal}^{vdW} = 1.15.

The LYP functional depends on four parameters a_{LYP}, b_{LYP}, c_{LYP}, and d_{LYP} that were determined from a fit to the He atom (see Table 2).

An evaluation of the BLYP-D functional with the original parameters and the modified dispersion correction ($s_6 = 1.00$ and $r_{scal}^{vdW} = 1.15$) gave an rmsd of 10.01 kcal mol^{-1}. During the fitting procedure, the rmsd was reduced by 17% and was converged to a value of 8.26 kcal mol^{-1}. The optimal parameters of the new oBLYP-D functional are also shown in Table 2. A reduction of the parameter values β_{B88} and b_{LYP} is observed, while the other values increased.

4.3. The oPWLYP-D Functional. The Perdew−Wang (PW) exchange[101] can be regarded as an enhanced form of B88 exchange, that additionally fulfills the Levy condition[102] and the Lieb−Oxford bound.[103] Its expression is shown in eq 9:

$$E_X^{mPW} = E_X^{LDA} -$$
$$\sum_\sigma \int \rho_\sigma^{4/3} \frac{b_{PW}x_\sigma^2 - (b_{PW} - \beta)x_\sigma^2 \exp(-c_{PW}x_\sigma^2) - 10^{-6}x_\sigma^{d_{PW}}}{1 + 6b_{PW}x_\sigma\sinh^{-1}x_\sigma - \dfrac{10^{-6}x_\sigma^{d_{PW}}}{A_x}}d^3r$$

(9)

with

$$\beta = 5(36\pi)^{-5/3}, \qquad A_x = -\frac{3}{2}\left(\frac{3}{4\pi}\right)^{1/3}$$ (10)

It depends on three parameters b_{PW}, c_{PW}, and d_{PW}. In order to enlarge the applicability of the PW functional, Adamo and Barone proposed an adjustment of these three parameters, leading to the modified Perdew−Wang exchange functional (mPW).[61] This adjustment was carried out as a fit to exact exchange energies of isolated atoms and to the differential exchange energies of the helium and neon dimers near their vdWs minima. These adjusted parameters are given in Table 3.

We started our reoptimization of the parameters with the mPWLYP-D functional, that yields an rmsd of 8.99 kcal mol^{-1}. Interestingly, the fitting procedure did not improve the rmsd value as much as for BLYP-D. In fact, the final rmsd value of the optimized PWLYP-D functional (oPWLYP-D) is exactly the same as that of oBLYP-D (8.26 kcal mol^{-1}).

All three parameter values of the exchange part were reduced. The final value of b_{PW} is almost the same as for β_{B88} in oBLYP-D (0.00402 compared to 0.00401 au). The value of c_{PW} was reduced by about 50%. The impact of the fitting procedure, though, is largest for the parameter d_{PW}. Its value decreased from 3.72 to 0.79. (Table 3). Adamo and Barone argued that this parameter is of particular importance for the long-range behavior of the functional. The observed large decrease can, thus, be explained by the fact that the

dispersion correction was applied throughout the fitting process, therefore, reducing the long-range influence inherent in the mPW functional. Due to the strongly reduced parameter values for c_{PW} and d_{PW} and the fact that b_{PW} has a similar value to β_{B88} of the reoptimized B88 exchange, we can conclude that the reoptimized PW exchange became more 'B88-like'. Evidence for this are the identical rmsd values for both oBLYP-D and oPWLYP-D.

The changes in the four LYP parameter values show similar tendencies as for the combination with B88 exchange, with the exception that here d_{LYP} also decreases. The exact values, though, are different than for oBLYP-D. All values of the new oPWLYP-D functional are shown in Table 3.

4.4. The oPBE-D Functional. The PBE exchange functional has the following form (eq 11) in which ε_X^{LDA} is the LDA exchange energy density and $F_X^{PBE}(s)$ the PBE enhancement factor (eq 12):[43]

$$E_X^{PBE} = \sum_\sigma \int \rho\varepsilon_X^{LDA}F_X^{PBE}(s_\sigma)dr$$ (11)

$$F_X^{PBE}(s) = 1 + \kappa_{PBE} - \frac{\kappa_{PBE}}{1 + \dfrac{\mu_{PBE}s_\sigma^2}{\kappa_{PBE}}}$$ (12)

κ_{PBE} and μ_{PBE} are functional parameters and $s_\sigma = x_\sigma/2(3\pi^2)^{1/3}$.

The correlation portion of the PBE functional can be written as a gradient expansion based on the correlation energy density of the uniform electron gas ε_C^{LDA} (using its PW parametrization) and on another reduced gradient variable t_σ (eqs 13 and 14):

$$E_C^{PBE} = \sum_\sigma \int \rho(\varepsilon_C^{LDA} + \beta_{PBE}t_\sigma^2 + ...)dr$$ (13)

with

$$t_\sigma \propto \frac{|\nabla\rho_\sigma|}{\phi(\zeta)\rho_\sigma}, \quad \phi(\zeta) = \frac{(1 + \zeta)^{2/3} + (1 - \zeta)^{2/3}}{2},$$

$$\zeta = \frac{\rho_\alpha - \rho_\beta}{\rho}$$ (14)

The parameter β_{PBE} controls the amount of gradient correction to the LDA part.

The original parameter values for κ_{PBE}, μ_{PBE}, and β_{PBE} are shown in Table 4. Several modifications of these were already published in the past and showed the sensitivity of the functional's results toward the parameters' values. Examples are the revised functionals revPBE,[52] RPBE,[53] mPBE,[54] PBEsol,[55] and other variants.[56,57]

When employing the PBE-D functional with the modified empirical dispersion correction (with s_6 and r_{scal}^{vdW} defined above), the rmsd for the complete fit set is very large with

Density Functional Thermochemistry

J. Chem. Theory Comput., Vol. 6, No. 1, 2010 **117**

Table 4. Original and Reoptimized Parameters of the PBE-D Functional

	κ_{PBE}	μ_{PBE}	β_{PBE}	rmsd[a]
PBE-D[b]	0.8040	0.21952	0.06672	17.11
oPBE-D[b]	1.2010	0.21198	0.04636	9.02

[a] Rmsd for the complete fit set in kcal mol^{-1}. All calculations were carried out with (aug)-def2-QZVP. [b] $s_6 = 1.00$ and $r_{scal}^{vdW} = 1.15$.

17.11 kcal mol^{-1}. The reparameterization gave an rmsd of 9.02 kcal mol^{-1}, which means a reduction of about 50%. The optimized parameter values are also shown in Table 4. A strong increase for κ_{PBE} can be observed. The final value is 1.2010, i.e., similar to that of revPBE (1.245).[52] The other two parameter values (μ_{PBE} and β_{PBE}) decrease.

4.5. The oTPSS-D Functional. Based on the PBE functional, Perdew, Kurth, Zupan, and Blaha derived a new *meta*-GGA functional called PKZB.[104] Further adjustments to PKZB were then undertaken by Tao, Perdew, Staroverov, and Scuseria resulting in the TPSS functional.[44]

The exchange part of the functional is similar to that of PBE in eq 11, but a new enhancement factor F_X^{TPSS} is defined (eq 15):

$$F_X^{TPSS} = 1 + \kappa_{PBE} - \frac{\kappa_{PBE}}{1 + \frac{x}{\kappa_{PBE}}} \quad (15)$$

κ_{PBE} is the same as for PBE. The variable x is given as (eq 16):

$$x = \left\{ \left[\frac{10}{81} + c_{TPSS} \frac{z^2}{(1+z^2)^2} \right] p + \frac{146}{2025} \tilde{q}_b^2 - \right.$$
$$\frac{73}{405} \tilde{q}_b \sqrt{\frac{1}{2} \left(\frac{3}{5} z \right)^2 + \frac{1}{2} p^2} + \frac{1}{\kappa_{PBE}} \left(\frac{10}{81} \right)^2 p^2 +$$
$$\left. 2 \sqrt{e_{TPSS}} \frac{10}{81} \left(\frac{3}{5} z \right)^2 + e_{TPSS} \mu_{PBE} p^3 \right\} / [(1 + \sqrt{e_{TPSS}} p)^2] \quad (16)$$

where

$$z = \frac{\tau^W}{\tau} \qquad \alpha = \frac{\tau - \tau^W}{\tau^{UEG}}$$
$$\tilde{q}_b = \frac{9}{20} \frac{(\alpha - 1)}{[1 + b_{TPSS} \alpha(\alpha - 1)]^{1/2}} + \frac{2p}{3} \quad (17)$$

p is s^2, τ the kinetic energy density, τ^W the von Weizsäcker kinetic energy density, and τ^{UEG} the uniform gas kinetic energy density. The μ_{PBE} parameter is the same as for PBE; b_{TPSS}, c_{TPSS}, and e_{TPSS} are new functional parameters (see Table 5).

The TPSS correlation functional is defined as follows (eq 18):

$$E_C^{TPSS} = \int \rho \varepsilon_C^{revPKZB} \left[1 + d_{TPSS} \varepsilon_C^{revPKZB} \left(\frac{\tau^W}{\tau} \right)^3 \right] d^3 r \quad (18)$$

with

$$\varepsilon_C^{revPKZB} = \varepsilon_C^{PBE}[\rho_\alpha, \rho_\beta, \nabla\rho_\alpha, \nabla\rho_\beta] \left[1 + C(\zeta, \xi) \left(\frac{\tau^W}{\tau} \right)^2 \right] -$$
$$[1 + C(\zeta, \xi)] \left(\frac{\tau^W}{\tau} \right)^2 \sum_\sigma \frac{\rho_\sigma}{\rho} \tilde{\varepsilon}_C \quad (19)$$

where

$$\tilde{\varepsilon}_C = \max[\varepsilon_C^{PBE}[\rho_\sigma, 0, \nabla\rho_\sigma, 0], \varepsilon_C^{PBE}[\rho_\alpha, \rho_\beta, \nabla\rho_\alpha, \nabla\rho_\beta]]$$
$$C(\zeta, \xi) = \frac{0.53 + 0.87\zeta^2 + 0.50\zeta^4 + 2.26\zeta^6}{\left[1 + \xi^2 \frac{(1+\zeta)^{-4/3} + (1-\zeta)^{-4/3}}{2} \right]^4}$$
$$\xi = \frac{|\nabla\zeta|}{2(3\pi^2\rho)^{1/3}} \quad (20)$$

As defined in eq 14, ζ is the relative spin polarization. The TPSS correlation part depends on two parameters. These are d_{TPSS}, as shown in eq 18, and β_{PBE}, which is part of the PBE correlation functional ε_C^{PBE} and of $\tilde{\varepsilon}_C$ (ref 44 gives a detailed description of all the necessary variables in the TPSS functional). In 2007, Perdew et al. published a reparameterized version of TPSS, with different values for μ_{PBE}, c_{TPSS}, and e_{TPSS} (Table 5).[58] In this study, we will refer to this modified variant as 'mod-TPSS'. Very recently, another revised version of TPSS (revTPSS) was presented.[59]

In total, we chose to optimize seven parameters as shown in Table 5. Initially, TPSS-D yielded an rmsd of 9.69 kcal mol^{-1}, which was reduced by about 30% to 6.81 kcal mol^{-1}. This is the lowest rmsd obtained for the fit set in this study. Lifting all physical constraints, that were imposed on the original derivation of TPSS, has a great influence on all seven parameter values (see Table 5). In particular, b_{TPSS}, e_{TPSS}, and d_{TPSS} change significantly. The original PBE parameters show the opposite trend for oTPSS-D than for oPBE-D, i.e., κ_{PBE} decreases, whereas μ_{PBE} and β_{PBE} strongly increase.

5. Results and Discussion

5.1. The GMTKN24 Set. *5.1.1. oBLYP-D and oPWLYP-D.* The MADs for all subsets of the GMTKN24 database are shown for the BLYP-D and oBLYP-D functionals in Figure 2. The actual MAD and the rmsd values for these functionals with and without dispersion correction are shown in Tables S26 and S27 of the Supporting Information. Reparameterizing the functional lowers the MAD for the MB08−165 subset by 1 kcal mol^{-1} (from 9.2 to 8.2 kcal mol^{-1}). Atomization energies, on the other hand, are better described by the original parameters (the MAD increases by about 1 kcal mol^{-1} for oBLYP-D). Ionization potentials and electron affinities are not affected by the reparameterization. Proton affinities are slightly better described by 0.4 kcal mol^{-1} with oBLYP-D. The effect of the reparameterization on SIE related problems either is negligible (see the almost identical MADs for BHPERI) or leads to slightly worse results: the MADs for the SIE11 and BH76 sets increase by 0.5 kcal mol^{-1} each.

The impact of the new parameters on reaction energies depends on their type. Whereas the values for the BH76RC,

Table 5. Original and Reoptimized Parameters of the TPSS-D Functional

	b_{TPSS}	c_{TPSS}	e_{TPSS}	μ_{PBE}	κ_{PBE}	β_{PBE}	d_{TPSS}	rmsd[a]
TPSS-D[b]	0.40	1.59096	1.537	0.21952	0.804	0.06672	2.8	9.69
'modTPSS'[c]	0.40	1.39660	1.380	0.25000	0.804	0.06672	2.8	—
oTPSS-D[b]	3.43	0.75896	0.165	0.41567	0.778	0.08861	0.7	6.81

[a] Rmsd for the complete fit set in kcal mol^{-1}. All calculations were carried out with (aug)-def2-QZVP. [b] $s_6 = 1.00$ and $r_{scal}^{vdW} = 1.15$. [c] Modified TPSS variant taken from ref 58. No rmsd value was calculated for this functional.
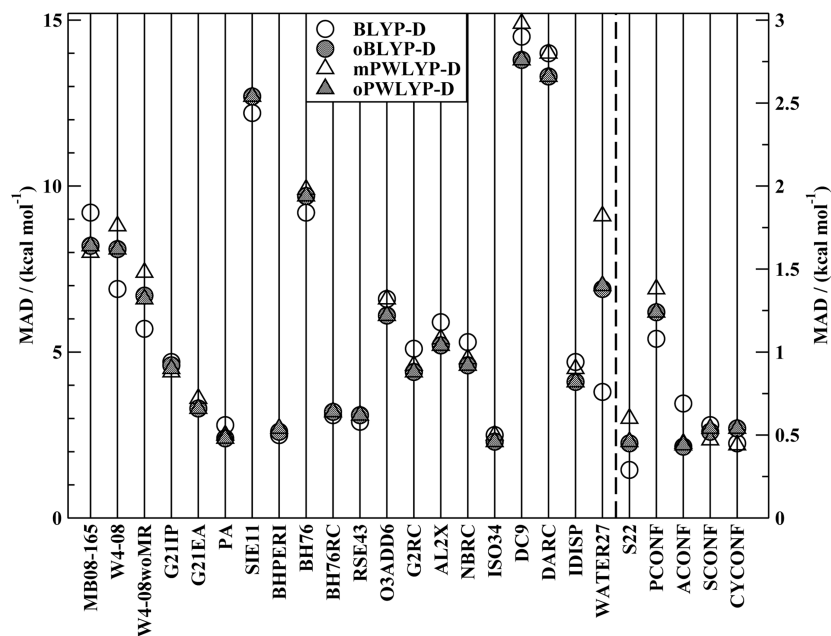
Figure 2. MADs of the (o)BLYP-D and o/mPWLYP-D methods for the GMTKN24 benchmark set. For a better visualization, a different scale is used for the last five data sets. All calculations were carried out with (aug)-def2-QZVP.

RSE43, and ISO34 sets do not change much, improvements for oBLYP-D can be observed for O3ADD6 (improvement by 0.5 kcal mol^{-1}), G2RC, AL2X, and NBRC (0.7 kcal mol^{-1}, each). The MADs for the difficult cases (DC9) and Diels−Alder reactions (DARC) also decrease, although they are still at a high level with 13.8 and 13.3 kcal mol^{-1}, respectively.

The description of intramolecular dispersion effects improves (from 4.7 to 4.1 kcal mol^{-1}). For the WATER27 set, though, a peculiar behavior is observed. The MAD value increases from 3.8 to 6.9 kcal mol^{-1}. On the contrary, oBLYP without dispersion correction shows an MAD of 4.1 kcal mol^{-1} (compared to 9.9 kcal mol^{-1} for BLYP). This can be primarily attributed to the large $(H_2O)_{20}$ clusters that contain many hydrogen bonds. When applying the dispersion correction to such systems, the results are very prone to the scale parameter of the vdW radii. On the other hand, the chosen functional also seems to be important, and compensating effects between functional and dispersion correction cannot be always foreseen. Another example is the S22 test set for which the original BLYP-D shows an extraordinary good result (MAD of 0.29 kcal mol^{-1}), which is in the range of double-hybrid functionals (see Tables S26 and S35 in the Supporting Information). The oBLYP-D method yields an MAD of 0.45 kcal mol^{-1}, which is worse than BLYP-D but still a good result compared to other functionals.

The four conformer subsets benefit for both BLYP and oBLYP from the dispersion correction. But for these sets, a heterogeneous behavior can be observed. While the values

increase for PCONF (by 0.14 kcal mol^{-1}) and CYCONF (by 0.09 kcal mol^{-1}), ACONF and SCONF are better described by oBLYP-D (by 0.26 and 0.04 kcal mol^{-1}).

The mPWLYP-D and oPWLYP-D functionals (Figure 2 and Tables S28 and S29 in the Supporting Information) show a different behavior. The MAD of mPWLYP-D for MB08−165 is already very good for a GGA functional with 8.0 kcal mol^{-1}. It worsens slightly by 0.2 kcal mol^{-1} for oPWLYP-D. For most of the subsets, the MAD almost stays the same when changing the parameters. Improvements are observed for atomization energies (by 0.6 kcal mol^{-1}), O3ADD6 (0.5 kcal mol^{-1}), DC9 (1.1 kcal mol^{-1}), DARC (0.7 kcal mol^{-1}), IDISP (0.4 kcal mol^{-1}), WATER27 (2.1 kcal mol^{-1}), and S22 (by 0.14 kcal mol^{-1}). The description of conformers improves slightly for PCONF, does not change at all for ACONF, and worsens slightly for SCONF and CYCONF.

A direct comparison between BLYP-D and mPWLYP-D clearly shows that in some cases both functionals differ significantly from each other, while in others they show similar results. The reparameterization, though, has the effect that both, oBLYP-D and oPWLYP-D yield almost identical MADs for all 24 subsets. This underlines the statement already made in the previous section, that the PW exchange part became more 'B88-like', and that a mathematically simpler functional performs almost identically to a more complicated one.

5.1.2. oPBE-D and oTPSS-D. The behavior of PBE-D and oPBE-D is more heterogeneous than for the functionals discussed above (Figure 3 and Tables S30 and S31 in the
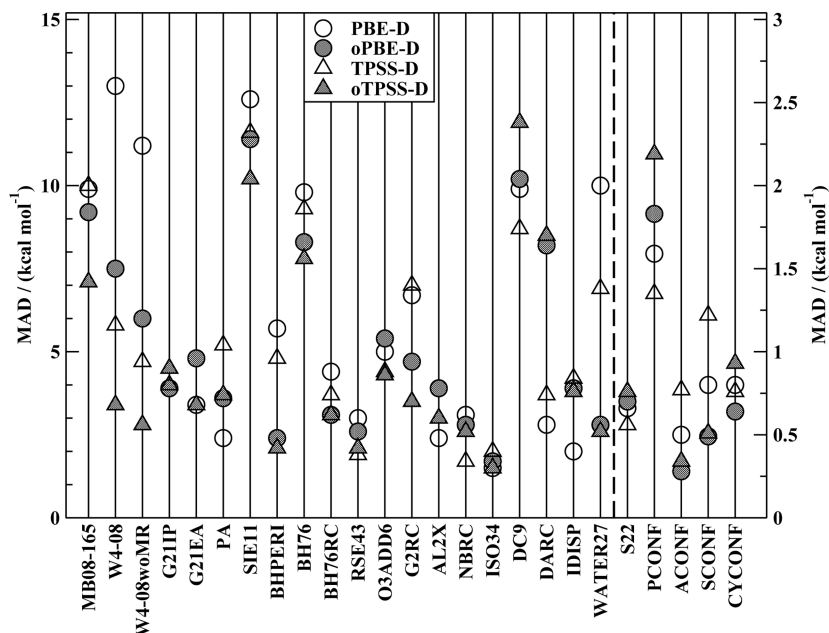
Density Functional Thermochemistry

J. Chem. Theory Comput., Vol. 6, No. 1, 2010 **119**

Figure 3. MADs of the (o)PBE-D and (o)TPSS-D methods for the GMTKN24 benchmark set. For a better visualization, a different scale is used for the last five data sets. All calculations were carried out with (aug)-def2-QZVP.

Supporting Information). In many cases, oPBE-D performs better than PBE-D. The MAD for the MB08−165 subset decreases by 0.7 to 9.2 kcal mol^{-1}, although this value is still 1 kcal mol^{-1} higher than for oBLYP-D. A large improvement is observed for atomization energies, which is in accordance with the parameter value of κ_{PBE} becoming more 'revPBE-like'. The MAD for W4−08 is reduced by more than 40% from 13.0 to 7.4 kcal mol^{-1}. The MAD for the SIE11 test set is reduced by 1.2 kcal mol^{-1}. A closer look at the barrier height subsets reveals that the original PBE-D approach shows worse results than the BLYP-D functional (e.g., 5.7 compared to 2.5 kcal mol^{-1} for BHPERI and 9.8 vs 9.2 kcal mol^{-1} for BH76). The optimized version though yields better MADs than that of oBLYP-D (2.4 vs 2.6 kcal mol^{-1} for BHPERI and 8.3 vs 9.7 kcal mol^{-1} for BH76).

Improvements for oPBE-D are also observed for the 'small molecule' reaction energy test sets, as can be seen for BH76RC, RSE43, and G2RC. For the latter one, the MAD is 2 kcal mol^{-1} lower than for PBE-D. The other reaction subsets show more or less similar results (O3ADD6, NBRC, ISO34, and DC9). This is also the case for the ionization potentials for which neither the dispersion correction nor the reparameterization have any significant effect.

Worse MADs are observed for the description of electron and proton affinities and the AL2X, DARC, and IDISP subsets. For the DARC subset, the very good MAD of 2.8 kcal mol^{-1} for PBE-D (better than any other functional in this study) increases by a factor of 3, although the MAD of 8.2 kcal mol^{-1} for oPBE-D is still better than those of the other optimized functionals.

For WATER27, the functionals again exhibit a peculiar behavior. Adding the dispersion correction with the originally proposed scale factors leads to an increased MAD from 3.2 (PBE) to 10.0 kcal mol^{-1} (PBE-D). The opposite behavior is observed for the optimized functional with different scale factors for the dispersion correction. Here, the MAD for

oPBE is quite large with 12.1 kcal mol^{-1}, but it decreases to a very small value of 2.8 kcal mol^{-1} for oPBE-D.

The MAD for the S22 set is slightly larger (by 0.04 kcal mol^{-1}) for oPBE-D than for PBE-D. The MAD increases also for the tripeptide conformers. On the other hand, the alkane, sugar, and cysteine conformers are much better described by oPBE-D.

Similar trends can also be observed for the TPSS-D and oTPSS-D functionals (Figure 3 and Tables S32 and S33 in the Supporting Information). Although located on a higher rung on Jacob's Ladder, TPSS-D does not perform better for MB08−165 than the GGA functionals (MAD of 10.0 kcal mol^{-1}). On the contrary, oTPSS-D performs very well with 7.1 kcal mol^{-1}, which is a value that comes close to that of hybrid functionals. Large improvements are also observed for atomization energies, proton affinities, SIE related problems, and barrier heights and the BH76RC, G2RC, ISO34, and IDISP subsets. On the other hand, MADs worsen for G21IP, NBRC, DC9, and DARC, but only the results for the last two sets can be regarded as 'outliers' for the complete database (MADs of 11.9 and 8.5 kcal mol^{-1}). The combination of the new functional parameters and slightly modified dispersion correction parameters performs better for IDISP and WATER27. In fact, the MAD of oTPSS-D for WATER27 is with 2.6 kcal mol^{-1} the best of all functionals tested in this study. On the other hand, the MAD for the S22 test increases by 0.2 kcal mol^{-1}. The description of the tripeptide conformers also deteriorates (1.4 kcal for TPSS-D vs 2.2 kcal mol^{-1} for oTPSS-D). The MADs for ACONF and SCONF improve by about 60%. CYCONF, though, shows a slightly worse MAD for oTPSS-D (0.76 vs 0.93 kcal mol^{-1}).

Another way to compare the oTPSS-D functional with TPSS-D is shown in Figure 4, part a. There the ratios of the MADs of both functionals [i.e., MAD(oTPSS-D)/MAD(TPSS-D)] are shown. A value smaller than 1 means that oTPSS-D
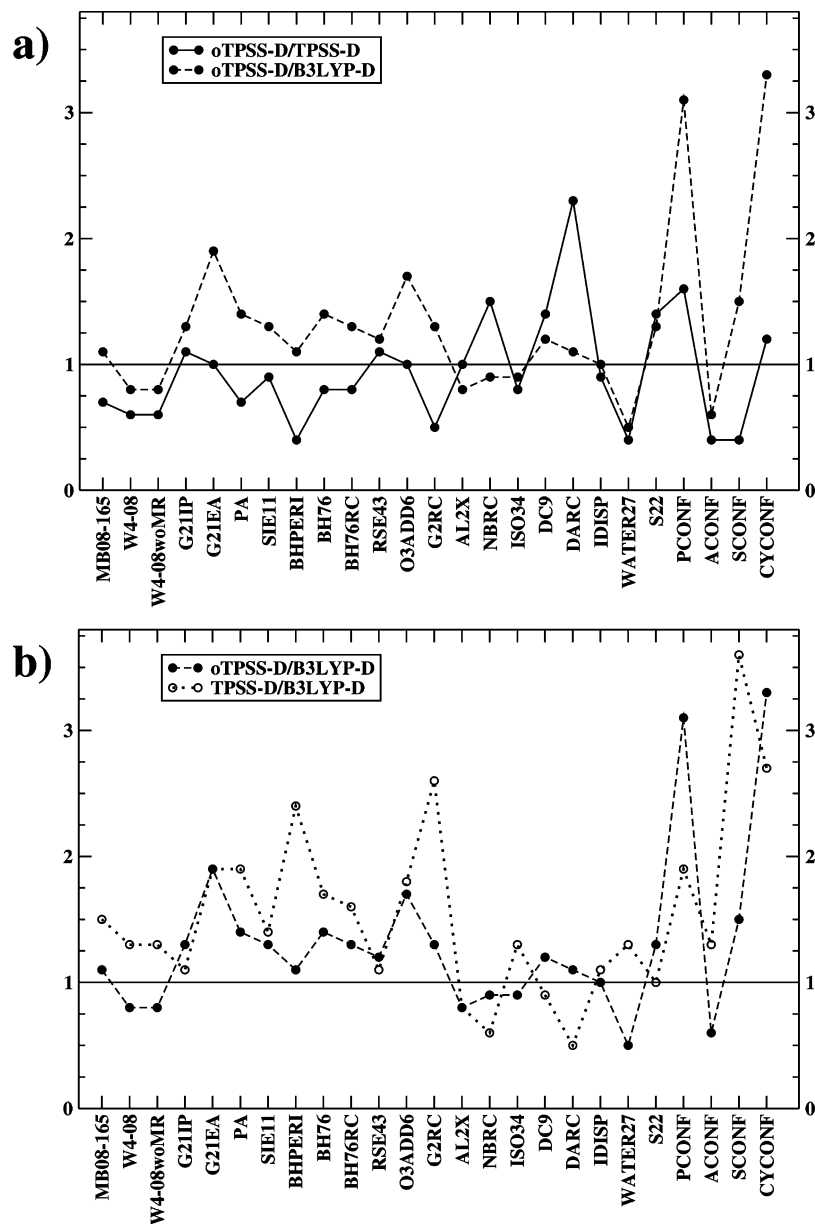
Figure 4. Ratios of the MADs of oTPSS-D and TPSS-D (a), oTPSS-D and B3LYP-D (a and b), and TPSS-D and B3LYP-D (b) for the complete GMTKN24 database. The lines between the data points are just drawn to guide the eye.

performs better than TPSS-D and vice versa. Values close to 1 indicate only minor changes. The curve clearly shows the reoptimized functional's improved performance for most of the considered subsets. Additionally, we tested the modified TPSS variant ('modTPSS') by Perdew et al. for the complete GMTKN24 database. The MADs and rmsds are shown in the Supporting Information, Table S34. A comparison between oTPSS-D, TPSS-D, and 'mod-TPSS-D' is shown in Figure S1 in the Supporting Information. It can clearly be seen that 'mod-TPSS-D' often yields results that are similar to TPSS-D and that it is also outperformed by oTPSS-D.

As the TPSS functional belongs to a higher rung on Jacob's Ladder, it is also more expensive than, e.g., PBE, due to the calculation of the kinetic energy density. This increase in computing time, however, is less than the corresponding increase when going to hybrids, and using TPSS would be adequate if its accuracy and robustness were significantly higher than for PBE.

The GMTKN24 database allows a direct comparison between PBE and TPSS, and thus, it is possible to evaluate the cost−benefit ratio for TPSS. In only five cases, the TPSS-D approach shows an improvement of more than 1 kcal mol^{-1} compared to that of PBE-D: W4−08, SIE11, RSE43, NBRC, and DC9. In two cases, PBE-D is better by more than 1 kcal mol^{-1} (PA and IDISP). In all of the other cases the PBE-D and TPSS-D results lie close to each other, and there is no real improvement when applying the *meta*-GGA functional.

When comparing the optimized versions with each other, one sees that the number of cases for which the *meta*-GGA functional is, on average, better by more than 1 kcal mol^{-1} increases to six: MB08−165, W4−08, G21EA, SIE11, O3ADD6, and G2RC. On the other hand, oPBE-D shows superior behavior only for the DC9 and CYCONF subsets.

5.1.3. B3LYP-D and B2PLYP-D. Additional calculations were carried out with the B3LYP-D and B2PLYP-D methods. The results are shown in Figure 5 and in the Supporting
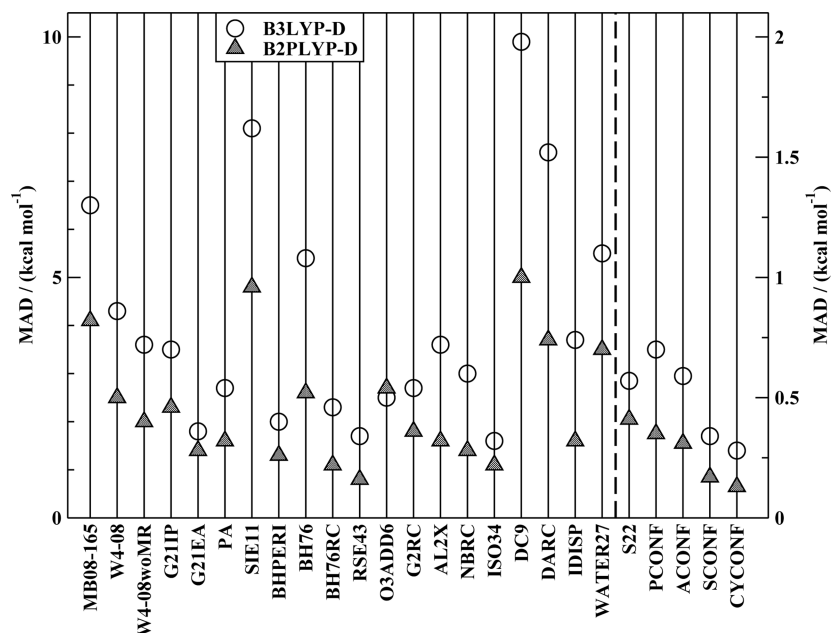
Figure 5. MADs of the B3LYP-D and B2PLYP-D methods for the GMTKN24 benchmark set. For a better visualization, a different scale is used for the last five data sets. All calculations were carried out with (aug)-def2-QZVP.

Information, Tables S35 and S36. Not unexpectedly, we find that B2PLYP-D clearly outperforms the allegedly 'state-of-the-art' B3LYP functional in all cases. In most of them, the MAD is reduced by 50% or more. Only for G21EA and O3ADD6, the results are quite similar. Both functionals are the only methods in this study that yield an MAD lower than 1 kcal mol^{-1} for the PCONF subset (0.70 for B3LYP-D and 0.35 for B2PLYP-D). A comparison between B3LYP-D and the original and optimized (*meta*-)GGA functionals shows that the latter ones sometimes yield better or comparable results. The oTPSS-D functional shows lower or very similar MADs in eight cases: W4-08, BHPERI, AL2X, NBRC, ISO34, IDISP, WATER27, and ACONF. From the results, it can be seen that the other methods also partially outperform B3LYP-D, though not in so many cases as for oTPSS-D (five cases for TPSS-D, seven cases for oPBE-D and PBE-D, and one case for BLYP-D, oBLYP-D, mPWLYP-D, and oPWLYP-D). In Figure 4, the ratios of the MADs of oTPSS-D and B3LYP-D [i.e., MAD(oTPSS-D)/MAD(B3LYP-D)] and of TPSS-D and B3LYP-D [i.e., MAD(TPSS-D)/MAD(B3LYP-D)] are given. The curves clearly show that, in the case of oTPSS-D, the ratios are closer to 1 and in many cases even smaller. On the other hand, the curve for TPSS-D shows that it is by far outperformed by B3LYP-D in the majority of cases.

Compared to B2PLYP-D, better or similar results are obtained for WATER27 (by oTPSS-D and oPBE-D), S22 (by BLYP-D), and ACONF (by oTPSS-D and oPBE-D). Still, B2PLYP-D shows for the majority of cases the best results of all functionals investigated in this study.

5.1.4. Overall Statistical Analysis. The analysis of the GMTKN24 database is completed by an overall statistical evaluation. In the spirit of the work by Truhlar and co-workers, we define a weighted total mean absolute deviation (WTMAD) to combine all obtained MADs to one final number for each tested method. Of course, such a value can be defined in several ways, and there is no real right or wrong. We tested many schemes, and the overall interpreta-

tion was not altered by the actual way of calculating the WTMADs. In the scheme, which we finally present here, each of the 24 MAD values is weighted by the number of entries of each subset (see eq 21). This takes into account the size of each set. Furthermore, each subest is weighted by an additional factor that was calculated as the ratio between the MADs of BLYP and B2PLYP-D [i.e., MAD-(BLYP)/MAD(B2PLYP-D)]. This takes into account the difficulty of a certain subset. As one of the worst methods without dispersion correction in this study, BLYP and, as the best method, B2PLYP-D are chosen. The actual values of these scale factors are usually in a range between 2.0 and 3.0 for reaction energies, atomization energies, ionization potentials and proton and electron affinities. They are significantly larger for SIE11, BHPERI, AL2X, NBRC, DC9, and DARC, and for subsets where London dispersion effects are important. The final formula is:

$$
\begin{aligned}
\text{WTMAD} = [&2.7 \times 165 \times \text{MAD(MB08-165)} + \\
&2.8 \times 99 \times \text{MAD(W4-08)} + \\
2.0 \times 36 \times \text{MAD(G21IP)} + &2.4 \times 25 \times \text{MAD(G21EA)} + \\
1.6 \times 12 \times \text{MAD(PA)} + &2.4 \times 11 \times \text{MAD(SIE11)} + \\
&4.5 \times 26 \times \text{MAD(BHPERI)} + \\
&3.2 \times 76 \times \text{MAD(BH76)} + \\
&3.0 \times 30 \times \text{MAD(BH76(RC))} + \\
&4.4 \times 43 \times \text{MAD(RSE43)} + \\
&2.2 \times 6 \times \text{MAD(O3ADD6)} + \\
3.1 \times 25 \times \text{MAD(G2RC)} + &7.1 \times 7 \times \text{MAD(AL2X)} + \\
6.8 \times 6 \times \text{MAD(NBRC)} + &2.9 \times 34 \times \text{MAD(ISO34)} + \\
4.1 \times 9 \times \text{MAD(DC9)} + &6.2 \times 14 \times \text{MAD(DARC)} + \\
&12.9 \times 6 \times \text{MAD(IDISP)} + \\
&2.8 \times 27 \times \text{MAD(WATER27)} + \\
&11.7 \times 22 \times \text{MAD(S22)} + \\
&13.8 \times 10 \times \text{MAD(PCONF)} + \\
&3.5 \times 15 \times \text{MAD(ACONF)} + \\
&5.2 \times 17 \times \text{MAD(SCONF)} + \\
&5.0 \times 10 \times \text{MAD(CYCONF)}]/2682.5 \quad (21)
\end{aligned}
$$

122 *J. Chem. Theory Comput., Vol. 6, No. 1, 2010*

Goerigk and Grimme

Table 6. WTMADs for functionals without (DFT) and with dispersion correction (DFT-D)[a]

functional	DFT	DFT-D[b]
BLYP	7.6	5.3
oBLYP	6.8	5.3
mPWLYP	6.8	5.6
oPWLYP	6.8	5.3
PBE	6.2	5.9
oPBE	6.6	4.9
TPSS	5.8	5.0
'modTPSS'[c]	6.3	5.0
oTPSS	5.5	4.0
B3LYP	5.4	3.6
B2PLYP	3.0	2.0

[a] In kcal mol^{-1}. All calculations were carried out with (aug)-def2-QZVP. [b] Empirical dispersion correction. For the optimized functionals with s_6 =1.00 and r_{scal}^{vdW} = 1.15; for the other functionals with r_{scal}^{vdW} = 1.1 and different s_6 values: 1.20 (BLYP-D), 0.90 (mPWLYP-D), 0.75 (PBE-D), 1.00 (TPSS-D and 'mod-TPSS-D'), 1.05 (B3LYP-D) and 0.55 (B2PLYP-D). [c] 'modTPSS' is the modified TPSS variant taken from ref 58.

The WTMADs for all functionals with and without dispersion correction are listed in Table 6. For all methods, one can see the importance of adding the empirical dispersion correction, as the WTMADs are lowered significantly. The only exception is the PBE functional, where the WTMAD stays nearly the same, due to compensation effects. This is mainly due to the typical overbinding behavior of PBE (e.g., for atomization energies or hydrogen bonds), which is further increased by the dispersion correction.

A comparison between the original and reparameterized versions of BLYP-D and mPWLYP-D shows that, overall, the reparameterization does not change the WTMADs significantly. In the case of BLYP-D and oBLYP-D, the WTMADs have identical values (5.3 kcal mol^{-1}); the WTMAD of oPWLYP-D is also 5.3 kcal mol^{-1} and is just 0.3 kcal mol^{-1} lower than that of mPWLYP-D. While the PBE-D functional at 5.9 kcal mol^{-1} has a higher WTMAD than the 'LYP-based' ones, oPBE-D yields a value slightly lower than oBLYP-D and oPWLYP-D (4.9 kcal mol^{-1}). Thus, all GGA functionals yield WTMADs of about 5 kcal mol^{-1} or more. The WTMAD for TPSS-D is 5.0 kcal mol^{-1}. This again emphasizes that TPSS-D cannot be regarded as an improvement compared to GGA functionals. This statement is also valid for the modified TPSS variant ('mod-TPSS-D'; WTMAD = 5.0 kcal mol^{-1}). The only reparameterized functional with a value significantly smaller than 5.0 kcal mol^{-1} is oTPSS-D. With 4.0 kcal mol^{-1}, it is even close to B3LYP-D (3.6 kcal mol^{-1}). B2PLYP-D shows the lowest WTMAD of all tested functionals with 2.0 kcal mol^{-1}, underlining again its superior performance.

5.2. Benchmark Study of Geometries. To test the influence of the reparameterization on molecular structures, the original and optimized (*meta*-)GGA functionals were applied to three geometry benchmark sets. The first one contains 36 bond lengths of 31 small molecules containing first-row elements.[105] The second test set comprises 42 bond lengths of 32 small molecules containing second-row elements.[106] The third test set is made up from 24 transition-metal compounds (28 bond lengths).[107,108] All reference values were derived from experiments. Table 7 shows the mean (MD), MAD, rmsd, smallest (min), and largest

deviations (max) for all test sets and functionals. The actual deviations for each molecule are listed in the Supporting Information, Tables S37−S39.

The results for the light element test set indicates that the reparameterization only has a small influence on the MDs, MADs, and rmsds and the error range. BLYP-D and oBLYP-D yield an MAD of 1.2 and 1.1 pm, respectively. Both mPWLYP-D and oPWLYP-D yield geometries of the same quality with MADs of 1.2 pm. Also for the other functionals the MAD does only change marginally: 1.0 pm for PBE-D, 1.2 pm for oPBE-D, 0.8 pm for TPSS-D, and 0.9 pm for oTPSS-D.

The MADs for the heavy element test set are higher than for the first one, but the same trends can be observed as before. There is only a marginal improvement for oBLYP-D and oPWLYP-D, and similar to the GMTKN24 database, both functionals give identical MADs with 2.2 pm. Both oPBE-D and oTPSS-D yield slightly worse results with 2.0 and 1.6 pm compared to 1.6 (PBE-D) and 1.3 (TPSS-D).

The errors for the transition-metal test set are in the same range as for the second one. Again, there is only a small improvement for the 'LYP-based' functionals. Compared to its original version, oPBE-D worsens by 0.6 pm. The MAD of oTPSS-D is larger by 0.3 pm compared to that of TPSS-D.

For all test sets, the reparameterization has only a small impact on the quality of the results. In all three cases, the *meta*-GGA functionals yield the best bond lengths.

6. Conclusions

In this study, we presented a new benchmark database for applications to general main group thermochemistry, kinetics, and noncovalent interactions (GMTKN24). It is an unprecedented compilation of 24 different, chemically relevant subsets, that either were taken from already existing databases or are presented here for the first time. The new subsets are benchmarks for self-interaction error-related problems (SIE11), barrier heights of pericyclic reactions (BHPERI), reaction energies for small closed-shell molecules (G2RC), reaction sets for ammonina/borane systems (NBRC), intramolecular London dispersion interactions (IDISP) and for cases that are difficult to treat with DFT methods (DC9). Furthermore, new reference data for a set of sugar conformers (SCONF) were presented. The complete set comprises 1.049 single point calculations and 731 reference energies, based on accurate (excluding zero point vibrational energy and thermal corrections) theoretical or experimental data. We additionally suggested a scheme for calculating a weighted total mean absolute deviation (WTMAD) with which we combine the MADs of all subsets to one final statistical number, thus enabling an overall evaluation of each investigated quantum chemical method. We regard this new combination of sets as particularly useful for the evaluation of DFT methods. This was demonstrated by applying common density functionals on the (*meta*-)GGA, hybrid-GGA, and double-hybrid-GGA levels, including the empirical London dispersion correction developed in our group. Furthermore, we carried out a systematic study on the reparameterization of (*meta*-)GGA functionals to investigate the effect of an empirical parameter fitting procedure on the performance for the

Density Functional Thermochemistry

J. Chem. Theory Comput., Vol. 6, No. 1, 2010 **123**

Table 7. MD, MAD, rmsd, min, and max Deviations for Bond Lengths in pm for the Original and Reoptimized Functionals for Three Test Sets[a]

	BLYP-D	oBLYP-D	mPWLYP-D	oPWLYP-D	PBE-D	oPBE-D	TPSS-D	oTPSS-D
Light Element Test Set[b]								
MD	1.2	1.1	1.2	1.1	1.0	1.2	0.7	0.8
MAD	1.2	1.1	1.2	1.2	1.0	1.2	0.8	0.9
rmsd	1.4	1.3	1.4	1.3	1.2	1.3	1.0	1.2
min	−0.1	−0.2	−0.2	−0.2	−0.6	0.0	−0.5	−1.1
max	3.3	2.8	3.2	2.9	2.8	3.3	2.9	3.2
Heavy Element Test Set[c]								
MD	2.4	2.2	2.3	2.2	1.6	2.0	1.3	1.4
MAD	2.4	2.2	2.3	2.2	1.6	2.0	1.3	1.6
rmsd	2.9	2.6	2.8	2.7	1.8	2.3	1.6	1.9
min	0.3	0.3	0.2	0.4	0.3	0.7	0.1	−1.6
max	7.6	6.3	7.2	6.4	3.4	4.7	4.5	6.0
Transition-Metal Test Set[d]								
MD	2.6	2.3	2.5	2.3	0.7	1.8	0.7	0.3
MAD	2.7	2.4	2.6	2.5	1.5	2.1	1.4	1.7
rmsd	3.2	3.1	3.2	3.1	1.8	2.6	1.8	2.1
min	−1.2	−1.6	−1.3	−1.6	−3.8	−2.6	−3.6	−4.7
max	8.3	9.7	9.1	9.7	3.4	6.2	3.9	3.7

[a] Deviations are defined as theory−experiment. All calculations were carried out with def2-QZVP. The particular s_6 and r_{scal}^{vdW} values for each functional can be found in the footnote of Table 6. [b] Experimental data taken from ref 105. [c] Experimental data taken from ref 106. [d] Experimental data taken from refs 107 and 108.

GMTKN24 database and of three different geometry benchmark sets. The refitting was carried out using a fit set containing 143 systems and seven chemically different problems. Our study led to the following conclusions:

(1) The influence of the new parameters is small for molecular structures (bond lengths). The MADs for the oBLYP-D and oPWLYP-D methods improve by a few tenths of a picometer compared to the original methods. The MADs for oPBE-D and oTPSS-D worsen slightly. As the quality of geometries is not significantly altered, one only has to evaluate the influence of the new parameters on energetics.

The reparameterized oBLYP-D version shows, in many cases, slight improvements compared to that of the original functional. On the other hand, the MADs of some subsets are worse or remain unchanged. Optimizing the parameters of the mPWLYP-D functional led to the oPWLYP-D functional, which yields results almost identical to oBLYP-D. The optimized PW-exchange seems to be more 'B88-like'. In the case of oPBE-D (which is more 'revPBE-like') and oTPSS-D, the influence of the new parameters is stronger than for oBLYP-D and oPWLYP-D. The description of many subsets is improved, as shown for the 'mindless-benchmark' set, atomization energies, barrier heights, some reaction energies, water clusters, and relative energies of alkane and sugar conformers. On the other hand, this study also shows that reaching a homogeneous, well-balanced behavior by just refitting existing functionals is difficult, as the description of other properties worsened, like for proton affinities, difficult cases for DFT, the description of Diels−Alder reactions, and relative energies of tripeptide and cysteine conformers.

(2) A comparison between the B3LYP-D and B2PLYP-D results for the GMTKN24 set shows that the double-hybrid exhibits superior performance by halving the MADs of B3LYP-D and by yielding the best results for the majority of subsets.

(3) An analysis of the WTMADs shows that including the empirical dispersion correction is crucial and that it reduces the values by about 1 kcal mol^{-1} or more, in most cases. The reparameterization has a small influence on the GGA functionals. The WTMADs are all around 5 kcal mol^{-1}. The TPSS-D method is in the same range, whereas a significant improvement is found for the WTMAD of oTPSS-D, which is comparable to that of B3LYP-D. This clearly indicates that the *meta*-GGA functional benefits most from lifting all physical constraints. B2PLYP-D yields by far the smallest WTMAD value (2.0 kcal mol^{-1}).

(4) oTPSS-D outperforms the GGA functionals, particularly for the MB08−165, W4−08, G21EA, SIE11, O3ADD6, and G2RC subsets. It also shows in eight cases better or comparable performance than B3LYP-D. Only for the DC9, DARC, and PCONF subsets is the applicability significantly worsened compared to that of TPSS-D. The above-discussed WTMAD value also underlines oTPSS-D's good performance, and we can recommend it in general and in particular for the calculation of atomization and reaction energies, electron affinities, ionization potentials, barrier heights, and noncovalent interactions. The very good result for the difficult WATER27 set is also striking. We cannot recommend it for self-interaction error-related problems, but note that it performs better than all other semilocal approximations. Functionals of at least hybrid-GGA quality (including a London dispersion correction) should be applied for the description of tripeptide conformers. Our study seems to be the first one that can confirm on very solid grounds previous statements that *meta*-GGAs can be almost as accurate as hybrid functionals.

(5) The new GMTKN24 database turned out to be effective for the evaluation of a given density functional's overall performance, and we strongly suggest it in future validation works of new functionals with regards to their applicability to chemically relevant problems. We regard this collection of databases as an open project. Whenever new, promising benchmark sets are proposed, we may consider to add them to our compilation, which will always be actualized (also regarding new density functionals) on our Web site.[67]

Supporting Information Available: All entries and reference data of the GMTKN24 database (Tables S1−S24), all entries of the parameters fit set (Table S25), and all results for the GMTKN24 and geometry benchmark sets (Tables S26−S39 and Figure S1). This material is available free of charge via the Internet at http://pubs.acs.org.

References

(1) Curtiss, L. A.; Raghavachari, K.; Redfern, P. C.; Pople, J. A. *J. Chem. Phys.* **1997**, *106*, 1063–1079.

(2) Curtiss, L. A.; Raghavachari, K.; Redfern, P. C.; Pople, J. A. *J. Chem. Phys.* **2000**, *112*, 7374–7383.

(3) Curtiss, L. A.; Redfern, P. C.; Raghavachari, K. *J. Chem. Phys.* **2005**, *123*, 124107.

(4) Lynch, B. J.; Truhlar, D. G. *J. Phys. Chem. A* **2003**, *107*, 8996–8999.

(5) Zhao, Y.; Truhlar, D. G. *J. Phys. Chem. A* **2006**, *110*, 10478–10486.

(6) Zhao, Y.; Truhlar, D. G. *J. Chem. Theory Comput.* **2005**, *1*, 415–432.

(7) Zhao, Y.; Truhlar, D. G. *J. Phys. Chem. C* **2008**, *112*, 6860–6868.

(8) Zhao, Y.; Lynch, B. J.; Truhlar, D. G. *J. Phys. Chem. A* **2004**, *108*, 2715–2719.

(9) Zhao, Y.; González-García, N.; Truhlar, D. G. *J. Phys. Chem. A* **2005**, *109*, 2012–2018.

(10) Zhao, Y.; Tishchenko, O.; Gour, J. R.; Li, W.; Lutz, J. J.; Piecuch, P.; Truhlar, D. *J. Phys. Chem. A* **2009**, *113*, 5786–5799.

(11) Zhao, Y.; Truhlar, D. G. *Theor. Chem. Acc.* **2008**, *120*, 215–241.

(12) Zhao, Y.; Truhlar, D. G. *J. Chem. Theory Comput.* **2009**, *5*, 324–333.

(13) Jurečka, P.; Sponer, J.; Cerny, J.; Hobza, P. *Phys. Chem. Chem. Phys.* **2006**, *8*, 1985–1993.

(14) Grimme, S.; Steinmetz, M.; Korth, M. *J. Org. Chem.* **2007**, *72*, 2118–2126.

(15) Korth, M.; Grimme, S. *J. Chem. Theory Comput.* **2009**, *5*, 993–1003.

(16) Karton, A.; Tarnopolsky, A.; Lamere, J. F.; Schatz, G. C.; Martin, J. M. L. *J. Phys. Chem. A* **2008**, *112*, 12868–12886.

(17) Curtiss, L. A.; Raghavachari, K.; Trucks, G. W.; Pople, J. A. *J. Chem. Phys.* **1991**, *94*, 7221–7230.

(18) Parthiban, S.; Martin, J. M. L. *J. Chem. Phys.* **2001**, *114*, 6014–6029.

(19) Guner, V.; Khuong, K. S.; Leach, A. G.; Lee, P. S.; Bartberger, M. D.; Houk, K. N. *J. Phys. Chem. A* **2003**, *107*, 11445–11459.

(20) Ess, D. H.; Houk, K. N. *J. Phys. Chem. A* **2005**, *109*, 9542–9553.

(21) Grimme, S.; Mück-Lichtenfeld, C.; Würthwein, E.-U.; Ehlers, A. W.; Goumans, T. P. M.; Lammertsma, K. *J. Phys. Chem. A* **2006**, *110*, 2583–2586.

(22) Dinadayalane, T. C.; Vijaya, R.; Smitha, A.; Sastry, G. N. *J. Phys. Chem. A* **2002**, *106*, 1627–1633.

(23) Neese, F.; Schwabe, T.; Kossmann, S.; Schirmer, B.; Grimme, S. *J. Chem. Theory Comput.* **2009**, *5*, 3060–3073.

(24) Johnson, E. R.; Mori-Sánchez, P.; Cohen, A. J.; Yang, W. *J. Chem. Phys.* **2008**, *129*, 204112.

(25) Piacenza, M.; Grimme, S. *J. Comput. Chem.* **2004**, *25*, 83–99.

(26) Woodcock, H. L.; Schaefer, H. F., III; Schreiner, P. R. *J. Phys. Chem. A* **2002**, *106*, 11923–11931.

(27) Schreiner, P. R.; Fokin, A. A.; Pascal, R. A.; de Meijere, A. *Org. Lett.* **2006**, *8*, 3635–3638.

(28) Lepetit, C.; Chermette, H.; Gicquel, M.; Heully, J.-L.; Chauvin, R. *J. Phys. Chem. A* **2007**, *111*, 136–149.

(29) Lee, J. S. *J. Phys. Chem. A* **2005**, *109*, 11927–11932.

(30) Grimme, S. *J. Chem. Phys.* **2006**, *124*, 034108.

(31) Schwabe, T.; Grimme, S. *Phys. Chem. Chem. Phys.* **2007**, *9*, 3397–3406.

(32) Grimme, S. *Angew. Chem., Int. Ed.* **2006**, *45*, 4460–4464.

(33) Bryantsev, V. S.; Diallo, M. S.; van Duin, A. C. T.; Goddard III, W. A. *J. Chem. Theory Comput.* **2009**, *5*, 1016–1026.

(34) Řeha, D.; Valdes, H.; Vondrasek, J.; Hobza, P.; Abu-Riziq, A.; Crews, B.; de Vries, M. S. *Chem.—Eur. J.* **2005**, *11*, 6803–6817.

(35) Gruzman, D.; Karton, A.; Martin, J. M. L. *J. Phys. Chem. A* **2009**, *113*, 11974–11983.

(36) Csonka, G. I.; French, A. D.; Johnson, G. P.; Stortz, C. A. *J. Chem. Theory Comput.* **2009**, *5*, 679–692.

(37) Wilke, J. J.; Lind, M. C.; Schaefer III, H. F.; Császár, A. G.; Allen, W. D. *J. Chem. Theory Comput.* **2009**, *5*, 1511–1523.

(38) Kurth, S.; Perdew, J. P.; Blaha, P. *Int. J. Quantum Chem.* **1999**, *75*, 889–909.

(39) Becke, A. D. *J. Chem. Phys.* **1993**, *98*, 5648–5652.

(40) Stephens, P. J.; Devlin, F. J.; Chabalowski, C. F.; Frisch, M. J. *J. Phys. Chem.* **1994**, *98*, 11623–11627.

(41) Grimme, S. *J. Comput. Chem.* **2006**, *27*, 1787–1799.

(42) Perdew, J. P.; Ruzsinszky, A.; Tao, J.; Staroverov, V. N.; Scuseria, G. E.; Csonka, G. *J. Chem. Phys.* **2005**, *123*, 62201.

(43) Perdew, J. P.; Burke, K.; Ernzerhof, M. *Phys. Rev. Lett.* **1996**, *77*, 3865–3868.

Density Functional Thermochemistry

J. Chem. Theory Comput., Vol. 6, No. 1, 2010 **125**

(44) Tao, J.; Perdew, J. P.; Staroverov, V. N.; Scuseria, G. E. *Phys. Rev. Lett.* **2003**, *91*, 146401.

(45) Boese, A. D.; Doltsinis, N. L.; Handy, N. C.; Sprik, M. *J. Chem. Phys.* **2000**, *112*, 1670–1678.

(46) Zhao, Y.; Schultz, N. E.; Truhlar, D. G. *J. Chem. Phys.* **2005**, *123*, 161103.

(47) Zhao, Y.; Schultz, N. E.; Truhlar, D. G. *J. Chem. Theory Comput.* **2006**, *2*, 364–382.

(48) Zhao, Y.; Truhlar, D. G. *J. Chem. Phys.* **2006**, *125*, 194101.

(49) Zhao, Y.; Truhlar, D. G. *J. Phys. Chem. A* **2007**, *110*, 13126–13130.

(50) Zhao, Y.; Truhlar, D. G. *J. Chem. Theory Comput.* **2008**, *4*, 1849–1868.

(51) Grimme, S.; Schwabe, T. *Phys. Chem. Chem. Phys.* **2006**, *8*, 4398–4401.

(52) Zhang, Y.; Yang, W. *Phys. Rev. Lett.* **1998**, *80*, 890–890.

(53) Hammer, B.; Hansen, L. B.; Norskov, J. K. *Phys. Rev. B: Condens. Matter* **1999**, *59*, 7413–7421.

(54) Adamo, C.; Barone, V. *J. Chem. Phys.* **2002**, *116*, 5933–5940.

(55) Perdew, J. P.; Ruzsinszky, A.; Csonka, G. I.; Vydrov, O. A.; Scuseria, G. E.; Constantin, L. A.; Zhou, X.; Burke, K. *Phys. Rev. Lett.* **2008**, *100*, 136406.

(56) Vela, A.; Medel, V.; Trickey, S. B. *J. Chem. Phys.* **2009**, *130*, 244103.

(57) Thakkar, A. J.; McCarthy, S. P. *J. Chem. Phys.* **2009**, *131*, 134109.

(58) Perdew, J. P.; Ruzsinszky, A.; Tao, J.; Csonka, G. I.; Scuseria, G. E. *Phys. Rev. A: At., Mol., Opt. Phys.* **2007**, *76*, 042506.

(59) Perdew, J. P.; Ruzsinszky, A.; Csonka, G. I.; Constantin, L. A.; Sun, J. *Phys. Rev. Lett.* **2009**, *103*, 026403.

(60) Tognetti, V.; Adamo, V. *J. Phys. Chem. A* **2009**, DOI: 10.1021/jp903672e (accessed Nov 12, 2009).

(61) Adamo, C.; Barone, V. *J. Chem. Phys.* **1998**, *108*, 664–675.

(62) Poater, J.; Duran, M.; Solà, M. *J. Comput. Chem.* **2001**, *14*, 1666–1678.

(63) Graham, D. C.; Menon, A. S.; Goerigk, L.; Grimme, S.; Radom, L. *J. Phys. Chem. A* **2009**, *113*, 9861–9873.

(64) Perdew, J. P.; Burke, K.; Ernzerhof, M. *Phys. Rev. Lett.* **1998**, *80*, 891.

(65) Becke, A. D. *Phys. Rev. A: At., Mol., Opt. Phys.* **1988**, *38*, 3098–3100.

(66) Lee, C.; Yang, W.; Parr, R. G. *Phys. Rev. B: Condens. Matter* **1988**, *37*, 785–789.

(67) Prof. Stefan Grimme Research Web Site. http://www.uni-muenster.de/Chemie.oc/grimme/en/index.html.

(68) Martin, J. M. L.; de Oliveira, G. *J. Chem. Phys.* **1999**, *111*, 1843–1856.

(69) Ruzsinszky, A.; Perdew, J. P.; Csonka, G. I.; Vydrov, O. A.; Scuseria, G. E. *J. Chem. Phys.* **2007**, *126*, 104102.

(70) Mori-Sanchez, P.; Cohen, A. J.; Yang, W. *J. Chem. Phys.* **2006**, *125*, 201102.

(71) Zhang, Y.; Yang, W. *J. Chem. Phys.* **1998**, *109*, 2604–2608.

(72) Gritsenko, O.; Ensing, B.; Schipper, P. R. T.; Baerends, E. J. *J. Phys. Chem. A* **2000**, *104*, 8558–8565.

(73) Bally, T.; Sastry, G. N. *J. Phys. Chem. A* **1997**, *101*, 7923–7925.

(74) Grimme, S. *J. Chem. Phys.* **2003**, *118*, 9095–9102.

(75) Schäfer, A.; Huber, C.; Ahlrichs, R. *J. Chem. Phys.* **1994**, *100*, 5829–5835.

(76) Raghavachari, K.; Trucks, G. W.; Pople, J. A.; Head-Gordon, M. *Chem. Phys. Lett.* **1989**, *157*, 479–483.

(77) Jurečka, P.; Hobza, P. *Chem. Phys. Lett.* **2002**, *365*, 89–94.

(78) Halkier, A.; Helgaker, T.; Jørgensen, P.; Klopper, W.; Koch, H.; Olsen, J.; Wilson, A. K. *Chem. Phys. Lett.* **1998**, *286*, 243–252.

(79) Dunning, T. H., Jr. *J. Chem. Phys.* **1989**, *90*, 1007–1023.

(80) Zipse, H. *Top. Curr. Chem.* **2006**, *263*, 163–189.

(81) Gilbert, T. M. *J. Phys. Chem. A.* **2004**, *108*, 2550–2554.

(82) Kendall, R. A.; Dunning, T. H.; Harrison, R. J. *J. Chem. Phys.* **1992**, *96*, 6796–6806.

(83) Adamo, C.; Barone, V. *J. Chem. Phys.* **1999**, *110*, 6158–6170.

(84) Repasky, M. P.; Chandrasekhar, J.; Jorgensen, W. L. *J. Comput. Chem.* **2002**, *23*, 1601–1622.

(85) Sattelmeyer, K. W.; Tirado-Rives, J.; Jorgensen, W. L. *J. Phys. Chem. A* **2006**, *110*, 13551–13559.

(86) Grimme, S.; Mück-Lichtenfeld, C. *Chem. Phys. Chem.* **2002**, *2*, 207–209.

(87) Werner, H.-J.; Knowles, P. J.; Lindh, R.; Manby, F. R.; Schütz, M.; Celani, P.; Korona, T.; Rauhut, G.; Amos, R. D.; Bernhardsson, A.; Berning, A.; Cooper, D. L.; Deegan, M. J. O.; Dobbyn, A. J.; Eckert, F.; Hampel, C.; Hetzer, G.; Lloyd, A. W.; McNicholas, S. J.; Meyer, W.; Mura, M. E.; Nicklaβ, A.; Palmieri, P. Pitzer, R.; Schumann, U.; Stoll, H.; Stone, A. J.; Tarroni R.; Thorsteinsson, T. *MOLPRO*, Version 2006.1; University College Cardiff Consultants Limited: Wales, U.K.; see http://www.molpro.net (accessed Nov 12, 2009).

(88) Grimme, S. *RICC*; University of Münster: Münster, Germany, 2007.

(89) Ahlrichs, R.; Furche, F.; Hättig, C.; Klopper, W. M.; Sierka, M.; Weigend, F. *TURBOMOLE*, Version 5.9; TURBOMOLE GmbH: Karlsruhe, Germany; http://www.turbomole.com (accessed Nov 12, 2009).

(90) Ahlrichs, R.; Bär, M.; Häser, M.; Horn, H.; Kölmel, C. *Chem. Phys. Lett.* **1989**, *162*, 165–169.

(91) Eichkorn, K.; Treutler, O.; Öhm, H.; Häser, M.; Ahlrichs, R. *Chem. Phys. Lett.* **1995**, *240*, 283–289.

(92) Hättig, C.; Weigend, F. *J. Chem. Phys.* **2000**, *113*, 5154–5161.

(93) Weigend, F.; Ahlrichs, R. *Phys. Chem. Chem. Phys.* **2005**, *7*, 3297–3305.

(94) Eichkorn, K.; Weigend, F.; Treutler, O.; Ahlrichs, R. *Theor. Chem. Acc.* **1997**, *97*, 119–124.

(95) Weigend, F. *Phys. Chem. Chem. Phys.* **2002**, *4*, 4285–4291.

(96) Weigend, F.; Häser, M.; Patzelt, H.; Ahlrichs, R. *Chem. Phys. Lett.* **1998**, *294*, 143–152.

(97) NIST Standard Reference Database. http://webbook.nist. gov/chemistry/ (accessed Nov 12, 2009).

(98) Davidson, E. R.; Hagstrom, S. A.; Chakravorty, S. J.; Umar, V. M.; Fischer, C. F. *Phys. Rev. A* **1991**, *44*, 7071–7083.

(99) Colle, R.; Salvetti, O. *Theoret. Chim. Acta* **1975**, *37*, 329–334.

(100) Miehlich, B.; Savin, A.; Stoll, H.; Preuss, H. *Chem. Phys. Lett.* **1989**, *157*, 200–206.

(101) Perdew, J. P. In *Proceedings of the 21st Annual International Symposium on the Electronic Structure of Solids*; Ziesche, P., Eschrig, H., Eds.; Akademie Verlag: Berlin, 1991.

(102) Levy, M.; Perdew, J. P. *Phys. Rev. B: Condens. Matter* **1993**, *48*, 11638–11645.

(103) Lieb, E. H.; Oxford, S. *Int. J. Quantum Chem.* **1981**, *19*, 427–439.

(104) Perdew, J. P.; Kurth, S.; Zupan, A.; Blaha, P. *Phys. Rev. Lett.* **1999**, *82*, 2544–2547.

(105) Gerenkamp, M.; Grimme, S. *Chem. Phys. Lett.* **2004**, *392*, 229–235.

(106) Coriani, S.; Marchesan, D.; Gauss, J.; Hättig, C.; Helgaker, T.; Jørgensen, P. *J. Chem. Phys.* **2005**, *123*, 184107.

(107) Neese, F.; Schwabe, T.; Grimme, S. *J. Chem. Phys.* **2007**, *126*, 124115.

(108) Hyla-Kryspin, I.; Grimme, S. *Organometallics* **2004**, *23*, 5581–5592.

JCTC Journal of Chemical Theory and Computation

The RPA Atomization Energy Puzzle

Adrienn Ruzsinszky,*[,†] John P. Perdew,[†] and Gábor I. Csonka[‡]

Department of Physics and Quantum Theory Group, 2001 Percival Stern Hall, Tulane University, New Orleans, Louisiana 70118 and Department of Inorganic and Analytical Chemistry, Budapest University of Technology and Economics, Szt. Gellért tér 4, Budapest, H-1111, Hungary

Abstract: There is current interest in the random phase approximation (RPA), a "fifth-rung" density functional for the exchange−correlation energy. RPA has full exact exchange and constructs the correlation with the help of the unoccupied Kohn−Sham orbitals. In many cases (uniform electron gas, jellium surface, and free atom), the correction to RPA is a short-ranged effect that is captured by a local spin density approximation (LSDA) or a generalized gradient approximation (GGA). Nonempirical density functionals for the correction to RPA were constructed earlier at the LSDA and GGA levels (RPA+), but they are constructed here at the fully nonlocal level (RPA++), using the van der Waals density functional (vdW-DF) of Langreth, Lundqvist, and collaborators. While they make important and helpful corrections to RPA total and ionization energies of free atoms, they correct the RPA atomization energies of molecules by only about 1 kcal/mol. Thus, it is puzzling that RPA atomization energies are, on average, about 10 kcal/mol lower than those of accurate values from experiment. We find here that a hybrid of 50% Perdew−Burke−Ernzerhof GGA with 50% RPA+ yields atomization energies much more accurate than either one does alone. This suggests a solution to the puzzle: While the proper correction to RPA is short-ranged in some systems, its contribution to the correlation hole can spread out in a molecule with multiple atomic centers, canceling part of the spread of the exact exchange hole (more so than in RPA or RPA+), making the true exchange−correlation hole more localized than in RPA or RPA+. This effect is not captured even by the vdW-DF nonlocality, but it requires the different kind of full nonlocality present in a hybrid functional.

1. Introduction: Local, Semilocal, and Fully Nonlocal Density Functionals

Modern electronic structure calculations for atoms, molecules, and solids are usually made within the Kohn−Sham density functional theory.[1,2] The many-electron problem is replaced by the computationally efficient self-consistent one-electron problem, in a way that is formally exact for the ground-state energy and the electron spin densities. In

practice, some approximation must be made for the exchange−correlation energy E_{xc} as a functional of the electron spin densities $n_\uparrow(\vec{r})$ and $n_\downarrow(\vec{r})$. E_{xc} is the correction to the Hartree approximation without self-interaction correction and provides most of the binding between atoms. Its functional derivative $\delta E_{xc}/\delta n_\sigma(\vec{r})$ is the exchange−correlation potential seen by the fictitious noninteracting electrons.

The exact E_{xc} can be expressed[3−5] as the electrostatic interaction between an electron at position $\vec{r}$ and the density $n_{xc}(\vec{r},\vec{r}')$ at $\vec{r}'$ of the coupling constant averaged exchange−correlation hole that surrounds it:

$$E_{xc} = (1/2) \int d^3 r n(\vec{r}) \int d^3 r' n_{xc}(\vec{r}, \vec{r}')/|\vec{r}'-\vec{r}| \quad (1)$$

Here $n_{xc} = n_x + n_c$ is the sum of the separate exchange and correlation holes. The exchange hole density is non-

* Corresponding author. Telephone: (504) 862-8144. E-mail: aruzsinszky@gmail.com.

† Department of Physics and Quantum Theory Group, Tulane University.

‡ Department of Inorganic and Analytical Chemistry, Budapest University of Technology and Economics.

positive and integrates over $\vec{r}'$ to -1 and is the same as in the Hartree−Fock theory (apart from the difference between Kohn−Sham and Hartree−Fock orbitals). The correlation hole density integrates over $\vec{r}'$ to zero. It is negative and Coulomb cusped at a small interelectronic separation $u = |\vec{r}' - \vec{r}|$ but typically positive at a large separation, where (in the system and spherical average of eq 1 that determines E_{xc}) it tends to cancel some or all of the exchange hole density. The exact exchange−correlation hole density is bounded by the electron density: $n_{xc}(\vec{r},\vec{r}') \geq - n(\vec{r}')$.

Semilocal approximations:

$$E_{xc}^{sl}[n_\uparrow, n_\downarrow] = \int d^3 r n \varepsilon_{xc}^{sl}(n_\uparrow, n_\downarrow, \nabla n_\uparrow, \nabla n_\downarrow, ...) \quad (2)$$

where $n = n_\uparrow + n_\downarrow$, are simple and computationally tractable and are sometimes usefully accurate. The local spin density approximation (LSDA),[1,6,7] which employs only the local spin densities as arguments in eq 2, is exact for a uniform electron gas and is still often used to describe solids. The generalized gradient approximation (GGA),[8] which adds the gradients of the local spin densities, can give a much better description of atoms and molecules, and in particular of the atomization energy of a molecule. LSDA and GGA are the first two rungs of a ladder of density functional approximations.[9] The third or *meta*-GGA rung, which can be accurate for both molecules[10,11] and solids[10] near equilibrium, adds the spin-resolved noninteracting kinetic energy densities of the occupied orbitals, $\tau_\sigma(\vec{r}) = \sum_\alpha |\nabla \psi_{\alpha\sigma}(\vec{r})|^2/2$. Although the Kohn−Sham orbitals $\psi_{\alpha\sigma}$ are fully nonlocal functionals of the electron spin densities, *meta*-GGA is also semilocal in the sense that it employs only the information in an infinitesimal neighborhood of position $\vec{r}$, that is available in any Kohn−Sham calculation. The added arguments in eq 2 can be used to satisfy additional exact constraints, and in fact, the three semilocal rungs of the ladder have been constructed in this way without empirical parameters.[7,8,10] Semilocal functionals require only a single integration over $\vec{r}$, while fully nonlocal functionals require (at least in principle) a double integration over $\vec{r}$ and $\vec{r}'$.

Models for the spherically- and system-averaged hole exist for many of the semilocal functionals. In some cases, the functionals are derived from models for this hole. In other cases, the hole models are "reverse engineered"[12,13] from the functionals. Sophisticated semilocal holes $n_{xc}^{sl}(\vec{r},'\,\vec{r}')$ are found to be of shorter range than the LSDA hole and are necessarily not long ranged in the separation $|\vec{r}' - \vec{r}|$, since they employ only information from an infinitesimal separation. To the extent that the exact exchange−correlation hole is also of short or intermediate range, sophisticated semilocal approximations can work well. Because the exact exchange−correlation hole is typically deeper and more short-ranged for exchange and correlation together than for exchange, semilocal functionals are typically more accurate for exchange and correlation together than for either of them separately.[14] This error cancellation between semilocal exchange and correlation manifests much more strongly in the atomization energies of molecules than it does in the surface energy of jellium, where a sophisticated semilocal functional can accurately predict the separate exchange and correlation contributions.[10]

As argued in greater detail in ref 14, making the exchange−correlation hole density more localized around its electron leads to a lower total energy. This effect is manifested in the atomization energy of a molecule, the total energy difference between the free component atoms and the molecule, all at rest. Exact exchange without correlation underbinds chemically, underestimating the atomization energy, because the exact exchange hole in a molecule is too spread out in comparison with the exact exchange−correlation hole. LSDA overbinds molecules, overestimating the atomization energy, because it makes the holes too diffuse, more so in the free atoms than in the molecule. GGA overbinds less, producing a realistic hole localization in the free atoms but somewhat too much hole localization in the molecule or solid. Further improvement of the molecular atomization energy and the solid-state properties can be achieved by using *meta*-GGA, or using a global hybrid functional (mixing in with GGA or *meta*-GGA a little exact exchange, which yields more hole delocalization in the molecule or solid), or by using both.

To the extent that the *exact* exchange−correlation hole is long-ranged, as it can be in systems with multiple atomic centers, sophisticated semilocal functionals fail, and fully nonlocal ones are needed.[14] This problem can become increasingly worse for stretched bonds and for dissociation limits,[15] where it can be solved to some extent by fourth-rung functionals or hyper-GGA's that employ information about exact exchange, such as global, local, or range-separated hybrid functionals (all of which rely on empirical parameters).[14] These dissociation problems of "many-electron self-interaction freedom"[15] are distinct from the problem of long-range van der Waals attraction, which is not accounted for even by the fourth-rung or hybrid functionals. Recently, Langreth, Lundqvist and their Rutgers−Chalmers collaborators have proposed a useful double-integral nonlocal functional for the van der Waals interaction[16] (vdW-DF), which does not employ exact exchange and so probably does not correct the dissociation limit problems.

Fifth-rung functionals employ the unoccupied as well as the occupied Kohn−Sham orbitals in a fully nonlocal way that can potentially solve both these problems. The simplest fifth-rung functional is the random phase approximation ("in a density functional context"[3,5,17]), as discussed in Section 2.

Yan, Perdew and Kurth[18] found LSDA and GGA corrections to RPA (nearly the same in GGA as in LSDA) by taking the difference between the same semilocal functional constructed beyond and within RPA. Their corrected RPA is called RPA+. They claimed that the correction to RPA is a short- or intermediate-range effect and, thus, is well modeled at the semilocal level. That claim is correct in the uniform electron gas,[7,12] the jellium surface,[19] and the free atom.[18,20] (In the free atom, the exact and RPA holes cannot be long-ranged.) Their corrections were accurate for the total energies of atoms (where RPA energies are too negative by about 0.02 hartree/electron, due to a too-negative on-top hole

RPA Atomization Energy Puzzle

J. Chem. Theory Comput., Vol. 6, No. 1, 2010 **129**

density $n_{xc}^{RPA}(\vec{r},\vec{r})$).[12,13] Jiang and Engel[20] found that these corrections also improve the RPA ionization energies of free atoms.

The approach of ref 18 unfortunately has no natural extension to find a *meta*-GGA for the correction to RPA, since a constraint used in the construction of the beyond RPA *meta*-GGA,[10] zero correlation energy for all one-electron densities, has no analog within RPA (and another constraint on the low-density limit would require new calculations). For the one-electron density of the molecule H_2^+, the RPA correlation energy is small for compressed and equilibrium bond lengths but is disturbingly large for long bond lengths.[21]

Reference 18 also computed the LSDA and GGA corrections to RPA atomization energies. Atomization energies were increased by typically 1 kcal/mol, suggesting that RPA would be accurate for atomization energies and that RPA+ still more so. The smallness of the computed correction is easy to understand: If the correction to RPA were +0.02 hartree/electron, then it would exactly cancel out of the atomization energy since there are as many electrons in the component free atoms as in the molecule. Puzzlingly, the careful RPA calculations of molecular atomization energies by both Furche[22] and Harl and Kresse[23] found that these atomization energies were too low by typically 10 kcal/mol, in comparison to experiment. We will argue here that the correction to RPA in molecules requires full nonlocality of the kind found in fourth-rung or hybrid functionals. This correction is too long-ranged for LSDA and GGA, although it is still possible that the RPA hole is correct at a longer range. RPA is computationally much more expensive than GGA or *meta*-GGA,[22−28] but in view of the good performance of RPA and RPA+ for solids[24−27] and surfaces[19,25] and of continuing improvements in RPA implementation,[28] it is important to find a general (hence fully nonlocal) correction. After discussing RPA in Section 2, we will mention some of the nonlocal corrections already proposed and tested.

2. The Random Phase Approximation

The roots of RPA go back to the plasma theory of electron correlation by Bohm and Pines[29,30] in the 1950s. In those days, the focus was on the uniform electron gas, for which finite-order perturbation theory in the electron−electron interaction diverges in second order, requiring a partial resummation to all orders. The orbitals for the electron gas are just plane waves in both the Hartree and Kohn−Sham schemes, but before the Kohn−Sham theory was proposed, the Hartree orbitals would likely have been chosen even for inhomogeneous systems, where they yield unrealistic densities. The work of Langreth and Perdew[3,5,17] brought RPA into the density functional context by introducing the Kohn−Sham orbitals for inhomogeneous systems, which depend only on the true electron density and are, therefore, independent of the coupling constant. Quantum chemists may recognize RPA as a ring coupled cluster doubles approach;[31] a coupled cluster code can be simplified to do RPA.

The RPA is the simplest member of the family of adiabatic-connection fluctuation−dissipation theorem density functional methods.[3−5,17,25,32,33] The Kohn−Sham nonin-

teracting system and the real interacting system are assumed to be adiabatically connected through a series of systems, all at the same electron density, in which the electron−electron interaction is $\lambda/|\vec{r}' - \vec{r}|$, where $0 \leq \lambda \leq 1$. The adiabatic-connection functionals employ exact exchange. Because they also require the unoccupied orbitals (and the orbital energies) for correlation, they stand at the top of the Jacob's ladder[9] of approximations, more sophisticated and more computationally demanding than lower-rung functionals. The zero-temperature fluctuation−dissipation theorem is used to express the ground-state correlation energy functional in terms of the imaginary part of the frequency-dependent density−density response function $\chi_\lambda(\vec{r},\vec{r}';\omega)$:

$$E_c = -\frac{1}{2} \int_0^1 d\lambda \int_0^\infty \frac{d\omega}{\pi} \int d^3r\,d^3r'\,\mathrm{Im}[\chi_\lambda(\vec{r},\vec{r}';\omega) - \chi_0(\vec{r},\vec{r}';\omega)]/|\vec{r}'-\vec{r}| \quad (3)$$

where $\chi_\lambda(\vec{r},\vec{r}';\omega)$ satisfies the Dyson equation:

$$\chi_\lambda = \chi_0 + \chi_0 * (\lambda v_{Coul} + f_{xc,\lambda}) * \chi_\lambda \quad (4)$$

$$\chi_0(\vec{r},\vec{r}';\omega) = \sum_{\alpha,\alpha',\sigma} \frac{\theta(\mu - \varepsilon_\alpha) - \theta(\mu - \varepsilon_{\alpha'})}{\omega + i0^+ + \varepsilon_\alpha - \varepsilon_{\alpha'}} \psi_\alpha^*(\vec{r})\psi_{\alpha'}(\vec{r})\psi_{\alpha'}^*(\vec{r}')\psi_\alpha(\vec{r}') \quad (5)$$

$f_{xc,\lambda}$ is the exchange−correlation kernel and is not known exactly as an explicit density functional. We can relate eqs 3 to 1 by defining:

$$n(\vec{r})n_c(\vec{r},\vec{r}') = -\int_0^1 d\lambda \int_0^\infty \frac{d\omega}{\pi} \mathrm{Im}[\chi_\lambda(\vec{r},\vec{r}';\omega) - \chi_0(\vec{r},\vec{r}';\omega)] \quad (6)$$

The simple or direct RPA we discuss here sets $f_{xc,\lambda} = 0$ (time-dependent Hartree response). (There is also a more elaborate "RPA with exchange" (RPAE), which sets $f_{xc,\lambda} = f_{x,\lambda}$ time-dependent exact-exchange-only response, so that for a one-electron density $\chi_\lambda = \chi_0$ and $E_c = 0$.) RPA becomes relatively exact for the uniform gas[7,12] in the high-density limit. It includes a reasonable description of the long-ranged van der Waals interaction. It is even able to describe the strong static correlation in the dissociation of the H_2 molecule in a spin-restricted formalism.[34] The RPA correlation energy can also be expressed as the change in the zero-point energy of the plasmons or the collective density oscillations.[28] In many cases, RPA provides a good description of the long-range exchange−correlation hole, but it has too much short-range correlation, making a total-energy error of roughly −0.02 hartree/electron at high and normal electron densities.

The correction to RPA in the high-density limit is the second-order exchange energy. More generally, the dominant correction is a higher order exchange effect, which in finite systems provides a kind of self-interaction correction[35,36] to RPA correlation. Thus, one might make a Perdew−Zunger[35] self-interaction-corrected RPA:

$$E_c^{RPASIC} = E_c^{RPA}[n_\uparrow, n_\downarrow] - \sum_{\alpha\varsigma}^{occup} E_c^{RPA}[n_{\alpha\sigma}, 0] \quad (7)$$

where $n_{\alpha\sigma}(\vec{r}) = |\psi_{\alpha\sigma}(\vec{r})|^2$ is the one-electron density of an occupied orbital. For the H atom, this SIC correction is +0.02 hartree (the value also predicted by the GGA correction), but for infinitely stretched H_2^+, the SIC correction is +0.17 hartree.[21] This fact suggests that the correction to RPA can be highly nonlocal in stretched bond situations. Of course, eq 7 is not very practical, requiring an RPA calculation for each occupied orbital density. (To satisfy the uniform-gas limit, it would be better to replace RPA by RPA+ in eq 7.)

A different fully nonlocal correction models the exchange−correlation kernel $f_{xc,\lambda}(\vec{r},\vec{r};\omega')$.[32,33] Another, at greater cost, is the RPAE defined above. Still another makes an RPA-based range-separated hybrid functional.[37,38] In the range separation approach, the Coulomb interaction between electrons is smoothly divided into a short- and long-ranged part, with the help of an empirical range separation parameter. Then the long-range part of eq 1 is evaluated using RPA or related methods, while the short-range part is evaluated using a modified semilocal functional. While these various nonlocal corrections are sometimes successful, they have not provided a clear conceptual answer to the RPA atomization energy puzzle, and they are computationally demanding. We will discuss simpler corrections to RPA in the rest of this paper.

3. Additive Density Functional Correction of RPA

Yan, Perdew, and Kurth[18] have presented a semilocal (sl) short-range correction to RPA correlation. Their RPA+ is

$$E_c^{RPA+}[n_\downarrow, n_\uparrow] = E_c^{RPA}[n_\downarrow, n_\uparrow] + \{E_c^{sl}[n_\downarrow, n_\uparrow] - E_c^{slRPA}[n_\downarrow, n_\uparrow]\} \quad (8)$$

The semilocal functional can be either LSDA or GGA, and there is typically little difference between these two choices. Their beyond-RPA GGA was PBE,[8] while their within-RPA GGA was constructed by a real-space cutoff of the RPA gradient expansion for correlation, similar to the one that (beyond RPA) yields PBE.[39] Since RPA was expected to be exact at long-range and LSDA or GGA is accurate at short-range, RPA+ was expected to provide an accurate correction.[18] RPA+ dramatically improves total energies of free atoms,[18] without damaging jellium surface energies.[19] More generally, RPA+ provides a useful correction to RPA in a free atom or an atomic ion, where the exchange−correlation hole and every component of it are well-localized around the electron and, thus, can be accurately described by a semilocal approximation. Numerical evidence for this can be found in the work of Jiang and Engel.[20] For neutral atoms (He, Li, Be, N, Ne, Mg, P, and Ar), they found that the RPA correlation energy is too negative, on average, by 0.021 hartree/electron, while the RPA+ correlation energy is too negative by only 0.002 hartree/electron. For eight free atoms and atomic ions (Li, Be^+, Be, B^+, Na, Mg^+, Mg, and Al^+), they found that the RPA first ionization energy is too large, on average, by 0.017 hartree, while the RPA+ first ionization energy is too large by only 0.002 hartree. Unfortunately, as described in Section 1, RPA+ significantly underestimates the atomization energy of a molecule, by an average of about

10 kcal/mol,[22,23] while the PBE−GGA overestimates them by about the same amount. In one sense, this is still a good result.[22,28] For atomization energies, RPA+ makes about the same absolute error as PBE, but without the strong error cancellation between exchange and correlation that PBE demonstrates. But greater accuracy is desired, especially since the RPA calculation is expensive.

Since a fully nonlocal correction to RPA is needed, the natural next step beyond eq 8 is

RPA++:

$$E_c^{RPA++}[n_\uparrow, n_\downarrow] = E_c^{RPA}[n_\uparrow, n_\downarrow] + \{E_c^{nl}[n_\uparrow, n_\downarrow] - E_c^{nlRPA}[n_\uparrow, n_\downarrow]\} \quad (9)$$

where nl is a fully nonlocal approximation that can be constructed both beyond and within RPA. The last requirement can only be satisfied by a nonempirical functional. If the fully nonlocal approximation happens to be a functional of the total density $n = n_\uparrow + n_\downarrow$, we define

$$E_c^{RPA++}[n_\uparrow, n_\downarrow] = E_c^{RPA+}[n_\uparrow, n_\downarrow] + \{E_c^{nl}[n] - E_c^{nlRPA}[n]\} - \{E_c^{sl}[n] - E_c^{slRPA}[n]\} \quad (10)$$

which starts from RPA+ and then corrects it for the difference between nl and sl applied to the total density. From now on, we will take the semilocal functional to be sl = GGA.

4. vdW-DF Fully Nonlocal Functional

The vdW-DF correlation energy[16] is a nonempirical fully nonlocal functional of the total density:

$$E_c^{vdW-DF}[n] = E_c^{LDA}[n] + \Delta E_c^{nl}[n] \quad (11)$$

and, thus, a candidate for our eq 10. (Its variant of ref 40 is a functional of the spin densities and, thus, a candidate for our eq 9.) In eq 11, the first term is the local density approximation (LDA). The second term is a double integral over position space:

$$\Delta E_c^{nl} = (1/2) \int d^3r \int d^3r' n(\vec{r}) \varphi([n]; \vec{r}, \vec{r}') n(\vec{r}') \quad (12)$$

constructed to vanish for a uniform density and to provide a van der Waals interaction between isolated fragments of electron density. The uniform-gas correlation energy per particle appears in both terms of eq 11, and we know this quantity both beyond and within RPA,[7] so we can use eq 11 to construct a nonempirical and fully nonlocal correction to RPA, one which is certainly correct in its LDA term. Of course, the authors of the vdW-DF never intended it to be used to find a correction to RPA.

Our RPA+ approximation of eq 8 for the correlation energy can be written as

$$RPA + = RPA + \{GGAsdf\} \quad (13)$$

where a curly bracket denotes a deviation of beyond-RPA from within-RPA correlation energy, and the argument of the curly bracket denotes the functional employed to find this deviation; for example, GGAsdf is the spin-density functional GGA. Then our RPA++ approximation of eq 10 can be written as

RPA Atomization Energy Puzzle

J. Chem. Theory Comput., Vol. 6, No. 1, 2010 **131**

$$RPA + + = RPA + \{sl\} + \{\Delta nl\} \quad (14)$$

where

$$\{sl\} = \{LDA\} + \{GGAsdf\} - \{GGAdf\} \quad (15)$$

is the semilocal part of the correction, GGAdf is the total-density functional GGA, and $\{\Delta nl\}$ is the fully nonlocal part of the correction:

$$\{\Delta nl\} = \Delta E_c^{nl} - \Delta E_c^{nlRPA} \quad (16)$$

where ΔE_c^{nl} is given by eq 12.

For numerical evaluation, we have taken 10 molecular atomizations from ref 22. The semilocal part of the correction, eq 15, was computed from a modified GAUSSIAN03 code,[41] using a fixed accurate molecular geometry, the 6-311+G(3df,2p) basis set and a ultrafine grid. For each of the various semilocal correlation functionals, a self-consistent calculation was made with the fixed spin-density PBE−GGA exchange energy functional; this ensured that all considered electron densities for a particular atom or molecule were realistic and similar. For a given level of correlation functional (say the total-density PBE−GGA), the density difference between the within- and beyond-RPA versions was even smaller because the correlation potentials differed by a nearly constant 0.02 hartree over most of the density. Our RPA+ values from Tables 1 and 2 agree fully with those of ref 22. The fully nonlocal part of eq 14, a computationally expensive double integral, was evaluated non-self-consistently from the PBE density using a smaller grid and a special approach, as described in the Appendix.

Table 1 shows how the semilocal parts of the correction to RPA, from eq 15, contribute to the atomization energies. The individual terms in Table 1 are rather small and tend to cancel one another when combined together. Table 2 shows the RPA and experimental atomization energies from ref 22 as well as the corrected RPA+ and RPA++ atomization energies (including the fully nonlocal contribution $\{\Delta nl\}$). Our RPA++ method improves over RPA+, but neither gives significant improvement over RPA. The vdW-DF, on which our RPA++ results are based, is fully nonlocal in the way needed to describe dispersion interaction but not in the way needed to correct RPA atomization energies.

Table 1. Semilocal Contributions of Eq 15 to the RPA++ Correction to the RPA Atomization Energy, in kcal/mol, and the Total Semilocal Contribution[a]

molecule	{LDA}	{GGAsdf}	{GGAdf}	{sl}[b]
H_2	−1.2	1.1	−1.6	1.5
N_2	−1.9	0.1	−2.8	0.9
O_2	−1.4	−1.2	−2.2	−0.4
F_2	−0.8	−1.4	−1.6	−0.6
Si_2	−1.0	0.2	−1.7	0.9
CO	−2.0	−1.4	−2.8	−0.6
CO_2	−3.8	−3.6	−5.5	−1.9
H_2O	−2.6	−0.7	−3.9	0.5
C_2H_2	−4.5	−2.3	−6.6	−0.2
HF	−1.4	−0.6	−2.0	0.1

[a] (1 hartree = 627.5 kcal/mol). [b] {sl} = {LDA} + {GGAsdf} − {GGAdf}.

Table 2. Ground-State Atomization Energies from RPA (ref 22), RPA+, and RPA++ Compared to the Experimental Results from Ref 22[a]

molecule	RPA	RPA+	RPA++	(PBE + RPA+)/2	expt
H_2	109	110	110	108	109
N_2	223	223	225	234	228
O_2	113	111	113	128	121
F_2	30	29	30	41	38
Si_2	70	70	71	76	75
CO	244	242	244	266	259
CO_2	364	360	364	388	389
H_2O	223	222	224	228	232
C_2H_2	381	378	381	397	405
HF	133	132	133	137	141
ME	−11	−12	−10	−1	
MAE	11	12	10	4	

[a] Both the calculated and corrected experimental values are for static nuclei. All calculations, including RPA, use PBE orbitals. RPA+ is the GGA correction of eqs 8 and 13. RPA++ is the vdW-DF-based correction of eqs 10 and 14 with its nonlocal term $\{\Delta nl\}$evaluated on a cubic grid (roughly 60 × 60 × 60) and with a spacing of roughly 0.17 bohr. We also show the empirical hybrid of eq 17, which averages the PBE and RPA+ exchange−correlation energies. All results are shown in kcal/mol. ME is the mean error, and MAE is the mean absolute error.

5. Global Hybrid Functional for Corrected RPA Atomization Energies

Correction of RPA atomization energies requires full nonlocality but (as can be seen from Table 2) not the full nonlocality responsible for the van der Waals interaction. The other familiar kind of nonlocality is that of the global, local, and range-separated hybrids.[14,37,38] We have found empirically that the global hybrid of 50% RPA+ with 50% PBE−GGA:

$$E_{xc}^{hyb} = (1/2)[E_{xc}^{RPA+} + E_{xc}^{PBE-GGA}] = E_{xc}^{RPA+} + 0.5[E_{xc}^{PBE-GGA} - E_{xc}^{RPA+}] \quad (17)$$

i.e.:

$$E_c^{hyb} = E_c^{RPA+} + 0.5[E_{xc}^{PBE-GGA} - E_{xc}^{RPA+}] \quad (18)$$

yields accurate atomization energies, as shown in Table 2. Equation 18 is exact for the uniform or slowly varying electron gas, but its empirical construction makes it somewhat unsatisfactory as a general correction to RPA. Moreover, it shares with other global hybrids the defect that its correlation energy for an inhomogeneous system scales improperly,like exchange in the high-density limit.[42] However, it does suggest the physics that a proper correction must have: RPA+ atomization energies are too low because the RPA+ exchange−correlation hole is too spread out in a molecule. The PBE−GGA atomization energies are too high because the PBE−GGA exchange−correlation hole is not spread out enough in a molecule. The hybrid of eq 17 achieves about the right spread of the exchange−correlation hole in a molecule.

Our global hybrid of RPA+ with PBE differs in detail from the more standard global hybrids of GGA or *meta*-GGA with a fraction of exact exchange. GGA's or *meta*-GGA's tend to be the most accurate near the upper or

Table 3. Jellium Surface Exchange−Correlation Energies σ_{xc} in erg/cm^2. The bulk density is $n = 3/(4\pi r_s^3)$, with r_s in bohr[a]

r_s	LDA	RPA	RPA+	ISTLS	(PBE + RPA+)/2
2.00	3354	3467	3413	3417	3337
2.07	2961	3064	3015	3026	2948
2.30	2019	2098	2060	2072	2011
2.66	1188	1240	1214	1227	1183
3.00	764	801	781	800	761
3.28	549	579	563	580	547
4.00	261	278	268	(281)	260
6.00	53	58	54	(60.5)	53

[a] The electron density at the surface is more slowly varying for smaller r_s. All calculations, including RPA, use LDA orbitals. The exact surface exchange−correlation energy probably (ref 19) falls in the narrow range between LDA and RPA. RPA and ISTLS values from ref 19 are compared to LDA and RPA+ values from ref 18. While RPA+ makes a GGA correction to RPA, ISTLS makes a promising fully nonlocal correction. The last column is from our global hybrid of eq 17. Note that the exchange−correlation contribution can far exceed the total surface energy.

physical limit of the coupling onstant integration[3] and the least accurate at the lower limit, where exchange dominates. But RPA+ is actually exact at the lower limit and makes its greatest error near the upper limit.

Reference 38 presents two range-separated hybrids that use a RPA or scaled RPA exchange−correlation hole at long-range and a LSDA hole at short-range. One of the authors (B. Janesko) of ref 38 kindly provided us with the errors for our 10 molecules. The MAEs are 5.8, 4.2, and 4.2 kcal/mol for their one- and two-parameters and for our one-parameter hybrids, respectively. Range-separated hybrids might achieve higher accuracy through the replacement of LSDA by GGA or *meta*-GGA holes.

In Table 3, we test the global hybrid of eqs 17 and 18 for the jellium surface energy. While the exact surface ex change−correlation energy is unknown, it probably[19] falls in the narrow range between LDA and RPA. Our global hybrid values fall at or a little below the lower end of this range (while PBE−GGA falls well below).

6. Conclusions

The random phase approximation (RPA) is a promising[18−20,22−28,34] fifth-rung density functional, but one that requires a correction. The correction to the total[18,20] and the ionization[20] energies of a free atom, or to the surface energy of a solid,[19,25] is a short-range correlation describable by LSDA or GGA (RPA+), but RPA molecular atomization

energies[22,23] surprisingly require a fully nonlocal correction, which we argue arises due to the multiple atomic centers of the molecule. The nonlocal RPA++ correction, based upon the vdW-DF,[16] is, however, not very different from RPA+. (And probably the vdW-DF correlation functional, like the LSDA and the GGA, does not have the kind of nonlocality that would make it compatible with exact exchange for molecular atomization energies.) The needed kind of nonlocality is present instead in the global hybrid functional of eq 17. The RPA, RPA+, and RPA++ exchange−correlation holes in a molecule can be more localized around an electron than that of the exact exchange hole but still too spread out in comparison to the exact exchange−correlation hole. While the global hybrid of eq 17 is not a satisfactory general correction to RPA, its accuracy strongly suggests this conclusion. RPA may still be nearly correct at longer range in normal systems, justifying range-separated hybrids, such as refs 37 and 38. However, the range-separated hybrids share two drawbacks with the global hybrids: the appearance of an empirical parameter and the incorrect behavior under uniform density-scaling to the high-density limit.[43,42]

A satisfactory fully nonlocal correction should be constructed by constraint satisfaction, without empirical parameters. A nonempirical self-interaction correction to RPA correlation is intrinsic to the inhomogeneous Singwi−Tosi−Land−Sjoelander (ISTLS) functional.[44,19] ISTLS is nearly exact for the uniform electron gas and yields jellium surface energies close to those of RPA+ (Table 3). So it would be interesting to see what ISTLS predicts for molecular atomization energies. Equally interesting would be atomization energy and surface energy tests of the "RPA with exchange", as defined in Section 2, with a small LSDA additive correction (RPAE+). RPAE already shows promise for the correlation energies of atoms.[45] References 19 and 46 suggest that, while the spatial dependence of $f_{x,\lambda}(\vec{r},\vec{r}';\omega)$ might be important, the frequency dependence might not be. The fully nonlocal second-order screened exchange correction to RPA, related to RPAE, has been used recently by Grueneis et al.[47]

7. Appendix

Numerical Double Integration on a Three-Dimensional Grid. Semilocal functionals (eq 2) require only a single integration over a three-dimensional grid of M points, with a computation time proportional to M. Fully nonlocal functionals require a double integration, with a computation time proportional to M^2. Thus, grids commonly used for

Table A1. Contribution of the Beyond-RPA vdW-DF Nonlocal Energy ΔE_c^{nl} (Hartree) of Eq 12 to the Atomization Energy of the N$_2$ Molecule vs the Spacing of the Grid Points (Bohr)[a]

spacing of the grid points	nonlocal contribution	core elimination	gradient calculation
0.237−0.224	0.01528	no	numeric
0.197−0.186	0.01227	no	numeric
0.168−0.159	0.01063	no	numeric
0.200	0.01343	no	analytic
0.200	0.01151	yes	numeric
0.200	0.01192	yes	analytic
0.150	0.01083	yes	analytic

[a] The effect of making the same core elimination for free atoms and molecules is shown in the last three lines. Where two spacings are given on one line, the first is for the molecule, and the second is for the free atom.

RPA Atomization Energy Puzzle

J. Chem. Theory Comput., Vol. 6, No. 1, 2010 **133**

Table A2. Convergence of $\{\Delta nl\} = \Delta E_c^{nl} - \Delta E_c^{nlPRA}$ (Hartree) vs the Spacing of the Grid Points (Bohr)[a]

system	spacing of the grid points	nonlocal correction	core elimination	gradient calculation	atomization
N_2	0.237	0.01231	no	numeric	1.15
N_2	0.197	0.01257	no	numeric	1.00
N_2	0.168	0.01268	no	numeric	0.92
N_2	0.200	0.01249	no	numeric	1.00
N_2	0.200	0.01280	yes	numeric	0.95
N_2	0.200	0.01310	no	analytic	0.98
N_2	0.200	0.01309	yes	analytic	0.98
N_2	0.150	0.01329	yes	analytic	0.96
N	0.224	0.00707	no	numeric	
N	0.186	0.00708	no	numeric	
N	0.159	0.00707	no	numeric	
N	0.200	0.00704	no	numeric	
N	0.200	0.00716	yes	numeric	
N	0.200	0.00732	no	analytic	
N	0.200	0.00733	yes	analytic	
N	0.150	0.00741	yes	analytic	

[a] ΔE_c^{nl} is the nonlocal expression of eq 12. The last column shows the contribution (kcal/mol) of $\{\Delta nl\}$ to the N_2 atomization energy. For example, for spacing = 0.0150 bohr, with core elimination and analytic gradients, this is $2(0.00741) - 0.01329$ hartree $= 0.00153$ hartree $= 0.96$ kcal/mol.

semilocal functionals can be impractical for fully nonlocal ones. For the contributions of $\{\Delta nl\}$ to the RPA++ atomization energies of Table 2, we used cubic grids (roughly $60 \times 60 \times 60$) with spacings of roughly 0.17 bohr. The grids for the molecule and the free atom were slightly different. The high-density cores were eliminated, somewhat as in the pseudopotential approach usually employed with the vdW-DF: Where $n > 1$ ($r_s < 0.6$), we set $n = 1$ and $\nabla n = 0$. With this core elimination, we can achieve a given level of convergence with a coarser grid, as shown in Table A1.

Later we devised the more elaborate methods described below, which confirmed our earlier result of Table 2 for N_2 and C_2H_2, and could be used for future work. These methods take maximum advantage of the error cancellation between molecule and free atoms. (We have not attempted to use the efficient implementation of the vdW-DF presented in ref 48).

For dissociation energy calculations of diatomic molecules, we use a cubic grid centered on the bond critical point of the molecule. This grid is typically displaced with respect to the atomic nuclei. The same displacement and density grid were used for the free atom. This way the electron density and its gradient are directly comparable for free atoms and molecules; the grid points have exactly the same arrangement around the nucleus.

In our calculations of Table 2, the density gradients were evaluated numerically on the grid. In Tables A1 and A2, we also check the effect of using analytic gradients instead of numerical ones.

Tables A1 and A2 show that, while the nonlocal contribution to the beyond-RPA correlation energy and the nonlocal correction to the RPA correlation energy are not so well converged, the nonlocal correction to RPA atomization energies is well converged.

References

(1) Kohn, W.; Sham, L. J. *Phys. Rev.* **1965**, *140*, A1133.

(2) *A Primer in Density Functional Theory*; Fiolhais C., Nogueira F., Marques M., Eds.; Springer: Berlin, Germany, 2003.

(3) Langreth, D. C.; Perdew, J. P. *Solid State Commun.* **1975**, *17*, 1435.

(4) Gunnarsson, O.; Lundqvist, B. I. *Phys. Rev. B: Solid State* **1976**, *13*, 4274.

(5) Langreth, D. C.; Perdew, J. P. *Phys. Rev. B: Solid State* **1977**, *15*, 2884.

(6) Von Barth, U.; Hedin, L. *J. Phys. C* **1972**, *5*, 1629.

(7) Perdew, J. P.; Wang, Y *Phys. Rev. B: Condens. Matter* **1992**, *45*, 13244, and references therein.

(8) Perdew, J. P.; Burke, K.; Ernzerhof, M *Phys. Rev. Lett.* **1996**, *77*, 3865, and references therein.

(9) Perdew J. P.; Schmidt K. In *Density Functional Theory and Its Applications to Materials*; Van Doren V. E., Van Alsenoy K., Geerlings P., Eds.; American Institute of Physics: Melville, NY, 2001, pages 1−20.

(10) Perdew, J. P.; Ruzsinszky, A.; Csonka, G. I.; Constantin, L. A.; Sun, J *Phys. Rev. Lett.* **2009**, *103*, 026403, and refences therein.

(11) Ruzsinszky, A.; Perdew, J. P.; Csonka, G. I. *J. Phys. Chem. A* **2005**, *109*, 11006.

(12) Giori-Giorgi, P.; Perdew, J. P. *Phys. Rev. B: Condens. Matter* **2002**, *66*, 165118.

(13) Constantin, L. A.; Perdew, J. P.; Tao, J. *Phys. Rev. B: Condens. Matter* **2006**, *73*, 205104, and references therein.

(14) Perdew, J. P.; Staroverov, V. N.; Tao, J.; Scuseria, G. E. *Phys. Rev. A: At., Mol., Opt. Phys.* **2008**, *78*, 052513, and references therein.

(15) Ruzsinszky, A.; Perdew, J. P.; Csonka, G. I.; Vydrov, O. A.; Scuseria, G. E. *J. Chem. Phys.* **2007**, *126*, 104102, and references therein.

(16) Dion, M.; Rydberg, H.; Schroeder, E.; Langreth, D. C.; Lundqvist, B. I. *Phys. Rev. Lett.* **2004**, *92*, 246401.

(17) Langreth, D. C.; Perdew, J. P. *Phys. Rev. B: Condens. Matter* **1980** *21*, 5469.

(18) Yan, Z.; Perdew, J. P.; Kurth, S. *Phys. Rev. B: Condens. Matter* **2000**, *61*, 16430.

(19) Constantin, L. A.; Pitarke, J. M.; Dobson, J. F.; Garcia-Lekue, A.; Perdew, J. P. *Phys. Rev. Lett.* **2008**, *100*, 036401, and references therein.

(20) Jiang, H.; Engel, E. *J. Chem. Phys.* **2007**, *127*, 184108.

(21) Mori-Sanchez P.; Cohen A. J.; Yang W. arXiv: 0903.4403.

(22) Furche, F. *Phys. Rev. B: Condens. Matter* **2001**, *64*, 195120.

(23) Harl, J.; Kresse, G. *Phys. Rev. B: Condens. Matter* **2008**, *77*, 045136.

(24) Gruening, M.; Marini, A.; Rubio, A. *J. Chem. Phys.* **2006**, *124*, 154108.

(25) Garcia-Gonzalez, P.; Fernandez, J. J.; Marini, A.; Rubio, A. *J. Phys. Chem. A* **2007**, *111*, 12458.

(26) Harl, J.; Kresse, G. *Phys. Rev. Lett.* **2009**, *103*, 056401.

(27) Ren, X. G.; Rinke, P.; Scheffler, M. *Phys. Rev. B: Condens. Matter* **2009**, *80*, 045402.

(28) Furche, F. *J. Chem. Phys.* **2008**, *129*, 114105.

(29) Bohm, D.; Pines, D. *Phys. Rev.* **1952**, *85*, 332.

(30) Bohm, D.; Pines, D. *Phys. Rev.* **1953**, *92*, 609.

(31) Scuseria, G. E.; Henderson, T. M.; Sorensen, D. C. *J. Chem. Phys.* **2008**, *129*, 231101.

(32) Furche, F.; Van Voorhis, T. *J. Chem. Phys.* **2005**, *122*, 164106.

(33) Dobson, J. F.; Wang, J.; Dinte, B. P; McLennan, K.; Le H. M, *Int. J. Quantum Chem.* **2005**, *101*, 579.

(34) Fuchs, M.; Niquet, Y.-M.; Gonze, X.; Burke, K. *J. Chem. Phys.* **2005**, *122*, 094116.

(35) Perdew, J. P.; Zunger, A. *Phys. Rev. B: Condens. Matter* **1981**, *23*, 5048.

(36) Cole, L. A.; Perdew, J. P. *Phys. Rev. A: At., Mol., Opt. Phys.* **1982**, *25*, 1265.

(37) Toulouse, J.; Gerber, I. C.; Jansen, G.; Savin, A.; Ángyán, J. G. *Phys. Rev. Lett.* **2009**, *102*, 096404.

(38) Janesko, B. G.; Henderson, T. M.; Scuseria, G. E. *J. Chem. Phys.* **2009**, *130*, 081105.

(39) Perdew, J. P.; Burke, K.; Wang, Y. *Phys. Rev. B: Condens. Matter* **1996**, *54*, 16533.

(40) Vydrov, O. A.; Van Voorhis, T. *Phys. Rev. Lett.* **2009**, *103*, 063004.

(41) Frisch, M. J., Trucks, G. W., Schlegel, H. B., Scuseria, G. E., Robb, M. A., Cheeseman, J. R., Montgomery, J. A., Vreven, T., Kudin, K. N., Burant, J. C., Millam, J. M., Iyengar, S. S., Tomasi, J., Barone, V., Mennucci, B., Cossi, M., Scalmani, G., Rega, N., Petersson, G. A., Nakatsuji, H., Hada, M., Ehara, M., Toyota, K., Fukuda, R., Hasegawa, J., Ishida, M., Nakajima, T., Honda, Y., Kitao, O., Nakai, H., Klene, M., Li, X., Knox, J. E., Hratchian, H. P., Cross, J. B., Bakken, V., Adamo, C., Jaramillo, J., Gomperts, R., Stratmann, R. E., Yazyev, O., Austin, A. J., Cammi, R., Pomelli, C., Ochterski, J. W., Ayala, P. Y., Morokuma, K., Voth, G. A., Salvador, P., Dannenberg, J. J., Zakrzewski, V. G., Dapprich, S., Daniels, A. D., Strain, M. C., Farkas, O., Malick, D. K., Rabuck, A. D., Raghavachari, K., Foresman, J. B., Ortiz, J. V., Cui, Q., Baboul, A. G., Clifford, S., Cioslowski, J., Stefanov, B. B., Liu, G., Liashenko, A., Piskorz, P., Komaromi, I., Martin, R. L., Fox, D. J., Keith, T., Laham, A. M. A., Peng, C. Y., Nanayakkara, A., Challacombe, M., Gill, P. M. W., Johnson, B., Chen, W., Wong, M. W., Gonzalez, C., Pople, J. A.; *GAUSSIAN03*, Revision D.01 ed.; Gaussian Inc.: Wallingford, CT, 2004.

(42) Perdew J. P.; Tao J. *J. Mol. Struct. - Theochem*, Special Issue on Conceptual Insights from Density Functional Theory (to appear).

(43) Vydrov, O. A.; Scuseria, G. E.; Perdew, J. P. *J. Chem. Phys.* **2007**, *126*, 154109.

(44) Dobson, J.; Wang, J.; Gould, T. *Phys. Rev. B: Condens. Matter* **2002**, *66*, 081108.

(45) Hellgren, M.; von Barth, U. *Phys. Rev. B: Condens. Matter* **2008**, *78*, 115107; Hellgren M.; von Barth, U., unpublished.

(46) Lein, M.; Gross, E. K. U.; Perdew, J. P. *Phys. Rev. B: Condens. Matter* **2000**, *61*, 13431.

(47) Grueneis, A.; Marsman, M.; Harl, J.; Schimka, L.; Kresse, G. *J. Chem. Phys.* **2009**, *131*, 154115.

(48) Roman-Perez, G.; Soler, J. M. *Phys. Rev. Lett.* **2009**, *103*, 096102.

CT900518K

JCTC Journal of Chemical Theory and Computation

Accelerating Correlated Quantum Chemistry Calculations Using Graphical Processing Units and a Mixed Precision Matrix Multiplication Library

Roberto Olivares-Amaya,[†,§] Mark A. Watson,[†,§] Richard G. Edgar,[†] Leslie Vogt,[†] Yihan Shao,[‡] and Alán Aspuru-Guzik*,[†]

Department of Chemistry and Chemical Biology, Harvard University, 12 Oxford Street, Cambridge, Massachusetts 02138 and Q-Chem, Inc., 5001 Baum Boulevard, Suite 690, Pittsburgh, Pennsylvania 15213

Abstract: Two new tools for the acceleration of computational chemistry codes using graphical processing units (GPUs) are presented. First, we propose a general black-box approach for the efficient GPU acceleration of matrix−matrix multiplications where the matrix size is too large for the whole computation to be held in the GPU's onboard memory. Second, we show how to improve the accuracy of matrix multiplications when using only single-precision GPU devices by proposing a heterogeneous computing model, whereby single- and double-precision operations are evaluated in a mixed fashion on the GPU and central processing unit, respectively. The utility of the library is illustrated for quantum chemistry with application to the acceleration of resolution-of-the-identity second-order Møller−Plesset perturbation theory calculations for molecules, which we were previously unable to treat. In particular, for the 168-atom valinomycin molecule in a cc-pVDZ basis set, we observed speedups of 13.8, 7.8, and 10.1 times for single-, double- and mixed-precision general matrix multiply (SGEMM, DGEMM, and MGEMM), respectively. The corresponding errors in the correlation energy were reduced from −10.0 to −1.2 kcal mol^{-1} for SGEMM and MGEMM, respectively, while higher accuracy can be easily achieved with a different choice of cutoff parameter.

1. Introduction

Ever since scientists began to solve the equations of molecular quantum mechanics using numerical methods and computational tools, the interplay between fundamental theory and application has been inextricably linked to exponential advances in hardware technology. Indeed, many influential contributions to quantum chemistry have been motivated by insights into how best to utilize the available computational resources within the same theoretical model. One example is Almlöf's appreciation of the discrepancy that had appeared between data storage capacity and raw processor speed.[1] His subsequent introduction of the direct SCF technique transformed calculations from being memory (or disk) bound into being processor bound; previously impossible applications could be attempted by using additional processor time.

We are now witnessing yet another era in the optimization of quantum chemistry codes, following an explosion of interest in the application of coprocessors, such as graphics processing units (GPUs) to general scientific computing.[2] This interest in GPUs and related massively parallel processors is largely driven by their tremendous cost to performance ratio (in operation counts per second per unit of currency), which arises from the economies of scale in their manufacture and in their great demand in numerous multimedia applications. Another key factor in their widespread uptake for scientific use is the recent release of NVIDIA's compute unified device architecture (CUDA) programming interface

---

* Corresponding author. E-mail: aspuru@chemistry.harvard.edu.

† Harvard University.

‡ Q-Chem, Inc.

§ Contributed equally to this work.

that allows development of algorithms for the GPU using a relatively simple extension of the standard C language.[2]

A GPU is an example of a stream-processing architecture[3] and can outperform a general-purpose central processing unit (CPU) for certain tasks because of the intrinsic parallelization within the device, which uses the single-instruction, multiple data (SIMD) paradigm. Typical GPUs contain multiple arithmetic units (streaming processors), which are typically arranged in groups of eight to form multiprocessors that share a fast access memory and an instruction unit; all eight processors execute the same instruction thread simultaneously on different data streams. In contrast, in multiple-core or parallel CPU architectures, each thread must have an instruction explicitly coded for each piece of data. One of the most recent GPU cards, the Tesla C1060 from NVIDIA, contains 240 streaming processors, can provide up to 933 GFLOPS of single-precision computational performance, and has a cost which is approximately 1 order of magnitude less than an equivalent CPU cluster.

GPUs are, therefore, well-suited for high-performance applications with dense levels of data parallelism where very high accuracy is not required. (Although double-precision cards are available, in the case of NVIDIA GPUs, they have a peak FLOP count approximately 10 times less than those of single precision cards.) The challenge for scientists wanting to exploit the efficiency of the GPU is to expose the SIMD parallelism in their problem and to efficiently implement it on the new architecture. A key component of this task is a careful consideration of the memory hierarchy to efficiently hide memory access latency.

Already, GPUs have been recruited extensively by the scientific community to treat a wide range of problems, including finite-difference time-domain algorithms[4] and *n*-body problems in astrophysics.[5] For computational chemistry, GPUs are emerging as an extremely promising architecture for molecular dynamics simulations,[6,7] quantum Monte Carlo,[8] density functional theory, self-consistent field calculations,[9−14] and correlated quantum chemistry[15] methods. Efficiency gains of between one and three orders of magnitude using NVIDIA graphics cards have been reported compared to conventional implementations on a CPU. In this way, new domains of scientific application have become amenable to calculation where, previously, extremely expensive and rare supercomputing facilities would have been required.

As an example of the more general impact of accelerator technologies, Brown et al.[16] have accelerated density functional theory up to an order of magnitude using a Clearspeed coprocessor. The Clearspeed hardware is a proprietary compute-oriented stream architecture promising raw performance comparable to that of modern GPUs, while offering double-precision support and an extremely low power consumption. The challenges of efficiently utilizing the Clearspeed boards are similar to those of GPUs, requiring a fine-grained parallel programming model with a large number of lightweight threads. Thus, the algorithmic changes suggested for their work and for ours have a common value independent of the precise hardware used, which will of course change with time.

In the current work, we introduce two new techniques with general utility for the adoption of GPUs in quantum chemistry. First, we propose a general approach for the efficient GPU acceleration of matrix−matrix multiplications, where the matrix size is too large for the whole computation to be held in the GPU's onboard memory, requiring the division of the original matrices into smaller pieces. This is a major issue in quantum chemical calculations where matrix sizes can be very large.

Second, we describe how to improve the accuracy of general matrix−matrix multiplications when using single-precision GPUs, where the 6−7 significant figures are often insufficient to achieve 'chemical accuracy' of 1 kcal mol^{-1}. To solve this problem, we have implemented a new algorithm within a heterogeneous computing model, whereby the numerically large contributions to the final result are computed and accumulated on a double-precision device (typically the CPU), and the remaining small contributions are efficiently treated by the single-precision GPU device.

We have applied these ideas in an extension of our previously published GPU-enabled implementation of resolution-of-the-identity second-order Møller−Plesset perturbation theory (RI-MP2).[17−20] Thus, the paper begins in Section 2 with an overview of the RI-MP2 method and our previous GPU implementation. In Sections 3 and 4, we discuss our new matrix-multiplication library and its performance. In Section 5, we examine the accuracy and the speedups achieved when applying the technology to RI-MP2 calculations on molecules with up to 168 atoms, and we end the paper with some brief conclusions.

2. GPU Acceleration of RI-MP2

One of the most widely used and computationally least expensive correlated treatments for electronic structure is the second-order Møller−Plesset perturbation theory (MP2). MP2 is known to produce equilibrium geometries of comparable accuracy to density functional theory (DFT),[21] but unlike many popular DFT functionals is able to capture long-range correlation effects, such as the dispersion interaction. For many weakly bound systems where DFT results are often questionable, MP2 is essentially the least expensive and most reliable alternative.[22] The expression for computing the MP2 correlation energy takes the form:

$$E^{(2)} = \sum_{ijab} \frac{(ia|jb)^2 + \frac{1}{2}[(ia|jb) - (ib|ja)]^2}{\varepsilon_i + \varepsilon_j - \varepsilon_a - \varepsilon_b} \quad (1)$$

in terms of the $\{i, j\}$ occupied and $\{a, b\}$ virtual molecular orbitals (MOs) that are eigenfunctions of the Fock operator with eigenvalues $\{\varepsilon\}$. The MO integrals:

$$(ij|ab) = \sum_{\mu\nu\lambda\sigma} C_{\mu i} C_{\nu j} C_{\lambda a} C_{\sigma b} (\mu\nu|\lambda\sigma) \quad (2)$$

are obtained by contracting two-electron integrals over the (real) atomic orbital (AO) basis functions:

$$(\mu\nu|\lambda\sigma) = \int \int \phi_\mu(\mathbf{r}_1)\phi_\nu(\mathbf{r}_1)\phi_\lambda(\mathbf{r}_2)\phi_\sigma(\mathbf{r}_2)d\mathbf{r}_1 d\mathbf{r}_2 \quad (3)$$

where **C** is the matrix of MO coefficients describing the

Correlated Quantum Chemistry Calculations

J. Chem. Theory Comput., Vol. 6, No. 1, 2010 **137**

expansion of each MO as a linear combination of the AOs. One way to considerably reduce the computational cost associated with traditional MP2 calculations (which formally scales as $O(N^5)$ with the number of basis functions) is to exploit the linear dependence inherent in the product space of atomic orbitals. This allows one to expand products of AOs as linear combinations of atom-centered auxiliary basis functions, P:

$$\rho_{\mu\nu}(\mathbf{r}) = \mu(\mathbf{r})\nu(\mathbf{r}) \approx \tilde{\rho}_{\mu\nu}(\mathbf{r}) = \sum_P C_{\mu\nu,P} P(\mathbf{r}) \qquad (4)$$

and to, therefore, approximate all the costly four-center, two-electron integrals in terms of only two- and three-center integrals:

$$\overline{(\mu\nu|\lambda\sigma)} = \sum_{P,Q} (\mu\nu|P)(P|Q)^{-1}(Q|\lambda\sigma) \qquad (5)$$

where we have assumed that the expansion coefficients are determined by minimizing the Coulomb self-repulsion of the residual density. The result is equivalent to an approximate insertion of the resolution-of-the-identity (RI).

All our work is implemented in a development version of Q-Chem 3.1,[23] where the RI-MP2 correlation energy is evaluated in five steps, as described elsewhere.[15] Previously we showed that step 4, the formation of the approximate MO integrals, was by far the most expensive operation for medium- to large-sized systems and requires the matrix multiplication:

$$\overline{(ia|jb)} \approx \sum_Q B_{ia,Q} B_{jb,Q} \qquad (6)$$

where:

$$B_{ia,Q} = \sum_P (ia|P)(P|Q)^{-1/2} \qquad (7)$$

The evaluation of eq 6 is typically an order of magnitude more expensive than eq 7. We shall concentrate on these two matrix multiplications in this work. Consistent with our previous paper,[15] we will repeatedly refer to these evaluations as steps 3 (eq 7) and 4 (eq 6) as we investigate the accuracy and the efficiency of our new GPU implementation.

Included in the CUDA software development toolkit is an implementation of the BLAS linear algebra library, named CUBLAS.[24] As previously reported,[15] we accelerated the matrix multiplication in eq 6 by simply replacing the BLAS *GEMM routines with corresponding calls to CUBLAS SGEMM. This initial effort achieved an overall speedup of 4.3 times for the calculation of the correlation energy of the 68-atom doeicosane ($C_{22}H_{46}$) molecule with a cc-pVDZ basis set using a single GPU. At this early stage in development, we used the GPU purely as an accelerator for *GEMM and made no effort to keep data resident on the device.

In the present work, we further explore the acceleration of our RI-MP2 code through the application of CUBLAS combined with two new techniques. These enable us to perform more accurate calculations on larger molecules and basis sets involving larger matrices, while also mitigating the errors associated with single-precision GPUs. We discuss both techniques in the following section.

3. GPU Acceleration of GEMM

In large-scale quantum chemistry calculations, the size of the fundamental matrices typically grows as the square of the number of atomic basis functions (even if the number of non-negligible elements is much smaller). Moreover, inter-mediate matrices are sometimes even larger, such as the **B** matrices of eq 7.

A GPU can only accelerate a calculation that fits into its onboard memory. While the most modern cards designed for research can have up to 4 GiB of RAM, consumer level cards may have as little as 256 MiB (with some portion possibly devoted to the display). If we wish to run large calculations, but only have a small GPU available, then some means of dividing the calculation up and staging it through the GPU must be found.

Next, we consider the question of accuracy arising from the use of single-precision GPU cards. It turns out, that many operations do not require full double-precision support to achieve acceptable accuracy for chemistry, but nevertheless, single precision is not always sufficient.[13] Double-precision capable GPUs have only become available within the past year and so are not yet widespread. Moreover, we cannot rely on the support of double-precision cards by manufacturers in the future, since the commercial driving force behind such processors is the wealth of multimedia applications that do not require high precision. We address this problem with the introduction of a new way to balance the desire for GPU acceleration with a need for high accuracy.

3.1. Cleaving GEMMs. Consider the matrix multiplication:

$$\mathbf{C} = \mathbf{A} \cdot \mathbf{B} \qquad (8)$$

where **A** is a $(m \times k)$ matrix, and **B** is a $(k \times n)$ matrix, making **C** an $(m \times n)$ matrix. We can divide **A** into a column vector of $r + 1$ matrices:

$$\mathbf{A} = \begin{pmatrix} \mathbf{A}_0 \\ \mathbf{A}_1 \\ \vdots \\ \mathbf{A}_r \end{pmatrix} \qquad (9)$$

where each entry $\mathbf{A}_i$ is a $(p_i \times k)$ matrix, and $\sum_{i=0}^r p_i = m$. In practice, all the p_i will be the same, with the possible exception of p_r, which will be an edge case. In a similar manner, we can divide **B** into a row vector of $s + 1$ matrices:

$$\mathbf{B} = (\mathbf{B}_0 \quad \mathbf{B}_1 \quad \cdots \quad \mathbf{B}_s) \qquad (10)$$

where each $\mathbf{B}_j$ is an $(k \times q_j)$ matrix, and $\sum_{j=0}^s q_j = n$. Again all the q_j will be the same, with the possible exception of q_s. We then form the outer product of these two vectors:

$$\mathbf{C} = \begin{pmatrix} \mathbf{A}_0 \\ \mathbf{A}_1 \\ \vdots \\ \mathbf{A}_r \end{pmatrix} \cdot (\mathbf{B}_0 \quad \mathbf{B}_1 \quad \cdots \quad \mathbf{B}_s) \qquad (11)$$

$$= \begin{pmatrix} \mathbf{A}_0 \cdot \mathbf{B}_0 & \mathbf{A}_0 \cdot \mathbf{B}_1 & \cdots & \mathbf{A}_0 \cdot \mathbf{B}_s \\ \mathbf{A}_1 \cdot \mathbf{B}_0 & \mathbf{A}_1 \cdot \mathbf{B}_1 & & \mathbf{A}_1 \cdot \mathbf{B}_s \\ \vdots & & \ddots & \\ \mathbf{A}_r \cdot \mathbf{B}_0 & & & \mathbf{A}_r \cdot \mathbf{B}_s \end{pmatrix} \qquad (12)$$

Each individual $\mathbf{C}_{ij} = \mathbf{A}_i \mathbf{B}_j$ is a $(p_i \times q_j)$ matrix and can be computed independently of all the others. Generalizing this

to a full *GEMM implementation, which includes the possibility of transposes being taken, is tedious but straightforward.

We have implemented this approach for the GPU, as a complete replacement for *GEMM. The p_i and q_j values are chosen such that each submultiplication fits within the currently available GPU memory. Each multiplication is staged through the GPU, and the results assembled on the CPU. This process is hidden from the user code, which simply sees a standard *GEMM call.

3.2. Heterogeneous Computing with MGEMM. With the problem of limited memory solved, we will now demonstrate how to overcome the lack of double precision GPU hardware. Again, consider the matrix multiplication:

$$\mathbf{C} = \mathbf{A} \cdot \mathbf{B} \qquad (13)$$

We can split each matrix element-wise into 'large' and 'small' components, giving:

$$\begin{aligned} \mathbf{C} &= (\mathbf{A}^{\text{large}} + \mathbf{A}^{\text{small}})(\mathbf{B}^{\text{large}} + \mathbf{B}^{\text{small}}) \\ &= \mathbf{A} \cdot \mathbf{B}^{\text{large}} + \mathbf{A}^{\text{large}} \cdot \mathbf{B}^{\text{small}} + \mathbf{A}^{\text{small}} \cdot \mathbf{B}^{\text{small}} \end{aligned}$$

The $\mathbf{A}^{\text{small}}\mathbf{B}^{\text{small}}$ term consists entirely of 'small' numbers and can be run in single precision on the GPU (using the cleaving approach described above, if needed). The other two terms contain 'large' numbers and need to be run in double precision. However, since each of the 'large' matrices should be sparse, these terms each consist of a dense-sparse multiplication. We only store the nonzero terms of the $\mathbf{A}^{\text{large}}$ and $\mathbf{B}^{\text{large}}$ matrices, cutting the computational complexity significantly. Consider:

$$C'_{ik} = A_{ij} B^{\text{large}}_{jk} \qquad (14)$$

Only a few B^{large}_{jk} will be nonzero, and we consider each in turn. For a particular scalar B^{large}_{jk}, only the kth column of $\mathbf{C}'$ will be nonzero and is equal to the product of B^{large}_{jk} and the jth column vector of $\mathbf{A}$. This nonzero column vector C'_{ik} can be added to the final result, $\mathbf{C}$, and the next B^{large}_{jk} can be considered. A similar process can be applied to the $\mathbf{A}^{\text{large}}\mathbf{B}^{\text{small}}$ term (producing *row* vectors of $\mathbf{C}$). Again, this approach can be generalized to a full *GEMM implementation, including transposes.

The remaining question is that of splitting the matrices. We have taken the simple approach of defining a cutoff value, δ. If $|A_{ij}| > \delta$, that element is considered 'large,' otherwise it is considered to be 'small.'

We have implemented our algorithm we have dubbed MGEMM for mixed-precision general matrix multiply. It operates similarly to the other *GEMM routines but takes one extra argument—the value of δ.

4. MGEMM Benchmarks

We will now discuss some benchmarks for MGEMM. Our aim is to assess the speed and accuracy of MGEMM for various matrix structures and the choice of cutoff tolerance compared to a DGEMM call on the CPU. In particular, it is important to benchmark how much computational speed is gained using the mixed-precision MGEMM with the GPU as a function of the loss in accuracy compared to DGEMM.
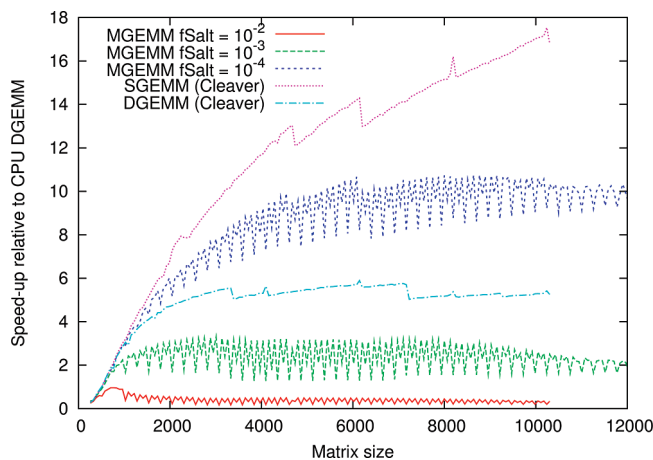

Figure 1. Speedup for various *GEMM calls as a function of (square) matrix size (averaged over 10 runs). Most elements were in the range $[-1, 1]$, with the 'salt' values in the range $[90, 110]$. Times are scaled relative to running DGEMM on the CPU.

Throughout this section, CPU calculations were made using an Intel Xeon E5472 (Harpertown) processor clocked at 300 GHz attached to an NVIDIA Tesla C1060 (packaged into a Tesla S1070). The GPU calls were limited to 256 MiB of RAM to model a more restricted GPU in a typical BOINC (Berkeley Open Infrastructure for Network Computing) client.[25,26]

4.1. Using Model Matrices. In Figure 1 we show the speedup for a variety of *GEMM calls using matrices of increasing (square) size. Three different types of matrices were considered, based on the number of randomly scattered 'large' elements. All the matrices were initialized with random values in the range $[-1, 1]$, forming the 'background' and 'salted' with a fraction f_{salt} of random larger values in the range $[90, 110]$. The size of the MGEMM cutoff parameter δ was chosen such that all the salted elements were considered 'large'.

There are three MGEMM curves plotted, for different values of $f_{\text{salt}} = 10^{-2}$, 10^{-3}, and 10^{-4}. The SGEMM(cleaver) curve corresponds to doing the full matrix multiplication on the GPU using the GEMM(cleaver) and includes the time taken to down convert the matrices to single precision on the CPU. The DGEMM(cleaver) curve corresponds to a full double-precision matrix multiplication on the GPU, which is possible for modern cards, and we include it for completeness. Square matrices were used in all cases, with no transpositions in the *GEMM calls. All the runs were performed 10 times, and speedups are obtained relative to the time taken for the corresponding DGEMM call on the CPU.

Examining the results, we see that SGEMM on the GPU gives a speedup of 17.1 times over running DGEMM on the CPU for a matrix of size $10\,048 \times 10\,048$ and is even faster for larger matrices. This represents an upper bound for the speedups we can hope to obtain with MGEMM for such matrices. The speedups increase significantly as the matrices become larger due to the masking of memory access latencies and due to other overheads when employing the GPU for more compute-intensive processes.
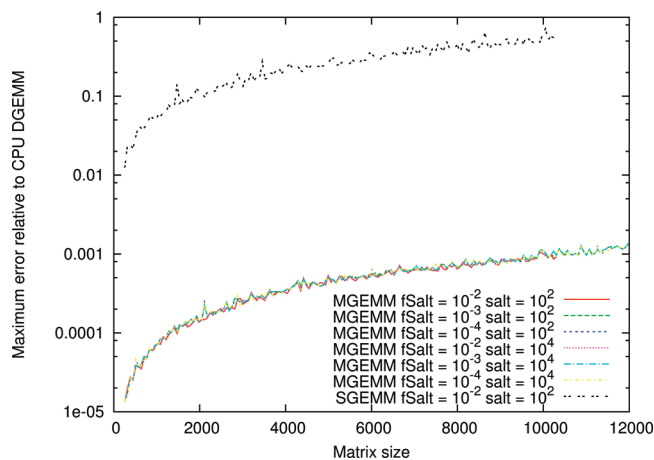
Correlated Quantum Chemistry Calculations

J. Chem. Theory Comput., Vol. 6, No. 1, 2010 **139**

Figure 2. Maximum absolute error in a single element for various GEMM calls as a function of matrix (square) size. Most elements were in the range $[-1, 1]$, with the 'salt' values in the range $[90, 110]$ or $[9\,990, 10\,010]$. A CPU DGEMM call was taken as the reference calculation.

Considering the MGEMM results, we see that the speedups are strongly dependent on the number of large elements which must be evaluated in double precision on the CPU. For the relatively high value of $f_{salt} = 10^{-2}$, running MGEMM was actually slower than running DGEMM on the CPU alone. This is understandable when one considers the extra steps in the MGEMM algorithm. In addition to down converting the matrices to single precision, the CPU has to perform cache-incoherent operations on the 'large' multi-plications. We store our matrices column major, so the operations performed in eq 14 are cache coherent. However, it is easy to see that the corresponding operations for $\mathbf{C}' = \mathbf{A}^{large}\mathbf{B}^{small}$ will be cache incoherent for both $\mathbf{C}'$ and $\mathbf{B}^{small}$ (recall that $\mathbf{A}^{large}$ will be stored as individual elements). This brings a huge penalty over a standard *GEMM implementa-tion, which is tiled for cache coherency.

In contrast, for $f_{salt} = 10^{-4}$, there is much less penalty to running MGEMM over SGEMM on the GPU, due to the small fraction of large elements computed on the CPU. Speedups of approximately 10 times are observed for the largest matrices. For $f_{salt} = 10^{-3}$, the performance is naturally reduced, and speedups of approximately 2 times relative to CPU DGEMM are obtained for the largest matrices. In this case, MGEMM runs approximately 2.5 times slower than full DGEMM on the GPU (available in the most modern cards). We may also note that the thresholds for matrix cleaving can be discerned. They start at matrix sizes of 3 344 for double precision and 4 729 for single precision. These are detectable on the curves but do not alter the times significantly.

In Figure 2, we examine the accuracy of MGEMM for various matrix structures. Shown in the figure are the maximum absolute errors of a single element (relative to the CPU DGEMM result) plotted as a function of matrix size, for different fractions f_{salt} and sizes of salted values. As before, all the matrices were initialized with random values in the range $[-1, 1]$, but now the salting sizes were grouped into two ranges: $[90, 110]$ and $[9\,990, 10\,010]$. There is one curve using SGEMM corresponding to a fraction of salted

values, $f_{salt} = 0.01$, in the range $[90, 110]$, and several MGEMM curves.

Looking at the figure, we see that the salted SGEMM calculation produces substantial errors for the largest matri-ces, which are of the same order of magnitude as the background elements themselves. In contrast, the errors are significantly reduced when using MGEMM and are the same regardless of the fraction or size of the salted elements. In fact, these limiting MGEMM errors are the same as the errors observed when using SGEMM on a pair of unsalted random matrices. Essentially, MGEMM is limiting the maximum error in any element to that of the 'background' matrix computed in single precision, since the cutoff tolerance guarantees that all the salted contributions will be computed in double precision on the CPU.

The order of magnitude of the limiting error can be rationalized from a consideration of the number of single-precision contributions per output element (approximately $1\,000-10\,000$ in this case) and the expected error in each (approximately $10^{-6}-10^{-7}$ for input matrices with a random background on $[-1, 1]$). A consequence of this observation is that an upper bound to the maximum error can be estimated from a consideration of only the matrix size and the cutoff parameter δ, although this estimate will be very conservative in cases where there is no obvious 'constant background', as we shall see in the following.

4.2. Using RI-MP2 Matrices. For a more realistic as-sessment of MGEMM for quantum chemistry applications, we also ran benchmarks on two pairs of matrices taken from an RI-MP2 calculation on the taxol molecule in a cc-pVDZ basis, as described below in Section 5. In this case, the MGEMM cutoff parameter δ will no longer be dimensionless but rather will take the same units as the input matrix elements, which, for eqs 6 and 7, are all computed in atomic units. For simplicity, we have dropped these units in the following discussion and assumed their implicit understand-ing based on the matrices that the δ-value is referring to.

As summarized in Section 2, our RI-MP2 implementation has two steps involving significant matrix multiplications: the evaluation of eqs 6 and 7. As described in the section and as consistent with our previous work,[15] we shall refer to these two matrix multiplications as step 3 (eq 7) and step 4 (eq 6) throughout the following discussion. Although step 3 is typically an order of magnitude faster than step 4, we need to take care to study it since we are interested not only in speed but also error accumulation using MGEMM.

For the case of taxol in a cc-pVDZ basis, the full $(P|Q)^{-1/2}$ matrix is of size $4\,186 \times 4\,186$. However, in the Q-Chem implementation, the full $(ia|P)$ and $B_{ia, Q}$ matrices do not need to be explicitly constructed. Instead, it is sufficient to loop over discrete batches of i, depending on available memory. As seen above, larger matrices deliver a greater speedup when multiplied on the GPU, thus, there is a motivation for choosing as large a batch size (over i) as possible in our GPU calculations. In these test benchmarks, we chose batch sizes of one and seven based on the available CPU memory, such that the $(ia|P)$ and $B_{ia, Q}$ matrices have dimensions of $897 \times 4\,186$ and $6\,279 \times 4\,186$, respectively. We do not batch the step 3 matrices since there are only $O(N)$
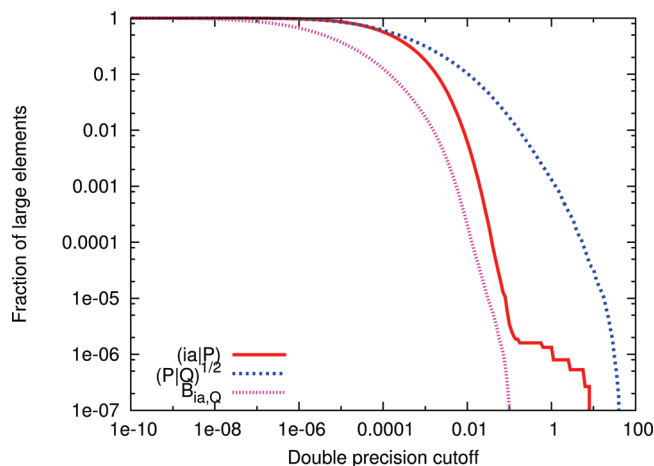
Figure 3. Fraction of 'large' elements as a function of the cutoff parameter, δ, for the taxol RI-MP2 matrices in steps 3 (eq 7) and 4 (eq 6) of the algorithm outlined in Section 2.

multiplications taking place, and the more computationally intensive process is step 4, which has order $O(N^2)$ operations.

We note that the structure of these matrices was found to be very different from the model matrices considered in the previous subsection, Section 4.1. Specifically, the distribution of large and small elements was structured, as described below. In the case of the $(P|Q)^{-1/2}$ matrix, involving only the auxiliary basis set, the large elements were heavily concentrated on the top left-hand corner in a diagonal fashion, while the other matrices were observed to have a striped vertical pattern of large elements. In the current implementation, the main issue affecting the efficiency of MGEMM is the ratio of large to small elements in the input matrices, but in general we can also expect the sparsity structure to impact performance. In cases where the structure is known in advance, a more specialized treatment could give worthwhile speedups, but this is beyond the scope of the current work.

The precise fractions of large and small elements for the taxol case are plotted in Figure 3 with varying cutoff parameter δ for both step 3 and 4 matrices. We should note that these curves are only for one particular i-batch, as explained above, and not for the full matrices. However, to ensure that the results are representative of the full matrix, we checked the distributions from the other batches, and we chose the most conservative matrices for our plots, which had large elements across the broadest range of δ-values.

Looking at the curves, it is significant that the step 3 matrices have a greater fraction of large elements than the step 4 matrices, and specifically, the $(P|Q)^{-1/2}$ matrix has the largest elements of all. This means that for a constant δ-value, we can expect MGEMM to introduce larger errors in the step 3 matrix multiplications than in step 4. In future work, it could be advantageous to tailor the δ-value for different steps in an algorithm, or even different input matrices, but in this first study, we use a constant δ-value throughout any given calculation.

In the model matrices of the previous subsection, Section 4.1, the distribution would have resembled a step function around $\delta = 1.0$, rapidly dropping from 1.0 to the chosen
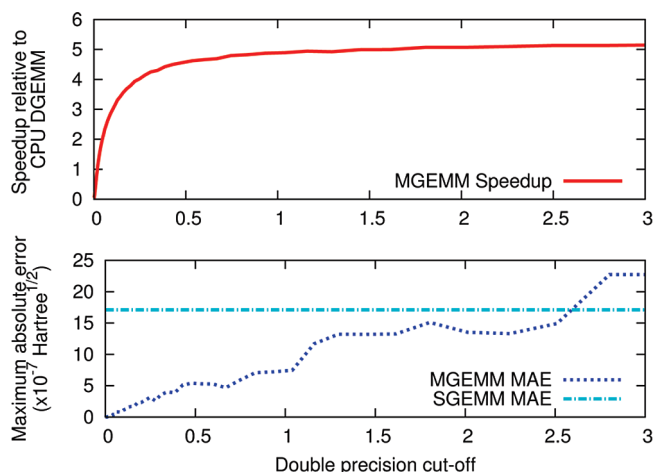

Figure 4. Results from the step 3 (eq 7) matrix multiplication in a taxol RI-MP2 calculation as a function of the cutoff variable δ. Top: MGEMM speedups relative to a CPU DGEMM calculation. Bottom: Maximum absolute error (Hartree$^{1/2}$) in a single element of the output matrix for MGEMM and SGEMM runs.
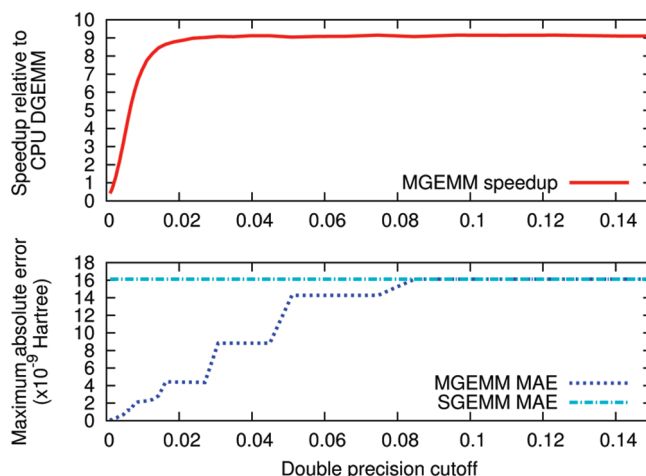

Figure 5. Results from the step 4 (eq 6) matrix multiplication in a taxol RI-MP2 calculation as a function of the cutoff variable δ. Top: MGEMM speedups relative to a CPU DGEMM calculation. Bottom: Maximum absolute error (Hartree) in a single element of the output matrix for MGEMM and SGEMM runs.

fraction of salted values for $\delta > 1.0$ and rapidly stepping again to 0 for δ-values beyond the salt size. In contrast, we see a continuous decay of element values in the real matrices across many orders of magnitude. In Figure 1, MGEMM was seen to outperform DGEMM for a fraction of salts of order 10^{-4}. Comparing to Figure 3, this suggests that δ should be greater than 0.01 to ensure significant MGEMM speedups when considering the $(ia|P)$ and $B_{ia,Q}$ matrices, while the fraction of large elements in the $(P|Q)^{-1/2}$ matrices only becomes this small for δ-values of order 10.

Having analyzed the distributions, we can consider their effect on the accuracy and the speedups compared to those of the model benchmarks. On the top plots of Figures 4 and 5, we show how the speedup for various *GEMM calls (compared to a CPU DGEMM call) varies with δ, averaged over 10 calls. We see that the MGEMM performance varies

Correlated Quantum Chemistry Calculations

J. Chem. Theory Comput., Vol. 6, No. 1, 2010 **141**

continuously from being almost the same speed as CPU DGEMM to reaching the GPU SGEMM limit for sufficiently large cutoff values. As expected, for the step 4 matrices, significant speedups are only observed for δ-values greater than approximately 0.01. Similarly, for step 3, the greatest speedups are only observed for much larger δ-values, approximately 1 to 2 orders of magnitude greater than for step 4. The limiting values for the speedups are approximately five and nine times for steps 3 and 4, respectively. This difference is mainly due to the different sizes of the matrices used in each benchmark, recognizing that the smaller matrices used in step 3 will give smaller speedups (cf. Figure 1).

Considering the MGEMM accuracy, the bottom plots in Figures 4 and 5 show the maximum absolute errors of a single element (relative to the CPU DGEMM result) plotted as a function of δ. As δ increases, the MGEMM errors steadily increase, as expected, with the single precision limit being approached for sufficiently large δ. Again we see significant differences between steps 3 and 4, as expected from the element distributions. First, the errors in step 3 are approximately 2 orders of magnitude greater than in step 4. Moreover, in step 4, the errors reach the SGEMM limit for $\delta \sim 0.1$, while the errors in step 3 continue to increase for cutoff values an order of magnitude larger. Examining Figure 3, it is expected that the relatively large fraction of elements greater than 1.0 in the $(P|Q)^{-1/2}$ matrix are responsible for these observations.

Unexpectedly, however, the errors are not seen to steadily converge to the SGEMM limit for step 3 in the same way as for step 4, with errors larger than SGEMM being observed for $\delta > 2.5$. We have performed additional tests to understand why this may be happening, and our conclusion is that it results from error cancellation effects. To verify this idea, we repeated similar calculations replacing all matrix elements with their absolute values, so that any error cancellation would be essentially removed. The result was a monotonic curve much more similar to that observed for step 4, showing the same steady convergence to the SGEMM limit (not shown).

We may now consider the advantages of using MGEMM over SGEMM in terms of accuracy and speed. Comparing the subplots in Figures 4 and 5, we can see that for a rather modest performance decrease from approximately five to four times and nine to seven times for steps 3 and 4, respectively, an order of magnitude reduction in the errors can be obtained. However, it might be noted that in all cases the maximum errors are rather small in these tests, being only of order 10^{-6} in the worst case. Considering real RI-MP2 applications, we might, therefore, expect the final errors in the molecular energy to be almost negligible, using single precision only. However, in Section 5, the benchmarks show that for larger molecules, the errors propagate such that the resulting correlation energy errors are too large to be acceptable.

Finally, from Figure 2, we can estimate an upper bound on the maximum absolute error of each element for different δ-values. Since the matrix dimension is approximately 4 000, the choice $\delta = 0.1$ would give a conservative error bound of approximately $4\,000 \times 10^{-6} \times 0.1$, which is of order 10^{-4}.

However, because the matrices do not have a 'constant background' of 0.1, this estimate is very conservative, and the observed error in Figure 5 is much less.

5. RI-MP2 Acceleration Benchmarks

In this section, our intention is to perform full RI-MP2 quantum chemistry calculations on real molecules and to benchmark the speedups and the accuracy in the resulting molecular energy that can be obtained when using the GPU. In this case, we include in the timings all steps required to compute the RI-MP2 correlation energy (after the SCF cycle has finished), while the GPU *GEMM libraries are used to accelerate the matrix multiplications in steps 3 (eq 7) and 4 (eq 6), as described in the previous sections. As a result, the observed speedups will be reduced compared to the previous benchmarks, since not all steps are accelerated.

For all these benchmarks, we used an AMD Athlon 5600+ CPU clocked at 300 GHz, combined with an NVIDIA Tesla C1060 GPU with 4 GiB of RAM. For some calculations, the GPU was limited to 256 MiB of RAM, as described below.

We emphasize that only the latest GPU cards have double-precision support to enable CUBLAS DGEMM, while older cards also have limited memory, which significantly constrains the size of even the CUBLAS SGEMM matrix multiplications. Our previous attempts to use GPUs to accelerate RI-MP2 calculations were limited to molecular systems with less than 500 basis functions[15] due to this constraint. However, using the matrix cleaver in the (MGEMM) library, we are now able to run calculations of a size limited only by the CPU specification, independent of the GPU memory.

For our test systems, we chose a set of linear alkanes (C_8H_{18}, $C_{16}H_{34}$, $C_{24}H_{50}$, $C_{32}H_{66}$, and $C_{40}H_{82}$) as well as two molecules of pharmaceutical interest, taxol ($C_{47}H_{51}NO_{14}$) and valinomycin ($C_{54}H_{90}N_6O_{18}$), and we considered the cc-pVDZ and cc-pVTZ[27] basis sets.

The matrix cleaver and MGEMM were implemented in a modified version of the Q-Chem 3.1 RI-MP2 code previously described.[15] Concerning the batching over occupied orbitals, as discussed in Section 4.2, only the step 4 matrices were batched. For all molecules, the batch size was chosen dynamically based on the matrix sizes and the available CPU memory (for taxol, this results in a batch size of seven, as used before). However, in these benchmarks the batching issue is less important, since we were limited to only 256 MiB of GPU RAM, which means that large batches would have to be cleaved by the MGEMM library in any case.

First, in Table 1, we benchmarked the reference case of either CUBLAS SGEMM or DGEMM for each test molecule using the double-ζ basis set. The table shows the speedup in computing the RI-MP2 correlation energy and the error relative to a standard CPU calculation (for SGEMM only). The speedups and SGEMM errors are seen to be greater for the larger molecules, as expected, with the largest speedups observed for valinomycin at 13.8 and 7.8 times, using SGEMM and DGEMM, respectively. However, while CUBLAS DGEMM gives essentially no loss of accuracy, the

142 *J. Chem. Theory Comput., Vol. 6, No. 1, 2010*

Olivares-Amaya et al.

Table 1. Speedups using CUBLAS SGEMM and DGEMM and Total Energy Errors Relative to CPU DGEMM for Various Molecules in a cc-pVDZ Basis

| molecule | speedup | | SGEMM energy error (kcal mol^{-1}) |
	SGEMM	DGEMM	
C_8H_{18}	2.1	1.9	−0.05616
$C_{16}H_{34}$	4.5	3.7	−0.12113
$C_{24}H_{50}$	6.9	5.2	−0.62661
$C_{32}H_{66}$	9.0	6.4	−0.75981
$C_{40}H_{82}$	11.1	7.2	−1.12150
taxol	11.3	7.1	−6.26276
valinomycin	13.8	7.8	−9.99340

Table 2. MGEMM Speedups and Total Energy Errors with Respect to CPU DGEMM for Various Molecules in a cc-pVDZ and a cc-pVTZ Basis

| molecule | speedup | | energy error (kcal mol^{-1}) | |
	double-ζ	triple-ζ	double-ζ	triple-ζ
C_8H_{18}	1.9	2.7	−0.01249	−0.03488
$C_{16}H_{34}$	3.8	5.6	−0.00704	−0.04209
$C_{24}H_{50}$	5.8	8.2	−0.14011	−0.33553
$C_{32}H_{66}$	7.9	9.2	−0.08111	−0.29447
$C_{40}H_{82}$	9.4	10.0	−0.13713	−0.51186
taxol	9.3	10.0	−0.50110	−1.80076
valinomycin	10.1	−	−1.16363	−

SGEMM error is approximately −10.0 kcal mol^{-1}, which is well beyond what is generally accepted as chemical accuracy.

The results from Table 1 highlight the need for MGEMM to reduce the errors when double-precision GPUs are unavailable. As an initial test of MGEMM for this purpose, we repeated the calculation of the taxol molecule in the double-ζ basis set (1 123 basis functions) for various choices of cutoff value δ. Figure 6 shows the speedup relative to CPU DGEMM as well as the absolute error in the energy.

As the cutoff increases, the MGEMM speedup increases rapidly to the asymptotic limit of 10.6 times, which is slightly less than the SGEMM limit of 11.3 times due to the MGEMM overhead. In contrast, the energy error in this range increases almost linearly toward the SGEMM limit. Recalling Figures 4 and 5, it seems that the errors are dominated by the step 3 operations, where we form the $B_{ia, Q}$ matrices, since these errors are also seen to steadily increase over the range of cutoff values considered in Figure 6. The overall speedups are also seen to have a similar shape to the step 3 speedups but are approximately twice as large. This reflects the greater speedups in step 4, noting that step 4 on the CPU is the most expensive step in the algorithm.

To achieve a target accuracy of 1.0 kcal mol^{-1}, Figure 6 shows that a cutoff value of $\delta < 2.0$ in the case of taxol
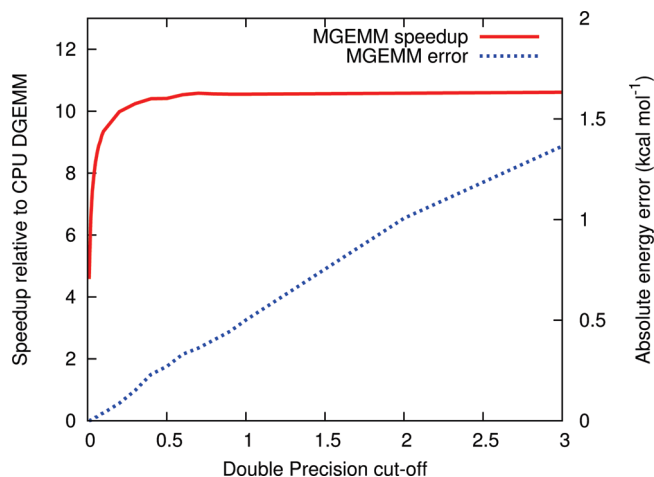
Figure 6. Taxol MGEMM calculation using a double-ζ basis set with respect to the double precision cutoff (δ). We plot the MGEMM speedup relative to CPU DGEMM, and it shows a rapid increase with δ toward an asymptotic value of 10.6 times. We also show the energy difference relative to CPU DGEMM, which is seen to increase steadily over the range of δ-values chosen but is significantly less than the previously computed SGEMM error of 6.6276 kcal mol^{-1}.

in a double-ζ basis is necessary. However, trading the accuracy and the speedup, a good choice of cutoff would be $\delta = 1.0$. This gives an error of 0.5 kcal mol^{-1}, which is an order of magnitude smaller than using SGEMM, with a speedup very close to the MGEMM limit and with only about 7% less than that of the SGEMM limit.

In Table 2, we explore the performance of MGEMM using a constant cutoff value of $\delta = 1.0$. The table shows the speedups and the total energy errors for each molecule in both the double- and triple-ζ basis sets. In this particular case, we have limited the GPU to use only 256 MiB of RAM to mimic the capability of older cards and to emphasize the use of the MGEMM cleaver. This will naturally result in a loss of speedup compared to utilizing a larger GPU memory. In the case of taxol, the reduction is approximately 20%, but obviously still much faster than a calculation using only the CPU.

Looking at Table 2, the trends are the same as in Table 1, but the MGEMM errors are seen to be approximately an order of magnitude less than the SGEMM errors (for the larger molecules). For valinomycin in the cc-pVDZ basis, the SGEMM speedup is reduced from 13.8 to 10.1 times using MGEMM, but the error in the total energy is also reduced from −10.0 to −1.2 kcal mol^{-1}, which is now very close to chemical accuracy. Moreover, while CUBLAS DGEMM clearly has the advantage (when available) of not introducing errors, if −1.2 kcal mol^{-1} is an acceptable accuracy, MGEMM may even be favored, since the DGEMM speedup is only 7.8 times compared to that of 10.1 times. Moreover, since the error increases as δ is increased, there will be a substantial error cancellation when obtaining energy differences. Thus, the apparent error in MGEMM will approach the DGEMM value.

It is unsurprising that the errors are larger when using the triple-ζ basis. The manner in which the errors grow can be anticipated using the arguments mentioned in Section 4, where we estimate an upper bound on the maximum absolute error from MGEMM by consideration of a constant background of elements no larger than the cutoff threshold and the size of the input matrices. In practice, this upper bound can be rather conservative. Moreover, if the quantity of interest is the final energy, we must also take into account how the matrices are used after the application of MGEMM (e.g., if they are multiplied by large numbers). Nevertheless, a topic of future study could be the search for a more

Correlated Quantum Chemistry Calculations

J. Chem. Theory Comput., Vol. 6, No. 1, 2010 **143**

sophisticated method for determining a safe and optimal δ-value for a given size of acceptable error in the final energy.

6. Conclusion

We have developed and implemented two new tools for the acceleration of computational chemistry codes using graphical processing units (GPUs). First, we proposed a general black-box approach for the efficient GPU acceleration of matrix−matrix multiplications, where the matrix size is too large for the whole computation to be held in the GPU's onboard memory. Second, we have shown how to improve the accuracy of matrix multiplications when using only single-precision GPU devices by proposing a heterogeneous computing model whereby both single- and double-precision operations are evaluated in a mixed fashion on the GPU and CPU, respectively.

This matrix cleaver and mixed-precision matrix multiplication algorithm have been combined into a general library named MGEMM,[28] which may be called like a standard SGEMM function call with only one extra argument, the cutoff parameter δ, which describes the partitioning of single- and double-precision work. Benchmarks of general interest have been performed to document the library's performance in terms of accuracy and speed.

Compared to a CPU DGEMM implementation, MGEMM is shown to give speedups approaching the CUBLAS SGEMM case when very few operations require double precision, corresponding to a large δ-value (which is equivalent to having a large fraction of small elements in the input matrices). However, when the fraction of large elements approaches 0.1% or greater, much less benefit is seen. Concerning accuracy, MGEMM restricts the maximum error in an element of the output matrix to an upper bound, based on the size of the matrix and the choice of δ-value. In practice, this upper bound is usually conservative. In general, the precise performance achieved with MGEMM is strongly dependent on the distribution of large and small values in the input matrices, as we have shown.

To illustrate the utility of MGEMM for quantum chemistry, we have implemented it into the Q-Chem program package to accelerate RI-MP2 calculations. We have considered both the use of modern high-end GPU cards, with up to 4 GiB of memory and with double-precision capability, as well as legacy cards, with only single-precision capability and with potentially only 256 MiB of RAM. Greater speedups but also larger absolute errors in the correlation energy were observed with the larger test molecules. In particular, for the 168-atom valinomycin molecule in a cc-pVDZ basis set, we observed speedups of 13.8, 10.1, and 7.8 times for SGEMM, MGEMM, and DGEMM, respectively. The corresponding errors in the correlation energy were -10.0, -1.2 kcal mol^{-1}, and essentially zero, respectively. The MGEMM δ-value was chosen as 1.0 for these benchmarks.

We have also suggested ways in which the size of the MGEMM error may be parametrized in terms of a conservative error bound. In addition, we have observed that the correlation energy error grows approximately linearly with the choice of δ-value, which may suggest a route to the *a priori* determination of the δ for a given target accuracy.

As we submit this paper for publication, we have become aware of the planned release of the next-generation GPU from NVIDIA, currently code-named Fermi. This card will have double-precision support with a peak performance only a factor of 2 less than that of single-precision operations. However, despite the emergence of double-precision GPU devices, it is our hope that the current work will provide a framework for thinking about other mixed-precision algorithms. Even with the more widespread availability of double-precision cards in the future, we have seen how MGEMM can run faster than CUBLAS DGEMM, if a specified level of accuracy is tolerated. Indeed, practical calculations on GPUs are very often bound by memory bandwidth to/from the device, rather than raw operation count. In these cases, the transfer and processing of only single-precision data could effectively double the performance compared to that of naive double-precision calculations.

Moreover, we are interested in the use of commodity GPUs as part of a grid-computing environment, such as the BOINC network. CUDA capable GPUs are extremely common in legacy gaming devices, but most of the client machines will not host the latest high-end hardware. We, therefore, see a significant application for MGEMM in leveraging these large numbers of legacy cards to overcome their lack of RAM and double-precision arithmetic. We are, therefore, optimistic overall about the role MGEMM can play in helping to accelerate computations using GPUs in the near future.

References

(1) Almlöf, J.; Taylor, P. R. In *Advanced Theories and Computational Approaches to the Electronic Structure of Molecules*; Dykstra, C., Ed.; D. Reidel: Dordrecht, 1984.

(2) *CUDA Programming Guide*; NVIDIA: Santa Clara, CA; http://developer.download.nvidia.com/compute/cuda/2_0/docs/NVIDIA_CUDA_Programming_Guide_2.0.pdf. Accessed September 30, 2009.

(3) Kapasi, U. J.; Rixner, S.; Dally, W. J.; Khailany, B.; Ahn, J. H.; Mattson, P.; Owens, J. D. *Computer* **2003**, *36*, 54.

(4) Krakiwsky, S. E.; Turner, L. E.; Okoniewski, M. M. Graphics processor unit (GPU) acceleration of finite-difference time-domain (FDTD) algorithm. *ISCAS* **2004**, (5), 265.

(5) Hamada, T.; Iitaka, T. The Chamomile Scheme: An Optimized Algorithm for N-body simulations on Programmable Graphics Processing Units. 2007, arXiv:astroph/073100.arXiv.org e-Print archive. http://arxiv.org/abs/astro-ph/0703100 (accessed Dec. 7, 2009).

(6) Stone, J. E.; Phillips, J. C.; Freddolino, P. L.; Hardy, D. J.; Trabuco, L. G.; Schulten, K. *J. Comput. Chem.* **2007**, *28*, 2618.

(7) Anderson, J. A.; Lorenz, C. D.; Travesset, A. *J. Comput. Phys.* **2008**, *227*, 5342.

(8) Anderson, A. G.; Goddard-III, W. A.; Schröder, P. *Comput. Phys. Commun.* **2007**, *177*, 298.

(9) Yasuda, K. *J. Comput. Chem.* **2008**, *29*, 334.

(10) Yasuda, K. *J. Chem. Theory Comput.* **2008**, *4*, 1230.

(11) Ufimtsev, I. S.; Martinez, T. J. *J. Chem. Theory Comput.* **2008**, *4*, 222.

(12) Ufimtsev, I. S.; Martinez, T. J. *Comput. Sci. Eng.* **2008**, *10*, 26.

(13) Ufimtsev, I. S.; Martinez, T. J. *J. Chem. Theory Comput.* **2009**, *5*, 1004.

(14) Ufimtsev, I. S.; Martinez, T. J. *J. Chem. Theory Comput.* **2009**, *5*, 2619.

(15) Vogt, L.; Olivares-Amaya, R.; Kermes, S.; Shao, Y.; Amador-Bedolla, C.; Aspuru-Guzik, A. *J. Phys. Chem. A* **2008**, *112*, 2049.

(16) Brown, P.; Woods, C.; McIntosh-Smith, S.; Manby, F. R. *J. Chem. Theory Comput.* **2008**, *4*, 1620.

(17) Feyereisen, M.; Fitzgerald, G.; Komornicki, A. *Chem. Phys. Lett.* **1993**, *208*, 359.

(18) Weigend, F.; Häser, M.; Patzelt, H.; Ahlrichs, R. *Chem. Phys. Lett.* **1998**, *294*, 143.

(19) Werner, H. J.; Manby, F. R. *J. Chem. Phys.* **2006**, *124*, 054114.

(20) Maschio, L.; Usvyat, D.; Manby, F. R.; Casassa, S.; Pisani, C.; Schültz, M. *Phys. Rev. B: Condens. Matter* **2007**, *76*, 075101.

(21) Frenking, G.; Antes, I.; Böhme, M.; Dapprich, S.; Ehlers, A. W.; Jonas, V.; Neuhaus, A.; Otto, M.; Stegmann, R.; Veldkamp, A.; Vyboishchikov, S. F. In *Reviews in Computational Chemistry*, Vol. 8; Lipkowitz, K. B., Boyd, D. B., Eds.; VCH: New York, 1996.

(22) Weigend, F.; Köhn, A.; Hättig, C. *J. Chem. Phys.* **2002**, *116*, 3175.

(23) Shao, Y. *Phys. Chem. Chem. Phys.* **2006**, *8*, 3172.

(24) *CUBLAS Library 1.0*; NVIDIA: Santa Clara, CA; http://developer.download.nvidia.com/compute/cuda/1_0/CUBLAS_Library_1.0.pdf. Accessed September 30, 2009.

(25) Bohannon, J. *Science* **2005**, *308*, 310.

(26) *Clean Energy Project*; Harvard University: Cambridge, MA; http://cleanenergy.harvard.edu. Accessed September 30, 2009.

(27) Dunning, T., Jr. *J. Chem. Phys.* **1989**, *90*, 1007.

(28) *SciGPU-GEMM* , *v0.8*; sciGPU.org, Harvard University: Cambridge, MA; http://scigpu.org/content/scigpu-gemm-v08-release. Accessed September 30, 2009.

JCTC Journal of Chemical Theory and Computation

Fisher Information Study in Position and Momentum Spaces for Elementary Chemical Reactions

Sheila López-Rosa,[†,‡] Rodolfo O. Esquivel,*[,‡,§] Juan Carlos Angulo,[†,‡] Juan Antolín,[‡,||]
Jesús S. Dehesa,[†,‡] and Nelson Flores-Gallegos[§]

*Departamento de Física Atómica, Molecular y Nuclear, Universidad de Granada,
18071-Granada, Spain, Instituto Carlos I de Física Teórica y Computacional,
Universidad de Granada, 18071-Granada, Spain, Departamento de Química,
Universidad Autónoma Metropolitana, 09340-México D.F., México, and Departamento
de Física Aplicada, EUITIZ, Universidad de Zaragoza, 50018-Zaragoza, Spain*

Abstract: The utility of the Fisher information measure is analyzed to detect the transition state, the stationary points of a chemical reaction, and the bond breaking/forming regions of elementary reactions such as the simplest hydrogen abstraction and the identity S_N2 exchange ones. This is performed by following the intrinsic reaction path calculated at the MP2 and QCISD(T) levels of theory with a 6-311++G(3df, 2p) basis set. Selected descriptors of both position and momentum space densities are utilized to support the observations, such as the molecular electrostatic potential (MEP), the hardness, the dipole moment, along with geometrical parameters. Our results support the concept of a continuum of transient of Zewail and Polanyi for the transition state rather than a single state, which is also in agreement with reaction force analyses.

Introduction

Notwithstanding that Fisher information of a probability distribution was introduced in the 1920s,[1] its utility for the informational description of relevant physical and chemical systems and/or processes, such as atoms,[2,3] molecules,[4] ionization,[5] and reactions, among many others, has been assessed until recently. Its appealing features differ appreciably from other information measures because of its "local" character,[6] in contrast with the "global" nature of several functionals, such as the variance or the Shannon, Tsallis, and Renyi entropies.

The local character of Fisher information provokes an enhanced sensitivity to strong changes, even over a very small-sized region in the domain of definition, because of its definition as a functional of the distribution gradient, as

will be described below. This is not the case for the global information measures (e.g., Shannon entropy, disequilibrium, variance),[7] whose values are conditioned by the behavior of the density over the whole domain and display much lower variations as a consequence of the strongly localized changes on its values.

Aside from the relevance of the Fisher information itself for the interpretation of different physical and chemical phenomena within an information-theoretical framework, mainly for one-particle densities in conjugated spaces for many-electron systems (e.g., atoms and molecules) and processes (e.g., ionization dissociation or reactions), among others, it is also a component of different complexity measures,[8] a concept that nowadays constitutes a hot topic for study as a tool for the informational analysis of the aforementioned systems and processes. Different complexities include in their definition the Fisher information as an essential ingredient to quantify the level of localization or organization for the considered distribution. Such is the case, for instance, of the recently introduced "Fisher−Shannon"[3] and "Cramer−Rao"[8] complexities, where information on randomness or uncertainty is provided, respectively, by the

---

* Corresponding author e-mail: esquivel@xanum.uam.mx.

† Departamento de Física Atómica, Universidad de Granada.

‡ Instituto Carlos I de Física Teórica y Computacional, Universidad de Granada.

§ Universidad Autónoma Metropolitana.

|| Universidad de Zaragoza.

Shannon entropy and the variance. Exhaustive recent studies of these complexities for atomic systems can be found in ref 9.

Moreover, the concept of Fisher information for a given distribution has given rise to the introduction of information functionals with the aim of establishing a comparative measure between two different densities retaining the aforementioned local character of the quantifier for performing such a comparison. Such is the case of the initially defined "relative Fisher information",[10] following a procedure similar to that done in the Shannon case for defining the so-called "Kullback−Leibler" relative entropy,[11] and later by symmetrizing the relative Fisher information, with the aim of being interpreted as a distance between distributions, resulting in a measure known as "Fisher Divergence",[12] in a similar way as the "Jensen−Shannon Divergence"[13] arises from the Shannon entropy. Most applications of the Fisher Divergence regard the comparison of a relevant density describing a given system with an a priori one, usually chosen according to a simplified model or by considering specifically known properties of the system under study, by imposing them on the reference or a priori one.

Theoretical chemistry has witnessed a great deal of research to study the energetics of chemical reactions.[14] For instance, a variety of calculations of potential energy surfaces have been performed at various levels of sophistication.[15] Within the broad scope of these investigations, particular interest has been focused on extracting information about the stationary points of the energy surface. Despite the fact that minima, maxima, and saddle points are useful mathematical features of the energy surface to reaction-path following,[16] it has been difficult to attribute too much chemical or physical meaning to these critical points.[17] Whereas the reaction rate and the reaction barrier are chemical concepts, which have been rigorously defined and experimentally studied since the early days of the transition state (TS) theory,[18] the structure of the TS remains as a quest of physical organic chemistry. Understanding the TS is a fundamental goal of chemical reactivity theories, which implies the knowledge of the chemical events that take place to better understand the kinetics and the dynamics of a reaction. On the other hand, a variety of density descriptors have been employed to study chemical reactions.[18,19] Among them, it is worthy to mention the reaction force studies on the potential energy of reactions, which have been employed to characterize changes in the structural and/or electronic properties in chemical reactions.[20,21] However, to the best of our knowledge, none of them has been able to conceptually describe the reaction mechanism of elementary reactions in a simple and direct fashion.

In past years, there has been an increasing interest to analyze the electronic structure of atoms and molecules by applying information theory (IT).[22] These works have shown that information-theoretic measures are capable of providing simple pictorial chemical descriptions of atoms and molecules and the processes they exert through the localized/delocalized behavior of the electron densities in position and momentum spaces. In a recent study,[23] we have provided evidence that supports the utility of the information-theoretic

measures in position and momentum spaces to detect the transition state and the stationary points of elementary chemical reactions so as to reveal the bond breaking/forming regions of the simplest hydrogen abstraction and the identity of S_N2 exchange chemical processes.

To the best of our knowledge, no studies have been reported on the application of Fisher information on chemical reactions. The goal of the present study is to follow the IRC (internal reaction coordinate) path of some selected elementary chemical reactions to analyze the course of the reactions by use of the Fisher information in position and momentum spaces as well as other charge density descriptors such as the molecular electrostatic potential (MEP) along with some reactivity parameters of DFT, the hardness "η", and softness "S", so as to witness the density changes exerted by the molecular structures during the chemical process. Two elemental reactions were chosen: the chemical probes under study are the simplest hydrogen abstraction reaction $H^{\bullet} + H_2 \rightarrow H_2 + H^{\bullet}$ and the identity S_N2 reaction $H^- + CH_4 \rightarrow CH_4 + H^-$.

Theoretical Details

The central quantities under study are the Fisher information

$$I_r = \int \frac{|\vec{\nabla}\rho(\vec{r})|^2}{\rho(\vec{r})} \mathrm{d}^3 r \qquad (1)$$

in position space and

$$I_p = \int \frac{|\vec{\nabla}\gamma(\vec{p})|^2}{\gamma(\vec{p})} \mathrm{d}^3 p \qquad (2)$$

in momentum space, where $\rho(\vec{r})$ and $\gamma(\vec{p})$ denote the normalize-to-unity electron density distributions in the position and momentum spaces, respectively. The total electron density of a molecule, in the independent particle approximation, consists of a sum of contributions from electrons in occupied orbitals. Thus, in momentum space, the contribution from an electron in a molecular orbital $\varphi_i(\vec{p})$ to the total electron density is given by $|\varphi_i(\vec{p})|^2$. The orbitals $\varphi_i(\vec{p})$ are then related by Fourier transforms to the corresponding orbitals in position space $\phi_i(\vec{r})$. Standard procedures for the Fourier transformation of position space orbitals generated by ab initio methods have been described.[24] The orbitals employed in ab initio methods are linear combinations of atomic basis functions, and because analytic expressions are known for the Fourier transforms of such basis fuctions,[25] the transformations of the total molecular electronic wave function from position to momentum space are computationally straightforward.[26]

The position Fisher information, which is closely connected to the kinetic energy,[27] is a spreading measure of the electron density all over the space with a locality property because it is a function of its gradient. In contrast with the Shannon entropy (which is a global spreading measure), it measures the spatial pointwise concentration of the electronic probability cloud and quantifies the gradient content of the electron distribution, so revealing the irregularities of the density and providing a quantitative estimation of its (strong) oscillatory character. Next, it is very sensitive to the

Fisher Information Study in Position and Momentum Spaces

J. Chem. Theory Comput., Vol. 6, No. 1, 2010 **147**

electronic fluctuations so that it allows us to explore the changes of the electronic distributions in an accurate manner. A similar interpretation follows for the momentum Fisher information. Moreover, the position and momentum Fisher information are reciprocal measures that satisfy the uncertainty relation $I_r I_p \geq 4D^2$ for D-dimensional quantum systems.[28] So, for three-dimensional systems, they fulfill the inequality $I_r I_p \geq 36$.

In recent studies, we have assessed the utility of employing other chemical descriptors to interpret information-theoretic measures. In this study, we find it interesting to use the MEP, the hardness, geometrical parameters, dipole moment, and vibrational frequencies.

The MEP represents the molecular potential energy of a proton at a particular location near a molecule,[29] say at nucleus A. The electrostatic potential, V_A, is then defined as

$$V_A = \left(\frac{\partial E^{\text{molecule}}}{\partial Z_A} \right)_{N, Z_{B \neq A}} = \sum_{B \neq A} \frac{Z_B}{|R_B - R_A|} - \int \frac{\rho(\vec{r}) \, d\vec{r}}{|\vec{r} - R_A|} \tag{3}$$

where $\rho(\vec{r})$ is the molecular electron density and Z_A is the charge on nucleus A, located at R_A. Generally speaking, negative electrostatic potential corresponds to an attraction of the proton by the concentrated electron density in the molecules from lone pairs, π-bonds, etc. (colored in shades of red in contour diagrams). Positive electrostatic potential corresponds to a repulsion of the proton by the atomic nuclei in regions where low electron density exists and the nuclear charge is incompletely shielded (colored in shades of blue in contour diagrams).

We have also evaluated some reactivity parameters that may be useful to analyze the chemical reactivity of the processes. Parr and Pearson proposed a quantitative definition of hardness (η) within conceptual DFT:[30]

$$\eta = \frac{1}{2S} = \frac{1}{2} \left(\frac{\partial \mu}{\partial N} \right)_{v(\vec{r})} \quad \text{where} \quad \mu = \left(\frac{\partial E}{\partial N} \right)_{v(\vec{r})} \tag{4}$$

is the electronic chemical potential of an N electron system in the presence of an external potential $v(\vec{r})$, E is the total energy, and "S" is called the softness. Using finite difference approximation, eq 4 would be

$$\eta = \frac{1}{2S} \equiv (E_{N+1} - 2E_N + E_{N-1})/2 = (I - A)/2 \tag{5}$$

where E_N, E_{N-1}, and E_{N+1} are the energies of the neutral, cationic, and anionic systems; and I and A are the ionization potential (IP) and electron affinity (EA), respectively. Applying Koopmans' theorem,[31] eq 4 can be written as:

$$\eta = \frac{1}{2S} \equiv \frac{\varepsilon_{\text{LUMO}} - \varepsilon_{\text{HOMO}}}{2} \tag{6}$$

where ε denotes the frontier molecular orbital energies. In general terms, hardness and softness are good descriptors of chemical reactivity; the former measures the global stability of the molecule (larger values of η means less reactive molecules), whereas the S index quantifies the polarizability of the molecule.[32] Thus, soft molecules are more polarizable and possess predisposition to acquire

additional electronic charge.[33] The chemical hardness "η" is a central quantity for use in the study of reactivity and stability, through the hard and soft acids and bases principle.[34]

Results and Discussion

The electronic structure calculations performed in this study were carried out with the Gaussian 03 suite of programs.[35] Reported TS geometrical parameters for the abstraction,[36] and the S_N2 exchange,[37] reactions were employed. Calculations for the IRC were performed at the MP2 (UMP2 for the abstraction reaction) level of theory with at least 35 points for each one of the directions (forward/reverse) of the IRC. Next, a high level of theory and a well-balanced basis set (diffuse and polarized orbitals) were chosen for determining all of the properties for the chemical structures corresponding to the IRC. Thus, the QCISD(T) method was employed in addition to the 6-311++G** basis set, unless otherwise stated. The hardness and softness chemical parameters were calculated by use of eqs 5 and 6 and the standard hybrid B*3*LYP (UB3LYP for the abstraction reaction) functional.[35] Molecular frequencies corresponding to the normal modes of vibration depend on the roots of the eigenvalues of the Hessian (its matrix elements are associated with force constants) at the nuclei positions of the stationary points. We have found it illustrative to calculate these values for the normal mode associated with the TS (possessing one imaginary frequency or negative force constant), which were determined analytically for all points of the IRC path at the MP2 (UMP2 for the abstraction reaction) level of theory.[35] The molecular Fisher information in position and momentum spaces for the IRC was obtained in this study by employing software developed in our laboratory along with 3D numerical integration routines[38] and the DGRID suite of programs.[26] The bond breaking/forming regions along with electrophilic/nucleophilic atomic regions were calculated through the MEP by use of MOLDEN.[39] Atomic units are employed throughout the study except for the dipole moment (debye), vibration frequencies (cm^{-1}), and geometrical parameters (angstroms).

Abstraction Reaction. The reaction $H_a^{\bullet} + H_2 \rightarrow H_2 + H_b^{\bullet}$ is the simplest radical abstraction reaction involving a free radical (atomic hydrogen) as a reactive intermediate. This kind of reaction involves at least two steps (S_N1 reaction type): in the first step, a new radical (atomic hydrogen in this case) is created by homolysis, and in the second one the new radical recombines with another radical species. Such homolytic bond cleavage occurs when the bond involved is not polar and there is no electrophile or nucleophile at hand to promote heterolytic patterns. When the bond is made, the product has a lower energy than the reactants, and it follows that breaking the bond requires energy.

Our calculations for this reaction were performed at two different levels: the IRC was obtained at the UMP2/6-311G level, and all properties at the IRC were obtained at the QCISD(T)/6-311++G** level of theory. As a result of the IRC, 72 points evenly distributed between the forward and
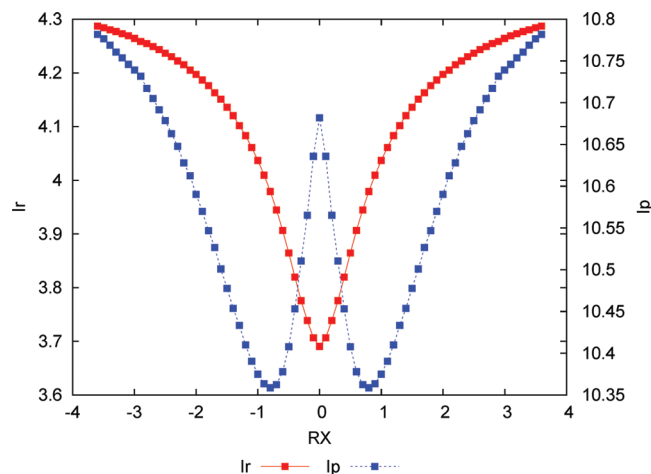
Figure 1. Fisher entropies in position (red line) and momentum (blue line) spaces for the IRC of $H_a^\bullet + H_2 \rightarrow H_2 + H_b^\bullet$.
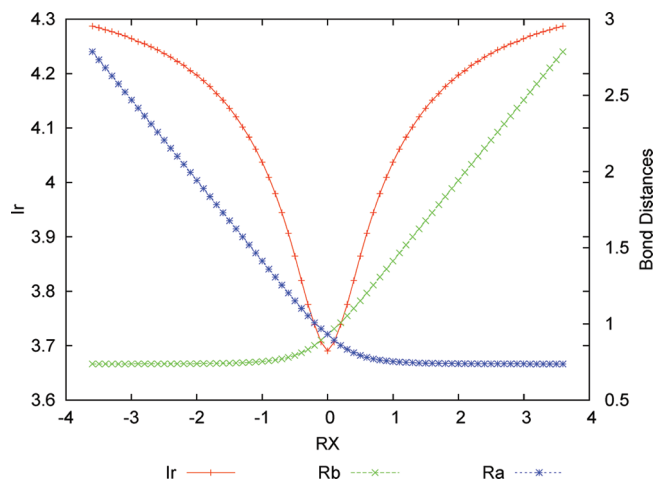

Figure 2. Fisher information in momentum space (red line) and the bond distances $R_a \equiv R(H_a-H)$ (blue line for the entering hydrogen) and $R_b \equiv R(H-H_b)$ (green line for the leaving hydrogen) for the IRC of $H_a^\bullet + H_2 \rightarrow H_2 + H_b^\bullet$.

reverse directions of the IRC were obtained. A relative tolerance of 1.0×10^{-5} was set for the numerical integrations.[38]

In Figure 1 is depicted the Fisher information in both position and momentum spaces. At a first glance, we observe that both quantities behave in a similar way toward the reactive complexes ($H_a^\bullet \cdots H-H$ and $H-H \cdots H_b^\bullet$) and tend to decrease toward the TS region, but with a very important difference that we analyze below. It is worth mentioning that, according to a previous study,[23] we have insight into the structural features of the distributions in both spaces, that is, concerning the spreading (localization/delocalization) of the densities. However, the behavior of the densities about their local changes (uniformity/irregularity) can only be provided by a local measure such as the Fisher information.

Both position and momentum Fisher information measures possess more structure at the vicinity of the TS as it may be observed from Figure 1. It is worthy to remark that this phenomenon is not present in the energy profile. By closer inspection, we note that the Fisher information I_r possesses a global minima at the TS, whereas the momentum one, I_p, possesses a local maxima and two local minimum at the vicinity of the TS (approximately $R_X \simeq 0.9$). This is interesting on chemical grounds because the structure observed for the Fisher information in momentum space at the vicinity of the TS can be associated with a process of bond breaking/forming (depending on the reaction direction) followed by stabilization of the structure at the TS.[23]

The chemical picture proceeds in this way: as the intermediate radical (H_a) approaches the molecule at the TS region, the molecular density exerts important changes so as to undergo the homolysis. This represents a physical situation where the density in position space gets localized in preparation for the bond rupture, which in turn results in a local increase of the kinetic energy. This provides explanation for the well-known fact that bond breaking requires energy. Next, the bond is formed, and, as a consequence, the TS structure shows lower kinetic energy than the reactant/product complex (H_a or H_b). Interestingly, from an information-theoretical point of view, all of the above happens: both I_r and I_p decrease as the radical intermediate approaches the

molecule at the TS region, which means that the gradient of the density distributions (in both spaces) becomes smaller; that is, these densities are less irregular and more uniform. For the position space the Fisher information reaches a minimum at the TS; that is, at this point the position space density is the most uniform and delocalized (structurally less distorted with low kinetic energy and null dipole moment, see below) among all other structures at the vicinity of the TS. In momentum space, the Fisher information shows minima at the vicinity of the TS ($R_X \simeq |0.9|$) corresponding to a delocalized and uniform momentum density. It is worth noting that it is at these minima where the processes of bond breaking/forming occur.[23] At the TS, the Fisher information, I_p, is maximum corresponding with the least uniform and the highest localized momentum density with respect to the structures in its neighborhood. It is interesting to mention that minima of the Fisher information in momentum space coincide with the BCER (bond cleavage energy reservoir) defined in ref 23, and hence they might be characterized by the Fisher measure in momentum space.

To better understand the shape of the Fisher information, in Figure 2 are plotted the bond distances between the entering/leaving hydrogen radicals and the central hydrogen atom. This clearly shows that in the vicinity of the TS a bond breaking/forming chemical situation is occurring because the $R_b \equiv R(H-H_b)$ is elongating at the right side of the TS and the $R_a \equiv R(H_a-H)$ is stretching at the left side of the TS. It is worth noting that the chemical process does not happen in a synchronous manner; that is, the homolytic bond breaking occurs first, and then the molecule stabilizes by forming the TS structure, which is clearly observed in Figure 2. As the incoming radical approaches the molecule, the bond breaks. Because the Fisher information represents the gradient of a probability distribution, it is natural to associate this with the change in the corresponding density. Therefore, from Figure 2, one can see that as the incoming hydrogen approaches, the bond enlarges in the region where the Fisher information in momentum space increases more rapidly. In contrast, the Fisher information in position space is not describing the bond breaking/forming process.
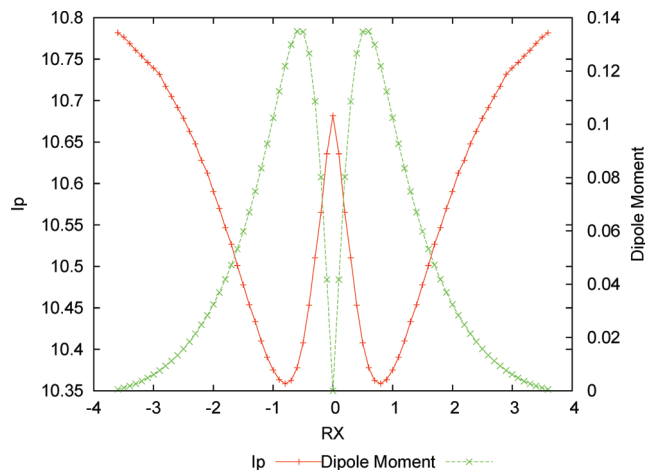
Figure 3. Fisher information in momentum space (red line) and the dipole moment values (green line) for the IRC of $H_a^{\bullet}$ + $H_2 \rightarrow H_2 + H_b^{\bullet}$.

Figure 4. Fisher information in momentum space (red line) and the eigenvalues of the Hessian (green line) for the IRC of $H_a^{\bullet} + H_2 \rightarrow H_2 + H_b^{\bullet}$. It should be noted that negative values actually correspond with imaginary numbers (roots of negative force constants) so that the negative sign only represents a flag.

Next, we would like to test the nonpolar bond pattern characteristic of homolytic bond breaking reactions, which should be reflected through the dipole moment of the molecules at the IRC. This is indeed observed in Figure 3, where these values along with the ones of the momentum Fisher information are depicted for comparison purposes. At the TS the dipole moment is zero, and the same behavior is observed as the process tends to the reactants/products in the IRC, reflecting the nonpolar behavior of the molecule in these regions. However, it is also interesting to observe, from this property, how the molecular densities get distorted, reaching maximal values at the vicinity of the TS. In contrast, the behavior of the momentum Fisher information is totally opposite: this quantity decreases (increases) when the dipole moment increases (decreases), being minimum (maximum) approximately at the same points that the dipole moment reaches its maximum (minimum) value. It means that in the regions where the molecule has a nonpolar behavior, the momentum electronic density has a higher gradient content corresponding to a high irregular and localized density.

In Figure 4 are depicted the eigenvalues of the Hessian for the normal mode associated with the TS along the IRC of the reaction, along with the momentum Fisher information values. The Hessian values represent the transition vector "frequencies", which show maxima at the vicinity of the TS and a minimal value at the TS. Several features are worth mentioning: the TS corresponds indeed to a saddle point, and maxima at the Hessian correspond to high kinetic energy values (largest "frequencies" for the energy cleavage reservoirs correspond to the BCER[23]). In contrast, at the TS, the Hessian reaches a minimum value; this means that in this point the kinetic energy is the lowest one (minimal molecular frequency),[23] and, as we can see, it corresponds to a maximal Fisher information in momentum space. So it seems viable that I_p resembles the behavior of the TS vector. In connection with the Fisher information also depicted in Figure 4, it is interesting to note that in the transition state region (where the frequencies become imaginary[23,40]) the Fisher information exerts its largest change as a gradient of the distribution in momentum space.
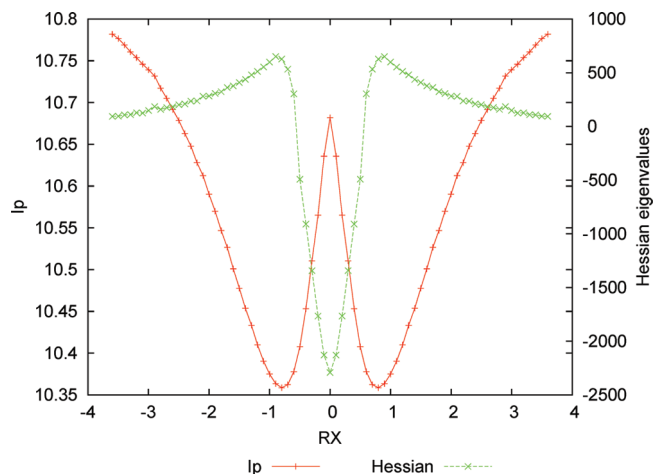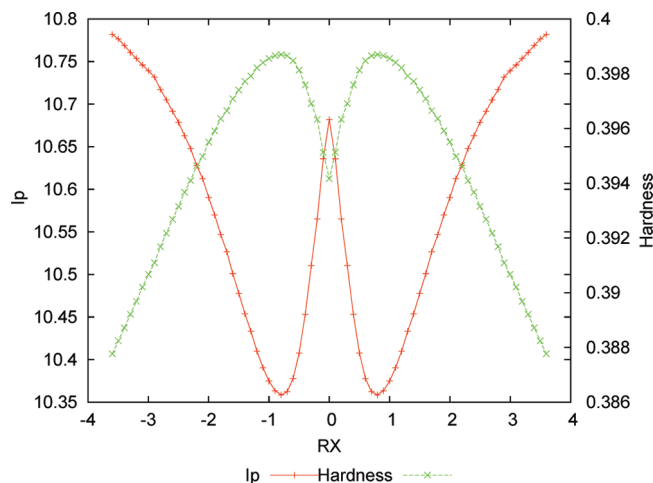

Figure 5. Fisher information in momentum space (red line) and the hardness values (green line) for the IRC of $H_a^{\bullet} + H_2 \rightarrow H_2 + H_b^{\bullet}$.

There are several density descriptors used in chemistry to determine the reactivity behavior such as the hardness and softness (see the previous section). In Figure 5 we have plotted the values for the hardness along with the Fisher information in momentum space for comparison purposes. From a DFT conceptual point of view, we may interpret Figure 5 as that chemical structures at the maximal hardness (minimal softness) values possess low polarizability and hence are less prone to acquire additional charge (less reactive). These regions correspond to minimal Fisher information regions in momentum space associated with a highly uniform momentum density. According to considerations discussed above, these structures are found at the defined (in a previous work[23]) BCER regions; that is, they are maximally distorted, with highly delocalized momentum densities (maximal dipole moment values; see Figure 3). In contrast, hardness values are minimal at the reactant complexes regions, which correspond with localized momentum densities[23] with null dipole moments, and hence they are
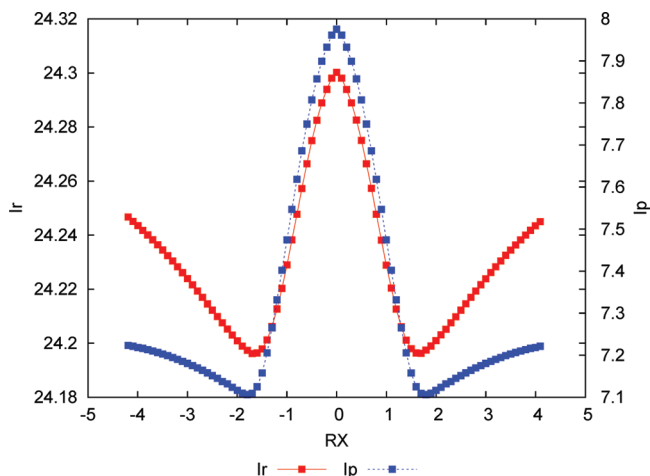
Figure 6. Fisher information in position (red line) and momentum (blue line) spaces for the IRC of $H_a^- + CH_4 \rightarrow CH_4 + H_b^-$.

more prone to react (more reactive). At the TS, a local minimum for the hardness may be observed; then it is locally more reactive and leaning to acquire charge because its dipole moment is null.

From the point of view of Fisher information, the TS represents a more irregular distribution. It is interesting to note that the I_r in Figure 1 can only be associated with the hardness at the TS (Figure 5), in that more reactive structures correspond to the most uniform density in position space.

Nucleophilic Substitution Reaction. In this part of the work, we analyze a typical nucleophilic substitution (S_N2) reaction whose chemical process involves only one step in contrast with the abstraction reaction studied before, which involves two steps. In the anionic form, the S_N2 mechanism can be depicted as

$$Y^- + RX \rightarrow RY + X^- \qquad (7)$$
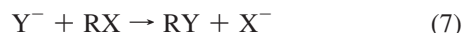
which is characterized by being kinetically of second order (first order in each of the reactants: the nucleophile Y^- and the substrate R_X, where X^- is the nucleofuge or leaving atom). For identity S_N2 reactions, $X = Y$. It was postulated that the observed second-order kinetics is the result of passage through the well-known Walden inversion transition state where the nucleophile displaces the nucleofuge (leaving group) from the backside in a single concerted reaction step.

The $H_a^- + CH_4 \rightarrow CH_4 + H_b^-$ represents the typical identity S_N2 reaction, and we proceed with the calculations as follows: because diffuse functions are important to adequately represent anionic species,[20] we have performed calculations for the IRC at the MP2/6-311++G** level of theory, which generated 93 points evenly distributed between the forward and reverse directions of the IRC. Next, Fisher information in both position and momentum spaces and geometrical parameters at the IRC were calculated at the QCISD(T)/6-311++G** level of theory, which has been reported to be adequate for this kind of reaction.[41] A relative tolerance of 1.0×10^{-5} was set for the numerical integrations.[38]

If we represent both Fisher informations, I_r and I_p, in the same picture, Figure 6, we can observe that they show a

similar structure, both possessing a maximum at the TS and minimal regions at its vicinity. This behavior is significantly different from the abstraction reaction analyzed before in that the position Fisher information shows the opposite behavior as compared to the momentum Fisher information at the TS region.

From a previous study[23] with Shannon entropies, we found a delocalized position density and a localized momentum density in the TS region, that is, corresponding with a chemically relaxed structure (structurally less distorted with low kinetic energy and null dipole moment, see below). In contrast, the reactive complexes toward reactants/products show more localized densities with less delocalized momentum densities; that is, the chemical structures at these regions are structurally distorted and possess more kinetic energy as compared to the TS. In the vicinity of the TS, at around $R_X \simeq |1.7|$, critical points for these measures are observed; they correspond to ionic complexes that characterize position densities, which are highly localized and with highly delocalized momentum densities and high kinetic energies. At a first glance, it seems likely that these regions correspond with BCER[23] where bond breaking may start occurring.

One of the principal differences between the S_N2 reaction with respect to the abstraction one is that for the former the course of the reaction occurs by an heterolytic rupture with an exchange of charge, whereas for the latter the mechanism is homolytic; that is, a spin coupling process occurs. In this reaction, as the incoming hydrogen approaches the molecule, it transfers charge, through the carbon bonding, to the leaving hydrogen so as to reach an equally charged distribution among the incoming/leaving hydrogens. As this process evolves, the gradient of the distribution involved in the position Fisher information I_r increases so as to reach a maximum at the TS.

To further support the charge transfer process mentioned above, we can witness the heterolytic bond/breaking process through the contour values of the MEP at several stages of the S_N2 reaction in the plane of the $[H_a \cdots C \cdots H_b]^-$ atoms. We may observe from Figure 7a the initial step of the bond breaking process for the leaving hydrogen (nucleofuge) at $R_X = -1.5$ (forward direction), by noting that this particular atom is losing bonding charge as it leaves (in the region where the potential is positive). This is in contrast with the entering hydrogen, which possesses the nucleophilic power of an hydride ion (in the region where the potential is negative). It is also interesting to note that the remaining attached hydrogen atoms possess the expected electrophilic nature of the molecular bonding environment, although its "philic" nature barely changes. In Figure 7b at $R_X = -0.9$ in the forward direction of the reaction, the $C-H_b$ bond cleavage is about to complete as the H_b atom has lost bonding charge (maximum electrophilic power) and the nucleophilic hydrogen is about to form a new bond by losing charge (nucleophilic power). In Figure 7c, we have depicted the MEP at the TS where we can observe the point where the gradient of the position density reaches its maximum due to the charge becoming equalized according to Figure 6.

To analyze in detail this reaction, we find it instructive to plot the distances between the nucleophilic hydrogen (H_a)
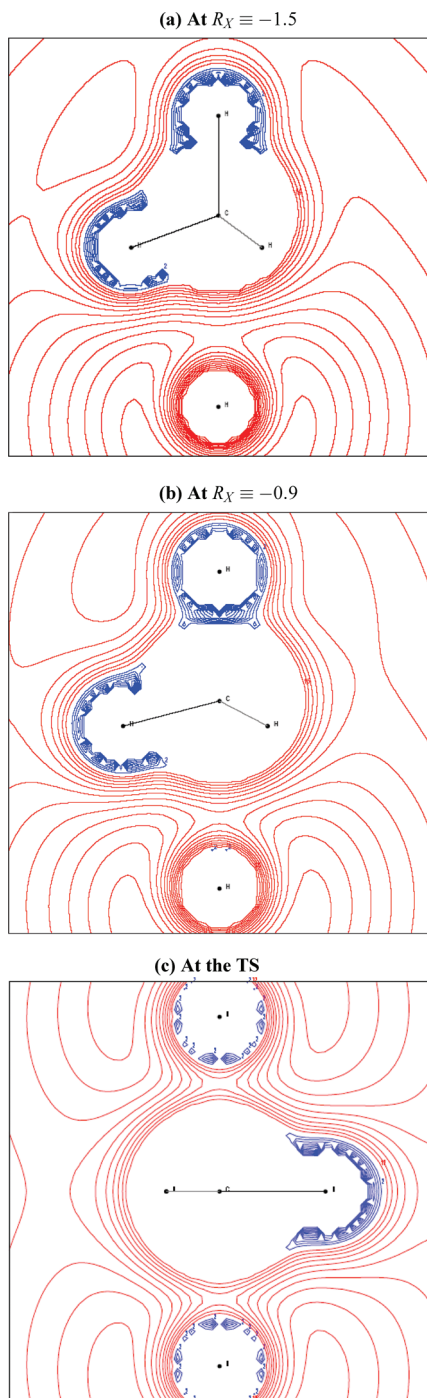
(a) At $R_X \equiv -1.5$

(b) At $R_X \equiv -0.9$

(c) At the TS

Figure 7. The MEP contour lines in the plane of $[H_a\cdots C\cdots H_b]^-$ (H_a stands for the nucleophilic atom and H_b is the nucleofuge, on bottom and top, respectively) showing nucleophilic regions (blue contour lines) and electrophilic regions (red contour lines) at several reaction coordinates for the S_N2 reaction at (a) $R_X = -1.5$, (b) $R_X = -0.9$, and (c) the TS.

Figure 8. Fisher entropy in momentum space (red line) and the bond distances $R_a \equiv R(H_a-C)$ (green line, where H_a stands for the nucleophile) and $R_b \equiv R(C-H_b)$ (blue line, where H_b stands for the nucleofuge) for the IRC of $H_a^- + CH_4 \rightarrow CH_4 + H_b^-$.

Figure 9. Fisher information in momentum space (red line) and the internal angle $H_a^-\cdots C-H$ (green line, where H_a stands for the nucleophile and H stands for any hydrogen attached to the methyl molecule) in degrees for the IRC of $H_a^- + CH_4 \rightarrow CH_4 + H_b^-$.

and the leaving hydrogen (H_b) in Figure 8. Distances show the stretching/elongating features associated with the bond forming/breaking situation that we have anticipated before. In contrast with the previous analyzed abstraction reaction, the S_N2 reaction occurs in a concerted and synchronous manner; that is, the bond breaking/forming occurs at unison. An interesting feature that might be observed from Figure 8 is that, whereas the elongation of the carbon–nucleofuge
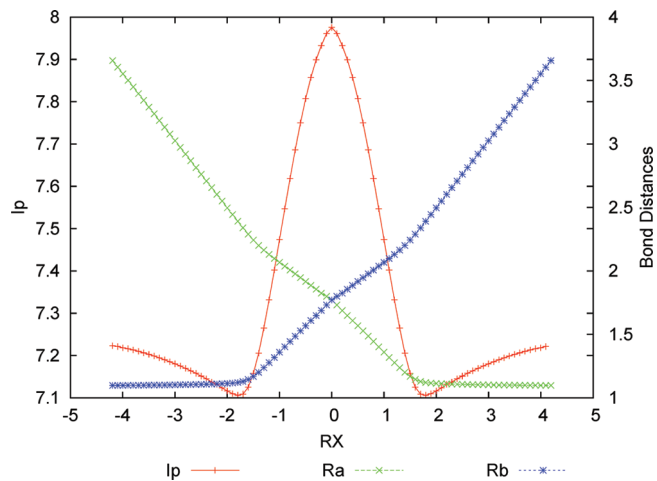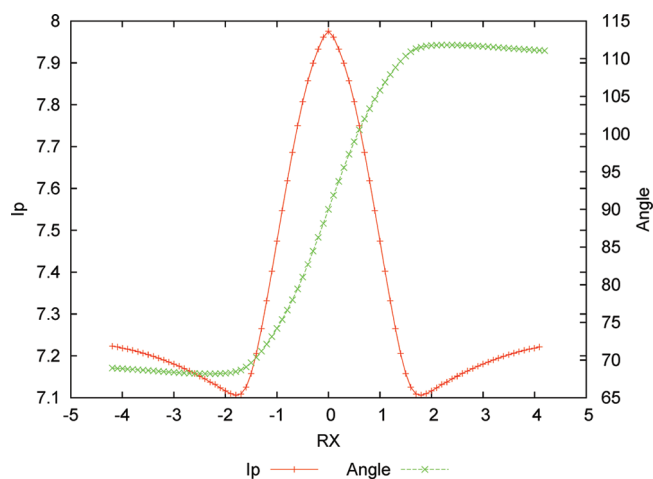
bond (R_b) changes its curvature significantly at $R_X \simeq -1.7$ (forward direction of the reaction), the stretching of the nucleophile–carbon bond does it in a smooth way, due to the repulsive forces that the ionic molecule exerts as the nucleophile approaches, which provokes the breaking of the carbon–nucleofuge to happen as the molecule starts liberating its kinetic energy. In this sense is that the reaction occurs in a concerted manner; that is, the bond breaking/dissipating energy processes occur simultaneously. It is interesting to note that minima for the momentum Fisher information coincide with the bond breaking/forming regions and that the change in the curvature of the bond distances marks the region where the gradient of the density in momentum space starts increasing.

In Figure 9, we have plotted the internal angle between $H_a^-\cdots C-H$ along with the Fisher information in momentum space for comparison purposes. Thus, the internal angle shows clearly that the molecule starts exerting the so-called
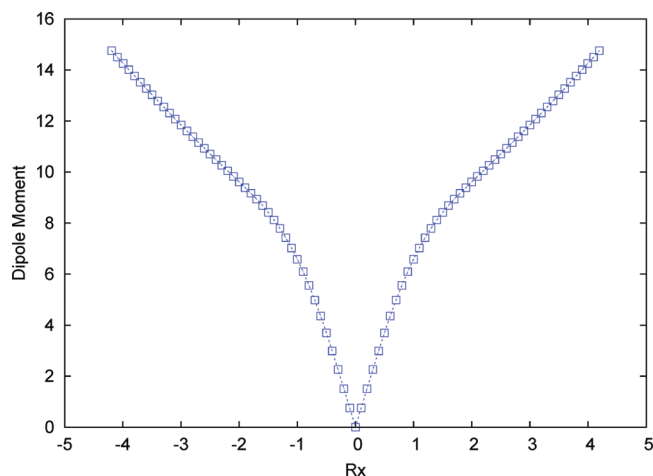
Figure 10. Dipole moment for the IRC of $H_a^- + CH_4 \rightarrow CH_4 + H_b^-$.

"inversion of configuration" at around $R_X \simeq -1.7$, where the nucleophile starts displacing the nucleofuge from the backside of the molecule in a single concerted reaction step. This starts occurring at the BCER regions.[23] We may observe from the figure that I_p possesses two minimum values that coincide with the inflection points of the angle, so marking the regions where the inversion of configuration occurs, that is, the region where the gradient increases and the momentum density distribution becomes less irregular.

The S_N2 reaction is a good probe to test the polar bond pattern characteristic of heterolytic bond breaking (with residual ionic attraction because of the ionic nature of the products), which should be reflected through the dipole moment of the molecules at the IRC. This is indeed observed in Figure 10, where these values along with the ones of the Fisher momentum information are depicted for comparison purposes. At the TS, the dipole moment is zero, showing the nonpolar character of the TS structure with both nucleophile/nucleofuge atoms repelling each other evenly through its carbon bonding. As the ionic complexes approach the reactants/products regions, the dipole moment increases monotonically, reflecting the polar bonding character of these ionic molecules with a significant change of curvature at the TS vicinity at around $R_X \simeq |1.0|$ (a change of curvature was already noted for Fisher information in momentum space at the same region). In going from reactants to products, it is evident that the inversion of the dipole moment values reflects clearly the inversion of configuration of the molecule (this reaction starts and ends with a tetrahedral sp^3 carbon in the methyl molecule passing through a trigonal bipyramid at the TS), which is an inherent feature of S_N2 reactions. At these regions, the gradient increases up to a maximum at the TS.

We found it illustrative to include the hardness values of the IRC in the analysis, which is depicted in Figure 11. We can observe that the hardness shows largest values toward the reactant/product regions and minima at the TS, where the Fisher information in momentum space gets a maximum value. The TS corresponds with a metastable structure with a lowest hardness (largest softness); that is, it is the most polarizable structure as compared to the rest at the IRC, and
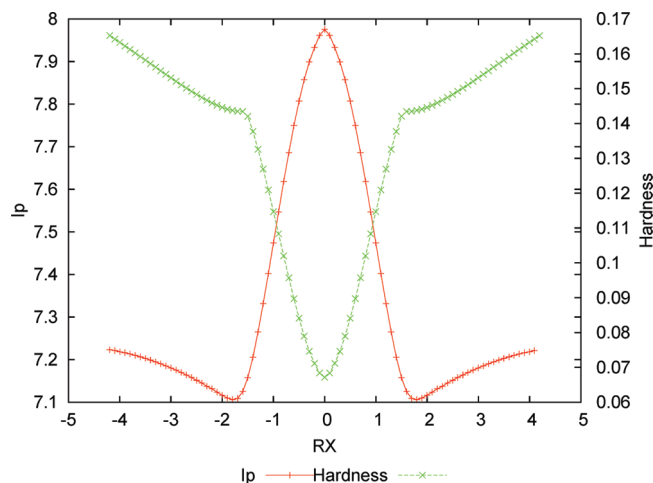

Figure 11. Fisher information in momentum space (red line) and the hardness values (green line) for the IRC of $H_a^- + CH_4 \rightarrow CH_4 + H_b^-$.
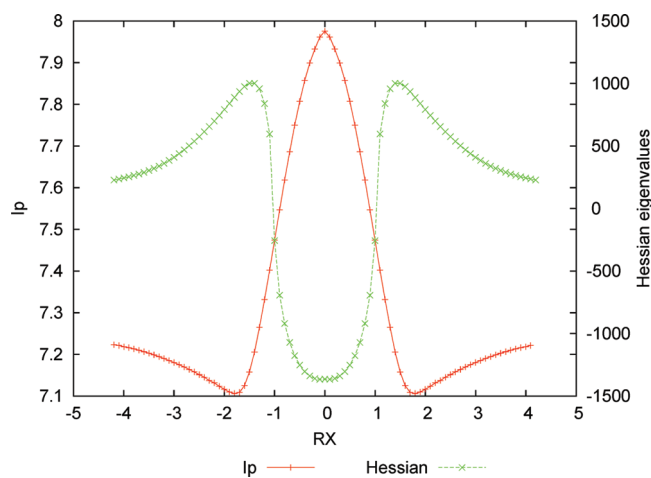
Figure 12. Fisher entropy in momentum space (red line) and the Hessian eigenvalues (green line) for the IRC of $H_a^- + CH_4 \rightarrow CH_4 + H_b^-$. It should be noted that negative values actually correspond with imaginary numbers (roots of negative force constants) so that the negative sign only represents a flag.

hence it is the most reactive. Also, it may be observed that the reactive complexes toward the reactant/product regions possess the largest hardness (lowest softness), which corresponds to highly stable molecules that are less prone to acquire additional charge. In the vicinity of the TS, we find "hardness bassins" at the BCER that we interpret to be chemically metastable and energetically reactive regions. We note from Figure 11 that the momentum Fisher information reflects the behavior above-described as an increment of the gradient.

The eigenvalues of the Hessian for the normal mode associated with the TS along the IRC of the reaction are depicted in Figure 12 along with the Fisher information values in momentum space. As it may be observed from this figure, the Hessian values show maxima at the BCER and reach its minimal value at the TS. The former are associated with high kinetic energy values (high vibrational frequencies), which seem to coincide with the minimal values in the momentum Fisher information profile. The TS at the saddle point is associated with a low kinetic energy structure

Fisher Information Study in Position and Momentum Spaces

J. Chem. Theory Comput., Vol. 6, No. 1, 2010 **153**

at the minimal molecular frequency value of the Hessian profile and with a maximum value of the Fisher information in momentum space, which corresponds to a density with the highest gradient content (very irregular density). It is important to mention that in the region where the frequencies become imaginary a transient of continuum has been established by Zewail and Polanyi[42] for the transition region, and this is clearly reflected by the zone where the gradient increases in momentum space and, consequently, the associated Fisher information increases too.

Conclusions

In this work, we have shown the usefulness of the information-theoretic measures of the Fisher type to characterize elementary chemical reactions. In a previous work,[23] the Shannon entropy of elementary chemical reactions was studied as a global measure that quantifies the localization/delocalization of the density; however, the behavior of the densities about their local changes (uniformity/irregularity) can only be provided by a local measure such as the Fisher information. In the previous sections, we have verified that the local character of Fisher information indeed provokes an enhanced sensitivity to changes on the position and momentum densities along the chemical reaction paths. One of the manifestations of the local changes excerted by the densities is due to the charge transfer process, which is directly reflected in the heterolitic behavior of the S_N2 reaction in contrast with the abstraction reaction whose mechanims are homolitic; that is, the Fisher information is capable of differentiating between both types of mechanims because of its local character.

The TS structure, at least for the studied reactions in this work, was clearly predicted by Fisher information in both spaces, whereas the stationary points that delimit the TS region are predicted by the momentum Fisher information solely. Besides, through the chemical probes we were capable of observing the basic chemical phenomena of bond breaking/forming showing that the Fisher information measures are highly sensitive in detecting these chemical events, mainly in momentum space.

It is interesting to mention that the uncertainty relation $I_r I_p \geq 36$, recently pointed out[28] for three-dimensional quantum systems, has been corroborated for the atomic and molecular systems involved in this study, which is a further check of our results.

According to Fisher information in position space, it is possible to detect differences in the mechanism for both reactions in that for the S_N2 the measure is able to witness the charge exchange process where the Fisher information is maximum at the TS. It remains to be studied whether the overall behavior of the abstraction reaction as compared to the exchange S_N2 reactions represents a manner of studying reaction mechanisms for Fisher information measures. We are aware of the fact that more chemical probes are necessary to pose more general statements.

References

(1) Fisher, R. A. *Proc. Cambridge Philos. Soc.* **1925**, *22*, 700.

(2) González-Férez, R.; Dehesa, J. S. *Eur. J. Phys. D* **2005**, *32*, 39.

(3) Angulo, J. C.; Antolín, J.; Sen, K. D. *Phys. Lett. A* **2008**, *372*, 670.

(4) Nalewajski, R. F. *Information Theory of Molecular Systems*; Elsevier Science: New York, 2006.

(5) Sen, K. D.; Panos, C. P.; Chatzisavvas, K. Ch.; Moustakidis, Ch. C. *Phys. Lett. A* **2007**, *368*, 286.

(6) Frieden, B. R. *Science from Fisher Information*; Cambridge University Press: New York, 2004.

(7) Cover, T. M.; Thomas, J. A. *Elements of Information Theory*; Wiley-Interscience: New York, 1991.

(8) Angulo, J. C.; Antolín, J. *J. Chem. Phys.* **2008**, *128*, 164109.

(9) Panos, C. P.; Chatzisavvas, K. C.; Moustakidis, C. C.; Kyrkou, E. *Phys Lett. A* **2007**, *363*, 78. Borgoo, A.; de Proft, F.; Geerlings, P.; Sen, K. D. *Chem. Phys. Lett.* **2007**, *444*, 183. Antolin, J.; Angulo, J. C. *Int. J. Quantum Chem.* **2009**, *109*, 586.

(10) Taneja, I. J.; Pardo, L.; Morales, D.; Menendez, M. L. *Questiio* **1989**, *13*, 47.

(11) Kullback, S.; Leibler, A. *Ann. Math. Stat.* **1951**, *22*, 79.

(12) Antolin, J.; Angulo, J. C.; López-Rosa, S. *J. Chem. Phys.* **2009**, *130*, 074110.

(13) Lin, J. *IEEE Trans. Inf. Theory* **1991**, *37*, 145.

(14) Hoffman, R.; Shaik, S.; Hiberty, P. C. *Acc. Chem. Res.* **2003**, *36*, 750.

(15) Schlegel, H. B. *Adv. Chem. Phys.* **1987**, *67*, 249.

(16) Fukui, K. *Acc. Chem. Res.* **1981**, *14*, 363.

(17) Shaik, S.; Ioffe, A.; Reddy, A. C.; Pross, A. *J. Am. Chem. Soc.* **1994**, *116*, 262.

(18) Eyring, H. *J. Chem. Phys.* **1935**, *3*, 107. Wigner, E. *Trans. Faraday Soc.* **1938**, *34*, 29.

(19) Hammond, G. S. *J. Am. Chem. Soc.* **1955**, *77*, 334. Leffler, J. E. *Science* **1953**, *117*, 340.

(20) Shi, Z.; Boyd, R. J. *J. Am. Chem. Soc.* **1991**, *113*, 1072.

(21) Bader, R. F. W.; MacDougall, P. J. *J. Am. Chem. Soc.* **1985**, *107*, 6788. Balakrishnan, N.; Sathyamurthy, N. *Chem. Phys. Lett.* **1989**, *164*, 267. Ho, M.; Schmider, H. L.; Weaver, D. F.;

Smith, V. H., Jr.; Sagar, R. P.; Esquivel, R. O. *Int. J. Quantum Chem.* **2000**, *77*, 376. Knoerr, E. H.; Eberhart, M. E. *J. Phys. Chem. A* **2001**, *105*, 880. Tachibana, A. *J. Chem. Phys.* **2001**, *115*, 3497.

(22) Gadre, S. R. In *Reviews of Modern Quantum Chemistry: A Celebration of the Contributions of Robert G. Parr*; Sen, K. D., Ed.; World Scientific: Singapore, 2003; Vol. 1, pp 108–147. Koga, T.; Morita, M. *J. Chem. Phys.* **1983**, *79*, 1933. Ghosh, S. K.; Berkowitz, M.; Parr, R. G. *Proc. Natl. Acad. Sci. U.S.A.* **1984**, *81*, 8028. Angulo, J. C.; Dehesa, J. S. *J. Chem. Phys.* **1992**, *97*, 6485. Massen, S. E.; Panos, C. P. *Phys. Lett. A* **1998**, *246*, 530. Nalewajski, R. F.; Parr, R. G. *J. Phys. Chem. A* **2001**, *105*, 7391. Nagy, A. *J. Chem. Phys.* **2003**, *119*, 9401. Romera, E.; Dehesa, J. S. *J. Chem. Phys.* **2004**, *120*, 8906. Karafiloglou, P.; Panos, C. P. *Chem. Phys. Lett.* **2004**, *389*, 400. Sen, K. D. *J. Chem. Phys.* **2005**, *123*, 074110. Parr, R. G.; Nalewajski, R. F.; Ayers, P. W. *J. Phys. Chem. A* **2005**, *109*, 3957. Guevara, N. L.; Sagar, R. P.; Esquivel, R. O. *J. Chem. Phys.* **2005**, *122*, 084101. Shi, Q.; Kais, S. *J. Chem. Phys.* **2005**, *309*, 127. Chatzisavvas, K. Ch.; Moustakidis, Ch. C.; Panos, C. P. *J. Chem. Phys.* **2005**, *123*, 174111. Sen, K. D.; Katriel, J. *J. Chem. Phys.* **2006**, *125*, 074117. Nagy, A. *Chem. Phys. Lett.* **2006**, *425*, 154. Ayers, P. W. *Theor. Chem. Acc.* **2006**, *115*, 253. Martyusheva, L. M.; Seleznev, V. D. *Phys. Rep.* **2006**, *426*, 1. Liu, S. *J. Chem. Phys.* **2007**, *126*, 191107. Borgoo, A.; Jaque, P.; Toro-Labbé, A.; Van Alsenoy, Ch.; Geerlings, P. *Phys. Chem. Chem. Phys.* **2009**, *11*, 476.

(23) Esquivel, R. O.; Flores-Gallegos, N.; Iuga, C.; Carrera, E.; Angulo, J. C.; Antolin, J. *Theor. Chem. Acc.* **2009**, *124*, 445–460.

(24) Rawlings, D. C.; Davison, E. R. *J. Phys. Chem.* **1985**, *89*, 969.

(25) Kaijser, P.; Smith, V. H., Jr. *Adv. Quantum Chem.* **1997**, *10*, 37.

(26) Kohout, M. *Program DGRID, version 4.2*; 2007.

(27) Hamilton, I. P.; Mosna, R. A. *J. Comput. Appl. Math.* **2010**, *233*, 1542–1547.

(28) Dehesa, J. S.; Gonzalez-Ferez, R.; Sanchez-Moreno, P. *J. Phys. A* **2007**, *40*, 1845.

(29) Politzer, P.; Truhlar, D. G. *Chemical Applications of Atomic and Molecular Electrostatic Potentials*; Academic Press: New York, 1981.

(30) Parr, R. G.; Pearson, R. G. *J. Am. Chem. Soc.* **1983**, *105*, 7512. Parr, R. G.; Yang, W. *Density-Functional Theory of Atoms and Molecules*; Oxford University Press: New York, 1989. Geerlings, P.; De Proft, F.; Langenaeker, W. *Chem. Rev.* **2003**, *103*, 1793.

(31) Koopmans, T. *Physica A* **1933**, *1*, 104. Janak, J. F. *Phys. Rev. B* **1978**, *18*, 7165.

(32) Ghanty, T. K.; Ghosh, S. K. *J. Phys. Chem.* **1993**, *97*, 4951. Roy, R.; Chandra, A. K.; Pal, S. *J. Phys. Chem.* **1994**, *98*, 10447. Hati, S.; Datta, D. *J. Phys. Chem.* **1994**, *98*, 10451. Simon-Manso, Y.; Fuenteaelba, P. *J. Phys. Chem. A* **1998**, *102*, 2029.

(33) Chattaraj, P. K.; Sarkar, U.; Roy, D. R. *Chem. Rev.* **2006**, *106*, 2065.

(34) Pearson, R. G. *J. Am. Chem. Soc.* **1963**, *85*, 3533. Pearson, R. G. *Hard and Soft Acids and Bases*; Dowen, Hutchinson and Ross: Stroudsberg, 1973. Pearson, R. G. *Chemical Hardness*; Wiley-VCH: New York, 1997.

(35) Frisch, M. J.; Trucks, G. W.; Schlegel, H. B.; Scuseria, G. E.; Robb, M. A.; Cheeseman, J. R.; Montgomery, J. A., Jr.; Vreven, T.; Kudin, K. N.; Burant, J. C.; Millam, J. M.; Iyengar, S. S.; Tomasi, J.; Barone, V.; Mennucci, B.; Cossi, M.; Scalmani, G.; Rega, N.; Petersson, G. A.; Nakatsuji, H.; Hada, M.; Ehara, M.; Toyota, K.; Fukuda, R.; Hasegawa, J.; Ishida, M.; Nakajima, T.; Honda, Y.; Kitao, O.; Nakai, H.; Klene, M.; Li, X.; Knox, J. E.; Hratchian, H. P.; Cross, J. B.; Bakken, V.; Adamo, C.; Jaramillo, J.; Gomperts, R.; Stratmann, R. E.; Yazyev, O.; Austin, A. J.; Cammi, R.; Pomelli, C.; Ochterski, J. W.; Ayala, P. Y.; Morokuma, K.; Voth, G. A.; Salvador, P.; Dannenberg, J. J.; Zakrzewski, V. G.; Dapprich, S.; Daniels, A. D.; Strain, M. C.; Farkas, O.; Malick, D. K.; Rabuck, A. D.; Raghavachari, K.; Foresman, J. B.; Ortiz, J. V.; Cui, Q.; Baboul, A. G.; Clifford, S.; Cioslowski, J.; Stefanov, B. B.; Liu, G.; Liashenko, A.; Piskorz, P.; Komaromi, I.; Martin, R. L.; Fox, D. J.; Keith, T.; Al-Laham, M. A.; Peng, C. Y.; Nanayakkara, A.; Challacombe, M.; Gill, P. M. W.; Johnson, B.; Chen, W.; Wong, M. W.; Gonzalez, C.; Pople, J. A. *Gaussian 03*, revision D.01; Gaussian, Inc.: Wallingford, CT, 2004.

(36) Johnson, B. A.; Gonzales, C. A.; Gill, P. M. W.; Pople, J. A. *Chem. Phys. Lett.* **1994**, *221*, 100.

(37) Shi, Z.; Boyd, R. J. *J. Am. Chem. Soc.* **1989**, *111*, 1575.

(38) Pérez-Jordá, J. M.; San-Fabián, E. *Comput. Phys. Commun.* **1993**, *77*, 46. Pérez-Jordá, J. M.; Becke, A. D.; San-Fabián, E. *J. Chem. Phys.* **1994**, *100*, 6520.

(39) Schaftenaar, G.; Noordik, J. H. *J. Comput.-Aided Mol. Des.* **2000**, *14*, 123.

(40) Toro-Labbé, A.; GutiÃl'rrez-Oliva, S.; Murray, J. S.; Politzer, P. J. *Mol. Model.* **2009**, *15*, 707. Toro-Labbé, A.; GutiÃl'rrez-Oliva, S.; Murray, J. S.; Politzer, P. *Mol. Phys.* **2007**, *105*, 2619. Murray, J. S.; Toro-Labbé, A.; Clark, T.; Politzer, P. J. *Mol. Model.* **2009**, *15*, 701. Jaque, P.; Toro-Labbé, A.; Geerlings, P.; De Proft, F. *J. Phys. Chem. A* **2009**, *113*, 332.

(41) Glukhovtsev, M. N.; Pross, A.; Radom, L. *J. Am. Chem. Soc.* **1995**, *117*, 2024.

(42) Polanyi, J. C.; Zewail, A. H. *Acc. Chem. Res.* **1995**, *28*, 119.

JCTC Journal of Chemical Theory and Computation

Spatially Homogeneous QM/MM for Systems of Interacting Molecules with on-the-Fly ab Initio Force-Field Parametrization

Ali Sebetci[†,‡] and Gregory J. O. Beran*[,†]

Department of Chemistry, University of California, Riverside, California 92521

Abstract: Quantum and classical mechanics are combined in a hybrid many-body interaction model to enable the computationally affordable study of systems containing many interacting molecules. This model treats intramolecular and pairwise intermolecular interactions quantum mechanically, while many-body electrostatic induction effects are approximated using a polarizable force field. In this paper, we demonstrate that parametrizing the force field with distributed multipoles and atom-centered polarizabilities obtained on-the-fly from ab initio quantum mechanical monomer calculations makes the model very accurate and eliminates nearly all empiricism. Test calculations on water, formamide, hydrogen fluoride, and glycine−water clusters, all of which exhibit strong many-body interactions, are presented. The performance of the hybrid model is competitive with related point-charge embedding models.

1. Introduction

Molecular clusters, liquids, and solids display complex and interesting behaviors, many of which are not well understood. Ab initio quantum chemistry would be an extremely helpful tool for modeling such systems, but its high computational expense and the difficulty in treating intermolecular interactions accurately limits its applicability at present. Reliable, inexpensive approximations to a full quantum mechanical treatment of such systems are greatly needed.

One such approach lowers the computational cost in systems of interacting molecules by using a truncated many-body interaction (MBI) expansion to describe the total system energy in terms of interacting molecules/fragments. This idea is quite old, and many groups have studied it in recent years. For example, symmetry-adapted perturbation theory techniques,[1,2] the fragment molecular orbital method,[3−5] the effective fragment potential,[6,7] electrostatically embedded many-body expansions,[8−11] molecular mechanics for clusters,[12] accurate polarizable force fields,[13−18] and other

studies[19−26] all utilize MBI expansions. Notably, the importance of including three-body and higher ("many-body") effects is a recurring theme in most of these works.

Many-body effects include contributions from exchange−repulsion, electrostatic induction (also called polarization), and dispersion forces. However, for systems of interacting polar molecules, induction typically dominates the many-body effects. Induction effects are particularly important when strong electrostatic interactions or hydrogen-bond cooperativity[27] are present.

One of us recently investigated[28] a hybrid quantum mechanics/molecular mechanics (QM/MM) model for describing systems of interacting molecules. This hybrid many-body interaction (HMBI) model partitions the system based on the order of intermolecular interactions in the many-body interaction series: the most important intermolecular interactions are modeled quantum mechanically, while smaller, computationally expensive contributions are approximated classically. Specifically, the one- and two-body interactions are computed quantum mechanically, while the three-body and higher interactions are approximated with an inexpensive classical polarizable force field that describes electrostatic induction. Many-body dispersion and exchange-repulsion effects are completely neglected in this model. Similar partitioning is used very successfully in constructing spec-

* To whom correspondence should be addressed: E-mail: gregory.beran@ucr.edu.
† University of California, Riverside.
‡ Current address: Computer Engineering Department, Zirve University, 27260 Gaziantep, Turkey. E-mail: alisebetci@zirve.edu.tr.

troscopically accurate polarizable force fields/potential energy surface models, such as the TTM-xF models for water.[13,14] The key difference here is that we perform all calculations on-the-fly instead of fitting to a fixed classical functional form.

Unfortunately, the incorporation of a force field into the model raises the question of force-field parametrization. Previously,[28] we tested the Amoeba[29] polarizable force field for approximating the many-body induction effects. While Amoeba works reasonably well, it can exhibit systematic errors in predicting the many-body induction contributions (as compared to quantum mechanical results). For example, Amoeba systematically overestimated the many-body induction energies in a set of water clusters.[28] In addition, like most standard force fields, Amoeba has only been parametrized for a relatively small number of molecules, and its existing parameters are not necessarily transferable to new systems.

In this paper, we demonstrate that force-field parameters needed for the HMBI model can be obtained on-the-fly in an ab initio fashion, virtually eliminating the need for empirical parameters in the model. At each given molecular geometry of a system, the one- and two-body interactions are computed quantum mechanically, and a force field is parametrized to reproduce the many-body induction effects for that specific geometry.

In general, ab initio force-field (AIFF) parametrization is a difficult problem that many research groups have studied.[6,7,15,30−38] However, HMBI simplifies the task in two ways. First, the HMBI model only uses the many-body electrostatic induction effects from the force field. Intramolecular, two-body dispersion, two-body exchange-repulsion, and two-body electrostatic/induction effects are all treated quantum mechanically. Many-body dispersion and exchange−repulsion are neglected (at least in the model's current form). Thus, HMBI requires only an AIFF model for self-consistent polarization. Second, while many-body effects are frequently too large to neglect, their energetic contribution remains relatively small. In water clusters, which have significant many-body effects, these effects account for only about 15% of the total interaction energy[39] (though in small clusters these effects can be much larger[40,41]). In other words, HMBI requires a fairly simple force field, and the relatively small size of its contribution reduces the impact of inadequacies in the force field. As explained in section 2.2, we use existing techniques to determine the actual force-field parameters.

Polarizable force fields come in many forms.[15,42−44] The ones considered here are based on atom-centered distributed multipole expansions and atomic polarizabilities, for which we use ab initio parametrization methods developed in other groups.[34,45−47] In section 2, we discuss the HMBI model and the techniques used for constructing the force fields from first principles. After explaining the computational details in section 3, we demonstrate the method on a series of test clusters exhibiting large many-body effects in section 4.

2. Theory

2.1. The HMBI Model. The particular hybrid many-body interaction (HMBI) expansion approach for modeling systems of interacting molecules used here has been presented previously,[28] so we only briefly review the formalism. The total energy of a system of interacting molecules can be viewed in terms of the energies of individual molecules, their two-body (or pairwise) interactions, and the three-body and higher ("many-body") intermolecular interaction corrections, according to the many-body interaction expansion:

$$E_{\text{total}} = \sum_i E_i + \sum_{ij} \Delta^2 E_{ij} + \sum_{ijk} \Delta^3 E_{ijk} + ... \quad (1)$$

where E_i is the energy of the ith molecule, $\Delta^2 E_{ij}$ is the pairwise-interaction energy between two molecules i and j ($\Delta^2 E_{ij} = E_{ij} - E_i - E_j$, where E_{ij} is the total dimer energy), $\Delta^3 E_{ijk}$ is the three-body interaction correction between molecules i, j, and k ($\Delta^3 E_{ijk} = E_{ijk} - \Delta^2 E_{ij} - \Delta^2 E_{ik} - \Delta^2 E_{jk} - E_i - E_j - E_k$, where E_{ijk} is the total trimer energy), etc.

Though they typically contribute less than the one- and two-body terms, the many-body interactions are often non-negligible. In systems containing polar molecules, these many-body terms are typically dominated by induction, which can be approximated relatively easily.[8,26,28] In particular, a classical polarizable force field can approximate these terms at very low computational cost. With this approximation and some straightforward rearrangement, we obtain:[28]

$$E_{\text{total}}^{\text{HMBI}} = E_{\text{total}}^{\text{MM}} + \sum_i (E_i^{\text{QM}} - E_i^{\text{MM}}) +$$
$$\sum_{ij} (\Delta^2 E_{ij}^{\text{QM}} - \Delta^2 E_{ij}^{\text{MM}}) \quad (2)$$

We emphasize that this HMBI model differs from conventional QM/MM models in that it partitions the system based on the type of interaction rather than by using a spatial criterion. HMBI's spatially homogeneous treatment of the entire system makes it ideal for treating molecular condensed-phase systems in which the important chemistry arises through intermolecular interactions dispersed over a large spatial area.

In addition HMBI sums many-body terms through all orders. Subsequent higher-order terms in the MBI expansion often alternate in sign. Truncating the series at a given order can introduce surprisingly large errors due to the absence of cancelation from higher-order terms.[28] By summing through all orders, HMBI avoids this pitfall.

2.2. Ab Initio Force Field (AIFF) Parameterization. The accuracy of an HMBI model depends critically on the polarizable force field used to approximate the many-body induction effects. The Amoeba force field tested previously performed moderately well, but evidence suggests it could be improved.[28] In this article, we demonstrate that an AIFF for many-body induction, in which the parameters are obtained directly from quantum mechanical monomer calculations, significantly improves results while simultaneously reducing the need for user-intervention during the force-field parametrization.

Specifically, we use a force field based on an atom-centered distributed-multipole representation[48−50] of the electron density and atom-centered local polarizabilities. To compute the polarizabilities, the molecular static polarizability is calculated using Kohn−Sham linear-response theory. The molecular polarizability is then distributed and localized to individual atoms according to the Williams−Stone−Misquitta procedure.[34,46,47] No intramolecular or two-body intermolecular force-field terms are required, because these are treated at the QM level.

The use of such procedures to parametrize a force field is not unique to our work. These particular procedures have been used to parametrize successful force fields for predicting the structures of molecular crystals,[51] for example. More generally, distributed multipoles (and sometimes polarizabilities) are widely used in force fields today (see, for example, refs 6, 7, 15, 34−38). However, these properties are rarely recomputed at every new geometry or point of interest on a potential energy surface to obtain a geometry-specific force field for many-body induction. In a purely classical model, doing such calculations would computationally overwhelm the relatively small effort required to evaluate the force field. Compared to the cost of evaluating the two-body quantum mechanical interactions in eq 2, however, the evaluation of these force-field parameters is reasonable. This means that the many-body induction force-field parameters can be recomputed as needed in HMBI. The repeated QM calculations (both one- and two-body energies and parametrizing the AIFF) obviously make HMBI much much more expensive than a simple force-field evaluation, but it is also widely applicable without requiring substantial hand reparameterization from the user.

Several important technical issues arise in constructing the force field. First, the distributed multipoles and local polarizabilities can be computed to different ranks. Previous studies have found that up to rank 4 (hexadecapole) multipole moments on non-hydrogen atoms and rank 1 moments (dipole) on hydrogen atoms, along with up to rank 2 (quadrupole) polarizabilities, perform well for general-purpose force fields,[34,47] so we use these same ranks here. In other words, the polarization model includes up to induced quadrupole effects.

Second, approximating electrostatic interactions with multipole interactions is only rigorously valid at long ranges. Therefore, it is necessary to introduce a damping function to attenuate the induction energy at short-range and to avoid the "polarization catastrophe." Numerous approaches to damp these interactions exist.[52−57] We apply the commonly used damping function proposed by Tang and Toennies,[58]

$$f_n(R) = 1 - \sum_{k=0}^{n} \left(\frac{(\beta R)^k}{k!} \right) e^{-\beta R} \qquad (3)$$

to damp a R^{-n} term in the multipolar interaction. This damping function requires a (usually empirical) damping factor β. Misquitta and co-workers have analyzed these issues in some detail,[47] and they proposed a simple model for predicting the damping factor β single-molecule-containing system based on the ionization potential I,

$$\beta_{\text{pred}} = 2(2I)^{1/2} \qquad (4)$$

They also proposed a related expression for systems containing multiple species. We will test this damping factor in our systems, and we will also explore treating this damping factor as an empirical parameter. Though the latter option is contrary to the spirit of the AIFF, we find it is unfortunately necessary in most of the cases examined here.

Third, one would ideally compute the multipoles and polarizabilities separately for each molecule in the cluster (and at each step in a molecular dynamics simulation or geometry optimization). However, the calculation of the polarizabilities in particular can be time-consuming. In practice, the polarizabilities of a water molecule, for example, will need to be computed repeatedly at slightly varying geometries. The polarizabilities do not change substantially with moderate changes in the molecular geometry, suggesting that computational savings might be obtained by approximating the polarizabilities by using the values obtained at similar geometries. In contrast, we find the multipole moments to be more sensitive to geometry. Computation of the multipole moments, however, requires much less computational effort than the polarizabilities. The effect of approximating these quantities with their equilibrium geometry values will be investigated below.

Fourth, here we only consider systems in which each molecule is completely contained within a given "monomer" (as in a set of small, interacting molecules). Monomer boundaries never cross a covalent bond. If instead the monomers were composed of molecular fragments, the "many-body" effects will include intramolecular interactions. These interactions are much stronger and harder to approximate with simple classical electrostatics/induction than intermolecular many-body effects. On the other hand, methods such as the fragment molecular orbital method[4,5] have been adapted to such cases with good results, so such partitioning merits future investigation.

3. Computational Details

The HMBI model requires the specification of both the quantum mechanical method and the polarizable force field. Unless otherwise specified, we use resolution-of-the-identity second-order Møller−Plesset (RI-MP2)[59−61] theory with the Dunning aug-cc-pVTZ basis set[62] and its corresponding auxiliary set[63] in the frozen core approximation for the QM calculations in eq 2. The aug-cc-pVTZ basis provides a reasonable balance between basis-set completeness and computational affordability. Dual-basis Hartree−Fock (HF)/MP2 algorithms accelerate the RI-MP2 calculations further.[64−66] These approximations make the benchmark MP2 calculations on the full clusters considered here affordable while introducing insignificant errors in relative energies. MP2 cannot describe all intermolecular interactions,[67−69] but more accurate methods would make the benchmark calculations unfeasible. MP2 serves as a compromise between accuracy and computational affordability here. Integral thresholds and HF energy convergence criteria were set to 10^{-14} and 10^{-8} a.u., respectively, to minimize numerical noise issues in

computing the many-body energies. These calculations were performed using a development version of Q-Chem, version 3.1.[70]

We compare six different approximations for the many-body (MM) terms in eq 2. In the first approximation, we neglect the many-body terms, which corresponds to setting all MM terms in eq 2 to zero. This approximation is labeled as "no MB" in the tables and figures below, and it serves as a measure of the importance of many-body effects. The second approximation uses supermolecular HF calculations to approximate the many-body induction effects quantum mechanically. This is equivalent to models explored by several other groups.[23,25,26,71] HF can describe many-body induction very accurately, and it serves as a target for the other five methods. Unfortunately, it is very expensive to perform the supermolecular HF calculation on the entire system. Using fast modern MP2 algorithms, the HF step is often the computational bottleneck in a large MP2 calculation.[72] The models that approximate many-body induction classically are much less expensive. In the third approximation, many-body induction is treated using the standard Amoeba polarizable force field,[29] as implemented in the Tinker[73] software package, just as was done in ref 28.

In the fourth approximation, we construct and use the AIFF described in section 2.2. The CamCasp[74] software package, which invokes the Dalton[75] quantum chemistry package, is used to construct the AIFF by predicting the distributed multipoles and polarizabilities from quantum mechanical calculations on each monomer in the system. Multipole moments are computed to rank 4 (hexadecapole) on heavy atoms and rank 1 (dipole) on hydrogen atoms.

The polarizabilities are computed to rank 2 (rank 1 on hydrogen atoms) using the Coupled Kohn−Sham (CKS) propagator. These ranks have been shown to reproduce DFT-based symmetry-adapted perturbation theory induction energies well.[47] Unless otherwise specified, the underlying Dalton calculations use the aug-cc-pVTZ basis and the hybrid PBE0[76] exchange and correlation functional. Our procedure uses two calculations per monomer: one to determine the RI-MP2 energy and another to find the force-field parameters with DFT. This is done to allow the use of pre-existing CamCasp software routines when determining the force-field parameters. The cost of performing an extra single-point energy calculation for each monomer is negligible compared to the other parts of the calculations. Ionization potentials of 0.4638 (water),[77] 0.3720 (formamide),[78] 0.5896 (hydrogen fluoride),[79] 0.3595 (glycine neutral), and 0.3042 au (glycine zwitterion) are employed in an asymptotic correction[80,81] for the PBE0 calculations. The two glycine vertical ionization potentials were calculated at the B3LYP/6-311++G(3df,2pd) level by taking the difference in energies between each molecule and its singly ionized cation. The Orient[82] software package is used to calculate self-consistent induction energies for the clusters based on the CamCasp multipole moments and polarizabilities.

Two different damping factors were considered for truncating short-range multipolar interactions for most systems. First, we used the damping factor predicted by eq 4 and the ionization potentials listed above. Second, we

treated the damping factor as an adjustable parameter and loosely optimized it to obtain both a small mean error and a narrow error distribution across the different clusters in each test set. Having a small mean error is required for accurate binding energies, while having a narrow range of errors is critical for accurate relative energies.

The fifth model examined is the electrostatically embedded pairwise-additivity (EE-PA) model of Dahlke and Truhlar.[8] Like the "no MB" case, EE-PA neglects many-body terms; rather, it uses an alternative approach for capturing many-body induction effects. The monomers and dimers are polarized by embedding them in a field of B3LYP/6-31G* Mulliken point charges centered at the nuclear positions of all other monomers. A more accurate variation on EE-PA also includes three-body effects, but that model is substantially more expensive than either EE-PA or the HMBI model discussed here, so we do not consider it. See ref 8 for further details on EE-PA.

The sixth and final model we consider is the self-consistent charge (or charge + dipole) embedded binary interaction scheme of Kamiya and co-workers.[11] In accord with ref 11, we refer to these methods as "binary+ESP" and "binary+ESP-dipole", respectively. Binary+ESP is essentially the same as EE-PA, except that the embedding charges are determined self-consistently by fitting to the electrostatic potential. Binary+ESP-dipole also includes some explicit dipole fitting. Both methods include counterpoise (CP) corrections[83] for basis set superposition error (BSSE). See the original work for more details. The self-consistent treatment of point charges helps capture induction effects through all orders. Because we do not have our own implementation of this method, we present binary+ESP-type results only for two test systems (water hexamers and glycine−water clusters) for which published data is already available.

These approximations are compared to the full RI-MP2 results on water clusters (Test Sets A−D), formamide clusters (Test Sets E and F), hydrogen fluoride clusters (Test Set G), and glycine−water clusters (Test Set H). All of these clusters exhibit strong many-body effects and therefore represent challenging test cases for HMBI models. To facilitate comparisons between the various systems, we report size-intensive energies obtained by dividing the resulting energies by the number of monomers.

Structures for the test clusters in Test Sets B, C, F, and G are provided as Supporting Information. The geometries used in Test Sets A, D, E, and H come from the literature, as discussed below. Tables containing all raw data used to generate the statistical results presented below are also available as Supporting Information.

4. Results and Discussion

4.1. Water Clusters. Water clusters have been investigated extensively in the last two decades because of both their general interest and strong many-body effects,[8,10,11,19,23,40,71,84−91] which means that they provide a challenging test case for approximate MBI expansion methods. We first consider the ability of the approximate methods to reproduce the binding energies of a series of

Table 1. Mean Signed Errors, Standard Deviations, and Total Error Ranges (in kJ/mol per molecule) for Various HMBI Many-Body Approximations Relative to RI-MP2[a]

	HF[b]	AIFF/β_{pred}[b]	AIFF/β_{opt}[b]	Amoeba[b]	EE-PA[c]	no MB[d]
			errors due to approximate many-body treatment			
	Test Set A: 16 $(H_2O)_n$ Clusters, $n = 5-20$					
mean	−0.03	−1.53	−0.04	−0.86	0.11	5.47
std dev	0.05	0.23	0.10	0.17	0.15	0.62
range	0.19	0.73	0.34	0.57	0.53	2.09
	Test Set B: 50 $(H_2O)_8$ Configurations					
mean	−0.02	−1.17	−0.01	−0.65	0.04	4.32
std dev	0.07	0.38	0.17	0.21	0.08	0.61
range	0.35	1.99	0.82	0.90	0.41	2.93
	Test Set C: 36 $(H_2O)_{10}$ Rotation PES Points					
mean	−0.06	−0.66	−0.24	−0.67	−0.43	1.54
std dev	0.09	0.58	0.12	0.54	0.13	1.91
range	0.27	1.86	0.48	1.78	0.59	6.55
	Test Set D: 8 $(H_2O)_6$ Configurations (see Table 2)					
	Test Set E: 51 $(HCONH_2)_8$ Configurations					
mean	0.04	−0.30	−0.04	1.20	0.32	3.06
std dev	0.10	0.19	0.17	0.32	0.18	0.83
range	0.43	0.97	0.71	1.50	0.79	4.00
	Test Set F: 50 Additional $(HCONH_2)_8$ Configurations					
mean	0.00	−0.37	−0.07	1.02	0.34	3.15
std dev	0.07	0.16	0.12	0.25	0.12	0.69
range	0.37	0.67	0.52	1.18	0.51	2.54
	Test Set G: 8 Cyclic $(HF)_n$ Clusters, $n = 3-10$					
mean	0.16	0.69	e	f	1.46	13.42
std dev	0.02	0.10	e	f	0.33	3.90
range	0.08	0.33	e	f	0.93	11.18
	Test Set H: Glycine·$(HO_2)_7$ Clusters (see Table 4)					

[a] For the AIFF, two different damping factors are considered. β_{pred} is the factor computed from eq 4 and β_{opt} is the value that approximately minimizes the mean error and range of errors. The actual β values are given in the text. [b] Technique used to approximate many-body terms in HMBI. [c] The EE-PA method from ref 8. [d] Many-body effects are neglected entirely in eq 2. [e] $\beta_{opt} = \beta_{pred}$, so the results are identical. [f] The Amoeba force field has not been parametrized for the HF molecule.

small- and medium-sized water clusters. Then we investigate how well these methods can reproduce potential energy surface (PES) energetics away from the minimum energy structures. Finally, we examine the ability of these methods to discriminate between a series of low-lying water hexamer isomers.

4.1.1. Performance on Optimized Water Clusters: Test Set A. We begin by computing the binding energies of 16 clusters containing 5 to 20 water molecules (Test Set A) with RI-MP2 and the various approximate many-body models, using optimized structures obtained from the Cambridge Cluster Database.[92,93] These particular clusters have been examined in similar studies previously[8,28] and therefore provide a useful comparison.

Summary statistics comparing HMBI and various treatments of many-body induction interactions with benchmark full-cluster RI-MP2 energies are presented in Table 1. Figure 1 shows the error distributions for each many-body induction approximation as obtained by combining the results from this test set and those from Test Sets B and C. As can be seen in the table, simply neglecting the many-body terms introduces both a large mean error (with error defined as $E_{approx} - E_{MP2}$) and a wide range of errors (defined as the difference between the two most extreme errors in the distribution). In contrast, the HF approximation for many-body induction is extremely accurate, giving a narrow error distribution peaked near zero. Its mean signed error is −0.03
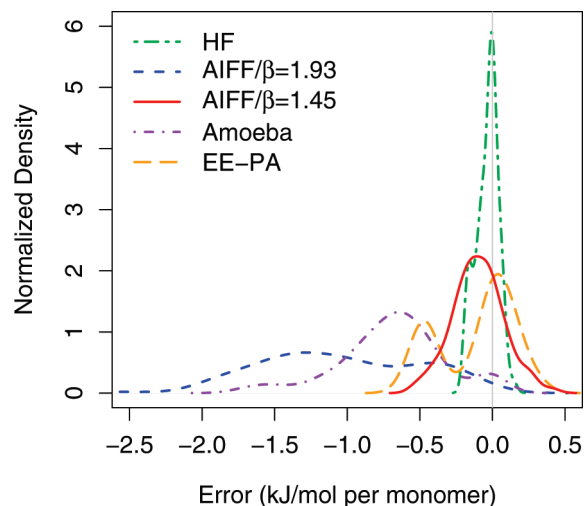
Figure 1. Error distributions for approximate many-body HMBI treatments relative to RI-MP2/aug-cc-pVTZ in 102 water clusters (Test Sets A−C combined).

kJ/mol per monomer, and the range of errors is 0.19 kJ/mol per monomer. As noted previously,[28] approximating the HMBI many-body induction terms with Amoeba is much better than simply neglecting them, but Amoeba significantly overestimates the many-body contribution in these water clusters, with a mean error of −0.86 kJ/mol per monomer

and a range three times wider than that of the HMBI/HF many-body approximation.

Next we consider the HMBI/AIFF results using two different damping factors. The first, $\beta_{pred} = 1.93$, is obtained using eq 4 and 0.4638 au for the ionization potential of water. For these water clusters, this damping factor appears to be a poor choice for the HMBI model, and the HMBI/AIFF/β_{pred} errors (mean error of -1.53 kJ/mol per monomer) are notably worse than those of the Amoeba.

If we loosely optimize β to minimize the mean error and error range for HMBI/AIFF, we find $\beta_{opt} = 1.45$. With this damping factor, the AIFF substantially out-performs the Amoeba force field for describing many-body induction. Though they are not as accurate as the HMBI/HF many-body results, the HMBI/AIFF/β_{opt} results exhibit a mean error and range of only -0.04 and 0.34 kJ/mol per monomer, respectively, and the cost of HMBI/AIFF is orders of magnitude cheaper than HMBI/HF for systems containing many monomers. The EE-PA point-charge embedding method[8] gives a larger mean error and range of errors (-0.11 and 0.53 kJ/mol per monomer, respectively).

One might be concerned that fitting β to these optimized water structures could bias the many-body force field toward these particular structures. However, this β value also performs well for the other water test sets examined below, which were not used in fitting β_{opt}. Therefore, $\beta_{opt} = 1.45$ appears to be a "universal" value for damping water−water interactions in this AIFF.

4.1.2. Performance across the Potential Energy Surface: Test Sets B and C. To examine the performance of the model away from equilibrium, we consider two different test sets. The first, Test Set B, consists of 50 $(H_2O)_8$ cluster geometries sampled at uniform intervals from a classical molecular dynamics simulation, which is representative of the potential energy surface sampling that occurs in typical condensed-phase studies. The second, Test Set C, consists of a series of points along a one-dimensional potential energy surface (PES) coordinate that disrupts the hydrogen bonding networks. Test Set C demands that the approximate method is able to describe widely varying intermolecular interactions accurately. As mentioned above, we continue to use $\beta_{opt} = 1.45$ for these test sets. Statistical results for both test sets are summarized in Table 1. See also Figure 1.

Optimized water clusters (e.g., Test Set A) often achieve enhanced stability through strong hydrogen bond cooperativity effects. In contrast, clusters sampled along a dynamics trajectory (Test Set B) will frequently exhibit a weaker and less homogeneous distribution of many-body effects. On the basis of the errors in the "no MB" column of Table 1, we observe that the mean many-body effects are smaller for Test Set B (-4.3 kJ/mol per monomer) than for Set A (-5.5 kJ/mol per monomer), and the distribution of many-body effects spans a broader range in Set B (2.9 vs 2.1 kJ/mol per monomer), as expected. The ability to reproduce this broad range of interactions is just as important as reproducing equilibrium structures.

The HMBI/AIFF/β_{opt} mean error for Test Set B is similar to the one for Test Set A. The range of errors is quite a bit larger in this set, but a significant increase in the range of
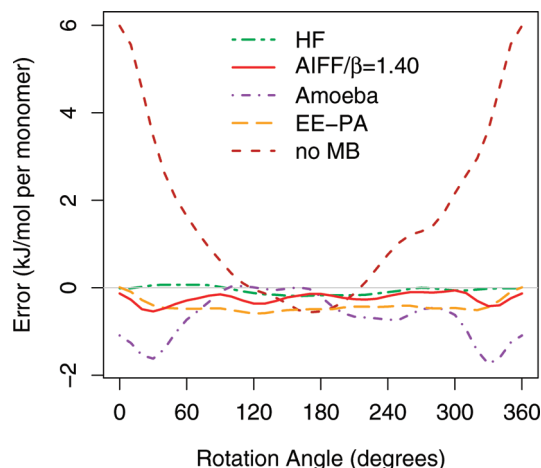

Figure 2. Errors (in kJ/mol per monomer) in binding energies for $(H_2O)_{10}$ relative to RI-MP2/aug-cc-pVTZ as each water molecule is rotated in place, disrupting the hydrogen bonding network (Test Set C).

errors is observed for the other HMBI models as well. This observation suggests that the varied many-body effects are indeed harder to approximate in these nonequilibrium structures. Nevertheless, the HMBI/AIFF model still provides good accuracy. EE-PA performs particularly well for this test set, exhibiting a range of errors similar to HMBI/HF and much smaller than HMBI/AIFF.

Next we examine the performance of these models along a challenging coordinate of the potential energy surface, Test Set C. Starting with the $(H_2O)_{10}$ structure from Test Set A, we generate a PES slice by simultaneously rotating each water molecule in place about the global coordinate *x*-axis passing through its center of mass (the geometries are available as Supporting Information). Energies were evaluated at $10°$ intervals in the range $0-360°$. This rotation completely disrupts the hydrogen bonding network and the corresponding hydrogen-bond cooperativity effects. In fact, the rotation reduces the many-body contribution from -6 kJ/mol per monomer at $0°$ to $+0.5$ kJ/mol per monomer (anticooperative effects) at $180°$, as reflected by the "no MB" line in Figure 2. The binding energy of this cluster ranges from roughly -40 kJ/mol per monomer (at $0°$) to $+10$ kJ/mol per monomer (at $180°$).

As always, HF approximates the many-body induction effects well, and the mean error and standard deviation along the PES slice are quite small. Both the HMBI/AIFF/β_{opt} and EE-PA many-body induction approximations perform well, too. While HMBI/AIFF is slightly more faithful to the RI-MP2 PES than EE-PA across much of the surface (as exhibited by its smaller mean error), the maximum HMBI/AIFF errors are similar to those of EE-PA (as exhibited by their similar standard deviations and error ranges). In either case, the errors are small relative to the overall binding energies. In addition, this system further demonstrates the superiority of the AIFF over an off-the-shelf force field such as Amoeba for our purpose. Amoeba has particular difficulties describing the wide range of interactions present along this PES slice. Together, the results from Test Sets B and C demonstrate that HMBI/AIFF performs well across the PES

On-the-Fly ab Initio Force Field Parametrization

J. Chem. Theory Comput., Vol. 6, No. 1, 2010 **161**

Table 2. Errors (in kJ/mol per monomer) in Predicted Counterpoise-Corrected MP2/aug-cc-pVDZ(Cartesian functions) Binding Energies for Low-Lying $(H_2O)_6$ Isomers (Test Set D)[a]

	binding energy	errors due to approximate many-body treatment				
isomer	MP2[b]	aug-cc-pVDZ AIFF[c]	Sadlej AIFF[c]	binary+ESP[d]	binary+ESP-dipole[d]	EE-PA
Book2	−28.88	0.54	0.32	−0.58	−0.69	0.80
C8	−29.01	0.67	0.33	−0.52	−0.64	0.83
C4	−27.53	0.68	0.42	−0.71	−0.79	0.73
C6	−28.59	0.77	0.45	−0.59	−0.70	0.92
Prism3	−28.07	0.55	0.35	−0.70	−0.85	0.79
Cage	−29.09	0.64	0.47	−0.58	−0.71	0.85
Chair	−28.71	0.98	0.43	−0.36	−0.50	1.02
C	−27.90	1.00	0.46	−0.40	−0.51	0.93
mean error		0.73	0.40	−0.55	−0.67	0.86
mean rel error[e]		0.08	−0.07	0.03	0.04	0.01
range		0.46	0.15	0.36	0.36	0.29

[a] Aug-cc-pVDZ and Sadlej in the column headings refer to the basis sets used to compute the AIFF parameters only. [b] Valiron-Mayer[97] counterpoise-corrected result, from ref 11. [c] Using $\beta_{opt} = 1.45$, as determined in section 4.1. [d] From ref 11. [e] Errors in energies relative to the Cage isomer.

and that the optimized damping factor β_{opt} works for water−water interactions well-away from equilibrium structures.

4.1.3. Ability To Differentiate between Low-Lying Isomers of $(H_2O)_6$: Test Set D. Finally, we examine a set of low-lying water hexamer isomers (Test Set D) that were used to benchmark the self-consistent charge-embedding binary interaction method of Kamiya and co-workers.[11] The geometries for these clusters originate from ref 94. The small relative energy differences in these clusters make their accurate prediction difficult. For these particular cluster geometries and MP2 energy calculations, the Cage isomer is the most stable. However, many possible isomers exist even within a single structural motif (such as a prism), and these isomers can differ substantially in energy. In contrast to the results for these particular isomers, recent accurate calculations predict that a Prism isomer, rather than a Cage isomer, is the most stable.[95,96] Nevertheless, our purpose is simply to compare the degree to which the various approximate many-body interaction models can reproduce the MP2 energies for these specific isomers, rather than to try to identify the globally optimal water hexamer structure.

To match the results from ref 11, we use canonical MP2/aug-cc-pVDZ (with Cartesian basis functions and no dual-basis approximation), and we found it necessary to correlate all electrons. Because ref 11 focuses on counterpoise-corrected results, we also apply a standard BSSE CP correction when evaluating each two-body HMBI interaction here. Table 2 presents the errors in binding energies predicted by HMBI, EE-PA, and two binary-interaction methods from ref 11.

Initially we computed the AIFF parameters in the aug-cc-pVDZ basis. However, this basis is too small to predict reliable polarizabilities, and the HMBI/AIFF model with aug-cc-pVDZ AIFF parameters performs much worse than if the compact Sadlej triple-ζ basis set[98,99] is used for parametrizing the AIFF. The Sadlej basis set predicts these polarizabilities with nearly aug-cc-pVTZ quality using roughly half the basis functions. The deficiencies in the aug-cc-pVDZ polarizabilities are not overcome by reoptimizing the damping factor β (rather, we continue to use the same $\beta_{opt} = 1.45$ parameter for all water clusters). Using the aug-cc-pVDZ basis for the MP2 one- and two-body calculations and the Sadlej basis

for predicting the AIFF parameters, we obtain a mean error of 0.40 and an error range of 0.15 kJ/mol per monomer relative to the CP-corrected MP2 binding energies. Both EE-PA and the binary-interaction models predict notably larger mean errors and error ranges than the AIFF(Sadlej) model, though they perform similar to or better than the AIFF(aug-cc-pVDZ) many-body induction model. Unfortunately, using a triple-ζ basis to compute the monomer polarizabilities substantially increases the cost of the double-ζ quality HMBI calculation, particularly in such small clusters. On the other hand, triple-ζ or larger basis sets are frequently important when describing intermolecular interaction without excessive BSSE.

If we consider relative energies instead of binding energies, the mean errors decrease substantially for all models. The HMBI/AIFF mean relative error is slightly larger than those for EE-PA and the binary interaction models, but it still performs very well. However, while several of the methods incorrectly order one of more isomers relative to the MP2 results, HMBI/AIFF(Sadlej) alone fails to predict the Cage structure as the most stable. It places the C8 isomer 0.06 kJ/mol per monomer *below* the Cage isomer. While the ordering is incorrect, the energy gap between them is very small and well within there margin of errors for the method. Furthermore, the ordering is corrected if the one- and two-body energies are computed in the aug-cc-pVTZ basis. Furthermore, the AIFF correctly predicts the prism as being more stable than the cage in the two water hexamer geometries considered in Test Set A, in agreement with both our own RI-MP2 calculations and highly accurate calculations.[95,96]

Overall, HMBI with the AIFF represents a good approximation for both single point energies of equilibrium structures (Test Sets A and D) and across the potential energy surface (Test Sets B and C) for small- and medium-sized water clusters. The combined results from Test Sets A−C in Figure 1 demonstrate the importance of using the proper damping factor ($\beta_{opt} = 1.45$ here), and the improvement of the AIFF over the Amoeba force field for describing many-body induction is clear. EE-PA performs similarly to the HMBI/AIFF model here, though it does exhibit slightly broader error distributions. Next, we evaluate the perfor-
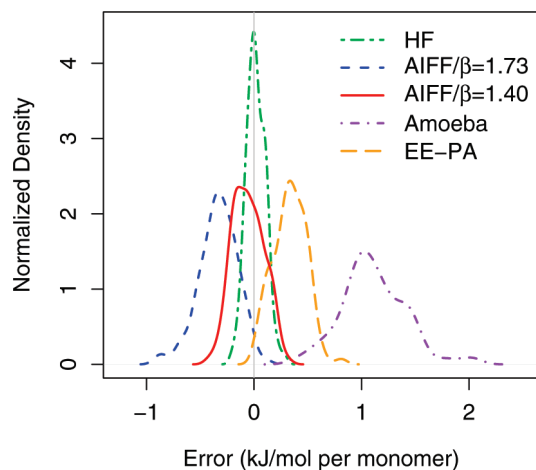
Figure 3. Error distributions for approximate many-body HMBI treatments relative to RI-MP2/aug-cc-pVTZ for 101 formamide clusters (Test Sets E and F combined).

mance of these models on formamide clusters, which also exhibit strong many-body effects.

4.2. (HCONH$_2$)$_8$ Clusters: Test Sets E and F. Formamide clusters are also noted for their strong many-body effects, and they have been studied by many groups.[100−107] We revisit the 51 formamide octamer geometries (Test Set E) considered in ref 28 with the AIFF. Once again, the two different damping factors are considered. Equation 4 predicts $\beta_{pred} = 1.73$, while optimization gives $\beta_{opt} = 1.40$. The error distributions relative to RI-MP2 for both Test Sets E and F are plotted in Figure 3, and statistical summaries are presented in Table 1.

As before, the AIFF/β_{opt} substantially out-performs Amoeba for approximating the RI-MP2 many-body induction. It also provides a significant improvement over neglecting many-body induction entirely. The mean HMBI/AIFF/β_{opt} error is only −0.04 kJ/mol per monomer (compared to the HMBI/HF error of 0.04 kJ/mol per monomer and an HMBI/Amoeba error of 1.20 kJ/mol per monomer). The HMBI/AIFF/β_{opt} error range of 0.71 kJ/mol per monomer is similar to what was observed for water/Test Set B. Again, this error distribution is broader than that of HMBI/HF, but the AIFF still does a remarkable job of approximating many-body induction effects. The range of the EE-PA error distribution (0.79 kJ/mol per monomer) is slightly broader than for HMBI/AIFF/β_{opt}, and the relatively large EE-PA mean error (0.32 kJ/mol per monomer) reflects a somewhat systematic underestimation of many-body effects.

We test the optimized β_{opt} value for transferability on 50 new (HCONH$_2$)$_8$ configurations (Test Set F). As listed in Table 1, the AIFF performs very well on this set too. The many-body effects are more uniform in size across the configurations sampled in the second set (compare the error ranges in the "no MB" columns for both Test Sets E and F), and the error ranges for the approximate models are commensurately smaller. Again, HMBI/AIFF/β_{opt} out-performs EE-PA by more than 0.3 kJ/mol per monomer in the mean error, while the error ranges are fairly similar. Overall, HMBI/AIFF/β_{opt} reproduces the total binding energies of these (HCONH$_2$)$_8$ clusters with a mean absolute percent error of 0.66%, compared to 1.70% for EE-PA and

Table 3. Binding Energies and Errors Arising from the Approximate Treatment of Many-Body Interactions (in kJ/mol per monomer) As Compared To Full RI-MP2 Binding Energies for a Series of Cyclic Hydrogen Fluoride Clusters, (HF)$_n$ (Test Set G)

	binding energy	errors due to approximate many-body treatment			
n	RI-MP2[a]	HF[a]	AIFF/β_{pred}[a]	EE-PA[b]	no MB[c]
3	−21.67	0.12	0.81	0.73	4.64
4	−30.24	0.18	0.71	1.19	10.90
5	−33.20	0.14	0.48	1.52	14.24
6	−33.96	0.16	0.64	1.65	15.17
7	−34.17	0.16	0.68	1.65	15.39
8	−34.34	0.16	0.71	1.64	15.63
9	−34.38	0.15	0.70	1.64	15.60
10	−34.66	0.20	0.82	1.65	15.82

[a] Technique used to approximate many-body terms in HMBI. [b] The EE-PA method from ref 8. [c] Many-body effects are neglected entirely in eq 2.

5.59% for HMBI/Amoeba. The vastly more expensive HMBI/HF approximation reduces the mean absolute percent error in binding energies to 0.35%.

We also investigate the use of the compact Sadlej triple-ζ basis set for computing the AIFF parameters for formamide clusters. As mentioned above, water polarizabilities were poorly reproduced in the aug-cc-pVDZ basis, but they can be predicted accurately with the Sadlej basis set, which is about half the size of the aug-cc-pVTZ basis set. The HMBI/AIFF/β_{opt} mean error, standard deviation, and range of errors for Test Set E with Sadlej-based AIFF are −0.05, 0.16, and 0.70 kJ/mol per monomer, which are essentially identical to the aug-cc-pVTZ results. Predicted many-body contributions for individual cluster geometries differ by only a few hundredths of a kJ/mol per monomer between the two basis sets. As recognized previously,[47] the Sadlej basis set provides a useful compromise between basis set size and accuracy in parametrizing the AIFF.

4.3. Cyclic (HF)$_n$ (n = 3−10) Clusters: Test Set G. Next, we consider a series of increasingly large cyclic hydrogen fluoride clusters (Test Set G). Hydrogen fluoride clusters are noted for their extraordinarily strong many-body effects, making them an extremely challenging test case. Many experimental[108−110] and theoretical[111−121] studies on HF clusters have been performed to understand their cluster and condensed-phase behavior.

Table 1 (statistical summary) and Table 3 (detailed results) demonstrate the performance of HMBI on these cyclic hydrogen fluoride clusters. The Amoeba force field has not been parametrized for the HF molecule, so we do not report HMBI/Amoeba results for these clusters. The large many-body hydrogen-bond cooperativity effects are clearly evident in Table 3, and we observe (as has been reported previously[111]) that they saturate at almost 16 kJ/mol per monomer for clusters of eight monomers or more.

As always, Hartree−Fock theory reproduces the many-body induction effects very well, though the mean error of 0.16 kJ/mol per monomer is significantly larger than for any of the other systems examined here. HMBI/AIFF/β_{pred} = 2.17 also performs rather well, but the mean error (0.69 kJ/mol per monomer) is again much larger than for formamide or water. On the other hand, the width of the error distribution

On-the-Fly ab Initio Force Field Parametrization

J. Chem. Theory Comput., Vol. 6, No. 1, 2010 **163**

Table 4. Predicted Energy Difference ($\Delta E = E_{neut} - E_{zwit}$ in kJ/mol) between Neutral and Zwitterionic Glycine$-(H_2O)_7$ Clusters (Test Set H) Using Frozen-Core MP2/aug-cc-pVDZ(Cartesian functions) with and without Counterpoise Correction

	full	HMBI approximate many-body treatment					
isomer	MP2[a]	HF	AIFF, single β[b]	AIFF, three βs[c]	binary+ESP[d]	EE-PA	no MB
ΔE	29.0	28.8	32.8	32.4	n/a	35.4	47.1
CP-ΔE	15.5	15.0	19.0	18.6	20.5	19.1	33.3

[a] Valiron-Mayer[97] counterpoise-corrected result, from ref 11. [b] AIFF determined with Sadlej basis, using $\beta_{opt} = 1.5$. [c] AIFF determined with Sadlej basis, using $\beta_{H_2O-H_2O} = 1.45$, $\beta_{neut-H_2O} = 1.51$, and $\beta_{zwit-H_2O} = 1.44$. [d] From ref 11.

is only 0.33 kJ/mol per monomer. Thus, the AIFF systematically underestimates the many-body effects by about 5% in the larger clusters, which amounts to an average 2.3% error in the total binding energies. Unlike the water and formamide test cases above, no improvement is found by optimizing β. Increasing β decreases the mean error further but at the expense of increasing the error range. For this particular test set, eq 4 provides a useful prediction for β.

Although the HMBI/AIFF errors are more pronounced in these hydrogen fluoride clusters than in the water or formamide clusters examined above, they are substantially smaller than the EE-PA errors. The mean EE-PA error is nearly 1.5 kJ/mol per monomer (nearly 4.5% in the total binding energy), more than twice that of HMBI/AIFF. Likewise, the EE-PA error range is almost three times as wide as that of HMBI/AIFF.

Reference 11 presents results on a similar set of cyclic HF clusters containing 4−9 molecules. They find that binary+ESP gives a mean error and error range of 1.04 and 0.33 kJ/mol per monomer, respectively, while the binary+ESP-dipole model gives a mean error and error range of 0.32 and 0.08 kJ/mol per monomer. These numbers cannot be compared directly to our own because they use slightly different clusters/geometries, smaller basis sets, and include CP corrections. Nevertheless, a loose comparison suggests that HMBI/AIFF is probably performing with accuracy intermediate between binary+ESP and binary+ESP-dipole here.

4.4. Glycine in Water: Test Set H. As a final test, Table 4 presents the energy difference, $\Delta E = E_{neutral} - E_{zwitterion}$, between the neutral and zwitterionic forms of glycine microsolvated with seven water molecules (Test Set H)[10,11] using CP-corrected, frozen-core canonical MP2/aug-cc-pVDZ(Cartesian). These conditions were chosen to enable direct comparison with ref 11. As observed previously, BSSE effects are substantial in this system and basis set, and CP-correction reduces the energy gap by almost a factor of 2.[11] The microsolvated zwitterion is more stable than its neutral counterpart before and after the CP correction. Unsurprisingly, HMBI/HF faithfully reproduces the energy gap to within 0.5 kJ/mol with or without the CP correction. Note that we did not counterpoise-correct the HF many-body contribution. Valiron-Mayer CP corrections for many-body effects become prohibitively expensive for large clusters and cannot be used in practice for most systems. BSSE effects in the many-body terms tend to be less significant than in the two-body terms.[21]

The presence of two different species (or even three if the neutral and zwitterionic forms of glycine are considered distinct) raises the question of how best to treat the damping

in the AIFF. Various approaches for handling damping in mixed systems have been proposed and tested in the literature (see, for example, refs 47, 55, 56). Here, we compare two different damping models on a training set of MP2 results from 18 glycine$-(H_2O)_2$ clusters (nine with neutral and nine with zwitterionic glycine), using the Sadlej basis set for the AIFF. The first model uses a single, system-wide empirical damping factor, just as in the examples described previously. We find that $\beta = 1.5$ is approximately optimal here, which is similar to the value obtained for pure water.

The second model uses three separate damping factors: one to describe water−water interactions (which we set to $\beta = 1.45$, as before) and additional parameters to describe water−neutral glycine and water−zwitterionic glycine interactions (which we optimized). We find $\beta_{neutral-H_2O} = 1.51$ and $\beta_{zwitterion-H_2O} = 1.44$.

Both damping models reproduce the counterpoise-corrected binding energy gap to within 3−3.5 kJ/mol. The three-parameter model performs 0.4 kJ/mol better, albeit at the undesirable expense of additional parameters. Once again, the AIFF parametrized in the aug-cc-pVDZ basis set performs slightly worse, predicting an energy gap that is 1.5 kJ/mol larger than the Sadlej AIFF gap. In this difficult system, counterpoise-corrected HMBI/AIFF, EE-PA, and binary+ESP all produce the correct qualitative trend, but they each predict an energy gap that is several kJ/mol to large. In contrast, the HMBI/HF predicted gap differs from the full MP2 one by only 0.5 kJ/mol. This discrepancy may stem from limitations in describing higher-order multipole induction effects in the simple classical models.

4.5. Approximating the AIFF Parameters. Finally, we briefly examine the possibility that the AIFF parameters can be approximated using the distributed multipoles and polarizabilities computed at the equilibrium geometry of a species. This would eliminate the need to compute these properties repeatedly for each monomer structure.

For the water clusters in Test Set A, using the multipoles and polarizabilities for water determined at its equilibrium geometry moderately degrades the results. It produces a mean error, standard deviation, and a range of errors of 0.18, 0.09, and 0.36, respectively. The geometries of individual water molecules do not differ too much in these clusters, so this result is unsurprising.

Formamide molecules, on the other hand, exhibit greater flexibility in our test sets. As can be seen for Test Set E in Table 5 and Figure 4, approximating the moments/polarizabilities with their equilibrium geometry values severely degrades the quality of the HMBI/AIFF approximation. The mean errors increase from −0.04 to 0.12 kJ/mol per monomer, while the range of errors more than doubles, from
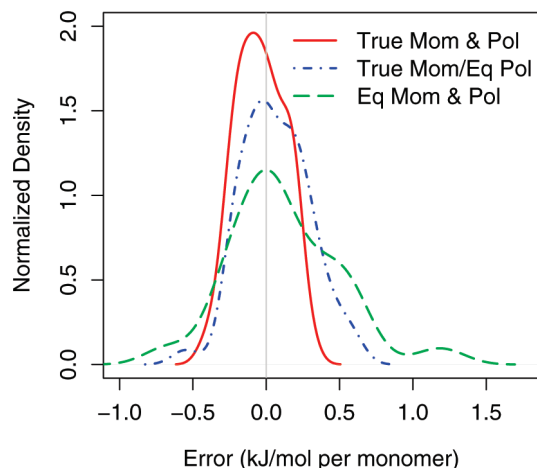
Figure 4. Distribution of errors relative to RI-MP2/aug-cc-pVTZ results as a function of the multipole moments and polarizabilities used in the AIFF/β_{opt} force field for the binding energies in 51 formamide octamer clusters (Test Set E).

Table 5. The Effect of Replacing the True Distributed Multipoles and Polarizabilities in the AIFF/β_{opt} with Those Computed at the Equilibrium Structure of an Isolated Formamide Molecule Using 51 $(HCONH_2)_8$ Configurations (Test Set E)[a]

	true moments and polarizabilities	true moments and equilib. polarizabilities	equilib. moments and polarizabilities
mean	−0.04	0.06	0.12
std dev	0.17	0.23	0.38
range	0.71	1.12	1.97

[a] Errors are given in kJ/mol per monomer.

0.71 to 1.97 kJ/mol per monomer. In contrast, using the equilibrium polarizabilities with the true distributed multipole moments is a much better approximation, with the mean error and range increasing to only 0.06 and 1.12 kJ/mol per monomer, respectively.

Physically, the polarizabilities are essentially an atomic property, even if the specific localization procedure is geometry dependent. So one expects that they will not vary too much with moderate conformational changes in the molecule. On the other hand, the density will likely be more sensitive to the details of the geometry and orbital overlap between atoms. This approximation is also computationally beneficial: calculating polarizabilities by solving the coupled Kohn–Sham equations requires substantially more effort than fitting distributed multipoles to the electron density. Of course, in systems containing many monomers, the QM calculation of the two-body effects will still be the computationally dominant step. In any case, these results make it clear that one should compute both the polarizabilities and multipoles for each molecule if very accurate results are needed. Similar results have been observed in developing more general force fields for flexible molecules.[122]

5. Conclusions

HMBI approximations represent interesting QM/MM models for studying large systems of interacting molecules at very low computational cost. It combines a quantum mechanical treatment of monomers and their pairwise interactions with a classical polarizable force-field approximation for many-body induction effects. Key advantages of HMBI include its quantum/classical partitioning based on the type of intermolecular interaction, its approximate inclusion of all orders in the many-body interaction expansion, and its ability to reproduce full quantum mechanical calculations accurately at much lower computational cost. The biggest weakness of an HMBI-type model has been its need for a parametrized polarizable force field. In this paper, we largely eliminate this weakness and demonstrate that very good HMBI results can be obtained when the force field is constructed on-the-fly from first-principles quantum mechanical calculations on the monomers.

We tested the model on water, formamide, hydrogen fluoride, and mixed glycine–water clusters, all of which exhibit strong many-body effects and test it strenuously. In each case, HMBI with the ab initio polarizable force field performed well. We also demonstrated that one can tolerably approximate the atomic polarizabilities by computing them at a single (or perhaps a few) representative geometries.

The performance of the HMBI/AIFF model demonstrated here is competitive with the related EE-PA and self-consistently embedded binary interaction methods. Using a supermolecular HF calculation to approximate the many-body effects[23,25,71] is significantly more accurate than any of the other approximations considered here, but it becomes cost-prohibitive for larger systems. The HMBI/AIFF formulation exhibits advantages and disadvantages compared to these other methods. The expense of computing distributed polarizabilities is probably similar to the cost of determining self-consistent embedding charges for the binary interaction method, for example. Both of those methods are more expensive than EE-PA, which uses simple fixed B3LYP/6-31G* point charges. While the cost of computing the distributed polarizabilities to evaluate the force field is nontrivial, there are only a linear number of monomers, versus a locally quadratic number of two-body interactions (assuming local truncations are applied, though that is not done here). Therefore, the cost of evaluating the QM two-body interactions will dominate in larger systems.

Implementing software routines to parametrize the AIFF requires more effort than does the implementation of the other methods. Nuclear gradients of the AIFF require derivatives of the multipole moments and polarizabilities, which are also more complicated to implement. On the other hand, the use of point charges in EE-PA and the self-consistent binary interaction method introduces additional computational complexity. The point charges cause the gradient of each one-body and two-body term to depend on all three N_{atoms} coordinates of the entire system, instead of depending only on the coordinates of the atoms of a particular monomer or dimer. The implementation and efficiency of HMBI/AIFF nuclear gradients will be addressed in a future study. All of the methods examined here are very promising, and further investigation is needed to understand their strengths and weaknesses better.

The errors in HMBI can be attributed primarily to (1) the limitations of the classical multipolar description of induction effects and (2) the neglect of many-body dispersion and

exchange−repulsion effects. Describing these latter effects accurately and inexpensively remains a challenge. The largest outstanding difficulty in the former is the need to dampen short-range multipolar interactions. In our tests, we found it necessary to treat this damping factor as an empirical adjustable parameter. On the other hand, optimizing this parameter is relatively straightforward compared to the more general problem of force-field parametrization, and it can in principle be done by running several small cluster benchmark calculations to optimize the damping factor(s) before proceeding with more elaborate studies, just as we did in the glycine−water cluster example.

The procedure used here to compute the distributed polarizabilities can be extended readily to monomers containing a few dozen atoms. Furthermore, the computational cost of evaluating the multitude of quantum mechanical two-body interaction energies will typically dominate over the cost of constructing the force field, at least for systems containing many interacting molecules. Given its low cost and good accuracy, HMBI holds much promise for studying a wide range of interesting condensed-phase chemical systems, and we plan to report on such applications in the near future.

Supporting Information Available: Tables containing the RI-MP2 binding energies and many-body contributions for each method. Geometries for Test Sets B, C, F, and G. This material is available free of charge via the Internet at http://pubs.acs.org.

References

(1) Jeziorski, B.; Moszynski, R.; Szalewicz, K. *Chem. Rev.* **1994**, *94*, 1887–1930.

(2) Podeszwa, R.; Szalewicz, K. *J. Chem. Phys.* **2007**, *126*, 194101.

(3) Kitaura, K.; Sawai, T.; Asada, T.; Nakano, T.; Uebayasi, M. *Chem. Phys. Lett.* **1999**, *312*, 319–324.

(4) Kitaura, K.; Ikeo, E.; Asada, T.; Nakano, T.; Uebayasi, M. *Chem. Phys. Lett.* **1999**, *313*, 701–706.

(5) Fedorov, D. G.; Kitaura, K. *J. Phys. Chem. A* **2007**, *111*, 6904–6914.

(6) Gordon, M. S.; Freitag, M. A.; Bandyopadhyay, P.; Jensen, J. H.; Kairys, V.; Stevens, W. J. *J. Phys. Chem. A* **2001**, *105*, 293–307.

(7) Gordon, M. S.; Slipchenko, L. V.; Li, H.; Jensen, J. H. *Annu. Rep. Comput. Chem.* **2007**, *3*, 177.

(8) Dahlke, E. E.; Truhlar, D. G. *J. Chem. Theory Comput.* **2007**, *3*, 46–53.

(9) Hirata, S. *J. Chem. Phys.* **2008**, *129*, 204104.

(10) Hirata, S.; Valiev, M.; Dupuis, M.; Xantheas, S. S.; Sugiki, S.; Sekino, H. *Mol. Phys.* **2005**, *103*, 2255–2265.

(11) Kamiya, M.; Hirata, S.; Valiev, M. *J. Chem. Phys.* **2008**, *128*, 074103.

(12) Dykstra, C. E. *J. Am. Chem. Soc.* **1989**, *111*, 6168–6174.

(13) Ganourgakis, G. S.; Xantheas, S. S. *J. Phys. Chem. A* **2006**, *110*, 4100–4106.

(14) Ganourgakis, G. S.; Xantheas, S. S. *J. Chem. Phys.* **2008**, *128*, 074506.

(15) Cisneros, G. A.; Darden, T. A.; Gresh, N.; Reinhardt, P.; Parisel, O.; Pilme, J.; Piquemal, J.-P. Design of next generation polarizable force fields from ab initio computations: Beyond point charges. In *Multi-scale Quantum Models for Biocatalysis: Modern Techniques and Applications*; Springer-Verlag: London, 2009; pp 137−172.

(16) Bukowski, R.; Szalewicz, K.; Groenenboom, G. C.; van der Avoird, A. *Science* **2007**, *315*, 1249.

(17) Bukowski, R.; Szalewicz, K.; Groenenboom, G. C.; van der Avoird, A. *J. Chem. Phys.* **2008**, *128*, 094314.

(18) Wang, Y.; Shepler, B. C.; Braams, B. J.; Bowman, J. M. *J. Chem. Phys.* **2009**, *131*, 054511.

(19) Xantheas, S. S. *J. Chem. Phys.* **1994**, *100*, 7523–7534.

(20) Tauer, T. P.; Sherrill, C. D. *J. Phys. Chem. A* **2005**, *109*, 10475–10478.

(21) Christie, R. A.; Jordan, K. D. *Struct. Bonding (Berlin)* **2005**, *116*, 27–41.

(22) Pedulla, J. M.; Kim, K.; Jordan, K. D. *Chem. Phys. Lett.* **2006**, *291*, 78–84.

(23) Tschumper, G. S. *Chem. Phys. Lett.* **2006**, *427*, 185–191.

(24) Elsohly, A. M.; Shaw, C. L.; Guice, M. E.; Smith, B. D.; Tschumper, G. S. *Mol. Phys.* **2007**, *105*, 2777–2782.

(25) Paulus, B.; Rosciszewski, K.; Gaston, N.; Schwerdtfeger, P.; Stoll, H. *Phys. Rev. B* **2004**, *70*, 165106.

(26) Hermann, A.; Schwerdtfeger, P. *Phys. Rev. Lett.* **2008**, *101*, 183005.

(27) Steiner, T. *Angew. Chem., Int. Ed.* **2002**, *41*, 48–76.

(28) Beran, G. J. O. *J. Chem. Phys.* **2009**, *130*, 164115.

(29) Ren, P.; Ponder, J. W. *J. Phys. Chem. B* **2003**, *107*, 5933–5947.

(30) Tabacchi, G.; Mundy, C. J.; Hutter, J.; Parrinello, M. *J. Chem. Phys.* **2002**, *117*, 1416–1433.

(31) Izvekov, S.; Parrinello, M.; Burnham, C. J.; Voth, G. A. *J. Chem. Phys.* **2004**, *120*, 10896–10913.

(32) Masia, M. *J. Chem. Phys.* **2008**, *128*, 184107.

(33) Bukowski, R.; Szalewicz, K.; Groenenboom, G. C.; van der Avoird, A. *Science* **2007**, *315*, 1249–1252.

(34) Stone, A. J.; Misquitta, A. J. *Int. Rev. Phys. Chem.* **2007**, *26*, 193–222.

(35) Popelier, P. L. A.; Rafat, M. *Chem. Phys. Lett.* **2003**, *376*, 148–153.

(36) Rafat, M.; Popelier, P. L. A. *J. Chem. Phys.* **2005**, *123*, 204103.

(37) Darley, M. G.; Handley, C. M.; Popelier, P. L. A. *J. Chem. Theory Comput.* **2008**, *4*, 1435–1448.

(38) Plattner, N.; Bandi, T.; Doll, J. D.; Freeman, D. L.; Meuwly, M. *Mol. Phys.* **2008**, *106*, 1675–1684.

(39) Mas, E. M.; Bukowski, R.; Szalewicz, K. *J. Chem. Phys.* **2003**, *118*, 4404–4413.

(40) Hodges, M. P.; Stone, A. J.; Xantheas, S. S. *J. Phys. Chem. A* **1997**, *101*, 9163–9168.

(41) Milet, A.; Moszynski, R.; Wormer, P. E. S.; van der Avoird, A. *J. Phys. Chem. A* **1999**, *103*, 6811–6819.

(42) Halgren, T. A.; Damm, W. *Curr. Opin. Struct. Biol.* **2001**, *11*, 236–242.

(43) Ponder, J. W.; Case, D. A. *Adv. Protein Chem.* **2003**, *66*, 27–85.

(44) Warshel, A.; Kato, M.; Pisliakov, A. V. *J. Chem. Theory Comput.* **2007**, *3*, 2034–2045.

(45) Stone, A. J. *The Theory of Intermolecular Forces*; Clarendon Press: Oxford, 2002.

(46) Misquitta, A. J.; Stone, A. J. *J. Chem. Theory Comput.* **2008**, *4*, 7–18.

(47) Misquitta, A. J.; Stone, A. J.; Price, S. L. *J. Chem. Theory Comput.* **2008**, *4*, 19–32.

(48) Stone, A. J. *Chem. Phys. Lett.* **1981**, *83*, 233–239.

(49) Stone, A. J.; Alderton, M. *Mol. Phys.* **1985**, *56*, 1047–1064.

(50) Stone, A. J. *J. Chem. Theory Comput.* **2005**, *1*, 1128–1132.

(51) Misquitta, A. J.; Welch, G. W. A.; Stone, A. J.; Price, S. L. *Chem. Phys. Lett.* **2008**, *456*, 105–109.

(52) Thole, B. T. *Chem. Phys.* **1981**, *59*, 341–350.

(53) Miller, K. J. *J. Am. Chem. Soc.* **1990**, *112*, 8543–8551.

(54) LeSueur, C. R.; Stone, A. J. *Mol. Phys.* **1993**, *78*, 1267–1291.

(55) Piquemal, J.-P.; Perera, L.; Cisneros, G. A.; Ren, P.; Pedersen, L. G.; Darden, T. A. *J. Chem. Phys.* **2006**, *125*, 054511.

(56) Masia, M.; Probst, M.; Rey, R. *Chem. Phys. Lett.* **2006**, *420*, 267–270.

(57) Slipchenko, L. V.; Gordon, M. S. *Mol. Phys.* **2009**, *107*, 999–1016.

(58) Tang, K. T.; Toennies, J. P. *J. Chem. Phys.* **1984**, *80*, 3726–3741.

(59) Dunlap, B. I. *J. Chem. Phys.* **1983**, *78*, 3140–3142.

(60) Feyereisen, M. W.; Fitzgerald, G.; Komornicki, A. *Chem. Phys. Lett.* **1993**, *208*, 359–363.

(61) Eichkorn, K.; Treutler, O.; Öhm, H.; Häser, M.; Ahlrichs, R. *Chem. Phys. Lett.* **1995**, *240*, 283–289.

(62) Dunning, T. H., Jr. *J. Chem. Phys.* **1989**, *90*, 1007–1023.

(63) Weigend, F.; Köhn, A.; Hättig, C. *J. Chem. Phys.* **2002**, *116*, 3175–3183.

(64) Liang, W. Z.; Head-Gordon, M. *J. Phys. Chem. A* **2004**, *108*, 3206–3210.

(65) Steele, R. P.; Distasio, R. A., Jr.; Shao, Y.; Kong, J.; Head-Gordon, M. *J. Chem. Phys.* **2006**, *125*, 074108.

(66) Steele, R. P.; Distasio, R. A., Jr.; Head-Gordon, M. *J. Chem. Theory Comput.* **2009**, *5*, 1560–1572.

(67) Chalasinski, G.; Szczesniak, M. M.; Kendall, R. A. *J. Chem. Phys.* **1994**, *101*, 8860–8869.

(68) Jurecka, P.; Sponer, J.; Cerný, J.; Hobza, P. *Phys. Chem. Chem. Phys.* **2006**, *8*, 1985–1993.

(69) Podeszwa, R. *J. Phys. Chem. A* **2008**, *112*, 8884–8885.

(70) Shao, Y.; et al. *Phys. Chem. Chem. Phys.* **2006**, *8*, 3172–3191.

(71) Dahlke, E. E.; Truhlar, D. G. *J. Chem. Theory Comput.* **2007**, *3*, 1342–1348.

(72) Distasio, R. A., Jr.; Jung, Y.; Head-Gordon, M. *J. Chem. Theory Comput.* **2005**, *1*, 862–876.

(73) Ponder, J. W. TINKER v4.2, 2004, http://dasher.wustl.edu/tinker/, accessed Jan 23, 2008.

(74) Misquitta A. J. Stone, A. J. CamCasp v5.2 (2008), http://www-stone.ch.cam.ac.uk/programs.html#CamCASP, accessed Oct 16, 2008.

(75) DALTON, a molecular electronic structure program, Release 2.0 (2005), http://www.kjemi.uio.no/software/dalton/dalton.html. Accessed October 16, 2008.

(76) Adamo, C.; Barone, V. *J. Chem. Phys.* **1999**, *110*, 6158.

(77) Joshipura, K. N.; Gangopadhyay, S.; Limbachiya, C. G.; Vinodkumar, M. *J. Phys.: Conf. Ser.* **2007**, *80*, 012008.

(78) Faubel, M.; Steiner, B.; Toennies, J. P. *J. Electron Spectrosc. Relat. Phenom.* **1998**, *95*, 159–169.

(79) Bruna, P. J.; Grein, F. *J. Chem. Phys. A* **2006**, *110*, 4906–4917.

(80) Tozer, D. J.; Handy, N. C. *J. Chem. Phys.* **1998**, *109*, 10180–10189.

(81) Tozer, D. J. *J. Chem. Phys.* **2000**, *112*, 3507–3515.

(82) Dullweber, A. Engkvist, O. Fraschini, E. Hodges, M. P. Meredith, A. Popelier, P. L. A. Wales, D. J. Stone, A. J. Orient v4.6 (2006) http://www-stone.ch.cam.ac.uk/programs.html#Orient, accessed Oct 16, 2008.

(83) Boys, S. F.; Bernardi, F. *Mol. Phys.* **1970**, *19*, 553–566.

(84) Laasonen, K.; Parrinello, M.; Car, R.; Lee, C.; Vanderbilt, D. *Chem. Phys. Lett.* **1993**, *207*, 208–213.

(85) Kim, J.; Majumdar, D.; Lee, H. M.; Kim, K. S. *J. Chem. Phys.* **1999**, *110*, 9128–9134.

(86) Kozmutza, C.; Kryachko, E. S.; Tfirst, E. *J. Mol. Struct. (THEOCHEM)* **2000**, *501*, 435–444.

(87) Day, P.; Pachter, R.; Gordon, M. S.; Merrill, G. N. *J. Chem. Phys.* **2000**, *112*, 2063–2073.

(88) Upadhyay, D. M.; Shukla, M. K.; Mishra, P. C. *Int. J. Quantum Chem.* **2001**, *81*, 90–104.

(89) Bulusu, S.; Yoo, S.; Apra, E.; Xantheas, S.; Zeng, X. C. *J. Phys. Chem. A* **2006**, *110*, 11781–11784.

(90) Olson, R. M.; Bentz, J. L.; Kemdall, R. A.; Schmidt, M. W.; Gordon, M. S. *J. Chem. Theory Comput.* **2007**, *3*, 1312–1328.

(91) Maheshwary, S.; Patel, N.; Sathyamurthy, N.; Kulkarni, A. D.; Gadre, S. R. *J. Phys. Chem. A* **2001**, *105*, 10525–10537.

(92) Maheshwary, S.; Patel, N.; Sathyamurthy, N.; Kulkarni, A. D.; Gadre, S. R. *J. Phys. Chem. A* **2001**, *105*, 10525–10537.

(93) Geometries obtained from the Cambridge Cluster Database. Wales, D. J.; Doye, J. P. K.; Dullweber, A.; Hodges, M. P.; Naumkin F. Y.; Calvo, F.; Hernandez-Rojas, J.; Middleton, T. F. http://www-wales.ch.cam.ac.uk/CCD.html, accessed Aug 21, 2008.

On-the-Fly ab Initio Force Field Parametrization

J. Chem. Theory Comput., Vol. 6, No. 1, 2010 **167**

(94) Ohno, K.; Okimura, M.; Akai, N.; Katsumoto, Y. *Phys. Chem. Chem. Phys.* **2005**, *7*, 3005.

(95) Dahlke, E. E.; Olson, R. M.; Leverentz, H. R.; Truhlar, D. G. *J. Phys. Chem. A* **2008**, *112*, 3976–3984.

(96) Bates, D. M.; Tschumper, G. S. *J. Phys. Chem. A* **2009**, *113*, 3555–3559.

(97) Valiron, P.; Mayer, I. *Chem. Phys. Lett.* **1997**, *275*, 46–55.

(98) Sadlej, A. J. *Collect. Czech. Chem. Commun.* **1988**, *53*, 1995–2016.

(99) Sadlej, A. J. *Theor. Chim. Acta* **1991**, *79*, 123–140.

(100) Suhai, S. *J. Chem. Phys.* **1995**, *103*, 7030–7039.

(101) Bende, A.; Vibok, A.; Halasz, G. J.; Suhai, S. *Int. J. Quantum Chem.* **2001**, *84*, 617–622.

(102) Fogarasi, G.; Szalay, P. G. *J. Phys. Chem. A* **1997**, *101*, 1400–1408.

(103) Bellissent-Funel, M.-C.; Nasr, S.; Bosio, L. *J. Chem. Phys.* **1997**, *106*, 7913–7919.

(104) Nasr, S.; Bosio, L. *J. Chem. Phys.* **1998**, *108*, 2297–2301.

(105) Cabaleiro-Lago, E. M.; Rios, M. A. *J. Chem. Phys.* **1999**, *110*, 6782–6791.

(106) Tsuchida, E. *J. Chem. Phys.* **2004**, *121*, 4740–4746.

(107) Mardyukov, A.; Sanchez-Garcia, E.; Rodziewicz, P.; Doltsinis, N. L.; Sander, W. *J. Phys. Chem. A* **2007**, *111*, 10552–10561.

(108) Pine, A. S.; Lafferty, W. L. *J. Chem. Phys.* **1983**, *78*, 2154–2162.

(109) Andrews, L.; Bondybev, V. E.; English, J. H. *J. Chem. Phys.* **1984**, *81*, 3452–3457.

(110) Micheal, D. W.; Lisy, J. M. *J. Chem. Phys.* **1986**, *85*, 2528–2538.

(111) Guedes, R. C.; do Couto, P. C.; Costa Cabral, B. J. *J. Chem. Phys.* **2003**, *118*, 1272–1281.

(112) Hendricks, S. B.; Wulf, O.; Hilbert, G. E.; Liddell, U. *J. Am. Chem. Soc.* **1936**, *58*, 1991–1996.

(113) Quack, M.; Schmitt, U.; Suhm, M. A. *Chem. Phys. Lett.* **1993**, *208*, 446–452.

(114) del Bene, J. E.; Person, W. B.; Szczepaniak, K. *J. Phys. Chem.* **1995**, *99*, 10705–10707.

(115) Hirata, S.; Iwata, S. *J. Phys. Chem. A* **1998**, *102*, 8426–8436.

(116) Hodges, M. P.; Stone, A. J.; Lago, E. C. *J. Phys. Chem. A* **1998**, *102*, 2455–2465.

(117) Halkier, A.; Klopper, W.; Helgaker, T.; Jørgensen, P.; Taylor, P. R. *J. Chem. Phys.* **1999**, *111*, 9157–9167.

(118) Rankin, K. N.; Boyd, R. J. *J. Comput. Chem.* **2001**, *22*, 1590–1597.

(119) Rincon, L.; Almeida, R.; Garcia-Aldea, D.; y Riega, H. D. *J. Chem. Phys.* **2001**, *114*, 5552–5561.

(120) Raynaud, C.; Maron, L.; Jolibois, F.; Daudey, J.-P.; Esteves, P. M.; Ramirez-Solis, A. *Chem. Phys. Lett.* **2005**, *414*, 161–165.

(121) Aviles, M. W.; Gray, P. T.; Curotto, E. *J. Chem. Phys.* **2006**, *124*, 174305.

(122) Murdachaew, G.; Szalewicz, K. *Faraday Discuss.* **2001**, *118*, 121–142.

JCTC Journal of Chemical Theory and Computation

Accurate Intermolecular Interaction Energies from a Combination of MP2 and TDDFT Response Theory

Michal Pitoňák*[,†,‡] and Andreas Heßelmann*[,§]

Institute of Organic Chemistry and Biochemistry, Academy of Sciences of the Czech Republic, v. v. i., Flemingovo nám. 2, 166 10 Praha 6, Czech Republic, Department of Physical and Theoretical Chemistry, Faculty of Natural Sciences, Comenius University, Mlynská Dolina, 842 15 Bratislava 4, Slovak Republic, and Lehrstuhl für Theoretische Chemie, Universität Erlangen-Nürnberg, Egerlandstrasse 3, D-91058 Erlangen

Abstract: A new method is presented that improves the supermolecular second-order Møller–Plesset (MP2) method for dimer systems with strong dispersion interactions while preserving the generally good performance of MP2 for other types of intermolecular interactions, e.g., hydrogen-bonded systems. This is achieved by adding a correction term to the supermolecular MP2 energy that is determined using time-dependent density functional (TDDFT) response theory and that accounts for the error of the dispersion energy contained in the supermolecular MP2 method. It is shown for the S22 database set of noncovalent complexes and some potential energy curves of noncovalent bound aromatic dimers that the approach gives strong improvements over MP2 if compared to coupled-cluster singles, doubles, and perturbative triples (CCSD(T)) reference energies. An efficient computer implementation of the method is presented that is shown to scale only with the fourth power of the system size and thus leads only to a slightly higher computational cost than that of the supermolecular MP2 itself.

1. Introduction

Highly accurate interaction energies of noncovalent bound molecular complexes and clusters are of high interest in the wide community of both computational chemists and experimentalists. However, to achieve the desired, so-called chemical accuracy (~1 kcal/mol) with present wave-function theory (WFT) computational methods is often a very demanding task. For notoriously known problematic interaction types, such as $\pi-\pi$ stacking, highly sophisticated theories such as CCSD(T) have to be applied to achieve such an accuracy. But even with ever improving computer technologies and algorithms (as implemented in various computer programs such as MOLCAS,[1] PSQ,[2] GAMESS,[3] ACES3,[4] etc.), an $\mathcal{N}^7$ scaling of the CCSD(T) method with

the system size allows the applicability of this method to be widened very slowly. According to a recently published series of benchmark calculations of noncovalent complexes,[5–8] CCSD(T) interaction energies close to the complete basis set (CBS) limit can nowadays be obtained for systems with about 30−50 second row atoms and hydrogen. Though this was just a dream a few years ago, such complexes are still too small to serve even as reliable models in biochemistry, nanoclusters, etc. To extend the investigated systems size beyond models to a "real-life" dimension is clearly impossible. Approximations of the CCSD(T) method within the strict WFT formalism for the calculation of noncovalent interactions is hardly possible. Following the series of increasing order of perturbation theory, i.e., second (MP2), third (MP3, MP4(SD), MP4(SDQ), CCSD), and fourth (MP4, CCSD(T)), none of these methods lower than fourth order is reliable enough.[9] For the problematic types of noncovalent interactions, this series often converges in an oscillatory way, third-order "overcorrecting" errors of the second order, etc. According to this, one could conclude that the proper

* To whom correspondence should be addressed. E-mail: pitonak@fns.uniba.sk (M.P.); andreas.hesselmann@chemie.uni-erlangen.de (A.H.).

† Academy of Sciences of the Czech Republic.

‡ Comenius University.

§ Universität Erlangen-Nürnberg.

description of noncovalent interactions in WFT theory necessarily requires at least an $\mathcal{N}^7$ scaling algorithm. This is clearly unpractical for several reasons, one of which is the long-range nature of the intermolecular dispersion contribution that asymptotically decays as R^{-6} with the distance (R) of the interacting fragments.

A possible conceptual remedy lies in the (fourth and higher order) approaches based on the idea of locality of the electron-correlation, which are, however, still not accurate, robust, or "black-box" enough. A major problem in the application of these methods on noncovalent interaction is that certain parts of the interaction energy, mainly the dispersion, is certainly not short-ranged nor can be approximated accurately enough by lower-order scaling methods, as already mentioned. Currently more practical, but computationally still quite expensive, options seem to be the empirical, $\mathcal{N}^6$ scaling MP2.5[9] and SCS-CCSD methods.[10] Though being quite accurate, as demonstrated in several benchmark calculations,[8–11] chemical accuracy is certainly not guaranteed, and error propagation with increasing molecular complex size is, especially for the latter one, SCS-CCSD, not known yet. Empirical $\mathcal{N}^5$ scaling methods, mostly based on the idea of SCS-MP2,[12] such as SCSN-MP2,[13] SCS(MI)-MP2,[14] or JMP2[15] are surprisingly accurate and have a much lower cost than the methods mentioned above, but as they are parametrized for only certain interaction types and molecular complex dimensions, their performance outside their training sets can be quite unpredictable.

A different approach would be to leave the WFT concept and follow the, in general computationally much more economic, route of density functional theory (DFT). Conventional DFT based on the local density approximation (LDA) or the generalized gradient approximation (GGA) does not account, however, for the important long-range correlation or dispersion contribution to the intermolecular interaction energy. The reason for this is that these density functionals are only locally dependent on the density and its gradients and therefore are not able to describe electron correlations between remote parts of the molecular complex. As this failure of standard DFT is widely known, a number of possible extensions have been developed in the past few years.[16–21]

A deeper investigation of the reasons of failure of the otherwise often quite accurate MP2 method for $\pi-\pi$ stacked complexes was done by Cybulski and Lytle[22] and Hesselmann.[23] The source of error was identified to be the 10–20% overestimated uncoupled Hartree–Fock (UCHF) dispersion energy component of the supermolecular MP2 interaction energy. In both works the same idea of substituting the inaccurate UCHF dispersion energy by the more accurate dispersion energy obtained from either scaled time-dependent Hartree–Fock (TDHF)[22] or time-dependent DFT (TDDFT)[23] has been proposed. Note that this approach is related to recent developments of new types of exchange-correlation functionals that are based on the random phase approximation (RPA),[24–26] because the RPA method itself is known to account for long-range correlation energies on a coupled Hartree–Fock level.[27] Both the approach from ref 23 and

from ref 22 seems to alleviate the problem of the overestimation of the dispersion contribution in the problematic complexes. It was found that the TDDFT-based approach is most accurate if an exchange-only potential from the localized Hartree–Fock method[28] combined with an exchange-only adiabatic local density approximation (ALDA) kernel is employed. In both works, results for several test cases, such as rare-gas dimers, hydrogen-bonded (H-bonded) complexes of small diatomic molecules, and DNA base pairs, were presented, strongly validating this approach. Similar to this approach, Tkatchenko et al.[29,30] recently proposed the so-called MP2+ΔvdW method. The main idea is to improve the long-range interaction MP2 potential by using the series of $\Delta C_n R^{-n}$ (ΔC_6, ΔC_8, ..., being differences between the MP2 and the "accurate" dispersion coefficient for $n = 6, 8, ...$; R being the distance between the interacting molecules) in combination with a proper damping function for short distances. This approach was shown also to be also quite accurate and can, in contrast to the method presented in this work, also be applied to study intramolecular dispersion effects if the scheme presented in refs 29 and 30 is extended by deriving intermolecular dispersion coefficients from atomic contributions. However, as with corresponding DFT+dispersion methods, it relies on an empirically determined damping function which has to reduce the double counting of correlation effects for short intermonomer distances. Moreover, in the MP2+ΔvdW method, the multipolar expansion of the long-range dispersion energy is restricted to the C_6 and C_8 terms and will therefore not be accurate for short intermonomer distances.

The main goal of this work is to extend the tests of the new MP2 "coupled" (MP2C) approach from ref 23 to the systematic S22 database of noncovalent complexes of Hobza et al.,[31] as well as to several challenging noncovalent complexes, such as the benzene dimer in several conformations, the H-bonded and stacked uracil dimer, and the methyl-adenine···methyl-thymine dimer (mAmT), for which highly accurate CCSD(T) benchmark interaction energies were published.[5–8] Because the balanced performance, not only of the equilibrium geometries but over a wide area of the potential energy surface (PES), is important, we selected a few cuts through the PES, i.e., potential energy curves (PEC), of the benzene dimer and nitrogen-substituted heterocyclic derivatives of the benzene dimer as well. Finally, we will also present an efficient implementation of the correction scheme, due to which the overall MP2C method is computationally by 1 order of magnitude less demanding than the supermolecular MP2 itself.

2. Method

The supermolecular MP2 interaction energy can be obtained from the energy difference:

$$E_{\text{int}}^{\text{MP2}} = E_{\text{AB}}^{\text{MP2}} - E_{\text{A}}^{\text{MP2}} - E_{\text{B}}^{\text{MP2}} \tag{1}$$

where $E_{\text{AB}}^{\text{MP2}}$ is the total energy of the dimer and $E_{\text{A, B}}^{\text{MP2}}$ are the monomer energies of the two systems A and B. Note that the use of eq 1 introduces the so-called basis set superposition error (BSSE) if finite basis sets are used. An effective

elimination of this error can however be achieved by using the Boys–Bernardi counterpoise correction[32] in which all individual energy calculations are done using the same (dimer centered) basis set.

Using intermolecular perturbation theory, it was observed a while ago[27,33,34] that the supermolecular MP2 interaction energy of eq 1 contains certain correlation terms that are of second order in the intermolecular interaction, namely the uncoupled Hartree–Fock (UCHF) dispersion energy, the corresponding Hartree–Fock exchange-dispersion energy, and a deformation-correlation term. The exchange-dispersion contribution stems from exchange interactions between the monomers when the monomer distance decreases and vanishes for larger distances while the deformation correlation term includes exchange-penetration, induction, and charge-transfer interactions. The uncoupled Hartree–Fock dispersion energy can exactly be written in terms of the monomer Hartree–Fock orbitals and orbital energies:

$$E_{\text{disp}}^{(2)}(\text{UCHF}) = -4 \sum_{ia,jb} \frac{|(i^A a^A | j^B b^B)|^2}{\varepsilon_a^A - \varepsilon_i^A + \varepsilon_b^B - \varepsilon_j^B} \quad (2)$$

where A, B label monomer A or B, indices i, j denote occupied orbitals, a, b denote unoccupied orbitals, $(ia|jb)$ is a two-electron repulsion integral in chemist's notation and ε_i is the orbital energy of orbital i. Note that closed-shell formalism will be used throughout. Using the Casimir–Polder integral transform, it can easily be seen that eq 2 can be rewritten as:

$$E_{\text{disp}}^{(2)}(\text{UCHF}) =$$
$$-\frac{1}{2\pi} \int_0^\infty d\omega \int d\mathbf{r}_1 d\mathbf{r}_2 d\mathbf{r}_3 d\mathbf{r}_4 \chi_0^A(\mathbf{r}_1, \mathbf{r}_3, \omega) \chi_0^B(\mathbf{r}_2, \mathbf{r}_4, \omega) \frac{1}{r_{12}} \frac{1}{r_{34}} \quad (3)$$

where the ω-integral runs over imaginary frequencies ω and χ_0^A and χ_0^B are the uncoupled Hartree–Fock response functions of monomers A and B given by:

$$\chi_0(\mathbf{r}_1, \mathbf{r}_2, \omega) = 4 \sum_{ia} \frac{\varepsilon_{ia}}{\varepsilon_{ia}^2 + \omega^2} \phi_{ia}(\mathbf{r}_1) \phi_{ia}(\mathbf{r}_2) \quad (4)$$

with the occupied-virtual orbital products $\phi_{ia}(\mathbf{r}) = \phi_i(\mathbf{r})\phi_a(\mathbf{r})$ and $\varepsilon_{ia} = \varepsilon_a - \varepsilon_i$. It is well-known that the dispersion energy on the UCHF level (eq 2) often poorly describes the dispersion energy, e.g., in case of stacked $\pi-\pi$ interactions the uncoupled HF dispersion energy can overestimate the dispersion energy by 15% and more.[22,35,36] Because of this, in refs 22 and 23 a correction was introduced to the supermolecular MP2 interaction energy that replaces the implicitly included UCHF dispersion contribution with the coupled dispersion energy on the time-dependent Hartree–Fock (TDHF) or time-dependent density-functional (TDDFT) level. Using coupled TDDFT dispersion energies, the corrected MP2 interaction energies are thus obtained with:

$$E_{\text{int}}^{\text{MP2C}} = E_{\text{int}}^{\text{MP2}} - E_{\text{disp}}^{\text{UCHF}} + E_{\text{disp}}^{\text{TDDFT}} \quad (5)$$

with the acronym MP2C denoting MP2 'coupled'. The decomposition of the supermolecular MP2 energy into the uncoupled HF dispersion energy and a remainder term is based on an explicit decomposition of the total system into two subsystems. Because of this, the approach described in this work is not capable to improve the MP2 method also for intramolecular dispersion effects. The dispersion energies from the TDDFT method can be obtained from:

$$E_{\text{disp}}^{(2)}(\text{TDDFT}) =$$
$$-\frac{1}{2\pi} \int_0^\infty d\omega \int d\mathbf{r}_1 d\mathbf{r}_2 d\mathbf{r}_3 d\mathbf{r}_4 \chi_{\text{coup}}^A(\mathbf{r}_1, \mathbf{r}_3, \omega) \chi_{\text{coup}}^B(\mathbf{r}_2, \mathbf{r}_4, \omega) \frac{1}{r_{12}} \frac{1}{r_{34}} \quad (6)$$

where $\chi_{\text{coup}}^{A,B}$ denote the coupled response functions of monomers A and B which can be obtained from the Dyson-type equation:

$$\chi_{\text{coup}}(\mathbf{r}_1, \mathbf{r}_2, \omega) = \chi_0(\mathbf{r}_1, \mathbf{r}_2, \omega) +$$
$$\int d\mathbf{r}_3 d\mathbf{r}_4 \chi_0(\mathbf{r}_1, \mathbf{r}_3, \omega) W(\mathbf{r}_3, \mathbf{r}_4, \omega) \chi_{\text{coup}}(\mathbf{r}_4, \mathbf{r}_2, \omega) \quad (7)$$

with W denoting the interelectronic interaction operator comprising Coulomb, exchange, and correlation effects:

$$W(\mathbf{r}_1, \mathbf{r}_2, \omega) = \frac{1}{r_{12}} + f_{\text{xc}}(\mathbf{r}_1, \mathbf{r}_2, \omega) \quad (8)$$

where $1/r_{12}$ is the Coulomb-operator and f_{xc} is the exchange-correlation (xc) kernel that in general is nonlocal and frequency-dependent. In the framework of TDDFT the xc-kernel almost always is approximated by the adiabatic local density approximation (ALDA) kernel:

$$f_{\text{xc}}(\mathbf{r}_1, \mathbf{r}_2, \omega) \approx f_{\text{xc}}^{\text{ALDA}}(\mathbf{r}_1)\delta(\mathbf{r}_1 - \mathbf{r}_2) \quad (9)$$

that is the frequency-independent second derivative of the LDA xc-functional. Note that in order to obtain the coupled response functions via eq 7 an iterative procedure has to be used, as χ_{coup} appears on both sides of the equation.

It has to be noted here that the MP2C approach (eq 5) does not account for also correcting the corresponding exchange-dispersion energy term ($E_{\text{exch-disp}}^{(2)}$) that is also described on an uncoupled Hartree–Fock level only in the supermolecular MP2 method. The calculation of $E_{\text{exch-disp}}^{(2)}$ is much more computationally demanding than the calculation of the dispersion energy and would therefore lead to a much more expensive method if explicitly corrected in addition. However, the exchange-dispersion energy is generally much smaller than the dispersion energy itself and decreases exponentially for larger intermonomer distances. It has been found that in the intermediate distance range the ratio between coupled and uncoupled exchange-dispersion energies is about the same as with the corresponding dispersion energies. Because, in contrast to the dispersion energy, the $E_{\text{exch-disp}}^{(2)}$ contribution is always positive, it is found that in most cases the uncoupled exchange-dispersion energy overestimates the coupled one and leads to slightly higher total intermolecular interaction energies. This may be the reason why it has been found that the correction scheme of eq 5 works best if the TDDFT dispersion energy is calculated with an exchange-only approach and not by using more accurate exchange-correlation (xc) potentials and kernels for the calculation of the coupled response functions of eq 7.[23] The

Combination of MP2 and TDDFT Response Theory

J. Chem. Theory Comput., Vol. 6, No. 1, 2010 **171**

TDDFT dispersion energies on the exchange-only level usually are only slightly less negative than the uncoupled HF dispersion energies, while the corresponding dispersion energies from more accurate xc potentials deviate more from the uncoupled HF dispersion energies; see ref 23. Thus the error from the coupled exchange-only approximation in the dispersion energy is reduced by accounting for the exchange-dispersion contribution on an uncoupled Hartree−Fock level.

In the following, a density-fitting implementation for the calculation of uncoupled and coupled dispersion energies will be described that scales only with $\mathcal{N}^3 - \mathcal{N}^4$ with the molecular size $\mathcal{N}$ if local xc-kernels are used, and that therefore can be used for relatively large molecular systems. We start by transforming the uncoupled response function of eq 4 in a local auxiliary basis set g_P:

$$(\chi_0)_{PQ} = \sum_{ia} (P|\eta|ia)\lambda_{ia}(ia|\eta|Q) \tag{10}$$

where $\lambda_{ia} = 4\varepsilon_{ia}/(\varepsilon_{ia}^2 + \omega^2)$ and $(P|\eta|ia)$ is a three-index integral over an auxiliary basis function g_P (indices $P, Q, R, \ldots$ are labeling auxiliary basis functions) and the occupied-virtual orbital product ϕ_{ia}. The operator η conventionally is chosen as the Coulomb-operator: $\eta = 1/r_{12}$. The idea is now that the number of auxiliary basis functions N_{aux} that are used to span the occupied-virtual space is much smaller than the product of occupied times virtual orbitals: $N_{aux} \ll N_{occ} \times N_{virt}$. As the number of auxiliary functions only increases linearly with the system size, it can be shown that the computation of the matrix χ_0 scales only as $\mathcal{N}^4$. Using eq 10, the uncoupled dispersion energy of eq 3 can be written as:

$$E_{disp}^{UCHF} = -\frac{1}{2\pi} \int_0^\infty d\omega (\mathbf{S}^{-1}\boldsymbol{\chi}_0^A\mathbf{S}^{-1})\mathbf{J}(\mathbf{S}^{-1}\boldsymbol{\chi}_0^B\mathbf{S}^{-1})\mathbf{J} \tag{11}$$

where $S_{P,Q} = (P|\eta|Q)$ is the metric matrix in the auxiliary basis set and $J_{PQ} = (P|1/r_{12}|Q)$ is a two-indexed Coulomb matrix in the auxiliary basis. It can readily be seen that the computation of the dispersion energy using eq 11 scales only with $\mathcal{N}^3$.

In order to obtain the coupled response functions in the auxiliary basis set, the Dyson eq 7 is expanded in this basis and one obtains:

$$\boldsymbol{\chi}_{coup} = \boldsymbol{\chi}_0 + \boldsymbol{\chi}_0\mathbf{W}\boldsymbol{\chi}_{coup} \tag{12}$$

where χ_0 is defined in eq 10 and

$$W_{PQ} = \left(P\left|\frac{1}{r_{12}}\right|Q\right) + (P|f_{xc}|Q) \tag{13}$$

is the interaction operator in the auxiliary basis set. The solution to eq 12 can easily be calculated:

$$\boldsymbol{\chi}_{coup} = \boldsymbol{\chi}_0\mathbf{S}^{-1}\mathbf{W}(\mathbf{S} - \boldsymbol{\chi}_0\mathbf{S}^{-1}\mathbf{W})^{-1}\boldsymbol{\chi}_0 \tag{14}$$

requiring only an inversion of a matrix of the dimension N_{aux}. The dispersion energy can then be obtained analogous to eq 11 by:

$$E_{disp}^{TDDFT} = -\frac{1}{2\pi} \int_0^\infty d\omega (\mathbf{S}^{-1}\boldsymbol{\chi}_{coup}^A\mathbf{S}^{-1})\mathbf{J}(\mathbf{S}^{-1}\boldsymbol{\chi}_{coup}^B\mathbf{S}^{-1})\mathbf{J} \tag{15}$$

It has been found that the computation of the two-indexed xc-kernel integrals $(P|f_{xc}|Q)$ turns out to be the computational bottleneck in the calculation of the dispersion energy. As this contribution usually is determined using numerical quadrature, the total cost of its computation is $N_{grid} \times N_{aux}^2$ where N_{grid} is the number of grid points. Though the scaling is only of the order $\mathcal{N}^3$, the prefactor is rather high because N_{grid} usually has values of 10^5 to 10^6 for larger molecular systems. Therefore, here an alternative way to compute the xc-kernel integrals is presented that reduces the computational cost of numerical quadratures by introducing a gridfree-based algorithm identical to gridfree DFT methods introduced by Almlöf and others:[37−39] we start by determining the matrix $(P|\rho|Q)$ where ρ is the electron density and P, Q are auxiliary basis functions by:

$$M_{PQ} = (P|\rho|Q) = (PQ|R)[\mathbf{S}^{-1}]_{RS}(S|\eta|\mu\nu)\gamma_{\mu\nu} \tag{16}$$

with $(PQ|R)$ being a three-index overlap integral over three auxiliary functions, $\mathbf{S}^{-1}$ is the inverse of the metric, $(S|\eta|\mu\nu)$ is a three-index integral over one auxiliary function and two atomic-orbital (AO) basis functions, and $\gamma_{\mu\nu}$ is the density-matrix in the AO basis. The matrix $\mathbf{M}$ is then transformed into a new matrix $\tilde{\mathbf{M}}$ using an orthonormal basis set:

$$\tilde{\mathbf{M}}[\rho] = \mathbf{V}^T\mathbf{M}[\rho]\mathbf{V} \tag{17}$$

with $\mathbf{V}^T\mathbf{S}\mathbf{V} = \mathbf{1}$ (note that here $S_{PQ} = (P|\delta(\mathbf{r} - \mathbf{r}')|Q)$) and diagonalization of $\tilde{\mathbf{M}}$ gives $\tilde{\mathbf{M}} = \mathbf{U}\boldsymbol{\Lambda}\mathbf{U}^T$ where $\mathbf{U}$ contains the eigenvectors and $\boldsymbol{\Lambda}$ is a diagonal matrix containing the eigenvalues of $\tilde{\mathbf{M}}$. One can then write any matrix $(\tilde{P}|f(\rho)|\tilde{Q})$ of the orthogonal auxiliary basis and functions $f(\rho)$ as follows:

$$\tilde{\mathbf{M}}[f(\rho)] = \mathbf{U}f(\boldsymbol{\Lambda})\mathbf{U}^T \tag{18}$$

where the matrix $f(\boldsymbol{\Lambda})$ is a diagonal matrix containing the function values $f(\Lambda_i)$ for each eigenvalue Λ_i in its diagonal. In case of $f = f_{xc}^{ALDAx}$ (exchange-only ALDA kernel) the function f is given by $f_{xc}^{ALDAx}(\rho) = -C_x\rho^{-2/3}$ and C_x is the Slater−Dirac constant. Finally the matrix $\tilde{\mathbf{M}}[f(\rho)]$ has to be backtransformed to the original nonorthogonal auxiliary basis set using:

$$\mathbf{M}[f(\rho)] = \mathbf{S}\mathbf{V}\mathbf{U}f(\boldsymbol{\Lambda})\mathbf{U}^T\mathbf{V}^T\mathbf{S} \tag{19}$$

It can be seen that the computational cost of the gridfree-based algorithm is only N_{aux}^3 and $N_{aux} \times N_{orb}^2$ (N_{orb}: number of AO basis functions) with both $N_{aux} \ll N_{grid}$ and $N_{orb} \ll N_{grid}$.

3. Computational Details

Geometries of complexes from the S22 database[31] as well as the geometries of all conformers of the benzene dimer[5] ("TT","T","PD", and "S"), the uracil dimer[7] ("HB" and "S"), and the stacked methyl-adenine···methyl-thymine dimer[8] ("mAmT") were taken from respective original references.

Table 1. Total MP2, MP2C, and CCSD(T) Interaction Energies (in kcal/mol) for the S22 Complexes. MP2/"CBS S22" and CCSD(T)/CBS Values Were Taken from Ref 31[a]

| structure | MP2 | | | | MP2C | | | | CCSD(T) |
	aDZ	aTZ	aQZ	CBS (CBS S22)	aDZ	aTZ	aQZ	CBS	CBS
$(NH_3)_2$	−2.68	−2.99	−3.09	−3.16(−3.20)	−2.73	−3.11	−3.23	−3.32	−3.17
$(H_2O)_2$	−4.37	−4.69	−4.86	−4.98(−5.03)	−4.38	−4.77	−4.96	−5.10	−5.02
(formic acid)$_2$	−15.99	−17.55	−18.14	−18.57(−18.60)	−15.90	−17.62	−18.28	−18.76	−18.61
(formamide)$_2$	−13.95	−15.03	−15.50	−15.84(−15.86)	−13.97	−15.20	−15.72	−16.10	−15.96
(uracil)$_2$ HB[b]	−18.41	−19.60	−20.07	−20.41(−20.43)	−18.22	−19.55	−20.06	−20.43	−20.47
2-PO-2-AP[c]	−15.55	−16.64	−17.06	−17.37(−17.37)	−15.25	−16.48	−16.95	−17.29	−16.71
A···T[d] HB	−14.70	−15.80	−16.23	−16.54(−16.54)	−14.52	−15.76	−16.24	−16.59	−16.46[e]
$(CH_4)_2$	−0.39	−0.46	−0.48	−0.49(−0.51)	−0.44	−0.52	−0.55	−0.57	−0.53
(ethene)$_2$	−1.17	−1.46	−1.53	−1.58(−1.62)	−1.18	−1.50	−1.58	−1.64	−1.51
benzene···CH_4	−1.47	−1.71	−1.77	−1.81(−1.86)	−1.17	−1.44	−1.51	−1.56	−1.50
(benzene)$_2$ PD[f]	−4.25	−4.70	−4.85	−4.96(−4.95)	−1.93	−2.48	−2.65	−2.77	−2.73
(pyrazine)$_2$	−6.00	−6.56	−6.76	−6.91(−6.90)	−3.46	−4.04	−4.28	−4.46	−4.42
(uracil)$_2$ S[g]	−9.81	−10.63	−10.90	−11.10(−11.15)	−8.10	−8.99	−9.32	−9.56	−9.88
indole···benzene S	−7.14	−7.74	−7.94	−8.09(−8.12)	−3.56	−4.27	−4.51	−4.69	−4.66[e]
A···T S	−13.24	−14.26	−14.59	−14.83(−14.93)	−9.71	−10.81	−11.21	−11.50	−12.23
ethene···ethine	−1.39	−1.58	−1.63	−1.67(−1.69)	−1.31	−1.52	−1.57	−1.61	−1.53
benzene···H_2O	−2.98	−3.35	−3.46	−3.54(−3.61)	−2.69	−3.12	−3.24	−3.33	−3.28
benzene···NH_3	−2.21	−2.52	−2.60	−2.66(−2.72)	−1.87	−2.21	−2.30	−2.37	−2.35
benzene···HCN	−4.38	−4.92	−5.06	−5.16(−5.16)	−3.85	−4.44	−4.59	−4.70	−4.46
(benzene)$_2$ T[h]	−3.10	−3.46	−3.56	−3.63(−3.62)	−2.32	−2.72	−2.82	−2.89	−2.74
indole···benzene T	−6.10	−6.71	−6.86	−6.97(−7.03)	−5.00	−5.67	−5.84	−5.96	−5.73
(phenol)$_2$	−6.79	−7.36	−7.59	−7.76(−7.76)	−6.19	−6.85	−7.11	−7.30	−7.05

[a] aXZ stands for Dunning's[42] aug-cc-pVXZ basis sets, X = D, T, Q. MP2/CBS and MP2C/CBS values correspond to Helgaker's[47] extrapolations from the aTZ and aQZ basis sets. [b] HB = hydrogen-bonded. [c] 2-PO-2-AP = 2-pyridoxine-2-aminopyridine. [d] A···T = adenine···thymine. [e] In ref 31 for A···T HB and indole···benzene S complexes, −16.37 and −5.22 kcal/mol estimated CCSD(T)/CBS results were calculated as MP2/CBS + ΔCCSD(T)/dz. Because the ΔCCSD(T)/dz values, 0.21 and 2.90 kcal/mol, are significantly underestimated for these systems, more accurate ΔCCSD(T)/aDZ values, of 0.08 and 3.46 kcal/mol, are used instead. [f] PD = parallel displaced. [g] S = stacked. [h] T = "T"-shaped −16.37.

PES studies were based on geometries taken from the work of Grimme et al.[40] ("PD-to-IP" and "T-to-S") and on geometries taken from the work of Wang and Hobza,[41] with modified intermonomer distances as explained in detail in section 4.3.

All MP2, MP2C, and CCSD(T) calculations were done in the frozen-core approximation and using the (aug-)cc-pVXZ basis sets ((a)XZ) of Dunning and co-workers.[42] MP2 and MP2C results were obtained with MOLPRO[43] using corresponding JKfit density-fitting basis sets of Weigend[44] for the Hartree−Fock and Localized Hartree−Fock calculations and the MP2fit basis sets from Weigend et al.[45] for the MP2 and TDDFT calculations. For the LHF calculations, the computational-efficient scheme described in ref 46 was used.

CCSD(T) calculations were carried out with the MOLCAS 7[1] package using a Cholesky decomposition of two-electron integrals with a threshold of $10^{−6}$ Hartree on both SCF and the CCSD(T) levels. This calculation setup was previously validated to be in agreement with the exact two-electron integral-based calculations beyond 0.01 kcal/mol in interaction energies.

4. Results and Discussion

4.1. S22 Test Set. Tables 1−3 show results obtained for the S22 data set in two different ways. In Table 1 total MP2 and MP2C interaction energies with the respective aTZ→aQZ extrapolations according to Helgaker et al.[47] are presented along with the estimated CCSD(T)/CBS reference values from ref 31. In Table 2 the total MP2 interaction energies are displayed along with the " ΔMP2C" and " ΔCCSD(T)"

energies, defined as $\Delta X = X$-MP2, where X stands for MP2C or CCSD(T). The last table on the S22 results, Table 3, shows a statistical evaluation of errors of estimated MP2/CBS and MP2C/CBS results with respect to the estimated CCSD(T)/CBS for each type of interactions separately as well as for the whole test set.

Let us first analyze the performance of the MP2C method on total interaction energies shown in Table 1. MP2 and MP2C values obtained in the series of aXZ (X = D, T, and Q) basis sets are presented to demonstrate the similar rate of convergence of these methods toward the CBS. Two different numbers appear in the CBS column for MP2, one being obtained by us from the extrapolation from aTZ and aQZ basis sets, another one in parentheses from the original S22 paper.[31] These numbers differ slightly, typically a few hundreds of kcal/mol, at most by 0.1 kcal/mol for the stacked adenine···thymine complex, which is because mostly un-augmented, but of one order of cardinality higher, cc-pVXZ basis sets were used. Another, but less important, deviation could also arise from using different density-fitting basis sets. The performance of MP2C for H-bonded complexes is excellent, just like the performance of uncorrected MP2 itself, with an average error of ∼0.2 kcal/mol. The only exception is the 2-pyridoxine-2-aminopyridine, for which the error of MP2 and MP2C is 0.66 and 0.58 kcal/mol, respectively. The performance of MP2 and MP2C is, however, dramatically different for dispersion-dominated complexes, as expected. Here the maximum error of MP2C is obtained for the adenine···thymine stacked complex, being −0.73 kcal/mol. Note that the actual error is probably by ∼0.1 kcal/mol less negative, due to the inconsistency with the MP2/CBS value

Combination of MP2 and TDDFT Response Theory

J. Chem. Theory Comput., Vol. 6, No. 1, 2010 **173**

Table 2. Total MP2 and ΔMP2C and ΔCCSD(T) Corrections to the MP2 Interaction Energies (in kcal/mol) for the S22 Complexes[a]

	MP2			ΔMP2C					ΔCCSD(T)	
structure	aDZ	aTZ	aQZ	aDZ	aTZ	aQZ	S22[b]		aDZ	S22[b]
$(NH_3)_2$	−2.68	−2.99	−3.09	−0.06	−0.12	−0.14	−0.04	(qz)	0.06	0.03
$(H_2O)_2$	−4.37	−4.69	−4.86	−0.02	−0.09	−0.11	−0.01	(qz)	0.03	0.00
(formic acid)$_2$	−15.99	−17.55	−18.14	0.09	−0.07	−0.14	0.09	(tz)	0.03	−0.02
(formamide)$_2$	−13.95	−15.03	−15.50	−0.02	−0.17	−0.22	−0.02	(tz)	−0.02	−0.11
(uracil)$_2$ HB[c]	−18.41	−19.60	−20.07	0.19	0.05	0.00	0.22	(tz-fd)	−0.06	−0.03
2-PO-2-AP[d]	−15.55	−16.64	−17.06	0.31	0.16	0.11	0.34	(tz-fd)	0.63	0.66
A···T[e] HB	−14.70	−15.80	−16.23	0.18	0.04	−0.01	0.18	(dz)	0.08	0.21
$(CH_4)_2$	−0.39	−0.46	−0.48	−0.05	−0.06	−0.07	−0.01	(qz)	−0.03	−0.02
(ethene)$_2$	−1.17	−1.46	−1.53	−0.00	−0.04	−0.05	0.05	(qz)	0.10	0.11
benzene···CH$_4$	−1.47	−1.71	−1.77	0.30	0.27	0.26	0.35	(tz-fd)	0.35	0.36
(benzene)$_2$ PD[f]	−4.25	−4.70	−4.85	2.32	2.23	2.20	2.32	(adz)	2.22	2.22
(pyrazine)$_2$	−6.00	−6.56	−6.76	2.54	2.52	2.48	2.52	(tz-fd)	2.57	2.48
(uracil)$_2$ S[g]	−9.81	−10.63	−10.90	1.71	1.63	1.58	1.69	(tz-fd)	1.26	1.28
indole···benzene S	−7.13	−7.74	−7.94	3.57	3.47	3.42	3.08	(dz)	3.46	2.90
A···T S	−13.24	−14.26	−14.59	3.54	3.45	3.38	2.91	(dz)	2.76	2.70
ethene···Ethine	−1.39	−1.58	−1.63	0.08	0.06	0.05	0.10	(tz)	0.16	0.18
benzene···H$_2$O	−2.98	−3.35	−3.46	0.29	0.23	0.22	0.30	(tz-fd)	0.28	0.33
benzene···NH$_3$	−2.21	−2.52	−2.60	0.35	0.31	0.30	0.37	(tz-fd)	0.33	0.37
benzene···HCN	−4.38	−4.92	−5.06	0.53	0.49	0.47	0.56	(tz-fd)	0.64	0.70
(benzene)$_2$ T[h]	−3.10	−3.46	−3.56	0.78	0.74	0.73	0.78	(adz)	0.88	0.88
indole···benzene T	−6.10	−6.71	−6.86	1.10	1.05	1.02	0.93	(dz)	1.34	1.30
(phenol)$_2$	−6.79	−7.36	−7.59	0.60	0.51	0.48	0.61	(tz-fd)	0.69	0.71

[a] ΔCCSD(T)/S22 values were taken from the ref 31. [b] Basis sets used in ref 31 for calculation of ΔCCSD(T), i.e., (a)XZ = (aug-)cc-pVXZ; tz-fd = cc-pVTZ with less diffuse d- and all f-functions removed. [c] HB = hydrogen-bonded. [d] 2-PO-2-AP = 2-pyridoxine-2-aminopyridine. [e] A···T = adenine···thymine. [f] PD = parallel displaced. [g] S = stacked. [h] T = "T"-shaped.

Table 3. Root Mean Squared Errors (RMS), Mean Absolute Deviations (MAD), Mean Signed Deviations (MSD), and Maximum Absolute Errors (MAX) (in kcal/mol) to the Estimated CCSD(T) Interaction Energies of the S22 Complexes from Table 1[a]

	H-bonded	dispersion	mixed	all
rms	0.26/0.25	1.86/0.34	0.71/0.17	1.20/0.24
MAD	0.16/0.18	1.48/0.24	0.61/0.15	0.78/0.17
MSD	0.08/0.17	1.47/−0.16	0.61/0.15	0.75/0.07
MAX	0.66/0.58	2.87/0.73	1.24/0.25	2.87/0.73

[a] MP2 values are the first and the MP2C errors are the second number in each column.

from S22, as mentioned above. The second largest deviation with respect to the S22 CCSD(T)/CBS was found for the stacked complex of indole···benzene, being −0.53 kcal/mol, which almost completely diminishes (to −0.03 kcal/mol) after improving the quality of the estimated CCSD(T)/CBS benchmark, from −5.22 to −4.66 kcal/mol, by calculating ΔCCSD(T) in the aDZ instead of the DZ basis set. The description of "mixed" type complexes by MP2C is the most balanced with average errors of ~0.15 kcal/mol and the largest error occurring for the phenol dimer, with only 0.25 kcal/mol (the error of MP2 is ~0.7 kcal/mol for this system).

A deeper insight into the magnitude and the basis set dependence of the TDDFT dispersion contribution can be acquired from Table 2. Because the MP2C and the CCSD(T) method can both be viewed as "corrections" to MP2, we can formally separate the respective correction term, as already mentioned. For MP2C it would be more methodologically correct to show the subtracted UCHF and the added TDDFT dispersion energy, but this would not serve the assessment we would like to address. The separation of the ΔCCSD(T) correction was shown to be extremely helpful

especially in benchmark calculations,[48] because it was observed that the ΔCCSD(T) converges typically much faster with the basis set size than the MP2 interaction energy itself, thus making it sufficient to be calculated in small- to medium-sized diffuse basis sets. It would also be advantageous to observe a similar feature in MP2C, so we could avoid TDDFT calculations (though not more expensive than the supermolecular MP2 itself) in large basis sets.

Generally, the ΔCCSD(T) correction for typical H-bonded complexes (e.g., the first four complexes in Table 2) is small and clustered around zero kcal/mol (see the results in Table 2), and this trend is slightly underestimated on the MP2C/CBS level. The last three H-bonded complexes have a significantly larger contribution from the dispersion energy, from which the uracil dimer and the adenine···thymine complexes are described fairly accurately, errors being −0.04 and 0.13 kcal/mol, respectively, after recalculating the ΔCCSD(T) for the adenine···thymine complex in the aDZ basis set (the error with respect to the original S22 CCSD(T)/CBS value is also acceptable with a value of 0.23 kcal/mol). The most problematic H-bonded complex, with an error of 0.58 kcal/mol, is the already mentioned 2-pyridoxine-2-aminopyridine. So far we do not have an explanation or numerical evidence for such a deviation of the MP2C method for this complex. Perhaps the intermolecular correlation beyond the second order is important for electrostatics, exchange, and deformation contributions. The basis set convergence of ΔMP2C for these complexes in percentile scale is rather slow; changes of ΔMP2C from the aTZ to the aQZ basis set account for 20 to 125%. These large numbers might be a bit misleading, because the ΔMP2C correction changes in absolute values only by −0.04 kcal/mol on average.

Table 4. Total MP2C and CCSD(T) Interaction Energies and Respective ΔMP2C and ΔCCSD(T) Energy Corrections (in kcal/mol) for a Few Selected Benchmark Complexes

structure	MP2C				CCSD(T)				ΔMP2C			ΔCCSD(T)		
	aDZ	aTZ	aQZ	CBS	aDZ	aTZ	aQZ	CBS	aDZ	aTZ	aQZ	aDZ	aTZ	aQZ
B_2[a] TT	−2.53	−2.81	−2.90	−2.97	−2.44	−2.66	−2.75	−2.78 ± 0.03	0.68	0.65	0.63	0.75	0.80	0.79
B_2 T	−2.37	−2.72	−2.82	−2.89	−2.28	−2.57	−2.65	−2.69 ± 0.02	0.72	0.69	0.68	0.82	0.85	0.85
B_2 PD	−2.06	−2.58	−2.74	−2.85	−2.15	−2.49	−2.63	−2.70 ± 0.04	2.20	2.11	2.09	2.11	2.20	2.19
B_2 S	−1.19	−1.58	−1.70	−1.79	−1.27	−1.51	−1.61	−1.64 ± 0.04	1.70	1.61	1.58	1.62	1.68	1.67
U_2[b] HB	−18.22	−19.55	−20.06	−20.41	−18.43	−19.81	−	−20.50 ± 0.14	0.19	0.05	0.00	−0.02	−0.21	−
U_2 S	−8.10	−8.99	−9.32	−9.55	−8.54	−9.33	−	−9.68 ± 0.11	1.71	1.63	1.58	1.26	1.29	−
mAmT[c]	−11.07	−12.74	−	−13.45	−11.61	−13.06	−	−13.70 ± 0.04	4.71	4.57	−	4.16	4.25[d]	−

[a] B_2 = benzene dimer, TT = "T"-shaped tilted, T = "T"-shaped, PD = parallel displaced, S = sandwich. For details on structures, see ref 5. [b] U_2 = uracil dimer, HB = hydrogen-bonded, S = stacked. For details on structures, see ref 7. [c] mAmT = methyl-adenine···methyl-thymine. For details on structure, see ref 8. [d] ΔSCS(MI)-MP2/cc-pV(DT)Z and ΔSCS(MI)-MP2/cc-pVQZ values are 2.87 and 2.65 kcal/mol, respectively.

Trends in the basis set convergence of the ΔMP2C term can be better observed for the dispersion-dominated complexes, because of much larger absolute values of the interaction energies, especially for the π−π stacked complexes. First of all, in all π−π stacked complexes investigated by us[5–8] or other authors (for instance see ref 49), the ΔCCSD(T) (thus ΔMP2C as well) values are repulsive. What is different is that the ΔCCSD(T), unlike the ΔMP2C, converges with the basis set from below, i.e., the repulsion is increasing with the basis set size. Surprisingly (see, for instance, results for the stacked uracil dimer in Table 2), the ΔMP2C correction decreases when going from the aDZ to the aQZ basis set. This means that for these kinds of complexes the total MP2C interaction energy (in attractive equilibrium complex geometries) is increasing with the basis set size, unlike the total CCSD(T) interaction energy, which is decreasing. Because we do not have systematic CCSD(T) results for the whole S22 set, few selected complexes, shown in Table 4, will be analyzed separately in section 4.2. The ΔMP2C values for dispersion-dominated complexes converge rather fast, both in percentile and absolute scale. The average change of ΔMP2C for the dispersion-bound complexes (methane and ethene dimers, benzene···methane complex) from the aDZ to the aTZ basis set is −0.03 kcal/mol (∼15%), while from the aTZ to the aQZ basis set it is only −0.01 kcal/mol (∼13%). For the stacked complexes (benzene, pyrazine, and uracil dimers and adenine···thymine complex), the average change of the ΔMP2C from aDZ to aTZ basis set is only 0.08 kcal/mol (∼3%), while from aTZ to aQZ it is even less, 0.05 kcal/mol (∼2%). This is similar to the rate of convergence of the ΔCCSD(T) term, as discussed further. The largest error from the dispersion dominated complexes as well as for the whole S22 set is obtained for the adenine···thymine stacked complex, estimated to be about 0.6 kcal/mol. As in case of 2-pyridoxine-2-aminopyridine, we have no clear explanation where this discrepancy stems from. We can only hypothesize that here maybe contributions to the intermolecular interaction other than the dispersion energy are approximated poorly on the intra- and/or intermolecular MP2 level. The convergence of ΔMP2C for the "mixed" complexes is also monotonous and "from above" (the repulsion due to the corrected dispersion energy decreases with the basis set size). Changes of ΔMP2C from aDZ to aTZ are on average 0.05 kcal/mol (∼9%), while

from the aTZ to aQZ basis sets, the average change decreases to only 0.02 kcal/mol (∼4%).

A statistical evaluation of errors via rms (root-mean-squared deviation), MAD (mean absolute deviation), MSD (mean signed deviation), and MAX (maximum absolute error) is summarized in Table 3. It is found that errors similar to those of the SCS(MI)-MP2[14] or the MP2.5[9] are obtained. However, both of these two methods contain empirical parameters, and furthermore the spin energy component scaling parameters utilized in the SCS(MI)-MP2 method were optimized exactly for the S22 data set. The performance of the first of these methods on complexes outside its training set is clearly deteriorating, as shown in the footnote of Table 4. Results for several systems from the S22 can also be compared with those used for the testing of the MP2+ΔvdW method in ref 29. For water and ammonia H-bonded dimers errors of the best and the worst performing damping functions are 0.09−0.21 kcal/mol and 0.09−0.23 kcal/mol, respectively. For "mixed" and dispersion bound complexes such as "T"-shaped benzene dimer and parallel-displaced (PD) conformations, errors of −0.09−0.35 kcal/mol and −0.05−0.60 kcal/mol were obtained.

4.2. Other Benchmarks. The growing number of highly accurate, systematically calculated CCSD(T)/CBS benchmarks for medium-sized (according to the applicability of the coupled-cluster theory) noncovalent complexes allows us to assess the accuracy of the MP2C approach even more critically. Table 4 shows the comparison of MP2C with the CCSD(T)/CBS results gathered from a few publications.[5,7,8] The first four lines show the performance of the MP2C method on various conformers of the benzene dimer. The rates of convergence of the ΔMP2C and ΔCCSD(T) terms are very similar, values being practically converged toward the CBS already in the aTZ basis set. A further increase of the basis set size amounts to changes of only 0.01−0.03 kcal/mol. Comparing the MP2C and the CCSD(T) values in the CBS limit, an almost uniform overestimation of 0.15−0.20 kcal/mol by the MP2C method is observed. When ΔMP2C and ΔCCSD(T) values are compared, for instance, in the aQZ basis set, a similar underestimation of the ΔCCSD(T) by 0.09−0.17 kcal/mol is found. What is, however, of key importance is that the CCSD(T)/CBS relative stability of different structures is well reproduced by the MP2C method. PD and T, almost isoenergetic structures according to the

CCSD(T)/CBS results, differ only by 0.04 kcal/mol with MP2C/CBS. The energetic separation of the TT structure from both PD and T, being ~0.1 kcal/mol on the CCSD(T)/CBS level, is well reproduced on the MP2C/CBS level, with values of 0.08−0.12 kcal/mol.

An excellent agreement of the MP2C/CBS and the CCSD(T)/CBS within ~0.1 kcal/mol is achieved also for the H-bonded and stacked uracil dimers. For these complexes the CCSD(T)/aQZ results are not available because of the enormous computational requirements. At least for the stacked structure, judged according to the convergence of the ΔCCSD(T) correction in aDZ and aTZ basis sets, the estimated CCSD(T)/CBS value is supposed to be very close to its exact basis set limit. The accuracy of the CCSD(T)/CBS value for the H-bonded dimer is, however, a bit more uncertain.

The last of the complexes in Table 4, the stacked methyl-adenine···methyl-thymine dimer, was thoroughly investigated in ref 8, motivated by its previously estimated[31] large repulsive higher-order correlation contribution to the interaction energy. The difference between ΔCCSD(T) and ΔMP2C is decreasing from −0.55 kcal/mol in the aDZ to −0.32 kcal/mol in the aTZ basis set. Just like for the rest of the complexes in Table 4, the same inverse slope of convergence of ΔMP2C compared to ΔCCSD(T), as for the S22 data set, is observed. The total MP2C/CBS interaction energy is finally only slightly underestimated by ~0.25 kcal/mol (~2%) compared to the CCSD(T)/CBS value. This is an excellent result, especially taking into consideration that the total MP2C/aTZ calculation of the BSSE corrected interaction energy was done in 12 h on a single Intel Core2 Quad 2.40 GHz processor, while only the (T) part of the coupled-cluster calculation of this complex in the aTZ basis set took almost 7 days on 80 four-core Xeon E5430 2.66 GHz processors.

4.3. PEC for Dimers of Aromatic Systems. Generally applicable methods for calculating noncovalent interactions should deliver accurate results not only for the minima but also over the wide region of the PES. This is a strong requirement for applications, for instance in biology, where the interacting fragments of protein, DNA, etc., often appear in distorted geometries or where a superposition of weak but numerous middle- to long-range interactions occurs. The first three figures show the "dissociation" of the parallel-displaced conformation of the benzene dimer (Figure 1), benzene···pyrimidine (Figure 2), and benzene···1,2,4,5-pentazine (Figure 3) calculated with MP2C/CBS (aTZ→aQZ extrapolation) and estimated with CCSD(T)/CBS (MP2 from aTZ→aQZ extrapolation, ΔCCSD(T) calculated in the aDZ basis set). For a more refined view, ΔMP2C and ΔCCSD(T) curves are plotted along the curves of total interaction energies. These systems were selected for known strong π−π interactions[41] which increase with the number of nitrogen heteroatoms. The increase of polarity from benzene to 1,2,4,5-pentazine results in a decrease of the optimal vertical displacement of the rings in the complex and consequently an increase of the interaction energy from −2.32 through −3.50 to −5.13 kcal/mol. Starting from the optimized structures of Wang and Hobza[41] (the acronyms "B0P", "B2P", and "B5P" were used in this publication), the distance
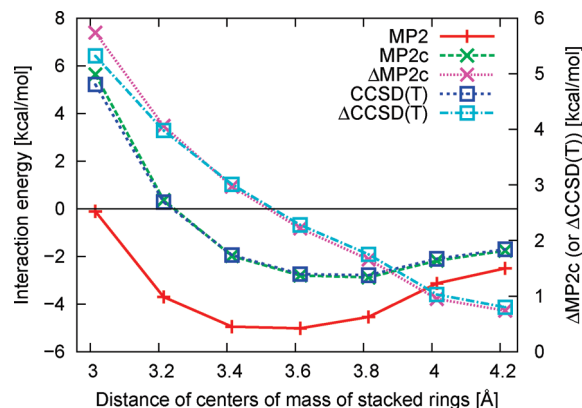

Figure 1. Vertical stretch of stacked benzene rings calculated on MP2C/CBS and estimated CCSD(T)/CBS levels.
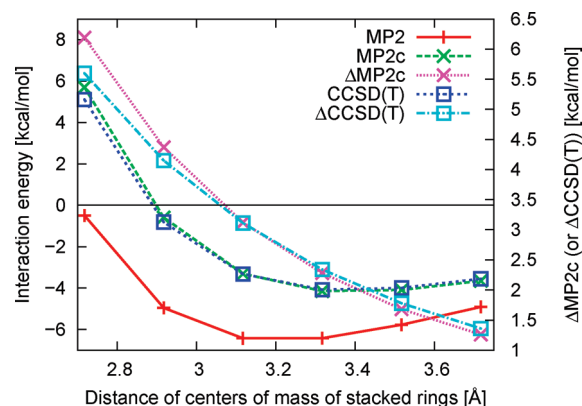

Figure 2. Vertical stretch of stacked benzene and pyrimidine rings calculated on MP2C/CBS and estimated CCSD(T)/CBS levels.
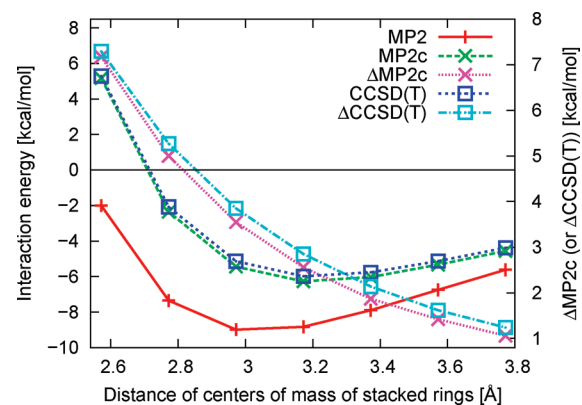

Figure 3. Vertical stretch of stacked benzene and 1,2,4,5-pentazine rings calculated on MP2C/CBS and estimated CCSD(T)/CBS levels.

between the centers of mass of the stacked rings was sampled by 0.2 Å to cover both repulsive and attractive regions around ~1.2 R_0 (R_0 being the equilibrium distance) in both directions. As can be clearly seen from Figures 1−3, MP2C well reproduces the CCSD(T) curve. Some deviations can be seen, for instance, in the strongly repulsive region for benzene···pyrimidine (more clearly visible on the ΔMP2C and ΔCCSD(T) curves) or as a small constant shift of ~0.2 kcal/mol along the whole PEC for benzene···1,2,4,5-pentazine. Deviations in the repulsive region probably originate from
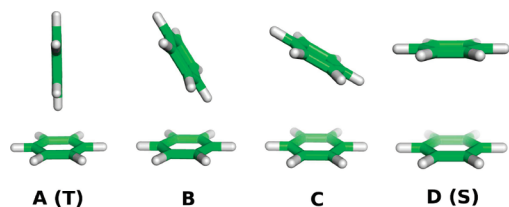
Figure 4. Structures on the "T-to-S" benzene dimer conversion potential energy curve.
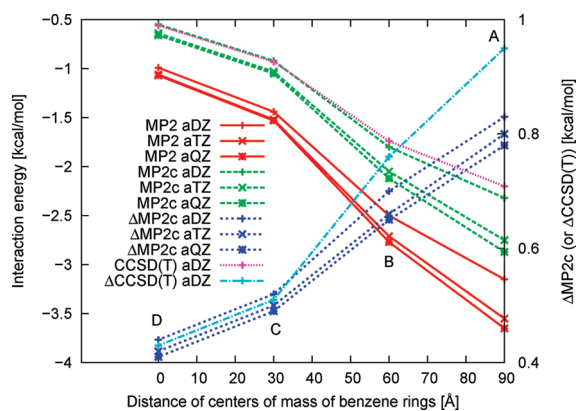

Figure 5. "T-to-S" benzene dimer conversion potential energy curve calculated on CCSD(T)/aug-cc-pVDZ and MP2C/aug-cc-pVXZ, X = 2, 3, 4, levels.
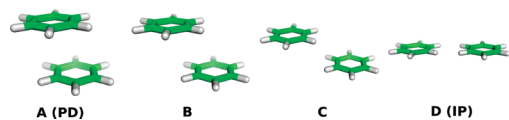

Figure 6. A few selected structures on the "PD-to-IP" benzene dimer conversion potential energy curve.

the intrinsic error of the MP2C method, while the constant shift on the curve for benzene···1,2,4,5-pentazine could be caused by a deficiency of the aDZ basis set used in the calculation of the estimated CCSD(T)/CBS reference.

The last two examples are PECs of the T-shaped benzene dimer conversion to the sandwich (S) structure, Figure 4 and Figure 5, and the parallel displaced (PD) benzene dimer conversion to the in-plane (IP) arrangement, Figure 6 and Figure 7. Geometries for all structures on these PECs were taken from the work of Grimme et al.[40] On both Figure 5 and Figure 7, MP2 and MP2C total interaction energies in the aDZ to aQZ basis sets are shown, along with the corresponding ΔMP2C correction. As references, CCSD(T) and ΔCCSD(T) in the aDZ basis set (unlike the estimated CCSD(T)/CBS used in previous figures, i.e., Figure 1−3) are plotted as well. A common feature in Figures 5 and 7 is the trend of convergence of the MP2 and the ΔMP2C energies with an increase of the basis set size. For the total MP2 interaction energy, a convergence toward a stronger stabilization is observed and in the case of MP2C a decrease of the "destabilization" due to a decrescent value of ΔMP2C occurs. As analyzed by Grimme et al.,[40] the contribution from the intermolecular interaction of $\pi-\pi$ orbitals is doubled (from 17% to 36% of the MP2/aDZ level) going from the T to the S structure. This can be tracked by more than a doubled rise of the ΔCCSD(T) (and ΔMP2C as well) in Figure 5.
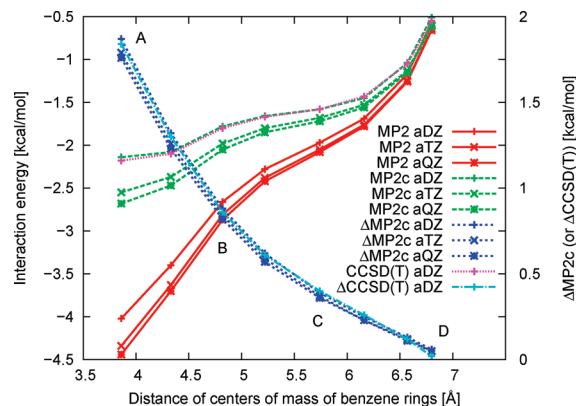

Figure 7. "PD-to-IP" benzene dimer conversion potential energy curve calculated on CCSD(T)/aug-cc-pVDZ and MP2C/aug-cc-pVXZ, X = 2, 3, 4, levels.

The error of the MP2C is also following this trend, being the largest for the sandwich structure, 0.12 kcal/mol in the aDZ basis set. On the basis of the trends of convergence of the ΔCCSD(T) and ΔMP2C correction terms (see Table 4), this discrepancy has a tendency to further increase upon an improvement of the basis set quality, because they converge in opposite directions. The overall quality of the total MP2C interaction energy is still excellent, with an error compared to the CCSD(T)/aDZ being smaller than 6% along the whole PEC.

The character of interaction is also significantly changing along the PD-to-IP PEC: the PD structure (A) has a strong $\sigma-\pi$ (49%) and $\pi-\pi$ (34%) character,[40] while for the IP structure (D) the importance of the intermolecular $\pi-\pi$ interaction decreases only to 9% ($\sigma-\pi$ decreases only slightly to 36%). This change of interaction character can be tracked in Figure 7 by a decrease of the ΔCCSD(T) and the ΔMP2C term from 1.84 and 1.87 kcal/mol for PD to almost zero for the IP structure. However, at the same time the total CCSD(T) and MP2C interaction energies decrease by ∼2 kcal/mol, because the repulsive ΔCCSD(T) and ΔMP2C terms correct the overestimation of the interaction energy on the MP2 level occurring only for structures with significant overlap of the stacked rings. MP2C/aDZ accurately reproduces the CCSD(T)/aDZ values along the whole PEC within 0.04 kcal/mol, leading to percentile errors of at most 8% (obtained for the IP structure).

5. Conclusions

The recently developed[23] dispersion correction scheme (termed MP2C, i.e., MP2 'coupled', in this work) for the supermolecular MP2 method has been extensively tested for different types of dimer systems containing both strong electrostatic and/or strong dispersion interaction energy contributions. While it is well-known that the supermolecular MP2 method is for some types of noncovalent interactions (such as hydrogen-bonding, etc.) capable of accurately reproducing CCSD(T) interaction energies, it has been shown in this work that the correction used in the MP2C approach does not worsen this performance. In fact it has been found that for the set of seven hydrogen-bonded complexes contained in the S22 benchmark set (see Table 1) the root

Combination of MP2 and TDDFT Response Theory

J. Chem. Theory Comput., Vol. 6, No. 1, 2010 **177**

mean squared errors to the estimated CCSD(T)/CBS results for MP2 and MP2C are of about the same magnitude and amount to 0.25 kcal/mol.

In contrast to this, a clear difference between the MP2 and MP2C method is observed for the $\pi-\pi$ stacked complexes where the intermolecular dispersion interactions are dominant. Here the MP2 method does not give reliable estimates of the interaction energy because of large overestimations of the dispersion interaction component contained in the supermolecular MP2 energy. This stems from the fact that the MP2 method accounts for dispersion interactions only on an uncoupled Hartree−Fock level, and this can typically lead to errors of 15% and more in this interaction energy component. In the MP2C method the uncoupled Hartree−Fock dispersion energy contribution is replaced by the coupled dispersion energy calculated using the exchange-only time-dependent density functional theory employing local Hartree−Fock (LHF) orbitals and eigenvalues and the exchange-only adiabatic local density approximation kernel (ALDAx). It has been shown that this approach leads to strong improvements over the MP2 method for the dispersion-dominated and mixed complexes of the S22 dimer set. Root mean square errors of MP2 to the CCSD(T) interaction energies are reduced from 1.86 to 0.36 kcal/mol for the dispersion-dominated complexes and from 0.71 to 0.17 kcal/mol for the mixed type complexes. Therefore, in contrast to the supermolecular MP2 method, the MP2C approach yields accurate and balanced estimates of the intermolecular interaction energy for all diverse types of interactions.

While the S22 benchmark data set contains only complexes in their equilibrium geometries, we have extended the testing of the MP2C method on several cuts through the potential energy surface of the benzene dimer and benzene···pyrimidine and benzene···1,2,4,5-pentazine dimers. In all three cases the MP2C curves do not only agree well with the CCSD(T) reference curves in the region of the minimum of the potential, but they also nicely reproduce the CCSD(T) curves for repulsive and stretched dimer distances. Another challenging test presented here are the potential energy curves corresponding to the transition of the benzene dimer from "T"-shaped to sandwich arrangement and from the parallel-displaced to the in-plane arrangement. CCSD(T) reference curves are reproduced within ∼0.1 kcal/mol accuracy, despite the fact that the character of interaction, especially for the latter one, is changing from strong $\pi-\pi$ to $\sigma-\sigma$ dominated. These examples strongly support the validity of the MP2C approach even for the prediction of wide areas of potential energy surfaces of noncovalent complexes with a good accuracy.

A computer implementation of the correction term used in the MP2C method is presented that scales only as $\mathcal{N}^4$ with the system size and is therefore 1 order of magnitude lower than that of conventional density-fitting MP2 implementations. As an example, the additional computational cost over the standard supermolecular MP2 in the calculation of one of the largest dimers studied in this work, namely the adenine···thymine base pair, amounts to only ∼27% of the total CPU time. Moreover, it was found that the basis set dependence of the ΔMP2C correction is less dependent on the basis set size than the total interaction energy (compare Table 1 and Table 2) and therefore can be, if needed, accurately approximated using smaller basis sets.

References

(1) Aquilante, F.; Vico, L. D.; Ferre, N.; Malmqvist, P.-Å.; Neogrády, P.; Pedersen, T.; Pitoňák, M.; Reiner, M.; Roos, B. O.; Serrano-Andrés, L.; Urban, M.; Veryazov, V.; Lindh, R. *J. Comput. Chem.* **2010**, *31*, 224.

(2) PQS, version 2.3, Parallel Quantum Solutions, 2013 Green Acres Rd., Fayetteville, AR 72703.

(3) Schmidt, M. W.; Baldridge, K. K.; Boatz, J. A.; Elbert, S. T.; Gordon, M. S.; Jensen, J. H.; Koseki, S.; Matsunaga, N.; Nguyen, K. A.; Su, S.; Windus, T. L.; Dupuis, M.; Montgomery, J. A. J. *J. Comput. Chem.* **1993**, *14*, 1347.

(4) Lotrich, V.; Flocke, N.; Ponton, M.; Yau, A. D.; Perera, A.; Deumens, E.; Bartlett, R. J. *J. Chem. Phys.* **2008**, *128*, 194104.

(5) Pitoňák, M.; Neogrády, P.; Rezáč, J.; Jurečka, P.; Urban, M.; Hobza, P. *J. Chem. Theory Comput.* **2008**, *4*, 1829.

(6) Janowski, T.; Pulay, P. *Chem. Phys. Lett.* **2007**, *447*, 27.

(7) Pitoňák, M.; Riley, K. E.; Neogrády, P.; Hobza, P. *Chem. Phys. Chem.* **2008**, *9*, 1636.

(8) Pitoňák, M.; Janowski, T.; Neogrády, P.; Pulay, P.; Hobza, P. *J. Chem. Theory Comput.* **2009**, *5*, 1761.

(9) Pitoňák, M.; Neogrády, P.; Čërný, J.; Grimme, S.; Hobza, P. *Chem. Phys. Chem.* **2009**, *10*, 282.

(10) Takatani, T.; Hohenstein, E. G.; Sherrill, C. D. *J. Chem. Phys.* **2008**, *128*, 124111.

(11) Sherrill, C. D.; Takatani, T.; Hohenstein, E. G. *J. Phys. Chem. A* **2009**, *113*, 10146.

(12) Grimme, S. *J. Chem. Phys.* **2003**, *118*, 9095.

(13) Hill, J. G.; Platts, J. A. *J. Chem. Theory Comput.* **2007**, *3*, 80.

(14) DiStasio, R. A.; Head-Gordon, M. *Mol. Phys.* **2007**, *105*, 1073.

(15) Janesko, B. G.; Scuseria, G. E. *Phys. Chem. Chem. Phys.* **2009**, *11*, 9677.

(16) Grimme, S. *J. Comput. Chem.* **2004**, *25*, 1463.

(17) Becke, A. D.; Johnson, E. R. *J. Chem. Phys.* **2005**, *122*, 154104.

(18) Bartlett, R. J.; Lotrich, V. F.; Schweigert, I. V. *J. Chem. Phys.* **2005**, *123*, 062205.

(19) Furche, F.; Van Voorhis, T. *J. Chem. Phys.* **2005**, *122*, 164106.

(20) Goll, E.; Werner, H.-J.; Stoll, H.; Leininger, T.; Gori-Giorgi, P.; Savin, A. *Chem. Phys.* **2006**, *329*, 276.

(21) Chakarova-Käck, S. D.; Schröder, E.; Lundqvist, B. I.; Langreth, D. C. *Phys. Rev. Lett.* **2006**, *96*, 146107.

(22) Cybulski, S. M.; Lytle, M. L. *J. Chem. Phys.* **2007**, *127*, 141102.

(23) Heßelmann, A. *J. Chem. Phys.* **2008**, *128*, 144112.

(24) Harl, J.; Kresse, G. *Phys. Rev. Lett.* **1009**, *103*, 056401.

(25) Toulouse, J.; Gerber, I. C.; Jansen, G.; Savin, A.; Angyan, J. *Phys. Rev. Lett.* **2009**, *102*, 096404.

(26) Janesko, B. G.; Henderson, T. M.; Scuseria, G. E. *J. Chem. Phys.* **2009**, *131*, 034110.

(27) Szabo, A.; Ostlund, N. S. *J. Chem. Phys.* **1977**, *67*, 4351.

(28) Della Sala, F.; Görling, A. *J. Chem. Phys.* **2001**, *115*, 5718.

(29) Tkatchenko, A.; DiStasio, R. A.; Head-Gordon, M.; Scheffler, M. *J. Chem. Phys.* **2009**, *131*, 094106.

(30) Tkatchenko, A.; DiStasio, R. A.; Head-Gordon, M.; Scheffler, M. *J. Chem. Phys.* **2009**, *131*, 129901.

(31) Jurečka, P.; Šponer, J.; Cěrný, J.; Hobza, P. *Phys. Chem. Chem. Phys.* **2006**, *8*, 1985.

(32) Bernardi, F.; Boys, S. F. *Mol. Phys.* **1970**, *19*, 553.

(33) Chalasinski, G.; Szczesniak, M. M. *Mol. Phys.* **1987**, *63*, 205.

(34) Cybulski, S. M.; Chalasinski, G.; Moszynski, R. *J. Chem. Phys.* **1990**, *92*, 4357.

(35) Heβelmann, A.; Jansen, G. *Chem. Phys. Lett.* **2003**, *367*, 778–784.

(36) Heβelmann, A.; Jansen, G.; Schütz, M. *J. Chem. Phys.* **2005**, *122*, 014103.

(37) Zheng, Y. C.; Almlöf, J. *Chem. Phys. Lett.* **1993**, *214*, 397.

(38) Zheng, Y. C.; Almlöf, J. J. *Mol. Struct. (THEOCHEM)* **1996**, *388*, 277.

(39) Glaesemann, K. R.; Gordon, M. S. *J. Chem. Phys.* **1998**, *108*, 9959.

(40) Grimme, S.; Mück-Lichtenfeld, C.; Anthony, J. *Phys. Chem. Chem. Phys.* **2008**, *10*, 3327.

(41) Wang, W.; Hobza, P. *Chem. Phys. Chem.* **2008**, *9*, 1003.

(42) Kendall, R. A.; Dunning, T. H. J.; Harrison, R. J. *J. Chem. Phys.* **1992**, *96*, 6796.

(43) Werner, H.-J., et al. MOLPRO, version 2009.2, a package of ab initio programs, 2009, see http://www.molpro.net.

(44) Weigend, F. *Phys. Chem. Chem. Phys.* **2002**, *4*, 4285.

(45) Weigend, F.; Köhn, A.; Hättig, C. *J. Chem. Phys.* **2002**, *116*, 3175.

(46) Hesselmann, A.; Manby, F. *J. Chem. Phys.* **2005**, *123*, 164116.

(47) Helgaker, T.; Klopper, W.; Koch, H.; Noga, J. *J. Chem. Phys.* **1997**, *106*, 9639.

(48) Jurečka, P.; Hobza, P. *Chem. Phys. Lett.* **2002**, *365*, 89.

(49) Min, S. K.; Lee, E. C.; Lee, H. M.; Kim, D. Y.; Kim, D.; Kim, K. S. *J. Comput. Chem.* **2008**, *29*, 1208.

JCTC Journal of Chemical Theory and Computation

Ab Initio Study of the Diels−Alder Reaction of Cyclopentadiene with Acrolein in a Ionic Liquid by KS-DFT/3D-RISM-KH Theory

Cinzia Chiappe, Marco Malvaldi,* and Christian Silvio Pomelli

Dipartimento di Chimica e Chimica Industriale, via Risorgimento 35, 56126 Pisa, Italy

Abstract: We study the Diels−Alder reaction between cyclopentadiene and acrolein in a model room-temperature ionic liquid ([mmim][PF$_6$]) as a solvent. The calculations have been performed with the KS-DFT/3D-RISM-SCF theory, where the reactants and transition state (TS) have been represented at a QM level, while the solvent is represented by a 3D distribution of classical (charge + LJ) sites obtained by solving the 3D-RISM integral equation. We show that this method, being computationally efficient, is able to reproduce the main experimental features displayed by the experiments, concerning the reaction rate enhancement and augmentation of the endo/exo ratio in ionic liquids (ILs). We find that the IL distorts noticeably the transition state geometry, inverting the order of the frontier orbitals and leading to an enhancement of the asynchronicity of the reaction. Finally, we find, in agreement with recent work, that formation of the hydrogen bond between the unique C2 hydrogen of the imidazolium ring is not essential to explain the peculiar features of these reactions in ILs.

Introduction

Ionic liquids (ILs) are salts generally constituted by a bulky organic cation and a polyatomic anion, liquid at or near room temperature, whose popularity has expanded dramatically in the last 10 years due to their recognition as new green chemicals with unique and highly tunable physicochemical properties.[1] They are now being explored in virtually all areas of chemistry as process chemicals (solvents, separation media, etc.), performance chemicals (lubricants, electrolytes, etc.), and materials. Studies of organic reactions and catalyzed processes performed in ILs suggest that for many reactions ILs give improved results in terms of yields, selectivity, and rate. Constituted exclusively by ions, ILs represent a reaction environment completely different from molecular solvents.[2] The strong ion−ion interactions present in ILs lead to highly structured materials, three-dimensional supermolecular polymeric networks of anions and cations linked by H bonds and/or Coulombic interactions, often permeated by nonpolar regions due to the presence of sufficiently long alkyl chains on cation.[3] Like many other organized systems, the ILs environment can display not only

dynamic but also local heterogeneity; molecules are trapped for a relatively long period in a quasistatic local solvent cage.[4] However, despite this complexity, reactivity and selectivity in ILs are generally explained considering the ability of the constituting cations and anions to act as hydrogen-bond donors/acceptors and the degree of charge delocalization in the anion.[5,6] In other words, they are normally rationalized on the basis of microscopic properties of these media, neglecting the solvent effects that can arise from the bulk and its supermolecular organization.

Generally, solvent effects on chemical reactions may be considered at the theoretical level; however, whereas for molecular solvents a continuum method[7] can be used with good results, the nature of ILs requires the definition of a more appropriate computational model. Recently, we have shown the possibility to adopt the KS-DFT/3D-RISM-KH method to study the solvation ability of ILs.[8] The method predicts the IL properties in remarkable agreement with conclusions drawn from MD simulations: the three-dimensional solvation structure is reproduced well, and the solvent environment effect of the constituents of the IL is described correctly.

---

* Corresponding author e-mail: marco@dcci.unipi.it.

The study described herein aims to apply this approach to the treatment of organic reactions in ILs. In particular, we report here data on the Diels−Alder reaction of cyclopentadiene with acrolein in dimethylimidazolium hexafluorophosphate, [mmim][PF$_6$].

Diels−Alder reaction has been widely investigated also in ILs.[9] Recently, in collaboration with the group of Welton, we evidenced[10] that the stereochemical and kinetic behavior of reaction of cyclopentadiene with three different dienophiles (including acrolein) in ILs is a function of *both* the solvent and the solute. Using multiparameter linear solvation energy relationships, the primary role of the solvent hydrogen-bond donation ability (α) has been evidenced in the reactions of acrolein and methyl acrylate but not of acrylonitrile. An attempt to study the same reaction at the DFT level using a supermolecular approach, i.e., considering a three molecule system constituted by diene, dienophile, and IL cation, has shown[11] that the IL cation coordination affects the equilibrium geometries and electronic structures of the reacting species throughout the reaction pathway, leading to changes in reactivity and selectivity. On the other hand, this approach did not allow the evaluation of more concerted interactions. The "clamp" effect, arising from the ability of the cation to interact with the dienophile and from the fact that in the IL the freedom of motion of the cation is strongly limited by the Coulombic interactions with the solvent bulk, could be only hypothesized using this approach.[11]

In the present work, we focused on understanding the role of the electronic and solvation energies on the catalytic and selectivity effects displayed by ionic liquids in Diels−Alder reactions by a multicomponent QM/classical method relying on 3D-RISM/SCF theory developed[12] in recent years and recently applied by some of us to ionic liquids.[8]

It is however noteworthy that during the writing of this paper a communication on the Diels−Alder reaction of cyclopentadiene with methyl acrylate in dimethylimidazolium chloride, [mmim]Cl, using the multicomponent reference interaction site model (RISM) has been published.[13] Therefore, results obtained adopting KS-DFT/3D-RISM-KH will be discussed in light of the experimental results taking into account the recently published data.

Computational Method

In this study, we chose 1,3-dimethylimidazolium hexafluorophosphide ([mmim][PF6]), which we consider a reasonable approximation to 1-butyl-3-methylimidazolium hexafluorophosphide ([bmim][PF6]), one of the most popular ILs on which experimental results for Diels−Alder reactions are available.[10]

The KS-DFT/3D-RISM-SCF procedure has been described in detail in previous work; here, we summarize only the main outline of the procedure.

The presence of the solvent is accounted for by a 3D distribution of solvent sites (described as rigid molecules) around the solute molecule, which is obtained[12] by the standard 3D-RISM integral equation ([3D-RISM]); the solute is described by its electron density distribution in space plus the nuclei charge (which describe the Coulomb interaction), while the dispersion interaction is described by Lennard−

Table 1. Free Energy of the Reagents (in kcal/mol) in the Gas Phase (gas) and in the Ionic Liquids Solution (IL) Together with Electronic (ΔE_{el}), Solvation (μ), and Thermal Correction (kinetic contribution + zero-point energy)

	ΔE_{el}	ΔG_{therm}	$\Delta \mu$	ΔG_{total}
cis-acrolein (gas)	−1618.40	12.45		−1605.95
trans-acrolein (gas)	−1627.95	13.08		−1614.87
cyclopentadiene (gas)	−2207.97	32.00		−2175.97
cis-acrolein (IL)	−1626.91	13.36	22.63	−1590.92
trans-acrolein (IL)	−1627.38	13.14	24.38	−1589.86
cyclopentadiene (IL)	−2207.33	31.82	25.51	−2150.00

Jones sites centered on each nucleus. The electronic structure of the solute (reagents, TS, products) and the 3D solvent structure are then obtained self-consistently.

The KS-DFT/3D-RISM-SCF were performed on a grid of 32 × 32 × 32 points spaced by 0.5 Å. The RISM equations were solved together with the partially linearized hypernetted chain (PLHNC) closure, which has been shown to give the most reliable results for ionic liquids.[14]

The geometries of the reactants, transition states, and products were optimized both in the gas phase and in the solvent at the DFT level with the TZ2P basis set and the OLYP XC functional. The vibrational frequencies were calculated on each final geometry at the same level. Since in the Diels−Alder reaction the $\pi-\pi$ interaction plays a crucial role, the final electronic energy changes on optimized structures were calculated with the M06−2X functional, which is to date most accurate in predicting the $\pi-\pi$ dispersion interaction.[15]

The frequency calculations in the IL solvent gave some spurious imaginary frequencies at very low wavenumbers in addition to the imaginary frequency relative to the reaction coordinate; this effect has been ascribed to the presence of the solvent, whose 3D distribution remains frozen during the frequency run. To evaluate the thermal contribution, the frequencies were then recalculated on the TS geometries fully optimized in IL but in a subsequent run without the solvent.

The correct finding of transition states and of the reaction coordinate was confirmed by performing an IRC run on each TS[16] in order to verify that the actual products (in the forward direction) and reagents (in the backward direction) were obtained.

All computations were performed with a development version of the ADF code.[17]

Results and Discussion

We start our analysis by examining the different reactions that can take place in both the gas phase and IL solution. In Table 1 the relative activation free energies $\Delta G^{\ddagger}$ are reported for transition state (TS) barriers.

The first thing that we note is that the reaction pathways to be considered change when switching from the gas phase to the IL solvent. The dienophile can be found in two different conformations, which are usually referred to as "cis" or "trans" according to the position that the double bonds can take with respect to the single C−C bond. Furthermore, dienophile can interact with cyclopentadiene following the endo or exo approach to give the corresponding adducts;

Table 2. Activation Free Energy $\Delta G^{\ddagger}$ (in kcal/mol) in the Gas Phase (gas) and in the Ionic Liquids solution (IL) Together with Electronic (ΔE_{el}), Solvation (μ), and Thermal Correction (kinetic contribution + zero-point energy) Contributions, and Numerical Value of the Imaginary Frequency of the Normal Mode Corresponding to the Reaction Coordinate

	ΔE_{el}	$\Delta\mu$	ΔG_{therm}	$\omega(cm^{-1})$	$\Delta G^{\ddagger}$
X−T(gas)	12.86		19.29	378.20	32.15
N−T(gas)	12.29		19.05	376.40	31.84
X−T(IL)	16.73	−10.05	19.82	359.78	26.50
N−T(IL)	15.88	−10.15	19.70	358.98	25.43
X−C(IL)	12.38	−6.47	19.48	338.57	25.39
N−C(IL)	10.74	−6.69	19.31	339.22	23.36

therefore, four possible structures for the TSs (endocis(N−C), endotrans(N−T), exocis(X−C), and exotrans(X−T)) must be considered.

Figure 1. 3D distribution function of the anion (yellow) and cation (N site, light blue) around the transition state optimized in the IL solvent.

Figure 2. Radial distribution function of cation sites with respect to the distance *r* from the transition state geometric center.

Figure 3. Radial distribution function of cation sites as a function of distance *r* with respect to the carbonyl oxygen of the TS.

In the void, the dienophile can be found only as a trans conformer due to the large energy difference ($\Delta G = 8.92$ kcal/mol, see Table 1) between the two isomers; thus, the reaction in the gas phase can take place only through the exotrans and endotrans TSs. This is the first difference with the work by Sato and co-workers,[13] where only the cis structure was considered due to their lower TS energies. In solution (see Table 1) both conformers are present, with a cis:trans ratio of about 75:25; in addition, the reaction free energy barrier height is lower (about 2 kcal/mol, see Table 2) for the endocis TS with respect to both TSs with the trans isomer. Thus, the cis route is actually the more important pathway to products, but the presence of the trans isomer in solution is not negligible.

The presence of the ionic liquid solvent implies changes at an electronic and a structural level on the transition state; on the other side, the thermal contribution to free energy was found to change negligibly (at most by 0.2 kcal/mol) when passing from the optimized structure in the gas phase to the optimized structure in the IL. To such effects, the solvation free energy contribution $\Delta\mu$ must be added to understand the effect of the solvent on the reaction.

Interaction with the Solvent. The interaction of the transition state with the solvent can be analyzed on the basis of the 3D distribution functions of the anion and cation around the transition state, presented in Figures 1−3. The cation density around the transition states has its peaks mainly at the carbonyl oxygen and in two regions above and below the TS, parallel to the diene and the dienophile planes. Thus, the interaction is driven by oxygen−hydrogen coupling, but also stacking interactions between the TS and the cation can be detected. The anion is located on the imaginary plane which is about perpendicular to the reaction coordinate, less close than the cation to the TS. It appears then that the first solvation shell of the TS could be described by three cations (one coordinated with the carbonyl and two stacked above and below the TS) and three anions.

This can be confirmed by inspection of the 1D averaged pair distribution functions (Figure 2), where the TS-cation has two peaks at short distance: the first is given by the cation directly interacting with the carbonyl while the second by

the stacked ones. It is noteworthy that the interaction of the carbonyl oxygen is stronger with the methyl groups and the twin CW sites than with the single CR group; thus, in agreement with precedent findings by Jorgensen,[18] this suggests that the hydrogen bond with the single hydrogen posed on CR is not a key factor and that interactions with other hydrogen sites are more important in driving the reaction.

Structural Level. The ionic liquid changes the geometry of the TS for all four pathways considered, deforming the diene−dienophile stacking geometry and enhancing the asynchronicity of the reaction when performed in these solvents. This aspect has been evidenced in previous theoretical studies[19] in which a single cation was allowed to interact with the TS, forming a hydrogen bond with the carbonyl oxygen; this aspect was not considered in the work of Sato,[13] where the geometries considered were those obtained in the gas phase. Also, the subsequent reduction of the imaginary frequency for the solvated TS when compared to the gas phase one, found in previous studies,[14] has been reproduced by us without the need for a specific quantum-mechanical interaction between the IL cation and the substrate. Then, even if it appears consolidated that the asynchronicity of the reaction is enhanced in ILs, it appears from our calculations that this aspect is not necessarily related to the presence of strong hydrogen bonding between the unique ring hydrogen and the dienophile (this aspect was first suggested by Acevedo and Jorgensen[18]).

Electronic Level. The presence of the ionic liquid raises the electronic energy of the TS by about 2−5 kcal/mol; this rise is accompanied by a switching of the order of the two frontier orbitals HOMO and HOMO−1. The combined effect of geometry distortion and electronic modification of the TSs leads to a large modification of the dipole moment of the TS, passing from 4.11 to 6.09 D for the exocis form and from 4.24 to 5.97 D for the endotrans form. The energy of these levels is slightly lower in the endo-TS with respect to the exo-TS; nevertheless, the electronic energy of the endocis transition state is lower than the exocis by 1.64 kcal/mol (see Table 2). This will play a key role in selectivity, as will be shown in the following discussion.

Solvation Free Energy. The most important effect on the reaction rate is given by the solvation free energy. The difference in $\Delta\mu$ between the isolated reagents and the transition state amounts to 8−10 kcal/mol, giving a substantial contribution to the barrier lowering in ILs, very similar to what happens in water.[20] This conclusion, already evidenced in the very recent paper by Sato and co-workers,[13] can be further investigated by inspecting the contribution of electronic and solvation contributions to free energy, which are reported in Figure 4; here, it can be appreciated that there is a minimum in solvation energy in correspondence of the TS geometry. The presence of a generalized solvophobic effect on neutral solutes in ILs with features very similar to that of water has been recently pointed out;[21] at present, it is believed that the (generally positive) solvation free energy of a neutral solute in a ionic liquid is dominated by the unfavorable process of creating a cavity of suitable size to accommodate the solute, which for an ionic liquid requires
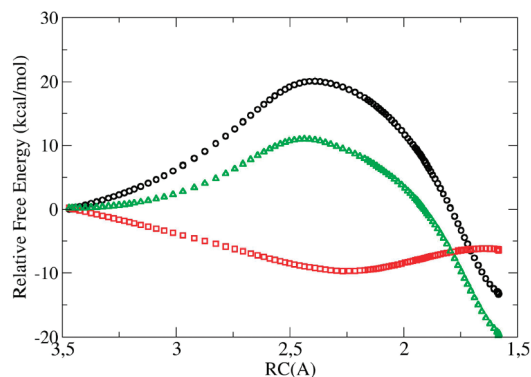

Figure 4. Contribution of electronic energy (black circles) and solvation energy (red squares) to reaction free energy (green triangles) as a function of reaction coordinate. The thermal and zero-point correction to free energy are not reported here.

a considerable amount of work due to the lowering of the Coulombic interactions, which cannot be recovered by dipole−ion (or even less efficient) interaction.[22]

For this reason, the aggregation of the organic moieties in ILs is strongly favorable, and this aspect drives the reaction rate in ionic liquids. A more detailed discussion of this aspect will be presented in the following discussion.

Endo/Exo Ratio. The endo/exo ratio has been studied and found, on the basis of M06-2X results, to be consistent with experiments and previous calculations; the difference in energy between the endocis-TS and the exocis-TS is found to be 2.03 kcal/mol, while the one between endotrans and the exotrans is 1.07 kcal/mol. Taking into account the relative equilibrium amount of *cis*- and *trans*-acrolein, an endo/exo ratio of 88:12 was found, while the corresponding ratio in the void was found to be about 70:30. The ionic liquid thus enhances the endo selectivity of the reaction, in agreement with experiments.[10] By inspection of Table 2, it can be readily seen that the origin of this enhancement is due to the electronic contribution to the free energy, which is lower in the endocis structure; conversely, the excess solvation free energy, which enhances the importance of the trans reaction route, appears to play a negligible role on the selectivity rise. This appears to go in the opposite direction with respect to water, in which the endo selectivity enhancement was found to be due to excess free energy of solvation, as already shown;[13] nevertheless, the electronic origin of the enhanced selectivity was not investigated in detail.

This favorable electronic reorganization energy in the endo TS conformer has been suggested by some of us to be due to the relative orientation of the π system of the diene with respect to the activated dienophile.[11] To confirm this, the obtained structures have been analyzed by taking into account the energies obtained at the OLYP level, which is not as good as M06-2X, to take into account the $\pi-\pi$ interaction.[15] At the OLYP level, the obtained endo/exo ratio was 1.40 in the IL, while in the void the exo product was slightly more probable than the endo product.

The ionic liquid can be probably thought to enhance the $\pi-\pi$ dispersion interaction between the reactants: from comparison of the two different functionals, it is nevertheless

Reaction of Cyclopentadiene with Acrolein

J. Chem. Theory Comput., Vol. 6, No. 1, 2010 **183**

evident that a proper description of $\pi-\pi$ interaction is mandatory to obtain reliable results about the endo selectivity.

Conclusions

In this work, we applied KS-DFT/3D-RISM-SCF to the Diels−Alder reaction in room-temperature ionic liquids. This method is able to obtain results in general agreement with experiment and proposes itself as a very powerful analysis method for processes in ionic liquids. Our results are in general agreement with results displayed by Sato and co-workers, which for the first time applied a mixed QM/RISM approach to this reaction in a ionic liquid. We go further on the direction pointed by this last work by analyzing the effect of the IL on the electronic and geometric structure of adducts.

The structure of the TS is deformed by the presence of the IL, and the asynchronicity of the reaction is augmented; the frequency of the barrier passing is nevertheless slightly lowered in ILs.

The importance of the hydrogen bonding between unique CR and carbonyl oxygen has been revised and found to be not of capital importance for the reaction. Both aspects were already noticed by Jorgensen with much more sophisticated calculations.

The rate acceleration observed in ILs is given by the free energy of solvation, which promotes aggregation of nonionic molecules in ILs solutions. On the other side, the endo selectivity enhancement in ILs is driven by electronic energy, which comes probably from the most favorable $\pi-\pi$ interaction between the reactants, which is enhanced in IL.

References

(1) Ionic Liquids IIIB: Fundamentals, Progress, Challenges, and Opportunities-Transformations and Processes. *ACS Symposium Series 902*; Rogers, R. D., Seddon, K. R., Eds.; American Chemical Society: Washington, D.C., 2005. Ionic Liquids IIIA: Fundamentals, Progress, Challenges, and Opportunities-Properties and Structure. *ACS Symposium Series 901*; Rogers, R. D., Seddon, K. R., Eds.; American Chemical Society: Washington, D.C., 2005. In *Ionic Liquids in Synthesis*, 2nd ed.; Wasserscheid, P., Welton, T., Eds.; Wiley-VCH: Weinheim, 2007.

(2) Chiappe, C.; Pieraccini, D. *J. Phys. Org. Chem.* **2005**, *18*, 275.

(3) (a) Lopes, J. N. A.; Padua, A. A. H. *J. Phys. Chem B* **2006**, *110*, 3330. (b) Chiappe, C. *Monatsh. Chem.* **2007**, *137*, 1035. (c) Xiao, D.; Rajian, J. R.; Hines, L. G.; Li, S.; Bartsch, R. A.; Quitevis, E. L. *J. Phys. Chem B* **2008**, *112*, 13316. (d) Consorti, C, S.; Suarez, P. A. Z.; de Souza, R. F.; Burrow, R. A.; Farrar, D. H.; Lough, A. J.; Loh, W.; da Silva, L. H. M.; Dupont, J. *J. Phys. Chem. B* **2005**, *109*, 4341.

(4) Hu, Z.; Margulis, C. J. *Proc. Natl. Acad. Sci. U.S.A.* **2006**, *103*, 831.

(5) (a) Lancaster, N. L.; Welton, T. *J. Org. Chem.* **2004**, *69*, 5986. (b) Anderson, J. L.; Ding, J.; Welton, T.; Armstrong, D. W. *J. Am. Chem. Soc.* **2002**, *124*, 14247. (c) Crowhurst, L.; Lancaster, N. L.; Perez Arlandis, J. M.; Welton, T. *J. Am.*

Chem. Soc. **2004**, *126*, 11549. (d) Lancaster, N. L.; Salter, P. A.; Welton, T.; Young, G. B. *J. Org. Chem.* **2002**, *67*, 8855. (e) Chiappe, C.; Pieraccini, D. *J. Org. Chem.* **2004**, *69*, 6059. (f) Grodkowski, J.; Neta, P.; Wishart, J. F. *J. Phys. Chem. A* **2003**, *107*, 9794. (g) Skrzypczak, A.; Neta, P. *J. Phys. Chem. A* **2003**, *107*, 7800. (h) D'Anna, F.; Frenna, V.; Noto, R.; Pace, V.; Spinelli, D. *J. Org. Chem.* **2006**, *71*, 5144. (i) Chiappe, C.; Pieraccini, D.; Sullo, P. *J. Org. Chem.* **2003**, *68*, 6710. (l) Bini, R.; Chiappe, C.; Pieraccini, D.; Piccioli, P.; Pomelli, C. S. *Tetrahedron Lett.* **2005**, *46*, 6675. (m) Crowhurst, L.; Falcone, R.; Lancaster, N. L.; Llopsis-Mestre, V.; Welton, T. *J. Org. Chem.* **2006**, *71*, 8847. (n) Hallet, J. P.; Liotta, C. L.; Ranieri, G.; Welton, T. *J. Org. Chem.* **2009**, *74*, 1864.

(6) Harper, J. B.; Kobrak, M. N. *Mini-Rev. Org. Chem.* **2006**, *3*, 253.

(7) Tomasi, J.; Mennucci, B.; Cammi, R. *Chem. Rev.* **2005**, *105*, 2999.

(8) Malvaldi, M.; Bruzzone, S.; Chiappe, C.; Gusarov, S.; Kovalenko, A. *J. Phys. Chem. B,* **2009**, *113*, 3536.

(9) (a) Lee, C. W. *Tetrahedron Lett.* **1999**, *40*, 2461. (b) Agarwal, A.; Lancaster, N. L.; Sethi, A. R.; Welton, T. *Green Chem.* **2002**, *4*, 517. (c) Earle, M. J.; McCormac, P. B.; Seddon, K. R. *Green Chem.* **1999**, *1*, 23. (d) Fischer, T.; Sethi, A. R.; Welton, T.; Woolf, J. *Tetrahedron Lett.* **1999**, *40*, 793. Howarth, J.; Hanlon, K.; Fayne, D.; McCormac, P. *Tetrahedron Lett.* **1997**, *38*, 3097. (e) Vidis, A.; Ohlin, C. A.; Laurenczy, G.; Küster, E.; Sedelmeier, G.; Dyson, P. J. *Adv. Synth. Catal.* **2005**, *347*, 266. Silvero, G.; Arévalo, A. J.; Bravo, J. L.; Jiménez, J. L.; López, I. *Tetrahedron* **2005**, *61*, 7105. (f) Sarma, D.; Kumar, A. *Appl. Catal., A* **2008**, *335*, 1.

(10) Bini, R.; Chiappe, C.; Llopsis Mestre, V.; Pomelli, C. S.; Welton, T. *Org. Biomol. Chem.* **2008**, *6*, 2522.

(11) Bini, R.; Chiappe, C.; Llopsis Mestre, V.; Pomelli, C. S.; Welton, T. *Theor. Chem. Acc.* **2009**, *123*, 347.

(12) Kovalenko, A.; Hirata, F. *Chem. Phys. Lett.* **1998**, *290*, 237. Kovalenko, A.; Hirata, F. *J. Chem. Phys.,* **1999**, *110*, 10095.

(13) Hayaki, S.; Kido, K.; Yokogawa, D.; Sato, H.; Sakaki, S. *J. Phys. Chem. B* **2009**, *113*, 8230.

(14) Malvaldi, M.; Bruzzone, S.; Chiappe, C. *Phys. Chem. Chem. Phys.* **2007**, *9*, 5576.

(15) Zhao, Y.; Truhlar, D. G. *Acc. Chem. Res.* **2008**, *41*, 157.

(16) Deng, L.; Ziegler, T. *Int. J. Quantum Chem.* **1994**, *52*, 731.

(17) ADF2008.01, SCM, Theoretical Chemistry, Vrije Universiteit, Amsterdam, The Netherlands, http://www.scm.com (accessed June 8, 2009).

(18) Acevedo, O.; Jorgensen, W. L.; Evanseck, J. D. *J. Chem. Theory Comput.* **2007**, *3*, 132.

(19) Sun, H.; Zhang, D.; Ma, C.; Liu, C. *Int. J. Quantum Chem.* **2007**, *107*, 875.

(20) Harano, Y.; Sato, H.; Hirata, F. *J. Am. Chem. Soc.* **2000**, *122*, 2289.

(21) Koddermann, T.; Paschek, D.; Ludwig, R. *Phys. Rev. Lett.* **2008**, *100*, 115901.

(22) Kobrak, M. N. *J. Phys. Chem. B* **2007**, *111*, 4755. Pomelli, C.; Malvaldi, M.; Chiappe, C. *Pure Appl. Chem.* **2009**, *81*, 767.

JCTC Journal of Chemical Theory and Computation

Free Energy Barriers for the N-Terminal Asparagine to Succinimide Conversion: Quantum Molecular Dynamics Simulations for the Fully Solvated Model

Ilya Kaliman,*[,†] Alexander Nemukhin,[†,‡] and Sergei Varfolomeev[†,‡]

*Department of Chemistry, M.V. Lomonosov Moscow State University, Moscow 119991,
Russian Federation, and N.M. Emanuel Institute of Biochemical Physics,
Russian Academy of Sciences, Moscow 119334, Russian Federation*

Abstract: Deamidation of asparagine residues represents one of the main routes for the post-translational modification of protein sequences. We computed the estimates of the free energy barriers for three stages of the deamidation process, deprotonation, cyclization, and deamination, of the conversion of asparagine to the succinimide intermediate within the fully solvated model with explicit water molecules. The Born−Oppenheimer molecular dynamics in the Gaussian and Plane Wave (GPW) approximation as implemented in the CP2K quantum chemistry package was utilized to sample the configurational space. By applying the metadynamics technique, the estimates of the free energy barriers were obtained for three separated stages of the reaction. In agreement with the experimental kinetic measurements, the estimated activation barriers do not exceed 21 kcal/mol. We demonstrate that the use of fully solvated models is the critical issue in theoretical studies of these reactions. We also conclude that more extensive sampling is necessary to obtain full free energy profiles and accurate barriers for the reaction stages.

Introduction

Spontaneous deamidation of asparagine residues leading to aspartic acid residues presents one of the pathways of protein degradation that affects structure and function of proteins.[1] The immense importance of this process is due to its relevance to the development of Alzheimer's disease.[2] The instability of glutaminyl and asparaginyl residues in proteins has been suggested to play a central biological role, and it is proposed that these residues serve as some sort of biological "clocks" for the regulation of processes in cells.[3] It was also proposed that accumulation of protein defects resulting from these processes may be one of the root causes of human aging.[4] The isomerization and racemization processes are known to play an important role not only in vivo but also during purification, storage and, transformation of proteins and polypeptides.[5]

The process of isomerization proceeds through formation of a cyclic imide intermediate.[1,6] This succinimide can be later hydrolyzed leading to aspartate and isoaspartate in the proportion 1:3.[7] A competent summary of what is known about the asparagine deamidation mechanism from the experimental side is presented in the paper of Peters and Trout,[8] and there is no need to retell it in full. For the goals of the present work, it is essential to underline the following: (i) the deamidation mechanism in a protein is the same as in a model peptide;[9] (ii) the conversion of asparagine to succinimide is the rate limiting step;[10] (iii) the rates of deamidation of model peptides obey the Arrhenius equations with the activation energies near 22 kcal/mol at pH 5−7.5.[11]

The tentative mechanism of succinimide ring formation proposed by Capasso et al.[12] can be illustrated in Scheme 1. In the first stage, the deprotonation of a peptide group occurs which may be stimulated either by basic pH or by presence of a nearby molecular group that plays the role of a base. Therefore, such a reaction route can be substantiated in proteins. Next, the cyclization to the tetrahedral intermediate takes place as a result of nucleophilic attack of nitrogen from

---

* Corresponding author e-mail: ilya.kaliman@gmail.com.
† M.V. Lomonosov Moscow State University.
‡ Russian Academy of Sciences.

Free Energy Barriers for Asparagine to Succinimide

J. Chem. Theory Comput., Vol. 6, No. 1, 2010 **185**

Scheme 1. Stages of the Succinimide Ring Formation from Asparagine
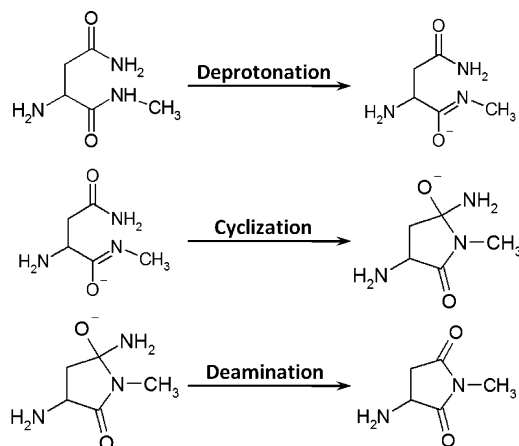
the peptide group on the carbonyl C atom. Finally, leaving of the NH_2 group occurs (the deamination stage) resulting in a cyclic imide product. This stage may be facilitated by general base catalysis.

Beyond experimental investigations, the asparagine isomerization was also studied by the methods of quantum chemistry. The reaction mechanisms for the molecular rearrangements shown in Scheme 1 were modeled by using density functional theory (DFT) calculations corrected by the polarized continuum model (PCM).[13−15] The results qualitatively agree with the mechanism proposed by Capasso et al.[12] Related theoretical studies[16,17] have been performed to rationalize the observation that aspartyl and asparagine residues racemize rapidly compared to other amino acid residues in proteins and peptides. This effect has been attributed to the increased acidity of the α-carbon atoms of succinimide residues. In a series of papers by Catak et al.,[18−20] it is shown that inclusion of an explicit aqueous environment in modeling these reactions is a very important issue. With the help of DFT-based calculations, the authors studied the water-assisted mechanisms of succinimide formation with different amounts of explicit water molecules. They concluded that the most favorable reaction mechanism corresponded to the formation of a succinimide intermediate and involved tautomerization of the asparagine amide to the corresponding imidic acid in the initial reaction step. Peters and Trout[8] simulated a network of elementary reactions for asparagine deamidation also by using the DFT-based quantum chemistry methods corrected for the effects of aqueous environment in the continuum solvent model.

Significantly, all the quantum chemical calculations[8,13−15,18−20] resulted in activation barriers that grossly overestimated, by at least 10 kcal/mol, the experimental value of 22 kcal/mol.[11] Substantial lowering of energy barriers from around 50 kcal/mol was achieved when explicit water molecules were added to the model system. It was suggested[18] that molecular dynamics simulations within the fully solvated model that also accounts for water assistance should be necessary to accurately simulate these processes. In this work, we describe the application of a quantum molecular dynamics procedure within the fully solvated model for estimates of free energy reaction profiles for the stages illustrated in Scheme 1. This approach allows us to obtain the results for the water-assisted mechanism quantitatively consistent with the experimental data. As a model system, we consider the peptide shown in Scheme 1, which was also used in earlier works.[13−15]

Methods and Computational Details

All simulations were performed by using the CP2K program (http://cp2k.berlios.de). The Quickstep module[21] of the CP2K program was utilized for electronic structure calculations. This approach provides the $O(n)$ implementation of the density functional theory calculations allowing simulations for hundreds of atoms. It relies on the pseudopotential and plane wave methodology in addition to the conventional Gaussian basis set approximations (the Gaussian and Plane Wave method, GPW)[22] to make practical calculations for extended systems.

The method of metadynamics[23,24] was used to obtain free energy profiles for the reaction stages. At present, the available computational resources do not allow observation of such rare events as chemical reactions in model systems by using equilibrium methods of molecular dynamics due to the prohibitively large volume of the configurational space to be explored. The method of metadynamics is one of nonequilibrium-based approaches that allows one to perform simulation of chemical reactions in feasible time.[25] This method was recently used for studies of bacterial chloride channels,[26] deprotonation of formic acid,[27] flexible ligand docking,[28] and a study of decarboxylation mechanism in orotidine-5′-monophosphate decarboxylase.[29]

The method of metadynamics assumes that a small set $s_i(n)$ of relevant collective variables (CVs) can be selected allowing one to construct projections of the free energy surface $F(s)$ on these collective variables. The CVs may be specific functions of atomic coordinates including distances, angles, coordination numbers, dihedral angles, and so forth. The history-dependent Gaussian hills are added to the biasing potential during the simulation (eq 1). This potential builds up until it counterbalances the underlying free energy well, allowing the system to escape via a saddle point to a nearby local minimum, where the procedure is repeated. When all minima are "filled" with Gaussian potential hills, the system moves barrier-free among the different states. The free energy is obtained as a negative sum of added Gaussian hills (eq 2).[30]

$$V_{\text{bias}}(\mathbf{s}, t) = \sum_{t_i} H \exp\left(-\frac{|\mathbf{s} - \mathbf{s}(t_i)|^2}{2\omega^2}\right) \qquad (1)$$

$$F(\mathbf{s}) = -V_{\text{bias}}(\mathbf{s}, t) \qquad (2)$$

In the limit of the infinitely long trajectory, the biasing potential exactly cancels the underlying free energy surface along the collective variable.

Our model system was composed of 333 atoms including the peptide and 104 water molecules. The periodic boundary conditions were imposed to simulate the bulk. The dimensions of the model cell were $15 \times 15 \times 15$ Å^3 (Figure 1).
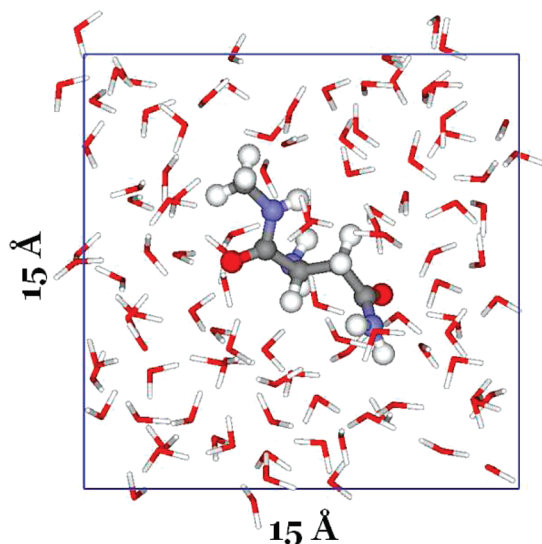
Figure 1. Schematic presentation of the model system.

We used the largest possible cell that allowed us to complete simulations in feasible time. However, the size of this cell does not allow us to pretend for description of such macroscopic properties as pH or concentration.

A dual basis set was used in which the wave functions were described by the Gaussian functions and the electronic density was described by auxiliary plane waves. The TZV2P Gaussian basis set[31,32] was used in all GPW calculations. The plane wave basis was extended to the density cutoff of 280 Ry. We utilized the pseudopotential of Goedeker, Teter, and Hutter (GTH)[33] to describe the core electrons. The BLYP gradient corrected functional was used to compute exchange-correlation contributions.[34,35] To sample the configurational space, we used the Born—Oppenheimer molecular dynamics in which the convergence criterion for the SCF procedure was set to 10^{-7} au at each step. An orbital transformation scheme[36] that is known to substantially accelerate convergence of the SCF procedure was used. The time step of 0.5 fs was utilized in all molecular dynamic calculations. The CSVR (canonical sampling through velocity rescaling)[37] scheme was applied for thermolization of the system. All simulations were performed at 300 K. The metadynamics parameters chosen were 0.001 au for the hill height and 0.5 au for the hill width. The mass of virtual particle in metadynamics simulations was selected to be 100 au.

The initial equilibration of the entire system was performed by using the empirical CHARMM force field.[38] After solvation and energy minimization, the system was equilibrated for 500 ps. Next, the equilibration with fully quantum description was performed for additional 20 ps. For modeling of the second and the third stages of the reaction (Scheme 1), the initial conformations and velocities were extracted from the metadynamics simulation of previous stage with preliminary equilibration for another 10 ps. The trajectory lengths for metadynamics simulations were 25—30 ps.

Results and Discussion

In our molecular dynamics simulations, we use the Gaussian and Plane Wave method to describe the electronic structure of the model system. Here, we provide an additional check of this approach against the conventional all-electron density functional theory with the B3LYP functional. The latter approach, known as an adequate tool for molecular modeling, was used in previous studies of this reaction.[8,13–15,18–20] The 6-311++G(d,p) basis set was used in all DFT/B3LYP calculations with the PC GAMESS quantum chemistry package (http://classic.chem.msu.su/gran/gamess/index.html).[39] We compared the computed equilibrium geometry configurations and relative energies for the stationary points of the model peptide referred to the reagent, transition state, intermediate, and product structures shown in insets of Table 1. These calculations were performed without water environment.

The comparison of optimized geometries shows almost perfect agreement between the Gaussian and Plane Wave based method on one hand and the all-electron B3LYP approach on the other hand: the deviation between the structures obtained with these two methods does not exceed 0.1 Å for internuclear distances and 2° for angles. Comparison of the relative energies shows that the GPW method describes the potential energy surface of the model system accurately enough (Table 1) but requires much less computational resources.
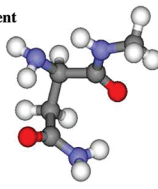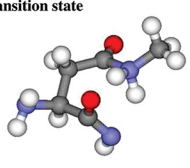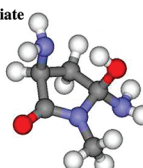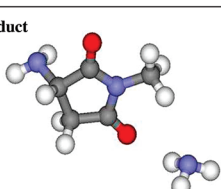
Next, we describe and discuss the resulting free energy profiles for the three stages of the mechanism of succinimide formation shown in Scheme 1: deprotonation, cyclization, and deamination, inside the shell of water molecules (Figure 1).

Deprotonation Stage. For modeling this stage, we select the distance between N and H atoms, describing cleavage of the N—H bond from the initial value of 1.08 Å, as the collective variable. The computed free energy profile along this collective variable for the deprotonation stage is presented in Figure 2 showing the activation barrier not exceeding 21 kcal/mol.

Initially, the system is located in the potential energy minimum near $r_{\text{N–H}} \approx 1$ Å. As soon as this minimum is filled with Gaussians, the N—H bond breaks, and the proton moves to the bulk phase. We notice that, upon cleavage of the N—H bond, the zwitterionic species is formed. We also notice that the leaving proton is transferred to the nearby water molecule but not directly to the amino group. The result of the subsequent hydrogen-bond reorganization is a transfer of another proton to the amino group leading to the zwitterionic conformation. We see that the proton that protonates the $-\text{NH}_2$ group is not physically the proton from the collective variable so we cannot reliably sample the corresponding conformations. An important issue is that the zwitterionic species is stable only in the presence of solvent water molecules. Attempts to optimize the corresponding structure without a water environment resulted in the back transfer of the proton to the nitrogen atom.

The outer minimum refers to the system in which the proton from the collective variable is in the bulk. Because of the difficulties to sample the corresponding conformations, it is hardly possible to accurately estimate the free energy of this product state. The shape and depth of the outer minimum should depend on concentration and the

Free Energy Barriers for Asparagine to Succinimide

J. Chem. Theory Comput., Vol. 6, No. 1, 2010 **187**

Table 1. Computed Relative Energies of Four Structures of the Model Peptide (kcal/mol)

Structure		GTH/BLYP/TZV2P/280Ry	B3LYP/6-311++G(d,p)
Reagent		0.0	0.0
Transition state		55.1	55.4
Intermediate		19.9	16.7
Product		6.4	7.7

size of the cell. However, this does not affect estimates of the activation barrier heights. We think that the presence of the minimum near $r_{N-H} \approx 2.5$ Å might also be attributed to the difficulties of sampling the region with the proton in the bulk.

In Figure 3, the CV dynamics graph is shown. From this picture, it is clear that the backward reaction is not observed because the process is not reversible. From this fact, we conclude that the negative metadynamics biasing potential gives us only an estimate of the reaction barrier. On the basis

of the observed bumps in free energy profile, we conclude that the error should be within 5 kcal/mol. To obtain a full free energy profile and a more accurate value for the barrier, one needs to conduct a much longer simulation. However, it is unclear whether it is possible to see the backward reaction in a feasible time during the simulation.

Cyclization Stage. Next, we modeled the cyclization stage corresponding to the formation of the succinimide ring. It results from the attack of the peptide bond nitrogen on the carbon from the amide group. For this stage, we

Figure 2. Free energy profile for the deprotonation stage. Collective variable is marked with the green line and squares.
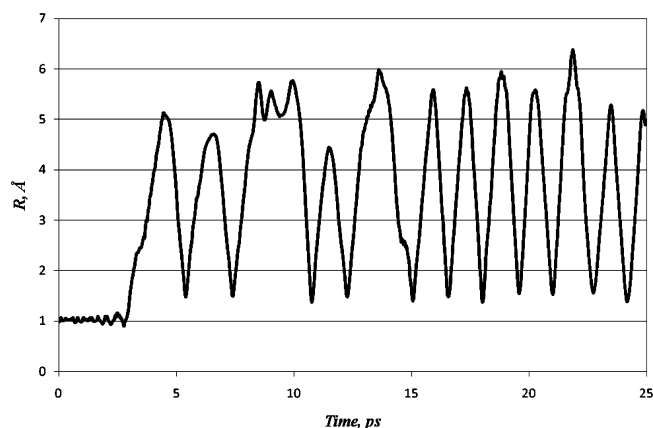
Figure 3. Dynamics of the N–H distance.
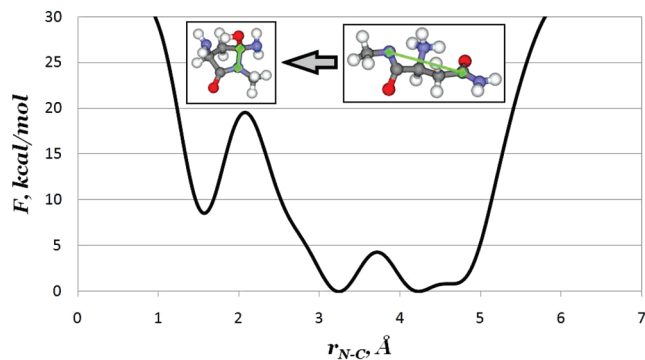
Figure 4. Free energy profile for the cyclization stage. Collective variable is marked with the green line and squares.
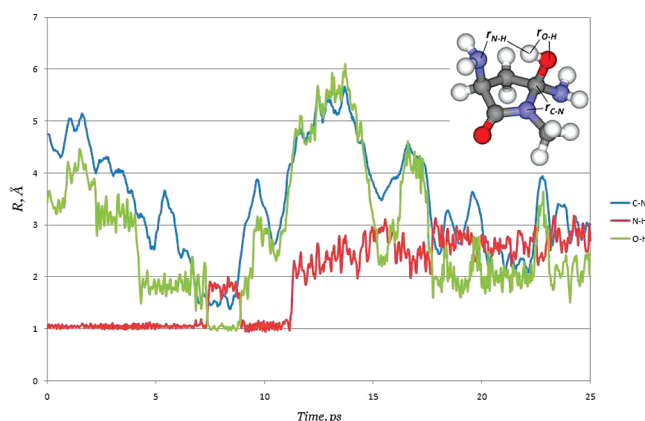
Figure 5. Dynamics of the C−N, N−H, and O−H distances.

Figure 6. Free energy profile for the deamination stage. Collective variable is marked with the green line and squares.
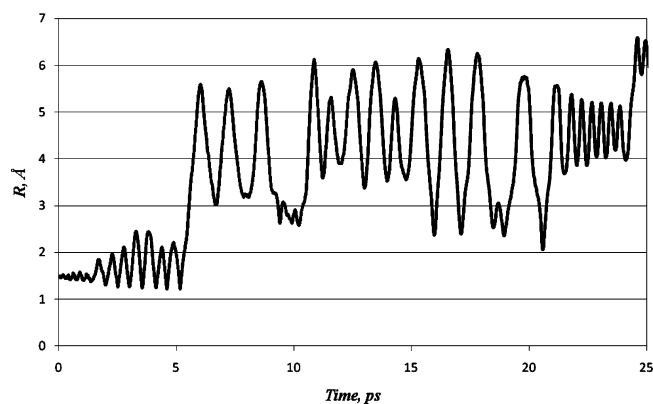
Figure 7. Dynamics of the C−N distance.

used the distance between N and C as the collective variable. The resulting free energy profile is shown in Figure 4. The calculated free energy barrier is about 20 kcal/mol. Initially, the system resided in a rather wide energy well (between 3.2 and 4.8 Å) that was accounted for by an unconstrained motion of the peptide chain. We think that the small maximum near $r_{N-C} \approx 3.7$ Å can be attributed to the insufficient sampling. When this well is "filled" with Gaussian functions, the system moved to another local minimum at $r_{N-C} \approx 1.5$ Å, and the chemical bond was formed between N and C atoms yielding the succinimide ring.

We notice that the excess proton from the amino group was transferred to the newly formed negatively charged oxygen leading to hydroxyl formation accompanied by the hydrogen bonding with the nearby amino group. In Figure 5, we show the dynamics of the C−N, N−H, and O−H distances. From the graph, it is clear that, as soon as the ring is formed (about 7 ps), the proton is transferred to the oxygen (it is worth noting similarities in the behavior of the C−N and O−H distances). But after the system recrosses the barrier and the ring is broken, we observe the back transfer of the proton.

Deamination Stage. Finally, the free energy profile for the deamination process was calculated. The collective variable chosen for this stage was the distance between the nitrogen atom from the leaving amino group and the adjacent carbon atom (the C−N bond distance). The resulting free

energy profile is shown in Figure 6. The computed free energy barrier for this stage is about 15 kcal/mol. The profile shows that this stage is characterized by the lowest free energy barrier that suggests that the deamination stage should proceed relatively easily compared to the first two stages. From the metadynamics trajectory, we see that the state of the living group is NH_3. The leaving -NH_2 group of the peptide is protonated by the excess proton formed in the deprotonation stage.

The peak in the profile near 4 Å on the CV axis may be attributed to insufficient sampling in the regions where the formed ammonia is far from the newly formed succinimide. As in the case with the deprotonation stage, it is difficult to sample the region of the outer minimum, and its shape should depend on concentration and the size of the cell.

In Figure 7, the dynamics of the C−N collective variable is shown. As in the case of deprotonation reaction, we are unable to see the recrossing of the barrier because the process is not reversible so the negative metadynamics biasing potential gives us only an estimate of the activation barrier for the given process.

Conclusion

Following the results of quantum simulations for separate stages of the mechanism of the cyclic imide formation from the asparagine residue in aqueous solution with an explicit treatment of water molecules, we conclude that the rate limiting stage refers either to deprotonation or to cyclization.

Free Energy Barriers for Asparagine to Succinimide

J. Chem. Theory Comput., Vol. 6, No. 1, 2010 **189**

The corresponding free energy barriers of these steps are estimated as 20−21 kcal/mol. The estimated free energy barrier for the deamination stage is 15 kcal/mol. Based on the observed bumps in free energy profiles, the error of obtained free energy barriers should be about 5 kcal/mol. We conclude that longer trajectories and better sampling are necessary to obtain full free energy profiles and more accurate barriers for the reaction stages. However, it is unclear whether it is possible to observe a backward reaction for stages 1 and 3 in feasible simulation time. Nevertheless, our estimates for the free energy barriers are consistent with the available experimental kinetic measurements showing the Arrhenius activation barrier of about 22 kcal/mol.[11]

If solvent molecules are ignored, the unrealistic energy barriers (above 50 kcal/mol) are predicted in quantum calculations. We show that one of the reaction intermediates can be stabilized only in the presence of water molecules. Therefore, the results of simulations demonstrate that the use of fully solvated models and implication of extensive sampling are the critical issues in theoretical studies of these reactions.

References

(1) Reissner, K. J.; Aswad, D. W. *Cell. Mol. Life Sci.* **2003**, *60*, 1281–1295.

(2) Payan, I. L.; Chou, S.; Fisher, G. H.; Man, E. H.; Emory, C.; Frey, W. H. *Neurochem. Res.* **1992**, *17*, 187–191.

(3) Robinson, N. E.; Robinson, A. B. *Proc. Natl. Acad. Sci. U.S.A.* **2001**, *98*, 944–949.

(4) Clarke, S. *Aging Res. Rev.* **2003**, *2*, 263–285.

(5) Kerrow, J. H.; Robinson, A. B. *Anal. Biochem.* **1971**, *42*, 565–568.

(6) Capasso, S.; Mazzarella, L.; Sica, F.; Zagari, A. *J. Peptide Res.* **1989**, *2*, 195–200.

(7) Geiger, T.; Clarke, S. *J. Biol. Chem.* **1987**, *262*, 785–794.

(8) Peters, B.; Trout, B. L. *Biochemistry* **2006**, *45*, 5384–5392.

(9) Capasso, S.; Salvadori, S. *J. Peptide Res.* **1999**, *54*, 377–382.

(10) Capasso, S.; Kirby, A.; Salvadori, S.; Sica, F.; Zagari, A. *J. Chem. Soc. Perkin Trans. 2* **1993**, 437–442.

(11) Patel, K.; Borchardt, R. T. *Pharm. Res.* **1990**, *7*, 703–711.

(12) Capasso, S.; Mazzarella, L.; Sica, F.; Zagari, A.; Salvadori, S. *J. Chem. Soc. Perkin Trans. 2* **1993**, 679–682.

(13) Konuklar, F. A.; Aviyente, V.; Sen, T. Z.; Bahar, I. *J. Mol. Model.* **2001**, *7*, 147–160.

(14) Konuklar, F. A.; Aviyente, V.; Ruiz-Lopez, M. F. *J. Phys. Chem. A* **2002**, *106*, 11205–11214.

(15) Konuklar, F. A.; Aviyente, V. *Org. Biomol. Chem.* **2003**, *1*, 2290–2297.

(16) Radkiewicz, J. L.; Zipse, H.; Clarke, S.; Houk, K. N. *J. Am. Chem. Soc.* **1996**, *118*, 9148–9155.

(17) Radkiewicz, J. L.; Zipse, H.; Clarke, S.; Houk, K. N. *J. Am. Chem. Soc.* **2001**, *123*, 3499–3506.

(18) Catak, S.; Monard, G.; Aviyente, V.; Ruiz-Lopez, M. F. *J. Phys. Chem. A* **2006**, *110*, 8354–8365.

(19) Catak, S.; Monard, G.; Aviyente, V.; Ruiz-Lopez, M. F. *J. Phys. Chem. A* **2008**, *112*, 8752–8761.

(20) Catak, S.; Monard, G.; Aviyente, V.; Ruiz-Lopez, M. F. *J. Phys. Chem. A* **2009**, *113*, 1111–1120.

(21) VandeVondele, J.; Krack, M.; Mohamed, F.; Parrinello, M.; Chassaing, T.; Hutter, J. *Comput. Phys. Commun.* **2005**, *167*, 103–128.

(22) Lippert, G.; Hutter, G.; Parrinello, M. *Mol. Phys.* **1997**, *92*, 477–487.

(23) Laio, A.; Parrinello, M. *Proc. Natl. Acad. Sci. U.S.A.* **2002**, *99*, 12562–12566.

(24) Iannuzzi, M.; Laio, A.; Parrinello, M. *Phys. Rev. Lett.* **2003**, *90*, 238302–238305.

(25) Ensing, B.; Laio, A.; Parrinello, M.; Klein, M. L. *J. Phys. Chem. B* **2005**, *109*, 6676–6687.

(26) Gervasio, F. L.; Parrinello, M.; Ceccarelli, M.; Klein, M. L. *J. Mol. Biol.* **2006**, *361*, 390–398.

(27) Lee, J. G.; Asciutto, E.; Babin, V.; Sagui, C.; Darden, T.; Roland, C. *J. Phys. Chem. B* **2006**, *110*, 2325–2331.

(28) Gervasio, F. L.; Laio, A.; Parrinello, M. *J. Am. Chem. Soc.* **2005**, *127*, 2600–2607.

(29) Stanton, C. L.; Kuo, I. W.; Mundy, C. J.; Laino, T.; Houk, K. N. *J. Phys. Chem. B* **2007**, *111*, 12573–12581.

(30) Ensing, B.; De Vivo, M.; Liu, Z.; Moore, P.; Klein, M. L. *Acc. Chem. Res.* **2006**, *39*, 73–81.

(31) VandeVondele, J.; Hutter, J. *J. Chem. Phys.* **2007**, *127*, 114105–114113.

(32) Schaefer, A.; Huber, C.; Ahlrichs, R. *J. Chem. Phys.* **1994**, *100*, 5829–5835.

(33) Goedecker, S.; Teter, M.; Hutter, J. *Phys. Rev. B* **1996**, *54*, 1703–1710.

(34) Becke, A. D. *Phys. Rev. A* **1988**, *38*, 3098–3100.

(35) Lee, C.; Yang, W.; Parr, R. G. *Phys. Rev. B* **1988**, *37*, 785789.

(36) VandeVondele, J.; Hutter, J. *J. Chem. Phys.* **2003**, *118*, 4365–4369.

(37) Bussi, G.; Donadio, D.; Parrinello, M. *J. Chem. Phys.* **2007**, *126*, 14101–14107.

(38) MacKerrell, A. D., Jr; Bashford, D.; Bellott, M.; Dunbrack, R. L., Jr; Evanseck, J. D.; Field, M. J.; Fischer, S.; Gao, J.; Guo, H.; Ha, S.; Joseph-McCarthy, D.; Kuchnir, L.; Kuczera, K.; Lau, F. T. K.; Mattos, C.; Michnick, S.; Ngo, T.; Nguyen, D. T.; Prodhom, B.; Reiher, W. E., III; Roux, B.; Schlenkrich, M.; Smith, J. C.; Stote, R.; Straub, J.; Watanabe, M.; Wiórkiewicz-Kuczera, J.; Yin, D.; Karplus, M. *J. Phys. Chem. B* **1998**, *102*, 3586–3616.

(39) Granovsky, A. A. PC GAMESS, version 7.1; Department of Chemistry, M. V. Lomonosov Moscow State University: Moscow, Russia, 2007.

JCTC Journal of Chemical Theory and Computation

Gaussian Multipole Model (GMM)

Dennis M. Elking,[†] G. Andrés Cisneros,[†] Jean-Philip Piquemal,[‡] Thomas A. Darden,[†]
and Lee G. Pedersen*[,†,§]

*Laboratory of Structural Biology, National Institute of Environmental Health Sciences,
P.O. Box 12233, MD K3-16, Research Triangle Park, North Carolina 27709,
Laboratoire de Chimie Théorique, UMR 7616 CNRS, Université
Pierre-et-Marie-Curie, Case Courier 137, 4, Place Jussieu, 75252 Paris, France, and
University of North Carolina, Department of Chemistry,
Chapel Hill, North Carolina 27599*

Abstract: An electrostatic model based on charge density is proposed as a model for future force fields. The model is composed of a nucleus and a single Slater-type contracted Gaussian multipole charge density on each atom. The Gaussian multipoles are fit to the electrostatic potential calculated at the B3LYP/6-31G* and HF/aug-cc-pVTZ levels of theory and tested by comparing electrostatic dimer energies, intermolecular density overlap integrals, and permanent molecular multipole moments with their respective ab initio values. For the case of water, the atomic Gaussian multipole moments Q_{lm} are shown to be a smooth function of internal geometry (bond length and angle), which can be approximated by a truncated linear Taylor series. In addition, results are given when the Gaussian multipole charge density is applied to a model for exchange−repulsion energy based on the intermolecular density overlap.

1. Introduction

Force fields are routinely used to simulate biological molecules in order to study structure and function. Recently, attention has been focused on developing accurate force field models that are able to provide a more realistic account of intermolecular interactions. For example, polarization models[1−6] have been incorporated into force fields[7−16] in order to account for many-body effects[17−20] in polar environments. In the SIBFA[10−12] force field, multipoles are placed on atoms and bond barycenters in order to accurately account for the anisotropy in electrostatic interactions. AMOEBA[13−16] places multipoles on atoms and has been developed as a force field for protein simulations. In addition, electrostatic models, which employ geometry-dependent charges, are being investigated.[21−24]

Atomic point multipole models derived from distributed multipole expansions[25−28] or fit to the electrostatic potential[29] (ESP) have been proposed to improve the description of electrostatic interactions. However, at short-range, it has been noted[25,30,31] that atomic point multipole electrostatic models significantly underestimate electrostatic interactions at dimer distances. This effect, called penetration error, becomes important at dimer distances where there is significant overlap of molecular charge densities. Damping functions[31−34] have been proposed as a short-range correction to atomic point multipoles in order to account for penetration effects.

Another approach for calculating short-range electrostatic interactions has been to model the electron density. For example, simple Gaussian charge densities[35−37] have been used in models for liquids. Wheatley[38,39] has studied Cartesian Gaussian multipole charge distributions,[40,41] which are obtained by differentiating simple normalized Gaussian functions. It was shown that at long-range, the interactions between Gaussian multipole charge densities behave asymptotically as point multipoles.[38] As an example, consider a Cartesian Gaussian dipole charge distribution ρ_μ with dipole moment $\vec{\mu}$, exponent α, and nuclear center $\vec{R}$ given by

---

* Corresponding author.lee_pedersen@unc.edu.

† Laboratory of Structural Biology, National Institute of Environmental Health Sciences.

‡ Laboratoire de Chimie Théorique, Université Pierre-et-Marie-Curie.

§ University of North Carolina, Department of Chemistry.

$$\rho_\mu(\vec{r}) \equiv \vec{\mu} \cdot \nabla_R \left(\frac{\alpha^2}{\pi}\right)^{3/2} \exp(-\alpha^2 |\vec{r} - \vec{R}|^2) \qquad (1)$$

where $\vec{r}$ is the field point and ∇_R is the Cartesian gradient with respect to the nuclear center $\vec{R}$. The electrostatic potential $\phi_\mu(\vec{r})$ arising from ρ_μ is given by

$$\phi_\mu(\vec{r}) = \int d^3r' \frac{\rho_\mu(\vec{r}')}{|\vec{r} - \vec{r}'|} = \vec{\mu} \cdot \nabla_R \frac{\text{erf}(\alpha|\vec{r} - \vec{R}|)}{|\vec{r} - \vec{R}|} \qquad (2)$$

where $\text{erf}(x)$ is the error function defined by

$$\text{erf}(x) \equiv \frac{2}{\sqrt{\pi}} \int_0^x \exp(-u^2) du \qquad (3)$$

Note that for large x, $\text{erf}(x) \approx 1$. Thus, for large exponents or separations, the electrostatic potential arising from a Gaussian dipole behaves as a point dipole, i.e.

$$\phi_\mu(\vec{r}) \approx \vec{\mu} \cdot \nabla_R \frac{1}{|\vec{r} - \vec{R}|} \qquad \alpha|\vec{r} - \vec{R}| >> 1 \qquad (4)$$

Recently, Giese and York[42] have derived the electrostatic energy integral, the density overlap integral, and the gradients of their matrix elements between contracted solid harmonic Gaussian (multipole) charge densities in the spherical tensor framework. In analogy to taking derivatives of simple normalized Gaussian functions to create Cartesian Gaussian multipoles, spherical tensor Gaussian multipoles can be constructed by contracting spherical tensor multipole moments Q_{lm} with the solid harmonic gradient operator[43,44] $C_{lm}(\nabla)$ acting upon a simple Gaussian function. In the Supporting Information, a summary of the mathematical background[43–47] used in this work, including definitions and theorems for the solid harmonic function $C_{lm}(x, y, z)$ and the solid harmonic gradient operator $C_{lm}(\nabla)$, is provided.

Methods of calculating the Gaussian charge density parameters are also being explored. Previously, we have proposed the Gaussian Electrostatic Model (GEM)[10,48–51] as an electrostatic model based on Gaussian charge density. The GEM density $\rho(r)$ is represented by a linear expansion of conventional auxiliary Gaussian basis sets. The density coefficients are fit to the ab initio density $\rho^{QM}(r)$ through a least-squares fit to the error in self-interaction electrostatic energy[52–56] ΔE_{self} given by

$$\Delta E_{\text{self}} = \langle \rho^{QM}(r) - \rho(r) | \frac{1}{r} | \rho^{QM}(r) - \rho(r) \rangle \qquad (5)$$

GEM has been shown to accurately reproduce intermolecular electrostatic interaction energies at both short- and long-range distances. In addition, it was also shown that a GEM-type model can be constructed by fitting to the electrostatic potential (ESP) numerically on a grid.[57] When fitting to ESP, it was found that fewer Gaussian basis functions were needed to reproduce ab initio intermolecular electrostatic energies as compared to fitting to the error in self-interaction electrostatic energy ΔE_{self}. In that work, we have also given some preliminary results for fitting a single s-type Gaussian charge function on each atom to the ESP. It was found that a simple model consisting of a single negative Gaussian charge distribution and positive nucleus on each atom is able to account for a large fraction of the penetration error and that it represents a significant improve-

ment over atomic point charge models for short-range electrostatic interactions.

In the present study, we propose a natural extension to the single (uncontracted) s-type Gaussian charge model by generalizing to a model based on a single diffuse contracted Gaussian multipole charge density on each atom. The radial part of the Gaussian multipole charge density is a Slater-type[58,59] contracted Gaussian function fit to $\exp(-\lambda r)$. For each atom, the Gaussian multipole moments Q_{lm} and a single Slater-type exponent parameter λ are fit to the ESP surrounding the molecule calculated at the B3LYP/6-31G* or HF/aug-cc-pVTZ levels of theory. The model is tested by comparing electrostatic dimer energies, intermolecular density overlap integrals, and permanent molecular moments with their reference ab initio values. In addition, a significantly improved method of fitting the Gaussian multipoles to the ESP numerically on a grid is adopted. In particular, angular grids available in most quantum chemistry codes are used, and a smooth weighting function, similar to the one proposed by Hu[60] et al., is used to filter out points near the nuclear centers.

In this work, we will show that a single diffuse contracted Gaussian multipole (shell) on each atom is capable of reproducing ab initio intermolecular electrostatic energies and density overlap integrals on hydrogen-bonded dimers at equilibrium geometries. For intermolecular electrostatic energies, the accuracy attained by Gaussian multipoles is shown to be approximately 0.1 kcal/mol, which is comparable to that of our original GEM model. Since the GEM model is represented by an auxiliary Gaussian basis set consisting of many uncontracted Gaussian shells (multipoles) on each atom, the proposed single Gaussian multipole model is expected to be an efficient model suitable for developing a force field for molecular dynamics simulations. In addition, since there are fewer fitted parameters used in Gaussian multipoles, the fit is more stable. Based on this property, the atomic Gaussian multipoles Q_{lm} are shown to be a continuous function of internal geometry (bond lengths and angles, etc). More specifically, it is shown that the atomic Gaussian multipole moments Q_{lm} can be approximated as a truncated linear Taylor series in both bond length and angle for the case of water.

The intermolecular density overlap integral calculated by Gaussian multipoles can be applied to the exchange–overlap model proposed by Wheatley and Price[61,62] for the exchange–repulsion energy. The first order intermolecular exchange–repulsion energy E_{exch} is defined as the total ab initio dimer energy minus the intermolecular electrostatic energy calculated using the frozen monomer wave functions. The ab initio exchange–repulsion energy E_{exch} can be modeled by fitting a proportionality constant K to the intermolecular density overlap integral S by

$$E_{\text{exch}} \cong K S^a \qquad (6)$$

where a is an empirical exponent parameter used to improve the quality of fit.[62] The expression in eq 6 is commonly generalized to a pairwise sum over atom–atom[61,62] contributions between the two monomers. One of the challenges of developing parameters and applying the exchange–overlap

model is first finding an accurate and convenient representation of the molecular charge density. In a previous work,[48,50] we have applied the exchange−overlap model in eq 6 to the GEM molecular charge density. A molecular pair K parameter was fit to the ab initio exchange−repulsion energy for the water−water dimer over several randomly oriented water−water geometries. Although fitting molecular pair K parameters over atomic pair parameters may not be ideal for constructing a general force field, we are interested in studying the effects of applying an anisotropic charge density to the exchange−overlap model. In the present study, a single molecular pair K parameter (eq 6) is fit to the ab initio exchange energies using the intermolecular density overlap integrals calculated by atomic Gaussian monopoles, dipoles, and quadrupoles for small molecule hydrogen-bonded dimers. Including anisotropy in the description of charge density is shown to make a significant improvement in reproducing ab initio exchange−repulsion energies.

In the following section, a Gaussian multipole charge density is defined, and expressions for the electrostatic potential, the electrostatic energy, and the density overlap integral are given. Details on fitting Gaussian multipoles to the electrostatic potential are provided along with a discussion on how the model is tested with ab initio intermolecular electrostatic energies, intermolecular density overlap integrals, and permanent molecular multipole moments. This is followed by a brief discussion on how the intermolecular density overlap integrals calculated by Gaussian multipoles are applied to the exchange−overlap model. In the next section, results for Gaussian multipoles are presented. Intermolecular electrostatic energies, intermolecular density overlap integrals, and permanent molecular multipole moments calculated by Gaussian multipoles are compared with their respective ab initio values. The geometry dependence of atomic Gaussian multipole moments Q_{lm} is presented for the case of water. Results are given when the Gaussian multipole intermolecular density overlap integrals are applied to the exchange−overlap model. Lastly, the results are summarized and future applications are discussed in the Conclusion Section.

2. Methods

In this section, a definition of a contracted Gaussian multipole charge density is given along with expressions for the electrostatic potential, electrostatic energy, and density overlap integrals. This is followed by a brief discussion of Slater-type contracted Gaussian functions and a description of how the Gaussian multipoles are fit to the ESP. In the next subsection, computational details on the calculation of ab initio electrostatic energies and intermolecular density overlap integrals are discussed. The calculation of permanent molecular multipole moments are described. This section concludes with computational details of how the exchange− overlap parameters are fit.

2.1. Gaussian Multipoles. The definition we have used for a contracted Gaussian multipole charge density is similar to the one given by Giese and York.[42] In that work,[42] expressions for efficiently calculating electrostatic and density overlap matrix element integrals between real regular solid harmonic contracted Gaussian functions are given along with

gradients of their matrix elements. In order to test the model for Gaussian multipole charge density, we have implemented similar expressions using complex solid harmonic Gaussian (multipole) functions, which are given below. A derivation of the following results along with a summary of necessary mathematical background[43−47] are given in the Supporting Information for the interested readers. Many of the theorems quoted in the Supporting Information have been used in the evaluation of integrals between solid harmonic Gaussian basis functions[63−65] for quantum chemistry calculations.

In the Introduction, it was mentioned that a spherical tensor Gaussian multipole charge distribution can be defined in terms of multipole moments Q_{lm} and of the solid harmonic gradient operator $C_{lm}(\nabla)$ acting upon a normalized Gaussian function. As shown in the Supporting Information, the solid harmonic gradient operator is especially useful in deriving integral quantities, such as electrostatic energies and density overlap integrals. In the following discussion, the final results for the electrostatic energy and the overlap integral between two Gaussian multipole charge densities are given after all derivative operations have been evaluated.

A contracted Gaussian multipole charge density $\rho(\vec{r}, \vec{R})$ with moments Q_{lm} and nuclear center $\vec{R}$ evaluated at the point $\vec{r}$ is given by

$$\rho(\vec{r}, \vec{R}) \equiv \sum_{l=0}^{l_{max}} \sum_{|m| \leq l} \frac{Q_{lm} C_{lm}^*(\vec{r} - \vec{R})}{(2l-1)!!} \rho_l(|\vec{r} - \vec{R}|; \alpha_\mu) \tag{7}$$

where l_{max} is the maximum order of the Gaussian multipoles (e.g., $l_{max} = 0$ for monopoles, 1 for dipoles, etc.), C_{lm}^* is the complex conjugate of a solid harmonic function, and ρ_l is a derivative of a contracted Gaussian charge density defined by

$$\rho_l(r; \alpha_\mu) \equiv \left(-\frac{1}{r}\frac{d}{dr}\right)^l \sum_{\mu=1}^{N_c} c_\mu \left(\frac{\alpha_\mu^2}{\pi}\right)^{3/2} \exp(-\alpha_\mu^2 r^2) \tag{8}$$

where N_c is the degree of contraction. For $l = 0$, the density ρ_0 is normalized to unity, $(\sum_\mu c_\mu = 1)$. The multipole moments of the charge density $\rho(\vec{r}, \vec{R})$ with respect to the center $\vec{R}$ are the coefficients Q_{lm}, i.e.

$$\int d^3 r \rho(\vec{r}, \vec{R}) C_{lm}(\vec{r} - \vec{R}) = Q_{lm} \tag{9}$$

The electrostatic potential ϕ arising from ρ in eq 7 is given by

$$\phi(\vec{r}) = \int d^3 r' \frac{\rho(\vec{r}', \vec{R})}{|\vec{r} - \vec{r}'|}$$

$$= \sum_{l=0}^{l_{max}} \sum_{|m| \leq l} \frac{Q_{lm} C_{lm}^*(\vec{r} - \vec{R})}{(2l-1)!!} \phi_l(|\vec{r} - \vec{R}|; \alpha_\mu) \tag{10}$$

where ϕ_l is defined by

$$\phi_l(r; \alpha_\mu) \equiv \left(-\frac{1}{r}\frac{d}{dr}\right)^l \sum_{\mu=1}^{N_c} c_\mu \frac{\text{erf}(\alpha_\mu r)}{r} \tag{11}$$

and $\text{erf}(x)$ is the error function defined in eq 3.

Gaussian Multipole Model (GMM)

J. Chem. Theory Comput., Vol. 6, No. 1, 2010 **193**

The electrostatic interaction energy between two Gaussian multipole charge densities $\rho_1(\vec{r},\vec{R}_1)$ and $\rho_2(\vec{r},\vec{R}_2)$ and their nuclei Z_1 and Z_2 is given by

$$U = \int\int d^3r d^3r' \frac{\rho_1(\vec{r},\vec{R}_1)\rho_2(\vec{r}',\vec{R}_2)}{|\vec{r} - \vec{r}'|} + Z_1\phi_2(\vec{R}_1) +$$
$$Z_2\phi_1(\vec{R}_2) + \frac{Z_1 Z_2}{|\vec{R}_1 - \vec{R}_2|} \quad (12)$$

where $\phi_2(\vec{R}_1)$ is the potential at $\vec{R}_1$ due to ρ_2 and $\phi_1(\vec{R}_2)$ is defined by a similar expression. The density overlap integral S between two Gaussian multipole charge densities is defined by

$$S = \int d^3r \rho_1(\vec{r})\rho_2(\vec{r}) \quad (13)$$

The electrostatic and density overlap integrals in eqs 12 and 13 can be expressed by[42]

$$\int\int d^3r d^3r' \rho_1(\vec{r})O(\vec{r},\vec{r}')\rho_2(\vec{r}') =$$
$$\sum_{l_1,m_1}\sum_{l_2,m_2} Q^1_{l_1 m_1} T_{l_1 m_1; l_2 m_2} Q^2_{l_2 m_2} \quad (14)$$

where $O(\vec{r},\vec{r}') \equiv 1/|\vec{r} - \vec{r}'|$ for the electrostatic integral, $O(\vec{r},\vec{r}') \equiv \delta(\vec{r} - \vec{r}')$ for the density overlap integral, and the interaction matrix $T_{l_1 m_1; l_2 m_2}$ is given below. The electrostatic energy and density overlap integrals between two normalized contracted Gaussian monopole charge densities with unit charge are given by

$$F_0(R) \equiv \sum_{\mu,\nu} c^1_\mu c^2_\nu \frac{\text{erf}(\alpha_{\mu\nu}R)}{R} \quad (15a)$$

$$F_0(R) \equiv \sum_{\mu,\nu} c^1_\mu c^2_\nu \left(\frac{\pi}{\alpha^2_{\mu\nu}}\right)^{3/2} \exp(-\alpha^2_{\mu\nu}R^2) \quad (15b)$$

where R is the distance between nuclear centers and α_μ is the Gaussian product exponent defined by

$$R \equiv |\vec{R}_1 - \vec{R}_2| \qquad \alpha_{\mu\nu} \equiv \frac{\alpha_\mu \alpha_\nu}{\sqrt{\alpha^2_\mu + \alpha^2_\nu}} \quad (16)$$

In addition, the constants A_{lm} and B_{lm} are defined by

$$A_{lm} \equiv \sqrt{(l+m)!(l-m)!}, \qquad B_{lm} \equiv \frac{A_{lm}}{(2l-1)!!} \quad (17)$$

for $l \neq 0$, and $A_{00} = B_{00} = 1$. The scaled solid harmonic function is defined by $R_{lm}(\vec{r}) \equiv C_{lm}(\vec{r})/A_{lm}$. The interaction matrix $T_{l_1 m_1; l_2 m_2}$ from eq 14 is given by

$$T_{l_1 m_1; l_2 m_2} = B_{l_1 m_1} B_{l_2 m_2} \sum_{l=0}^{\min(l_1, l_2)} \sum_{m=-l}^{l} \frac{(-1)^{l_2+m}}{A_{lm}B_{lm}} \times$$
$$R^*_{l_2-l,m_2+m}(\vec{R})R^*_{l_1-l,m_1-m}(\vec{R})F_{l_2+l_1-l}(R) \quad (18)$$

where $F_l(R) \equiv 2^l (d/dR^2)^l F_0(R)$. Finally, the point multipole results for both electrostatic potential and energy can be found by considering an uncontracted Gaussian multipole ($N_c = 1$), taking the large exponent limit ($\alpha \rightarrow \infty$) and noting $\text{erf}(x) \rightarrow 1$ as $x \rightarrow \infty$.

The atomic Gaussian multipole moments Q_{lm} are commonly defined[25] with respect to a local frame of the atom Q^{local}_{lm} and then rotated to a system or global frame $Q^{\text{global}}_{lm} \equiv Q_{lm}$ through Wigner rotation matrices $\mathbf{D}^l_{m'm}$

$$Q^{\text{global}}_{lm} = \sum_{m'} \mathbf{D}^l_{m'm}[\mathbf{R}^{-1}]Q^{\text{local}}_{lm'} \quad (19)$$

Recursion formulas for evaluating $\mathbf{D}^l_{m'm}$ have been given in Choi[66] et al. For each atom, the Cartesian transformation matrix $\mathbf{R}$ between the local and global frames is defined with respect to the relative positions of the atom and of its neighbors.[13,67,68]

2.2. Slater-Type Contracted Gaussian functions. The contraction coefficients d_μ and exponents α_μ are fit to a simple Slater function $\exp(-r)$ over all space for $N_c = 1 - 14$

$$\exp(-r) \cong \sum_{\mu=1}^{N_C} d_\mu \exp(-\alpha^2_\mu r^2) \quad (20)$$

For $N_c = 1 - 6$, the optimized exponents agree with those used in the development of the original STONG basis sets.[58,59] The contraction coefficients d_μ and exponents α_μ fit to $\exp(-r)$ are used to find the corresponding coefficients and exponents for $\exp(-\lambda r)$ by a scaling argument. The final expression for a normalized Slater-type charge density with unit charge and with exponent λ is given by

$$\frac{\lambda^3}{8\pi} \exp(-\lambda r) \cong \sum_{\mu=1}^{N_C} c_\mu \left(\frac{\alpha^2_\mu \lambda^2}{\pi}\right)^{3/2} \exp(-\alpha^2_\mu \lambda^2 r^2) \quad (21)$$

where $c_\mu \equiv d_\mu/8\pi \times (\pi/\alpha^2_\mu)^{3/2}$. A full list of contracted coefficients and exponents for $\exp(-r)$ can be found in the Supporting Information for $N_c = 1 - 14$.

2.3. Nonlinear Fit to Potential. The model for molecular charge density presented in this work consists of an effective nuclear charge Z_{eff} and a set of contracted Gaussian multipole moments Q_{lm} with a single diffuse Slater exponential parameter λ centered on each atom. Only the valence charge density is modeled, and the core electron density near the nuclear centers is neglected by using screened nuclear charges $Z_{\text{eff}} = Z - N_{\text{core}}$, where Z is the true nuclear charge and N_{core} is the number of core electrons. The number of core electrons N_{core} is taken to be 0 for hydrogen, 2 for the first-row elements, and 10 for the second-row elements. Thus, the screened nuclear charges Z_{eff} are set to 1.0 for H, 4.0 for C, 5.0 for N, 6.0 for O, 7.0 for F, and 7.0 for Cl. Initially, we experimented with using the true nuclear charges, e.g. $Z = 8$ for O. However, when the true nuclear charges are used, the intermolecular density overlap integrals at equilibrium dimer distances are consistently overestimated by $10-15\%$. If the true nuclear charges are used, then the model is forced to account for both the core and valence electron density with a single diffuse Slater-type Gaussian function. By only modeling the valence charge density, we had found that using effective screened nuclear charges gave significantly smaller errors when comparing to the ab initio intermolecular electrostatic energy and the density overlap integral.

The model for Gaussian multipole molecular charge density ρ^{GM} evaluated at the point $\vec{r}$ is represented as a sum over atomic Gaussian multipole charge densities given by

$$\rho^{\mathrm{GM}}(\vec{r}) = \sum_a \sum_{l=0}^{l_{\max}} \sum_{|m|\le l} \frac{Q_{lm,a}C_{lm}^*(\vec{r}-\vec{R}_a)}{(2l-1)!!}\rho_l(|\vec{r}-\vec{R}_a|;\lambda_a\alpha_\mu) \tag{22}$$

where $\vec{R}_a$ is the nuclear center of atom a, $Q_{lm,a}$ is the atomic Gaussian multipole moments of atom a, λ_a is the Slater exponent on atom a, and ρ_l is defined by eq 8. The electrostatic potential due to the effective nuclear charges and the Gaussian multipole charge density can be found from eq 10 as

$$\phi(\vec{r};Q_{lm,a},\lambda_a) = \sum_a \frac{Z_{\mathrm{eff},a}}{|\vec{r}-\vec{R}_a|} +$$
$$\sum_{l=0}^{l_{\max}} \sum_{|m|\le l} \frac{Q_{lm,a}C_{lm}^*(\vec{r}-\vec{R}_a)}{(2l-1)!!}\phi_l(|\vec{r}-\vec{R}_a|,\lambda_a\alpha_\mu) \tag{23}$$

where $\vec{r}$ is the field point, $Z_{\mathrm{eff},a}$ is the effective nuclear charge of atom a, and ϕ_l is defined by eq 11. For each atom, $Q_{lm,a}$ and λ_a are treated as optimizable parameters and fit to the ab initio electrostatic potential ϕ^{QM} surrounding the molecule. Gaussian quadrupoles are defined by $l_{\max} = 2$, i.e., a Gaussian monopole, dipole, and quadrupole with the same atomic exponent parameter λ_a are placed on a given atom a. Similarly, Gaussian dipoles are defined by $l_{\max} = 1$, i.e., a Gaussian monopole and dipole with the same atomic exponent parameter λ_a are placed on a given atom a.

Points near the nuclei are either filtered out or discarded by using a weighting function $w(\vec{r})$. The weighting function $w(\vec{r})$ used in this work is a modified version of a weighting function taken from Hu et al.[60] In this present study, $w(\vec{r})$ is a sigmoid function of the form:

$$w(\vec{r}) \equiv \begin{cases} \exp\{-\sigma[\ln\rho^{QM}(\vec{r}) - \ln K_0]^2\} & \rho^{QM}(\vec{r}) \ge K_0 \\ 1 & \rho^{QM}(\vec{r}) \le K_0 \end{cases} \tag{24}$$

where ρ^{QM} is the ab initio electron density. The weighting function $w(\vec{r})$ is small for regions of high electron density, while $w(\vec{r}) = 1$ for regions of low electron density. The adjustable parameters σ and $\ln K_0$ control the curvature and the location of the sigmoid function, respectively. In the limit of large σ, $w(\vec{r})$ becomes a step function. For Gaussian multipoles, the σ and $\ln K_0$ parameters are set to 0.3 and -6.0, respectively. The σ and $\ln K_0$ parameters are selected by performing a two-dimensional (2D) scan of parameters and by observing the average error in electrostatic dimer energy of hydrogen-bonded dimers at equilibrium geometries. A plot of the average root-mean-square deviation (rmsd) error in electrostatic dimer energy is given in Figure 1 for the case of contracted ($N_c = 4$) Gaussian quadrupoles fit to the ESP calculated at the B3LYP/6-31G* level. The surface is flat, and a range of values perform equally well, e.g., $(\sigma, \ln K_0)$ = (0.2, −7), (0.3, −6), (0.4, −5), etc. Similar parameter scans were performed with Gaussian monopoles, dipoles, and quadrupoles at various degrees of contraction N_c, and the same set of parameters were found to be local minima. In Hu et al.,[60] a weighting function for fitting atomic point charges to the ab initio ESP is proposed. There, it was shown that the point charges are stable with respect to varying
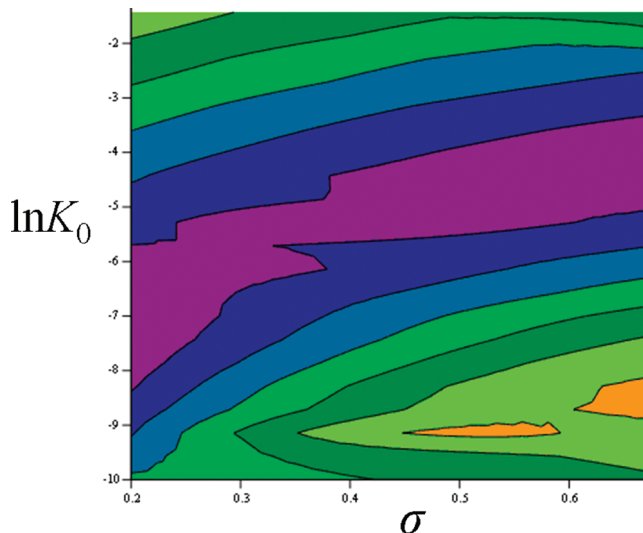
Figure 1. Contour plot of the average rmsd error in electrostatic dimer energy (kcal/mol), as a function of parameters σ and $\ln K_0$ for the ESP weighting function $w(\vec{r})$. The electrostatic energies are calculated on hydrogen-bonded dimers at equilibrium geometries using B3LYP/6-31G* Gaussian quadrupoles ($N_c = 4$). The dark-purple running through the center represents minima in the average rmsd error in electrostatic dimer energy.

conformations. The main differences between the weighting function $w(\vec{r})$ used in this work and the one proposed by Hu[60] et al. are that the ab initio electron density ρ^{QM} is used rather than an empirical model for ρ^{QM} and that points far away from the molecule are given a weight of 1.0. We have also fit atomic point multipoles to the ESP using the σ and $\ln K_0$ weight parameters of 0.8 and -9.0 given by Hu[60] et al.

The fitting function χ^2 is given by

$$\chi^2(Q_{lm},\lambda) = \int d^3r w(\vec{r})[\varphi^{\mathrm{GM}}(Q_{lm},\lambda;\vec{r}) - \varphi^{QM}(\vec{r})]^2 \tag{25}$$

where ϕ^{GM} and ϕ^{QM} are the ESPs calculated by Gaussian multipoles (eq 23) and by ab initio, respectively. χ^2 is approximated numerically on a coarse grain molecular grid taken from a modified version of NWChem[69,70] and optimized using a Levenberg−Marquardt nonlinear least-squares fit algorithm.[71] The ab initio ESP is calculated at both the B3LYP/6-31G* or HF/aug-cc-pVTZ levels using the Gaussian 03 software package.[72] Earlier in our study, we had experimented with using rectangular grids similar to the CHELPG-type[73] grids used in optimizing atomic point charges. A relatively fine grid spacing of 0.05 Å was used, and points within 1 Å of any nuclei were discarded. For uncontracted Gaussian multipole ($N_c = 1$), this procedure gave Gaussian multipole parameters which predicted electrostatic energies in approximate agreement to the results presented here, using the molecular grids with a smooth weighting function. However, for water, the number of rectangular grid points needed was on the order of 10^6-10^7, which can be compared to 10^3-10^4 grid points used in the coarse grain molecular grids.

Gaussian Multipole Model (GMM)

J. Chem. Theory Comput., Vol. 6, No. 1, 2010 **195**

2.4. Ab initio Dimer Energy and Molecular Density Overlap Test. The model is tested by comparing intermolecular electrostatic dimer energies and density overlap integrals on equilibrium dimer geometries of various molecules hydrogen bonded to water. The geometries of the dimers are optimized at both the B3LYP/6-31G* or HF/aug-cc-pVTZ levels, while keeping the monomers rigid in their respective monomer-optimized geometries. For the model fit to B3LYP/6-31G* data, the model is tested by comparing to the ab initio electrostatic energies calculated by the constrained space orbital variation (CSOV) decomposition[74] method, using a modified version of the HONDO[75,76] quantum chemistry program. For the model fit to HF/aug-cc-pVTZ data, ab initio electrostatic energies are calculated by the reduced variational space[77,78] (RVS) decomposition method, using the GAMESS[79] quantum chemistry program. In addition, we have developed code to calculate ab initio intermolecular density overlap integrals from the ab initio density matrix using the McMurchie–Davidson algorithm.[80]

For the water–water dimer, the model is tested by calculating intermolecular electrostatic energies and density overlap integrals on nonequilibrium dimer geometries. Several water–water dimer geometries are generated by rigidly translating one water molecule with respect to the other in the direction of the intermolecular H···O hydrogen bond. The intermolecular electrostatic energies and density overlap integrals calculated by Gaussian multipoles are plotted as a function of H···O distance and compared to their ab initio values. In addition, 100 water–water dimer geometries are generated in random orientations, while the relative center of masses lie between 2.5 and 5.0 Å. Scatter plots of the intermolecular electrostatic energy and density overlap integral are presented, comparing the results calculated by Gaussian quadrupoles with their ab initio values.

2.5. Molecular Multipole Moments. The Gaussian multipoles are further tested by comparing permanent molecular dipoles ($l = 1$), quadrupoles ($l = 2$), octapoles ($l = 3$), and hexadecapoles ($l = 4$) with their ab initio molecular multipoles. The atomic Gaussian multipole moments Q_{lm} at position $\vec{R}$ are translated to the origin by the following expression:[25]

$$Q_{lm}^{\text{orgin}} = \sum_{l_1=0}^{l_{\max}} \sum_{m_1=-l_1}^{l_1} \sqrt{\binom{l+m}{l_1+m_1}\binom{l-m}{l_1-m_1}} Q_{l_1 m_1} C_{l-l_1, m-m_1}(\vec{R}) \quad (26)$$

where C_{lm} is a solid harmonic function. Note that $Q_{lm}^{\text{origin}} \neq 0$ for all values of l and m. For example, an atomic Gaussian dipole (with respect to its atomic position) contributes to the total molecular dipole, quadrupole, octapole, etc. (with respect to the origin). The translated atomic Gaussian multipoles at the origin Q_{lm}^{origin} are summed to give the total spherical tensor molecular moment. Expressions for converting real spherical tensor multipoles into traceless Cartesian multipoles can be found in Özdoğan.[81] Below, the results for converting complex spherical tensor multipoles $Q_{lm} \equiv Q^r_{lm} + iQ^i_{lm}$ into their traceless Cartesian forms are given. For $l = 1$, the Cartesian dipole μ_α is related to Q_{1m} by

$$\mu_x = -\sqrt{2}Q^r_{11} \quad \mu_y = -\sqrt{2}Q^i_{11} \quad \mu_z = Q_{10} \quad (27)$$

For $l = 2$, the traceless Cartesian quadrupoles $\Theta_{\alpha\beta}^{\text{TL}}$ are related to Q_{2m} by

$$\Theta_{xx}^{\text{TL}} = \frac{1}{2}(-Q_{20} + \sqrt{6}Q^r_{22}) \qquad \Theta_{xz}^{\text{TL}} = -\sqrt{\frac{3}{2}}Q^r_{21}$$

$$\Theta_{yy}^{\text{TL}} = \frac{1}{2}(-Q_{20} - \sqrt{6}Q^r_{22}) \qquad \Theta_{yz}^{\text{TL}} = -\sqrt{\frac{3}{2}}Q^i_{21}$$

$$\Theta_{zz}^{\text{TL}} = Q_{20} \qquad \Theta_{xy}^{\text{TL}} = \sqrt{\frac{3}{2}}Q^r_{22}$$

$$(28)$$

Note the trace of the quadrupoles is zero, i.e., $\text{Tr}(\Theta^{\text{TL}}) = \Theta_{xx}^{\text{TL}} + \Theta_{yy}^{\text{TL}} + \Theta_{zz}^{\text{TL}} = 0$. For the conversion formulas of traceless Cartesian octapoles ($l = 3$) and hexadecapoles ($l = 4$) from their complex spherical tensor moments, see the Supporting Information. The ab initio molecular multipole moments are calculated by Gaussian 03[72] and then converted to their traceless forms.[25] For example, the expression for converting Cartesian quadrupoles $\Theta_{\alpha\beta}$ into traceless Cartesian quadrupoles $\Theta_{\alpha\beta}^{\text{TL}}$ is given by

$$\Theta_{\alpha\beta}^{\text{TL}} = \frac{3}{2}\Theta_{\alpha\beta} - \frac{1}{2}\delta_{\alpha\beta}\sum_p \Theta_{pp} \quad (29)$$

Similar expressions for converting Cartesian octapoles and hexadecapoles into their traceless forms are given in the Supporting Information.

2.6. Gaussian Multipole Geometry Dependence. The atomic Gaussian multipole moments Q_{lm}^{local} in the local frame (eq 19) are calculated as a function of both bond length and angle for a water molecule. The geometry of water is optimized at the B3LYP/6-31G* level. Several geometries of water are found by performing two separate one-dimensional (1D) scans of perturbing one of the bond lengths and the bond angle away from equilibrium in increments of 0.1 Å and 1°, respectively. Atomic Gaussian quadrupoles Q_{lm} and exponent parameters λ ($N_c = 4$) are fit to the B3LYP/6-31G* ESP for the optimized water geometry. For each perturbed geometry, new atomic Gaussian quadrupoles are fit the B3LYP/6-31G* ESP calculated for that geometry, while the exponent parameters λ are kept at their geometry optimized values. The atomic Gaussian multipoles in the local frame Q_{lm}^{local} are plotted as a function of both bond length and angle.

2.7. Overlap–Exchange Model. The exchange–overlap model[61,62] is tested using the model for Gaussian multipole charge density for hydrogen-bonded dimer pairs. For a given dimer, several geometries are generated by translating one of the monomers in increments of 0.1 Å along the axis defined by the two atoms forming the hydrogen bond. For each dimer geometry, the B3LYP/6-31G* exchange energy E_{exch} is calculated through CSOV decomposition. Only dimer geometries for which the total dimer energy is within +5 kcal/mol of the total minimum dimer energy are kept. Typically, this entails 40–60 dimer geometries of which the exchange energy lies between 0 and 30 kcal/mol. For example, the exchange–overlap model for the water–water dimer is fit to 63 geometries, whose exchange energies lie between 0 and 27 kcal/mol. For each dimer pair, a single

molecular pair K parameter is fit to the ab initio exchange energy (eq 6), using the intermolecular density overlap integrals S calculated by Gaussian multipoles with $a = 0.95$.

3. Results

In this section, results for Gaussian monopoles, dipoles, and quadrupoles are presented. Recall that 'Gaussian quadrupoles' refers to a model in which Gaussian monopoles, dipoles, and quadrupoles with the same atomic exponent parameter λ are placed on each atom. In the next few subsections, results for intermolecular electrostatic energy, density overlap integral, and permanent molecular multipole moment, calculated by Gaussian multipoles, are compared with their respective ab initio values. For the case of water, the atomic local frame Gaussian multipole moments Q_{lm}^{local} are plotted as a function of bond length r and bond angle θ. Lastly, results are given when Gaussian multipoles are applied the exchange−overlap model.

The dependence of intermolecular electrostatic energy and density overlap integral on the degree of Slater-type contraction N_c is studied. For $N_c = 1$, the model for charge density is a single Gaussian function. In the limit of large N_c, the model for charge density is equivalent to using a Slater function $\exp(-\lambda r)$. For Gaussian multipoles fit to the B3LYP/6-31G* ESP, the results for energy and density overlap favored $N_c = 4$. However, for the Gaussian multipoles fit to the HF/aug-cc-pVTZ ESP, the errors in intermolecular electrostatic energy and density overlap decreased for larger values of N_c. The results indicate the optimal degree of contraction N_c depends on the size of the ab initio basis set. The smaller 6-31G* basis set favors a smaller degree of contraction, while the larger aug-cc-pVTZ basis set prefers a larger degree of contraction. The values of $N_c = 4$ and $N_c = 8$ are chosen for the Gaussian multipoles fit to the B3LYP/6-31G* and HF/aug-cc-pVTZ ESPs, respectively. For more details on the N_c dependence, see the Supporting Information.

3.1. Electrostatic Energy. Electrostatic dimer energies for several molecules hydrogen bonded to water are calculated at their equilibrium geometries. In Table 1, electrostatic dimer energies are given for Gaussian monopoles, dipoles, and quadrupoles with $N_c = 4$, which are fit to the ESP calculated at the B3LYP/6-31G* level. The Gaussian multipole electrostatic dimer energies are compared with their reference B3LYP/6-31G* values. The rmsd errors in the electrostatic dimer energy are 0.568, 0.567, and 0.094 kcal/mol for Gaussian monopoles, dipoles, and quadrupoles, respectively. On average, the errors for Gaussian monopoles and dipoles ($N_c = 4$) are quite similar, while a significant improvement is gained for Gaussian quadrupoles. As a representative example, the electrostatic dimer energies of the water−methanol[(1)] dimer are −8.751, −8.103, and −8.558 kcal/mol for Gaussian monopoles, dipoles, and quadrupoles, respectively. The superscript (1), (2), and (3) denote multiple dimer geometries. These numbers can be compared to the reference ab initio electrostatic energy for the water−methanol[(1)] dimer of −8.524 kcal/mol. Gaussian quadrupoles are found to be particularly important in predicting the electrostatic dimer energies of organic halides with water. For example, the ab initio electrostatic energy

Table 1. Electrostatic Energies (kcal/mol) for Equilibrium Hydrogen-Bonded Dimers (X−Water)[a]

X	E_M	E_{DM}	E_{QDM}	CSOV
formamide[(1)]	−13.59	−12.82	−13.42	−13.68
formamide[(2)]	−8.723	−7.849	−8.554	−8.545
formamide[(3)]	−7.618	−7.089	−7.627	−7.679
N-methylformamide	−9.330	−8.058	−8.186	−8.285
water[(1)]	−7.934	−7.730	−8.195	−8.235
water[(2)]	−4.697	−4.582	−4.780	−4.879
water[(3)]	−3.517	−3.192	−3.129	−3.179
methanol[(1)]	−8.751	−8.103	−8.558	−8.524
methanol[(2)]	−7.263	−7.712	−8.217	−8.296
CH_3Cl[(1)]	−1.070	−0.719	−0.362	−0.372
CH_3Cl [(2)]	−2.297	−2.564	−2.714	−2.768
CH_2Cl_2[(1)]	−0.580	−0.274	−0.029	−0.035
CH_2Cl_2[(2)]	−4.237	−4.211	−4.618	−4.693
CH_3F[(1)]	−3.187	−2.731	−2.481	−2.538
CH_3F[(2)]	−1.639	−1.889	−1.922	−2.003
CH_2F_2	−2.211	−1.803	−1.673	−1.743
CH_2F_2[(2)]	−2.904	−3.160	−3.233	−3.358
ammonia[(1)]	−10.60	−11.04	−11.95	−12.04
ammonia[(2)]	−3.360	−3.263	−3.538	−3.629
methylamine	−11.61	−11.76	−12.35	−12.43
formaldehyde	−6.046	−5.330	−6.113	−6.145
acetaldehyde[(1)]	−7.676	−6.762	−7.541	−7.717
acetaldehyde [(2)]	−6.943	−6.156	−7.036	−7.025
acetone	−8.427	−7.541	−8.424	−8.545
dimethyl ether	−7.457	−7.849	−8.300	−8.185
rmsd	0.568	0.567	0.094	

[a] The electrostatic energies predicted by Gaussian monopoles E_M, dipoles E_{DM}, and quadrupoles E_{QDM} ($N_c = 4$) are compared to their reference B3LYP/6-31G* electrostatic dimer energies calculated using the CSOV decomposition method. The superscript (1), (2), and (3) denote multiple dimer geometries. 1 kcal/mol = 4.184 kJ/mol.

for the water−CH_3Cl[(1)] dimer is −0.372 kcal/mol. This result can be compared to the electrostatic dimer energies predicted by Gaussian monopoles, dipoles, and quadrupoles of −1.070, −0.719, and −0.362 kcal/mol, respectively.

A similar analysis is performed at the HF/aug-cc-pVTZ level. Gaussian multipoles ($N_c = 8$) are fit to the ESP calculated at the HF/aug-cc-pVTZ level, while the reference ab initio electrostatic energies are calculated at the same level of theory using the RVS decomposition method. Due to computational limitations, 11 of the original 25 hydrogen-bonded dimers are studied at this level. The dimers with the smallest monomers are chosen (water, ammonia, methanol, CH_3F, and CH_2F_2). As expected, a significant improvement is found by increasing the multipole order from Gaussian monopoles to quadrupoles. The rmsd errors in electrostatic dimer energy are 0.885, 0.366, and 0.133 kcal/mol for Gaussian monopoles, dipoles, and quadrupoles, respectively. As an example, the electrostatic energies for the water−methanol[(1)] dimer predicted by Gaussian monopoles, dipoles, and quadrupoles ($N_c = 8$) are −9.233, −8.187, and −8.847 kcal/mol, respectively. These results can be compared to the HF/aug-cc-pVTZ electrostatic energy of −8.753 kcal/mol. For more individual results, see the Supporting Information.

The results for intermolecular electrostatic energy, given above, are calculated on equilibrium dimer geometries. For nonequilibrium dimer geometries, the intermolecular electrostatic energy is calculated for the water−water dimer. The
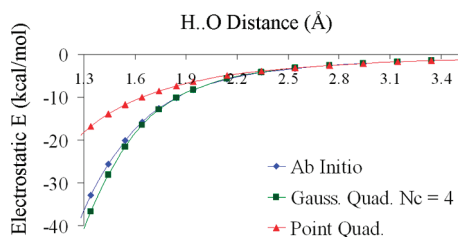
Gaussian Multipole Model (GMM)

J. Chem. Theory Comput., Vol. 6, No. 1, 2010 **197**

Figure 2. The electrostatic energy (kcal/mol) calculated by atomic point and Gaussian quadrupoles and by ab initio is plotted as a function of H···O distance for the water−water dimer.
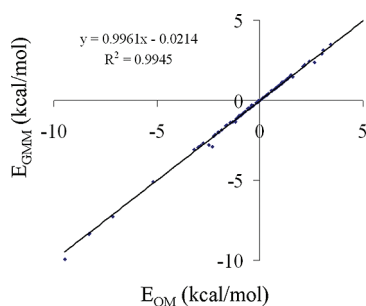

Figure 3. The intermolecular electrostatic energy (kcal/mol) calculated by Gaussian quadrupoles (*y*-axis) and by ab initio (*x*-axis) is plotted for randomly oriented water−water dimer geometries.

electrostatic energies calculated by Gaussian quadrupoles ($N_c = 4$) and by ESP-fitted atomic point quadrupoles are plotted for various hydrogen-bond distances H···O in Figure 2 for the water−water dimer and compared to their reference B3LYP/6-31G* values. As in the case of Gaussian quadrupoles, we call 'atomic point quadrupoles' as a model in which ESP-fitted atomic point monopoles, dipoles, and quadrupoles are placed on each atom. The optimized equilibrium dimer H···O distance is found to be 1.94 Å at the B3LYP/6-31G* level. At the equilibrium dimer separation, Gaussian quadrupoles predict an electrostatic energy of −8.195 kcal/mol and atomic point quadrupoles predict −6.422 kcal/mol, while the reference ab initio result is −8.235 kcal/mol. The underestimation of the atomic point quadrupole energy is an example of the penetration error[25,30,31] for atomic point multipoles. At long-range H···O distances, beyond 2.3 Å, both Gaussian and atomic point quadrupoles accurately reproduce the ab initio electrostatic energy. At short-range H···O distances, less than 1.64 Å, the Gaussian quadrupole electrostatic energy begins to slowly deviate from its reference B3LYP/6-31G* result. For example at 1.54 Å, the B3LYP/6-31G* ab initio electrostatic energy is −20.11 kcal/mol, which can be compared to the result of −21.54 kcal/mol calculated by Gaussian quadrupoles and −11.74 kcal/mol calculated by atomic point quadrupoles. In Figure 3, the intermolecular electrostatic energies calculated by Gaussian quadrupoles are compared with their ab initio reference values for several randomly oriented water−water dimers. The electrostatic energies calculated by Gaussian quadrupoles agree with their ab initio reference values for energies ranging from −10 kcal/mol to +5 kcal/mol. Additional scatter plots of intermolecular electrostatic energy can be found in the

Supporting Information for randomly oriented hydrogen-bonded dimers.

In order to compare Gaussian multipoles with the Gaussian Electrostatic Model (GEM),[57] electrostatic dimer energies are calculated on 10 water dimers,[82,83] which represent local minima on the water−water potential energy surface. Previously, GEM[57] was fit to the B3LYP/6-31G* ESP using the A1 and P1 auxiliary Gaussian basis sets (ABS). Two GEM models for water were developed. In a three-point GEM water model, ABS's have been placed on atomic centers only. A second GEM water model has been developed by placing ABS's on both the atomic centers and the bond midpoints, resulting in a five-point GEM water model. The average absolute errors in the electrostatic energy for the three-point GEM water model are 0.11 and 0.12 kcal/mol for the A1 and P1 basis sets, respectively. Including basis functions on bond midpoints results in an improved fit for GEM. The errors in the five-point GEM water fit to the ESP are 0.06 and 0.04 kcal/mol for the A1 and P1 basis sets, respectively. The average errors in electrostatic dimer energy for GEM can be compared to the error of 0.06 kcal/mol for Gaussian quadrupoles ($N_c = 4$). The GEM five-point water model with the A1 and P1 basis sets have a total of 110 and 213 primitive Gaussian functions, respectively. The total number of uncontracted basis functions in the GEM water models can be compared to the total number of contracted Gaussian quadrupoles of 27.

3.2. Molecular Density Overlap Integral. The model for Gaussian multipoles is further tested by comparing intermolecular density overlap integrals with their ab initio values. In Table 2, the intermolecular density overlap integrals are given for the hydrogen-bonded dimers at their equilibrium geometries. The intermolecular density overlap integrals for Gaussian monopoles, dipoles, and quadrupoles ($N_c = 4$) are compared with their respective B3LYP/6-31G* values. On average, there is a significant improvement in going up in multipole order from Gaussian monopoles to quadrupoles. The rmsd errors in intermolecular density overlap integrals are 2.571-, 0.752-, and 0.195 × 10^{-3} $e^2/Å^3$ for Gaussian monopoles, dipoles, and quadrupoles, respectively. A representative example is the water−methylamine complex at equilibrium, which has an ab initio value of 15.89 × 10^{-3} $e^2/Å^3$. This value can be compared to the intermolecular density overlap calculated by Gaussian monopoles, dipoles, and quadrupoles of 19.78-, 17.05-, and 15.56 × 10^{-3} $e^2/Å^3$, respectively. Similar trends can be found for the Gaussian multipoles fit to the HF/aug-cc-pVTZ ESP. At the HF/aug-cc-pVTZ level, the rmsd errors in intermolecular density overlap integral are 2.668-, 0.502-, and 0.268 × 10^{-3} $e^2/Å^3$ for Gaussian monopoles, dipoles, and quadrupoles ($N_c = 8$), respectively. For individual results on HF/aug-cc-pVTZ Gaussian multipoles, see the Supporting Information.

The results given in Table 2 are for intermolecular density overlap integrals calculated at equilibrium dimer distances. For nonequilibrium dimer geometries, the intermolecular density overlap integrals are compared with their ab initio values for the water−water dimer. In Figure 4, the intermolecular density overlap integrals calculated by B3LYP/6-31G* Gaussian quadrupoles ($N_c = 4$) and the B3LYP/6-31G*

198 *J. Chem. Theory Comput., Vol. 6, No. 1, 2010*

Elking et al.

Table 2. Intermolecular Density Overlap Integrals ($\times 10^{-3}$ $e^2/\text{Å}^3$) for Equilibrium Hydrogen-Bonded Dimers (X–Water)[a]

X	S_M	S_{DM}	S_{QDM}	S_{QM}
formamide[1]	20.29	17.30	16.76	16.99
formamide[2]	15.47	11.05	11.25	10.88
formamide[3]	8.283	7.201	7.577	7.399
N-methylformamide	16.36	12.04	11.43	11.37
water[1]	11.28	9.969	9.133	9.061
water[2]	2.871	2.513	2.503	2.698
water[3]	1.189	0.958	0.930	1.084
methanol[1]	15.40	12.70	11.47	11.30
methanol[2]	8.783	10.21	9.470	9.518
CH_3Cl[1]	0.662	0.461	0.243	0.308
CH_3Cl[2]	1.790	2.469	3.238	3.250
CH_2Cl_2[1]	0.329	0.217	0.116	0.162
CH_2Cl_2[2]	3.812	3.704	5.341	5.440
CH_3F[1]	5.679	3.358	2.886	3.086
CH_3F[2]	2.542	2.561	2.738	2.881
CH_2F_2[1]	3.635	2.044	1.806	2.036
CH_2F_2[2]	4.477	4.016	4.275	4.569
ammonia[1]	15.63	13.75	13.21	13.39
ammonia[2]	3.647	4.297	4.230	4.327
methylamine	19.78	17.05	15.56	15.89
formaldehyde	10.71	8.028	8.060	7.871
acetaldehyde[1]	12.77	9.957	9.584	9.657
acetaldehyde[2]	12.63	9.390	9.573	9.241
acetone	14.30	11.37	11.18	11.12
dimethyl ether	15.56	14.34	12.58	12.25
rmsd	2.571	0.752	0.195	

[a] The overlap integrals predicted by Gaussian monopoles S_M, dipoles S_{DM}, and quadrupoles S_{QDM} ($N_c = 4$) are compared to their reference B3LYP/6-31G* values. The superscripts (1), (2), and (3) denotes multiple dimer geometries. 10^{-3} $e^2/\text{Å}^3 = 1.482 \times 10^{-4}$ e^2/a_0^3, where a_0 is the Bohr radius.
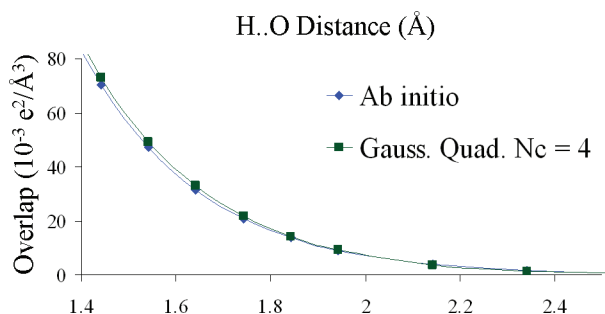
H..O Distance (Å)

Figure 4. The intermolecular density overlap integral ($\times 10^{-3}$ $e^2/\text{Å}^3$) calculated by atomic Gaussian quadrupoles and by ab initio is plotted as a function of H···O distance (Å) for the water–water dimer.

reference values are plotted as a function of H···O distance. The intermolecular overlap integrals predicted by Gaussian quadrupoles agree with their ab initio values for H···O distances ranging from 2.3 to 1.7 Å. For shorter separations, the intermolecular overlap integrals predicted by Gaussian quadrupoles begin to overestimate the ab initio result. In Figure 5, the intermolecular density overlap integral calculated by Gaussian quadrupoles is compared with its respective ab initio value for several randomly oriented water–water geometries. The intermolecular overlap integrals range from 0 to 30.0×10^{-3} $e^2/\text{Å}^3$. There is a small overestimation (~6%) of the intermolecular density overlap integrals calculated by Gaussian quadrupoles as compared with their ab initio values. In the Supporting Information, additional
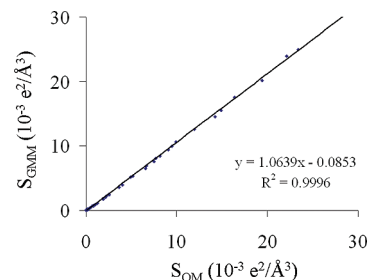
Figure 5. The intermolecular density overlap integral ($\times 10^{-3}$ $e^2/\text{Å}^3$) calculated by Gaussian quadrupoles (*y*-axis) and by ab initio (*x*-axis) is plotted for randomly oriented water–water dimer geometries.

Table 3. Non-Zero Components of the Molecular Quadrupole Moment D-Å of Ammonia for Gaussian Monopoles, Dipoles, And Quadrupoles ($N_c = 4$) Fit to B3LYP/6-31G* ESP

atomic	*xx*	*yy*	*zz*	rmsd
Gaussian monopoles	0.9211	0.9211	−1.8422	0.39291
Gaussian dipoles	1.2701	1.2700	−2.5400	0.04402
Gaussian quadrupoles	1.3139	1.3138	−2.6278	0.00015
B3LYP/6-31G*	1.3140	1.3140	−2.6281	

Table 4. Average Rmsd Error (Δ) in Traceless Molecular Dipole, Quadrupole, Octapole, and Hexadecapole Moments[a]

atomic	Δdip (10^{-3} D)	Δquad (D-Å)	Δoct (D-Å^2)	Δhex (D-Å^3)
Gaussian monopoles	9.489	0.1947	0.9970	3.402
Gaussian dipoles	2.495	0.0453	0.2154	0.969
Gaussian quadrupoles	1.045	0.0061	0.0381	0.130

[a] Averaged over 14 molecules for Gaussian multipoles ($N_c = 4$) fit to the B3LYP/6-31G* ESP.

scatter plots of intermolecular density overlap integral can be found for other randomly oriented hydrogen bonded dimers.

3.3. Molecular Multipole Moments. The permanent molecular multipole moments up to hexadecapole are calculated for the atomic Gaussian monopole, dipole, and quadrupole models ($N_c = 4$) and compared with their reference B3LYP/6-31G* values. As an example, the nonzero components of the molecular quadrupole for ammonia are given in Table 3. A significant improvement is found by increasing the atomic Gaussian multipole order from Gaussian monopoles to quadrupoles. For example, the ab initio Q_{xx} component of the molecular quadrupole is 1.3140 D-Å, which can be compared to the value predicted by Gaussian monopoles, dipoles, and quadrupoles of 0.9211, 1.2701, and 1.3139 D-Å, respectively.

The results for molecular multipole moments given for ammonia are representative of the other 14 monomers studied in this work. The rmsd errors in molecular multipole moment up to hexadecapole are averaged over all the molecules and presented in Table 4. As expected, there is a significant decrease in average rmsd error for increasing atomic Gaussian multipole order. For example, the average rmsd errors in molecular hexadecapole are 3.402 for atomic Gaussian monopoles, 0.969 for Gaussian dipoles, and 0.130 D-Å^3 for
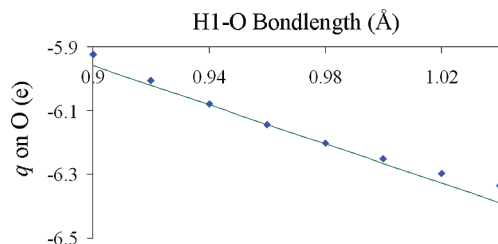
Gaussian Multipole Model (GMM)

J. Chem. Theory Comput., Vol. 6, No. 1, 2010 **199**

Figure 6. Atomic Gaussian monopole moment q (e) on oxygen in a water molecule as a function of H1−O bond length. The B3LYP/6-31G* equilibrium H1−O bond length is 0.9684 Å.
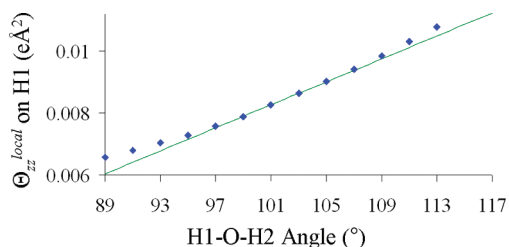

Figure 7. Atomic local frame Gaussian quadrupole moment Θ_{zz}^{local} (eÅ^2) on the 'H1' hydrogen in a water molecule as a function of H1−O−H2 bond angle. The B3LYP/6-31G* equilibrium H1−O−H2 bond angle is 103.66°.

Gaussian quadrupoles. For more individual results, see the Supporting Information.

3.4. Gaussian Multipole Geometry Dependence. The atomic Gaussian multipole moments are investigated as a function of bond length r and bond angle θ for the case of water. Gaussian quadrupoles ($N_c = 4$) are calculated at the B3LYP/6-31G* level for several geometries of water obtained by perturbing either the O−H1 bond length or the H1−O−H2 bond angle. The atomic Gaussian multipole moments in the local frame (eq 19) are converted to their traceless Cartesian moments (eqs 27 and 28). In Figure 6, the atomic Gaussian monopole moment q on oxygen is plotted when the H1−O bond length is varied. The Gaussian monopole charge q is a smooth function of bond length, which can be approximated as a straight line for bond lengths between 0.92 and 1.00 Å (the equilibrium bond length is 0.9684 Å). In addition, the zz component of the local frame traceless Cartesian quadrupole moment Θ_{zz}^{local} on the H1 hydrogen is plotted as a function of H1−O−H2 bond angle in Figure 7. Θ_{zz}^{local} can be approximated as a straight line for bond angles between 95° and 111° (the equilibrium bond angle is 103.66°). In both Figures 6 and 7, the straight lines are determined by the value of the local frame atomic multipoles Q_{lm}^{local} at the equilibrium geometry and by the finite difference derivative of Q_{lm}^{local} with respect to the bond length or bond angle at the equilibrium geometry. The results given in Figures 6 and 7 are examples, and the other atomic Gaussian moments Q_{lm}^{local} follow similar trends (see the Supporting Information for more examples). For small internal geometry perturbations, the above results suggest that the local frame atomic Gaussian multipole moments can be approximated by a truncated linear Taylor series as a function of the two bond lengths r_1 (H1−O) and r_2 (H2−O) and the bond angle θ (H1−O−H2) as

$$Q_{lm}^{local}(r, \theta) \cong Q_{lm}^{local,0} + (r_1 - r_1^0)\frac{\partial Q_{lm}^{local,0}}{\partial r_1} +$$
$$(r_2 - r_2^0)\frac{\partial Q_{lm}^{local,0}}{\partial r_2} + (\theta - \theta^0)\frac{\partial Q_{lm}^{local,0}}{\partial \theta} \quad (29)$$

where $Q_{lm}^{local,0}$ is the atomic Gaussian multipole at the geometry optimized equilibrium structure. Evaluated at the equilibrium structure, $\partial Q_{lm}^{local,0}/\partial r_1$, $\partial Q_{lm}^{local,0}/\partial r_2$, and $\partial Q_{lm}^{local,0}/\partial\theta$ are the finite difference partial derivatives of $Q_{lm}^{local,0}$ with respect to r_1, r_2, and θ, respectively.

3.5. Exchange−Overlap Model. The exchange−overlap model is fit to exchange−repulsion energies calculated at the B3LYP/6-31G* level through CSOV decomposition as described in Section 2.7. The intermolecular density overlap integrals are calculated from Gaussian quadrupoles ($N_c = 4$) fit to the B3LYP/6-31G* ESP. For the water−water dimer, the rmsd error of fit is 0.350 kcal/mol for Gaussian quadrupoles, over a range of exchange energies from 0.0 to 27.0 kcal/mol. At the equilibrium water−water dimer distance, the exchange energy calculated by the exchange−overlap model is 5.449 kcal/mol, compared to the ab initio result of 5.362 kcal/mol. In Figure 8, the water−water exchange energy calculated by the model is compared with the ab initio value and plotted as a function of H···O distance. A similar analysis is performed on the other hydrogen-bonded dimers. The rmsd fit errors are averaged over all the dimers and given by 0.764, 0.379, and 0.275 kcal/mol for Gaussian monopoles, dipoles, and quadrupoles, respectively. This result indicates that including anisotropy into the model for charge density makes a significant improvement when applying the exchange−overlap model. At equilibrium distances, the exchange energies lie between 0.1 and 10 kcal/mol. The rmsd in exchange energy at the equilibrium dimer distance averaged over the hydrogen-bonded dimers are 1.782, 0.262, and 0.276 kcal/mol for Gaussian monopoles, dipoles, and quadrupoles, respectively. For Gaussian quadrupoles, the molecular pair K parameters range from 0.5786 kcal/mol ($\times 10^3$ Å^3/e^2)$^{0.95}$ for the water−CH$_3$F dimer to 0.7499 for the water−ammonia dimer. The average value of the molecular pair K parameter over all the dimers is 0.6607. Because of the variability of the K parameters, a single molecular pair K parameter may not be sufficient for larger molecules or for when a large amount of configuration space is sampled. For more individual
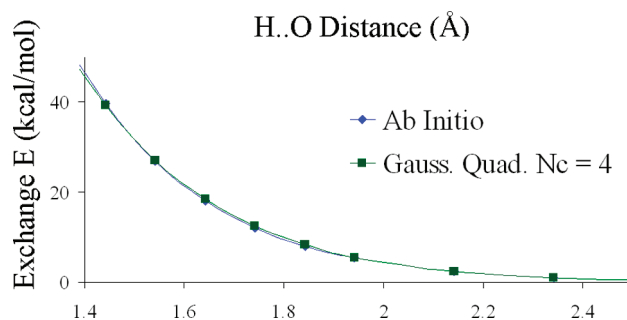

Figure 8. The exchange energy calculated by Gaussian quadrupoles and by ab initio is plotted as a function of H···O distance for the water−water dimer.

results, including exchange parameters K, rmsd errors, and exchange dimer energies, see the Supporting Information.

4. Conclusion

We have proposed a model based on contracted Gaussian multipole charge density. The atomic Gaussian multipoles are fit to the ab initio electrostatic potential and are shown to reproduce ab initio electrostatic dimer energies, intermolecular density overlap integrals, and permanent molecular multipole moments. For the case of water, the local frame atomic Gaussian multipole moments Q_{lm}^{local} are shown to be a smooth function of bond length r and bond angle θ, which can be approximated as a truncated linear Taylor series. In a follow up work, we will present analytic atomic force expressions for geometry-dependent Gaussian multipoles and show that geometry-dependent electrostatic models are capable of reproducing ab initio electrostatic atomic forces. In addition, the intermolecular density overlap integrals calculated by Gaussian multipoles have been applied to a model[61,62] for exchange−repulsion energy based on intermolecular density overlap integral. A molecular pair K parameter is fit to the ab initio exchange−repulsion energy for hydrogen-bonded dimers. A significant improvement is found in going from Gaussian monopoles to quadrupoles, indicating that including anisotropy in the description of atomic charge density is important. Though the preliminary results of applying the exchange−overlap model to the Gaussian multipole charge density are encouraging, a more extensive investigation would be useful, possibly by studying atomic pair K parameters fit to a larger molecular data set. We plan to further study the exchange−overlap model using Gaussian multipoles, and we hope to propose a general set of transferable exchange−overlap parameters in the near future.

Supporting Information Available: There are three parts available. Part I contains additional mathematical details and background. Elementary properties of spherical, solid, and scaled solid harmonic functions are given along with some theorems for the solid harmonic function and the solid harmonic gradient operator. Expressions for electrostatic energy and density overlap integral are derived for complex Gaussian multipoles along with the Cartesian gradients of their matrix elements. In addition, formulas for converting complex spherical tensor multipole moments into their traceless Cartesian forms are given. In part II, additional results for Gaussian multipoles are presented. The dependence on the degree of Slater-type contraction N_c is discussed. Additional tables and figures of electrostatic dimer energies and intermolecular density overlap integrals are presented.

For the case of water, additional plots of Q_{lm}^{local} as a function of bond length and bond angle are given. For the exchange−overlap model, exchange−repulsion energies, molecular pair K parameters, and rmsd of fits are provided for B3LYP/6-31G* Gaussian multipoles. In part III, the Gaussian multipole parameters, the Slater-type contraction coefficients/exponents, and the equilibrium dimer geometries are given. This material is available free of charge via the Internet at http://pubs.acs.org.

References

(1) Thole, B. T. *Chem. Phys.* **1981**, *59*, 341–350.

(2) Elking, D. M.; Darden, T.; Woods, R. J. *J. Comput. Chem.* **2007**, *28*, 1261–1274.

(3) Lamoureux, G.; MacKerell, A. D.; Roux, B. *J. Chem. Phys.* **2003**, *119* (10), 5185–5197.

(4) Rick, S. W.; Stuart, S. J.; Berne, B. J. *J. Chem. Phys.* **1994**, *101* (7), 6141–6156.

(5) Stern, H. A.; Kaminski, G. A.; Banks, J. L.; Zhou, R.; Berne, B. J.; Friesner, R. *J. Phys. Chem.* **1999**, *103*, 4730–4737.

(6) Piquemal, J.-P.; Chelli, R.; Procacci, P.; Gresh, N. *J. Phys. Chem. A* **2007**, *111*, 8170–8176.

(7) Patel, S.; Brooks, C. L., III *J. Comput. Chem.* **2004**, *25*, 1–16.

(8) Patel, S.; MacKerell, A. D.; Brooks III, C. L. *J. Comput. Chem.* **2004**, *25*, 1504–1514.

(9) Kaminski, G. A.; Stern, H. A.; Berne, B. J.; Friesner, R. *J. Phys. Chem. A* **2004**, *108*, 621–627.

(10) Gresh, N.; Cisneros, G. A.; Darden, T. A.; Piquemal, J.-P. *J. Chem. Theory Comput.* **2007**, *3*, 1960–1986.

(11) Gresh, N. *J. Comput. Chem.* **1995**, *16*, 856–882.

(12) Piquemal, J-P; Chevreau, H.; Gresh, N. *J. Chem. Theory Comput.* **2007**, *3*, 824–837.

(13) Ren, P.; Ponder, J. W. *J. Phys. Chem. B* **2003**, *107*, 5933–5947.

(14) Ren, P.; Ponder, J. W. *J. Comput. Chem.* **2002**, *23*, 1497–1506.

(15) Grossfield, A.; Ren, P.; Ponder, J. W. *J. Am. Chem. Soc.* **2003**, *125*, 15671–15682.

(16) Piquemal, J.-P.; Perera, L.; Cisneros, G. A.; Ren, P.; Pedersen, L. G.; Darden, T. A. *J. Chem. Phys.* **2006**, *125*, 054511.

(17) Iuchi, S.; Izvekov, S.; Voth, G. A. *J. Chem. Phys.* **2007**, *126*, 124505–124512.

(18) Paesani, F.; Iuchi, S.; Voth, G. A. *J. Chem. Phys.* **2007**, *127* (7), 074506−074515.

(19) Wang, F.; Jordan, K. D. *J. Chem. Phys.* **2002**, *116*, 6973–6981.

(20) Jiang, H.; Jordan, K. D.; Taylor, C. E. *J. Phys. Chem. B* **2007**, *111*, 6486–6492.

(21) Koch, U.; Popelier, P. L. A.; Stone, A. *J. Chem. Phys. Lett.* **1995**, *2*, 253–260.

(22) Koch, U.; Stone, A. J. *J. Chem. Soc., Faraday Trans.* **1996**, *92* (10), 1701–1708.

(23) Cho, K.; Kang, Y. K.; No, K. T.; Scheraga, H. A. *J. Phys. Chem. B* **2001**, *105*, 3624–3634.

(24) Mankoo, P.; Keyes, T. *J. Chem. Phys.* **2008**, *129*, 034504−034509.

(25) Stone, A. J. *The Theory of Intermolecular Forces*; Oxford University Press: Oxford, U.K., 2000.

(26) Stone, A. J. *Chem. Phys. Lett.* **1981**, *83*, 233–239.

(27) Vigné-Maeder, F.; Claverie, P. *J. Chem. Phys.* **1998**, *88*, 4934–4948.

(28) Náray-Szabó, G; Ferenczy, G. G. *Chem. Rev.* **1995**, *95* (4), 829–847.

(29) Ángyán, J. G.; Chipot, C.; Dehez, F.; Hättig, C.; Jansen, G.; Millot, C. *J. Comput. Chem.* **2003**, *24*, 997–1008.

(30) Qian, W.; Krimm, S. *J. Phys. Chem. A* **2005**, *109*, 5608–5618.

(31) Freitag, M. A.; Gordon, M. S.; Jensen, J. H.; Stevens, W. J. *J. Chem. Phys.* **2000**, *112* (17), 7300–7306.

(32) Piquemal, J-P; Gresh, N.; Giessner-Prettre, C. *J. Phys. Chem. A* **2003**, *107*, 10353–10359.

(33) Cisneros, G. A.; Tholander, S. Na-Im; Elking, D. M.; Darden, T. A.; Parisel, O.; Piquemal, J-P *Int. J. Quantum Chem.* **2008**, *108*, 1905–1912.

(34) Slipchenko, L. V; Gordon, M. S. *Mol. Phys.* **2009**, *107*, 999–1016.

(35) Chelli, R.; Righini, R.; Califano, S.; Procacci, P. *J. Mol. Liq.* **2002**, *96−97*, 87–100.

(36) Masia, M.; Probst, M.; Rey, R. *J. Chem. Phys.* **2005**, *123*, 164505–13.

(37) Paricaud, P.; Předota, M.; Chialvo, A.; Cummings, P. *J. Chem. Phys.* **2005**, *122*, 244511–244514.

(38) Wheatley, R. J. *Mol. Phys.* **1993**, *79*, 597–610.

(39) Wheatley, R. J.; Mitchell, J. B. O. *J. Comput. Chem.* **1994**, *15*, 1187–1198.

(40) Hall, G. G. *Adv. At. Mol. Phys.* **1985**, *20*, 41–63.

(41) Martin, D.; Hall, G. G. *Theor. Chim. Acta* **1981**, *59*, 281–290.

(42) Giese, T. J.; York, D. M. *J. Chem. Phys.* **2008**, *128* (6), 064104−6.

(43) Hobson, E. W. *The Theory of Spherical and Ellipsoidal Harmonics*; Chelsea: New York, 1955, pp 93.

(44) Bayman, B. F. *J. Math. Phys.* **1978**, *19*, 2558–2562.

(45) Chakrabarti, S.; Dewangan, D. P. *J. Phys. B: At. Mol. Opt. Phys.* **1995**, *28*, L769–774.

(46) Helgaker, T.; Jorgensen, P.; Olsen, J. *Molecular Electronic-Structure Theory*; Wiley: Chichester, U.K., 2004, pp 337−424.

(47) Arken, G. B. *Mathematical Methods for Physicists*, 5th ed.; Academic Press: San Diego, CA, 2000, pp 693−765.

(48) Cisneros, G. A.; Piquemal, J.-P.; Darden, T. A. *J. Chem. Phys.* **2005**, *123*, 044109−044110.

(49) Cisneros, G. A.; Piquemal, J.-P.; Darden, T. A. *J. Chem. Phys.* **2006**, *125* (18), 184101–184116.

(50) Piquemal, J.-P.; Cisneros, G. A.; Reinhardt, P.; Gresh, N.; Darden, T. A. *J. Chem. Phys.* **2006**, *124* (10), 104101–104112.

(51) Cisneros, G. A.; Darden, T. A.; Gresh, N.; Reinhardt, P.; Parisel, O.; Pilmé, J.; Piquemal, J.-P. Design of Next Generation Force Fields from Ab Initio Computations: Beyond Point Charges. In *Electrostatics Multi-scale Quantum Models for Biocatalysis: Modern Techniques and Applications, for the*

Book Series: Challenges and Advances in Computational Chemistry and Physics; York, D. M., Lee, T.-S., Eds.; Springer Verlag: New Amsterdam, The Netherlands, 2009; Vol. 7, pp 137−172.

(52) Dunlap, B. I.; Connolly, W. D.; Sabin, J. R. *J. Chem. Phys.* **1979**, *71*, 4993–4999.

(53) Köster, A. M. *J. Chem. Phys.* **1996**, *104*, 4114–4124.

(54) Köster, A. M. *J. Chem. Phys.* **2003**, *118*, 9943–9951.

(55) Eichkorn, K.; Treutler, O.; Ohm, H.; Haser, M.; Ahlrichs, R. *Chem. Phys. Lett.* **1995**, *240*, 283–289.

(56) Jung, Y; Sodt, A; Gill, P. M. W. Gill; Head-Gordon, M. *Proc. Natl. Acad. Sci. U.S.A.* **2005**, *102*, 6692−6697.

(57) Cisneros, G. A.; Elking, D. M.; Piquemal, J-P; Darden, T. A. *J. Phys. Chem. A* **2007**, *111*, 12049–12056.

(58) Hehre, W. J.; Stewart, R. F.; Pople, J. A. *J. Chem. Phys.* **1969**, *51* (6), 2657–2664.

(59) Stewart, R. F. *J. Chem. Phys.* **1970**, *52* (1), 431–438.

(60) Hu, H; Lu, Z; Yang, W. *J. Chem. Theory Comput.* **2007**, *3*, 1004–1013.

(61) Wheatley, R. J.; Price, S. L. *Mol. Phys.* **1990**, *69*, 507–533.

(62) Mitchell, J. B. O.; Price, S. L. *J. Phys. Chem. A* **2000**, *104*, 10958–10971.

(63) Dunlap, B. I. *Phys. Rev. A: At., Mol., Opt. Phys.* **1990**, *42* (3), 1127–1137.

(64) Dunlap, B. I. *Int. J. Quantum Chem.* **2001**, *81*, 373–383.

(65) Dunlap, B. I. *J. Chem. Phys.* **2003**, *118* (3), 1036–1043.

(66) Choi, C. H.; Ivanic, J.; Gordon, M. S.; Ruedenberg, K. *J. Chem. Phys.* **1999**, *11*, 8825–8831.

(67) Toukmaji, A.; Sagui, C.; Board, J. A.; Darden, T. A. *J. Chem. Phys.* **2000**, *113*, 10913–10927.

(68) Sagui, C.; Pedersen, L. G.; Darden, T. A. *J. Chem. Phys.* **2004**, *120*, 73–87.

(69) Bylaska, E. J.; de Jong, W. A.; Govind, N.; Kowalski, K.; Straatsma, T. P.; Valiev, M.; Wang, D.; Apra, E.; Windus, T. L.; Hammond, J.; Nichols, P.; Hirata, S.; Hackler, M. T.; Zhao, Y.; Fan, P.-D.; Harrison, R. J.; Dupuis, M.; Smith, D. M. A.; Nieplocha, J.; Tipparaju, V.; Krishnan, M.; Wu, Q.; Van Voorhis, T.; Auer, A. A.; Nooijen, M.; Brown, E.; Cisneros, G.; Fann, G. I.; Fruchtl, H.; Garza, J.; Hirao, K.; Kendall, R.; Nichols, J. A.; Tsemekhman, K.; Wolinski, K.; Anchell, J.; Bernholdt, D.; Borowski, P.; Clark, T.; Clerc, D.; Dachsel, H.; Deegan, M.; Dyall, K.; Elwood, D.; Glendening, E.; Gutowski, M.; Hess, A.; Jaffe, J., Johnson, B.; Ju, J.; Kobayashi, R.; Kutteh, R.; Lin, Z.; Littlefield, R.; Long, X.; Meng, B.; Nakajima, T.; Niu, S.; Pollack, L.; Rosing, M.; Sandrone, G.; Stave, M.; Taylor, H.; Thomas, G.; van Lenthe, J.; Wong, A.; Zhang, Z. *NWChem, A Computational Chemistry Package for Parallel Computers*, version 5.1(a modified version); Pacific Northwest National Laboratory: Richland, WA, 2007.

(70) Kendall, R. A.; Aprà, E.; Bernholdt, D. E.; Bylaska, E. J.; Dupuis, M.; Fann, G. I.; Harrison, R. J.; Ju, J.; Nichols, J. A.; Nieplocha, J.; Straatsma, T. P.; Windus, T. L.; Wong, A. T. High Performance Computational Chemistry: an Overview of NWChem a Distributed Parallel Application. *Comput. Phys. Commun.* **2000**, *128*, 260–283.

(71) Press, W. H.; Flannery, B. P.; Teukolsky, S. A.; Vetterling, W. T. *Numerical Recipes in C: The Art of Scientific*

Computing, 2nd ed.; Cambridge University Press: Cambridge, 1992; p. 683.

(72) Frisch, M. J.; Trucks, G. W.; Schlegel, H. B.; Scuseria, G. E.; Robb, M. A.; Cheeseman, J. R.; Montgomery, Jr., J. A.; Vreven, T.; Kudin, K. N.; Burant, J. C.; Millam, J. M.; Iyengar, S. S.; Tomasi, J.; Barone, V.; Mennucci, B.; Cossi, M.; Scalmani, G.; Rega, N.; Petersson, G. A.; Nakatsuji, H.; Hada, M.; Ehara, M.; Toyota, K.; Fukuda, R.; Hasegawa, J.; Ishida, M.; Nakajima, T.; Honda, Y.; Kitao, O.; Nakai, H.; Klene, M.; Li, X.; Knox, J. E.; Hratchian, H. P.; Cross, J. B.; Bakken, V.; Adamo, C.; Jaramillo, J.; Gomperts, R.; Stratmann, R. E.; Yazyev, O.; Austin, A. J.; Cammi, R.; Pomelli, C.; Ochterski, J. W.; Ayala, P. Y.; Morokuma, K.; Voth, G. A.; Salvador, P.; Dannenberg, J. J.; Zakrzewski, V. G.; Dapprich, S.; Daniels, A. D.; Strain, M. C.; Farkas, O.; Malick, D. K.; Rabuck, A. D.; Raghavachari, K.; Foresman, J. B.; Ortiz, J. V.; Cui, Q.; Baboul, A. G.; Clifford, S.; Cioslowski, J.; Stefanov, B. B.; Liu, G.; Liashenko, A.; Piskorz, P.; Komaromi, I.; Martin, R. L.; Fox, D. J.; Keith, T.; Al-Laham, M. A.; Peng, C. Y.; Nanayakkara, A.; Challacombe, M.; Gill, P. M. W.; Johnson, B.; Chen, W.; Wong, M. W.; Gonzalez, C.; and Pople, J. A. *Gaussian 03, Revision C.02*; Gaussian, Inc.: Wallingford, CT, 2004.

(73) Breneman, C. M.; Wiberg, K. B. *J. Comput. Chem.* **1990**, *11*, 361–373.

(74) Bagus, P. S.; Hermann, K.; Bauschlicher, C. W., Jr. *J. Chem. Phys.* **1984**, *80*, 4378–4386.

(75) Piquemal, J.-P.; Marquez, A.; Parisel, O.; Giessner-Prettre, C. *J. Comput. Chem.* **2005**, *26*, 1052–1062.

(76) Dupuis, M.; Marquez, A.; Davidson, E. R. *HONDO95.3*; Indiana University: Bloomington, IN, 1995.

(77) Stevens, W. J; Fink, W. H. *Chem. Phys. Lett.* **1987**, *139* (1), 15–22.

(78) Chen, W.; Gordon, M. S. *J. Phys. Chem.* **1996**, *100*, 14316–14328.

(79) Schmidt, M. W.; Baldridge, K. K.; Boatz, J. A.; Elbert, S. T.; Gordon, M. S.; Jensen, J. J.; Koseki, S.; Matsunaga, N.; Nguyen, K. A.; Su, S.; Windus, T. L.; Dupuis, M.; Montgomery, J. A. *J. Comput. Chem.* **1993**, *4*, 1347.

(80) McMurchie, L. E.; Davidson, E. R. *J. Comp. Phys.* **1978**, *26*, 218–231.

(81) Özdoğan, T. *J. Math. Chem.* **2006**, *42* (2), 201–214.

(82) Tschumper, G. S.; Leininger, M. L.; Hoffman, B. C.; Valeev, E. F.; Schaffer, H. F.; Quack, M. *J. Chem. Phys.* **2002**, *116*, 690–701.

(83) van Duijneveldt-van, de; Rijdt, J. G. C. M.; Mooij, W. T. M.; Duijneveldt, F. B *Phys. Chem. Chem. Phys.* **2003**, *5*, 1169–1180.

CT900348B

JCTC Journal of Chemical Theory and Computation

Performance of Nonlinear Finite-Difference Poisson−Boltzmann Solvers

Qin Cai,[†,‡] Meng-Juei Hsieh,[‡] Jun Wang,[‡] and Ray Luo*[,†,‡]

Department of Biomedical Engineering and Department of Molecular Biology and Biochemistry, University of California, Irvine, California 92697

Abstract: We implemented and optimized seven finite-difference solvers for the full nonlinear Poisson−Boltzmann equation in biomolecular applications, including four relaxation methods, one conjugate gradient method, and two inexact Newton methods. The performance of the seven solvers was extensively evaluated with a large number of nucleic acids and proteins. Worth noting is the inexact Newton method in our analysis. We investigated the role of linear solvers in its performance by incorporating the incomplete Cholesky conjugate gradient and the geometric multigrid into its inner linear loop. We tailored and optimized both linear solvers for faster convergence rate. In addition, we explored strategies to optimize the successive over-relaxation method to reduce its convergence failures without too much sacrifice in its convergence rate. Specifically, we attempted to adaptively change the relaxation parameter and to utilize the damping strategy from the inexact Newton method to improve the successive over-relaxation method. Our analysis shows that the nonlinear methods accompanied with a functional-assisted strategy, such as the conjugate gradient method and the inexact Newton method, can guarantee convergence in the tested molecules. Especially the inexact Newton method exhibits impressive performance when it is combined with highly efficient linear solvers that are tailored for its special requirement.

Introduction

Electrostatic interaction plays a key role in determining the structure and function of biomolecules.[1−14] However, modeling of the electrostatic interaction in biomolecules remains a serious computational challenge. The difficulty in modeling a biomolecular system resides in its high dimensionality, especially when explicit solvents are used. Explicit solvents can provide a realistic description of the solution system but require expensive computational resources. In contrast, implicit solvent representation reduces the system degrees of freedom by capturing the average or continuum behavior of the solvent. To model the electrostatic interaction in the salt water solution, the Poisson−Boltzmann equation (PBE) has been widely used:

$$\nabla \cdot \varepsilon(\vec{r})\nabla\phi(\vec{r}) = -4\pi\rho_0 - 4\pi\lambda \sum_i ez_i c_i \times$$
$$\exp(-ez_i\phi(\vec{r})/k_\mathrm{B}T) \quad (1)$$

where $\varepsilon(\vec{r})$ is the dielectric constant, $\phi(\vec{r})$ is the electrostatic potential, ρ_0 is the solute charge density, λ is the ion-exclusion function with values of 0 within the Stern layer and the molecular interior and 1 outside the Stern layer, e is the unit charge, z_i is the valence of ion type i, c_i is the number density of ion type i, k_B is the Boltzmann constant, and T is the absolute temperature. For a solution with symmetric 1:1 salt, eq 1 can be simplified to

$$\nabla \cdot \varepsilon(\vec{r})\nabla\phi(\vec{r}) = -4\pi\rho_0 + \lambda\frac{\varepsilon_\mathrm{out}\kappa^2}{C}\sinh[C\phi(\vec{r})] \quad (2)$$

where $\kappa^2 = (8\pi e^2 I)/(\varepsilon_\mathrm{out}k_\mathrm{B}T)$ and $C = (ez)/(k_\mathrm{B}T)$. Here "out" denotes the outside solvent, I represents the ionic strength of the solution, and $I = z^2 c$. If the electrostatic

* To whom correspondence should be addressed. E-mail: rluo@uci.edu. Fax: (949) 824-9551.
† Department of Biomedical Engineering.
‡ Department of Molecular Biology and Biochemistry.

potential is weak and the ionic strength is low, the nonlinear PBE can be simplified to the linearized form[15]

$$\nabla \cdot \varepsilon(\vec{r})\nabla\phi(\vec{r}) = -4\pi\rho_0 + \lambda\varepsilon_{out}\kappa^2\phi(\vec{r}) \quad (3)$$

The linearized PBE is easier to solve, but it is not very accurate in modeling highly charged biomolecules, such as nucleic acids, while the nonlinear PBE predictions have been shown to yield good agreement with experiments and explicit ion simulations.[16−20] Solution of the nonlinear PBE has attracted much attention in the past. Just as linear PBE solvers, these methods can also be grouped into three categories according to how the PBE is discretized, that is, the finite difference method (FDM),[17,19,21−27] the finite element method (FEM),[28−34] and the boundary element method (BEM).[35−37] A combination of FDM and BEM[38] was also reported. Some of these methods have been incorporated into the widely used PB programs, including Delphi,[24,26] UHBD,[23] PBEQ,[24] and APBS.[28,31] This study intends to evaluate the existing nonlinear FDM solvers and explore strategies to improve their performance.

After the nonlinear PBE is discretized with FDM, a nonlinear system is generated as follows

$$\begin{aligned}
&\varepsilon^x_{i-1,j,k}[\phi_{i,j,k} - \phi_{i-1,j,k}] + \varepsilon^x_{i-1,j,k}[\phi_{i,j,k} - \phi_{i+1,j,k}] \\
&\varepsilon^y_{i,j-1,k}[\phi_{i,j,k} - \phi_{i,j-1,k}] + \varepsilon^y_{i,j-1,k}[\phi_{i,j,k} - \phi_{i+1,j,k}] \\
&\varepsilon^z_{i,j,k-1}[\phi_{i,j,k} - \phi_{i,j,k-1}] + \varepsilon^z_{i,j,k-1}[\phi_{i,j,k} - \phi_{i,j,k+1}] \quad (4) \\
&+ \lambda\frac{\varepsilon_{out}\kappa^2 h^2}{C}\sinh(C\phi_{i,j,k}) = 4\pi q_{i,j,k}/h
\end{aligned}$$

where i, j, and k are the grid indexes along x, y and z axes, respectively. $\varepsilon^x_{i,j,k}$ is the dielectric constant between grids (i, j, k) and ($i + 1$, j, k); $\varepsilon^y_{i,j,k}$ and $\varepsilon^z_{i,j,k}$ are defined similarly. h is the grid spacing in each dimension. $\phi_{i,j,k}$ is the potential at (i, j, k). $q_{i,j,k}$ is the total charge within the cubic volume centered at (i, j, k). The nonlinear system can then be denoted as

$$\mathbf{A}\phi + N(\phi) = \mathbf{b} \quad (5)$$

where $\mathbf{A}$ is the coefficient matrix for the linear part of the PBE, which is a positive-definite matrix, ϕ is the potential vector, $\mathbf{b}$ is the free charge vector, and $N(\phi)$ denotes the nonlinear term in the PBE. The discretized form of PBE can be solved by several numerical methods, such as the nonlinear relaxation methods as implemented in Delphi and PBEQ,[17,19,21,22,24,26,27] the nonlinear conjugate gradient method implemented in UHBD,[23] the nonlinear multigrid method,[25] and the inexact Newton method implemented in APBS.[16] The relaxation methods, extended from classical linear methods such as Gauss−Seidel and successive over-relaxation, were first attempted to solve the FDM version of the nonlinear PBE.[17,24] However, the convergence of such methods cannot be guaranteed.[16] The multigrid method was also attempted,[25] but it may diverge on certain applications.[16] More robust approaches, such as the conjugate gradient method[23] and the inexact Newton method,[16] were also reported for biomolecular applications. The conjugate gradient method is very slow due to considerable evaluations of the nonlinear term. The inexact Newton method is very

attractive and is proven to converge.[16,39] More importantly, the inexact Newton method can be combined with highly efficient linear FDM solvers to yield highly efficient methods.

Despite the early introduction of various nonlinear PBE solvers to biomolecular applications, a comparative and extensive analysis of these solvers is still in need. Such an analysis can guide future development and application of nonlinear PBE solvers. In this study, we implemented, evaluated, and improved when possible seven nonlinear PBE solvers in the FDM scheme. In the following, the tested algorithms of the nonlinear PBE solvers are first summarized. This is followed by a comprehensive analysis of their convergence and performance with a large number of high-quality crystal structures of DNAs, RNAs, and proteins.

Methods

The discretized nonlinear PBE, eq 5, cannot be solved directly for typical biomolecular systems. Even for a linear equation system, the cost to compute the inverse of the coefficient matrix $\mathbf{A}$ is prohibitively high. In practice, the discretized PBE is often solved iteratively in the following form

$$\phi^{t+1} = \phi^t + \delta\phi^t \quad (6)$$

where $\delta\phi^t$ is an update of ϕ^t at the tth iteration. The conjugate gradient method follows a minimization strategy. It first intends to find an update $\delta\phi^t$, which is $\mathbf{A}$-conjugate to all previous updates if the nonlinear term is eliminated. $\delta\phi^t$ is then scaled to minimize a predefined functional. In contrast, the inexact Newton method and the relaxation method are both derivatives of the root-finding Newton method for nonlinear functions, which uses the first-order Taylor expansion of the residual of eq 5, $\mathbf{g}(\phi) = \mathbf{A}\phi + N(\phi) - \mathbf{b}$, to obtain an appropriate update $\delta\phi^t$. The inexact Newton method also requires $\delta\phi^t$ to be scaled to descend a functional that is closely related to that used in the conjugate gradient method.

Conjugate Gradient Algorithm

Luty et al. first explored the use of the nonlinear conjugate gradient (CG) method to solve the nonlinear PBE.[23] The nonlinear conjugate gradient method is derived from the linear conjugate gradient method in a straightforward fashion. The CG method always tries to solve a minimization problem. The predefined functional $G(\phi)$ to be minimized is the integral form of $\mathbf{g}(\phi)$:

$$\min_{\phi}\left\{G(\phi):G(\phi) = \frac{1}{2}\phi^T\mathbf{A}\phi + \Delta\Pi - \mathbf{b}^T\phi\right\} \quad (7)$$

Here, superscript T represents the transpose of a vector or matrix, $\Delta\Pi = \sum_{i,j,k}\int N(\phi_{i,j,k})\,d\phi_{i,j,k}$. Therefore, the stationary point of $G(\phi)$ is also the solution of $\mathbf{g}(\phi) = 0$. It is difficult to build conjugacy between subsequent updates, $\delta\phi^t$, for a nonlinear equation system. Instead, the Fletcher−Reeves algorithm for the corresponding linear problem is used as an approximation, which was proven to converge.[40] Thus, $\delta\phi^t$ is computed in the following way:[41]

$$\delta\phi^t = -\mathbf{g}(\phi^t) + \beta^t\delta\phi^{t-1} \quad (8)$$

Finite-Difference Poisson−Boltzmann Solvers

J. Chem. Theory Comput., Vol. 6, No. 1, 2010 **205**

Chart 1. Pseudocode for the Nonlinear CG Algorithm

```
For i,j,k from 1 to xm,ym,zm
```
$$\varepsilon_{i,j,k} = \varepsilon^x_{i-1,j,k} + \varepsilon^y_{i,j-1,k} + \varepsilon^z_{i,j,k-1} + \varepsilon^x_{i,j,k} + \varepsilon^y_{i,j,k} + \varepsilon^z_{i,j,k}$$
$$g^0_{i,j,k} = \varepsilon_{i,j,k}\phi^0_{i,j,k} - \varepsilon^x_{i-1,j,k}\phi^0_{i-1,j,k} - \varepsilon^y_{i,j-1,k}\phi^0_{i,j-1,k} - \varepsilon^z_{i,j,k-1}\phi^0_{i,j,k-1}$$
$$- \varepsilon^x_{i,j,k}\phi^0_{i+1,j,k} - \varepsilon^y_{i,j,k}\phi^0_{i,j+1,k} - \varepsilon^z_{i,j,k}\phi^0_{i,j,k+1} - 4\pi q_{i,j,k}/h$$
$$\delta\phi^0_{i,j,k} = -g^0_{i,j,k}$$
```
End for i,j,k
Do until convergence
   For i,j,k from 1 to xm,ym,zm
```
$$\sigma_{i,j,k} = \varepsilon_{i,j,k}\delta\phi^t_{i,j,k} - \varepsilon^x_{i-1,j,k}\delta\phi^t_{i-1,j,k} - \varepsilon^y_{i,j-1,k}\delta\phi^t_{i,j-1,k} - \varepsilon^z_{i,j,k-1}\delta\phi^t_{i,j,k-1}$$
$$- \varepsilon^x_{i,j,k}\delta\phi^t_{i+1,j,k} - \varepsilon^y_{i,j,k}\delta\phi^t_{i,j+1,k} - \varepsilon^z_{i,j,k}\delta\phi^t_{i,j,k+1} .$$
```
   End for i,j,k
   Do until convergence
```
$$\text{Solve } (\delta\phi^t, g^t) + (\delta\phi^t, N(\phi^t + \alpha^t\delta\phi^t) - N(\phi^t)) + \alpha^t(\delta\phi^t, \sigma) = 0$$
```
         for α^t using Newton's root-finding method.
   End do
   For i,j,k from 1 to xm,ym,zm
```
$$\phi^{t+1}_{i,j,k} = \phi^t_{i,j,k} + \alpha^t\delta\phi^t_{i,j,k} .$$
$$g^{t+1}_{i,j,k} = g^t_{i,j,k} + N(\phi^{t+1}_{i,j,k}) - N(\phi^t_{i,j,k}) + \alpha^t\sigma_{i,j,k} .$$
```
   End for i,j,k
```
$$\beta^{t+1} = (g^{t+1}, g^{t+1})/(g^t, g^t) .$$
```
   For i,j,k from 1 to xm,ym,zm
```
$$\delta\phi^{t+1}_{i,j,k} = -g^{t+1}_{i,j,k} + \beta^{t+1}\delta\phi^t_{i,j,k} .$$
```
   End for i,j,k
```
$$t = t+1 .$$
```
End do
```

where $\beta^t = (\mathbf{g}(\phi^t), \mathbf{g}(\phi^t))/(\mathbf{g}(\phi^{t-1}), \mathbf{g}(\phi^{t-1}))$, which is used to enforce the **A**-conjugacy between $\delta\phi^t$ and all previous updates in the linear case. Here $(\boldsymbol{a},\boldsymbol{b})$ denotes the dot product of two vectors **a** and **b**. Note that $\delta\phi^t$ is scaled so that eq 6 becomes

$$\phi^{t+1} = \phi^t + \alpha^t\delta\phi^t \qquad (9)$$

where α^t is the scaling factor. By tuning α^t, the functional $G(\phi)$ is minimized. The pseudocode for the nonlinear CG algorithm is given as shown in Chart 1. In this chart, the superscript "0" represents the initial value and the superscript "t" represents the value at the tth iteration. Here, the inner Newton iterations are employed to find the scaling factor α^t that minimizes $G(\phi)$. Luty et al. showed that the nonlinear CG solver was about 4 times slower than the linear CG solver with otherwise identical conditions.[23]

Inexact Newton Method

The inexact Newton (NT) method starts from the standard Newton method.[42] The first-order Taylor expansion of $\mathbf{g}(\phi)$ at $\phi = \phi^t$ gives

$$\mathbf{g}(\phi^t + \delta\phi^t) = \mathbf{g}(\phi^t) + [\mathbf{g}'(\phi)|^t_\phi]\delta\phi^t =$$
$$\mathbf{g}(\phi^t) + [\mathbf{A} + \mathbf{N}'(\phi^t)]\delta\phi^t \quad (10)$$

where $\mathbf{N}'(\phi)$ is the Jacobian matrix of the vector $\mathbf{N}(\phi)$, and a diagonal matrix in this case. The ideal $\delta\phi^t$ would make the new ϕ^{t+1} the root of $\mathbf{g}(\phi) = 0$. Thus, we have

$$[\mathbf{A} + \mathbf{N}'(\phi^t)]\delta\phi^t = -\mathbf{g}(\phi^t) \qquad (11)$$

Chart 2. Pseudocode for the NT Algorithm

```
Do until convergence
   Calculate the nonlinear PB residual g(φ^t).
   Calculate the Jacobian matrix N'(φ^t).
```
$$\text{Let } A^L(\phi^t) = A + N'(\phi^t).$$
```
   Iteratively solve a linear problem
```
$$A^L(\phi^t)\delta\phi^t = -g(\phi^t) \text{ for } \delta\phi^t$$
$$\text{until } \|A^L(\phi^t)\delta\phi^t + g(\phi^t)\| < \|g(\phi^t)\| .$$
```
   Conduct line search along the direction δφ^t,
      i.e., looking for α^t, to satisfy
```
$$\|f(\phi^t + \alpha^t\delta\phi^t)\| < \|f(\phi^t)\| .$$
$$t = t+1 .$$
```
End do
```

In eq 11, the inverse of $[\mathbf{A} + \mathbf{N}'(\phi^t)]$ is difficult to compute and the corresponding $\delta\phi^t$ cannot be obtained within a few iterations, but it is actually unnecessary to solve eq 11 precisely for $\delta\phi^t$. Equation 11 is solved iteratively to the extent that a predefined functional $f(\phi)$ is ensured to decrease in the update direction $\delta\phi^t$, or in other words, a descent direction of $f(\phi)$ is found. Although the integral of $\mathbf{g}(\phi)$ in the above nonlinear CG algorithm is a natural choice for the functional,[23] a simpler form is also effective,[16]

$$\min_\phi\left\{ f(\phi) : f(\phi) = \frac{1}{2}\mathbf{g}(\phi)^T \cdot \mathbf{g}(\phi) \right\} \qquad (12)$$

It has been proven that if the following condition is satisfied

$$\|[\mathbf{A} + \mathbf{N}'(\phi^t)]\delta\phi^t + \mathbf{g}(\phi^t)\| < \|\mathbf{g}(\phi^t)\| \qquad (13)$$

a descent direction of $f(\phi)$ can always be obtained,[16] and the inexact Newton method can converge locally.[42] Next, a line search along the descent direction is conducted to ensure $f(\phi^{t+1}) < f(\phi^t)$, which can guarantee the global convergence of the inexact Newton method.[16] There are various ways to solve eq 11 inexactly, such as the multigrid (MG) method, the incomplete Cholesky conjugate gradient (ICCG) method, and the successive over-relaxation (SOR) method. In summary, the NT algorithm can be written as shown in Chart 2.

The two NT solvers tested in this study are combined with ICCG (NT-ICCG) and MG (NT-MG), respectively, which are employed to solve the inner linear problem for $\delta\phi^t$. The ICCG method is an optimized version by Luo et al.[43] In the MG method, we applied a four-level v-cycle implementation, where the restriction and prolongation were realized with a three-dimensional seven-banded version of Alcouffe's algorithm.[44] We employed the SOR method for the MG presmoothing and postsmoothing on fine grids and also for solving the linear problem on the coarsest grid. The relaxation parameter was set as 1.5 on fine grids and 1.9 on the coarsest grid. Both the presmoothing and postsmoothing use five SOR steps. Because eq 11 is solved inexactly, we adopted this simple and fast implementation, which would be otherwise unstable and unsuitable to solve a normal linear problem with tight convergence criterion.[45] Specifically, the convergence

Chart 3. Pseudocode for a Typical Nonlinear Relaxation Algorithm for the PBE

```
Do until convergence
   For i,j,k from 1 to xm,ym,zm
```

$$\sigma = \varepsilon^x_{i-1,j,k}\phi^{t+1}_{i-1,j,k} + \varepsilon^y_{i,j-1,k}\phi^{t+1}_{i,j-1,k} + \varepsilon^z_{i,j,k-1}\phi^{t+1}_{i,j,k-1}$$

$$+ \varepsilon^x_{i,j,k}\phi^t_{i+1,j,k} + \varepsilon^y_{i,j,k}\phi^t_{i,j+1,k} + \varepsilon^z_{i,j,k}\phi^t_{i,j,k+1}$$

$$\varepsilon_{i,j,k} = \varepsilon^x_{i-1,j,k} + \varepsilon^y_{i,j-1,k} + \varepsilon^z_{i,j,k-1} + \varepsilon^x_{i,j,k} + \varepsilon^y_{i,j,k} + \varepsilon^z_{i,j,k}$$

$$\phi^{t+1}_{i,j,k} = (1-\omega)\phi^t_{i,j,k} + \frac{\omega(\sigma + 4\pi q_{i,j,k}/h)}{\varepsilon_{i,j,k} + N'(\phi^t_{i,j,k})}$$

```
   End for i,j,k
   t = t+1
End do
```

criterion for the NT-MG method was set as $\|[\mathbf{A} + \mathbf{N}'(\phi^t)]\,\delta\phi^t + \mathbf{g}(\phi^t)\| < \|\mathbf{g}(\phi^t)\|$, and the convergence criterion for the NT-ICCG method was set as $\|[\mathbf{A} + \mathbf{N}'(\phi^t)]\,\delta\phi^t + \mathbf{g}(\phi^t)\| < 0.1 \times \|\mathbf{g}(\phi^t)\|$.

Relaxation Algorithms

Unlike the inexact Newton method, a nonlinear relaxation method uses a matrix $\mathbf{B}$ that is approximate to $[\mathbf{A} + \mathbf{N}'(\phi^t)]^{-1}$ in eq 11. Specifically, for the nonlinear SOR method,

$$\mathbf{B} = \omega[\mathbf{D} + \omega\mathbf{L} + \mathbf{N}'(\phi^t)]^{-1} \tag{14}$$

For the nonlinear Jacobi method,

$$\mathbf{B} = [\mathbf{D} + \mathbf{N}'(\phi^t)]^{-1} \tag{15}$$

For the nonlinear Gauss−Seidel (GS) method,

$$\mathbf{B} = [\mathbf{D} + \mathbf{L} + \mathbf{N}'(\phi^t)]^{-1} \tag{16}$$

In eq 14−16, $\mathbf{D}$ is a diagonal matrix, $\mathbf{L}$ is a strictly lower triangular matrix, so that $\mathbf{A} = \mathbf{D} + \mathbf{L} + \mathbf{L}^T$, where $\mathbf{L}^T$ denotes the transpose of $\mathbf{L}$. Each of the above approximate matrices can be easily inversed and the update ($\delta\phi^t$) can be obtained by forward substitutions.

The nonlinear relaxation algorithms are similar to their linear counterparts. The unknowns are updated iteratively in a main loop. At each step, however, a nonlinear term, either a sinh/cosh function[22,24,26,27] or a polynomial,[17,19,21] has to be evaluated on every grid point. A typical nonlinear relaxation algorithm for the PBE can be summarized as the pseudocode shown in Chart 3. In this chart, ω is the relaxation parameter: $\omega = 1$ corresponds to the nonlinear GS method, and $1 < \omega < 2$ corresponds to the nonlinear SOR method. $N'(\phi^t_{i,j,k})$ is a diagonal element of the matrix $\mathbf{N}'(\phi^t)$[22] or a corresponding approximate expression.[17,19,21,24] The above procedure works well for the nonlinear PBE in many situations, but there are cases where the iteration diverges.[24] The convergence failures can be reduced by optimizing the relaxation parameter ω and adding the nonlinearity gradually. For example, in the Delphi program, the nonlinear term is added to the PBE by 5% each time and the optimal ω is estimated adaptively on the basis of the average nonlinearity across the whole space.[26]

In this study, the nonlinear SOR solver uses a constant high-value ω; i.e., $\omega = 1.9$. Our previous analysis shows that the optimal relaxation parameter for the linear SOR method is between 1.9 and 1.95, depending on the structures.[45] We chose $\omega = 1.9$, because it gives a reasonable balance between convergence rate and convergence failure among tested molecules. Reducing ω further can lead to fewer convergence failures but much lower convergence rate. For example, $\omega = 1.8$ reduces convergence failures by 24% but simultaneously reduces the convergence rate by 49%. Instead of optimizing ω, we implemented two different strategies to reduce the convergence failures of SOR. In the first revised SOR, termed the adaptive SOR (ASOR) method, we initially use a high-value ω and then gradually lower it if the norm of the residual starts to increase. As will be shown below, ASOR can reduce the convergence failures of the original SOR method and retains its overall convergence rate. The second modified SOR method combines SOR with the same line search used in the two NT methods after $\delta\phi^t$ is calculated. The "damped" SOR (DSOR) method can also improve the convergence efficiently, though neither can guarantee convergence as will be shown below.

Simulation Details

We implemented seven nonlinear PBE solvers in the PBSA program of the AMBER 10 package,[46] including one implementation of GS, three implementations of SOR, one implementation of CG, and two implementations of NT. The relaxation solvers and the conjugate gradient solver all solve the corresponding linear PBE first and utilize the solution as the initial guess of the solution of the nonlinear PBE.

The dielectric constant was set to 1 within the molecular interior and it was set to 80 within the solvent. The solvent probe was set to be 1.5 Å to compute the solvent excluded surface that was used as the solute/solvent dielectric boundary. The ion probe was set to be 2.0 Å to compute the ion accessible surface that was used as the interface between the Stern layer and the bulk ion accessible solvent region. The finite-difference grid spacing was set as 0.5 Å. The ratio between the longest dimension of the finite-difference grid and that of the solute was set as 1.5. The convergence criterion for the nonlinear system was set to be 10^{-6} and the ionic strength was set to 150 mM if not otherwise mentioned. All floating point data were set in double precision to be consistent with the rest of the Amber 10 package.

We initially collected 588 high-resolution (at least 2 Å) nucleic acid structures with sequence diversity more than 30% from the Protein Data Bank. We first removed all ligand molecules and those structures with non-natural nucleotides unsupported by the Amber force field. Often the unsupported nucleotides are located in the terminal regions, so that the remaining structures can still be used if the terminal regions are deleted. Finally, the test set includes 364 nucleic acids. Hydrogen atoms were added in LEAP of the Amber 10 package.[46] These molecules were assigned the charges of Cornell et al.[47] and the radii of Tan et al.[48] The atom numbers of the nucleic acids range from 250 to 5569, and the numbers of grid points of the nucleic acids range from 313 551 to

Finite-Difference Poisson−Boltzmann Solvers

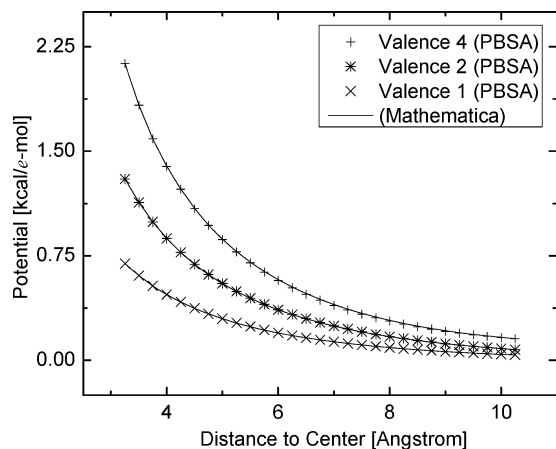*J. Chem. Theory Comput., Vol. 6, No. 1, 2010* **207**

Figure 1. Comparison between the numerical solutions from PBSA and Mathematica for the idealized system under different charges of the single ion. PBSA: numerical solutions in the PBSA program. Mathematica: numerical solutions from the Mathematica program. The charge of the single ion is set as 1*e*, 2*e*, and 4*e*, respectively. Ion concentration is 500 mM and ion valence is 1. Only potential in the ion accessible region is plotted.

Figure 2. Comparison between the numerical solutions from PBSA and Mathematica for the idealized system under different ion concentrations. Linear: solutions to the linearized PBE. Nonlinear: solutions to the full nonlinear PBE. Ion concentrations are set as 100 and 1000 mM, respectively. The charge of the single ion is 2*e* and ion valence is 1. Only potential in the ion accessible region is plotted.

Table 1. Solver Convergence and Relative Performance Statistics for the Test Set of 364 Nucleic Acids, Excluding the Ten Largest Ones[a]

solver	GS	SOR	ASOR	DSOR	CG	NT-ICCG	NT-MG
av rel	47.10	3.32	3.71	5.86	21.35	1.99	1.00
unconv	6	25	6	3	0	0	0

[a] Relative performance of a solver for a molecule is defined as the CPU time of the solver over the CPU time of the NT-MG solver for the same molecule; av rel, average relative performance over all tested molecules; unconv, number of convergence failures.

15 218 175. The PDB codes of the nucleic acids are given as an appendix.

The performance statistics of the seven solvers was collected on a computer cluster of 80 nodes with 1 GB of memory of 3.0 GHz P4 CPUs. For some methods, calculations on the ten largest molecules in the test of 364 nucleic acids require more than 1 GB of memory, so they were left out in the overall analysis. Next, we tested the two NT solvers with the 22 largest nucleic acids (>2000 atoms) in the test set, with the ten largest nucleic acids included, on a server node with 8 GB memory. We also tested the two NT solvers with the 26 largest proteins (>4000 atoms) from the Amber test set.[46] Finally, we analyzed the effects of different salt properties on the performance of the two NT solvers.

Results and Discussion

Idealized System Test. We first tested the nonlinear solvers with an idealized system, i.e., a single ion with radius of 1 Å and multiple charges in the salt−water solution. In this simple system, the grid spacing was set to be 0.25 Å. We compared the numerical solutions of the seven solvers with the solutions obtained from the predictor−corrector Adams method in Mathematica 6.0 under different conditions. Here different charges for the single ion and different ion concentrations were used. Figure 1 shows the results with different charges for the single ion while the ion concentration is 500 mM, and Figure 2 shows the results under different ion concentrations while the charge of the single ion is 2*e*. Note that the solutions of all seven tested numerical solvers are represented by the same symbol due to their virtually identical numerical values. Both figures demonstrate excellent agreements between the seven implemented solvers and the standard numerical method packaged in Mathematica for the tested systems.

Solver Convergence Statistics. We studied the convergence of all the solvers for the 364 nucleic acid test set,

excluding the 10 largest molecules due to the memory limitation of the computer cluster. The convergence statistics are shown in Table 1. Three out of the seven solvers can converge within 10 000 steps in all test cases, i.e., the CG method and the two NT methods, each of which makes use of a functional-assisted strategy. The original SOR method fails in most cases but is noticeably improved if ω is adaptively modified: 76% failed cases in the original SOR method converge with the ASOR method. After a damped step size is applied in the DSOR method, 88% failed cases in the original SOR method converge.

Since we first solve the corresponding linear problem in the nonlinear SOR solvers, the nonlinearity is weakened. This strategy was found to improve the convergence. Moreover, lower-value ω, or even under-relaxation, can obtain better convergence than high-value ω.[24,26] For example, in our test, the GS method converges in more test cases than the original SOR method, in spite of its much lower convergence rate. The minimal ω in the ASOR method is equal to 1, so it is expected that the ASOR method has the same number of convergence failures as the GS method, but it converges much faster because over-relaxation is initially used. The DSOR method conducts a line search to descend $f(\phi)$ in eq 12 but still cannot guarantee convergence, because the direction is not necessarily a descent direction. Note that for those test cases for which the original SOR method cannot

converge, the DSOR method shows better convergence rate than the ASOR method.

There is one way to improve the inexact Newton method, which is to use an appropriate convergence criterion to inexactly solve the inner linear equation at each step. This requires that each convergence criterion be different and deliberately designed to prevent under-solving or oversolving eq 11. Oversolving the equation means the convergence criterion is too tight. This is because the descent direction $\delta\phi^t$ no longer changes much when the appropriate convergence criterion is reached. That is to say, the extra computation in reaching the tighter convergence criterion does not result in noticeable improvement. Under-solving the equation means the convergence criterion is so loose that $\delta\phi^t$ is no longer a good descent direction, along which the functional can decrease little. This will lead to a significant increase in the Newton iteration steps. The set of convergence criteria is called the forcing terms. A study on local convergence of different sets of forcing terms was conducted in the litera-ture.[49] However, it is still hard to design appropriate forcing terms if the initial guess is far away from the solution. Note that NT-MG and NT-ICCG are in different situations. One linear MG cycle can substantially reduce the residual and probably oversolve the equation, while multiple ICCG cycles are necessary to reduce the residual to the same level. Therefore, we used a tighter inner convergence criterion for NT-ICCG (the average relative performance is 53.12 if the same inner convergence criterion as for NT-MG is used), and for the same reason, NT-ICCG is more likely to be improved by optimizing the forcing terms.

Finally, the convergence performance of SOR might be improved if a hybrid method is employed. For example, one would start with SOR and later switch to NT-MG when SOR becomes ineffective. The memory requirement is the same as in the more demanding method, i.e., NT-MG. This hybrid method can definitely guarantee convergence. However, it is useful only if SOR is superior to NT-MG during the initial iteration steps, which is actually not the case. Thus, more effort is definitely needed if a hybrid method is to be pursued.

Timing and Memory Requirement of Inexact Newton Methods. In the following, we focus on the two NT methods because of their significantly higher efficiency and robust-ness. First, we examined the timing and memory requirement of the two NT methods in solving PBEs for the test set of 364 nucleic acids, excluding the 10 largest ones. We utilized the APBS finite-difference solver as a reference in this round. All three solvers were compiled and tested under conditions as identical as possible, though it should be pointed out that the APBS solver has been adapted for parallel platforms, which may impact its single-CPU performance. Specifically the exactly same discretized nonlinear problems were solved. Figure 3 shows that the memory requirement and solver time of the three solvers are similar for smaller molecules, but their difference becomes obvious when the number of grid points increases. Both the memory and the timing trends for NT-MG are linear over the number of grid points. The memory trend for NG-ICCG is linear, but its timing trend remains linear only for smaller test cases and becomes nonlinear for larger test cases. On average, the APBS solver
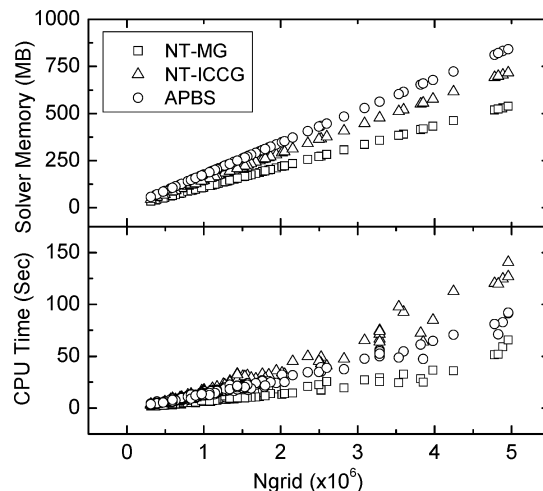
Figure 3. Scaling of solver CPU times and memory usages versus numbers of grid points of the two inexact Newton methods and the APBS solver for the test set of 364 nucleic acids, excluding the 10 largest ones.

Table 2. Solver Times (s) of Two Inexact Newton Methods for the 22 Largest Nucleic Acids in the Test Set of 364 Nucleic Acids[a]

nucleic acids	N_{atom}	N_{grid}	NT-MG	NT-ICCG
1EHZ	2509	7 258 191	51.71	131.35
1EVV	2509	6 650 175	46.76	108.97
1I2Y	2124	3 820 287	18.31	51.83
1NUJ	3112	7 498 575	53.54	140.65
1NUV	3112	7 498 575	53.97	142.65
1Q96	2616	4 887 087	31.08	80.03
1U8D	2145	3 285 711	20.83	44.12
1ZCI	2448	5 980 975	34.74	107.87
244D	3120	4 956 175	34.81	79.97
2DZ7	2032	2 597 023	17.35	28.18
2EES	2145	3 285 711	20.43	48.83
2EET	2147	3 285 711	20.89	46.78
2EEU	2145	3 285 711	20.71	46.67
2EEV	2147	3 285 711	20.75	48.43
2G3S	2580	4 779 775	26.27	77.83
2G9C	2144	3 285 711	20.67	48.07
2GWQ	3128	6 286 383	40.55	104.68
352D	3024	4 956 175	34.75	90.32
3BNN	2696	8 078 175	57.32	146.12
3D2V	4970	8 299 375	61.94	164.30
2Z75	4646	11 979 711	102.47	225.23
3DIL	5569	15 218 175	126.39	383.26

[a] N_{atom}, atom number; N_{grid}, number of grid points.

requires the most memory, the NT-ICCG consumes the most time, and the NT-MG needs less memory and less time than both the NT-ICCG and the APBS solver. Although our simple implementation of MG is superior under current circumstances, a more robust MG solver will probably bring more benefit if the convergence criterion for the nonlinear equation is tighter. In this case, the linear equation should be solved exactly in the last few Newton steps, because the linear equation is a very good approximation. Finally, it should be noted that the memory usages and the CPU times among the three solvers differ at most by a factor of 2. The difference may be overwhelmed by a higher grid resolution and by a different testing condition, such as in molecular dynamics, as our latest analysis has shown.[50]

Tables 2 and 3 list the solver time of the two NT methods for the 22 largest molecules in the test set of 364 nucleic acids and the 26 largest proteins in the Amber test set,

Finite-Difference Poisson−Boltzmann Solvers

J. Chem. Theory Comput., Vol. 6, No. 1, 2010 **209**

Table 3. Solver Times (s) of Two Inexact Newton Methods for the 26 Largest Proteins in the Amber Test Set

proteins	N_{atom}	N_{grid}	NT-MG	NT-ICCG
1B8O_A	4348	4 779 775	29.91	98.38
1C0P_A	5566	7 258 191	73.34	194.19
1D8V_A	4211	5 849 375	32.19	119.25
1DCI_A	4281	6 204 975	40.45	160.39
1DJ0_A	4176	5 759 775	44.74	115.93
1DS1_A	4916	4 869 375	45.02	121.30
1E19_A	4874	6 384 175	34.93	127.91
1E6Q_M	7819	8 816 751	74.85	193.63
1E6U_A	4966	5 180 175	49.82	103.80
1EZA_0	4034	4 921 631	29.07	69.93
1EZO_A	5735	8 392 815	49.42	147.62
1F24_A	6221	6 286 383	39.43	108.85
1HZY_A	5092	4 869 375	30.28	97.17
1IXH_0	4856	5 637 663	36.70	87.21
1MLA_0	4485	4 424 175	28.18	81.41
1PA2_A	4441	4 779 775	30.43	91.16
1QH4_A	5983	6 829 375	37.72	130.39
1QNR_A	5129	4 379 375	37.47	91.42
1QOP_B	5895	5 233 167	41.56	140.93
1QQF_A	4365	4 019 679	22.28	56.62
1QTW_A	4380	4 342 767	26.85	85.04
1YUB_0	4168	6 768 719	37.55	134.50
2CTC_0	4801	4 342 767	28.59	71.34
2OLB_A	8254	7 866 207	53.02	148.77
3SIL_0	5804	5 359 375	38.29	120.50
7A3H_A	4578	3 615 183	22.25	68.95

respectively. Since tested proteins are more compact than tested nucleic acids, the average number of grid points is similar for the two sets of molecules. It is apparent that the solver times are also comparable between the two sets of molecules, i.e., the solver efficiency mostly depends on the number of grid points. More importantly, for these largest tested molecules, NT-MG uses only a third of the time of NT-ICCG. Note that it uses about a half of the time of NT-ICCG in the overall test. This observation is consistent with the intrinsic advantage of the MG method on large systems.

Performance of Inexact Newton Methods versus Convergence Criterion. Next, the performance of the two NT methods under a variety of convergence criteria ranging from 10^{-1} to 10^{-9} was examined. Five nucleic acids of different sizes were selected as test cases in this round, 1SGS (1074 atoms), 1JRN (1564 atoms), 1U8D (2145 atoms), 1EHZ (2509 atoms), and 2GWQ (3128 atoms). Figure 4 shows that both methods can improve convergence without any steep jump in the solver time, indicating a constantly smooth convergence behavior. Specifically, a linear relationship exists between the solver time and the logarithm of the convergence criterion. The slope, however, increases with the complexity and size of tested molecules.

Performance of Inexact Newton Methods versus Ion Concentration. Finally, the effect of the ion concentration was studied, and the results are shown in Figure 5. The sample in this test consists five large nucleic acids, 1EHZ (2509 atoms), 3BNN (2696 atoms), 1NUV (3112 atoms), 2GWQ (3128 atoms), 3D2V (4970 atoms). Three different ion concentrations were tested, including 150, 500, and 1000 mM. Regardless of ion concentrations, the average solver time of NT-MG for the five molecules is more or less constant. On the contrary, the average solver time of NT-ICCG depends on the ion concentration: the solver uses about
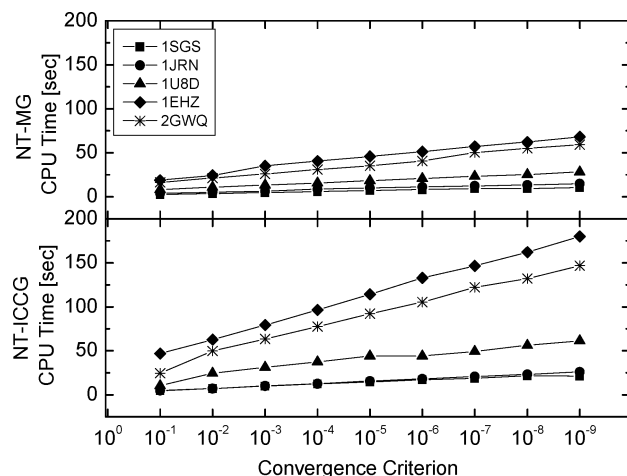
Figure 4. Solver CPU times versus convergence criteria of the two inexact Newton methods. Note that the flat region between adjacent convergence criteria results from the same number of iterations required to converge, even if the convergence criteria are different; i.e., the residual reduction is more than the specified convergence criterion reduction.
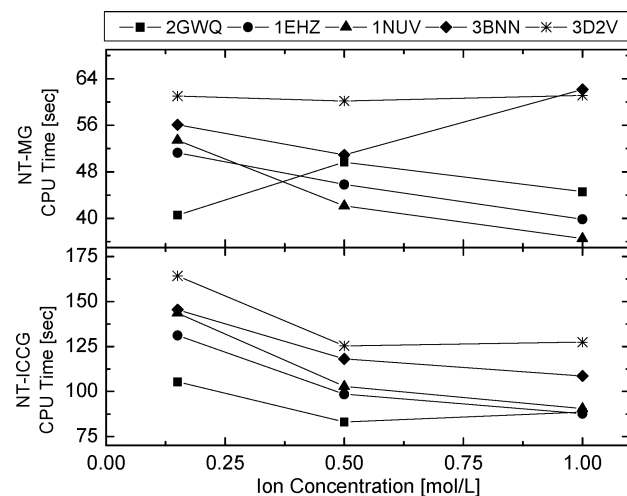
Figure 5. Solver CPU times versus ion concentrations of the two inexact Newton methods.

one-quarter less solver time when the ion concentration is high (≥ 500 mM). This observation indicates that NT-MG is probably more stable than NT-ICCG under different salt conditions in biomolecular applications.

We also tested the performance of the two NT methods when the ion valence is changed. However, no clear trend was observed. The average solver times of both the NT-MG method and the NT-ICCG method only increase slightly with the ion valence.

Conclusion

We implemented and optimized seven finite-difference solvers for the nonlinear Poisson−Boltzmann equation, including four relaxation methods, one CG method, and two NT methods. We tested the performance of the seven solvers with a large number of nucleic acids and proteins, with special attentions given to the robust NT algorithm. We investigated the role of linear solvers in its performance by

incorporating ICCG and MG into the algorithm. Specifically, a four-level v-cycle was applied in the MG method, where the restriction and prolongation were realized with a three-dimensional seven-banded version of Alcouffe's algorithm. In addition, the SOR method was applied for the multigrid presmoothing and postsmoothing on fine grids and also for solving the linear problem on the coarsest grid. We adopted this simple and fast implementation because the inner linear problem of the NT method does not need to be solved exactly. To accelerate the convergence of our implementation of NT-ICCG, we tightened the convergence criterion of the inner linear solver loop. In addition, we explored strategies to optimize the SOR method to reduce its convergence failures without too much sacrifice in its convergence rate. In the ASOR method, ω was designed to decrease when the norm of the residual starts to increase. This method reduces the convergence failures by 76% and retains much of the overall convergence rate of the original SOR method with a high-value ω. In the DSOR method, the damping strategy from the NT method was utilized to optimize the search step length and was found to reduce the convergence failures by 88%.

Our results show that only the nonlinear methods accompanied with a functional-assisted strategy can guarantee convergence, such as the CG method and the NT method, while the relaxation methods cannot. Especially the NT method exhibits impressive performance when it is combined with highly efficient linear solvers. Therefore, our analysis suggests that the functional-assisted strategies be used in existing numerical solvers for biomolecular applications if they intend to solve the nonlinear PBE for biomolecules.

Finally, it is instructive to discuss future directions in the optimization of nonlinear solvers for biomolecular applications. First point charges are widely used to represent atomic charge density distributions in current biomolecular models. Unfortunately, this practice introduces singularity into the right-hand side of PBE. The presence of charge singularity results in discontinuity in the electrostatic potential with large error when the finite-difference method is used. We have developed a new formulation to remove the charge singularity in the linear finite-difference solvers.[51] Given the current implementations of the nonlinear solvers, we are in a position to investigate the effect of charge singularity on the performance of the nonlinear finite-difference solvers. In addition, we plan to extend our analysis and optimization of the nonlinear finite-difference solvers in the context of molecular dynamics simulations. It is expected that the efficiency of the nonlinear solvers can be improved in molecular dynamics simulations, just as in our prior analysis of the linear solvers.[45] However, further development is necessary to fully take advantage of the potential update nature in molecular dynamics to achieve computational efficiency high enough for routine biomolecular applications.

Appendix: Test Set of 364 Nucleic Acids

The following molecular structures, in both the Amber format and the pqr format, can be downloaded from http://rayl0.bio.uci.edu/rayl/#Database: 100D, 109D, 110D, 118D, 126D, 127D, 131D, 137D, 138D, 151D, 152D, 157D, 158D, 160D, 161D, 165D, 181D, 182D, 184D, 190D, 191D, 192D, 196D, 198D, 1A2E, 1BD1, 1BNA, 1CSL, 1D10, 1D11, 1D12, 1D13, 1D15, 1D23, 1D32, 1D36, 1D37, 1D38, 1D39, 1D43, 1D44, 1D45, 1D46, 1D48, 1D49, 1D54, 1D56, 1D57, 1D58, 1D63, 1D67, 1D78, 1D79, 1D88, 1D8G, 1D8X, 1D96, 1DA0, 1DA9, 1DC0, 1DCG, 1DJ6, 1DL8, 1DN8, 1DNO, 1DNS, 1DNT, 1DNX, 1DNZ, 1DOU, 1DQH, 1EHV, 1EHZ, 1EN3, 1EN8, 1EN9, 1ENE, 1ENN, 1EVP, 1EVV, 1F27, 1FD5, 1FDG, 1FMQ, 1FMS, 1FN2, 1FQ2, 1FTD, 1G4Q, 1I0T, 1I1P, 1I2Y, 1I7J, 1ICG, 1ICK, 1ID9, 1IDW, 1IH1, 1IHA, 1IKK, 1IMR, 1IMS, 1JGR, 1JO2, 1JRN, 1JTL, 1K9G, 1KCI, 1KD3, 1KD4, 1KD5, 1L1H, 1L2X, 1L4J, 1LJX, 1M69, 1M6F, 1M6G, 1M6R, 1M77, 1MF5, 1MSY, 1NLC, 1NQS, 1NT8, 1NUJ, 1NUV, 1NVN, 1NVY, 1OOK, 1OFX, 1OSU, 1P20, 1P4Y, 1P4Z, 1P79, 1PFE, 1PJG, 1PJO, 1Q96, 1Q9A, 1QCU, 1QYK, 1QYL, 1R68, 1RQY, 1RXB, 1S23, 1S2R, 1SGS, 1SK5, 1T0E, 1U8D, 1UB8, 1UE4, 1V9G, 1VAQ, 1VJ4, 1VS2, 1VZK, 1WOE, 1WQY, 1XA2, 1XCS, 1XCU, 1XJX, 1XJY, 1XPE, 1XVK, 1XVN, 1XVR, 1Z3F, 1Z8V, 1ZCI, 1ZEV, 1ZEX, 1ZEY, 1ZEZ, 1ZF0, 1ZF1, 1ZF2, 1ZF3, 1ZF4, 1ZF5, 1ZF6, 1ZF7, 1ZF8, 1ZF9, 1ZFA, 1ZFB, 1ZFC, 1ZFF, 1ZFG, 1ZNA, 1ZPH, 1ZPI, 200D, 212D, 215D, 220D, 221D, 222D, 224D, 232D, 234D, 235D, 236D, 240D, 241D, 243D, 244D, 245D, 248D, 251D, 255D, 258D, 259D, 260D, 272D, 276D, 279D, 284D, 288D, 292D, 293D, 295D, 2A43, 2A7E, 2ADW, 2AVH, 2B0K, 2B1B, 2B2B, 2B3E, 2D47, 2D94, 2D95, 2DCG, 2DES, 2DYW, 2DZ7, 2EES, 2EET, 2EEU, 2EEV, 2F8W, 2G32, 2G3S, 2G9C, 2GB9, 2GPM, 2GQ4, 2GQ5, 2GQ6, 2GQ7, 2GVR, 2GW0, 2GWA, 2GWQ, 2GYX, 2HBN, 2HTO, 2I2I, 2I5A, 2IE1, 2O1I, 2O4F, 2OE5, 2OE8, 2OIY, 2OKS, 2PKV, 2PL4, 2PL8, 2PLB, 2PLO, 2PWT, 2Q1R, 2QEK, 2R22, 2V6W, 2V7R, 2VAL, 2Z75, 307D, 308D, 310D, 312D, 314D, 315D, 317D, 331D, 332D, 334D, 336D, 348D, 349D, 351D, 352D, 354D, 355D, 360D, 362D, 368D, 369D, 370D, 371D, 377D, 385D, 386D, 393D, 394D, 395D, 396D, 397D, 398D, 399D, 3BNN, 3C2J, 3C44, 3CGP, 3CGS, 3CJZ, 3CZW, 3D0M, 3D2V, 3DIL, 3DNB, 3ERU, 3EUM, 413D, 414D, 420D, 423D, 428D, 431D, 432D, 434D, 435D, 437D, 439D, 440D, 441D, 442D, 443D, 452D, 453D, 455D, 463D, 465D, 466D, 472D, 473D, 476D, 477D, 479D, 480D, 482D, 483D, 485D, 5DNB, 7BNA, 9BNA, 9DNA.

References

(1) Baker, N. A. *Curr. Opin. Struct. Biol.* **2005**, *15*, 137.

(2) Bashford, D.; Case, D. A. *Annu. Rev. Phys. Chem.* **2000**, *51*, 129.

(3) Chen, J. H.; Im, W. P.; Brooks, C. L. *J. Am. Chem. Soc.* **2006**, *128*, 3728.

(4) Cramer, C. J.; Truhlar, D. G. *Chem. Rev.* **1999**, *99*, 2161.

(5) Davis, M. E.; McCammon, J. A. *Chem. Rev.* **1990**, *90*, 509.

(6) Feig, M.; Chocholousova, J.; Tanizaki, S. *Theor. Chem. Acc.* **2006**, *116*, 194.

Finite-Difference Poisson−Boltzmann Solvers

J. Chem. Theory Comput., Vol. 6, No. 1, 2010 **211**

(7) Gilson, M. K. *Curr. Opin. Struct. Biol.* **1995**, *5*, 216.

(8) Honig, B.; Nicholls, A. *Science* **1995**, *268*, 1144.

(9) Im, W.; Chen, J. H.; Brooks, C. L. *Adv. Protein Chem.* **2006**, *72*, 173.

(10) Koehl, P. *Curr. Opin. Struct. Biol.* **2006**, *16*, 142.

(11) Lu, B. Z.; Zhou, Y. C.; Holst, M. J.; McCammon, J. A. *Commun. Comput. Phys.* **2008**, *3*, 973.

(12) Roux, B.; Simonson, T. *Biophys. Chem.* **1999**, *78*, 1.

(13) Sharp, K. A. *Curr. Opin. Struct. Biol.* **1994**, *4*, 234.

(14) Wang, J.; Tan, C. H.; Tan, Y. H.; Lu, Q.; Luo, R. *Commun. Comput. Phys.* **2008**, *3*, 1010.

(15) Hill, T. L. Dilute Electrolyte Solutions and Plasmas. In *An Introduction to Statistical Thermodynamics*; Dover Publications, Inc.: New York, 1986; pp 321−331.

(16) Holst, M. J.; Saied, F. *J. Comput. Chem.* **1995**, *16*, 337.

(17) Jayaram, B.; Sharp, K. A.; Honig, B. *Biopolymers* **1989**, *28*, 975.

(18) Prabhu, N. V.; Panda, M.; Yang, Q. Y.; Sharp, K. A. *J. Comput. Chem.* **2008**, *29*, 1113.

(19) Sharp, K. A.; Honig, B. *J. Phys. Chem.* **1990**, *94*, 7684.

(20) Ye, X.; Cai, Q.; Yang, W.; Luo, R. *Biophys. J.* **2009**, *97*, 554.

(21) Allison, S. A.; Sines, J. J.; Wierzbicki, A. *J. Phys. Chem.* **1989**, *93*, 5819.

(22) Forsten, K. E.; Kozack, R. E.; Lauffenburger, D. A.; Subramaniam, S. *J. Phys. Chem.* **1994**, *98*, 5580.

(23) Luty, B. A.; Davis, M. E.; McCammon, J. A. *J. Comput. Chem.* **1992**, *13*, 1114.

(24) Nicholls, A.; Honig, B. *J. Comput. Chem.* **1991**, *12*, 435.

(25) Oberoi, H.; Allewell, N. M. *Biophys. J.* **1993**, *65*, 48.

(26) Rocchia, W.; Alexov, E.; Honig, B. *J. Phys. Chem. B* **2001**, *105*, 6507.

(27) Xiang, Z. X.; Shi, Y. Y.; Xu, Y. W. *J. Comput. Chem.* **1995**, *16*, 200.

(28) Baker, N.; Holst, M.; Wang, F. *J. Comput. Chem.* **2000**, *21*, 1343.

(29) Chen, L.; Holst, M. J.; Xu, J. C. *SIAM J. Numer. Anal.* **2007**, *45*, 2298.

(30) Dyshlovenko, P. E. *Comput. Phys. Commun.* **2002**, *147*, 335.

(31) Holst, M.; Baker, N.; Wang, F. *J. Comput. Chem.* **2000**, *21*, 1319.

(32) Sayyed-Ahmad, A.; Tuncay, K.; Ortoleva, P. J. *J. Comput. Chem.* **2004**, *25*, 1068.

(33) Shestakov, A. I.; Milovich, J. L.; Noy, A. *J. Colloid Interface Sci.* **2002**, *247*, 62.

(34) Xie, D.; Zhou, S. Z. *BIT Numer. Math.* **2007**, *47*, 853.

(35) Rashin, A. A.; Malinsky, J. *J. Comput. Chem.* **1991**, *12*, 981.

(36) Vorobjev, Y. N.; Grant, J. A.; Scheraga, H. A. *J. Am. Chem. Soc.* **1992**, *114*, 3189.

(37) Zhou, H. X. *J. Chem. Phys.* **1994**, *100*, 3152.

(38) Boschitsch, A. H.; Fenley, M. O. *J. Comput. Chem.* **2004**, *25*, 935.

(39) Eisenstat, S. C.; Walker, H. F. *SIAM J. Optimization* **1994**, *4*, 393.

(40) Ortega, J. M.; Rheinboldt, W. C. Convergence of Minimization Methods. In *Iterative Solution of Nonlinear Equations in Several Variables*; Rheinboldt, W. C., Ed.; Academic Press, Inc.: New York, 1970; pp 509−512.

(41) Fletcher, R.; Reeves, C. M. *Comput. J.* **1964**, *7*, 149.

(42) Dembo, R. S.; Eisenstat, S. C.; Steihaug, T. *SIAM J. Numer. Anal.* **1982**, *19*, 400.

(43) Luo, R.; David, L.; Gilson, M. K. *J. Comput. Chem.* **2002**, *23*, 1244.

(44) Alcouffe, R. E.; Brandt, A.; Dendy, J. E.; Painter, J. W. *SIAM J. Sci. Stat. Comput.* **1981**, *2*, 430.

(45) Wang, J.; Luo, R. *J. Comput. Chem.* **2010**, *31*, in press.

(46) Case, D. A.; Darden, T. A.; Cheatham, T. E., III; Simmerling, C. L.; Wang, J.; Duke, R. E.; Luo, R.; Crowley, M.; Walker, R. C.; Zhang, W.; Merz, K. M.; Wang, B.; Hayik, S.; Roitberg, A.; Seabra, G.; Kolossváry, I.; Wong, K. F.; Paesani, F.; Vanicek, J.; Wu, X.; Brozell, S. R.; Steinbrecher, T.; Gohlke, H.; Yang, L.; Tan, C.; Mongan, J.; Hornak, V.; Cui, G.; Mathews, D. H.; Seetin, M. G.; Sagui, C.; Babin, V.; Kollman, P. A. *AMBER 10*; University of California: San Francisco, 2008.

(47) Cornell, W. D.; Cieplak, P.; Bayly, C. I.; Gould, I. R.; Merz, K. M.; Ferguson, D. M.; Spellmeyer, D. C.; Fox, T.; Caldwell, J. W.; Kollman, P. A. *J. Am. Chem. Soc.* **1995**, *117*, 5179.

(48) Tan, C. H.; Yang, L. J.; Luo, R. *J. Phys. Chem. B* **2006**, *110*, 18680.

(49) Eisenstat, S. C.; Walker, H. F. *SIAM J. Sci. Comput.* **1996**, *17*, 16.

(50) Cai, Q.; Luo, R. In preparation.

(51) Cai, Q.; Wang, J.; Zhao, H. K.; Luo, R. *J. Chem. Phys.* **2009**, *130*, 145101.

CT900381R

JCTC Journal of Chemical Theory and Computation

Conformational Analysis of Arabinofuranosides: Prediction of $^3J_{H,H}$ Using MD Simulations with DFT-Derived Spin−Spin Coupling Profiles

Hashem A. Taha,[†] Norberto Castillo,[†] Devin N. Sears,[†] Roderick E. Wasylishen,[†]
Todd L. Lowary,*[,†] and Pierre-Nicholas Roy*[,‡]

Department of Chemistry and Alberta Ingenuity Centre for Carbohydrate Science,
Gunning-Lemieux Chemistry Centre, University of Alberta, Edmonton, AB,
Canada T6G 2G2, and Department of Chemistry, University of Waterloo,
Waterloo, ON, Canada N2L 3G1

Abstract: A molecular dynamics (MD) investigation on a series of oligo-α-arabinofuranosides (**1**−**8**) using the AMBER force field and the GLYCAM carbohydrate parameter set is reported. The validation of the method was carried out by direct comparison of experimental vicinal proton−proton coupling constants ($^3J_{H,H}$) with those obtained by using an empirically determined Karplus equation and density functional theory (DFT)-derived relationships specifically tailored for α-arabinofuranosyl systems. A simple code was developed to implement the determination of $^3J_{H,H}$ by applying these relationships to the probability distributions of rotamers and ring conformations displayed by the simulations. The empirical Karplus relationship and the DFT-derived equations yielded, in most cases, the same trend as experiment for intra-ring $^3J_{H,H}$ values. This direct comparison circumvents additional sources of errors that may arise from the assumptions introduced by the deconvolution procedures often used to calculate population of rotamers and ring conformations from experimental $^3J_{H,H}$.

Introduction

Molecular dynamics (MD) simulations of glycoconjugates are an active area of research due to the role of carbohydrate-containing molecules in several life processes,[1−4] and it is now appreciated that the conformational preferences of these molecules are critical determinants of their biological activity.[5,6] The conformational analysis of complex carbohydrates is often too complex and challenging to be addressed completely by experimental methods and thus such investigations rely heavily on the tandem use of computational and experimental approaches (largely NMR spectroscopy and X-ray crystallography).[5,6] To complement these techniques, significant efforts have therefore been devoted to studying the conformational equilibrium of carbohydrates computationally.

Various accounts have described the development of methodologies for deriving force field parameters, including atomic charges, to simulate biomolecules,[7−12] and there are extensive reports describing molecular dynamics simulations on oligosaccharides containing pyranoside (six-membered) rings.[13−17] Software programs for the structural prediction of sugars have also been developed to investigate possible conformations not visited by nonergodic simulations.[18−20] Far fewer investigations of oligosaccharides containing one or more furanose (five-membered) rings have been reported.[21−27]

Our group has a long-standing interest in the furanoside-containing polysaccharides that are found in the cell wall structure of mycobacteria, including the pathogenic species *Mycobacterium tuberculosis* and *Mycobacterium leprae,* which cause tuberculosis and leprosy, respectively.[28] These glycoconjugates play a critical role in mycobacterial survival and pathogenicity. Conformational investigations of these molecules are of interest as the information gleaned will be of help in developing inhibitors of enzymes that process

---

* To whom correspondence should be addressed. E-mail: pnroy@uwaterloo.ca, todd.lowary@ualberta.ca.
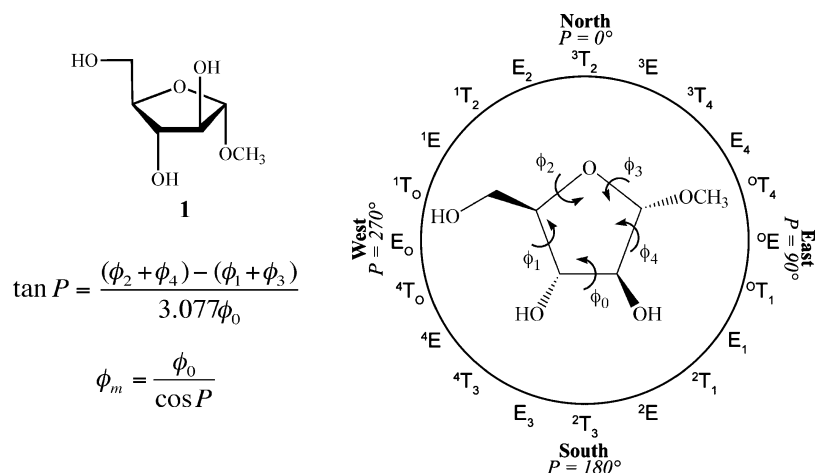† University of Alberta.
‡ University of Waterloo.

Conformational Analysis of Arabinofuranosides

J. Chem. Theory Comput., Vol. 6, No. 1, 2010 **213**

Figure 1. Pseudorotational itinerary for methyl α-D-arabinofuranoside, **1**.

furanose sugars.[29] However, conformational studies of oligofuranosides are more complex than comparable investigations on oligopyranosides, due to the inherent flexibility of five-membered rings.[21−26]

Furanoside rings can adopt a number of twist (T) and envelope (E) conformations, which can be depicted using the pseudorotational itinerary (Figure 1). Each conformer can be described by two coordinates: the Altona−Sundaralingam (AS) phase angle of pseudorotation (P), which represents the atoms that are displaced from the plane, and the AS puckering amplitude (ϕ_m), a measure of the maximum displacement from the planar ring form.[30] Given five endocyclic torsion angles of a given conformer, P and ϕ_m can be calculated through the use of the equations shown in Figure 1.[30] The interconversion barrier between these conformers is relatively low (<5 kcal/mol),[31] and this flexibility renders the theoretical description of furanosides challenging, as one must consider both the torsion angles of the ring (Figure 1) as well as any exocyclic dihedral angles.

Determination of the solution conformation of carbohydrates is most frequently performed using NMR spectroscopy,[32−34] and great effort has been devoted to the study of molecular conformations by analysis of both homo- and heteronuclear NMR coupling constants and their orientational dependence.[32−44] Experimental coupling constants, $^3J_{H,H}$, are measured as an average over the entire conformational space of the molecule and this average can be expressed by eq 1[45]

$$\langle J \rangle = \int_0^{360} J(\phi)\, \rho(\phi)\, d\phi \qquad (1)$$

where $J(\phi)$ is an extended Karplus equation that correlates the vicinal nuclear spin−spin coupling constants to the dihedral angle between the coupled spins and $\rho(\phi)$ is the probability distribution of dihedral angles about a particular bond.

The simplest method for assessing conformation about acyclic fragments is the "discrete model".[45] In this approach, it is assumed that a set of equilibrating rotamers of discrete dihedral angles (usually three staggered rotamers) adequately describes the conformational preferences about that bond. As an example, for the C4−C5 bond in methyl α-D-arabinofuranoside (**1**), three staggered rotamers about this
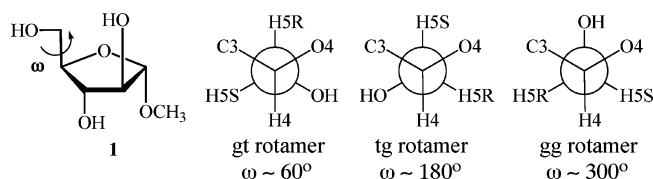
Figure 2. Definitions of the three staggered rotamers about the C4−C5 bond in **1**. The angle ω is defined as the O5−C5−C4−O4 torsion angle.

bond, gt, tg, and gg, can be defined (Figure 2) and are generally used in calculations of this type.

This approach is formally expressed by eq 2, where X_i (i = 1, 2, 3) are the unknown populations of the discrete rotamers, ϕ_i is the H4−C4−C5−H5R or H4−C4−C5−H5S dihedral angle in each of the three rotamers, and $\langle J \rangle$ is the measured average coupling constant.

$$\langle J \rangle = \sum_{i=1}^{3} X_i J(\phi_i) \quad \text{with} \quad \sum_{i=1}^{3} X_i = 1 \qquad (2)$$

This assumption leads to potential errors in the analysis, because it does not consider deviations from the staggered conformations and does not account for contributions from dihedral angles with low probability. In addition, for some systems more than three conformers may exist.

The search for alternatives to address the limitations arising from assumptions of the discrete model and thus to better define $\rho(\phi)$ gave rise to the generation of continuous models. The continuous probability distribution (CUPID)[45] is among the most popular continuous models used.[35] This method is based on the fact that the probability distribution of rotamers, $\rho(\phi)$, must be a periodic function of ϕ and therefore can be expressed as a Fourier series where the coefficients of the expansion are the parameters to be determined from eq 1. For practical reasons, the Fourier series must be truncated, and this constitutes the main limitation of the method. Aside from its use in determining rotamer populations about single bonds, CUPID has been adapted for use in the conformational analysis of five-membered ring systems (CUPID-5), incorporating the general principles of pseudorotation.[46] The use of CUPID-5 yielded generally more accurate fits to the experimental NMR coupling constants, compared to discrete
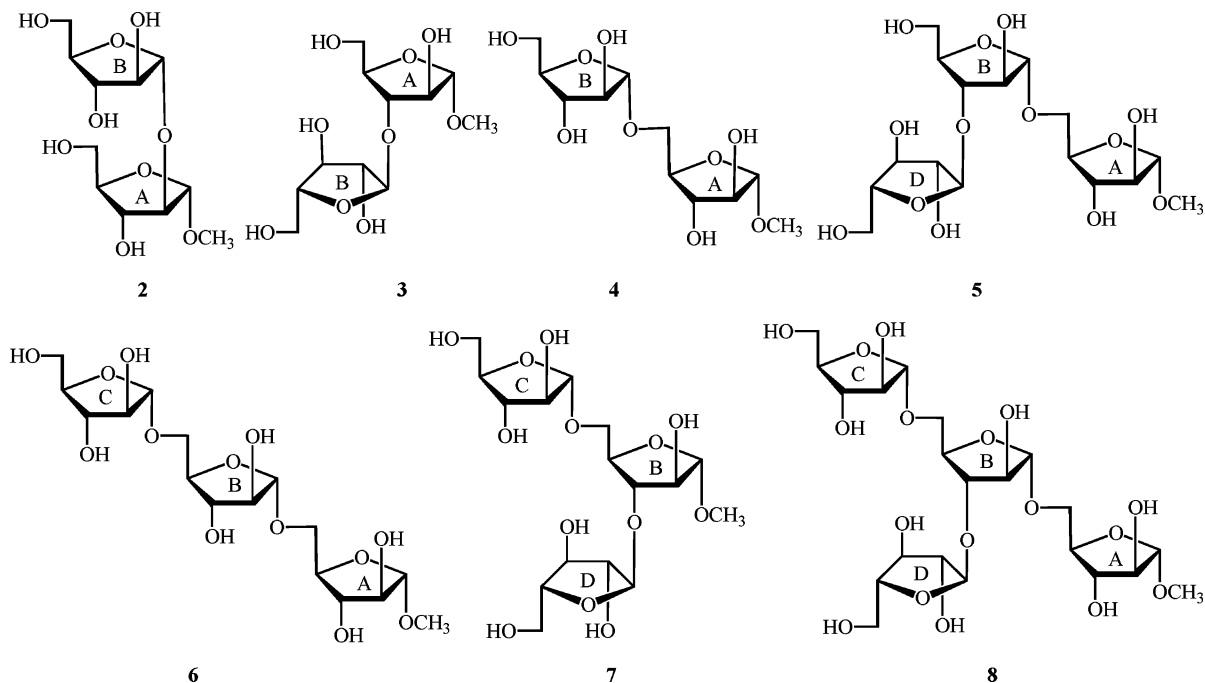
Figure 3. Oligoarabinofuranosides studied; rings have been lettered to facilitate comparison with **1**.

model approaches, e.g., PSEUROT analysis,[47] which assumes a two-state equilibrium for the five-membered ring.

The solution conformation of carbohydrates depends heavily on the interaction between the hydroxyl groups and solvent molecules.[48,49] Such interactions exhibit a strong electrostatic character (i.e., H-bonding) and thus requires a reliable set of atomic charges to properly model carbohydrates and to obtain acceptable simulation results compared to experiment.[50,51] Previously, we reported a procedure to obtain a set of atomic charges representative of the conformational equilibrium of **1**,[52] which has also been successfully applied to methyl β-D-arabinofuranoside.[53] This procedure reduced conformer-dependent charge variability, leading to better agreement between the C4−C5 bond rotamer distributions obtained from the MD simulations with those determined from NMR spectroscopic data.[54,55] In addition, these studies allowed us to gain insight into the ring conformation of **1** and its β anomer. However, here the agreement in the value of the pseudorotational phase angle, P, with experiment was less good. In particular for **1**, the MD simulations predicted a broad distribution of conformers centered around a single region of conformational space, whereas PSEUROT analysis of available $^3J_{H,H}$ data predicted an approximately 1:1 ratio of two conformers.

We describe here the use of probability distributions obtained from molecular dynamics simulations of **1** as the basis for calculating Boltzmann-averaged $^3J_{H,H}$ values using eq 1, which were then compared to those obtained experimentally. In one approach, we used an available generalized Karplus equation[56] (eq 3) for correlating each ring and exocyclic dihedral angle in all MD-derived conformers of **1** with $^3J_{H,H}$ values.

$$^3J_{HH} = 14.63 \cos^2 \phi - 0.78 \cos \phi + 0.60 +$$
$$\sum_i \lambda_i \{0.34 - 2.31 \cos^2[\xi_i\phi + 18.4|\lambda_i|]\} \quad (3)$$

In this equation, ϕ is the dihedral angle between the coupled protons, λ_i is the difference in electronegativities between a non-hydrogen substituent i and hydrogen, and ξ_i is equal to ± 1 depending on the relative orientation of substituents along the coupling path. A limitation of this approach is that the equation used for deriving these "Karplus relationships" was generated empirically by analyzing various substituted ethane fragments possessing a range of substituents with varying electronegativity. Thus, although this equation is generalizable, we questioned if better correlation of conformation and $^3J_{H,H}$ for **1** and larger oligomers could be obtained by using relationships more tailored to the α-arabinofuranose ring system. Hence, using density functional theory (DFT) calculations, we derived spin−spin coupling relationships for each ethanic fragment in **1**, which were then used in the calculation of $^3J_{H,H}$ values. Better agreement with experiment was indeed found using the DFT-derived equations. With this method in hand, we carried out MD simulations on a set of oligofuranosides (**2**−**8**, Figure 3) to determine the robustness of the method in these larger molecules.

Methods

Nomenclature. For clarity we will refer to the C4−C5 rotamers of each unit in the oligofuranosides as the rotamers of the corresponding ring, although they are not completely contained in these rings.

DFT $^3J_{H,H}$ Coupling Profiles. The accurate measurement of spin−spin coupling constants has aided in the structure determination of various molecules ranging from small organic molecules to large proteins.[57−63] The difficulty in calculating the spin−spin coupling tensor, which describes the interactions of nuclei through their interactions with the electrons of the molecule, arises from (1) the several mechanisms[64,65] that all contribute to the spin−spin coupling

Conformational Analysis of Arabinofuranosides

J. Chem. Theory Comput., Vol. 6, No. 1, 2010 **215**

tensor and therefore cannot be neglected a priori and (2) the involvement of not only singlet excitations (similar to those found in the expressions for shielding) but triplet excitations, which are nearly impossible to accurately calculate in the Hartree−Fock approximation. Therefore, a theoretical framework in which electron correlation is taken into consideration must be used for this purpose. For a detailed discussion of the calculation of spin−spin coupling constants and the implementation in quantum mechanical software packages, the reader is referred to reviews by Vaara et al.,[65] Autschbach and Le Guennic,[64] and Helgaker et al.[66,67,69]

DFT calculations of the spin−spin coupling constants were performed using the Gaussian 03 program[68] at the B3LYP/cc-pVTZ level of theory.[69,70] This level of theory was chosen on the basis of the results of $^3J_{H,H}$ calculations for ethane using several different functionals and basis sets (see Supporting Information). For these calculations, 10 envelope conformers of **1** were constructed; three C4−C5 rotamers and three C5−O5 rotamers were generated for each envelope, giving a total of 90 conformations. The geometries of all 90 conformations were then optimized at the B3LYP/6-31G* level of theory. A single endocyclic torsion angle (representing the four-atom plane of each envelope conformer) was fixed at 0° to maintain the envelope structure. For example, the E_O conformer was generated by fixing C1, C2, C3, and C4 in the plane. All other geometric parameters were allowed to vary during the geometry optimizations. In all cases, the preoptimized geometries were built to minimize intramolecular hydrogen bonds, i.e., the O−H bond of the C-3 hydroxyl group is oriented anti to C-4. This structural motif was maintained through all optimizations for the entire set of furanosides. For the spin−spin coupling calculations, all four contributions to the $^3J_{H,H}$ were computed, including Fermi contact (FC), spin dipolar (SD), paramagnetic spin−orbital (PSO), and diamagnetic spin−orbital (DSO). The resulting *J* data were extracted for all conformations (see Supporting Information for complete coupling constant data).

For a picture of the structural dependencies of $^3J_{H,H}$ on their respective H,H torsion angles, the Marquardt−Levenberg nonlinear least-squares algorithm[71] was used to fit the acquired coupling constants to a truncated Fourier series in the H,H dihedral angle (ϕ) (eq 4)[72]

$$^3J_{HH} = a + b\cos(\phi) + c\cos(2\phi) \qquad (4)$$

The coefficients *a*, *b*, and *c* can be determined from the fitting of the DFT data, and five equations can be obtained corresponding to the five three-bond H,H coupling pathways in the molecule (H1−C1−C2−H2, H2−C2−C3−H3, H3−C3−C4−H4, H4−C4−C5−H5*R*, H4−C4−C5−H5*S*).

Molecular Dynamics (MD) Simulations. All MD simulations were performed with the SANDER module of the AMBER 9.0 suite of programs[73] using the parm99 force field together with the GLYCAM (version 04f) parameters for carbohydrates.[74,75] The topology of the oligofuranosides was built by using the additivity principle[76,77] to the set of atomic charges obtained for monosaccharide **1**, which were determined, as previously reported,[52] to account for the flexibility of the ring. The starting geometries were also constructed

from multiple units of **1** using the Leap module in AMBER. The simulations were carried out in water and under NPT conditions coupled to an external temperature bath[78] at 300 K and to a pressure bath at 1 atm to be consistent with the NMR data available. Each oligofuranoside was put in a theoretical box of approximate dimensions of 30 Å × 30 Å × 30 Å filled with TIP3P[79] water. We used periodic boundary conditions and the SHAKE[80] algorithm to fix all hydrogen-containing bonds to their equilibrium value. A dielectric constant of unity was used and a cutoff of 8 Å was set for nonbonded (short- and long-range) interactions. The particle mesh Ewald algorithm was used for treatment of long-range electrostatics.[81,82]

The simulations were started by first minimizing the energy of the water molecules with the geometry of the sugar molecules constrained. This was followed by a total energy minimization. Fifty cycles of steepest decent energy minimization followed by 950 cycles of conjugate gradient were applied to these first two steps. An annealing run of 100 ps was further applied followed by a short equilibration MD run of 150 ps. After this short MD run, production dynamics were performed up to 240 ns keeping the same temperature and pressure of 300 K and 1 atm, respectively.

In our earlier work,[52,53] simulation times of over 200 ns were required to obtain accurate rotamer distributions. Moreover, the convergence of the gt:tg:gg populations as a function of simulation time was used to establish this >200 ns criterion used in the present research. Shorter simulations will result in errors of several units of percentage on the rotamer populations. New methodologies will be required in order to analyze larger oligomers to avoid prohibitive simulation times.

Calculation of $^3J_{H,H}$ Values from Conformational Ensembles Obtained from MD Simulations. For an accurate comparison of the DFT/MD-derived $^3J_{H,H}$ values to experiment, ensemble averaging must be carried out. This was done by calculating $^3J_{H,H}$ values for each relevant bond in compounds **1−8** using the DFT-determined equations and the generalized Karplus equation previously developed by Altona and co-workers (eq 3).[56] These $^3J_{H,H}$ values were then ensemble-averaged using eq 1.

Results and Discussion

Spin−Spin Coupling Profiles. The spin−spin coupling constant data were plotted as a function of the respective H,H torsion angles and fitted to eq 4 (Figures 4 and 5). Each curve resulted in an equation, which correlates the $^3J_{H,H}$ magnitude with each dihedral angle (eqs 5−9). The coupling profiles for the ring protons (Figure 4 and eqs 5−7) show reasonably well fitted curves, although it is apparent that the curves are not well parametrized at torsion angles near 0° (±90°). It should be appreciated, however, that these equations are well-defined *only* over the area of rotational space that is possible given the constraints of this ring system. In addition, in all of the dihedral angle distributions generated from the MD conformer ensemble, no conformers that adopt these configurations are visited (see Supporting Information). For angles that cannot be obtained while the ring structure
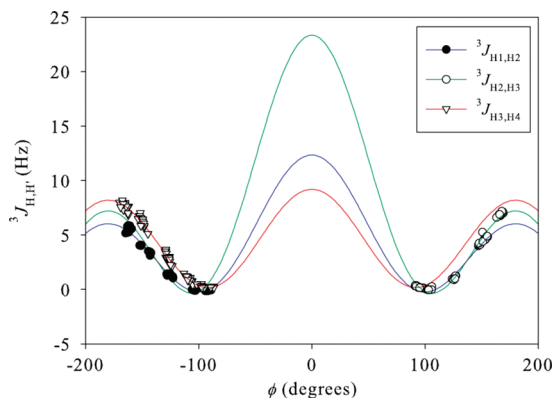
Figure 4. $^3J_{H,H}$ coupling profiles for the ring protons of methyl α-D-arabinofuranoside. All fits resulted in an R^2 value of 0.99.
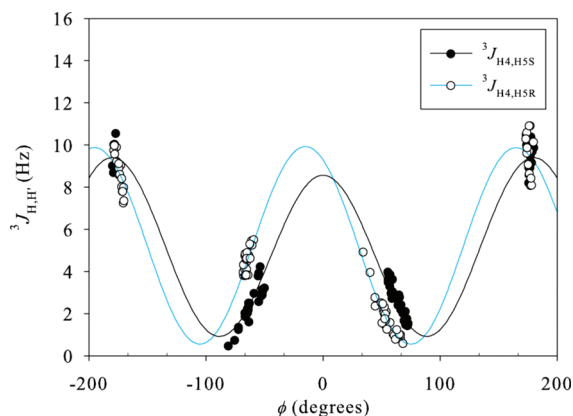

Figure 5. $^3J_{H,H}$ coupling profiles along the C4−C5 bond of methyl α-D-arabinofuranoside. ϕ is the H4−C4−C5−H5(R/S) dihedral angle.

is maintained (e.g., H2−C2−C3−H3 = 0°), use of a particular equation will give unrealistic values for the corresponding $^3J_{H,H}$ (i.e., $J > 20$ Hz).

$$^3J_{1,2} = 4.62 + 3.16 \cos(\phi) + 4.57 \cos(2\phi) \quad (5)$$

$$^3J_{2,3} = 8.04 + 8.07 \cos(\phi) + 7.24 \cos(2\phi) \quad (6)$$

$$^3J_{3,4} = 4.44 + 0.50 \cos(\phi) + 4.25 \cos(2\phi) \quad (7)$$

The coupling profiles along the C4−C5 bond (Figure 5 and eqs 8 and 9) also illustrate well-fitted ($R^2 = 0.97$) and well-defined Karplus-type relationships. Of particular note, the $^3J_{H4,H5R}$ curve is shifted by ca. 15° from the $^3J_{H4,H5S}$ curve. As a result, a phase factor has been added to eq 9 to obtain a better fit to the DFT data.

$$^3J_{4,5S} = 4.95 - 0.42 \cos(\phi) + 4.03 \cos(2\phi) \quad (8)$$

$$^3J_{4,5R} = 5.23 + 0.02 \cos(\phi + 15.1°) + 4.67 \cos(2\phi + 30.2°) \quad (9)$$

The dependence of the $^3J_{H,H}$ values on the rotation of the C5−O5 bond was also investigated. Some variation in the J values as a function of H5−O5−C5−C4 angle was observed, and this analysis is presented in the Supporting Information.

Comparison of DFT/MD-Derived and Experimental $^3J_{H,H}$ Values for 1. With the empirical and DFT-derived relationships (eqs 3 and 5−9, respectively) in hand, and with

Table 1. Comparison of Experimental and Theoretical ⟨$^3J_{H,H}$⟩ Values (in Hz) for **1**[a]

coupling	exp	EK[b]	DK[b]
⟨$^3J_{H1,H2}$⟩	1.7	2.8	2.4
⟨$^3J_{H2,H3}$⟩	3.4	5.2	3.8
⟨$^3J_{H3,H4}$⟩	5.8	8.5	5.8
⟨$^3J_{H4,H5R}$⟩	5.8	4.2	4.2
⟨$^3J_{H4,H5S}$⟩	3.3	1.4	3.2

[a] Exp = experimental, EK = empirical Karplus equation, DK = DFT-derived equations. [b] MD simulations led to a conformational distribution largely located in the northeast region of the pseudorotational itinerary (centered around $P \approx 45°$) and a C4−C5 rotamer distribution of approximately 37% gt, 7% tg, and 56% gg.

the use of eq 1, we calculated averaged $^3J_{H,H}$ values using the distribution of conformers we had previously obtained from an MD simulation of **1**.[52] This investigation had identified a single conformer family located in the northeastern portion of the pseudorotational itinerary (Figure 1). Presented in Table 1 is a comparison of these calculated $^3J_{H,H}$ values for **1** with those measured by NMR spectroscopy. Analysis of these data reveals that the DFT-derived eqs 5−9 yield results that are in better agreement with experimental $^3J_{H,H}$ than those calculated using the empirical relationship (eq 3). Indeed, this is observed for all coupling constants, with the exception of $^3J_{H4,H5R}$. The calculated ring couplings ($^3J_{H1,H2}$, $^3J_{H2,H3}$, and $^3J_{H3,H4}$) show the same trend as experiment, with a near perfect agreement observed for $^3J_{H3,H4}$. The calculated $^3J_{H1,H2}$ is slightly larger than the experimental value, which could be attributed to small errors in the conformer distributions obtained from the MD simulations.

There is good agreement with the DFT/MD-determined $^3J_{H4,H5S}$ value; however, for $^3J_{H4,H5R}$ significant deviations from experiment are observed. Again, a possible explanation for this discrepancy stems from small differences in the MD-predicted hydroxymethyl rotamer populations and those found in solution. The simulations overestimate the gg rotamer population (56%) compared to experiment (48%) and underestimate the gt rotamer population (37% compared to 45%). In the gt rotamer, H4 and H5R are trans to each other and hence the $^3J_{H,H}$ for this rotamer is large. This coupling is therefore the largest contributor to the average $^3J_{H,H}$, and if the population is underestimated in the MD simulations, then the calculated average coupling would be smaller than the experimental value. Better agreement with the experimental $^3J_{H4,H5R}$ values would be obtained if, in the MD simulation, the population of the gt rotamer is increased and the population of the gg rotamer is decreased. In contrast, the $^3J_{H4,H5S}$ values would remain less affected, as the $^3J_{H4,H5S}$ value is rather insensitive to the relative populations of the gt and gg rotamers (the largest coupling between H4 and H5S is present in the tg rotamer). More information can be found in the Supporting Information. It should be appreciated, however, that differences as low as 0.2 kcal/mol in the relative energies of two rotamers can lead to significantly different rotamer populations. Therefore, differences in energies between MD and solution would need to be less than 0.2 kcal/mol to obtain better agreement.

It is not surprising that the use of the DFT-derived relationships yields better results than the generalized equa-

Conformational Analysis of Arabinofuranosides

J. Chem. Theory Comput., Vol. 6, No. 1, 2010 **217**
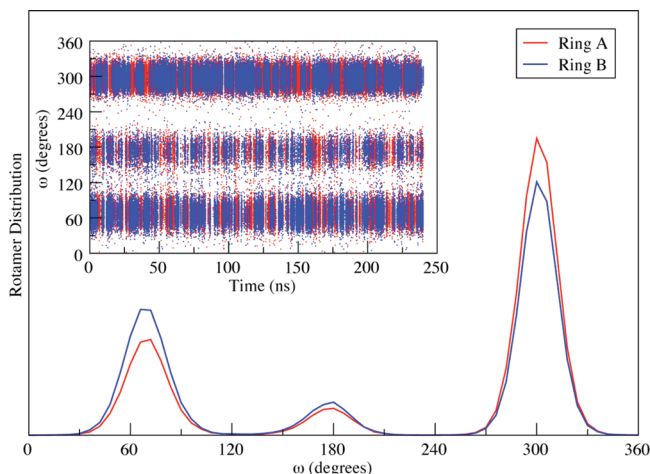
Figure 6. Time dependence of the ω angle (insets) and the resulting histograms obtained from the simulation of **2** for ring A (red) and ring B (blue).

tion. Nevertheless, the difference between the two is striking, with the $^3J_{H,H}$ values differing by an average 1.3 Hz (over a range of 0.4−2.6 Hz). An important implication of this finding is that the results of many previous conformational analyses of α-arabinofuranose rings,[31,83−85] which relied upon the use of generalized relationships such as eq 3, should now be re-evaluated. These previous studies also involved the analysis of $^3J_{H,H}$ by PSEUROT,[47] in which a two-state conformational model is assumed. The results in Table 1 and our previous MD simulations on **1**[52] suggest that the two-state model is not applicable for the α-arabinofuranose ring. Hence, the use of the PSEUROT approach in probing the conformation of these ring systems appears to be of questionable utility. Instead, an alternative approach would be to carry out an AMBER/GLYCAM MD simulation of the α-arabinofuranoside of interest and subsequently use the resulting conformer ensemble to calculate $^3J_{H,H}$ values that can be directly compared with those from experiment (see below). Moreover, use of the dihedral angle distributions from the MD simulations with the DFT-determined equations leads to significantly better agreement than the use of idealized geometrical parameters (e.g., H1−C1−C2−H2 = 180°; see Supporting Information), thus demonstrating that the DFT-determined equations must be used in conjunction with the MD conformer ensemble to reasonably predict the $^3J_{H,H}$ values.

Conformational Analysis of Larger α-Arabinofuranoside Oligomers (2−8). Having had success in applying this approach to monosaccharide **1**, we next turned our attention to larger oligosaccharides containing α-arabinofuranoside residues (**2−8**), the conformations of which we have previously investigated.[55] To begin, we carried out MD simulations on disaccharides **2−4**, which are the three possible isomeric methyl α-D-arabinofuranosyl-α-D-arabinofuranosides.

Rotamer Populations in 2−4. MD simulations of **2−4** required 240 ns for the rotamer populations to achieve convergence to reasonable uncertainties (errors in populations of 3% or less), a simulation time similar to that reported previously for **1**.[52] Figures 6−8 show the time dependence
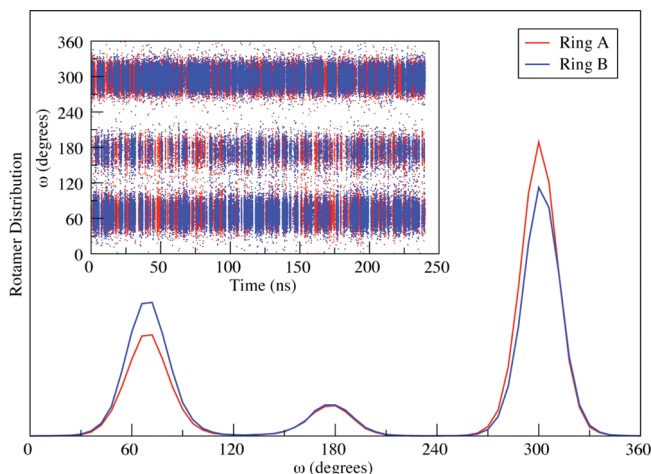
Figure 7. Time dependence of the ω angle (insets) and the resulting histograms obtained from the simulation of **3** for ring A (red) and ring B (blue).
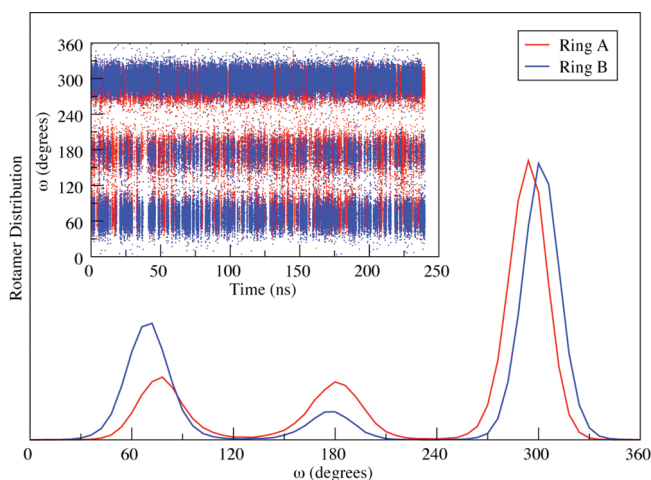
Figure 8. Time dependence of the ω angle (insets) and the resulting histograms obtained from the simulation of **4** for ring A (red) and ring B (blue).

Table 2. MD-Derived Rotamer Populations for Rings A and B of **2−4**[a]

	1	**2**		**3**		**4**	
		A	B	A	B	A	B
X_{gt}	37 (3)	25 (2)	34 (2)	27 (2)	35 (2)	17 (2)	30 (2)
X_{tg}	7 (1)	8 (1)	9 (1)	8 (1)	9 (1)	18 (2)	8 (1)
X_{gg}	56 (3)	67 (3)	57 (3)	65 (3)	56 (3)	65 (3)	62 (3)

[a] Standard errors were calculated according to Allen and Tildesley[88] and are reported in parentheses.

of the ω angle for both rings in each of **2−4**, as well as the resulting histograms. Table 2 summarizes the rotamer populations about the C4−C5 bond in each ring for the three disaccharides.

The results presented in Figures 6−8 and Table 2 demonstrate that the simulations yield three well-defined rotamers for the C4−C5 bond of each ring in disaccharides **2−4**. In the α-(1→2) and α-(1→3)-linked disaccharides, **2** and **3**, respectively, the rotamer populations of both rings exhibit the same trend, namely $X_{gg} > X_{gt} > X_{tg}$, which is in agreement with the results obtained for **1**,[52] as well as experiment.[54,55] However, different results are observed for

Table 3. $^3J_{H4,H5R}$ and $^3J_{H4,H5S}$ (in Hz) for Each Ring in **2**−**4** Obtained from Experiment and from MD Simulation Conformer Populations[a]

		ring A			ring B		
		Exp	EK	DK	Exp	EK	DK
2	R	5.8	2.4	3.4	5.8	3.8	4.0
	S	3.1	1.6	3.3	3.3	1.7	3.3
3	R	5.8	2.8	3.6	5.8	4.0	4.1
	S	3.4	1.6	3.3	3.4	1.7	3.3
4	R	5.5	2.6	3.5	5.5	3.2	3.7
	S	3.4	2.0	3.5	3.4	1.6	3.3

[a] $R = {}^3J_{H4,H5R}$, $S = {}^3J_{H4,H5S}$, Exp = experimental, EK = extended Karplus equation, DK = DFT-derived equation.

the α-(1→5)-linked disaccharide **4**. The rotamer populations of ring B follow the trend observed for the rings in **1**−**3** ($X_{gg} > X_{gt} > X_{tg}$) but those of ring A follow the trend $X_{gg} > X_{tg} \approx X_{gt}$. The results of the simulations in ring A of **4** thus differ from experimental data, which has shown that the C4−C5 bonds in both rings in **4** have similar rotameric distributions.[54] On the basis of these results and those obtained from **1**, it is clear that for "terminal" C4−C5 bonds (all those in **1**−**3** and ring B in **4**) the simulations provide rotamer populations similar to each other and also to experiment. However for "internal" C4−C5 bonds, as for ring A in **4**, poorer agreement with experiment is seen; although the gg rotamer is still the most populated, the tg rotamer is enhanced at the expense of the gt rotamer.

Shown in Table 3 are the $^3J_{H4,H5R}$ and $^3J_{H4,H5S}$ coupling constants measured by NMR spectroscopy,[26,27] as well as those calculated from the conformer ensemble obtained from the simulations by application of the empirical Karplus equation and the DFT-determined equations. These data demonstrate that agreement between the calculated $^3J_{H4,H5R}$ and $^3J_{H4,H5S}$ values and the experimental ones improves significantly by using the DFT-derived equations as opposed to the generalized relationship. In particular, the DFT-derived equation for $^3J_{H4,H5S}$ reproduces the experimental value essentially identically for all three molecules. With regard to $^3J_{H4,H5R}$, the calculated values are all significantly smaller than those obtained from experiment, which is consistent with the monosaccharide **1**, but again better agreement is observed using the DFT-derived equations. Again, this discrepancy may be due to the MD-predicted hydroxymethyl group conformation.

Rotamer Populations in 5−8. We next examined the C4−C5 rotamer populations in four larger oligosaccharides (**5**−**8**, Figure 3); results analogous to those seen in **2**−**4** were observed. Rotamers about C4−C5 bonds involved in an α-(1→5) linkage (rings A and B) exhibit similar dependencies of the ω angle and histograms to that of ring A in disaccharide **4**. In contrast, for terminal C4−C5 bonds (rings C or D), populations similar to those of both rings of disaccharides **2** and **3** and ring B of **4** are obtained (Table 4).

As would be expected from the similarity between the C4−C5 rotamer populations in **5**−**8** with those in **2**−**4**, the trends observed in the $^3J_{H4,H5R}$ and $^3J_{H4,H5S}$ magnitudes are analogous to those described above (Table 5). That is, the use of the DFT-derived equation significantly underestimates

Table 4. MD-Derived Rotamer Populations for the Rings A, B, C, and D of **5**−**8**[a]

		ring A	ring B	ring C	ring D
5	X_{gt}	14 (2)	24 (2)		30 (2)
	X_{tg}	15 (2)	7 (1)		8 (1)
	X_{gg}	71 (3)	69 (3)		62 (3)
6	X_{gt}	14 (2)	13 (2)	32 (2)	
	X_{tg}	16 (2)	15 (2)	8 (1)	
	X_{gg}	70 (3)	72 (3)	60 (3)	
7	X_{gt}		9 (1)	31 (2)	31 (2)
	X_{tg}		22 (2)	9 (1)	8 (1)
	X_{gg}		69 (3)	60 (3)	61 (3)
8	X_{gt}	17 (2)	11 (1)	28 (2)	34 (2)
	X_{tg}	18 (2)	22 (2)	7 (1)	10 (1)
	X_{gg}	65 (3)	67 (3)	65 (3)	56 (3)

[a] Standard errors were calculated according to Allen and Tildesley 86 and are reported in parentheses.

the $^3J_{H4,H5R}$ magnitude while accurately predicting the value for $^3J_{H4,H5S}$. Similar to the results for **2**−**4**, use of the empirical Karplus equation for the coupling pathways in **5**−**8** leads to the correct trend, however, the magnitudes agree very poorly with experiment, and particularly poor agreement is observed for ring B of **7** and **8**, which is glycosylated at both O5 and O3. In both molecules, the calculated C4−C5 rotamer populations are inverted relative to experiment, regardless of whether the DFT-derived or empirically derived curves are used to calculate the $^3J_{H,H}$. Consistent with the results for **1**-**4**, when the DFT-derived relationships (eqs 5−9) are used, the $^3J_{H4,H5S}$ values obtained for the C4−C5 bonds in **5**−**8** agreed well with experiment (in all cases within 0.4 Hz).

Distribution of Ring Conformers. Having investigated the C4−C5 rotamer populations in **1**−**8**, we turned our attention to the ring conformations in the oligomers and the related coupling constants, $^3J_{H1,H2}$, $^3J_{H2,H3}$, and $^3J_{H3,H4}$. Thus, the same analysis carried out for $^3J_{H4,H5R}$ and $^3J_{H4,H5S}$ was performed for the $^3J_{H,H}$ in each furanose residue of oligosaccharides **2**−**8**. As mentioned previously, direct comparison between experimental $^3J_{H,H}$ and those calculated by application of the various coupling relationships to the conformer ensemble obtained from the MD simulation will eliminate errors associated with the two-state model inherent in the PSEUROT[47] approach. Table 6 lists the $^3J_{H1,H2}$, $^3J_{H2,H3}$, and $^3J_{H3,H4}$ determined from NMR spectroscopy,[54] as well as those calculated from the simulations of oligofuranosides **2**−**8**. For the sake of comparison, the data for **1** are included again in Table 6.

Use of either the generalized Karplus equation or the DFT-derived relationships led to the same trend as experiment ($^3J_{H3,H4} > {}^3J_{H2,H3} > {}^3J_{H1,H2}$) in all the compounds. As was demonstrated for **1**, use of the DFT-derived equations lead to $^3J_{H,H}$ magnitudes that agree with experiment better than the use of the empirical relationship,[56] which uniformly overestimates the magnitudes. It should be noted that both equations yield the lowest magnitudes of $^3J_{H1,H2}$, $^3J_{H2,H3}$, and $^3J_{H3,H4}$ for rings substituted at C3, which is also observed experimentally. Taken together, these results suggest that these AMBER/GLYCAM MD simulations provide an accurate distribution of ring conformers and that the discrepancies with the absolute $^3J_{H,H}$ values stem from differences

Conformational Analysis of Arabinofuranosides

J. Chem. Theory Comput., Vol. 6, No. 1, 2010 **219**

Table 5. $^3J_{H4,H5R}$ and $^3J_{H4,H5S}$ (in Hz) for Each Ring in **5**–**8** Obtained from Experiment and from MD Simulation Conformer Populations[a]

		ring A			ring B			ring C			ring D		
		Exp	EK	DK	Exp	EK	DK	Exp	EK	DK	Exp	EK	DK
5	R	5.4	2.1	3.2	5.8	2.4	3.4				5.9	3.2	3.8
	S	3.1	1.5	3.3	3.2	1.5	3.3				3.1	1.6	3.3
6	R	5.9	2.2	3.3	5.7	2.0	3.2	5.8	3.5	3.9			
	S	3.2	1.8	3.4	3.2	1.7	3.3	3.3	1.7	3.3			
7	R				5.3	1.9	3.3	5.9	3.4	3.9	6.0	3.3	3.8
	S				3.0	2.4	3.7	3.4	1.7	3.4	3.3	1.6	3.3
8	R	5.4	2.5	3.5	5.4	2.2	3.4	5.7	2.9	3.6	5.7	3.9	4.1
	S	3.1	2.1	3.5	3.0	2.4	3.7	3.2	1.6	3.2	3.2	1.8	3.4

[a] $R = {}^3J_{H4,H5R}$, $S = {}^3J_{H4,H5S}$, Exp = experimental, EK = extended Karplus equation, DK = DFT-derived equations.

Table 6. Vicinal Coupling Constants (in Hz) for the Ring Protons for Each Ring in **1**–**8** Obtained from Experiment and from MD Simulation Conformer Populations[a]

		ring A[b]			ring B[b]			ring C[b]			ring D[b]		
		Exp	EK	DK	Exp	EK	DK	Exp	EK	DK	Exp	EK	DK
1	$^3J_{H1,H2}$	1.7	2.8	2.4									
	$^3J_{H2,H3}$	3.4	5.2	3.8									
	$^3J_{H3,H4}$	5.8	8.5	5.8									
2	$^3J_{H1,H2}$	1.6	0.9	1.7	1.6	1.7	2.0						
	$^3J_{H2,H3}$	3.5	3.6	3.0	3.4	4.4	3.5						
	$^3J_{H3,H4}$	6.3	7.5	5.3	6.1	8.2	5.6						
3	$^3J_{H1,H2}$	1.3	0.7	1.8	1.6	1.7	2.0						
	$^3J_{H2,H3}$	2.2	2.9	2.7	3.4	4.4	3.5						
	$^3J_{H3,H4}$	5.5	6.8	4.9	6.2	8.2	5.6						
4	$^3J_{H1,H2}$	1.6	2.4	2.2	1.6	2.5	2.3						
	$^3J_{H2,H3}$	3.1	4.6	3.6	3.1	4.9	3.7						
	$^3J_{H3,H4}$	5.8	8.0	5.5	6.1	8.3	5.7						
5	$^3J_{H1,H2}$	1.7	2.4	2.2	1.2	0.2	1.6				1.6	1.8	2.1
	$^3J_{H2,H3}$	3.4	4.4	3.5	2.2	2.5	2.6				3.4	4.5	3.5
	$^3J_{H3,H4}$	5.4	7.8	5.5	5.8	6.6	4.8				6.2	8.3	5.7
6	$^3J_{H1,H2}$	1.7	2.4	2.3	1.6	2.1	2.2	1.6	2.3	2.2			
	$^3J_{H2,H3}$	3.2	4.5	3.5	3.2	4.3	3.4	3.3	4.8	3.7			
	$^3J_{H3,H4}$	5.9	7.9	5.5	6.0	7.8	5.5	5.9	8.4	5.7			
7	$^3J_{H1,H2}$				1.1	0.5	1.7	1.6	2.0	2.1	1.6	1.8	2.1
	$^3J_{H2,H3}$				2.1	2.8	2.7	3.3	4.6	3.6	3.4	4.5	3.5
	$^3J_{H3,H4}$				5.3	7.0	5.0	5.9	8.4	5.7	6.0	8.3	5.7
8	$^3J_{H1,H2}$	1.8	2.3	2.2	1.2	0.1	1.6	1.6	2.3	2.2	1.6	1.6	2.0
	$^3J_{H2,H3}$	3.4	4.4	3.5	2.0	2.6	2.6	3.3	4.8	3.6	3.3	4.4	3.5
	$^3J_{H3,H4}$	5.9	7.8	5.5	5.5	7.0	5.0	5.8	8.5	5.8	6.0	8.2	5.6

[a] Exp = experimental, EK = extended Karplus equation, DK = DFT-derived equations. [b] See Figure 3 for definition of ring labels.

between the spin–spin coupling profiles derived for **1** and those that could be calculated, for larger, more complicated systems such as **2**–**8**.

We also evaluated the distribution of P for all of the rings in these compounds. Similar to what we observed for **1**,[52] unsubstituted rings, or those glycosylated at O2 and O5, display conformational distributions with a single conformer family, located in the northern hemisphere between −60° and 90° (Figure 9, left panel, and Supporting Information). In contrast, for rings substituted at O3 such as ring B of **3**, **5**, **7**, and **8** the distributions of the P display a second populated area of conformational space in the southern hemisphere, which is centered about P = 120° (Figure 9, right panel). Thus, attaching another sugar to the ring influences the ring conformation only when this group is attached at O3, not at O2 or O5. This corresponds well to the results obtained by the analysis of $^3J_{H,H}$.

Conclusions

We report here the combined use of AMBER/GLCYAM MD simulations and calculation of $^3J_{H,H}$ ($^3J_{H1,H2}$, $^3J_{H2,H3}$, $^3J_{H3,H4}$, $^3J_{H4,H5R}$, and $^3J_{H4,H5S}$) from the resulting conformer distribution to probe the conformation of a group of oligosaccharides consisting of one to four α-arabinofuranosyl residues (**1**–**8**). This approach allows for the direct comparison of vicinal coupling constants obtained from NMR spectroscopy and conformer populations from MD simulations, thereby circumventing possible sources of errors introduced by the model used to analyze NMR data (e.g., the two-state model inherent in PSEUROT[47] or the "discrete" model[45]).

The coupling constant values calculated from either the DFT-derived $^3J_{H,H}$ relationships or the empirically derived Karplus equation showed, for nearly all cases, the same trend as experiment. These results lend credence to the ability of AMBER/GLYCAM to provide accurate conformer distributions of oligosaccharides containing α-arabinofuranoside rings. Not surprisingly, the DFT-derived equations obtained for **1** lead to significantly better agreement between experiment and theory, compared to the use of an empirical Karplus equation. Indeed, for many of the $^3J_{H,H}$ nearly identical agreement between the calculated values and those obtained from experiment is observed.
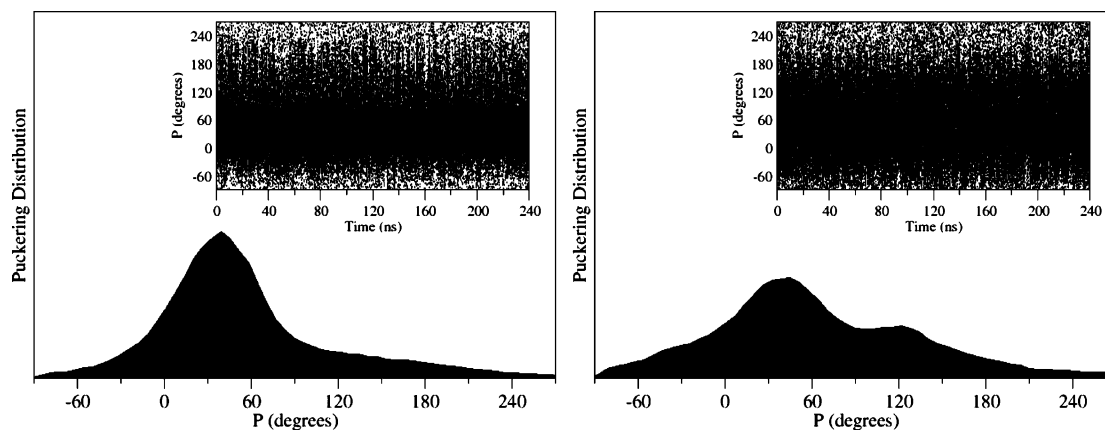
Figure 9. Time dependence of the *P* angle (insets) and the resulting histograms obtained by the simulation of disaccharide **3** ring A (right) and ring B (left).

As determined in earlier studies with monosaccharide **1**,[52] long simulation times (240 ns) are required to achieve convergence. The simulations yield three well-defined rotamers for each ring of the oligofuranosides **2**−**8**. In the particular cases of terminal rotamers, their populations exhibit the trend $X_{gg} > X_{gt} > X_{tg}$. However, internal rotamers, which are defined as those involved in an α-(1→5) linkage, follow a different trend, namely, $X_{gg} > X_{tg} = X_{gt}$; the results for these internal linkages do not agree with experimental data. In the search for the origin of this discrepancy, we evaluated the efficiency of the TIP3P model to represent the water−carbohydrate interactions in **2**−**8** by performing the same simulations using the TIP4P water model (data not shown). The use of this more sophisticated water model led to the same outcome as TIP3P, thus suggesting the difference with experiment is not related to the choice of water model. We postulate that the use of coupling relationships more tailored to these substituted linkages may lead to better agreement between the rotamer populations obtained from the simulations and those determined experimentally.

Another point of poor agreement is the $^3J_{H4,H5R}$ magnitudes in **2**−**8**, for which the calculated values are significantly smaller than those measured by NMR spectroscopy. In attempting to determine the origin of this discrepancy, we considered that it may result from the effect of C5−O5 bond rotation on the magnitude of this $^3J_{H,H}$. However, when this was investigated (see Supporting Information), we found that rotation about this bond has only a minor effect on the coupling across the C4−C5 bond, which is consistent with earlier work by Serianni and co-workers on computed $^3J_{H,H}$ values in hydroxymethyl groups in pyranosides.[39] Currently, investigations are ongoing to elucidate the lack of agreement between the computed and experimental values for $^3J_{H4,H5R}$. A possible alternative approach for the prediction of these couplings would be to sample the MD trajectories for a small set of representative conformers and to perform the DFT coupling calculations directly on these structures. This approach will avoid any possible errors that may be introduced in the fitting of the DFT data to obtain the coupling profiles. Moreover, the possibility that the MD simulations may not accurately predict the C4−C5 rotamer distributions may be a source of the discrepancy in the $^3J_{H4,H5R}$ values. For a more complete determination of the

solution conformation of the hydroxymethyl groups in **2**−**8**, measurements of $^2J_{C,H}$, $^3J_{C,H}$, and $^4J_{C,H}$ would provide additional insights. Similar studies have been conducted by Serianni and co-workers, where various coupling constants in ^{13}C-labeled carbohydrates were used to probe conformation.[38−41,86,87] Analogous studies on **1** are currently ongoing.

With regard to ring puckering, the simulations yield *P* distributions for the rings of oligofuranosides **2**−**8** that are essentially identical to those previously determined for the monomer, methyl α-D-arabinofuranoside **1**.[52] The conformers are distributed in the northern hemisphere and thus in a single region of the pseudorotational itinerary. These results confirm our earlier work on **1**, which suggested that the two-state conformational model for assessing ring conformation using PSEUROT is not valid for α-arabinofuranoside rings. On the basis of the simulations carried out here, a notable exception is for rings glycosylated at O3 (for ring B of **3** and **6**−**8**), where a second area of conformational space, centered in the southern hemisphere around $P = 120°$, is populated. The two-state model therefore appears to be valid for these substituted rings.

Supporting Information Available: Details on the determination of the spin−spin coupling profiles; analysis of different basis sets and functionals; table of all calculated $^3J_{H,H}$ values; details on the C5−O5 dependence of $^3J_{4,5R}$ and $^3J_{4,5S}$; distributions of H−H dihedral angles, C4−C5 rotamers, and ring pucker obtained from the MD simulations; details of MD/DFT coupling constant calculations; and elaboration on the discrepancies in $^3J_{H4,H5R}$ values. This information is available free of charge via the Internet at http://pubs.acs.org.

Conformational Analysis of Arabinofuranosides

J. Chem. Theory Comput., Vol. 6, No. 1, 2010 **221**

References

(1) Dwek, R. A. *Chem. Rev.* **1996**, *96*, 683–720.

(2) Rojo, J.; Morales, J. C.; Penades, S. *Top. Curr. Chem.* **2002**, *218*, 45–92.

(3) Koeller, K. M.; Wong, C. H. *Nat. Biotechnol.* **2000**, *18*, 835–841.

(4) Dwek, R. A.; Butters, T. D. *Chem. Rev.* **2002**, *102*, 283–284.

(5) Meyer, B.; Moller, H. *Top. Curr. Chem.* **2007**, *267*, 187–251.

(6) Wormald, M. R.; Petrescu, A. J.; Pao, Y. L.; Glithero, A.; Dwek, R. A. *Chem. Rev.* **2002**, *102*, 371–386.

(7) Wang, W.; Donini, O.; Reyes, C. M.; Kollman, P. A. *Annu. Rev. Biophys. Biomol. Struct.* **2001**, *30*, 211–243.

(8) Adcock, S. A.; McCammon, J. A. *Chem. Rev.* **2006**, *106*, 1589–1615.

(9) MacKerell, A. D., Jr.; Bashford, D.; Bellott, M.; Dunbrack, R. L., Jr.; Evanseck, J. D.; Field, M. J.; Fischer, S.; Gao, J.; Guo, H.; Ha, S.; Joseph-McCarthy, D.; Kuchnir, L.; Kuczera, K.; Lau, F. T. K.; Mattos, C.; Michnick, S.; Ngo, T.; Nguyen, D. T.; Prodhom, B.; Reiher, W. E., III; Roux, B.; Schlenkrich, M.; Smith, J. C.; Stote, R.; Straub, J.; Watanabe, M.; Wiorkiewicz-Kuczera, J.; Yin, D.; Karplus, M. *J. Phys. Chem. B* **1998**, *102*, 3586–3616.

(10) Oostenbrink, C.; Villa, A.; Mark, A. E.; Van Gunsteren, W. F. *J. Comput. Chem.* **2004**, *25*, 1656–1676.

(11) Jakalian, A.; Bush, B. L.; Jack, D. B.; Bayly, C. I. *J. Comput. Chem.* **2000**, *21*, 132–146.

(12) Jakalian, A.; Bush, B. L.; Jack, D. B.; Bayly, C. I. *J. Comput. Chem.* **2002**, *23*, 1623–1641.

(13) Almond, A.; Petersen, B. O.; Duus, J. *Biochemistry* **2004**, *43*, 5853–5863.

(14) Brisson, J.-R.; Uhrinova, S.; Woods, R. J.; Van der Zwan, M.; Jarrell, H. C.; Paoletti, L. C.; Kasper, D. L.; Jennings, H. J. *Biochemistry* **1997**, *36*, 3278–3292.

(15) Corzana, F.; Motawia, M. S.; Du Penhoat, C. H.; Perez, S.; Tschampel, S. M.; Woods, R. J.; Engelsen, S. B. *J. Comput. Chem.* **2004**, *25*, 573–586.

(16) Gonzalez-Outeirino, J.; Kadirvelraj, R.; Woods, R. J. *Carbohydr. Res.* **2005**, *340*, 1007–1018.

(17) Woods, R. J. *Glycoconjugate J.* **1998**, *15*, 209–216.

(18) Engelsen, S. B.; Cros, S.; Mackie, W.; Perez, S. *Biopolymers* **1996**, *39*, 417–433.

(19) Xia, J.; Daly, R. P.; Chuang, F.; Parker, L.; Jensen, J. H.; Margulis, C. J. *J. Chem. Theory Comput.* **2007**, *3*, 1620–1628.

(20) Xia, J.; Daly, R. P.; Chuang, F.; Parker, L.; Jensen, J. H.; Margulis, C. J. *J. Chem. Theory Comput.* **2007**, *3*, 1629–1643.

(21) Cros, S.; Hervé du Penhoat, C.; Pérez, S.; Imberty, A. *Carbohydr. Res.* **1993**, *248*, 81–93.

(22) French, A. D.; Mouhous-Riou, N.; Pérez, S. *Carbohydr. Res.* **1993**, *247*, 51–62.

(23) Hervé du Penhoat, C.; Engelsen, S. B.; Plusquellec, D.; Pérez, S. *Carbohydr. Res.* **1997**, *305*, 131–145.

(24) Mazeau, K.; Pérez, S. *Carbohydr. Res.* **1998**, *311*, 203–217.

(25) French, A. D.; Kelterer, A.-M.; Cramer, C. J.; Johnson, G. P.; Dowd, M. K. *Carbohydr. Res.* **2000**, *326*, 305–322.

(26) Cros, S.; Imberty, A.; Bouchemal, N.; Hervé du Penhoat, C.; Pérez, S. *Biopolymers* **1994**, *34*, 1433–1447.

(27) Hatcher, E.; Guvench, O.; MacKerell, A. D. *J. Phys. Chem. B* **2009**, 12466–12476.

(28) Brennan, P. J.; Nikaido, H. *Annu. Rev. Biochem.* **1995**, *64*, 29–63.

(29) Li, J.; Lowary, T. L. *Org. Lett.* **2008**, *10*, 881–884.

(30) Altona, C.; Sundaralingam, M. *J. Am. Chem. Soc.* **1972**, *94*, 8205–8212.

(31) Houseknecht, J. B.; Lowary, T. L.; Hadad, C. M. *J. Phys. Chem. A* **2003**, *107*, 5763–5777.

(32) Kato, K.; Sasakawa, H.; Kamiya, Y.; Utsumi, M.; Nakano, M.; Takahashi, N.; Yamaguchi, Y. *Biochim. Biophys. Acta* **2008**, *1780*, 619–625.

(33) Jimenez-Barbero, J.; Diaz, M. D.; Nieto, P. M. *Anti-Cancer Agents Med. Chem.* **2008**, *8*, 52–63.

(34) Homans, S. W. *Carbohydr. Chem. Biol.* **2000**, *2*, 947–968.

(35) Kraszni, M.; Szakacs, Z.; Noszal, B. *Anal. Bioanal. Chem.* **2004**, *378*, 1449–1463.

(36) Bock, K.; Duus, J. Ø. *J. Carbohydr. Chem.* **1994**, *13*, 513–543.

(37) Bose-Basu, B.; Klepach, T.; Bondo, G.; Bondo, P. B.; Zhang, W.; Carmichael, I.; Serianni, A. S. *J. Org. Chem.* **2007**, *72*, 7511–7522.

(38) Olsson, U.; Serianni, A. S.; Stenutz, R. *J. Phys. Chem. B* **2008**, *112*, 4447–4453.

(39) Pan, Q.; Klepach, T.; Carmichael, I.; Reed, M.; Serianni, A. S. *J. Org. Chem.* **2005**, *70*, 7542–7549.

(40) Klepach, T. E.; Carmichael, I.; Serianni, A. S. *J. Am. Chem. Soc.* **2005**, *127*, 9781–9793.

(41) Thibaudeau, C.; Stenutz, R.; Hertz, B.; Klepach, T.; Zhao, S.; Wu, Q.; Carmichael, I.; Serianni, A. S. *J. Am. Chem. Soc.* **2004**, *126*, 15668–15685.

(42) Minch, M. J. *Concepts Magn. Reson.* **1994**, *6*, 41–56.

(43) Contreras, R. H.; Peralta, J. E. *Prog. Nucl. Magn. Reson. Spectrosc.* **2000**, *37*, 321–425.

(44) Coxon, B. *Adv. Carbohydr. Chem. Biochem.* **2009**, *62*, 17–82.

(45) Dzakula, Z.; Westler, W. M.; Edison, A. S.; Markley, J. L. *J. Am. Chem. Soc.* **1992**, *114*, 6195–6199.

(46) Dzakula, Z.; DeRider, M. L.; Markley, J. L. *J. Am. Chem. Soc.* **1996**, *118*, 12796–12803.

(47) Deleeuw, F.; Altona, C. *J. Comput. Chem.* **1983**, *4*, 428–437.

(48) Gonzalez-Outeirino, J.; Kirschner, K. N.; Thobhani, S.; Woods, R. J. *Can. J. Chem.* **2006**, *84*, 569–579.

(49) Kirschner, K. N.; Woods, R. J. *Proc. Natl. Acad. U.S.A.* **2001**, *98*, 10541–10545.

(50) Basma, M. D.; Calgan, Varnali, T.; Woods, R. J. *J. Comput. Chem.* **2001**, *22*, 1125–1137.

(51) Woods, R. J.; Chappelle, R. *J. Mol. Struct.* **2000**, *527*, 149–156.

(52) Seo, M.; Castillo, N.; Ganzynkowicz, R.; Daniels, C.; Woods, R.; Lowary, T. L.; Roy, P.-N. *J. Chem. Theory Comput.* **2008**, *4*, 184–191.

(53) Taha, H. A.; Castillo, N.; Roy, P.-N.; Lowary, T. L. *J. Chem. Theory Comput.* **2009**, *5*, 430–438.

(54) D'Souza, F. W.; Ayers, J. D.; McCarren, P. R.; Lowary, T. L. *J. Am. Chem. Soc.* **2000**, *122*, 1251–1260.

(55) Houseknecht, J. B.; Altona, C.; Hadad, C. M.; Lowary, T. L. *J. Org. Chem.* **2002**, *67*, 4647–4651.

(56) Altona, C.; Francke, R.; de Haan, R.; Ippel, J. H.; Daalmans, G. J.; Hoekzema, A. J. A. W.; van Wijk, J. *Magn. Reson. Chem.* **1994**, *32*, 670–678.

(57) Sauer, S. *Int. J. Mol. Sci.* **2003**, *4*, 62–63.

(58) Alkorta, I.; Elguero, J. *Int. J. Mol. Sci.* **2003**, *4*, 64–92.

(59) Zaccari, D.; Barone, V.; Peralta, J. E.; Contreras, R. H.; Taurian, O. E.; Díez, E.; Esteban, A. *Int. J. Mol. Sci.* **2003**, *4*, 93–106.

(60) Zubkov, S. V.; Chertkov, V. A. *Int. J. Mol. Sci.* **2003**, *4*, 107–118.

(61) Ruud, K.; Frediani, L.; Cammi, R.; Mennucci, B. *Int. J. Mol. Sci.* **2003**, *4*, 119–134.

(62) Jackowski, K. *Int. J. Mol. Sci.* **2003**, *4*, 135–142.

(63) Pecul, M.; Helgaker, T. *Int. J. Mol. Sci.* **2003**, *4*, 143–157.

(64) Autschbach, J.; Le Guennic, B. *J. Chem. Educ.* **2007**, *84*, 156–171.

(65) Vaara, J.; Jokisaari, J.; Wasylishen, R. E.; Bryce, D. L. *Prog. Nucl. Magn. Reson. Spectrosc.* **2002**, *41*, 233–304.

(66) Vahtras, O.; Ågren, H.; Jørgensen, P.; Jensen, H. J. A.; Padkjaer, S. B.; Helgaker, T. *J. Chem. Phys.* **1992**, *99*, 6120–6125.

(67) Helgaker, T.; Jaszuñski, M.; Pecul, M. *Prog. Nucl. Magn. Reson. Spectrosc.* **2008**, *53*, 249–268.

(68) Frisch, M. J.; Trucks, G. W.; Schlegel, H. B.; Scuseria, G. E.; Robb, M. A.; Cheeseman, J. R.; Montgomery, J. A., Jr.; Vreven, T.; Kudin, K. N.; Burant, J. C.; Millam, J. M.; Iyengar, S. S.; Tomasi, J.; Barone, V.; Mennucci, B.; Cossi, M.; Scalmani, G.; Rega, N.; Petersson, G. A.; Nakatsuji, H.; Hada, M.; Ehara, M.; Toyota, K.; Fukuda, R.; Hasegawa, J.; Ishida, M.; Nakajima, T.; Honda, Y.; Kitao, O.; Nakai, H.; Klene, M.; Li, X.; Knox, J. E.; Hratchian, H. P.; Cross, J. B.; Bakken, V.; Adamo, C.; Jaramillo, J.; Gomperts, R.; Stratmann, R. E.; Yazyev, O.; Austin, A. J.; Cammi, R.; Pomelli, C.; Ochterski, J. W.; Ayala, P. Y.; Morokuma, K.; Voth, G. A.; Salvador, P.; Dannenberg, J. J.; Zakrzewski, V. G.; Dapprich, S.; Daniels, A. D.; Strain, M. C.; Farkas, O.; Malick, D. K.; Rabuck, A. D.; Raghavachari, K.; Foresman, J. B.; Ortiz, J. V.; Cui, Q.; Baboul, A. G.; Clifford, S.; Cioslowski, J.; Stefanov, B. B.; Liu, G.; Liashenko, A.; Piskorz, P.; Komaromi, I.; Martin, R. L.; Fox, D. J.; Keith, T.; Al-Laham, M. A.; Peng, C. Y.; Nanayakkara, A.; Challacombe, M.; Gill, P. M. W.; Johnson, B.; Chen, W.; Wong, M. W.; Gonzalez, C.; and Pople, J. A. *Gaussian 03, Revision E.01*; Gaussian, Inc.: Wallingford, CT, 2004.

(69) Helgaker, T.; Watson, M.; Handy, N. C. *J. Chem. Phys.* **2000**, *113*, 9402–9409.

(70) Becke, A. D. *J. Chem. Phys.* **1993**, *98*, 5648–5652.

(71) Marquardt, D. *SIAM J. Appl. Math.* **1963**, *11*, 431–441.

(72) Haasnoot, C. A. G.; De Leeuw, F. A. A. M.; Altona, C. *Tetrahedron* **1980**, *36*, 2783–2792.

(73) Case, D. A.; Darden, T. A.; Cheatham, T. E., III; Simmerling, C. L.; Wang, J.; Duke, R. E.; Luo, R.; Merz, K. M.; Pearlman, D. A.; Crowley, M.; Walker, R. C.; Zhang, W.; Wang, B.; Hayik, S.; Roitberg, G.; Seabra, G.; Wong, K. F.; Paesani, F.; Wu, X.; Brozell, S.; Tsui, V.; Gohlke, H.; Yang, L.; Tan, C.; Mongan, J.; Hornak, V.; Cui, G.; Beroza, P.; Mathews, D. H.; Schafmeister, C.; Ross, W. S.; Kollman, P. A. *AMBER 9*; University of California, San Francisco, 2006.

(74) Woods, R. J.; Dwek, R. A.; Edge, C. J.; Fraser-Reid, B. *J. Phys. Chem.* **1995**, *99*, 3832–3846.

(75) Case, D. A.; Cheatham, T. E.; Darden, T.; Gohlke, H.; Luo, R.; Merz, K. M.; Onufriev, A.; Simmerling, C.; Wang, B.; Woods, R. J. *J. Comput. Chem.* **2005**, *26*, 1668–1688.

(76) Cieplak, P.; Cornell, W. D.; Bayly, C.; Kollman, P. A. *J. Comput. Chem.* **1995**, *16*, 1357–1377.

(77) Cornell, W. D.; Cieplak, P.; Bayly, C.; Gould, I. R.; Merz, K. M., Jr.; Fergunson, D. M.; Spellmeyer, D. C.; Fox, T.; Caldwell, J. W.; Kollman, P. A. *J. Am. Chem. Soc.* **1995**, *117*, 5179–5197.

(78) Berendsen, H. J. C.; Postma, J. P. M.; van Gunsteren, W. F.; DiNola, A.; Haak, J. R. *J. Chem. Phys.* **1984**, *81*, 3684–3690.

(79) Jorgensen, W. L.; Chandrasekhar, J.; Madura, J. D.; Impey, R. W.; Klein, M. L. *J. Chem. Phys.* **1983**, *79*, 926–935.

(80) Ryckaert, J. P.; Ciccotti, G.; Berendsen, H. J. C. *J. Comput. Phys.* **1977**, *23*, 327–341.

(81) Darden, T.; York, D.; Pedersen, L. *J. Chem. Phys.* **1993**, *98*, 10089–10092.

(82) Essmann, U.; Perera, L.; Berkowitz, M. L.; Darden, T.; Lee, H.; Pedersen, L. G. *J. Chem. Phys.* **1995**, *103*, 8577–8593.

(83) Houseknecht, J. B.; McCarren, P. R.; Lowary, T. L.; Hadad, C. M. *J. Am. Chem. Soc.* **2001**, *123*, 8811–8824.

(84) Houseknecht, J. B.; Lowary, T. L.; Hadad, C. M. *J. Phys. Chem. A* **2003**, *107*, 372–378.

(85) Hoffmann, R. A.; Van Wijk, J.; Leeflang, B. R.; Kamerling, J. P.; Altona, C.; Vliegenthart, J. F. G. *J. Am. Chem. Soc.* **1992**, *114*, 3710–3714.

(86) Zhao, H.; Pan, Q.; Zhang, W.; Carmichael, I.; Serianni, A. S. *J. Org. Chem.* **2007**, *72*, 7071–82.

(87) Klepach, T.; Zhang, W.; Carmichael, I.; Serianni, A. S. *J. Org. Chem.* **2008**, *73*, 4376–4387.

(88) Allen, M. P.; Tildesley, D. J. *Computer Simulation of Liquids*; Oxford University Press Inc.: New York, 1987; pp 192.

JCTC Journal of Chemical Theory and Computation

Relativistic Zeroth-Order Regular Approximation Combined with Nonhybrid and Hybrid Density Functional Theory: Performance for NMR Indirect Nuclear Spin−Spin Coupling in Heavy Metal Compounds

Salvador Moncho

Departament de Química, Universitat Autonoma de Barcelona, 08193 Cerdanyola del Vallés, Spain

Jochen Autschbach*

Department of Chemistry, State University of New York at Buffalo, Buffalo, New York 14260-3000

Abstract: A benchmark study for relativistic density functional calculations of NMR spin−spin coupling constants has been performed. The test set contained 47 complexes with heavy metal atoms (W, Pt, Hg, Tl, Pb) with a total of 88 coupling constants involving one or two heavy metal atoms. One-, two-, three-, and four-bond spin−spin couplings have been computed at different levels of theory (nonhybrid vs hybrid DFT, scalar vs two-component relativistic). The computational model was based on geometries fully optimized at the BP/TZP scalar relativistic zeroth-order regular approximation (ZORA) and the conductor-like screening model (COSMO) to include solvent effects. The NMR computations also employed the continuum solvent model. Computations in the gas phase were performed in order to assess the importance of the solvation model. The relative median deviations between various computational models and experiment were found to range between 13% and 21%, with the highest-level computational model (hybrid density functional computations including scalar plus spin−orbit relativistic effects, the COSMO solvent model, and a Gaussian finite-nucleus model) performing best.

I. Introduction

Indirect nuclear spin−spin coupling (*J* coupling) is one of the most important nuclear magnetic resonance (NMR) observables. Because of its high sensitivity, the possibility of routine measurements, and its ability to provide useful data about the geometric as well as the electronic structure of chemical compounds, NMR is a widely used technique in chemistry and neighboring scientific disciplines. Consequently, calculations of NMR parameters based on first-principles theory are of high importance to help with the interpretation of experimental data and make predictions. Also, the computation of NMR parameters such as nuclear

magnetic shielding and *J* coupling offers new ways of analysis that can enhance the knowledge about NMR observables and improve our ability to understand the implications of experimental NMR data.[1−6]

On the theoretical side, apart from the evidently important topic of modeling NMR parameters, there are few molecular properties that are as sensitive to relativistic effects as *J* coupling: relativistic "corrections" exceeding 100% of the nonrelativistic result are rather common when elements from the sixth row of the periodic table are involved.[6] Moreover, indirect nuclear spin−spin coupling is quite sensitive to approximations used to describe the electron−electron interactions, the quality of the basis set, and just about every other approximation made in the computational model. *J* coupling is therefore an excellent testing ground for elec-

* To whom correspondence should be addressed. E-mail: jochena@buffalo.edu.

tronic structure methods, for relativistic quantum chemical methods, and for relativity−correlation, relativity−solvation, etc., "cross terms".

J couplings with heavy atoms can be challenging to obtain experimentally and reproduce computationally. The reliable calculation of coupling constants for heavy nuclei has some important theoretical requirements for the computational model, most importantly the inclusion of relativistic effects and electron correlation, basis sets that are capable of describing the large relativistic effects on *J* coupling, but also more 'exotic' features such as an adequate finite nuclei representation. Due to the variational instability of the perturbation operators it is also advantageous if the calculation makes use of analytical derivatives techniques instead of a finite-field differentiation.[78]

In recent years, first-principles codes for heavy atom spin−spin coupling constants have become available that consider most, if not all, of these aspects.[7−13] Relativistic effects were considered in these approaches in different ways, making use of four-component theory[7] and various approximate two-component methods (or their scalar relativistic versions) such as the zeroth-order[8,9,12,13] and infinite-order[10] regular approximations (ZORA, IORA), or Douglas−Kroll transformations.[11] Density functional theory (DFT) is usually the method of choice in calculations of heavy nuclei NMR properties in larger metal complexes because it includes electronic correlation at an affordable computational cost. In the past, relativistic NMR computations were a highly specialized research topic. In recent years a substantial body of computational data has become available, demonstrating that in particular relativistic DFT computations of heavy nucleus NMR parameters can be successfully undertaken even for large metal complexes. For a recent overview of theoretical methods and available case studies, see ref 6.

The availability of easy-to-apply relativistic NMR methods of affordable computational cost allows researchers who are not specialized in theory developments to routinely augment their work by first-principles calculations. As a consequence, it is very important to develop protocols for such computations with reasonably well-known and well-understood error bars, perhaps similar in spirit to the established model thermochemistries. It is the intent here to study of performance of a family of computational models for relativistic *J*-coupling computations and determine the error bars with respect to a substantial set of experimental data for coupling constants involving one or two heavy metals. In this way, adequate settings may be determined for an overall agreement of computed spin−spin coupling constants with experiment which allow for an estimation of the error bars of newly computed coupling constants or to gauge whether agreement with experiment has been obtained for 'good enough reasons'. For an assessment of the overall performance of the method a wide range of different couplings needs to be tested, including compounds with different heavy metals and spin−spin couplings through one, two, or more bonds. Having well-tested basis sets available for such computations is also extremely important.

A comparatively widely applied method for relativistic *J*-coupling computations is presently the analytic-derivative

ZORA relativistic approach described in refs 8, 9, 12, and 13 which includes scalar and spin−orbit relativistic effects, a finite nucleus model, and allows for nonhybrid as well as hybrid DFT computations. The program also includes several methods for chemically motivated analyses of the results.[14−17] A modest number of benchmark data (23 one-bond coupling constants) has been reported along with the original nonhybrid DFT scalar relativistic point-nucleus implementation,[8] indicating overall reasonable agreement with experiment. In this and other previous works, a mix of experimental structures and geometries optimized at various levels of theory have been used along with varying approximations in the exchange-correlation (XC) potential and the XC response kernel. Subsequent applications also have employed varying basis sets, geometries, and functionals. Combining the results from these previous studies into one data set would provide an inconsistent assessment of the method overall.

In this work, we will provide systematic data for 88 one-, two-, and multibond coupling constants involving heavy metal atoms based on a well-defined computational model that is easy to establish in routine computations (see computational details for references): All geometries were optimized at the scalar-ZORA/BP/TZP level of theory with inclusion of a continuum solvation model followed by *J*-coupling computations with a finite nucleus model, the continuum solvation model, and a basis set suitable for *J* coupling. Herein, scalar vs spin−orbit ZORA and nonhybrid vs a hybrid functional (PBE vs PBE0) computations will be compared with experimental data to determine the performance of each computational model with respect to reproducing experimental data. In addition to compiling data for benchmark systems from previous studies, a sizable number of new coupling constants were added and are computed here for the first time. Further, many coupling constants of previously studied systems are computed here for the first time at the hybrid DFT level of theory and including finite nucleus effects. The benchmark set contains 30 two-bond as well as several multibond couplings, a test set large enough to critically assess the performance of relativistic DFT methods using standard functionals to calculate coupling constants with heavy elements other than one-bond couplings.

The approximations leading to deviations between theory and experiment, defining the error bars for each method, are not only in the basis set and functional but also in the overall computational model since most of the experimental *J* couplings were determined in solution at finite temperature. Previous work from our group has highlighted the importance of solvent effects for *J* coupling in metal complexes[6,14,18−22] for which nonhybrid DFT computations have indicated that the use of a continuum model is not always sufficient. In the present benchmark study, errors from a lack of treating explicit solvation dynamically, which would be the most desirable computational model but also a very expensive one, will therefore contribute to the error bars of each computational model. Overall, the results are encouraging: the most sophisticated model (based on spin−orbit hybrid DFT computations) performs best, yielding a 12.5% median relative deviation from experiment.

Spin−Spin Coupling in Heavy Metal Compounds

J. Chem. Theory Comput., Vol. 6, No. 1, 2010 **225**

This paper is organized as follows. In section II details for the computational models, regarding the basis sets, and other technical details are provided. The benchmark data are provided and discussed in section III. The discussion focuses on general performance as well as on individual interesting cases or classes of compounds and classes of *J* couplings. A brief conclusion can be found in section IV.

II. Computational Details

All computations were performed with a pre-2009 release of the Amsterdam Density Functional (ADF) package.[23] Relativistic effects were incorporated in the computations with the zeroth-order regular approximation (ZORA)[24,25] using both the scalar (spin-free) and the two-component formalisms. Relativistic effects in this approach are considered in the one-electron part of the Hamiltonian (relativistic corrections to the kinetic energy of the electrons and to the electron−nucleus attraction as well as one-electron spin−orbit terms), along with relativistic corrections to the electron−electron interactions in a mean-field sense. Like in most applications of relativistic DFT NMR methodology, the spin−other-orbit term was not considered in the computations. Previous experience with two-electron spin−orbit contributions indicates that their *relative* importance decreases in comparison to their one-electron counterparts when the nuclear charges become larger,[26−28] and consequently, their effect on the coupling constants investigated here is expected to be small.

The calculations of spin−spin coupling (*J* coupling) reduced constants were performed using the CPL module of the ADF package.[8,9,12,13] "Pure", i.e., nonhybrid, DFT computations employed both the Vosko−Wilk−Nusair (VWN)[29] local density approximation (LDA) and Perdew−Burke−Ernzerhof (PBE)[30] generalized gradient approximation (GGA) terms; for simplicity, this functional will be referred to as PBE. Differences in the results compared to PBE proper, which was originally devised with a different local correlation functional, are very minor and will not affect the conclusions of this work. Hybrid DFT calculations used a corresponding PBE0 functional which includes 25% of Hartree−Fock exchange.[31] In order to facilitate the hybrid functional calculations orbital−pair density fitting techniques were applied.[12,32,33] For a better representation of the Kohn−Sham orbitals near the nuclei, the atomic nuclei were represented as Gaussian charge distributions, not as point charges as is usually done, because the effect of the nucleus representation in heavy metal spin−spin coupling calculations has been found to be significant. For details about the finite-nucleus implementation and benchmark data for *J*-coupling constants see ref 13. For the user of the software it is only required to provide a "NuclearModel Gaussian" input keyword. The nuclear radii are determined on the fly from atomic masses stored in the ADF software library.[13]

The heavy metal basis set used for obtaining the *J* couplings was an updated version of the 'JCPL' (short for *J* coupling) Slater-type orbitals (STO) basis set used in previous publications.[8,13] Since the time when some of these basis sets were first devised, the ZORA STO basis sets accompanying the ADF package have undergone minor

revisions and we decided to generate a fresh set of basis sets for this benchmark study and future computational work. This JCPL basis set will accompany future releases of the program. Like previous versions, for the sixth-row elements this basis is derived from the TZ2P basis of the ADF basis set library adapted for ZORA calculations which is a valence-triple-ζ and core-double-ζ all-electron STO basis set with two sets of polarization functions. For the sixth-row elements, basis functions with exponents $\gg Z$ (Z = nuclear charge) were replaced by an even-tempered set of 9 high-exponent 1s and 2p functions along with a set of accompanying density-fit functions. A ratio of 1.69 has been used to form the even-tempered set in order to reach exponents around 10 000 with relatively few functions. Previous work showed good performance of basis sets derived in this way.[13,15] Moreover, in finite nucleus computations, these basis sets yielded reasonably well-converged results with respect to the high-exponent augmentation without causing numerical problems,[13] and thus, they represent an economical yet reasonably accurate choice for routine computations. For lighter elements, four 1s basis functions with exponents 2 Z, 3 Z, 4 Z, and 100 Z were added following a recipe given by Watson et al.[34] but with corresponding density fit functions added.[15] Atom types not involved in spin−spin couplings were represented using a double-ζ all-electron STO basis set with one set of polarization functions for all atoms (DZP of the ADF basis set library). No frozen cores were used.

For verification, all coupling constants were also computed with the older version of the JCPL basis and with the basis TZ2P3 from ref 13, which was constructed in a similar way as JCPL but with STO exponents reaching 3×10^4 for the sixth-row metals for elements as heavy as Hg and Pb. The obtained coupling constants were very similar (the difference is less than a 1% in more than 95% of the couplings calculated with the PBE functional). In calculations of coupling constants with the TZ2P3 basis and the hybrid functional, PBE0 led to convergence problems in several compounds of Hg, W, and Pt. Convergence issues with PBE0 computations and basis sets with very high STO exponents were also noted previously in ref 13, where the basis set convergence in relativistic *J*-coupling DFT calculations was investigated. The convergence problems for very high exponent basis functions are tentatively attributed to the accuracy of the numerical integration/density fitting combination used to compute the exact exchange integrals. No convergence problems were found with the JCPL and the revised JCPL basis. Due to the similarity of the results it was decided only to report data obtained with the updated JCPL basis in this work. We note, however, that both in ref 13 and during the course of the present study we noticed a slower convergence of the PBE0 *J* couplings with respect to the high-exponent augmentation, in particular with a point-nucleus model. The finite-nucleus data reported here are likely to be better converged, but the difference in basis set convergence of nonhybrid vs hybrid DFT *J* couplings of heavy atoms may warrant further investigation.

For consideration of solvent effects, the ADF implementation of the conductor-like screening model (COSMO)[35] was applied. Dielectric constants of 20.7, 37.5, 2.3, 4.8, 2.6, 8.9,

Table 1. Molecules and Spin−Spin Couplings Computed for This Work. Part 1: Hg and Pt

metal	formula	solvent[a]	one bond	two bond	others	refs
Hg	$Hg(CN)_2$	CH_3OH	Hg−C			43
	$[Hg(CN)_4]^{2-}$	gas phase[b]	Hg−C			44
	$Hg(CH_3)Cl$	CH_3Cl	Hg−C	Hg−H		45
	$Hg(CH_3)Br$	CH_3Cl	Hg−C	Hg−H		45
	$Hg(CH_3)I$	CH_3Cl	Hg−C	Hg−H		45
	$Hg(CH_3)_2$	CH_3Cl	Hg−C	Hg−H		45
	$Hg(CH_3)(CF_3)$	$\varepsilon_r = 8.0$[c]		Hg−F, Hg−H		46
	$Hg(C_6H_5)_2$	CH_2Cl_2	Hg−C	Hg−C	Hg−C[d]	43
	$Hg(CCCl)_2$	DMSO	Hg−C	Hg−C		43
	$Hg(CH_3)CCH$	C_6H_6	Hg−C[e]	Hg−C		43
	$IrCl(SnCl_3)(HgCl)(CO)(PH_3)_2$[f]	CH_3Cl		Hg−Sn, Hg−P		47
Pt	$Pt(P(CH_3)_3)_4$	THF	Pt−P			48
	$Pt(PF_3)_4$	THF	Pt−P			49
	$[Pt(CO)_3]_2^{2+}$	H_2O	Pt−Pt, Pt−C[g]	Pt−C[g]		50
	$[Pt(CN)_5]_2^{4-}$	H_2SO_4(conc)	Pt−Pt, Pt−C[g]	Pt−C[g]		51
	cis-$PtH_2(P(CH_3)_3)_2$	CH_3COCH_3	Pt−P, Pt−H			52
	trans-$PtH_2(P(CH_3)_3)_2$	CH_3COCH_3	Pt−P, Pt−H			52
	cis-$PtCl_2(P(CH_3)_3)_2$	CH_2Cl_2	Pt−P			53
	trans-$PtCl_2(P(CH_3)_3)_2$	CH_2Cl_2	Pt−P			53
	cis-$PtI_2(NH_2CH_3)_2$	CH_3COCH_3		Pt−H, Pt−C		54
	trans-$PtI_2(NH_2CH_3)_2$	CH_3COCH_3		Pt−H, Pt−C		54
	$Pt(SnCl_3)(CH_2C(CH_3)CH_2)(C_2H_4)$	CH_3Cl	Pt−Sn, Pt−C[h]	Pt−C, Pt−H[i]	Pt−H[j]	55

[a] Solvent model used in calculations. [b] Experimental value corresponds to solid-state NMR of K salt. [c] Neat liquid. A dielectric constant of 8.0 representative of organic compounds with CF_3 groups was used. [d] Both three-bond and four-bond spin−spin couplings. [e] Two different couplings for both methyl and ethinyl ligands. [f] Experimental value for $IrCl(SnCl_3)(HgCl)(CO)(P(C_6H_5)_3)_2$. [g] Both cis and trans inequivalent couplings. [h] Four inequivalent couplings. [i] Five inequivalent couplings. [j] Three-bond coupling.

5.0, 46.7, 2.3, 32.6, 2.31, 2.78, 84.0, 7.58, 2.38, and 78.39 were used to describe the solvents acetone, acetonitrile, benzene, chloroform, CS_2, dichloromethane, dimethyl ether, DMSO, Freon 113, methanol, $Pb(CH_3)_4$, $PbCl_4$, sulfuric acid, THF, toluene, and water, respectively, along with default atomic radii.

Coupling computations were performed with the following settings for the numerical integration: a global parameter of 6.0 and an atomic core parameter of 8.0. These values roughly indicate the number of significant figures for the density integration.[36] The two-component relativistic analogs of the FC, SD, PSO, and DSO terms as well as spin−orbit cross terms were included in the spin−spin couplings, except where scalar relativistic calculations were performed, in which case the (often small) SD term was neglected to lower the computational expense.

Conversions between J coupling in Hertz and reduced coupling K were based on the following gyromagnetic ratios, in 10^7 rad/(T s): 26.7522128, 6.728284, 25.18148, 10.8394, 2.624198, −10.0317, 1.1282403, 5.8385, 4.8457916, 15.5393338, 15.6921808, and 5.58046 for ^{1}H, ^{13}C, ^{19}F, ^{31}P, ^{35}Cl, ^{119}Sn, ^{183}W, ^{195}Pt, ^{199}Hg, ^{203}Tl, ^{205}Tl, and ^{207}Pb, respectively.[37] Where applicable, the couplings constant reported in this work were obtained as the average of the computed constant for every equivalent atom pair in the molecule since experimentally equivalent atoms may be nonequivalent in the calculation, for instance due to the free rotation of alkyl groups and other ligands under experimental conditions. Further, the coupling constants reported here are unsigned because the sign is not always known experimentally. We note that for the TlX series of diatomics, calculations and experiment agree in that the isotropic coupling is negative and the coupling anisotropy is positive.[12] The Supporting Information provides the full set of coupling constants, including their signs, for each of the computational models employed here.

Molecular geometries used for the spin−spin coupling computations were obtained by full DFT optimizations. The scalar ZORA operator was used to include relativistic effects along with a triple-ζ all-electron basis with polarization functions optimized for ZORA calculations (TZP from the ADF basis set library) and small frozen cores (1s frozen for C, N, O, and F, 1s−2p for Cl and P, 1s−3p for Br, 1s−4p for Sn and I, and 1s−4d for W, Pb, Pt, Tl, and Hg). The XC functional chosen for optimizations was BP, the combination of the Becke88[38] and the Perdew86[39] generalized gradient approximations (GGAs), which has been shown in benchmarks to produce reliable local minimum structures for metal complexes.[40−42] For consistency with the *J*-coupling computations, solvent effects were included in the optimizations by the COSMO method using the dielectric constants listed above.

III. Results and Discussion

A. Benchmark Overview and Discussion of the Scalar ZORA PBE Results. For this study a comprehensive set of experimental *J*-coupling data has been compiled in order to include representative cases for a wide range of heavy metal spin−spin couplings. The major NMR nuclei of the sixth row of the periodic table have been studied: W, Pt, Hg, Pb, and Tl. For the analysis a total of 47 different systems have been calculated to obtain 88 different spin−spin couplings involving one or two heavy atoms. This study includes one-bond couplings, as in previous benchmarks, but also a considerable number of two-bond couplings and some couplings through more than two bonds. A list of the selected complexes and computed couplings, with references to the experimental measurements, is provided in Tables 1 and 2. The full data set, experimental and computed coupling constants, is provided in the Supporting Information.

Table 2. Molecules and Spin−Spin Couplings Computed for This Work. Part 2: W, Pb, and Tl

metal	structure	Solvent[a]	one bond	two bond	others	refs
W	$W(CO)_6$	CH_3Cl	W−C			56
	$W(CO)_5PF_3$	$CFCl_2CF_2Cl$[b]	W−P			57, 58
	$W(CO)_5PCl_3$	$CFCl_2CF_2Cl$[c]	W−P			58
	$W(CO)_5PI_3$	$CFCl_2CF_2Cl$[c]	W−P			58
	η^5-$(C_5H_5)W(CO)_3H$	CH_3CN[d]	W−H			59
	WF_6	CS_2	W−F			60
	$W(CCH_3)(CH_2CH_3)_3$[e]	C_6H_6		W−H		61
Pb	$PbCl_4$	$PbCl_4$[f]	Pb−Cl			62
	$Pb(CH_3)_4$	$Pb(CH_3)_4$[f]	Pb−C	Pb−H		63, 64
	$Pb(CH_3)_3H$	CH_3OCH_3	Pb−H	Pb−H		64
	$Pb(CH_3)_2H_2$	CH_3OCH_3	Pb−H	Pb−H		64
	$Pb(CH_3)_2(CF_3)_2$	$\varepsilon_r = 8.0$[g]		Pb−F, Pb−H		46
	$Pb(CH_3)_3CF_3$	$\varepsilon_r = 8.0$[g]		Pb−F, Pb−H		46
	PbH_4	CH_3OCH_3[h]	Pb−H			
	$Pb_2(CH_3)_6$	C_6H_6	Pb−C	Pb−C, Pb−H	Pb−H	65
Tl	TlF	gas phase	Tl−F			66
	TlCl	gas phase	Tl−Cl			66
	TlBr	gas phase	Tl−Br			66
	TlI	gas phase	Tl−I			66
	$Tl_4(OCH_3)_4$[i]	$C_6H_5CH_3$		Tl−Tl[i]		67
	$Tl(CN)_3$	H_2O	Tl−C			68
	$Tl(CN)_2Cl$	H_2O	Tl−C			68
	$Tl(CN)Cl_2$	H_2O	Tl−C			68

[a] Solvent used in calculations. [b] Experimental solvent quoted simply as Freon. We selected Freon 113 with its intermediate ε_r. [c] Experimental solvent unknown; selected $CFCl_2CF_2Cl$ for analogy with $W(CO)_5PF_3$. [d] Experimental measurement in liquid crystal (ZLI-1132 Merck/EBBA). [e] As a model for $W(CC(CH_3)_3)(CH_2C(CH_3)_3)_3$. [f] Neat liquid. [g] Neat liquid. A dielectric constant of 8.0, representative of organic compounds with CF_3 groups, was used. [h] Experimental value not known. The value used has been extrapolated from $Pb(CH_3)_3H$ and $Pb(CH_3)_2H_2$. [i] Experimental value for $Tl_4(OC(CH_3)_3)_4$, $^{205}T−^{203}Tl$.
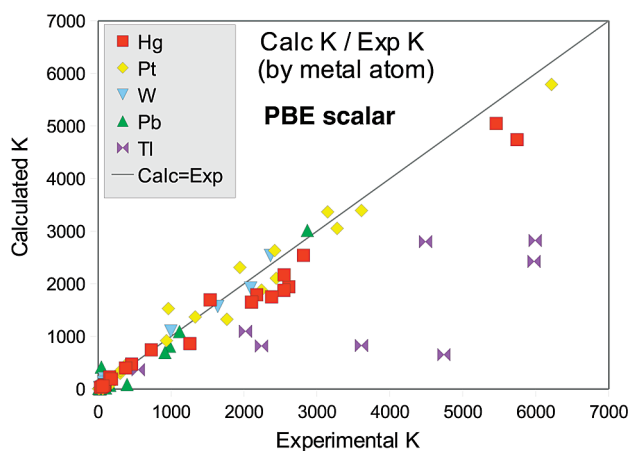

Figure 1. Computed absolute values of the reduced nuclear spin−spin coupling constants K versus absolute experimental values (in units of 10^{19} T^2 J^{-1}) for PBE, scalar ZORA calculations. Two coupling constants involving Sn and a heavy metal nucleus have been omitted due to their magnitude.

In Figure 1 most of the computed reduced spin−spin coupling (J-coupling) constants obtained from scalar ZORA computations using the nonhybrid PBE functional are plotted vs experiment. A good correlation can be observed for most of the computed couplings, although there are several large disagreements, in particular for the Tl systems. Apart from these outliers, the correlation appears to be reasonable at the scale of the plot.

Since the data set spans several orders of magnitude and includes some severe outliers one needs to be careful with assessing the performance numerically based on average or rms deviations. An overall assessment of the agreement with experiment can be obtained by comparing the average and median of the unsigned deviation for both the absolute and the relative errors, with associate variability measures as the standard deviation (SD) around the average and median unsigned deviation (MD)[79] around the median (see Table 3).

The most significant discrepancy between theory and experiment is the systematic underestimation of the coupling constant in the thallium systems. This is expected because previous works[12,15] have shown that in these Tl compounds the inclusion of spin−orbit coupling is crucial. The relative errors for couplings involving Pb are of similar magnitude. In this case there are a number of small coupling constants that are not well described at the scalar ZORA PBE level of theory. Besides Tl and Pb the most significant absolute deviation of the coupling constant is observed in the complex $IrCl(SnCl_3)(HgCl)(CO)(PH_3)_2$. For its huge Hg−Sn two-bond coupling constant, which is outside the plot range of Figure 1, the deviation of $11\,710 \times 10^{19}$ T^2 J^{-1} with respect to the experiment represents 23% of the total coupling of $-50\,838 \times 10^{19}$ T^2 J^{-1}.[47] This and most of the other significant discrepancies and selected cases will be discussed later in section III.E. Couplings involving Hg and a light ligand in linear Hg(II) complexes are reasonably close to experiment. We note already here that the hybrid DFT results for Hg−C couplings reported below agree very well with experiment. It should be noted, however, that explicit solvation was demonstrated to increase Hg−C couplings in linear Hg(II) complexes quite significantly,[21] and therefore, it is likely that an error compensation regarding the complexes structure, solvation effects on structure and J coupling, and approximations in the density functional, is influential both in the present computations as well as in previous work. By extrapolating the trends regarding solvation effects that were reported in ref 21 a dynamic model with explicit solvation

Table 3. Statistical Error Parameters for the PBE, ZORA Scalar Calculations

	absolute deviation[a]				relative deviation[a]			
	ΔK_{mean}	SD[b]	ΔK_{median}	MD[c]	ΔK_{mean}^{rel}	SD[b]	ΔK_{median}^{rel}	MD[c]
total	513.3	1462.7	71.1	68.4	39.6%	90.2%	17.6%	11.5%
Hg	753.4	2352.5	158.5	153.4	16.9%	10.3%	17.0%	7.3%
Pt	233.7	685.7	32.5	30.4	23.3%	23.5%	13.6%	7.5%
W	73.8	57.0	70.3	42.8	35.7%	46.2%	10.3%	8.7%
Pb	98.1	111.7	25.7	19.1	100.2%	192.9%	68.5%	18.3%
Tl	2226.0	2536.9	2235.2	1122.8	57.0%	55.2%	56.2%	14.5%
one bond	676.7	1043.6	324.7	241.1	46.7%	122.9%	18.3%	9.5%
two bond	352.0	1920.2	14.7	9.3	32.9%	33.3%	18.2%	9.4%
longer	4.3	2.8	3.7	1.9	18.7%	14.8%	11.4%	6.3%

[a] Mean and median unsigned absolute and relative deviations from experiment. Absolute deviations in 10^{19} T^2 J^{-1}. Relative deviation calculated as $\Delta K^{rel} = |(K_{calcd} - K_{exp})/K_{exp} \times 100\%|$ with unsigned K values. [b] Standard deviation (SD) calculated as $((1/N)\Sigma_{i=1}^{N}(\Delta K_i - \Delta K_{mean}))^{1/2}$. [c] Median unsigned deviation (MD) obtained as $median_i (|\Delta K_i - \Delta K_{med}|)$.

might eventually lead to an overestimation of these J couplings with respect to experiment at the level of theory employed for this study. However, this will have to be demonstrated explicitly in future work. Unlike previous computations,[21] here the full GGA response kernel is considered in the computations, along with the continuum model, the revised JCPL basis, and finite nucleus corrections, and the geometries were optimized which is an important factor. The combination of these effects lead to a less strong underestimation of Hg−C couplings calculated with a GGA functional when explicit solvation is omitted, as compared to previous work, which is beneficial for the performance of the computational model used here.

Overall, the pronounced discrepancy between average and median errors in the summary for all metals in Table 1 indicates that at this level of theory a considerable number of outliers taint the otherwise reasonable appearance of the data set in Figure 1. Regarding the performance of the computations for two-bond and higher couplings, the results are promising since the relative median deviations from experiment are comparable to the one-bond couplings.

B. Functional: PBE vs PBE0. Using a hybrid functional (PBE0) results in a clear improvement of the overall agreement of the computed coupling constants with experiment as can be observed in both the plot of computed couplings vs experiment (Figure 2) and the statistical parameters (Table 4). The outliers for Tl remain at this scalar relativistic level of theory. Most of the coupling constants are better represented with this functional (57 of the total 88 coupling constants improve toward experiment). However, when computing the overall deviation by metal, for molecules containing Hg, Pb, and W, worse average results are observed in the hybrid-DFT calculations. For mercury, however, this trend is coming from an individual exception, the huge ^2J(Hg−Sn) coupling constant in IrCl($SnCl_3$)(HgCl)-(CO)(PH_3)$_2$. It has a great absolute error in both sets of scalar relativistic calculations. Its calculated value is further away from experiment with PBE0, with an unsigned deviation around 100 times the second largest error among the Hg couplings. If this coupling is discarded, a very significant improvement of the overall mean deviations is obtained for both the PBE0 and the PBE sets of calculations. The change from the PBE calculations (average deviation = 255.4 10^{19} T^2 J^{-1}) to PBE0 (average deviation = 82.1) shows the general trend of improvement for Hg when including exact exchange

Figure 2. Computed vs experimental reduced couplings (in 10^{19} T^2 J^{-1}) for PBE0, scalar ZORA calculations. See also caption of Figure 1.

in the functional with results closer to experiment in 14 of the 23 calculated K (Hg−X) couplings. Regarding the W and Pb computations, a general trend is not observed in the absolute mean deviation. For example, the number of improved results for the W complexes (4) and of worse results (3) are similar, and so the overall accuracy for scalar relativistic PBE vs PBE0 is comparable. However, an improvement in the relative deviations is observed in the Pb and W results due to improvements of the calculations of the small J-coupling constants for which the relative error with PBE is often quite large. The small couplings will be discussed in more detail further below.

Regarding the relation of the coupling path length to the performance of the model, the hybrid functional yields better agreement with experiment for the one-bond couplings than for two- and multibond couplings. Although the inclusion of exact exchange in the functional reduces the one-bond coupling overall deviations to less than one-half, the agreement with experiment becomes worse for the long-range couplings (three and four bond). The improvement of the performance mainly for the one-bond couplings is also clearly visible in the relative mean and median errors. In the case of two-bond couplings, the mean absolute deviation increases from PBE to PBE0, but it is mostly due to the individual bad result of the Hg−Sn coupling, as mentioned above. When omitting the Hg−Sn coupling from the test

Spin−Spin Coupling in Heavy Metal Compounds

J. Chem. Theory Comput., Vol. 6, No. 1, 2010 **229**

Table 4. Statistical Error Parameters for the PBE0, ZORA Scalar Calculations

	absolute deviation[a]				relative deviation[a]			
	ΔK_{mean}	SD[b]	ΔK_{median}	MD[c]	ΔK_{mean}^{rel}	SD[b]	ΔK_{median}^{rel}	MD[c]
total	476.5	2500.5	33.9	30.9	22.4%	33.2%	12.2%	9.3%
Hg	1093.8	4746.0	32.9	17.0	16.4%	13.5%	7.5%	6.0%
Pt	118.9	238.7	13.6	10.8	15.1%	15.1%	10.8%	6.4%
W	87.8	122.9	35.0	27.3	19.1%	16.3%	15.7%	12.8%
Pb	98.8	186.7	28.2	27.1	42.4%	65.2%	20.2%	11.3%
Tl	1317.4	1598.9	1265.1	750.9	33.1%	35.9%	30.3%	18.3%
one bond	363.3	711.2	132.1	120.8	19.5%	41.0%	8.0%	18.2%
two bond	678.8	3890.0	8.5	8.4	25.7%	21.8%	18.2%	14.1%
longer	14.1	12.1	11.3	7.5	19.0%	11.5%	24.0%	10.4%

[a] Mean and median unsigned absolute and relative deviations. Absolute deviations in 10^{19} T^2 J^{-1}. See footnotes of Table 3 for details. [b] Standard deviation (SD). [c] Median unsigned deviation (MD).

Table 5. Statistical Error Parameters for the PBE, ZORA Spin−Orbit Calculations

	absolute deviation[a]				relative deviation[a]			
	ΔK_{mean}	SD[b]	ΔK_{median}	MD[c]	ΔK_{mean}^{rel}	SD[b]	ΔK_{median}^{rel}	MD[c]
total	466.1	1142.0	69.2	65.5	40.7%	97.1%	20.6%	11.6%
Hg	665.6	1633.6	171.0	170.4	20.0%	11.5%	17.8%	6.3%
Pt	290.2	861.0	35.4	32.2	24.5%	21.7%	16.2%	10.5%
W	99.3	80.9	50.0	45.8	38.4%	50.4%	12.1%	8.2%
Pb	122.4	130.1	53.9	39.0	106.7%	209.7%	56.7%	32.8%
Tl	1649.0	2068.0	1587.5	1092.7	38.5%	39.7%	38.7%	10.4%
one bond	662.6	1181.5	362.2	359.0	47.6%	132.1%	22.2%	11.8%
two bond	255.5	1359.7	17.2	14.0	34.1%	33.8%	19.9%	10.1%
longer	4.0	3.4	3.2	2.4	17.1%	16.5%	14.2%	8.3%

[a] Mean and median unsigned absolute and relative deviations. Absolute deviations in 10^{19} T^2 J^{-1}. See footnotes of Table 3 for details. [b] Standard deviation (SD). [c] Median unsigned deviation (MD).

Table 6. Statistical Error Parameters for the PBE0, ZORA Spin−Orbit Calculations

	absolute deviation[a]				relative deviation[a]			
	ΔK_{mean}	SD[b]	ΔK_{median}	MD[c]	ΔK_{mean}^{rel}	SD[b]	ΔK_{median}^{rel}	MD[c]
total	352.2	1934.4	43.4	39.0	22.4%	36.1%	12.5%	9.4%
Hg	856.8	3686.8	35.0	32.7	14.8%	12.5%	10.1%	7.4%
Pt	111.9	246.7	19.0	17.5	16.6%	15.0%	11.5%	7.9%
W	70.6	74.9	44.1	37.5	15.0%	16.0%	8.2%	5.5%
Pb	68.2	72.0	30.0	26.3	49.0%	72.2%	26.5%	16.5%
Tl	737.1	1019.6	487.0	258.8	22.0%	29.9%	13.3%	8.9%
one bond	235.8	465.3	96.7	87.6	17.2%	45.2%	7.4%	17.5%
two bond	545.2	3023.7	10.2	6.5	29.3%	21.3%	25.1%	11.8%
longer	11.3	9.2	9.1	5.2	18.3%	9.7%	22.3%	9.9%

[a] Mean and median unsigned absolute and relative deviations. Absolute deviations in 10^{19} T^2 J^{-1}. See footnotes of Table 3 for details. [b] Standard deviation (SD). [c] Median unsigned deviation (MD).

set the mean absolute deviations are comparable within the uncertainties of the averages (absolute average = 27.4 for PBE and 31.1 for PBE0), showing a similar performance in this case for both functionals for the two-bond couplings.

C. Spin−Orbit Effects. The inclusion of spin−orbit (SO) coupling in the ZORA computations has no systematic effect on the accuracy of the couplings when considering the whole data set. The calculation results are summarized in Tables 5 and 6 and Figures 3 and 4. In the PBE0 calculations, for example, 44 of the 88 computed couplings are improved by including SO coupling in the formalism. As a result, the absolute average deviation is improved but not the median, and the relative errors are very similar. As pointed out earlier, a systematic and large improvement is obtained for some of the couplings involving the Tl atom. SO effects on other molecules are less significant and variable, even decreasing the agreement with experiment in some examples. For most metals, the overall effect of including SO coupling is different

in hybrid and pure DFT calculations: in 34 of the computed couplings spin−orbit coupling improves the result only for one of the functionals.

The SO effect will be analyzed separately for the different kinds of couplings under consideration here. As a general finding, the overall deviations listed in Table 6 document that the combination of the PBE0 functional with the spin−orbit ZORA relativistic formalism yields the best agreement with experiment among the computational models tested here and that it is an overall well-performing method for this set of coupling constants. The results are somewhat reassuring because this computational model is also the most sophisticated among those tested here. Incidentally, it is the most expensive model too in terms of the required computing resources.

For the Hg compounds, including SO effects always reduces the absolute mean deviation from experiment, but the median of the absolute unsigned error increases. In the
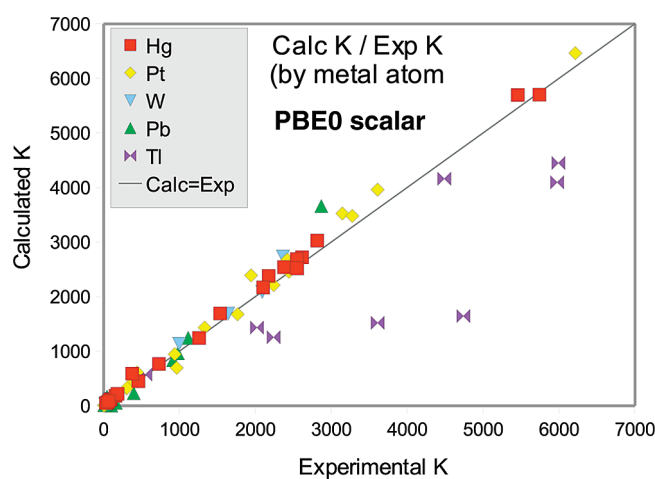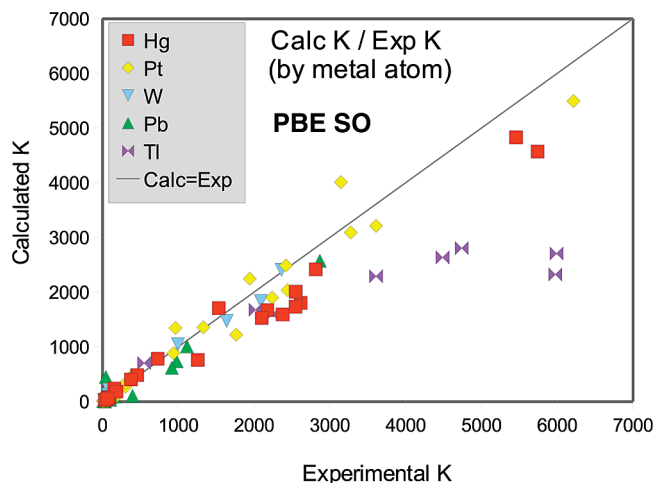
Figure 3. Computed vs experimental reduced couplings (in 10^{19} T^2 J^{-1}) for PBE, spin−orbit ZORA calculations. See also caption of Figure 1.

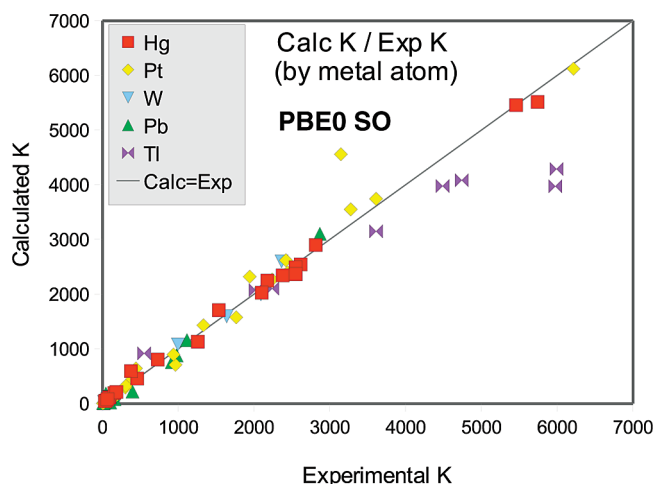**Figure 4.** Computed vs experimental reduced couplings (in 10^{19} T^2 J^{-1}) for PBE0, spin−orbit ZORA calculations. See also caption of Figure 1.

PBE calculation most of the individual Hg couplings (19 out of 23) have slightly less good agreement with experiment when including SO coupling, but the improvement in the very large ^2J(Hg−Sn) dominates the overall statistics. In the PBE0 calculations it is also the ^2J(Hg−Sn) coupling that dominates the absolute deviations, but here also the general trend is that SO coupling improves the results slightly. At the PBE0 level, 15 of the Hg coupling constants improve with respect to experiment when SO effects are considered. However, the average improvement (excluding the ^2J(Hg−Sn) coupling) is just on the order of 10×10^{19} T^2 J^{-1}.

For the Pt complexes the inclusion of SO coupling worsens the agreement with experiment for most of the J couplings (for 21 couplings with PBE and 20 with PBE0 out of a total of 34). On the other hand, the absolute mean deviation from experiment is smaller for the PBE0 calculations when comparing scalar with SO results but only by about 7×10^{19} T^2 J^{-1}. We emphasize the case of the Pt−Pt coupling in the $[Pt(CN)_5]_2^{4-}$ complex: In this case inclusion of SO coupling yields a large difference between theory and experiment (in

PBE0 calculation by more than 1000×10^{19} T^2 J^{-1}, which is 33% of the experimental value). This result highlights the difficulty of assessing approximate computational results in which potentially important effects are not included: a good agreement of scalar relativistic data with experiment might lead to the conclusion that the magnitude of SO effects is small, which is not correct in this case.

For complexes with W, opposite behaviors with respect to SO effects are observed with the two functionals. Spin−orbit effects in combination with the hybrid functional clearly improve the results, but they render the agreement of PBE with experiment worse. The combination of PBE0 with the SO relativistic formalism yields overall very good results, with a median relative deviation of 10%. These are the best results for any of the metals in terms of both absolute and relative deviations.

For compounds of Pb, it also depends on the functional whether SO effects improve the agreement with experiment or not. In the nonhybrid PBE calculations both relative and absolute deviations increase upon inclusion of SO effects. Despite the fact that the PBE0 absolute mean deviation is lower with SO coupling, there is an increase in the relative errors compared to scalar relativistic calculations, showing that spin−orbit coupling mainly improves the larger J couplings but renders the results worse for some of the Pb couplings with small magnitudes.

For complexes with Tl, the increase of the accuracy of the calculations upon the inclusion of SO coupling is very significant for the TlX (X = halide) series for both functionals. However, the SO effect in the Tl(CN)$_n$Cl$_{(3-n)}$ series and for Tl$_4$(OCH$_3$)$_4$ is to increase the deviation from experiment. Since the gain in accuracy for some of the systems is quite significant (around 40% of the experimental value) while the loss of accuracy for the cyanide series is relatively minor (around 3%), the overall result is a clear improvement of the Tl couplings upon inclusion of SO coupling in the computations. Therefore, for the Tl systems the best results for the reduced NMR spin−spin coupling constants are obtained from the spin−orbit relativistic hybrid PBE0 functional calculations.

Focusing on the one-bond couplings, despite the fact that the absolute mean deviation is always smaller when spin−orbit coupling is included, in the PBE calculations the absolute median and both the relative mean and the median deviations increase slightly. The meaning of this is that some of the worst results are improving, but there is somewhat less good agreement with experiment for some of the coupling constants that agreed quite well with experiment in the scalar relativistic calculations. Overall, with PBE there is only an improvement toward experiment for one-third of the couplings upon including SO coupling. When spin−orbit coupling is applied in combination with the hybrid functional, most of the results improve toward experiment, and as a consequence, all the statistic parameters improve.

For the two-bond couplings, although the absolute averages show better agreement with experiment when SO coupling is included, this is mainly due to the Hg−Sn case. If it is excluded from the test set the mean absolute deviations are slightly higher but just by 2×10^{19} T^2 J^{-1} for PBE and 11

Table 7. Statistical Error Parameters for Gas-Phase PBE0 ZORA Spin−Orbit *J*-Coupling Calculations[d]

	absolute deviation[b]				relative deviation[b]			
	ΔK_{mean}	SD[c]	ΔK_{median}	MD[d]	ΔK_{mean}^{rel}	SD[c]	ΔK_{median}^{rel}	MD[d]
total	241.9	549.2	44.5	43.2	24.4%	36.5%	13.9%	10.4%
Hg	188.7	266.9	61.0	55.1	13.5%	12.8%	13.8%	4.7%
Pt	186.0	417.1	31.9	31.5	23.2%	24.3%	11.6%	10.4%
W	65.9	64.7	33.9	26.6	18.3%	16.1%	8.7%	7.3%
Pb	53.7	68.8	18.0	9.9	42.8%	70.5%	25.2%	15.7%
Tl	1163.0	1695.1	559.1	463.0	29.5%	37.9%	23.6%	19.2%
one bond	396.6	795.7	137.4	129.7	22.6%	44.7%	10.9%	12.0%
two bond	61.3	155.4	10.8	6.1	27.4%	25.4%	21.5%	10.4%
longer	10.3	9.3	7.6	5.0	14.1%	6.4%	16.4%	4.8%

[a] Same as Table 6 and Figure 4 but without application of the continuum solvent model in the *J*-coupling computations (optimized geometries were the same as in Table 4 and Figure 4). [b] Mean and median unsigned absolute and relative deviations. Absolute deviations in 10^{19} T^2 J^{-1}. See footnotes of Table 3 for details. [c] Standard deviation (SD). [d] Median unsigned deviation (MD).

$\times 10^{19}$ T^2 J^{-1} for PBE0. At the same time the absolute median and both relative deviations worsen slightly.

The effect of SO coupling in the statistical parameters for longer range couplings is quite small, and general trends are not observed (the data set is also small, and not too much significance should be attributed to minor differences in the statistical parameters for different sets of computations). For the few data points we have available, one-half of the coupling constants improve and the other half become worse in comparison with experiment when SO coupling is included.

D. Overall Importance of the Solvent Model. One might wonder how large the influence from the continuum solvent model is in the calculations. In Table 7 the statistical data are provided for calculations at the PBE0 ZORA spin−orbit level but without the continuum model. The optimized geometries are the same as those used in all other computations in this paper. If we focus on the relative deviations from experiment, it is seen that the performance of the gas-phase calculations is not significantly worse than the calculations with the COSMO solvent model when taking the standard deviations of the mean and median into consideration. The breakdown per metal reveals similar performance of the gas-phase computations for Hg, Pt, and W, as quantified by the median relative deviations. The trends in the absolute deviations are strongly influenced by the Hg−Sn coupling (see the apparently remarkable improvement of the overall absolute average errors). As will be discussed in the next section, the large-magnitude Hg−Sn coupling tends to dominate the mean deviations in our data set and in the case of the gas-phase calculations this coupling constant happens to be close to experiment. Given the sensitivity of this coupling constant to the computational model, this Hg−Sn-bonded compound deserves further investigation. For the trigonal Tl systems such as Tl(CN)$_2$Cl we will demonstrate in the next section that a dynamic study with explicit solvent molecules (water) is likely to be necessary in order to reproduce the experimental *J* couplings within a 10% margin of error. Previous work by our group has reported large explicit solvent effects on *J* couplings in metal complexes with Tl.[14,18] The breakdown per metal in Table 5, in comparison with the COSMO data in Table 4, already shows improvements for Tl from the continuum model. However, just like in other Tl complexes that we investigated in the past, the continuum model alone, without explicit solvent, is not sufficient to reproduce experimental data obtained in solution.

E. Some Individual Cases. *1. Tl.* The *J* couplings in the Tl compounds are quite strongly dependent on the computational model. The pronounced SO effects have already been highlighted. The findings in this work further echo conclusions from previous studies of Pt−Tl coupling constants carried out in our group[14] in which a strong sensitivity of the results with respect to the computational model was noted. A spin−orbit relativistic formalism as well as the use of a hybrid functional appears to be overall beneficial for the computation of NMR parameters in Tl complexes. However, we pointed out already that spin−orbit coupling does not improve the results for some cyanide thallium complexes.

The *J* coupling in the Tl−X series of diatomics is particularly strongly affected by SO coupling. Figure 4 (see also the Supporting Information) shows that despite the strong improvement toward experiment the SO PBE0 results are still somewhat too small in magnitude. This is in part due to the structural aspect of the computational model: the BP-optimized bond lengths are larger than the experimentally determined equilibrium distances reported in ref 69. Figure 5 demonstrates that when experimental equilibrium distances are used for the TlX series the computed coupling magnitudes slightly overshoot the experimental ones. Remaining deviations from experiment are tentatively attributed to the approximations in the density functional as one of the major remaining sources of error.

For some examples, such as Tl(CN)$_2$Cl, the deviation between computations and experiment remain quite large even for the PBE0 SO calculation. It is likely that solvent effects need to be modeled explicitly in order to obtain *J* couplings that are within 5−10% of the experimental data. Previously, the importance of including solvent effects with explicit solvent molecules was demonstrated for complexes with vacant sites in their first coordination sphere.[14,18,21] In order to investigate this issue, for the Tl(CN)$_2$Cl complex an additional set of calculations was performed but now considering explicitly the solvent. Two water molecules, one above and one below the metal−ligand plane, were added in the calculations. The results show some improvement, reducing the deviation from experiment from 26% to 18%
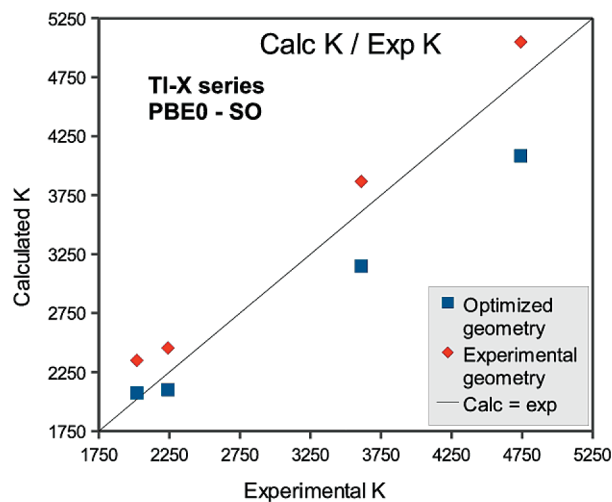
Figure 5. Computed vs experimental reduced couplings (in 10^{19} T^2 J^{-1}) of the Tl–X (X = F, Cl, Br, I) diatomics for PBE0, spin–orbit ZORA calculations: Optimized (BP/ZORA/TZP, blue square markers) and experimental bond lengths (orange diamond markers).

in the spin-free PBE0 calculation (which yields the best results for this molecule).

2. Small Couplings. It has been pointed out above that the hybrid functional performance is superior for most of the smallest coupling constants. This is shown explicitly in Figure 6 where the coupling constants are plotted on a smaller scale. In particular, for a group of very small Pb couplings, with magnitudes of less than 50×10^{19} T^2 J^{-1}, the inclusion of HF exchange in the functional brings the results closer to experiment. The same behavior is observed for the SO relativistic computations. For the small coupling constants, which may afford large relative deviations from experiment, the hybrid functional appears to be particularly beneficial.

3. Huge Sn Couplings. In this study, the performance of the functionals was also tested for some very large *J*-coupling constants. In general, reduced couplings involving Hg tend to be very large, and the 'world record' holders among coupling constants are therefore not surprisingly Hg–Hg one-bond couplings.[19,70−72] Herein, we considered some very large coupling constants between a heavy metal and the Sn nucleus. As seen above, for the largest coupling, ^2J(Hg–Sn) in IrCl(SnCl$_3$)(HgCl)(CO)(PH$_3$)$_2$, the deviation from experiment is always large, both in absolute and relative terms.

However, this is not a general behavior for Sn couplings. For example, the ^1J(Pt–Sn) coupling is within 1% of the experimental value (absolute deviation = 240×10^{19} T^2 J^{-1}). Also, the behavior of these couplings with respect to the functional is different: For the Hg–Sn coupling, the error is larger with PBE0 while the Pt–Sn coupling constant is closer to experiment with the hybrid functional.

4. Model Compounds. In order to reduce the computational resource requirements for some of the calculations a few large compounds considered in this study have been replaced by smaller models. These complexes are IrCl(SnCl$_3$)(HgCl)(CO)(P(C$_6$H$_5$)$_3$)$_2$, W(CC(CH$_3$)$_3$)(CH$_2$C-(CH$_3$)$_3$)$_3$, and Tl$_4$(OC(CH$_3$)$_3$)$_4$). For the Hg system, a model compound was calculated where triphenylphosphine was replaced by PH$_3$. For the other systems methyl has replaced *tert*-butyl. The models for the ligands along with a missing treatment of solvent and dynamic effects are likely responsible for part of the deviations between the computations and experiment. Whether the approximations for the ligands have a large impact, however, is unclear at this time. The Hg system has been discussed in the previous paragraph. For the W and Tl compounds, the absolute mean deviation from experiment is 61.3×10^{19} T^2 J^{-1}, and the relative mean deviation is 8.4% for the PBE spin–orbit calculations which agree best with experiment. The corresponding data are 197.4 $\times 10^{19}$ T^2 J^{-1} and 53.7%, respectively, for the PBE0 spin–orbit computations which agree worst with experiment. The performance of the calculations for these systems is similar to the average performances for the whole test set for three of the four computational models, except for PBE0 spin–orbit where ^2J(^{203}Tl$-^{205}$Tl) is strongly overestimated with this method.

IV. Concluding Remarks and Outlook

It is not easy to achieve good agreement between computations and experiment for heavy atom *J*-coupling constants in heavy metal systems. It has previously been pointed out that relativistic effects serve as a kind of 'magnifying glass' for subtle effects in the bonding in such systems,[4] which is one of the reasons for these difficulties. Any approximation in the computational model is 'felt' by this sensitive molecular property. Nonetheless, from the results in this benchmark study, a reasonably good performance of the hybrid functional PBE0 in the computations of spin–spin coupling constant with heavy metal atoms can be observed.
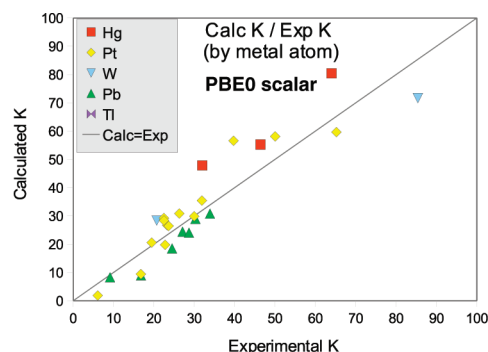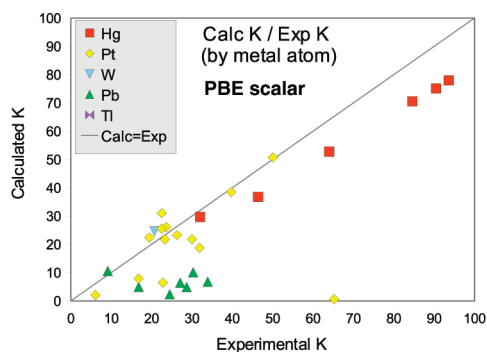

Figure 6. Computed vs experimental reduced couplings (in 10^{19} T^2 J^{-1}) for scalar ZORA, PBE vs PBE0, for |*K*| < 100: (left) PBE, (right) PBE0.

Spin−Spin Coupling in Heavy Metal Compounds

J. Chem. Theory Comput., Vol. 6, No. 1, 2010 **233**

The good performance includes the representation of two-bond coupling constants in heavy metal systems, which have not previously been benchmarked. The inclusion of spin−orbit coupling in the calculations does not consistently lead to improved agreement with experiment across the whole test set, and its application must be analyzed more carefully. This finding can only mean that exclusion of SO coupling is in some cases balancing errors resulting from other approximations.

The systematic use of DFT-optimized structures is considered beneficial for the purpose of this paper since it makes all computations subject to similar potential deficiencies in the geometries. This way, the errors in the *J* couplings due to the optimizations are part of the whole assessment of each computational model. Overall, the most sophisticated computational model in which the *J* couplings are computed with SO coupling and with the hybrid functional performs best on average with a $12.5 \pm 9.4\%$ median deviation. Outliers are still present in this computational model, as evidenced by the larger relative mean absolute error of 22.4%, which also has a large standard deviation. This computational model should be considered satisfactory for discussing trends in the *J* couplings for a wide range of sixth-row heavy atom spin−spin coupling constants and to analyze the results in chemically meaningful terms. Much better quantitative agreement with experiment, i.e., setting a goal of reducing these deviations by an order of magnitude, is likely to require dynamic models including sophisticated treatment of solvent effects along with better density functionals (or explicitly correlated wave function methods), more flexible basis sets, and possibly a more accurate treatment of relativistic effects beyond ZORA. Regarding the latter, numerical and basis set DFT calculations of ZORA hyperfine integrals of heavy atom semicore and valence orbitals needed for the calculations of *J* coupling have revealed that they are within less than 1% deviation of the four-component relativistic results.[73] Since *J* coupling is a valence property (i.e., in heavy element compounds the contributions from atomic core orbitals for which ZORA affords significant errors are negligible[15,74]), approximations other than the relativistic model are likely to be of higher importance.

Supporting Information Available: Optimized geometries for all systems in the test set, and calculated and experimental *J* couplings. This material is available free of charge via the Internet at http://pubs.acs.org.

References

(1) Facelli, J. C. Shielding Calculations. In *Encyclopedia of Nuclear Magnetic Resonance*; Grant, D. M., Harris, R. K., Eds.; John Wiley & Sons: Chichester, 2002; Vol. 9, pp 332−333.

(2) Helgaker, T.; Jaszuński, M.; Ruud, K. *Chem. Rev.* **1999**, *99*, 293–352.

(3) Kowalewski, J. *Annu. Rep. NMR Spectrosc.* **1982**, *12*, 81–176.

(4) Autschbach, J. *Coord. Chem. Rev.* **2007**, *251*, 1796–1821.

(5) Autschbach, J.; Ziegler, T. *Coord. Chem. Rev.* **2003**, *238/239*, 83–126.

(6) Autschbach, J.; Zheng, S. *Annu. Rep. NMR Spectrosc.* **2009**, *67*, 1–95.

(7) Enevoldsen, T.; Visscher, L.; Saue, T.; Jensen, H. J. A.; Oddershede, J. *J. Chem. Phys.* **2000**, *112*, 3493–3498.

(8) Autschbach, J.; Ziegler, T. *J. Chem. Phys.* **2000**, *113*, 936–947.

(9) Autschbach, J.; Ziegler, T. *J. Chem. Phys.* **2000**, *113*, 9410–9418.

(10) Filatov, M.; Cremer, D. *J. Chem. Phys.* **2004**, *120*, 11407–11422.

(11) Melo, J. I.; Ruiz de Azúa, M. C.; Peralta, J. E.; Scuseria, G. E. *J. Chem. Phys.* **2005**, *123*, 204112–7.

(12) Autschbach, J. *J. Chem. Phys.* **2008**, *129*, 094105–9. Autschbach, J. Erratum. *J. Chem. Phys.* **2009**, *130*, 209901.

(13) Autschbach, J. *ChemPhysChem* **2009**, *10*, 2274–2283.

(14) Le Guennic, B.; Matsumoto, K.; Autschbach, J. *Magn. Reson. Chem.* **2004**, *42*, S99–S116.

(15) Autschbach, J. *J. Chem. Phys.* **2007**, *127*, 124106–11.

(16) Boshaalaa, A. M. A.; Simpson, S. J.; Autschbach, J.; Zheng, S. *Inorg. Chem.* **2008**, *47*, 9279–9292.

(17) Autschbach, J.; Le Guennic, B. *J. Chem. Educ.* **2007**, *84*, 156–171.

(18) Autschbach, J.; Le Guennic, B. *J. Am. Chem. Soc.* **2003**, *125*, 13585–13593.

(19) Autschbach, J.; Sterzel, M. *J. Am. Chem. Soc.* **2007**, *129*, 11093–11099.

(20) Chen, W.; Liu, F.; Matsumoto, K.; Autschbach, J.; Le Guennic, B.; Ziegler, T.; Maliarik, M.; Glaser, J. *Inorg. Chem.* **2006**, *45*, 4526–4536.

(21) Autschbach, J.; Ziegler, T. *J. Am. Chem. Soc.* **2001**, *123*, 3341–3349.

(22) Autschbach, J.; Ziegler, T. *J. Am. Chem. Soc.* **2001**, *123*, 5320–5324.

(23) Baerends, E. J. *Amsterdam Density Functional, SCM*; Theoretical Chemistry, Vrije Universiteit: Amsterdam, The Netherlands, http://www.scm.com.

(24) van Lenthe, E.; Baerends, E. J.; Snijders, J. G. *J. Chem. Phys.* **1994**, *101*, 9783–9792.

(25) van Lenthe, E.; Ehlers, A.; Baerends, E. J. *J. Chem. Phys.* **1999**, *110*, 8943–8953.

(26) Okada, S.; Shinada, M.; Matsuoka, O. *J. Chem. Phys.* **1990**, *93*, 5013–5019.

(27) Ishikawa, Y.; Nakajima, T.; Hada, M.; Nakatsuji, H. *Chem. Phys. Lett.* **1998**, *283*, 119–124.

(28) Vaara, J.; Ruud, K.; Vahtras, O.; Ågren, H.; Jokisaari, J. *J. Chem. Phys.* **1998**, *109*, 1212–1222.

(29) Vosko, S. H.; Wilk, L.; Nusair, M. *Can. J. Phys.* **1980**, *58*, 1200–1211.

(30) Perdew, J. P.; Burke, K.; Ernzerhof, M. *Phys. Rev. Lett.* **1996**, *77*, 3865–3868.

(31) Adamo, C.; Barone, V. *J. Chem. Phys.* **1999**, *110*, 6158–6170.

(32) Ye, A.; Patchkovskii, S.; Autschbach, J. *J. Chem. Phys.* **2007**, *127*, 074104−13.

(33) Bryce, D.; Autschbach, J. *Can. J. Chem.* **2009**, *87*, 927–941.

(34) Watson, M. A.; Handy, N. C.; Cohen, A. J.; Helgaker, T. *J. Chem. Phys.* **2004**, *120*, 7252–7261.

(35) Pye, C. C.; Ziegler, T. *Theor. Chem. Acc.* **1999**, *101*, 396–408.

(36) te Velde, G.; Baerends, E. J. *J. Comput. Phys.* **1992**, *99*, 84–98.

(37) WebElements, http://www.webelements.com.

(38) Becke, A. D. *Phys. Rev. A* **1988**, *38*, 3098–3100.

(39) Perdew, J. P. *Phys. Rev. B* **1986**, *33*, 8822–8824.

(40) Waller, M. P.; Braun, H.; Hojdis, N.; Bühl, M. *J. Chem. Theory Comput.* **2007**, *3*, 2234–2242.

(41) Bühl, M.; Reimann, C.; Pantazis, D. A.; Bredow, T.; Neese, F. *J. Chem. Theory Comput.* **2008**, *4*, 1449–1459.

(42) Furche, F.; Perdew, J. P. *J. Chem. Phys.* **2006**, *124*, 044103−27.

(43) Sebald, A.; Wrackmeyer, B. *J. Magn. Reson.* **1985**, *63*, 397–400.

(44) Wu, G.; Kroeker, S.; Wasylishen, R. E. *Inorg. Chem.* **1995**, *34*, 1595–1598.

(45) Brown, A. J.; Howarth, O. W.; Moore, P. *J. Chem. Soc., Dalton Trans.* **1976**, 1589–1592.

(46) Eujen, R.; Lagow, R. J. *J. Chem. Soc., Dalton Trans.* **1978**, 541–544.

(47) Kretschmer, M.; Pregosin, P. S. *J. Org. Chem.* **1983**, *253*, 17–30.

(48) Benn, R.; Büch, H. M.; Reinhardt, R.-D. *Magn. Reson. Chem.* **1985**, *23*, 559–564.

(49) Hao, N.; McGlinchey, M. J.; Sayer, B. G.; Schrobilgen, G. J. *J. Magn. Reson.* **1982**, *46*, 158–162.

(50) Xu, Q.; Heaton, B. T.; Jacob, C.; Mogi, K.; Ichihashi, Y.; Souma, Y.; Kanamori, K.; Eguchi, T. *J. Am. Chem. Soc.* **2000**, *122*, 6862–6870.

(51) Maliarik, M.; Glaser, J.; Tóth, I. *Inorg. Chem.* **1998**, *37*, 5452–5459.

(52) Paonessa, R. S.; Trogler, W. C. *J. Am. Chem. Soc.* **1982**, *104*, 1138–1140.

(53) Goggin, P. L.; Goodfellow, R. J.; Haddock, S. R.; Knight, J. R.; Reed, F. J. S.; Taylor, B. F. *J. Chem. Soc., Dalton Trans.* **1974**, 523–533.

(54) Rochon, F. D.; Bubulei, V. *Inorg. Chim. Acta* **2004**, *357*, 2218–2230.

(55) Musco, A.; Pontellini, R.; Grassi, M.; Sironi, A.; Meille, S. V.; Rüegger, H.; Ammann, C.; Pregosin, P. S. *Organometallics* **1988**, *7*, 2130–2137.

(56) Mann, B. E. *J. Chem. Soc., Dalton Trans.* **1973**, 2012–2015.

(57) Keiter, R. L.; Verkade, J. G. *Inorg. Chem.* **1969**, *8*, 2115–2120.

(58) Fischer, E. O.; Knauss, L.; Keiter, R. L.; Verkade, J. G. *J. Organomet. Chem.* **1972**, *37*, C7−C10.

(59) Caldarelli, S.; Catalano, D.; Di Bari, L.; Pasquali, M.; Veracini, C. A. *Gazz. Chim. Ital.* **1990**, *120*, 211–213.

(60) Banck, J.; Schwenk, Z. *Z. Phys. B* **1975**, *20*, 75–80.

(61) Young, C. G.; Kober, E.; Enemark, J. H. *Polyhedron* **1987**, *6*, 255–259.

(62) Hawk, R. M.; Sharp, R. R. *J. Chem. Phys.* **1974**, *60*, 1009–1017.

(63) McFarlane, W. *Mol. Phys.* **1967**, *13*, 587–588.

(64) Schumann, C.; Dreeskamp, H. *J. Magn. Reson.* **1970**, *3*, 204–217.

(65) Clarck, R. J. H.; Davles, A. G.; Puddephatt, R. J.; McFarlane, W. *J. Am. Chem. Soc.* **1969**, *91*, 1334–1339.

(66) Bryce, D. L.; Wasylishen, R. E. *J. Am. Chem. Soc.* **2000**, *122*, 3197–3205.

(67) Zechmann, C. A.; Boyle, T. J.; Pedrotty, D. M.; Lang, D. P.; Scott, B. L. *Inorg. Chem.* **2001**, *40*, 2177–2184.

(68) Berg, K. E.; Blixt, J.; Glaser, J. *Inorg. Chem.* **1996**, *35*, 7074–7081.

(69) Huber, K.; Herzberg, G. Constants of Diatomic Molecules. In *NIST Chemistry WebBook, NIST Standard Reference Database Number 69*; Mallard, W. G., Linstrom, P. J., Eds.; National Institute of Standards and Technology: Gaithersburg MD, 2005; data prepared by J. W. Gallagher and R. D. Johnson, III. URL: http://webbook.nist.gov.

(70) Gillespie, R. J.; Granger, P.; Morgan, K. R.; Schrobilgen, G. J. *Inorg. Chem.* **1984**, *23*, 887–891.

(71) Malleier, R.; Kopacka, H.; Schuh, W.; Wurst, K.; Peringer, P. *Chem. Commun.* **2001**, 51–52.

(72) Autschbach, J.; Igna, C. D.; Ziegler, T. *J. Am. Chem. Soc.* **2003**, *125*, 4937–4942.

(73) Autschbach, J. *Theor. Chem. Acc.* **2004**, *112*, 52–57.

(74) Khandogin, J.; Ziegler, T. *Spectrochim. Acta* **1999**, *A 55*, 607–624.

(75) Moss, R. E.; Trivedi, H. P. *Mol. Phys.* **1979**, *38*, 1611–1619.

(76) Morrison, J. D.; Moss, R. E. *Mol. Phys.* **1980**, *41*, 491–507.

(77) Schwartz, C. *Ann. Phys.* **1959**, *2*, 156–169.

(78) There are classes of problems where low-order perturbation theory with variationally unstable operators yields well-defined results, although higher order perturbation theory may yield divergent terms. For examples involving operators with δ-function terms see refs 75−77. In such a situation finite-field differentiations can be difficult to keep under control, numerically.

(79) Calculated as MD = median$_i$($|X_i−$median$_j(X_j)|$).

CT900535D

JCTC Journal of Chemical Theory and Computation

New Formulation and Implementation of Vibrational Self-Consistent Field Theory

Mikkel B. Hansen,*,[†] Manuel Sparta,[†] Peter Seidler,[†] Daniele Toffoli,[†,‡] and Ove Christiansen[†]

The Lundbeck Foundation Center for Theoretical Chemistry, Center for Oxygen Microscopy and Imaging, Department of Chemistry, University of Aarhus, Langelandsgade 140, DK 8000 Aarhus C, Denmark, and Department of Chemistry, Middle East Technical University, 06531 Ankara, Turkey

Abstract: A new implementation of the vibrational self-consistent field (VSCF) method is presented on the basis of a second quantization formulation. A so-called active terms algorithm is shown to be a significant improvement over a standard implementation reducing the computational effort by one order in the number of degrees of freedom. Various types of screening provide even further reductions in computational scaling and absolute CPU time. VSCF calculations on large polyaromatic hydrocarbon model systems are presented. Further, it is demonstrated that in cases where distant modes are not directly coupled in the Hamiltonian, down to linear scaling of the required CPU time with respect to the number of vibrational modes can be obtained. This is illustrated with calculations on simple model systems with up to 1 million degrees of freedom.

1. Introduction

A central topic in modern theoretical chemistry is the search for linear scaling algorithms for the calculation of the electronic structure of molecular systems. By linear scaling it is meant that the computational effort scales linearly with the size of the system. While traditionally electronic structure methods have had much steeper computational scaling, there has been significant progress in reducing the computational scaling, in particular with respect to the self-consistent field types of methods including Hartree−Fock and density functional theory.[1−3] While linear scaling methods for more advanced and accurate electronic structure methods have been more slow in coming, there have been activity and progress along these lines as well.[3−6]

While calculation of the electronic structure is a very fundamental issue and in many cases the logical first step toward a theoretical description of a molecule, understanding the dynamics of large and complex systems is another fundamental challenge of modern theoretical chemistry. In that framework the working conditions have been significantly different. Classical molecular dynamics (MD) is probably still the most widely used tool for studying the dynamics of large molecular systems. However, classical MD per definition involves a fundamental error in the complete neglect of quantum effects. On the other hand, quantum dynamical methods have generally proven to have a very steep, often exponential, computational scaling with the size of the system. Thus, quantum dynamical methods have very rarely been applicable to larger systems.[7−9] Obviously, this is a problem as more and more research, both theoretical and experimental, focuses on large molecular systems.

The self-consistent field method in either time-independent form, known as vibrational self-consistent field (VSCF) theory,[10,11] or in the time-dependent form (TD-SCF), sometimes also denoted time-dependent Hartree (TDH), is complementary to classical MD in two ways: (i) the theory is completely quantum mechanical in nature in contrast to the classical MD; (ii) it involves the construction of the best possible separation of motion in a self-consistently determined mean field in contrast to the full correlation of the degrees of freedom in classical MD. In this study we shall discuss further the use of VSCF. As in electronic Hartree−

---

* Corresponding author e-mail: mbh@chem.au.dk.

† University of Aarhus.

‡ Middle East Technical University.

Fock theory, the VSCF method from the outset involves significant approximations. However, VSCF is sometimes good enough, and furthermore it acts as the stepping stone to a variety of more advanced approaches.

It has very recently been shown that for a Hamiltonian coupling at most two modes, advanced methods such as vibrational coupled cluster (VCC) with up to two-mode excitations (VCC[2]) can be made to scale cubically with the system size.[12] In the limit where each mode has only significant interactions with a limited set of other modes, essentially linear scaling was demonstrated for the key steps in the VCC algorithm. However, the relevance of this is based on the assumption that the VSCF state can be obtained in an insignificant amount of time, since usually VSCF provides the reference state and optimal one-mode basis functions. In this paper, we illustrate how VSCF in a simple implementation also scales cubically for a two-mode Hamiltonian, but a much improved active terms algorithm can bring down the scaling to quadratic. Introducing various screenings and other tricks, the scaling and absolute computational effort can be reduced even further. As for VCC, and with even lower computational cost, linear scaling can be obtained if the mode−mode interactions are only local when proceeding to systems with many degrees of freedom. Our new VSCF approach is based on a second quantization formulation.[13] The second quantization formulation of the many body problem was decisive for the development of the many-mode VCC approach. This work is the first detailed second quantization based realization of a VSCF implementation.

There are a few other perspectives on fast VSCF methods. A new approach for the construction of potential energy surfaces (PESs) denoted adaptive density guided approach[14] (ADGA) uses VSCF one-mode functions to construct one-mode densities which are used as auxiliary quantities in an iterative construction of the PES on a set of grids. The densities are used (i) to guide the addition of new grid points, (ii) to update the grid boundaries, and (iii) in the convergence checks of the iterative algorithm. Clearly, it is essential that the VSCF equations can be solved very efficiently to avoid overhead in this procedure. In addition to relying on the VSCF method, the final PES generated using ADGA may also provide savings in the vibrational structure calculations due to a more compact representation of the PES. Although our main focus will be on the VSCF algorithm itself, this paper also discusses further how the ADGA can provide additional savings with respect to both PES construction and vibrational wave function calculations using both VSCF and post-VSCF methods.

The number of vibrational states increases strongly with the size of the system. For larger molecules and significant temperatures, the population of many excited vibrational states introduces additional contributions to molecular properties in a thermodynamic framework. VSCF can also be a very useful tool in this respect. With the algorithms of this work VSCF is now so fast that it is in fact conceivable to calculate many millions of states explicitly. Furthermore, a recently introduced approach for combining anharmonic wave functions with statistical mechanics has the determination of the VSCF reference state as the rate limiting step.[15]

Fast VSCF methods are thus open for calculating quantum anharmonic partition functions and temperature-dependent vibrational contributions to properties.[15]

In section 2 we describe the theory behind our approach. We begin with a brief account of the construction and form of the Hamiltonian since that is used later. However, the choice and construction of the coordinates are not discussed in any detail. The CPU times and scalings discussed in this paper will focus on the anharmonic vibrational wave function step. The construction of the PES can certainly be the rate determining step in many calculations, but this depends on the cost of single points (high-accuracy correlated ab initio, density functional theory (DFT), semiempirical, or even classical force field) and only the number of single-point evaluations are discussed in this work. After this background we discuss a second quantization formulation of VSCF and an accompanying implementation. This includes the active terms algorithm and various additional steps taken to reduce scaling and absolute cost. All these aspects are then explored in test calculations on all fundamental vibrations in polyaromatic hydrocarbons (PAHs) of increasing size. The computational details are described in section 3, and the results are discussed in section 4. Finally, in section 5 we give a summary and outlook.

2. Theory

2.1. Representation of the Hamiltonian. In mass-weighted normal coordinates, the rovibrational Hamiltonian,

$$H = T + V \tag{1}$$

is given by the Watson operator.[16] In the simplest case where the interaction between rotation and vibration is neglected, the kinetic energy operator is approximated as a sum of one-mode operators, $T = -(1/2)\Sigma_m d^2/dq_m^2$. More generally, one can include the terms accounting for vibrational angular momentum and effective inverse moments of inertia which are of importance in some systems. However, this is only a minor detail in the context of this work and will not be considered further here.

The construction of the PES, V, is an area of much research; see, e.g., ref 17 and references therein. Normal modes are nonlocal by construction and may conveniently reduce some couplings in size, but the PES described in nonlocal coordinates may not exhibit in a useful way the expected decay of the size of couplings with distance. A converging series of approximate PESs is introduced,

$$V^{(1)}, \ V^{(2)}, \ ..., \ V^{(M)} \tag{2}$$

where $V^{(1)}$ corresponds to the uncoupled anharmonic oscillator approximation, $V^{(2)}$ includes all couplings among pairs of modes as well, etc. Eventually, the fully coupled M-mode PES, $V^{(M)}$, may be recovered. The use of such restricted mode coupling expansions has become widespread.[18−23] In practical terms, this means that the PES is written as a sum of low-dimensional subpotentials,

$$V = \sum_{\mathbf{m}} \bar{V}^{\mathbf{m}} \tag{3}$$

In eq 3 the subpotentials $\bar{V}^{\mathbf{m}}$ are functions only of the modes given in the mode combination (MC) $\mathbf{m}$ and defined such that the function is zero if any of the corresponding coordinates are zero. For instance, $\bar{V}^{m_1,m_2}$ embodies the true two-mode coupling between modes m_1 and m_2, and it is related to the original potential function as $\bar{V}^{m_1,m_2}(q_{m_1},q_{m_2}) = V(...,0,q_{m_1},0, ...,0, q_{m_2}, ...) - V(...,0,q_{m_1} = 0,0, ...,0, q_{m_2}, ...) - V(...,0,q_{m_1},0, ...,0, q_{m_2} = 0, ...)$.

It is computationally convenient to work with a Hamiltonian in the sum over products (SOP) form,

$$H = \sum_{t=1}^{N_t} c_t \prod_{m=1}^{M} h^{m,t} = \sum_{t=1}^{N_t} c_t \prod_{m \in \mathbf{m}^t} h^{m,t} = \sum_{t=1}^{N_t} c_t H^{\mathbf{m}^t} \quad (4)$$

where N_t is the number of terms in the operator and $\mathbf{m}^t$ is a MC denoting the set of modes that have one-mode operators $h^{m,t}$ different from the unit operator in that particular term.

It has previously been shown how a Hamiltonian in the form of eq 4 can be very useful for efficient implementation of quantum dynamics codes, e.g., within the multiconfigurational time-dependent Hartree (MCTDH) framework[24] and for VCC wave functions.[12] Clearly, the Hamiltonian is not directly given in the SOP form, and it must be part of our numerical procedure to construct it in this way.

The simplest method is based on a Taylor expansion of the PES around the equilibrium geometry which clearly provides the PES in the required SOP form. Another method involves the calculation of the PES on a set of grid points, and an analytical representation of the PES is then obtained by a least-squares fitting with a multivariate polynomial function of sufficiently high degree.[17] The combined use of the restricted mode coupling expansion, eq 3, and the fitting of the low dimensional subpotentials to a direct product polynomial basis ensures that the PES is eventually given in the SOP form, eq 4. A minor technical detail relevant later is that, for numerical stability, the fitting is done in frequency scaled normal coordinates, $\tilde{q}_i = (\omega_i)^{1/2} q_i$, ω_i being the harmonic frequency of the ith vibrational mode.

For both the Taylor expansion approach and the grid-based approach described above, the one-mode operators are simply normal coordinates in powers up to the degree of the polynomial expansion, D, i.e., q_m^i with $i = 1, 2, ..., D$, as well as second-order derivatives, $(\partial^2)/(\partial q_m^2)$. The integrals required for the implementation of VSCF using a Hamiltonian written in the SOP form are one-mode integrals of the type

$$h^{m,t}_{i^m j^m} = \langle \phi^m_{i^m}(q_m) | h^{m,t} | \phi^m_{j^m}(q_m) \rangle \quad (5)$$

Different ways of handling these integrals have been implemented depending on the form of the PES and the chosen basis set; see refs 14 and 17. In any case, there are only a few integrals per mode and the integral evaluation is one-dimensional and can thus be done simply and fast. In fact, due to the choice of a SOP operator, the integral part becomes independent of the dimensionality of the PES. The integral part always scales linearly with respect to the size of the system with a very low prefactor. The calculation and

storage of the one-mode integrals are therefore never limiting factors in the calculations and will not be discussed any further.

The above procedures for obtaining analytical representations of the potential part of the vibrational Hamiltonian relies on the ability to perform accurate fits to multidimensional grids of points. For systems with strongly coupled modes, this might not be straightforward, but the ability to use fairly high polynomium degrees (say on the order of 14) provides some flexibility. The problem is mentioned here for completeness. We also note in passing that other approaches circumventing this step are widespread.[18,25,26]

2.2. Adaptive Density-Guided Approach for the PES Construction. The ADGA was developed to provide a robust, accurate, and black-box procedure for constructing molecular PESs. ADGA uses the reduced density of the nuclear wave function to iteratively tailor the grids (both the spatial extension and mesh) onto which each of the potential energy functions are evaluated. By using the quantity $\rho V^{\mathbf{m}}$, where ρ is the density of the VSCF wave function and $V^{\mathbf{m}}$ is the potential energy function for the given MC, $\mathbf{m}$, the MCs containing modes which are not strongly coupled will be given a compact representation based on only a few single-point calculations. More important couplings will be given a more elaborate form based on many more sampling points. As a consequence, the number and placement of the single-point energy calculations are optimized, thus reducing considerably the CPU time spent in the construction of the PES and potentially improving accuracy at the same time. As an additional advantage, the more compact representation of in particular weak couplings can potentially improve the computational scaling of the vibrational wave function calculations. For instance, a weak two-mode coupling may in the most favorable case be represented simply through the terms $q_i q_j$, $q_i^2 q_j$, $q_i q_j^2$, and $q_i^2 q_j^2$, which is obviously computationally cheaper to handle than a high-order polynomial approximation. In fact, as the system grows larger, one can expect that the ratio between the number of weak and strong mode couplings increases and it is therefore essential to have a method capable of approximating with minimal cost the weak couplings. For a complete overview of the adaptive procedure we refer to refs 14 and 27.

2.3. Vibrational Self-Consistent Field Theory. We begin our derivation by noting that whereas previous formulations of VSCF theory have been done in first quantization, we choose to work in the second quantization formalism introduced in ref 13. Note that this second quantization formalism is different from the harmonic oscillator step-up/step-down operator formulation sometimes used in vibrational theory. The advantages of second quantization in relation to VSCF will become apparent during the course of the derivation.

The VSCF ansatz for the wave function of a system with M modes is written as

$$|\text{VSCF}\rangle = \exp(\kappa)|\Phi_{\mathbf{i}}\rangle = \exp\left(\sum_{m=1}^{M} \sum_{p^m q^m} \kappa^m_{p^m q^m} E^m_{p^m q^m} \right)|\Phi_{\mathbf{i}}\rangle$$

$$(6)$$

The reference state is given by

$$|\Phi_{\mathbf{i}}\rangle = \prod_{m=1}^{M} a_{i^m}^{m\dagger}|\text{vac}\rangle \tag{7}$$

where $\mathbf{i}$ is a vector indicating for each mode which modal is occupied in the reference state, and

$$E_{p^m q^m}^m = a_{p^m}^{m\dagger} a_{q^m}^m \tag{8}$$

The basic creation and annihilation operators, $a_{r^m}^{m\dagger}$ and $a_{r^m}^m$, satisfy the commutator relations

$$[a_{r^m}^m, a_{s^{m'}}^{m'\dagger}] = \delta_{mm'}\delta_{r^m s^{m'}} \tag{9}$$

$$[a_{r^m}^m, a_{s^{m'}}^{m'}] = [a_{r^m}^{m\dagger}, a_{s^{m'}}^{m'\dagger}] = 0 \tag{10}$$

and the killer condition,

$$a_{r^m}^m|\text{vac}\rangle = 0 \tag{11}$$

The operator κ is antihermitian such that $\exp(\kappa)$ is unitary and the exponential prefactor therefore generates rotations among the modals.

The optimal VSCF modals are obtained by invoking the variational principle on the modal rotation parameters, $\kappa_{p^m q^m}^m$, of the VSCF energy,

$$E_{\text{VSCF}} = \langle\Phi_{\mathbf{i}}|\exp(-\kappa)H\exp(\kappa)|\Phi_{\mathbf{i}}\rangle \tag{12}$$

giving

$$0 = \frac{\partial}{\partial\kappa_{r^m s^m}^m}\langle\Phi_{\mathbf{i}}|\exp(-\kappa)H\exp(\kappa)|\Phi_{\mathbf{i}}\rangle \tag{13}$$

By inserting the expression for the κ operator, eq 6, into eq 13, one obtains straightforwardly, for $\kappa = 0$, that the criterion for having an optimal $|\Phi_{\mathbf{i}}\rangle$ state is

$$0 = \langle\Phi_{\mathbf{i}}|[H, E_{r^m s^m}^m]|\Phi_{\mathbf{i}}\rangle \tag{14}$$

This is the VSCF analogue of the Brillouin condition. An effective mean-field operator for mode m, $F^{m,\mathbf{i}}$, may be introduced with matrix elements[13] (notice that there is an unfortunate sign error in eq 59 of ref 13).

$$F_{r^m s^m}^{m,\mathbf{i}} = \langle\Phi_{\mathbf{i}}|[[a_{r^m}^m, H], a_{s^m}^{m\dagger}]|\Phi_{\mathbf{i}}\rangle \tag{15}$$

By applying the basic second quantization commutator relations, the nonredundant elements, corresponding to occupied-virtual rotations, are given by

$$F_{i^m a^m}^{m,\mathbf{i}} = \langle\Phi_{\mathbf{i}}|[H, E_{a^m i^m}^m]|\Phi_{\mathbf{i}}\rangle \tag{16}$$

$$F_{a^m i^m}^{m,\mathbf{i}} = -\langle\Phi_{\mathbf{i}}|[H, E_{i^m a^m}^m]|\Phi_{\mathbf{i}}\rangle \tag{17}$$

where we have used i^m for occupied and a^m for virtual modals. The $F^{m,\mathbf{i}}$ matrix elements are thus directly related to the VSCF gradient terms, eq 14. A zero gradient for mode m may be obtained by diagonalizing the $F^{m,\mathbf{i}}$ matrix,

$$\mathbf{F}^{m,\mathbf{i}}\mathbf{C}^m = \mathbf{C}^m\boldsymbol{\varepsilon}^m \tag{18}$$

for all modes. In eq 18, $\mathbf{C}^m$ is a matrix containing the current set of optimized modals while $\boldsymbol{\varepsilon}^m$ is a diagonal matrix holding the corresponding modal energies. An outline of our VSCF procedure will be given in a subsequent section.

At this point, we note that the computationally demanding part of the self-consistent scheme is the construction of the $\mathbf{F}^{m,\mathbf{i}}$ matrix which involves the Hamiltonian. The Hamiltonian in SOP form, see eq 4, can in second quantization be represented as

$$H = \sum_t c_t \prod_{m'\in\mathbf{m}^t} \sum_{p^{m'} q^{m'}} h_{p^{m'} q^{m'}}^{m',t} E_{p^{m'} q^{m'}}^{m'} \tag{19}$$

where the integrals, $h_{p^{m'} q^{m'}}^{m',t}$, are given by eq 5. The effective operator in eq 15 may thus be written

$$F_{r^m s^m}^{m,\mathbf{i}} = \sum_t c_t \langle\Phi_{\mathbf{i}}|[[a_{r^m}^m, \prod_{m'\in\mathbf{m}^t} \sum_{p^{m'} q^{m'}} h_{p^{m'} q^{m'}}^{m',t} E_{p^{m'} q^{m'}}^{m'}], a_{s^m}^{m\dagger}]|\Phi_{\mathbf{i}}\rangle \tag{20}$$

This may be simplified by using the commutator relations

$$[A, B_1 B_2 ... B_N] = \sum_{i=1}^{N} B_1 B_2 ... B_{i-1}[A, B_i]B_{i+1}...B_N \tag{21}$$

$$[[a_{r^m}^m, E_{p^{m'} q^{m'}}^{m'}], a_{s^m}^{m\dagger}] = \delta_{r^m p^{m'}}\delta_{s^m q^{m'}}\delta_{mm'} \tag{22}$$

the latter of which follows directly from eqs 9–11.

From the $\delta_{mm'}$ in eq 22, it follows that if mode m is not contained in term t, it simply evaluates to zero and one needs not to consider that term in the construction of the $\mathbf{F}^{m,\mathbf{i}}$ matrix. This defines our active terms algorithm: In the process of evaluating the effective $\mathbf{F}^{m,\mathbf{i}}$ operator, we partition the terms of the Hamiltonian into two sets. The first set contains terms which are active for mode m, i.e., have a nonzero double commutator or, equivalently, have a nonunit one-mode operator for that mode. The other set contains the remaining terms which are inactive, i.e., only contain the unit operator for mode m. Mathematically, we are thus working with two sets of operator terms, $\{t_{\text{act.}}|t: \mathbf{m}^t \cap \{m\} = \{m\}\}$ and $\{t_{\text{inact.}}|t: \mathbf{m}^t \cap \{m\} = \{\}\}$.

For the active terms, eq 20 finally evaluates to

$$F_{r^m s^m}^{m,\mathbf{i}} = \sum_{t\in\{t_{\text{act.}}\}} c_t \prod_{m'\in\mathbf{m}^t\backslash n} h_{i^{m'} i^{m'}}^{m',t} \times$$
$$\sum_{p^m q^m} h_{p^m q^m}^{m,t}\langle\text{vac}|a_{i^m}^m[[a_{r^m}^m, E_{p^m q^m}^m], a_{s^m}^{m\dagger}]a_{i^m}^{m\dagger}|\text{vac}\rangle \tag{23}$$
$$= \sum_{t\in\{t_{\text{act.}}\}} z^{m,t} h_{r^m s^m}^{m,t}$$

where we have introduced the effective factor

$$z^{m,t} = c_t \prod_{m'\in\mathbf{m}^t\backslash n} h_{i^{m'} i^{m'}}^{m',t} \tag{24}$$

We now turn briefly to first quantization where the mean-field operator for mode m assumes the form

$$^{FQ}\mathbf{F}^{m,\mathbf{i}} = \langle\prod_{m'\neq m}^{M} \phi_{i^{m'}}^{m'}|H|\prod_{m'\neq m}^{M} \phi_{i^{m'}}^{m'}\rangle \tag{25}$$

Here, the integration is understood to be only over the $M - 1$ other degrees of freedom. For a SOP operator in first quantization, eq 4, this leads to the following matrix elements,

$$^{FQ}F_{u^mv^m}^{m,\mathbf{i}} = \langle \chi_{u^m}|^{FQ}\mathbf{F}^{m,\mathbf{i}}|\chi_{v^m}\rangle = \sum_t c_t \langle \chi_{u^m}^m|h^{m,t}|\chi_{v^m}^m\rangle \prod_{m'\in\mathbf{m}^t\backslash m} h_{i^{m'}i^{m'}}^{m',t}$$

(26)

where $h^{m,t}$ is a one-mode operator working on mode m. In eq 26 it is assumed that the modals are given as a linear combination of primitive basis functions, χ_{u^m}; see, e.g., ref 10. If the Hamiltonian is partitioned into active and inactive terms, the following contributions to the $^{FQ}\mathbf{F}^{m,\mathbf{i}}$ matrix are derived, assuming normalized basis functions,

$$^{FQ}F_{u^mv^m}^{m,\mathbf{i},[\text{act.}]} = \sum_{t\in\{t_{\text{act.}}\}} z^{m,t} h_{u^mv^m}^{m,t}$$

(27)

$$^{FQ}F_{u^mv^m}^{m,\mathbf{i},[\text{inact.}]} = \delta_{u^mv^m} \sum_{t\in\{t_{\text{inact.}}\}} C_t \prod_{m'\in\mathbf{m}^t} h_{i^{m'}i^{m'}}^{m',t}$$

(28)

i.e., the active part is the same as the second quantization effective operator $\mathbf{F}^{m,\mathbf{i}}$; see eq 23. The inactive part, which is absent in the second quantization operator defined by eq 15, merely adds a constant to the diagonal. This constant contribution may be safely neglected in the course of the optimization since a constant added to the diagonal of a matrix does not affect its eigenvectors. Thus, one can introduce the same algorithm as in second quantization. However, in the latter case, the terms inactive for a given mode are naturally found not to contribute to the optimization.

2.4. Active Terms VSCF Algorithm. The optimization of the VSCF reference state may proceed in many ways. In this paper we pursue a direct first-order algorithm based upon eqs 14−18. Second-order algorithms can be constructed on the basis of the Hessian, i.e., the second-order derivatives of the VSCF energy expectation value, eq 12. However, so far we have found the first-order procedure to be sufficiently stable. Our algorithm is based on a simple structure where we solve the VSCF eigenvalue equations for one mode at a time. This requires the construction of the VSCF mean-field operator, $\mathbf{F}^{m,\mathbf{i}}$, and its subsequent diagonalization. This defines a new set of one-mode functions for this particular mode. The new occupied one-mode function is used in the construction of the VSCF mean-field operators for the other modes.

Thus, the algorithm for solving the VSCF equations proceeds as follows:

Loop over VSCF iterations
   Loop over all modes m
      Construct the $\mathbf{F}^{m,\mathbf{i}}$ matrix
      Diagonalize $\mathbf{F}^{m,\mathbf{i}}$
      Update $h_{i^mi^m}^{m,t}$ list
   Calculate the VSCF energy and test for convergence

The diagonalization is in the space of one-mode functions for a single mode and the matrix dimension is therefore $N^m \times N^m$, where N^m is the size of the one-mode basis used for the expansion of the modals for mode m. Thus, it is a local diagonalization independent of the size of the system with a computational cost depending only on the size of the basis set for each single mode. The update step calculates the integrals, $h_{i^mi^m}^{m,t}$, for the occupied level of each mode such that these are readily available when needed in the calculation of $\mathbf{F}^{m,\mathbf{i}}$ for other modes as well as the energy,

$$E = \sum_t c_t \prod_{m\in\mathbf{m}^t} h_{i^mi^m}^{m,t}$$

(29)

Given the Hamiltonian operator in the SOP form, eq 4, the active terms part for calculating $\mathbf{F}^{m,\mathbf{i}}$ in the self-consistent algorithm sketched above, proceeds as follows: We initially determine for each mode m the corresponding set of active terms in the Hamiltonian. Given this set, we, for each mode m, make a pass through the active terms for m. For each term we first calculate the $z^{m,t}$ factor by looping through the modes in the particular term, excluding the target mode m. After the $z^{m,t}$ factor has been constructed, the relevant one-mode integrals for mode m are multiplied with $z^{m,t}$ and the result added to $\mathbf{F}^{m,\mathbf{i}}$.

To set the above considerations into perspective, we note that a M mode Hamiltonian which couples all pairs of modes through its potential part has $M(M-1)/2$ couplings. For such an operator, only $M-1$ couplings will be active in a given mode; the remaining $(M-1)(M-2)/2$ couplings are inactive. Thus, the computational cost of constructing the $\mathbf{F}^{m,\mathbf{i}}$ matrix is reduced by a power of M simply by construction as the inactive terms need not be considered. Indeed, this order of reduction of the computational effort is gained for all potentials, regardless of the order of the coupling in the Hamiltonian; i.e., the computational complexity for the construction of a $\mathbf{F}^{m,\mathbf{i}}$ matrix involving a N-mode coupled Hamiltonian is reduced by the active terms algorithm as

$$\mathcal{O}(M^N) \rightarrow \mathcal{O}(M^{N-1})$$

(30)

M of these matrices must be constructed in each iteration, Thus, the total computational complexity decreases from $\mathcal{O}(M^{N+1})$ to $\mathcal{O}(M^N)$.

Assume that the number of active terms for each mode in the system is limited. More precisely, each mode m is coupled directly to a limited set of modes much smaller than the total set of modes. This means that there are many other modes, m', having no terms containing operators for both m and m'. If the active terms algorithm is employed, the time required for construction of the $\mathbf{F}^{m,\mathbf{i}}$ matrix is thus expected to be fairly constant with respect to the size of the system though still linear in the number of active terms per mode. Thereby, the scaling of the whole VSCF algorithm becomes linear in the number of modes. In total, the computational scaling of the active terms implementation scales roughly as the number of modes times the number of active terms per mode.

2.5. Screening. It is possible at various stages in the VSCF algorithm to avoid calculation of contributions that are numerically negligible.

Most trivially, terms in the Hamiltonian with c_t coefficients less than a certain threshold can be neglected. This is relevant since the automatic procedures for determining the PES may generate terms with essentially zero coefficients. This form of screening is employed already when reading in the operator, before the VSCF calculation.

In relation to the algorithm outlined above, screening on the basis of the magnitude of the $z^{m,t}$ factor in eq 24 has also been implemented. If the absolute value of $z^{m,t}$ times the norm

(square root of the sum of element norms squared) of the $h^{m,t}$ integrals is less than a certain threshold times the expected norm of the target quantity, $\mathbf{F}^{m,\text{act.}}$, the scaling of the $h^{m,t}$ integrals and addition of the contribution to the $\mathbf{F}^{m,\mathbf{i}}$ matrix are avoided. The latter method defines a more rigorous screening strategy but on the other hand also requires significantly more computational work compared to the screening on the Hamiltonian coefficients. We will in the following investigate both of these types of screening as well as a combination of the two.

2.6. Combination of Terms in the Hamiltonian. Yet another method for reducing the number of terms in the Hamiltonian, and thereby the computational cost, may be introduced by combining terms in the operator. Consider the Hamiltonian in eq 4. Each term is a product of one-mode operators. The terms can be grouped into sets where only the operator for a single mode differs between the terms. Each of these sets can be reduced to a single term by isolating the mode where the difference occurs, for instance for modes 0 and 1:

$$c_1 q_0^n q_1^a + c_2 q_0^n q_1^b + c_3 q_0^n q_1^c = q_0^n(c_1 q_1^a + c_2 q_1^b + c_3 q_1^c) \tag{31}$$

Here three terms have been reduced to one by introducing an effective one-mode operator that is simply a linear combination of the original ones. As a realistic example, consider a two-mode Hamiltonian with simple kinetic energy operators given by the second derivatives of the normal coordinates and a Taylor expanded PES of order D. In this case the individual operators are d^2/dq^2, and q^n, with $n = 1, 2, ..., D$. By combining terms, the number of one-mode operator terms is reduced from $M(D + 1)$ to M. The number of two-mode operator terms is reduced from $M(M - 1)D(D - 1)/4$ to $M(M - 1)D/2$, i.e,. by a factor of $(D - 1)/2$. We note here that the Taylor PESs are usually of low polynomial order, and more significant savings may be observed for a grid-based potential. The computational cost for this reduction comes in terms of the extra integrals needed to be handled corresponding to the combined one-mode operators. These integrals can be stored or calculated on the fly.

Combining terms reduces the total number of terms in the Hamiltonian. The CPU time depends rather directly on the number of terms per mode so there are potentially significant savings in CPU time by combining terms. We note that the computational scaling with respect to the size of the system is not changed by combining operator terms. The drawback of combining terms is that it introduces in one form or another additional storage and logic in the handling of the operator information.

2.7. Program. The VSCF method is implemented in the MidasCpp (Molecular Interactions, Dynamics and Simulation in C++/Chemistry Program Package) program.[28] The MidasCpp program also includes the discussed static and adaptive grid methods for generating potential energy and property surfaces. Interfaces to widely known electronic structure programs including DALTON, ACESII, CFOUR, and GAMESS are available in order to perform the electronic structure calculations needed for the construction of potential energy and molecular property surfaces.

3. Computational Details

In this study, we have investigated polyaromatic hydrocarbons (PAHs) consisting of 1−24 fused benzene rings with at most four rings in each row. The PAHs will be denoted PAHn, $n = 1, 2, ..., 24$ corresponding to the number of fused benzene rings in the molecule. In Figure 1 we present a few examples of PAH structures.

The PAHs have been optimized at the PM3 level[29,30] using the GAMESS program.[31,32] A normal mode vibrational analysis has been performed by building the Hessian matrix numerically from analytical gradients. A step size of 5×10^{-4} au has been used. The MidasCpp suite of programs has been used to construct the PESs through an interface to the GAMESS quantum chemistry program. Both the static grid method as well as ADGA have been used. In the static grid method, $16_1 8_{3/4}$ sets of coarse grid points have been used (see ref 17 for notation). To these grids, a number of additional points have been added by spline interpolation. Analytical representations of the PESs have been obtained via least-squares fitting with a multivariate polynomial function of 12th degree and using a cutoff of 12 in the bidimensional fittings. No use of point group symmetry was made.

The thresholds used for the construction of the PESs with the ADGA procedure are as follows: the one-mode surfaces were converged with $\varepsilon_{\text{rel}} = 1 \times 10^{-2}$ and $\varepsilon_{\text{abs}} = 1 \times 10^{-6}$, while the two-mode surfaces were converged with $\varepsilon_{\text{rel}} = 5 \times 10^{-2}$ and $\varepsilon_{\text{abs}} = 5 \times 10^{-6}$ (see ref 14 for details). The boundaries of the one-mode grids were iteratively determined by requiring that 99.9% of the mean density constructed from the three lowest vibrational states for each vibrational mode was included in the boundaries of the one-mode grids.

As for the static grid approach, the maximum polynomial degree used for the fitting of the surfaces is 12. However, in the early cycles of the iterative procedure, when few evaluation points are available, the maximum degree of the fitting polynomials are reduced to $n - 1$ with n being the number of evaluation points.

The basis set used during the VSCF calculations (both during the ADGA and in the analysis of the VSCF and VCC performances) consists of 13 harmonic oscillator functions for each of the vibrational modes corresponding to vibrational quantum numbers $v = 0, 1, ..., 12$.

It should be noted that the energies and wave functions obtained from the VSCF calculations differ slightly between the ADGA and static grid PESs. The mean absolute deviation (MAD) between fundamental excitation energies is of the order of 1 cm^{-1} for all molecules.

The timings presented in the following are, with the exception of the results for the duplicated PAH7 systems, obtained on SUN Fire x2100 dual core servers (2.2 GHz, 2GB memory) and refer to one iteration in the VSCF part; i.e., PES construction and other time-consuming steps are not treated.

New Formulation and Implementation of VSCF Theory

J. Chem. Theory Comput., Vol. 6, No. 1, 2010 **241**
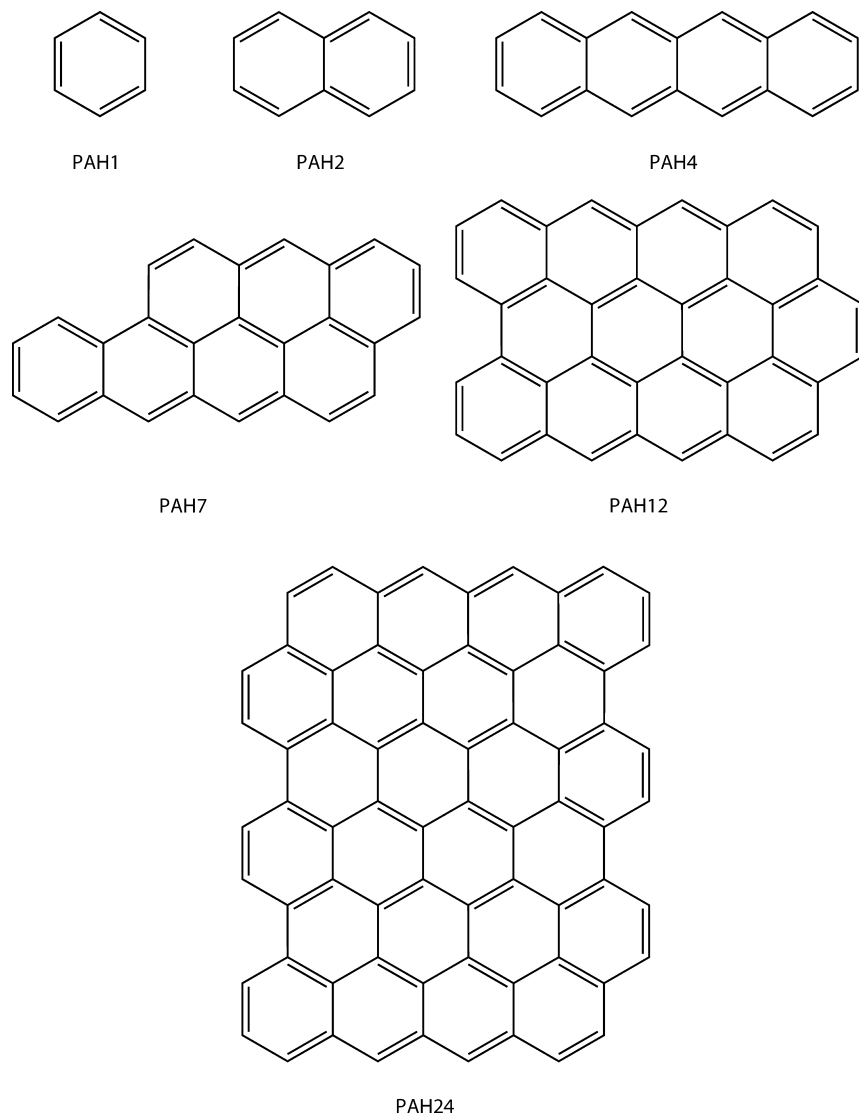
Figure 1. Examples of polyaromatic hydrocarbons.

4. Sample Calculations: Polyaromatic Hydrocarbons

In this section we describe some sample calculations. The VSCF approximation as such and most of its limitations have been extensively discussed in the literature, and we shall here primarily discuss aspects relating to our new implementation. Thus, the focus is on timings for systems of systematically increasing size. The PAHs define a class of molecules that can be extended in a systematic fashion with the normal coordinates still being able to provide a reasonable description of the systems.

4.1. PES Setup. In Figure 2 we present, as a function of system size, the number of terms in the Hamiltonian and the number of required single-point evaluations using the static grid approach and ADGA.

The static grid method provides a simple quadratic increase in the number of single-point evaluations and the number of terms in the Hamiltonian. This follows trivially from the number of mode-coupling pairs, $(1/2)M(M - 1)$, each of which requires a constant number of evaluation points and adds a constant number of terms to the Hamiltonian. In

ADGA, the same number of mode-couplings is handled but the number of single-point evaluations and terms varies among the couplings. From the inspection of Figure 2 it is clear that ADGA is more efficient than the static grid method in terms of single-point evaluations. The saving in single-point evaluations increases with increasing system size from 17% for PAH1 (benzene) to 77% for PAH24. Turning to the number of terms in the Hamiltonian, ADGA again offers quite large savings. For the largest systems investigated here, the analytical representation of the potential obtained with the ADGA contains only 12% of the number of terms present in the static grid Hamiltonian. This in turn provides computational savings in the vibrational structure calculations. The saving is significant for molecules of the size of PAH24 where the number of terms may otherwise easily exceed 1 million even for two-mode coupled potentials.

4.2. Scaling of Native VSCF versus Active Terms Algorithm. To investigate the performance of the active terms algorithm relative to the native VSCF algorithm in a simple setting, we initially use the static grid PESs which
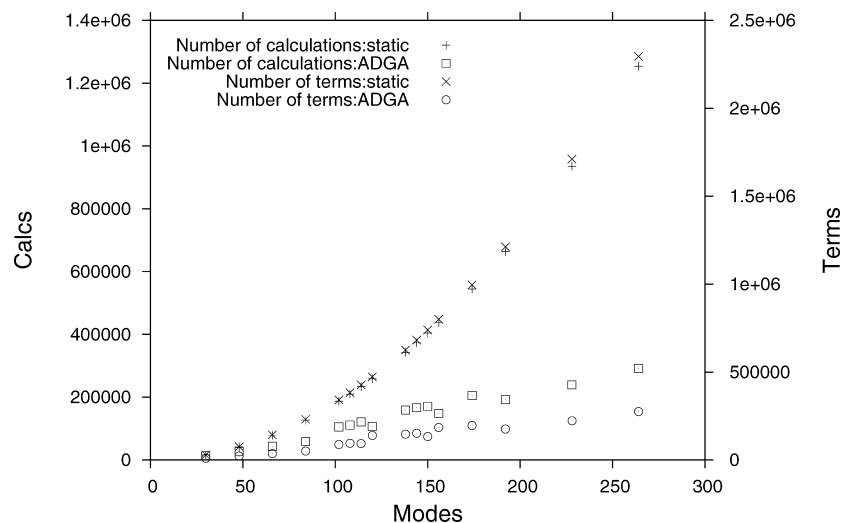
Figure 2. Number of single-point calculations (left) and the number of terms in the potential (right) in the static grid and ADGA potentials as a function of the number of vibrational degrees of freedom.

have a fixed number of terms per mode-coupling irrespective of the size of the system.

In the following, we assume that the CPU time for one VSCF iteration follows a simple equation of the type

$$t = 10^A M^B \tag{32}$$

or

$$\log t = A + B \log M \tag{33}$$

where M is the number of modes and A and B are fitting parameters. In the following we report computational scaling B and the prefactor 10^A. This allows for a very simple identification of the computational scaling as seen in Figure 3 which reports a log−log plot of the CPU time as a function of system size for the native and active terms algorithms. Linear least-squares fits are shown as well.

Due to the fact that the Hamiltonian couples all pairs of modes, and we in this subsection do not take any measures

to reduce the cost of evaluating all these couplings, the CPU time increases approximately proportional to some power of M as discussed in Theory. From Figure 3 it is seen that the native algorithm has a scaling of 2.6. The reason for this deviation from the expected cubic scaling is due to the fact that the leading order scaling is determined by the number of inactive terms in eq 28, which scales like M^2 (for all M modes) rather than the number of active terms in eq 27, which scales like M. However, the inactive terms are very simple to calculate (stored in memory at all times), making the prefactor on this term very low. This, in turn, results in comparable computational times for the active and inactive parts even for systems with 264 modes. The formula of eq 32 is too simple to capture this behavior.

For an operator with a mode-coupling level of two, one should obtain quadratic scaling when using the active terms algorithm. This is confirmed by the results reported in Figure 3. The difference in computational times between the active
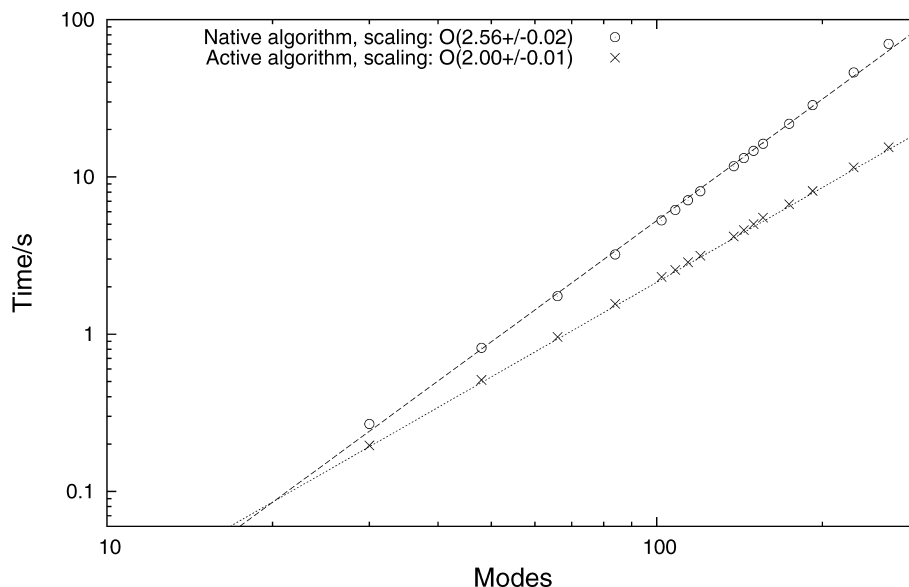
Figure 3. Time for a single VSCF iteration as a function of the size of the system (log−log scale). The broken and dotted lines represent the curves fitted to the data for the native and active terms, respectively.

Table 1. Computational Complexity of One VSCF Iteration When Screening Is Employed in the Active Terms Algorithm[a]

threshold(c_t)	threshold ($z^{m,t}$)	reorder[b]	scaling	prefactor	max(MAD)[c]	max(MAXAD)[d]
		no	2.00 ± 0.00	$10^{-3.67 \pm 0.01}$		
10^{-12}		no	1.89 ± 0.04	$10^{-3.68 \pm 0.08}$	1.3×10^{-4}	5.8×10^{-3}
10^{-10}		no	1.79 ± 0.05	$10^{-3.70 \pm 0.10}$	7.5×10^{-3}	3.5×10^{-2}
10^{-9}		no	1.82 ± 0.05	$10^{-3.91 \pm 0.10}$	7.2×10^{-2}	3.6×10^{-1}
	10^{-8}	no	1.86 ± 0.05	$10^{-3.87 \pm 0.10}$	1.1×10^{-8}	7.4×10^{-8}
	10^{-6}	no	1.79 ± 0.03	$10^{-4.01 \pm 0.07}$	4.4×10^{-6}	1.6×10^{-5}
	10^{-5}	no	1.84 ± 0.04	$10^{-4.14 \pm 0.07}$	8.3×10^{-4}	1.3×10^{-4}
	10^{-4}	no	1.57 ± 0.04	$10^{-3.94 \pm 0.09}$	3.2×10^{-2}	2.1×10^{-1}
10^{-9}	10^{-5}	no	1.71 ± 0.05	$10^{-4.09 \pm 0.11}$	8.0×10^{-2}	3.6×10^{-1}
10^{-9}	10^{-4}	no	1.48 ± 0.05	$10^{-3.79 \pm 0.10}$	9.4×10^{-2}	4.4×10^{-1}
10^{-9}	10^{-4}	yes	1.80 ± 0.04	$10^{-4.29 \pm 0.12}$	8.4×10^{-2}	3.7×10^{-1}

[a] The CPU time is assumed to be proportional to the number of modes to some scaling power multiplied by a prefactor. The scaling powers and the prefactors are listed in the table, given in terms of 10^A and B; see eqs 32−33. The errors (cm^{-1}) introduced are listed as well. [b] Specifies whether reordering of the operator terms has been used. [c] Largest value among the MAD for all molecules; see text for details. [d] Largest value among the MAXAD for all molecules; see text for details.

terms algorithm and the native algorithm is thus due to the inactive terms. For PAH2, PAH6, and PAH24, the fraction of time spent in the inactive terms part is 37, 59, and 78%, respectively, clearly indicating that for larger systems the computational effort of the native algorithm is dominated by the inactive part, and for sufficiently large systems cubic scaling is obtained.

Having clearly illustrated the better performance of the active terms algorithm over the native algorithm, we will in the following only use the active terms algorithm.

**4.3. Screening.** To reduce the scaling, one may use several types of screening. Here we investigate the computational speedup gained by (i) screening of the c_t coefficients, (ii) screening of the contributions to $\mathbf{F}^{m,\mathbf{i}}$ on the basis of $z^{m,t}$, and (iii) the combination of i and ii. In Table 1 the computational scalings and prefactors are presented for several thresholds of i and ii. The mean and maximum absolute deviations (MAD and MAXAD) of the VSCF fundamental frequencies with respect to the results obtained without screening were computed for all molecules, and their maximum values are presented for each threshold as well.

4.3.1. Screening of c_t. We begin our discussion by considering screening of the c_t coefficients in Table 1. In the three cases shown, the mean and maximum absolute deviations (MAD and MAXAD) of the VSCF fundamental frequencies with respect to the results obtained without screening are all below 0.5 cm^{-1}. This is certainly acceptable for VSCF fundamental frequencies. It is worth noting that many-mode correlation effects beyond VSCF and variations in the electronic structure methods for generating the individual PES points, as well as details in the construction of the PES may easily provide larger effects. Thus, 0.5 cm^{-1} is well below the accuracy expected in the full calculation. For the screening thresholds included in Table 1, the scaling is reduced compared to quadratic scaling but no clear trend is evident. Thresholds of 10^{-12}, 10^{-10}, and 10^{-9} yield scalings of 1.89, 1.79, and 1.82, respectively.

4.3.2. Screening on Contributions to $\mathbf{F}^{m,\mathbf{i}}$ on the Basis of $z^{m,t}$. The screening on the contributions to the elements of the $\mathbf{F}^{m,\mathbf{i}}$ matrices represents a perhaps more rigorous way of screening than the screening on the PES expansion coefficients.

In Table 1 we present the results obtained for PAHn, $n = 1$−24, using several thresholds for the screening of contributions to $\mathbf{F}^{m,\mathbf{i}}$ by inspecting $z^{m,t}$. The computational scaling

with the system size decreases compared to quadratic scaling when increasing the screening threshold above 10^{-10}. For screening thresholds of 10^{-8} to 10^{-5} the computational scalings are rather similar and within their respective standard errors. A threshold of 10^{-4} provide a computational scaling of $M^{1.57 \pm 0.04}$, which represents a significant reduction of the unscreened quadratic computational scaling. With a threshold of 10^{-4}, the maximum MAD and MAXAD errors are 0.03 and 0.2 cm^{-1}, which is clearly acceptable for systems of this size. For lower screening thresholds, the MAD and MAXAD errors are significantly lower.

4.3.3. Combined Screening. Figure 4 illustrates the computational scaling when using a threshold of 10^{-9} for the direct screening on the c_t coefficients and a threshold of 10^{-4} for the screening of $z^{m,t}$. The MAD/MAXAD for the VSCF fundamental frequencies for each molecule relative to those obtained without any screening are included as well. For completeness, the results from the combined screening are presented in short form in Table 1.

With these thresholds, we obtain a computational scaling of $M^{1.48 \pm 0.05}$ with respect to system size. This should be compared to the quadratic scaling when not exploiting screening. The scaling of $M^{1.48 \pm 0.05}$ is seen to be lower than the scaling found when using screening on $z^{m,t}$ or c_t alone. There is some synergistic effect when employing the two types of screening simultaneously, but the effect is fairly small compared to the $z^{m,t}$ screening alone. It is worth noting that the time for performing one VSCF iteration is about a half-second for the PAH24 molecule which consists of 264 modes. The unscreened active terms algorithm in comparison took 15.4 s, while the unscreened native algorithm takes 70.0 s per iteration. The errors introduced are rather similar to the ones found for the screening on c_t alone and are considered to be acceptable. In conclusion we may, by using the new active terms algorithm together with different screening strategies, bring down the VSCF iteration time very significantly compared to the standard VSCF algorithm, 2 orders of magnitude for a 264 mode system.

In addition to screening, one may consider the combination of operator terms as described in Theory. In Table 1 we include the scaling, prefactor, and errors obtained when employing this trick as well. It is evident that the computational scaling does not come out quite as favorable as in the case where we just employ two types of screening. The
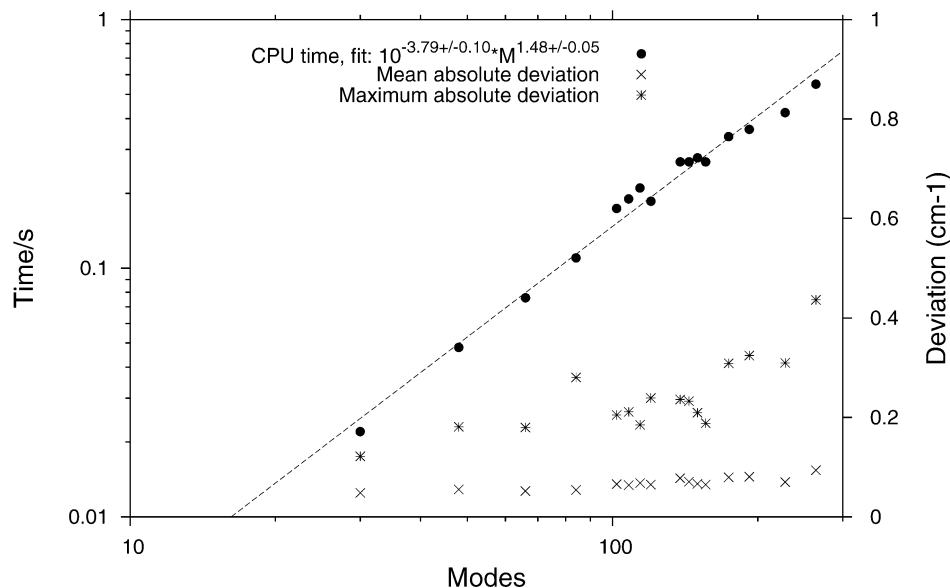
Figure 4. Time for a single VSCF iteration as a function of system size (log−log scale) when two kinds of screening are combined. The broken line represents the curve fitted to the CPU times.
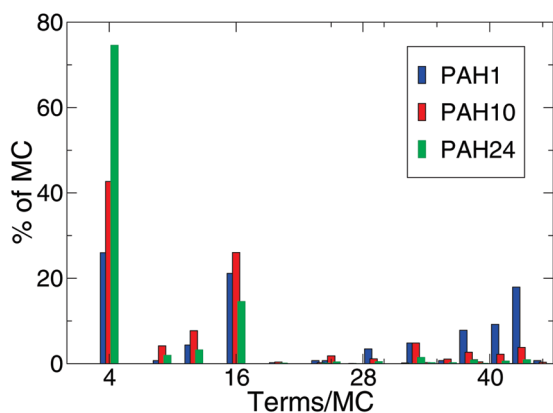

Figure 5. Distribution of operator terms per MC for PAH1, PAH10, and PAH24.

reason for this is the fact that lower fractions of the $z^{m,t}$ coefficients are screened away when employing the combination of operator terms. This trick generates more operator terms, and evidently more of these have nonnegligible contributions. For PAH10, the percentages of terms screened away with and without combination of operator terms are 70 and 84%, respectively, for the VSCF ground state.

4.4. ADGA PESs. The PESs constructed with the ADGA are particularly suitable for larger systems since, as discussed above, the ADGA is able to provide a more compact representation of weak couplings compared to a static grid approach. In this section we examine the performance of VSCF using these PESs. As stated in a previous section, a given two-mode MC may be approximated by as few as four terms in the most favorable case. In Figure 5 we present the distribution of operator terms per MC. Interestingly, the percentage of MCs which are represented by only four terms in the operator increases with increasing system size. This is of course intimately related to the savings in the number of single-point calculations observed in ADGA as compared to the static grid approach. For instance, only four single-point calculations are needed in the simplest case of four

terms in a coupling term. For PAH24, the biggest system tested, the percentage of MCs represented by four or 16 terms amounts to more than 90%.

At this point we note that the simple computational scaling formula, eq 32, is not strictly valid when using the ADGA, since the polynomial degree is allowed to adjust to the number of single-point evaluations. However, due to the very simple nature of this way of analyzing the results, we choose to use it for ADGA results as well.

The computational scaling obtained for the ADGA PESs is shown in Figure 6. A computational scaling of $M^{1.52\pm0.05}$ is obtained, with a significant reduction in the computational cost. One should also note that the asymptotic standard errors obtained in the fitting procedure are sufficiently small to justify the use of eq 32 in the fitting. The effect of the screening on contributions to the $\mathbf{F}^{m,i}$ matrices is shown in Figure 6 as well. A screening threshold of 10^{-4} on the $\mathbf{F}^{m,i}$ contributions changes the computational scaling to $M^{1.37\pm0.05}$, whereas a scaling of $M^{1.52\pm0.05}$ was found for the unscreened one. The prefactor also changes significantly, thus making the ADGA in combination with screening on $\mathbf{F}^{m,i}$ contributions very fast. The mean and maximum absolute deviations are less than 0.2 cm^{-1}, which is satisfactory for the VSCF method.

4.5. Predicted Important Coupling. A different method for screening away entire mode combinations is to employ the so-called predicted important coupling (PIC) schemes where the coupling strength of two different normal modes is estimated by their "atom-by-atom" overlap.[22] In the simplest of these works, and the one used by Pele et al.,[22] the criteria for judging whether a MC should be kept or neglected is based on whether the displacement vectors representing two normal coordinates introduce movement of the same atoms, though additional criteria may be introduced.

We tested the version of PIC in ref 22 (as well as others including additional criteria) but found that neglecting even a few MCs in this way resulted in large errors (mean and absolute) compared to the unscreened results. The neglect
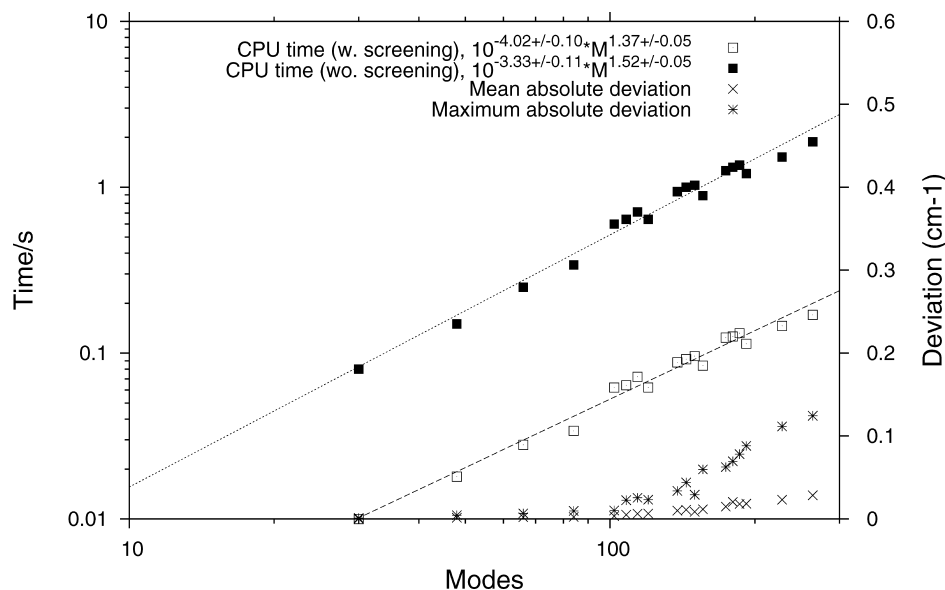
New Formulation and Implementation of VSCF Theory

J. Chem. Theory Comput., Vol. 6, No. 1, 2010 **245**

Figure 6. Time for a single VSCF iteration as a function of system size when ADGA PESs are used (log−log scale). Data both with and without screening are shown. The deviations of the screened results are provided on the right-hand scale. The broken and dotted lines represent the curves fitted to the CPU times of the screened and unscreened results.

of only 0.1 and 3% of the two-mode couplings, corresponding to specific coupling strength thresholds, resulted in MAD (MAXAD) of 0.14 (1.4) and 4.58 (40.8) cm^{-1}, respectively, for the PAH2 molecule. For a larger system represented by PAH4, neglecting 0.04 and 7% of the two-mode couplings resulted in MAD (MAXAD) of 0.16 (3.94) and 2.19 (12.5) cm^{-1}, respectively. These deviations are perhaps not too severe in comparison to the other approximations introduced, but, for these low thresholds, the computational gain in constructing the potentials as well as in the subsequent vibrational wave function calculations are rather limited.

There are certainly some nice features of the PIC schemes in terms of potentially lowering the computational scaling with respect to the number of modes. However, such intuitive schemes did not work well for the presented cases. How to remove MCs in an efficient, general, and accurate way is still an open issue.

We note that other ways of neglecting MCs are possible, for example the one advocated by Benoit.[23] Within this approach, the full PES must be calculated at a lower level of theory after which a measure of the coupling strengths are computed. On the basis of these coupling strengths MCs may be kept or neglected accordingly. The advantage of this method is that it provides a firmer measure of the coupling strengths; the drawback is that the full PES must be calculated in advance, although at a lower level of theory. This method has not been pursued in this work.

4.6. Duplicated PAH7 Molecules as a Model System. In this section we investigate the computational scaling of the VSCF algorithm for a model system consisting of noninteracting PAH7 molecules described by the ADGA potential. Within the individual subsystems, all operator terms are maintained; i.e., we do not exploit screening. The Hamiltonian thus consists of all one-mode terms and all two-mode terms in each subunit, i.e., no terms in the Hamiltonian couple modes belonging to different mono-

mers. In this case the number of terms in the Hamiltonian is given by (as follows we assume a static grid potential for simplicity, but the same arguments may be applied to an ADGA Hamiltonian),

$$N^T = N_{su}\left(DM_{su} + \frac{1}{2}M_{su}(M_{su} - 1)D(D - 1)\right) \quad (34)$$

where N_{su} and M_{su} denote the number of subunits and the number of modes in each subunit, respectively. The total number of modes is given by $M = M_{su}N_{su}$, and hence the total number of terms is

$$N^T = M\left(D + \frac{1}{2}(M_{su} - 1)D(D - 1)\right) \quad (35)$$

The number of terms thus scales linearly with the total number of modes in the system. By the scaling arguments used in the discussion of the native and active terms algorithms (section 2.3), one may thus expect quadratic scaling of the VSCF iteration times for the native algorithm, while linear scaling should be obtained for the active terms algorithm.

Figure 7 shows the computational scaling of one VSCF iteration as a function of the number of duplicates. The plot yields a slope of 1.01 ± 0.00 in perfect agreement with linear scaling. We note that similar calculations using the native algorithm confirm the expected quadratic scaling (results not shown). In connection with this we note that the VSCF iteration time for the largest system studied here (10^6 modes) is extrapolated to be more than 2.5 CPU years using the native algorithm. In comparison, the VSCF iteration time for the active terms algorithm is just under 2 h. It is comforting to see that MidasCpp runs VSCF calculations including more than 1 million modes without having to introduce any special treatments. This aspect of the active terms algorithm is important for efficiency also in other than
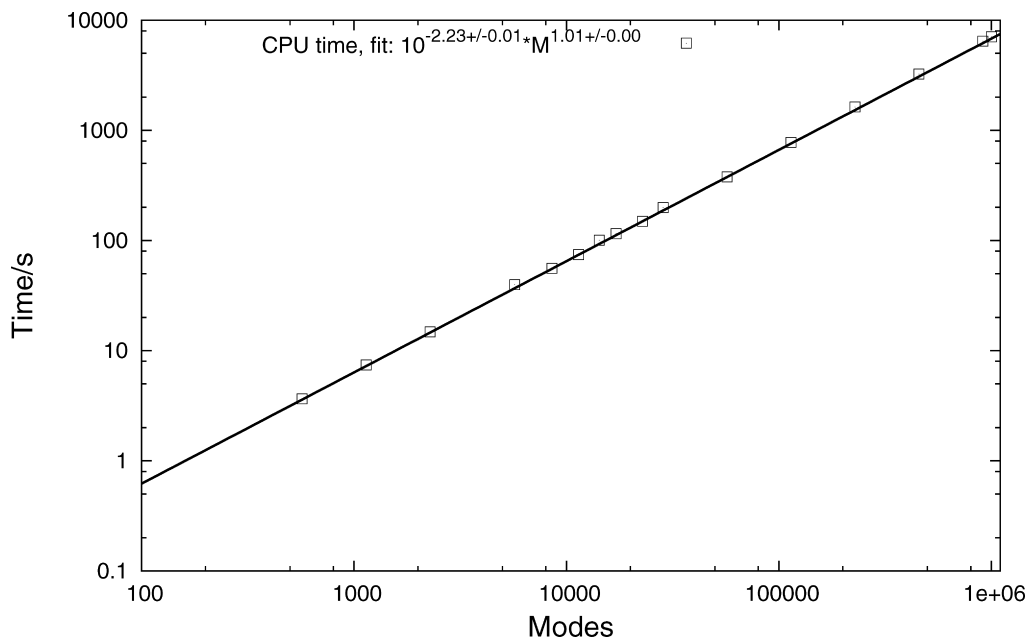
Figure 7. log−log plot of the CPU time for a single VSCF iteration as a function of the size of the system (number of modes) for duplicated PAH7 (see text).
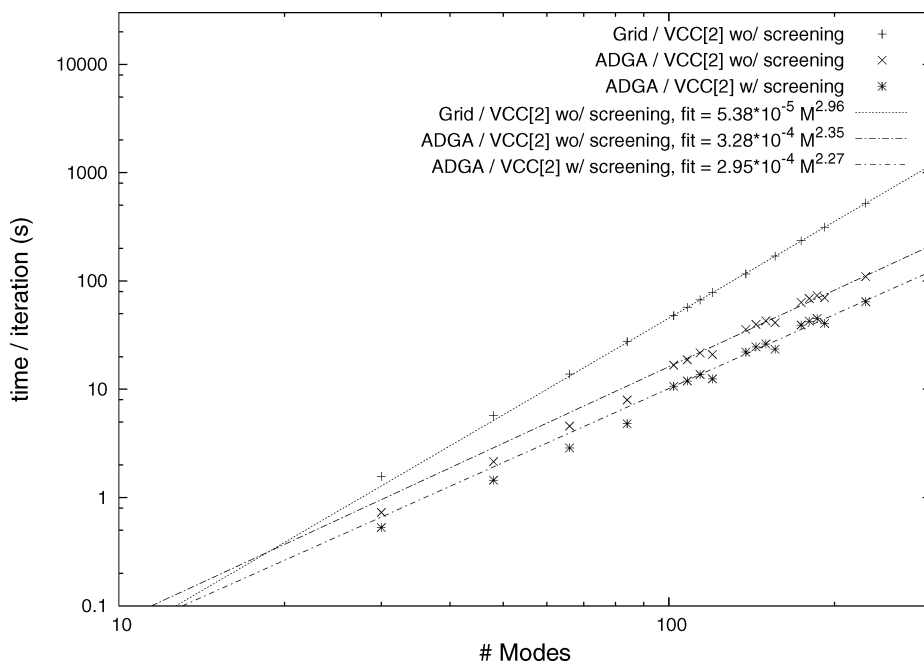
Figure 8. Scaling of the VCC[2] algorithm when applied to PAH systems described by static grid and ADGA based PESs with and without screening of the cluster amplitudes.

the present simple case. The computational cost of the active terms algorithm thus reflects the actual anharmonic coupling network.

4.7. Correlated Calculations. In a previous section it was shown how the use of ADGA PESs reduces the scaling of VSCF calculations. Though correlated calculations are not the focus of this paper, it is worthwhile to investigate whether the same is true for these kinds of calculations. For this purpose, we have used the VCC[2] algorithm reported in ref 12. For further details on basic VCC theory see ref 33. We note that the trick of combining terms in the Hamiltonian, discussed in section 2.6, is implicitly used by this algorithm. Furthermore, screening has been implemented but the details

are different from those of the VSCF algorithm since it is based primarily on the cluster amplitudes instead of the Hamiltonian terms; see ref 12 for details.

In the calculations reported here, all 13 optimal VSCF modals are included in the VCC part for each mode. Figure 8 shows the scaling of the VCC[2] algorithm applied to the series of PAHs in three different cases: Using a static grid based PES, the scaling is M^3 as previously reported.[12] More interestingly, the use of an ADGA-based PES reduces the scaling to $M^{2.35}$. The number of amplitudes in this calculation naturally remains the same as when using the static grid based PES, and the reduction is therefore simply due to the lower scaling of the number of terms in the potential part of

New Formulation and Implementation of VSCF Theory

J. Chem. Theory Comput., Vol. 6, No. 1, 2010 **247**

the Hamiltonian with respect to the system size; see Figure 2. Finally, a calculation with a screening threshold of 10^{-20} (see ref 12) shows that the screening method implemented in the VCC algorithm does not reduce the scaling but more generally improves performance. In this case the improvement is approximately 33%.

In conclusion, it is encouraging that correlated quantum mechanical calculations can be carried out for systems as large as PAH24. Furthermore, the ADGA is, also for correlated calculations, a very promising method for larger molecules.

5. Summary and Outlook

We have presented an efficient active terms algorithm for VSCF calculations. It has been demonstrated how the core part of the algorithm appears naturally by deriving the VSCF theory in second quantization formalism. It has further been demonstrated that the implementation allows for calculations on systems with many degrees of freedom. With up to a few hundred explicitly coupled degrees of freedom, a computational scaling of order $M^{1.5}$ per VSCF iteration per state was found together with a very low prefactor including two mode couplings in the Hamiltonian. The computational scaling was found to be as low as $M^{1.37}$ when using ADGA potentials in combination with screening. Sample calculations for model systems with up to 1 million degrees of freedom are reported, illustrating linear scaling when each mode interacts only with a limited set of other modes.

Even though the systems considered here are simple from some perspectives, the fact that such quantum mechanical calculations on systems of this size are possible is encouraging. In discussions of quantum methods versus classical methods it seems often to be assumed that quantum methods are inherently costly and only possible for small systems. Indeed, in many circumstances where classical mechanics is used today it is presently the only realistic option. Though there are many different bottlenecks that must be overcome in various areas of applications, this general statement need not be a valid standard assumption in the future. At least the presented very fast VSCF implementation in combination with the ADGA procedure provides a powerful tool and suggests that at least some of the conceived limitations can be removed. We will continue to work on many of the other bottlenecks of many mode quantum dynamics.

In this paper we have used normal coordinates throughout. For weakly anharmonic systems the normal coordinate harmonic oscillator description is a good reference point. However, standard normal coordinates will be a rather poor starting point for many floppy molecules, and their determination nontrivial for systems with thousands of atoms. Furthermore, it should be noted that normal coordinates, by construction, are nonlocal. True linear scaling, as observed when duplicating PAH7, may thus not be easily obtained in general using normal coordinates. The use of more local coordinates in combination with the present scheme is certainly a very attractive perspective for future research. One line of research here could be the use of internal coordinates, though complicated due to the cumbersome form of the kinetic energy operators. Another interesting perspective is the localization of normal coordinates, as suggested recently by Jacob and Reiher.[34]

The predicted importance coupling approach attempts to predict mode couplings which are not strongly coupled and neglect the suggested weakly coupled ones accordingly using only the form of the normal coordinates. This approach, however appealing, was found not to work for the molecules used in this study.

Correlation effects may also be considered in the construction of approximate wave function going beyond the single Hartree product description of VSCF. In particular, the VCC approach has the promise of maintaining the same accuracy for large systems compared to small systems, when the same level of wave function approximation is used. Some of the tricks employed in this paper also led to improvements in the scaling of VCC. Furthermore, the new active terms VSCF implementation fulfills that it is well below an optimal VCC implementation in computational scaling, which is in fact not quite the case with the native VSCF algorithm.

Supporting Information Available: Figures containing the raw data and fitted curves from which the computational scaling and prefactors are found. This material is available free of charge via the Internet at http://pubs.acs.org.

References

(1) White, C. A.; Johnson, B. G.; Gill, P. M. W.; Head-Gordon, M. *Chem. Phys. Lett.* **1994**, *230*, 8.

(2) Strain, M. C.; Scuseria, G. E.; Frisch, M. J. *Science* **1996**, *271*, 51.

(3) Ochsenfeld, C.; Kussmann, J.; Lambrecht, D. S. In *Linear-Scaling Methods in Quantum Chemistry*; Lipkowitz, K. B., Cundari, T. R., Eds.; VCH: New York, 2007; pp 1−82.

(4) Scuseria, G.; Ayala, P. *J. Chem. Phys.* **1999**, *111*, 8330.

(5) Subotnik, J.; Sodt, A.; Head-Gordon, M. *J. Chem. Phys.* **2006**, *125*, 074116.

(6) Christiansen, O.; Manninen, P.; Olsen, J.; Jørgensen, P. *J. Chem. Phys.* **2006**, *124*, 084103.

(7) Jelski, D. A.; Haley, R. D.; Bowman, J. M. *J. Comput. Chem.* **1996**, *17*, 1645.

(8) Makri, N. *Annu. Rev. Phys. Chem.* **1999**, *50*, 167.

(9) Roitberg, A.; Gerber, R. B.; Elber, R.; Ratner, M. A. *Science* **1995**, *268*, 1319.

(10) Bowman, J. M. *Acc. Chem. Res.* **1986**, *19*, 202.

(11) Gerber, R. B.; Ratner, M. A. *Adv. Chem. Phys.* **1988**, *70*, 97.

(12) Seidler, P.; Hansen, M. B.; Christiansen, O. *J. Chem. Phys.* **2008**, *128*, 154113.

(13) Christiansen, O. *J. Chem. Phys.* **2004**, *120*, 2140.

(14) Sparta, M.; Toffoli, D.; Christiansen, O. *Theor. Chem. Acc.* **2009**, *123*, 413.

(15) Hansen, M. B.; Christiansen, O.; Toffoli, D.; Kongsted, J. *J. Chem. Phys.* **2008**, *128*, 174106.

(16) Watson, J. K. G. *Mol. Phys.* **1968**, *15*, 479.

(17) Toffoli, D.; Kongsted, J.; Christiansen, O. *J. Chem. Phys.* **2007**, *127*, 204106.

(18) Jung, J. O.; Gerber, R. B. *J. Chem. Phys.* **1996**, *105*, 10332.

(19) Carter, S.; Culik, S. J.; Bowman, J. M. *J. Chem. Phys.* **1997**, *107*, 10458.

(20) Carter, S.; Bowman, J. M.; Harding, L. B. *Spectrochim. Acta, Part A* **1997**, *53*, 1179.

(21) Rauhut, G. *J. Chem. Phys.* **2004**, *121*, 9313.

(22) Pele, L.; Gerber, R. B. *J. Chem. Phys.* **2008**, *128*, 165105.

(23) Benoit, D. M. *J. Chem. Phys.* **2004**, *120*, 562–573.

(24) Beck, M. H.; Jäckle, A.; Worth, G. A.; Meyer, H.-D. *Phys. Rev.* **2000**, *324*, 1.

(25) Yagi, K.; Taketsugu, T.; Hirao, K.; Gordon, M. S. *J. Chem. Phys.* **2000**, *113*, 1005.

(26) Benoit, D. *J. Chem. Phys.* **2006**, *125*, 244110.

(27) Sparta, M.; Høyvik, I. M.; Toffoli, D.; Christiansen, O. *J. Phys. Chem. A* **2009**, *113*, 8712.

(28) MidasCpp (Molecular Interactions, Dynamics and Simulation Chemistry Program Package in C++), http://www.chem.au.dk/~midas, accessed Nov. 8, 2009.

(29) Stewart, J. J. P. *J. Comput. Chem.* **1989**, *10*, 209.

(30) Stewart, J. J. P. *J. Comput. Chem.* **1989**, *10*, 221.

(31) Schmidt, M. W.; Baldridge, K. K.; Boatz, J. A.; Elbert, S. T.; Gordon, M. S.; Jensen, J. H.; Koseki, S.; Matsunaga, N.; Nguyen, K. A.; Su, S.; Windus, T. L.; Dupuis, M.; Montgomery, J. A. *J. Comput. Chem.* **1993**, *14*, 1347.

(32) Gordon, M. S.; Schmidt, M. W. In *Advances in Electronic Structure Theory: GAMESS a Decade Later*; Dykstra, C. E., Frenking, G., Kim, K. S., Scuseria, G. E., Eds.; Elsevier: Amsterdam, 2005; pp 1167−1190.

(33) Christiansen, O. *J. Chem. Phys.* **2004**, *120*, 2149.

(34) Jacob, C. R.; Reiher, M. *J. Chem. Phys.* **2009**, *130*, 084106.

J. Chem. Theory Comput. **2010,** *6,* 249–256

249

JCTC Journal of Chemical Theory and Computation

Solvatochromic Shifts in Uracil: A Combined MD-QM/MM Study

Jógvan Magnus Olsen,[†] Kęstutis Aidas,[‡] Kurt V. Mikkelsen,[‡] and Jacob Kongsted*,[†]

Department of Physics and Chemistry, University of Southern Denmark, Campusvej 55, DK-5230 Odense M, Denmark, and Department of Chemistry, H. C. Ørsted Institute, University of Copenhagen, Universitetsparken 5, DK-2100 Copenhagen Ø, Denmark

Abstract: Uracil is a commonly occurring pyrimidine derivative found in RNA where it base pairs with adenine. Rationalizing the electronic properties of uracil in both gas phase and aqueous solution is of fundamental importance because of the significant biological role played by this molecule. This paper presents accurate predictions of the solvatochromic shifts of the lowest $\pi \rightarrow \pi^*$ and $n \rightarrow \pi^*$ vertical electronic excitation energies in uracil due to an aqueous solution. The calculations are conducted using a recently developed combined quantum mechanics/ molecular mechanics (QM/MM) method, and nuclear dynamical effects are accounted for through molecular dynamics simulations. The electronic structure is described using either density functional theory employing the CAM-B3LYP exchange-correlation functional or the coupled cluster singles and approximate doubles (CC2) method. The predicted solvatochromic shifts using CAM-B3LYP/MM and CC2/MM are -0.12 ± 0.01 eV and -0.20 ± 0.01 eV, respectively, for the $\pi \rightarrow \pi^*$ transition and 0.42 ± 0.03 eV and 0.43 ± 0.03 eV, respectively, for the $n \rightarrow \pi^*$ transition. Our best estimate of the solvatochromic shifts are derived using a self-consistent polarizable model in both the MD and QM/MM simulations and are -0.29 ± 0.01 eV and 0.45 ± 0.03 eV for the $\pi \rightarrow \pi^*$ and $n \rightarrow \pi^*$ transitions, respectively. The estimate is based on CC2 with electrostatic corrections defined from CAM-B3LYP and dispersion corrections derived from CC2 model system calculations. These solvatochromic shifts are in excellent agreement with experimental data, indicating the importance of explicit inclusion of polarization effects in MD-based QM/MM methods.

1. Introduction

Predictions of solvatochromic shifts have for a long time been a very active and important research area in theoretical chemistry. Because the polarities of the ground and excited states of a chromophore generally are different, a change in the solvent polarity will lead to a differential stabilization of the ground and excited states and thereby to a change in the energy difference between these two states. Consequently, variations in the position, intensity, and shape of the absorption spectra can be a direct measure of the specific interactions between the solute and solvent molecules.

Accurate predictions of molecular properties of large molecular samples, e.g., a solute in a solvent, represent one of the greatest challenges to modern quantum chemistry. The simplest approach would be to neglect all specific interactions between the solute and the solvent. This is the strategy followed in the dielectric continuum models.[1] However, these models may become too crude, and predictions of solvato-chromic shifts should be based on more advanced models. The complexity met when facing the condensed phase is tackled very effectively by combining classical and quantum mechanics (QM/MM) along with molecular dynamics (MD) simulations. For the description of the excited states, the use of quantum mechanics is mandatory. On the other hand, the

* To whom correspondence should be addressed. E-mail: kongsted@ifk.sdu.dk.

† University of Southern Denmark.

‡ University of Copenhagen.

part of the system not directly involved in the electronic processes can be described effectively, e.g., using classical mechanics. Even though linear scaling techniques are becoming more advanced and may be used to describe the total solute−solvent system, the question of conformational sampling still persists. This means that formulation of accurate effective Hamiltonian methods becomes of crucial importance. In fact, in order to pursue a direct comparison with experimental data it is mandatory to include the effects of nuclear dynamics. In the present work this issue is covered by performing classical molecular dynamics simulations. Here we proceed in a sequential manner, i.e., we first perform the MD simulations and then, using an appropriate number of solute−solvent configurations extracted from the classical MD simulations, simulate the electronic transitions. In this respect we neglect the effect of the electronic structure on the configurations, and the accuracy of our approach relies first of all on the use of an accurate classical potential to be used for the MD simulations.

The inclusion of explicit polarization into solvent models have received much attention in the past few years.[2] Generally, it is now recognized that polarization may contribute significantly to the specific solvation process. For example, polarization causes an up to 70% increase in the dipole moment of a water molecule in the liquid state and may in addition constitute as much as 50% of the total interaction energy.[3] The conventional, and indeed most easy, way of accounting for polarization is implicitly, i.e., through an artificial enhancement of the electrostatic pairwise model parameters so as to include polarization in an averaged fashion. By definition, this way of proceeding completely neglects the dynamical responses in the mutual interaction between the solute and solvent electronic densities caused by electric fields and changes in the chemical environment. For a molecule in its electronic ground state interacting only weakly with its local environment, it might be a reasonable approximation to neglect dynamical responses, e.g., explicit polarization. However, when considering electronic transitions, the electronic density in the active part of the system might undergo significant changes and dynamical solute−solvent response might be mandatory to include in the predictions. In addition, because of the Franck−Condon principle only the electronic polarization can be assumed to relax instantaneously to the excited state thereby leading to a nonequilibrium situation.

In this study we apply different QM/MM approaches[4−7] for the prediction of the solvatochromic shifts of the lowest $n \rightarrow \pi^*$ and $\pi \rightarrow \pi^*$ transitions in uracil due to water solvent. These QM/MM models are based on either Density Functional Theory (DFT) or Coupled Cluster (CC). Solvent polarization is included by means of the polarizable point-dipole model, and dynamical effects are included through MD simulations. Uracil is a commonly occurring pyrimidine derivative found in RNA where it base pairs with adenine and is replaced by thymine in DNA translation. Rationalizing the electronic properties of uracil in both gas phase and aqueous solution is thus of great importance because of the biological role played by this molecule, and the electronic spectrum of uracil has indeed been the subject of several

previous papers.[8−22] Uracil is capable of performing several hydrogen bonds to a protic solvent, and this must be reflected in the solvent model used for the rationalization. In the QM/MM approach this is naturally tackled by treating uracil quantum mechanically while the solvent, or at least the major part of it, is described using a discrete (yet polarizable) solvent model. The experimental electronic spectrum of uracil in aqueous solution is characterized by a large peak around 4.8 eV and a second peak above 6.0 eV.[23−26] The first peak is due to a strongly absorbing $\pi \rightarrow \pi^*$ transition and is red-shifted as compared to the corresponding transition in the isolated uracil.[24] All calculations in this paper refer to the diketo form of uracil because this conformer has previously been found to be the dominant one (see, for example, the discussion in ref 21).

2. Computational Details

The solvatochromic shifts are calculated as the difference between vertical excitation energies in uracil in aqueous solution and in vacuum. The QM/MM results were obtained using a development version of the Dalton quantum chemistry program[27] at the DFT and CC levels of theory.[4−7] The MD simulations were performed with the Molsim program[28] and the interface between Dalton and Molsim is provided by the Whirlpool program.[29] Geometry optimizations were done using the Gaussian 03 program.[30] Because of a difference in the implementation of the B3LYP[31−34] exchange-correlation (xc) functional in Gaussian 03 and Dalton, we denote the implementation of B3LYP in Gaussian 03 by B3LYP(G) and the corresponding implementation in Dalton by B3LYP. Furthermore, we used Gaussian 03 and the MOLCAS program[35] to calculate certain force-field parameters (specified below) needed for the MD simulations.

2.1. MD Simulations. We conducted classical MD simulations of a rigid uracil molecule and 511 rigid water molecules (see Figure 1). The solvated geometry of uracil was obtained from a geometry optimization at the B3LYP(G)/aug-cc-pVTZ/PCM[1,36−38] level of theory. The default PCM settings were used as implemented in Gaussian 03 except for the RMin and OFac parameters which were set to 0.5 and 0.8, respectively. The RMin parameter sets the minimum radius in angstroms for added spheres, and the OFac parameter specifies the overlap index between two interlocking spheres. Changing these parameters from the default to the specified values results in fewer added spheres between atoms. The cavity was built using the united atoms (UA0) model. We performed simulations using either a polarizable or a nonpolarizable force field. The nonpolarizable force field for water is the standard TIP3P[39] water model, and the polarizable force field is provided by Ahlström et al.[40] For uracil, we calculated the nonpolarizable force field parameters, i.e., the partial point charges, by employing the CHELPG procedure,[41] which fits the atomic charges to reproduce the molecular electrostatic potential, at the B3LYP(G)/aug-cc-pVTZ/PCM level using Gaussian 03. In addition, the charges were constrained to reproduce the electric dipole moment. For the polarizable force field, we used the B3LYP(G)/aug-cc-pVTZ based CHELPG point charges calculated in vacuum together with the constraint
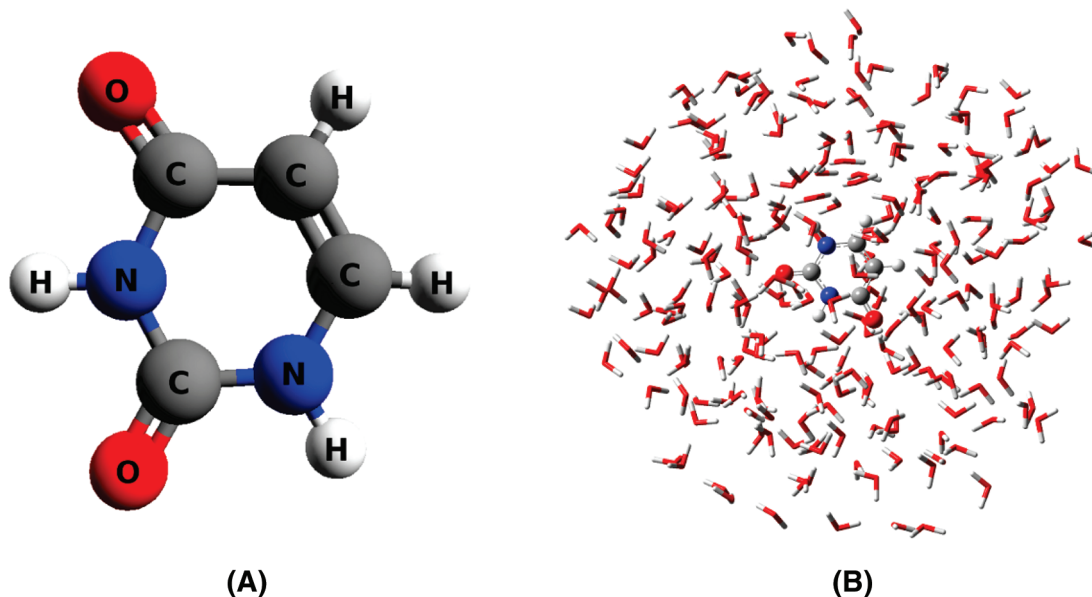
Solvatochromic Shifts in Uracil

J. Chem. Theory Comput., Vol. 6, No. 1, 2010 **251**

Figure 1. The structure of uracil (a) and an example of a molecular configuration with uracil in water extracted from a MD simulation (b).

on the dipole moment. We calculated the atomic polarizabilities at the B3LYP/aug-cc-pVTZ level using the LoProp approach[42] implemented in MOLCAS which is a method for obtaining localized properties. Nonelectrostatic intermolecular interactions were modeled with a 6−12 Lennard−Jones potential and Lorentz−Berthelot mixing rules. The Lennard−Jones parameters used for uracil were obtained from ref 43.

The MD simulations were performed in a cubic box within the NVT ensemble at a temperature of 298.15 K. The box length was set to 24.934 Å in order to reproduce the experimental density of liquid water. We employed periodic boundary conditions together with a spherical cutoff distance for the electrostatic interactions at half box length. To account for the long-range and polarization interactions, a reaction-field correction was used. The initial equilibration was carried out for 360 ps with a time step of 2 fs followed by the production run of 1.2 ns. The configurations were dumped every 10 ps in order to ensure that they were statistically uncorrelated. Thus, we obtained 120 molecular configurations to use in the subsequent QM/MM calculations.

2.2. Vacuum Calculations. The vacuum geometry of uracil was optimized at the B3LYP(G)/aug-cc-pVTZ level of theory. The vertical excitation energies were calculated with the CAM-B3LYP,[44,45] B3LYP,[31−34] B3PW91,[46] PBE0[47,48] xc-functionals, and CC2[49] together with the aug-cc-pVDZ basis set.[36,37] We used the frozen core approximation in the CC2 calculations. The CC2 method was used as a reference in gauging the accuracy of the considered xc-functionals. Furthermore, we calculated the excitation energies using Dunning's augmented correlation consistent basis sets of double- and triple-ζ quality[36,37] with the CAM-B3LYP xc-functional.

2.3. QM/MM Calculations. Excitation energies were calculated using the CAM-B3LYP xc-functional and the CC2 method with frozen core. The QM/MM implementation used for the calculations presented in this study allows for the use of either a nonpolarizable or an isotropically polarizable force field. We performed calculations using both types of

potentials allowing an examination of the importance of explicit treatment of polarization. The force fields for water were the same as the ones used in the MD simulations. We used a spherical solute−solvent cutoff distance of 12 Å which includes approximately 240 water molecules. This has previously been shown to be adequate.[50] However, calculations with cutoffs at 10 and 14 Å were performed to verify the convergence.

It has been shown that it might be necessary to include a number of explicit water molecules in the QM region to get accurate excitation energies.[6,50] This is especially important in the case of $\pi \rightarrow \pi^*$ transitions as these are very sensitive to nonelectrostatic intermolecular interactions.[50] Therefore, a series of calculations with increasing number of water molecules in the QM region were performed. The first step includes the hydrogen bonding water molecules and subsequent steps include those water molecules which are closest to the π electronic system of uracil.

It is well-known that DFT has difficulties in describing intermolecular interactions related to dispersion. In order to investigate the significance of this issue, we constructed a model system consisting of uracil and two water molecules. The entire system was geometry optimized at the B3LYP(G)/aug-cc-pVTZ level of theory. This leads to a structure where each water molecule appears to be hydrogen bonded twice to uracil, one through hydrogen to a carbonyl oxygen and one through oxygen to a hydrogen in a N−H group. We then proceeded with excitation energy calculations using the same methods as in the vacuum case. This was done on the complete system and also a single QM/MM calculation with the two water molecules confined to the MM region.

The reported excitation energies are averages over all the QM/MM calculations carried out on all the configurations extracted from the MD simulations. Therefore, it is appropriate to present the results with uncertainties which we define as $1.96 S_E$. The standard error of the mean, S_E, is defined as $S_E = s/n^{1/2}$, where s is the sample standard deviation and n is the number of samples, i.e., the number of configurations

252 *J. Chem. Theory Comput., Vol. 6, No. 1, 2010*

Olsen et al.

Table 1. The Lowest $\pi \rightarrow \pi^*$ and $n \rightarrow \pi^*$ Vertical Excitation Energies in Isolated Uracil Calculated with Different xc-Functionals and (frozen-core) CC2[a]

method	$\Delta E_{vac}^{\pi \rightarrow \pi^*}$ (eV)	$\Delta E_{vac}^{n \rightarrow \pi^*}$ (eV)
B3LYP	5.139	4.655
B3PW91	5.163	4.641
PBE0	5.253	4.784
CAM-B3LYP	5.384	5.052
CC2	5.406	4.933

[a] The aug-cc-pVDZ basis set and B3LYP(G)/aug-cc-pVTZ geometry was used.

in our case. This definition of uncertainty approximates a 95% confidence level.

3. Results and Discussion

A previous theoretical study of the nucleic acid bases by means of coupled cluster theory found that CC2 in combination with the aug-cc-pVDZ basis set provides very reasonable results.[12] This is attributed to the fact that the effects of larger basis counter the effects obtained from including higher levels of dynamic correlation, e.g., CC3. Our CC2/aug-cc-pVDZ results, shown in Table 1, are slightly higher than those reported in this study, but this is most likely related to differences in geometry. This is confirmed by a recent study of uracil by Krylov et al.[20] which reports 5.0 and 5.3 eV for the lowest $n \rightarrow \pi^*$ and $\pi \rightarrow \pi^*$ transitions, respectively, using CR-EOM-CCSD(T)/aug-cc-pVTZ on a geometry optimized at B3LYP/6-311G(2df,2pd) level. We predict almost identical results, about 4.9 and 5.4 eV (Table 1), using a very similar geometry; hence, what we observe is exactly the previously mentioned cancelation effect. Therefore, we expect our CC2/aug-cc-pVDZ results to be of high accuracy.

The excitation energies calculated with DFT and CC2 are listed in Table 1. The B3LYP and B3PW91 functionals give very similar results that are underestimated by about 0.25−0.30 eV compared to CC2. PBE0 performs better and underestimates the energies by about 0.15 eV. The best performance is exhibited by the CAM-B3LYP xc-functional which provides very good agreement with the corresponding CC2 results. The $\pi \rightarrow \pi^*$ transition is underestimated by about 0.02 eV while the $n \rightarrow \pi^*$ transition is overestimated by about 0.12 eV. The same tendencies are observed in our condensed phase model system (see Table 2), although all the xc-functionals predict a larger increase in the $n \rightarrow \pi^*$ transition than CC2 compared to vacuum. Thereby it seems that the PBE0 xc-functional performs better for this transition as compared to CC2; however, the shifts of the excitation energies, compared to vacuum, in the model system are comparable for all xc-functionals. Thus, we conclude that CAM-B3LYP provides the best quality results and is therefore our xc-functional of choice for the large scale QM/MM calculations.

The results from the calculations on the model system are presented in Table 2. As expected from the DFT calculations, we do not see any substantial change in the $\pi \rightarrow \pi^*$ excitation energy when the two water molecules are included in the QM calculation, whereas the CC2 method lowers it by a relatively large amount. We see that the error made in

the CAM-B3LYP/MM calculation is about 0.01 eV while the CC2/MM calculation is off by about 0.06 eV. Thus, the CC2 method recovers about 0.05 eV compared to CAM-B3LYP. This clearly shows that it is necessary to include water molecules in the QM region and also that DFT is not fully capable of describing certain intermolecular interactions. Calculations using CC2 with many water molecules in the QM region quickly become prohibitively expensive using our large scale MD-QM/MM scheme and, thus, the most viable solution is to use DFT. From the analysis of the model system we find that CAM-B3LYP will underestimate the solvatochromic shift of the $\pi \rightarrow \pi^*$ transition by at least 0.05 eV, mainly because of the lack of dispersion interactions.

A comparison of the vacuum and QM/MM (with the polarizable force field) excitation energies calculated with a series of basis sets of increasing size is presented in Table 3. Digits written in subscript are insignificant and are shown for the sake of a more detailed comparison. There is a slight dip in the excitation energies when an extra set of diffuse functions is added. This is most evident in the augmented double-ζ basis sets while this effect is very small in the augmented triple-ζ basis sets. This indicates that we are close to the basis set limit with respect to the excitation energies in question. In addition, the vacuum excitation energies calculated with the augmented double-ζ basis are very close to the results calculated with the doubly augmented triple-ζ basis and, on top of that, there is also a cancelation of errors when we calculate the solvatochromic shifts. The conclusion is therefore that the errors due to incomplete basis are negligible.

To further assess the quality of our results, we need to inspect certain aspects of the MD-QM/MM calculations, i.e., cenvergence with respect to the number of included molecular configurations, how many water molecules should be included in the MM region, the need to include water molecules in the QM region, and the effects of a polarizable force field. First, we address the question of convergence with respect to the number of molecular configurations. Previous studies have shown that around 100 molecular configurations are adequate to get converged excitation energies,[50] and this is indeed confirmed by our study. Figure 2 contains two plots made from the results from one of the MD-QM/MM calculations. The first plot (2a) shows the fluctuations of the excitation energies in each configuration, and the second (2b) shows the convergence of the average excitation energy as the number of molecular configurations increases. We see that the fluctuations of the $n \rightarrow \pi^*$ transition are much larger in magnitude than the $\pi \rightarrow \pi^*$ excitation energies which is reflected in the higher uncertainty of the former. This is mainly due to the fact that the $n \rightarrow \pi^*$ transition is much more sensitive to the strength and orientation of the hydrogen bonds to water than the $\pi \rightarrow \pi^*$ transition because the $n \rightarrow \pi^*$ transition leads to a significant weakening of the hydrogen bond. From the second plot we observe that the excitation energies are well converged with respect to the number of molecular configurations.

The second aspect is the number of water molecules needed in the MM region, i.e., at which cutoff distance are the excitation energies converged. Although the differences

Solvatochromic Shifts in Uracil

J. Chem. Theory Comput., Vol. 6, No. 1, 2010 **253**

Table 2. Results from the DFT and (frozen core) CC2 Calculations on the Model System (uracil + 2H$_2$O)[a]

method	QM(uracil)/MM(2H$_2$O)		QM(uracil+2H$_2$O)		relative error	
	$\Delta E^{\pi\rightarrow\pi^*}$ (eV)	$\Delta E^{n\rightarrow\pi^*}$ (eV)	$\Delta E^{\pi\rightarrow\pi^*}$ (eV)	$\Delta E^{n\rightarrow\pi^*}$ (eV)	$\Delta E^{\pi\rightarrow\pi^*}$ (eV)	$\Delta E^{n\rightarrow\pi^*}$ (eV)
B3LYP	5.027	4.840	5.022	4.826	−0.005	−0.014
B3PW91	5.051	4.827	5.046	4.816	−0.005	−0.011
PBE0	5.138	4.970	5.131	4.963	−0.007	−0.007
CAM-B3LYP	5.258	5.242	5.250	5.239	−0.008	−0.003
CC2	5.264	5.052	5.204	5.051	−0.060	−0.001

[a] The relative error is defined as the difference between $E_{QM(uracil+2H_2O)}$ and $E_{QM(uracil)/MM(2H_2O)}$.

Table 3. The Lowest $\pi \rightarrow \pi^*$ and $n \rightarrow \pi^*$ Vertical Excitation Energies in Uracil in Vacuum and in Water (polarizable force field) Calculated with CAM-B3LYP and Increasing Basis Set Size[a]

basis set	$\Delta E_{vac}^{\pi\rightarrow\pi^*}$ (eV)	$\Delta E_{vac}^{n\rightarrow\pi^*}$ (eV)	$\Delta E_{sol}^{\pi\rightarrow\pi^*}$ (eV)	$\Delta E_{sol}^{n\rightarrow\pi^*}$ (eV)
aug-cc-pVDZ	5.384	5.052	5.26$_9$ ± 0.01	5.47$_6$ ± 0.03
d-aug-cc-pVDZ	5.378	5.047	5.26$_1$ ± 0.01	5.47$_1$ ± 0.03
aug-cc-pVTZ	5.387	5.057	5.27$_1$ ± 0.01	5.48$_4$ ± 0.03
d-aug-cc-pVTZ	5.386	5.055	−	−

[a] The geometry was optimized at the B3LYP(G)/aug-cc-pVTZ level of theory.

are very small, and certainly negligible considering the uncertainties, we observe the largest differences between the cutoffs of 10 and 12 Å, namely −0.002 and 0.008 eV for the $\pi \rightarrow \pi^*$ and $n \rightarrow \pi^*$ transitions, respectively. The improvement from an increased cutoff of 14 Å is vanishingly small, −0.001 and 0.002 eV for the $\pi \rightarrow \pi^*$ and $n \rightarrow \pi^*$ transitions, respectively; hence, we can conclude that a cutoff of 12 Å is fully adequate.

Excitation energies can be more or less sensitive to the nonelectrostatic interactions with the surrounding solvent. However, QM/MM interactions are purely electrostatic, and it may therefore be necessary to include a number of solvent molecules in the QM region. A hydrogen bond analysis on the molecular configurations extracted from the MD simulation using the polarizable force field shows that on average, six hydrogen bonds are formed between uracil and the surrounding water molecules. A previous study of uracil in aqueous solution arrived at the same conclusion by means of Car−Parrinello molecular dynamics.[51] We used geometric criteria to define hydrogen bonds that were derived from an analysis of the radial and angular distribution functions.

Adding water molecules to the QM region decreases the $\pi \rightarrow \pi^*$ excitation energy (see Table 4). A comparison of the $\pi \rightarrow \pi^*$ excitation energy from both force fields and with no water molecules in the QM region shows that the polarizable force field performs much better. This is evident, first of all, when comparing the $\pi \rightarrow \pi^*$ excitation energies without any QM water molecules but also when comparing the change in the energy as water molecules are added to the QM region. Using the nonpolarizable force field, it drops by about 0.05 eV while it only drops by 0.01 eV when using the polarizable force field. This shows that calculations using the polarizable potential capture a large part of the solvent interactions that are missing in the nonpolarizable force field. The $\pi \rightarrow \pi^*$ transition exhibits very slow convergence with respect to the number of QM water molecules, showing the necessity of a good description of nonelectrostatic interac-

tions. With 12 QM water molecules the energy seems to be converged within the given uncertainty. The $n \rightarrow \pi^*$ excitation energy calculated using the polarizable force field is more or less unaffected as the number of QM water molecules increases, indicating that this transition is not very sensitive to nonelectrostatic interactions and that the hydrogen bonds are well described already at the MM level. This is not the case with the nonpolarizable force field where the $n \rightarrow \pi^*$ excitation energy increases as we add QM water molecules, again showing that it is inadequate for modeling solvatochromic shifts. A comparison between the CAM-B3LYP/MM and CC2/MM results without any QM water molecules and using the polarizable force field shows that both the $\pi \rightarrow \pi^*$ and $n \rightarrow \pi^*$ transitions are in reasonable agreement with the CC2/MM result. This is moreso for the $\pi \rightarrow \pi^*$ transition as it was in the vacuum case. Our best result for the excitation energies calculated with CAM-B3LYP is obtained with the polarizable potential and 12 QM water molecules, i.e., 5.23 ± 0.01 and 5.49 ± 0.03 eV for the $\pi \rightarrow \pi^*$ and $n \rightarrow \pi^*$ transitions, respectively.

In the following, we will only consider calculations where the polarizable potential was used unless stated otherwise. A comparison of the solvatochromic shifts (see Table 5) shows that our CAM-B3LYP/MM results are in fairly good agreement with the shifts predicted by CC2/MM. In fact, the shift of the $n \rightarrow \pi^*$ transition is essentially identical while the shift of the $\pi \rightarrow \pi^*$ transition is too low in magnitude, i.e., −0.12 ± 0.01 eV compared to −0.20 ± 0.01 eV for CC2/MM.

Both CAMB3LYP/MM and CC2/MM underestimate the shift of the $\pi \rightarrow \pi^*$ transition compared to experiment (see Table 6). The shift calculated with CC2/MM is off by 0.10 eV while CAM-B3LYP/MM is off by 0.18 eV; however, adding 12 QM water molecules lowers the error to 0.14 eV. This was expected based on the analysis of the model system because QM water molecules are needed to describe the $\pi \rightarrow \pi^*$ transition correctly and because DFT does not include dispersion effects which are important for this particular transition.

From the CAM-B3LYP/MM results presented in Table 5 we find that inclusion of 12 water molecules into the QM region modifies the shifts by −0.04 and 0.02 eV for the $\pi \rightarrow \pi^*$ and $n \rightarrow \pi^*$ transitions, respectively. Adding this correction, that is mainly due to nonelectrostatic effects, to the CC2/MM predictions in Table 5, we arrive at our best estimates for the solvatochromic shifts of the $\pi \rightarrow \pi^*$ and $n \rightarrow \pi^*$ transitions of −0.24 and 0.45 eV, respectively. Since solute−solvent dispersion is fairly short-ranged in nature, an estimate of this contribution to the specific excitation
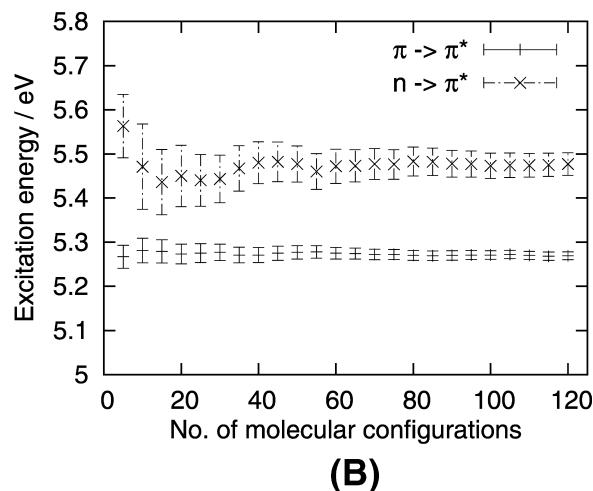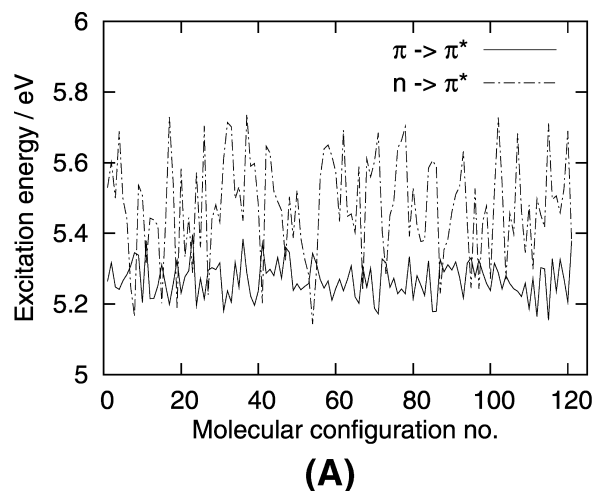
Figure 2. Fluctuations in the excitation energies in water-solvated uracil (a) and the average of the excitation energy as a function of the number of included molecular configurations in the averaging procedure (b). The results are obtained using CAM-B3LYP/aug-cc-pVDZ and the polarizable Ahlström water potential.

Table 4. The Lowest $\pi \rightarrow \pi^*$ and $n \rightarrow \pi^*$ Vertical Excitation Energies in Solvated Uracil Calculated with CAM-B3LYP and (frozen core) CC2 Using Either a Polarizable (Ahlström) or Nonpolarizable (TIP3P) Force Field and the Indicated Number of QM Water Molecules[a]

method	no. QM water	MM potential	$\Delta E_{sol}^{\pi \rightarrow \pi^*}$ (eV)	$\Delta E_{sol}^{n \rightarrow \pi^*}$ (eV)
CAM-B3LYP	0	TIP3P	5.32 ± 0.01	5.53 ± 0.02
	6		5.28 ± 0.01	5.57 ± 0.02
CAM-B3LYP	0	Ahlström	5.27 ± 0.01	5.48 ± 0.03
	6		5.25 ± 0.01	5.48 ± 0.03
	8		5.24 ± 0.01	5.49 ± 0.03
	10		5.23 ± 0.01	5.48 ± 0.03
	12		5.23 ± 0.01	5.49 ± 0.03
CC2	0	Ahlström	5.20 ± 0.01	5.37 ± 0.03

[a] The aug-cc-pVDZ basis set and B3LYP(G)/aug-cc-pVTZ geometry was used. The results are statistical averages over all molecular configurations extracted from MD simulations.

Table 5. The Solvatochromic Shifts of the Lowest $\pi \rightarrow \pi^*$ and $n \rightarrow \pi^*$ Vertical Excitation Energies in Uracil Due to Water Solvent Calculated with CAM-B3LYP and (frozen core) CC2 Using Either a Polarizable (Ahlström) or Nonpolarizable (TIP3P) Force Field and the Indicated Number of QM Water Molecules[a]

method	no. QM water	MM potential	$\Delta E_{shift}^{\pi \rightarrow \pi^*}$ (eV)	$\Delta E_{shift}^{n \rightarrow \pi^*}$ (eV)
CAM-B3LYP	0	TIP3P	-0.06 ± 0.01	0.47 ± 0.02
	6		-0.11 ± 0.01	0.51 ± 0.02
CAM-B3LYP	0	Ahlström	-0.12 ± 0.01	0.42 ± 0.03
	6		-0.13 ± 0.01	0.43 ± 0.03
	8		-0.14 ± 0.01	0.44 ± 0.03
	10		-0.15 ± 0.01	0.43 ± 0.03
	12		-0.16 ± 0.01	0.44 ± 0.03
CC2	0	Ahlström	-0.20 ± 0.01	0.43 ± 0.03

[a] The aug-cc-pVDZ basis set and B3LYP(G)/aug-cc-pVTZ geometry was used. The results are statistical averages over all molecular configurations extracted from MD simulations.

energies may be derived from the analysis of the model systems. Thus, based on the results for the model system a further decrease of 0.05 eV (due to solute−solvent dispersion) could be added to the shift affiliated with the $\pi \rightarrow \pi^*$ transition, thereby arriving at a final estimate of −0.29 eV

Table 6. The Solvatochromic Shifts of the Lowest $\pi \rightarrow \pi^*$ and $n \rightarrow \pi^*$ Vertical Excitation Energies in Uracil Due to Water Solvent from Our Study and Other Theoretical Studies as well as Experimental Data[a]

method	$\Delta E_{shift}^{\pi \rightarrow \pi^*}$ (eV)	$\Delta E_{shift}^{n \rightarrow \pi^*}$ (eV)
CAM-B3LYP/MM	-0.12 ± 0.01	0.42 ± 0.03
CAM-B3LYP[b]/MM	-0.16 ± 0.01	0.44 ± 0.03
CC2/MM	-0.20 ± 0.01	0.43 ± 0.03
CC2/CAM-B3LYP/MM	-0.29 ± 0.01	0.45 ± 0.03
PBE0/PCM[13]	-0.09	0.35
PBE0[c]/PCM[13]	-0.12	0.47
B3PW91[d]/PCM[11]	-0.17	0.59
INDO/CIS[11]	-0.19	0.50
PMM/B3LYP[14]	-0.18	0.38
PMM/CCSD[14]	-0.12	0.34
EOM-CCSDt(II)[e]/MM[20]	0.07	0.44
MRCI2/MM[22]	-0.05	0.41
FMO-MCSCF[22]	-0.19	0.44
experiment[f] [23−26]	-0.30 ± 0.02	-

[a] The CC2/CAM-B3LYP/MM is a best estimate based on CC2 with electrostatic corrections defined from CAM-B3LYP and dispersion corrections derived from CC2 model system calculations. [b] Uracil and 12 water molecules. [c] Uracil and 4 water molecules. [d] Uracil and 9 water molecules. [e] (10,10) active space, i.e., 10 electrons in 10 orbitals. [f] The quoted experimental value is an average over values obtained from 4 different studies.

for this shift and leading to results for both the $\pi \rightarrow \pi^*$ and $n \rightarrow \pi^*$ shifts in very good agreement with experimental findings. We note, however, that there is no convincing experimental value for the shift of the $n \rightarrow \pi^*$ transition available; however, other theoretical studies have assumed a shift of about 0.5 eV, and this is confirmed by our study as well.

In this study we have presented the most complete description of the solvatochromic shifts of the two lowest vertical excitations in water solvated uracil, wherein we have taken into account nuclear dynamical effects, electrostatic interactions, polarization, dispersion, nonelectrostatic repulsion, and electron correlation. There are several theoretical studies of the solvatochromic shifts in uracil[11,13,14,20,22] some of which are listed in Table 6 together with our best results. Gustavsson et al.[13] reported −0.09 and 0.35 eV for the shifts of the $\pi \rightarrow \pi^*$ and $n \rightarrow \pi^*$ transitions, respectively, using

Solvatochromic Shifts in Uracil

J. Chem. Theory Comput., Vol. 6, No. 1, 2010 **255**

PBE0 exchange correlation functional and PCM to model the solvent effects. Adding four explicit water molecules improved the shifts yielding −0.12 and 0.47 eV for the $\pi \rightarrow \pi^*$ and $n \rightarrow \pi^*$ transitions, respectively. This is consistent with other studies, e.g., Ludwig et al.[11] reported shifts of −0.17 and 0.59 eV using B3PW91 and PCM with nine explicit water molecules. Here we see the need for a quantum mechanical treatment of at least the first solvation shell, i.e., the shift of the $\pi \rightarrow \pi^*$ transition improves with increasing number of QM water molecules. Although it seems that the shift in the $n \rightarrow \pi^*$ transition also tends to increase with increasing number of QM water molecules which we also observed when using a nonpolarizable force field, it does not change significantly when using the polarizable force field, indicating that it provides a good description of the hydrogen bonding. Ludwig et al. also report shifts that are calculated using the semiempirical INDO/CIS method on uracil and 200 water molecules which predicted shifts of −0.19 and 0.50 eV for the $\pi \rightarrow \pi^*$ and $n \rightarrow \pi^*$ transitions, respectively. The perturbed matrix method (PMM) used with the B3LYP functional and CCSD method yields shifts of −0.18 and −0.12 eV, respectively, for the $\pi \rightarrow \pi^*$ transition and 0.38 and 0.34 eV, respectively, for the $n \rightarrow \pi^*$ transition.[14] Krylov et al.[20] predict a blue-shift of the $\pi \rightarrow \pi^*$ transition using an active space EOM-CCSDt/MM method whereas our CC2 results actually are in good agreement with experiment. Thus, the specific blue-shift based on CC cannot, as detailed in our investigation, be related to a less satisfactory performance of CC in prediction of solvatochromic shifts. Kistler and Matsika[22] employed the fragment molecular orbital (FMO) method in combination with MCSCF to benchmark MRCI2/MM calculations of the shifts. The MRCI2/MM results again show the need for QM treatment of the surrounding water molecules, because the predicted shift in the $\pi \rightarrow \pi^*$ transition is only −0.05 eV. FMO-MCSCF predicts the shifts to be −0.19 and 0.44 eV for the $\pi \rightarrow \pi^*$ and $n \rightarrow \pi^*$ transitions, respectively, which is very similar to our CC2/MM results.

4. Conclusions

The solvatochromic shifts of the lowest $\pi \rightarrow \pi^*$ and $n \rightarrow \pi^*$ vertical electronic excitation energies in uracil due to an aqueous solution were calculated using a polarizable MD-QM/MM method. The electronic structure calculations were performed using either density functional theory through the CAM-B3LYP xc-functional or CC2. Using CC2 as a benchmark, we found CAM-B3LYP to provide reliable results for the excited states considered. The CAM-B3LYP/MM method predicts solvatochromic shifts of −0.12 ± 0.01 eV and 0.42 ± 0.03 eV for the $\pi \rightarrow \pi^*$ and $n \rightarrow \pi^*$ transitions, respectively, while CC2/MM predicts −0.20 ± 0.01 eV 0.43 ± 0.03 eV. An analysis of a condensed phase model system, uracil with two hydrogen bonded water molecules, allowed for a quantification of the errors made by DFT due to incorrect description of dispersion interactions. We find that a polarizable force field is important for a complete description of the electrostatic solute−solvent interactions. Furthermore, a correct description of the $\pi \rightarrow \pi^*$ transition requires nonelectrostatic solute−solvent inter-

actions to be included by quantum mechanical calculations. Presently, this is only viable through DFT, and converged results were found by adding 12 water molecules in the QM region. Thus, our best estimate of the solvatochromic shifts are −0.29 ± 0.01 eV and 0.45 ± 0.03 eV for the $\pi \rightarrow \pi^*$ and $n \rightarrow \pi^*$ transitions, respectively, in excellent agreement with experimental data.

References

(1) Tomasi, J.; Mennucci, B.; Cammi, R. *Chem. Rev.* **2005**, *105*, 2999.

(2) Jørgensen, W. L. *J. Chem. Theory Comput.* **2007**, *3*, 1877.

(3) Yu, H.; van Gunsteren, W. F. *Comput. Phys. Commun.* **2005**, *172*, 69.

(4) Kongsted, J.; Osted, A.; Mikkelsen, K. V.; Christiansen, O. *J. Phys. Chem. A* **2003**, *107*, 2578. Kongsted, J.; Osted, A.; Mikkelsen, K. V.; Christiansen, O. *J. Chem. Phys.* **2003**, *118*, 1620. Osted, A.; Kongsted, J.; Mikkelsen, K. V.; Christiansen, O. *J. Chem. Phys.* **2004**, *108*, 8646.

(5) Osted, A.; Kongsted, J.; Mikkelsen, K. V.; Christiansen, O. *J. Chem. Phys.* **2006**, *124*, 124503.

(6) Kongsted, J.; Mennucci, B. *J. Phys. Chem. A* **2007**, *111*, 9890.

(7) Nielsen, C. B.; Christiansen, O.; Mikkelsen, K. V.; Kongsted, J. *J. Chem. Phys.* **2007**, *126*, 154112.

(8) Ismail, N.; Blancafort, L.; Olivucci, M.; Kohler, B.; Robb, M. A. *J. Am. Chem. Soc.* **2002**, *124*, 6818.

(9) Merchan, M.; Serrano-Andres, L. *J. Am. Chem. Soc.* **2003**, *125*, 8108.

(10) Matsika, S. *J. Phys. Chem. A* **2004**, *108*, 7584.

(11) Ludwig, V.; Coutinho, K.; Canuto, S. *Phys. Chem. Chem. Phys.* **2007**, *9*, 4907.

(12) Fleig, T.; Knecht, S.; Hättig, C. *J. Phys. Chem. A* **2007**, *111*, 5482.

(13) Gustavsson, T.; Bányász, A.; Lazzarotto, E.; Markovitsi, D.; Schalmani, G.; Frisch, M. J.; Barone, V.; Improta, R. *J. Am. Chem. Soc.* **2006**, *128*, 607.

(14) Zazza, C.; Amadei, A.; Sanna, N.; Grandi, A.; Chillemi, G.; Nola, A. D.; D'abramo, M.; Aschi, M. *Phys. Chem. Chem. Phys.* **2006**, *8*, 1385.

(15) Fulsher, M.; Serrano-Andres, L.; Roos, B. O. *J. Am. Chem. Soc.* **1997**, *119*, 6168.

(16) Shukla, M. K.; Leszczynski, J. *J. Phys. Chem. A* **2002**, *106*, 8642.

(17) Broo, A.; Holmen, A. *J. Phys. Chem. A* **1997**, *101*, 3589.

(18) Mennucci, B.; Toniolo, A.; Tomasi, J. *J. Phys. Chem. A* **2001**, *105*, 4749.

(19) Improta, R.; Barone, V. *J. Am. Chem. Soc.* **2004**, *126*, 14320.

(20) Epifanovski, E.; Kowalski, K.; Fan, P.-D.; Valiev, M.; Matsika, S.; Krylov, A. I. *J. Phys. Chem. A.* **2008**, *112*, 9983.

(21) Marian, C. M.; Schneider, F.; Kleinschmidt, M.; Tatchen, J. *Eur. Phys. J. D* **2002**, *20*, 357.

(22) Kistler, K. A.; Matsika, S. *J. Phys. Chem. A* **2009**, *113*, 12396.

(23) Voet, D.; Gratzer, W. B.; Cox, R. A.; Doty, P. *Biopolymers* **1963**, *1*, 193.

(24) Clark, L. B.; Peschel, G. G.; Tinoco, I., Jr. *J. Phys. Chem.* **1965**, *69*, 3615.

(25) Daniels, M.; Hauswirth, W. *Science* **1971**, *171*, 675.

(26) Du, H.; Fuh, R. A.; Li, J.; Corkan, A.; Lidsey, J. S. *Photochem. Photobiol.* **1998**, *68*, 141.

(27) DALTON, a molecular electronic structure program, release 2.0, 2005; see http://www.daltonprogram.org/.

(28) Linse, P.; MOLSIM; part of an integrated MD/MC/BD simulation program belonging to the MOLSIM package; Version 3.3.0, Dec 5, 2001.

(29) Aidas, K. *Whirlpool*: a QM/MM analysis program, University of Copenhagen, 2009.

(30) Frisch, M. J.; Trucks, G. W.; Schlegel, H. B.; Scuseria, G. E.; Robb, M. A.; Cheeseman, J. R.; Montgomery, J. A., Jr.; Vreven, T.; Kudin, K. N.; Burant, J. C.; Millam, J. M.; Iyengar, S. S.; Tomasi, J.; Barone, V.; Mennucci, B.; Cossi, M.; Scalmani, G.; Rega, N.; Petersson, G. A.; Nakatsuji, H.; Hada, M.; Ehara, M.; Toyota, K.; Fukuda, R.; Hasegawa, J.; Ishida, M.; Nakajima, T.; Honda, Y.; Kitao, O.; Nakai, H.; Klene, M.; Li, X.; Knox, J. E.; Hratchian, H. P.; Cross, J. B.; Bakken, V.; Adamo, C.; Jaramillo, J.; Gomperts, R.; Stratmann, R. E.; Yazyev, O.; Austin, A. J.; Cammi, R.; Pomelli, C.; Ochterski, J. W.; Ayala, P. Y.; Morokuma, K.; Voth, G. A.; Salvador, P.; Dannenberg, J. J.; Zakrzewski, V. G.; Dapprich, S.; Daniels, A. D.; Strain, M. C.; Farkas, O.; Malick, D. K.; Rabuck, A. D.; Raghavachari, K.; Foresman, J. B.; Ortiz, J. V.; Cui, Q.; Baboul, A. G.; Clifford, S.; Cioslowski, J.; Stefanov, B. B.; Liu, G.; Liashenko, A.; Piskorz, P.; Komaromi, I.; Martin, R. L.; Fox, D. J.; Keith, T.; Al-Laham, M. A.; Peng, C. Y.; Nanayakkara, A.; Challacombe, M.; Gill, P. M. W.; Johnson, B.; Chen, W.; Wong, M. W.; Gonzalez, C.; Pople, J. A. Gaussian 03, Revision E.01; Gaussian, Inc., Wallingford, CT, 2004.

(31) Becke, A. D. *J. Chem. Phys.* **1993**, *98*, 5648.

(32) Lee, C. T.; Yang, W. T.; Parr, R. G. *Phys. Rev. B* **1988**, *37*, 785.

(33) Vosko, S. H.; Wilk, L.; Nusair, M. *Can. J. Phys.* **1980**, *58*, 1200.

(34) Stephens, P. J.; Devlin, F. J.; Chabalowski, C. F.; Frisch, M. J. *J. Phys. Chem.* **1994**, *98*, 11623.

(35) Karlström, G.; Lindh, R.; Malmqvist, P.-Å.; Roos, B. O.; Ryde, U.; Veryazov, V.; Widmark, P.-O.; Cossi, M.; Schimmelpfennig, B.; Neogrady, P.; Seijo, L. *Comput. Mater. Sci.* **2003**, *28*, 222.

(36) Dunning, T. H., Jr. *J. Chem. Phys.* **1989**, *90*, 1007.

(37) Kendall, R. A.; Dunning, T. H.; Harrison, R. J. *J. Chem. Phys.* **1992**, *96*, 6796.

(38) Miertuš, S.; Scrocco, E.; Tomasi, J. *Chem. Phys.* **1981**, *55*, 117.

(39) Jørgensen, W. L. *J. Am. Chem. Soc.* **1981**, *103*, 335.

(40) Ahlström, P.; Wallqvist, A.; Engström, S.; Jönsson, B. *Mol. Phys.* **1989**, *68*, 563.

(41) Breneman, C. M.; Wiberg, K. B. *J. Comput. Chem.* **1990**, *11*, 361.

(42) Gagliardi, L.; Lindh, R.; Karlström, G. *J. Chem. Phys.* **2004**, *121*, 4494.

(43) Pranata, J.; Wierschke, S. G.; Jorgensen, W. L. *J. Am. Chem. Soc.* **1991**, *113*, 2810.

(44) Yanai, T.; Tew, D. P.; Handy, N. C. *Chem. Phys. Lett.* **2004**, *393*, 51.

(45) Peach, M. J. G.; Helgaker, T.; Sałek, P.; Keal, T. W.; Lutnæs, O. B.; Tozer, D. J.; Handy, N. C. *Phys. Chem. Chem. Phys.* **2006**, *8*, 558.

(46) Perdew, J.; Wang, Y. *Phys. Rev. B* **1992**, *45*, 13244.

(47) Ernzerhof, M.; Scuseria, G. E. *J. Chem. Phys.* **1999**, *110*, 5029.

(48) Adamo, C.; Barone, V. *J. Chem. Phys.* **1999**, *110*, 6158.

(49) Christiansen, O.; Koch, H.; Jørgensen, P. *Chem. Phys. Lett.* **1995**, *243*, 409.

(50) Aidas, K.; Møgelhøj, A.; Nilsson, E. J. K.; Johnson, M. S.; Mikkelsen, K. V.; Christiansen, O.; Söderhjelm, P.; Kongsted, J. *J. Chem. Phys.* **2008**, *128*, 194503.

(51) Gaigeot, M.-P.; Sprik, M. *J. Phys. Chem. B* **2004**, *108*, 7458.

JCTC Journal of Chemical Theory and Computation

Modeling the Excited States of Biological Chromophores within Many-Body Green's Function Theory

Yuchen Ma,*,[†] Michael Rohlfing,[†] and Carla Molteni[‡]

Fachbereich Physik, Universität Osnabrück, D-49069 Osnabrück, Germany, and Physics Department, King's College London, Strand, London WC2R 2LS, United Kingdom

Abstract: First-principle many-body Green's function theory (MBGFT) has been successfully used to describe electronic excitations in many materials, from bulk crystals to nanoparticles. Here we assess its performance for the calculations of the excited states of biological chromophores. MBGFT is based on a set of Green's function equations, whose key ingredients are the electron's self-energy Σ, which is obtained by Hedin's GW approach, and the electron−hole interaction, which is described by the Bethe−Salpeter equation (BSE). The GW approach and the BSE predict orbital energies and excitation energies with high accuracy, respectively. We have calculated the low-lying excited states of a series of model biological chromophores, related to the photoactive yellow protein (PYP), rhodopsin, and the green fluorescent protein (GFP), obtaining a very good agreement with the available experimental and accurate theoretical data; the order of the excited states is also correctly predicted. MBGFT bridges the gap between time-dependent density functional theory and high-level quantum chemistry methods, combining the efficiency of the former with the accuracy of the latter: this makes MBGFT a promising method for studying excitations in complex biological systems.

I. Introduction

The photoactive yellow protein (PYP) and rhodopsin are photoreceptors that transform light into biological signals. Their photocycles are initiated by the photoinduced trans/cis isomerization of their chromophores, which leads to successive conformational changes of the overall protein structure and ultimately produces the biological response.[1] PYP was first found in the halophilic purple bacterium *Ectothiorhodospira halophila* and is linked to the negative phototaxis to blue light; the chromophore of PYP is a deprotonated *p*-coumaric acid (*p*CA), linked to a cysteine in the protein via a thioester bond. The chromophore of rhodopsin is retinal in the protonated Schiff base form; light absorption induces isomerization of 11-*cis*-retinal to all-*trans*-retinal and initiates the visual cycle. The green fluorescent protein (GFP) was first isolated in the jellyfish *Aequorea victoria*; its chromophore is *p*-hydroxybenzylideneimida-zolinone (*p*-HBDI)[2] in its neutral or anionic form. GFP is widely used as a biological label, since it can be implanted into host proteins without affecting their normal properties; the host proteins, however, become fluorescent and can be detected in living cells and organisms.

Understanding the photochemical processes in photoactive proteins has attracted much interest in both experiments and theory. A wealth of work has been accomplished to investigate optical spectra, the isomerization processes of chromophores, and the role of solution and protein environment in the electronic excitations. Recent measurements of the optical absorption of chromophores in the gas phase provide an experimental benchmark for theoretical methods.[3−10]

Ab initio calculations for biological chromophores have been performed extensively at various levels of quantum chemistry theory. The methods used include time-dependent density functional theory (TDDFT),[4,6,11−14] second-order approximate coupled cluster singles and doubles model (CC2),[15,16] equation of motion coupled cluster theory (EOM-CCSD),[4,5,13,15,17,18] complete active space with second-order perturbation theory (CASPT2),[18−22] and the augmented

* Corresponding author e-mail: yuma@uos.de.
† Universität Osnabrück.
‡ King's College London.

version of the multiconfigurational quasi-degenerate perturbation theory (aug-MCQDPT2):[10,23] both accuracy and computational cost progressively increase from TDDFT, through CC2, EOM-CCSD, CASPT2 up to aug-MCQDPT2. Recently quantum Monte Carlo has also been used for evaluating excited states.[24,25]

Semiempirical methods, like ZINDO, also can give good approximations for the excited states of biological chromophores at a reduced computational cost,[14] but they might be less transferable to a wide range of systems than ab initio methods.

In spite of many efforts, the accurate calculation of the excited states in relative large molecules remains a challenge. In fact, highly reliable methods such as EOM-CCSD, CASPT2, and aug-MCQDPT2 can only be applied to small systems because of their large computational cost. In the last 2 decades, CASPT2 has been regarded as the standard ab initio method for calculating accurate excited-state properties of organic molecules;[26] however, the quality of CASPT2 excitation energies decreases if the complete active space self-consistent field (CASSCF) function is not a good reference and/or the basis set is not sufficiently large.[27] The average accuracy of EOM-CCSD is generally considered to be of 0.2−0.4 eV.[28,29] As an approximation to CCSD, the typical error in CC2 is within the range of 0.3−0.5 eV.[28,29] EOM-CCSD and CC2 can get good results for singlet excited states that are dominated by single-electron transitions.[26] Recent aug-MCQDPT2 calculations provided very good estimations (within 0.1 eV) for the lowest $\pi \rightarrow \pi^*$ excited state of some chromophore models;[23,27,30] however, the general performance of aug-MCQDPT2 for other excited states is still unknown, which prevents a systematic comparison with other quantum chemistry approaches. TDDFT is the fastest quantum chemistry method for calculating excited states of medium- and large-sized molecules of up to 200 second-row atoms. However, with the commonly used approximations, TDDFT yields substantial errors for excited states of molecules with extended π-systems, as well as for nonlocal electronic transitions such as charge-transfer excitations and excited states with little single-excitation character.[11,31,32] The order of the states and the oscillation strengths are also important factors to test the reliability of a method: at present there is no consensus on these for PYP chromophores, for example.[5] In summary, the applicability of quantum chemistry approaches depends strongly on the system under investigation.

In response to the limitations of traditional quantum chemistry methods, here we propose and test the use of many-body Green's function theory (MBGFT)[33−35] for the study of biological chromophores. We demonstrate that MBGFT can compute accurate excitation energies for chromophores that are in excellent agreement with experiments with a reasonable computational cost. MBGFT is well-known in the physics and materials science community to predict orbital and excitation energies with high accuracy. It has been widely and successfully used for describing optical excitations in many systems, including bulk crystals,[36−38] clusters,[39] polymers,[40,41] inorganic molecules (e.g., SiH$_4$,[39] CO,[42] NH$_3$[42]) and organic molecules[40,43] (e.g., benzene and
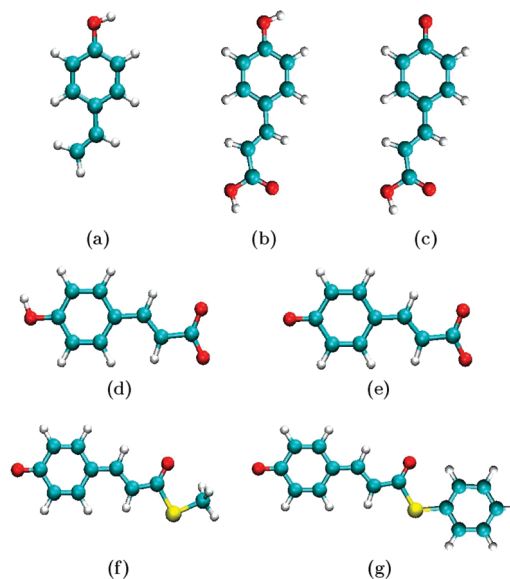
Figure 1. PYP chromophore models studied in this work: (a) pVP, (b) pCA, (c) pCA$^-$′, (d) pCA$^-$″, (e) pCA^{2-}, (f) TMpCA$^-$, and (g) pCT$^-$. Carbon, hydrogen, oxygen, and sulfur atoms are represented in cyan, gray, red, and yellow, respectively.
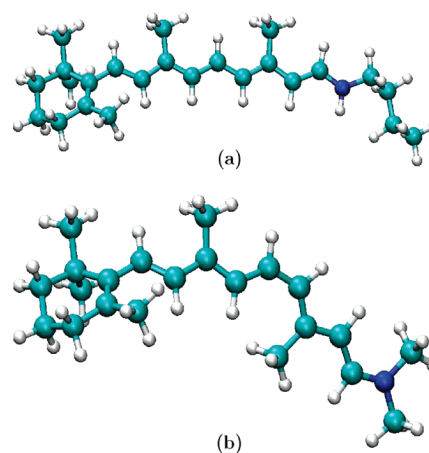
Figure 2. Retinal chromophore models studied in this work: (a) all-trans protonated Shiff base of retinal (PSBT); (b) 11-cis protonated Schiff base of retinal (PSB11).

naphthalene). The typical error for the excitation energies is within 0.1−0.2 eV.

Here, we present the calculations of the excitation energies of several chromophore models related to PYP, rhodopsin, and GFP, for which experimental data are available, to test the applicability of MBGFT method for biological chromophores. To the best of our knowledge, this work is the first that applies MBGFT method to biological chromophores.

II. Chromophore Models

The 12 chromophore models studied in this work are shown in Figure 1 (PYP chromophore models), Figure 2 (rhodopsin chromophore models), and Figure 3 (GFP chromophore models).

Optical absorption spectra have been measured for the chromophore models related to PYP: *p*-coumaric acid

Modeling Excited States of Biological Chromophores

J. Chem. Theory Comput., Vol. 6, No. 1, 2010 **259**
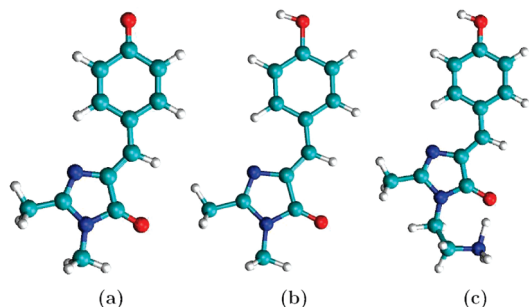
Figure 3. GFP chromophore models studied in this work: (a) *p*-HBDI⁻, (b) *p*-HBDI, and (c) *p*-HBDI⁺. Nitrogen atoms are represented in blue.

(*p*CA),[44] the methyloxy ester of *p*CA (OM*p*CA),[5] deprotonated *p*-coumaric acid (*p*CA⁻),[8,10,44] the double-anionic form of *p*-coumaric acid (*p*CA²⁻),[8,44] deprotonated thiomethyl *p*-coumaric acid (TM*p*CA⁻)[20] and deprotonated thiophenyl *p*-coumarate (*p*CT⁻);[8] the chromophore modes of rhodopsin: all-trans protonated Schiff base of retinal (PSBT)[3,9] and 11-cis protonated Schiff base of retinal (PSB11);[9] and the GFP chromophore *p*-HBDI in different charged states (anionic *p*-HBDI⁻,[7] neutral *p*-HBDI[45]) plus a cationic form of the GFP chromophore,[6] which we simply denote here as *p*-HBDI⁺, shown in Figure 3c.

For *p*CA⁻ the deprotonation can occur either at the phenol site or at the carboxyl site as shown in Figure 1c and d, respectively; we denote the two cases as *p*CA⁻′ and *p*CA⁻″, respectively. The absorption spectrum of *p*-vinylphenol (*p*VP), formed from *p*CA by thermal decarboxylation during the experiment, is also available.[4,46]

III. Methods and Computational Details

The ground-state geometries of the chromophore models are optimized within density functional theory (DFT) using the SIESTA code,[47] employing the PBE generalized gradient approximation (GGA)[48] for the exchange and correlation energy and norm-conserving Troullier−Martins pseudopotentials[49] to describe the interaction between the ion cores and the valence electrons. A double-ζ plus polarization (DZP) basis set made of atomic orbitals is used for the geometry optimization and gives converged structures. In fact, bond length differences between DZP basis set and a larger triple-ζ plus polarization basis set are smaller than 0.004 Å. The PBE exchange and correlation functional is widely used for materials and chemical systems. In comparison with results obtained with other popular functionals, e.g., BLYP[25] and the hybrid B3LYP,[17,50−52] the bond lengths calculated with PBE are on average longer by about 0.01−0.02 Å. Such differences in geometry influence the MBGFT excitation energy by less than 0.1 eV, which makes PBE geometries a reasonable starting point for excitation energy calculation within MBGFT. However, the influence of the DFT exchange-correlation functional on the MBGFT excitation energies deserves further studies.

The excited states of the ground-state geometries obtained as described above are then calculated within MBGFT. At variance from the geometry optimization where basis sets constructed by atomic orbitals were used, the basis set for all steps of the MBGFT calculations is made by atom-centered Gaussian orbitals which have the form

$$\phi_{ijk}(\mathbf{r}) = A_{ijk}x^iy^jz^k e^{-\alpha \mathbf{r}^2} \tag{1}$$

The same exchange and correlation functional and pseudopotentials are used. Four decay constants (α) are used for C, N, O, and S atoms (0.2, 0.5, 1.25, and 3.2 in atomic units (a_0^{-2})), whereas three decay constants are used for H atoms (0.1, 0.4, and 1.5 in atomic units). Gaussian orbitals with s, p, d, and s* symmetry are included for each atom. The number of Gaussian orbitals for each atom is 40 for C, N, O, S and 30 for H, respectively. The decay constants have been tested to give converged orbital and excitation energies. They are adjusted so that orbital energies calculated by the Gaussian orbital basis set reproduce (within 0.1 eV) those obtained by a well-converged plane-wave basis set. A larger basis set, which, besides the atom-centered Gaussian orbitals discussed above, contains additional Gaussian orbitals centered above and below the plane of the molecule to give a better description of the π and π^* orbitals, modifies the lowest excitation energy of *p*CA⁻ by only 0.03 eV. This shows that the basis set with only atom-centered Gaussian orbitals is able to give converged excitation energies and is suitable to study the selected chromophore models.

In DFT, one needs to solve the Kohn−Sham equation

$$\left\{-\frac{\hbar^2}{2m}\nabla^2 + V_{ps}(\mathbf{r}) + V_{H}(\mathbf{r}) + V_{xc}(\mathbf{r})\right\}\psi_n^{DFT}(\mathbf{r}) = E_n^{DFT}\psi_n^{DFT}(\mathbf{r}) \tag{2}$$

where V_{ps} and V_{H} are the pseudopotentials describing the electron−ion interaction and the Hartree potential, respectively, and V_{xc} is the exchange-correlation potential. Approximation to the exchange-correlation potential in DFT makes it fail to predict correctly the orbital energies. In MBGFT, accurate orbital energies can be obtained within the GW approximation (GWA), proposed by Hedin and Lundqvist.[33] An accurate prediction of the orbital energies is an essential prerequisite for the further excited-state calculation in MBGFT. GWA has been successfully applied to compute band structures of a large number of solids[53] and orbital energies of many molecules[42,43] including organic molecules.[43] Within GWA, V_{xc} in DFT is replaced by a nonlocal, energy-dependent self-energy operator $\Sigma(\mathbf{r}, \mathbf{r}', E)$, which fulfills the GW equation[54]

$$\left\{-\frac{\hbar^2}{2m}\nabla^2 + V_{ps}(\mathbf{r}) + V_{H}(\mathbf{r})\right\}\psi_n^{GWA}(\mathbf{r}) + \int \Sigma(\mathbf{r}, \mathbf{r}', E_n^{GWA})\psi_n^{GWA}(\mathbf{r}')\,d\mathbf{r}' = E_n^{GWA}\psi_n^{GWA}(\mathbf{r}) \tag{3}$$

The self-energy operator $\Sigma(\mathbf{r}, \mathbf{r}', E)$ can be evaluated by

$$\Sigma(\mathbf{r}, \mathbf{r}', E) = \frac{i}{2\pi}\int e^{-i\omega 0^+} G(\mathbf{r}, \mathbf{r}', E - \omega)W(\mathbf{r}, \mathbf{r}', \omega)\,d\omega \tag{4}$$

where *G* and *W* are the one-body Green function and the dynamically screened Coulomb interaction, respectively. *G* and *W* are in the forms

$$G(\mathbf{r}, \mathbf{r}', E) = \sum_n \frac{\psi_n(\mathbf{r})\psi_n^*(\mathbf{r}')}{E - E_n + i0^+ \, \mathrm{sgn}(E_n - \mu)} \tag{5}$$

and

$$W = \varepsilon^{-1}v \tag{6}$$

respectively, where ε and v are the dielectric function and the bare Coulomb interaction, respectively. μ is the chemical potential. G and W are evaluated based on the ground-state wave functions and energies obtained from eq 2. ε is calculated within the random-phase approximation.[54] Usually, the GWA orbital energies are evaluated perturbatively to first order by

$$E_n^{\mathrm{GWA}} = E_n^{\mathrm{DFT}} + Z_n \langle \psi_n^{\mathrm{DFT}} | \Sigma(E_n^{\mathrm{DFT}}) - V_{\mathrm{xc}} | \psi_n^{\mathrm{DFT}} \rangle \tag{7}$$

based on the assumption that the DFT wave function in eq 2 agrees well with the GWA wave function in eq 3 in most cases.[56] Z_n is the renormalization constant to take into account the energy dependence of the self-energy[56]

$$Z_n = 1 - \left[\frac{\partial \Sigma_n(E)}{\partial E} \Big|_{E=E_n^{\mathrm{GWA}}} \right]^{-1} \tag{8}$$

where $\Sigma_n(E) = \langle \psi_n^{\mathrm{DFT}} | \Sigma(E) | \psi_n^{\mathrm{DFT}} \rangle$.

By applying GWA, the original occupied orbitals within DFT are shifted down while the unoccupied orbitals are raised up, as shown in Figure 4 and discussed in the following section for pCA and pCA$^{-\prime}$. In some cases the order of energy levels may change from DFT to GWA; for example, in pCA HOMO $-$ 1 in DFT becomes HOMO $-$ 2 in GWA, while HOMO $-$ 2 in DFT turns out to be HOMO $-$ 1 in GWA.

If an electron is excited into a higher state it leaves a hole in its old state. The excited electron and the hole cannot be treated separately, since the electron feels the presence of the hole. Due to the Coulomb interaction between the excited electrons and holes, optical electron−hole excitations cannot be described by an effective one-particle picture. Instead, it is necessary to consider two-particle (electron and hole) states which can be described as

$$\chi(\mathbf{r}_e, \mathbf{r}_h) = \sum_\alpha^{\mathrm{occ}} \sum_\beta^{\mathrm{virt}} [A_{\alpha\beta}\psi_\beta(\mathbf{r}_e)\psi_\alpha^*(\mathbf{r}_h) + B_{\alpha\beta}\psi_\alpha(\mathbf{r}_e)\psi_\beta^*(\mathbf{r}_h)] \tag{9}$$

where $A_{\alpha\beta}$ and $B_{\alpha\beta}$ are resonant (occupied → virtual) and antiresonant (virtual → occupied) electron−hole amplitudes, respectively, and α and β denote the one-particle occupied and virtual orbitals, respectively. The motion of the electron−hole pair, well-represented by the two-particle Green's function, can be rigorously described by the Bethe−Salpeter equation (BSE).[34,35] For singlet-to-singlet excitations, the generalized BSE takes the form[34]

$$\begin{pmatrix} R & C \\ -C^* & -R^* \end{pmatrix} \begin{pmatrix} A \\ B \end{pmatrix} = \Omega \begin{pmatrix} A \\ B \end{pmatrix} \tag{10}$$
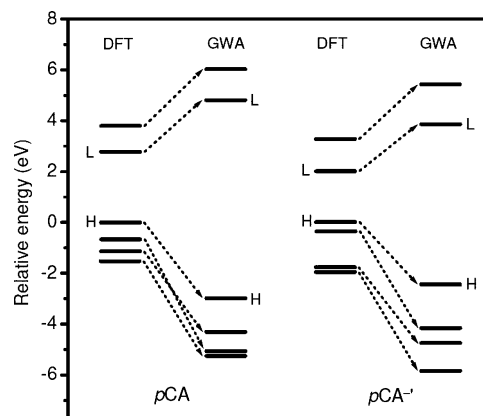
Figure 4. Energy levels (four occupied and two unoccupied) of pCA and pCA$^{-\prime}$ calculated within DFT and GWA. H and L denote the highest occupied molecular orbital (HOMO) and lowest unoccupied molecular orbital (LUMO), respectively. The energy levels in DFT and the corresponding ones in GWA are connected by dotted arrow lines. In both chromophore models, the energies of the highest occupied orbitals (H) within DFT are set to zero.

with $R = D + 2K^{R,x} + K^{R,d}$, $C = 2K^{C,x} + K^{C,d}$, and $D = E_{\mathrm{occ}}^{\mathrm{GWA}} - E_{\mathrm{virt}}^{\mathrm{GWA}}$.[35] R and $-R^*$ are the Hamiltonians corresponding to the resonant and antiresonant parts of the transitions, respectively, whereas C and $-C^*$ are the coupling terms between resonant and antiresonant transitions. D is the free interlevel transition energy between occupied and virtual orbitals. Ω is the excitation energy, i.e., the energy difference between the excited state and the ground state within the Franck−Condon approximation. $K^{R,x}$ ($K^{R,d}$) is the bare exchange term (screened direct term) of the electron−hole interaction kernel for the resonant transition, whereas $K^{C,x}$ ($K^{C,d}$) are corresponding terms for the coupling terms.

The procedure to compute the optical spectrum with MBGFT is that first, conventional DFT (here within PBE-GGA) is performed to calculate the ground-state orbital energies and wave functions; then, accurate orbital energies are computed within GWA with the ground-state orbital energies and wave functions as input parameters; finally, BSE is solved with the GWA orbital energies and ground-state wave functions (used to construct the excited state in eq 9) as input parameters. Indicatively, a GW + BSE calculation for one of the chromophore models studied in this work can usually be completed within half a day with a single CPU.

MBGFT calculations of the excitation energies for crystals, clusters, nanotubes, and polymers are usually done within Tamm−Dancoff approximation (TDA),[34] i.e., the coupling term C in eq 10 is omitted. The coupling term C is in fact nearly zero for these systems, and TDA only influences the excitation energy by about 0.1 eV. However, for the chromophores studied here, we find that the magnitude of the coupling term C is comparable to that of the resonant transition R in eq 10 so that the coupling term cannot be neglected, and we have to solve the full BSE. TDA only influences the excitation energy related to the $\pi \rightarrow \pi^*$ transitions. For example, for the lowest $\pi \rightarrow \pi^*$ transitions in all the chromophore models, TDA overestimates the excitation energy by at least 0.4 eV. In contrast, TDA has very weak influence on the energy for the $n \rightarrow \pi^*$ excitations.

Table 1. Selected Excitation Energies (in eV) of PYP, GFP, and Retinal Chromophore Models Calculated by Many-Body Green's Function Theory and Their Comparison with Reference Experimental Data and a Selection of Theoretical Values[a]

model	experiment	MBGFT		other theory
*p*VP	4.12 (ref 4)	S$_1$	4.17	4.19 (ref 4)[b], 4.57 (ref 11)[c], 4.66 (ref 4)[d]
	4.75 (ref 4)	S$_2$	4.60	4.52 (ref 4)[b], 5.43 (ref 4)[d]
*p*CA	4.06 (ref 5)[e], 4.00 (ref 44)[f]	S$_1$	3.94	3.78 (ref 12)[g], 4.15 (ref 5)[h], 4.20 (ref 11)[c], 4.69 (ref 5)[d], 4.92 (ref 17)[i]
	4.37 (ref 5)[e]	S$_2$	4.20	4.58 (ref 5)[h], 4.95 (ref 5)[d], 5.14 (ref 17)[i], 5.22 (ref 12)[g]
*p*CA$^{-\prime}$	2.88 (refs 8, 10)	S$_1$	2.95	2.79 (ref 10)[j], 2.82 (ref 10)[k], 3.10 (ref 10)[l], 3.24 (ref 12)[g], 3.40 (ref 10)[m]
*p*CA$^{-\prime\prime}$	4.36 (ref 8)[f], 4.39 (ref 44)[f]	S$_4$	4.37	2.85 (ref 30)[k], 4.70 (ref 10)[m], 4.79 (ref 10)[l], 5.17 (ref 27)[j]
*p*CA^{2-}	3.69 (ref 8)[f], 3.72 (ref 44)[f]	S$_2$	3.73	
TM*p*CA$^-$	2.78 (ref 20)[n]	S$_1$	2.80	2.58 (ref 20)[o], 2.89 (ref 15)[p], 3.18 (ref 15)[q], 3.32 (ref 11)[c]
*p*CT$^-$	2.70 (ref 8)	S$_1$	2.75	2.71 (ref 30)[k], 3.01 (ref 12)[g], 3.05 (ref 11)[c]
p-HBDI$^-$	2.59 (ref 7)	S$_1$	2.67	2.52 (ref 30)[r], 2.66 (ref 18)[s,t], 2.92 (ref 25)[u], 3.12 (ref 18)[s,v], 2.93 (ref 25)[w], 3.04 (ref 25)[x]
p-HBDI	3.12 (ref 45)[n]	S$_1$	3.17	3.46 (ref 6)[y], 3.85 (ref 18)[s,t], 3.58 (ref 25)[u], 4.21 (ref 18)[s,v], 3.20 (ref 25)[w]
p-HBDI$^+$	2.99 (ref 6)	S$_1$	2.93	3.34 (ref 6)[y], 3.21 (ref 25)[u], 3.21 (ref 25)[w], 3.36 (ref 25)[x]
PSBT	2.00 (ref 9), 2.03 (ref 3)	S$_1$	2.09	2.03 (ref 30)[z], 2.07 (ref 22)[aa], 2.28 (ref 51)[ab], 2.32 (ref 19)[ac]
	3.22 (ref 9)	S$_2$	3.10	2.85 (ref 22)[aa], 3.12 (ref 51)[ab], 3.51 (ref 19)[ac]
PSB11	2.03 (ref 9)	S$_1$	2.04	2.07 (ref 23)[z], 2.05 (ref 22)[aa], 2.27 (ref 51)[ab], 2.32 (ref 19)[ac], 2.14 (ref 16)[ad]
	3.18 (ref 9)	S$_2$	3.01	2.84 (ref 22)[aa], 3.10 (ref 51)[ab], 3.49 (ref 19)[ac], 3.21 (ref 16)[ad]

[a] Details of the theoretical methodologies and basis sets used for the calculation of the excited-state energies//ground-state geometries for the theoretical results are given. [b] TDDFT(BP86)/def-TZVP//DFT(BP86)/def-TZVP. [c] TDDFT(B3LYP)/cc-PVTZ//DFT(B3LYP)/cc-PVTZ. [d] EOM-CCSD/6-31+G*//CCSD/cc-pVDZ. [e] OM*p*CA. [f] In solution. [g] TDDFT(BP86)/TZP//DFT(BP86)/PW. [h] TDDFT(B3LYP)/def-TZVP//DFT(B3LYP)/def-TZVP. [i] EOM-CCSD/6-31G*//DFT(B3LYP)/6-31G**. [j] MRMP2/CASSCF(14,12)/(p-type d-aug)-cc-pVDZ/DFT(PBE0)/cc-pVDZ. [k] aug-MCQDPT2/CASSCF(14,12)/(p-type d-aug)-cc-pVDZ//DFT(PBE0)/cc-pVDZ. [l] RI-CC2/aug-cc-pVTZ//DFT(PBE0)/aug-cc-pVDZ. [m] TDDFT(CAM-B3LYP)/aug-cc-pVTZ//DFT(PBE0)/aug-cc-pVDZ. [n] In the protein. [o] MS-CASPT2/CASSCF(12,10)/ANO//CASSCF(12,10)/ANO. [p] CC2/SV(P)//HF/6-31G*. [q] EOM-CCSD/6-31G*//HF/6-31G*. [r] aug-MCQDPT2/CASSCF(16,14)/(p-type d-aug)-cc-pVDZ//DFT(PBE0)/cc-pVDZ. [s] A 2,3-dimethyl model. [t] SA-2-CAS(2,2)PT2/6-31G//SA-2-CAS(2,2)/6-31G. [u] CASPT2/CASSCF(14,14)/cc-pVDZ//DFT(BLYP)/cc-pVTZ. [v] EOM-CCSD/6-31G//SA-2-CAS(2,2)/6-31G. [w] TDDFT(SAOP)/ET-pVQZ//DFT(BLYP)/cc-pVTZ. [x] Diffusion Quantum Monte Carlo/cc-pVDZ//DFT(BLYP)/cc-pVTZ. [y] TDDFT(B3LYP)/6-311++G*//MP3. [z] aug-MCQDPT2/CASSCF(12,12)/(p-type d-aug)-cc-pVDZ//DFT(PBE0)/cc-pVDZ. [aa] CASPT2/CASSCF(12,12)/ANO//MP2/6-31G**. [ab] TDDFT(B3LYP)/6-311++G(d)//DFT(B3LYP)/6-31G(d). [ac] CASPT2/CASSCF(12,12)/6-31G*//CASSCF(12,12)/6-31G*. [ad] CC2/def2-TZVPP//MP2/TZVP.

Chromophores are quasi-zero-dimensional systems. The distribution of the excited electron and the hole is highly localized. It is the huge exchange interaction between the excited electron and the hole that makes the resonant−antiresonant coupling not negligible. When the dimension of the system increases, such as in polymers, nanotubes, and bulk solids, the excited electron and hole becomes delocalized and the influence of TDA decreases gradually.

We also include dynamical screening effects in the electron−hole interaction. In comparison to the results from calculations with only static screening, we find that the influence of dynamical screening on the excitation energies is about 0.1 eV for the lowest $\pi \rightarrow \pi^*$ transitions, but for the lowest $n \rightarrow \pi^*$ transitions the influence is larger, up to 0.25 eV.

IV. Results and Discussion

IV.A. Neutral PYP Chromophores. Ryan et al.[46] tried to measure the gas-phase optical absorption spectrum of *p*CA. However, de Groot and Buma[55] pointed out that the spectrum obtained should be attributed to *p*VP due to the decarboxylation of *p*CA in the experiment, which is proved by the excitation spectrum measurement on *p*VP itself.[4,55] The excitation spectrum of the methyloxy ester of *p*CA (OM*p*CA), with the hydrogen atom at the carboxyl group replaced by a methyl group, was recently obtained by de Groot et al.[5] EOM-CCSD calculations indicate that the influence of the methyl substituent on the excitation energies

is very small,[5] which is also confirmed by our MBGFT calculations. So the excitation energies from the OM*p*CA spectrum could be regarded as a good reference for those in *p*CA. The absorption spectrum of *p*CA was also measured by Putschögl et al.[44] in pH 1 aqueous solution, which gave the first absorption peak in energy close to that of the gas-phase OM*p*CA.

MBGFT gives excitation energies in good agreement with experiments for *p*VP and *p*CA, with discrepancy within 0.1 eV (10 nm) and 0.2 eV (20 nm) for the first (S$_1$) and second (S$_2$) excited states, respectively, as shown in Table 1.

The characters of the excitations are still an open question for *p*CA. For example, most of the TDDFT, EOM-CCSD, and CASPT2 calculations[5,12,17,50] showed that S$_1$ and S$_2$ are $\pi \rightarrow \pi^*$ states and S$_3$ is an $n \rightarrow \pi^*$ state, whereas the CASPT2 calculation by Li and Fang[57] predicted that S$_1$ is an $n \rightarrow \pi^*$ state and S$_2$ is a $\pi \rightarrow \pi^*$ state. On the basis of EOM-CCSD,[5,50] S$_1$ originates from the HOMO $\rightarrow$ LUMO + 1 transition, whereas S$_2$ has a dominant contribution from the HOMO $\rightarrow$ LUMO transition.

According to the MBGFT calculations, S$_1$ and S$_2$ are $\pi \rightarrow \pi^*$ states and S$_3$ is an $n \rightarrow \pi^*$ state with the excitation energy of 3.94, 4.20. and 4.30 eV, respectively. The oscillator strength of S$_1$ is larger than that of S$_2$. In DFT within PBE-GGA, HOMO − 2, HOMO, LUMO, and LUMO + 1 are π states, whereas HOMO − 1 is an n state. In GWA, which gives more accurate orbital energies, the order between HOMO − 1 and HOMO − 2 is interchanged as shown in

Figure 4, with HOMO − 2 the n state and HOMO − 1 the π state. S_3 originates from HOMO − 2 → LUMO transition (in this context, when discussing results obtained within MBGFT, orbitals are in the order computed within GWA). Both S_1 and S_2 contain contributions from HOMO → LUMO, HOMO → LUMO + 1, and HOMO − 1 → LUMO transitions, with HOMO → LUMO and HOMO → LUMO + 1 dominating S_1 and S_2, respectively.

For pVP, both MBGFT and EOM-CCSD[4] predict a much smaller oscillator strength for S_1 than S_2, which is in agreement with experiment.[4] S_1 and S_2 are dominated by HOMO → LUMO + 1 and HOMO → LUMO transitions, respectively, according to both methods.

IV.B. Anionic PYP Chromophores. *IV.B.1. pCA⁻ and pCA²⁻.* Electrospray ionization (ESI) is routinely used to produce gas-phase compounds, including PYP chromophores,[8] retinal chromophores,[3,9] and tyrosine.[58,59] Most of these species, such as pCA and tyrosine, have more than one acidic site, so the structure produced in electrospray technique is unclear. For pCA the carboxylic acid site is more acidic than the phenolic one in solution, so the gas-phase absorption spectrum of pCA⁻ was originally attributed to the model pCA⁻″,[8,30] as illustrated in Figure 1d in which the carboxylic group is deprotonated, similarly to the case in solution. Recent experiments on tyrosine[58,59] find that deprotonation in the gas phase occurs preferentially at the phenolic site if the compound was sprayed from a methanol solution through ESI. The gas-phase pCA⁻ used in the experiment was also produced from a methanol solution,[8] which makes the assignment of the absorption peak at 430 nm (2.88 eV) to pCA⁻″ questionable. In neutral aqueous solution, pCA⁻ preferentially exists in the form of pCA⁻″ as discussed above, so the absorption peak of pCA⁻″ in aqueous solution can be determined to be around 4.36 eV, according to the experiments performed by Nielsen et al.[8] and Putschögl et al.[44] In alkaline aqueous solution, pCA⁻″ transforms to pCA²⁻, which was observed to have an absorption maximum around 3.70 eV.[8,44] Very recently pCA⁻ was also experimentally studied in vacuo, together with two methyl derivatives of it, which allowed for the study of the phenoxide and carboxylate forms.[10] The absorption maximum for all three chromophores was again 430 nm (2.88 eV), suggesting that both the phenoxide and carboxylate forms might have the same absorption properties. However, the analysis of the photodissociation pathways of pCA⁻ suggested that only the phenoxide isomer was present in a substantial amount, and the presence of pCA⁻″ could not be verified.[10] DFT and RI-CC2 calculations also showed that pCA⁻′ is more stable than pCA⁻″ in vacuo.[10]

According to the MBGFT calculations, the absorption maxima of pCA⁻′, pCA⁻″, and pCA²⁻ are predicted at 2.95, 4.37, and 3.73 eV, respectively. If the gas-phase absorption peak measured by Nielsen et al.[8] and Rocha-Rinza et al.[10] is attributed to pCA⁻′ rather than pCA⁻″, our result is in very good agreement with the experiment as shown in Table 1. The absorption maximum in vacuo we obtained for pCA⁻″ is very close to those measured in solution.[8,44]

The excitations in pCA⁻′ are simple, with S_1 (2.95 eV) dominated by the HOMO → LUMO (π → π^*) transition

and S_2 (3.32 eV) dominated by the HOMO − 1 → LUMO (n → π^*) transition, with no reordering of the energy levels within GWA as shown in Figure 4. The situation in pCA⁻″ is more complex. With DFT within PBE-GGA, HOMO and HOMO − 1 are n states, HOMO − 2 and HOMO − 3 are π states, LUMO and LUMO + 2 are π^* states, whereas LUMO + 1 is a Rydberg-type orbital with appreciable electron density beyond the frame of the molecule. Within GWA, the highest four occupied orbitals are reordered, with the original HOMO − 3 in DFT becoming HOMO, while the order of the other three occupied orbitals remains. The energies of the lowest four excited states within MBGFT are calculated to be 3.47, 3.63, 3.87, and 4.37 eV. S_1 and S_2 are n → π^* excitations mainly induced by transitions from the highest two n orbitals to the lowest two π^* orbitals; S_3 and S_4 are π → π^* excitations mainly induced by HOMO → LUMO and HOMO → LUMO + 2 transitions, with S_3 dominated by HOMO → LUMO and S_4 by HOMO → LUMO + 2 transitions. The absorption peak observed in the experiments originates from S_4, which has the strongest oscillator strength.

Within GWA, for pCA²⁻, HOMO is a π state with electron density mainly localized at the phenolic oxygen, HOMO − 1 and HOMO − 2 are n states with electronic density localized on the two carboxylic oxygens, LUMO and LUMO + 2 are π^* orbitals, whereas LUMO + 1 is a Rydberg-type orbital. The lowest two excited states S_1 and S_2 are of π → π^* character, with energies of 3.37 and 3.73 eV, respectively. Both these states have contribution from HOMO → LUMO and HOMO → LUMO + 2 transitions. S_3 and S_4 are n → π^* excitations, and S_5 is a π → Rydberg excitation. S_2, with the highest oscillator strength, is responsible for the absorption maximum (∼3.70 eV) observed in experiments.

MRMP2 (multireference second-order Møller−Plesset perturbation theory) and aug-MCQDPT2 have been used to study pCA⁻″ by Nemukhin et al.[30] and Andersen and Bochenkova;[27] however, the calculated energies are quite different, 5.17 eV by the former and 2.85 eV by the latter. The results from TDDFT and CC2 are close to that from MRMP2 but deviate from the aug-MCQDPT2 value by around 2.0 eV;[10] MCQDPT2 results support the idea that pCA⁻′ and pCA⁻″ have very similar absorption properties,[10] whereas all the other theoretical methods, including MBGFT, suggest that pCA⁻′ is the isomer present in vacuo; if present in vacuo, pCA⁻″ would have an absorption peak similar to that measured in solution.

IV.B.2. TMpCA⁻ and pCT⁻. The optical absorption maximum of pCT⁻ in vacuo was measured by Nielsen et al. to be 2.70 eV.[8] pCT⁻ should have similar excitation properties to the chromophore in the protein. Comparison of its absorption maximum in vacuo with that in the protein at 2.78 eV[8,60] shows only a small influence (∼0.08 eV) of the protein environment on the absorption spectrum. Until now, there is no measurement on the absorption spectrum of TMpCA⁻ in vacuo besides the absorption spectrum in the protein which gives two excitation energies at 2.78 and 3.14 eV,[61] respectively. If the protein effects are small as concluded by Nielsen et al.,[8] these energies could be reasonable references for excitation energies of TMpCA⁻

Modeling Excited States of Biological Chromophores

J. Chem. Theory Comput., Vol. 6, No. 1, 2010 **263**

in vacuo, which should also not differ substantially from those of pCT$^-$.

The first absorption peaks of pCT$^-$ and TMpCA$^-$ have been attributed to $\pi \rightarrow \pi^*$ excitations. aug-MCQDPT2 obtained this excitation energy in excellent agreement with experiment for pCT$^-$.[30] For TMpCA$^-$, the excitation energies calculated with CC2,[15] EOM-CCSD,[15] and CASPT2[20] deviate from experimental values by 0.1, 0.4, and 0.2 eV, respectively. However, the excitation energy at 2.89 eV by CC2 for TMpCA$^-$ given in Table 1 is the second excited state, with the lowest excited state being an $n \rightarrow \pi^*$ state at the energy of 2.84 eV.[15] The experimental 3.14 eV excitation is thought to initiate an alternative route for PYP excitation photocycle and was considered to involve an excited state different from the lowest $\pi \rightarrow \pi^*$ excitation in TmpCA$^-$.[61] S_2 computed by CASPT2 is an $n \rightarrow \pi^*$ state at the energy of 2.95 eV and is regarded as the origin of the excitation at 3.14 eV observed in the experiment.[20] EOM-CCSD predicts an $n \rightarrow \pi^*$ state as the second excited state with the energy of 3.82 eV, deviating from the experimental value by 0.68 eV.

With MBGFT, the characters of S_1 and S_2 in TMpCA$^-$ and pCT$^-$ are similar to those of S_1 and S_2 in pCA$^{-\prime}$ since the electronic density involved in these two states does not exceed the carboxyl group in both compounds. S_1 is a $\pi \rightarrow \pi^*$ state dominated by the HOMO $\rightarrow$ LUMO transition, whereas S_2 is an $n \rightarrow \pi^*$ state dominated by the HOMO $-$ 1 $\rightarrow$ LUMO transition. The energies of S_1 for TMpCA$^-$ and pCT$^-$ are calculated to be 2.80 and 2.75 eV, respectively, deviating from the experimental values by 0.02 and 0.05 eV, respectively. The energy of S_2 for TMpCA$^-$ is calculated to be 3.19 eV, which is very close to the experimental excitation energy at 3.14 eV. Assuming that the protein effects are small, the agreement with the experiments is excellent.

IV.C. GFP Chromophores. GFP chromophores exhibit two absorption maxima at 3.12 and 2.60 eV in the protein,[7] which are attributed to the neutral (p-HBDI) and anionic (p-HBDI$^-$) forms shown in Figure 3, respectively. The absorption maximum of the neutral form has a weak dependence on the environment, e.g., protein and solvent.[62,63] The excitation energy of the neutral form in vacuo should therefore be very close to 3.12 eV. The absorption maximum of the anionic form in vacuo was measured to be at 2.59 eV,[7] also close to that in the protein, which indicates that the protein environment has little disturbance on the electronic structure of the chromophore.[64] Lammich et al. also measured in vacuo the spectrum of a cationic form of the GFP chromophore shown in Figure 3c, here simply denoted as p-HBDI$^+$, which exhibits an absorption peak at 2.99 eV.[6]

Within MBGFT, the absorption maxima for the neutral, anionic, and cationic forms of GFP chromophore are 3.17, 2.67, and 2.93 eV, deviating from the experimental data by at most 0.07 eV, respectively. All these excitations have HOMO $\rightarrow$ LUMO character.

GFP chromophores models have been theoretically studied with a range of techniques including TDDFT, CASPT2, EOM-CCSD, SOS-CIS(D), MRMP2, aug-MCQDPT2, and quantum Monte Carlo,[6,13,18,21,25,30] and comparison between the results obtained with different methods and approxima-

tions has been recently discussed;[13,25] a selection of these results is shown in Table 1.

IV.D. Retinal Chromophores. Successful measurement of the optical absorption spectra of isolated PSBT and PBS11 molecules in vacuo has stimulated a large number of quantum chemistry studies.[16,19,22,23,30] The computational requirement of TDDFT is the least; however, excitation energies calculated through TDDFT depend drastically on the exchange-correlation functional used[51] and they are not accurate.[52] In comparison to experimental values, CASPT2 calculations by Sekharan et al.[22] gave a good results for S_1, but the energies of S_2 was underestimated by 0.3−0.4 eV. Other CASPT2 calculations by Cembran et al.[19] overestimated the energies of both S_1 and S_2 by 0.3 eV. Recent high-level aug-MCQDPT2 calculations predicted good excitation energies for S_1;[23,30] however, its performance on S_2 is unknown. It is somehow surprising that the lower-level CC2 method succeeded in computing energies of both S_1 and S_2 for PSB11[16] with high accuracy, and the origin of this success needs to be further clarified.

With MBGFT, we get excellent S_1 excitation energies for both PSBT and PSB11, with accuracy at the same level as aug-MCQDPT2. The performance of MBGFT on S_2 is also good, with deviation from experimental results by 0.17 eV at most, which is about half the typical error of CASPT2 for S_2. In both PSBT and PSB11, S_1, which has mainly HOMO $\rightarrow$ LUMO character (90%), has an oscillator strength stronger than that of S_2, which has mainly HOMO $-$ 1 $\rightarrow$ LUMO (75%) character complemented by HOMO $\rightarrow$ LUMO + 1 (15%) contribution.

V. Conclusions

In this work, we have applied for the first time MBGFT to the study of the excited states of PYP, rhodopsin, and GFP chromophores. Its performance has been extensively tested on several chromophore models, including both neutral and charged ones. Excellent agreement with the available experiments are obtained for the excitation energies for all the models, with errors within 0.1 eV (10 nm) for the lowest absorption maximum with $\pi \rightarrow \pi^*$ character excitations and $n \rightarrow \pi^*$ excitations, whereas the accuracy for the second $\pi \rightarrow \pi^*$ excitations is within 0.2 eV. The order of the states is also reproduced correctly. More accurate prediction (within an error of 0.1 eV) of the second $\pi \rightarrow \pi^*$ state may require consideration of double excitations,[27] which is beyond the ability of the current MBGF method.

With respect to other theoretical methods, whose applicability depends drastically on the specific chromophore models, MBGFT has the advantages of high accuracy, good transferability, and reasonable computational cost, which become important for relatively large chromophores, like the protonated Schiff base of retinal. An important feature of MBGFT is the possibility to incorporate at minimal cost polarizability and screening effects outside the object under consideration, which may affect the excited states because of nonlocal correlation effects, in terms of the screened Coulomb interaction. This is particularly relevant for biological chromophores, where the protein environment tunes and catalyzes the photoreaction. Moreover, progress in the

calculation of forces in the excited state within MBGFT has recently been made,[42,65] opening the way to the study of isomerization processes and excited-state dynamics. All these features make MBGFT a very promising tool for the investigation of photoactive proteins.

We also find necessary to go beyond the Tamm−Dancoff approximation for the application of MBGFT in chromophores. The influence of the resonant−antiresonant transitions coupling on the absorption maximum is larger than 0.4 eV for chromophores, which is quite different from that in crystals and clusters. This provides guidelines for further applications of MBGFT to similar low-dimensional systems.

Supporting Information Available: DFT-PBE geometries of the model chromophores. This material is available free of charge via the Internet at http://pubs.acs.org.

References

(1) van der Horst, M. A.; Hellingwerf, K. J. *Acc. Chem. Res.* **2004**, *37*, 13.

(2) Shimomura, O. *FEBS Lett.* **1979**, *104*, 220.

(3) Andersen, L. H.; Nielsen, I. B.; Kristensen, M. B.; El Ghazaly, M. O. A.; Haacke, S.; Brøndsted Nielsen, M.; Åxman Petersen, M. *J. Am. Chem. Soc.* **2005**, *127*, 12347.

(4) de Groot, M.; Buma, W. J.; Gromov, E. V.; Burghardt, I.; Köppel, H.; Cederbaum, L. S. *J. Chem. Phys.* **2006**, *125*, 204303.

(5) de Groot, M.; Gromov, E. V.; Köppel, H.; Buma, W. J. *J. Phys. Chem. B* **2008**, *112*, 4427.

(6) Lammich, L.; Åxman Petersen, M.; Brøndsted Nielsen, M.; Andersen, L. H. *Biophys. J.* **2007**, *92*, 201.

(7) Nielsen, S. B.; Lapierre, A.; Andersen, J. U.; Pedersen, U. V.; Tomita, S.; Andersen, L. H. *Phys. Rev. Lett.* **2001**, *87*, 228102.

(8) Nielsen, I. B.; Boyé-Péronne, S.; El Ghazaly, M. O. A.; Kristensen, M. B.; Brøndsted Nielsen, S.; Andersen, L. H. *Biophys. J.* **2005**, *89*, 2597.

(9) Nielsen, I. B.; Lammich, L.; Andersen, L. H. *Phys. Rev. Lett.* **2006**, *96*, 018304.

(10) Rocha-Rinza, T.; Christiansen, O.; Rajput, J.; Gopalan, A.; Rahbek, D. B.; Andersen, L. H.; Bochenkova, A. V.; Granovsky, A. A.; Bravaya, K. B.; Nemukhin, A. V.; Christiansen, K. L.; Nielsen, M. B. *J. Phys. Chem. A* **2009**, *113*, 9442.

(11) Muguruza González, E.; Guidoni, L.; Molteni, C. *Phys. Chem. Chem. Phys.* **2009**, *11*, 4556.

(12) Sergi, A.; Grüning, M.; Ferrario, M.; Buda, F. *J. Phys. Chem. B* **2001**, *105*, 4386.

(13) Epifanovsky, E.; Polyakov, I.; Brigorenko, B.; Nemukhin, A.; Krylov, A. I. *J. Chem. Theory Comput.* **2009**, *5*, 1895.

(14) Wan, S. B.; Liu, S. S.; Zhao, G. J.; Chen, M. D.; Han, K. L.; Sun, M. T. *Biophys. Chem.* **2007**, *129*, 218.

(15) Gromov, E. V.; Burghardt, I.; Köppel, H.; Cederbaum, L. S. *J. Am. Chem. Soc.* **2007**, *129*, 6798.

(16) Send, R.; Sundholm, D. *Phys. Chem. Chem. Phys.* **2007**, *9*, 2862.

(17) Ko, C.; Levine, B.; Toniolo, A.; Manohar, L.; Olsen, S.; Werner, H. J.; Martínez, T. J. *J. Am. Chem. Soc.* **2003**, *125*, 12710.

(18) Toniolo, A.; Olsen, S.; Manohar, L.; Martínez, T. J. *Faraday Discuss.* **2004**, *127*, 149.

(19) Cembran, A.; González-Luque, R.; Altoè, P.; Merchán, M.; Bernardi, F.; Olivucci, M.; Garavelli, M. *J. Phys. Chem. A* **2005**, *109*, 6597.

(20) Molina, V.; Merchán, M. *Proc. Natl. Acad. Sci. U.S.A.* **2001**, *98*, 4299.

(21) Martin, M. E.; Negri, F.; Olivucci, M. *J. Am. Chem. Soc.* **2004**, *126*, 5452.

(22) Sekharan, S.; Weingart, O.; Buss, V. *Biophys. J.* **2006**, *91*, L07.

(23) Bravaya, K.; Bochenkova, A.; Granovsky, A.; Nemukhin, A. *J. Am. Chem. Soc.* **2007**, *129*, 13035.

(24) Schautz, F.; Buda, F.; Filippi, C. *J. Chem. Phys.* **2004**, *121*, 5835.

(25) Filippi, C.; Zaccheddu, M.; Buda, F. *J. Chem. Theory Comput.* **2009**, *5*, 2074.

(26) Schreiber, M.; Silva-Junior, M. R.; Sauer, S. P. A.; Thiel, W. *J. Chem. Phys.* **2008**, *128*, 134110.

(27) Andersen, L. H.; Bochenkova, A. V. *Eur. Phys. J. D* **2009**, *51*, 5.

(28) Christiansen, O.; Koch, H.; Jørgensen, P.; Olsen, J. *Chem. Phys. Lett.* **1996**, *256*, 185.

(29) Koch, H.; Christiansen, O.; Jørgensen, P.; Olsen, J. *Chem. Phys. Lett.* **1995**, *244*, 75.

(30) Nemukhin, A. V.; Bochenkova, A. V.; Bravaya, K. B.; Granovsky, A. A. *Proc. SPIE* **2007**, *6449*, 64490N.

(31) Cai, Z. L.; Sendt, K.; Reimers, J. R. *J. Chem. Phys.* **2002**, *117*, 5543.

(32) Dreuw, A.; Head-Gordon, M. *J. Am. Chem. Soc.* **2004**, *126*, 4007.

(33) Hedin, L.; Lundqvist, S. Effects of Electron−Electron and Electron−Phonon Interactions on the One-Electron States of Solids. *Solid State Physics: Advances in Research and Application*; Academic Press: New York, 1969; Vol. 23, pp 1−181.

(34) Onida, G.; Reining, L.; Rubio, A. *Rev. Mod. Phys.* **2002**, *74*, 601.

(35) Rohlfing, M.; Louie, S. G. *Phys. Rev. B* **2000**, *62*, 4927.

(36) Albrecht, S.; Reining, L.; Del Role, R.; Onida, G. *Phys. Rev. Lett.* **1998**, *80*, 4510.

(37) Ma, Y.; Rohlfing, M. *Phys. Rev. B* **2008**, *77*, 115118.

(38) Shirley, E. L. *Phys. Rev. Lett.* **1998**, *80*, 794.

(39) Rohlfing, M.; Louie, S. G. *Phys. Rev. Lett.* **1998**, *80*, 3320.

(40) Artacho, E.; Rohlfing, M.; Côté, M.; Haynes, P. D.; Needs, R. J.; Molteni, C. *Phys. Rev. Lett.* **2004**, *93*, 116401.

(41) Rohlfing, M.; Louie, S. G. *Phys. Rev. Lett.* **1999**, *82*, 1959.

(42) Ismail-Beigi, S.; Louie, S. G. *Phys. Rev. Lett.* **2003**, *90*, 076401.

Modeling Excited States of Biological Chromophores

J. Chem. Theory Comput., Vol. 6, No. 1, 2010 **265**

(43) Tiago, M. L.; Chelikowsky, J. R. *Phys. Rev. B* **2006**, *73*, 205334.

(44) Putschögl, M.; Zirak, P.; Penzkofer, A. *Chem. Phys.* **2008**, *343*, 107.

(45) Creemers, T. M. H.; Lock, A. J.; Subramaniam, V.; Jovin, T. M.; Völker, S. *Nat. Struct. Biol.* **1999**, *6*, 557.

(46) Ryan, W. L.; Gordon, D. J.; Levy, D. H. *J. Am. Chem. Soc.* **2002**, *124*, 6194.

(47) Soler, J. M.; Artacho, E.; Gale, J. D.; García, A.; Junquera, J.; Ordejón, P.; Sánchez-Portal, D. *J. Phys.: Condens. Matter* **2002**, *14*, 2745.

(48) Perdew, J. P.; Burke, K.; Ernzerhof, M. *Phys. Rev. Lett.* **1996**, *77*, 3865.

(49) Troullier, N.; Martins, J. L. *Phys. Rev. B* **1991**, *43*, 1993.

(50) Gromov, E. V.; Burghardt, I.; Köppel, H.; Cederbaum, L. S. *J. Phys. Chem. A* **2005**, *109*, 4623.

(51) Sun, M. T.; Ding, Y.; Cui, G. L.; Liu, Y. J. *J. Phys. Chem. A* **2007**, *111*, 2946.

(52) Wanko, M.; Hoffmann, M.; Strodel, P.; Koslowski, A.; Thiel, W.; Neese, F.; Frauenheim, T.; Elstner, M. *J. Phys. Chem. B* **2005**, *109*, 3606.

(53) Aulbur, W. G.; Jönsson, L.; Wilkins, J. W. Quasiparticle Calculations in Solids. *Solid State Physics: Advances in Research and Application*; Academic Press: New York, 2000; Vol. 54, pp 1−218.

(54) Rohlfing, M.; Krüger, P.; Pollmann, J. *Phys. Rev. B* **1995**, *52*, 1905.

(55) de Groot, M.; Buma, W. J. *J. Phys. Chem. A* **2005**, *109*, 6135.

(56) Hybertsen, M. S.; Louie, S. G. *Phys. Rev. B* **1986**, *34*, 5390.

(57) Li, Q. S.; Fang, W. H. *Chem. Phys.* **2005**, *313*, 71.

(58) Tian, Z. X.; Kass, S. R. *J. Am. Chem. Soc.* **2008**, *130*, 10842.

(59) Tian, Z. X.; Wang, X. B.; Wang, L. S.; Kass, S. R. *J. Am. Chem. Soc.* **2009**, *131*, 1174.

(60) Meyer, T. E. *Biochim. Biophys. Acta* **1985**, *806*, 175.

(61) Devanathan, S.; Pacheco, A.; Ujj, L.; Cusanovich, M.; Tollin, G.; Lin, S.; Woodbury, N. *Biophys. J.* **1999**, *77*, 1017.

(62) Bell, A. F.; He, X.; Wachter, R. M.; Tonge, P. J. *Biochemistry* **2000**, *39*, 4423.

(63) Dong, J.; Solntsev, K. M.; Tolbert, L. M. *J. Am. Chem. Soc.* **2006**, *128*, 12038.

(64) Sinicropi, A.; Andruniow, T.; Ferré, N.; Basosi, R.; Olivucci, M. *J. Am. Chem. Soc.* **2005**, *127*, 11534.

(65) Ma, Y.; Rohlfing, M. Unpublished work (2009).

JCTC Journal of Chemical Theory and Computation

An Improved Self-Consistent-Charge Density-Functional Tight-Binding (SCC-DFTB) Set of Parameters for Simulation of Bulk and Molecular Systems Involving Titanium

Grygoriy Dolgonos,* Bálint Aradi, Ney H. Moreira, and Thomas Frauenheim

Bremen Center for Computational Materials Science, University of Bremen, Am Fallturm 1, 28359 Bremen, Germany

Abstract: A new self-consistent-charge density-functional tight-binding (SCC-DFTB) set of parameters for Ti–X pairs of elements (X = Ti, H, C, N, O, S) has been developed. The performance of this set has been tested with respect to TiO_2 bulk phases and small molecular systems. It has been found that the band structures, geometric parameters, and cohesive energies of rutile and anatase polymorphs are in good agreement with the reference DFT data and with experiment. Low-index rutile and anatase surfaces were also tested. For molecular systems, binding and atomization energies close to their DFT analogues have been achieved. Large errors, however, have been found for systems in high-spin states and/or having multireference character of their wave functions. The correct performance of SCC-DFTB for surface reactions has been demonstrated via the water splitting on anatase (001) surface. The current SCC-DFTB set is a suitable tool for future in-depth investigation of chemical processes occurring on the surfaces of TiO_2 polymorphs as well as for other processes of physicochemical interest.

1. Introduction

Among 3d transition metals, titanium is the second most abundant element after iron that occurs in the Earth's crust.[1] It has plenty of interesting physical and chemical properties (i.e., low density, high thermal and mechanical strength, insensitivity to corrosion) that makes it the metal of choice for the construction of jet engines of many airplanes, of tanks, and of autoclaves for chemical processing, or even to create lustrous and exotic jewelry. In addition, titanium and its alloys serve as excellent dental implants due to their biocompatibility and corrosion resistance as well as due to the strong attachment of the implant to the bone (osseointegration).[2,3] Titanium also plays an important role in catalysis as its compounds (Ziegler–Natta catalysts) serve as coordination centers upon polymerization of α-olefins leading to stereoregular products.[4]

The major technologically important titanium compound is titanium dioxide, which is mainly used as a white pigment in many products ranging from paint and paper to ceramics and toothpaste. Moreover, titanium dioxide has also been shown to exhibit unique characteristics[5] suitable for gas sensing,[6,7] solar cells,[8] water photolysis,[9] and photocatalytic decomposition of organic and inorganic pollutants.[10–12] Given these exciting applications, it becomes necessary not only to synthesize such solid-state and molecular systems but also to reliably model their properties at an appropriate size and time scale.

Apparently, on the theoretical side, we are still limited to using the main electronic structure theories—Hartree–Fock (HF) or density-functional (DFT) ones—as the usage of highly correlated methods for large periodic/molecular systems is not feasible. However, even within a DFT framework, the results may sometimes suffer from incomplete treatment of electron correlation leading to underestimation of band gaps of TiO_2 polymorphs (rutile and anatase)[13] or to incorrect treatment of weakly bound (hy-

* Corresponding author e-mail: grygoriy.dolgonos@bccms.uni-bremen.de.

drogen-bonded and van der Waals) molecular systems.[14,15] Nevertheless, DFT usually provides acceptable results for the ground-state properties, which are in better agreement with experiment than HF ones. On the other hand, DFT-quality results can be also achieved by applying an approximate self-consistent-charge density-functional tight-binding (SCC-DFTB) method[16,17] provided that the corresponding Hamiltonian and respective integral tables have been thoroughly derived and tested. Due to its tight-binding-like nature, this method allows one to gain up to 2 orders of magnitude in speed compared to standard DFT without a significant loss of accuracy.[18] Therefore, SCC-DFTB serves as a computationally efficient method to investigate electronic, structural, and energetic properties of both molecules and bulk periodic systems.

Formerly, a SCC-DFTB parametrization for the pairs of elements involving titanium and carbon, hydrogen, nitrogen, and oxygen was created.[19] This parametrization has been directed mainly toward molecular systems and complexes, and according to our benchmark results, is not fully applicable to periodic systems such as respective solids and related surfaces. The aim of the current work is to remedy this shortcoming and to develop a new, widely transferable, SCC-DFTB data basis, which could be applied for both molecular and periodic structures. Since the main interest is concentrated on simulation of TiO_2 systems, a special accent in parametrization has been made on the reproducibility of rutile and anatase bulk structures and surfaces. Additionally, we also developed parameters for titanium−sulfur interactions as sulfur is one of the elements of great importance for the photocatalytic applications of TiO_2.

This paper is organized as follows. Section 2 contains a brief overview of the SCC-DFTB formalism and the parametrization details as well as the details of the reference DFT methodology. In section 3, a validation of the newly derived SCC-DFTB parameters is presented, and the conclusions follow in section 4.

2. Computational Methodology

2.1. SCC-DFTB Method. The SCC-DFTB method is based on the second-order expansion of the Kohn−Sham total energy with respect to charge density fluctuations (for a more detailed description, see refs 16−18 and 20). In other words, the total energy expression includes not only the standard tight-binding (TB) "band structure" E_{BS} and short-range repulsive terms E_{rep}, but also an electrostatic-interaction term $E_2(n, \Delta n)$ that accounts for the charge fluctuations:

$$E_{tot} = E_{BS} + E_{rep} + E_2(n, \Delta n) = \sum_i^{occ} n_i \langle \psi_i | \hat{H}^0 | \psi_i \rangle +$$

$$E_{rep} + \frac{1}{2} \sum_{a,b}^{M} \gamma_{ab} \Delta q_a \Delta q_b \quad (1)$$

The first term of eq 1 is the sum over the occupied electronic eigenstates ψ_i of the effective Kohn−Sham Hamiltonian $\hat{H}^0$, derived under the approximation that the initial electronic density of the many-atom system can be represented as a superposition of corresponding neutral atomic charge densities. The Hamiltonian $\hat{H}^0$ depends only on this properly chosen reference density. The second term E_{rep} accounts for the energy difference between the electronic part of the (SCC-)DFTB method and DFT for a given reference system and comprises a summation over the Coulombic and exchange double counting terms as well as the ion core−core repulsion. Finally, the second-order term $E_2(n, \Delta n)$ is represented by atomic charge fluctuations Δq_a and Δq_b (based on Mulliken charges) together with an analytical interpolating function γ_{ab}. This term becomes important for the systems bearing atoms with different electronegativities leading to the formation of covalent polar or ionic bonds.

Further, the SCC-DFTB method relies on the following assumptions:

1. Only valence electrons are treated explicitly.

2. Kohn−Sham orbitals are expanded within the LCAO approximation using minimal localized pseudoatomic Slater orbitals, which include the confinement harmonic potential $(r/r_0)^2$ for the orbital localization (where r_0 is called a "wave function confinement radius").

3. The effective one-electron Kohn−Sham potential of many-atom system is constructed using a superposition of unperturbed neutral (pseudo)atomic densities (obtained with PBE functional[21]) which are confined by an analogous $(r/r_0)^2$ potential (with r_0 as a "density confinement radius").

4. The nondiagonal Hamiltonian matrix elements are derived on the basis of a two-center approximation, whereas the diagonal elements correspond to the calculated atomic orbital energies.

5. The repulsive term is approximated as the sum over all pairs of atom−atom potentials, which in turn are determined as a difference between the SCC-DFTB electronic energy and DFT total energy as a function of interatomic distance for properly chosen reference systems.

The computational efficiency of the SCC-DFTB method originates from the use of tabulated values of Hamiltonian and overlap matrix elements over a large number of interatomic distances that allows one to obtain interpolated values at any distance and to skip the computationally intensive explicit evaluation of two-center integrals. In addition, repulsion profiles are validated to be transferable, leading to DFT-quality results for the ground-state properties of typical organic molecules and solid-state systems while retaining at the same time the speed of common semiempirical methods.[18]

2.2. SCC-DFTB Parametrization Procedure. The successful SCC-DFTB parametrization implies that the main properties of reference systems are well reproduced with respect to DFT. This can be achieved by adjusting the wave function and density confinement radii (see above) for a given element as well as by accurate construction of repulsion profiles for all Ti−X diatomic cases.

In our previous SCC-DFTB parametrization of zinc-related systems,[22] it was found that the density confinement radius plays a marginal role on the quality of the obtained parameters whereas the wave function confinement radius is mainly responsible for the quality of band structures for periodic systems. Therefore, we have used the previous[19] value of 14 bohr for the former parameter but have checked the influence of the latter one on the Ti hexagonal-close-

268 *J. Chem. Theory Comput., Vol. 6, No. 1, 2010*

Dolgonos et al.

Table 1. Reference Molecular Systems and Cutoff Values Used To Generate Ti−X (X = Ti, C, H, N, O, S) Repulsion Profiles

Ti−X pair	reference system	cutoff value, bohr	shift of repulsion curve
Ti−Ti	(singlet) Ti_2	5.68	no
Ti−O	TiO_2	5.49	no
Ti−H	TiH_4	3.60	no
Ti−C	$Ti(CH_3)_4$	5.78	upward by 0.7 eV/bond
Ti−N	$Ti(NH_2)_4$	6.60	upward by 0.5 eV/bond
Ti−S	TiS_2	7.48	no

packed (hcp) band structure. Early investigations on the DFTB parametrization of first-row elements and hydrogen[17] suggested that the wave function confinement radius should be approximately 2 times larger than the covalent radius of a given element (although this rule is not absolute for other elements). Therefore, after varying the value of the wave function confinement radius from 3 to 5 bohr, we have observed the best Ti band-structure reproducibility at 4.3 bohr and used this value throughout this study. It should be noted that this value is however slightly larger than the previously chosen one of 3.6 bohr.[19]

In the case of other elements (C, H, N, O, S), we have employed the same initial atomic parameters as have been reported earlier.[16] This ensures the applicability and transferability of our newly derived parameters among different molecular and periodic structures.

Repulsion profiles for Ti−X (X = Ti, C, H, N, O, S) pairs were generated by fitting with cubic splines the difference of DFT total energy and the electronic DFTB energy versus distance upon stretching Ti−X bonds in simple reference molecules. Different Ti−X repulsion profiles are characterized by different cutoff values indicating the distance at which the repulsion energy approaches zero. Table 1 gives an overview of parametrization details used for the generation of Ti−X repulsion profiles. It should be noted that in some cases (cf. Table 1, Ti−N and Ti−C pairs) the repulsion curve has to be shifted toward higher energies to reduce the errors associated with significant overbinding of reference systems.

All the reported parameters (set name "tiorg") can be downloaded from the DFTB webpage (see http://www.dftb.org/parameters/download).

2.3. Reference DFT Calculations. For molecular systems, we have employed the same methodology as was originally proposed by Zheng et al.:[19] all potential-energy-surface scans as well as geometry optimizations were performed using the hybrid Becke's three-parameter exchange functional with the Lee−Yang−Parr correlation functional (B3LYP)[23−25] in conjunction with a mixed SDD+ basis set. This basis set consists of a Stuttgart/Dresden SDD[26,27] effective core potential and basis set for titanium and Pople-style double-ζ 6-31G(d)[28] basis set for other elements. All these calculations were performed using the Gaussian 03 program package.[29]

For periodic systems, we have performed DFT calculations using Perdew, Burke, and Ernzerhof (PBE)[21] functional with double-ζ basis set including polarization functions as implemented in the SIESTA code.[30,31] The Troullier−Martins[32,33] scheme was employed to generate two types of pseudopo-

tentials assuming $3s^2 3p^6 3d^2 4s^2$ (PP I) and $3d^2 4s^2$ (PP II) valence electronic configurations for titanium atom. The valence electronic configuration of oxygen was always $2s^2 2p^4$ throughout this study. The *k*-point sampling was performed in the same manner as for the SCC-DFTB calculations (see below). In the case of anatase, we have also carried out reference DFT calculations using the screened Hartree−Fock hybrid exchange-correlation (HSE06) functional[34,35] with projector-augmented plane wave (PAW)[36,37] potentials and treating Ti 3p electrons as valence ones. These calculations were performed with the Vienna Ab initio Simulation Package (VASP 5.2)[38−41] using an energy cutoff of 420 eV.

2.4. SCC-DFTB Calculations. Single-point SCC-DFTB calculations and geometry optimizations were carried out with the DFTB+ program.[42,43] In the latter case, the conjugate gradient algorithm[44] with the maximum force component of 10^{-4} au was employed. Bulk titanium, rutile, and anatase structures were simulated with the $8 \times 8 \times 4$, $4 \times 4 \times 8$, and $10 \times 10 \times 4$ Monkhorst−Pack[45] grids for *k*-point sampling, respectively. The optimal lattice parameters were obtained after looking for a minimum-energy value from numerous single-point calculations having different *c*/*a* ratios, volumes, and internal *u* (for TiO_2 polymorphs) parameters. The rutile and anatase surfaces were modeled on the basis of periodic slabs for supercells having vacuum regions (>120 Å) and one *k*-point along the surface-normal directions. Cohesive, atomization, and binding energies were computed as the energy difference with respect to individual spin-polarized fragments (atoms). The mio-set[16,17] SCC-DFTB diatomic pairs involving carbon, hydrogen, oxygen, nitrogen, and sulfur were employed throughout this study.

3. Results and Discussion

In the following, our current parametrization results for some model systems involving Ti−X (X = Ti, C, H, N, O, S) Slater−Koster pairs will be presented in comparison to previous SCC-DFTB parametrization of Zheng et al.,[19] to DFT, and to available experimental data.

3.1. Ti−Ti Interactions: Ti hcp Structure. As mentioned earlier in section 2.2, we have found the best SCC-DFTB band-structure representation of Ti hcp phase using a titanium wave function confinement radius of 4.3 bohr. The corresponding band structure is depicted in Figure 1 together with the reference GGA-DFT one. One can easily see that the most of SCC-DFTB bands are compressed in comparison to their DFT analogues while retaining their shape. Such a behavior is typical for the SCC-DFTB method due to the minimal basis set employed and is commonly observed in the case of other elements.[22]

The equilibrium geometric parameters together with cohesive energies of Ti hcp bulk phase obtained using different SCC-DFTB parametrization sets, using DFT, and taken from experiment are given in Table 2. As seen from these data, the SCC-DFTB parametrization set of Zheng et al.[19] leads to the much shorter values of lattice constants *a* and *c* (although the *c*/*a* ratio is quite accurate) as a result of the strong overbinding of the Ti hcp phase. This trend may indicate that there is not enough contribution from the repulsion Ti−Ti energy near equilibrium bulk values. With
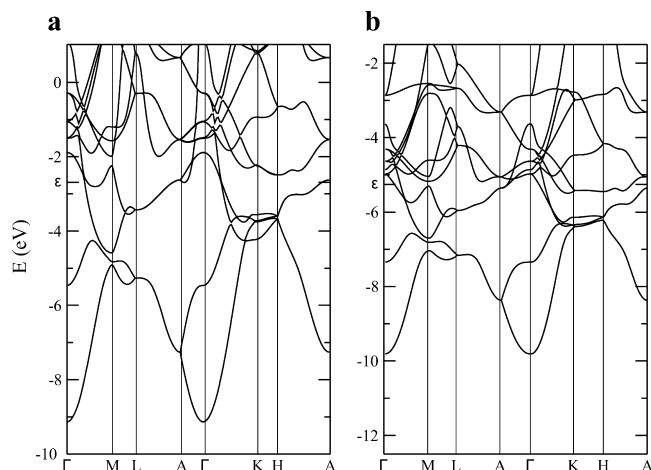
SCC-DFTB Set of Parameters for Ti−X Systems

J. Chem. Theory Comput., Vol. 6, No. 1, 2010 **269**

a   **b**

Figure 1. Titanium hcp band structures calculated with (a) GGA-DFT and (b) SCC-DFTB.

Table 2. Comparison of the Main Geometric and Energetic Parameters of Ti hcp Structure Calculated with SCC-DFTB and Obtained from Experiment

	SCC-DFTB		DFT			
parameter	set of Zheng et al.[19]	current set	LDA[a]	LDA[b]	PBE[b]	expt[c]
a, Å	2.380	2.998	2.866, 2.925	2.87	2.94	2.9508
c, Å	3.828	4.855	4.547, 4.666	4.526	4.642	4.6855
V, Å³	18.78	37.80	32.34, 34.57	32.28	34.75	35.33
c/a	1.608	1.619	1.586, 1.595	1.577	1.579	1.588
E_{coh}, eV	11.58	6.49	6.42,[d] 5.20	6.70	5.87	4.85

[a] Linearized augmented plane-wave (LAPW) results of Lu et al.[47] using exchange-correlation potentials of Hedin−Lundqvist and exchange-only Xα (α = 2/3), respectively. [b] Full-potential LAPW results of da Silva et al.[84] [c] See ref 47 and references therein. For cohesive energy, see also ref 50. [d] Slightly smaller LDA value of 6.29 eV has been reported by Philipsen and Baerends[46] calculated using an experimental Ti hcp geometry.

the current SCC-DFTB set, we observe a much closer agreement of investigated properties with experiment: the a value lies within 0.06 Å to experiment or PBE, whereas the c value is more overestimated (by 0.21 and 0.17 Å to PBE and experiment, respectively). It should be noted however that the Ti hcp cohesive energy is now equal to 6.49 eV (and is overestimated by only 1.6 eV to experiment), which is comparable to DFT with local density approximation (LDA) values (6.29,[46] 6.42[47] eV). This result is quite satisfactory taking into account the general overestimation trend of the SCC-DFTB method itself.

3.2. Ti−O Interactions. Since the main aim of the current parametrization is to properly reproduce the properties of periodic systems involving titanium, the performance of this parametrization set for the two main TiO_2 polymorphs, rutile and anatase, and their surfaces is presented below.

3.2.1. Properties of Rutile and Its Low-Index Surfaces. The band structures of bulk rutile calculated with the current SCC-DFTB method and with GGA-DFT are shown in Figure 2. It is well-known that pure LDA and GGA functionals usually yield much smaller band gap values whereas hybrid functionals tend to overestimate this quantity.[13] In accord with this finding, our GGA results lead to band gap values of 1.7−2.0 eV, which are lower by more than 1 eV than the experimental one. Interestingly enough, in the case of the

SCC-DFTB method we have found the minimal band gap at Γ of 3.13 eV that lies very close to the experimental value of 3.0 eV.[48,49] This presumably originates from the fortunate error cancellation associated with the minimal basis set used and other approximations of the SCC-DFTB method. However, the SCC-DFTB band structure differs significantly in the valence bands near the Γ-point from that obtained with DFT because of limitations of the SCC-DFTB method (cf. Figure 2c). This discrepancy cannot be cured by applying different wave function confinement radii for the oxygen atom nor by shifting the value of the oxygen 2s on-site energy.

Table 3 summarizes the main geometric and energetic characteristics of rutile bulk structure obtained with different DFT approaches and SCC-DFTB. We estimate the cohesive energy of rutile at 0 K by using the most recent CRC values[1] for the standard heats of formation of crystalline rutile and atomic oxygen as well as the cohesive energy of Ti hcp.[50] All less contributing terms such as thermal corrections and zero-point vibration energy of TiO_2 have been neglected. In general, all DFT methods overestimate the cohesive energy of rutile with hybrid functionals coming closer to the experimental value. Although SCC-DFTB also suffers from this deficiency, we managed to significantly reduce this overbinding trend in comparison to the previous set of Zheng et al.[19] and to bring down this property to 22.5 eV/TiO_2, which lies close to the PBE result of Lazzeri et al.[51] of 21.44 eV/TiO_2.

A comparison of rutile lattice parameters obtained with DFT and SCC-DFTB (see Table 3) indicates that, among GGA functionals, PBE generally reproduces the experimental values quite well whereas BLYP leads to larger a and c values. The previous SCC-DFTB set of Zheng et al.[19] gives too high a value of lattice constant a, while leading to the almost exact value of c. As a result, the corresponding c/a value is very low. The current SCC-DFTB parametrization overcomes this discrepancy and leads to a better agreement with experiment (though the c value is now only slightly overestimated). However, the bulk modulus of rutile is now determined less accurately (i.e., by ∼50 GPa lower to BLYP or PBE values and by ∼80 GPa to experiment) than the same property obtained using the parametrization set of Zheng et al.[19] (see Table 3).

To further validate our Ti−O parameters, we have also investigated the energetic characteristics of main low-index rutile surfaces. Table 4 gives the surface energies of (001) and (100) rutile calculated with SCC-DFTB in comparison to different DFT functionals within the slab approach. The surface energy E_{surf} is defined as the energy difference between the total energy of the slab (E_{slab}) and that of the regular crystal having the same number (n) of TiO_2 formula units (E_{bulk}) divided by twice the surface area (A) of the slab: $E_{surf} = (E_{slab} - nE_{bulk})/2A$. The calculated SCC-DFTB surface energy of the least stable (001) surface converges to 2.01 J/m² with the slab thickness that is slightly larger than the LDA result of Labat et al.[13] For the (100) surface, we observe small oscillations of the surface energy with the slab thickness reaching the final value of 1.192 J/m² that almost coincides with its LDA counterpart.[13] It should be noted that
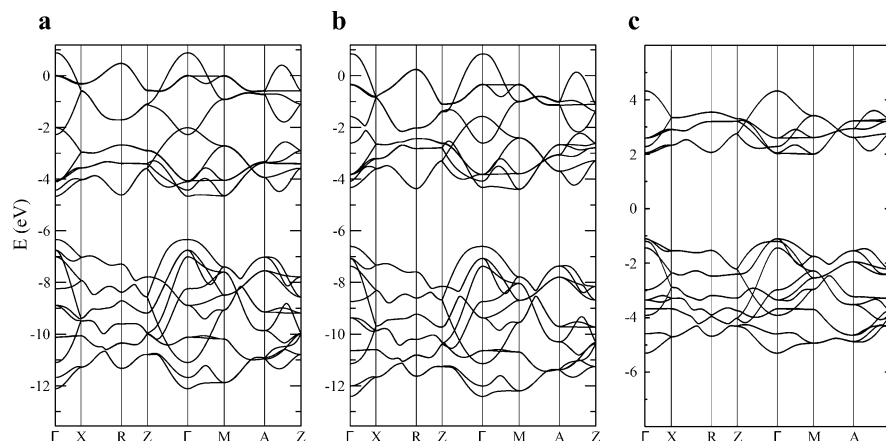
Figure 2. TiO$_2$ rutile band structures calculated with DFT-GGA using (a) PP I pseudopotential and (b) PP II pseudopotential, and (c) with current SCC-DFTB. For the description of PP I and PP II please refer to section 2.3.

Table 3. Comparison of the Geometric and Energetic Parameters of Bulk TiO$_2$ Rutile Structure Calculated with Different DFT Functionals, with SCC-DFTB Using Two Different Parametrization Sets, and Obtained from Experiment

				SCC-DFTB		
				set of	current	
property	LDA[a]	PBE[a]	BLYP[a]	Zheng et al.[19]	set	expt[b]
E_{coh}, eV	24.44	21.44	20.27	28.7	22.5	19.79
B_0, GPa	249	204	200	223	148	230 ± 20[c]
V_o, Å^3/TiO$_2$	30.2	31.8	32.7	33.0	32.8	31.217
a, Å	4.546	4.634	4.679	4.723	4.677	4.5936
c, Å	2.925	2.963	2.985	2.958	2.999	2.9587
c/a	0.643	0.639	0.638	0.626	0.641	0.6441
u	0.304	0.305	0.305	0.300	0.301	0.3048

[a] Literature values from ref 51; similar values were also reported by Labat et al.[13,53] for LDA and PBE functionals. [b] Structural parameters are taken from ref 85; cohesive energy E_{coh} is estimated on the basis of $\Delta H_f°(TiO_2,cr,298.15 \text{ K}) = -9.78$ eV,[1] $\Delta H_f°(O,g,298.15 \text{ K}) = 2.58$ eV,[1] and cohesive energy $E_{coh}(Ti,hcp)$ of 4.85 eV (cf. Table 2) as $E_{coh}(TiO_2) = E_{coh}(Ti) + 2\Delta H_f°(O,g,298.15K) - \Delta H_f°(TiO_2,cr,298.15K)$. [c] Literature value from ref 86.

the corresponding surface geometries agree well with their DFT analogues.

3.2.2. Properties of Anatase and Its Low-Index Surfaces. Figure 3 depicts the band structures of bulk anatase calculated with the hybrid HSE06[34,35] functional and SCC-DFTB. The indirect $\Gamma \rightarrow X$ band gap was found to be 3.7 and 3.2 eV with HSE06 and SCC-DFTB, respectively. The latter result is in a very close agreement with experimental band gap values of 3.2−3.3 eV.[52] The overall overestimation of band gaps with DFT using hybrid functionals is not surprising and was also reported earlier by Labat et al.[53] for the PBE0[54] functional. Unlike the rutile case, the SCC-DFTB band structure, apart from its compressed shape, reproduces well the main features of DFT band structure and is also in perfect agreement with experiment.

The main structural features and cohesive energies of bulk anatase calculated with DFT and SCC-DFTB together with experimental values are summarized in Table 5. With the current SCC-DFTB parametrization set, we obtain the cohesive energy of 22.3 eV/TiO$_2$. This value lies between the PBE result of Lazzeri et al.[51] of 21.5 eV and the hybrid HSE06[34,35] result of 22.9 eV. It should be noted that,

Table 4. Comparison of the Energetics of Different Low-Index Surfaces of Rutile TiO$_2$[a]

	(a) (001) surface					
		E_{surf} for (001-13L) surface with other methods,[b] J/m^2				
n	E_{surf}(SCC-DFTB), J/m^2	HF	LDA	PBE	B3LYP	PBE0
4	1.887					
8	2.003	2.077	1.876	1.393	1.452	1.587
16	2.010					

	(b) (100) Surface					
		E_{surf} for (100-5L) surface with other methods,[b] J/m^2				
n	E_{surf}(SCC-DFTB), J/m^2	HF	LDA	PBE	B3LYP	PBE0
4	1.193					
8	1.176	1.128	1.197	0.694	0.699	0.833
16	1.192					

[a] Each slab contains n unit cells. [b] Literature values from ref 13.
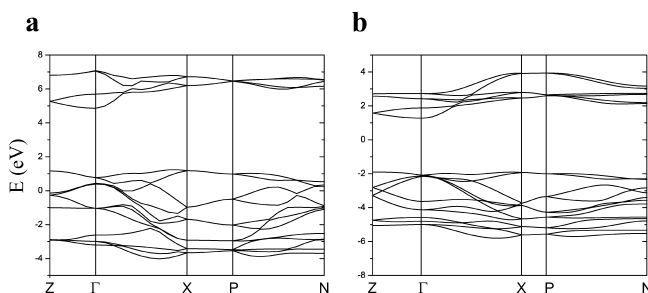
Figure 3. TiO$_2$ anatase band structures calculated with (a) HSE06 DFT functional and (b) SCC-DFTB with current parameters.

according to experimental observations,[53,55,56] rutile is the most stable TiO$_2$ polymorph and anatase should lie by up to 0.06 eV higher in energy than rutile. However, DFT functionals usually do not reproduce this stability order (except for LDA[53]). Surprisingly, the SCC-DFTB method gives the correct trend in stability with anatase being by 0.2 eV less stable than rutile and giving at the same time the

Table 5. Comparison of the Geometric and Energetic Parameters of Bulk TiO_2 Anatase Structure Calculated with Different DFT Functionals, with SCC-DFTB Using Two Different Parametrization Sets, and Obtained from Experiment

| | | | | | SCC-DFTB | | |
| | | | | | set of Zheng et al.[19] | current set | expt[c] |
property	LDA[a]	PBE[a]	BLYP[a]	HSE06[b]			
E_{coh}, eV	24.46	21.54	20.39	22.90	28.41	22.3	19.73
B_0, GPa	199	176	178	−	60	133	179 ± 2^d
V_o, Å³/TiO_2	33.25	34.89	35.83	33.72	35.70	33.75	34.06
a, Å	3.735	3.786	3.828	3.752	3.914	3.801	3.7842
c, Å	9.534	9.737	9.781	9.578	9.322	9.346	9.5146
c/a	2.553	2.572	2.555	2.552	2.382	2.459	2.5143
u	0.207	0.206	0.206	0.206	0.216	0.214	0.2081

[a] Literature values from ref 51; similar values were also reported by Labat et al.[13,53] for LDA and PBE functionals. [b] This work. [c] Structural parameters are taken from ref 87; cohesive energy E_{coh} is estimated to be by up to 0.06 eV smaller than that of rutile (Table 3) after taking into account the difference in binding energies of rutile and anatase reported by Labat et al.[53] (or from the difference in their standard heats of formation[55]). [d] Literature value from ref 88.

Table 6. Comparison of the Energetics of Different Low-Index Surfaces of Anatase $TiO_2{}^a$

	(a) (001) Surface			
		E_{surf} for (001-6L) surface with other DFT models,[b] J/m²		
n	E_{surf} (SCC-DFTB), J/m²	LDA unrelaxed/relaxed	PBE unrelaxed/relaxed	
2, 4, 8	1.10	1.46/1.38	1.12/0.98	

	(b) (100) Surface							
		E_{surf} for (100-6L) surface with other DFT models,[b] J/m²		E_{surf} for (100-8L) surface with other methods,[c] J/m²				
n	E_{surf} (SCC-DFTB), J/m²	LDA unrelaxed/relaxed	PBE unrelaxed/relaxed	HF	LDA	PBE	B3LYP	PBE0
2	0.97							
4	0.96	1.90/0.96	1.59/0.58	1.024	0.971	0.625	0.666	0.732
8	0.97							

[a] Each slab contains n unit cells. [b] Literature values from ref 51. [c] Literature values from ref 13.

values of cohesive energy much closer to experiment than those from LDA calculations.

As concerns geometric parameters, LDA geometries reported by Lazzeri et al.[51] are the most accurate among the listed pure DFT functionals and GGA functionals tend to provide slightly larger lattice parameters of anatase. Much better results can be obtained if one utilizes a screened Hartree−Fock hybrid exchange-correlation functional, for instance, HSE06,[34,35] for which the lattice parameters differ from experiment by only 0.032 and 0.063 Å for a and c, respectively. Current SCC-DFTB parametrization results in an accurate value of a (see Table 5), though the c value is by 1.8% smaller than its experimental counterpart. The corresponding internal u parameter, which represents the ratio of apical Ti−O bond length to c, slightly exceeds the experimental value. Similar to the rutile case, the bulk modulus calculated with current SCC-DFTB parameters is underestimated by approximately 40−50 GPa to DFT and experiment but outperforms the set of Zheng et al.,[19] which gives a too low B_0 value (Table 5).

If one compares the surface energies of low-index anatase surfaces (see Table 6), one can easily see that the current SCC-DFTB parametrization yields the corresponding values of at least LDA quality: in the case of (001) surface, the SCC-DFTB result is between the LDA and PBE ones

whereas for the (100) surface the SCC-DFTB result coincides with its LDA counterpart. The DFT stability order of these surfaces is also retained with SCC-DFTB.

3.2.3. Properties of Small Titanium Oxide Molecules. In the final step of verification of our SCC-DFTB Ti−O parameters with respect to DFT and to previous SCC-DFTB parameters of Zheng et al.,[19] we have investigated the geometric and energetic characteristics of small $(TiO)_n$ and $(TiO_2)_n$ molecules ($n = 1, 2$). The corresponding equilibrium geometries are given in Figure 4, whereas the total atomization energies are collected in Table 7.

The TiO molecule is the most well-characterized of all the systems presented in Figure 4, both experimentally and theoretically. It has a triplet ($^3\Delta$) ground state with an experimental bond length of 1.6202 Å[1] and atomization energy (D_0) of 158.4 ± 1.5 kcal/mol[57] that, after inclusion the zero-point-energy (ZPE) correction based on the experimental value of vibrational Ti−O frequency of 1009 cm⁻¹,[1] leads to the electronic atomization energy (D_e) value of 159.8 ± 1.5 kcal/mol. Both B3LYP and SCC-DFTB slightly underestimate the equilibrium bond length for the same state with the maximum error of 0.033 Å to experiment while the same geometric parameter for the singlet state is described with SCC-DFTB more accurately (within 0.01 Å to DFT and 0.02 Å to experiment (1.602 Å)).[58] The cal-
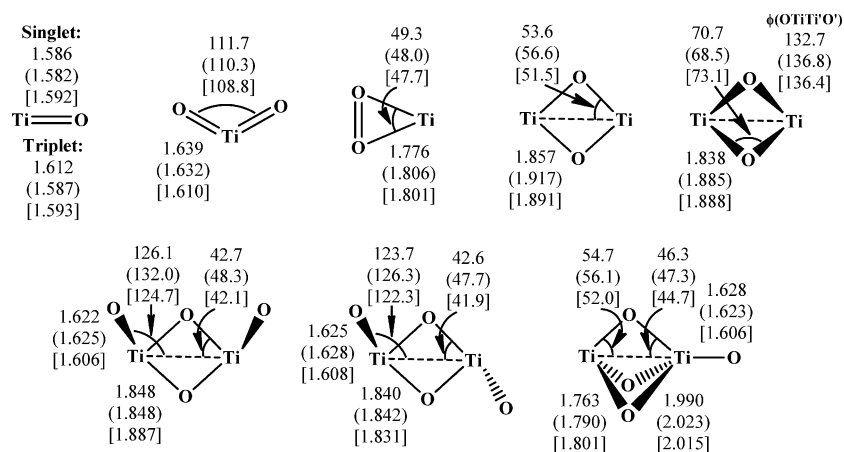
Figure 4. Schematic view of small isomeric $(TiO)_n$ and $(TiO_2)_n$ molecules ($n = 1, 2$) together with their equilibrium geometric parameters obtained with DFT (B3LYP/SDD+; without parentheses or brackets) and with SCC-DFTB using parameter set of Zheng et al.[19] (in parentheses) or using current set (in brackets).

Table 7. Total Atomization Energies[a] (TAEs, in kcal/mol) of Small Isomeric $(TiO)_n$ and $(TiO_2)_n$ Molecules ($n = 1, 2$) Calculated with DFT and SCC-DFTB

molecule	point group, multiplicity	DFT[b]	SCC-DFTB set of Zheng et al.[c]	current set
TiO	$C_{\infty v}$, 1	135.9	208.7	190.9
	$C_{\infty v}$, 3	162.5	229.3	211.5
TiO$_2$	C_{2v}, 1	300.1	428.2	389.7
Ti(O$_2$)	C_{2v}, 1	199.7	284.5	243.0
Ti$_2$O$_2$	D_{2h}, 1	353.0	572.4	440.7
	C_{2v}, 1	385.3	582.2	453.3
Ti$_2$O$_4$	C_{2v}, 1	713.1	1002.8	862.5
	C_{2h}, 1	719.5	1005.8	865.2
	C_{3v}, 1	702.7	1015.8	825.5

[a] Total atomization energies refer to the energies of Ti and O atoms in their ground spin (triplet) states. [b] B3LYP/SDD+ (see section 2.3) calculations; this work. [c] Using the SCC-DFTB parameters of Zheng et al.;[19] this work.

culated SCC-DFTB atomization energies suffer from severe overbinding with the current parametrization leading to a by almost 0.8 eV lower value (9.17 eV) for ^{3}TiO in comparison to the set of Zheng et al.[19] (9.94 eV). The current SCC-DFTB atomization energy of ^{3}TiO is however comparable to the SVWN, SP86, and SLYP results reported earlier.[59] Interestingly, the excitation energies to the lowest-lying closed shell singlet ($^1\Sigma^+$) state of TiO are determined much closer to experiment with SCC-DFTB than with B3LYP leading to 0.89 eV (with both parametrization sets) and 1.15 eV, respectively, compared to the experimental value of 0.70 eV (5650 cm^{-1}).[60]

TiO$_2$ in its singlet ground state is known experimentally to have a bond length of 1.62 ± 0.08 Å (as quoted by Ramana and Philips[61]) and a bond angle of 110 ± 15°[62] from early IR measurements refined later to be 113 ± 5°.[63] The current SCC-DFTB parametrization reproduces well these geometric features of TiO$_2$ with an absolute error to DFT of 0.029 Å and 2.9° for the Ti–O bond length and O–Ti–O bond angle, respectively. It should be noted that, according to the recent high-level coupled-cluster CCSD/LANL2DZ calculations of Qu et al.[64] and CCSD(T)/aug-cc-pVTZ-PP ones of Li et al.,[65,66] the equilibrium bond

length should be rather longer (1.672 and 1.666 Å, respectively) than the values commonly obtained by DFT using various functionals,[59] but the bond angle (112.6 and 112.4°) almost coincides with the best experimental estimate (see above) and is within 1° of our reference B3LYP value. The experimental $D_0(TiO_2)$ was reported to be 301.1 ± 2.9[67] and 304.0 ± 2.8 kcal/mol.[57] Because of lack of experimental values of the vibrational frequency for the O–Ti–O bending mode, it is not possible to calculate ZPE directly; therefore, a theoretical B3LYP/SDD+ ZPE correction of 3.4 kcal/mol is employed here leading to electronic atomization energies of 304.5 ± 2.9 and 307.4 ± 2.8 kcal/mol. Our reference DFT value of the TAE (300.1 kcal/mol) lies a few kilocalories per mole below the experimental estimates but agrees perfectly with the complete-basis-set extrapolated CCSD(T) value of 299.08 kcal/mol.[66] As in the case of TiO species, SCC-DFTB strongly overbinds TiO$_2$ with the current set being almost 90 kcal/mol above the reference DFT value.

Another TiO$_2$ isomer, cyclic peroxide Ti(O$_2$), has been investigated only theoretically. Our reference DFT Ti–O bond length (1.776 Å) and O–Ti–O bond angle (49.3°) are in a good agreement with previous BLYP/6-311+G* results of Uzunova et al.[68] (1.785 Å and 48.8°, respectively) but lie slightly below the B3LYP/LANL2DZ results of Qu et al.[64] (1.814 Å and 50.9°). SCC-DFTB with current parameters reproduces well the geometric features of Ti(O$_2$): the bond length deviates by 0.025 Å to DFT and the bond angle deviates by only 1.6°. The SCC-DFTB relative energies of singlet Ti(O$_2$) with respect to the ground-state TiO$_2$ are determined however less accurately: B3LYP/SDD+ leads to the value of 4.35 eV (in accord with previous DFT results of 4.49 eV,[68] 4.73 eV[64]), whereas both SCC-DFTB parametrizations give 6.2–6.4 eV, indicating a different overestimation degree of pure metal oxide and metal peroxide bond energies.

According to DFT, dibridged cyclic Ti$_2$O$_2$ can exist as a planar D_{2h} or nonplanar ("butterfly") C_{2v} isomer with the latter being the global-minimum structure in agreement with previous calculations and experiment.[63,69,70] The SCC-DFTB optimized geometries are determined now with slightly larger errors when in the case of TiO and TiO$_2$ molecules: the bond

length can differ by up to 0.05−0.06 Å to B3LYP whereas bond angles may vary by ±3° to the same functional. It should be mentioned that our reference B3LYP geometric parameters depend also on the basis set size and the effective-core-potential versus all-electron approach, as exemplified by the B3LYP/6-311+G* Ti−O bond length in the D_{2h} isomer of 1.846 Å[69] that reduces the SCC-DFTB vs DFT bond length error to 0.042 Å. Although SCC-DFTB gives the correct stability order for these two Ti_2O_2 isomers, the actual SCC-DFTB relative energies are too low in comparison to our reference DFT value with the largest error of 22.5 kcal/mol represented by the set of Zheng et al.[19] Nevertheless, the current parametrization set now gives closer to DFT atomization energies per Ti−O bond (with the energy difference of about 17−22 kcal/mol) compared to TiO_2 (44.8 kcal/mol).

Three main isomeric structures were proposed for Ti_2O_4: cis dibridged (C_{2v}), trans dibridged (C_{2h}), and tribridged (C_{3v}) (cf. Figure 4)—with the lowest-energy isomer corresponding to the trans dibridged (C_{2h}) structure.[64,65,71,72] SCC-DFTB optimization with current parameters leads to a good agreement of geometric characteristics of these isomers with reference DFT data: the maximum error is 0.039 Å in bond lengths and 2.7° in bond angles. In addition, our reference DFT bond lengths agree within 0.023 Å to the recent CCSD(T)/aug-cc-pVTZ-PP results of Li et al.[65] The SCC-DFTB parametrization set of Zheng et al.[19] usually tends to give more open structures for these isomers with the bond angles much larger (up to 6°) compared to reference DFT values. In addition, the same set does not reproduce the correct stability order of Ti_2O_4 isomers (see Table 7), leading to C_{3v} isomer as the most stable one. The current parametrization set overcomes this discrepancy, but the relative SCC-DFTB energies of Ti_2O_4 isomers still differ significantly from their reference DFT and high-level ab initio counterparts: the cis dibridged (C_{2v}) lies by 2.7 kcal/mol higher in energy above the global minimum (compared to 6.4 kcal/mol with B3LYP/SDD+ or to 5.5 kcal/mol with CCSD(T)/CBS[65]), whereas the tribridged (C_{3v}) isomer is higher by almost 40 kcal/mol (compared to 16.8 kcal/mol with B3LYP/SDD+ or to 12.8 kcal/mol with CCSD(T)/CBS[65]). The total atomization energy of trans dibridged (C_{2h}) isomer derived experimentally at 0 K is 721.1 ± 11.2 kcal/mol[73] that, after including the ZPE (B3LYP/SDD+) correction of 9.1 kcal/mol, leads to the electronic atomization energy of 730.2 ± 11.2 kcal/mol. Our reference DFT value for the same isomer lies close to the lower bound of experimental estimate. The SCC-DFTB atomization energies are overestimated in all cases, but the overestimation degree of the current set is almost twice as low compared to that of Zheng et al.[19]

Overall, the current SCC-DFTB parametrization gives an acceptable description of small titanium molecules with geometric characteristics lying close to their DFT analogues. The total atomization energies are however overestimated for all the systems, and the relative energies between different isomers may vary significantly from their DFT analogues and should be treated with caution, especially if an unusual spatial arrangement of atoms is present.

3.3. Ti−H Interactions. As stated in Table 1, we have generated the repulsion profile of Ti−H interactions on the

Table 8. Equilibrium Geometries and Total Atomization Energies[a] (TAEs) of Small Titanium Hydrides Calculated with DFT and SCC-DFTB Methods (r in Å, α and ϕ in deg, TAE in kcal/mol)

| | | | | SCC-DFTB | |
molecule	spin multiplicity	parameter	DFT[b]	set of Zheng et al.[c]	current set
TiH	2	r	1.723	1.678	1.690
	2	TAE	49.5	51.4	49.2
	4	r	1.760	1.698	1.701
	4	TAE	59.5	83.2	81.2
TiH$_2$	1	r	1.696	1.690	1.696
	1	α	111.8	102.6	102.4
	1	TAE	98.1	117.7	113.2
	3	r	1.755	1.694	1.698
	3	α	121.9	104.8	105.1
	3	TAE	125.9	137.9	133.6
TiH$_3$ (D_{3h})	2	r	1.725	1.699	1.748
	2	TAE	185.8	197.8	172.1
TiH$_4$ (T_d)	1	r	1.685	1.688	1.695
	1	TAE	242.1	271.9	263.5
Ti$_2$H$_2$ (dibridged)	1	r(Ti−Ti)	1.988	2.082	1.967
	1	r(Ti−H)	1.868	1.865	1.827
	1	α(Ti−Ti−H)	57.9	56.1	57.4
	1	ϕ(H−Ti−Ti−H)	90.5	101.9	98.0
	1	TAE	152.1	261.9	229.5
	3	r(Ti−Ti)	2.020	2.096	1.975
	3	r(Ti−H)	1.875	1.836	1.812
	3	α(Ti−Ti−H)	57.4	55.2	56.9
	3	ϕ(H−Ti−Ti−H)	126.3	139.8	133.7
	3	TAE	154.0	260.5	224.0

[a] Total atomization energies refer to the energies of Ti and H atoms in their ground spin states (triplet and doublet, respectively). [b] B3LYP/SDD+ (see section 2.3) calculations; this work. [c] Using the SCC-DFTB parameters of Zheng et al.;[19] this work.

basis of the titane (TiH$_4$) molecule in its T_d symmetry using the cutoff value of 3.60 bohr. Table 8 lists total atomization energies together with equilibrium bond lengths and angles of TiH$_x$ ($x = 1-4$) and dibridged C_{2v} Ti$_2$H$_2$ species. An inspection of these data reveals that the SCC-DFTB geometries of low-spin states are described quite accurately leading to the maximal Ti−H bond length error of 0.041 Å (for the singlet Ti$_2$H$_2$ case). Bond angles and dihedral angles are, however, the most sensitive parameters and may deviate up to 9.4° (for the singlet TiH$_2$ case) for low-spin systems in comparison to DFT values. This discrepancy usually originates from the very floppy profile of potential energy surfaces (PESs) associated with bending an angle or twisting a dihedral angle, on the one hand, or multireference character of the wave function that cannot be handled by single-reference methods without electron correlation, on the other. For example, the experimental value of the H−Ti−H angle of the ground ($^3B_1$) state of TiH$_2$ was found to be 145 ± 5°,[74] which is very far from our reference DFT and SCC-DFTB results. Moreover, its CISD/TZP(f,d) equilibrium geometry[75] is characterized by r(Ti−H) = 1.790 Å and α(H−Ti−H) = 142.1°, i.e., close to the experimental value. Demuynck and Schaefer[76] have predicted 10 possible electronic configurations of triplet TiH$_2$ in C_{2v} symmetry, some of which are low-lying. State-averaged CASSCF calculations of Kudo and Gordon[77] for the bent $^3B_1$ state lead to r(Ti−H) = 1.863 Å and α(H−Ti−H) = 140.7°, showing at the same time the corresponding floppy bending PES. A similar discrepancy is found for the lowest singlet

274 *J. Chem. Theory Comput., Vol. 6, No. 1, 2010*

Dolgonos et al.

$^1A_1$ state of the bent TiH$_2$ with the CASSCF values of r(Ti−H) = 1.899 Å and α(H−Ti−H) = 168.4°,[77] i.e., very different from our DFT and SCC-DFTB results. These observations clearly point out that our SCC-DFTB parametrization may not give the right answers in terms of geometries of triplet and singlet TiH$_2$ states as well as other high-spin states of titanium hydrides, having many low-lying electronic states and floppy bending PES profiles. It is interesting to note, however, that the SCC-DFTB triplet−singlet splitting (i.e., the energy difference between singlet and triplet) in TiH$_2$ was calculated to be 20.5 kcal/mol in excellent agreement with the state-averaged CASSCF result of 20.9 kcal/mol.[77]

For the total atomization energies (TAEs), the current SCC-DFTB parametrization generally yields more reasonable values close to their DFT analogues than the previous SCC-DFTB set.[19] In some cases, the SCC-DFTB TAEs however may differ by more than 1 eV from DFT as exemplified by the quartet TiH and both singlet and triplet Ti$_2$H$_2$ species. In addition, for planar TiH$_3$ radical we observe a different behavior of SCC-DFTB TAEs calculated with different parametrization sets with respect to the reference DFT one: the set of Zheng et al.[19] tends to overestimate TAE whereas our set underestimates TAE by almost the same amount as a result of different steepnesses of repulsion Ti−H profiles.

By comparing the high-spin → low-spin excitation energies (or splittings), one can see the correct performance of SCC-DFTB for TiH (4 → 2) and TiH$_2$ (3 → 1) species but the reverse behavior for the dibridged Ti$_2$H$_2$ (3 → 1) isomer, which is known to be triplet in its ground state.[78] This again indicates that the SCC-DFTB investigation of spatially strained systems, especially in their high-spin states, should be performed with caution.

3.4. Ti−C Interactions. As mentioned earlier, the Ti−C parameter set has been generated by using atomic parameters of carbon from the mio-set[16,17] and by applying a repulsion curve shift of 0.7 eV per Ti−C bond. To verify the applicability of this set for titanium−carbon compounds, we have performed a comparative investigation of the geometries and binding energies of one saturated Ti(CH$_3$)$_4$, one unsaturated Ti(CH$_3$)$_2$ molecule, and one complex of catalytic importance, Ti(C$_2$H$_4$)$^+$. The corresponding geometric characteristics together with total binding energies with respect to separate fragments (ligands) are presented in Table 9. The equilibrium geometry of Ti(CH$_3$)$_4$ agrees within 0.024 Å to DFT, and the binding energy is overestimated by 43.9 kcal/mol per four Ti−C bonds. Similar overestimation trends are also observed for Ti(CH$_3$)$_2$ species. However, new SCC-DFTB parameters result in much lower binding energies of Ti(C$_2$H$_4$)$^+$ complexes in comparison to their DFT analogues and to results of Zheng et al.[19] due to a much stronger contribution of repulsion energy to the total SCC-DFTB energy. Preliminary investigations indicate that it is possible to achieve the DFT-quality results for Ti(C$_2$H$_4$)$^+$ by applying smaller values for the repulsion curve shift; however, in such a case, the TAEs of covalently bound Ti(CH$_3$)$_4$ and Ti(CH$_3$)$_2$ systems will be overestimated by more than 1 eV per Ti−C bond that exceeds typical SCC-DFTB overbinding values

Table 9. Equilibrium Geometries, Binding Energies[a] (BEs), and High-Spin → Low-Spin Excitation Energies of Small Titanium−Carbon Compounds Calculated with DFT and SCC-DFTB Methods (r in Å, α in deg, BE in kcal/mol)

molecule	spin multiplicity	parameter	DFT[b]	SCC-DFTB set of Zheng et al.[19]	SCC-DFTB current set
Ti(CH$_3$)$_4$	1	r	2.072	2.034	2.096
	1	BE	242.7	419.4	286.6
Ti(CH$_3$)$_2$	1	r	2.038	2.033	2.096
	1	α	113.7	110.1	110.2
	1	BE	98.1	192.4	125.4
	3	r	2.100	2.040	2.103
	3	α	122.1	117.6	118.4
	3	BE	118.2	209.9	143.0
	3 → 1	ΔE	20.1	17.5	17.6
Ti(C$_2$H$_4$)$^+$	2	r	2.029	1.993	2.015
	2	BE	68.0	99.9	35.0
	4	r	2.337	2.276	2.259
	4	BE	76.2	93.6	32.4
	4 → 2	ΔE	8.23	−6.26	−2.6

[a] BEs are defined as follows: for Ti(CH$_3$)$_n$, BE = E(Ti) + nE(CH$_3$) − E(Ti(CH$_3$)$_n$); for Ti(C$_2$H$_4$)$^+$, BE = E(Ti$^+$) + E(C$_2$H$_4$) − E(Ti(C$_2$H$_4$)$^+$). [b] B3LYP/SDD+ (see section 2.3) calculations; this work.

Table 10. Equilibrium Geometries and Binding Energies[a] (BE) of small Titanium−Nitrogen Compounds Calculated with DFT and SCC-DFTB Methods (r in Å, α in deg, BE in kcal/mol)

molecule	spin multiplicity	parameter	DFT[b]	SCC-DFTB set of Zheng et al.[19]	SCC-DFTB current set
Ti(NH$_2$)$_4$ (S_4 symm)	1	r	1.899	1.874	1.902
	1	BE	358.9	383.5	361.6
H$_3$TiNH$_2$	1	r	1.846	1.859	1.898
	1	BE	91.6	104.5	118.0
HN=Ti=NH	1	r	1.707	1.692	1.703
	1	α	114.8	114.2	114.7
	1	BE	91.7	124.1	113.3

[a] BEs are defined as follows: for Ti(NH$_2$)$_4$, BE = E(Ti) + $4E$(NH$_2$) − E(Ti(NH$_2$)$_4$); for H$_3$TiNH$_2$, BE = E(TiH$_3$) + E(NH$_2$) − E(H$_3$TiNH$_2$); for Ti(NH)$_2$, BE = E(Ti) + E(N$_2$H$_2$) − E(Ti(NH)$_2$). [b] B3LYP/SDD+ (see section 2.3) calculations; this work.

found for other Ti−X systems as well as for test systems of mio-set.[16,17]

It is worth noting that the SCC-DFTB high-spin → low-spin excitation energy for the Ti(C$_2$H$_4$)$^+$ complex has an opposite sign with respect to the DFT value. Such a result again confirms that the treatment of high-spin systems may not be adequate within the SCC-DFTB framework. Nevertheless, the current parametrization generally leads to an acceptable description of covalently bound titanium−carbon systems and may be applied further to molecules and bulk systems but may not give the right answer for charged coordination complexes, particularly, in their high-spin states.

3.5. Ti−N and Ti−S Interactions. Ti−N SCC-DFTB parametrization exemplifies another case where there was a need to shift the repulsion curve toward higher energies to diminish the degree of overbinding of reference systems (see Table 1). Table 10 contains the reference DFT and SCC-DFTB equilibrium geometries and binding energies of some small titanium−nitrogen-containing molecules. We can see

SCC-DFTB Set of Parameters for Ti−X Systems

J. Chem. Theory Comput., Vol. 6, No. 1, 2010 **275**

Table 11. Equilibrium Geometries and Total Binding Energies[a] (BEs) of Titanium Sulfides Calculated with DFT and SCC-DFTB Methods (r in Å, α in deg, BE in kcal/mol)

molecule	spin multiplicity	parameter	DFT[b]	SCC-DFTB[c]
TiS$_2$ (C_{2v})	1	r(Ti−S)	2.079	2.107
	1	α(S−Ti−S)	112.9	109.3
	1	BE	199.7	235.9
Ti$_2$S$_3$ (D_{3h})	1	r(Ti−S)	2.297	2.269
	1	BE	416.3	428.3
TiS ($C_{\infty v}$)	1	r(Ti−S)	2.021	2.007
	1	BE	82.6	113.8

[a] Total binding energy is calculated with respect to the energies of separate Ti and S atoms in their ground spin states. [b] B3LYP/SDD+ (see section 2.3) calculations; this work. [c] Current SCC-DFTB parametrization set.

that the current SCC-DFTB results almost coincide now with their DFT counterparts for the reference Ti(NH$_2$)$_4$ molecule. However, for another saturated compound, H$_3$TiNH$_2$, the current set gives a slightly larger Ti−N equilibrium bond length and binding energy. On the other hand, for the unsaturated Ti(NH)$_2$ compound, the current set is coming closer to the DFT values than the previous set.[19] Therefore, the current Ti−N set should be considered as generally applicable to model such systems and should not cause significant errors.

Finally, we have also performed the new SCC-DFTB parametrization of Ti−S interactions. Unlike the Ti−N case, for this pair of elements it was possible to apply a relatively large cutoff value in order to avoid the usage of the repulsion energy shift. The resulting SCC-DFTB parameters were tested against a few gas-phase titanium sulfides, and the obtained results are given in Table 11. It has been found that the reference TiS$_2$ molecule is characterized by only marginal Ti−S bond elongation as well as a small decrease of bond angle using the SCC-DFTB method in comparison to DFT. For other titanium sulfides tested, a small decrease in bond lengths (up to 0.028 Å) is observed. Concerning the total binding energies, the largest overbinding (of 36.2 kcal/mol) is found for the TiS$_2$ molecule whereas other sulfides are described with smaller absolute energy differences. Hence, the new SCC-DFTB set for titanium−sulfur interactions should yield relatively accurate equilibrium geometries of such sulfur-containing systems while slightly overbinding these compounds.

3.6. Water Splitting on (001) Anatase Surface: Test Case. It has been well established in the literature that the high reactivity of anatase nanoparticles should be associated with the minority (001) anatase surface,[79] which exhibited an unusually strong tendency to cause spontaneous water dissociation.[80,81] In turn, this high reactivity also originates from an unusual structural feature and high strain of the (001) surface, having two inequivalent Ti−O bonds and a large Ti−O−Ti bond angle.[51]

Vittadini et al.[81] have found three different adsorption modes for water adsorption on the (001) surface based on GGA calculations: dissociative, molecular, and mixed. Figure 5 depicts the corresponding local-minimum structures of adsorbed water on (001) anatase obtained with SCC-DFTB and DFT. Although we did not perform preliminary molec-
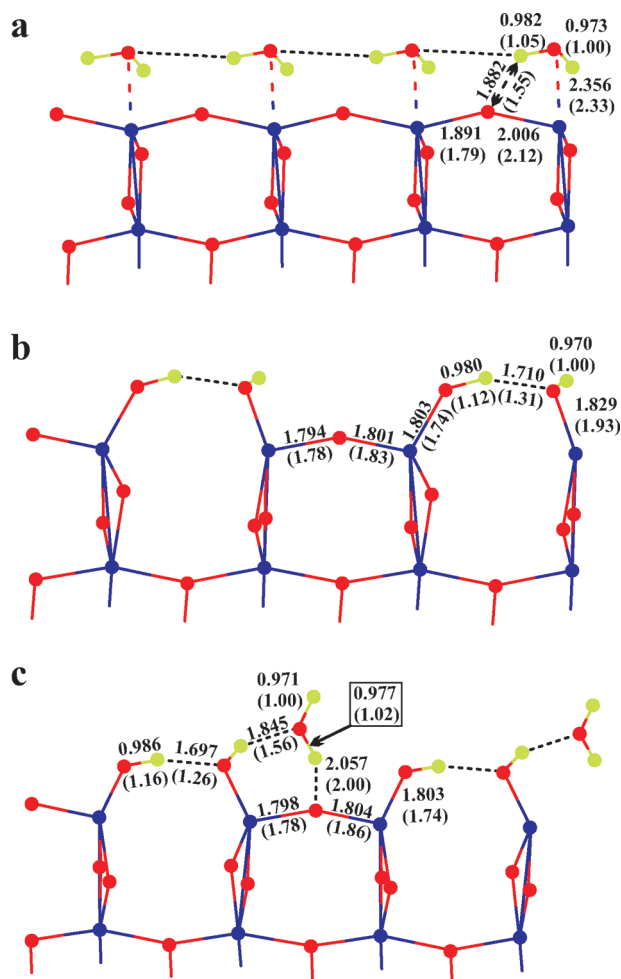

Figure 5. Structures of (001) anatase surfaces with adsorbed water molecules via (a) molecular, (b) dissociated, and (c) mixed adsorption modes. Bond lengths (in Å) without parentheses refer to SCC-DFTB ones obtained with current parametrization set, whereas those with parentheses are DFT values taken from Vittadini et al.[81] Titanium atoms are shown in blue, oxygen atoms are in red, and hydrogen atoms are in green. Hydrogen bonds are denoted with black dashed lines.

ular dynamics simulations using different orientations of water molecules near the (001) surface in order to find more energetically preferable structures, but rather relied on the SCC-DFTB optimization itself, we were able to locate the main structures for these three modes with geometric characteristics close to their DFT analogues. The largest deviation in bond lengths has been found for the hydrogen-bonded −O···H distances that exceeded sometimes 0.4 Å in comparison to DFT ones, indicating that the corresponding potential energy surface may contain many close-lying minima not easily obtained through a simple energy minimization.

If one compares the energetic characteristics, i.e., adsorption energies per H$_2$O molecule, for different adsorption modes and capacities (shown in Table 12), one can also see a satisfactory agreement with DFT results of Vittadini et al.[81] SCC-DFTB also confirms that at coverages θ below 0.5 the dissociative mode is preferred over other modes whereas at $\theta > 0.5$ the mixed mode is more energetically favorable.

276 *J. Chem. Theory Comput., Vol. 6, No. 1, 2010*

Dolgonos et al.

Table 12. Water Adsorption Energies (in eV/H_2O) on (001) Anatase Surface Calculated for the Different Adsorption Modes Using SCC-DFTB and DFT

adsorption mode	coverage,[a] θ	DFT[b]	SCC-DFTB[c]
molecular	0.5	0.81	0.66
	1	0.82	0.51
dissociative	0.5	1.44	1.59
mixed	1	1.01	0.96

[a] Coverage is defined as $n(H_2O)/n(5\text{-Ti})$, where $n(H_2O)$ and $n(5\text{-Ti})$ are the number of adsorbed water molecules and five-coordinated surface titanium atoms, respectively. [b] GGA results of Vittadini et al.[81] [c] Using current SCC-DFTB parametrization set.

Given the limitations of SCC-DFTB methods, on the one hand, and the difference in geometries for our SCC-DFTB and Vittadini et al.'s[81] DFT structures, on the other, the energy differences of 0.3 eV and smaller between SCC-DFTB and Vittadini et al.'s[81] corresponding DFT values should be considered as acceptable.

4. Conclusions

A new improved SCC-DFTB parametrization for titanium and its interactions with carbon, hydrogen, nitrogen, oxygen, and sulfur has been developed in order to get the best possible description of periodic and molecular systems involving these elements. This new SCC-DFTB set has been shown to give accurate values of the band gaps of the main TiO_2 polymorphs: rutile and anatase. The corresponding energetic and structural SCC-DFTB parameters of these bulk phases and their low-index surfaces are also in a good agreement with experimental and reference DFT results, outperforming the previous set of Zheng et al.[19] In addition, the careful generation of repulsion profiles for each pair of interacting elements allowed us to achieve much better binding (and/or atomization) energies of small molecular systems that generally lie close to their DFT counterparts and do not suffer from significant overbinding. However, it should be emphasized that the current SCC-DFTB set may rather not be applicable to small molecular systems in their high-spin states and with floppy potential energy surfaces or to systems whose wave functions exhibit significant multireference character. Nevertheless, the current set should serve as an excellent tool for the preliminary investigation of the adsorption of small molecules on rutile and anatase surfaces using considerably less computational resources as would be the case with ab initio methods.

When this work was finished, another SCC-DFTB parametrization involving titanium has been published by Luschtinetz et al.,[82] reporting structural and electronic characteristics of rutile and anatase bulk phases in a close agreement with our results. However, our set relies on the previously derived SCC-DFTB parameters for the first-row elements (mio-set) that have been shown[16−18,83] to perform well for many organic molecules and, therefore, this work should be considered as an attempt to generate the most suitable mio-based Ti−X (X = Ti, C, H, N, O, S) set to be applied to metal−organic compounds, to periodic (mainly, TiO_2) systems, and to systems involving small molecular adsorbates on rutile and/or anatase surfaces.

References

(1) Lide, D. R. *CRC Handbook of Chemistry and Physics*; CRC Press: Boca Raton, FL, 2005.

(2) Albrektsson, T.; Branemark, P. I.; Hansson, H. A.; Lindstrom, J. *Acta Orthop. Scand.* **1981**, *52* (2), 155–170.

(3) Jones, F. H. *Surf. Sci. Rep.* **2001**, *42* (3−5), 79–205.

(4) Corradini, P.; Guerra, G.; Cavallo, L. *Acc. Chem. Res.* **2004**, *37* (4), 231–241.

(5) Diebold, U. *Surf. Sci. Rep.* **2003**, *48* (5−8), 53–229.

(6) Buso, D.; Post, M.; Cantalini, C.; Mulvaney, P.; Martucci, A. *Adv. Funct. Mater.* **2008**, *18* (23), 3843–3849.

(7) Karunagaran, B.; Uthirakumar, P.; Chung, S. J.; Velumani, S.; Suh, E. K. *Mater. Charact.* **2007**, *58* (8−9), 680–684.

(8) Nazeeruddin, M. K.; Pechy, P.; Renouard, T.; Zakeeruddin, S. M.; Humphry-Baker, R.; Comte, P.; Liska, P.; Cevey, L.; Costa, E.; Shklover, V.; Spiccia, L.; Deacon, G. B.; Bignozzi, C. A.; Gratzel, M. *J. Am. Chem. Soc.* **2001**, *123* (8), 1613–1624.

(9) Fujishima, A.; Honda, K. *Nature* **1972**, *238* (5358), 37–38.

(10) Bannat, I.; Wessels, K.; Oekermann, T.; Rathousky, J.; Bahnemann, D.; Wark, M. *Chem. Mater.* **2009**, *21* (8), 1645–1653.

(11) Kalousek, V.; Tschirch, J.; Bahnemann, D.; Rathousky, J. *Superlattices Microstruct.* **2008**, *44* (4−5), 506–513.

(12) Menendez-Flores, V. M.; Friedmann, D.; Bahnemann, D. W. *Int. J. Photoenergy* **2008**; 280513/1-11.

(13) Labat, F.; Baranek, P.; Adamo, C. *J. Chem. Theory Comput.* **2008**, *4* (2), 341–352.

(14) Johnson, E. R.; DiLabio, G. A. *Chem. Phys. Lett.* **2006**, *419* (4−6), 333–339.

(15) Janowski, T.; Pulay, P. *Chem. Phys. Lett.* **2007**, *447* (1−3), 27–32.

(16) Elstner, M.; Porezag, D.; Jungnickel, G.; Elsner, J.; Haugk, M.; Frauenheim, T.; Suhai, S.; Seifert, G. *Phys. Rev. B* **1998**, *58* (11), 7260–7268.

(17) Porezag, D.; Frauenheim, T.; Köhler, T.; Seifert, G.; Kaschner, R. *Phys. Rev. B* **1995**, *51* (19), 12947–12957.

(18) Elstner, M.; Frauenheim, T.; Suhai, S. *J. Mol. Struct. (THEOCHEM)* **2003**, *632*, 29–41.

(19) Zheng, G. S.; Witek, H. A.; Bobadova-Parvanova, P.; Irle, S.; Musaev, D. G.; Prabhakar, R.; Morokuma, K.; Lundberg, M.; Elstner, M.; Köhler, C.; Frauenheim, T. *J. Chem. Theory Comput.* **2007**, *3* (4), 1349–1367.

(20) Elstner, M. *J. Phys. Chem. A* **2007**, *111* (26), 5614–5621.

(21) Perdew, J. P.; Burke, K.; Ernzerhof, M. *Phys. Rev. Lett.* **1996**, *77* (18), 3865–3868.

(22) Moreira, N. H.; Dolgonos, G.; Aradi, B.; da Rosa, A. L.; Frauenheim, T. *J. Chem. Theory Comput.* **2009**, *5* (3), 605–614.

(23) Becke, A. D. *J. Chem. Phys.* **1988**, *88* (2), 1053–1062.

(24) Lee, C. T.; Yang, W. T.; Parr, R. G. *Phys. Rev. B* **1988**, *37* (2), 785–789.

SCC-DFTB Set of Parameters for Ti−X Systems

J. Chem. Theory Comput., Vol. 6, No. 1, 2010 **277**

(25) Stephens, P. J.; Devlin, F. J.; Chabalowski, C. F.; Frisch, M. J. *J. Phys. Chem.* **1994**, *98* (45), 11623–11627.

(26) Dolg, M.; Wedig, U.; Stoll, H.; Preuss, H. *J. Chem. Phys.* **1987**, *86* (2), 866–872.

(27) Wedig, U.; Dolg, M.; Stoll, H.; Preuss, H. In *Quantum Chemistry: The Challenge of Transition Metals and Coordination Chemistry*; Veillard, A., Ed.; Reidel: Dordrecht, The Netherlands, 1986; Vol. 176, p 79.

(28) Frisch, M. J.; Pople, J. A.; Binkley, J. S. *J. Chem. Phys.* **1984**, *80* (7), 3265–3269.

(29) Frisch, M. J.; Trucks, G. W.; Schlegel, H. B.; Scuseria, G. E.; Robb, M. A.; Cheeseman, J. R.; Montgomery, J. A., Jr.; Vreven, T.; Kudin, K. N.; Burant, J. C.; Millam, J. M.; Iyengar, S. S.; Tomasi, J.; Barone, V.; Mennucci, B.; Cossi, M.; Scalmani, G.; Rega, N.; Petersson, G. A.; Nakatsuji, H.; Hada, M.; Ehara, M.; Toyota, K.; Fukuda, R.; Hasegawa, J.; Ishida, M.; Nakajima, T.; Honda, Y.; Kitao, O.; Nakai, H.; Klene, M.; Li, X.; Knox, J. E.; Hratchian, H. P.; Cross, J. B.; Bakken, V.; Adamo, C.; Jaramillo, J.; Gomperts, R.; Stratmann, R. E.; Yazyev, O.; Austin, A. J.; Cammi, R.; Pomelli, C.; Ochterski, J. W.; Ayala, P. Y.; Morokuma, K.; Voth, G. A.; Salvador, P.; Dannenberg, J. J.; Zakrzewski, V. G.; Dapprich, S.; Daniels, A. D.; Strain, M. C.; Farkas, O.; Malick, D. K.; Rabuck, A. D.; Raghavachari, K.; Foresman, J. B.; Ortiz, J. V.; Cui, Q.; Baboul, A. G.; Clifford, S.; Cioslowski, J.; Stefanov, B. B.; Liu, G.; Liashenko, A.; Piskorz, P.; Komaromi, I.; Martin, R. L.; Fox, D. J.; Keith, T.; Al-Laham, M. A.; Peng, C. Y.; Nanayakkara, A.; Challacombe, M.; Gill, P. M. W.; Johnson, B.; Chen, W.; Wong, M. W.; Gonzalez, C.; Pople, J. A. *Gaussian 03*, Revision B.04; Gaussian, Inc.: Wallingford, CT, 2004.

(30) Sánchez-Portal, D.; Ordejón, P.; Artacho, E.; Soler, J. M. *Int. J. Quantum Chem.* **1997**, *65* (5), 453–461.

(31) Soler, J. M.; Artacho, E.; Gale, J. D.; García, A.; Junquera, J.; Ordejón, P.; Sánchez-Portal, D. *J. Phys.: Condens. Matter* **2002**, *14* (11), 2745–2779.

(32) Kleinman, L.; Bylander, D. M. *Phys. Rev. Lett.* **1982**, *48* (20), 1425–1428.

(33) Troullier, N.; Martins, J. L. *Phys. Rev. B* **1991**, *43* (3), 1993–2006.

(34) Heyd, J.; Scuseria, G. E.; Ernzerhof, M. *J. Chem. Phys.* **2003**, *118* (18), 8207–8215.

(35) Vydrov, O. A.; Heyd, J.; Krukau, A. V.; Scuseria, G. E. *J. Chem. Phys.* **2006**, *125* (7), 224106/1-5.

(36) Blochl, P. E. *Phys. Rev. B* **1994**, *50* (24), 17953–17979.

(37) Kresse, G.; Joubert, D. *Phys. Rev. B* **1999**, *59* (3), 1758–1775.

(38) Kresse, G.; Furthmüller, J. *Phys. Rev. B* **1996**, *54* (16), 11169–11186.

(39) Kresse, G.; Furthmüller, J. *Comput. Mater. Sci.* **1996**, *6* (1), 15–50.

(40) Kresse, G.; Hafner, J. *Phys. Rev. B* **1993**, *47* (1), 558–561.

(41) Kresse, G.; Hafner, J. *Phys. Rev. B* **1994**, *49* (20), 14251–14269.

(42) Aradi, B.; Hourahine, B.; Frauenheim, T. *J. Phys. Chem. A* **2007**, *111* (26), 5678–5684.

(43) DFTB+ version 1.0 (p1); see http://www.dftb-plus.info (accessed Sept 30, 2009).

(44) Hestenes, M. R.; Stiefel, E. *J. Res. Natl. Bur. Stand.* **1952**, *49* (6), 409–436.

(45) Monkhorst, H. J.; Pack, J. D. *Phys. Rev. B* **1976**, *13* (12), 5188–5192.

(46) Philipsen, P. H. T.; Baerends, E. J. *Phys. Rev. B* **1996**, *54* (8), 5326–5333.

(47) Lu, Z. W.; Singh, D.; Krakauer, H. *Phys. Rev. B* **1987**, *36* (14), 7335–7341.

(48) Pascual, J.; Camassel, J.; Mathieu, H. *Phys. Rev. Lett.* **1977**, *39* (23), 1490–1493.

(49) Pascual, J.; Camassel, J.; Mathieu, H. *Phys. Rev. B* **1978**, *18* (10), 5606–5614.

(50) Kittel, C. *Introduction to Solid State Physics*, 7th ed.; John Wiley & Sons: New York, 1996; p 57.

(51) Lazzeri, M.; Vittadini, A.; Selloni, A. *Phys. Rev. B* **2001**, *6315* (15), 155409/1-9.

(52) Tang, H.; Berger, H.; Schmid, P. E.; Lévy, F.; Burri, G. *Solid State Commun.* **1993**, *87* (9), 847–850.

(53) Labat, F.; Baranek, P.; Domain, C.; Minot, C.; Adamo, C. *J. Chem. Phys.* **2007**, *126* (15), 154703/1-12.

(54) Adamo, C.; Barone, V. *J. Chem. Phys.* **1999**, *110* (13), 6158–6170.

(55) Fahmi, A.; Minot, C.; Silvi, B.; Causá, M. *Phys. Rev. B* **1993**, *47* (18), 11717–11724.

(56) Ranade, M. R.; Navrotsky, A.; Zhang, H. Z.; Banfield, J. F.; Elder, S. H.; Zaban, A.; Borse, P. H.; Kulkarni, S. K.; Doran, G. S.; Whitfield, H. J. *Proc. Natl. Acad. Sci. U.S.A.* **2002**, *99*, 6476–6481.

(57) Hildenbrand, D. L. *Chem. Phys. Lett.* **1976**, *44* (2), 281–284.

(58) Merer, A. J. *Annu. Rev. Phys. Chem.* **1989**, *40*, 407–438, and references therein.

(59) Bergström, R.; Lunell, S.; Eriksson, L. A. *Int. J. Quantum Chem.* **1996**, *59* (6), 427–443.

(60) Wu, H. B.; Wang, L. S. *J. Chem. Phys.* **1997**, *107* (20), 8221–8228.

(61) Ramana, M. V.; Phillips, D. H. *J. Chem. Phys.* **1988**, *88* (4), 2637–2640.

(62) McIntyre, N. S.; Thompson, K. R.; Weltner, J., W. *J. Phys. Chem.* **1971**, *75* (21), 3243–3249.

(63) Chertihin, G. V.; Andrews, L. *J. Phys. Chem.* **1995**, *99* (17), 6356–6366.

(64) Qu, Z. W.; Kroes, G. J. *J. Phys. Chem. B* **2006**, *110* (18), 8998–9007.

(65) Li, S. G.; Dixon, D. A. *J. Phys. Chem. A* **2008**, *112* (29), 6646–6666.

(66) Li, S. G.; Hennigan, J. M.; Dixon, D. A. *J. Phys. Chem. A* **2009**, *113* (27), 7861–7877.

(67) Balducci, G.; Gigli, G.; Guido, M. *J. Chem. Phys.* **1985**, *83* (4), 1909–1912.

(68) Uzunova, E. L.; Mikosch, H.; Nikolov, G. S. *J. Chem. Phys.* **2008**, *128* (9), 094307/1-12.

(69) Gong, Y.; Zhang, Q. Q.; Zhou, M. F. *J. Phys. Chem. A* **2007**, *111* (18), 3534–3539.

(70) Xiang, J.; Yan, X. H.; Xiao, Y.; Mao, Y. L.; Wei, S. H. *Chem. Phys. Lett.* **2004**, *387* (1−3), 66–69.

(71) Albaret, T.; Finocchi, F.; Noguera, C. *J. Chem. Phys.* **2000**, *113* (6), 2238–2249.

(72) Hagfeldt, A.; Bergstrom, R.; Siegbahn, H. O. G.; Lunell, S. *J. Phys. Chem.* **1993**, *97* (49), 12725–12730.

(73) Balducci, G.; Gigli, G.; Guido, M. *J. Chem. Phys.* **1985**, *83* (4), 1913–1916.

(74) Xiao, Z. L.; Hauge, R. H.; Margrave, J. L. *J. Phys. Chem.* **1991**, *95* (7), 2696–2700.

(75) Ma, B. Y.; Collins, C. L.; Schaefer, H. F. *J. Am. Chem. Soc.* **1996**, *118* (4), 870–879.

(76) Demuynck, J.; Schaefer, H. F. *J. Chem. Phys.* **1980**, *72* (1), 311–315.

(77) Kudo, T.; Gordon, M. S. *J. Chem. Phys.* **1995**, *102* (17), 6806–6811.

(78) Papai, I. *Theor. Chem. Acc.* **2000**, *104* (2), 131–139.

(79) Gong, X. Q.; Selloni, A. *J. Phys. Chem. B* **2005**, *109* (42), 19560–19562, and references therein.

(80) Vittadini, A.; Casarin, M.; Selloni, A. *Theor. Chem. Acc.* **2007**, *117* (5−6), 663–671.

(81) Vittadini, A.; Selloni, A.; Rotzinger, F. P.; Gratzel, M. *Phys. Rev. Lett.* **1998**, *81* (14), 2954–2957.

(82) Luschtinetz, R.; Frenzel, J.; Milek, T.; Seifert, G. *J. Phys. Chem. C* **2009**, *113* (14), 5730–5740.

(83) Niehaus, T. A.; Elstner, M.; Frauenheim, T.; Suhai, S. *J. Mol. Struct. (THEOCHEM)* **2001**, *541*, 185–194.

(84) Da Silva, J. L. F.; Stampfl, C.; Scheffler, M. *Surf. Sci.* **2006**, *600* (3), 703–715.

(85) Abrahams, S. C.; Bernstein, J. L. *J. Chem. Phys.* **1971**, *55* (7), 3206–3211.

(86) Gerward, L.; Olsen, J. S. *J. Appl. Crystallogr.* **1997**, *30*, 259–264.

(87) Horn, M.; Schwerdtfeger, C. F.; Meagher, E. P. *Z. Kristallogr.* **1972**, *136* (3−4), 273–281.

(88) Arlt, T.; Bermejo, M.; Blanco, M. A.; Gerward, L.; Jiang, J. Z.; Olsen, J. S.; Recio, J. M. *Phys. Rev. B* **2000**, *61* (21), 14414–14419.

JCTC Journal of Chemical Theory and Computation

Local Bonding Effects in the Oxidation of CO on Oxygen-Covered Au(111) from Ab Initio Molecular Dynamics Simulations

Thomas A. Baker,[†] Cynthia M. Friend,*[,†,‡] and Efthimios Kaxiras[†,‡,§]

*Department of Chemistry and Chemical Biology, Harvard University, 12 Oxford St,
Cambridge, Massachusetts 02138, School of Engineering and Applied Sciences,
Harvard University, Cambridge, Massachusetts 02138, and Department of Physics,
Harvard University, 16 Oxford St., Cambridge, Massachusetts 02139*

Abstract: A fully dynamical approach using ab initio molecular dynamics (AIMD) simulations is applied to the investigation of CO oxidation on O-covered Au(111). We investigate how the activity of gold depends upon temperature, oxygen coverage, and surface structure. On clean Au(111) at 500 K, CO binds transiently on top of Au atoms, spending a small fraction (~7%) of the total simulation time adsorbed on the surface. The presence of O on the surface increases the residence time for CO by more than 4 times on a surface containing 0.22 ML of O. On the other hand, the probability for CO adsorption decreases with oxygen coverage from 31% at 0.22 ML of oxygen to 15% at 0.55 ML of oxygen. Our simulations show that the activity for CO reaction with O to yield CO_2 decreases with increasing oxygen coverage. We attribute this decrease of activity to (1) the decrease in the CO adsorption probability as the oxygen coverage increases and (2) the decreasing amount of reactive chemisorbed oxygen (oxygen bound in a 3-fold site) with increasing total oxygen coverage. We show that oxygen bound in sites of local 3-fold coordination (chemisorbed oxygen) is nearly 2 times more reactive than other oxygen species observed on the surface, namely, surface and subsurface oxide. Our work demonstrates the value and feasibility of using AIMD to study surface reactions.

I. Introduction

Since the discovery[1–8] that gold nanoparticles supported on reducible metal oxides are catalytically active for many processes, including CO oxidation,[9] there is renewed interest in the potential use of gold as a material for low-temperature selective oxidation catalysis. The detailed understanding of the interaction of adsorbed oxygen and CO with the Au(111) surface is important because oxidized Au(111) is a model system for understanding chemical processes relevant to heterogeneous catalysis. While the oxidation of CO on gold has been studied extensively both experimentally[10–20] and

theoretically,[21–39] there are still unanswered questions regarding the activity of gold. One specific issue is how the local bonding of oxygen affects the activity for CO oxidation. It is, therefore, critical to determine the oxygen species and structure that prevail under different conditions.

Previous experimental studies[16] showed that ozone efficiently dissociates to form atomic oxygen on Au(111) and that the local bonding and surface morphology depend on the surface temperature during exposure to O_3. In turn, the state of the surface has a significant effect on the activity for CO oxidation. Scanning tunneling microscopy (STM) studies revealed differences in the surface morphology depending on the temperature used for oxidation or the coverage of atomic oxygen.[11] High-resolution electron energy loss and X-ray photoelectron spectroscopies also showed that the local bonding of oxygen depends on the oxidation temperature and the oxygen coverage. Detailed studies of

---

* Corresponding author. Tel: 617-495-4052. Fax: 617-496-8410.
E-mail: friend@chemistry.harvard.edu.

[†] Department of Chemistry and Chemical Biology.

[‡] School of Engineering and Applied Sciences.

[§] Department of Physics.

the activity for CO oxidation on O-covered Au(111) suggested that the activity for CO oxidation varies significantly for different types of oxygen (chemisorbed versus a surface oxide).

In addition to local bonding of O, the structure of the Au is thought to play a role in determining reactivity. Liu et al.,[26] using density functional theory (DFT) calculations, reported that the energy barrier for CO oxidation depends on the crystal face of the stepped surface. Recently, we also found differences in the calculated energy barrier, depending on the type of surface defect used, for the reaction of propene with atomic oxygen on Au(111).[40] Structure also plays a vital role for oxide-supported Au nanoparticles, since the size[41,42] and the particle shape[43] have a substantial effect on the reactivity, with rate constants differing by as much as 2 orders of magnitude.[32] It is clear that the oxygen surface species and surface morphology, which are strongly correlated for the Au−O interaction, play an important role in the reactivity of the gold surface.

While experimental studies clearly show that atomic O bound to Au is highly active for CO oxidation, there is still controversy about the types of oxygen that react with the CO. Clearly, atomic O is very active for CO oxidation; however, O_2 dissociation is required. A second reaction scenario involves molecular O_2 adsorption followed by CO adsorption and reaction to make a peroxo-like, $OC\cdots O_2$ complex, which leads to CO_2 and residual atomic oxygen. Criticism of the first mechanism is based on the fact that the dissociation rate of O_2 on gold surfaces is low, consistent with DFT calculations that find a high energy barrier for O_2 dissociation even on small clusters,[26,44−46] and on recent work showing the role of molecular O_2 in oxidation.[13,47] In contrast to other transition-metal surfaces, there is no appreciable O_2 dissociation on extended single crystals of Au.[48] As a result, experimental studies use other sources of oxygen to produce atomic oxygen on the surface.[49−53] Nevertheless, atomic oxygen is ultimately formed even in the scenario where O_2 reacts directly with CO; thus, it is important to understand the reactivity of O on gold.

Temperature is an important factor in determining the morphology and ultimately the reactivity of the surface. Treatment of surface temperature is a major challenge for theoretical studies, and for this reason, previous theoretical investigations of CO oxidation on Au surfaces have generally used static, zero-temperature DFT calculations. Kinetic Monte Carlo (kMC) is a popular theoretical technique for modeling the dynamical temperature dependence on the reactivity of a surface[54] and has been effectively used to model CO oxidation on RuO_2(110).[55] Unfortunately, kMC methods presume prior knowledge of all the events important to the dynamics of the system. Furthermore, the spatial degrees of freedom of the system are typically reduced to a simple lattice. The interaction of oxygen with Au is complex because of the role of defects and metal atom release. Therefore, it is impossible to know all the important events a priori and it is unrealistic to confine these events within the context of a lattice. Ideally, one wants to capture all the relevant effects in a fully atomistic molecular dynamics simulation with accurate forces between ions and under realistic external conditions (temperature and oxygen concentration).

Molecular dynamics is an important tool for simulating reactions and other dynamical chemical behavior for a variety of systems, including surfaces.[56] Classical force fields, which can be derived from many sources including first-principle methods or empirical observations, are used to describe the interaction of atoms and have been used in many applications. These force fields can be useful because they are computationally cheap, giving the ability to simulate large systems for long time scales (easily thousands of atoms for nanoseconds). The disadvantage of these force fields is their poor accuracy—classical or course-grained methods often do not capture complex chemical behavior, including bond breaking and formation. Ab initio molecular dynamics (AIMD), that is, using first-principles for calculating forces, provides a more accurate alternative to classical methods and has been used in many situations to understand surfaces.[57,58] Typically, AIMD calculations employ the Born−Oppenheimer approximation, but it is important to point out that for catalytic reactions on surfaces there are some cases where there is electronic nonadiabatic coupling, making the Born−Oppenheimer approximation invalid.[59,60] Other important molecular dynamics methods that could be useful for understanding the dynamics of surfaces include (but are not limited to) Car−Parrinello dynamics[61] or Ehrenfest dynamics.[62,63] The challenge in performing AIMD simulations is the restriction to short time scales because the calculations are computationally expensive.

Recently, we have developed the ability to use AIMD simulations to model the *dynamic* restructuring of the Au(111) surface due to the adsorption of atomic oxygen and have obtained results that are in agreement with vibrational spectroscopy experiments.[64] We find that the morphology and fraction of various O bonding configurations depend on the coverage and temperature at the tested coverages of 0.22, 0.33, and 0.55 monolayers (ML), and at 200, 500, and 800 K.[64] We categorized oxygen into three different types: chemisorbed oxygen, surface oxide, and subsurface oxide, as illustrated in Figure 1. These three types represent, respectively, an oxygen atom bound on top of the surface in a 3-fold hollow site, an oxygen atom bound to a gold atom that has been pulled out of the surface, and an oxygen atom buried below the first layer of gold. At low oxygen coverage (<0.33 ML) or temperature (200 K), the Au(111) surface is smooth and contains mostly chemisorbed oxygen, while at higher coverage (>0.33 ML) or temperature (500, 800 K), it is oxidized, containing a higher concentration of surface and subsurface oxide. By matching calculated vibrational spectra with the experimental results under conditions that produce the most reactive surface for CO and olefin oxidation (low coverage and low temperature), we suggested that chemisorbed oxygen was the more reactive type of oxygen for CO oxidation on Au(111).

Herein, we report a detailed study of CO oxidation on O-covered Au(111) using AIMD. We directly confirm that chemisorbed oxygen, i.e., O bound to sites of local 3-fold coordination, is most reactive. We also discuss the underlying
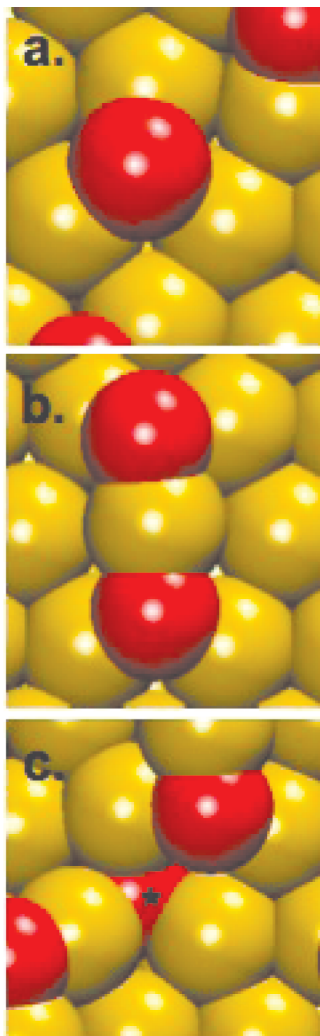
Figure 1. Model (top view) of three oxygen types: (a) chemisorbed, (b) surface oxide, and (c) subsurface oxide (labeled by an asterisk). Yellow and red spheres represent gold and oxygen atoms, respectively.

physical reasons for this different reactivity and place it in a broader context of using AIMD to model the dynamics of surface reactions.

II. Calculational Details

We performed the AIMD simulations in the canonical ensemble,[65] with a time step of 2 fs, for the reaction of carbon monoxide with atomic oxygen covered Au(111) in the framework of density functional theory using the VASP code[66] with the GGA-PW91[67] functional and ultrasoft pseudopotentials.[68,69] We used a plane-wave cutoff energy of 300.0 eV, an electronic convergence tolerance of 10^{-3} eV, and $2 \times 2 \times 1$ Monkhorst−Pack reciprocal space (k-point) sampling. The surface is modeled by a slab consisting of four layers in the (111) direction, with a 3×3 supercell in the lateral directions; the three uppermost layers of the slab were allowed to relax, with the bottom layer fixed at the ideal bulk positions.

We considered four different conditions: clean Au(111) and Au(111) with O coverages of 0.22, 0.33, and 0.55 ML at 500 K. The simulation temperature of 500 K represents

an optimal balance of adsorption and reaction, thus minimizing the total simulation time needed to observe important events in the system. The surfaces were prepared as follows:[64] oxygen was randomly placed above an equilibrated Au(111) substrate and the system then simulated at 500 K for 2 ps to allow for adsorption and rearrangement of the surface. To model the reaction of CO with these substrates, one CO molecule (0.11 ML coverage) was introduced to each system with a zero initial velocity, ∼3 Å above the surface. For this reason, we are unable to find a sticking probability to compare with experiment, defined as the ratio of the adsorption rate to impingement rate,[70] since for a molecular beam or a background gas there would be molecules hitting the surface with either a nonzero constant velocity or Maxwell−Boltzmann distribution of velocities. In contrast, our simulations are limited to CO molecules with a zero initial velocity above the surface so as to increase the probability of adsorption, thus significantly overestimating the true sticking probability.

At each oxygen coverage, 100 independent simulations were performed, each lasting 8 ps. All results are obtained after a sufficient equilibration time, as evaluated by the point in time at which fluctuations in the average energy, temperature, and other measurable quantities were small (<5%). For example, the average C−O distance during adsorption of $CO_{(a)}$ was found by averaging the distance at each time step during adsorption, excluding steps that were less than 600 fs after adsorption and before desorption. If the lifetime of $CO_{(a)}$ on the surface was not long enough to provide sufficient statistics (<1600 fs), the MD run was not used for calculating the C−O distance. We defined a process as adsorption (desorption) if the carbon from CO was within (greater than) 2.7 Å of the closest gold atom for a minimum of 300 fs.

III. Results

A. Simulations of CO Adsorption on Oxygen-Free Au(111). The adsorption of CO on clean Au(111)-(1 × 1) is weak and leads to a short surface lifetime. The adsorption of CO was simulated on clean Au(111) at 500 K using a $p(3 \times 3)$ unit cell and an unreconstructed Au(111) surface as the starting point. The clean (1 × 1)-Au(111) surface is used in contrast to the herringbone reconstructed surface for two reasons: first, the experimentally observed herringbone reconstruction of the clean Au(111) surface is often lifted upon adsorption, and second, the difference in surface energy between the ideal (1 × 1) surface and the surface with the herringbone reconstruction is actually quite small, ∼0.02 eV per surface Au atom.[71] At 500 K, CO should have a very short lifetime on the surface due to its weak adsorption: experimental[72] and theoretical[73] adsorption energies are ∼0.4 and 0.34 eV, respectively. For example, CO adsorption is not detected experimentally at 300 K on Au(111) until high pressures (>0.5 Torr).[74,75] No measurable adsorption of CO at low pressures on Au(110)[15] is detected above 125 K or above 100 K on the oxygen-covered Au(111) surface.[10] We observe qualitatively similar behavior in our simulations: a CO molecule spends only ∼7% of the total simulation time
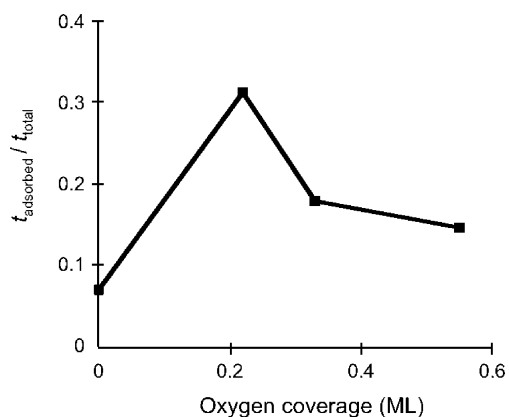
Figure 2. The ratio of time CO spends adsorbed on the surface ($t_{adsorbed}$) to the total simulation time (t_{total}) at different oxygen coverages.

(8 fs) on the surface. Of the 100 independent runs, each of duration 8 fs, CO adsorbs at some point during the simulation for 40% of the runs but quickly desorbs, spending an average of only 861 fs on the surface per adsorption event, resulting in a short overall surface lifetime.

Carbon monoxide preferentially binds to top sites on the (1×1)-Au(111) surface, with the carbon interacting with the surface. This is in agreement with experimental[73] and theoretical findings,[76] although one theoretical study finds the 3-fold site to be preferred for CO binding.[26] In our work, we find that the C−O bond is slightly elongated during adsorption, with the gas phase C−O bond of 1.144 Å extending to 1.151 Å during adsorption. These bond distances agree with experimental estimates and static DFT calculations. The experimental gas phase C−O distance[77] is 1.128 Å, while the DFT calculated distance is 1.142 Å in the gas phase and 1.149 Å during adsorption.[63] This elongation is attributed to a slight weakening of the C−O bond, which can be understood as the transfer of electrons from the σ state of CO to the gold surface and back-transfer of electrons from the metal to the π^* state of CO.[78] The C−O bond will increase in length as the binding of CO to gold becomes stronger due to surface defects.[79]

B. CO Adsorption on Oxygen-Covered Au(111). Preadsorption of O on the Au(111) surface increases the surface lifetime of CO and leads to reactive events. Simulations of CO adsorption and oxidation to CO_2 were performed on oxygen-covered Au(111) at three different O coverages—0.22, 0.33, and 0.55 ML—at 500 K. In all cases, CO spends much more time bound to the oxygen-covered surface compared to clean Au(111). For example, CO spends 31% of the total simulation time on the 0.22 ML oxygen-covered surface (Figure 2), compared to 7% of the total simulation time spent adsorbed on the clean surface.

Although lower coverages of O increase the surface lifetime, an increase in the O coverage decreases the residence time of CO compared to adsorption on lower oxygen coverages, to 18% for an O coverage of 0.55 ML. We find the average time CO spends on the surface per adsorption event increase from 861 fs on the clean surface to 2662 fs on 0.22 ML of oxygen on Au(111). Interestingly, this residence time increases to 2903 fs for 0.33 ML of oxygen but then decreases to 2398 fs for 0.55 ML oxygen.
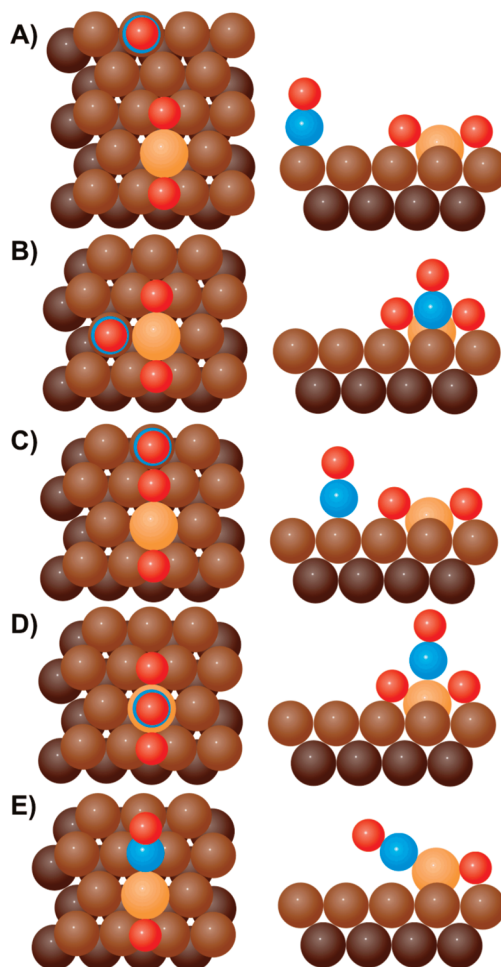

Figure 3. Models of adsorption sites for CO on the oxygen-covered surface, used for the classification of reactions; in the actual simulations, small variations and combinations of these idealized situations are encountered. Brown, gold, blue, and red spheres represent the first layer of gold atoms, a gold adatom lifted out of the first layer of the surface, a carbon atom, and oxygen atom, respectively. In site E, a CO molecule binds on the same gold atom opposite an oxygen atom adsorbed on the surface, causing the gold atom to be lifted from the surface with the CO not bound perpendicular to the surface.

Table 1. Ratio of CO Adsorption Sites at Each Oxygen Coverage[a]

CO site	0.22 ML	0.33 ML	0.55 ML
A	0.63	0.24	0.25
B	0.17	0.11	0.16
C	0.21	0.47	0.00
D	0.00	0.02	0.52
E	0.01	0.16	0.07

[a] The sites are illustrated in Figure 3.

The preferred binding site for CO on the oxygen-covered Au(111) surface is the top site of a gold atom with the CO molecule binding perpendicular to the surface, similar to the clean surface. This configuration clearly predominates for low oxygen coverage (<0.33 ML), since gold adatoms are not as readily formed. Figure 3 and Table 1 illustrate the observed binding sites and distribution of these sites at each coverage.

Local Bonding Effects in the Oxidation of CO

J. Chem. Theory Comput., Vol. 6, No. 1, 2010 **283**

At higher O coverage, there is a transition in the preferred binding site for CO, partly due to an increase in the number of binding sites around the surface oxide, because this species is more prevalent under these conditions. A transition in CO adsorption sites occurs, changing from sites A and C to site D (Figure 3), as the oxygen coverage increases from 0.33 to 0.55 ML. This corresponds to a change in adsorption from around the AuO_2 surface oxide complex to the site on top of the surface oxide. This is most likely the result of site blocking around the surface oxide complex by oxygen, which leaves only the top of the complex as available binding sites. We also find that CO can pull gold atoms from the surface. Site E (Figure 3) illustrates an adsorption geometry in which a CO molecule binds on a gold atom, which is also bound to an adsorbed oxygen atom. Upon adsorption, this gold atom is lifted from the surface, creating a chain starting with the adsorbed oxygen, a gold adatom, the carbon of the CO, and finally the oxygen from the CO. This configuration has many variations, depending on the type of oxygen surrounding the chain, and it is clear from the wide variation of systems we observed that the coadsorbed system is quite complex and dynamical in nature.

Our calculations also show that there is a strong dependence on the reactivity of oxygen as a function of coverage, in agreement with experiment. Min et al.[16] showed that the reactivity of CO depends on the oxygen coverage: Au(111) oxidized by dosing ozone at 200 K is most reactive at a coverage of ~0.5 ML, with the reactivity decreasing almost linearly with coverage, for either higher or lower oxygen coverage in a classic Langumuir−Hinshelwood behavior. Qualitatively, similar behavior is exhibited in our simulations. For example, reactivity is highest for 0.22 ML oxygen, with about 26% of the independent simulation runs resulting in CO_2 formation. The reactivity decreases to 12% conversion at 0.33 ML and to 8% at 0.55 ML of atomic oxygen coverage.

An ensemble of oxidation reaction pathways exist, with all observed reactions following the Langmuir−Hinshelwood mechanism in which CO adsorption is followed by subsequent reaction, in agreement with the experimental observations of Lazaga et al.[10] Lazaga found a negative activation energy for CO oxidation on Au(111) that was independent of oxygen coverage or CO pressure. The negative activation energy ruled out the possibility of a single elementary reaction step, indicating that CO oxidation does not proceed via an Eley−Rideal mechanism, in which a reaction would occur without CO first adsorbing on the surface. Experimental studies of CO oxidation on Au(111) also are consistent with a Langmuir−Hinshelwood mechanism when O is deposited at low temperature.[16] For clarification, we did occasionally observe CO reaction immediately following adsorption, especially for reaction pathway A_2 in Figure 4, but in all cases CO spends at least a few (>5) vibrational lifetimes on the surface; thus, we define all observed reactions as Langmuir−Hinshelwood. It is important to point out that because of our unphysical initial introduction of CO into the simulation (with zero velocity), we cannot absolutely rule out the possibility of the Eley−Rideal mechanism. However, many adsorption and desorption events occurred during each
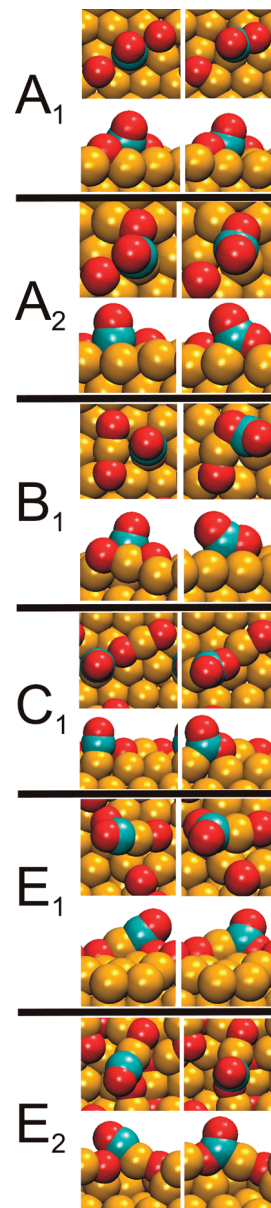

Figure 4. Snapshots (top and side views) of reaction pathways for CO oxidation to CO_2 on oxygen-covered Au(111) surfaces. Yellow, blue, and red spheres represent gold, carbon, and oxygen atoms, respectively. The first column represents the "start" of the reaction, while the second column is approximately the transition state. These defined reaction pathways are used in Table 2. Reactions E_1 and E_2 differ in that CO reacts with a chemisorbed oxygen in the former, while CO reacts with a surface oxide in the latter.

run, allowing at least the possibility for such a reaction to proceed which we did not observe, in agreement with experimental conclusions.

Reactions that involve chemisorbed oxygen atoms proceed primarily through the pathway labeled A_1 in Figure 4. In this pathway, a CO molecule is bound on top of a gold atom neighboring a 3-fold site. During reaction, the CO molecule migrates to the bridge site and toward the oxygen. At the same time, the O atom moves toward the CO through the same 2-fold site. The C of the CO molecule meets the adsorbed oxygen atom, forming CO_2, which then desorbs from the surface since the interaction of CO_2 with the surface

Table 2. Fractional Contribution of Reaction Pathways as a Function of Oxygen Coverage

| reaction[a]	0.22 ML	0.33 ML	0.55 ML
A_1	0.77	0.42	0.00
A_2	0.08	0.08	0.50
B_1	0.04	0.00	0.00
C_1	0.12	0.17	0.00
E_1	0.00	0.33	0.00
E_2	0.00	0.00	0.50

[a] The capital letter of each reaction signifies the starting adsorption site (Figure 3) and the subscript refers to each different reaction. Examples of each reaction are illustrated in Figure 4.

is extremely weak.[10] A second, less frequent pathway (see Table 2) for CO reaction with chemisorbed oxygen, labeled A_2 in Figure 4, occurs when CO binds to a gold atom to which oxygen is also bound in a neighboring 3-fold site. The reaction following adsorption is fast due to the instability of the system and because the CO molecule can easily find the adsorbed oxygen atom. Oxidation pathways involving an adsorbed surface oxide complex are initiated in the easiest way from adsorption site C (see Figure 3). A reaction occurs when the CO molecule diffuses toward the adsorbed oxygen. Other reactions involve adsorption site E and occur when the carbon reacts with chemisorbed oxygen (E_1) or the surface oxide or subsurface oxide (E_2). Table 2 lists the ratio of each reaction pathway by coverage. At lower oxygen coverage, reaction pathways involving chemisorbed oxygen (A_1 and A_2 in Figure 4) are dominant; at 0.22 ML of oxygen, chemisorbed oxygen accounts for 88% of the observed reactions. At higher coverages (0.33 and 0.55 ML), reactions with the subsurface oxide and other complicated pathways occur as is commented on in more detail in the Discussion.

IV. Discussion

Using AIMD, we identify two main factors that control the reactivity of CO on oxygen-covered Au(111): (1) the ability of CO to adsorb on the surface and (2) the local binding of the adsorbed oxygen. Our simulations are in general agreement with experiment and prior static DFT calculations. We find that the structure of the oxygen-covered surface and the oxygen coverage affect the CO oxidation pathways that contribute. CO oxidation was studied in a number of static DFT calculations; Su et al.[25] found a barrier of 0.29 eV for the oxidation on the Au(111) surface, while Liu et al.[26] found a barrier of 0.25 eV for the same reaction on the Au(221) surface. The careful recent DFT work of Wang et al. also showed how the barrier and rate for CO oxidation could strongly depend on surface structure and coordination of gold atoms.[80] We find similar trends, but importantly, we find the most reactive surface to be the one with 0.22 ML of oxygen, which contains oxygen mostly bound in 3-fold sites.

We attribute the increased binding of CO to the oxygen-covered surface to the presence of under-coordinated gold atoms that form upon adsorption of oxygen. Earlier theoretical[64] and experimental[81] work has shown that the gold surface becomes rough upon adsorption of oxygen, leading to a higher concentration of under-coordinated surface gold atoms as the O concentration increases. Under-coordinated Au atoms have been proposed to enhance the activity for
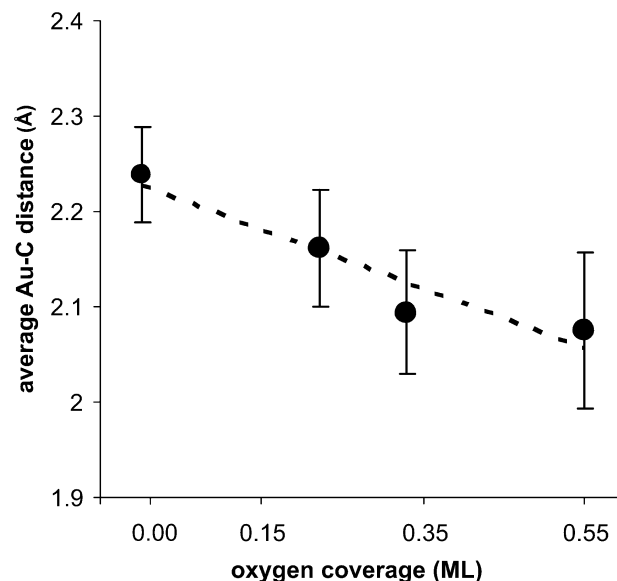
Figure 5. Average Au−$C_{(CO)}$ distance for adsorbed CO as a function of oxygen coverage.

O_2 dissociation for a variety of systems, including supported Au nanoparticles[32,39,76,82,83] and Au clusters on Au(111).[46,80]

The increasing roughness of the surface with oxygen coverage is expected to increase the binding strength of CO, based on studies by Wang et al.,[80] who found that the CO adsorption strength was inversely proportional to the coordination of the gold atom to which the CO is bound. In fact, by analyzing the average bond length of the carbon atom within CO to the gold atom on the surface to which it is bound, we observe a slight, but systematic, decrease in the bond length with increasing oxygen coverage (Figure 5), suggesting that CO adsorption is stronger on the rougher surface, which contains a larger number of under-coordinated gold. However, at O coverages greater than 0.22 ML, we observe a decrease in the CO surface lifetime, in agreement with previous experimental observations.[17] This suggests that while the binding of CO to the surface is stronger at higher oxygen coverage, the additional adsorbed oxygen is blocking sites for adsorption.

Since the reaction follows the Langmuir−Hinshelwood mechanism, adsorption of CO is an important first step to reaction. We find a strong correlation between the CO surface lifetime and the rate of oxidation. Despite the stronger CO adsorption at higher oxygen coverage, due to site blocking, the CO spends less time adsorbed on the surface. Since CO spends less time on the surface, there is less probability to react, leading to a lower oxidation rate.

It is important to understand the role of the type of oxygen involved in the reaction, that is, whether oxygen is chemisorbed or takes the form of a surface or subsurface oxide. The probability of CO adsorption alone cannot explain the reactivity trends, since the reaction rate decreases as a function of coverage, even when the reaction probability is normalized by the fraction of time CO spends adsorbed on the surface. We also expect that the reaction energy barriers and the availability to attack should significantly differ, depending on the oxygen species.

Local Bonding Effects in the Oxidation of CO

J. Chem. Theory Comput., Vol. 6, No. 1, 2010 **285**

Table 3. Ratio of Chemisorbed Oxygen and Surface Oxide on the Surface before CO Oxidation (Surface Species) and the Oxygen Atom Type Consumed during Oxidation (Reactive Species) along with the Relative Rate and Normalized Relative Rate (By Oxygen Type) for the Reaction for Each Oxygen Type on 0.22 and 0.33 ML Oxygen Covered Au(111)

	0.22 ML		0.33 ML	
	chemisorbed	surface oxide	chemisorbed	surface oxide
surface species	0.80	0.20	0.60	0.40
reactive species	0.88	0.12	0.83	0.17
relative rate	7.7	1.0	5.0	1.0
normalized relative rate	1.9	1.0	3.3	1.0

We find chemisorbed oxygen to be the most reactive oxygen species for CO oxidation. This effect is illustrated in Table 3, which compares the amounts of each oxygen type present at 0.22 and 0.33 ML relative to the probability that they react with CO to form CO_2. At both oxygen coverages, the chemisorbed oxygen contributes to the majority of the oxidation reactions. For 0.22 ML of oxygen coverage, initially 80% of the surface is covered with chemisorbed oxygen while 20% is covered with surface oxide. However, of the oxygen types responsible for oxidation, 88% is chemisorbed oxygen. The same is true for 0.33 ML of oxygen coverage: the surface is covered with 60% of chemisorbed oxygen, yet chemisorbed oxygen makes up 83% of the reactive atoms, illustrating that the chemisorbed oxygen is the most reactive type on the surface. Table 3 also illustrates the calculated relative reaction rate for each oxygen type. Even when the rate is normalized to take into account the ratio of each oxygen species on the surface (bottom line of Table 3), the relative rate for reaction with chemisorbed oxygen is significantly higher than surface oxide.

V. Conclusions

Realistic simulation of catalytic reactions on surfaces is an important endeavor that requires substantial computational resources. Generally, two key factors need to be taken into consideration when simulating such systems: the ability to accurately describe the important characteristics of the system (such as the forces between nuclei, charge transfer, etc.) and the need to minimize the computational cost of the simulation so that the dynamics of the system can be modeled for long time scales. Coarse-grained and lattice-based methods, such as kMC, are capable of investigating processes over a long time scale, but these methods must simplify the complicated electronic and ionic system using approximations or reduce the dimensionality of the fully atomistic system to a lattice. For systems as complicated as the interaction of oxygen on gold, neither of these approximations is acceptable, because oversimplifying the system features makes the simulation unreliable. To avoid this problem, we have used a fully atomistic simulation with forces between nuclei accurately calculated using DFT. This level of accuracy is computationally costly, resulting in dynamical runs that extend only for ∼10 ps and small unit cells, which may artificially restrict the possible structures that could be observed computation-

ally. Furthermore, we cannot model the effect of the initial CO velocity on the reaction, since we introduced CO into the system with a zero velocity because of computational cost. Nevertheless, a number of useful conclusions can be obtained from these simulations.

The oxidation of CO on Au(111) is a prototypical model system for ab initio molecular dynamics simulations, due to its inherent interest, involving a representative simple molecule that can be oxidized and an originally inert solid surface on which atomic-scale features can play an important role in reactivity. We carried out an extensive study of this system, using AIMD simulations. We find the highest rate of CO oxidation for 0.22 ML of oxygen coverage, with decreasing activity at the other two oxygen-coverage conditions we considered, 0.33 and 0.55 ML. The difference in reactivity that we found is most likely due to two factors: the type of oxygen atoms present on the surface during reaction and the ability of CO to adsorb on the surface. We have identified chemisorbed oxygen as the most reactive type of oxygen atoms. Furthermore, we observe a decrease in the adsorption probability for CO with increasing oxygen coverage, despite the increase in the strength of CO adsorption. The decrease in the probability for CO adsorption results in a decrease in reactivity as the oxygen coverage increases.

References

(1) Haruta, M. *Chem. Rec.* **2003**, *3*, 75.

(2) Haruta, M.; Date, M. *Appl. Catal. A-Gen.* **2001**, *222*, 427.

(3) Meyer, R.; Lemire, C.; Shaikhutdinov, S. K.; Freund, H. *Gold Bull.* **2004**, *37*, 72.

(4) Haruta, M.; Yamada, N.; Kobayashi, T.; Iijima, S. *J. Catal.* **1989**, *115*, 301.

(5) Hayashi, T.; Tanaka, K.; Haruta, M. *J. Catal.* **1998**, *178*, 566.

(6) Grisel, R. J. H.; Kooyman, P. J.; Nieuwenhuys, B. E. *J. Catal.* **2000**, *191*, 430.

(7) Jang, B. W. L.; Spivey, J. J.; Kung, M. C.; Kung, H. H. *Energy Fuels* **1997**, *11*, 299.

(8) Thompson, D. *Gold Bull.* **2000**, *33*, 40.

(9) Haruta, M.; Kobayashi, T.; Sano, H.; Yamada, N. *Chem. Lett.* **1987**, 405.

(10) Lazaga, M. A.; Wickham, D. T.; Parker, D. H.; Kastanas, G. N.; Koel, B. E. *ACS Symp. Ser.* **1993**, *523*, 90.

(11) Min, B. K.; Friend, C. M. *Chem. Rev.* **2007**, *107*, 2709.

(12) Kim, J.; Samano, E.; Koel, B. E. *J. Phys. Chem. B* **2006**, *110*, 17512.

(13) Stiehl, J. D.; Kim, T. S.; McClure, S. M.; Mullins, C. B. *J. Am. Chem. Soc.* **2004**, *126*, 13574.

(14) Gottfried, J. M.; Christmann, K. *Surf. Sci.* **2004**, *566*, 1112.

(15) Outka, D. A.; Madix, R. J. *Surf. Sci.* **1987**, *179*, 351.

(16) Min, B. K.; Alemozafar, A. R.; Pinnaduwage, D.; Deng, X.; Friend, C. M. *J. Phys. Chem. B* **2006**, *110*, 19833.

(17) Ojifinni, R. A.; Froemming, N. S.; Gong, J.; Pan, M.; Kim, T. S.; White, J. M.; Henkelman, G.; Mullins, C. B. *J. Am. Chem. Soc.* **2008**, *130*, 6801.

(18) Kim, T. S.; Gong, J.; Ojifinni, R. A.; White, J. M.; Mullins, C. B. *J. Am. Chem. Soc.* **2006**, *128*, 6282.

(19) Gottfried, J. M.; Christmann, K. *Surf. Sci.* **2004**, *566*, 1112.

(20) Yoon, B.; Hakkinen, H.; Landman, U.; Worz, A. S.; Antonietti, J. M.; Abbet, S.; Judai, K.; Heiz, U. *Science* **2005**, *307*, 403.

(21) Broqvist, P.; Molina, L. M.; Gronbeck, H.; Hammer, B. *J. Catal.* **2004**, *227*, 217.

(22) Molina, L. M.; Rasmussen, M. D.; Hammer, B. *J. Chem. Phys.* **2004**, *120*, 7673.

(23) Molina, L. M.; Hammer, B. *Phys. Rev. B* **2004**, *69*, 155424.

(24) Coquet, R.; Howard, K. L.; Willock, D. J. *Chem. Soc. Rev.* **2008**, *37*, 2046.

(25) Su, H. Y.; Yang, M. M.; Bao, X. H.; Li, W. X. *J. Phys. Chem. C* **2008**, *112*, 17303.

(26) Liu, Z. P.; Hu, P.; Alavi, A. *J. Am. Chem. Soc.* **2002**, *124*, 14770.

(27) Prestianni, A.; Martorana, A.; Ciofini, I.; Labat, F.; Adamo, C. *J. Phys. Chem. C* **2008**, *112*, 18061.

(28) Fajin, J. L. C.; Cordeiro, M.; Gomes, J. R. B. *J. Phys. Chem. C* **2008**, *112*, 17291.

(29) Chen, Y.; Crawford, P.; Hu, P. *Catal. Lett.* **2007**, *119*, 21.

(30) Wang, C. M.; Fan, K. N.; Liu, Z. P. *J. Am. Chem. Soc.* **2007**, *129*, 2642.

(31) Ganesh, R.; Pala, S.; Liu, F. *J. Chem. Phys.* **2006**, *125*, 5.

(32) Lopez, N.; Janssens, T. V. W.; Clausen, B. S.; Xu, Y.; Mavrikakis, M.; Bligaard, T.; Norskov, J. K. *J. Catal.* **2004**, *223*, 232.

(33) Zhang, C. J.; Hu, P. *J. Am. Chem. Soc.* **2000**, *122*, 2134.

(34) Molina, L. M.; Lesarri, A.; Alonso, J. A. *Chem. Phys. Lett.* **2009**, *468*, 201.

(35) Liu, L. M.; McAllister, B.; Ye, H. Q.; Hu, P. *J. Am. Chem. Soc.* **2006**, *128*, 4017.

(36) Liu, Z. P.; Jenkins, S. J.; King, D. A. *Phys. Rev. Lett.* **2004**, *93*, 156102.

(37) Liu, Z. P.; Gong, X. Q.; Kohanoff, J.; Sanchez, C.; Hu, P. *Phys. Rev. Lett.* **2003**, *91*, 266102.

(38) Kandoi, S.; Gokhale, A. A.; Grabow, L. C.; Dumesic, J. A.; Mavrikakis, M. *Catal. Lett.* **2003**, *93*, 93.

(39) Remediakis, I. N.; Lopez, N.; Norskov, J. K. *Angew. Chem., Int. Ed.* **2005**, *44*, 1824.

(40) Baker, T. A.; Xu, B.; Friend, C. M.; Kaxiras, E. Unpublished, 2009.

(41) Valden, M.; Lai, X.; Goodman, D. W. *Science* **1998**, *281*, 1647.

(42) Valden, M.; Pak, S.; Lai, X.; Goodman, D. W. *Catal. Lett.* **1998**, *56*, 7.

(43) Comotti, M.; Li, W. C.; Spliethoff, B.; Schuth, F. *J. Am. Chem. Soc.* **2006**, *128*, 917.

(44) Xu, Y.; Mavrikakis, M. *J. Phys. Chem. B* **2003**, *107*, 9298.

(45) Yoon, B.; Hakkinen, H.; Landman, U. *J. Phys. Chem. A* **2003**, *107*, 4066.

(46) Mills, G.; Gordon, M. S.; Metiu, H. *J. Chem. Phys.* **2003**, *118*, 4198.

(47) Stiehl, J. D.; Kim, T. S.; McClure, S. M.; Mullins, C. B. *J. Am. Chem. Soc.* **2004**, *126*, 1606.

(48) Deng, X. Y.; Min, B. K.; Guloy, A.; Friend, C. M. *J. Am. Chem. Soc.* **2005**, *127*, 9267.

(49) Wang, J.; Voss, M. R.; Busse, H.; Koel, B. E. *J. Phys. Chem. B* **1998**, *102*, 4693.

(50) Gottfried, J. M.; Elghobashi, N.; Schroeder, S. L. M.; Christmann, K. *Surf. Sci.* **2003**, *523*, 89.

(51) Biener, M. M.; Biener, J.; Friend, C. M. *Surf. Sci.* **2005**, *590*, L259.

(52) Canning, N. D. S.; Outka, D.; Madix, R. J. *Surf. Sci.* **1984**, *141*, 240.

(53) Saliba, N.; Parker, D. H.; Koel, B. E. *Surf. Sci.* **1998**, *410*, 270.

(54) Battaile, C. C.; Srolovitz, D. J. *Annu. Rev. Mater. Res.* **2002**, *32*, 297.

(55) Reuter, K.; Scheffler, M. *Phys. Rev. B* **2006**, *73*, 045433.

(56) Rapaport, D. C. *The Art of Molecular Dynamics Simulation*; Cambridge University Press: Cambridge, 2004; pp 1−10.

(57) Radeke, M. R.; Carter, E. A. *Annu. Rev. Phys. Chem.* **1997**, *48*, 243.

(58) Marx, D.; Hutter, J. *Ab Initio Molecular Dynamics: Basic Theory and Advanced Methods*; Cambridge University Press: Cambridge, 2009; pp 369−406.

(59) Wodtke, A. M.; Tully, J. C.; Auerbach, D. J. *Int. Rev. Phys. Chem.* **2004**, *23*, 513.

(60) Tully, J. C. *Annu. Rev. Phys. Chem.* **2000**, *51*, 153.

(61) Car, R.; Parrinello, M. *Phys. Rev. Lett.* **1985**, *55*, 2471.

(62) Tully, J. C. In *Modern Methods for Multidimensional Dynamics Computations in Chemistry*; Thompson, D. L., Ed.; World Scientific: Singapore, 1998; pp 34−72.

(63) Tully, J. C. In *Classical and Quantum Dynamics in Condensed Phase Simulations*; Berne, B. J., Ciccotti, G., Coker, D. F., Eds.; World Scientific: Singapore, 1998; pp489−514.

(64) Baker, T. A.; Xu, B.; Liu, X.; Friend, C. M.; Kaxiras, E. *J. Phys. Chem.* **2009**, *113*, 16561.

(65) Nose, S. *Mol. Phys.* **2002**, *100*, 191.

(66) Kresse, G.; Hafner, J. *Phys. Rev. B* **1993**, *47*, 558.

(67) Vanderbilt, D. *Phys. Rev. B* **1990**, *41*, 7892.

(68) Kresse, G.; Hafner, J. *J. Phys.-Condes. Matter* **1994**, *6*, 8245.

(69) Perdew, J. P.; Wang, Y. *Phys. Rev. B* **1992**, *45*, 13244.

(70) King, D. A.; Wells, M. G. *Surf. Sci.* **1972**, *29*, 454.

(71) Wang, Y.; Hush, N. S.; Reimers, J. R. *Phys. Rev. B* **2007**, *75*, 233416.

(72) Elliott, G. S. Thesis, University of California, San Diego, 1988.

(73) Piccolo, L.; Loffreda, D.; Ladete Santos Aires, F. J.; Deranlot, C.; Jugnet, Y.; Sautet, P.; Bertolini, J. C. *Surf. Sci.* **2004**, *566−568*, 995.

Local Bonding Effects in the Oxidation of CO

J. Chem. Theory Comput., Vol. 6, No. 1, 2010 **287**

(74) Nakamura, I.; Takahaski, A.; Fujitani, T. *Catal. Lett.* **2009**, *129*, 400.

(75) Peters, K. F.; Steadman, P.; Isern, H.; Alvarez, J.; Ferrer, S. *Surf. Sci.* **2000**, *467*, 10.

(76) Mavrikakis, M.; Stoltze, P.; Morskov, J. K. *Catal. Lett.* **2000**, *64*, 101.

(77) *CRC Handbook of Chemistry and Physics*, 77th ed.; Lide, D. R., Ed.; CRC Press: New York, 1996; pp 9−17.

(78) Shriver, D.; Atkins, P. *Inorganic Chemistry*; W. H. Freeman and Co.: New York, 2003; pp 544−546.

(79) Loffreda, D.; Sautet, P. *J. Phys. Chem. B* **2005**, *109*, 9596.

(80) Wang, H. F.; Gong, X. Q.; Guo, Y. L.; Guo, Y., G. L.; Hu, P. *J. Phys. Chem. C* **2009**, *113*, 6124.

(81) Min, B. K.; Deng, X.; Pinnaduwage, D.; Schalek, R.; Friend, C. M. *Phys. Rev. B* **2005**, *72*, 4.

(82) Lopez, N.; Norskov, J. K. *J. Am. Chem. Soc.* **2002**, *124*, 11262.

(83) Lemire, C.; Meyer, R.; Shaikhutdinov, S.; Freund, H. J. *Angew. Chem., Int. Ed.* **2004**, *43*, 118.

JCTC Journal of Chemical Theory and Computation

Computational Analysis of Solvent Effects in NMR Spectroscopy

Martin Dračínský* and Petr Bouř*

Institute of Organic Chemistry and Biochemistry, Academy of Sciences,
Flemingovo nám. 2, 166 10 Prague, Czech Republic

Abstract: Solvent modeling became a standard part of first principles computations of molecular properties. However, a universal solvent approach is particularly difficult for the nuclear magnetic resonance (NMR) shielding and spin−spin coupling constants that in part result from collective delocalized properties of the solute and the environment. In this work, bulk and specific solvent effects are discussed on experimental and theoretical model systems comprising solvated alanine zwitterion and chloroform molecules. Density functional theory computations performed on larger clusters indicate that standard dielectric continuum solvent models may not be sufficiently accurate. In some cases, more reasonable NMR parameters were obtained by approximation of the solvent with partial atomic charges. Combined cluster/continuum models yielded the most reasonable values of the spectroscopic parameters, provided that they are dynamically averaged. The roles of solvent polarizability, solvent shell structure, and bulk permeability were investigated. NMR shielding values caused by the macroscopic solvent magnetizability exhibited the slowest convergence with respect to the cluster size. For practical computations, however, inclusion of the first solvation sphere provided satisfactory corrections of the vacuum values. The simulations of chloroform chemical shifts and CH *J*-coupling constants were found to be very sensitive to the molecular dynamics model used to generate the cluster geometries. The results show that computationally efficient solvent modeling is possible and can reveal fine details of molecular structure, solvation, and dynamics.

1. Introduction

NMR spectroscopy is extremely sensitive to molecular structure, conformational, and environmental effects.[1−3] Ab initio computations of magnetic shielding[4,5] and indirect spin−spin coupling constants[6] were implemented in many software packages and have become standard tools for a more complete interpretation of the experiment ever since. However, due to the computational cost, these computations are still prohibitive for larger molecular systems. For solution data, it is therefore desirable to find reasonably accurate approximations that would allow accounting for the molecular environment.

The effect of solvent on the NMR parameters is relatively complex. It is difficult to separate the bulk medium effect from more specific interactions.[7] Both the solute and the solvent molecules can also be polarized by electrostatic interactions, make specific bonds involving an electron transfer, and change the conformation in a solution.

Standard polarizable continuum models (PCM) may be used for an estimation of molecular energies and conformations;[8,9] to some extent, they also improve computed vibrational properties.[10] These methods are, however, particularly inaccurate for polar solvents where a directional interaction, typically the hydrogen bond, influences the spectra or conformation.[11−14] Lately, a H⋯π interaction was also detected as an important factor for NMR of aromatic compounds.[15] Similarly, for modeling of properties involving electronically excited states, explicit solvent molecules are a better option.[16−20]

In theoretical modeling of NMR parameters, the PCM methodology certainly improves the vacuum results.[21−23]

---

* To whom correspondence should be addressed. E-mail: dracinsky@uochb.cas.cz (M.D.), bour@uochb.cas.cz (P.B.).

Computational Analysis of Solvent Effects

J. Chem. Theory Comput., Vol. 6, No. 1, 2010 **289**

Nevertheless, the discrete character of real solvents plays an important role also for the NMR spectroscopic response, particularly for polar systems and aqueous solutions.[2,21,24−29]

Previously, we found that the structure of the alanine hydration shell was crucial for understanding the fine chemical shift and spin−spin coupling changes caused by molecular protonation.[24] Also, other studies suggest that the solvent effects cannot be explained on the basis of a simple continuum approach.[26,27] In this study, we analyze a larger set of computational approaches and molecular model systems including both polar and nonpolar compounds to obtain a deeper physical insight into the mechanism of the solvent action. To estimate the bulk effect, the size of the water−alanine clusters was systematically varied, and various solvent models quantitatively were compared in terms of their influence on NMR spectra. The computational modeling is extended by less polar chloroform in various organic solvents. Solvated chloroform also proved to be a convenient model system, as the solute is small, halomethane NMR spectra exhibit a strong dependence on the solvent,[30] and the experiment is relatively straightforward.

Particular attention is paid to the bulk magnetizability that has often been ignored in previous modeling. Yet, it may cause comparatively large differences in chemical shifts with respect to those coming from internal molecular structural changes.[31,32] For a reliable comparison, NMR shifts obtained with different machines or conditions thus have to be corrected for the bulk effects, including factors reflecting shapes of the cells where the sample and the standard were measured.[33]

In this work, we also qualitatively discuss the bulk influence of isotropic and oriented solvent shells on molecular shielding. Other effects including electrostatic and charge-transfer interactions are analyzed in clusters of water and alanine charged forms. The calculated chemical shifts and *J* couplings are compared to the experimental values reported previously.[22] Finally, NMR data for chloroform were measured in various solvents and interpreted on the basis of cluster ab initio computations combined with molecular dynamics (MD) averaging. Although the precision of the Hartree−Fock (HF) and density functional methods is somewhat limited for NMR,[34−36] we are using these approximations because they are computationally efficient and still provide a deep physical insight into the solvation phenomena.

The computed data agree well with observed trends for the NMR parameter changes in various solvents. Both the chemical shift and *J*-coupling values, however, were found unexpectedly strongly dependent on the molecular dynamics model. This suggests that a similar dependence observed for water[24] is quite general, and the NMR parameters also reflect the fine arrangement of other solvent molecules around the solute. Only the combined MD/ab initio strategy is thus able to reliably include the environmental factors and provide means for a more precise NMR determination of molecular structures, dynamics, and interactions with the solvent.

Magnetic Continuum. To better understand the NMR solvation effects, we find it useful to briefly recall the behavior of a magnetic continuum. It has been recognized
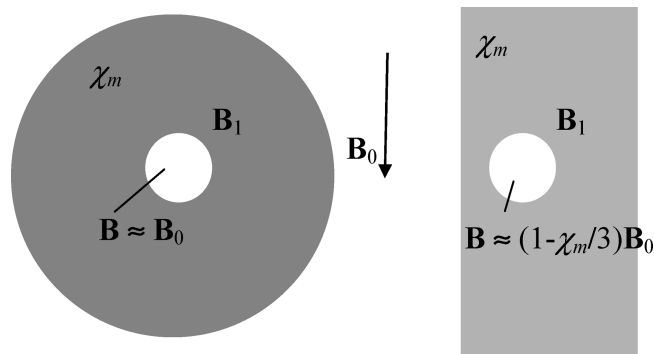

Figure 1. Spherical cavities in a magnetizable sphere and a rod.

that the influence of bulk on measured values of the isotropic magnetic shielding may be very large if compared with the differences originated in fine changes of molecular structure.[31] Modern spectrometers provide various ways of how to compensate these effects, including carefully chosen standards and cell-shape correction factors.[33] Nevertheless, the continuum part must also be considered in the modeling.

Isotropic Continuum Magnetizability. The magnetizability of an isotropic solvent is $\mathbf{M} = (d\mathbf{m})/(dV) = \rho\mathbf{m}N_A/M_w$, where ρ [kg/m^3] is the density, $\mathbf{m}$ [m^{2}A] is the molecular magnetic dipole moment, $N_A = 6.022045 \times 10^{23}$ is Avogadro's number, and M_w [kg/mol] is the molecular weight. The bulk magnetizibility thus can be related to the microscopic dipole $\mathbf{m} = \chi\mathbf{B}$ that is induced by a local magnetic field $\mathbf{B}$ [*T*]; χ [J/T^2] is the (isotropic) susceptibility.

Using the definition of magnetic polarization, $\mathbf{J} = \mu_0\mathbf{M} = \chi_m\mathbf{B}$, we can conveniently introduce dimensionless molecular susceptibility as $\chi_m = \mu_0\rho N_A\chi/M_w$, where $\mu_0 = 4\pi \times 10^{-7}$ [J/(mA^2)] is the vacuum permeability. The local (total) field $\mathbf{B}$ is related to the external field $\mathbf{B}_0$ via

$$\mathbf{B} = (1 + \chi_m)\mathbf{B}_0 = \mu_r\mathbf{B}_0 \qquad (1)$$

where μ_r is the relative permeability.[32,37]

In a NMR experiment, an external field of a magnet ($\mathbf{B}_0$) must be differentiated from the actual field in the solvent ($\mathbf{B}_1$) and that acting on a molecule ($\mathbf{B}$). As illustrative examples, consider a cavity in a magnetic "solvent" in the form of a sphere and a long rod (Figure 1). For the sphere, we get a uniform magnetization[31,37] $\mathbf{B}_1 = (1 + \chi_m)/(1 + \chi_m/3)\mathbf{B}_0 \approx (1 + 2\chi_m/3)\mathbf{B}_0$ and $\mathbf{B} = (1 - 2\chi_m/3)\mathbf{B}_1 \approx \mathbf{B}_0$, resulting in a zero bulk shielding. Similarly, for the rod, $\mathbf{B}_1 \approx (1 + \chi_m)\mathbf{B}_0$ and $\mathbf{B} = (1 - \chi_m/3)\mathbf{B}_0$, which corresponds to an NMR shift $\sigma = \chi_m/3$ induced by the solvent. Note that the NMR spectra are typically measured in long tubes that can be well approximated by the rod. Obviously, shapes of generally nonspherical molecules will modify the bulk influence in a more complicated way.

Anisotropic Solvation Shell. The continuum approximation also provides useful qualitative information about a partially oriented solvent layer around a dissolved molecule. In this anisotropic case, the susceptibility of the solvent becomes a position-dependent tensor, $\chi(\mathbf{r})$. An external magnetic field induces in each volume element dV a magnetic dipole of

$$dm = n\chi \cdot \mathbf{B} dV \qquad (2)$$

where $n = \rho N_A/M_w$ is a particle density. For small χ, we suppose that $\mathbf{B} \approx \mathbf{B_0}$. Note the final anisotropic dimensionless shift does not depend on the field. The magnetic field $\mathbf{B(0)}$ sensed by a molecule placed at the origin is a sum of the external field $\mathbf{B_0}$ and the contributions from the solvent minute dipoles:

$$\mathbf{B(0)} = \mathbf{B_0} + \frac{\mu_0}{4\pi} \int \frac{3\mathbf{rr} \cdot d\mathbf{m} - r^2 d\mathbf{m}}{r^5} \qquad (3)$$

For simplicity, we suppose that the solvent is oriented radially around the solute, with corresponding radial and angular susceptibility components, χ_{rr} and χ_{vv}, that are constant in a hydration shell limited by radii $r_1...r_2$. Then, we can also decompose the induced magnetic moment, $d\mathbf{m} = d\mathbf{m_r} + d\mathbf{m_v}$, where $dm_r = nB_0\chi_{rr}\cos(v)\,dV$ and $dm_v = nB_0\chi_{vv}\sin(v)\,dV$ (Figure 2). Because of the symmetry, only the scalar z-field components need to be considered $\mathbf{B_z(0)} = \mathbf{B(0)}$, with the ring volume element $dV = 2\pi r^2 \sin(v)\,dvdr$:

$$
\begin{aligned}
B(0) - B_0 &= \frac{\mu_0}{4\pi} \int \frac{3dm_r \cos(v) - dm_z}{r^3} \\
&= \frac{\mu_0}{4\pi} \int \frac{3dm_r \cos(v) - dm_r \cos(v) - dm_v \sin(v)}{r^3} \\
&= \frac{\mu_0 nB_0}{2} \int \frac{2\chi_{rr}\cos^2(v) - \chi_{vv}\sin^2(v)}{r} \sin(v)\,dv\,dr \\
&= \frac{2\mu_0 nB_0}{3}(\chi_{rr} - \chi_{vv})\ln\frac{r_2}{r_1} \qquad (4)
\end{aligned}
$$

Using the dimensionless susceptibilities, we obtain an NMR shift of $\sigma = (2/3)(\chi_{m,rr} - \chi_{m,vv})\ln(r_2/r_1)$. In other words, the orientation of the solvent molecules in the solvation spheres may result in an additional contribution to the solvent shift.

Normally, we can suppose that the oriented solvent layer does not extend too far from the solute. For small molecules, such as alanine and chloroform in the solvents studied below, $r_1 \sim 2$ Å and $r_2 \sim 6$ Å, so that $\ln(r_2/r_1) \sim 1$. Approximating very roughly $\chi_{m,rr} - \chi_{m,vv} \sim \chi_m/2$, we thus get at least a crude estimation of the shift as $\sigma \sim \chi_m/3$. That means that the anisotropic contribution is on the same order as those coming from the bulk. Note that the difference $\chi_{m,rr} - \chi_{m,vv}$
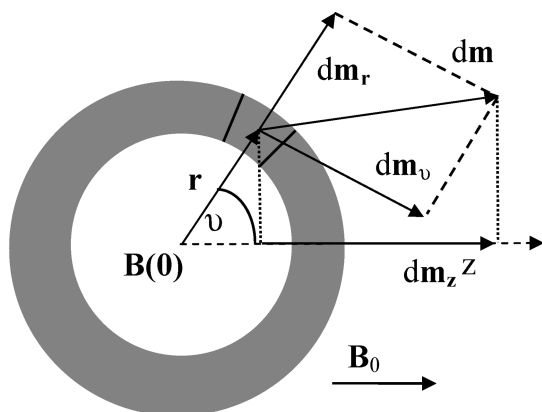

Figure 2. Spherical hydration sphere with a nonisotropic magnetization.

can be both positive and negative, so that the orientated solvent around can either amplify or neutralize the bulk shielding. Indeed, this is consistent with the more quantitative cluster computations presented in this study.

2. The Methods

Experimental Section. The experimental chemical shifts and spin−spin coupling constants obtained for isotopically labeled L-alanine (^{13}C, 98%; ^{15}N, 98%) were reported elsewhere.[22] Three NMR parameter sets for the zwitterionic (AZW, pH = 7), cationic (A$^+$, pH = 2), and anionic (A$^-$, pH = 12) amino acid forms in aqueous (H$_2$O/D$_2$O) mixtures were considered.

Carbon and hydrogen chemical shifts and indirect spin−spin coupling constants in chloroform were measured in six solvents, with the Bruker Avance II-600 spectrometer (600.1 MHz for ^{1}H and 150.9 MHz for ^{13}C). Pure chloroform (CHCl$_3$, 25 μL) was dissolved in a NMR tube with 0.5 mL of deuterated chloroform (CDCl$_3$), benzene, acetonitrile, acetone, methanol, and DMSO. A capillary ($\sim$0.2 mm in diameter) with 30 μL of chloroform was coaxially inserted into the tube as a standard. The ^{1}H and ^{13}C spectra were acquired, and solvent-induced chemical shifts were calculated as a difference between the chemical shifts in the solution and those in the capillary. Alternatively, the spectrometer solvent-correction functions were disabled, and the samples were referenced directly to pure chloroform, which, however, produced nearly the same results. The C−H coupling constants were determined from the distance between ^{13}C satellites in the ^{1}H NMR spectra. We estimate the accuracy of the measured chemical shifts as $\sim$0.01 and 0.001 ppm for σ_C and σ_H, respectively, and $\sim$0.2 Hz for the coupling.

Molecular Dynamics. Aqueous alanine (AZW) solvation shells were modeled with the Tinker molecular dynamics (MD) package,[38] using the Amber99 force field[39] that includes the TIP3P[40] water model. One alanine molecule was placed in a (18.56 Å)^3 cubic box, and the molecular dynamics were run using the periodic boundary conditions, NVT ensemble ($T = 295$ K), and a 1 fs integration step. After 10 ps of equilibration, solvent shells were selected from the MD snapshot each 10 ps. Additionally, an arbitrary water force field was used for the same MD runs, where atomic partial charges were set to zero ($q_O = q_H = 0$) and all other TIP3P and Amber99 parameters were unchanged. This choice led to solvation shells where the "water" molecules interacted weakly, which resulted in their different (more irregular) orientations and, consequently, different NMR parameters of alanine.

Alternatively, a larger (37.12 Å^3) cubic periodic box containing one alanine and 1708 water molecules was used in MD with Tinker using the same conditions. After 10 and 15 ps equilibration stages, the geometries were minimized (Amber99/TIP3P), and solvation shells and layers of various sizes specified below (e.g., containing water molecules closer than r_{max} and farther than r_{min} from the solute) were selected with our own Fortran code. Results obtained with the two MD snapshots were very similar with respect to the size-convergence behavior, and thus only the 10 ps case is shown.

Computational Analysis of Solvent Effects

J. Chem. Theory Comput., Vol. 6, No. 1, 2010 **291**

Table 1. Calculated and Experimental Solvent Magnetic Susceptibilities

solvent	$\chi^{a,b}$	$\chi^{a,c}$	ρ^d	$\chi_m^{c,e}$	$\chi_m^{\text{exptl } f}$
water	−220	−235	1.00	−9.9	−8.91
methanol	−355	−364	0.79	−6.8	−6.91
chloroform	−991	−1087	1.49	−10.3	−9.19
acetone	−555	−569	0.78	−5.8	−5.67
DMSO	−765	−778	1.10	−8.3	−7.81
benzene	−930	−931	0.87	−7.9	−
acetonitrile	−406	−419	0.79	−6.1	−6.57

[a] Molecular magnetic susceptibility, in 10^{-30} J T^{-2}. [b] B3LYP/6-31G** calculation. [c] B3LYP/6-311++G** calculation. [d] Density (g/mL) used. [e] Relative bulk magnetic susceptibility, in parts per million. [f] Ref 33, in parts per million.

To obtain a deeper physical insight into the influence of the solvent on the NMR calculations, we also used four alanine/water clusters that were previously obtained with the Car−Parrinello molecular dynamics (CPMD).[24] The more demanding CPMD simulation did not enable the inclusion of larger clusters, but water distribution obtained by this method is more realistic and provides NMR data more comparable with experimental results than from the classical MD.[24,41] The ab initio dynamics were based on the BLYP[42] functional and Vanderbilt[43] ultrasoft pseudopotentials; an energy cutoff of 25 Ry and a 4 au integration time step were used under temperatures of 300 K. A shorter time step than for the classical dynamics had to be used to allow for the relaxation of the electronic wave function, which is performed on the fly in CPMD.[44] Four cluster sets were selected, at 1.5, 5.0, 5.5, and 10 ps. Our own scripts were used to reduce the number of water molecules to for to nine so that hydrogen-bonded water molecules closer than 3.6 Å to the solute were retained only.[24] The distance of 3.6 Å allows to fully include the first hydration sphere. These "smaller" clusters were used by default. Similarly, larger clusters were made where all water molecules up to 4.5 Å were retained. In the resultant clusters, the alanine geometry was optimized ab initio with a fixed geometry of the water molecules.

Similarly as for the alanine, chloroform solvation, and solvent dependence of the NMR parameters was investigated with the aid of clusters obtained by the Tinker[38] MD and MM3[45] force field. Periodic cubic boxes of chloroform (sized 35.98 Å) and chloroform in the benzene (35.99 Å), methanol (36.00 Å), acetone (36.01 Å), acetonitrile (36.01 Å), and dimethylsulfoxide (CH₃SOCH₃, DMSO, 35.52 Å) solvents were subjected to equilibration MD runs for 10 ps. Both NVT and NpT thermodynamical ensembles were investigated at a temperature of 295 K and a pressure of 1 atm. For the NpT simulations, the solvent could more easily relax and orient itself around the solute than for NVT ensembles, but equilibrated solvent NpT densities were lower (by ∼25%) than the experimental ones (Table 1) due to force field inaccuracies. A total of 10 MD snapshots at 10 ps intervals were used to generate solvated chloroform molecules where all solvent molecules closer than 9 Å were retained. On average, the clusters with central solvated chloroform contained 44 MeOH, 20 CHCl₃, 18 acetone, 33 acetonitrile, 14 C₆H₆, and 18 DMSO molecules. Resultant clusters were subjected to constrained normal mode optimization of the geometry.[46,47] Vibrational modes with wavenumbers within

−300 to + 300 cm^{-1} were fixed (imaginary frequencies were considered as negative), so that the MD solvent distribution could be approximately conserved, but molecular geometry, particularly the bond lengths and angles, could relax at a higher, BPW91[48]/6-31G** level.

NMR Computations and Solvent Models. The NMR parameters were computed ab initio for simplified solvent models that included (1) solute in the gas phase, (2) solvent molecules explicitly included in the CPMD and MD clusters, (3) CPMD clusters surrounded by a polarizable PCM continuum,[49] (4) clusters where the solvent molecules were replaced by TIP3P[40] partial atomic charges ($q_O = -0.834$, $q_H = 0.417$, for water) and electrostatically fitted charges[50] from Gaussian (for the nonaqueous solvents), (5) using the same point charges surrounded by a PCM continuum, and (6) the solute in plain PCM. To investigate the "pure" polarizability effects (7), water molecules were also replaced by neon atoms placed at the water oxygen positions. Finally, (8) the nucleus-independent chemical shift (NICS)[32,51] was calculated for the CPMD and MD clusters where the solute molecule was removed from the cluster and only its solvation shell remained. For the ghost atoms in NICS, the *J* coupling was also calculated and related to the nuclear momenta of the substituted atoms.

Molecular magnetic susceptibilities, NMR isotropic shielding, and indirect spin−spin coupling (*J* coupling) were calculated with the Gaussian program.[52] All four *J*-coupling terms (Fermi-contact, spin-dipolar, diamagnetic, and paramagnetic spin−orbital)[6] were included. The hybrid B3LYP[42] functional with 6-31G** and 6-311++G** Pople-type basis sets was used for the susceptibilities. The default GIAO orbitals were used[4] in all calculations. Some alanine NMR parameters were obtained for CPMD clusters from ref 24 at the B3LYP/6-311++G** level. The Hartree−Fock (HF)/6-31G approximation was used for the larger (MD) clusters of alanine and water, because the DFT methods (B3LYP and BPW91) exhibited numerical instabilities for very large clusters. NMR shielding and *J* coupling in chloroform solvated by the organic solvents were calculated with the B3LYP and BPW91 functionals and 6-31G** basis set. Other basis sets were also tried (IGLOII and IGLOIII, not shown) but did not bring new insight. The accuracy of NMR properties is known to be significantly dependent on the quality of the basis set;[2] however, in this study, similarly as in previous works,[22,24,53] other limitations, such as the accuracy of the DFT methods, appear more important.

3. Results and Discussion

The Bulk Influence. The isotropic shielding caused by the bulk environment (cf. eq 1) can often be suppressed by suitable experimental conditions.[33] Its detailed modeling at the atomic level is beyond the main scope of this study; nevertheless, we can estimate at least its approximate magnitude from Table 1, where calculated (B3LYP/6-31G** and B3LYP/6-311++G**) dimensionless susceptibilities, χ_m, are compared to the experimental values from ref 33. Note that for a spherical cavity in a rod (Figure 1) the bulk shielding would be $\sigma = \chi_m/3$ and so forth. Such a geometry model is appropriate for most NMR experiments with
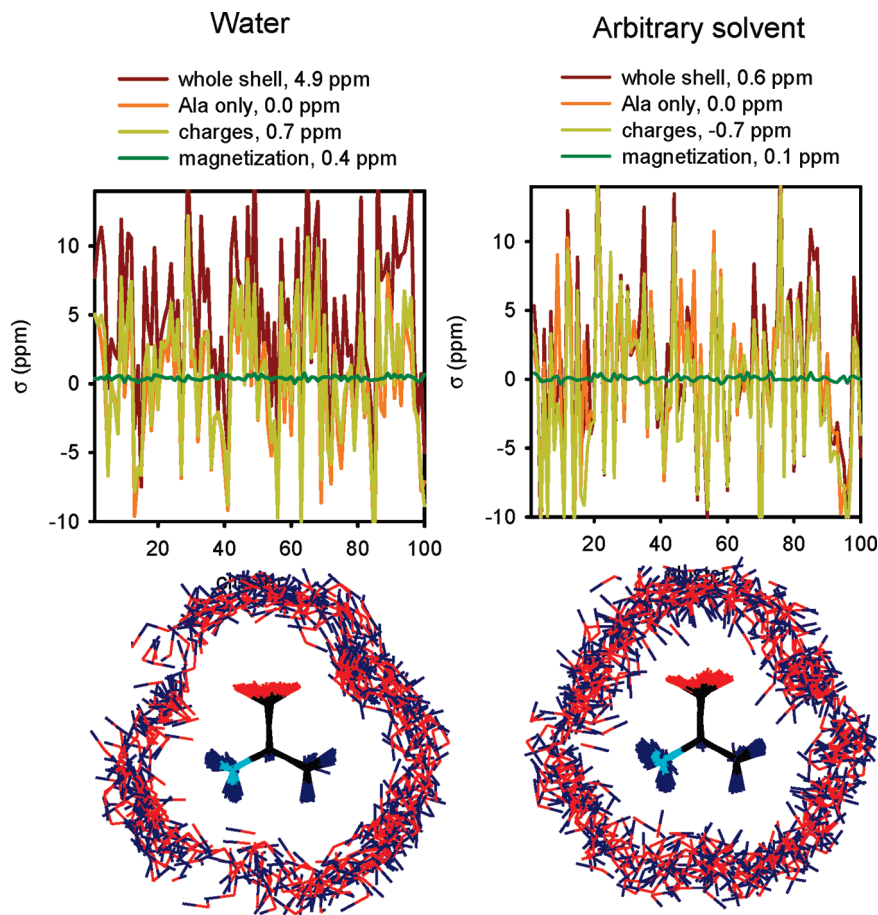
Figure 3. Example of water (left) and a less-oriented (right, "water" without charges) alanine solvation shell (3−4 Å). For 100 MD clusters, calculated (HF/6-31G) average and immediate nitrogen chemical shift changes (σ) are plotted as caused by the shell (maroon), alanine distorsions only (orange, the average is taken as a reference), partial charges mimicking the water molecules (yellow, $q_H = 0.42$, $q_O = -0.84$), and the magnetic NICS contribution (green). In the bottom, cross-sections 1-Å-thick through the overlapped hydration shells are plotted.

approximately spherical molecules measured in a prolonged (rotating) capillary. As apparent from the table, the ab initio computations with the 6-31G** and 6-311++G** basis sets produced similar results, and the calculated values very well (within 2−12%) agreed with the experiment. Clearly, the bulk magnetizability can cause chemical shift differences of several parts per million between various solvents, and as such it cannot be neglected in precise modeling.

The Solvent Orientation Effect. We have seen (eq 4) that oriented solvent can specifically contribute to the bulk influence, depending on the fine structure and extent of the solute hydration sphere. For oriented solvents and crystals, the derived logarithmic dependence of the shielding contribution on the distance means that clusters of limited sizes are not relevant for the theoretical modeling. Fortunately, for usual solvents, the solvent ordering is restricted to the first hydration sphere and thus better susceptible to modeling at the atomic level. On the example of a hydrated alanine zwitterion (Figure 3), we can follow both immediate and average hydration effects on the isotropic shielding of nitrogen. The behavior of other atomic shifts was similar.

In the solvent shell selected in Figure 3, immediate solvent configurations disperse the nitrogen shift within a large interval, ~-10 to $+13$ ppm if compared to the reference vacuum value. After averaging, the oriented aqueous solvent

produces a significantly different average shift of 4.9 ppm (left of Figure 3) than the chargeless artificial "water" model (0.6 ppm, Figure 3, right). A replacement of the water atoms by atomic partial charges (yellow curves) produces qualitatively similar dispersion to that of the explicit model, but corresponding average shift values obtained with the normal and chargeless water models (0.7 and −0.7 ppm, respectively) are quite different again. We can also see that the water magnetizability itself (green line) makes only a tiny contribution to the overall solvent effect. Its dispersion is also very small. Nevertheless, its average cannot be ignored for precise modeling. The more oriented case provides a value (0.4 ppm) that is significantly larger than that for the less-oriented model (0.1 ppm). This computational exercise is consistent with many cluster NMR studies,[24,26,27] indicating that the shift dispersion caused by the solvent configuration is huge, and a relatively large amount of MD configurations has to be taken for converged results.

Cluster Size Convergence. The cluster size convergence of the shielding caused by the bulk magnetazibility is rather slow (cf. eqs 3 and 4). It also strongly depends on the cluster shape (cf. Figures 1 and 2). However, this contribution is relatively minor (cf. Figure 3, green lines), and for practical computations, the principal solvent effects on NMR shielding can be reasonably approximated by a finite cluster of the
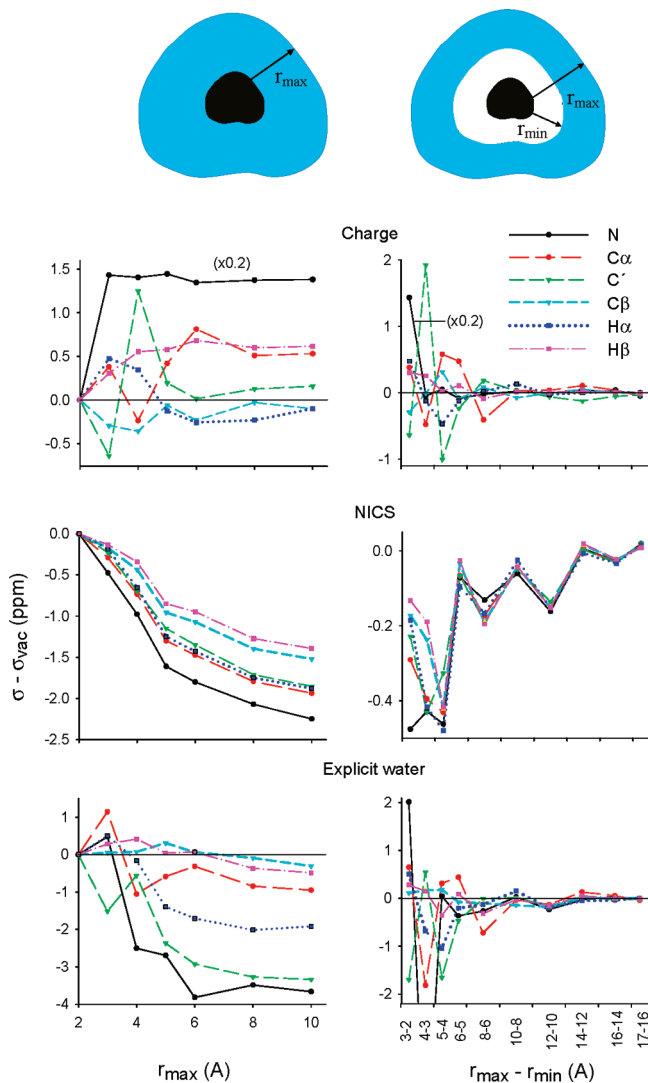
Computational Analysis of Solvent Effects

J. Chem. Theory Comput., Vol. 6, No. 1, 2010 **293**

Figure 4. Calculated (HF/6-31G) dependence of chemical shifts in the alanine zwitterion on the hydration shell radius (left) and the chemical shifts obtained with variously sized shell layers (right). A randomly selected MD cluster was used; the shifts are referenced to alanine in a vacuum.

solvent molecules around the solute. Indeed, as shown in Figure 4 (left) where alanine zwitterion shielding changes with respect to the vacuum caused by variously sized solvation shells are plotted, solvation shells of $\sim 8-10$ Å seem to provide reasonably converged results. The contributions obtained with the partial atomic charges and NICS are plotted separately in Figure 4. The size of the full shells with explicit water molecules is limited to $r_{max} \leq 10$ Å because of the computer time and memory limits. For example, the HF/6-31G NMR computation took 11 min for the 4 Å sphere (14 waters, 250 basis functions, about 50 MB of memory needed) and 7 h for the 8 Å sphere (100 waters, 1368 b.f., ~ 1 GB) if related to one 2.6 GHz AMD processor. Nevertheless, on the basis of previous analysis in Figure 3, we can suppose that averaging of the water orientations in the shell layers will further limit the influence of a distant hydration. Most of the shielding changes occur up to ~ 5 Å thickness (Figure 4); nevertheless, for example, the chemical shift of the hydrophobic C^{α} carbon is still notably influenced by solute molecules at a distance of ~ 6 Å from the solute.

A pure electrostatic influence of the solvent simulated by the partial atomic charges fades relatively quickly, at $r_{max} \sim$ 5 Å. This suggests that other effects are important for the total solvent-induced shift, such as making the hydrogen bonds associated with partial electronic transfer and polarization of the solvent by the solute, also neglected in the charge model. Particularly, the NICS "bulk" magnetizability (the middle row of graphs in Figure 4) converges very slowly. In accord with the above-mentioned discussion, the NICS values are similar for all atoms ($\sim 1.3-2.2$ ppm for the 10 Å shell) and qualitatively correspond to the shielding in a spherical aqueous cavity ($\chi_m/3 \sim 3$ ppm, cf. Table 1).

An alternate view is provided by the contributions from variously distant hydration layers plotted at the right-hand side of Figure 4. This approach allowed for a slightly larger distances ($r_{max} \leq 17$ Å) because the layers contained fewer water molecules than the full shells. In addition to the dependencies discussed for the full shells, we see that the contributions from individual layers of similar thickness diminish much faster with the maximum distance than for the full shells at the left-hand side of the figure, although the layers still contain a number of water molecules increasing as $\sim r^2$. Their decreasing influence on the chemical shifts is not monotonic, but it is modulated by actual water distribution/orientation in the layer. This is consistent with the shift dispersion caused by the solvent observed for a fixed-sized shell in Figure 3.

A relatively large basis set superposition error was found for the smallest alanine/water clusters (not shown), especially for the nitrogen shift, where it caused variations up to 1.5 ppm. Therefore, a fixed number of basis functions corresponding to all water molecules and $r_{max} = 4$ Å was kept in clusters smaller than this value.

Hydration Shell Additivity. Because the hydration layers influence the solute shifts in a relatively complex way, their effect is additive only roughly. This is demonstrated in Figure 5 for a 5–6 Å layer obtained from MD (Amber99/Tinker). For example, the addition of a layer-1-Å thick to the 5 Å shell does not noticeably change the original nitrogen σ_{xx} shielding density (top of Figure 5). In the bottom of Figure 5, in a more quantitative way, the approximate additivity is illustrated on individual AZW chemical shifts (with respect to the vacuum). Indeed, the shifts obtained with the 5–6 Å solvent layer follow the differences of shifts obtained with the complete 6 Å and 5 Å clusters. Other solvent shells (e.g., 3–4, 4–5 Å, not shown) behaved similarly. In the present example, a considerable deviation from additivity appears, namely, for the polar nitrogen atom. Nevertheless, on the basis of these observations, we can conclude that the NMR solvent effect is primarily caused by through-space electric and magnetic "additive" interactions rather than an electron transfer and similar solvent-mediated effects.

Solvent Contributions to NMR Shielding. Although we cannot separate individual mechanisms taking part in the solvent effect, they can be partially deduced from the comparison of various solvation models. In Figure 6, we compare isotropic shielding (relative to vacuum) of selected nuclei in the alanine zwitterion as obtained with several solvent approximations. The results for the other two A^+
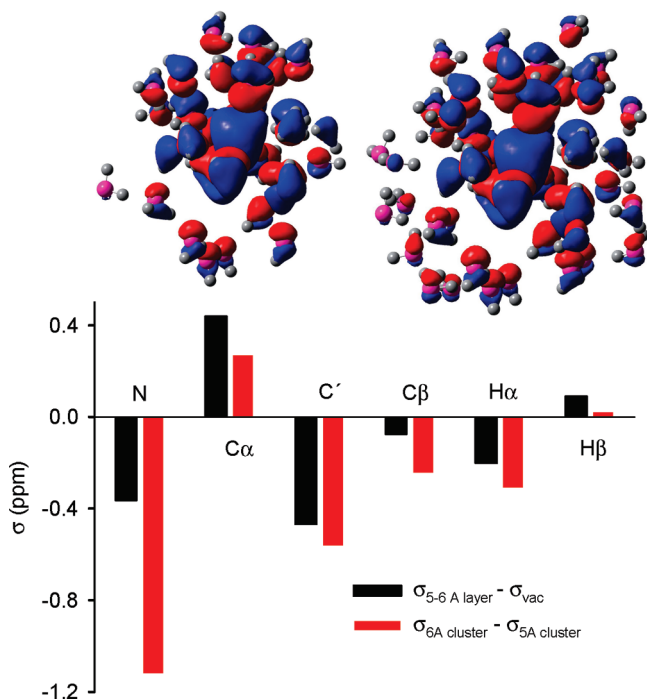
Figure 5. (Top) Nuclear shielding density (HF/6-31G, σ_{xx} isovalues at 0.02 au) calculated for the nitrogen atom in AZW surrounded by 5 Å (left) and 6 Å (right) hydration spheres. (Bottom) Difference of the chemical shifts obtained with the full 5 Å and 6 Å hydration shells (red, and the shift changes caused by the 5−6 Å layer only (black).
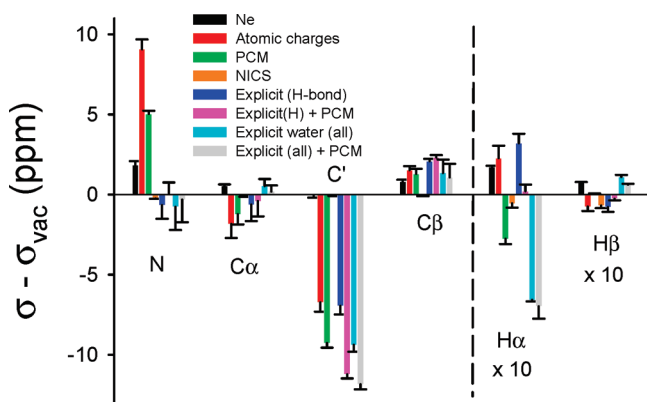

Figure 6. AZW chemical shifts calculated (B3LYP/6-311++G**) with various solvent models: (black) water molecules replaced by neon atoms and BSSE-corrected, (red) water molecules replaced by TIP3P atomic partial charges, (green) plain PCM, (yellow) the NICS contribution, (blue) explicit hydrogen-bond water clusters, (magenta) the clusters surrounded by PCM dielectric, (aqua and gray) larger clusters where also non-hydrogen-bonded water molecules were included, without and with the PCM environment. Results obtained as an average of four (two for the last two models) CPMD clusters are shown.

and A⁻ charged forms were similar to AZW and are not shown. For example, replacing the solvent by neon atoms placed at the water oxygen positions already causes significant chemical shift changes. This effect is relatively large for the hydrogen nuclei. It does not correspond well to the last, presumably most accurate, large cluster/PCM model. Nevertheless, the "plain polarization", in this case that of

the electrically neutral Ne atoms, significantly contributes to the NMR solvent effect. It should be noted that neon polarizability is a fraction (∼20%) of the aqueous one; modeling with other rare gas species, however, was problematic because of their large van der Waals radii. The neon radius, on the other hand, is very close to that of oxygen.

The C′ and C$^\beta$ shifts induced by the atomic partial charges (cf. Figure 6) copy the benchmark results (the last model in Figure 6) much more faithfully. The charge approximation, however, is fully inadequate for the nitrogen shielding, differing by ∼10 ppm from the more advanced approximations. More importantly, the widely used PCM model (green bars in Figure 6) also fails for the nitrogen. Clearly, for accurate calculation of NMR parameters, explicit water molecules are needed to model the hydrogen bonding and electron transfer associated with the solvation of the NH₃⁺ group. Similarly, computations of amide electronic excitations are required to include the water molecules explicitly.[18] On the other hand, the charge approximation could be used for modeling of the vibrational amide properties.[12,54]

The PCM model also gives rather erratic results for H$^\alpha$ and H$^\beta$ shifts. Even the models comprising H-bond waters in smaller clusters (blue and magenta bars in Figure 6) fail in this case. Clearly, for the aliphatic hydrogen magnetic shielding, the inclusion of all water molecules around the solute is more important than for the heavy atoms. This can be understood since H$^\alpha$ and H$^\beta$ do not form hydrogen bonds that were used for the water selection in the smaller clusters. Nevertheless, the addition of the PCM model seems to be still important for the largest clusters, where the longer-range polarization forces can significantly modulate the NMR shielding. It should be noted that experimental chemical shift variations for hydrogen, for example, in proteins, are much smaller than those for heavy atoms, which corresponds to the smaller absolute values for shifts comprising the H$^\alpha$ and H$^\beta$ atoms (cf. the y scale in Figure 6). Relative chemical shift variations for hydrogen and heavy atoms are dependent on the chosen reference (standard) and can generally be comparable.

The NICS contributions caused by the water magnetization only seem to be negligible for the heavy atoms. Presumably, they are overpowered by the currents magnetically induced inside the alanine molecule. However, they are very important for the hydrogen atoms, which are surrounded by a sparser electron density and clearly more susceptible to the magnetic currents induced in the solvent. Note that the size of the NICS effect is about the same for all atoms, similar to the bulk effect discussed before, which also makes it more important for the hydrogens where the absolute shifts are small.

These findings are supported by the data in Table 2, where the calculated chemical shifts of A⁻ and A⁺ (with respect to AZW) are compared to the experiment. In particular, although the point charge model was not adequate for the nitrogen shielding, it provides on average better results than PCM. The NICS bulk magnetic contribution is negligibly small, except for the hydrogen shielding of A⁻. As expected, the largest clusters surrounded by the PCM dielectric lead to the most accurate results.

Computational Analysis of Solvent Effects

J. Chem. Theory Comput., Vol. 6, No. 1, 2010 **295**

Table 2. Chemical Shifts (ppm) in the Charged A$^+$ and A$^-$ Forms Referenced to the Corresponding Nuclei in AZW as Calculated (B3LYP/6-311++G**) with Different Solvent Models[a]

	vacuum	PCM[b]	point charge	NICS	charge+PCM	cluster	cluster+PCM	exptl[b]
				$\sigma(A^+) - \sigma(AZW)$				
N	−3.54	−3.32	−2.84	0.02	−3.89	−1.79	−1.82	−2.20
C′	1.79	−1.04	−1.17	0.05	−1.24	−1.42	−1.80	−1.77
C$^\alpha$	3.12	−1.38	−0.44	0.09	−1.53	−0.23	−1.86	−3.11
C$^\beta$	−3.09	−2.60	−1.68	0.03	−2.42	−0.87	−1.30	−0.83
H$^\alpha$	0.67	0.75	0.65	0.08	0.70	0.62	0.75	0.37
H$^\beta$	0.51	0.25	0.32	0.02	0.27	0.28	0.22	0.08
$\Delta\sigma$[c]	2.35	0.98	0.88		0.99	0.69	0.44	0.00
				$\sigma(A^-) - \sigma(AZW)$				
N	−12.97	−11.62	−8.28	−0.23	−10.65	−8.96	−8.34	−6.60
C′	2.48	0.98	0.92	−0.18	1.03	0.47	0.77	0.93
C$^\alpha$	14.96	12.71	12.87	−0.08	12.57	11.53	10.28	8.94
C$^\beta$	3.03	4.08	3.73	−0.15	4.49	3.03	3.11	4.25
H$^\alpha$	−0.97	−0.90	−0.73	−0.22	−0.88	−0.56	−0.63	−0.48
H$^\beta$	−0.63	−0.43	−0.53	−0.15	−0.33	−0.40	−0.28	−0.26
$\Delta\sigma$[c]	2.67	1.60	1.11		1.41	1.14	0.76	0.00

[a] The calculated shifts were obtained as an average from four clusters based on geometries from ref 24. [b] Ref 22. [c] Mean absolute deviation.
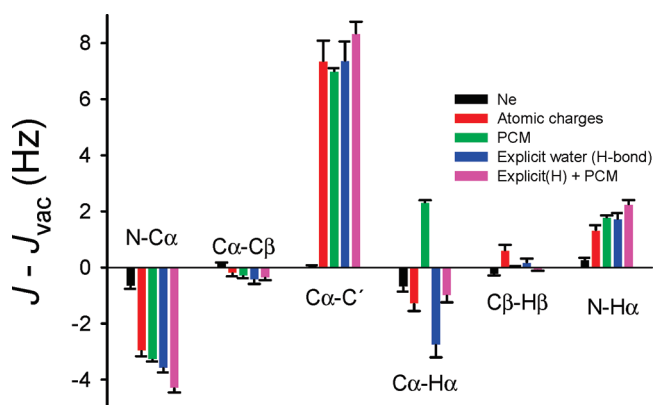
Figure 7. Calculated (B3LYP/6-311++G**) changes of selected AZW *J*-coupling constants caused by five different solvation models (cf. Figure 6). Cluster results were averaged for four CPMD AZW/H$_2$O geometries.

AZW *J* Coupling. As discussed previously, the indirect spin−spin coupling is a significantly more local property than the chemical shift.[24,36] Consequently, its dependence on the solvent is limited: The polarization neon model (the first in Figure 7) has a minor influence on calculated AZW coupling constants. On the other hand, the lower-level point charge and PCM solvent models provide changes that are all comparable with the most advanced explicit/PCM approximation (Figure 7). However, the PCM model fails for the *J*(C$^\alpha$−H$^\alpha$) constant. This may be an accident, as both the DFT approximation itself and neglecting the vibrational averaging significantly contribute to an overall error of the calculated *J*-coupling constants.[2,24,36,55] In any case, the importance of the solvent for the nonpolar C$^\alpha$−H$^\alpha$ moiety is rather surprising.

On average, the PCM results reasonably well explain the experimental solvent influence on the *J*-coupling constants for the three alanine charged forms, as documented in Table 3, where also other solvent models and the experimental values are listed. Very good solvent correction is obtained also with a computationally cheap atomic partial charge model combined with the PCM environment.

NMR Shielding and Coupling in Nonaqueous Solvents. Further insight into the mechanisms of the solvation effects can be obtained by comparison of more solvents. We plotted the calculated shift and spin−spin coupling constant changes caused in the chloroform molecule by the acetone, acetonitrile, benzene, chloroform, dimethylsulfoxide, and methanol solvents in Figure 8. The NMR parameters were evaluated at the BPW91/6-311++G**(6-31+G* for the solvent) level. The GGA BPW91 functional works approximately as well as B3LYP, but the calculations are significantly faster. As above, we consider the last ("explicit+PCM") model to be the most reliable. Unlike for water (Figures 6 and 7), the replacement of the organic solvents by the partial atomic charges does not provide reliable solvent effects. The carbon chemical shifts obtained with PCM are not realistic, while this approximation gives reasonable hydrogen shifts for some polar solvents (acetone, acetonitrile, and DMSO). The electrostatic (charge and PCM) models particularly fail for benzene; for this molecule, we can observe an exceptionally large NICS "bulk" magnetizability contribution, as can be expected because of its aromatic character. The aromaticity causes the experimentally well-known ring current effects.[32] The aromatic solvent-induced shift (ASIS) has been firstly observed with pyridine and benzene used as solvents and soon systematically was investigated in a series of steroidal compounds.[56] In our case, perhaps surprisingly, the NICS shielding is also important for the chloroform hydrogen solvent shift, where it causes about 80% of the total "explicit + PCM" change.

For the coupling, we defined "NICS" coupling values, in an analogy to the shift, as a coupling constant between two solute nuclei. The nuclei were treated as pseudo(ghost)-atoms, without electrons and a basis set, so that the coupling was enabled by the solvent electrons only. Such coupling thus represents a direct magnetic interaction between the solute nuclei mediated by the solvent. As expected, this effect is rather small (orange bars in the bottom panel in Figure 8) but may become important for more precise computations in the future. According to our knowledge, it has never been estimated before.

Table 3. Calculated and Experimental Indirect Spin−Spin Coupling Constants (Hz) for the Three Alanine Forms

	C^α	vacuum	cluster	point charge	PCM	point charge+PCM	cluster+PCM	exptl.[a]
AZW	$N-C^\alpha$	0.1	−3.5	−2.8	−3.2	−3.4	−4.2	−5.7
	$C^\alpha-C^\beta$	33.6	33.1	33.3	33.2	33.3	33.2	34.9
	$C^\alpha-C'$	45.4	52.8	52.8	52.4	52.9	53.8	54.0
	$C^\alpha-H^\alpha$	142.8	140.0	141.5	145.1	144.4	141.8	145.1
	$C^\beta-H^\beta$	123.4	123.6	124.0	123.4	123.5	123.3	129.7
	$N-H^\alpha$	−3.4	−1.7	−2.1	−1.6	−1.7	−1.2	0.0
	$N-C^\beta$	0.0	−0.1	−0.1	−0.2	−0.2	−0.4	0.0
	$N-C'$	0.1	−0.1	−0.1	−0.1	−0.1	−0.1	0.0
	$C^\alpha-H^\beta$	−2.5	−2.9	−2.8	−2.8	−2.8	−3.0	−4.4
	$C^\beta-H^\alpha$	−2.4	−2.7	−2.7	−3.0	−2.9	−3.0	−4.6
	$C'-C^\beta$	−1.0	−1.1	−1.2	−1.1	−1.2	−1.1	−1.2
	$C'-H^\alpha$	−3.8	−3.6	−3.8	−4.0	−4.0	−3.6	−5.0
	$N-H^\beta$	−3.8	−3.2	−3.6	−3.5	−3.5	−3.0	−3.1
	$C'-H^\beta$	2.9	3.6	3.5	3.5	3.6	3.9	4.2
	$H^\alpha-H^\beta$	5.8	6.2	6.0	6.1	6.1	6.4	7.3
	ΔJ^b	2.5	1.7	1.6	1.4	1.4	1.4	0.0
A^+	$N-C^\alpha$	−5.2	−5.9	−6.0	−6.0	−6.2	−6.0	−6.6
	$C^\alpha-C^\beta$	31.5	32.8	32.4	33.3	33.2	33.5	34.1
	$C^\alpha-C'$	63.1	61.6	62.7	62.2	62.4	60.9	59.6
	$C^\alpha-H^\alpha$	141.4	138.1	139.7	143.5	142.8	141.5	146.6
	$C^\beta-H^\beta$	128.1	126.3	127.3	125.7	125.9	125.0	131.0
	$N-H^\alpha$	−1.1	−0.2	−0.6	−0.3	−0.2	0.0	0.0
	$N-C^\beta$	−0.2	−0.2	−0.3	−0.4	−0.4	−0.3	0.0
	$N-C'$	−0.5	−0.7	−0.5	−0.4	−0.4	−0.6	0.0
	$C^\alpha-H^\beta$	−3.0	−3.3	−3.2	−3.3	−3.3	−3.4	−4.6
	$C^\beta-H^\alpha$	−3.8	−3.9	−3.9	−4.1	−4.1	−4.2	−4.9
	$C'-C^\beta$	−1.4	−1.1	−1.2	−1.3	−1.3	−1.1	−1.3
	$C'-H^\alpha$	−6.2	−5.7	−5.9	−6.2	−6.1	−5.8	−6.0
	$N-H^\beta$	−4.1	−3.1	−3.6	−3.5	−3.4	−2.9	−3.0
	$C'-H^\beta$	4.3	4.4	4.4	4.4	4.4	4.5	4.6
	$H^\alpha-H^\beta$	6.5	6.7	6.6	6.5	6.6	6.7	7.3
	ΔJ^b	1.5	1.5	1.4	1.1	1.2	1.2	0.0
A^-	$N-C^\alpha$	−3.3	−3.1	−3.5	−2.8	−3.4	−2.8	−4.3
	$C^\alpha-C^\beta$	36.3	35.6	36.2	36.2	35.9	35.5	35.2
	$C^\alpha-C'$	49.6	50.3	50.9	50.4	51.0	50.0	52.7
	$C^\alpha-H^\alpha$	130.5	130.5	130.2	132.9	132.1	131.9	138.4
	$C^\beta-H^\beta$	118.1	120.3	119.7	120.2	121.1	120.9	127.6
	$N-H^\alpha$	−3.4	−2.5	−2.8	−2.7	−2.5	−2.3	−2.2
	$N-C^\beta$	−4.9	−3.3	−3.9	−4.3	−3.6	−0.3	0.0
	$N-C'$	0.9	1.1	1.0	0.9	1.1	1.1	0.0
	$C^\alpha-H^\beta$	−3.0	−3.2	−3.1	−3.2	−3.1	−3.2	−4.3
	$C^\beta-H^\alpha$	−2.9	−3.6	−3.4	−3.4	−3.5	−3.7	−4.7
	$C'-C^\beta$	0.3	0.2	0.3	0.4	0.1	0.2	0.0
	$C'-H^\alpha$	−3.7	−3.1	−3.3	−3.4	−3.3	−3.0	−4.3
	$N-H^\beta$	−3.5	−3.3	−3.5	−3.5	−3.6	−3.3	−3.0
	$C'-H^\beta$	3.1	3.6	3.4	3.6	3.6	3.8	4.3
	$H^\alpha-H^\beta$	6.0	6.3	6.2	6.2	6.2	6.4	7.1
	ΔJ^b	2.4	2.0	2.1	2.0	1.8	1.6	0.0

[a] Ref 22. [b] Mean absolute deviation.

Another important difference between the solvated alanine and chloroform is the indifference of the carbon and hydrogen NMR parameters to the addition of the PCM continuum around the explicit cluster. Only for the J(CH) coupling constant in DMSO and methanol solvents does the addition of PCM cause larger changes. This can be explained by the absence of a strong chloroform-solvent hydrogen-bond-like interaction, lower polarity of the organic solvents, and their comparatively larger size (against H_2O). Indeed, as apparent from the radial distribution functions in Figure 9, the used cutoff of 9 Å allows inclusion of most of the orientation effects associated with the arrangement of the solvent in the first solvation sphere. For larger radii, the radial distribution functions (solvent densities) quickly converge to the experimental values (cf. also Table 1), although minor oscillations can still be seen even at larger distances, in particular for DMSO.

DFT Functional and Basis Set Dependence. For control computations, we also estimated the influence of a functional (BPW91 → B3LYP) and basis set applied used for the solvent (6-31+G*→6-311++G**) on the predicted solvent effects in Figure 8. This did not bring significant qualitative changes. For absolute values, however, the basis set change still caused differences up to 0.4 ppm and 0.1 ppm for the carbon and hydrogen chemical shifts and 0.8 Hz for the C−H coupling, for example. The results obtained with the different functionals differed much less (∼0.1 ppm for the shifts and ∼0.2 Hz for the coupling).

Comparison to Experimental Chloroform NMR Spectra. As an ultimate test, the NMR parameters calculated with the MD solvent/chloroform clusters are compared to experimental results. In Figure 10, ^{13}C and ^{1}H chemical shifts (with respect to pure chloroform) are plotted as calculated and

Computational Analysis of Solvent Effects

J. Chem. Theory Comput., Vol. 6, No. 1, 2010 **297**

Figure 9. Radial distribution densities of the six solvents surrounding the chloroform molecule obtained by the NVT Amber99 MD simulations. The density was integrated with respect to the CHCl$_3$ carbon atom.
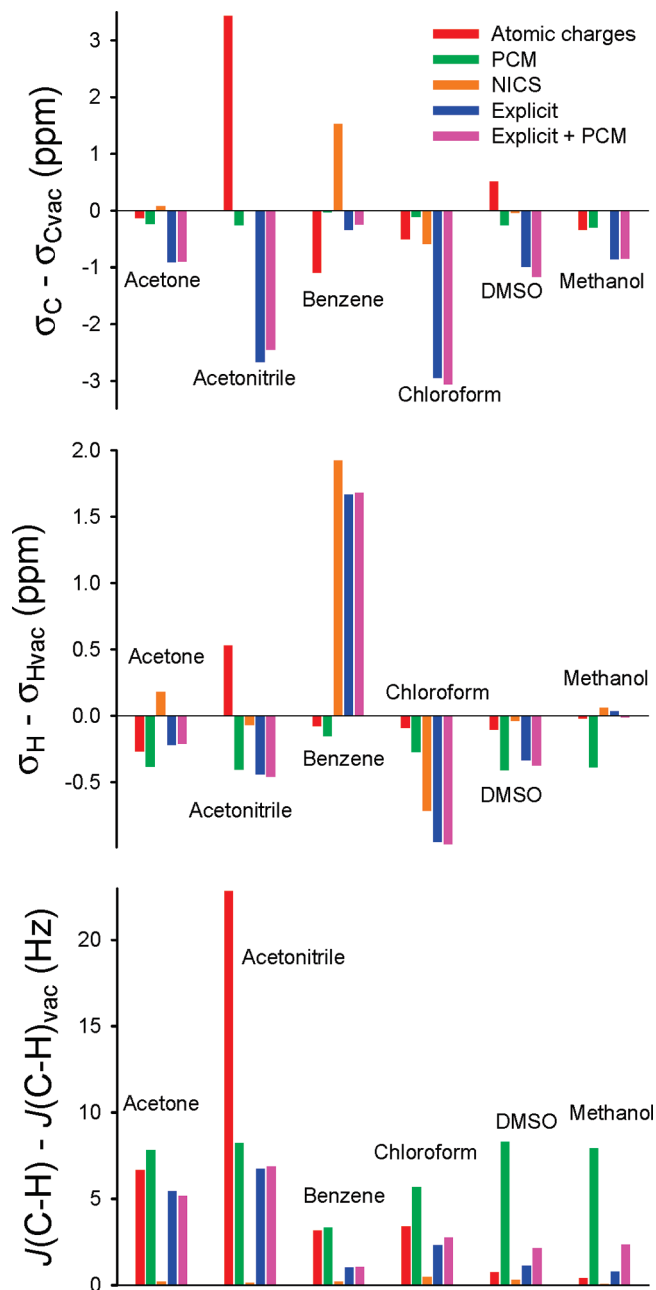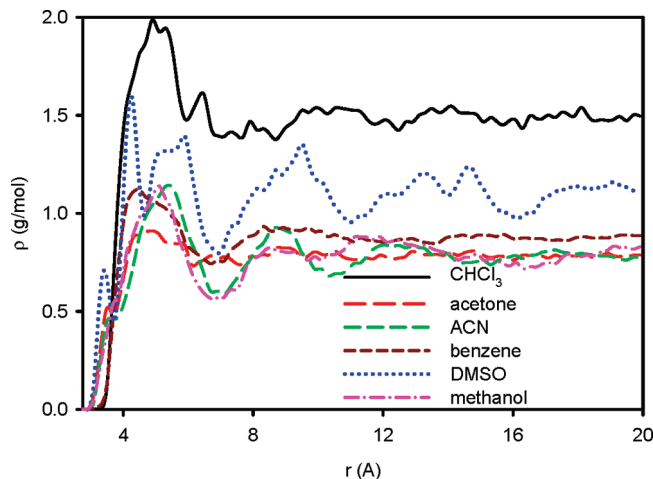

Figure 8. Calculated (BPW91/6-311++G**/6-31+G*) solvent-induced carbon (top) and hydrogen (middle) chemical shifts and changes of the C−H coupling constant (bottom) for chloroform in different solvents. Five solvent approximations were adopted as indicated.

shielding to the MD model has already been observed for the alanine,[24] where the CPMD simulation gave better results than a classical MD. For the larger chloroform/solvent clusters, unfortunately, the CPMD computations take too long.

A very good overall agreement can also be observed between the calculated and experimental solvent changes in the *J*(CH) coupling (Figure 11). Here, the NVT geometries provided somewhat better results than those from the NpT simulation. This can be attributed to more realistic NVT solvent densities; the NpT simulation underestimates both densities and coupling solvent effects. The solvent coupling effect on *J*(CH) seems to be primarily driven by the polarity of the solvent. The DMSO induces the biggest changes with respect to the nonpolar solvents, but the dependence does not follow the electric permittivity for similarly polar solvents blindly (the respective permittivities for CHCl$_3$, C$_6$H$_6$, CD$_3$CN, MeOH, acetone, and DMSO are ε_r = 4.7, 2.3, 35.7, 32.6, 20.5, and 46.9). The good agreement with the experiment and the variation of the results with the MD parameters also indicate desirable improvements in future simulations of the NMR parameters. Inevitably, solvent and solute molecular dynamics have to become more reproducible.

4. Conclusions

On several models, we have investigated various factors that are important for an understanding and reliable modeling of the solvent effects on NMR chemical shifts and indirect spin−spin coupling constants. In spite of the complexity, such as the delocalized character of the magnetic phenomena, the cluster models, where the geometry is derived from relatively accurate MD simulations and properly averaged over a modest number of configurations, recover the most important changes observed for the NMR parameters in the experiment. Needless to say, ab initio molecular dynamics, when possible, provide more reliable results than empirical MD force fields.

For the shielding, a correct description of the solvent orientation in the first solvation sphere appeared particularly

measured for the six solvents. A total of 10 clusters were averaged for each point, and the standard error of the mean is indicated. Overall, the main trends are well-reproduced; the results obtained with the MD solvent clusters could further be improved when the bulk influence was arbitrarily added as 1/3 of the relative magnetic susceptibility (Table 1) for all solvents, mimicking thus a spherical cavity. The BPW91 and B3LYP functionals provide nearly the same results. The calculated solvent effects (the slope in the graphs, compare to the line $y = x$) are overestimated for ^{13}C and underestimated for ^{1}H in comparison with the experiment. Interestingly, the NVT dynamics provided much larger solvent effects than NpT. Such a sensitivity of the NMR
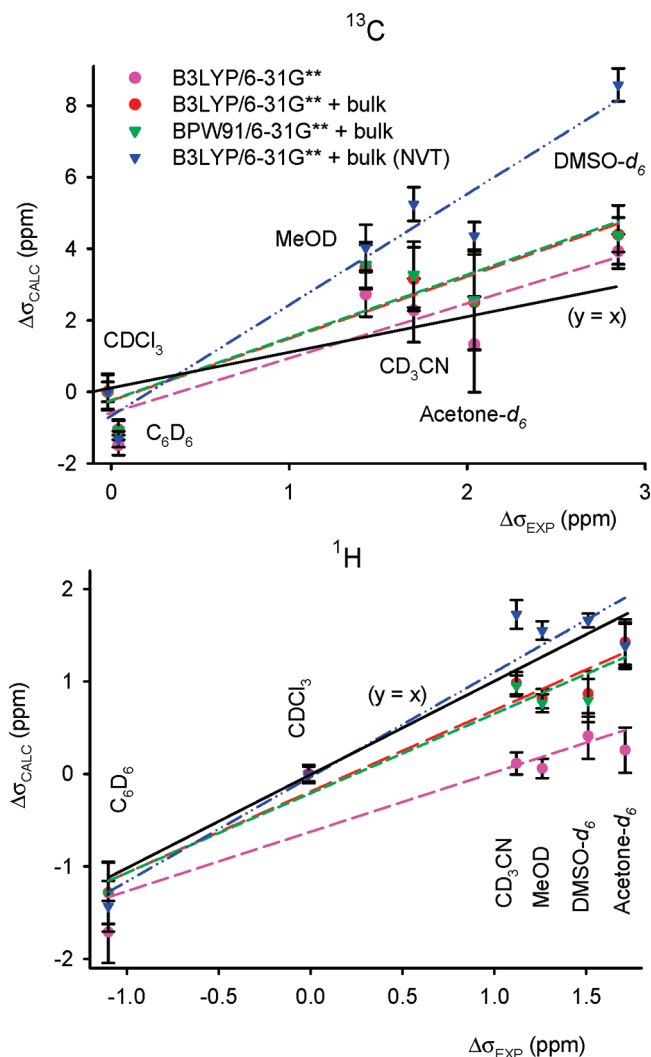
Figure 10. Experimental versus calculated ^{13}C (top) and ^1H (bottom) chemical shifts of chloroform in various solvents, referenced to pure $CHCl_3$. The calculated solvent shifts were obtained as averages of 10 independent MD geometries. By default, the NpT thermodynamic ensemble was used. Errors of the means are indicated.
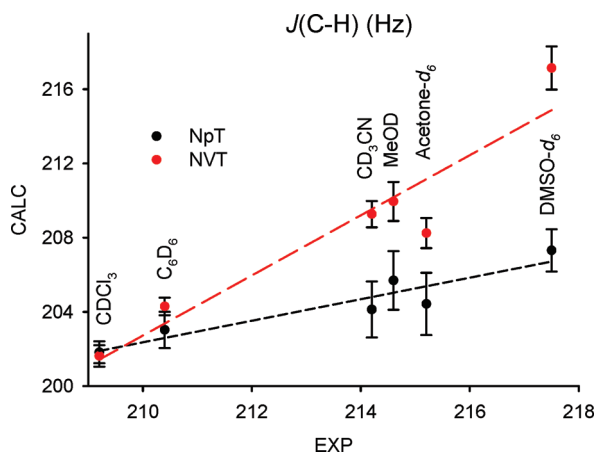

Figure 11. Correlation of experimental and calculated (B3LYP/6-31G**) chloroform C–H coupling constants in various solvents. For results obtained as averages of 10 random clusters from NpT or NVT MD simulations, the errors of the mean are indicated.

crucial for precise results. The far-ranging bulk influence could be estimated only roughly from computations on large clusters or from the solvent magnetic susceptibility. The isotropic shielding was found to be very sensitive to specific solvent−solute interactions and solvent orientation in the hydration spheres.

The indirect spin−spin coupling behaved as a much more local phenomenon than the shielding. The solvent effects, primarily dependent on electrostatic interactions, could be modeled at a relatively low level of approximation, for example, with the atomic partial charges or a polarizable continuum.

The modeling provided chemical shifts and indirect spin−spin coupling constants for the alanine charged forms that compared well with the previous experimental results. Similarly for the chloroform NMR data, the calculated results reasonably well explained differences observed experimentally for six organic solvents. The calculated results were strongly dependent on the adopted molecular dynamics model. Nevertheless, the modeling revealed the large potential of the NMR spectroscopy to study not only molecular structure and conformation, but also the specific solvent−solute interactions and structures of the solvation shells.

References

(1) Evans, J. N. S. *Biomolecular NMR Spectroscopy*; Oxford University Press: Oxford, U. K., 1995.

(2) Kaupp, M.; Bühl, M.; Malkin, V. G. *Calculation of NMR and EPR Parameters: Theory and Applications*; Wiley-VCH: Weinheim, Germany, 2004.

(3) Otting, G.; Liepinsh, E. *Acc. Chem. Res.* **1995**, *28*, 171.

(4) Ditchfield, R. *Mol. Phys.* **1974**, *27*, 789.

(5) Cheeseman, J. R.; Trucks, G. W.; Keith, T.; Frisch, M. J. *J. Chem. Phys.* **1996**, *104*, 5497.

(6) Sychrovský, V.; Gräfenstein, J.; Cremer, D. *J. Chem. Phys.* **2000**, *113*, 3530.

(7) Luhmer, M.; Bartik, K. *J. Phys. Chem. A* **1997**, *101*, 5278.

(8) Cossi, M.; Rega, N.; Scalmani, G.; Barone, V. *J. Comput. Chem.* **2002**, *24*, 669.

(9) Caricato, M.; Ingrosso, F.; Mennucci, B.; Tomasi, J. *J. Chem. Phys.* **2005**, *122*, 154501.

(10) Cossi, M.; Barone, V. *J. Chem. Phys.* **1998**, *109*, 6246.

(11) Jalkanen, K. J.; Nieminen, R. M.; Frimand, K.; Bohr, J.; Bohr, H.; Wade, R. C.; Tajkhorshid, E.; Suhai, S. *Chem. Phys.* **2001**, *265*, 125.

(12) Bouř, P.; Michalík, D.; Kapitán, J. *J. Chem. Phys.* **2005**, *122*, 144501.

(13) Bouř, P. *J. Chem. Phys.* **2004**, *121*, 7545.

(14) Bouř, P.; Keiderling, T. A. *J. Chem. Phys.* **2003**, *119*, 11253.

Computational Analysis of Solvent Effects

J. Chem. Theory Comput., Vol. 6, No. 1, 2010 **299**

(15) Ebrahimi, A.; Habibi, M.; Masoodi, H. R. *Chem. Phys. Lett.* **2009**, *478*, 120.

(16) Cammi, R.; Mennucci, B.; Tomasi, J. *J. Phys. Chem. A* **2000**, 104.

(17) Caricato, M.; Mennucci, B.; Tomasi, J.; Ingrosso, F.; Cammi, R.; Corni, S.; Scalmani, G. *J. Chem. Phys.* **2006**, *124*, 124520.

(18) Šebek, J.; Kejík, Z.; Bouř, P. *J. Phys. Chem. A* **2006**, *110*, 4702.

(19) Šebek, J.; Bouř, P. *J. Phys. Chem. A* **2008**, *112*, 2920.

(20) Šebek, J.; Gyurscik, B.; Šebestík, J.; Kejík, Z.; Bernárová, L.; Bouř, P. *J. Phys. Chem. A* **2007**, *111*, 2750.

(21) Ruud, K.; Åstrand, P. O.; Taylor, P. R. *J. Am. Chem. Soc.* **2001**, *123*, 4826.

(22) Sychrovský, V.; Buděšínský, M.; Benda, L.; Špirko, V.; Vokáčová, Z.; Šebestík, J.; Bouř, P. *J. Phys. Chem. B* **2008**, *112*, 1796.

(23) Bouř, P.; Buděšínský, M.; Špirko, V.; Kapitán, J.; Šebestík, J.; Sychrovský, V. *J. Am. Chem. Soc.* **2005**, *127*, 17079.

(24) Dračínský, M.; Kaminský, J.; Bouř, P. *J. Phys. Chem. B* **2009**, *113*, 16698.

(25) Woodford, J. N.; Harbison, G. S. *J. Chem. Theory Comput.* **2006**, *2*, 1464.

(26) Kongsted, J.; Nielsen, C. B.; Mikkelsen, K. V.; Christiansen, O.; Ruud, K. *J. Chem. Phys.* **2007**, *126*, 034510.

(27) Aidas, K.; Møgelhøj, A.; Kjær, H.; Nielsen, C. B.; Mikkelsen, K. V.; Ruud, K.; Christiansen, O.; Kongsted, J. *J. Phys. Chem. A* **2007**, *111*, 4199.

(28) Autschbach, J.; Ziegler, T. *J. Am. Chem. Soc.* **2001**, *123*, 3341.

(29) Buehl, M.; Golubnychiy, V. *Magn. Reson. Chem.* **2008**, *46*, S36.

(30) Watts, V. S.; Goldstein, J. H. *J. Phys. Chem.* **1966**, *70*, 3887.

(31) Hoffman, R. E. *J. Magn. Reson.* **2003**, *163*, 325.

(32) Gomes, J. A. N. F.; Mallion, R. B. *Chem. Rev.* **2001**, *101*, 1349.

(33) Hoffman, R. E. *J. Magn. Reson.* **2006**, *178*, 237.

(34) Kümmel, S.; Kronik, L.; Perdew, J. P. *Phys. Rev. Lett.* **2004**, *93*, 213002.

(35) Vignale, G.; Rasolt, M. *Phys. Rev. B* **1988**, *37*, 10685.

(36) Dračínský, M.; Kaminský, J.; Bouř, P. *J. Phys. Chem.* **2009**, *130*, 094106.

(37) Horák, Z.; Krupka, F. *Fyzika*; SNTL: Praha, Czech Republic, 1981.

(38) Ponder, J. W. *Tinker, Software Tools for Molecular Design, 3.8*; Washington University School of Medicine: Saint Louis, MO, 2000.

(39) Wang, J.; Cieplak, P.; Kollman, P. A. *J. Comput. Chem.* **2000**, *21*, 1049.

(40) Jorgensen, W. L.; Chandrasekhar, J.; Madura, J. D. *J. Chem. Phys.* **1983**, *79*, 926.

(41) Asher, J. R.; Doltsinis, N. L.; Kaupp, M. *Magn. Reson. Chem.* **2005**, *43*, S237.

(42) Becke, A. D. *J. Chem. Phys.* **1993**, *98*, 5648.

(43) Vanderbilt, D. *Phys. Rev. B* **1990**, *41*, 7892.

(44) Car, R.; Parrinello, M. *Phys. Rev. Lett.* **1985**, 55.

(45) Lii, J. H.; Allinger, N. L. *J. Comput. Chem.* **1998**, *19*, 1001.

(46) Bouř, P.; Keiderling, T. A. *J. Chem. Phys.* **2002**, *117*, 4126.

(47) Bouř, P. *Collect. Czech. Chem. Commun.* **2005**, *70*, 1315.

(48) Becke, A. *Phys. Rev. A* **1988**, *38*, 3098–3100.

(49) Mennucci, B.; Cancès, E.; Tomasi, J. *J. Phys. Chem. B* **1997**, *101*, 10506.

(50) Besler, B. H.; Merz, K. M.; Kollman, P. A. *J. Comput. Chem.* **1990**, *11*, 431.

(51) Chen, Z.; Corminboeuf, C.; Heine, T.; Bohmann, J.; Schleyer, P. R. *J. Am. Chem. Soc.* **2003**, *125*, 13930.

(52) Frisch, M. J.; Trucks, G. W.; Schlegel, H. B.; Scuseria, G. E.; Robb, M. A.; Cheeseman, J. R.; Montgomery, J. A., Jr.; Vreven, T.; Kudin, K. N.; Burant, J. C.; Millam, J. M.; Iyengar, S. S.; Tomasi, J.; Barone, V.; Mennucci, B.; Cossi, M.; Scalmani, G.; Rega, N.; Petersson, G. A.; Nakatsuji, H.; Hada, M.; Ehara, M.; Toyota, K.; Fukuda, R.; Hasegawa, J.; Ishida, M.; Nakajima, T.; Honda, Y.; Kitao, O.; Nakai, H.; Klene, M.; Li, X.; Knox, J. E.; Hratchian, H. P.; Cross, J. B.; Bakken, V.; Adamo, C.; Jaramillo, J.; Gomperts, R.; Stratmann, R. E.; Yazyev, O.; Austin, A. J.; Cammi, R.; Pomelli, C.; Ochterski, J. W.; Ayala, P. Y.; Morokuma, K.; Voth, G. A.; Salvador, P.; Dannenberg, J. J.; Zakrzewski, V. G.; Dapprich, S.; Daniels, A. D.; Strain, M. C.; Farkas, O.; Malick, D. K.; Rabuck, A. D.; Raghavachari, K.; Foresman, J. B.; Ortiz, J. V.; Cui, Q.; Baboul, A. G.; Clifford, S.; Cioslowski, J.; Stefanov, B. B.; Liu, G.; Liashenko, A.; Piskorz, P.; Komaromi, I.; Martin, R. L.; Fox, D. J.; Keith, T.; Al-Laham, M. A.; Peng, C. Y.; Nanayakkara, A.; Challacombe, M.; Gill, P. M. W.; Johnson, B.; Chen, W.; Wong, M. W.; Gonzalez, C.; Pople, J. A. *Gaussian 03*, revision C.02; Gaussian, Inc.: Wallingford, CT, 2004.

(53) Bouř, P.; Raich, I.; Kaminský, J.; Hrabal, R.; Čejka, J.; Sychrovský, V. *J. Phys. Chem. A* **2004**, *108*, 6365.

(54) DeCamp, M. F.; DeFlores, L.; McCracken, J. M.; Tokmakoff, A.; Kwac, K.; Cho, M. *J. Phys. Chem. B* **2005**, *2005*, 11016.

(55) Ruden, T. A.; Lutnaes, O. B.; Helgaker, T.; Ruud, K. *J. Chem. Phys.* **2003**, *118*, 9572.

(56) Laszlo, P. *Prog. NMR Spectrosc.* **1967**, *3*, 231.

JCTC Journal of Chemical Theory and Computation

Using Correlated Monte Carlo Sampling for Efficiently Solving the Linearized Poisson−Boltzmann Equation Over a Broad Range of Salt Concentration

Marcia O. Fenley,*,† Michael Mascagni,*,‡ James McClain,§ Alexander R. J. Silalahi,‖ and Nikolai A. Simonov⊥,#

Department of Physics and Institute for Molecular Biophysics, Departments of Computer Science, Mathematics, and Scientific Computing, Department of Computer Science, and Department of Physics, Florida State University, Tallahassee, Florida 32306, and Institute of Computational Mathematics and Mathematical Geophysics, Novosibirsk 630090, Russia

Abstract: Dielectric continuum or implicit solvent models provide a significant reduction in computational cost when accounting for the salt-mediated electrostatic interactions of biomolecules immersed in an ionic environment. These models, in which the solvent and ions are replaced by a dielectric continuum, seek to capture the average statistical effects of the ionic solvent, while the solute is treated at the atomic level of detail. For decades, the solution of the three-dimensional Poisson−Boltzmann equation (PBE), which has become a standard implicit-solvent tool for assessing electrostatic effects in biomolecular systems, has been based on various deterministic numerical methods. Some deterministic PBE algorithms have drawbacks, which include a lack of properly assessing their accuracy, geometrical difficulties caused by discretization, and for some problems their cost in both memory and computation time. Our original stochastic method resolves some of these difficulties by solving the PBE using the Monte Carlo method (MCM). This new approach to the PBE is capable of efficiently solving complex, multidomain, and salt-dependent problems in biomolecular continuum electrostatics to high precision. Here, we improve upon our novel stochastic approach by simultaneouly computing electrostatic potential and solvation free energies at different ionic concentrations through correlated Monte Carlo (MC) sampling. By using carefully constructed correlated random walks in our algorithm, we can actually compute the solution to a standard system including the linearized PBE (LPBE) at all salt concentrations of interest, simultaneously. This approach not only accelerates our MCPBE algorithm, but seems to have cost and accuracy advantages over deterministic methods as well. We verify the effectiveness of this technique by applying it to two common electrostatic computations: the electrostatic potential and polar solvation free energy for calcium binding proteins that are compared to similar results obtained using mature deterministic PBE methods.

1. Introduction

Many biological molecules, such as weakly charged proteins embedded in either their normal cellular or in vitro milieu,

---

* Corresponding author e-mail: mfenley@sb.fsu.edu.

† Department of Physics and Institute for Molecular Biophysics, Florida State University.

‡ Departments of Computer Science, Mathematics, and Scientific Computing, Florida State University.

§ Department of Computer Science, Florida State University.

‖ Department of Physics, Florida State University.

are surrounded by water, ions, and other small molecules. Both experimental measurements and theoretical results have shown that subtle and small changes in salt concentration can have a strong effect on a broad spectrum of protein properties. For instance, the stability of proteins as well the protein's association with molecules ranging from small

---

⊥ Institute of Computational Mathematics and Mathematical Geophysics.

Current address: Russian Science Center, Baker Hughes B.V., Novosibirsk, Russia.

Correlated MC Sampling for Solving the Linearized PBE

J. Chem. Theory Comput., Vol. 6, No. 1, 2010 **301**

charged peptides and drugs to larger proteins and polysaccharides at both the kinetic and the thermodynamic levels can be altered by changing the salt type and concentration.[1−6] We still lack a complete theoretical understanding of why increasing the salt concentration and changing the salt type can either enhance or diminish protein stability and binding to charged ligands (e.g., other charged proteins), depending upon the geometry and charge distribution of the protein or its complexes. To interpret this simple yet fundamental experimental observation, it will be necessary to understand the long-range salt-mediated electrostatic interactions and hydration effects at the molecular level of detail.

The enzymatic and catalytic activity, folding landscape, precipitation, and recognition behavior of proteins can also be modulated by small changes in salt concentration.[5,7−11] In a recent contribution to the literature, it has been demonstrated how changes in salt concentration can have an important role in producing more potent therapeutic vaccines consisting of cationic lipid and proteins.[12] Thus, a better understanding of how nonspecific and bulk salt-mediated electrostatic interactions modulate the stability, biological activity, aggregation, and recognition processes involving proteins will have a significant impact in drug design efforts where the target is proteins. This will clearly be of tremendous value in biopharmaceutical applications.

Implicit solvent or dielectric continuum model-based approaches, such as the PBE, which ignore the explicit treatment of water and ions but fully account for the geometric and 3D structural details of the protein charge distribution, have already shown to be quite successful in predicting some biophysically important nonspecific salt-mediated properties such as thermodynamic and kinetic binding parameters, and stability data under low to moderate physiological salt conditions, where ion-type specific (e.g., Hofmeister effects) and hydration effects can safely be ignored.[13,14] In principle, the explicit solvent molecular dynamics (MD) of large-scale proteins and their complexes are capable of modeling salt-mediated electrostatic and hydration effects at the molecular level of detail with higher accuracy when compared to implicit solvent models. However, very few studies of salt effects on biomolecular properties have appeared in the literature,[15] some of which are only based on simple model systems.[16] This is probably due to issues concerning adequate metal ion force field parameters, the long-equilibration times required to obtain converged and reliable ion distributions surrounding large biomolecules under the appropriate salt conditions, periodic boundary condition effects,[17] and other problems. Of course, in time this scenario may quickly change with the push to develop better force fields (e.g., polarizable) and enhanced sampling techniques.[18] In fact, a few very elegant all-atom molecular dynamics simulations examining both salt specific and nonspecific effects on the stability and binding of small charged peptides and proteins have appeared in the past few years.[15,19,20]

To better account for conformational flexibility in both stability and binding studies of proteins and other biomolecules, it has become common practice to use MD or MCMs techniques along with the PBE to compute the thermodynamic/

kinetic stability or association energetics, which entails doing so at several thousands of PB calculations.[21] Clearly, in one such approach, known as the MM-PBSA protocol,[22] which is now being widely used in pharmaceutical companies,[23] robust PBE solvers that provide both accurate and fast electrostatic or polar salvation free energy predictions are important prerequisites. It should also be pointed out that MC simulations that use a dielectric continuum model for the solvent but treat ions explicitly are very valuable, and some recent studies have appeared in the literature.[24] Interestingly, some of these studies lend further support to the use of the LPBE due to the good agreement between the predictions of two fundamentally different computational approaches when examining salt-dependent behavior of proteins. Of course, when studying ion distributions surrounding proteins, the more accurate MC approach should be the method of choice.

On the basis of the above discussion, it seems that implicit solvent-based approaches such as the PBE still appear to be the best alternative when modeling nonspecific salt effects in biomolecular systems given their accurate, fast prediction, and ease of use for interpreting and/or predicting pertinent salt-dependent properties of biomolecules when compared to the more expensive and complex explicit solvent molecular dynamics or explicit ion/dielectric solvent MC-based molecular simulation tools. Because of the above facts, the development of faster and more accurate predictions of nonspecific salt-dependent electrostatic properties is still an important research endeavor, because they will provide powerful software tools for diverse applications in far reaching settings, including the pharmaceutical and biotechnology industries. With this goal in mind, here we discuss a novel implicit-solvent-based LPBE approach that can deliver very accurate nonspecific salt-dependent electrostatic properties, over a broad range of salt concentrations, in a single PB calculation and with very high accuracy due to the inherent properties of our MC-based algorithm.

In this work, we first provide a detailed description of the random walk-MC approach for solving the LPBE for biomolecules of arbitrary size, shape, and charge distribution. The use of correlated sampling in the MC simulations and its advantages over uncorrelated sampling for solving the LPBE over a broad range of salt concentrations is presented. Next, we discuss the errors and cost in CPU time and memory of the MC-based LPBE algorithm. We then employ the MC-based LPBE approach to compute some electrostatic properties (e.g., electrostatic solvation free energy, electrostatic potential) of four different EF-hand calcium binding proteins of varying net charge. We choose these because salt-mediated electrostatic interactions are important for their stability and calcium binding affinity behavior.[14] To validate the proposed correlated sampling scheme, we compare the computed electrostatic properties of these important proteins over a broad spectrum of salt concentrations with similar results obtained with a robust deterministic LPBE approach (Boschitsch and Fenley, in preparation).
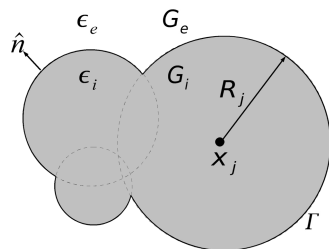
Figure 1. A solvated biomolecule with interior dielectric region defined by G_i and with dielectric permittivity ε_i. The exterior ionic solvent region, G_e, with dielectric permittivity ε_e. The boundary Γ separating the interior and exterior regions of the solvated biomolecules of interest is here defined by the van der Waals (vdW) surface: the union of the spherical atomic surfaces defined by the van der Waals radius of each atom j, R_j, in the molecule.

2. Methods

The PBE provides the electrostatic potential and other important derived quantities, such as electrostatic solvation free energies and electrostatic forces at varying ionic conditions. Thus, we will specialize our discussion to these computations using the PBE as the basic electrostatic model.[25,26] In the past three decades, various deterministic approaches such as boundary element,[27−40] finite-difference,[41−51] and finite-element methods[52−57] have been reported in the literature. In this work, we focus on the novel MC-based solution of the PBE and when possible make comparisons with the more mature deterministic methods.

We are interested in describing a specific computational method to solve a well-defined class of electrostatics problems of biophysical significance in various fields.[58] To do this, we will begin by defining the general problem for a prototypical large biomolecule composed of many spherical atoms that is immersed in an aqueous ionic solution. In Figure 1, the jth atom is modeled as a sphere of radius, R_j, with a fixed charge of magnitude q_j (in units of e, the protonic charge) located at its center, x_j, and the biomolecule in question is the union of such intersecting atomic spheres. In the interior region, G_i, the dielectric constant, ε_i, is equal to that of the solute. Thus, the electrostatic potential in the interior region of the biomolecule satisfies the Poisson equation:

$$\Delta u_i = -\frac{e \sum_{j=1}^{N} q_j \delta(x - x_j)}{k_b T \varepsilon_i} \quad (1)$$

where u_i is the normalized electrostatic potential (in units of $k_b T/e$) in the interior region, N is the number of atoms, $\Delta = \nabla^2$ is the Laplace operator, and $\delta(x - x_j)$ is the Dirac delta function. The Dirac delta function is used because each atom is assumed to have its (partial) charge localized at the center of its atomic sphere.

In the exterior region, G_e, we have an aqueous ionic solution with the free ions distributed via a Boltzmann distribution, which is a standard assumption underlying the derivation of the PBE. Here, the exterior dielectric constant, ε_e, is also assumed to be constant but equal to that of the

high dielectric aqueous ionic solvent. Thus, the normalized electrostatic potential (in units of $(k_b T)/(e)$) in the exterior region containing a 1:1 salt, u_e, obeys the full PBE:

$$\Delta u_e = \kappa^2 \sinh(u_e) \quad (2)$$

with $\kappa^2 = (2 N_A e^2 I_c)/(k_b T \varepsilon_e)$; κ is called the Debye−Hückel constant. Here, $I_c = \frac{1}{2} \sum_k c_b^k z_k^2$ is the ionic strength of the solvent, c_b is the bulk salt concentration in moles (M), z_b is the ionic valence, N_A is Avogadro's number, k_b is Boltzmann's constant, ε_e is the solvent dielectric constant, e is the protonic charge, and T is the absolute temperature of the system (in K). For small potentials, $u_e \ll 1$, one can linearize eq 2 to obtain the so-called LPBE:

$$\Delta u_e = \kappa^2 u_e \quad (3)$$

In the subsequent discussion, we will only consider systems involving the LPBE.

At the biomolecule's boundary, Γ, which is defined by the van der Waals (vdW) surface, the electrostatic potential, u, and the normal component of the dielectric displacement, $\varepsilon(\partial u/\partial n)$, are both continuous. These two boundary conditions arise from consideration of bound surface charge density at the dielectric interface. Note that for a vdW boundary, the normal vector is not uniquely defined on the intersections of spherical surfaces. However, the mathematical singularities on these curves are integrable under the condition that the molecular surface as a whole is regular.[59] Because of the geometry of the molecule, possible internal cavities are treated as if they were the exterior region.[60] Since we have evidence that treating these internal cavities as exterior as opposed to interior regions can affect the computed electrostatic properties in a future communication, we will examine this issue in more detail, which will require some very minor algorithmic changes. Thus, the electrostatic potential inside and outside of the molecule must satisfy the following boundary conditions on Γ:

$$\begin{aligned} u_i &= u_e \\ \varepsilon_i \frac{\partial u_i}{\partial n} &= \varepsilon_e \frac{\partial u_e}{\partial n} \end{aligned} \quad (4)$$

In addition, the potential must go to zero as we move away from the molecule:

$$\lim_{\|x\| \to \infty} u_e(x) = 0 \quad (5)$$

We have now defined a system of elliptic partial differential equations (PDE) with appropriate boundary conditions, eqs 1, 3, 4, and 5, whose solution gives the electrostatic potential everywhere (e.g., at charge sites and in exterior domain). This system of equations, with the previously mentioned molecular geometry, defines our model problem.

The fixed charges in the interior region are seen as the source of the electrostatic potential (field), and because these are modeled as point charges, they introduce singularities in the electrostatic potential. These singularities can be removed by expressing the overall electrostatic potential as the sum of a Coulombic part, which is the solution when

Correlated MC Sampling for Solving the Linearized PBE

J. Chem. Theory Comput., Vol. 6, No. 1, 2010 **303**

the exterior solvent is replaced by the interior dielectric medium (i.e., the Coulombic potential generated by atomic charges in a uniform medium with interior dielectric constant throughout the whole space), and the so-called reaction field potential.

$$u_i = u_i^{Coulomb} + u_i^{RF} \tag{6}$$

where

$$u_i^{Coulomb} = \sum_{j=1}^{N} \frac{eq_j}{k_b T \varepsilon_i |x - x_j|} \tag{7}$$

This explicit separation of the total electrostatic potential into two terms results in the singularity-free reaction field potential satisfying the Laplace equation in the interior region, G_i:

$$\Delta u_i^{RF} = 0 \tag{8}$$

It should be noted that this decomposition of the potential is very useful, because it conveniently removes charge singularities that are inherent and problematic to some deterministic schemes. These charge singularities lead to numerical accuracy and convergence issues as well as the need to perform two LPBE computations, one as reference, as opposed to the single computation needed in the method described here. However, boundary-element and some finite-difference implementations of the LPBE[39,61,61−64] also use a similar decomposition of the electrostatic potential, thus leading to more accurate solutions and CPU time gains due to the need to perform only a single computation to evaluate the reaction field potential.

While the quantity to be solved for in the above discussion is clearly the electrostatic potential, in most cases it is difficult to experimentally measure this quantity in a biochemical setting. However, some recent experimental studies have reported electrostatic potentials for some interesting biomolecular systems.[65,66] However, there are certain scalar quantities that involve the electrostatic potential that also cannot be measured; these include the electrostatic free energy and some of its differences, such as the polar solvation and binding free energies. On the other hand, one can measure the salt dependence of the binding affinity[14] and the stability of biomolecules[4] using thermodynamic and kinetic techniques and compare these results directly with similar LPBE computational predictions.

To compute the electrostatic solvation free energy, which is the electrostatic free energy change involved in transferring the solute from vacuum into the ionic solution, we need to calculate the reaction field term at the center, x_j, of each atomic sphere in G_i that has a nonzero static charge, $q_i \neq 0$. Specifically, we must compute the electrostatic free energy change with the exterior dielectric constant, $\varepsilon_e = \varepsilon_{solv}$ (solvent) and $\varepsilon_e = 1$ (vacuum). This quantity involves only a finite number of computations for the reaction-field potential at two different exterior dielectric constants:

$$\Delta G^{solv} = \frac{1}{2} \sum_{j=1}^{N} q_j [u^{RF}(x_j)(\varepsilon_e = \varepsilon_{solv}) - u^{RF}(x_j)(\varepsilon_e = 1)] \tag{9}$$

Because we are using $\varepsilon_i = 1$ in our study, the last term in eq 9 is zero because it is computed at zero salt concentration and with no dielectric discontinuity, $\varepsilon_i = \varepsilon_e$. Thus, only the first term needs to be computed in this specific case.

2.1. Monte Carlo Solution of the Electrostatic Equations. The traditional ways to solve a system of equations like eqs 1, 3, 4, and 5 are all based on replacing this continuous PDE system with some sort of discrete approximate system. While the details vary considerably, this is the way the finite-difference, finite-element, and boundary-element methods approach this problem.[25]

Once the finite-dimensional approximate systems are formed, an approximate solution is obtained by solving the resulting systems of (linear) equations. These methods of solution are all deterministic in nature and lead to errors that are commonly studied by numerical analysts. These errors are the discretization error, caused by replacing the original, continuous, system by the appropriate deterministic approximation, and the roundoff error introduced in solving the resulting system of linear equations using floating-point arithmetic on a digital computer. Roundoff error is a function of the precision of the computer and the algorithms' design. On the other hand, discretization error can be controlled by replacing a given finite approximation with improved techniques such as "focusing".[67] This usually requires setting up a new computation with many more unknowns and thus leads to an increase in the memory and CPU requirements for computing the solution. In this Article, we use a Monte Carlo method (MCM)[68−74] to solve this same system, eqs 1, 3, 4, and 5. Monte Carlo methods (MCMs) are fundamentally different from deterministic methods. If we have a quantity of interest, v, and we want to design a MCM to numerically determine v, we need to define a random variable, ν, that approximates v in a statistical sense. This means that the expected value $E[\nu] = v + \beta$, where β is the bias (a type of MCM error), and if $\beta = 0$, then ν is called an unbiased estimator of v. Given ν, we need to have a way to statistically sample it through simulation, and then we can use our simulation to provide a MC estimate through this simulation. Because ν is a random variable, we simulate ν_i, $i = 1,..., M$, and then use $\Sigma_{i=1}^{M}\nu_i = \bar{\nu}$ as our MCM estimate. We know its mean and can sample the variance, $\sigma_{\bar{\nu}}^2$, of $\bar{\nu}$, and so can form a confidence interval that contains the correct value with a specified probability. The width of this confidence interval is traditionally used as an a posteriori estimate of the error and is proportional to the square root of the sample variance, $M^{-1/2}\sigma_\nu$.

The errors in a MCM are qualitatively different from those in deterministic numerical methods. There are two errors in MCMs: the first is the bias, β, and has been described above. In this Article, we have either $\beta = 0$ or its dependence on computational parameters will be explicitly known. It is important to note that the bias, when there is one, is the difference between the MCM's estimate and the solution to the PDE. When the estimate is unbiased, the MCM samples

the solution to the PDE directly, as opposed to all of the deterministic methods known, which incur a discretization error because they solve a related approximate problem, but not the actual PDE. The other error in MCMs is the so-called sampling error and is the width of the confidence interval of the mean. As mentioned above, this is proportional to $M^{-1/2}\sigma_\nu$, where the constant of proportionality is based on the confidence level desired in the estimate. Thus, the sampling error can be reduced by either reducing the sample variance, which is called variance reduction, or increasing the number of samples, M. Increasing M can be achieved in many ways, such as using multiple processors, as MCMs are naturally parallel, but sampling error in MCMs scales as $M^{-1/2}$. This is often viewed as a weakness of MCMs, but this sampling error is often the only significant error in a particular MCM, and reducing it does not require solving a different problem as with deterministic methods, only doing more computations on the same problem. In addition, this error is often robustly independent of other problem parameters, the problem's dimension (not important in this case), and problem geometry.

2.2. The Monte Carlo Method. The goal of this Article is to show how the MCM method we previously developed can be redeployed efficiently to solve these electrostatics problems over a broad range of salt concentrations. We deploy a correlated sampling technique, but to understand the technique we need to describe certain quantitative aspects of the underlying MCM. However, it is not appropriate to detail the technique here as it has been published in great detail elsewhere.[71,72,74,75]

The qualitative nature of the MC algorithm is that it creates a statistical sample of the solution of the PDE system at a point by starting a Brownian motion process at that point. Each time the Brownian motion hits the surface of the molecule, the Coulombic contribution of the potential at the hitting point is accumulated. The process then leaves the surface by entering either the molecule or the exterior region. In the interior region, the process eventually hits the vdW surface again, while outside the process may return to the surface, but also can be terminated with a probability that is related to the length of the process in the exterior solvent region. In addition, this probability is related to κ: higher values of κ increase the termination probability and thus reduce the length of the process.

Some more detail is appropriate here, but still the publication of the full algorithm[71,72,74,75] should be consulted for those interested in all of the algorithmic and mathematical details.

2.3. Acceleration Techniques. The technique we use requires the simulation of a complicated Brownian motion process, and specifically we need to be able to correctly sample the hitting locations of the process on the surface of the molecule. If one uses standard techniques from Brownian dynamics or stochastic differential equations, this is a complicated task. However, we can use sampling techniques based on the walk on spheres (WOS) method[69,70,74,76,77] to accomplish this while also accelerating the computations. Because we need to only sample the hitting locations, this can be done by creating our walks in subregions where the

first hitting location can be sampled exactly. Spheres are such regions, as the distribution of first hitting of a Brownian motion started anywhere within a sphere is both known and easy to sample from. In addition, because we are dealing with a problem geometry based on molecules made up of spherical atoms, the WOS technique can further take advantage of this geometry. Thus, when we start our Brownian processes, we walk from point to point on the surface of spheres using WOS.

When we begin our walks, at a point in the interior, we use the WOS algorithm where our spheres are the atoms making up the molecule under consideration. There are two issues in this interior WOS scheme. The first is that often we need to walk from a point that is not the center of the sphere to a point on the sphere's surface. Fortunately, the exact first passage distribution is known via the well-known Poisson kernel. Moreover, sampling random points from the distribution defined by the Poisson kernel is very straightforward to implement. When a new point, x, has been sampled with the Poisson kernel, there is a geometric issue: determining if x is on the surface of the molecule, Γ, or if it is on an atom's surface but still in the molecule's interior. The algorithm for answering this question is very efficient and described elsewhere.[71,72,74,75] To determine if a point on the surface of an atom is inside a molecule, we make use of the fact that in our model atoms are represented as spheres. The distance from a point to a sphere is equal to the distance from the point to the sphere's center less its radius. The function that computes the distance from a point to the closest atom of the molecule makes use of this fact; it will return a negative distance in response to a point that is inside of the molecule. A point that is on the surface of an atom but inside of the molecule can be recognized by noting the sign of the response from the distance function.

When the walk reaches the surface of the molecule, a decision is made as to whether one continues the walk inside or outside the molecule. The probability of returning inside is $p_i = (\varepsilon_i)/(\varepsilon_i + \varepsilon_e)$, while with probability $p_e = 1 - p_i = (\varepsilon_e)/(\varepsilon_i + \varepsilon_e)$ the walk continues outside the molecule. Because $\varepsilon_e \gg \varepsilon_i$, the chance of exiting the molecule is close to one. In addition to these probabilities, the location of the walker is chosen with the help of a small auxiliary sphere with radius r_{aux}. The use of the auxiliary sphere causes our MC estimate to be biased with a bias of $O(r_{aux}^3)$.[72] When outside the molecule, the regular WOS algorithm is used. If we are at a point outside the molecule, x, then we draw the largest sphere with center at x that is completely outside the molecule. The closure of this sphere touches the molecule at only a single point, in most cases. Next, a point is chosen uniformly on this sphere to give us our new x. Because these spheres touch the molecule at only a few points at most, the WOS process can never return to the sphere in a finite number of steps. To fix this, we add a small capture region of thickness $\bar{\varepsilon} \ll 1$, which is defined as all of the points outside the molecule within distance $\bar{\varepsilon}$ of the surface, $C_{\bar{\varepsilon}} = \{x$ outside of the molecule $|\mathrm{dist}(x, \Gamma) \le \bar{\varepsilon}\}$. In addition, to sample the solution to the LPBE outside the molecule, we have to either weight our sample or terminate the walk with probability equal to this weight. Each WOS step outside the
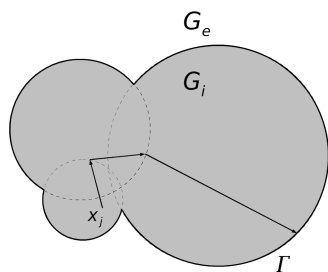
Figure 2. Random walk constructed by consecutive walks on spheres in the interior region, G_i.
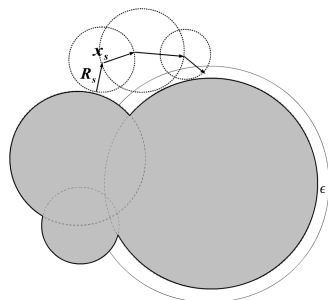

Figure 3. Random walk constructed by consecutive walks on spheres $B(x_s, R_s)$ in the exterior solvent region G_e. The walk will eventually come back to the boundary Γ with probability less than one. An absorbing layer with thickness $\bar{\varepsilon}$ is introduced to reduce the number of walks in the exterior region.
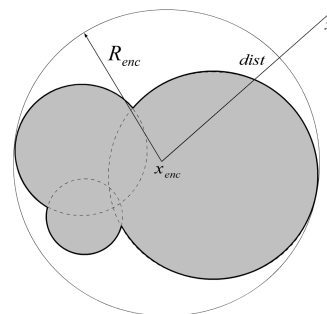

Figure 4. An enclosing sphere around the molecule being studied is used for the $\kappa = 0$ MC simulation. This sphere is centered at x_{enc} and has radius R_{enc} that is large enough to enclose the molecule. In the region outside this sphere, the electrostatic potential satisfies only the LPBE, and one can use $p_0 = R_{enc}/dist$ as the survival probability for any walk starting from a distance "dist" from the center of the sphere.

molecule occurs on a sphere with a radius, d, and this allows us to define the probability that the walker terminates with this step as $p_{term} = 1 - p_{surv} = 1 - (\kappa d)/(\sinh(\kappa d))$.

2.4. Correlated Sampling. The second acceleration technique that we use is one that allows the simultaneous computation of the solution to the problem at all of the salt concentrations of interest. In the previous three sections, we have described the random walk algorithm and the description of the probabilistic method to treat the boundary conditions. Suppose we want to compute the reaction field potential in the interior region for several different values of κ. The random walk algorithm in the interior region, as shown in Figure 2, is dependent only on the geometry and does not depend on the value of κ. Thus, the trajectories in the interior region generated for one value of κ can be reused for all other values of κ. The same thing is also true for the boundary treatment, because the probability of reentering or leaving the molecule depends only on the dielectric constant of the two regions. On the other hand, the survival probability $p_{surv}(x, y)$ for a random walk in the exterior region depends on the value of κ.

However, for every walk in the exterior region, the radius of the WOS sphere does not depend on κ, but depends only on the geometry, as shown in Figure 3. Furthermore, we also know that the value of $p_{surv}(x, y)$ lies in the interval [0,1] and decreases monotonically as the value of κ increases. This means the smaller is the value of κ, the longer is the walk taken in the exterior region. Thus, for a computation for several different values of κ, one could reuse the trajectory of the smallest nonzero κ for computing the trajectories at the other κ values. This correlated computation brings us two advantages. First, it reduces the amount of CPU time

by making it possible to do an electrostatic potential computation simultaneously over a range of κ values. The second advantage relates to the nature of MCMs; by having the same reference trajectory, the estimate for different κ values will be correlated with each other. This correlation makes it possible to take the difference of two MCM estimates without introducing unacceptable levels of random error in the difference.

Although the correlation algorithm can be used for the computation of electrostatic properties over a range of κ values, it is limited to only $\kappa > 0$. The reason for this is that at $\kappa = 0$ the survival probability $p_{surv}(x, y)$ is 1, and so walks do not terminate in the exterior. Yet, for $\kappa = 0$ the LPBE in the exterior turns into the Laplace equation, and one can use another exactly known probability distribution to accelerate this situation. Suppose the walk is started at the point x in $G_e \backslash B(x_{enc}, R_{enc})$, as described in Figure 4. For this unbounded region, there is a nonzero probability $p_{inf} = 1 - (R_{enc})/(dist)$ that the walk goes to infinity in a single step. When the walker is outside a sphere that completely encloses the molecule, the probability of walking to infinity (and termination) is p_{inf}, while with probability $1 - p_{inf}$ a point on the surface of $B(x_{enc}, R_{enc})$ is sampled on the basis of the Poisson kernel p'_{pk}, as the next point of the walk. The correct Poisson kernel for exterior region is given by $p'_{pk} = (1/4\pi R_{enc})[(x^2 - R_{enc}^2)/(|y - x|^3)]$, where y is the point on the sphere $B(x_{enc}, R_{enc})$.

Although we now have a new algorithm for the special case of $\kappa = 0$, the algorithm for $\kappa \neq 0$ can also be used here. It is important to relate the $\kappa = 0$ trajectory with the $\kappa \neq 0$ algorithm to make it possible to compute the electrostatic potential for a range of κ values, which includes $\kappa = 0$, and to preserve correlation. One possible way to do this is by first generating a trajectory for the smallest nonzero κ, and to reuse that trajectory for all other values of κ, including $\kappa = 0$. Once the walk for the smallest nonzero κ terminates, the walk for $\kappa = 0$ is continued with its random walk algorithm. This ensures the correlation between the two algorithms.

2.4.1. Computational Error and Time. The statistical error of the MCM estimate, ν, (width of confidence interval), is

measured in units of $\sigma_\nu M^{-(1)/(2)}$, where $\sigma_\nu^2 = \mathrm{VAR}[\nu]$ is the estimate's variance, and M is number of trajectories. Therefore, to guarantee a statistical error of δ, we have to simulate $\sim \sigma_\nu^2 \delta^{-2}$ samples. This means that for a given δ, the total computational time (theoretical complexity of the algorithm) is $\sim \sigma_\nu^2 \delta^{-2} t$, where t is the mean time needed for computing a single trajectory. The length of the trajectory depends on several parameters: the coefficient κ, the width of the strip near the boundary $\bar{\varepsilon}$, and the radius of the auxiliary sphere r_{aux}.

Brownian motion trajectories in the exterior region either terminate or return to the molecular surface, Γ. Thus, the overall number of simulated points depends linearly on the number of boundary hits. The probability of terminating the walk depends linearly on the initial distance from the boundary in the exterior domain. This means that the average number of steps in the walk before revisiting the boundary is finite and proportional to the inverse of the initial distance: $(r_{\mathrm{aux}}/2)^{-1}$. For a given boundary strip width, $\bar{\varepsilon}$, the number of steps between two consecutive boundary hits scales like $\log \|\bar{\varepsilon}\|$. Our computations show that the dependence on κ is also weak, and the length of the random walk scales like $O(\log \kappa)$.

The terminating condition for the walk depends on κ and the distance to the boundary. The walk in the interior is done in a bounded region, while the exterior walk is done in unbounded region. This means that the length of the Brownian trajectory is dominated by the part of the trajectory in the exterior region. Thus, the CPU time is dominated by the walk in the exterior rather than by any other processes. For every walk in the exterior region, one needs to find the closest boundary point and compute the distance to the boundary. In a linear search, this will take time $O(N)$, where N is the number of atoms in the molecule. In our Article, we use the approximate nearest neighbor (ANN) algorithm, which scales as $O(\log(N))$.

2.4.2. Correlated versus Uncorrelated Random Walk Sampling. The mean μ and statistical error $\sigma/\sqrt{M}$ come from the scoring function u^{Coulomb}, where its evaluation depends on the location of the charges and the geometry of the molecule. In uncorrelated sampling, both μ and $\sigma/\sqrt{M}$ for different values of κ are computed from independent trajectories. Therefore, for an arbitrary number of trajectories, M, there is no guarantee of a monotonic behavior of μ versus κ. In this case, a plot of μ versus κ would give an oscillating curve, which would converge to a smooth curve as $M \rightarrow \infty$. Thus, it will be difficult to draw information of salt derivative of electrostatic property, which is the slope of the function. On the other hand, the simulation in correlated sampling of a set of κ employs the survival probability, p_{surv}, in all trajectories, which guarantees the monotonic behavior of μ versus κ. Therefore, the salt derivative of any electrostatic properties can be computed with very high accuracy using correlated sampling.

2.5. Structure Preparation. Four calcium binding proteins of varying net charges and charge densities were selected from the RCSB database (http://www.rcsb.org) with the following PDB ids: 3ICB (net charge $= -7$e, surface charge density $= -0.055704$ e/A^2, 1EDM (net charge $=$

-14e, surface charge density $= -0.27852$ e/A^2, 3CLN (net charge $= -22.5$e, surface charge density $= -0.17684$ e/A^2, and 1PRW (net charge $= -24.5$e, surface charge density $= -0.17525$ e/A^2. Preparation of the calcium binding proteins was done following two simple protocols because in this work we are not attempting to make any comparison with experimental data, only to similar deterministic LPBE results. In both protocols, missing protein side chains were not modeled, and all cofactors, calcium ions, and water molecules were removed from all structures prior to any further calculations.

In the first protocol, hydrogen atoms were not added to the structures because we are employing a simplified formal charge model. Moreover, the structures were not subjected to any energy minimization procedure. The ionization state at physiological pH was adopted, that is, ionized forms for side chains of Arg, Lys, Asp, Glu, and C-terminus residues, and ionized forms for the His side chains. In the simplified formal charge model, all atoms had zero net charge with the exception of the following atoms whose charges were assigned as follows: Arg (NH1 $= +0.5$e, NH2 $= +0.5$e), Lys (NZ $= +1$e), Asp (OD1 $= -0.5$e, OD2 $= -0.5$e), Glu (OE1 $= -0.5$e, OE2 $= -0.5$e), C-terminus (OXT $= -1$e), and His (ND1 $= 0.25$e, NE2 $= 0.25$e). The following Bondi radii[78] were assigned: C $= 1.7$ Å, O $= 1.4$ Å, N $= 1.4$ Å, and S $= 1.8$ Å. With the formal charge assignment, there is a significant CPU savings because the walks in MC simulation only need to be started at sites where charges are nonzero. However, because atoms with zero charges are not necessarily modeled as point charges, their geometries are still accounted for in the MC simulation. For some of the atoms that are assigned to have zero radius, the random walk is started in the same way as at other atoms.

In some of our LPBE calculations, the pdb2pqr server (http://pdb2pqr-1.wustl.edu/pdb2pqr)[79] was used to obtain a pqr file based on the Charmm or Amber molecular mechanics force fields. In these cases, the default settings of the pdb2pqr software were used. Hydrogen atoms were added to the structures, and the radii and charge were assigned according to the Charmm[80] or Amber[81] force fields.

In section 3.3, the Amber force field was used to generate the charges and radii of the atoms for "hypothetical molecules" that were constructed from the initial vitamin D-dependent calcium binding protein structure (PDB id: 3icb). We generated several different unphysical molecules from four 3icb molecules by stacking the three molecules that were shifted by 2 Å in x, y, and z directions to the original 3icb molecules. We then made a spherical cut of this molecule with several different radius so that we have several molecules with globular shapes and varying size: 503, 601, 702, 800, 984, 2973, and 4257 atoms. The CPU time is geometrically dependent; thus by using the same geometry for all test cases we fix the dependence on geometry while varying the number of atoms.

2.6. Monte Carlo-Based LPBE Calculations. As in any deterministic LPBE solver, the user is required to provide an input file containing the coordinates, charge, and radii for each of the atoms of the biomolecule (e.g., a pqr file obtained from the pdb2pqr software (see above)). The other

Correlated MC Sampling for Solving the Linearized PBE

J. Chem. Theory Comput., Vol. 6, No. 1, 2010 **307**

usual and standard PBE parameters such as temperature of the solution, interior solute, and exterior solvent dielectric constants have to be provided by the user in an input file. The specification of boundary conditions and other grid-based parameters is not necessary due to the nongrid-based and stochastic nature of the MCM. The radii and charge values used in this study are given in section 2.5, while the solvent and protein dielectric constants were 78.5 and 1, respectively. The temperature of the solution was fixed at 298 K (room temperature). The 1:1 salt (i.e., NaCl) concentration varied in the range of 0−1 M (0, 0.0001, 0.0002, 0.0005, 0.001, 0.002, 0.005, 0.01, 0.02, 0.05, 0.1, 0.2, 0.5, and 1 M).

Some important code parameters that are intrinsic to the MC approach that need to be specified by the user are: the absorbing layer[82,83] width, which was set to 0.0001 Å, the auxiliary sphere radius,[72] which was set to 0.01 Å, and the number of trajectories, which was set to several different values depending on the problem being studied. The choices of these parameters were based on the trade off between the CPU time and the desired accuracy of the MC simulation. The optimal values of the first two parameters depend on the geometry of the molecule.

2.7. Deterministic Finite-Difference versus MC LPBE Calculations.

For any new algorithm to become mainstream and made available to the user community, it is very important to validate it against different algorithms that solve the same problem. So with this goal in mind, here we compared the MC LPBE solver with results obtained with an innovative and mature deterministically based (i.e., multigrid finite-difference) PBE solver (Boschitsch and Fenley, in preparation). We had already established that this latter deterministic PBE solver is in very good agreement with other PBE solvers and analytical results (results not shown).

As in the MCM method, in this deterministic PBE solver only the reaction field potential is computed in the interior region, thus eliminating singularities at the charge sites and eliminating the need for a fine mesh or complications of self-energy effects in the vicinity of these sites. In the exterior region, the total potential is calculated. Here, we examine the predictions of two important electrostatic properties: the electrostatic potential at user specified sites and the electrostatic solvation free energies. Both of these are required to examine the role of electrostatic interactions in processes such as binding, folding, and recognition of biomolecular systems.

The dielectric boundary separating the solute and solvent regions was the vdW surface generated by the union of spheres centered at each atom. For consistency with the MC results, no ion-exclusion region was employed. To estimate the error of the PBE calculations due to grid resolution, the calculations were repeated at the finest grid spacings of 1.5, 1.0, 0.8, 0.4, 0.2, and 0.1 Å. Our results are stable and converged for resolutions as coarse as 0.4 Å (results not shown). To strike a compromise between accuracy and efficiency, we used a fine grid spacing of 0.3 Å. The dimensions of the grid were set to 3 times the largest dimension of the molecule.

3. Results and Discussion

3.1. Correlated versus Uncorrelated Random Walk Sampling.

One of the motivations for accurately computing salt-dependent electrostatic solvation free energies resides on their use in helping experimentalists interpret salt-dependent thermodynamic stability data for moderate to highly charged biomolecules, such as certain halophilic and thermophilic proteins.[13,84,85]

Here, we focus on an overall anionic vitamin D-dependent calcium binding protein (PDB id: 3icb), which, as shown in Figure 5, has significant negative potential over most of its surface. Note also that the calcium binding pockets, which consist of anionic Asp (D) and Glu (E) residues (a DEEE pattern at the calcium binding sites) in its surroundings, generate a characteristic negative electrostatic patch near the two calcium binding sites. This characteristic potential surface patch at calcium binding sites is a general characteristic of all calcium binding proteins here studied (see Figure 5).

In this section, we examine the salt dependence of the electrostatic solvation free energy of vitamin D-dependent calcium binding protein, which has a significant salt-dependent electrostatic solvation free energy, using both the uncorrelated and the correlated sampling MC approaches. Our goal here is to show the importance of using the correlated MC sampling in terms of both its CPU time and enhanced accuracy when calculating the salt-dependent electrostatic solvation free energies, ΔG_{solv}^{elec}, of arbitrarily complex-shaped biomolecules.

As shown in Figure 6, the electrostatic solvation free energies of the vitamin D-dependent calcium binding protein are plotted as a function of the logarithm of the NaCl concentration in the range of 0.001−1 M (for a total of 14 salt concentrations). We generated 500, 1500, and 4500 trajectories for the uncorrelated MC sampling computations as opposed to 500 trajectories for the correlated sampling MC computations. As shown in Figure 6, the uncorrelated random walk sampling gives a very nonsmooth (i.e., jagged) ΔG_{solv}^{elec} versus log(salt concentration) curve. It is clear that this behavior is more pronounced when the number of trajectories is smaller because the fluctuation of the peaks is larger and thus the plot is more visibly jagged. These large fluctuations of ΔG_{solv}^{elec} are a reflection of the fact that the simulations at the different salt concentrations were carried out independently; that is, they are uncorrelated with each other.

It would be difficult to extract any salt derivatives of electrostatic solvation free energy at specified salt concentrations using finite-differencing techniques when the uncorrelated sampling approach is employed. This can be remedied by using a large number of trajectories. However, this approach is not practical from the CPU time point of view. On the other hand, by using the correlated sampling method, one can attain highly accurate salt-dependent electrostatic properties with a very low CPU time cost because a single PBE run is required for any user specified number of salt concentrations. In the correlated MC simulations, the survival probability of the random walk in the exterior region is
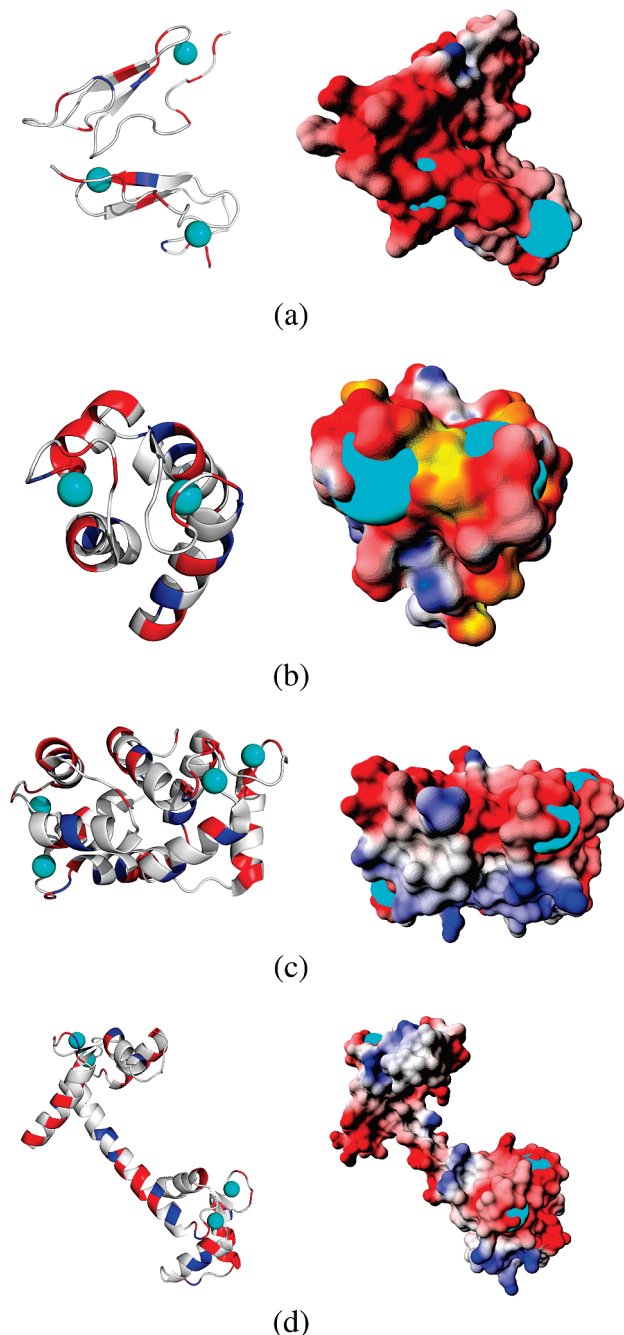
(a)

(b)

(c)

(d)

Figure 5. The 3D structures of four calcium binding proteins (given by their PDB ids) along with their surface electrostatic potential maps are displayed: (a) 1edm, (b) 3icb, (c) 1prw, and (d) 3cln. The calcium ions are shown as cyan colored spheres. Note that for all four calcium binding proteins an extensive patch of negative electrostatic potential lies around the calcium binding sites, which are created by unique patterns of Asp and Glu residues. The color scheme used in these surface electrostatic potential maps is as follows: yellow is the most negative and green is the most positive. White is neutral. Red and blue represent negative and positive potentials, respectively.

independent of the geometry of the molecule. Thus, with the same trajectory one can obtain energy estimates for all different salt concentrations. On the other hand, in the implementation of the uncorrelated random walk sampling, separate and independent walks are done for each of the salt
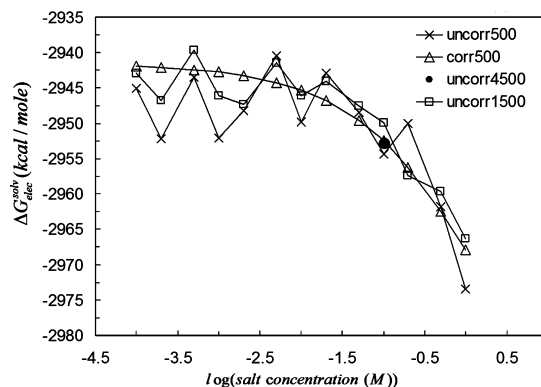

Figure 6. Electrostatic solvation free energy (ΔG_{elec}^{solv}) of the vitamin D-dependent calcium binding protein (PDB id: 3icb) calculated using four different protocols: uncorrelated sampling with 500 trajectories at each salt concentration, uncorrelated sampling with 1500 trajectories at each salt concentration, uncorrelated sampling with 4500 iterations at each salt concentration, and correlated sampling with 500 trajectories.

concentrations. Therefore, for the same level of accuracy, the CPU time for a correlated MC simulation with $N_{\text{concentration}}$ salt concentrations is on the order of $N_{\text{concentration}}$ times smaller than in the uncorrelated MC approach.

In the low salt region where the MC trajectory takes longer to complete, there are consequently larger fluctuations in the energies as reflected in Figure 6. As expected, we also observe that the uncorrelated random walk data points fluctuate around the smooth line of the correlated sampling energy values. As one increases the number of trajectories from 500 to 1500, the computed data points of ΔG_{solv}^{elec} for uncorrelated sampling approach to the computed ΔG_{solv}^{elec} curve for correlated sampling. This implies that by increasing the number of trajectories the uncorrelated random walk energies approach the smooth line generated by the correlated sampling energy curve.

Here, we also computed the fluctuations of the energies relative to its normalized mean values $(\sigma)/(\mu\sqrt{M})$ for both types of sampling: correlated and uncorrelated. To get the same level of accuracy for the energies computed at 0.1 M NaCl using a correlated MC approach requires only 500 trajectories, whereas for uncorrelated MC simulation at least 4500 trajectories are necessary. This means that for this specific case, the correlated sampling gives an overall advantage of about a factor 126, which is obtained from the relationship: $N_{\text{concentration}} \times (M_{\text{traject}}^{\text{uncorr}}/M_{\text{traject}}^{\text{corr}})$.

3.2. CPU Cost and Statistical Error of the LPBE MCM. As shown in section 3.1, the fluctuations of the MCM energy estimates depend on the number of trajectories employed as well as the specified range of salt concentration. It was also shown that the correlated sampling algorithm provides a significant CPU savings because the computations for a set of salt concentrations are done all in one PBE calculation. Moreover, this approach also provides a smaller statistical error for the same number of generated trajectories. In the MC simulation for the vitamin D-dependent calcium binding protein, which was done using 500 trajectories, the fluctuation (or error) of the electrostatic solvation free energy for $\kappa = 0$ is about 0.1%, which is a very small error as

compared to what can be attained with some deterministic PBE methods. If such a small error is not required for a particular electrostatic property being computed with MCM, one can reduce the number of trajectories and therefore save significant CPU time.

As an example, we computed the salt dependence of the electrostatic solvation free energy of calmodulin (CaM) (PDB id: 3cln). The 3D structure of CaM along with its characteristic electrostatic potential map are shown in Figure 5. If one requires a very small error of 0.1% in the electrostatic solvation free energy, the MCM simulation will require 625 trajectories. On the other hand, a less stringent, but still very good level of accuracy of about 0.5% only requires 25 trajectories and takes 33 min to complete on a machine with a 2.8 GHz AMD Opteron 8220 Dual-Core processor.

We can obtain a significant CPU time gain on the order of 25, by simply increasing the error level from 0.1% to 0.5%, which still leads to extremely accurate values for salt-dependent electrostatic properties. Therefore, it is more straightforward to control the accuracy level of electrostatic properties with our MCM as opposed to the more mature deterministic PBE methods. With deterministic PBE solvers, the end-user needs to do some further analysis to determine the accuracy of the PBE solution.

3.3. The Dependence of CPU Time on the Size of the Biomolecule. For any new PBE algorithm to become mainstream in the community, it is important to assess how its accuracy and CPU time scale with system size. Thus, in this section, we address how the CPU time of our MCM-based PBE computation scales with the size of the biomolecular system and how this compares with the scaling of alternate deterministic PBE methods.

In this section, we use an "unphysical" biophysical system to preserve the globularity of the hypothetical biomolecule. The requirement of using similar geometries for these unphysical molecules is done so that all molecules have the same CPU time dependence on the geometry. Thus, we computed the dependence of the CPU time on the number of atoms for an unphysical toy model.

We already described how we constructed "hypothetical biomolecules" of comparable globularity but with different numbers of atoms (i.e., 503, 601, 702, 800, 984, 2973, and 4257 atoms). We evaluated how the CPU time taken in the computation of the salt dependence of the electrostatic solvation free energy of such "toy biomolecules" scales with the number of atoms.

The nature of the discretization required in deterministic finite-difference PBE solvers limits the computational domain to a bounded region. These intrinsic limitations of the popular finite-difference solvers combined with their computational box effect limit its ability to accurately compute electrostatic properties of large-scale biomolecular systems such as viruses, which can have a million or more atoms, without the need for sophisticated computer platforms.[86]

In our MCM algorithm, the random walk done in the interior region is bounded by the molecular surface, whereas the exterior random walk is unbounded. The walk in the exterior region is terminated with the complement of its survival probability, $1 - p_{surv}$. In principle, there is no error
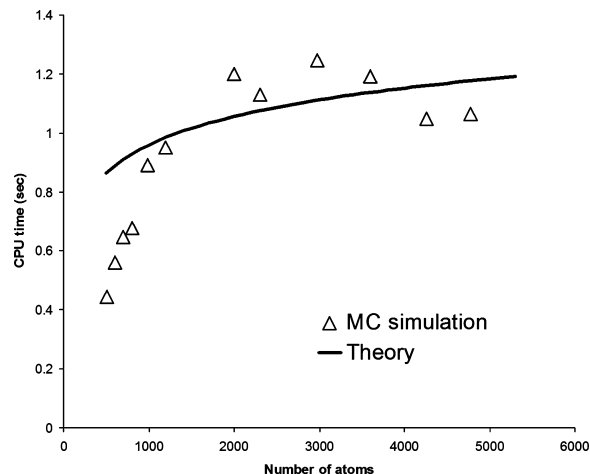

Figure 7. The CPU time per atom per trajectory as a function of the number of atoms of hypothetical globular-like molecules. For a small number of atoms, the CPU time scales linearly with the number of atoms, whereas for larger molecules the scaling approaches a logarithmic behavior.

associated with computational box effects. Because of the intrinsic nature of the MCM algorithm, the simulation time is dominated by the walk in the exterior region rather than other processes (e.g., walk in the interior region, evaluation of the Coloumbic potential). The CPU time as a function of the number of atoms for a random walk is thus $O(\ln(N))$.

In Figure 7, we plot the CPU time as a function of the number of atoms (N) for molecules of differing sizes. As can be inferred from this figure, our results show that for molecules with a small number of atoms the CPU time per atom per trajectory follows a linear scaling, while for molecules with a large number of atoms this gets closer to a logarithmic scaling. Although we compute the CPU time of the MCM for "hypothetical biomolecules", this trend should also apply to any arbitrary and realistic biomolecule.

3.4. Stochastic versus Deterministic Predictions of the Salt Dependence of the Electrostatic Solvation Free Energy of Calcium Binding Proteins. The salt dependence of the electrostatic solvation free energy of four calcium binding proteins (PDB ids: 1prw, 3cln, 1edm, and 3icb) obtained with the MCM is compared against similar finite-difference-based predictions. On the basis of previous results, we anticipate that the salt sensitivity of the electrostatic solvation free energies of the four calcium binding proteins will be different given their differing charge densities. In fact, the salt dependence of the electrostatic solvation free energies is expected to be more pronounced for proteins with higher charge densities. As shown in Figure 8, our MCM results are in excellent agreement with similar deterministic PBE results, thus showing the excellent accuracy of two fundamentally different numerical solutions to the same PDE.

Figure 8 shows the salt dependence of $\Delta\Delta G_{elec}^{solv}$ for all four proteins, where $\Delta\Delta G_{elec}^{solv}$ is the electrostatic solvation free energy at a finite salt concentration relative to that at zero salt concentration as defined by the following equation:

$$\Delta\Delta G_{elec}^{solv} = \Delta G_{elec}^{solv}(\kappa \neq 0) - \Delta G_{elec}^{solv}(\kappa = 0) \quad (10)$$

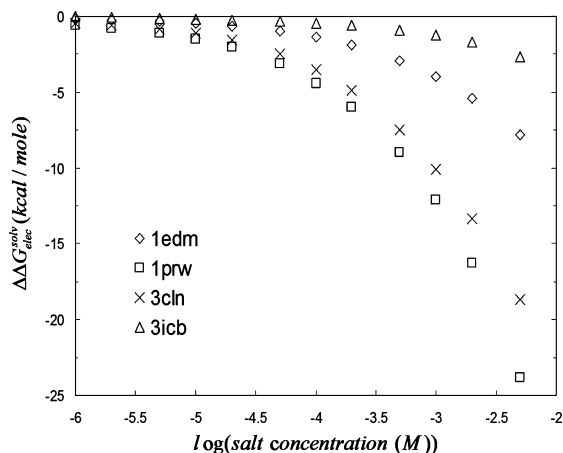Figure 8 shows that the proteins exhibit different salt-dependent behavior in the medium to high salt range. The

Figure 8. Relative electrostatic solvation free energy ($\Delta \Delta G_{\text{elec}}^{\text{solv}}(\kappa) - \Delta G_{\text{elec}}^{\text{solv}}(\kappa = 0)$) versus the logarithmic of the bulk 1:1 salt concentration (in M units). In the limit of zero salt concentration, the slope of the curve also tends to zero. The magnitude of the slope of the curves is larger for the calcium binding proteins with higher net charges.
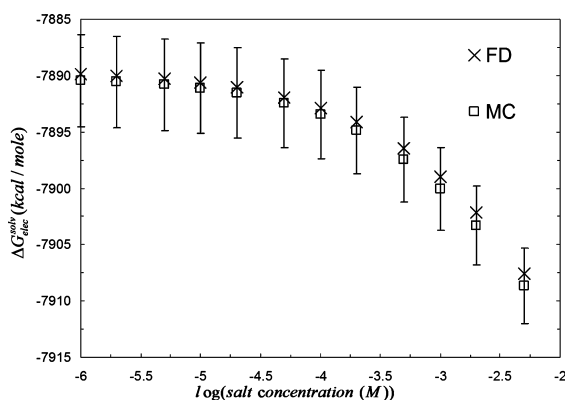

Figure 9. Comparison of the salt dependence of the electrostatic solvation free energy ($\Delta G_{\text{elec}}^{\text{solv}}$) of calmodulin (PDB id: 3cln) obtained with two independent and very distinct PB solvers: MC and deterministic. The graph shows that the deterministic results fall well within the 95% confidence interval of MC energy values at all salt concentrations. Moreover, in the limit of zero salt concentration, the salt derivative of $\Delta G_{\text{elec}}^{\text{solv}}$ is equal to zero for both deterministic and LPBE MCM.

more pronounced salt sensitivity of $\Delta \Delta G_{\text{elec}}^{\text{solv}}$ for calmodulin (PDB id: 1prw) is a reflection of its larger net charge (charge density).

Figure 9 shows the limiting behavior of the electrostatic solvation free energy with respect to log(salt concentration) computed with MCM and the deterministic PBE method. In the limit of zero salt concentration, the salt derivative of the electrostatic solvation free energy of calmodulin (PDB id: 3cln) computed with both codes converges to zero. This also shows that the deterministic energy result falls well within the 95% confidence interval of similar MCM energies. As a comparison, we also plot the salt derivative of the electrostatic solvation free energy with respect to κ at extremely low salt concentration. Figure 10 shows that both PB codes predict comparable salt derivatives in the limit of $\kappa = 0$ (differing by 20%). For the other three calcium binding proteins, smaller differences were observed (results not
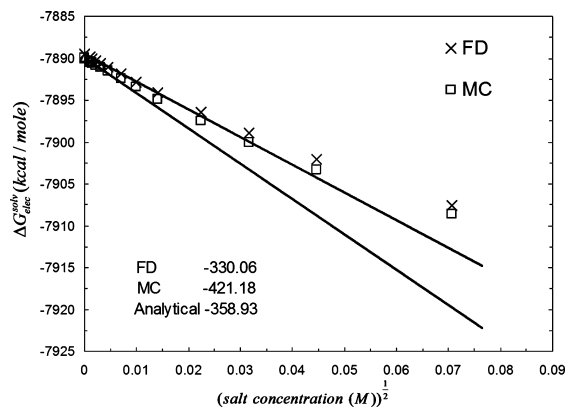

Figure 10. The behavior of the salt derivative of $\Delta G_{\text{elec}}^{\text{solv}}$ (with respect to κ) at the limit of $\kappa = 0$. The plot shows that both deterministic and MCM predict a comparable salt behavior in an extremely low salt regime.

shown). The derivation of the expressions for the limiting behavior of the two different salt derivatives of the electrostatic solvation free energies is given in the Appendix.

3.5. Calcium Binding Site Potentials. It is well established that the electrostatic environment plays a key role in metal binding to proteins, including calcium binding proteins.[87] Locating potential metal binding sites in proteins and nucleic acids using implicit solvent models, such as the PBE, is now a common and practical approach, but there is still room for improvement, especially when one is interested in predicting "hot spot" regions in large-scale assemblies such as viruses and ribosomes, which require a huge computational box (huge memory cost) for deterministic PBE methods.[88]

One of such prediction strategies relies on computing surface electrostatic potentials using PBE methods. We anticipate that our approach will be superior as compared to mainstream methods in determining "'hot spot'" regions, and the binding strength of a ligand for particular sites, due to the MCM ability to compute local electrostatic metrics in a very fast and accurate manner. However, before developing postprocessing tools to allow the end-user to expediently analyze hot spot regions on biomolecules of interest, it is necessary to determine the accuracy and CPU time associated with such electrostatic potential computations.

For a calcium binding protein (PDB id: 1EDM), which has three calcium binding sites (see Figure 5), we computed the electrostatic potential at the center of each site, in the absence of the calcium ions, using both deterministic and MCMs, to assess the accuracy of these two fundamentally different PBE codes. As shown in Figure 5, two of the calcium sites are very close to the molecular surface, while the third calcium ion is much further away. In fact, by analyzing the structural data for this protein, we noted that the B-factor for this latter site is very large, indicating a significant variability for its positioning, whereas the other two calcium positions had similar and smaller B-factors. Therefore, we anticipate that the third calcium ion is more loosely bound, and thus the electrostatic potential surrounding it is probably not as strong as that at the other two sites. Our results confirm this hypothesis, and the electrostatic potential map also shows a stronger negative potential around the first two sites (results not shown).
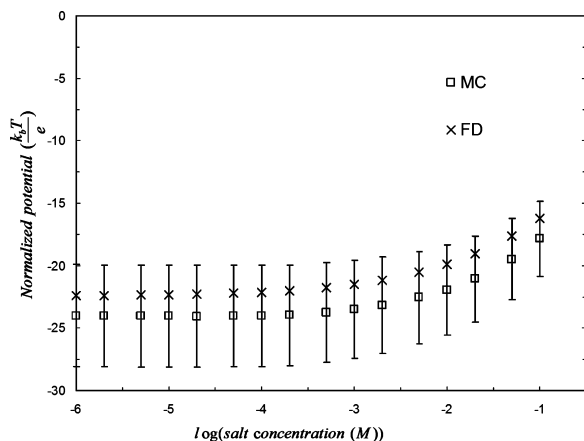
Correlated MC Sampling for Solving the Linearized PBE

J. Chem. Theory Comput., Vol. 6, No. 1, 2010 **311**

Figure 11. Electrostatic potential at one of the calcium binding sites for the epidermal growth factor-like calcium binding protein (PDB id: 1EDM). The electrostatic potential is computed for salt concentrations ranging from 0.000001 to 0.1 M.

Moreover, the electrostatic potentials at the specified sites obtained with these two fundamentally different PBE approaches are in excellent agreement. More precisely, as observed in Figure 11, the electrostatic potential values for all calcium sites obtained with the deterministic code fall well within the 95% confidence interval of the MCM results and obey the same salt behavior.

In the MCM, the electrostatic potential at any arbitrary site is calculated via a random walk starting from that precise 3D location, which implies that to compute the electrostatic potential at one particular location, one does not need to solve the LPBE over the entire 3-D computational domain as required in deterministic-based PBE approaches. Moreover, deterministic-PBE approaches do not provide site potentials directly; they only provide electrostatic potentials at the grid points and thus require the use of interpolation schemes to obtain potential values at any specified 3D-location. When we performed site electrostatic potential calculations for the epidermal growth factor protein using the Charmm force-field, we noted a large discrepancy (up to 20%) between MCM and deterministic results, which is due to the presence of internal voids that are caused by the small hydrogen atoms (radius = 0.2245 Å). It should be pointed out that if we considered the internal cavities as external regions in the deterministic computations as is done in the MCM solver, the agreement between the potential values obtained with both PBE algorithms would be restored. Moreover, we also noticed that the existence of internal cavities near one of the calcium binding sites leads to extremely high electrostatic potentials, on the order of $80(k_{\mathrm{b}}T)/(e)$, when such voids are treated as external regions.

To ensure small errors in the electrostatic potential, calculations using the MCM simulations were performed with 1000 trajectories. The computations took at most 3 min to complete for any of the three calcium binding sites. We observed that the CPU time is smaller the further away the calcium site is from the molecular boundary. The CPU time can be further reduced by fine-tuning code parameters such as the absorbing layer width, $\bar{\varepsilon}$, and the auxiliary sphere radius, a. Our results suggest that the evaluation of electro-

static potential at putative recognition sites for large-scale biomolecular assemblies such as viruses and ribosomes using the proposed MCM will be of great interest to the structural biology and bioinformatics communities due to its low cost and high accuracy.

4. Conclusions

We demonstrated the accuracy, memory, and CPU time advantages of an alternative, stochastic-based, LPBE solver for obtaining salt-dependent electrostatic properties of biomolecules. In particular, we presented a detailed description of how correlated sampling is essential for obtaining accurate electrostatic properties of biomolecules over a broad range of salt concentration in a single MC-based PBE computation, thus significantly reducing the CPU cost and increasing the accuracy of the predictions of salt dependent electrostatic properties. We then validated the LPBE MCM by comparing the electrostatic potential and solvation free energies of calcium binding proteins against similar results obtained with a mature deterministic PBE solver. The excellent agreement between results obtained with two such fundamentally different techniques gives us confidence for further optimizing the present algorithm to make it a viable complementary LPBE solver for the general scientific community. We expect that our LPBE MCM will be very useful in predicting both the electrostatic potential at user-specified sites for large-scale biomolecular assemblies (e.g., viruses and ribosomes) and the salt-dependent solvation free energies of proteins. The latter is important when examining the salt sensitivity of the stability of charged proteins.[13] Of course, we anticipate that in the future it may be possible to create hybrid stochastic-deterministic PBE solvers, where we combine the strengths of each of these two fundamentally different numerical techniques.

Future work will include the applications of the LPBE MCM solver to the computation of other electrostatic properties (e.g., Born radii, electric field). In addition, there are many different quantities of biophysical interest (e.g., electrostatic binding free energy, pK_a shift) that we wish to compute, and further algorithmic and code development is needed on the MCM. There are also many opportunities to improve the performance of MCM by using clever computational geometric algorithms. Finally, we anticipate that this approach will be increasingly beneficial to the general scientific community as these stochastic methods become both better developed and more widely deployed.

Appendix

Dependence of the Electrostatic Solvation Free Energy on κ. For the LPBE, the electrostatic free energy of a biomolecule immersed in a 1:1 salt solution is given as follows:[89]

$$G_{\text{elec}} = \int (\rho^f \phi - 4\pi c_b \phi^2 - 2\pi \varepsilon \bar{E}^2) \, d^3 r \qquad (11)$$

where ρ^f is the charge density of the biomolecule, ϕ is the electrostatic potential, c_b is the bulk salt concentration, ε is the dielectric constant, and $\bar{E}$ is the electric field. From this equation, one can derive two salt derivatives of the electrostatic free energy, $dG_{\text{elec}}/d\kappa$ and $dG_{\text{elec}}/d\log(c_b)$, where

$$c_b = \frac{k_b T \varepsilon_e}{2e^2} \kappa^2 \qquad (12)$$

In eq 12, k_b is the Boltzmann constant, T is the temperature, ε_e is the external dielectric constant, and e is the protonic charge.

The limiting behavior of these two salt derivatives of the electrostatic free energy at zero bulk salt concentration was first derived by Boschitsch et al.[39,90] and is given by the following.

(i) The salt derivative of the electrostatic free energy with respect to κ:

From eq 11, one can derive the expression

$$\frac{dG_{\text{elec}}}{d\kappa} = S - 4\pi\kappa \frac{(k_b T)^2 \varepsilon_e}{e^2} \int u_e^2 \, d^3 r \qquad (13)$$

where $S = -\int_A \varepsilon_e (d\phi_e/dn)(d\phi_e/d\kappa) \, dA$ is the surface integral, ϕ_e is the electrostatic potential in the exterior region, and u_e is the normalized potential $u_e = (e\phi_e)/(k_b T)$.

At large distances from the biomolecule, the biomolecule can be treated effectively as a single central charge with total charge Q_{net} located in the center of a cavity of radius a_{cav}, which reflects the dimension of the biomolecule. In this region, the dielectric constant is ε_e, and the electrostatic potential, ϕ_e, has the following asymptotic form:

$$\phi_e = \frac{Q_{\text{net}}}{4\pi r \varepsilon_e (1 + \kappa a_{\text{cav}})} \exp(-\kappa(r - a_{\text{cav}})) \qquad (14)$$

By using eqs 14 and 12, as $r \to \infty$, the limit of the derivative of ϕ_e with respect to κ at $\kappa \to 0$ can be evaluated and is given by $-(Q_{\text{net}})/(4\pi \varepsilon_e)$. By using this, one can evaluate the surface integral S, in the limit of $\kappa \to 0$, as follows:

$$S = -\lim_{r \to \infty} \int_A \varepsilon_e \frac{d\phi_e}{dn} \frac{d\phi_e}{d\kappa} \, dA$$
$$= \frac{Q_{\text{net}}}{4\pi \varepsilon_e} \lim_{r \to \infty} \int_A \varepsilon_e \frac{d\phi_e}{dn} \, dA \qquad (15)$$
$$= \frac{Q_{\text{net}}^2}{4\pi \varepsilon_e}$$

The volume integral in eq 13 cannot generally be evaluated for arbitrary geometries. However, the limiting behavior at $\kappa \to 0$ can be computed exactly. The exterior region can be divided into a region outside a spherical volume of radius R_s, called V_2, and its complementary volume V_1. Therefore, the volume integral can be rewritten as:

$$I = I(V_1) + I(V_2)$$
$$= 4\pi k \frac{(k_b T)^2 \varepsilon_e}{e^2} \left(\int_{V_1} u_e^2 \, d^3 r + \int_{V_2} u_e^2 \, d^3 r \right) \qquad (16)$$

The radius R_s is chosen to be large so that in region V_2 the molecule looks like a spherical object. Using the expression for the normalized electrostatic potential obtained from Kirkwood,[91] the limit of $I(V_2)$ at $\kappa \to 0$ can be calculated and is equal to $(Q_{\text{net}}^2)/(8\pi \varepsilon_e)$ for any finite R_s. Because I is independent of R_s, then it has to be true that the $\lim_{\kappa \to 0} I(V_1) = 0$. Therefore, the limit of salt gradient at $\kappa \to 0$ is given by:

$$\lim_{\kappa \to 0} \frac{dG_{\text{elec}}}{d\kappa} = \frac{Q_{\text{net}}^2}{8\pi \varepsilon_e} \qquad (17)$$

as first shown by Boschitsch et al.[39,90]

(ii) The salt derivative of the electrostatic free energy with respect to $\log(c_b)$:

We begin by using the relationship

$$\frac{dG_{\text{elec}}}{d\log(c_b)} = \frac{\kappa}{2} \frac{dG_{\text{elec}}}{d\kappa}$$

$$= \kappa S - 2\pi\kappa^2 \frac{(k_b T)^2 \varepsilon_e}{e^2} \int u_e^2 \, d^3 r \qquad (18)$$

In the limit as $\kappa \to 0$, the right terms of eq 18 are equal to zero, given the fact that the limiting behavior of S is defined by eq 15, and the limiting behavior of volume integral I is given by $(Q_{\text{net}}^2)/(8\pi \varepsilon_e)$. Therefore, for any arbitrary geometry, the following relation is valid:

$$\lim_{\kappa \to 0} \frac{dG_{\text{elec}}}{d\log(c_b)} = 0 \qquad (19)$$

(iii) The salt derivative of the electrostatic solvation free energy with respect to κ and $\log(c_b)$:

Because $G_{\text{elec}}^{\text{solv}}$ is defined as

$$G_{\text{elec}}^{\text{solv}} = G_{\text{elec}}(\kappa, \varepsilon_e = \varepsilon_{\text{solv}}) - G_{\text{elec}}(\varepsilon_e = 1) \qquad (20)$$

where the $G_{\text{elec}}(\varepsilon_e = 1)$ is independent of κ, it is straightforward to calculate the limiting behavior of the two salt derivatives of $G_{\text{elec}}^{\text{solv}}$ as $\kappa \to 0$ as

$$\lim_{\kappa \to 0} \frac{dG_{\text{elec}}^{\text{solv}}}{d\kappa} = \lim_{\kappa \to 0} \frac{dG_{\text{elec}}}{d\kappa} = \frac{Q_{\text{net}}^2}{8\pi \varepsilon_e} \qquad (21)$$

and

$$\lim_{\kappa \to 0} \frac{dG_{\text{elec}}^{\text{solv}}}{d\log(c_b)} = \lim_{\kappa \to 0} \frac{dG_{\text{elec}}}{d\log(c_b)} = 0 \qquad (22)$$

References

(1) Richard, A. J.; Liu, C.-C.; Klinger, A. L.; Todd, M. J.; Mezzasalma, T. M.; LiCata, V. J. *Biochim. Biophys. Acta* **2006**, *1764*, 1546–1552.

(2) Niiranen, L.; Altermak, B.; Brandsal, B.; Leiros, H.-K.; Helland, R.; Smalas, A.; Willassen, N. *FEBS J.* **2008**, *275*, 1593–1605.

(3) Kloss, E.; Barrick, D. *J. Mol. Biol.* **2008**, *383*, 1195–1209.

(4) Lindman, S.; Xue, W.; Szczepankiewicz, O.; Bauer, M. C.; Nilsson, H.; Linse, S. *Biophys. J.* **2006**, *90*, 2911–2921.

Correlated MC Sampling for Solving the Linearized PBE

J. Chem. Theory Comput., Vol. 6, No. 1, 2010 **313**

(5) Suh, J.-Y.; Tang, C.; Clore, G. M. *J. Am. Chem. Soc.* **2007**, *129*, 12954–12955.

(6) Henry, B. L.; Connell, J.; Liang, A.; Krishnasamy, C.; Desai, U. R. *J. Biol. Chem.* **2009**, *284*, 20897–20908.

(7) Song, B.; Cho, J.-H.; Raleigh, D. *Biochemistry* **2007**, *46*, 14206–14214.

(8) Majhi, P. R.; Ganta, R. R.; Vanam, R. P.; Seyrek, E.; Giger, K.; Dubin, P. L. *Langmuir* **2006**, *22*, 9150–9159.

(9) Müller-Santos, M.; de Souza, E. M.; de O. Pedrosa, F.; Mitchell, D. A.; Longhi, S.; Carrière, F.; Canaan, S.; Krieger, N. *Biochim. Biophys. Acta* **2009**, *1791*, 719–729.

(10) Liu, S.; Low, N. H.; Nickerson, M. T. *J. Agric. Food Chem.* **2009**, *57*, 1521–1526.

(11) Watanabe, E. O.; Popova, E.; Miranda, E. A.; Maurer, G.; de Alcântara Pessôa Filho, P. *Fluid Phase Equilib.* **2009**, *281*, 32–39.

(12) Yan, W.; Huang, L. *Int. J. Pharm.* **2009**, *368*, 56–62.

(13) Dominy, B. N.; Perl, D.; Schmid, F. X.; Brooks, C. L. *J. Mol. Biol.* **2002**, *319*, 541–554.

(14) Bertonati, C.; Honig, B.; Alexov, E. *Biophys. J.* **2007**, *2*, 1891–1899.

(15) Formaneck, M. S.; Ma, L.; Cui, Q. *J. Am. Chem. Soc.* **2006**, *128*, 9506–9517.

(16) Thomas, A. S.; Elcock, A. H. *J. Am. Chem. Soc.* **2006**, *128*, 7796–7806.

(17) Ye, X.; Cai, Q.; Yang, W.; Luo, R. *Biophys. J.* **2009**, *97*, 554–562.

(18) Min, D.; Li, H.; Li, G.; Berg, B. A.; Fenley, M. O.; Yang, W. *Chem. Phys. Lett.* **2008**, *454*, 391–395.

(19) Dzubiella, J. *J. Am. Chem. Soc.* **2008**, *130*, 14000–14007.

(20) Feng, J.; Wong, K.-Y.; Lynch, G. C.; Gao, X.; Pettitt, B. M. *J. Phys. Chem. B* **2009**, *113*, 9472–9478.

(21) Li, L.; Liang, S.; Pilcher, M. M.; Meroueh, S. O. *Protein Eng. Des. Sel.* **2009**, *22*, 575–586.

(22) Massova, I.; Kollman, P. A. *Perspect. Drug Discovery* **2000**, *18*, 113–115.

(23) Fujiwara, S.; Amisaki, T. *Biophys. J.* **2008**, *94*, 95–103.

(24) Boda, D.; Valiskó, M.; Henderson, D.; Gillespie, D.; Eisenberg, B.; Gilson, M. K. *Biophys. J.* **2009**, *96*, 1293–1306.

(25) Lu, B.; Zhou, Y.; Holst, M.; McCammon, J. A. *Commun. Comput. Phys.* **2008**, *3*, 973–1009.

(26) Grochowski, P.; Trylska, J. *Biopolymers* **2007**, *89*, 93–113.

(27) Miertus, S.; Scrocco, E.; Tomasi, J. *Chem. Phys.* **1981**, *55*, 117–129.

(28) Hoshi, H.; Sakurai, M.; Inoue, Y.; Chûjô, R. *J. Chem. Phys.* **1987**, *87*, 1107–1115.

(29) Zauhar, R.; Morgan, R. *J. Comput. Chem.* **1988**, *9*, 171–187.

(30) Rashin, A. A. *J. Phys. Chem.* **1990**, *94*, 1725–1733.

(31) Yoon, B.; Lenhoff, A. *J. Comput. Chem.* **1990**, *11*, 1080–1086.

(32) Juffer, A.; Botta, E.; Vankeulen, B.; Vanderploeg, A.; Brendsen, H. *J. Comput. Phys.* **1991**, *97*, 144–171.

(33) Zhou, H.-X. *Biophys. J.* **1993**, *65*, 955–963.

(34) Bharadwaj, R.; Windemuth, A.; Sridharan, S.; Honig, B.; Nicholls, A. *J. Comput. Chem.* **1995**, *16*, 898–913.

(35) Purisima, E.; Nilar, S. *J. Comput. Chem.* **1995**, *16*, 681–689.

(36) Liang, J.; Subramaniam, S. *Biophys. J.* **1997**, *73*, 1830–1841.

(37) Vorobjev, Y. N.; Scheraga, H. A. *J. Comput. Chem.* **1997**, *18*, 569–583.

(38) Totrov, M.; Abagyan, R. *Biopolymers* **2001**, *60*, 124–133.

(39) Boschitsch, A.; Fenley, M.; Zhou, H.-X. *J. Phys. Chem. B* **2002**, *106*, 2741–2754.

(40) Lu, B.; Cheng, X.; Huang, J.; McCammon, J. A. *Proc. Natl. Acad. Sci. U.S.A.* **2006**, *103*, 19314–19319.

(41) Hagstrom, I.; Fine, R.; Sharp, K.; Honig, B. *Proteins* **1986**, *1*, 47–59.

(42) Gilson, M.; Sharp, K.; Honig, B. H. *J. Comput. Chem.* **1988**, *9*, 327–335.

(43) Davis, M.; McCammon, J. *J. Comput. Chem.* **1989**, *10*, 386–391.

(44) Nicholls, A.; Honig, B. *J. Comput. Chem.* **1991**, *12*, 435–445.

(45) Luty, B.; Davis, M.; McCammon, J. *J. Comput. Chem.* **1992**, *13*, 1114–1118.

(46) Holst, M.; Saied, F. *J. Comput. Chem.* **1993**, *14*, 105–113.

(47) Forsten, K.; Kozack, R.; Lauffenburger, D.; Subramaniam, S. *J. Phys. Chem.* **1994**, *98*, 5580–5586.

(48) Im, W.; Beglov, D.; Roux, B. *Comput. Phys. Commun.* **1998**, *111*, 59–75.

(49) Rocchia, W.; Alexov, E.; Honig, B. *J. Phys. Chem. B* **2001**, *105*, 6507–6514.

(50) Luo, R.; David, L.; Gilson, M. *J. Comput. Chem.* **2002**, *23*, 1244–1253.

(51) Bashford, D. *Lecture Notes Comput. Sci.* **1997**, *1343*, 233–240.

(52) Cortis, C.; Friesner, R. *J. Comput. Chem.* **1997**, *18*, 1591–1608.

(53) Baker, N. A.; Holst, M.; Wang, F. *J. Comput. Chem.* **2000**, *21*, 1343–1352.

(54) Holst, M.; Baker, N.; Wang, F. *J. Comput. Chem.* **2000**, *21*, 1319–1342.

(55) Shestakov, A.; Milovich, J.; Noy, A. *J. Colloid Interface Sci.* **2002**, *247*, 62–79.

(56) Chen, L.; Holst, M.; Xu, J. *Siam J. Numer. Anal.* **2007**, *45*, 2298–2320.

(57) Xie, D.; Zhou, S. *BIT* **2007**, *47*, 853–871.

(58) Bhardwaj, N.; Stahelin, R. V.; Langlois, R. E.; Cho, W.; Lu, H. *J. Mol. Biol.* **2006**, *359*, 486–495.

(59) Freidlin, M. *Functional Integration and Partial Differential Equations*; Princeton University Press: Princeton, NJ, 1985.

(60) Tjong, H.; Zhou, H.-X. *J. Chem. Theory Comput.* **2008**, *4*, 507–514.

(61) Geng, W.; Yu, S.; Wei, G. *J. Chem. Phys.* **2007**, *127*, 114106.

(62) Wang, J.; Cai, Q.; Li, Z.-L.; Zhao, H.-K.; Luo, R. *Chem. Phys. Lett.* **2009**, *468*, 112–118.

(63) Cai, Q.; Wang, J.; Zhao, H.-K.; Luo, R. *J. Chem. Phys.* **2009**, *130*, 145101.

(64) Zhou, Z.; Payne, P.; Vasquez, M.; Khn, N.; Levitt, M. *J. Comput. Chem.* **1996**, *11*, 1344–1351.

(65) Lu, J.; Deutsch, C. *J. Mol. Biol.* **2008**, *384*, 73–86.

(66) Lu, J.; Kobertz, W. R.; Deutsch, C. *J. Mol. Biol.* **2007**, *371*, 1378–1391.

(67) Gilson, M. K.; Honig, B. H. *Nature* **1987**, *330*, 84–86.

(68) Fleming, C.; Mascagni, M.; Simonov, N. *Lecture Notes Comput. Sci.* **2005**, *3516*, 760–765.

(69) Hwang, C.-O.; Mascagni, M. *Appl. Phys. Lett.* **2001**, *78*, 787–789.

(70) Karaivanova, A.; Mascagni, M.; Simonov, N. *Monte Carlo Methods Appl.* **2004**, *10*, 311–320.

(71) Mascagni, M.; Simonov, N. *SIAM J. Sci. Comput.* **2004**, *26*, 339–357.

(72) Simonov, N. *Dokl. Math.* **2006**, *74*, 656–659.

(73) Simonov, N. *Lecture Notes Comput. Sci.* **2007**, *4310*, 181–188.

(74) Mascagni, M.; Simonov, N. A. *J. Comput. Phys.* **2004**, *195*, 465–473.

(75) Simonov, N. A.; Mascagni, M.; Fenley, M. O. *J. Chem. Phys.* **2007**, *127*, 185105.

(76) Elepov, B.; Mikhailov, G. *Sov. Math. Dokl.* **1973**, *14*, 1276–1280.

(77) Ettelaie, R. *J. Phys. Chem.* **1995**, *103*, 3657–3667.

(78) Bondi, A. *J. Phys. Chem.* **1964**, *68*, 441–451.

(79) Dolinsky, T. J.; Nielsen, J. E.; McCammon, J. A.; Baker, N. A. *Nucleic Acids Res.* **2004**, *32*, 665–667.

(80) Brooks, B. R.; Bruccoleri, R. E.; Olafson, B. D.; States, D. J.; Swaminathan, S.; Karplus, M. *J. Comput. Chem.* **1983**, *4*, 187–217.

(81) Cornell, W. D.; Cieplak, P.; Bayly, C. I.; Gould, I. R.; Merz, K. M.; Ferguson, D. M.; Spellmeyer, D. C.; Fox, T.; Caldwell, J. W.; Kollman, P. A. *J. Am. Chem. Soc.* **1995**, *117*, 5179–5197.

(82) Muller, M. *Ann. Math. Stat.* **1956**, *27*, 569–589.

(83) Sabelfeld, K. *Monte Carlo Methods in Boundary Value Problems*; Springer-Verlag: Berlin/Heidelberg/New York, 1991.

(84) Bandyopadhyay, A. K.; Sonawat, H. M. *Biophys. J.* **2000**, *79*, 501–510.

(85) Lanyi, J. K. *Microbiol. Mol. Biol. Rev.* **1974**, *38*, 272–290.

(86) Baker, N. A.; Sept, D.; Joseph, S.; Holst, M. J.; McCammon, J. A. *Proc. Natl. Acad. Sci. U.S.A.* **2001**, *98*, 10037–10041.

(87) Penfold, R.; Warwicker, J.; Jönsson, B. *J. Phys. Chem. B* **1998**, *102*, 8599–8610.

(88) Jones, S.; Shanahan, H. P.; Berman, H. M.; Thornton, J. M. *Nucleic Acids Res.* **2003**, *31*, 7189–7198.

(89) Sharp, K. A.; Honig, B. *J. Phys. Chem.* **1990**, *94*, 7684–7692.

(90) Boschistsch, A. H.; Fenley, M. O. *J. Comput. Chem.* **2004**, *25*, 935–955.

(91) Kirkwood, J. G. *J. Chem. Phys.* **1934**, *2*, 351–361.

JCTC Journal of Chemical Theory and Computation

A Nonradial Coarse-Grained Potential for Proteins Produces Naturally Stable Secondary Structure Elements

Davide Alemani,[†] Francesca Collu,[‡] Michele Cascella,*,[‡] and Matteo Dal Peraro*,[†]

Laboratory for Biomolecular Modeling, Ecole Polytechnique Fédérale de Lausanne (EPFL), CH-1015 Lausanne, Switzerland and Departement für Chemie und Biochemie, Universität Bern, Freiestrasse 3, CH-3012 Bern, Switzerland

Abstract: We introduce a nonradial potential term for coarse-grained (CG) molecular simulations of proteins. This term mimics the backbone dipole−dipole interactions and accounts for the needed directionality to form stable folded secondary structure elements. We show that α-helical and β-sheet peptide chains are correctly described in dynamics without the need of introducing any a priori bias potentials or ad hoc parametrizations, which limit broader applicability of CG simulations for proteins. Moreover, our model is able to catch the formation of supersecondary structural motifs, like transitions from long single α-helices to helix−coil−helix or β-hairpin assemblies. This novel scheme requires the structural information of C_α beads only; it does not introduce any additional degrees of freedom to the system and has a general formulation, which allows it to be used in synergy with various CG protocols, leading to an improved description of the structural and dynamic properties of protein assemblies and networks.

1. Introduction

Molecular dynamics (MD) simulations have proven to be a powerful tool to investigate the structure and function of biomolecular systems. Among different approaches to modeling proteins, nucleic acids, and biological membranes, all-atom MD has been shown to provide a reasonable compromise between the accuracy of the force fields used to describe molecular interactions and the computational cost required to simulate relevant systems.[1] The continuous increase in computational power allows a routine application of such techniques to systems as large as 10^2 kDa at the multi-nanosecond time scale, when using high-performance-computing resources. Moreover, benefiting from such improved throughput, the scientific community has been recently very active in testing the reliability of current force fields[2,3] and in developing new models, protocols, and algorithms to increase both the accuracy and the performance of current MD codes. Nonetheless, within the atomistic framework, it remains computationally unaffordable to thoroughly sample size and time scales that are critical to most of the biological processes both in vitro and in vivo. In fact, fundamental events like protein folding, signal transduction, or DNA transcription, while all triggered by interactions at atomistic dimensionality, occur at very different time scales (from the femtosecond to the second and more) and span over different sizes (from few tens to millions of atoms). Such a scale range implies a dimensionality of the corresponding phase-space so large that its complete sampling by brute-force all-atom MD remains at the moment unfeasible.[4]

To extend the boundaries of time and size, one can abandon the atomistic representation for a coarser description of molecular systems. From the original framework of elastic networks used by Levitt and Warshel[5] and Go and Scheraga[6,7] to describe protein folding, more recent coarse-grained (CG) models make use of beads to represent groups of atoms that interact through effective potentials, which have a functional form similar to that of atomistic force fields. Successful CG models were introduced to describe polar/nonpolar interactions, such as in lipid self-assembly processes in water.[8−10] On the basis of these seminal works, new generations of CG models were developed to study aqueous surfactant solutions,[11,12] and membrane lipid assemblies.[13−16] Current

---

* Corresponding author e-mail: michele.cascella@iac.unibe.ch (M.C.); matteo.dalperaro@epfl.ch (M.D.P.).

† EPFL.

‡ Universität Bern.

computational power allows using these schemes to access size scales on the order of 10^6 CG particles (i.e., ≈10 million atoms) and time scales approaching relevant experimental regimes (i.e., millisecond).[4] Recently, effective potentials based on similar atom-to-bead mapping have been extended to proteins[17−20] and nucleosomes.[21−25] These models have been used in the past years to study very large membrane−protein complexes, showing promising results for the study of structural rearrangements, which are functional to many biological processes.[26−36] Even coarser levels of approximating protein potentials have been proposed on the basis of a single bead representation of amino acids[37−39] or extended to describe well-defined structural intraprotein domains or even single proteins in multimolecular assemblies.[26,40]

Progressive efforts in linking CG models to the atomistic descriptions have also been produced by the computational community, with the scope of developing multiscale frameworks able to synergically exploit the complementary advantages of descriptions of molecular systems at different levels of resolution.[25,41−53]

Nonetheless, to date, many issues still afflict CG schemes, which limit in turn their general applicability to a vast class of relevant biological problems. The functional form of CG potentials is not univocally defined and strongly depends on the level of coarse-graining one chooses to adopt.[52,54] Moreover, accurate potential function parameters for CG MD simulations are still laking full transferability; therefore, they have to be recalibrated according to the system of interest.[55,56] The lack of both universality and transferability results in significant drawbacks, which reduce their general applicability. In particular, fully transferable CG models based on pair potentials can face difficulties in reproducing anisotropic properties, which are crucial for accounting for both stability in secondary structure elements and correct tertiary structure assembling. One possibility to circumvent such problems is to maintain a higher resolution (atomistic or quasi-atomistic) at least in the backbone region.[57−59] In the case where a one-bead per backbone unit mapping is chosen, it is usually necessary to introduce additional bias potentials, which are defined on a target conformation and do not naturally adapt to secondary structure modifications, which may occur during dynamics.[17,26,31]

In the past years, significant results have been achieved by Scheraga and co-workers, by defining coarse-grained potentials where dipole−dipole interactions for the backbone are explicitly taken into account.[60−63] Such a model has proven to be particularly effective for energy calculations in folding predictions. Recently, backbone dipole−dipole interactions within a similar scheme were also implemented in a MD scheme.[64]

In a recent previous paper, we have shown how the orientation of the backbone dipole can be directly reconstructed from the positions of C_α atoms only.[65] From that standpoint, we have here formulated a computational protocol able to account for the intrinsic nonradial nature of backbone−backbone interactions in a CG−molecular dynamics framework using a single-bead representation for backbone units. We have evaluated its performance in a series of test systems, finding that our designed potential term

is able to naturally stabilize secondary structure motifs, such as α-helices and β-sheets, to describe basilar structure rearrangements and to reliably modulate structural transitions into supersecondary assemblies. The proposed potential energy term is computationally very efficient, as it is fully defined as a function of the backbone C_α coordinates; therefore, it does not introduce any additional degrees of freedom to the system. Together with analytical modifications in the bending and torsional potentials, also discussed in this work, this novel scheme represents a promising step toward the development of a CG force field, which can accurately describe the structural and dynamic properties of protein assemblies and networks.

2. Computational Methods

Parameterized potential functions in all-atom (AA) molecular dynamics usually take the form

$$V_{\text{AA}} = \sum_{\text{bonds}} k_r(r - r_0)^2 + \sum_{\text{angles}} k_\gamma(\gamma - \gamma_0)^2 +$$
$$\sum_{\text{dihedrals}} [1 + \cos(n\varphi + \delta)] + \sum_{i<j}\left[\frac{A_{ij}}{R_{ij}^{12}} - \frac{B_{ij}}{R_{ij}^6}\right] + \sum_{i<j} \frac{q_i q_j}{R_{ij}} \quad (1)$$

where the first three terms represent stretching, bending, and torsional potentials, and the last two terms are nonbonded van der Waals and Coulomb interactions. Our model potential for CG backbone beads is expressed in a similar form, but with some important modifications. In particular, we change the functional form of the angular potential, we introduce a correlation term for consecutive dihedral angles, and we replace point-charge Coulombic interactions with backbone dipole−dipole interactions:

$$V_{\text{CG}} = \sum_{\text{bonds}} k_r(r - r_0)^2 + \sum_{\text{angles}} k_\gamma P^4(\gamma - \gamma_0) +$$
$$\sum_{\text{dihedrals}} k_\varphi[1 + \cos(n\varphi + \delta)] + \sum_{\text{dihedrals}-1} k_{\text{corr}}(\varphi_i - \varphi_{i+1})^2 +$$
$$\sum_{k<l}\left(\frac{A_{kl}}{R_{kl}^{12}} - \frac{B_{kl}}{R_{kl}^6}\right) + \sum_{i<j} V[\boldsymbol{\mu}_i(C_{\alpha,i-1}, C_{\alpha,i}, C_{\alpha,i+1}),$$
$$\boldsymbol{\mu}_j(C_{\alpha,j-1}, C_{\alpha,j}, C_{\alpha,j+1})] \quad (2)$$

In this expression, indices k and l run on all beads, while indices i and j run on all groups of three consecutive bonded $C_{\alpha, i-1}$, $C_{\alpha, i}$, and $C_{\alpha, i+1}$ beads (called C_i triplet hereafter, Figure 1).

2.1. Dipole−Dipole Interactions. Backbone atomistic dipole−dipole interactions are modeled as directional interactions between two C_i triplets. An electrostatic dipole $\boldsymbol{\mu}_i$ is associated with each C_i triplet. $\boldsymbol{\mu}_i$ mimics the electrostatic dipole associated with the peptide bond located between amino acids i and $i + 1$ (Figure 1). The geometrical orientation of these dipoles is constrained to that of the C_i triplet to which they belong. In this way, forces acting on dipoles can be transmitted to the relative C_α beads, without increasing the number of degrees of freedom to be propagated during dynamics.

The protocol works as follows (Figure 2):

• Determination of the spatial orientation of all dipoles $\{\boldsymbol{\mu}_i\}$ starting from the coordinates of all C_i triplets
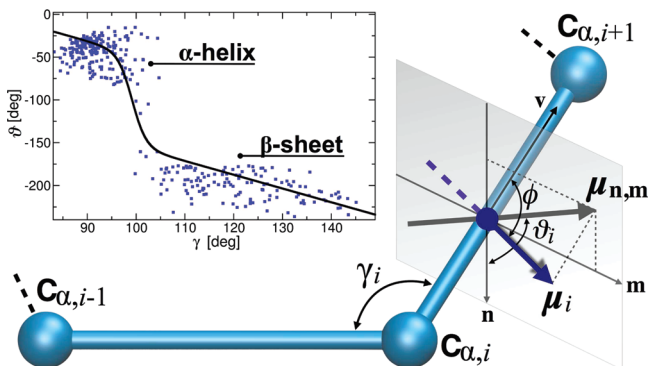
A Nonradial Coarse-Grained Potential for Proteins

J. Chem. Theory Comput., Vol. 6, No. 1, 2010 **317**

Figure 1. Backbone dipole reconstruction. The backbone dipole moment μ_i as a function of the local reference system (v, n, m) associated with the C_i triplet. ϕ is the angle between the μ_i and the v axis. ϑ_i is the angle between the component of μ_i on the plane n, m ($\mu_{n,m}$), and the n axis. The inset shows the statistical distribution of θ_i as a function of γ extracted from the PDB (square symbols) and its analytical fitting function (solid line). The local reference system is represented at the middle point of the $C_{\alpha,i}-C_{\alpha,i+1}$ bond for the sake of clarity.

• Computation of forces F_{ij} and torques τ_{ij} acting on each dipole μ_i, due to dipole−dipole interactions
• Distribution of F_{ij} and τ_{ij} to the corresponding C_i triplet
• Time propagation of C_i coordinates, following classical equations of motion (EoM)

Below, each step of this protocol is explained in detail.

Computation of the Backbone Dipole Moment. Given a triplet C_i, let γ_i be the angle formed by the C_α beads of the triplet and S_i be the local reference system of axes (v, n, m), centered at $C_{\alpha,i}$, defined as follows: v is directed along the direction given by $C_{\alpha,i}$ and $C_{\alpha,i+1}$; n is orthogonal to the plane formed by the C_i triplet; m is orthogonal to v and n (Figure 1 and Figure 2, panel 2).

In a recent paper,[65] we showed that the components of the backbone dipole along such axes can be obtained with good approximation by fitting their experimental measurements from the PDB databank as functions of the angle γ. For the purposes of this work, we have reformulated such a fit by using the following representation in spherical coordinates:

$$\mu_{i,v} = \mu_0 \cos \phi$$
$$\mu_{i,n} = \mu_0 \sin \phi \cos \vartheta$$
$$\mu_{i,m} = \mu_0 \sin \phi \sin \vartheta \qquad (3)$$

where μ_0 is the modulus of the vector μ (3.6 D, modeled as two charges of ± 0.33 au, located at a distance $\delta = 2.273$ Å, mimicking the atomistic intensity)[66] and ϕ and ϑ are defined as in Figure 1. In this way, by construction, the angle ϕ is a constant, with $\cos \phi = 0.177$. The angle ϑ_i remains as the only variable, which is fitted as a function of the angle γ_i:

$$\vartheta_i = -1.607\gamma_i + 0.094 + \frac{1.883}{\exp\left[\dfrac{(\gamma_i - \gamma_0)}{\sigma}\right] + 1} \qquad (4)$$

where $\gamma_0 = 1.730$ rad and $\sigma = 0.025$ rad (see inset of Figure 1).
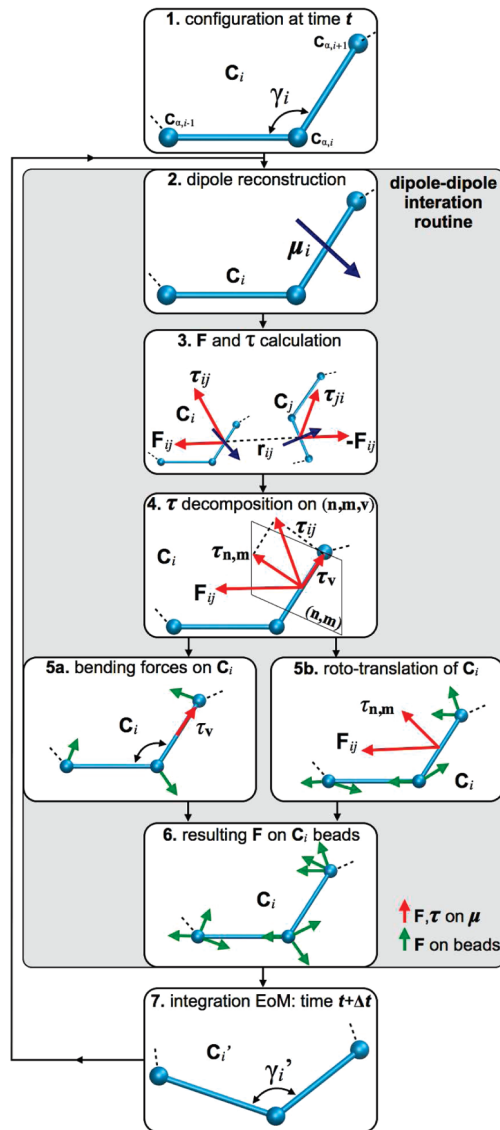
Figure 2. Dipole−dipole interaction protocol. The theoretical protocol of the new algorithm used to describe the dipole−dipole interactions.

Computation of Forces and Torques. The electrostatic dipole−dipole interaction potential reads

$$V(\mu_i, \mu_j) = \frac{\mu_i \cdot \mu_j}{r^3} - \frac{3}{r^5}(\mu_i \cdot r)(\mu_j \cdot r) \qquad (5)$$

where r is the vector connecting the two dipoles. Forces F_{ij} and torques τ_{ij} and τ_{ji} acting between dipole couples are derived accordingly (Figure 2, panel 3):

$$F_{ij} = \frac{3}{r^5}(\mu_i \cdot \mu_j)r - \frac{15}{r^7}(\mu_i \cdot r)(\mu_j \cdot r)r + \frac{3}{r^5}[(\mu_j \cdot r)\mu_i + (\mu_i \cdot r)\mu_j] \qquad (6)$$

and

$$\tau_{ij} = -\frac{1}{r^3}(\mu_i \times \mu_j) + \frac{3}{r^5}(\mu_j \cdot r)(\mu_i \times r)$$
$$\tau_{ji} = -\frac{1}{r^3}(\mu_j \times \mu_i) + \frac{3}{r^5}(\mu_i \cdot r)(\mu_j \times r) \qquad (7)$$

Equations 6 and 7 are valid under the condition that the dipole length δ is much shorter than the distance between the same dipoles, that is, $\delta \ll |\mathbf{r}|$. At short distances, that is, when δ is on the same order of magnitude as $|\mathbf{r}|$, the dipole−dipole interactions are treated by considering the opposite charges of absolute value $q = 0.33$ au, placed at the edges of the dipole and at a fixed distance of δ, and computing point-charge interactions.

Dynamics of the C_i Triplets. The spatial orientation of the dipole $\boldsymbol{\mu}_i$ is fully determined by the geometry of the C_i triplet. Therefore, forces and torques acting on the dipole can be explicitly transformed into forces acting on the three beads forming C_i.

In fact, because any γ_i angle is associated with the respective ϑ_i angle via eq 4, the application of a torque on $\boldsymbol{\mu}_i$, which produces a variation of ϑ_i, is necessarily associated with a variation of γ_i (Figure 1 and Figure 2, panel 5a). On the contrary, the angle ϕ is constrained to a fixed values, therefore, torques that would produce a modification of that angle will instead result into a rigid rotation of the triplet (Figure 1 and Figure 2, panel 5b).

Specifically, the torque $\boldsymbol{\tau}_i$,

$$\boldsymbol{\tau}_i = \sum_j \boldsymbol{\tau}_{ij} \tag{8}$$

which is the total torque acting on $\boldsymbol{\mu}_i$ due to the interactions of $\boldsymbol{\mu}_i$ with all of the other dipoles $\boldsymbol{\mu}_j$, is expressed as the sum of two components:

$$\boldsymbol{\tau}_i = \boldsymbol{\tau}_{n,m} + \boldsymbol{\tau}_v \tag{9}$$

$\boldsymbol{\tau}_{n,m}$ is the projection of $\boldsymbol{\tau}_i$ on the plane $(\mathbf{n}, \mathbf{m})$, and $\boldsymbol{\tau}_v$ is the component along the v axis (Figure 2, panel 4). The $\boldsymbol{\tau}_v$ component, associated with a rotation around v, affects ϑ only (Figure 2, panel 5a). Therefore, by inverting the biunivocal relationship between ϑ_i and γ_i (eq 4), such precession can be easily transformed into a bending force, $\mathbf{B}_i(\gamma_i)$ acting on the γ_i angle:

$$\mathbf{B}_i(\gamma_i) = \boldsymbol{\tau}_v \frac{\partial \vartheta_i}{\partial \gamma_i} \tag{10}$$

The $\boldsymbol{\tau}_{n,m}$ component is associated with a rotation of μ_i on a plane containing the $C_{\alpha,i}$, $C_{\alpha,i+1}$ direction, thus with a variation of the constrained angle ϕ. Therefore, this rotation of μ_i has to be rigidly transferred to the triplet C_i (Figure 2, panel 5b).

In practice, interactions among dipoles result into rigid rototranslations of the triplets, produced by the combined action of $\boldsymbol{\tau}_{n,m}$, and forces $\mathbf{F}_{ij}$, and bending motions, under the action of $\boldsymbol{\tau}_v$ (Figure 2, panel 6).

Integration of the EoM. Our procedure rigorously transforms all forces acting on dipoles into forces acting on C_α beads (Figure 2); therefore, integration of the equations of motion is performed on C_α's only, without the introduction of additional degrees of freedom to the system or the need to impose any fictitious dipole dynamics. The generation of dipole geometries and the redistribution of forces from dipoles to beads constitute negligible additional computational costs to the simulations. In fact, they are constituted by simple operations, most of which (like the determination
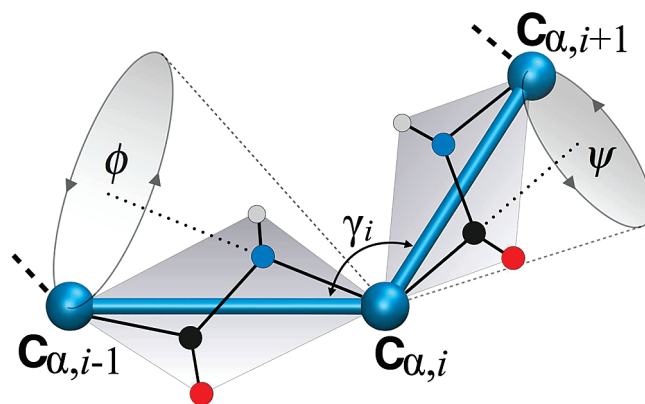

Figure 3. Relationship between the CG angle γ_i and the all-atom Ramachandran angles ϕ and Ψ. The all-atom structure is sketched in lines; the CG beads are represented in cyan balls-and-sticks. Rotation of any Ramachandran angle corresponds to a precession of the respective CG bead, resulting in a variation of the angle γ_i.

of internal reference systems and computation of the γ angles) are already routinely required for bending interactions and, thus, performed by standard MD operations. The only non-negligible cost is related to the dipole−dipole interaction part, which has to be added ex novo to the nonbonded interactions. Anyway, its cost is comparable to that of an additional nonbonded solute−solute interaction, which typically constitutes less than 1% of the total simulation cost per step, thus being acceptable for simulation-speedup criteria in CG simulations.

2.2. Bending Potential. Within the harmonic approximation for bending motion, only small oscillations of the angle γ formed by three consecutive backbone beads around a defined equilibrium value γ_0 are allowed. Instead, variations in such angles are related, in the respective all-atom representation, to structural variations of the Ramachandran torsional angles (Figure 3). Therefore, we decided to use a double-well potential to describe angular interactions. The angular potential function takes the form of a fourth degree polynomial function in the $(\gamma - \gamma_0)$ variable:

$$P^4(\gamma - \gamma_0) = \frac{1}{2}k_1(\gamma - \gamma_0)^2 - \frac{1}{3}k_2(\gamma - \gamma_0)^3 + \frac{1}{4}k_3(\gamma - \gamma_0)^4 \tag{11}$$

where γ_0 is 91°.

Such a kind of potential form for the CG bending term, originally proposed by Warshel and Levitt,[5] and recently successfully used in studies on CG modeling of HIV-1 protease,[22,37−39] allows the determination of two local minima, corresponding to the α-helical and β-strand basins. Thus, this allows for a more general description of CG interactions, without the need of specifying *biasing* secondary structure-dependent angular potentials. Rather, by modulating its shape, secondary structure propensities can be attributed to local portions of the amino acid (aa) sequence, thus making conformational transitions possible at finite energy costs. The two parameter sets chosen for simulations in this paper (see Table 1) are meant to reproduce the qualitative shape of a Boltzmann inversion of the statistical distributions coming

Table 1. Potential Energy Parameters[a]

structure	k_φ, n, δ	k_{corr}	γ_0	k1	k2	k3
α-helix	0.8, 3, 0.0	>0.4	1.588	100.0	295.3	218.0
β-sheet	0.8, 3, 0.0 and 2.6, 1, 0.0	0.6	1.588	70.0	308.5	302.2

[a] Different secondary structure propensities are modeled using the reported values. n = multiplicity of dihedral term; [γ_0], [δ] = rad; [k_φ], [k_{corr}] = kcal mol^{-1}; [k1] = kcal mol^{-1} rad^{-2}; [k2] = kcal mol^{-1} rad^{-3}; [k3] = kcal mol^{-1} rad^{-4}.

from triplets of amino acids with high α and high β propensities, respectively.

2.3. Dihedral Correlation Potential. The final modification of the molecular Hamiltonian consists of defining a correlation potential term for consecutive dihedrals:

$$V_{corr}(\varphi_i, \varphi_{i+1}) = k_{corr}(\varphi_i - \varphi_{i+1})^2 \qquad (12)$$

This effective potential is meant to account for all of those steric and electrostatic interactions that would be present among those atoms that are represented by neighboring CG beads, and which result in a decreased rigidity of the chain. With such a potential, structures which are characterized by large variations in consecutive dihedral angles will pay for extra potential energy. In particular, the potential in eq 12 disfavors randomly collapsed structures, and it enhances the formation of ordered structures that show local conformational self-identity along the sequence. Rather, a minimal number of deformations (e.g., turns) can be allowed whenever they account for any favorable pairing of structural elements, like in β-hairpin or α-helical assemblies. Different values of k_{corr} can in principle be used for different portions of the chain, to represent local variations in its chemical-physical nature.

2.4. Choice of Simulation Parameters. Different parameter sets where chosen, as reported in Table 1, representing different physical natures of the peptide chain. In particular, we define increasing rigid polymers by progressively increasing the values of k_{corr}, and we modulate the α or β propensity by modulating the shape of the bending and torsional potentials (see Table 1). The van der Waals parameters were modeled as alanine beads of the MARTINI[17] potential (equilibrium distance, 5.28 Å; binding energy, 0.836 kcal mol^{-1}). Solvent−solute interactions were also taken from the MARTINI potential (equilibrium distance, 5.28 Å; binding energy, 0.741 and 1.195 kcal mol^{-1} for solute−solvent and solvent−solvent interactions, respectively). Dihedral potentials are in general expressed as a combination of multiple cosine terms. The dipole−dipole, bending, dihedral, and dihedral correlation potential terms account, on average, for ≈−0.29, +0.21, +0.13, and +0.02 kcal mol^{-1} per bead, respectively (data taken from simulation of the short helix, see below). Stretching distances were constrained to their equilibrium value (3.8 Å). In our simulations, interactions within consecutive dipoles were excluded. All interactions were screened by a relative global dielectric constant of 10.

2.5. Molecular Dynamics Simulations. Molecular dynamics simulations of different test systems were performed. In particular, we first tested the structural stability of 10-aa-long peptides in initial helical conformation and that of 25-
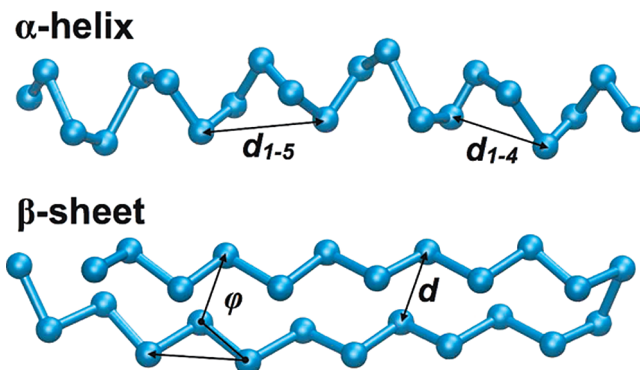

Figure 4. Structural parameters for α-helices and β-sheets. d_{1-5} and d_{1-4} are the distances between the helical pitches of five and four consecutive beads, respectively. d is the interstrand distance, and ϕ is the interstrand torsional angle.

aa-long peptides in initial antiparallel β-sheet conformation for different values of the potential parameters. This part of the work allowed us to define basins of stability for α-helices and β-sheet structural elements. Then, longer (25 to 30 aa) peptides in the helical conformation were studied, to investigate the capabilities of our model in predicting structural reorganizations of the polymer.

The systems were first minimized by 2000 steps of conjugate gradients; then they were slowly heated up from 0 to 300 K in 10 ns and simulated in the canonical ensemble on the nanosecond to microsecond time scales. We tested the use of different timesteps, starting from 1 fs and progressively increasing them. We found our simulations to be consistent among themselves for timesteps up to 20 fs. For larger timesteps, problems in conservation of the energy start to arise, leading eventually to inconsistent simulations.

Our potential function was implemented in the LAMMPS suite of programs[67−69] for MD, all simulations were run with the same program.

3. Results

Molecular dynamics runs were performed on model systems representing fundamental secondary and supersecondary structure elements. In this way, we tested the capability of our new potential function of predicting such motifs as locally stable structures. We have compared our results to those obtained with the MARTINI force field,[17] which is, at present, one of the most successful and reliable CG force fields proposed in the literature.

Short α-Helices. We simulated helical peptides composed of 10 units for 1.5 μs. Helices are stable in a regime of k_{corr} > 0.4 kcal mol^{-1} rad^{-2} and for bending potentials which define a strong helical propensity (Table 1). The helical structures remain stable along all of the simulation times, with average values for the 1−4 and 1−5 pitches in the helical turn of d_{1-4} = 5.2 ± 0.2 Å and d_{1-5} = 5.9 ± 0.5 Å, respectively (Figure 4). The structural data are in good agreement with the experimental measurement as obtained from PDB structures (Table 2).

Simulations with different dihedral potential intensities show the same behavior and do not lead to significant

Table 2. Structural Parameters for α-Helices and β-Sheets in CG MD[a]

	present results	PDB exptl. values
α-helices	$d_{1-4} = 5.2 \pm 0.2$ $d_{1-5} = 5.9 \pm 0.5$	$d_{1-4} = 5.1 \pm 0.1$ $d_{1-5} = 6.2 \pm 0.1$
β-sheets	$d_{is} = 5.1 \pm 0.1$ $\varphi_{is} = 91 \pm 8$	$d_{is} = 4.8 \pm 0.1$ $\varphi_{is} = 90 \pm 6$

[a] Values for 1−4 and 1−5 helical pitches and interstrand distances (d_{1-4}, d_{1-5}, d_{is}, respectively) are reported in Å; values for interstrand torsional angles are given in degrees.

differences in their results. The stability of the structure is not affected by variations of the dihedral energy term. The structures fluctuate with an average rmsd of 1.2 ± 0.2 Å from the initial structure, which corresponds to a mobility similar to that found using the MARTINI force field.[17]

Antiparallel β-Sheets. Molecular dynamics simulations of two antiparallel strands kept their average structural parameters close to optimal values. In particular, the interstrand distance and orientation (Figure 4) are $d = 5.1 \pm 0.1$ Å and $\phi = 91 \pm 8°$. These relevant structural parameters are in very good agreement with experimental values (Table 2). The β-hairpin structure remains within a rmsd as small as 1.6 ± 0.2 Å from the initial native geometry. In particular, the structure shows conserved eclipsed configurations between corresponding C_α's in the two strands and the correct overall average parallel orientation of their planes (Table 2). β-sheet geometries are stabilized by dihedral potential terms with an absolute minimum at $\varphi = 180°$, which corresponds to defining a stiff rigidity for the chain. Structural features characterizing the β-sheet pair cannot be easily described using standard CG models with radial nonbonded interactions. In fact, radial potentials do not discriminate among all those configurations that keep a similar number of contacts between the two strands (e.g., structures with wrongly oriented strand planes or with coiled strands). This results in a disordered ensemble of structures, different from the native one, which are found during CG MD runs with the MARTINI-ff and present a higher rmsd (3.0 ± 0.3 Å). The only way of overcoming this problem would be to explicitly define contact potentials between the two strands, which would, on the other hand, bias the structure. In our model, the presence of dipole interactions among strands automatically introduces preferential directionality, thus, producing the right geometry without the need of external biases.

Long α-Helices. Single long α-helices with nonspecific aa sequences are usually not stable and tend to undergo conformational transitions leading to supersecondary structure elements like, for example, helix−coil−helix or β-hairpin motifs.[70] We have tested the behavior of our backbone potential by simulating a 25-aa-long chain starting from an α-helical conformation. Attributing parameters previously found to produce stable helices, we find that the initial structure corresponds to a local minimum of the energy, but MD simulations at 300 K univocally lead to rapid conformational transition, to form helix−loop−helix structures (Figure 5). Such transition is induced by the attractive coupling between the finite electrostatic dipoles associated with the two antiparallel helical portions formed when the initial structure breaks. Our protocol, in fact, intrinsically
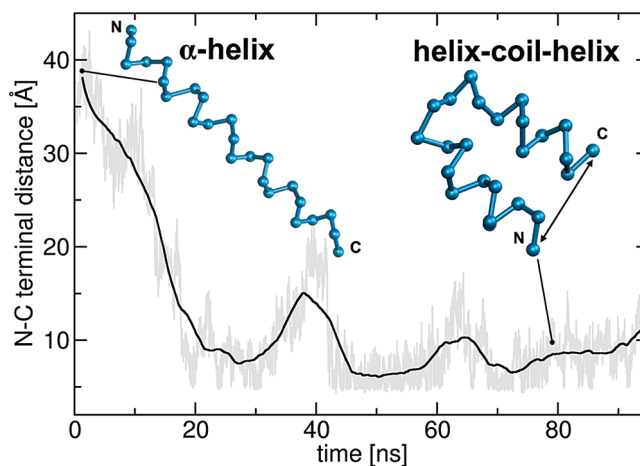

Figure 5. Helix−coil−helix formation. The N−C terminal distance as a function of the simulation time for a 25-aa-long chain. Averaged distances are represented with a solid black line. The insets show the conformational transition undergone by the initial helical structure into a supersecondary helix−coil−helix structure.

takes into account the interaction between macromolecular dipoles induced by backbone helical packing and therefore is able to correctly describe helical N-to-C polarity, which is a fundamental ingredient for the correct assembling of helical bundles. We note that in our simulations the terminal residues were not bringing any zwitterionic charge. Therefore, no instabilities due to attraction of the ends of the chain were present. The new structure is stable for values of k_{corr} of $0.4-0.5$ kcal mol^{-1} rad^{-2}. For lower values of k_{corr}, instead, we find that, after formation of the helix−coil−helix motif, the two helices tend to break again, yielding collapsed structures that resemble a four-helix bundle (which cannot be fully formed due to the shortness of the peptide chain).

α-Helix−β-Hairpin Transition. Our potential was tested toward the possibility of describing α−β structural transitions. We used again the 25-aa-long α-helical peptide as a starting conformation and potential parameters, as in Table 1, which reproduce stable β-sheet structures. Within such potential parameters, the α-helix is only marginally stable and rapidly unfolds when heated up to 300 K. The peptide chain tends to stretch into an extended structure, which eventually bends to pair its two arms, leading to a β-hairpin structure (Figure 6). For smaller values of k_{corr}, the reorganization into a three-antiparallel-sheet structure is also observed.

β-Helix. Finally, we tested the stability of parallel β-sheets, by modeling an 81-aa-long peptide in a β-helical conformation. We used the core structure of the antifreeze protein from *Choristoneura fumiferana* (pdb code: 1M8N[71]) as a template model (Figure 7). Parallel β-sheet pairings are not characterized by optimal dipole alignment, and therefore they fold only in the presence of other stabilizing factors, for example, side-chain packing in supersecondary assemblies. In fact, the template protein presents a compact hydrophobic core in the middle of the helix, which stabilizes the whole structure. Therefore, we modeled our helix by filling the inner space with nonbonded hydrophobic beads with a VdW radius of 2.0 Å. We find that, apart from an initial sudden shrinking
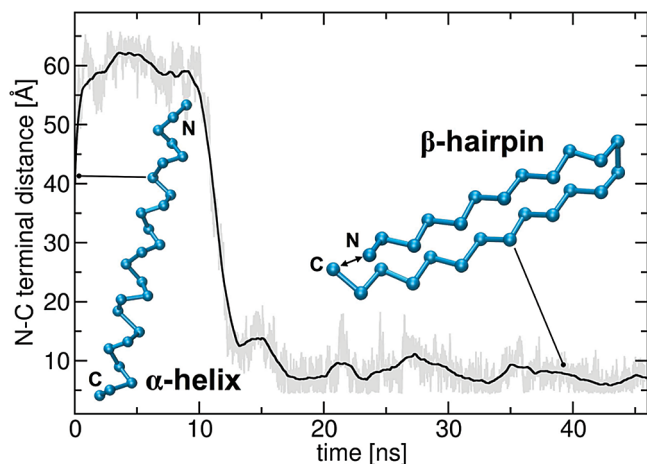
A Nonradial Coarse-Grained Potential for Proteins

J. Chem. Theory Comput., Vol. 6, No. 1, 2010 **321**

Figure 6. α-helix$-\beta$-hairpin transition. The N$-$C terminal distance as a function of the simulation time for a 25-aa-long chain. Averaged distances are represented with a solid black line. The insets show the conformational transition from the initial helical configuration to a β-hairpin structure.
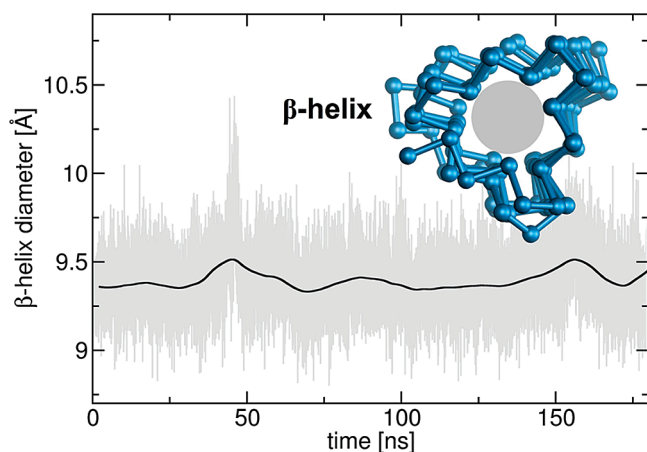

Figure 7. β-Helix structure. Diameter of a 81-aa-long peptide in a β-helical conformation as a function of the simulation time. The equilibrated structure is shown in the inset (PDB code: 1M8N).[71] The average diameter value remains stable during the simulation time.

of the structure, which has to be attributed to a nonoptimal space-filling by the hydrophobic-core mimicking beads, our model structure remains stable along the 160 ns of MD (Figure 7). Importantly, we see that the major deformations of the structure are associated with local distortions occurring at the vertices of the triangular assembly. The three β-sheet edges, on the contrary, keep all their contacts paired, as in the canonical structure of parallel β-sheets.

4. Discussion

Published data based on toy potentials and statistical mechanics modeling[72] showed that the minimal ingredients required to reproduce folded states of proteins are backbone flexibility and relative hydrophobicity of the chain, while H-bonding is required to ensure diversification, modulation, and ordered assembly of folded motifs. More generally, structuring of polymer chains can be associated with an

induced coupling between consecutive Frenet terns, that is, of the relative orientations of the local reference systems associated with each bead.[73] While CG models based on molecular potentials (eq 1) can easily treat hydrophobicity (e.g., through relative solute$-$solute, solute$-$solvent, and solvent$-$solvent nonbonded interactions), both H-bonding and flexibility remain a more complex issue. In fact, H-bonds are intrinsically determined by the relative spatial orientation of objects (atoms) smaller than the resolution of the same CG models. The amino acid chain flexibility, at the all-atom level, is determined by the mixture of bonded and nonbonded energy terms which drive interactions of atoms in neighboring amino acids. This means that energy contributions for bonded interactions in CG should be able to represent such a mixture of both bonded and nonbonded interactions from the all-atom picture. In fact, in the CG picture, the pseudo-bonds which link the backbone beads are connecting objects that, in the all-atom picture, can be topologically distant. Therefore, simple harmonic approximations for bonded interactions, like those used in all-atom molecular Hamil-tonians, can be too limiting for a correct description of the physics of the amino acid chain.

Our model potential for the protein backbone introduces an effective directional potential which mimics the presence of permanent electrostatic dipoles at peptide bond locations. Such directional interaction enables the reproduction of, at short-range, the local structure of contacts formed by the H-bonding network in all-atom systems, which is funda-mental to defining secondary structure elements (Figure 4, Table 1). At the same time, it introduces long-range interactions which are able to drive the recognition and pairing of elements and, thus, formation of supersecondary structure assemblies, like in the case of the collapse of long helical structures into helix$-$coil$-$helix arrangements (Figure 5). Such assembly is favored by the presence of macromo-lecular dipoles associated to each helix, which pair in an energetically advantageous configuration. Such a feature is well represented by our model; in fact, within its representa-tion, unspecific packing of backbone beads does not neces-sarily lead to an energy gain, and therefore it is not necessarily stabilized. This is confirmed by the results from our simulations, where we see the spontaneous assembly of ordered helix$-$turn$-$helix (Figure 5) and β-hairpin (Figure 6) motifs. In particular, our model predicts a very good relative orientation of two paired β-strands with respect to that predicted by potentials based on radial nonbonded interactions only (see Results section).

The improved performances of our model can be related to the intrinsic anisotropic character of the electrostatic potential of proteins. In fact, the nonbonded potential terms for CG beads have to effectively describe, among the others, the electrostatic interactions between the different groups of atoms they represent. As the electrostatic potential of a group of atoms, expressed as a function of a single center, is formally defined by its multipolar expansion, it is reasonable to think that a fully transferable radial potential would be particularly suited in those cases where CG beads map groups of atoms with a non-negligible total charge Q_{tot}, or in the assumption that characteristic times for multipole reorganiza-

tion are much faster than the typical times of CG dynamics. On the contrary, the protein backbone is characterized by the presence of strong permanent dipoles localized at peptide bonds between C_α atoms, an orientation that is not free but directly correlated to the local conformational geometry (Figure 3). As the conformation of the polymer is a piece of information explicitly present at the CG-resolution, directional nonbonded contributions due to the presence of permanent dipoles remain a relevant quantity to describe the physics of proteins.[74]

More sophisticated modeling for bonded terms than the harmonic approximation also turns out to be useful for the stabilization and modulation of secondary structure elements. In particular, we make use of a double-well potential for bending, representing the two principal stable basins in the Ramachandran plot. Moreover, we introduce a correlation potential energy term for consecutive dihedrals. These modifications ensure a direct control on the flexibility properties of the polymer. Specifically, such potential disfavors random orientations of the chain, which would eventually lead to collapsed structures, promoting structures characterized by conformational self-identity along the chain, like in extended (e.g., β-strands) or coiled structures (e.g., helical motifs). For parameters corresponding to highly flexible polymers ($k_{corr} < 0.4$ kcal mol^{-1} rad^{-2}), random collapsed structures tend to appear. On the contrary, for high values of k_{corr}, combined with strong dihedral potentials of multiplicity $n = 1$ and $k_\varphi > 2.8$ kcal mol^{-1}, all initial structures tend to form single, long, stretched motifs. Our findings on the correlation between flexibility and structure stability are in very good qualitative agreement with the phase diagram reported in ref 72.

Our potential energy term for nonbonded interactions does not need to be defined according to the starting secondary structure; rather, it allows for structural reorganizations or deformations which can lead to energetically more favorable assemblies. This was seen in our simulations of long α-helical structures, where, starting from the same conformation, for two peptides with different defined secondary structure propensities, we observed the spontaneous formation of helix−coil−helix or β-hairpin motifs, respectively. This is also confirmed by the structural deformations seen in the β-helix simulations, where the strain of the structure due to nonoptimal modeling of the hydrophobic core remains localized at the ends of the β-sheets, keeping ordered elements in their place. We remark on the fact that we did not define different specific potentials for the beads in the sheets and in the turns; rather, the system itself finds it energetically convenient to pay for some strain in the turn regions, while keeping the strands paired, as expected. The possibility of explicitly defining bead-specific bending, dihedral, and correlation terms makes possible the future development of new CG force fields based on the proposed functional form, able to incorporate both local flexibility and secondary-structure propensity into the backbone potential.

The presented algorithm allows for a full description of dipole locations and orientations as functions of the coordinates of the C_α beads, and, thus, representation of their interactions with forces acting on the same C_α beads.

Therefore, it does not introduce further degrees of freedom to the system, limiting the increase of computational time to the explicit evaluation of the dipole−dipole interactions. The possibility of reconstructing structural features from the C_α coordinates in proteins was already shown in the case of side-chain localization[75] and effectively used to improve the performance of CG network models.[76,77] The dipolar interactions, within our model, have to be considered as an effective potential which represents, through an explicit potential energy term, the energy gain in the formation of ordered contacts in a folded protein backbone. Its functional form is such that it allows it to be easily incorporated into any CG representation of proteins which make use of C_α beads. In this respect, the intensity of the dipoles, as well as that of the interactions in general, can be in principle rescaled or re-equilibrated to optimally match pre-existing CG models or the multiscaling criteria used to develop the original CG potential.

The use of a dipole that has a definition consistent with the corresponding permanent electrostatic dipole of a protein backbone has specific advantages. In fact, we had already shown that, within a very similar approach,[65] electrostatic potentials of proteins can be reproduced by CG structural information, in particular by accounting for the contribution only of backbone and side-chain permanent dipoles. Therefore, such multipolar definition of CG electrostatics can be helpful in describing more reliably protein−protein assemblies or protein−ligand recognition in multiscale frameworks.

5. Concluding Remarks

In conclusion, our protocol is able to introduce backbone dipole interactions in CG MD simulations of proteins, which, in turn, allows for an unbiased representation of stable secondary structure elements, as well as prediction of their dynamical arrangement into supersecondary structure assemblies. The proposed directional potential has a general form and can in principle be coupled to existing CG protocols (single or multibead), which retain structural information of the C_α trace of proteins. Together with modifications of the bonded energy terms, with respect to simplest harmonic approximations (in particular, of bending and dihedrals), our scheme constitutes a promising step toward the development of a more universal and transferable CG force field for proteins, not plagued with knowledge-based biases on the secondary structure. In particular, the directionality of the backbone structure is directly connected to the bending angle. Thus, the secondary structure propensity of amino acids, which is chemically encoded in the side-chain, can be elegantly controlled by using the backbone bending potential as an order parameter. The present results anticipate the development of a new CG force field able to take into account the intrinsic anisotropy of protein structures, leading to an improved description of the structural and dynamic properties of protein assemblies and networks.

A Nonradial Coarse-Grained Potential for Proteins

J. Chem. Theory Comput., Vol. 6, No. 1, 2010 **323**

References

(1) Karplus, M.; McCammon, J. *Nat. Struct. Biol.* **2002**, *9*, 646–652.

(2) Hornak, V.; Abel, R.; Okur, A.; Strockbine, B.; Roitberg, A.; Simmerling, C. *Proteins* **2006**, *65*, 712–725.

(3) Perez, A.; Marchan, I.; Svozil, D.; Sponer, J.; Cheatham, T.; Laughton, C.; Orozco, M. *Biophys. J.* **2007**, *92*, 3817–3829.

(4) Klein, M. L.; Shinoda, W. *Science* **2008**, *321*, 798–800.

(5) Levitt, M.; Warshel, A. *Nature* **1975**, *253*, 694–698.

(6) Go, N.; Scheraga, H. A. *Macromolecules* **1976**, *9*, 535–542.

(7) Tanaka, S.; Sheraga, H. A. *Macromolecules* **1976**, *9*, 945–950.

(8) Shelley, J. C.; Shelley, M. Y.; Reeder, R. C.; Bandyopadhyay, S.; Klein, M. L. *J, Phys. Chem. B* **2001**, *105*, 4464–4470.

(9) Shelley, J. C.; Shelley, M. Y.; Reeder, R. C.; Bandyopadhyay, S.; Klein, M. L. *J, Phys. Chem. B* **2001**, *105*, 9785–9792.

(10) Saiz, L.; Klein, M. L. *Acc. Chem. Res.* **2002**, *35*, 482–489.

(11) Shinoda, W.; DeVane, R.; Klein, M. L. *Soft Matter* **2008**, *4*, 2454–2462.

(12) Shinoda, W.; Devane, R.; Klein, M. L. *Mol. Simulat.* **2007**, *33*, 27–36.

(13) Marrink, S. J.; de Vries, A.; Mark, A. *J. Phys. Chem. B* **2004**, *108*, 750–760.

(14) Brannigan, G.; Lin, L. C. L.; Brown, F. L. H. *Eur. Biophys. J.* **2006**, *35*, 104–124.

(15) Shi, Q.; Izvekov, S.; Voth, G. A. *J. Phys. Chem. B* **2006**, *110*, 15045–15048.

(16) Lu, L.; Voth, G. A. *J. Phys. Chem. B* **2009**, *113*, 1501–1510.

(17) Monticelli, L.; Kandasamy, S.; Periole, X.; Larson, R.; Tieleman, D.; Marrink, S. J. *J. Chem. Theory Comput.* **2008**, *4*, 819–834.

(18) Arkhipov, A.; Freddolino, P.; Imada, K.; Namba, K.; Schulten, K. *Biophys. J.* **2006**, *91*, 4589–4597.

(19) DeVane, R.; Shinoda, W.; Moore, P. B.; Klein, M. L. *J. Chem. Theory Comput.* **2009**, *5*, 2115–2124.

(20) Basdevant, N.; Borgis, D.; Ha-Duong, T. *J. Phys. Chem. B* **2007**, *111*, 9390–9399.

(21) Voltz, K.; Trylska, J.; Tozzini, V.; Kurkal-Siebert, V.; Langowski, J.; Smith, J. *J. Comput. Chem.* **2008**, *29*, 1429–1439.

(22) Trylska, J.; Tozzini, V.; Chang, C.; McCammon, J. *Biophys. J.* **2007**, *92*, 4179–4187.

(23) Trovato, F.; Tozzini, V. *J. Phys. Chem. B* **2008**, *112*, 13197–13200.

(24) Villa, E.; Balaeff, A.; Schulten, K. *Proc. Natl. Acad. Sci. U. S. A.* **2005**, *102*, 6783–6788.

(25) Ayton, G. S.; Voth, G. A. *Curr. Opin. Struct. Biol.* **2009**, *19*, 138–144.

(26) Arkhipov, A.; Yin, Y.; Schulten, K. *Biophys. J.* **2008**, *95*, 2806–2821.

(27) Treptow, W.; Marrink, S. J.; Tarek, M. *J. Phys. Chem. B* **2008**, *112*, 3277–3282.

(28) Yelimov, S.; van der Giessen, E.; Onck, P.; Marrink, S. J. *Biophys. J.* **2008**, *94*, 2994–3002.

(29) Marrink, S. J.; Mark, A. *J. Am. Chem. Soc.* **2003**, *125*, 11144–11145.

(30) Risselada, H.; Marrink, S. J. *Proc. Natl. Acad. Sci. U. S. A.* **2008**, *105*, 17367–17372.

(31) Bond, P.; Wee, C.; Sansom, M. S. P. *Biochemistry* **2008**, *47*, 11321–11331.

(32) Carpenter, T.; Bond, P.; Khalid, S.; Sansom, M. S. P. *Biophys. J.* **2008**, *95*, 3790–3801.

(33) Marrink, S. J.; de Vries, A. H.; Tieleman, D. P. *BBA Biomembr.* **2009**, *1788*, 149–168.

(34) Balali-Mood, K.; Bond, P. J.; Sansom, M. S. P. *Biochemistry* **2009**, *48*, 2135–2145.

(35) Klingelhoefer, J. W.; Carpenter, T.; Sansom, M. S. P. *Biophys. J.* **2009**, *96*, 3519–3528.

(36) Sherwood, P.; Brooks, B. R.; Sansom, M. S. P. *Curr. Opin. Struct. Biol.* **2008**, *18*, 630–640.

(37) Tozzini, V.; McCammon, J. *Chem. Phys. Lett.* **2005**, *413*, 123–128.

(38) Tozzini, V.; Trylska, J.; Chang, C.; McCammon, J. *J. Struct. Biol.* **2007**, *157*, 606–615.

(39) Tozzini, V.; McCammon, J. *Protein Sci.* **2004**, *13*, 194–194.

(40) Arkhipov, A.; Freddolino, P.; Schulten, K. *Structure* **2006**, *14*, 1767–1777.

(41) Delle Site, L.; Abrams, C. F.; Alavi, A.; Kremer, K. *Phys. Rev. Lett.* **2002**, *89*, 156103.

(42) Villa, E.; Balaeff, A.; Mahadevan, L.; Schulten, K. *Multiscale Modell. Simulat.* **2004**, *2*, 527–553.

(43) Neri, M.; Anselmi, C.; Cascella, M.; Maritan, A.; Carloni, P. *Phys. Rev. Lett.* **2005**, *95*, 218102.

(44) Lyman, E.; Ytreberg, F. M.; Zuckerman, D. M. *Phys. Rev. Lett.* **2006**, *96*, 028105.

(45) Lyman, E.; Zuckerman, D. M. *J. Chem. Theory. Comput.* **2006**, *2*, 656–666.

(46) Izvekov, S.; Voth, G. A. *J. Phys. Chem. B* **2005**, *109*, 2469–2473.

(47) Izvekov, S.; Voth, G. A. *J. Chem. Theory Comput.* **2006**, *2*, 637–648.

(48) Ayton, G. S.; Voth, G. A. *J. Struct. Biol.* **2007**, *157*, 570–578.

(49) Ensing, B.; Nielsen, S. O.; Moore, P. B.; Klein, M. L.; Parrinello, M. *J. Chem. Theory Comput.* **2007**, *3*, 1100–1105.

(50) Heyden, A.; Truhlar, D. G. *J. Chem. Theory Comput.* **2008**, *4*, 217–221.

(51) Zacharias, M. *J. Chem. Theory Comput.* **2008**, *4*, 477–487.

(52) Ayton, G.; Noid, W.; Voth, G. A. *Curr. Opin. Struct. Biol.* **2007**, *17*, 192–198.

(53) Cascella, M.; Dal Peraro, M. *CHIMIA* **2009**, *63*, 14–18.

(54) Tozzini, V. *Curr. Opin. Struct. Biol.* **2005**, *15*, 144–150.

(55) Noid, W.; Chu, J.; Ayton, G.; Krishna, V.; Izvekov, S.; Voth, G. A.; Das, A.; Andersen, H. *J. Chem. Phys.* **2008**, *128*, 244114.

(56) Noid, W.; Liu, P.; Wang, Y.; Chu, J.; Ayton, G.; Izvekov, S.; Andersen, H.; Voth, G. A. *J. Chem. Phys.* **2008**, *128*, 244115.

(57) Bereau, T.; Deserno, M. *J. Chem. Phys.* **2009**, *130*, 235106.

(58) Maupetit, J.; Tuffery, P.; Derremaux, P. *Proteins* **2007**, *69*, 394–408.

(59) Gopal, S. M.; Mukherjee, S.; Cheng, Y.-M.; Feig, M. *Proteins* **2009**, DOI: 10.1002/prot.22645.

(60) Liwo, A.; Oldziej, S.; Pincus, M. R.; Wawak, R. J.; Rackovsky, S.; Scheraga, H. A. *J. Comput. Chem.* **1997**, *18*, 849–873.

(61) Liwo, A.; Pincus, M. R.; Wawak, R. J.; Rackovsky, S.; Oldziej, S.; Scheraga, H. A. *J. Comput. Chem.* **1997**, *18*, 874–887.

(62) Liwo, A.; Oldziej, S.; Czaplewski, C.; Kozlowska, U.; Scheraga, H. A. *J. Phys. Chem. B* **2004**, *108*, 9421–9438.

(63) Liwo, A.; Khalili, M.; Scheraga, H. A. *Proc. Natl. Acad. Sci. U. S. A.* **2005**, *102*, 2362–2367.

(64) Májek, P.; Elber, R. *Proteins* **2009**, *76*, 822–836.

(65) Cascella, M.; Neri, M. A.; Carloni, P.; Dal Peraro, M. *J. Chem. Theory Comput.* **2008**, *4*, 1378–1385.

(66) van Gunsteren, W. F.; Billeter, S. R.; Eising, A. A.; Hünenberg, P. H.; Krüger, P.; Mark, A. E.; Scott, W. R. P.; Tironi, I. G. *Biomolecular Simulation: The GROMOS96 Manual and User Guide*; Hochschulverlag AG an der ETH Zurich: Zurich, Switzerland, 1996.

(67) LAMMPS Molecular Dynamics Simulator. http://lammps.sandia.gov/ (accessed November 25th, 2009).

(68) Plimpton, S. J. *J. Comp. Phys.* **1995**, *117*, 1–19.

(69) Plimpton, S. J.; Pollock, R.; Stevens, M. Particle-Mesh Ewald and rRESPA for Parallel Molecular Dynamics Simulations. In *Proceedings of the Eighth SIAM Conference on Parallel Processing for Scientific Computing* Minneapolis, 1997; SIAM, ISBN 0-89871-395-1.

(70) Forood, B.; Perezpaya, E.; Houghten, R.; Blondelle, S. *Biochem. Biophys. Res. Commun.* **1995**, *211*, 7–13.

(71) Leinala, E.; Davies, P.; Doucet, D.; Tyshenko, M.; Walker, V.; Jia, Z. *J. Biol. Chem.* **2002**, *277*, 33349–33352.

(72) Hoang, T. X.; Trovato, A.; Seno, F.; Banavar, J. R.; Maritan, A. *Proc. Natl. Acad. Sci. U. S. A.* **2004**, *101*, 7960–7964.

(73) Banavar, J. R.; Cieplak, M.; Hoang, T. X.; Maritan, A. *Proc. Natl. Acad. Sci. U. S. A.* **2009**, *106*, 6900–6903.

(74) Warshel, A.; Russell, S. *Q. Rev. Biophys.* **1984**, *17*, 283–422.

(75) Park, B.; Levitt, M. *Proteins* **1996**, *258*, 367–392.

(76) Micheletti, C.; Carloni, P.; Maritan, A. *Proteins* **2004**, *55*, 635–645.

(77) Neri, M.; Cascella, M.; Micheletti, C. *J. Phys., Condens. Matter* **2005**, *17*, S1581–S1593.

JCTC Journal of Chemical Theory and Computation

On the Validation of Molecular Dynamics Simulations of Saturated and *cis*-Monounsaturated Phosphatidylcholine Lipid Bilayers: A Comparison with Experiment

David Poger*,[†] and Alan E. Mark[†,‡]

School of Chemistry and Molecular Biosciences and Institute for Molecular Bioscience, University of Queensland, Brisbane St Lucia, QLD 4072, Australia

Abstract: Molecular dynamics simulations of fully hydrated pure bilayers of four widely studied phospholipids, 1,2-dilauroyl-*sn*-glycero-3-phosphocholine (DLPC), 1,2-dimyristoyl-*sn*-glycero-3-phosphocholine (DMPC), 1,2-dioleoyl-*sn*-glycero-3-phosphocholine (DOPC), and 2-oleoyl-1-palmitoyl-*sn*-glycero-3-phosphocholine (POPC) using a recent revision of the GROMOS96 force field are reported. It is shown that the force field reproduces the structure and the hydration of bilayers formed by each of the four lipids with high accuracy. Specifically, the solvation and the orientation of the dipole of the phosphocholine headgroup and of the ester carbonyls show that the structure of the primary hydration shell in the simulations closely matches experimental findings. This work highlights the need to reproduce a broad range of properties beyond the area per lipid, which is poorly defined experimentally, and to consider the effect of system size and sampling times well beyond those commonly used.

1. Introduction

Pure phospholipid bilayers have been extensively studied as models for biomembranes.[1,2] Although lipids may exhibit a wide diversity of phases (such as the gel and liquid-crystalline phases), the most biologically relevant state under physiological conditions is the fluid phase (alternatively named the liquid crystal, L_α phase or, more correctly, the liquid-disordered phase L_d) in which the lipid chains are flexible and disordered. The fluidity of membranes precludes the accurate determination of their structure at an atomic level.[1] As a consequence, theoretical techniques, especially molecular dynamics (MD) simulations, have contributed greatly to our understanding of the structure and the dynamical properties of membrane systems as well as to the interpretation of experimental results. The basic features of the mechanisms of fundamental processes, such as vesicle formation[3] and fusion,[4] peptide-induced[5,6] and peptide-free[7] pore formation, ion permeation through membranes,[8−12] lipid flip-flop,[13,14] spontaneous lipid aggregation into a bilayer,[15]

and formation of gel[16] and ripple[17] phases, have been modeled using MD simulations.

The quality and the validity of the results from such MD simulation studies depend heavily on the fidelity with which the underlying model, or force field, used describes the interatomic interactions. Biomolecular force fields are being continuously improved and updated. Currently, the most widely used force fields for lipid systems are the all-atom CHARMM[18,19] and the united-atom GROMOS96[20] force fields and the parameter set proposed by Berger et al.[21] The latest revision of the GROMOS96 force field (parameter set 53A6)[22] was based on the reproduction of the solvation properties (free enthalpies of hydration) of small molecule analogues of biomolecules. The G53A6 parameter set has been extensively studied and validated for the simulation of peptides, proteins and DNA in water.[23,24] However, it failed to reproduce the properties of phosphatidylcholine lipids—a major component of biological membranes—in the fluid phase.[25] We recently reported a correction of the G53A6 parameter set (G53A6$_L$), which greatly improved the fluidity of 1,2-dipalmitoyl-*sn*-glycero-3-phosphocholine (DPPC) lipid bilayers.[25] Specifically, the repulsion between the choline methyl groups and the nonester phosphate oxygens was

* E-mail: d.poger@uq.edu.au.
† School of Chemistry and Molecular Biosciences.
‡ Institute for Molecular Bioscience.

Table 1. Summary of Published Areas Per Lipid A_L (in nm^2) Measured in Experiments and in Simulations in Fluid-Phase DLPC, DMPC, DPPC, DOPC and POPC Bilayers[a]

	lipid bilayer				
source	DLPC	DMPC	DPPC	DOPC	POPC
Experiment	0.69 (RT)[94]	0.58 (297)[95]	0.665 (317)[96]	0.70 (275)[97]	0.54 (275)[98]
	0.665 (293)[96]	0.67 (298)[99]	0.625 (318)[100]	0.82 (RT)[94]	0.63 (297)[95]
	0.572 (293)[101]	0.652 (300)[102]	0.643 (318)[100]	0.594 (296)[103]	0.683 (303)[48]
	0.594 (295)[104]	0.65 (300)[94]	0.57 (323)[105]	0.82 (298)[102]	0.66 (310)[106]
	0.687 (298)[102]	0.595 (303)[107]	0.712 (323)[102]	0.718 (298)[100]	0.62 (323)[98]
	0.71 (298)[99]	0.597 (303)[108]	0.69 (323)[99]	0.726 (298)[100]	
	0.626 (303)[65]	0.596 (303)[1]	0.71 (323)[94]	0.722 (303)[60]	
	0.632 (303)[47]	0.60 (303)[65]	0.717 (323)[109]	0.725 (303)[1]	
		0.660 (303)[28]	0.629 (323)[110]	0.721 (303)[32]	
		0.589 (303)[111]	0.633 (323)[65]	0.724 (303)[48]	
		0.606 (303)[47]	0.64 (323)[1]	0.674 (303)[29]	
		0.657 (309)[96]	0.642 (323)[64]	0.724 (303)[30]	
		0.600 (309)[101]	0.628 (323)[29]		
		0.622 (310)[104]	0.631 (323)[29]		
			0.695 (338)[104]		
Simulation literature	0.629 (303)[27 b]	0.577 (300)[112 d]	0.61 (323)[21 c]	0.651 (303)[38 c]	0.693 (298)[26 b]
	0.630 (303)[27 b]	0.577 (300)[113 d]	0.62 (323)[15 c]	0.65 (310)[87 f]	0.655 (300)[114 h]
	0.660 (323)[115 c]	0.618 (303)[27 b]	0.635 (323)[116 c]	0.658 (303)[27 b]	0.668 (303)[117 f]
		0.621 (303)[27 b]	0.66 (323)[118 c]	0.660 (303)[27 b]	
		0.592 (305)[119 e]	0.636 (323)[27 b]		
		0.602 (310)[120 b]	0.637 (323)[27 b]		
		0.558 (310)[87 f]	0.60−0.64 (325)[121 b]		
		0.625 (314)[26 b]	0.691 (325)[122 c]		
		0.611−0.635 (323)[37 c]	0.50−0.57 (325)[123 b]		
		0.656 (323)[124 c]	0.604 (325)[125 b]		
		0.57 (325)[86 b]	0.645 (325)[125 g]		
			0.623 (325)[26 b]		
			0.65 (350)[126 c]		
G53a6$_L$	0.632 (303)	0.616 (323)	0.631 (323)[25]	0.649 (303)	0.638 (303)

[a] Temperatures (in K) are indicated in parentheses (room temperature, RT). The data are presented in a chronological order for each temperature. [b–h] The force field parameter sets used in simulations are: [b] as described in the reference; [c] Berger parameters;[21] [d] AMBER94;[33] [e] CHARMM22;[36] [f] GAFF;[34] [g] CHARMM27;[19] and [h] CHARMM19[35] (partial charges from CHARMM22[36]).

enhanced by increasing the van der Waals radius of the atom of oxygens for this particular interaction. The structural properties of these bilayers (area and volume per lipid, electron density profiles, bilayer thickness and hydration, ordering and conformation of acyl chains) were in very good agreement with experiment. The self-assembly of DPPC into a bilayer in water was also simulated, demonstrating that a bilayer is the thermodynamically preferred state.

Two recently developed lipid force fields include alternative GROMOS96-derived parameter sets. In the parameter set proposed by Kukol[26] and based on the GROMOS 53A6 parameter set, the repulsion between DPPC molecules was enhanced by increasing the van der Waals radius of the two carbonyl carbons in the glycerol moiety. This new parameter set was used to model various phospholipid bilayers in a fluid phase, and it was found that the area per lipid (A_L) was reproduced correctly for 1,2-dimyristoyl-*sn*-glycero-3-phosphocholine (DMPC), 2-oleoyl-1-palmitoyl-*sn*-glycero-3-phosphocholine (POPC), and DPPC and for simulations up to 40 ns. In contrast, Chiu et al.[27] partly reparameterized the GROMOS96 43a1 parameter set, specifically the bond and the van der Waals parameters. The new parameter set called 43a1-S3 was used to simulate pure lipid bilayers of 1,2-lauroyl-*sn*-glycero-3-phosphocholine (DLPC), 1,2-dioleoyl-*sn*-glycero-3-phosphocholine (DOPC), DMPC or DPPC

in the fluid phase. The structural parameters of the bilayers calculated from the simulations, such as the area and the volume per lipid, the bilayer thickness, the deuterium order parameters, and the form factor, were in good agreement with experiment.

A_L is often used as the primary target property in the validation of lipid force field parameters to assess their ability to reproduce the correct phase of a membrane. However, there is considerable uncertainty in regard to the true value of A_L for a given lipid bilayer in the fluid phase.[1] In the last two decades, values of A_L derived from X-ray methods, NMR, and neutron diffraction have varied dramatically. For example, as shown in Table 1, in the case of the DMPC L_α phase, values of A_L as low as 0.596 nm^{2} [1] and as high as 0.660 nm^{2} [28] have been proposed in the last nine years. Similarly, recent values of A_L for the L_α phase of DOPC, published even by the same group of authors, range from 0.674 nm^{2} [29] to 0.724 nm^{2} [30] at 303 K. One reason for the scatter in the values of A_L obtained experimentally is that the area per lipid is frequently not measured directly but inferred from other quantities, such as order parameters from NMR spectroscopy.[31] Fluctuations in the structure of lipid bilayers, which are inherent in the bilayer being in a fluid phase, also make the accurate determination of this structural quantity difficult.[32]

Validation of Molecular Dynamics Simulations

J. Chem. Theory Comput., Vol. 6, No. 1, 2010 **327**

In contrast, the areas per lipid obtained in simulations appearing in the literature fall in a narrow range, regardless of the parameter set used (such as Berger,[21] GROMOS,[20] AMBER[33,34] or CHARMM)[18,19,35,36] and regardless of whether the simulations required or not the application of a surface tension to reproduce a value of the area per lipid compatible with a fluid bilayer. They are also seemingly independent of the length of the simulation and the extent to which the specific system was equilibrated. This is surprising as structural relaxation times in bilayer systems can be long (>100 ns) and, even at equilibrium, the area per lipid in simulations of systems (including relatively small ones) under periodic boundary conditions can fluctuate on a time scale of tens of nanoseconds.[37−39] The uniformity in the values from simulations is all the more striking given the variation in the methodology used, such as the method for the treatment of the long-range electrostatic interactions (particle mesh Ewald,[40,41] reaction field,[42] straight cutoff, or shift function).[43] Furthermore, corrections for the effects of undulations in the membrane and other artifacts inherent in the quantity measured experimentally are rarely—if ever—considered. Instead A_L is normally determined simply as the area of the simulation box divided by the number of lipids, not by modeling the experiment. It is also noteworthy that a reasonable agreement of a value of A_L obtained from simulations with experiment can be misleading. For example, a value of 0.56 nm^2 was found when simulating a hydrated DPPC bilayer with the original GROMOS 53A6 force field.[25] Despite this value being considered low, it is still almost within the range of experimental values listed in Table 1 (0.57−0.717 nm^2). However, other properties, such as the electron density profile across the bilayer, were characteristic of bilayers in a gel-like phase. The simulation of hydrated DLPC, DMPC, and POPC bilayers with the original GRO-MOS 53A6 force field showed a similar behavior (data not shown). Therefore, the ability of a parameter set to model a fluid bilayer must be judged based on a combination of several properties and not only on the area per lipid.

In this work, the ability of the G53A6$_L$ parameter set to reproduce the structural and hydration properties of pure bilayers of DLPC, DMPC, DOPC, and POPC in a L$_\alpha$ phase is examined. Together with DPPC bilayers, these phospholipids bilayers have been best characterized experimentally.[1,44] The myristoyl, oleoyl and palmitoyl acyl chains are also among the major fatty tails found in biologically relevant phospholipids.[45] For example, POPC is the most abundant lipid in animal cells.[46] The results from the simulations are compared to a wide range of structural properties (including the area and volume per lipid, the isothermal area compressibility modulus, the bilayer thickness, the deuterium order parameters, and the conformation of the acyl chains as well as the orientation and hydration of the headgroups and the carbonyls). The results demonstrate that the G53A6$_L$ parameter set is well suited for simulating a range of phosphatidylcholine lipids in the fluid phase. In addition, by collecting and tabulating the range of experimental results that have been obtained for these properties experimentally, we not only provide a measure of the uncertainty in these values but also underline the need to validate models against a range

of properties, in contrast to just a specific value of, for example, the area per lipid.

2. Methods

2.1. Simulation Systems. Four different systems were simulated. Each system consisted of a pure lipid bilayer containing either DLPC (12:0/12:0), DMPC (14:0/14:0), DOPC (18:1c9/18:1c9), or POPC (16:0/18:1c9). The lipids were described using the recently derived GROMOS 53A6 parameter set for phosphatidylcholines (G53A6$_L$).[25] Each system consisted of a hydrated 128-lipid bilayer (64 lipids in each leaflet) initially constructed by replicating a pair of lipids on an 8 × 8 grid. The area per lipid for each membrane was set initially to the experimentally measured area per lipid of the appropriate bilayer in the L$_\alpha$ phase. The areas per lipid used were 0.632 nm^2 for DLPC,[47] 0.606 nm^2 for DMPC,[47] 0.724 nm^2 for DOPC,[30] and 0.683 nm^2 for POPC.[48] Sufficient water molecules were added to give the desired level of hydration for fluid bilayers (with a ratio of 35−40 H$_2$O per lipid).

2.2. Simulation Parameters. All simulations were performed using the GROMACS package, version 3.2.1[49] under periodic boundary conditions in a rectangular box. The temperature of the system was maintained by independently coupling the lipids and the solvent to an external temperature bath at the reference temperature of 303 K with a coupling constant τ_T of 0.1 ps using a Berendsen thermostat.[50] The temperature for each system (303 K) was chosen above the gel→liquid-crystalline phase transition temperature (276.4, 296.9, 255.7, and 270.5 K for DLPC, DMPC, DOPC and POPC, respectively[51−54]). The pressure was kept at 1 bar in the lateral and normal directions by weakly coupling to a semi-isotropic pressure bath,[50] using an isothermal compressibility of 4.6 × 10^{-5} bar^{-1} and a coupling constant τ_P of 1 ps. Covalent bond lengths in the lipid were constrained using the LINCS algorithm.[55] The geometry of the simple point charge (SPC) water molecules[56] was constrained using SETTLE.[57] A 2-fs time step was used. Nonbonded interactions were evaluated using a twin-range cutoff scheme: interactions within the 0.8-nm short-range cutoff were calculated every step, whereas interactions within the 1.4-nm long-range cutoff were updated every 5 steps together with the pair list. A reaction-field correction was applied to the electrostatic interactions beyond the long-range cutoff[42] using a relative dielectric permittivity constant of 62, as appropriate for SPC water.[58] The force field parameters (G53A6$_L$) used to calculate the inter- and intramolecular interactions in lipids have been described previously.[25] This parameter set was derived from the GROMOS 53A6 force field.[22] Specifically, the repulsion between the choline methyls and the nonester phosphate oxygens was enhanced.

Each system was initially energy-minimized and then simulated at 50 K for 10 ps. The temperature was then increased gradually over 100 ps until the final simulation temperature was reached. Each system was simulated twice. The equilibration of the systems was monitored by examining the time evolution of the potential energy and the area per lipid of the system. Once the systems were equilibrated, data

Table 2. Overview of the Systems Simulated

lipid bilayer	total time (ns)	sampling time (ns)
DLPC	220, 350	120
DMPC	235, 245	120
DOPC	260, 300	120
POPC	245, 250	120

were collected for 120 ns. An overview of the simulations performed is given in Table 2.

3. Results

3.1. Area and Volume Per Lipid and Isothermal Area Compressibility Modulus. The area A_L per lipid was calculated from the lateral dimensions of the simulation box divided by the number of lipids in each leaflet. A_L is often used to judge the convergence of simulations of lipid bilayers. Similarly, the volume per lipid V_L was calculated by subtracting the volume occupied by the water molecules from the volume V of the simulation box:

$$V_L = \frac{V - n_w V_w}{n_L} \tag{1}$$

where n_L and n_w are the number of lipid (128) and water molecules, respectively. V_w is the volume per water molecule. V_w was determined from an independent 15-ns simulation of 1 728 SPC water molecules at 303 K and at a pressure of 1 bar. The value of V_w obtained was 3.09×10^{-2} nm^3. The average values of A_L and V_L from the simulations are reported in Table 3 together with the values obtained experimentally. As found previously in regard to DPPC, the G53A6 force field[25] yields are in good agreement with experiment for both properties for each of the systems simulated (DLPC, DMPC, DOPC, and POPC). The A_L's calculated from the simulations are in general agreement with the experimental values measured for fluid bilayers listed in Table 1. The simulated values of V_L fall within less than 2% of the experimental values.

The isothermal area compressibility modulus K_A is related to the fluctuations of A_L:

$$K_A = \frac{2k_B \langle T \rangle \langle A_L \rangle}{n_L \sigma_A^2} \tag{2}$$

where k_B is the Boltzmann constant, $\langle T \rangle$ is the average temperature, $\langle A_L \rangle$ is the average area per lipid and σ_A^2 is the variance associated to A_L. The average area compressibility moduli calculated from the simulations are given in Table 3, along with the alternative experimental values of 234 ± 23 for DMPC,[59] 188,[60] 254,[30] 265 ± 18[59] for DOPC, and $180-330$ mN·m^{-1}[61] for POPC in the fluid phase. As previously found in the case of the simulation of a fluid DPPC bilayer with the G53A6$_L$ parameter set,[25] the values of K_A derived from the simulations are about a factor of 2 larger than the experimental values. Nonetheless, they are consistent with previous estimates of K_A obtained from simulation studies, which were in the range of $200-600$ mN·m^{-1}.[37,43] The discrepancy with experiment is mainly due to the values of σ_A^2 being low, which leads to an overestimation of K_A.[37,62]

3.2. Electron Density Profiles. The structure of the bilayers was compared with the available X-ray scattering data by calculating an electronic density profile from the simulations. Ideally, one would directly compare the simulation and experimental data in reciprocal space but, to make the comparison direct, the spacing of the layers in the simulations would have to match those in the experiment exactly. Alternatively, the electron density profiles across the bilayer for DLPC, DMPC, DOPC, and POPC shown in Figure 1 are a straightforward, common way to compare qualitatively with experiment. The two main peaks in the density profiles are due to the phosphorus atoms, the most electron-dense atoms in the bilayers. The bilayer thickness can be characterized in several ways. The thickness D_{HH} of a bilayer is commonly taken as the distance between the two phosphate peaks. Alternatively, the Luzzati thickness D_B is defined as[1]

Table 3. Summary of Structural Properties of Bilayers at Equilibrium Measured in Experiments and in the Simulations[a]

lipid bilayer	A_L (nm^2)	V_L (nm^3)	K_A (mN·m^{-1})	D_{HH} (nm)	D_B (nm)
DLPC					
experiment	0.54−0.71[b]	0.991[47]	—	3.08[47]	3.14[47]
simulation	0.632 (3)	0.969 (1)	461 (96)	2.85 (1)	3.07 (4)
DMPC					
experiment	0.58−0.67[b]	1.0955[28]	234 (23)[59]	3.44[108]	3.63[47]
		1.101[1,47]		3.53[47]	3.69[1,108]
				3.60[1]	
simulation	0.616 (1)	1.077 (1)	475 (10)	3.27 (3)	3.49 (3)
DOPC					
experiment	0.594−0.82[b]	1.303[1,29,30,48,60]	188[60]	3.53[60]	3.59[1]
			254[30]	3.67[29,30]	3.61[32,60]
			265 (18)[59]	3.69[1]	3.87[29]
				3.71[32]	
simulation	0.649 (2)	1.284 (1)	389 (19)	3.63 (2)	3.89 (1)
POPC					
experiment	0.54−0.683[b]	1.223[98]	180−330[61]	3.70[48]	3.68[48]
		1.256[48]			
simulation	0.638 (4)	1.232 (1)	404 (55)	3.46 (4)	3.87 (1)

[a] A_L, area per lipid; V_L, volume per lipid; K_A, isothermal area compressibility modulus; D_{HH}, bilayer thickness; D_B, Luzzati bilayer thickness. The numbers in parentheses are error estimates in the last digit(s) of the averages.
[b] See Table 1.

Validation of Molecular Dynamics Simulations

J. Chem. Theory Comput., Vol. 6, No. 1, 2010 **329**

$$D_B = b_z - \int_{-b_z/2}^{b_z/2} \rho_w(z)dz \qquad (3)$$

where b_z is the z-dimension of the simulation box and $\rho_w(z)$ is the probability distribution of water along z. $\rho_w(z)$ was calculated from the time-averaged histogram of the distribution of water along the z-axis with a bin width of dz:

$$\rho_w(z) = \frac{n_w(z)V_w}{dV} \qquad (4)$$

where $n_w(z)$ is the time-averaged number of water molecules per slice and dV is the time-averaged volume of a slice.[27] The values of D_{HH} and D_B observed in the simulations are reported in Table 3. Again, the values calculated are consistent with the values obtained from experimental studies of lipid bilayers in the fluid phase. D_{HH} and D_B values obtained in the simulations are within 9% of those measured experimentally and are listed in Table 3.

The decomposition of the overall electron density into the contributions from different groups—namely water, choline moieties (Cho), phosphate groups (P), glycerol and carbonyls groups (Gro/CO), methylenes (CH_2) and terminal methyls (CH_3) of the acyl chains, and CH=CH groups in the oleoyl chains of DOPC and POPC (CH)—are also presented in Figure 1. The profiles are relatively symmetric, indicating that the bilayers are equilibrated. Water was found to penetrate into the bilayers up to the Gro/CO groups,[63] while the terminal methyl groups in the acyl chains were dehydrated, in agreement with experiment.[47,48,64]

3.3. Ordering of the Acyl Chains. The deuterium order parameters S_{CD} of the lauroyl (Lau), myristoyl (Myr), palmitoyl (Pam), and oleoyl (Ole) acyl chains, in the simulations of DLPC, DMPC, DOPC, and POPC, were calculated and compared to the available experimental data. S_{CD} measures the relative orientation of the C—D bonds with respect to the bilayer normal. The order parameter S_{CD} of a methylene group is defined as

$$S_{CD} = \frac{1}{2}\langle 3\cos^2\theta - 1\rangle \qquad (5)$$

where θ is the angle between a C—D bond of the methylene in the given acyl chain and the normal to the bilayer (z-axis). The angular brackets indicate an ensemble average. As the GROMOS force field uses an united-atom representation, the positions of the deuterons were constructed based on the positions of the neighboring carbons assuming tetrahedral geometry. The $|S_{CD}|$ profiles of the lipid sn-1 and sn-2 acyl chains of DLPC, DMPC, DOPC, and POPC, together with various experimental profiles based on NMR measurements, are presented in Figure 2. In all cases, the $|S_{CD}|$ values are lower than 0.25, which indicates than the aliphatic chains are disordered. The variation in $|S_{CD}|$ and in the magnitudes for the DLPC and DMPC bilayers are very similar to the values of Petrache et al.[65] and Douliez et al.[66] obtained experimentally. There is some discrepancy for the methylenes 2 and 3 in the Lau tails, but Douliez et al.[66] reported that the $|S_{CD}|$ for the second methylene could not be determined accurately.

In the case of POPC, the simulations reproduced the differences between the $|S_{CD}|$ values of the sn-1 Pam and sn-2 Ole chains observed experimentally.[67–69] The sn-1 Pam chain shows a continuous decrease in $|S_{CD}|$ characteristic of saturated chains. In contrast, the profile of the sn-2 Ole chain has a distinctive dip, corresponding to the double bond between carbons 9 and 10. The sn-2 Ole chain is also clearly less ordered than the saturated chain.[68,69] To our knowledge, no experimental values of $|S_{CD}|$ for the oleoyl chains in DOPC have been published. However, the two Ole tails show similar variations to the $|S_{CD}|$ of sn-2 Ole in POPC, as expected.

3.4. Conformation of Acyl Chains. Another structural parameter that can be inferred from experiment is the preference for given rotamers and sequences of rotamers in the acyl chains. Fourier transform infrared (FTIR) spectroscopy can be used to determine the number of *trans* (t) and *gauche* (g) conformers in an acyl chain and the sequences of t and g (end *gauche eg*, *gg*, *gtg* and kinks *gtg′*). The combinations observed are characteristic of a given lipid phase with, for example, the gel-to-fluid phase transition being associated with an increase in the number of *gauche* conformers and of kinks in the acyl chains.[70–72] In the simulations of DLPC, DMPC, DOPC, and POPC, the torsion

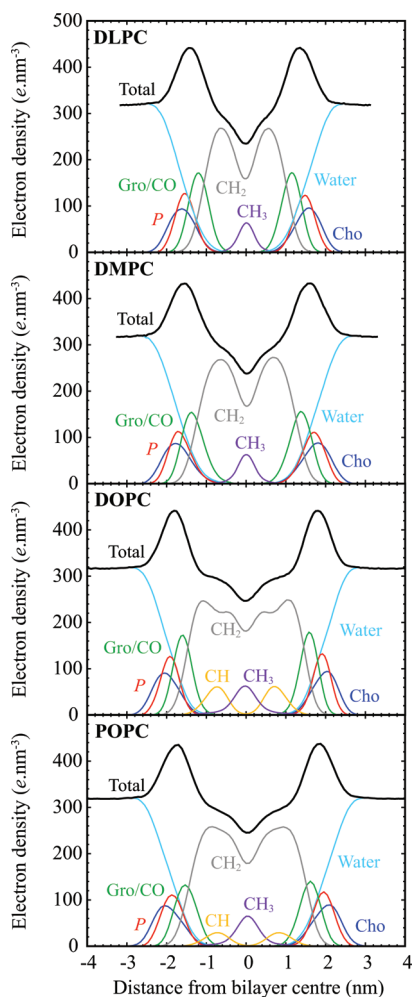**Figure 1.** Electron density profiles of the whole hydrated DLPC, DMPC, DOPC, and POPC bilayers and of the contribution of their individual components (Cho: contribution from the choline moieties; P: phosphate groups; Gro/CO: contribution of the glycerol and carbonyl groups; CH_2: methylenes of the acyl chains; CH: CH=CH groups in the oleoyl chains; CH_3: terminal methyls of the acyl chains).
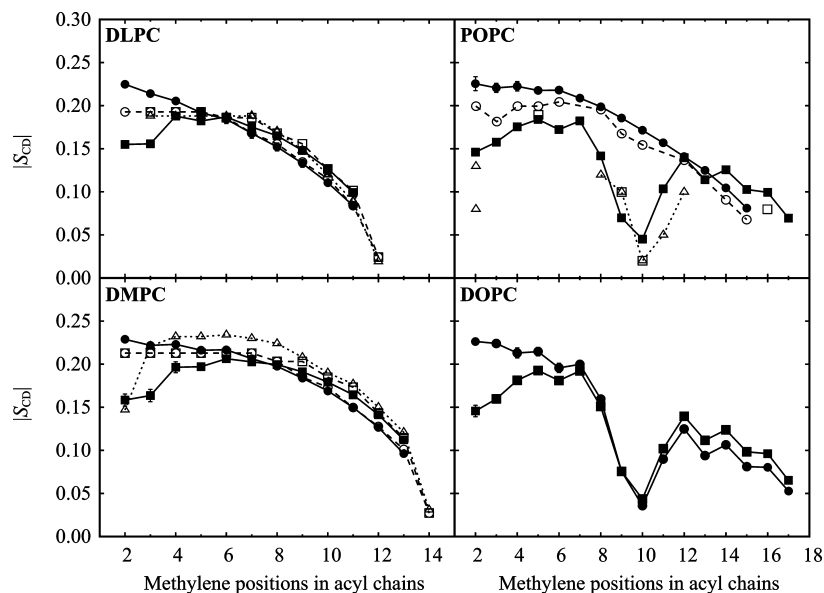
Figure 2. Deuterium order parameter $|S_{CD}|$ profiles of the *sn*-1 (●) and *sn*-2 (□) fatty acyl chains of hydrated DLPC, DMPC, DOPC, and POPC bilayers calculated from the simulations (Lau, 12:0; Myr, 14:0; Pam, 16:0; and Ole, 18:1c9). The $|S_{CD}|$ values are averaged over all the lipid *sn*-1 and -2 acyl chains in the systems and over the two simulations. Experimental $|S_{CD}|$ values: for DLPC and DMPC, $|S_{CD}|$ measured by Petrache et al.[65] for the *sn*-1 (○) and *sn*-2 (□) acyl chains; for DLPC, *sn*-2 Lau at 308 K from Douliez et al.[66] (△); for DMPC, *sn*-2 Myr from Douliez et al.[66] (△); for POPC, *sn*-1 Pam from Seelig and Seelig at 300 K[67] (○), *sn*-2 Ole from Perly et al.[69] (□), and from Seelig and Waespe-Šarčević[68] (△).

Table 4. Occurrence of Rotamer Sequences in Acyl Chains (*eg*, *gg*, *gtg'*, and *gtg'* + *gtg*) Estimated from Experiment and in the Simulations[a]

	number of bonds or bond sequences per chain								
	experiment					simulation			
rotamer	DLPC[74]	DMPC[76]	DPPC	DPPE[75]	POPE[75]	DLPC	DMPC	DOPC	POPC
eg	0.45	0.38	0.54[74] 0.38[76] 0.4[75]	0.1	0.05	0.34 (1)	0.31 (0)	0.31 (0)	0.31 (0)
gg	0.32	0.67	0.40[74] 0.57[76] 0.4[75]	0.2	0.2	0.37 (0)	0.50 (0)	0.41 (0)	0.45 (0)
gtg'	0.88[b]	—	1.19[74] [b]	—	—	0.29 (0)	0.36 (1)	0.31 (0)	0.37 (0)
gtg' + *gtg*	—	0.44	0.46[76] 1.0[75]	1.0	0.8	0.56 (0)	0.66 (0)	0.59 (0)	0.69 (1)

[a] The numbers between the parentheses are error estimates in the last digit of the averages. [b] The *gtg'* sequence may be ascribed to a *gtg'* + *gtg* sequence.[72]

angles ϕ in the acyl chains were classified as *t* ($\phi < -150°$ or $\phi > 150°$), g^- ($-90° \leq \phi < -30°$) or g^+ ($30° < \phi \leq 90°$).[73] The results are listed in Table 4 together with the available experimental values.[74−76] The estimates of *eg* and *gg* from the simulations of DLPC and DMPC are in good agreement with experiment. As noted previously in regard to DPPC,[25] apparent discrepancies for *gtg'* and *gtg* + *gtg'* are due mainly to experimental uncertainties in the assignment of *gtg* and *gtg'* methylene wagging modes.[72] No experimental data is available for DOPC and POPC. Nevertheless, given the experimental data available for phosphatidylcholines and phosphatidylethanolamines shown in Table 4, it is possible to judge the quality of the simulations of the DOPC and POPC bilayers. As is evident from Table 4, experimentally, there are marked differences in the incidence of specific rotameric sequences between DPPC (0.38−0.54 *eg*,[74−76] 0.40−0.57 *gg*,[74−76] and 0.46−1.0 *gtg'* + *gtg*[75,76] per

palmitoyl chain) and DPPE (0.1 *eg*, 0.2 *gg*, and 1.0 *gtg'* + *gtg*)[75] in the L_α phase. By comparing the propensity of palmitoyl chains to have *eg*, *gg*, and *gtg'* + *gtg* rotamers in DPPC and DPPE bilayers in the fluid phase, Senak et al.[75] estimated there were gains of 0.3−0.4 in *eg*, 0.2 in *gg*, and 0.1 in *gtg'* + *gtg* per chain going from a DPPC to a DPPE bilayer. By extrapolating their observations to fluid POPC and POPE bilayers, the number of *eg*, *gg*, and *gtg'* + *gtg* rotamer sequences per acyl chain, calculated from the simulation of a POPC bilayer (0.31 *eg*, 0.45 *gg*, and 0.69 *gtg'* + *gtg*), seems consistent with those obtained experimentally from a POPE bilayer in the L_α phase (0.05 *eg*, 0.2 *gg*, and 0.8 *gtg'* + *gtg*).[75]

No experimental values for DOPC were found, but the trend observed in the simulation of a DOPC fluid bilayer is similar to that of POPC, with a higher population of kinks
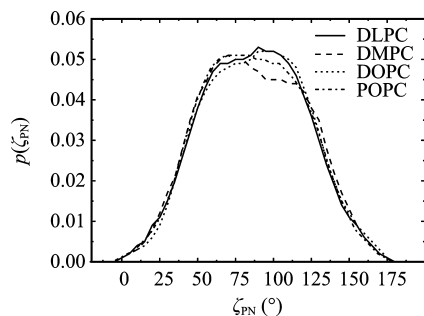
Validation of Molecular Dynamics Simulations

J. Chem. Theory Comput., Vol. 6, No. 1, 2010 **331**

Figure 3. Probability distribution function of the angle ζ_{PN} between the bilayer normal pointing away from the middle of the bilayer to bulk water and the lipid headgroup $P^- \rightarrow N^+$ vectors in the simulations of DLPC, DMPC, DOPC, and POPC.
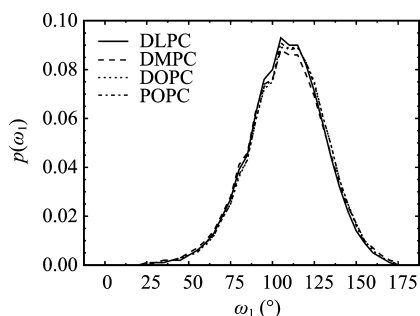

Figure 4. Probability distribution function of the angle ω_1 between the bilayer normal pointing away from the middle of the bilayer to bulk water and the *sn*-1 carbonyl $O \rightarrow C$ vectors in the simulations of DLPC, DMPC, DOPC and POPC.

$+$ *gtg* than that of *eg* and *gg* sequences, as previously noticed by Chia and Mendelsohn.[77]

3.5. Orientation of the Headgroups and of the Carbonyls. Büldt et al.[78] have shown that the dipole moment along the $P^- \rightarrow N^+$ vector in the phosphocholine headgroup lies almost parallel to the surface of the membrane. Figure 3 shows the probability distribution function of the angle ζ_{PN} between the $P^- \rightarrow N^+$ dipole and the outward bilayer normal. The distributions of ζ_{PN} obtained from the simulations of DLPC, DMPC, DOPC, and POPC are similar with most probable angles ζ_{PN} being 88°, 87°, 91°, and 86°, respectively. Accordingly, the headgroups, on average, lie nearly parallel to the bilayer surface.

The orientation of the *sn*-1 and -2 carbonyl $O^{\delta-} \rightarrow C^{\delta+}$ dipoles with respect to the outward bilayer normal was also calculated (angles ω_1 and ω_2, respectively). The probability distributions of ω_1 and ω_2 are shown in Figures 4 and 5, respectively. Again, the distributions are similar in all systems, with the most probable value for the angle ω_1 being 107° for DLPC, DMPC, DOPC, and POPC. The most probable value of ω_2 was 132°, 127°, 132°, and 135° for DLPC, DMPC, DOPC, and POPC, respectively.

3.6. Hydration of the Headgroups and Glycerol/ Carbonyls Moieties. The distribution of the water molecules around the atoms within the headgroup, the glycerol group as well as the *sn*-1 and *sn*-2 carbonyls, were calculated. Figure 6 illustrates the distribution of the distance between the oxygens of water and the nearest phosphocholine headgroup atom in the simulations of DLPC, DMPC, DOPC,
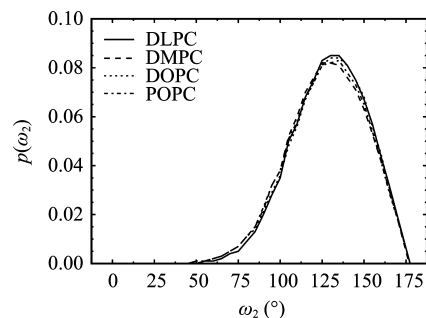

Figure 5. Probability distribution function of the angle ω_2 between the bilayer normal pointing away from the middle of the bilayer to bulk water and the *sn*-2 carbonyl $O \rightarrow C$ vectors in the simulations of DLPC, DMPC, DOPC, and POPC.

and POPC. The curves obtained in all simulations are essentially identical with three peaks at 0.27, 0.34, and 0.63 nm, indicating that the interaction of water with the headgroups does not depend upon the nature of the lipid tails. The integration of the distributions up to the second peak shows that there are 14.5, 14.3, 14.9, and 14.9 water molecules per lipid headgroup for DLPC, DMPC, DOPC, and POPC, respectively (Table 5). These results are in accord with experiment from which a ratio of about 11−20 water molecules per lipid in a fluid phase has been estimated.[79−82] The decomposition of the distributions of *P*Cho into the individual contributions of the choline (Cho) and phosphate (*P*) groups, together with the distributions of the water oxygens to the nearest glycerol (Gro), *sn*-1 carbonyl (CO^{sn-1}) and -2 carbonyl (CO^{sn-2}) groups are depicted in Figure 7. All four bilayers show similar distributions with a distinct first peak at 0.34 nm for Cho, 0.28 nm for *P*, 0.29 nm for Gro, 0.27 nm for CO^{sn-1}, and 0.26 nm for CO^{sn-2}. *P* and Gro also have a clear second peak at 0.47 and 0.38 nm, respectively. As listed in Table 5, it was found that there were, on average, 13−14 water molecules around the choline groups at 0.34 nm, about 3 and 10−11 water molecules around phosphates at 0.28 and 0.47 nm, respectively, and 1.6 water molecules around the carbonyls at the *sn*-2 positions at 0.26 nm. Despite the presence of a peak at 0.29 nm for Gro and at 0.27 nm for CO^{sn-1}, the integration of the peaks shows that they correspond to less than one water molecule on average.

4. Discussion

Overall, the GROMOS 53A6 force field parameters have been shown to be effective in representing a range of phosphatidylcholine lipids in a fluid phase and are able to reproduce a range of structural properties, such as the area per lipid, the volume per lipid, the deuterium order parameters, the hydration properties in close agreement with experiment, and, to a lesser extent, the isothermal compressibility modulus. The validation of simulation studies of membranes in a fluid phase is, however, a difficult task. Phospholipids are amphipathic molecules with the central polar glycerol group bound to one or two long, hydrophobic acyl chains and to a polar or charged headgroup. As a consequence, the phase behavior of a lipid bilayer is the result of a subtle balance between inter- and intramolecular
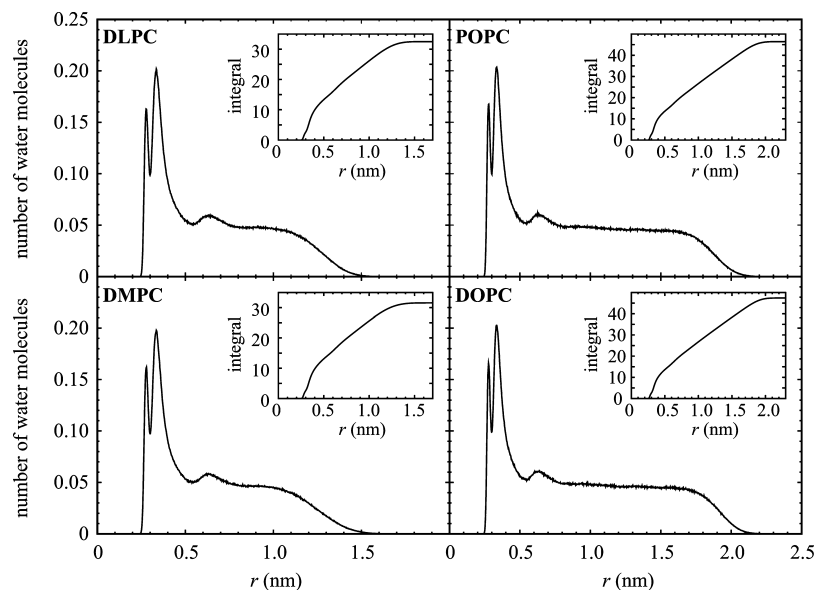
Figure 6. Distribution of the distance between the oxygen of water and the nearest lipid headgroup atom in the simulations of DLPC, DMPC, DOPC, and POPC. Insets: Integral of the distribution.

Table 5. Number of Water Molecules Per Lipid Hydrating the Phosphocholine Headgroup and the Different Polar Moieties in Lipids[a]

	number of water molecules per group					
lipid bilayer	$PCho$	Cho	P	Gro	CO^{sn-1}	CO^{sn-2}
DLPC	2.6	13.5	3.2	0.2	0.6	1.6
	14.5		10.2	3.3		
DMPC	2.5	13.3	3.3	0.2	0.6	1.6
	14.3		10.3	3.5		
DOPC	2.6	14.0	3.2	0.2	0.6	1.6
	14.9		10.9	3.4		
POPC	2.7	13.6	3.3	0.2	0.6	1.6
	14.9		10.9	3.3		

[a] Phosphocholine ($PCho$), choline (Cho), phosphate (P), glycerol (Gro), and carbonyls at the sn-1 (CO^{sn-1}) and sn-2 (CO^{sn-2}) positions. The values correspond to the integration up to the first peak in the distribution of water in Figure 6 for $PCho$ and in Figure 7 for the other groups. In the case of $PCho$, P and Gro, the second values correspond to the integration up to the second peak.

interactions[83] as well as the balance between interactions within the headgroup and tail regions. The compactness of a bilayer also means that structure and dynamics are strongly correlated. For example, in a gel phase, lipids pack more closely and are more highly ordered than in a L_α phase. The degree of ordering is often estimated by the area per lipid A_L, but this is generally measured indirectly, and the range of alternative experimental values is broad (see Table 1). In simulations, A_L is dependent on the sampling time, the size of the system, and the methodology used.[37−39,43] As a result, A_L is just one of a range of properties that need to be considered during the validation of force field parameters for lipids. In this work, a range of structural properties (A_L, bilayer thicknesses D_{HH} and D_B, S_{CD}, conformation of the acyl chains, and orientation of the headgroups) were used to validate the G53A6 parameter set. As shown in Table 3 and Figure 2, a good agreement was found with experiment not only for A_L but also for all the structural properties investigated. Although high, the estimates obtained for the

isothermal area compressibility modulus in all the bilayers (within the range of 389−475 mN·m^{-1}, see Table 3) are consistent with the range of 200−600 mN·m^{-1} obtained in previous simulation studies by Anézo et al.[43] This said, it must be noted that the Berendsen weak-coupling method[50] was used in both studies to maintain constant temperature and pressure, which might account for the discrepancy. The Berendsen thermostat and barostat do not give rise to an exact *NPT* ensemble. In particular, the weak-coupling method can suppress short-time fluctuations in the temperature and the pressure even though the long-time averages are correct. In this regard, it should be stressed that, while the fluctuations in the temperature and the pressure in the simulations occur on a 1−10-ps time scale, the fluctuations in A_L occur on a 10−100 ns time scale. Thus, fluctuations in A_L are not expected to be strongly affected or biaised by the relaxation time used in the weak coupling of temperature ($\tau_T = 0.1$ ps) and pressure ($\tau_P = 1$ ps). Other factors that could lead to an underestimation of the fluctuations in A_L include the suppression of the fluctuations due to the small size of the system and/or the time scale over which the fluctuations were accumulated. To determine the extent to which the values of K_A reflect the size of the system and the length of the sampling time, two additional simulations of a POPC bilayer at equilibrium with 361 lipids per leaflet were performed under the same conditions described in Section 2, the Methods section. The variation in K_A as a function of the extent of sampling time for the POPC bilayers in the fluid phase containing either 64 or 361 lipids per leaflet is shown in Figure 8. It is evident in Figure 8 that the apparent value of K_A depends strongly on both the size of the system simulated and the time scale over which σ_A^2 is determined; the value of K_A becoming closer to experiment the longer the sampling time or the larger the bilayer for a fixed sampling time. For example, with a sampling time of 60 ns, K_A is almost a factor of 2 lower in the bilayer comprising 361 POPC per leaflet ($K_A = 454 \pm 89$ mN·m^{-1}) than in the

Validation of Molecular Dynamics Simulations

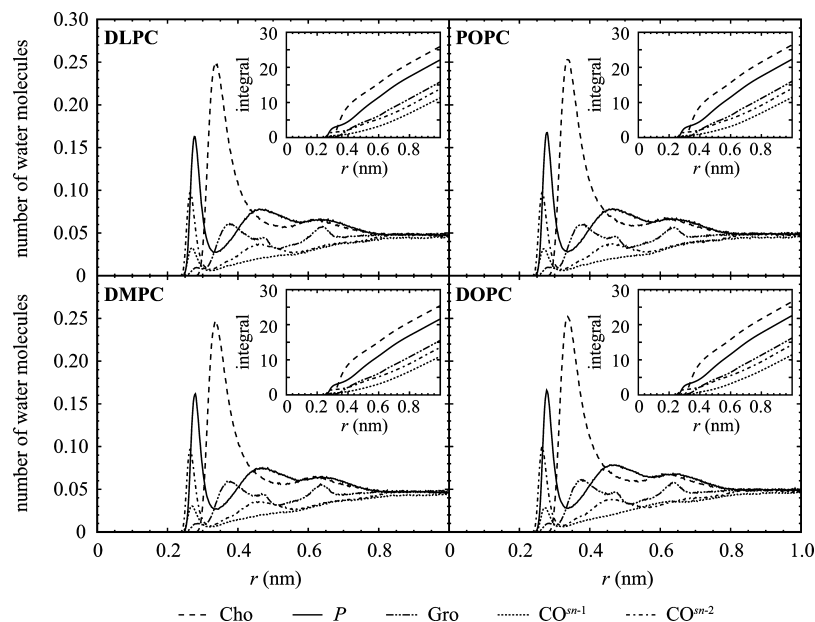*J. Chem. Theory Comput., Vol. 6, No. 1, 2010* **333**

Figure 7. Distribution of the distance between the oxygen of water and the nearest atom of the choline (Cho), phosphate (P), glycerol (Gro), sn-1 (CO^{sn-1}), and sn-2 (CO^{sn-2}) carbonyl groups in the simulations of DLPC, DMPC, DOPC, and POPC. Insets: Integrals of the distributions.
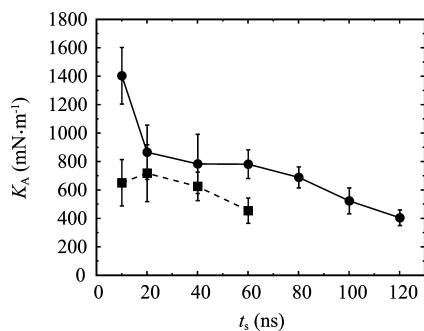

Figure 8. Isothermal area compressibility modulus K_A calculated over different sampling times t_s from the simulations of a fluid POPC bilayer comprising 64 (●) or 361 (■) lipids per leaflet. For each value of t_s, the initial time t_i for sampling was determined using the total time of the simulation t_t such that $t_i = t_t - t_s$. The error bars show the standard deviation of the average K_A over two independent simulations for a given value of t_s for each system.

bilayer with 64 lipids per leaflet ($K_A = 781 \pm 101$ mN·m^{-1}). In both cases, the average value of A_L is consistent with experiment (0.638 nm^2 in the 361 lipid per leaflet bilayer and 0.630 nm^2 in the 64 lipid per leaflet bilayer). In the smaller system, variations of A_L due to undulatory and peristaltic (thickness fluctuations) motions in bilayers,[37] which determined the value of σ_A^2 used in eq 2, were occurring on a time scale of 50−100 ns. This accounts for the decrease in K_A with increased sampling. In the larger system which contained almost six times the number of lipids per leaflet, the value of σ_A^2 converged more rapidly as expected. Note that the error bars shown in Figure 8 reflect the standard deviations of the average values of K_A calculated over the two independent equilibrium trajectories for a given sampling time. While in principle a larger bilayer is expected to reduce the effects of periodic boundary conditions and improve convergence, larger bilayers have the added com-

plication that collective properties, such as the bending of the bilayer, must also be taken into account. In this case, alternative formulas to eq 2 must be used.[37] This underlines the need to consider not only a wide range of properties but also the effect of sampling time and of system size when validating models.

While the overall structural properties such as A_L are central to validating force field parameters, the local properties, such as the sequences of rotameric states or the interaction with interfacial water, are equally important. Hydration forces play a critical role in the structure of fluid lipid bilayers.[84,83] Chandrasekhar et al.[85] showed that the balance between the water−water, lipids−lipids, and interfacial water−lipids interactions is crucial to allow a sufficient number of water molecules to interact with headgroups. NMR spin−lattice relaxation measurements, as a function of lipid hydration, suggested a ratio of 11−16 H$_2$O per lipid,[79] and more specifically 14−20 water molecules per lipid in the case of DOPC, in a liquid crystalline phase.[80,81] Lairión et al.[82] estimated the number of interfacial waters to be 12−16 in reversed micelles. The first hydration shell of lipids corresponds to the first two peaks in Figure 6. Figure 7 shows that the phosphate and carbonyl groups mainly contribute to the inner peak, whereas the choline and glycerol moieties are to a greater extent responsible for the outer peak. The integration of the distributions of the distances of the water oxygens to the closest lipid headgroup in the simulations is illustrated in the insets in Figure 6. This shows that there are approximately 14−15 water molecules up to the second peak: 14.5, 14.3, 14.9, and 14.9 water molecules per headgroup for DLPC, DMPC, DOPC, and POPC, respectively (Table 5). This is in good agreement with the NMR results and with previous simulation studies on DMPC,[86,87] DPPC,[88] POPC,[89] and DOPC[87,89,90] fluid bilayers, for example. Note, the splitting of the first hydration shell into separate peaks for the phosphate and choline groups at 0.27

and 0.34 nm in the distribution function, in Figure 6, observed in all the simulations has been previously seen in simulations of DOPC[89,90] and POPC[89] performed with united-atom models (with peaks at approximately 0.25−0.27 and 0.32−0.36 nm) but not in the all-atom simulations of DMPC and DOPC by Rosso and Gould.[87] This highlights the extent to which local properties of a model may vary even if general properties, such as the area per lipid, are similar.

The two ester carbonyl groups are not equivalent in phospholipids. Infrared spectroscopic studies of fully hydrated DMPC bilayers[91,92] suggested that, whereas the *sn*-1 carbonyl is largely buried, the *sn*-2 carbonyl interacts strongly with water. In the simulations, similar features are found with CO^{sn-1} being almost desolvated, while CO^{sn-2} is bound to 1.6 water molecules on average (Table 5).

Polar and charged groups give rise to the existence of several dipoles in lipids, namely the $P^- \rightarrow N^+$ dipole in phosphocholines and the $O^{\delta-} \rightarrow C^{\delta+}$ dipoles of the *sn*-1 and *sn*-2 carbonyls, which show preferential orientations with respect to the surrounding water molecules. Using neutron diffraction, Büldt et al.[78] showed that the P−N dipole in phosphocholine headgroups lies almost parallel to the surface of the bilayer. Furthermore, the X-ray structure of DMPC dihydrate[93] shows that the *sn*-1 carbonyl lies flat in the plane of the bilayer, whereas the oxygen of the *sn*-2 carbonyl is directed toward water. Using the G53A6 parameter set, the appropriate orientation of the three dipoles was found consistent for all four lipid bilayers: the P−N dipole is parallel to the surface of the bilayer ($\zeta_{PN} \approx 90°$) and the dehydrated *sn*-1 carbonyl adopts a comparable orientation but with the O→C vector slightly pointing outward from the bilayer ($\omega_1 \approx 107°$), whereas the *sn*-2 carbonyl has its oxygen clearly directed toward water ($\omega_2 \approx 132°$).

5. Conclusion

The simulations of common phospholipids of varying length (DLPC and DMPC) and degree of saturation (DOPC and POPC) of the acyl chains demonstrate that the G53A6 parameter set is well suited for the simulation of phosphatidylcholine bilayers in the biologically relevant liquid-crystalline phase. The structural properties of the bilayers were validated using a broad range of experimental data for each lipid. Critically, the extent of hydration of the lipid headgroups was found to be in agreement with NMR, X-ray, and neutron diffraction as well as infrared spectroscopic data. The work underlines the fact that to validate simulation models, especially those used to model lipid bilayers, there is a critical need to examine a range of experimental data as opposed to focusing on a single parameter, such as the area per lipid in isolation.

Supporting Information Available: The topology files of the lipid molecules and the atomic coordinates of equilibrated fluid bilayers of DLPC, DMPC, DOPC, and POPC are provided. This information is available at http://compbio.chemistry.uq.edu.au/~david/research/lipids.htm and on the GROMOS Automated Topology Builder and Repository (http://compbio.chemistry.uq.edu.au/atb). This material is available free of charge via the Internet at http://pubs.acs.org.

References

(1) Nagle, J. F.; Tristram-Nagle, S. *Biochim. Biophys. Acta* **2000**, *1469*, 159–195.

(2) Vigh, L.; Escribá, P.; Sonnleitner, A.; Sonnleitner, M.; Piotto, S.; Maresca, B.; Horváth, I.; Harwood, J. L. *Prog. Lipid Res.* **2005**, *44*, 303–344.

(3) de Vries, A. H.; Mark, A. E.; Marrink, S.-J. *J. Am. Chem. Soc.* **2004**, *126*, 4488–4489.

(4) Marrink, S.-J.; Mark, A. E. *J. Am. Chem. Soc.* **2003**, *125*, 11144–11145.

(5) Leontiadou, H.; Mark, A. E.; Marrink, S.-J. *J. Am. Chem. Soc.* **2006**, *128*, 12156–12161.

(6) Sengupta, D.; Leontiadou, H.; Mark, A. E.; Marrink, S.-J. *Biochim. Biophys. Acta* **2008**, *1778*, 2308–2317.

(7) Leontiadou, H.; Mark, A. E.; Marrink, S.-J. *Biophys. J.* **2004**, *86*, 2156–2164.

(8) Marrink, S.-J.; Jähnig, F.; Berendsen, H. J. *Biophys. Chem.* **1996**, *71*, 632–647.

(9) Leontiadou, H.; Mark, A. E.; Marrink, S.-J. *Biophys. J.* **2007**, *92*, 4209–4215.

(10) Khavrutskii, I. V.; Gorfe, A. A.; Lu, B.; McCammon, J. A. *J. Am. Chem. Soc.* **2009**, *131*, 1706–1716.

(11) Vernier, P. T.; Ziegler, M. J.; Sun, Y.; Chang, W. V.; Gundersen, M. A.; Tieleman, D. P. *J. Am. Chem. Soc.* **2006**, *128*, 6288–6289.

(12) Gurtovenko, A. A.; Anwar, J. *J. Phys. Chem. B* **2007**, *111*, 10453–10460.

(13) Tieleman, D. P.; Marrink, S.-J. *J. Am. Chem. Soc.* **2006**, *128*, 12462–12467.

(14) Gurtovenko, A. A.; Vattulainen, I. *J. Phys. Chem. B* **2007**, *111*, 13554–13559.

(15) Marrink, S.-J.; Lindahl, E.; Edholm, O.; Mark, A. E. *J. Am. Chem. Soc.* **2001**, *123*, 8638–8639.

(16) Marrink, S.-J.; Risselada, J.; Mark, A. E. *Chem. Phys. Lipids* **2005**, *135*, 223–244.

(17) de Vries, A. H.; Yefimov, S.; Mark, A. E.; Marrink, S.-J *Proc. Natl. Acad. Sci. U.S.A.* **2005**, *102*, 5392–5396.

(18) MacKerell, A. D., Jr.; et al. *J. Phys. Chem. B* **1996**, *102*, 3586–3616.

(19) Feller, S. E.; MacKerell, A. D., Jr. *J. Phys. Chem. B* **2000**, *104*, 7510–7515.

(20) van Gunsteren, W. F.; Billeter, S. R.; Eising, A. A.; Hünenberger, P. H.; Krüger, P.; Mark, A. E.; Scott, W. R. P.; Tironi, I. G. *Biomolecular Simulation: The GROMOS96 Manual and User Guide*; vdf Hochschulverlag AG an der ETH Zürich and BIOMOS B.V.: Zürich, Switzerland, 1996.

(21) Berger, O.; Edholm, O.; Jähnig, F. *Biophys. J.* **1997**, *72*, 2002–2013.

(22) Oostenbrink, C.; Villa, A.; Mark, A. E.; van Gunsteren, W. F. *J. Comput. Chem.* **2004**, *25*, 1656–1676.

(23) Oostenbrink, C.; Soares, T. A.; van der Vegt, N. F.; van Gunsteren, W. F *Eur. Biophys. J.* **2005**, *34*, 273–284.

(24) Villa, A.; Fan, H.; Wassenaar, T.; Mark, A. E. *J. Phys. Chem. B* **2007**, *111*, 6015–6025.

(25) Poger, D.; van Gunsteren, W. F.; Mark, A. E. *J. Comput. Chem.* **2009**, In press (DOI: 10.1002/jcc.21396)

(26) Kukol, A. *J. Chem. Theory Comput.* **2009**, *5*, 615–626.

(27) Chiu, S.-W.; Pandit, S. A.; Scott, H. L.; Jakobsson, E. *J. Phys. Chem. B* **2009**, *113*, 2748–2763.

(28) Costigan, S. C.; Booth, P. J.; Templer, R. H. *Biochim. Biophys. Acta* **2000**, *1468*, 41–54.

(29) Kučerka, N.; Nagle, J. F.; Sachs, J. N.; Feller, S. E.; Pencer, J.; Jackson, A.; Katsaras, J. *Biophys. J.* **2008**, *95*, 2356–2367.

(30) Pan, J.; Tristram-; Nagle, S.; Kučerka, N.; Nagle, J. F. *Biophys. J.* **2008**, *94*, 117–124.

(31) van Gunsteren, W. F.; Dolenc, J.; Mark, A. E. *Curr. Opin. Struct. Biol.* **2008**, *18*, 149–153.

(32) Liu, Y.; Nagle, J. F. *Phys. Rev. E: Stat. Phys., Plasmas, Fluids, Relat. Interdisc. Top.* **2004**, *69*, 040901.

(33) Cornell, W. D.; Cieplak, P.; Bayly, C. I.; Gould, I. R.; Merz, K. M.; Ferguson, D. M.; Spellmeyer, D. S.; Fox, T.; Caldwell, J. W.; Kollman, P. A. *J. Am. Chem. Soc.* **1995**, *117*, 5179–5197.

(34) Wang, J.; Wolf, R. M.; Caldwell, J. W.; Kollman, P. A.; Case, D. A. *J. Comput. Chem.* **2004**, *25*, 1157–1174.

(35) Brooks, B. R.; Bruccoleri, R. E.; Olafson, B. D.; States, D. J.; Swaminathan, S.; Karplus, M. *J. Comput. Chem.* **1983**, *4*, 187–217.

(36) MacKerell, A. D., Jr.; et al. *J. Phys. Chem. B* **1998**, *102*, 3586–3616.

(37) Lindahl, E.; Edholm, O *Biophys. J.* **2000**, *79*, 426–433.

(38) de Vries, A. H.; Mark, A. E.; Marrink, S.-J. *J. Phys. Chem. B* **2004**, *108*, 2454–2463.

(39) de Vries, A. H.; Chandrasekhar, I.; van Gunsteren, W. F.; Hünenberger, P. H. *J. Phys. Chem. B* **2005**, *109*, 11643–11652.

(40) Darden, T.; York, D.; Pedersen, L. *J. Chem. Phys.* **1993**, *98*, 10089–10092.

(41) Essmann, U.; Perera, L.; Berkowitz, M. L.; Darden, T.; Lee, H.; Pedersen, L. G. *J. Chem. Phys.* **1995**, *103*, 8577–8593.

(42) Tironi, I. G.; Sperb, R.; Smith, P. E.; van Gunsteren, W. F. *J. Chem. Phys.* **1995**, *102*, 5451–5459.

(43) Anézo, C.; de Vries, A. H.; Höltje, H.-D.; Tieleman, D. P.; Marrink, S.-J. *J. Phys. Chem. B* **2003**, *107*, 9424–9433.

(44) Tieleman, D. P.; Marrink, S.-J.; Berendsen, H. J. C. *Biochim. Biophys. Acta* **1997**, *1331*, 235–270.

(45) van der Rest, M. E.; Kamminga, A. H.; Nakano, A.; Anraku, Y.; Poolman, B.; Konings, W. N. *Microbiol. Rev.* **1995**, *59*, 304–322.

(46) Tattrie, N. H.; Bennett, J. R.; Cyr, R *Can. J. Biochem* **1968**, *46*, 819–824.

(47) Kučerka, N.; Liu, Y.; Chu, N.; Petrache, H. I.; Tristram-Nagle, S.; Nagle, J. F. *Biophys. J.* **2005**, *88*, 2626–2637.

(48) Kučerka, N.; Tristram-Nagle, S.; Nagle, J. F. *J. Membr. Biol.* **2005**, *208*, 193–202.

(49) van der Spoel, D.; Lindahl, E.; Hess, B.; Groenhof, G.; Mark, A. E.; Berendsen, H. J. C. *J. Comput. Chem.* **2005**, *26*, 1701–1718.

(50) Berendsen, H. J. C.; Postma, J. P. M.; van Gunsteren, W. F.; DiNola, A.; Haak, J. R. *J. Chem. Phys.* **1984**, *81*, 3684–3690.

(51) Mabrey, S.; Sturtevant, J. M. *Proc. Natl. Acad. Sci. U.S.A.* **1976**, *73*, 3862–3866.

(52) Davis, P. J.; Fleming, B. D.; Coolbear, K. P.; Keough, K. M. W. *Biochemistry* **1981**, *20*, 3633–3636.

(53) Huang, C. H.; Lapides, J. R.; Levin, I. W. *J. Am. Chem. Soc.* **1982**, *104*, 5926–5930.

(54) Lewis, R. N. A. H.; Sykes, B. D.; McElhaney, R. N. *Biochemistry* **1988**, *27*, 880–887.

(55) Hess, B.; Bekker, H.; Berendsen, H. J. C.; Fraaije, J. G. E. M. *J. Comput. Chem.* **1997**, *18*, 1463–1472.

(56) Berendsen, H. J. C.; Postma, J. P. M.; van Gunsteren, W. F.; Hermans, J. Interaction models for water in relation to protein hydration. In *Intermolecular Forces*; Pullman, B., Ed.; Reidel: Dordrecht, The Netherlands, 1981; pp 331−342.

(57) Miyamoto, S.; Kollman, P. A. *J. Comput. Chem.* **1992**, *13*, 952–962.

(58) Heinz, T. N.; van Gunsteren, W. F.; Hünenberger, P. H. *J. Chem. Phys.* **2001**, *115*, 1125–1136.

(59) Rawicz, W.; Olbrich, K. C.; McIntosh, T.; Needham, D.; Evans, E. *Biophys. J.* **2000**, *79*, 328–339.

(60) Tristram-Nagle, S.; Petrache, H. I.; Nagle, J. F. *Biophys. J.* **1998**, *75*, 917–925.

(61) Binder, H.; Gawrisch, K. *J. Phys. Chem. B* **2001**, *105*, 12378–12390.

(62) Marrink, S.-J.; Mark, A. E. *J. Phys. Chem. B* **2001**, *105*, 6122–6127.

(63) Simon, S. A.; McIntosh, T. J. *Methods Enzymol.* **1986**, *127*, 511–521.

(64) Kučerka, N.; Tristram-Nagle, S.; Nagle, J. F. *Biophys. J.* **2006**, *90*, L83–L85.

(65) Petrache, H. I.; Dodd, S. W.; Brown, M. F *Biophys. J.* **2000**, *79*, 3172–3192.

(66) Douliez, J.-P.; Léonard, A.; Dufourc, E. J. *Biophys. J.* **1995**, *68*, 1727–1739.

(67) Seelig, A.; Seelig, J. *Biochemistry* **1977**, *16*, 45–50.

(68) Seelig, J.; Waespe-Šarčević, N. *Biochemistry* **1978**, *17*, 3310–3315.

(69) Perly, B.; Smith, I. C. P.; Jarrell, H. C. *Biochemistry* **1985**, *24*, 1055–1063.

(70) Snyder, R. G.; Strauss, H. L.; Elliger, C. A. *J. Phys. Chem.* **1982**, *86*, 5145–5150.

(71) Mendelsohn, R.; Senak, L. Quantitative determination of conformational disorder in biological membranes by FTIR spectroscopy. In *Biomolecular spectroscopy*; Clark, R. J. H., Hester, R. E., Eds.; Wiley: New York, 1993; pp 339−380.

(72) Cates, D. A.; Strauss, H. L.; Snyder, R. G. *J. Phys. Chem.* **1994**, *98*, 4482–4488.

(73) Moss, G. P. *Pure Appl. Chem.* **1996**, *68*, 2193–2222.

(74) Casal, H. L.; McElhaney, R. N. *Biochemistry* **1990**, *29*, 5423–5427.

(75) Senak, L.; Davies, M. A.; Mendelsohn, R. *J. Phys. Chem.* **1991**, *95*, 2565–2571.

(76) Tuchtenhagen, J.; Ziegler, W.; Blume, A. *Eur. Biophys. J.* **1994**, *23*, 323–335.

(77) Chia, N.-C.; Mendelsohn, R. *Biochim. Biophys. Acta* **1996**, *1283*, 141–150.

(78) Büldt, G.; Gally, H. U.; Seelig, A.; Seelig, J.; Zaccai, G. *Nature* **1978**, *271*, 182–184.

(79) Borle, F.; Seelig, J. *Biochim. Biophys. Acta* **1983**, *735*, 131–136.

(80) Ulrich, A. S.; Volke, F.; Watts, A. *Chem. Phys. Lipids* **1990**, *55*, 61–66.

(81) Ulrich, A. S.; Watts, A *Biophys. J.* **1994**, *66*, 1441–1449.

(82) Lairión, F.; Filler, R.; Disalvo, E. A. *Colloids Surf., B* **2002**, *25*, 369–371.

(83) Lewis, R. N. A. H.; Pohle, W.; McElhaney, R. N. *Biophys. J.* **1996**, *70*, 2736–2746.

(84) Gawrisch, K.; Ruston, D.; Zimmerberg, J.; Parsegian, V. A.; Rand, R. P.; Fuller, N *Biophys. J.* **1992**, *61*, 1213–1223.

(85) Chandrasekhar, I.; Oostenbrink, C.; van Gunsteren, W. F. *Soft Mater.* **2004**, *2*, 27–45.

(86) Chiu, S.-W.; Clark, M.; Balaji, V.; Subramaniam, S.; Scott, H. J.; Jakobsson, E. *Biophys. J.* **1995**, *69*, 1230–1245.

(87) Rosso, L.; Gould, I. R. *J. Comput. Chem.* **2008**, *29*, 24–37.

(88) Åman, K.; Lindahl, E.; Edholm, O.; Håkansson, P.; Westlund, P.-O. *Biophys. J.* **2003**, *84*, 102–115.

(89) Chiu, S.-W.; Clark, M. M.; Jakobsson, E.; Subramaniam, S.; Scott, H. L. *J. Phys. Chem. B* **1999**, *103*, 6323–6327.

(90) Mashl, R. J.; Scott, H. L.; Subramaniam, S.; Jakobsson, E. *Biophys. J.* **2001**, *81*, 3005–3015.

(91) Wong, P. T. T.; Mantsch, H. H. *Chem. Phys. Lipids* **1988**, *46*, 213–224.

(92) Hübner, W.; Blume, A. *Chem. Phys. Lipids* **1998**, *96*, 99–123.

(93) Pearson, R. H.; Pascher, I. *Nature* **1979**, *281*, 499–501.

(94) Rand, R. P.; Parsegian, V. A. *Biochim. Biophys. Acta* **1989**, *988*, 351–376.

(95) Smaby, J. M.; Momsen, M. M.; Brockman, H. L.; Brown, R. E. *Biophys. J.* **1997**, *73*, 1492–1505.

(96) Lewis, B. A.; Engelman, D. M. *J. Mol. Biol.* **1983**, *166*, 211–217.

(97) Gruner, S. M.; Tate, M. W.; Kirk, G. L.; So, P. T.; Turner, D. C.; Keane, D. T.; Tilcock, C. P.; Cullis, P. R. *Biochemistry* **1988**, *27*, 2853–2866.

(98) Pabst, G.; Rappolt, M.; Amenitsch, H.; Laggner, P. *Phys. Rev. E: Stat. Phys., Plasmas, Fluids, Relat. Interdiscip. Top.* **2000**, *62*, 4000–4009.

(99) De Young, L. R.; Dill, K. A. *Biochemistry* **1988**, *27*, 5281–5289.

(100) Mills, T. T.; Toombes, G. E.; Tristram-Nagle, S.; Smilgies, D. M.; Feigenson, G. W.; Nagle, J. F. *Biophys. J.* **2008**, *95*, 669–681.

(101) Balgavý, P.; Dubničková, M.; Kučerka, N.; Kiselev, M. A.; Yaradaikin, S. P.; Uhríková, D. *Biochim. Biophys. Acta* **2001**, *1512*, 40–52.

(102) Lis, L. J.; McAlister, M.; Fuller, N.; Rand, R. P.; Parsegian, V. A. *Biophys. J.* **1982**, *37*, 657–666.

(103) Wiener, M. C.; White, S. H. *Biophys. J.* **1992**, *61*, 434–447.

(104) Janiak, M. J.; Small, D. M.; Shipley, G. G. *J. Biol. Chem.* **1979**, *254*, 6068–6078.

(105) Büldt, G.; Gally, H. U.; Seelig, J.; Zaccai, G. *J. Mol. Biol.* **1979**, *134*, 673–679.

(106) Hyslop, P. A.; Morel, B.; Sauerheber, R. D. *Biochemistry* **1990**, *29*, 1025–1038.

(107) Koenig, B. W.; Strey, H. H.; Gawrisch, K. *Biophys. J.* **1997**, *73*, 1954–1966.

(108) Petrache, H. I.; Tristram-Nagle, S.; Nagle, J. F. *Chem. Phys. Lipids* **1998**, *95*, 83–94.

(109) Thurmond, R. L.; Dodd, S. W.; Brown, M. F. *Biophys. J.* **1991**, *59*, 108–113.

(110) Nagle, J. F.; Zhang, R.; Tristram-Nagle, S.; Sun, W.; Petrache, H. I.; Suter, R. M. *Biophys. J.* **1996**, *70*, 1419–1431.

(111) Kučerka, N.; Kiselev, M. A.; Balgavý, P. *Eur. Biophys. J.* **2004**, *33*, 328–334.

(112) Moore, P. B.; Lopez, C. F.; Klein, M. L *Biophys. J.* **2001**, *81*, 2484–2494.

(113) Lopez, C. F.; Nielsen, S. O.; Klein, M. L.; Moore, P. B. *J. Phys. Chem. B* **2004**, *108*, 6603–6610.

(114) Heller, H.; Schaefer, M.; Schulten, K. *J. Phys. Chem.* **1993**, *97*, 8343–8360.

(115) de Joannis, J.; Jiang, Y.; Yin, F.; Kindt, J. T. *J. Phys. Chem. B* **2006**, *110*, 25875–25882.

(116) Hofsäß, C.; Lindahl, E.; Edholm, O. *Biophys. J.* **2003**, *84*, 2192–2206.

(117) Jójárt, B.; Martinek, T. A. *J. Comput. Chem.* **2007**, *28*, 2051–2058.

(118) Patra, M. *Eur. Biophys. J.* **2005**, *35*, 79–88.

(119) Zubrzycki, I. Z.; Xu, Y.; Madrid, M.; Tang, P. *J. Chem. Phys.* **2000**, *112*, 3437–3441.

(120) Pasenkiewicz-Gierula, M.; Takaoka, Y.; Miyagawa, H.; Kitamura, K.; Kusumi, A. *Biophys. J.* **1999**, *73*, 1228–1240.

(121) Tieleman, D. P.; Berendsen, H. J. C. *J. Chem. Phys.* **1996**, *105*, 4871–4880.

(122) Repáková, J.; Čapková, P.; Holopainen, J. M.; Vattulainen, I. *J. Phys. Chem. B* **2004**, *108*, 13438–13448.

(123) Chandrasekhar, I.; Bakowies, D.; Glättli, A.; Hünenberger, P.; Pereira, C.; van Gunsteren, W. F. *Mol. Simulat.* **2005**, *31*, 543–548.

(124) Gurtovenko, A. A.; Patra, M.; Karttunen, M.; Vattulainen, I. *Biophys. J.* **2004**, *86*, 3461–3472.

(125) Sonne, J.; Jensen, M. O.; Hansen, F. Y.; Hemmingsen, L.; Peters, G. H. *Biophys. J.* **2007**, *92*, 4157–4167.

(126) Leekumjorn, S.; Sum, A. K. *Biophys. J.* **2006**, *90*, 3951–3965.

J. Chem. Theory Comput. **2010,** *6,* 337–343

337

Flexibility of Catalytic Zinc Coordination in Thermolysin and HDAC8: A Born−Oppenheimer ab Initio QM/MM Molecular Dynamics Study

Ruibo Wu,[†,‡] Po Hu,[†] Shenglong Wang,[†] Zexing Cao,[‡] and Yingkai Zhang*,[†]

Department of Chemistry, New York University, 100 Washington Square East, New York 10003, and Department of Chemistry and State Key Laboratory of Physical Chemistry of Solid Surfaces, College of Chemistry and Chemical Engineering, Xiamen University, Xiamen 361005, China

Abstract: The different coordination modes and fast ligand exchange of zinc coordination has been suggested to be one key catalytic feature of the zinc ion which makes it an invaluable metal in biological catalysis. However, partly because of the well-known difficulties for zinc to be characterized by spectroscopy methods, evidence for dynamic nature of the catalytic zinc coordination has so far mainly been indirect. In this work, Born−Oppenheimer ab initio Quantum Mechanical/Molecular Mechanical (QM/MM) molecular dynamics (MD) simulation has been employed, which allows for a first-principle description of the dynamics of the metal active site while properly including effects of the heterogeneous and fluctuating protein environment. Our simulations have provided direct evidence regarding inherent flexibility of the catalytic zinc coordination shell in thermolysin (TLN) and histone deacetylase 8 (HDAC8). We have observed different coordination modes and fast ligand exchange during the picosecond's time scale. For TLN, the coordination of the carboxylate group of Glu166 to zinc is found to continuously change between monodentate and bidentate manner dynamically, while for HDAC8, the flexibility mainly comes from the coordination to a nonamino acid ligand. Such distinct dynamics in the zinc coordination shell between two enzymes suggests that the catalytic role of zinc in TLN and HDAC8 is likely to be different in spite of the fact that both catalyze the hydrolysis of the amide bond. Meanwhile, considering that such Born−Oppenheimer ab initio QM/MM MD simulations are very much desired but are widely considered to be too computationally expensive to be feasible, our current study demonstrates the viability and powerfulness of this state-of-the-art approach in simulating metalloenzymes.

   Zinc is relatively abundant in biological materials. Approximately 10% of the total human proteome have been identified to bind with zinc in vivo from a bioinformatics investigation,[1] and they play very crucial roles in all forms of life.[2−6] For mononuclear zinc enzymes, a typical metal coordination environment contains three amino acid side chain ligands (His, Glu, Asp, and Cys) and one or two small molecules.[3,7,8] The flexibility of zinc coordination, which allows different coordination modes and fast ligand exchange, has been suggested to be one key catalytic feature of the zinc ion which makes it an invaluable metal in biological catalysis.[9] However, partly because of the well-known difficulties for zinc to be characterized by spectroscopy methods,[10,11] evidence for dynamic nature of the catalytic zinc coordination has so far mainly been indirect coming from determined X-ray crystal structures[5,12] and geometry optimizations of model complexes with electronic structure methods.[13,14]

* To whom correspondence should be addressed. E-mail: yingkai.zhang@nyu.edu. Telephone: (212) 998 7882.

† New York University.

‡ Xiamen University.

A classical example of the flexible zinc coordination is thermolysin (TLN), one of the best experimentally characterized zinc proteases with one Glu and two His amino acid side chains as ligands.[15] Extensive structural studies have indicated that besides the simple tetrahedron coordination, its catalytic zinc ion can also be five- or six-coordinated[16−19] especially for the carboxylate of Glu/Asp whose coordination is highly flexible. The different coordination mode of carboxylate to zinc with a continuous range between monodentate and bidentate manner has been observed in model complexes as well as in other zinc enzymes with one Glu or Asp as ligands.[12] It has been suggested that the coordination of carboxylate to zinc could be dynamic in the catalytic process, known as carboxylate shift, which has been suggested to be important in the function of zinc enzymes.[13,14,20−22] Intriguingly, for zinc-dependent histone deacetylases (HDACs), in which the catalytic zinc ion is coordinated to one His and two Asp residues, only the monodentate mode has been observed for the carboxylate coordination in several crystal structures.[23−26] HDACs, which catalyze the removal of acetyl group from histone tails, have emerged to be critical in gene regulation and are among the most promising targets for the development of antitumor therapeutics. For example, the recently FDA approved anticancer drug SAHA is an HDAC inhibitor which is directly coordinated to the zinc.[27,28]

To provide deep insights into the dynamics and flexibility of the zinc catalytic site, which would be essential in characterizing their catalytic mechanisms and rational design of novel inhibitors for zinc enzymes, we have carried out density functional theory (DFT) QM/MM Born−Oppenheimer molecular dynamics (BOMD) simulations on TLN and HDAC8. Although semiempirical QM/MM BOMD simulations of some zinc-dependent enzymes have been carried out,[29−32] one main concern is the accuracy and transferability of the semiempirical QM Hamiltonian in describing the zinc coordination shell and the enzyme reaction profile. Often, some parameters of the semiempirical Hamiltonian need to be reoptimized for specific systems and reactions to obtain reasonable results,[30,32−35] which significantly reduce its transferability and predictability. Thus, in our current DFT QM/MM molecular dynamics simulations, the zinc ion and its ligands are treated by B3LYP hybrid functional with a Stuttgart ECP/basis set[36] for the zinc atom and a 6-31G* basis set for all other QM atoms. Our employed theoretical approach, which has recently been demonstrated to be feasible and powerful in several enzymatic studies,[37−40] allows for a first-principle description of the dynamics of the metal active site while properly including effects of the heterogeneous and fluctuating protein environment.

Computational Methods

I. Preparation of Simulation Systems. As illustrated in Figure 1 and listed in Tables 1 and 2, four TLN and two HDAC8 simulation systems have been prepared on the basis of their respective experiment crystal structures: TLNa, a substrate-free structure of TLN (pdb code: 1LNF[16]); TLNb, a TLN-inhibitor complex which mimics the reactant state (pdb code: 1ZDP[17]); TLNc, a TLN-inhibitor complex which

(a) TLN: $[Zn(Glu)(His)_2(M)_x]^y$

(b) HDAC8: $[Zn(Asp)_2(His)(M)_2]^0$
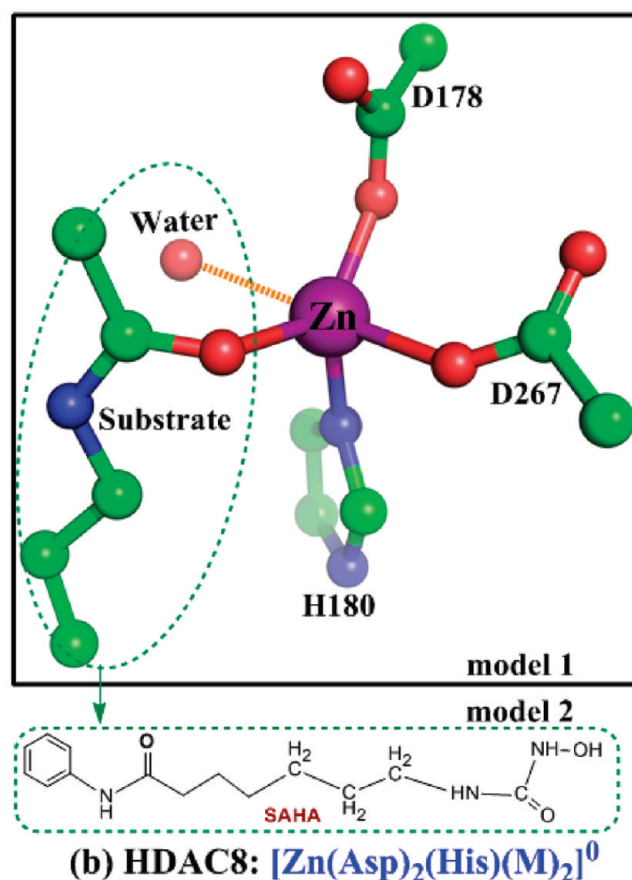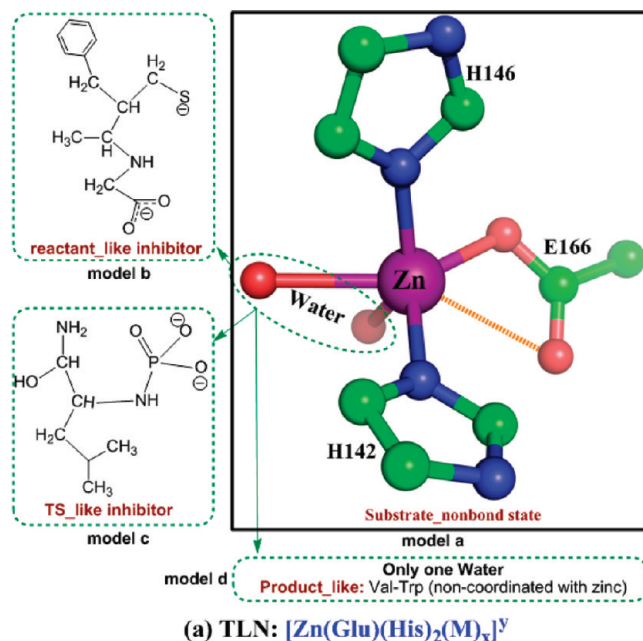
Figure 1. Illustration of various zinc coordination shells in our simulated TLN and HDAC8 enzyme complexes.

mimics the transition state (pdb code: 2TMN[18]); TLNd, a TLN-product complex (pdb code: 3TMN[19]); model 1, a complex of the Y306F mutant of HDAC8 and its substrate (pdb code: 2V5W[25]); model 2, an HDAC8-SAHA complex (pdb code: 1T69[24]). Representative active site structures of TLN and HDAC8 enzymes are illustrated in Figure 2.

Thermolysin and HDAC8 Catalytic Zinc Coordination

J. Chem. Theory Comput., Vol. 6, No. 1, 2010 **339**

Table 1. Interaction Distances in the Zinc Coordination Sphere of Thermolysin[a]

models	CN[b]	Zn–N (H142) d_1	Zn–N (H146) d_2	Zn–O$_{e1}$(E166) d_3	Zn–O$_{e2}$(E166) d_4	d_5	d_6
expt (1LNF)[c]	6	1.980	1.987	2.378	2.242	2.384[g]	2.276[g]
TLNa	5.6 ± 0.4	2.063 ± 0.063	2.152 ± 0.076	**2.216 ± 0.289**	2.150 ± 0.069	2.186 ± 0.093[g]	2.158 ± 0.086[g]
expt (1ZDP)[d]	4	2.141	2.096	2.002	2.955	2.414[h]	n/a
TLNb	4.0 ± 0.1	2.031 ± 0.051	2.066 ± 0.060	2.053 ± 0.062	**3.117 ± 0.140**	2.330 ± 0.060[h]	n/a
expt (2TMN)[e]	4	2.119	2.102	2.148	2.887	2.792[i]	2.065[i]
TLNc	5.3 ± 0.4	2.043 ± 0.051	2.235 ± 0.116	**2.940 ± 0.409**	2.131 ± 0.335	**2.220 ± 0.223**[i]	**2.083 ± 0.128**[i]
expt (3TMN)[f]	4	2.119	2.117	2.167	2.800	2.129[j]	n/a
TLNd	4.5 ± 0.4	1.991 ± 0.050	2.078 ± 0.062	**2.173 ± 0.272**	**2.466 ± 0.415**	2.089 ± 0.071[j]	n/a

[a] The flexible distances are highlighted in bold (n/a, not applicable). Å are used for Zn–O, 2.40 and 2.65 for Zn–S, respectively. These values are chosen on the basis of very recent analysis on databases of zinc enzyme structures database.[5] [b] CN means the coordination number. CN is 1 if Zn–N ≤ 2.15 Å, equals 0 if Zn–N ≥ 2.40 Å, and is a linear scalar between 0 and 1 if Zn–N is between 2.15 and 2.40 Å. Similarly, the values of 2.20 and 2.60. [c] Ref 15. Resolution: 1.7 Å. [d] Ref 16. Resolution: 1.7 Å. [e] Ref 17. Resolution: 1.6 Å. [f] See from ref 18. Resolution: 1.7 Å. [g] It is Zn–O distance between Zn^{2+} and crystal water. [h] It is Zn–S distance between Zn^{2+} and inhibitor. [i] It is Zn–O distance between Zn^{2+} and phosphate group in inhibitor. [j] It is Zn–O distance between Zn^{2+} and crystal water.

Table 2. Interaction Distances in the Zinc Coordination Sphere of HDAC8

models	CN	Zn–O (D178) r_1	Zn–N (D180) r_2	Zn–O (D267) r_3	Zn–(water/SAHA) r_4	Zn–(sub./SAHA) r_5
expt (2 V5W)[a]	5	1.955	2.074	1.947	2.238	1.994
model 1 (Y306F)	4.4 ± 0.4	1.938 ± 0.047	1.996 ± 0.049	2.002 ± 0.085	**2.422 ± 0.219**	2.103 ± 0.064
expt (1T69)[b]	5	2.131	1.789	1.908	1.953	1.975
model 2 (SAHA)	4.8 ± 0.2	1.992 ± 0.056	2.154 ± 0.078	1.969 ± 0.052	**2.247 ± 0.111**	2.171 ± 0.083

[a] Reference 25. Resolution: 2.0 Å. [b] Reference 24. Resolution: 2.9 Å.

For each simulation system, its initial structure was prepared on the basis of its respective crystal structure with molecular modeling and dynamics simulations. First, missing residues were added with the Swiss-PdbViewer.[41] Protonation states of charged residues in the enzyme complex were determined via H++ program[42] and by carefully examining local hydrogen bond networks. In all TLN models, His142 and His146 were identified as singly protonated, whereas His231 was doubly protonated, which are the same as previous studies.[43,44] For HDAC8 models, His180 was determined as singly protonated on δ site, while His142 and His143 were determined as singly protonated on ε site. Then, each prepared system was solvated into a rectangular box with a 10 Å buffer distance between the solvent box wall and the nearest solute atom. Finally, to neutralize each simulation system, one to six sodium ions were added at the protein surface by employing the Amber Tool. All sodium ions were located more than 17 Å away from the zinc active site. The resulting simulation system was about 45 000 atoms for each model. The Zn^{2+} ion was modeled with the Stote's scheme.[45] Considering that the zinc coordination shell is very difficult to be well described by a molecular mechanical force field,[46−49] ~1500 kcal/mol harmonic restraint was placed on ~15 atoms in the zinc bind site to retain the zinc coordination structure during the MM equilibrations. The rest of protein and solvent molecules were first minimized, and then more than 3 ns MD simulations were carried out for each system with periodic boundary condition. A time step of 2 fs was used. Berendsen thermostat method[50] was used to control the system temperature at 300 K. All MD simulations were performed with AMBER10 molecular dynamics package.[51] The Amber99SB[52−54] force field for the protein and TIP3P model[55] for water molecules were employed, and the force field parameters for substrate in HDAC8 and inhibitors in these simulation models were generated from AMBER GAFF force field[56] via AMBER tools. The SHAKE algorithm[57] was applied to constrain all bonds involving hydrogen atoms with tolerance of 10^{-5} Å, and 12 Å cutoffs were used for both van der Waals and electronic interactions.

II. Born−Oppenheimer ab Initio QM/MM Molecular Dynamic Simulations. Considering that the trajectory was very stable after 2 ns for all these classical MD simulations, the resulting snapshot after 3 ns MD simulation was employed as the initial structure for the preparation of ab initio QM/MM MD simulations. Each QM/MM model was prepared by deleting the solvent molecules beyond 30 Å from the zinc atom. The resulting QM/MM system had a total of ~13 000 atoms. The detailed QM/MM partition for all these TLN and HDAC8 models are presented in Figure 1 of the Supporting Information. The QM subsystem, including the zinc and its coordinating ligands, was treated with B3LYP functional using Stuttgart ECP/basis set[36] for the zinc atom and 6-31G(d) basis set for all other atoms, which has been previously tested and employed successfully to describe zinc coordination shell.[14,21,58−60] The QM/MM boundary was described by improved pseudobond approach.[61−64] All other atoms were described by the same molecular mechanical force field used in classical MD simulations. The spherical boundary condition had been applied so that atoms beyond 22 Å from the zinc atom were fixed. The 18 and 12 Å cutoffs were employed for electrostatic and van der Waals interactions, respectively. There was no cutoff for electrostatic interactions between QM and MM regions. The prepared system was first minimized by QM/MM calculations. Finally, more than 20 ps ab initio QM/MM MD simulations were carried out with 1 fs as the time step, and the Beeman algorithm[65] was used to integrate the Newton equations of motion. To further check the convergence of our simulations, we also extended the ab initio QM/MM MD simulations to 40 ps for the TLNa system. As shown in Table 1 of the Supporting Information, the difference of average distances and the fluctuation for the zinc coordination shell in TLNa are very similar for different time periods. The Berendsen
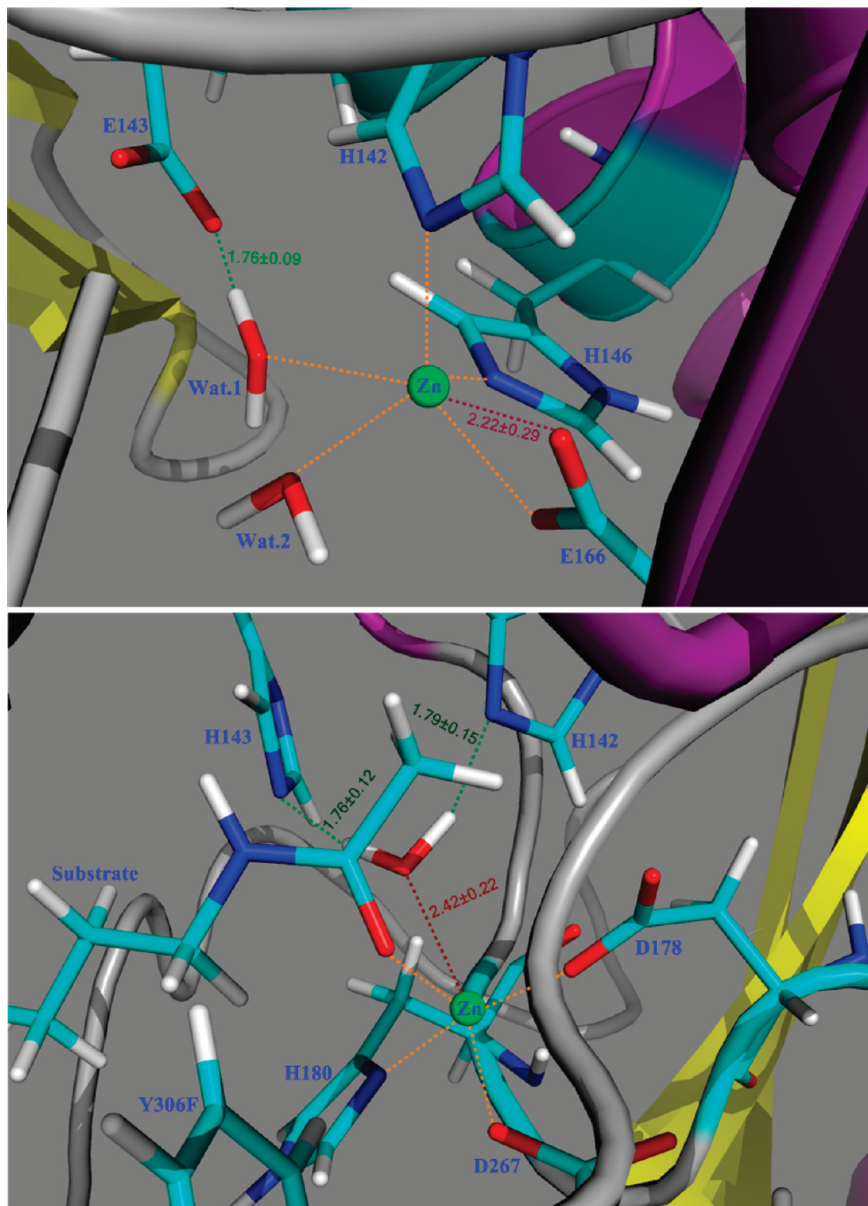
Figure 2. The representative active site of TLN complex (TLNa) and HDAC8 (model 1). The coordination shell is indicated by a dash line in orange (the most flexible bond is highlighted in purple), and the important hydrogen bonds are shown in green.

thermostat method[50] was used to control the system temperature at 300 K. The last 20 ps trajectory, which has achieved the equilibrated temperature (300 K), is adopted as data analysis. To make sure that the fluctuation of the zinc coordination shell is not due to the higher temperature of the QM subsystem, we have monitored it along our QM/MM MD simulation trajectories. We found that most of the time the temperature of the QM subsystem is not higher than 300 K, and the fluctuation is reasonable. All ab initio QM/MM calculations were performed with modified Q-Chem[66] and Tinker[67] programs.

Results and Discussion

For TLN, we simulated four enzyme complexes of TLN with different coordinating ligands starting from their respective crystal structures as illustrated in Figure 1a. In the model
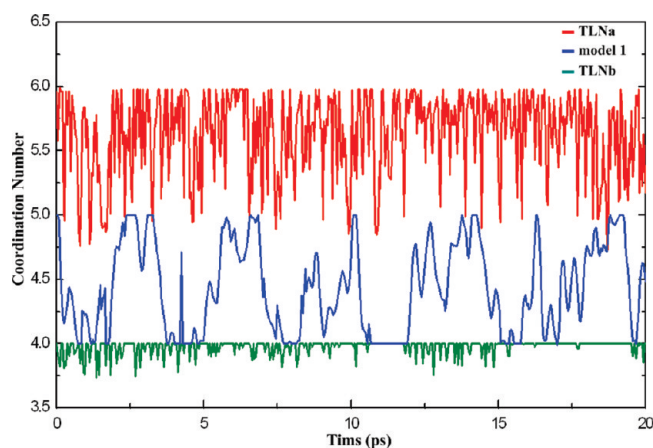
Figure 3. The coordination number change during the DFT QM/MM MD simulations.

Figure 4. The change of the coordination distance to zinc during the DFT QM/MM MD simulations.

TLNa, in which no substrate is bound to the active site, the zinc ion is six-coordinated with a bidentate carboxyl group and two water molecules in the crystal structure. From Table 1, we can see that our MD simulation results not only reproduced the coordination shell very well but also clearly indicated the flexibility and dynamics of the zinc catalytic site. The coordination between Zn^{2+} and Glu166:OE1 i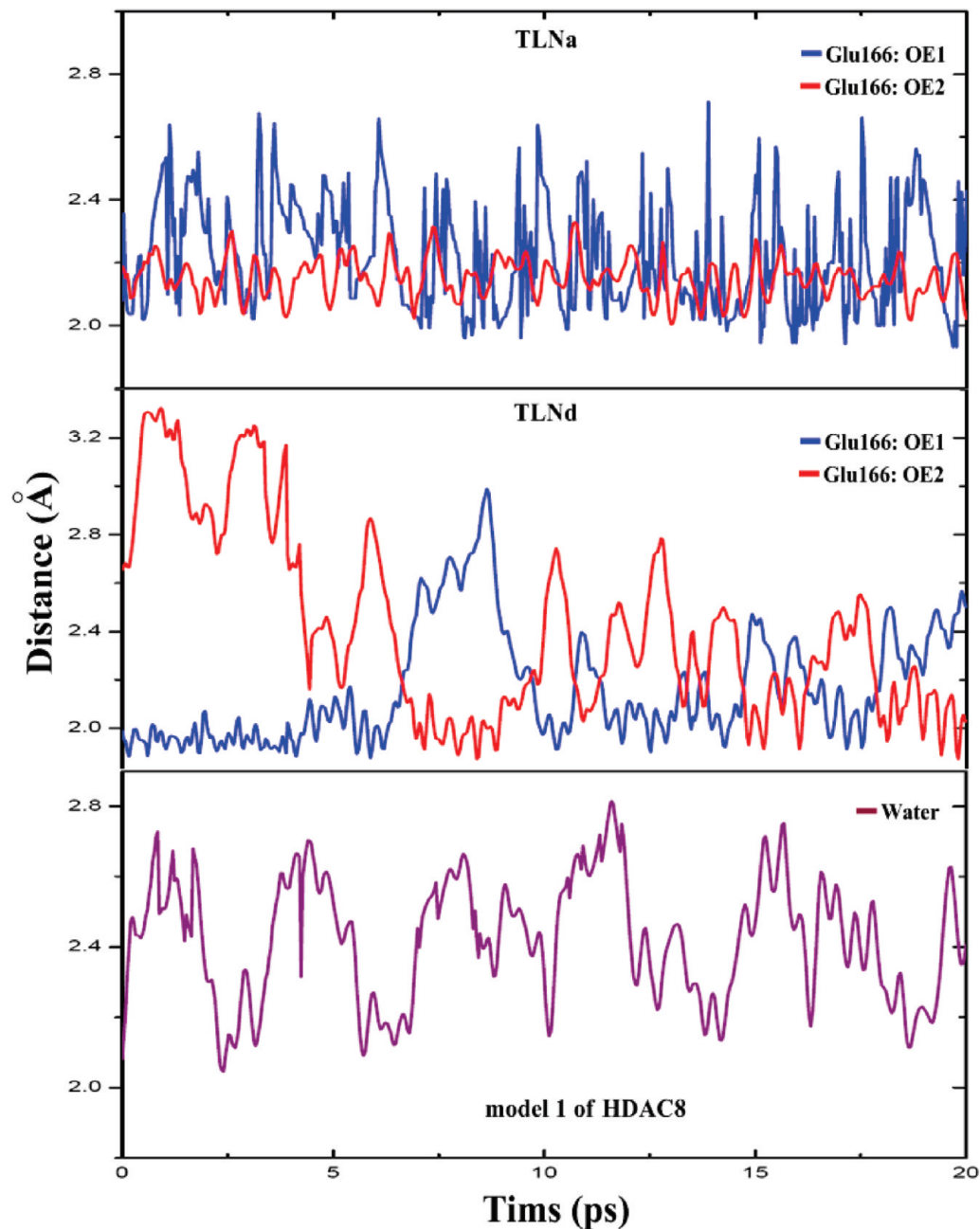s demonstrated to be most dynamic, and the zinc–carboxylate coordination fluctuates between mono- and bidentate manners as shown in Figures 3 and 4. Interestingly, in the model TLNb, in which the inhibitor is bound to Zn^{2+} with a thiolate, its zinc coordination is much less flexible which is manifested by the small standard deviation (SD) and is kept to be tetrahedral as in the crystal structure most of the time (see Figure 3). Meanwhile, in models TLNc and TLNd, which have been suggested to mimic the reaction transition state and product, respectively, their zinc active sites are found

to be even more flexible than that in model TLNa. For both models, the zinc–carboxylate coordination is the most flexible and continuously changes between monodentate and bidentate manner dynamically. We can also see that the ligand exchange in zinc coordination is very fast and can occur at the picoseconds scale as illustrated in Figure. 4.

For HDAC8, a key distinct feature of its active site is that there are two carboxylate groups coordinated to zinc instead of only one carboxylate in TLN. From structural studies, only monodentate mode of carboxylate coordination has been observed.[23–26] Considering the medical and biological significance of HDACs, it would be of particular interest to probe the dynamics of its zinc active site. Here, we have simulated two HDAC8 complexes starting from their respective crystal structures: model 1 is a Y306F mutant in complex with its substrate acetyl-lysine,[25] and model 2 is the wild-type HDAC8 binding with its superstar inhibitor SAHA[24]

as shown in Figure 1b. From Table 2, we can see that the average distances are consistent with the experimental data, and fluctuations indicate the flexibility of the zinc coordination sphere. Although the zinc active sites in both models are still quite dynamic, the carboxylate coordination is very stable, which is manifested by the small fluctuation, and is always kept in the monodentate mode. As shown in Figures 3 and 4, in the mutant−substrate complex (model 1), its zinc coordination number fluctuates between 4 and 5 and its main flexibility comes from the coordination of the water molecule. In the HDAC8-SAHA complex, its 5-fold zinc coordination is considerably more stable. SAHA is coordinated to the zinc in the bidentate manner most of the time, but it remains to be more flexible than other amino acid ligands, which is indicated by the relatively large standard deviation in Table 2. Thus, our simulations clearly indicate that the dynamics of the zinc active site of HDAC8 is quite different from thermolysin and suggest that HDAC8 is not likely to employ the carboxylate-shift mechanism in its catalytic cycle.

As noted in Figure 1, the first coordination shell in TLN is 2His+Glu, and for HDAC8 is 1His+2Asp, so the total charge for the coordination shell is different. This would be an important factor which leads to their different flexibility of zinc-binding sites. Such distinct dynamics in the zinc coordination shell also suggests that the catalytic role of zinc in TLN and HDAC8 is likely to be different in spite of the fact that both catalyze the hydrolysis of amide bond.

In summary, with ab initio QM/MM MD simulations, we have provided direct evidence regarding the inherent flexibility of the catalytic zinc coordination in both TLN and HDAC8 and have observed different coordination modes and fast ligand exchange. For TLN, the coordination of the carboxylate group of Glu166 is found to be most flexible, which can continuously change between monodentate and bidentate manner dynamically. For HDAC8, its coordination to all three amino acid ligands, including two carboxylate groups of Asp, is very stable. Its flexibility mainly comes from a nonamino acid ligand. Such distinct dynamics in their zinc coordination shell suggest that the catalytic role of zinc in TLN and HDAC8 is likely to be different in spite of the fact that both catalyze the hydrolysis of amide bond. Furthermore, our work demonstrates the feasibility and applicability of Born−Oppenheimer ab initio QM/MM MD simulations in simulating metalloenzymes and sets the stage for more detailed understanding of catalysis and inhibition in TLN and HDAC8.

Supporting Information Available: The illustration of QM/MM partition for selected model systems and the data for 40 ps ab initio QM/MM MD results. This information is available free of charge via the Internet at http://pubs.acs.org

References

(1) Andreini, C.; Banci, L.; Bertini, I.; Rosato, A. *J. Proteome Res.* **2006**, *5*, 196–201.

(2) Odell, B. L. *Nutr. Rev.* **1992**, *50*, 48–50.

(3) Lipscomb, W. N.; Strater, N. *Chem. Rev.* **1996**, *96*, 2375–2433.

(4) Christianson, D. W.; Cox, J. D. *Annu. Rev. Biochem.* **1999**, *68*, 33–57.

(5) Parkin, G. *Chem. Rev.* **2004**, *104*, 699–767.

(6) Anzellotti, A. I.; Farrell, N. P. *Chem. Soc. Rev.* **2008**, *37*, 1629–1651.

(7) Karlin, S.; Zhu, Z. Y. *Proc. Natl. Acad. Sci. U.S.A.* **1997**, *94*, 14231–14236.

(8) Lee, Y. M.; Lim, C. *J. Mol. Biol.* **2008**, *379*, 545–553.

(9) McCall, K. A.; Huang, C. C.; Fierke, C. A. *J. Nutr.* **2000**, *130*, 1437S–1446S.

(10) Sigel, H.; Martin, R. B. *Chem. Soc. Rev.* **1994**, *23*, 83–91.

(11) Parkin, G. *Chem. Commun.* **2000**, *20*, 1971–1985.

(12) Tamames, B.; Sousa, S. F.; Tamames, J.; Fernandes, P. A.; Ramos, M. J. *Proteins: Struct., Funct., Bioinf.* **2007**, *69*, 466–475.

(13) Robert, V.; Lemercier, G. *J. Am. Chem. Soc.* **2006**, *128*, 1183–1187.

(14) Sousa, S. F.; Fernandes, P. A.; Ramos, M. J. *J. Am. Chem. Soc.* **2007**, *129*, 1378–1385.

(15) Matthews, B. W. *Acc. Chem. Res.* **1988**, *21*, 333–340.

(16) Holland, D. R.; Hausrath, A. C.; Juers, D.; Matthews, B. W. *Protein Sci.* **1995**, *4*, 1955–1965.

(17) Roderick, S. L.; Fourniezaluski, M. C.; Roques, B. P.; Matthews, B. W. *Biochemistry* **1989**, *28*, 1493–1497.

(18) Tronrud, D. E.; Monzingo, A. F.; Matthews, B. W. *Eur. J. Biochem.* **1986**, *157*, 261–268.

(19) Holden, H. M.; Matthews, B. W. *J. Biol. Chem.* **1988**, *263*, 3256–3260.

(20) Kimura, E. *Acc. Chem. Res.* **2001**, *34*, 171–179.

(21) Sousa, S. F.; Fernandes, P. A.; Ramos, M. J. *Biophys. J.* **2005**, *88*, 483–494.

(22) Szeto, M. W. Y.; Mujika, J. I.; Zurek, J.; Mulholland, A. J.; Harvey, J. N. *J. Mol. Struct.: THEOCHEM* **2009**, *898*, 106–114.

(23) Vannini, A.; Volpari, C.; Filocamo, G.; Casavola, E. C.; Brunetti, M.; Renzoni, D.; Chakravarty, P.; Paolini, C.; De Francesco, R.; Gallinari, P.; Steinkuhler, C.; Di Marco, S. *Proc. Natl. Acad. Sci. U.S.A.* **2004**, *101*, 15064–15069.

(24) Somoza, J. R.; Skene, R. J.; Katz, B. A.; Mol, C.; Ho, J. D.; Jennings, A. J.; Luong, C.; Arvai, A.; Buggy, J. J.; Chi, E.; Tang, J.; Sang, B. C.; Verner, E.; Wynands, R.; Leahy, E. M.; Dougan, D. R.; Snell, G.; Navre, M.; Knuth, M. W.; Swanson, R. V.; McRee, D. E.; Tari, L. W. *Structure* **2004**, *12*, 1325–1334.

(25) Vannini, A.; Volpari, C.; Gallinari, P.; Jones, P.; Mattu, M.; Carfi, A.; De Francesco, R.; Steinkuhler, C.; Di Marco, S. *EMBO Rep.* **2007**, *8*, 879–884.

(26) Dowling, D. P.; Gantt, S. L.; Gattis, S. G.; Fierke, C. A.; Christianson, D. W. *Biochemistry* **2008**, *47*, 13554–13563.

(27) Mann, B. S.; Johnson, J. R.; Cohen, M. H.; Justice, R.; Pazdur, R. *Oncologist* **2007**, *12*, 1247–1252.

(28) Marks, P. A.; Breslow, R. *Nat. Biotechnol.* **2007**, *25*, 84–90.

Thermolysin and HDAC8 Catalytic Zinc Coordination

J. Chem. Theory Comput., Vol. 6, No. 1, 2010 **343**

(29) Park, H.; Brothers, E. N.; Merz, K. M. *J. Am. Chem. Soc.* **2005**, *127*, 4232–4241.

(30) Wong, K. Y.; Gao, J. *Biochemistry* **2007**, *46*, 13352–13369.

(31) Elstner, M.; Cui, Q.; Munih, P.; Kaxiras, E.; Frauenheim, T.; Karplus, M. *J. Comput. Chem.* **2003**, *24*, 565–581.

(32) Lopez-Canut, V.; Marti, S.; Bertran, J.; Moliner, V.; Tunon, I. *J. Phys. Chem. B* **2009**, *113*, 7816–7824.

(33) Brauer, M.; Kunert, M.; Dinjus, E.; Klussmann, M.; Doring, M.; Gorls, H.; Anders, E. *J. Mol. Struct.: THEOCHEM* **2000**, *505*, 289–301.

(34) Lopez, X.; York, D. M. *Theor. Chem. Acc.* **2003**, *109*, 149–159.

(35) Xu, D. G.; Guo, H. *J. Am. Chem. Soc.* **2009**, *131*, 9780–9788.

(36) Dolg, M.; Wedig, U.; Stoll, H.; Preuss, H. *J. Chem. Phys.* **1987**, *86*, 866–872.

(37) Hu, P.; Wang, S.; Zhang, Y. *J. Am. Chem. Soc.* **2008**, *130*, 3806–3813.

(38) Hu, P.; Wang, S.; Zhang, Y. *J. Am. Chem. Soc.* **2008**, *130*, 16721–16728.

(39) Wang, S. L.; Hu, P.; Zhang, Y. K. *J. Phys. Chem. B* **2007**, *111*, 3758–3764.

(40) Ke, Z. H.; Zhou, Y. Z.; Hu, P.; Wang, S. L.; Xie, D. Q.; Zhang, Y. K. *J. Phys. Chem. B* **2009**, *113*, 12750–12758.

(41) Guex, N.; Peitsch, M. C. *Electrophoresis* **1997**, *18*, 2714–2723.

(42) Gordon, J. C.; Myers, J. B.; Folta, T.; Shoja, V.; Heath, L. S.; Onufriev, A. *Nucleic Acids Res.* **2005**, *33*, W368–W371.

(43) Antonczak, S.; Monard, G.; Ruiz-Lopez, M. F.; Rivail, J. L. *J. Am. Chem. Soc.* **1998**, *120*, 8825–8833.

(44) Blumberger, J.; Lamoureux, G.; Klein, M. L. *J. Chem. Theory Comput.* **2007**, *3*, 1837–1850.

(45) Stote, R. H.; Karplus, M. *Proteins: Struct., Funct., Genet.* **1995**, *23*, 12–31.

(46) Liang, J. Y.; Lipscomb, W. N. *Proc. Natl. Acad. Sci. U.S.A.* **1990**, *87*, 3675–3679.

(47) Pang, Y. P. *Proteins: Struct., Funct., Genet.* **2001**, *45*, 183–189.

(48) Yan, C. L.; Xiu, Z. L.; Li, X. H.; Li, S. M.; Hao, C.; Teng, H. *Proteins: Struct., Funct., Bioinf.* **2008**, *73*, 134–149.

(49) Karjiban, R. A.; Rahman, M. B. A.; Basri, M.; Salleh, A. B.; Jacobs, D.; Wahab, H. A. *Protein J.* **2009**, *28*, 14–23.

(50) Berendsen, H. J. C.; Postma, J. P. M.; Vangunsteren, W. F.; Dinola, A.; Haak, J. R. *J. Chem. Phys.* **1984**, *81*, 3684–3690.

(51) Case, D. A.; Darden, T. A.; Cheatham, T. E., III; Simmerling, C. L.; Wang, J.; Duke, R. E.; Luo, R.; Crowley, M.; Walker, R. C.; Zhang, W.; Merz, K. M.; Wang, B.; Hayik, S.; Roitberg, A.; Seabra, G.; Kolossváry, I.; Wong, K. F.; Paesani, F.; Vanicek, J.; Wu, X.; Brozell, S. R.; Steinbrecher, T.; Gohlke, H.; Yang, L.; Tan, C.; Mongan, J.; Hornak, V.; Cui, G.; Mathews, D. H.; Seetin, M. G.; Sagui, C.; Babin, V. Kollman,

P. A. *AMBER 10* University of California: San Francisco, CA, 2008.

(52) Cornell, W. D.; Cieplak, P.; Bayly, C. I.; Gould, I. R.; Merz, K. M.; Ferguson, D. M.; Spellmeyer, D. C.; Fox, T.; Caldwell, J. W.; Kollman, P. A. *J. Am. Chem. Soc.* **1995**, *117*, 5179–5197.

(53) Wang, J. M.; Cieplak, P.; Kollman, P. A. *J. Comput. Chem.* **2000**, *21*, 1049–1074.

(54) Hornak, V.; Abel, R.; Okur, A.; Strockbine, B.; Roitberg, A.; Simmerling, C. *Proteins: Struct., Funct., Bioinf.* **2006**, *65*, 712–725.

(55) Jorgensen, W. L.; Chandrasekhar, J.; Madura, J. D.; Impey, R. W.; Klein, M. L. *J. Chem. Phys.* **1983**, *79*, 926–935.

(56) Wang, J. M.; Wolf, R. M.; Caldwell, J. W.; Kollman, P. A.; Case, D. A. *J. Comput. Chem.* **2004**, *25*, 1157–1174.

(57) Ryckaert, J. P.; Ciccotti, G.; Berendsen, H. J. C. *J. Comput. Phys.* **1977**, *23*, 327–341.

(58) Corminboeuf, C.; Hu, P.; Tuckerman, M. E.; Zhang, Y. K. *J. Am. Chem. Soc.* **2006**, *128*, 4530–4531.

(59) Xiao, C. Y.; Zhang, Y. K. *J. Phys. Chem. B* **2007**, *111*, 6229–6235.

(60) Sousa, S. F.; Fernandes, P. A.; Ramos, M. J. *Proteins: Struct., Funct., Bioinf.* **2007**, *66*, 205–218.

(61) Zhang, Y. K. *Theor. Chem. Acc.* **2006**, *116*, 43–50.

(62) Zhang, Y. K.; Lee, T. S.; Yang, W. T. *J. Chem. Phys.* **1999**, *110*, 46–54.

(63) Zhang, Y. K.; Liu, H. Y.; Yang, W. T. *J. Chem. Phys.* **2000**, *112*, 3483–3492.

(64) Zhang, Y. K. *J. Chem. Phys.* **2005**, *122*, 024114.

(65) Beeman, D. *J. Comput. Phys.* **1976**, *20*, 130–139.

(66) Shao, Y.; Molnar, L. F.; Jung, Y.; Kussmann, J.; Ochsenfeld, C.; Brown, S. T.; Gilbert, A. T. B.; Slipchenko, L. V.; Levchenko, S. V.; O'Neill, D. P.; DiStasio, R. A.; Lochan, R. C.; Wang, T.; Beran, G. J. O.; Besley, N. A.; Herbert, J. M.; Lin, C. Y.; Van Voorhis, T.; Chien, S. H.; Sodt, A.; Steele, R. P.; Rassolov, V. A.; Maslen, P. E.; Korambath, P. P.; Adamson, R. D.; Austin, B.; Baker, J.; Byrd, E. F. C.; Dachsel, H.; Doerksen, R. J.; Dreuw, A.; Dunietz, B. D.; Dutoi, A. D.; Furlani, T. R.; Gwaltney, S. R.; Heyden, A.; Hirata, S.; Hsu, C. P.; Kedziora, G.; Khalliulin, R. Z.; Klunzinger, P.; Lee, A. M.; Lee, M. S.; Liang, W.; Lotan, I.; Nair, N.; Peters, B.; Proynov, E. I.; Pieniazek, P. A.; Rhee, Y. M.; Ritchie, J.; Rosta, E.; Sherrill, C. D.; Simmonett, A. C.; Subotnik, J. E.; Woodcock, H. L.; Zhang, W.; Bell, A. T.; Chakraborty, A. K.; Chipman, D. M.; Keil, F. J.; Warshel, A.; Hehre, W. J.; Schaefer, H. F.; Kong, J.; Krylov, A. I.; Gill, P. M. W.; Head-Gordon, M. *Q-Chem*, version 3.0; Q-Chem, Inc.: Pittsburgh, PA, 2006.

(67) Ponder, J. W. *TINKER, Software Tools for Molecular Design*, version 4.2; 2004.

(68) Maret, W.; Li, Y. *Chem. Rev.* **2009**, *109*, 4682–4707.

CT9005322

JCTC Journal of Chemical Theory and Computation

A Transferable H-Bonding Correction for Semiempirical Quantum-Chemical Methods

Martin Korth,[†] Michal Pitoňák,[†,‡] Jan Řezáč,[†] and Pavel Hobza*[,†,§]

*Institute of Organic Chemistry and Biochemistry, Academy of Sciences of the Czech Republic
and Center for Biomolecules and Complex Systems, 16610 Prague 6, Czech Republic,
Department of Physical and Theoretical Chemistry, Faculty of Natural Sciences,
Comenius University, 84215 Bratislava 4, Slovak Republic, and Department of
Physical Chemistry, Palacky University, 771 46 Olomouc, Czech Republic*

Abstract: Semiempirical methods could offer a feasible compromise between ab initio and empirical approaches for the calculation of large molecules with biological relevance. A key problem for attempts in this direction is the rather bad performance of current semiempirical methods for noncovalent interactions, especially hydrogen-bonding. On the basis of the recently introduced PM6-DH method, which includes empirical corrections for dispersion (D) and hydrogen-bond (H) interactions, we have developed an improved and transferable H-bonding correction for semiempirical quantum chemical methods. The performance of the improved correction is evaluated for PM6, AM1, OM3, and SCC-DFTB (enhanced by standard empirical dispersion corrections) with several test sets for noncovalent interactions and is shown to reach the quality of current DFT-D approaches for these types of problems.

1. Introduction

The ability to perform fast and accurate computer simulations of biomolecular systems has the potential to bring new insight and application opportunities in several scientific fields, for example, the development of selective receptors, catalysts, and enzyme inhibitors in computational drug design. Complementary computational methods for de novo drug design and virtual screening have already made striking successes possible, for example, through computer-aided drug lead generation and optimization.[1,2] Although these approaches can support and complement drug design, they can not be seen as fully mature, because both the modeling tools used and our understanding of protein−ligand recognition principles are still limited, especially regarding the effects of protein flexibility and solvation.[3]

Even though many advanced and accurate computational methods exist, their application to large-scale simulations of biomolecules is not possible, because these methods are computationally too demanding. As a result, the method of choice for these applications is molecular mechanics (MM). Although MM performs well in many cases, it has several drawbacks: By design, it cannot describe quantum effects like, for example, changes in electronic structure, such as chemical reactions or charge transfer, and most MM models also neglect polarization effects, which were shown to be important, for example, for the solvation of biomolecules.[4] Promising tools to overcome these limitations while maintaining efficiency (allowing extensive sampling of biologically relevant molecular systems) are semiempirical (SE) quantum mechanical methods.

The application of current SE methods to biochemical problems is unfortunately not straightforward, because the structure and function of biomacromolecules are dominantly influenced by noncovalent interactions like dispersion and hydrogen-bonding,[5] that generally need very high-level quantum chemical methods to be modeled with sufficient accuracy.[6] Despite this, the past few years have seen great success with the incorporation of dispersion effects via

* To whom correspondence should be addressed. E-mail: pavel.hobza@marge.uochb.cas.cz.
† Academy of Sciences of the Czech Republic and Center for Biomolecules and Complex Systems.
‡ Comenius University.
§ Palacky University.

empirical corrections for a wide range of DFT[7,8] and also SE (e.g., PM3-D, AM1-D[9]) methods. But because substrate recognition and binding is most often dominated by electrostatics, the accurate description of these effects and especially the hydrogen-bond interactions are also of fundamental importance for any biomolecular modeling approach. Examples for the importance of hydrogen-bonding for molecular recognition are, for example, DNA base pairing, protein folding, enzyme activity, crystal structures, properties of liquids, and pharmaceutical drug solubility and activity. While electrostatics in general are not a problem for SE methods, current SE methods are known to be deficient in the description of hydrogen-bonding (with hydrogen core−core terms, missing polarization functions on hydrogen, missing orthogonalization corrections, and in general parametrization as discussed reasons, see refs 10 and 11 and references therein). We see this to be the major obstacle limiting the accuracy of SE methods when applied to biomolecules.

As classical modeling approaches are further pushed to their limit, and more and more pitfalls are coming to light,[12] the interest in improving SE for biomolecular modeling purposes grew substantially over the past few years and has led to a number of related publications: As a result of the first biomolecular application attempts with OMn[13] and SCC-DFTB[14] and explorative approaches to describe protein ligand docking with PM3[15,16] and AM1,[17] it became clear that the (earlier known) deficiencies of SE methods for the description of hydrogen bonding[18,19] are of crucial importance in these applications.[16,20] On the other hand, first large-scale SE modeling of protein structures gave promising results[21−23] and showed that the capability of SE methods to detect native structures from collections of decoys is quite remarkable.[12] In order to surpass the accuracy of the description of noncovalent interactions by MM force fields, improving the description of hydrogen-bonding interactions in SE methods is clearly necessary.

A number of approaches offering improvement in this direction have been suggested in the literature so far, for example, on the basis of additional or modified core−core terms (like PM3-PIF[24,25] and PDDG/PM3[26]), third-order terms, and modified parameters for SCC-DFTB[27] and also reformulated QM/MM interaction terms (to improve hydrogen bonding at the QM/MM interface[28]). An overview of the problem and the proposed solutions can be found in refs 10 and 11. While a significantly better performance is observed when applying these techniques, the results still leave large space for further improvements. (It is nevertheless hard to understand why a recent comparison of the performance of semiempirical QM/MM approaches with force fields[29] ignores all developments except the PDDG approaches.) Concerning force field and ab initio results, the following has to be kept in mind: A recent study that evaluated the performance of a set of widely used force fields by calculating the geometries and stabilization energies for a large collection of intermolecular complexes showed that the magnitude of hydrogen-bonding interactions are severely underestimated by all of the force fields tested.[30] And albeit much better, also the performance of DFT methods for the

calculation of (especially the relative) strength of hydrogen-bond interactions is not always of satisfactorily high accuracy (see ref 31 and references therein).

Recently, our group managed to successfully open up a new path to improve SE methods for hydrogen-bonding interactions: We augmented the new PM6 method[32] with empirical corrections for dispersion and hydrogen-bonding interactions (referred to as PM6-DH1 in the following)[33] and were able to achieve large improvements in accuracy for interaction energies of biologically relevant, noncovalently bound systems. PM6 was chosen, because this model is parametrized for 80 elements and was shown to be one of the most accurate SE approaches for a wide range of problems.[32] Furthermore, PM6 is implemented also as a linear-scaling, localized molecular orbital algorithm (termed MOZYME[34]) in Mopac2009[35] and VAMP 10.0, which allows the modeling of most of the proteins in the PDB (with less than about 5000 atoms) on standard desktop computers.[34] While our first-generation H-bonding correction was already a major step forward in accuracy, we have found further improvement possible, to be presented in the following.

2. Empirical H-Bonding Corrections for Semiempirical Quantum Chemical Methods

The First-Generation Correction. To incorporate the major characteristics of hydrogen-bond interactions, the first-generation correction made use of the charges q on the acceptor (A) and hydrogen (H) atoms, the H-bond distance r between these atoms, and a cosine term that promotes a 180° bonding situation for the A···H−D (with the donor atom D) angle:

$$E_{\text{H-bond}} = a\left[\frac{q_A \times q_H}{r^2} \times \cos(\theta) + b \times c^r\right] \qquad (1)$$

The parameters a, b, and c were optimized for eight different bond types, leading to overall 24 parameters for the description of common H bonds involving nitrogen and oxygen acceptor and donor atoms. As the discussion of the results in section 4 will illustrate, this approach leads to a significantly improved performance of PM6 for the description of H-bond interactions.

An in-depth analysis of our correction revealed the following improvement opportunities: While the H-bond distance and the 180° condition for the A···H−D angle are the most important geometrical features of hydrogen-bonding, two additional internal coordinates are needed to complete the sterical description by taking care of the "orientation of the lone pair" at the acceptor atom. We will show later that the full description of all important geometrical features of hydrogen-bonding in the second-generation correction is the major reason for its improved accuracy and reliability. It turns out that the change to a physically more sound description of hydrogen bonding allows us to fix two other problems of the first-generation correction: First, the second term in eq 1 is only dependent on the H-bond distance coordinate. This leads to discontinuous potentials around values of 90° for the A···H−D angle. Second, for some H-bond types, the second−meant to be

346 *J. Chem. Theory Comput., Vol. 6, No. 1, 2010*
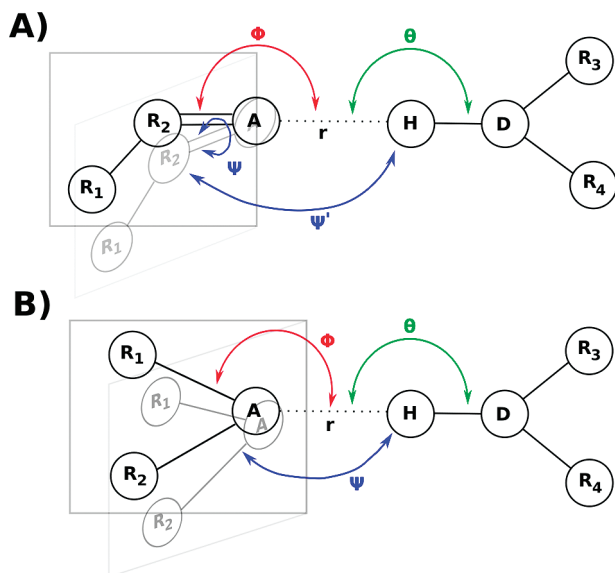
Korth et al.

A)

B)

Figure 1. Illustration of the geometric features of hydrogen-bonding; see text for explanation.

repulsive—term is of an attractive nature (the optimization of the *b* parameter with constraints on the sign was tested but discarded because of a diminished accuracy of the results). By fixing these two problems in the new version, we are able to significantly increase the robustness of our empirical correction approach.

To prevent problems with the optimization of very strong H bonds (like in the case of the formic acid dimer), we had to keep the distance cutoff of the first-generation correction (see ref 33 for a more detailed discussion of this approximation). The cutoff is applied in such a way that H-bond distances below 1.8 Å are set to 1.8 Å for the calculation of the hydrogen-bond energy. It acts like a damping function that forces the correction to a constant value in the repulsive region, where the description seems to be quite deficient otherwise. For molecular dynamics simulations, this cutoff will be implemented with an interpolating polynomial to prevent kinks in the potential surface. We also tried multiplication by a damping function for the second generation correction but found no advantages over the cutoff distance solution.

The application of the above listed changes in the second-generation correction furthermore allows us to change from bond-type to atom-type parameters and to apply our ansatz also to other semiempirical methods.

The Second-Generation Correction. The sterical arrangement of the two system parts involved in a H bond can be defined with six internal coordinates (see Figure 1 for an illustration of the following explanations): the H-bond distance *r*, the two angles A···H—D (termed Θ) and R_2—A···H (termed Φ, with R_2 being a donor "base atom"), and the corresponding three torsional angles of which only one directly influences the H-bond interaction energy, R_1R_2A···H (termed Ψ). The first two mentioned coordinates, the H-bond distance and the angle Θ between acceptor, hydrogen, and donor atoms were incorporated into the first-generation correction. The second two mentioned coordinates define the relative position of the acceptor atom system part

(or so to say the spatial arrangement of the acceptor lone pair), which is important to prevent nonphysical contributions to the H-bond interaction energies (e.g., through other atoms or in the case of purely dispersion-bound complexes). Figure 1 shows r, Θ, Φ, and Ψ for two different cases, an sp^2 oxygen-type acceptor atom (a) and sp^2 nitrogen or general sp^3-type acceptor atoms (b), which require a different choice of atoms for the definition of the torsion angle coordinate. Note that, for our choice of coordinates, the out-of-plane "movement" in case a (described by Ψ') is actually realized by a combined change of the two internal coordinates Φ and Ψ. As a result of these considerations, the new version of our empirical H-bonding correction takes the following form:

$$E_{\text{H-bond}} = \left[a \times \frac{q_A \times q_H}{r^b} + c \times d^r \right] \times$$
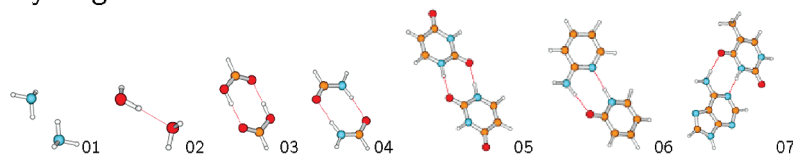$$\cos(\theta) \times \cos(\phi) \times \cos(\psi) \quad (2)$$

with ϕ as the deviation of the R_2—A···H angle from the idealized optimal H-bond angle (taken as 109.48° for sp^3 and 120° for sp^2 structures) and ψ as the deviation of the R_1R_2A···H torsion angle from the idealized optimal H-bond torsion angle (taken to be 109.48° for N sp^3, 109.48/2° for other sp^3 structures, and 0° for sp^2 structures). Two special cases arise: For sp^2 oxygen acceptor atoms, not only 120° but also 180° has to be considered as the idealized optimal H-bond angle; the one with the smaller deviation to the actual binding situation is chosen for the calculation. For NR_3 nitrogen acceptor atoms, the possible planarization of this group has to be taken into account; we chose to calculate the idealized optimal ϕ and ψ values by linear extrapolation between the tetrahedral and planar values (109.48 and 90 for ϕ, 109.48/2 and 90 for ψ) subject to the actual value of the torsion angle between R_1R_2A and the remaining third of the NR_3 group. An alternative (but considering gradient derivations unnecessarily complicated) implementation of our general approach would be to use a cosine term for the angle between the H-bond and an "idealized lone-pair orientation" vector.

The resulting equation was analyzed for the importance of the different terms and parametrized for acceptor atom types in a stepwise optimization process that led to some remarkable observations illustrated by data for the H-bonded complexes of the S26 set (the S22 benchmark set[6] for noncovalent interactions, extended with four singly hydrogen-bonded complexes,[36] see also Figure 2) in Table 1:

• Even when using only the attractive term, $(q_A \times q_H)/(r^b) \times \cos(\theta) \times \cos(\phi) \times \cos(\psi)$, with overall only a single parameter (termed P1 in Table 1: $b = 3.2$) to correct PM6-D for all different types of nitrogen and oxygen hydrogen-bond interactions, our new correction leads to very good (PM6-DH1-quality) values for almost all S26 H-bond interaction energies (please note that the intermediate parametrization results are given to show the robustness of our approach and that the Pn parametrizations are therefore not meant to be some kind of "intermediate" methods).

• The additional distinction between nitrogen and oxygen acceptor atom types (resulting in overall two parameters

H-Bonding Correction for Quantum-Chemical Methods

J. Chem. Theory Comput., Vol. 6, No. 1, 2010 **347**

Hydrogen-bond dominated:

Dispersion dominated:
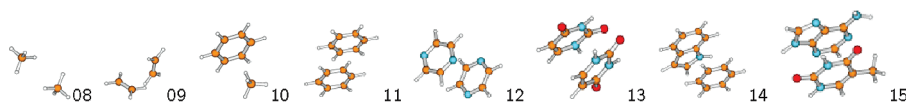
Mixed complexes:

Figure 2. The S22 benchmark set for noncovalent interactions.[6]

Table 1. Intermediate Results from the Optimization Process[a]

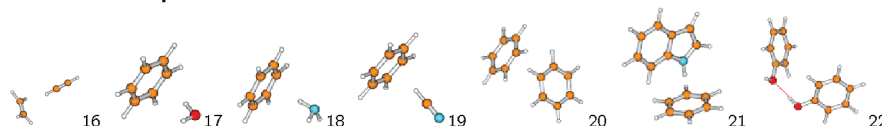| S26 entry	reference	PM6	PM6-D	PM6-DH1	P1[b]	P2[b]	P3[b]	PM6-DH2	AM1-D*	AM1-D*/P1[b]	DFTB-D	DFTB-D/P1[b]	OM3-D	OM3-D/P1[b]
ammonia dimer	−3.17	0.86	0.33	−0.55	−0.14	−0.32	−0.33	−0.04	1.45	0.55	2.57	2.23	−0.28	−0.89
water dimer	−5.02	1.08	0.70	0.35	−1.18	−0.95	−0.05	0.12	1.16	−1.78	1.80	0.09	−5.44	4.15
formic acid dimer	−18.61	7.47	6.47	1.23	−0.08	0.63	−0.08	−0.03	18.26	6.62	2.49	−3.57	−2.53	0.49
formamide dimer	−15.96	3.40	2.18	0.56	−2.21	−1.70	0.34	0.09	7.74	−1.44	2.67	−0.33	−2.12	−0.66
uracil dimer C_{2h}	−20.65	7.32	5.55	1.82	0.37	0.96	0.37	−0.56	11.76	0.43	3.74	−0.17	−0.60	−0.07
2-pyridoxine/2-aminopyridine	−16.71	6.72	4.50	−0.64	0.69	0.41	0.18	0.37	8.09	0.83	4.84	2.49	−2.47	1.08
adenine/thymine Watson/Crick	−16.37	7.30	4.89	−1.46	0.67	0.20	−0.02	−0.09	7.65	−0.68	5.80	3.29	−0.49	−0.07
phenol dimer	−7.05	3.67	1.32	0.31	0.06	0.21	0.06	−0.01	0.96	−0.93	3.02	1.96	−1.84	0.00
methanol dimer	−5.70	2.20	1.35	0.26	−0.25	−0.06	−0.25	−0.55	2.45	−0.15	2.45	1.04	−1.42	0.88
methanol/formaldehyde	−5.31	1.89	1.23	0.47	0.12	0.26	0.12	0.10	1.78	−0.09	2.46	1.62	−2.27	2.26
methyl amide dimer (α)	−6.69	1.76	0.38	−0.34	−0.93	−0.84	−0.27	0.31	1.59	−1.48	0.92	0.07	−0.85	−0.01
methyl amide dimer (β)	−7.65	1.78	0.72	−0.05	−1.00	−0.80	−0.01	−0.02	3.98	0.49	1.59	0.45	−0.68	−0.15
MSE		3.79	2.47	0.16	−0.32	−0.17	0.01	0.04	5.57	0.20	2.86	0.76	−1.75	0.60
MUE		3.79	2.47	0.67	0.64	0.61	0.19	0.19	5.57	1.29	2.86	1.44	1.75	0.89
RMSE		4.56	3.26	0.85	0.88	0.76	0.28	0.24	7.57	2.12	3.15	1.89	2.22	1.47
$\Delta_{\text{Max−Min}}$		6.61	6.13	3.28	2.90	2.66	0.93	0.84	17.30	8.40	4.88	6.86	5.16	5.05

a Errors, mean signed error (MSE), mean unsigned error (MUE), root mean square error (RMSE), and the error span $\Delta_{\text{Max−Min}}$ with respect to the benchmark CCSD(T)/CBS interaction energies are presented. All values in kcal/mol. AM1-D* refers to standard AM1 with a standard empirical dispersion correction, unlike AM1-D, see text for details. *b* For explanation see text, PM6-D and PM6-D/Pn with PM6-DH1 dispersion parameters.

(termed P2)), then leads to comparably small but still significant improvements.

• In the case of PM6-D, the accurate description of H-bonding interactions involving water and peptide systems requires the inclusion of at least one additional atom-type parameter (termed P3).

• Also for AM1-D* (not AM1-D, see next paragraph for explanation), SCC-DFTB-D and OM3-D, a significant improvement is found with only a single parameter ($b = 2.2$ for AM1, 3.2 for DFTB, and 3.1 for OM3). For these methods, no additional parameters for water or peptide systems are necessary, but one additional parameter is required for the proper description of acid acceptor atoms.

We decided not to use the AM1-D method published by McNamara and Hillier[9] with our correction scheme, because their method is not simply AM1 with a standard empirical dispersion correction but is additionally based on a refit of 18 AM1 parameters that also account to some extent for

hydrogen bonding. The variant we use here, termed AM1-D* in the following, refers to standard AM1 with a standard empirical dispersion correction of the Jurečka type.[8] The optimization of the D parameters for the dispersion-bound complexes of the S22 benchmark set led to the values $s_r = 0.91$, $\alpha = 56.0$, and $s_6 = 1.18$. This way, the mean unsigned error for the dispersion-bound S22 complexes was decreased from 6.7 kcal/mol for AM1 to 0.4 kcal/mol for AM1-D*, slightly lower than the 0.6 kcal/mol found for AM1-D.[9]

We also adjusted the dispersion correction for PM6, because we have found that PM6-DH1 overestimates dispersion effects in saturated systems. The new parameters are $s_r = 1.04$, $\alpha = 20.0$, and $s_6 = 0.89$ (instead of $s_r = 1.07$, $\alpha = 11.0$, and $s_6 = 1.00$ for the old version), in combination with $c_6 = 0.95$ for sp³ carbon and $c_6 = 1.65$ for other carbon atoms (instead of $c_6 = 1.65$ for all carbon atoms) and a hydrogen van der Waals radius of 156 pm (instead of 120 pm). The effects of these changes are very small for the

systems investigated here but become significant, for example, for large, saturated hydrocarbon chains. We decided to nevertheless include these changes here to avoid spreading the details of PM6-DH2 over multiple publications.

As a training set for the stepwise H-bonding correction parameter optimization procedure, the equilibrium structures of the original H-correction training set[33] (105 hydrogen-bond interaction energies) were extended with the (non-charged) 37 hydrogen-bonded DNA base pairs and 13 peptide interaction energies from the JSCH2005 set.[6] Another optimization run on the much smaller S26 test led to essentially the same parameter values, showing on one hand the stability of our approach with respect to the chosen parameters and on the other hand the usefulness of this test set for the parametrization of new methodological developments for H-bonding interactions. (Due to the implications of the limited size of the S26 complexes we do not assume this to be equally true for empirical dispersion corrections).

Because the fitting of correction terms only to equilibrium structure data is prone to result in problems in real-life applications, we extended in the next step the S26 set with the S22 × 4 set,[37] which contains four nonequilibrium structures with high-level reference data for each of the S22 complexes. While not necessary at all for the description of the equilibrium structures, the second (constrained to be repulsive) term in eq 2 was included to further improve the accuracy at short distances, especially in the case of very strong hydrogen bonds like those found in the formic acid dimer.

The inclusion of more parameters for a (reasonably) larger number of acceptor atom types or additional parameters for donor atom types led to no significant improvements. In addition, it was found that method-independent values can be chosen for the parameters b, c, and d in eq 2, because slight differences are absorbed by the method-dependent a parameters. For the final parametrization of the new correction for the PM6-D, AM1-D*, OM3-D, and SCC-DFTB-D methods on the combined S26/S22 × 4 set, fixed values of b, c, d, and five acceptor atom types with different a parameters were chosen. Albeit a significant improvement can already be found with only one a parameter, the additional increase of accuracy (especially for water and peptides in the case of PM6-D) outweighed our concerns of using five different acceptor-atom-type-based a parameters. This view was further supported by the rather well-behaved nature of the parameters (that nicely reflect the capabilities of the underlying SE methods to describe hydrogen bonding) and the overall number of parameters in SE methods.

As a result, the outlined procedure led to three global and five method-dependent parameters for the description of common H bonds involving nitrogen and oxygen acceptor and donor atoms. One additional method-dependent parameter for the description of H bonds involving sulfur acceptor atoms was generated accordingly for every method (except OM3, where no sulfur SE parameters were available to us), using the sulfur hydrogen-bonded DNA base pairs from the JSCH2005 set.[6] The final parameters are shown in Table 2. We believe that the differences of the individual parameter values are more likely to reflect advantages and deficiencies

Table 2. Final Parameters

parameter	element	PM6	AM1	OM3	DFTB
		Global			
b	all	3.0			
c	all	0.65			
d	all	5.0			
		Method-Dependent			
a	N	1.48	4.54	0.86	4.41
	O	1.56	3.75	0.75	1.84
	O$_{acid}$	1.55	5.55	1.51	1.15
	O$_{peptide}$	0.96	3.46	0.78	1.56
	O$_{water}$	0.76	3.52	0.49	1.57
	S	0.85	1.05	—[a]	0.53

[a] OM3 sulfur parameters unavailable.

of the parametrization of the underlying SE methods, rather than physical issues of different H-bonding interactions. As noted before, the qualitative parameter differences between methods nicely reflect the initial capability of the underlying SE methods to describe hydrogen bonding (with a rather bad performance of AM1 and a quite good performance of OM3 at the two ends of the scale).

We also tested our correction with third-order SCC-DFTB with and without a modified γ parameter for an improved description of hydrogen bonding[27] but ended up with the same accuracy as with SCC-DFTB-DH2 (which is significantly higher than third-order SCC-DFTB with a modified γ parameter, giving an MAD of 1.0 and an error span of 6.0 kcal/mol for the S26 test set).

As the last step, an analytical gradient for the proposed correction was implemented. This was done analogously to the first-generation correction, that is, without derivatives of the atom charges. This approximation was found to have only a minor impact for the cases investigated here and allows us to keep our approach simple and fast but surely needs deeper investigation in the future.

3. Computational Details

Semiempirical PM6 and AM1 calculations applying the MOZYME algorithm were done with MOPAC2009,[35] OM3 calculations with MNDO2005, and SCC-DFTB calculations with DFTB+.[38] TPSS[39] and B3-LYP[40,41] DFT calculations with empirical dispersion corrections of the Jurecka type[8] were done with Turbomole 5.10[42] using TZVPP[43] Gaussian AO basis sets and the RI approximation[44,45] for two-electron integrals. The second-generation H-bonding correction is implemented as an add-on correction to MOPAC2009, mndo99 and DFTB+ in our own development code (the latest version of this software can be obtained from the authors upon request), and will be included in a future release of MOPAC2009.

4. Results and Discussion

Tables 3−8 show results of PM6, AM1, OM3, and SCC-DFTB calculations with dispersion correction and first- and second-generation H-bonding corrections for the S26 (Table 3), S22 (Table 4, in additional comparison to literature data), and S26+S22 × 4 benchmark sets (Table 5), the PM6-DH1 training set of 105 small hydrogen-bonded complexes (Table

Table 3. Results for the S26 Set[a]

S26 entry	CCSD(T)/CBS	PM6	PM6-D	PM6-DH1	PM6-DH2	TPSS-D[a]	B3LYP-D[a]	AM1	AM1-D*	AM1-DH2	DFTB	DFTB-D	DFTB-DH2	OM3	OM3-D	OM3-DH2
ammonia dimer	−3.17	0.86	0.57	−0.57	−0.04	0.57	0.71	2.38	1.45	0.67	2.82	2.57	1.12	1.24	0.49	0.06
water dimer	−5.02	1.08	0.91	0.35	0.12	1.31	1.49	2.13	1.16	−1.43	1.82	1.80	−0.63	0.93	0.28	0.09
formic acid dimer	−18.61	7.47	6.76	1.23	−0.03	0.85	0.70	20.14	18.26	1.09	2.74	2.49	−1.11	7.06	5.44	0.26
formamide dimer	−15.96	3.40	2.49	0.56	0.09	0.17	0.47	10.23	7.74	−0.97	3.40	2.67	−0.32	4.28	2.53	1.07
uracil dimer C_{2h}	−20.65	7.32	5.88	1.82	−0.56	−0.14	0.37	14.85	11.76	−0.30	4.98	3.74	−1.64	4.47	2.12	0.28
2−pyridoxine/2−aminopyridine	−16.71	6.72	4.97	−0.64	0.37	1.16	1.06	12.25	8.09	0.15	6.45	4.84	−0.91	5.36	2.47	1.51
adenine/thymine Watson/Crick	−16.37	7.30	5.37	−1.46	−0.09	0.71	0.78	12.08	7.65	−2.27	7.58	5.80	−1.54	5.03	1.84	0.39
methane dimer	−0.53	0.56	0.18	−0.10	0.18	0.17	−0.03	0.85	−0.18	−0.18	0.54	0.06	0.06	0.67	−0.08	−0.08
ethene dimer	−1.51	1.11	0.45	−0.01	0.45	0.17	0.11	1.38	−1.25	−1.25	1.32	0.70	0.70	1.65	−0.17	−0.17
benzene/methane	−1.50	1.02	0.11	−0.25	0.11	−0.39	−0.41	1.90	−0.70	−0.70	1.32	0.29	0.29	1.63	−0.01	−0.01
benzene dimer stacked	−2.73	2.84	−0.85	−0.90	−0.85	−0.31	−0.88	6.24	−0.38	−0.38	3.10	−0.37	−0.37	3.86	−1.14	−1.14
pyrazine dimer	−4.42	2.60	−0.93	−1.00	−0.93	−0.75	−0.98	6.91	−0.16	−0.16	4.11	0.79	0.79	3.74	−1.47	−1.47
uracil dimer C_2	−10.12	5.66	0.70	0.42	0.67	−1.04	−0.52	10.23	−0.02	−0.06	6.17	1.94	1.92	6.16	−1.29	−1.30
indole/benzene stacked	−5.22	5.28	0.16	0.01	0.16	−1.00	−1.64	10.60	0.77	0.77	5.46	0.63	0.63	6.60	−0.76	−0.76
adenine/thymine stacked	−12.23	7.29	0.57	−0.55	0.54	−1.07	−0.84	15.14	0.08	0.04	8.34	2.10	2.08	8.93	−1.87	−1.89
ethene/ethine	−1.53	0.98	0.58	0.42	0.58	0.02	−0.09	1.18	0.13	0.13	0.99	0.54	0.54	0.85	0.10	0.10
benzene/water	−3.28	1.00	0.10	−0.13	0.10	0.49	0.43	2.59	0.54	0.54	2.00	1.62	1.62	1.53	−0.01	−0.01
benzene/ammonia	−2.35	0.82	−0.20	−0.42	−0.20	−0.10	−0.13	2.02	−0.41	−0.41	1.84	0.77	0.77	1.58	−0.04	−0.04
benzene/HCN	−4.46	2.48	1.48	1.27	1.48	−0.64	−0.77	3.65	1.53	1.53	2.73	1.64	1.64	2.78	0.77	0.77
benzene dimer T−shaped	−2.74	1.98	0.15	−0.10	0.15	−0.81	−0.95	3.10	−0.53	−0.53	2.42	0.69	0.69	2.85	0.09	0.09
indole/benzene T−shaped	−5.73	3.32	0.79	0.42	0.79	−0.84	−1.25	4.67	0.44	0.44	4.05	1.71	1.71	4.56	0.79	0.79
phenol dimer	−7.05	3.67	1.84	0.31	−0.01	0.11	0.52	5.69	0.96	−0.85	4.25	3.02	1.19	3.89	0.60	0.24
methanol dimer	−5.70	2.20	1.72	0.26	−0.55	1.28	1.51	4.00	2.45	−0.10	2.66	2.45	0.07	2.58	1.42	1.11
methanol/formaldehyde	−5.31	1.89	1.51	0.47	0.10	0.12	0.61	3.39	1.78	0.16	2.77	2.46	1.29	3.28	2.27	2.38
methylamide dimer (α)	−6.69	1.76	0.74	−0.34	0.31	0.08	0.34	3.81	1.59	0.49	1.98	0.92	0.39	2.44	0.85	0.53
methylamide dimer (β)	−7.65	1.78	0.99	−0.05	−0.02	−0.15	0.36	5.85	3.98	0.36	2.38	1.59	0.40	1.93	0.68	0.03
					Complete S26 Set											
MSE		3.17	1.42	0.04	0.11	−0.00	0.04	6.43	2.57	−0.12	3.39	1.83	0.44	3.46	0.61	0.11
MUE		3.17	1.58	0.54	0.36	0.56	0.69	6.43	2.85	0.61	3.39	1.85	0.94	3.46	1.14	0.64
RMSE		3.94	2.46	0.71	0.51	0.69	0.82	8.18	5.17	0.81	3.93	2.31	1.10	4.04	1.63	0.91
$\Delta_{Max-Min}$		6.91	7.69	3.28	2.41	2.38	3.15	19.29	19.51	3.80	7.80	6.17	3.72	8.26	7.31	4.27
					Hydrogen-Bonded Systems											
MSE		3.79	2.81	0.16	−0.03	0.51	0.74	8.07	5.57	−0.25	3.65	2.86	−0.14	3.54	1.75	0.66
MUE		3.79	2.81	0.67	0.19	0.55	0.74	8.07	5.57	0.74	3.65	2.86	0.88	3.54	1.75	0.66
RMSE		4.56	3.55	0.85	0.27	0.73	0.84	9.77	7.57	0.96	4.05	3.15	1.01	3.95	2.22	0.96
$\Delta_{Max-Min}$		6.61	6.19	3.28	0.93	1.46	1.17	18.01	17.30	3.36	5.76	4.88	2.93	6.13	5.16	2.35

[a] TZVP basis set. [a] Errors, mean signed error (MSE), mean unsigned error (MUE), root mean square error (RMSE), and the error span $\Delta_{Max-Min}$ with respect to the benchmark CCSD(T)/CBS interaction energies are presented. All values in kcal/mol.

Table 4. Results for the S22 Set[a]

method	MUE
MP2/CBS	0.8[c]
B3LYP-D/TZVP	0.7
TPSS-D/TZVP	0.6
M08-HX/6-311+G(3df,2p)/CP	0.5[c]
M06−2X/6-311+G(3df,2p)/CP	0.4[c]
TPSS-D/6-311++G(3df,3pdf)	0.3[d]
B2-PLYP-D/TZVPP/0.5CP	0.3[e]
PM3$_{BP}$	5.2[f]
SCC-DFTB-D	1.9
OM3-D	1.1
PM3-D[b]	0.9[f]
AM1-D[b]	0.9[f]
PM6-DH1	0.6
SCC-DFTB-DH2	1.0
AM1-DH2	0.7
OM3-DH2	0.6
PM6-DH2	0.4

[a] Comparison of mean unsigned errors (MUE) with respect to the benchmark CCSD(T)/CBS interaction energies for various wave function theory, density-function theory and enhanced semiempirical quantum chemical methods are presented. All values in kcal/mol. (0.5)CP stands for (half) counter-poise corrected values. [b] With 18 adjusted AM1/PM3 parameters, see ref 9. [c] From ref 46. [d] From ref 8. [e] From ref 47. [f] From ref 9.

6), the 37 noncharged, H-bonded DNA base pair complexes from the JSCH2005 set (table 7), and the 13 noncharged,

H-bonded peptide-structures from the JSCH2005 test set (Table 8) with corresponding TPSS-D/TZVP and B3-LYP/TZVP data for comparison. Each table shows the reference interaction energy at the CCSD(T)/CBS level, errors relative to these values for the investigated methods, followed by statistical measures overs these errors: the mean signed error (MSE), mean unsigned error (MUE), root-mean-square error (RMSE), and the error span ($\Delta_{Max-Min}$). The errors are calculated so that a positive error means that the investigated method underestimates the binding energy and vice versa.

The general trends for the different benchmark sets are very similar, so that the observations can be summarized altogether in the following way: The standard SE semiempirical methods perform quite badly for both dispersion and hydrogen-bonding interactions, but PM6, OM3, and SCC-DFTB (S26 MUEs around 3 kcal/mol) are significantly more accurate than AM1 (S26 MUE around 6 kcal/mol). The inclusion of empirical dispersion corrections is a great improvement for all tested semiempirical methods. With these corrections, the semiempirical methods are able to model dispersion bound complexes with comparably high accuracy (MUEs between 1 and 3 kcal/mol), so that the largest remaining errors are found for hydrogen-bond interactions.

Table 5. Results for the Combined S26+S22 × 4 Sets (114 Entries)[a]

	PM6	PM6-D	PM6-DH2	TPSS-D[b]	B3LYP-D[b]	AM1	AM1-D*	AM1-DH2	DFTB	DFTB-D	DFTB-DH2	OM3	OM3-D	OM3-DH2
MSE	2.23	1.04	0.14	−0.56	−0.63	4.43	1.86	0.06	2.42	1.34	0.38	2.20	0.51	−0.10
MUE	2.23	1.17	0.36	0.58	0.63	4.43	2.23	0.89	2.42	1.49	0.68	2.20	0.88	0.72
RMSE	3.21	2.07	0.61	0.69	0.72	7.00	4.87	1.72	3.20	2.18	0.88	2.98	1.49	1.29
$\Delta_{Max-Min}$	9.62	9.69	4.96	1.68	1.46	28.52	29.15	14.40	10.21	10.64	4.35	8.97	9.76	7.71

[a] Mean signed error (MSE), mean unsigned error (MUE), root mean square error (RMSE), and the error span $\Delta_{Max-Min}$ with respect to the benchmark CCSD(T)/CBS interaction energies are presented. All values in kcal/mol. [b] TZVP basis set.

Table 6. Results for 105 Small, Hydrogen-Bonded Complexes of the PM6-DH1 Training Set[a]

	PM6	PM6-D	PM6-DH2	TPSS-D[b]	B3LYP-D[b]	AM1	AM1-D*	AM1-DH2	DFTB	DFTB-D	DFTB-DH2	OM3	OM3-D	OM3-DH2
MSE	−2.63	−1.66	−0.43	0.90	1.01	−5.06	−2.55	−0.12	−3.19	−2.33	−0.40	−2.67	−0.88	−0.51
MUE	2.64	1.76	1.15	0.91	1.01	5.06	2.70	1.59	3.21	2.36	0.85	2.67	0.91	0.66
RMSE	3.16	2.35	1.54	1.08	1.15	6.07	4.03	2.12	3.56	2.79	1.06	2.87	1.14	0.86
$\Delta_{Max-Min}$	9.22	9.61	7.37	3.66	3.52	22.75	22.64	12.13	10.32	10.47	5.15	6.73	6.52	4.48

[a] Mean signed error (MSE), mean unsigned error (MUE), root mean square error (RMSE), and the error span $\Delta_{Max-Min}$ with respect to the benchmark CCSD(T)/CBS interaction energies are presented. All values in kcal/mol. [b] TZVP basis set.

Table 7. Results for the Noncharged Hydrogen-Bonded JSCH2005 DNA Base Pairs (37 Entries)[a]

	PM6	PM6-D	PM6-DH2	TPSS-D[b]	B3LYP-D[b]	AM1	AM1-D*	AM1-DH2	DFTB[c]	DFTB-D[c]	DFTB-DH2[c]	OM3[d]	OM3-D[d]	OM3-DH2[d]
MSE	−8.07	−6.06	−0.83	0.42	0.55	−14.08	−9.56	−0.01	−7.21	−5.34	2.09	−5.67	−2.41	−0.80
MUE	8.07	6.06	1.85	0.72	0.70	14.08	9.56	2.20	7.21	5.34	2.78	5.67	2.49	1.21
RMSE	8.23	6.23	2.36	0.97	0.97	14.71	10.33	2.84	7.47	5.64	3.25	5.89	2.79	1.44
$\Delta_{Max-Min}$	8.73	7.67	8.84	3.97	3.86	18.85	16.43	12.43	7.88	6.85	9.58	7.01	6.81	4.53

[a] Mean signed error (MSE), mean unsigned error (MUE), root mean square error (RMSE), and the error span $\Delta_{Max-Min}$ with respect to the benchmark CCSD(T)/CBS interaction energies are presented. All values in kcal/mol. [b] TZVP basis set. [c] Without adenine/fluorotoluene Watson/Crick complex because of missing fluorine parameters. [d] Without seven thio base pairs because of missing sulfur parameters.

Table 8. Results for the Hydrogen-Bonded JSCH2005 Peptides (13 Entries)[a]

	PM6	PM6-D	PM6-DH2	TPSS-D[b]	B3LYP-D[b]	AM1	AM1-D*	AM1-DH2	DFTB	DFTB-D	DFTB-DH2	OM3[c]	OM3-D[c]	OM3-DH2[c]
MSE	−2.97	−0.19	−0.13	−0.35	−0.45	−4.49	1.40	1.47	−3.77	−0.80	−0.72	−3.96	0.33	0.36
MUE	2.97	0.68	0.71	0.67	0.60	4.49	1.49	1.56	3.77	0.87	0.79	3.96	0.60	0.62
RMSE	3.24	0.87	0.89	0.80	0.82	4.95	1.91	2.00	4.01	1.01	0.94	4.21	0.80	0.81
$\Delta_{Max-Min}$	4.56	3.44	3.41	2.53	2.59	7.31	4.30	4.27	5.34	2.91	2.84	5.20	2.81	2.79

[a] Mean signed error (MSE), mean unsigned error (MUE), root mean square error (RMSE), and the error span $\Delta_{Max-Min}$ with respect to the benchmark CCSD(T)/CBS interaction energies are presented. All values in kcal/mol. [b] TZVP basis set. [c] Without seven thio base pairs because of missing sulfur parameters.

As mentioned before, the inclusion of our first-generation H-bonding correction in PM6-DH1 is already a major step toward a higher accuracy for these interactions (with a MUE of 0.7 kcal/mol for the hydrogen-bonding interactions in the S26 set). The largest errors are found for double hydrogen bonds, because of the parametrization to single hydrogen bonds and the higher likeliness of nonphysical contributions to the H-bonding correction in these cases.

The new correction manages to reach even higher accuracy (with a corresponding MUE of 0.2 kcal/mol) and greatly reduced error span (from 3.3 to 0.8 kcal/mol). Furthermore, it can be seen that the new H-bonding correction does not lead to nonphysical interaction energy contributions for purely dispersion-bound complexes (the values for PM6-DH being essentially the same as for PM6-D). Albeit a less accurate final performance is found for AM1, OM3, and DFTB when compared to PM6, the large decrease of errors (especially for AM1) is still impressive for these SE methods. As we focused on PM6 during the initial development phase, we do not want to exclude the possibility that further improvements are possible, especially for AM1, for which the chosen repulsive term seems to fit least well.

While the results for the hydrogen-bonded complexes of the PM6-DH1 training set and the hydrogen-bonded JSCH2005 peptides (both with smaller interaction energies of −6.2 and −4.4 kcal/mol and quite good values already for the "pure" SE methods) are less impressive, the hydrogen-bonded JSCH2005 DNA base pairs set (with an average interaction energy of −19.5 kcal/mol) shows how large the gain of applying the second generation H-bonding correction can be, if H-bonding interaction energies become larger. We believe that the rather poor performance for the peptide test set stems at least partly from an unbalanced description of dispersion and hydrogen-bond interactions through the combination of the two empirical corrections, which will be addressed in our future work.

It can nevertheless be stated that the obtained quality of the PM6-DH2, AM1-DH2, OM3-DH2, and DFTB-DH2 calculations reaches the accuracy of DFT-D methods (with TPSS-D/TZVP being one of the most accurate for the noncovalent interactions) for a large part of the investigated cases, while being several orders of magnitude faster. For the S22 set (included in our fit set, but also used as fit set for DFT corrections), PM6-DH2 (MUE 0.4 kcal/mol) nearly

H-Bonding Correction for Quantum-Chemical Methods

J. Chem. Theory Comput., Vol. 6, No. 1, 2010 **351**

catches up even with very sophisticated DFT approaches, like B2-PLYP-D/TZVPP/0.5CP[47] (MUE 0.3 kcal/mol) and M06−2X/6-311+G(3df,2p)/CP[46] (MUE 0.4 kcal/mol).

5. Concluding Remarks

With the presented work, we have made an attempt to alleviate the problem of the deficient description of H bonding in semiempirical quantum-chemical methods, a problem that is of vital importance for any application of these methods in computer simulations of biomolecular systems. We have proposed a transferable H-bonding correction for semiempirical methods that was shown to improve the performance of PM6, AM1, OM3, and SCC-DFTB for several test sets of H-bonding interactions by up to an order of magnitude.

The most appealing features of the new H-bonding correction are as follows:

1. Compared to the existing core−core term modifications for the improvement of the description of hydrogen bonding, our solution is able to achieve higher accuracy through the incorporation of the geometric features of H bonding.

2. Compared to the first version of our correction scheme, the new version avoids physically unsound equation terms and parameters and is now more robust and furthermore transferable between different semiempirical methods.

3. Even with only a single parameter, the new correction scheme gives significantly better results than most published correction schemes.

4. With the final parametrization (based on three global and five method-dependent parameters), the new scheme outperforms all other published H-bonding corrections by a significant margin and yields results comparable with current DFT-D approaches for a large part of the investigated cases.

5. Several details (e.g., well-behaved parameter values within and between methods, etc.) indicate the robustness of our general idea (it should nevertheless be kept in mind that our purely additive scheme cannot correct possible artifacts of the underlying methods, for example, in the case of dissociation curves).

A remaining major drawback, and subject to our future work, is the inability of our scheme to model processes where the acceptor atom-type changes, for example, proton transfer reactions. A second important step would be the combination of the second-generation H-bonding correction with an improved dispersion correction beyond a simple parameter refit of the current approach (as now the dispersion correction has become the overall less accurate part of PM6 with empirical dispersion and H-bonding corrections). From a longer perspective, we would expect it to be fruitful to incorporate empirical DH corrections directly into the parametrization process of semiempirical methods to avoid double counting and allow for a better balance of the different interactions types.

References

(1) Jorgensen, W. L. Acc. Chem. Res. 2009, DOI: 10.1021/ar800236t.

(2) Jorgensen, W. L. *Science* **2004**, *303*, 1813.

(3) Klebe, G. *Drug Discovery Today* **2006**, *11*, 580.

(4) van der Vaar, A.; Merz, K. M., Jr. *J. Am. Chem. Soc.* **1999**, *121*, 9182.

(5) Hobza, P.; Müller-Dethlefs, K. *Non-Covalent Interactions. Theory and Experiment*: RSC Publishing: London, 2010; pp 1−220.

(6) Jurecka, P.; Sponer, J.; Cerny, J.; Hobza, P. *Phys. Chem. Chem. Phys.* **2006**, *8*, 1985.

(7) Grimme, S. *J. Comput. Chem.* **2004**, *25*, 1436.

(8) Jurecka, P.; Cerny, J.; Hobza, P.; Salahub, D. R. *J. Comput. Chem.* **2007**, *28*, 555.

(9) McNamara, J. P.; Hillier, I. H. *Phys. Chem. Chem. Phys.* **2007**, *9*, 2362.

(10) Clark, T. J. *THEOCHEM* **2000**, *530*, 1.

(11) Winget, P.; Selcuki, C.; Horn, A. H. C.; Martin, B.; Clark, T. *Theor. Chem. Acc.* **2003**, *110*, 254.

(12) Wollacott, A. M.; Merz Jr, K. M. *J. Chem. Theory Comput.* **2007**, *3*, 1609.

(13) Möhle, K.; Hofmann, H.-J.; Thiel, W. *J. Comput. Chem.* **2001**, *22*, 509.

(14) Elstner, M.; Jalkanen, K. J.; Knapp-Mohammady, M.; Frauenheim, T.; Suhai, S. *Chem. Phys.* **2001**, *263*, 203.

(15) Nikitina, E.; Sulimov, V.; Zayets, V.; Zaitseva, N. *Int. J. Quantum Chem.* **2004**, *97*, 747.

(16) Nikitina, E.; Sulimov, V.; Grigoriev, F.; Kondakova, O.; Luschekina, S. *Int. J. Quantum Chem.* **2006**, *106*, 1943.

(17) Vasilyev, V.; Bliznyuk, A. *Theor. Chem. Acc.* **2004**, *112*, 313.

(18) Dannenberg, J. J. *THEOCHEM* **1997**, *401*, 279.

(19) Csonka, G. I.; Angyan, J. G. *THEOCHEM* **1997**, *393*, 31.

(20) Villar, R.; Gil, M. J.; Garcia, J. I.; Martinez-Merino, V. *J. Comput. Chem.* **2005**, *26*, 1347.

(21) Raha, K.; Merz, K. M., Jr. *J. Med. Chem.* **2005**, *48*, 4558.

(22) Raha, K.; Peters, M. B.; Wang, B.; Yu, N.; Wollacott, A. M.; Westerhoff, L. M.; Merz, K. M., Jr. *Drug Discovery Today* **2007**, *12*, 725.

(23) Thiriot, E.; Monard, G. *THEOCHEM* **2009**, *898*, 31.

(24) Bernal-Uruchurtu, M. I.; Ruiz-Lopez, M. F. *Chem. Phys. Lett.* **2000**, *330*, 118.

(25) Monard, G.; Bernal-Uruchurtu, M. I.; Van Der Vaart, A.; Merz, K. M., Jr.; Ruiz-Lopez, M. F. *J. Phys. Chem. A* **2005**, *109*, 3425.

(26) Repasky, M. P.; Chandrasekhar, J.; Jorgensen, W. L. *J. Comput. Chem.* **2002**, *23*, 1601.

(27) Yang, Y.; Yu, H.; York, D.; Cui, Q.; Elstner, M. *J. Phys. Chem. A* **2007**, *111*, 10861.

(28) Wang, Q.; Bryce, R. A. *J. Chem. Theory Comput.* **2009**, DOI: 10.1021/ct9002674.

(29) Seabra, G. M.; Walker, R. C.; Roitberg, A. E. *J. Phys. Chem. A.* **2009**, DOI: 10.1021/jp903474v.

(30) Paton, R. S.; Goodman, J. M. *J. Chem. Inf. Model.* **2009**, *49*, 944.

(31) Rao, L.; Ke, H.; Fu, G.; Xu, X.; Yan, Y. *J. Chem. Theory Comput.* **2009**, *5*, 86.

(32) Stewart, J. J. P. *J. Mol. Mod.* **2007**, *13*, 1173.

(33) Řezáč, J.; Fanfrlik, J.; Salahub, D.; Hobza, P. *J. Chem. Theory Comput.* **2009**, *5*, 1749.

(34) Stewart, J. P. *J. Mol. Mod.* **2009**, *15*, 765.

(35) OPENMOPAC. www.openmopac.net (accessed Aug 31, 2009).

(36) Riley, K. E.; Hobza, P. *J. Phys. Chem. A* **2007**, *111*, 8257.

(37) Grafova, L.; Pitonak, M.; Hobza, P. To be published.

(38) DFTBplus. http://www.dftb-plus.info (accessed Aug 31, 2009).

(39) Tao, J.; Perdew, J. P.; Staroverov, V. N.; Scuseria, G. E. *Phys. Rev. Lett.* **2003**, *91*, 146401.

(40) Becke, A. D. *J. Chem. Phys.* **1993**, *98*, 5648.

(41) Stephens, P. J.; Devlin, F. J.; Chabalowski, C. F.; Frisch, M. J. *J. Phys. Chem.* **1994**, *98*, 11623.

(42) Ahlrichs, R.; Bär, M.; Häser, M.; Horn, H.; Kölmel, C. *Chem. Phys. Lett.* **1989**, *162*, 165.

(43) Schäfer, A.; Huber, C.; Ahlrichs, R. *J. Chem. Phys.* **1994**, *100*, 5829.

(44) Eichhorn, K.; Treutler, O.; öhm, H.; Häser, M.; Ahlrichs, R. *Chem. Phys. Lett.* **1995**, *242*, 652.

(45) Eichhorn, K.; Weigend, F.; Treutler, O.; Ahlrichs, R. *Theor. Chem. Acc.* **1997**, *97*, 119.

(46) Zhao, Y.; Truhlar, D. G. *J. Chem. Theory Comput.* **2008**, *4*, 1849.

(47) Grimme, S. *Phys. Chem. Chem. Phys.* **2007**, *9*, 3397.